3D Modelling and Inversion of Audio-Magnetotelluric (AMT) data from McArthur River, Athabasca Basin, using Unstructured Tetrahedral Grids

by

©Ekrem Bekin

A thesis submitted to the School of Graduate Studies in

partial fulfillment of the requirements for the degree of

Master of Science

Department of Earth Sciences

Memorial University of Newfoundland

October, 2021

St. John's Newfoundland & Labrador

Abstract

The main aim of this study is to do trial-and-error 3D forward modelling and inversion for the AMT data collected in the McArthur River area of the Athabasca Basin. For the forward modelling and inversion, the ideas are not new, but the tools used in this study have not been used previously for the corresponding AMT data set. In the McArthur River area, the P2 fault is a thrust fault in the basement formed within pelitic gneiss, and the mineralization of the unconformity-type uranium found in the Athabasca Basin is often related to the P2 fault - which is originally a graphitic unit. Different geophysical and geological surveys have provided information about parts of the substructure; however, none of the studies so far presented have provided a better understanding of the P2 fault of the McArthur River mine area at depth. All previous studies, including electrical and electromagnetic (EM) surveys, had pointed out the increasing need for imaging the deep parts of the P2 fault. Consequently, a natural source method, the Audio-Frequency Magnetotelluric (AMT) method, was performed in 2002 within the scope of EXTECH IV (EXploration science and TECHnology) project by other researchers to image greater depths at low costs.

In this study, a synthetic model is first created by trial and error based on previous studies. The accuracy of the model is checked by comparing the calculated apparent resistivity and phase values with the measurements. According to the results obtained from the forward modelling calculations, the accuracy of the model is satisfactory.

From a data inversion point of view, this study consists of four inversions. The first is the inversion of the synthetic data for the model constructed by the trial-and-error forward modelling. This allows for the capabilities of the inversion process to be assessed. The other three are the inversions of the real data. For the synthetic data inversion, ten frequencies were used, and the data were fit successfully. The real data inversions were performed using three different forms of the data uncertainties. In the first scenario, the variances estimated from the data processing were considered as uncertainties. In the other two real-data inversions, uncertainties of 3% and 5% were used. Results of the real-data inversion were compared to those of previous inversion studies. The results from all three real-data inversions show good consistency with those of earlier studies.

General Summary

The Audio-Frequency Magnetotelluric (AMT) method is a variant of the Magnetotelluric method that helps to image the subsurface of the Earth down to 5 km using the electrical and magnetic properties of the geological structures in the subsurface. The theory of the method follows the electromagnetic (EM) principles in physics. The source of the method is natural, and application cost and effort cheaper than some other geophysical EM prospection methods.

In geophysics, the researchers endeavour to model the subsurface on computers. The next steps are the process of determining the physical parameters, e.g., conductivities for EM methods, of this model mathematically, either using inversion, guessing or using geological knowledge. Then, there is the process of calculating the data for that model, i.e., calculating for the model the same quantities (values of electric and magnetic fields, values of apparent resistivities and phases) as are measured in a survey. If the data fit is satisfactory, it is more likely that the synthetic model is close to the real subsurface of the Earth. This way of calculation helps to understand the geological features effectively beneath the surface of the Earth. In literature, this is so-called "modelling and inversion of the geophysical data".

In the present study, the modelling and inversion of the AMT data collected in the vicinity of the McArthur River area of the Athabasca Basin are presented. The main idea of this thesis is imaging the P2 fault, which plays a key role in the unconformity-type uranium mineralization in the area.

Acknowledgments

I would like to thank The Ministry of National Education of Turkey for funding me during this study and the head of The Education Attache Office in Toronto for their support whenever I needed it.

I would first like to state that I cannot show enough gratitude to Prof. Colin G. Farquharson. I felt his support and encouragement all the time regarding all issues. He always enlightened and helped me to stay on the right track. All the time, it was easy to reach him when I needed to ask questions, even in the pandemic via online meetings. It was a great honour for me to be a member of his research group for around two years.

I would like to thank my other supervisory committee member Dr. Charles Hurich for his valuable comments and suggestions.

I would like to thank Dr. Hormoz Jahandari for sharing his code with me to accomplish this study. I also would like to thank Ph.D. candidate Mitra Kangazian for her efforts to help me regarding the issues. I always learned something new from her, and it would have been tough to finish this study without her help. I would like to thank all members of Prof. Colin Farquharson's research group for their valuable contributions.

Lastly, I would like to thank my wife, Guner Bekin, for being with me all the time and for her permanent support, especially during this period. I would also like to thank my friends Deniz Ertuncay, Rıdvan Örsvuran and Fatih Turhan for their supports. I would like to send last thanks to all members of my family.

Table of Contents

ABSTRACT II
GENERAL SUMMARY IV
ACKNOWLEDGMENTS V
TABLE OF CONTENTS VI
LIST OF TABLES VIII
LIST OF FIGURES IX
1 INTRODUCTION 1
2 GEOLOGY AND THE PREVIOUS STUDIES OF THE MCARTHUR RIVER MINE AREA 7
2.1. Introduction 7
2.2. Geological Characteristics 9
2.3. Previous Geophysical Studies 16
2.3.1. Geophysical Properties of the Rocks in the McArthur River Area 16
2.3.2. Regional-Scale Surveys 18
2.3.2.1. Airborne Radiometric Methods 18
2.3.2.2. Aeromagnetic Exploration 20
2.3.2.3. Regional Gravity Exploration 21
2.3.2.4. Airborne Electromagnetic (EM) Surveys 22
2.3.3. District-Scale Studies 25
2.3.3.1. Magnetic Studies 25
2.3.3.2. Gravity Studies 27
2.3.3.3. Seismic Studies 29
2.3.3.4. Well-Logging (Borehole) Studies 32
2.3.3.5. Joint Earth Modeling and Inversion Study 35
2.3.3.6. Electromagnetic (EM) Studies (TDEM, VLF, CSAMT) 36
2.3.3.7. Audio-Frequency Magnetotelluric (AMT) Surveys 37
2.4. Summary 48
3 THE AUDIO-FREQUENCY MAGNETOTELLURIC METHOD 49
3.1. Introduction 49
3.2. Source of Audio-Frequency Magnetotelluric (AMT) Method 49
3.3. Maxwell's Equations 52
3.4. The Constitutive Relations 55
3.5. Electromagnetic (EM) Impedance and the Impedance Tensor 58
3.6. Earth Models in Magnetotellurics 60
3.6.1. One-Dimensional Earth Models 60
3.6.2. Two-Dimensional Earth Models 61
3.6.3. Three-Dimensional Earth Models 65
3.7. Magnetic Transfer Functions 65
3.8. Apparent Resistivity and Impedance Phase 67
3.9. Skin Depth 68
3.10. Summary 69
4 FORWARD MODELLING AND INVERSION OF AMT DATA 70

4.1. Introduction 70
4.2. 3D Model Creation Software: FacetModeller 71
4.3. Generation of the Tetrahedral Meshes (Tetrahedral and Voronoï Grids) 73
4.4. The Forward Problem 77
4.5. The Inverse Problem 80
4.6. Summary 85

5 RESULTS 86

5.1. Introduction 86
5.2. Collected AMT Data and Plots 86
5.2.1. Collected AMT Data *86*
5.2.2. Plots: Apparent Resistivity and Phase (TE & TM Only) *88*
5.3. Forward Model and Results 93
5.3.1. Forward Model *93*
5.3.2. Results of Forward Modelling: Apparent Resistivity and Phase Plots (TE-TM Only) *99*
5.4. Comparison of Collected Data and the Forward Model Results 104
5.5. Inversion Model Details and Results for the Forward-Modelled Data 108
5.5.1. Introduction *108*
5.5.2. Inversion Model Details *108*
5.5.3. Inversion Results for the Synthetic Data *111*
5.6. Inversion of the Real AMT Data 118
5.6.1. Inversion Results for the Real AMT Data *119*
5.6.1.1 Inversion with Variances 120
5.6.1.2 Inversion with 3% Measurement Uncertainties 127
5.6.1.3 Inversion with 5% Uncertainties 132
5.7. Summary 138

6 DISCUSSION AND CONCLUSION 140

6.1. Discussion 140
6.2. Conclusion 148

REFERENCES 151

APPENDIX A – STATION NAMES 165

APPENDIX B – APPARENT RESISTIVITIES AND PHASES FROM MEASURED DATA AND SYNTHETIC DATA (TE-TM ONLY) 171

APPENDIX C – FIT PLOTS OF IMPEDANCES, APPARENT RESISTIVITIES AND PHASES FOR INVERSION OF THE SYNTHETIC DATA 179

APPENDIX D – FIT PLOTS OF IMPEDANCES, APPARENT RESISTIVITIES AND PHASES FOR INVERSION WITH VARIANCES 312

APPENDIX E – FIT PLOTS OF IMPEDANCES, APPARENT RESISTIVITIES AND PHASES FOR INVERSION WITH 3% UNCERTAINTIES 445

APPENDIX F – FIT PLOTS OF IMPEDANCES, APPARENT RESISTIVITIES AND PHASES FOR INVERSION WITH 5% UNCERTAINTIES 578

List of Tables

Table 5.1: List of frequencies used for the forward modelling................................ 100

Table 5.2: The twenty frequencies considered in all inversions of the real data-set. 120

Table 6.1: Summary of the previous inversion studies of the McArthur River AMT data set. 140

Table 6.2: Data misfit values for each frequencies for the inversion with variances as uncertainties, 3% uncertainties, and 5% uncertainties...................................... 143

List of Figures

Figure 1.1: a) Geological map showing the local exploration areas, including the McArthur River mine area of the Athabasca Basin (modified after Long, 2007; Card et al., 2007; Portella and Annesley, 2000; Ramaekers et al., 2007; Thomas et al., 2002). The red rectangle highlights the location of the McArthur River mine area. b) Stratigraphy of the Athabasca Basin. The red arrow shows the location of the McArthur River area. (Modified after Rainbird et al., 2007.) 3

Figure 2.1: Geological map of the Athabasca Basin (modified after Jefferson, 2006). The bold red cross on the map shows the location of the study area, the McArthur River Mine. 8

Figure 2.2: a) Locations of the western Churchill province, the Athabasca Basin, and the two major orogenic belts (modified after Jefferson et al., 2007; Thomas, 2000). b) The stratigraphic units of the Athabasca Basin (modified after Jefferson et al., 2007; Ramaekers, 1990; Ramaekers et al., 2007). MF denotes the Manitou Falls Formation; MFw is Warnes Member. c) Hydrothermal fluid flow types (modified after Jefferson et al., 2007). 10

Figure 2.3: A cross-section of the P2 Fault and local stratigraphy in the vicinity of the McArthur River Mine (modified from Cameco Report, 2018). 15

Figure 2.4: Electrical resistivities of rock types and materials in the Athabasca Basin (modified after Tuncer, 2007; Cristall and Brisbin, 2006; Irvine and Witherly, 2006). 17

Figure 2.5: The radioactivity maps of the Athabasca Basin. The solid black line represents the boundary of the Basin. The map at the top shows the total count map,

the middle panels demonstrate the eU, eTh, and K concentrations in the region, and the bottom panels show the ratios (taken from Tuncer, 2007). 19

Figure 2.6: Residual total magnetic field of the Athabasca Basin. The solid black line denotes the Athabasca Basin boundary, and the rectangular area highlighted with the dashed black line corresponds to the corridor between the Mudjatik and Wollaston domains. The black plus signs show uranium deposit locations (modified after Matthews et al., 1997; Tuncer, 2007; Darijani, 2019)................ 21

Figure 2.7: Bouguer gravity anomaly map of the Athabasca Basin (modified from Matthews et al., 1997) 22

Figure 2.8: Comparison of MEGATEM, VTEM, and ground resistivity inversion results. The first two panels show the spatial variation of the vertical magnetic field with time. The panels with the abbreviation LEI represent Layered Earth Inversions results for the respective data sets. The bottom panel is the ground resistivity depth section. (Modified from Irvine and Witherly, 2006.) 23

Figure 2.9: The 2D magnetic modelling results for the McArthur River Mine area. a) Total magnetic intensity map of the area. Lines P1 and P2 show the magnetic measurement profiles across the area; Line B-B’ corresponds to the path of the gravity and seismic, the dashed white line is the boundary between the Mudjatik and Wollaston domains, the dashed black lines indicate the fault locations and the solid black lines denote the geological contacts (the bold one indicates mineralization locations) (modified from Thomas and McHardy, 2007). b) The upper panel shows the fit between the data calculated for the 2D magnetic model and the observed data, the middle panel shows the model constraints such as

seismic reflection results, magnetic susceptibilities, and densities, and the bottom panel indicates the various geological units. 26

Figure 2.10: Gravity model created by Thomas and Wood (2007) using the seismic constraints for line B-B'(see Figure 2.9). The McArthur River area is located at point G. 28

Figure 2.11: a) Seismic lines for survey by Györfi et al. (2007) superimposed on the map of the magnetic vertical derivative. b) Geological interpretation of Line 12. c) Geological interpretation of Line 14.. 29

Figure 2.12: a) The locations of the seismic profiles in the study by Hajnal et al. (2007) superimposed on the total magnetic field map. b) The upper 3 s of the time-migrated section of line B-B'. UC: Unconformity zone, P2: the P2 Fault, BR: Bright reflector. (Modified from Hajnal et al., 2007 and Györfi et al., 2007.)..... 31

Figure 2.13: Geophysical logs from drill hole MAC-218 at McArthur River indicating total-count gamma-ray, density, velocity, and resistivity (from Mwenifumbo et al., 2007). RD: Read Formation; MFb, MFc, MFd: Bird, Collins, and Dunlop members of Manitou Falls Formation; Ovb = overburden; Chlor: chlorite; Kaol: kaolinite; RES: electrical resistivity). 34

Figure 2.14: Geophysical logs for hole RL-88 in the McArthur River area indicating total-count gamma-ray, density, velocity, and resistivity (Mwenifumbo et al., 2007). RD: Read Formation; MFb, MFc, MFd: Bird, Collins, and Dunlop members of Manitou Falls Formation; Ovb = overburden; Chlor: chlorite; Kaol: kaolinite; RES: electrical resistivity. 35

Figure 2.15: The top panel shows the VLF data, and the bottom panel shows the CSAMT result (modified after McGill et al., 1993; and Tuncer, 2007)............... 37

Figure 2.16: The tensor decomposition results for the McArthur River AMT data. a) Map of the best-fitting strike direction at each observation location. b) RMS error map; the lower RMS values indicate that the 2D assumption is valid for the area. (Modified from Tuncer et al., 2006.) 39

Figure 2.17: The 2D inversion results for the McArthur River AMT data-set by Tuncer et al. (2006). The left column shows the results of TE-TM-T_{zy} inversion; the right column shows the results of TE-TM inversion (taken from Tuncer et al., 2006). 40

Figure 2.18: The comparison of 2D and 3D inversion results as depth slices of the McArthur River AMT data. The left panel shows the depth slices of the 2D TE-TM-Tzy inversion, the middle panel shows the results of only TE-TM inversion, and the right panel shows the depth slices of the 3D inversion (modified from Tuncer et al., 2006). 42

Figure 2.19: 2D and 3D inversion results of the McArthur River AMT data-set. The left column corresponds to the 2D inversion results presented in Tuncer et al. (2006). The middle two columns correspond to the 3D inversion results of algorithms mentioned in Siripunvaraporn et al. (2005a) and Mackie et al. (2001), respectively. The right column shows the 3D inversion result calculated using the algorithm introduced by Farquharson et al. (2002). (Modified from Craven et al., 2006.) .. 43

Figure 2.20: Map, on the left-hand side, showing the AMT sounding locations (black dots, the red rectangle of the data-set considered in Craven et al. (2007), and on the right-hand side, the cross-section is the result of the 2D TE-TM data inversion (modified after Craven et al. 2007). 45

Figure 2.21: Vertical sections of the 3D inversion results for each profile (from Farquharson et al., 2009). 47

Figure 3.1: An example of a signal in the dead band for the AMT method (modified from Gracia and Jones, 2008). A) Time series with a transient caused by lightning. B) Wavelet transform to show the spectral and temporal structure of the transient. The spectrum has minimal values at around f=2000 hz, $\log_{10}(f)=3.3$ and this area corresponds to the AMT dead band at each graph. 51

Figure 3.2: Conductivities of Earth's rock types (modified after Palacky, 1988). 57

Figure 3.3: A basic 2D model example made up of two structures having different conductivities at a vertical contact. As a result of the conservation of charge at the discontinuity (vertical contact), EY is discontinuous. The x-direction is parallel to the strike in this example. The AMT or MT response decouples into two polarizations, one with the electric field aligned along strike (TE mode) and one with electric field aligned perpendicular to the strike (TM mode) (modified after Simpson and Bahr, 2005). 63

Figure 4.1: A) Left panel is an example of a 3D PLC. The pinkish side is a polygon, including a hole and the edges and vertices floating in it. The blue side is an example of an interior polygon. The second figure on the right shows non-PLCs (taken from Wi, 2015). B) a screenshot presenting the GUI of facetmodeller. The left side corresponds to the 2D horizontal depth sections, whereas the one on the right corresponds to the 3D view panel. Different colours indicate the different geological structures. 72

Figure 4.2: Tetrahedral (Delaunay cell, black) and Voronoï cells (red). The edges of the Delaunay cells meet at the center of a Voronoï cell. Moreover, the edges of the tetrahedra are orthogonal to the faces of the Voronoï cells (and vice versa). (modified after Jahandari and Farquharson, 2014; Lu, 2020.) 74

Figure 4.3: A view of an example unstructured tetrahedral mesh for a 3D model. 76

Figure 5.1: A topography map of the study area. (Topography data was downloaded from the Canada Digital Elevation Map website.) Black triangles indicate the AMT sounding locations. The yellow star shows the approximate location of the McArthur River mine. 87

Figure 5.2: Plots of apparent resistivity and phase for profile L224. The left panel corresponds to the TE mode, and the right panels correspond to the TM mode. . 89

Figure 5.3: Plots of apparent resistivity and phase for profile L254. The left panels correspond to the TE-mode, and the right panels correspond to the TM-mode. .. 90

Figure 5.4: Plots of apparent resistivity and phase for profile L276. The left panels correspond to the TE mode, and the right panels correspond to the TM mode.... 91

Figure 5.5: Plots of apparent resistivity and phase for profile L304. The left panels correspond to the TE mode, and the right panels correspond to the TM-mode. .. 92

Figure 5.6: Schematic cross-section of the study area. (Modified from Tuncer et al., 2006; Tuncer, 2007; Farquharson and Craven, 2009.) 93

Figure 5.7: Induction arrow maps of the study area (modified from Tuncer et al., 2006). a) Induction arrow map of the measured data at 100 Hz. b)The same map with red circles showing the reversals indicating the possible location of the graphitic fault (P2 Fault). 94

Figure 5.8: Different views of the forward model. a) The model with the outer shell, in which the dark blue portion corresponds to the homogeneous half-space (earth), and the lighter blue part corresponds to the air layer. b) The area of interest of the model, where refinements at the top indicate the AMT sounding locations, and the

refinement on the front side corresponds to the P2 Fault. c) Horizontal slice through the mesh and model at the earth-air interface. 96

Figure 5.9: A transparent view of the area of interest. The lighter meshes belong to the Athabasca layer and the refinements around the AMT sounding points. The darker meshes belong to structures located below this layer. 98

Figure 5.10: Plots of calculated apparent resistivity and phase for profile L224 over the model in Figures 5.8 and 5.9. The left panels correspond to the TE mode, and the right panels correspond to the TM mode. 100

Figure 5.11: Plots of calculated apparent resistivity and phase for profile L254 over the model in Figures 5.8 and 5.9. The left panels correspond to the TE mode, and the right panels correspond to the TM mode. 101

Figure 5.12: Plots of calculated apparent resistivity and phase for profile L276 over the model in Figures 5.8 and 5.9. The left panels correspond to the TE mode, and the right panels correspond to the TM mode. 102

Figure 5.13: Plots of calculated apparent resistivity and phase for profile L304 over the model in Figures 5.8 and 5.9. The left panels correspond to the TE mode, and the right panels correspond to the TM mode. 103

Figure 5.14: a) Synthetic induction arrow map at 100 Hz presented in Tuncer et al. (2006). Grey rectangles indicate the location of the top of the graphitic conductor (P2 Fault). b) Synthetic induction arrow map at 128 Hz (the closest frequency to 100 Hz) in the present study. The red dashed line shows the two segments of the P2 fault in the model considered here. 106

Figure 5.15: The mesh used for the inversion of the synthetic data. a) Outer shell of the model. The darker layer corresponds to the air, and the lighter one indicates the

second padding zone. b) Top view of the ground-surface cut of the model. The outer lighter part belongs to the second padding zone, the pinkish beige part is the first padding zone (homogeneous half-space /earth), and the inner burgundy area is the area of interest. Concentrated refinements in the area of interest indicate the AMT sounding locations. 109

Figure 5.16: The first padding region and the area of interest of the mesh shown in Figure 5.15. a) The burgundy area is the area of interest, and b) is a vertical clipped section through the part of the mesh shown in panel a...................................... 110

Figure 5.17: Convergence curves for the synthetic data inversion. The curves correspond to the data misfit, objective function and model parameter variations with respect to iterations for the given cooling parameter (0.9). The left vertical axis is for the data parameters, and the right vertical axis is for the model parameters.. 112

Figure 5.18: Data-fit curves of the impedance, in NS-EW coordinate system, data at ten frequencies for station 13 (the red dot on the left-hand side). Error bars indicate the standard deviation of the noise added to the synthetic data. The lines show the calculated data for the final inversion model. Black and red colours indicate the real and imaginary parts of the impedance data. 113

Figure 5.19: Data-fit curves in terms of apparent resistivity and phase at ten frequencies for station 13 (see Figure 5.18 for the station location). Lines indicated calculated data for the final model. The dots indicate the (noisy) synthetic data going into the inversion. Black and red colours indicate real and imaginary parts.................. 114

Figure 5.20: Left panel shows the vertical cross-sections of the synthetic model, and the right panel shows the final inversion model for the synthetic data (first 6 profiles).

Black dots show the AMT-sounding locations in both panels. The red arrows indicate the P2 Fault in the synthetic model. 116

Figure 5.21: Figure 5.20 continued (last five profiles). The left panel shows the vertical cross-sections of the synthetic model, and the right panel shows the final inversion model for the synthetic data. Black dots show the AMT-sounding locations in both panels. The red arrows indicate the P2 Fault in the synthetic model. 117

Figure 5.22: Horizontal slices from final inversion model of the synthetic data. The leftmost panel shows the field orientation where black dots show the observation points and the black rectangle shows the other four panels' boundaries. 118

Figure 5.23: Convergence curves for the real-data inversion using variances to give estimates of the data uncertainties. The cooling parameter was equal to 0.9, shown by the slope of the blue curve. The left vertical axis belongs to the data parameters, and the right vertical axis is for the model parameters. 122

Figure 5.24: Data-fit plots for the impedance data in the NS-EW coordinate system for the 20 frequencies of station 105 (the red dot in the window on the left-hand side). Error bars indicate the uncertainties assigned to the data (equal to the square roots of the variances provided with the data). Lines indicate the calculated data. Black and red colours correspond to the real and imaginary parts respectively of the impedance data. 123

Figure 5.25: Data-fit curves in terms of the apparent resistivity and phase values for the TE and TM modes (with respect to the geoelectric strike) for station 105. (See Figure 5.24 for station location.) Black dots indicate the observed data, whereas the red lines indicate the calculated data for the inversion result (the inversion using the variances to give the measurement uncertainties). 124

Figure 5.26: Vertical cross-sections of the final inversion model for the inversion of the real data-set using the variances for estimates of uncertainties. Black dots show the AMT-sounding locations. Ellipses show the appearance of the P2 Fault. 126

Figure 5.27: Convergence curves for the real data inversion with 3% uncertainties. This graph shows the data and model parameter variations with respect to iteration for the given cooling parameter (0.9). The left vertical axis belongs to the data parameters, and the right vertical axis is for the model parameters. 128

Figure 5.28: Data-fit curves of the impedance data, in the NS-EW coordinate system, for the 20 frequencies of station 70 (for the station location, see the red dot in the window on the left-hand side). The error bars indicate the uncertainties assigned to the data (3%). The lines show the calculated data. Black and red colours indicate the real and imaginary parts of the impedance data. 129

Figure 5.29: Fit curves of apparent resistivity and phase values for TE and TM modes of station 70. (See Figure 5.28 for the station location.) Black dots indicate the observed data, whereas the red line stands for the results of inversion with the variances as error floors. 130

Figure 5.30: Vertical cross-sections of the final inversion model for the inversion with 3% uncertainties. Black dots show the AMT-sounding locations. Ellipses show the response of the P2 Fault. 131

Figure 5.31: Convergence curves for the real data inversion with 5% uncertainties. The graph shows the data and model parameter variations with respect to iterations for the given cooling parameter (0.9). The left vertical axis belongs to the data parameters, and the right vertical axis is for the model parameters. 134

Figure 5.32: Data-fit curves of the impedance data – in NS-EW coordinate system –for 20 frequencies of station 70 (station location presented as the red dot on the left-hand side window) for the inversion with 5% uncertainties. Lines indicate the calculated data. Black and red colours indicate the real and imaginary parts of the impedance data. 135

Figure 5.33: Data-fit curves shown in terms of apparent resistivity and phase values for TE and TM modes of station 70 – see Figure 5.32 for the station location. Black dots indicate the observed data, whereas the red lines stand for the results of the inversion. 136

Figure 5.34: Vertical cross-sections of the final inversion model for the inversion with 5% uncertainties. Black dots show the AMT-sounding locations. Ellipses show the response of the P2 Fault... 137

Figure 6.1: Comparison of the inversion results for the McArthur River AMT data-set. a) Results from previous studies (modified from Craven et al., 2006). b) Results of the three different inversion attempts in the present study. 144

Figure 6.2: a) Horizontal slices from previous AMT inversion studies (modified from Craven et al., 2007). b) Horizontal slices from different inversions conducted in this study. 146

Figure 6.3: Comparison of the vertical cross-section of L224. a) Vertical cross-section modified from Tuncer et al. (2006). b) Resulting vertical cross-section of the inversion with the 5% uncertainties for L224. The small white dashes indicate the depth of unconformity zone and the larger white dashed line indicates the response of the P2 Fault.. 148

1 Introduction

The main idea behind geophysical exploration methods is imaging subsurface features using physical principles. Imaging of the geological structures beneath the surface can be achieved either by collecting the data at the surface directly or in the air using aircraft. The next step is analyses of the collected data in which the physical properties of the subsurface can be revealed. In general, these analyses consist of the forward modelling and the inversion of the collected data. In most geophysical exploration methods, such as seismic, gravity, magnetic, and EM methods, these analyses are used frequently.

In the present study, the Audio-Frequency Magnetotelluric (AMT) method, a particular application of the Magnetotelluric (MT) method that considers data at relatively high frequencies between 10 Hz –10,000 Hz, is used to image a mineral exploration target at depth. The source field of the technique is natural, meaning the MT method can be described as passive. In the AMT method, signals above 1 Hz are generally produced by lightning discharges in the ionosphere (Simpson and Bahr, 2005). The frequency range of the method is nearly 10 Hz –10,000 Hz, and the frequency range between 1 and 5 kHz represents the AMT dead band where signals are weak and are challenging to measure accurately by AMT sensors (Garcia and Jones, 2002; Ferguson, 2012). Theoretically, the time-varying Earth's magnetic field induces electric currents to flow in the subsurface. The strength of these currents and where they flow depends on the rocks and formations and structures in the subsurface.

The Athabasca basin, located between the northwestern part of Saskatchewan and the northeastern part of Alberta (Figure 1.1.a), is a host of unconformity-type high-grade uranium. More than one-third of the unconformity-type uranium, which has grades 3 to 100 times higher than the other types, is found in the Athabasca and Thelon Basins in Canada (Jefferson et al., 2007). The highest grades and tonnages of U can be found in the Cigar Lake and McArthur River mine areas. In Cigar Lake, considering both east and west zones, the amount of uranium is 131,400 tonnes, whereas this supply rises to 192,085 tonnes in the McArthur River mine area (Jefferson, 2006). The Athabasca Group (namely Manitou Falls Formation) - which comprises the Dunlop (MFd), Collins (MFc), Birds (MFb), and the Read Formation (formerly MFa, nowadays RD) - is located above the unconformity (Jefferson et al., 2007). Beneath the unconformity, the eastern Mudjatik and Wollaston basement domains underlie the Athabasca Group. In these domains, graphitic metapelitic gneiss plays a key role in forming weak zones through processes such as faulting (McGill et al., 1993) (see Figure 1.1.b). That is to say, the graphite is concentrated by the hydrothermal fluids that use the fault zone as a path for flow, and this is the same for the uranium concentration. As a result of this, the fault zone is more conductive than the surrounding graphitic metapelitic gneiss.

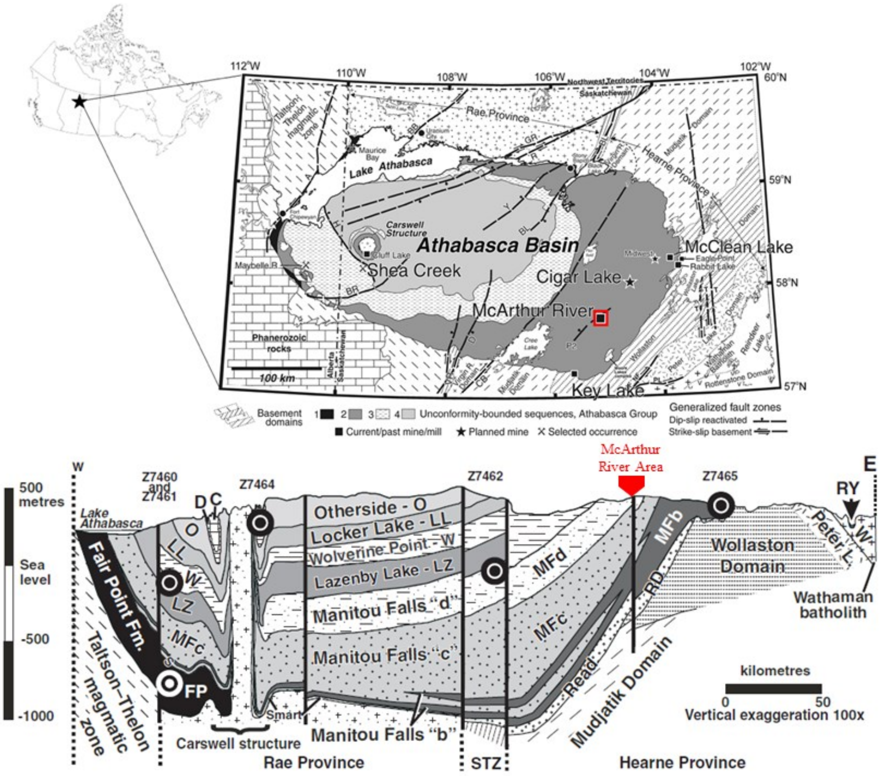

Figure 1.1: a) Geological map showing the local exploration areas, including the McArthur River mine area of the Athabasca Basin (modified after Long, 2007; Card et al., 2007; Portella and Annesley, 2000; Ramaekers et al., 2007; Thomas et al., 2002). The red rectangle highlights the location of the McArthur River mine area. b) Stratigraphy of the Athabasca Basin. The red arrow shows the location of the McArthur River area. (Modified after Rainbird et al., 2007.)

Graphitic units in the Athabasca Basin have a vital role in the exploration of uranium deposits. In particular, the footwall of the P2 Fault, which is the primary shear zone in the McArthur River mine area, consists of pelitic gneiss, including graphitic zones, which are good targets for EM exploration methods because of having low resistivity values (Jefferson, 2006; Jefferson, 2007). For the Athabasca Group (sandstone), low resistivity anomalies are associated with the clay alteration, and silicification causes high resistivity anomalies. For the graphitic zones (graphitic metapelite gneiss) in the basement, the quartz dissolution causes low resistivity. A detailed description of the geology of the study area is given in Chapter 2.

Various geophysical exploration methods and geological surveys have been carried out in the Athabasca Basin and the McArthur River mine area. These researches include both regional-scale surveys (the Athabasca Basin) that have been performed using aircraft and district-scale surveys (the McArthur River mine area in this study) that have generally been ground-based methods. Several geophysical and geological surveys have revealed information about the subsurface; on the other hand, none have presented successful results of accurately imaging the P2 fault of the McArthur River mine area at depth. Previously, several electrical and EM methods such as direct current (DC) resistivity, transient EM methods, horizontal loop EM methods (HLEM) and very low frequency (VLF) methods have been applied. Still, they are less effective for imaging targets at a depth of the P2 fault (around 500 m) compared to the AMT method. Controlled-source EM methods need larger loops to reach those kinds of depths; thus, it increases the cost and efforts (Tuncer et al., 2006). All previous studies have pointed out the increasing need for imaging the deep parts of the P2 fault. Therefore, the AMT method was applied because it uses natural sources and lower frequencies, which allows for more in-depth investigation and reduces the cost of exploration. AMT data were collected at 132 stations in 2002 as part of the EXTECH IV (EXploration science and TECHnology) Project (Jefferson et al., 2003; Tuncer et al., 2006).

Since data collection, several studies of modelling and inverting the AMT data-set have been presented (Tuncer et al., 2006; Craven et al., 2006; Farquharson and Craven, 2009). All of these have used different inversion algorithms. Tuncer et al.

(2006) carried out the inversion using a 2D approach, inverting the data for each line separately, whereas the others have used 3D inversion approaches. A brief description of these studies is presented in Chapter 2.

As for most geophysical surveys, after collecting the data, geophysical modelling is essential for AMT studies. Quantitative interpretation of the AMT method comprises two steps: 1) forward modelling and 2) inversion of the observed data. Forward modelling can be considered the process of constructing a synthetic Earth model, getting the calculated data to match the observed, then the inference that the constructed model should represent the true subsurface. In contrast, the main idea of inversion is to fit the calculated data to the observed using a process in which the model is automatically adjusted to improve the data fit. In the present study, the algorithm presented in Jahandari and Farquharson (2017) is used for the forward modelling and inversion of the AMT data-set. This algorithm uses a minimum-structure approach and unstructured tetrahedral grids for parameterizing the Earth model. Using unstructured grids is advantageous compared to structured grids because the latter typically requires more cells than the former for the same discretization level. Additionally, unstructured grids are also better at representing general features in Earth models, including dipping fault zones. Local refinement using unstructured grids is very straightforward and practical; an arbitrary area of interest or the geological target, and the observation locations, can be refined more than other parts in the model (Lelièvre et al., 2012; Jahandari and Farquharson, 2017).

The general motivation of this study is doing both trial-and-error 3D forward modelling and inversion to try to fit the McArthur River AMT data. The forward-modelling ideas applied in the present study are not new, but the tools used, such as

FacetModeller (Lelièvre et al., 2012) and unstructured tetrahedral meshes, are. This allows for more accurate representations of graphitic fault zones in the models. The inversions are also done using unstructured tetrahedral meshes. Using these tools should enable a better reference model of the P2 fault zone at McArthur River to be built.

This thesis comprises five chapters. Chapter 2 provides the geological background of the study area and summarizes the previous studies in the area. Chapter 3 describes the theory of the AMT method. In Chapter 4, the theoretical details of the forward-modelling and inversion steps are explained. As well as the theoretical basics of these steps, the software and codes used in the study are also described in this chapter. The details of the models constructed during this study, both from the forward modelling and inversion, can be found in Chapter 5. The last chapter focuses on a discussion and conclusions, in which the interpretations of the results and comparisons can be found.

2 Geology and the Previous Studies of the McArthur River Mine Area

2.1. Introduction

The Athabasca Basin starts from the northwestern part of Saskatchewan and extends widely to the northeastern part of Alberta (Figure 2.1). The geological features of the Athabasca Basin have been studied by numerous researchers and industry-university co-operative projects (e.g., EXTECH IV) over decades. It is a sedimentary, chiefly flat-lying, un-metamorphosed, but mostly altered, late Paleoproterozoic to Mesoproterozoic strata (Jefferson et al., 2006). Mineralization associated with uranium (such as pods, veins, lenses) is generally situated between Paleoproterozoic to Mesoproterozoic sandstone and Archean to Paleoproterozoic strongly metamorphosed granitoid rocks (Jefferson et al., 2006).

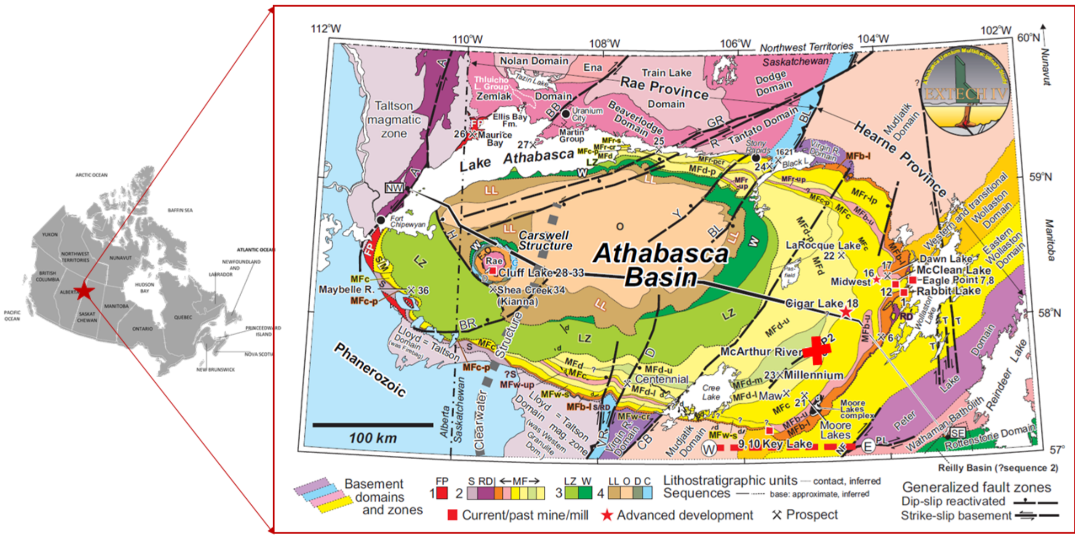

Figure 2.1: Geological map of the Athabasca Basin (modified after Jefferson, 2006). The bold red cross on the map shows the location of the study area, the McArthur River Mine.

The Athabasca basin is a major source of unconformity-type high-grade uranium. The highest grades and tonnages of uranium can be found in Cigar Lake and McArthur River mine areas. In Cigar Lake, considering both east and west zones, the amount of U is 131,400 tonnes (nowadays it is around 97,550 tonnes), whereas this amount rising to 192,085 tonnes (nowadays it is around 167,700 tonnes) in the McArthur River mine area (Jefferson, 2006, and World Nuclear Association).

The deposits, consisting of uranium (U), can be classified into two categories. In the first category, polymetallic deposits (U, Ni, Co, As, and traces of Au) typically appear within the unconformity zone, whereas in the second category, the monometallic deposits (U) occur either underneath or rarely on top of the unconformity zone. Exceptionally, the monometallic deposit directly exists in the unconformity zone in the McArthur River mine area (Ruzicka, 1996).

In the Athabasca Basin, graphitic units play a crucial role in the exploration for uranium deposits. The unconformity-type uranium mineralization is located at the intersection of the basement and the graphitic units. For instance, the footwall of the P2 fault, which is the primary shear zone in the McArthur River mine area, consists of pelitic gneiss, including graphitic zones (Jefferson 2006, 2007). The main target of this study is to delineate this graphitic fault in the McArthur River mine area. The next sub-sections of this chapter will focus mostly on the geology of the McArthur River area. The remaining sub-sections will then summarize the other geophysical surveys that have been done in the area.

2.2. Geological Characteristics

The Athabasca Basin is located in the western Churchill province between the eroded remnants of two orogenic belts. One of these belts is the Taltson magmatic zone to Thelon tectonic zone, which has an age of approximately 1.9 Ga, and the other is the 1.8 Ga Trans-Hudson Orogen. The Rae and Hearne sub-provinces of the Churchill Province were formed due to the transpression undergone by these belts during the convergence of the Slave and Superior provinces (Figure 2.2) (Jefferson et al., 2007).

a)

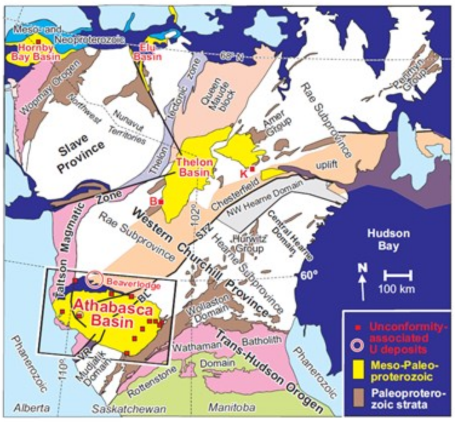

b)

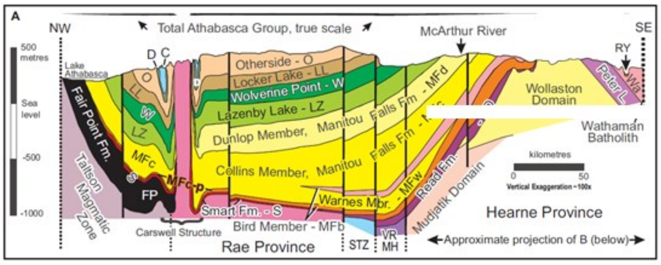

c)

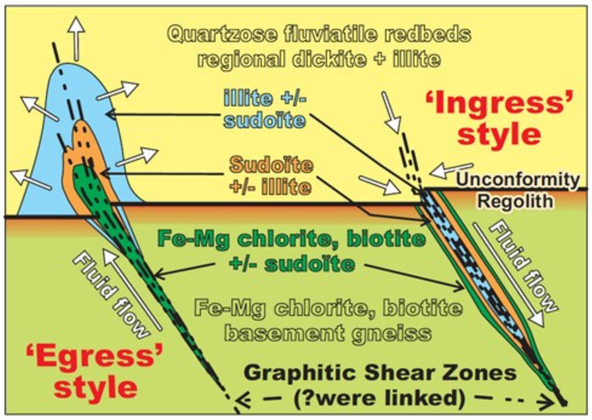

Figure 2.2: a) Locations of the western Churchill province, the Athabasca Basin, and the two major orogenic belts (modified after Jefferson et al., 2007; Thomas, 2000). b) The stratigraphic units of the Athabasca Basin (modified after Jefferson et al., 2007; Ramaekers, 1990; Ramaekers et al., 2007). MF denotes the Manitou Falls Formation; MFw is Warnes Member. c) Hydrothermal fluid flow types (modified after Jefferson et al., 2007).

The McArthur River mine area is situated at the southeastern part of the Athabasca Basin, and this location is near the boundary of the Wollaston and Mudjatik Domains. The boundary between these domains separates the strong northeastern patterns of the Wollaston Domain from the curvilinear features of the Mudjatik Domain (Marlatt et al., 1992). In the McArthur River mine area, graphitic gneisses at this boundary are where the faulting occurs and are the main sources of the uranium deposits (Marlatt et al., 1992).

In the McArthur River mine area, the stratigraphical units start from the Athabasca Group (namely Manitou Falls Formation), which comprises the Dunlop (MFd), Collins (MFc), Birds (MFb), and the Read Formation members (formerly MFa, nowadays RD) of the Manitou Falls formation, respectively (Jefferson et al., 2007). The eastern Mudjatik and Wollaston basement domains underlie the Athabasca Group in the study area. In the corresponding domains, graphitic metapelitic gneiss sections exhibit weak zones (i.e., faulting or thrusting in the area). In addition, the concentration of graphite in weak zones allows the circulation of hydrothermal fluids. The basement rocks include two types of metasedimentary rocks. These are pelite rocks, which occur in the hanging wall rocks of the basement faults, and hence the P2 Fault, and quartzite, which occurs in the footwall (McGill et al., 1993).

In the study area, the hydrothermal fluid flow is categorized into two classes in terms of flow direction. When the hydrothermal flow direction is from the basement to the sandstone units, this is called the egress type. In this fluid flow class, the generated uranium deposit is called “egress type uranium deposit”. If the hydrothermal fluid flow is from the sandstone to the basement structure, it is called the ingress type. In this class, the alteration is weak compared to the former one (see Figure 2.2.c).

- **Mudjatik and Wollaston Domains**

The eastern Mudjatik and Wollaston basement domains underlie the McArthur River mine area. Substantial amounts of quartzose, pelitic, and arkosic paragneiss can be observed across these domains. Those rocks were folded isoclinally and interleaved with Archean orthogneiss, and intruded by numerous pegmatite. In these domains, graphitic metapelitic gneiss forms weak zones, which are the foci of the deformation during folding, thrusting, and then brittle deformation (Jefferson, 2007).

- **Manitou Falls Formation (Athabasca Group)**

The Manitou Falls Formation was first described in Raemaekers (1979), and has since been categorized into four units (MFa to MFd) in Raemaekers (1990). It was defined, by Raemaekers (1979), as nearly up to 1.4 km of a trench in which quartz sandstone layers flat and cross-stratified and deposited with 1 to 20% interstitial clay and minor conglomerate supported by clasts (Long, 2007).

MFa includes a sequence of interbedded fluvial and marine units, consisting of sandstone and conglomerate and extends to a depth of up to 600 m. Following research conducted in the vicinity (e.g., in EXTECH IV, etc.), this unit was divided into two sub-sections: the original part of the unit is now identified as the Warnes Member (MFw), and the remaining lower part is named the Read Formation (RD) (see Figure 2.2b) (Long, 2007).

MFb, the Bird Member of the Manitou Falls Formation, is described as interbedded sandstone and minor conglomerate depending on the surface exposures

(Raemaekers, 1990; Long, 2007). This unit is located immediately above the MFa unit, and it is approximately 125 metres thick (Figure 2.2.b).

MFc, where the c denotes the Collins Member of the Manitou Falls Formation, is defined in Raemaekers (1990) as sandstone layers that lack conglomerate beds thicker than 2 cm and involves 1% clay interclasts (Long, 2007).

MFd is the Dunlop Member of the Manitou Falls Formation, and it is the shallowest unit (Figure 2.2.b). This unit comprises well-sorted sandstone with 1% mudstone interclasts underlain by the MFc unit (Long, 2007).

- **Alteration**

The alteration in the study area includes by silicification, with weak bleaching of the sandstone, and hydrothermal clay alteration (Jefferson et al., 2007; Marlatt et al., 1992). The lower 225 m of the sandstone has been affected by common bleaching, and beneath this depth, the sandstone possesses colours varying from pink to purple due to primarily unbleached or weakly bleached hematite. The upper level of the sandstone is silicified weakly. The intensity of this silicification rises progressively to the depth of 375 m, while it shows a drastic increase below this depth. The fine-grained dravite (having blue-green colour) occurs in the upper sandstone — the amount of dravite increases from the northeastern part to the southeastern part of the study area. Alteration of the lower sandstone is similar but mostly associated with post-mineralization. In locations of the geological disruption, hydrothermal fluids access with ease and have caused intense alteration. The hanging wall rocks of the P2 fault have been exposed to a strong hydrothermal alteration, although the footwall rocks have only been subjected to weak alteration such as paleoweathering. The alteration of feldspar and biotite to sericite, illite, and quartz is prevalent in both of these mineral types. In the lower sandstone layer, the illite and chlorite alteration is intense around the fault zones. On the other hand, the alteration signs are weak in the footwall minerals such as apatite, dravite, and chlorite (Marlatt et al., 1992).

- **P2 Fault**

In the study area, the mineralization of the unconformity-type uranium is linked with the P2 fault, which was originally a reverse thrust fault (Marlatt et al., 1992) (see Figure 2.3). The P2 thrust faults have reactivated the thrust fault planes within lower 25 m of the hanging wall basement rocks in the Athabasca Basin. Seismic studies have revealed that the geometrical interrelations (such as folds and thrusts) of P2 fault dates back to the Trans Hudson Orogeny (Jefferson et al., 2007). The P2 fault, a graphitic fault formed as a result of weak pelitic gneiss, offsets the unconformity vertically with 80 m at the northeast part of the McArthur River Area and 60 m at the southwestern part by elevating the Wollaston Domain rocks to a level beneath the lower unit of the unconformity (Figure 2.3) (Marlatt et al., 1992; Jefferson et al., 2007). The analysis of drill core has pointed that the P2 fault dips to the southeast with a dip angle that varies between 40° and 65° (Jefferson et al., 2007).

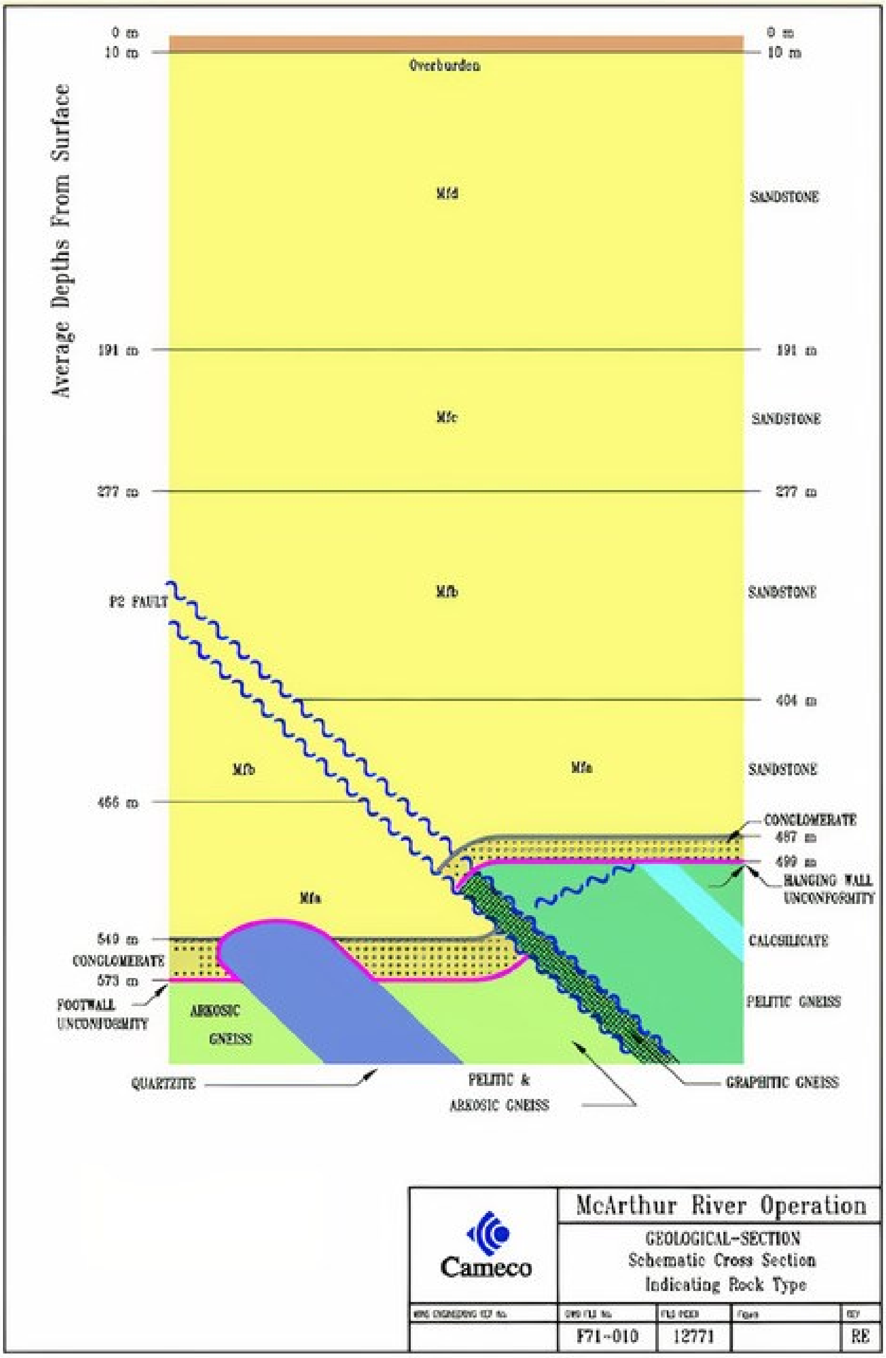

Figure 2.3: A cross-section of the P2 Fault and local stratigraphy in the vicinity of the McArthur River Mine (modified from Cameco Report, 2018).

2.3. Previous Geophysical Studies

Various geophysical research has been conducted in the Athabasca Basin and the McArthur River mine area. The results from previously published geophysical studies in the vicinity of the study area are described in this section. The studies may be classified into two categories: 1) regional-scale studies, in which the measurements were mostly performed with an aircraft, and 2) district-scale surveys that generally used ground-based methods. The combination of geophysical exploration methods — such as seismic imaging, well-logging, airborne and ground-based EM, gravity, and magnetic studies — helps researchers illuminate the subsurface structure of the study area. In this way, researchers can benefit from different complementary strengths of different methods to overcome the weaknesses of any one method.

The next sub-sections summarize the results of the regional-scale and district-scale geophysical surveys that have been done in the Athabasca Basin and in the vicinity of the McArthur River mine.

2.3.1. Geophysical Properties of the Rocks in the McArthur River Area

In the study area, the physical properties of the deposits – including mineral ore bodies, faults, alteration zones – might cause a change in geophysical responses. Figure 2.4 shows the electrical resistivities of the rock types in the Athabasca Basin. In the study area, graphitic faults are good electrical conductors, and this feature makes them a primary objective for electrical and EM methods (Tuncer, 2007). Typically, alteration involves a reduction in silica and an increase in clay concentration. This kind of alteration might cause responses as follows: high conductivity, lower density, lower magnetic susceptibilities, and low-velocity values (Tuncer, 2007). In contrast, the increasing silica content in the alteration zones results in a rise in the geophysical responses such as high resistivities, high velocities.

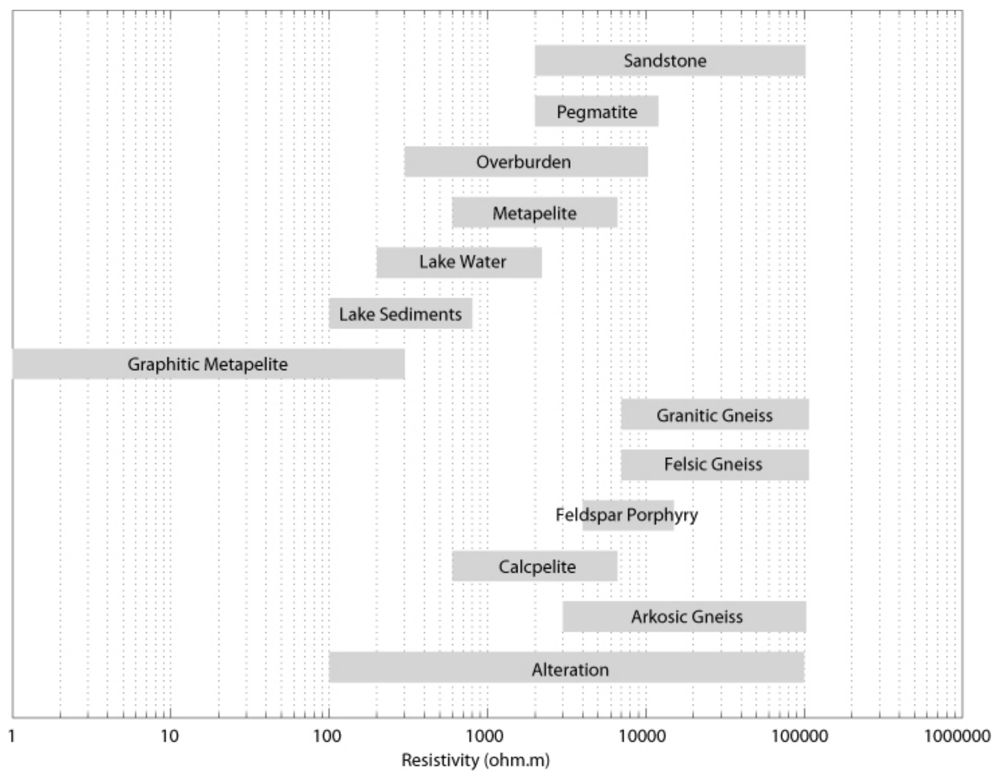

Figure 2.4: Electrical resistivities of rock types and materials in the Athabasca Basin (modified after Tuncer, 2007; Cristall and Brisbin, 2006; Irvine and Witherly, 2006).

2.3.2. Regional-Scale Surveys

2.3.2.1. Airborne Radiometric Methods

Radiometric surveys can be carried out by measuring the alpha and beta particles (a helium nucleus and electrons, respectively) (Milsom, 1989) – modern surveys involve measurements of spectral gamma ray responses. In the Athabasca Basin, the radiometric data has been collected over the entire region, where it indicates the surface composition to a depth of between 30 cm to 1 m (Campbell et al., 2002). Equivalent thorium (eTh), equivalent uranium (eU), and potassium (K) were measured in this survey. The generated radioactivity map of the Athabasca Basin is presented in Figure 2.5. As can be inferred from the map, the radioactive element concentration over the majority of the Athabasca Basin is less than in the eastern part of the basin. In the eastern part, especially around the McArthur River area, the concentration of eTh is high, and the K and eU concentrations are low. In addition to that, eTh-K ratio is very high on the western side of the basin and high in the McArthur area. The reason for the high values might be because the Read and Bird members of the Manitou Falls Formation (MFa and MFb, respectively) contain high amounts of Th. However, no significant amount of U can be observed in the Athabasca Basin. The lack of U concentration might be due to the mineralization of radioactive elements being at deeper locations (i.e., basement rocks) compared to the sandstone (Campbell et al., 2002; Tuncer, 2007). The radiometric method seems to be less effective in terms of monitoring the U-rich areas in the Athabasca Basin because it is a shallow-seeing method, and the uranium is at depth.

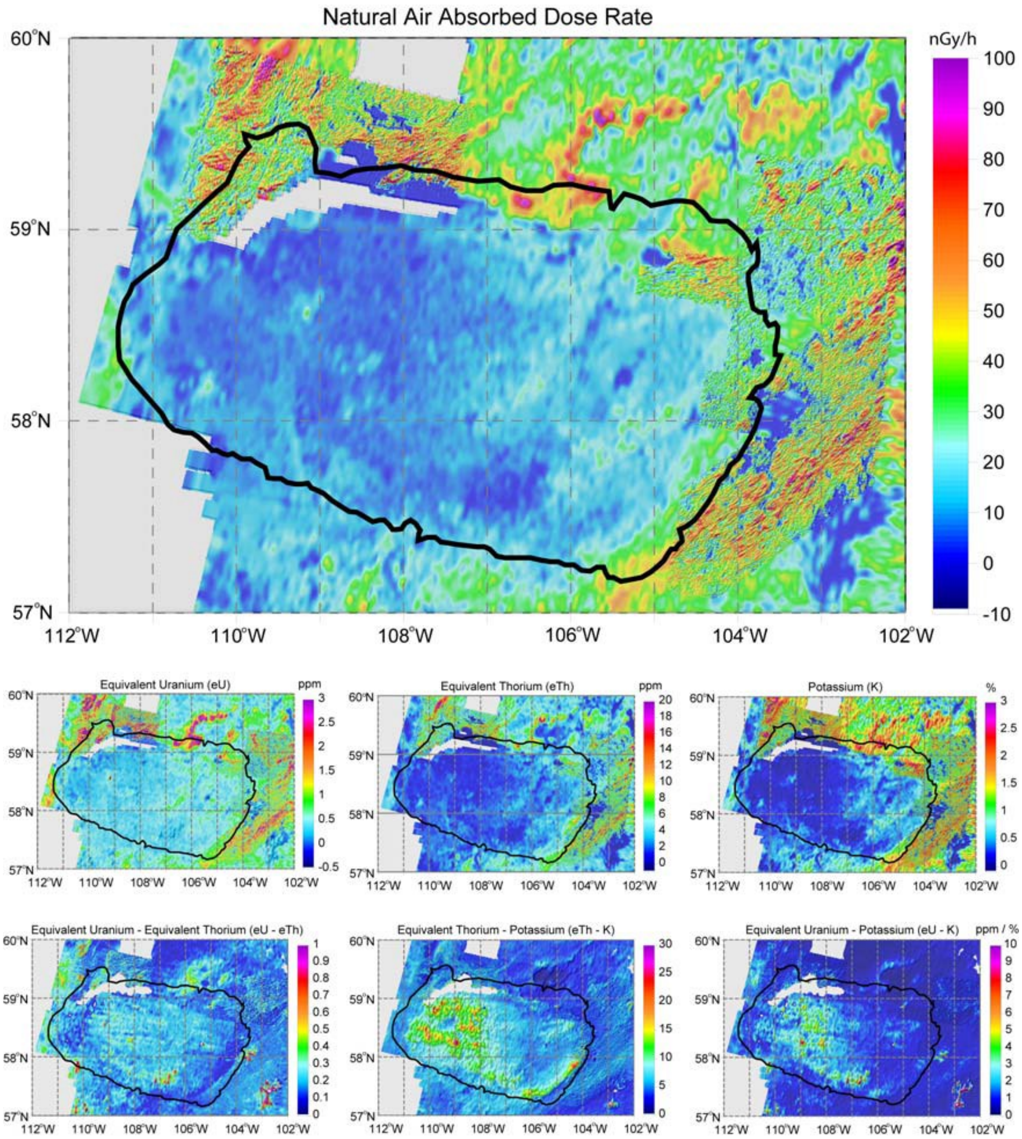

Figure 2.5: The radioactivity maps of the Athabasca Basin. The solid black line represents the boundary of the Basin. The map at the top shows the total count map, the middle panels demonstrate the eU, eTh, and K concentrations in the region, and the bottom panels show the ratios (taken from Tuncer, 2007).

2.3.2.2. Aeromagnetic Exploration

Aeromagnetic surveys are generally applied for regional reconnaissance surveys. This method has been used to detect the boundaries between basement rocks with fault and alteration systems focusing on intensity differences (Matthews et al., 1997). The residual total magnetic field map of the Athabasca Basin is presented in Figure 2.6. The corridor-shaped low-intensity zones correspond to the boundary between the Mudjatik and Wollaston basement domains. Additionally, Thomas and McHardy (2007) linked these narrow magnetic low-intensity zones with the graphitic content that includes pelitic-psammopelitic gneiss.

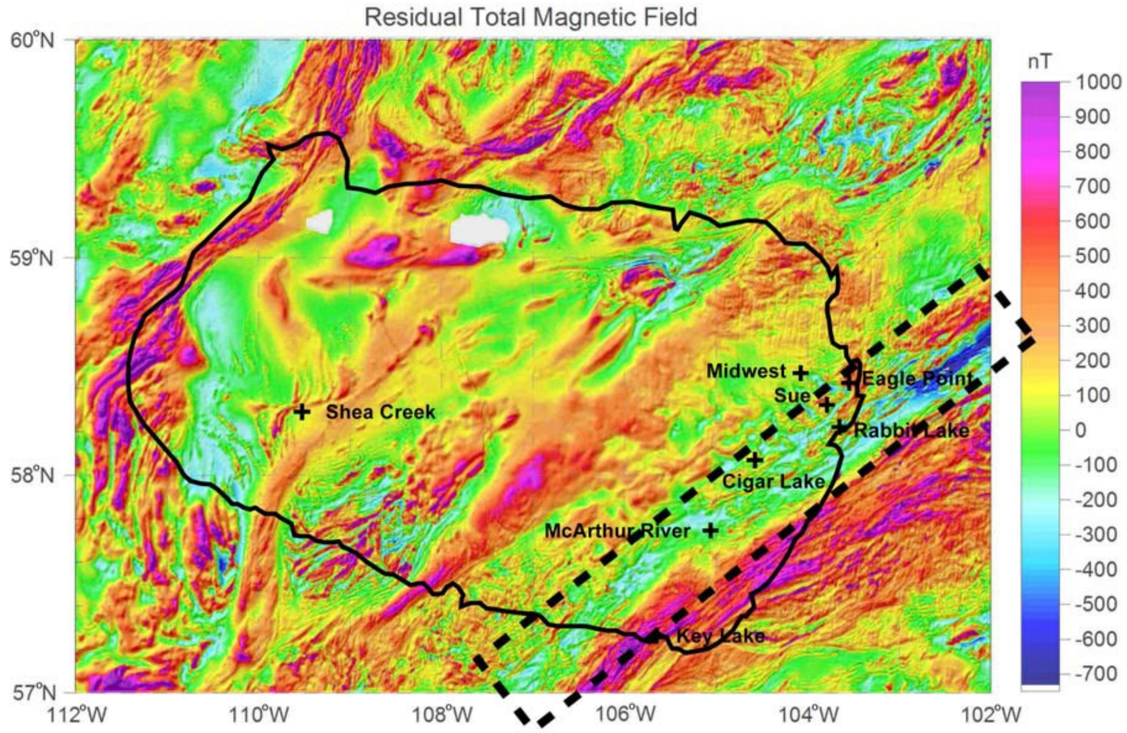

Figure 2.6: Residual total magnetic field of the Athabasca Basin. The solid black line denotes the Athabasca Basin boundary, and the rectangular area highlighted with the dashed black line corresponds to the corridor between the Mudjatik and Wollaston domains. The black plus signs show uranium deposit locations (modified after Matthews et al., 1997; Tuncer, 2007; Darijani, 2019).

2.3.2.3. Regional Gravity Exploration

The regional gravity data are predominantly affected by the basement structure of the Athabasca Basin (see Figure 2.7). Matthews et al. (1997) presented the Bouguer gravity anomaly map (Figure 2.7). In the Bouguer gravity map, low-gravity values are thought to be associated with the Archean crustal blocks, whereas high-gravity values are thought to be related to the Hudsonian mylonite zones (Matthews et al., 1997; Tuncer, 2007; Darijani 2019).

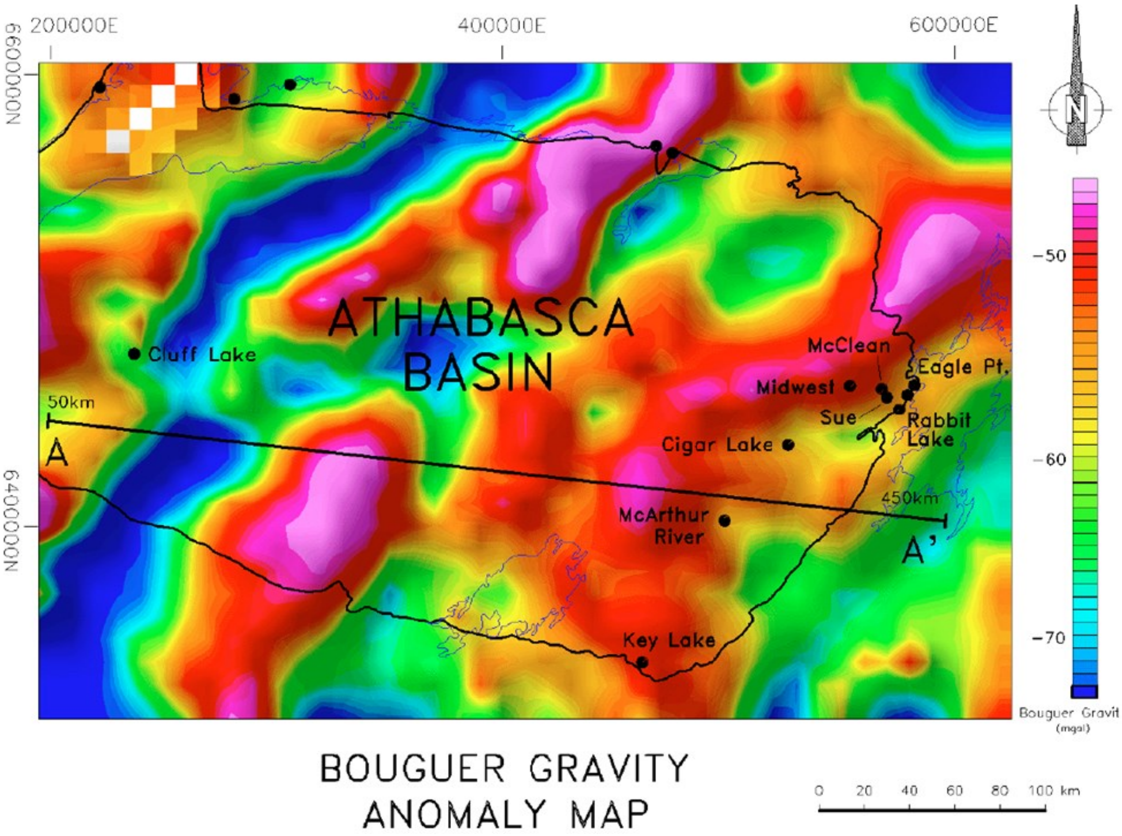

Figure 2.7: Bouguer gravity anomaly map of the Athabasca Basin (modified from Matthews et al., 1997)

2.3.2.4. Airborne Electromagnetic (EM) Surveys

As mentioned above, the unconformity-type uranium deposits are linked with the graphitic faults in the Athabasca Basin (Irvine and Witherly, 2006; Jefferson et al., 2007). Due to the high electrical conductivity of these structures, EM-based exploration methods may have the potential to help delineate these fault zones. Irvine and Witherly (2006) carried out modelling and inversion of airborne time-domain EM data-sets (i.e., MEGATEM and VTEM) and compared their results to the ground resistivity cross-sections (see Figure 2.8). MEGATEM was first introduced by Smith et al. (1998), and it is an airborne transient EM system that has a larger transmitter loop that enables an increasing value of the dipole moment of the system more than one million Am^2 (Smith and Lemieux, 2009). VTEM is a time-domain helicopter system that provides a high signal/noise ratio by providing a large primary field at the exploration depth (Witherly et al., 2004).

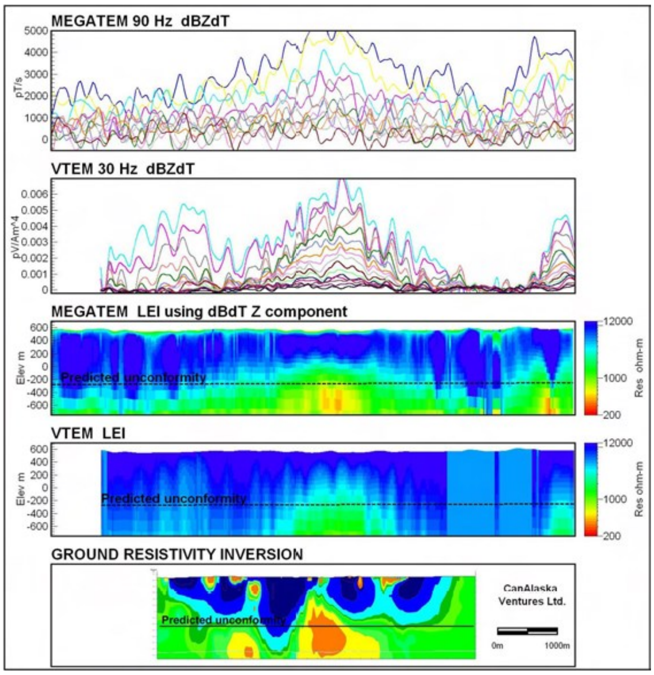

Figure 2.8: Comparison of MEGATEM, VTEM, and ground resistivity inversion results. The first two panels show the spatial variation of the vertical magnetic field with time. The panels with the abbreviation LEI represent Layered Earth Inversions results for the respective data sets. The bottom panel is the ground resistivity depth section. (Modified from Irvine and Witherly, 2006.)

Irvine and Witherly (2006) considered data from three different locations. In the first case, the depth to the unconformity was approximately 30 m, and the assumed model correlated well with the VTEM data. The response was very high at 61 m, while it decreased at a depth of 800 m. In the second case, where the depth to the unconformity is around 650 m, data from both MEGATEM and VTEM methods were inverted, and the results have been compared to the ground resistivity data cross-section. The strong response of the conductor was observed in all results, although the response of the conductor was not as wide in the VTEM layered earth inversion and the ground resistivity cross-sections. On the other hand, the MEGATEM layered earth inversions contain some conductive bodies near the surface, which may correspond to the same features as the near-surface conductive structures seen in the ground resistivity section. A relatively small conductive response was observed near the strong response in the VTEM layered inversion result, but there was no indication of this structure in both the MEGATEM and ground resistivity results.

In the third case that Irvine and Witherly (2006) considered, the depth to the unconformity was approximately 800 m. MEGATEM, VTEM, and ground resistivity methods were all considered, as in the second case. The comparative results are presented in Figure 2.8. In the panels of Figure 2.8, the conductor thought to be a graphitic fault in the basement were broadened. Moreover, differences in the conductivity responses of MEGATEM, VTEM and the ground resistivity inversion results can be observed. These discrepancies indicate a strong need for another EM exploration method to delineate the conductor without having monitoring problems with the layer thickness above it. These studies showed that both the MEGATEM and

VTEM methods are struggling to see to the depths of the graphitic fault zones in the parts of the basin where the unconformity is down at multiple hundreds of metres depth.

2.3.3. District-Scale Studies

2.3.3.1. Magnetic Studies

Thomas and Wood (2007) proposed a 2D magnetic susceptibility model for the McArthur River Mine area (see Figure 2.9). Thomas and Wood (2007) included seismic reflection, drill-hole densities, and magnetic susceptibilities for modelling the subsurface structures in the area along line B-B’.

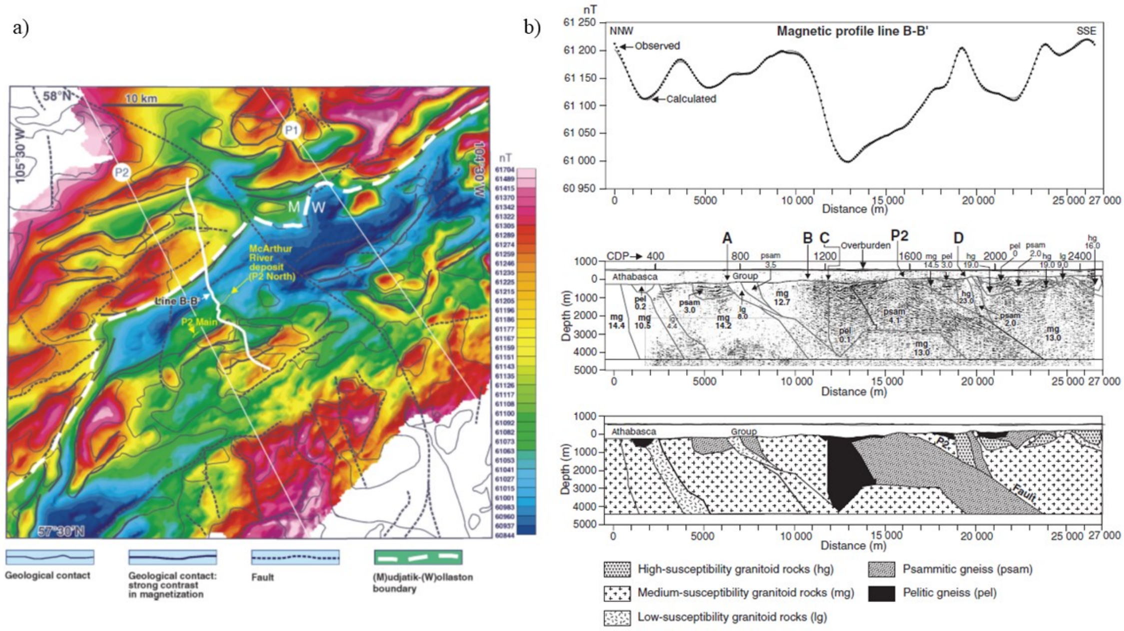

Figure 2.9: The 2D magnetic modelling results for the McArthur River Mine area. a) Total magnetic intensity map of the area. Lines P1 and P2 show the magnetic measurement profiles across the area; Line B-B' corresponds to the path of the gravity and seismic, the dashed white line is the boundary between the Mudjatik and Wollaston domains, the dashed black lines indicate the fault locations and the solid black lines denote the geological contacts (the bold one indicates mineralization locations) (modified from Thomas and McHardy, 2007). b) The upper panel shows the fit between the data calculated for the 2D magnetic model and the observed data, the middle panel shows the model constraints such as seismic reflection results, magnetic susceptibilities, and densities, and the bottom panel indicates the various geological units.

In the modelling by Thomas and Wood (2007), the overburden layer and the Athabasca Group were assumed to be non-magnetic. In the middle panel of Figure 2.9.b, the northern side of point A is dominated by the granitoid rocks having susceptibility values that are interpreted to be moderate (i.e., 10.5-14.5×10^{-3} SI). A steeply dipping structure cuts these rocks, and a graphitic unit having weak susceptibility was put on top of these units to explain the general downward (to the north) trend of the measured total magnetic intensity (TMI). On the southern side of point A, a psammitic gneiss or possibly a granitoid unit having weak magnetic susceptibility was modelled. A dramatic decrease in the TMI between point B and the P2 Fault was linked to the structure having a synformal pattern. A southward dipping strong magnetic psammitic gneiss body to the south of a weakly magnetic pelitic gneiss block was incorporated in the model between the mentioned locations to fit the data. According to the results, the boundary near point C might be a strike-slip fault that originated from a flower structure. Strong magnetic granitoid rock units explain the increase in the TMI above the P2 Fault and near point D. The low response in TMI near point D can be explained by the psammitic gneiss. Here, the P2 Fault plays a vital role as the boundaries of these units are moved upward (i.e., splaying off upthrust, Thomas and Wood, 2007).

2.3.3.2. Gravity Studies

In another study, Thomas and Wood (2007) used the seismic constraints to construct a density model along the same line as the magnetic modelling (Figure 2.9). In the cross-section shown in Figure 2.10, the McArthur River area is denoted with point G. The proposed model reveals that the highly silicified McArthur River area corresponds to a gravity low of 0.4 mGal; the low density is more likely the consequence of the stratigraphic variation (or alteration) rather than variation in the overburden thickness.

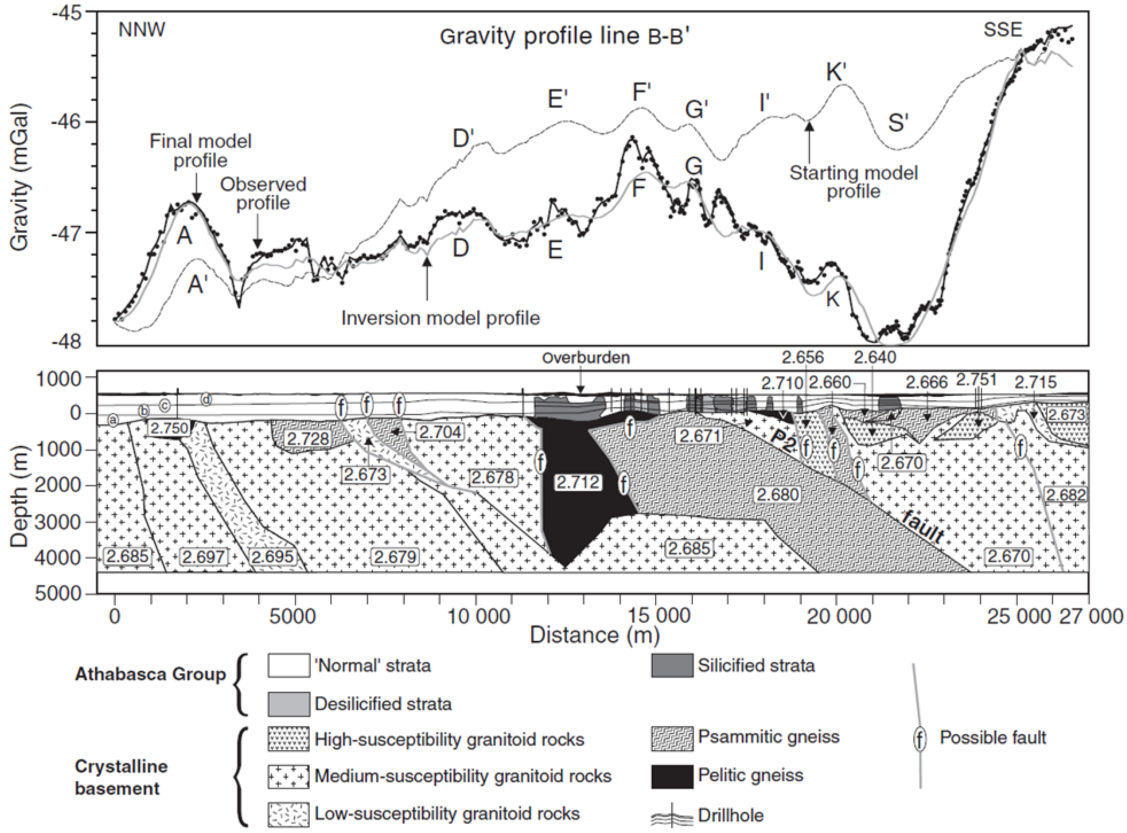

Figure 2.10: Gravity model created by Thomas and Wood (2007) using the seismic constraints for line B-B'(see Figure 2.9). The McArthur River area is located at point G.

Darijani (2019) carried out 3D modelling and inversion of the gravity data in the McArthur River area. Numerous models were created to investigate the contributions of the various geological structures to the gravity data. The results showed that the difference in the densities of the alteration zone and Athabasca Group plays a crucial role in detecting the signature of the alteration zone in the Bouguer anomaly data.

Darijani (2019) also found that the different basement units had an influence on the observed Bouguer anomaly data.

2.3.3.3. Seismic Studies

Györfi et al. (2007) targeted the P2 zone in detail with a high-resolution survey. The seismic data unveiled a detailed 3D picture of the P2 Fault zone and new structures around the zone, in addition to the internal details of the basement rocks. The survey was conducted along two survey lines in the McArthur River area (Figure 2.11).

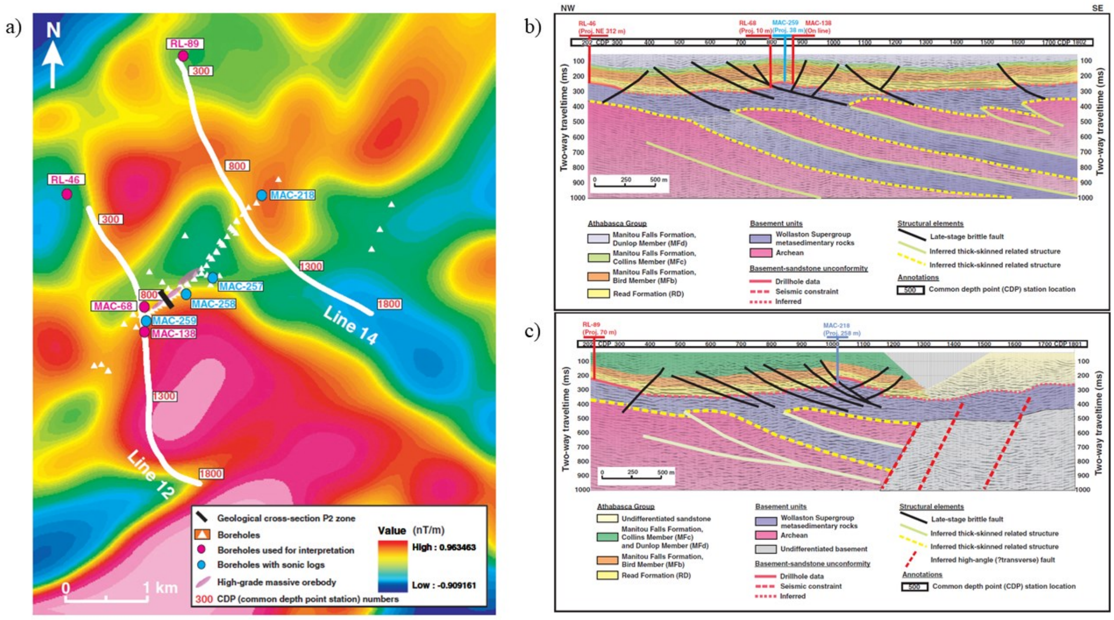

Figure 2.11: a) Seismic lines for survey by Györfi et al. (2007) superimposed on the map of the magnetic vertical derivative. b) Geological interpretation of Line 12. c) Geological interpretation of Line 14.

According to Györfi et al. (2007), the seismic signatures of the Athabasca Group could not be distinguished in Line 12 (Figure 2.11.b). In other words, the different Manitou Falls Formation layers (MFa or RD, MFb, MFc, MFd) could not be observed within the seismic data. It is reported in Györfi et al. (2007) that a 50 ms thick sandstone layer has been observed, although it is hard to convert this time to a distance without drill hole data on seismic studies. The southeast dipping basement reflectivity was observed in the center and at the southern parts of the profile. The seismic cross-section survey has revealed that the vertical offset of the basement interpreted at a 20 ms range in two-way travel time in the seismic section which corresponds to the 45 m compared to the drill hole information (Györfi et al., 2007).

The interpretation of Line 14 (Figure 2.11.c) demonstrates that the nature of the reflectivity is more complicated than for Line 12. However, a rotated sandstone bed has been interpreted at the P2 fault. In Line 12 and 14 the responses are different from each other in terms of the structures. Furthermore, the basement offset is about 75 m at the rotated sandstone bed.

For both lines, the study shows that it is hard to interpret the details of the subsurface without drill-hole data, even if the geological features or history is known. The paleoweathered structure (the ancient regolith) varies laterally along the profiles, and its occurrence causes problems in the seismic mapping (Györfi et al., 2007).

Seismic reflection results are also presented in Hajnal et al. (2007). The migrated seismic reflection sections indicate that the P2 Fault has a thickness of approximately 2 km, and it comes up to the unconformity. A bright reflector is observed at around 2 ms beneath the P2 Fault zone on the two-way travel-time section (Figure 2.12.b; Hajnal et al., 2007). Comparing the results of Hajnal et al. (2007) and Györfi et al. (2007), the sections presented in Figures 2.11.c and 2.12.b both indicate rotated sandstone beds in the vicinity of the P2 Fault.

a)

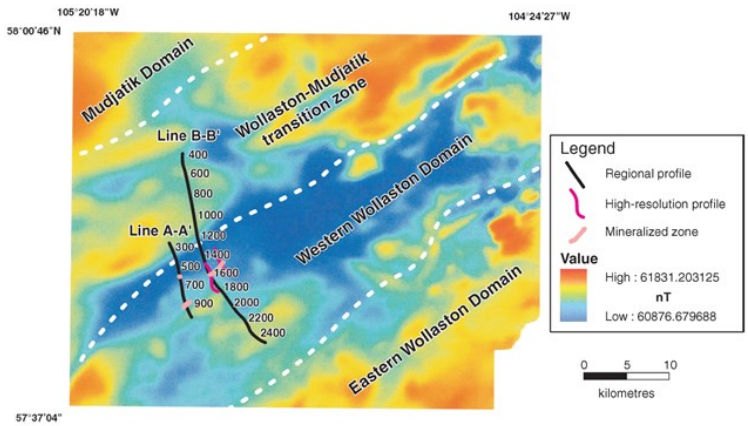

b)

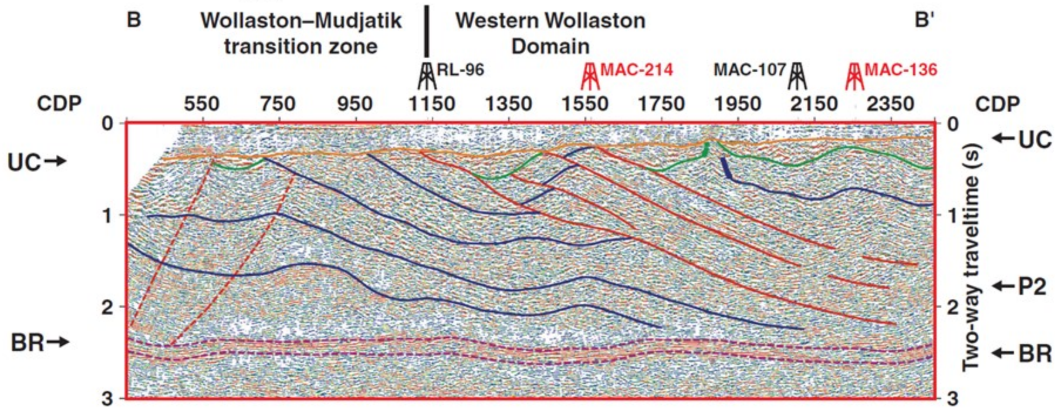

Figure 2.12: a) The locations of the seismic profiles in the study by Hajnal et al. (2007) superimposed on the total magnetic field map. b) The upper 3 s of the time-migrated section of line B-B’. UC: Unconformity zone, P2: the P2 Fault, BR: Bright reflector. (Modified from Hajnal et al., 2007 and Györfi et al., 2007.)

The seismic survey conducted by White et al. (2007) showed that the P2 Fault had been located successfully, and the unconformity zone had been imaged well. However, it is not certain that their 3D seismic data indicate the precise location of the orebodies in the vicinity of the McArthur River area. White et al. (2007) also could not define the stratigraphy and recommended further geophysical logging and vertical seismic profiling (VSP) surveys to obtain the response of the ore zone in addition to defining the stratigraphy. In addition to these, White et al. (2007) suggested a porosity survey to check the silicification degree and believed that a true 3D seismic study instead of a limited one would be beneficial to define the stratigraphy and delineate the orebody.

Shi et al. (2014) proposed a 2D synthetic model with 2500 m in width and 1500 m in depth, considering the Athabasca sandstones in two sub-units. These units in the model are a layer with a gradually increasing velocity starting from top to a depth of 350 m, and the RD (MFa) formation goes down to approximately 650 m – the first 50 m of this layer is a thin sedimentary sequence. The P-wave velocity of the first layer varies between 4500 and 4800 m/s, whereas the RD formation has a P-wave velocity of approximately 5300 m/s. The basement has a P-wave velocity value of approximately 5800 m/s. Along the unconformity zone, the velocity contrast is low, having a value of 500 m/s. The mineralization zone and the fault were considered to have different S-wave velocities from the other surrounding rocks.

2.3.3.4. Well-Logging (Borehole) Studies

A comparative geophysical multiparameter downhole study was carried out in the vicinity of the McArthur River area by Mwenifumbo et al. (2007). The previous radiometry results have already been discussed in sub-section 2.3.2.1. In this subsection, only variation of the geophysical parameters with depth gathered from MAC-218 and

RL-88 are described in this sub-section even though the study also consisted of gamma-ray (radiometry) results.

The data from borehole MAC-218 indicates that the hydrothermal quartz dissolution or hydrothermal silicification is less intense in the Collins member of the Manitou Falls Formation, thus causing a low electrical resistivity. In contrast, there is no correlated effect observed in gamma, velocity, and density logs. In contrast, the Manitou Falls Formation members that involve dickite (Lower Birds member and Read Formation) show a dramatic increase in electrical resistivity. In this case, the higher percentage of dickite causes increases in the velocity and density logs, although not as dramatic as in the electrical resistivity. A smooth decrease in the velocity and density logs after 400 m can be considered a result of increasing porosity (Figure 2.13; Mwenifumbo et al., 2007). It seems that the formations that comprise chlorite-kaolinite-dravite have different geophysical parameters compared to others.

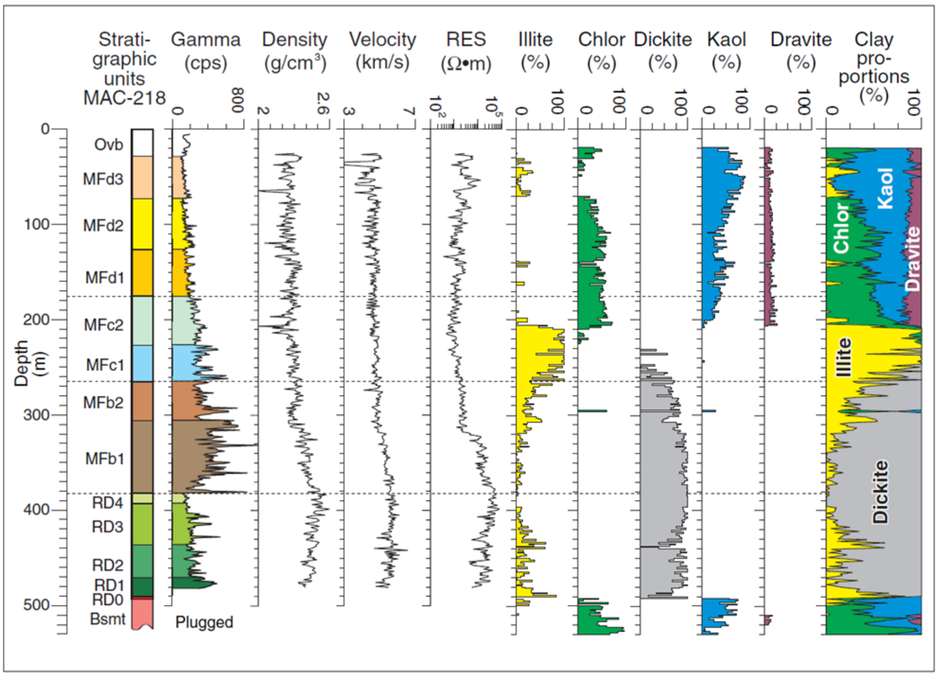

Figure 2.13: Geophysical logs from drill hole MAC-218 at McArthur River indicating total-count gamma-ray, density, velocity, and resistivity (from Mwenifumbo et al., 2007). RD: Read Formation; MFb, MFc, MFd: Bird, Collins, and Dunlop members of Manitou Falls Formation; Ovb = overburden; Chlor: chlorite; Kaol: kaolinite; RES: electrical resistivity).

The slight decrease with depth in the resistivity, seismic p-wave velocity, and density logs of hole RL-88 may be due to the porosity after desilicification between the depths of approximately 190 and 300 m (Figure 2.14). The depth ranges where the electrical resistivity, p-wave velocity, and density logs show increases correspond to the silicified zones (Mwenifumbo et al., 2007).

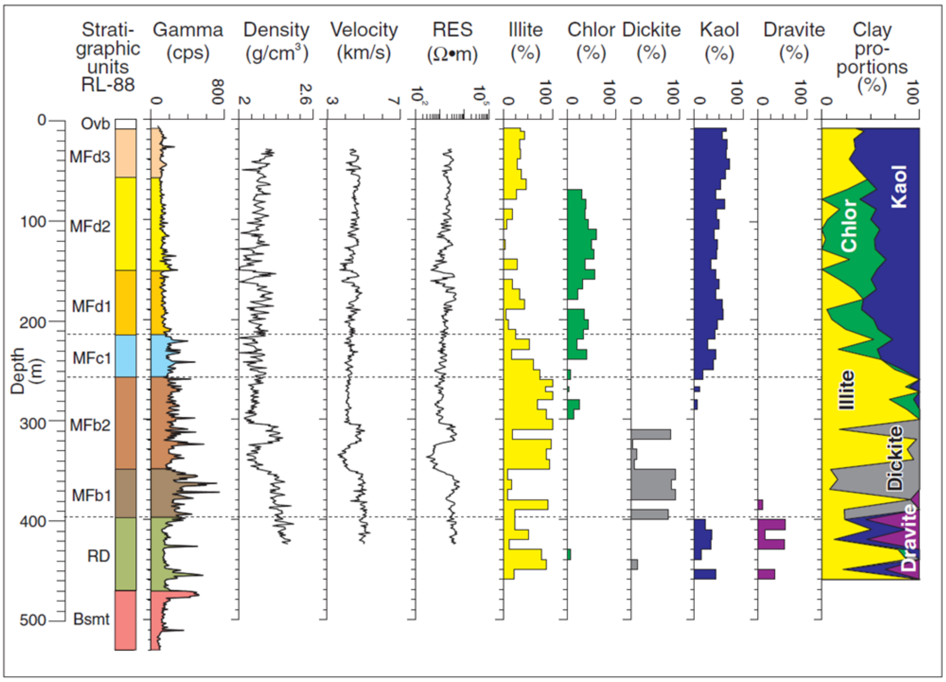

Figure 2.14: Geophysical logs for hole RL-88 in the McArthur River area indicating total-count gamma-ray, density, velocity, and resistivity (Mwenifumbo et al., 2007). RD: Read Formation; MFb, MFc, MFd: Bird, Collins, and Dunlop members of Manitou Falls Formation; Ovb = overburden; Chlor: chlorite; Kaol: kaolinite; RES: electrical resistivity.

2.3.3.5. Joint Earth Modeling and Inversion Study

Darijani et al. (2021) performed a 3D gravity and magnetic data joint inversion. The independent 3D inversions of the magnetic and gravity data were also performed in the study. Different attempts were applied in the study to get close fits in the inversion process, such as using fuzzy c-mean clustering. Although the independent inversions have not provided satisfactory results, the 3D constrained joint inversion with the clustering method enabled better results. That is to say, the locations of the overburden layer, P2 Fault and the unconformity zone are clearly visible in the results of the constrained inversion.

2.3.3.6. Electromagnetic (EM) Studies (TDEM, VLF, CSAMT)

The graphitic conductors, such as the P2 Fault, can be detected using EM methods. Several ground-based EM methods have been carried out to locate and delineate the P2 Fault in the McArthur River area. A time-domain EM method, DEEPEM, was used in 1984, with results revealing that the P2 Fault extends more than 13 km along the strike direction. In 1988, a Geonics EM37, a time-domain EM (TDEM) survey, was carried out after the discovery of the McArthur River area. Some 1500 km of fixed-loop TDEM surveys were conducted between 1980 and 1992. All of these surveys indicated a strong conductor response at a depth of 500 m (Matthews et al., 1997; Tuncer, 2007). Also, the University of Toronto EM system (UTEM), a moving loop system, has indicated a deep and dominant conductor response around the P2 Fault. Data processing and modelling of the UTEM data have suggested that the structure is located at a depth of around 400 m from the top having a conductivity of 30 S/m and dips with an angle of 75° to the east (Matthews et al., 1997; Tuncer, 2007). As well as the TDEM surveys, a VLF survey was performed in the area. However, because of the frequencies of the method, the data could not image to the depths of the P2 conductor. A Controlled Sourced Audio-Frequency Magnetotelluric (CSAMT) survey was also carried out in the study area. Theoretically, this method is very close to the Audio-Frequency Magnetotelluric (AMT) method, but the source field of the former one is not natural, whereas the source field of the latter is natural. The results provided by the CSAMT survey showed that a resistive pattern occurred above the P2 conductor, which has been interpreted as originating from silicification (Figure 2.15). On the other hand, the result did not show a basement conductor even at a frequency of 16 Hz (Tuncer, 2007).

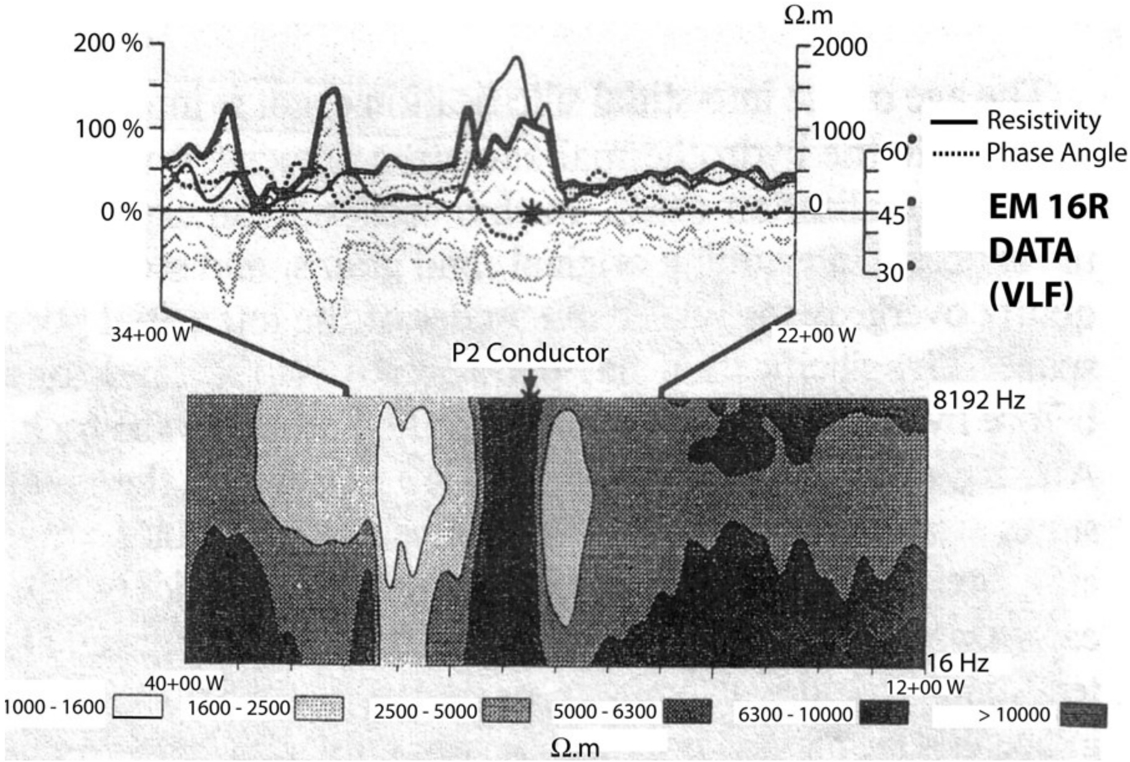

Figure 2.15: The top panel shows the VLF data, and the bottom panel shows the CSAMT result (modified after McGill et al., 1993; and Tuncer, 2007).

2.3.3.7. Audio-Frequency Magnetotelluric (AMT) Surveys

An Audio-Frequency Magnetotelluric (AMT) survey was carried out in the vicinity of the McArthur River mine within the scope of the EXTECH-IV (Exploration science and TECHnology) initiative. The AMT data were collected at 132 stations in 2002. The fundamental aim of Tuncer et al. (2006) was to determine the subsurface structure, which has not been resolved with other studies. The work published by Tuncer et al. (2006) hoped to image deeper parts of the survey area (from the surface to more than 1 km) and the deeper parts of the P2 Fault.

In Tuncer et al. (2006), 2D modelling of the area was preferred given the predominant strike of the area corresponding to the P2 Fault. Geoelectric strike analysis of the data was performed to determine the validity of the 2D assumption and the direction of the geoelectric strike. The strike determination approach of McNeice and Jones (2001) was used. The frequency range between 1000 and 1 Hz of the AMT data-set was analyzed, and the results show that the area is mostly 2D, having a geoelectric strike of N45°E (Figure 2.16). Having determined the geoelectric strike, all data were then transformed into a new coordinate system, for which the new x-axis points N45°E.

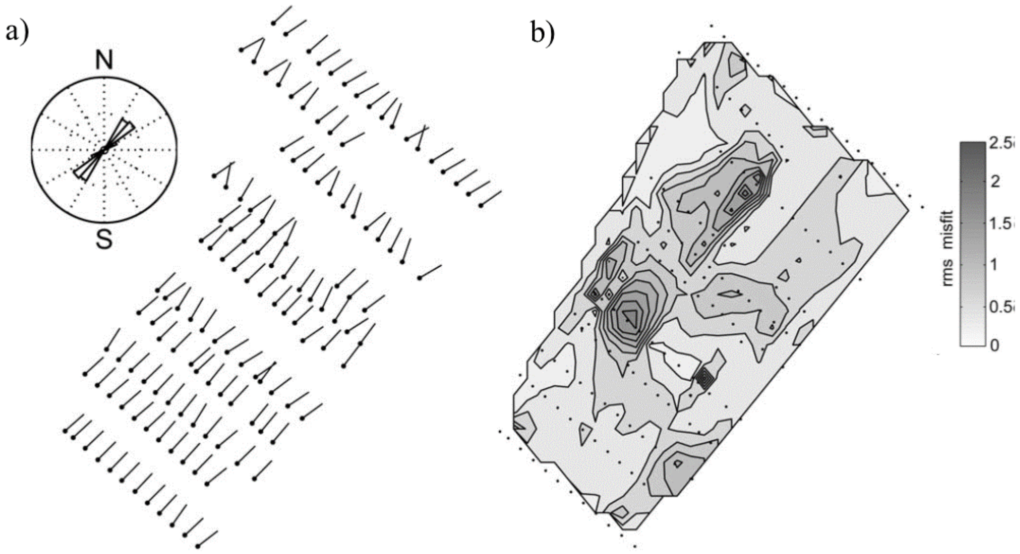

Figure 2.16: The tensor decomposition results for the McArthur River AMT data. a) Map of the best-fitting strike direction at each observation location. b) RMS error map; the lower RMS values indicate that the 2D assumption is valid for the area. (Modified from Tuncer et al., 2006.)

For the inversion of the AMT data, Tuncer et al. (2006) used the 2D inversion algorithm of Rodi and Mackie (2001), which uses the non-linear conjugate-gradients method. The electrical resistivity cross-sections for every profile are shown in Figure 2.17. These results consist of two different inversions, the left panel of Figure 2.17 corresponds to the results of TE-TM-T_{zy} inversion, and the right panel the results of TE-TM inversions.

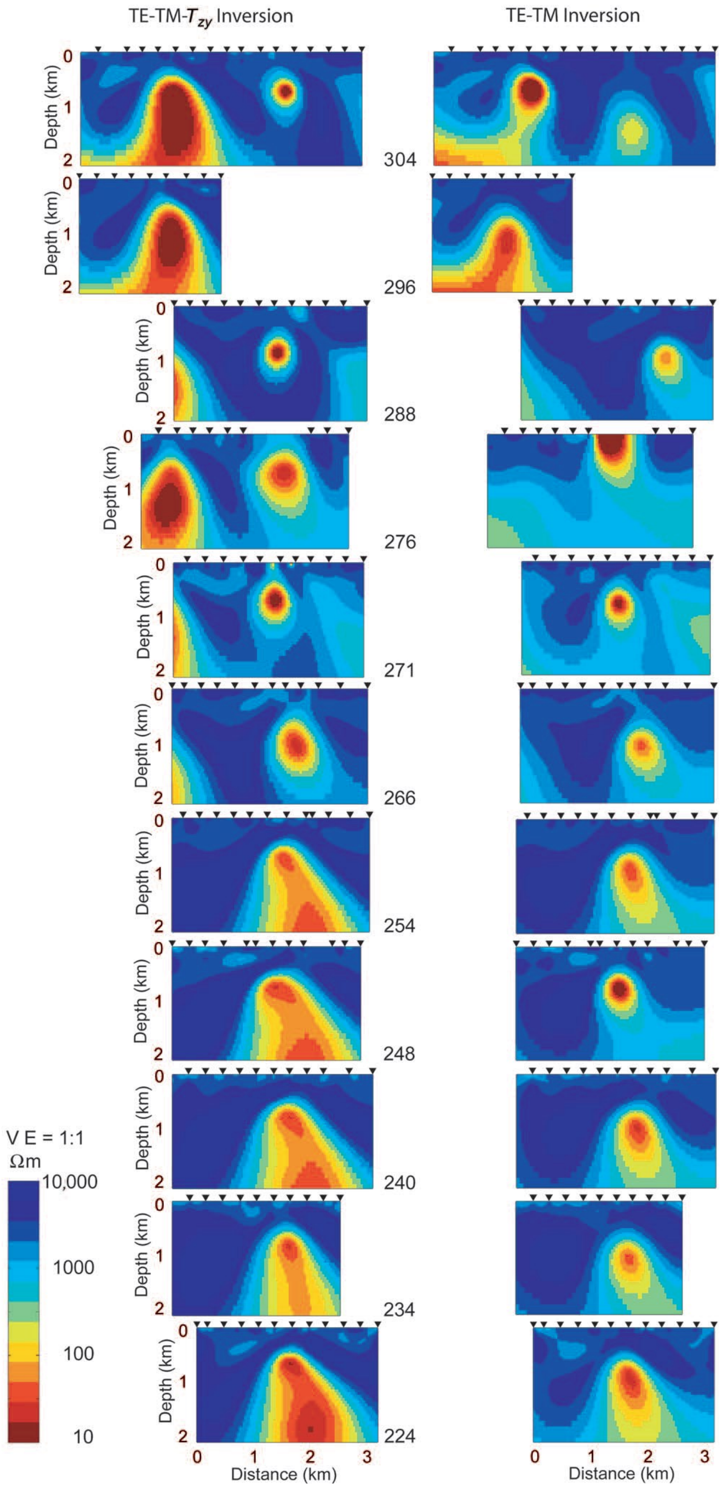

Figure 2.17: The 2D inversion results for the McArthur River AMT data-set by Tuncer et al. (2006). The left column shows the results of TE-TM-T_{zy} inversion; the right column shows the results of TE-TM inversion (taken from Tuncer et al., 2006).

According to interpretations in Tuncer et al. (2006) the RMS values are higher around the mine area (line 276) due to the gap between stations. The higher RMS values were also linked with cultural noise at the mine site, even though its effect had not been observed in the time-series data. According to their interpretation, the resulting misfits of the TE-TM-Tzy inversions are better for lines 224-254, whereas the TE-TM inversions gave reliable results for the other profiles. In Figure 2.17, the inversion results show that a strong conductor effect is observed in the northwestern parts of the northern profiles (from lines 266 to 304), whereas there is no indication of this conductor in the southern profiles (lines 224-254). This strong conductor is thought to be an effect of another graphitic fault in the area. It can be inferred from lines 224-254 that the P2 Fault dips to the southeast. Tuncer et al. (2006) point out the presence of a resistive halo above the conductor in the inversion results, emphasizing that it could be a regularization artifact produced by inversion. Tuncer et al. (2006) also compare the results of a 3D inversion with a 2D inversion. The 3D inversion was performed using the algorithm presented by Siripunvaraporn et al. (2005a). For this inversion, 16 frequencies at 131 sites were used (Tuncer et al., 2006). The depth slices of both 2D and 3D inversions (Figure 2.18) show similarities, such as the resistive halo that surrounds the conductor. The resistivity patterns have been interpreted as being similar-looking at depths below 500 m.

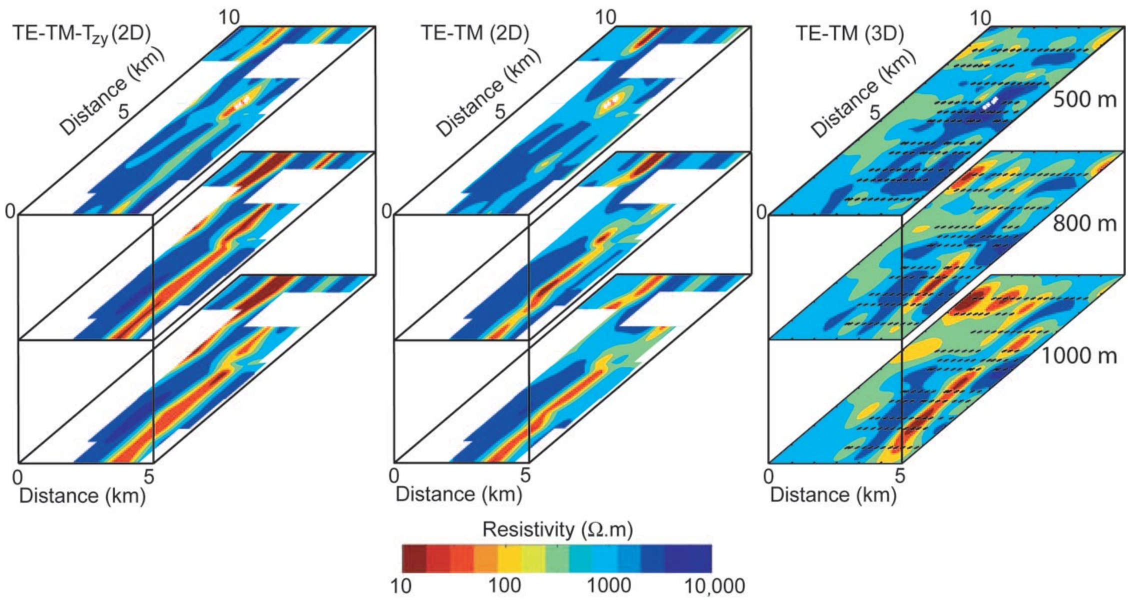

Figure 2.18: The comparison of 2D and 3D inversion results as depth slices of the McArthur River AMT data. The left panel shows the depth slices of the 2D TE-TM-Tzy inversion, the middle panel shows the results of only TE-TM inversion, and the right panel shows the depth slices of the 3D inversion (modified from Tuncer et al., 2006).

Craven et al. (2006) present a comparative study that considers multiple results obtained by different inversion algorithms for the same AMT data-set. In Figure 2.19, the cross-sections of the inversion results for specific profiles are shown. The left column corresponds to the results mentioned above (in Figure 2.18). The next column shows the results calculated using the algorithm of Siripunvaraporn (2005a). The last two columns on the right side are the results acquired by using the algorithms mentioned in Mackie et al. (2001) and Farquharson et al. (2002), respectively. All of the results, except those presented by Tuncer et al. (2006), are 3D. Although all results coincide roughly with each other (i.e., the dipping nature of the graphitic conductor, a second conductor on the northern profiles, i.e., lines 276 & 304), these results do not support each other in detail. For example, significant differences can be observed for line 224 in the cross-sections of the Siripunvaraporn inversion compared to others. Moreover, a similar discrepancy can also be viewed for line 254 in the 2D Tuncer et al. results and the Mackie et al. results compared to the other two results in terms of the shape of the graphitic conductor.

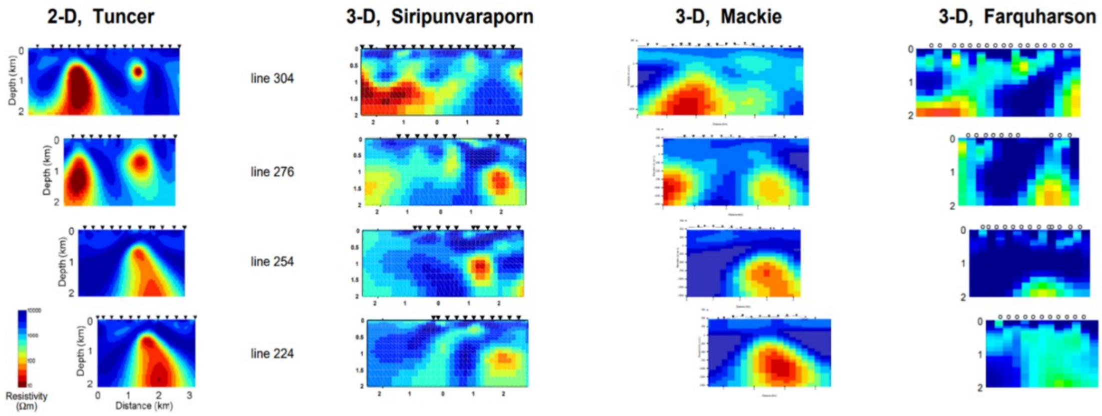

Figure 2.19: 2D and 3D inversion results of the McArthur River AMT data-set. The left column corresponds to the 2D inversion results presented in Tuncer et al. (2006). The middle two columns correspond to the 3D inversion results of algorithms mentioned in Siripunvaraporn et al. (2005a) and Mackie et al. (2001), respectively. The right column shows the 3D inversion result calculated using the algorithm introduced by Farquharson et al. (2002). (Modified from Craven et al., 2006.)

Craven et al. (2007) present an inversion of the AMT data collected at 15 stations in 2001 in the main McArthur River area. In Craven et al. (2007), the approach of Groom and Bailey (1989) was applied to the data for the geoelectric strike determination. Only TE-TM data were considered for inversion, and the inversion was performed by using the algorithm of Rodi and Mackie (2001). Figure 2.20 shows the location of the fifteen-station profile and the result of this inversion study. In the resistivity cross-section, feature A is thought to be an indication of the graphitic conductor dipping to the southeast. According to the interpretation of the results, this feature is consistent with the induction arrow plots at a particular frequency (i.e., 100 Hz – corresponding to the data seeing down to the fault). Although the data and induction arrows support feature A, the source of feature B remains unknown since the sounding locations are not close enough to the feature to yield reliable data. At the western side of the P2 Fault, or feature A, a resistive body – feature C – is observed, which is linked with the widespread metamorphic quartzite. The small conductive body, feature D, is thought to be associated with fractures and alteration-based faults (Craven et al., 2007).

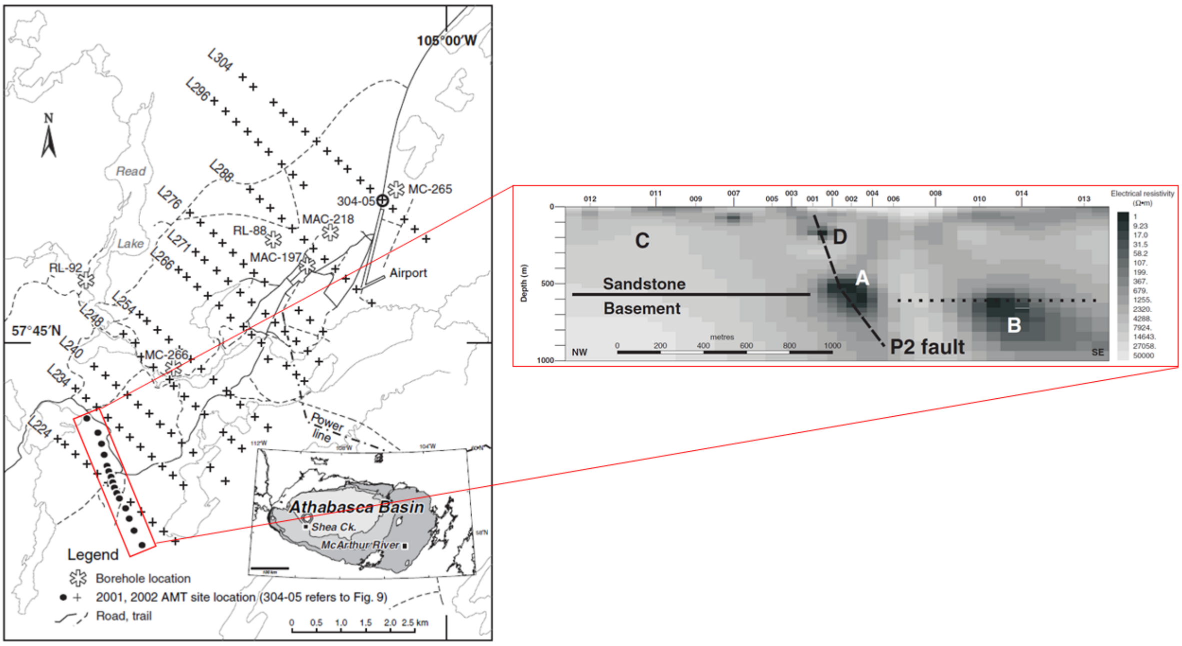

Figure 2.20: Map, on the left-hand side, showing the AMT sounding locations (black dots, the red rectangle of the data-set considered in Craven et al. (2007), and on the right-hand side, the cross-section is the result of the 2D TE-TM data inversion (modified after Craven et al. 2007).

Another inversion attempt on the AMT data studied in Tuncer et al. (2006) was carried out and presented in Farquharson and Craven (2009). The inversion algorithm uses the minimum-structure method. Only impedance data for 11 frequencies were considered for the inversion in the study. In addition, frequencies higher than 1280 Hz were not included in the inversion because of a lack of small enough cells. The model was embedded in a half-space having a conductivity of 10^{-4} S/m. The vertical slices representing the inversion results for every profile are shown in Figure 2.21. The results show consistency in terms of the dip of the graphitic conductor compared to the other inversion studies mentioned above. The fundamental difference with this study is the depth of the top parts of the second conductor located in the northwestern parts of the northern profiles. The features in the model near the surface (upper few 100 metres) are interpreted as reasonable, suggesting that they are real subsurface structures and not artifacts from static shift effects in the data. In addition to this idea, the deep conductive features have been linked with the nature of the MT method and the smoothing procedure of the minimum structure method because they do not extend to the known depths (i.e., top of the fault, around the depths of 500 m and 1 km) (Farquharson and Craven, 2009).

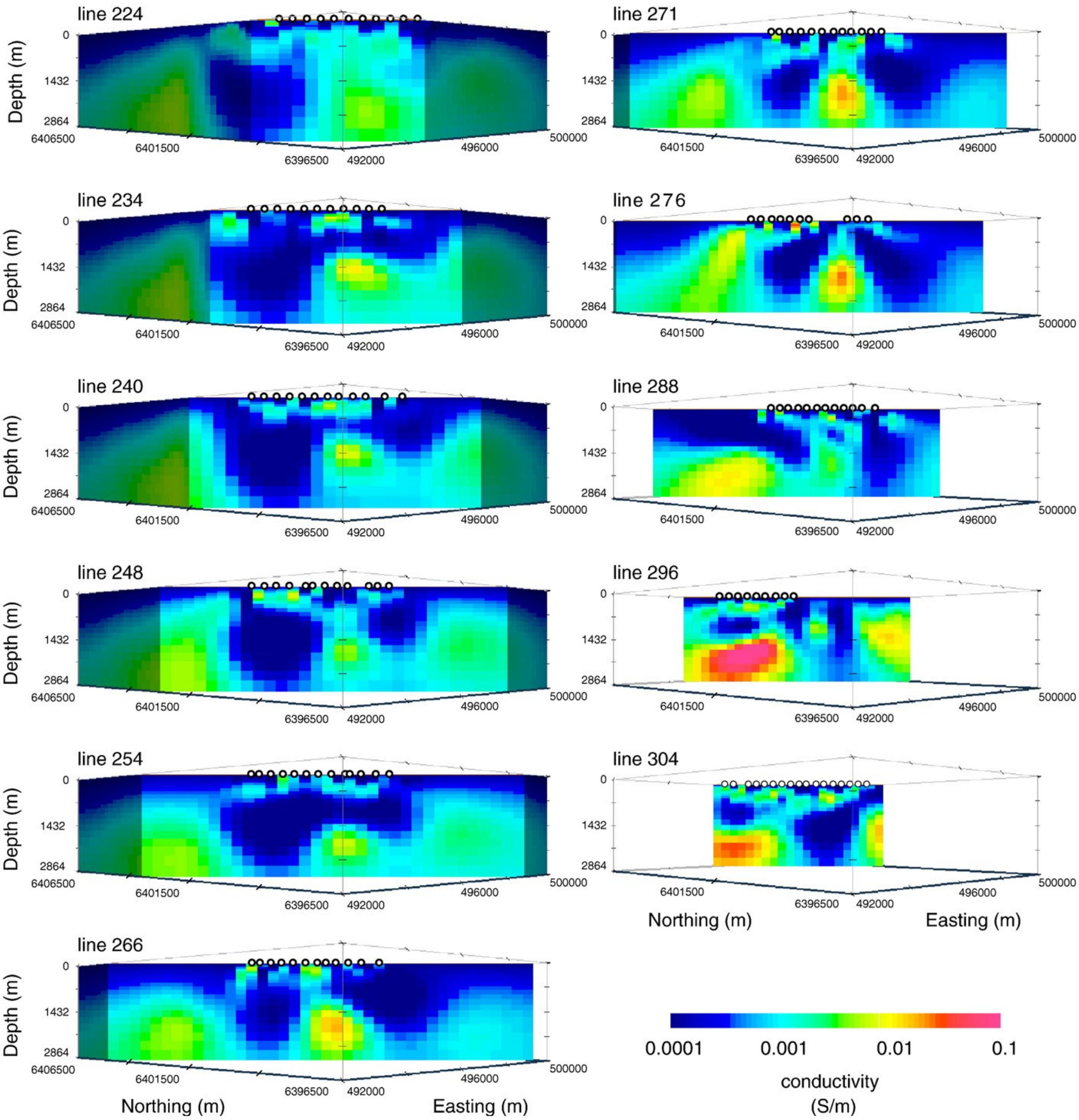

Figure 2.21: Vertical sections of the 3D inversion results for each profile (from Farquharson et al., 2009).

2.4. Summary

The geological background of the Athabasca Basin, and hence the McArthur River area, has been described in this chapter. In addition to the geology, geophysical surveys that help image and explain the geological features have also been summarized. The physical properties of the subsurface, such as magnetic susceptibility, density, or electrical conductivity, have an impact on the geophysical measurements. These properties sometimes permit complementary studies, such as using two different data sets (the combination of borehole data and gravity densities or seismic imaging data) to resolve the geological structure. Moreover, it can be inferred from this chapter that different geophysical surveys may be effective for monitoring some specific structures.

Furthermore, previous EM methods showed that the first 600 m might be imaged well, although there is a strong need for monitoring the depths beneath 600 m. For this purpose, the AMT method has been carried out in the McArthur River area, both for imaging the unconformity-type uranium body and delineating the P2 Fault. The inversion results of the collected AMT data in the same area have shown discrepancies in some aspects whilst the general scenario, southeast-dipping graphitic conductor, is the same for all. Inverting this data set with some new tools enabling better inversion results is the main objective of the present study. For instance, using tetrahedral meshes provides refinement around the observation points and this yields adding more frequencies for inversion. Moreover, the tetrahedral meshes help to focus on the relatively important structures in the model by deciding the size of them – i.e., finer meshes for the target structures and larger meshes for the remaining parts of the model. The details of the methodology and results will be discussed in the next chapters.

3 The Audio-Frequency Magnetotelluric Method

3.1. Introduction

The Magnetotelluric (MT) method is one of the most widely used EM prospecting methods in Geophysics. Several different versions of the MT method exist based on the frequency range of the measurements: the Long-Period Magnetotelluric Method (LMT), Broad-Band Magnetotelluric Method (BBMT), Audio-Frequency Magnetotelluric (AMT) Method, Control-Sourced Audio-Frequency Magnetotelluric (CSAMT) Method, Seafloor Magnetotelluric (SFMT) Method, and Radio Magnetotelluric (RMT) Method. In this study, AMT data are considered. The theory behind the AMT method is the same as that of the MT method. The frequency range of AMT soundings is at the high end of MT frequencies, approximately 10 Hz –10,000 Hz (Strangway et al.1973; Zonge and Hughes, 1991; Ferguson, 2012). These high frequencies correspond to seeing the shallower depth ranges that are possible using the MT method, and so are more appropriate for mineral exploration compared to crustal and upper mantle studies.

3.2. Source of Audio-Frequency Magnetotelluric (AMT) Method

The AMT method (like the general MT method) is a passive EM method. In other words, the source field of the method is natural. In MT, the “natural” source of the method is produced by meteorological events such as lightning activities and the variations in the Earth's magnetic field in response to the bombardment by charged particles from the solar wind.

The source field of the AMT method with frequencies above 1 Hz is generated as a result of the meteorological activities, i.e., lightning or thunderstorm energy. These types of signals comprise a wide range of EM frequencies, and they are called 'sferics'. It is sferics, especially from the exceedingly disturbed equatorial regions, that have the greatest importance because they propagate around the globe within a waveguide enclosed by the ionosphere and the Earth's surface (Simpson and Bahr, 2005).

The natural signal used in the AMT method shows the characteristically lower amplitudes in the frequency range of 1 to 5 kHz. This range is called the AMT dead band. The MT response at frequencies in this range provides important information on conductive bodies at 500 to 1500 m depth embedded in resistive host rocks. In this case, it is only possible to detect the geometrical features and the physical parameters of the conducting body satisfactorily if the response is known over the full bandwidth (Garcia and Jones, 2002). When the skin depth is too small compared to the dimensions of the conductor, the magnetic field will penetrate it before dampening out. In the limit where $\omega\mu\sigma \rightarrow \infty$, the induced current will be a surface current. However, for very small values of $\omega\mu\sigma$, the magnetic field penetrates into the conductor whilst the current field will be vanishingly small. If l is the dimension of the conductor, in the case when $\omega\mu\sigma l^2 \gg 1$, the magnetic field will vanish in the conductor. If $\omega\mu\sigma l^2 \gg 1$, the conductor will have a slight impact on the field. It is expected that the conductor should perturb the field between these two extremes (Grant and West, 1965).

An example of an AMT signal in the dead band caused by lightning is shown in Figure 3.1. Figure 3.1.a shows a transient caused by lightning. Figure 3.1.b shows the wavelet transform of the time series presented in Figure 3.1.a. It is clear that the spectrum has low values between 1 and 5 kHz.

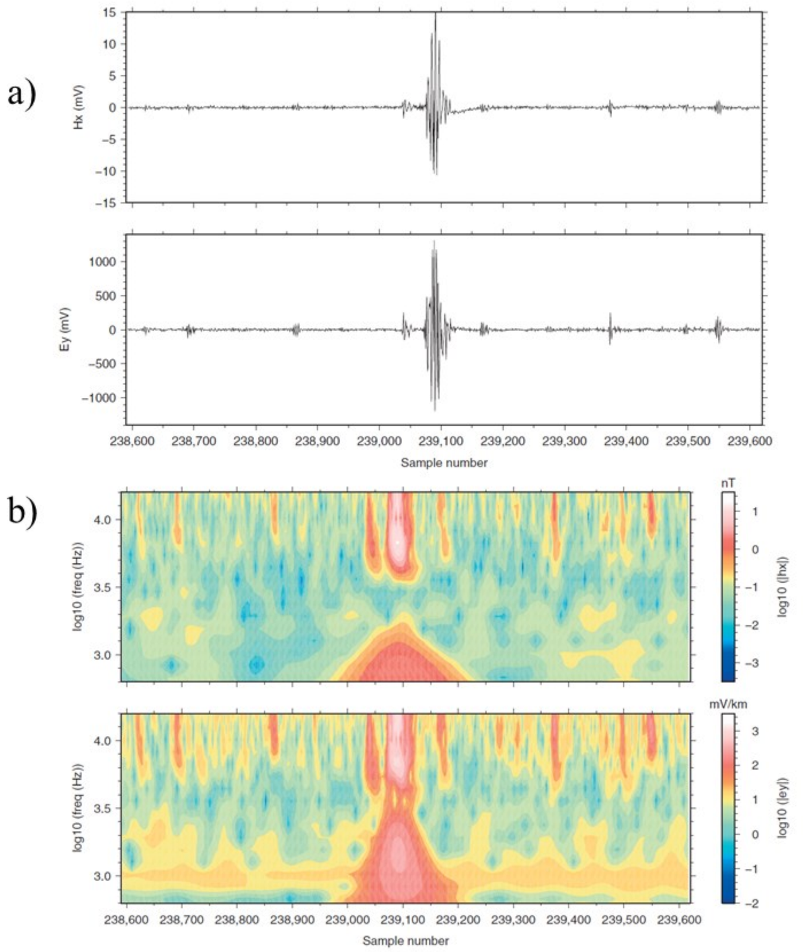

Figure 3.1: An example of a signal in the dead band for the AMT method (modified from Gracia and Jones, 2008). A) Time series with a transient caused by lightning. B) Wavelet transform to show the spectral and temporal structure of the transient. The spectrum has minimal values at around f=2000 hz, $\log_{10}(f)=3.3$ and this area corresponds to the AMT dead band at each graph.

For the MT and AMT methods, the ionospheric current systems are another source of the variations in the geomagnetic field, and therefore the field that induces the currents in the Earth. Besides, the impedance (i.e., the ratio of electric and magnetic fields, which will be explained later) on the Earth's surface is assumed to not depend on the electric and magnetic fields themselves but only on the Earth's electrical conductivity. EM fields are assumed to be plane waves that penetrate into the Earth at essentially vertical incidence (Cagniard, 1953; Kaufmann and Keller, 1981; Simpson and Bahr, 2005).

3.3. Maxwell's Equations

The fundamental theory of electromagnetics can be described by Maxwell's equations. Maxwell gathered together Gauss's, Ampère's, and Faraday's laws to define electromagnetics mathematically and physically (Griffiths, 1999). The differential form of Maxwell's equations in the frequency domain can be represented as:

$$\boldsymbol{\nabla} \times \mathbf{E} + i\mu\omega\mathbf{H} = 0 \qquad 3.1$$

$$\boldsymbol{\nabla} \times \mathbf{H} - (\sigma + i\varepsilon\omega)\mathbf{E} = 0 \qquad 3.2$$

$$\boldsymbol{\nabla}.\mathbf{D} = \rho \qquad 3.3$$

$$\boldsymbol{\nabla}.\mathbf{B} = 0 \qquad 3.4$$

where **E** is the electric field intensity in V/m, **H** is the magnetic field intensity in A/m, **B** is the magnetic induction in Teslas, **D** is the dielectric displacement in C/m^2, ω is the angular frequency, σ is conductivity, ε is dielectric permittivity, and ρ is the electric charge density in C/m^3 (e.g., Ward and Hohmann, 1988).

The basis of the theory consists of two main assumptions regarding the quasi-static approximation. One specific assumption for Maxwell's equations is about Ampère's Law, which, in the frequency domain, is

$$\boldsymbol{\nabla} \times \mathbf{H} = \sigma\mathbf{E} - i\omega\varepsilon\mathbf{E} \qquad 3.5$$

where ω is the angular frequency, σ is conductivity, and ε is dielectric permittivity. (The dielectric permittivity is a measure of how a material is polarized with an applied electric field and quantifies how a material transmits an electric field). The electric permittivity is assumed to be its value $\varepsilon = \varepsilon_0 = 8.854\times10^{-12}$ F/m in free space (Keller, 1988; Miensopust, 2010). On the right-hand side of equation (3.5), the first term is the conduction currents, and the second term is the displacement currents ($\mathbf{D} = \varepsilon\mathbf{E}$).

Should homogeneous Earth materials have a conductivity of 10^{-4} S/m or greater, free charge ρ_e scatters in less than 10^{-6} s (Ward and Hohmann, 1988). Because of the quasistatic approximation, which is neglecting the electric permittivity in non-magnetic media because it is too small and this approximation is valid for MT theory in terms of its frequency range, displacement currents are minimal when compared with conduction currents (Ward and Hohmann, 1988). For the MT method, and hence for the AMT method, Ampère's Law is assumed to be

$$\nabla \times \mathbf{H} = \sigma\mathbf{E} \tag{3.6}$$

For frequencies less than 10^5 Hz, $\partial\rho_e/\partial t \sim 0$, and by taking the divergence of Ampère's Law, it can be obtained that

$$\nabla . \mathbf{J} = 0 \tag{3.7}$$

Another particular assumption for Maxwell's equations is about Gauss's Law. The original form of Gauss's Law for the electric field is:

$$\nabla . \mathbf{E} = \rho \tag{3.8}$$

and this equation is true only for a region of uniform conductivity. However, in the electro-quasi-static approximation, neglecting the electric permittivity in the non-magnetic media due to it being too small and the time-varying displacement currents negligible compared with the time-varying conducting currents, the divergence of the electric field is equal to zero, and Gauss's Law for the electric field takes the form:

$$\nabla . \mathbf{E} = 0 \tag{3.9}$$

(Kaufmann and Keller, 1981; Ward and Hohmann, 1988; Simpson and Bahr, 2005).

3.4. The Constitutive Relations

The constitutive relations define the relationships between the current density and electric field, and between the magnetic field and magnetic intensity. Because the dielectric displacement is neglected because of the quasi-static approximation, it will not be explained here. These relationships depend on the material. It is typically assumed that the medium is linear and isotropic. Moreover, the electrical properties of the medium are assumed to be independent, which are independent of time, temperature, or pressure.

One of the constitutive relation equations explains the relationship between the magnetic field intensity (**H**) and the magnetic field induction (**B**), considering the magnetic permeability. It can be stated as

$$\mathbf{B} = \mu\mathbf{H} \tag{3.10}$$

where μ is the magnetic permeability of the medium in H/m. The magnetic permeability, μ, is a measure of how matter is magnetized, having been exposed to a magnetic field. Explicitly, when dealing with the EM fields in the MT (AMT) method, any variation in magnetic properties of the rocks, and hence any effect that this might have on the magnetic fields, is negligible compared to the impact on the EM fields from EM induction happening due to the conductivity of the subsurface materials. It is really a tensor quantity in all cases by simplifies to a scalar in isotropic media. The assumptions regarding a medium mentioned above yield to work with a scalar value; the magnetic permeability is assumed to be that of free space $\mu = \mu_0 = 4\pi\times10^{-7}$ (Keller,1988).

Another constitutive relation equation is the general statement of Ohm's Law. It describes the relationship between the electric field (E) and the current density (J) with conductivity. Ohm's Law can be written as

$$\mathbf{J} = \sigma\mathbf{E} \tag{3.11}$$

where σ is the electrical conductivity (in S/m) of the medium (Ward and Hohmann, 1988). Since E and J are vector identities, σ is a tensor quantity. However, the tensor takes a more straightforward form if the two orthogonal coordinate directions are chosen to lie in the principle directions (maximum and minimum conductivity directions) of the tensor. In this case, all of the tensor's non-diagonal elements are zero. Also, the principal elements are equal to each other in an isotropic medium. That is to say, the conductivity tensor can be considered as a scalar (Keller, 1988).

The reciprocal of the conductivity (σ) is called resistivity (ρ), and its unit is Ohm metres (Ωm). Numerous environmental factors may cause a change in the resistivity value of rock, such as time, pressure, and temperature (Keller, 1988). In Figure 3.2, the conductivity (resistivity) characteristics of various rock types are presented.

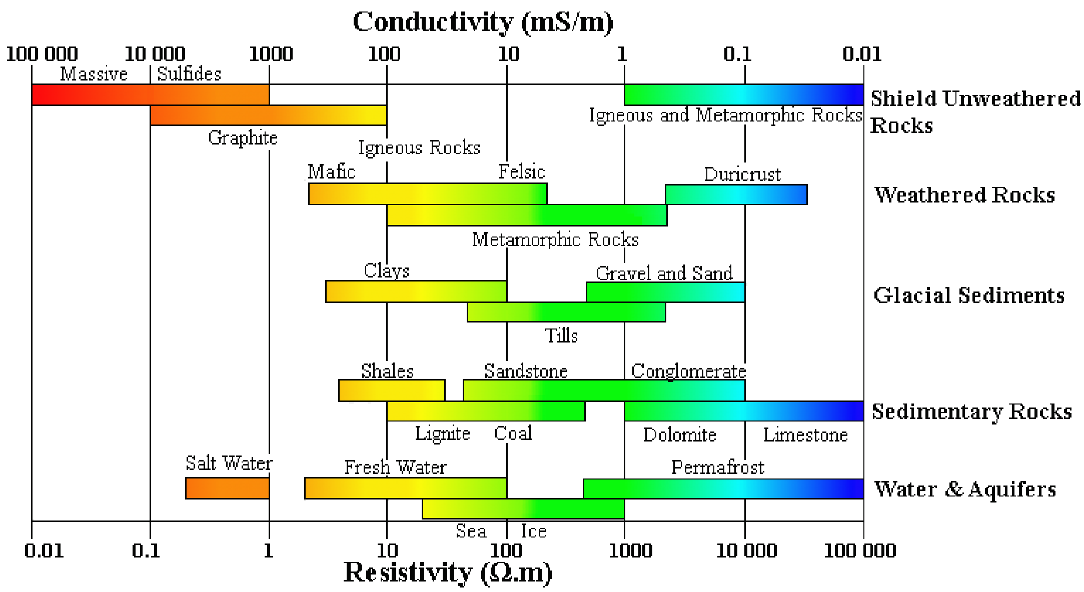

Figure 3.2: Conductivities of Earth's rock types (modified after Palacky, 1988).

The flow of electric currents in the Earth may be classified into electrolytic, electronic, and dielectric conduction. In the case of electrolytic conduction, the ions are responsible for the electric current flow in materials. In electronic conduction, or namely Ohmic conduction, the current flows classically in materials that possess free electrons, such as metal. For dielectric conduction, as mentioned above, the current flow occurs under the effect of a varying external field. This field causes a separation of negative and positive charges in the material, known as dielectric polarization. As a result of this, a current is produced, and this current is called displacement current (Telford, et al., 1990).

Electronic conduction plays a role in metallic ore minerals such as hematite and magnetite. In EM studies, the conduction in graphite is of particular importance. It is electronic conduction that takes place in single-crystalline graphite, whereas it is electrolytic conduction in non-crystalline (amorphous) graphite (Simpson and Bahr, 2005). As a result of dissolution of the salt in water, electrolytic conduction occurs in saline water. Similarly, electrolytic conduction occurs in the partial melts generated by asthenospheric upwelling and adiabatic decompression or high temperatures (Simpson and Bahr, 2005).

As shown in Figure 3.2, volcanic-based massive sulphides possess lower resistivity values (as low as 1 Ωm). The resistivity range of graphite varies between 0.1 and 10 Ωm, and is very close to massive sulphides. Basement rocks such as metamorphic rocks and igneous rocks have the highest resistivities between 10^3 and 10^5 Ωm. In sedimentary rocks such as sandstones, the porosity, clay and fluid contents decrease resistivity levels. In general, the resistivity of sandstone varies between 50 Ωm and 1000 Ωm. The resistivity in saline water varies between 0.2 Ωm and 1 Ωm (Palacky, 1988).

3.5. Electromagnetic (EM) Impedance and the Impedance Tensor

In the MT and AMT methods, the interrelation between horizontal components of the electric field (i.e., E_X, E_Y) and horizontal components of the magnetic field (i.e., H_X, H_Y) is diagnostic of the resistivities beneath the Earth's surface at a certain frequency. Tikhonov (1950) and Cagniard (1953) described the impedances, i.e., the ratio of **E** and **H** (Simpson and Bahr, 2005). For a uniform or layered Earth, the mutually orthogonal components of the electric and the magnetic fields are proportional to each other, i.e., E_X and H_Y (Tikhonov, 1950; Cagniard, 1953). The impedance can be represented as:

$$\mathbf{Z}_{ij}(\omega) = \frac{E_i(\omega)}{H_j(\omega)} \qquad 3.12$$

where **Z** is the EM impedance, and i and j indicate either X and Yor Y and X. Because **E** and **H** are complex-valued in the frequency domain representation, impedance is a complex number. In the general case of a 2D or 3D subsurface, **Z** can be defined as a second rank tensor (see equation 3.14) (Cagniard, 1953; Swift, 1967; Kaufmann and Keller, 1981, Simpson and Bahr, 2005). When calculating the impedance tensor in forward modelling, any two polarizations (e.g., North and East or TE and TM) of the electric and magnetic fields are considered. Suppose that **A** is the matrix of the horizontal electric fields of the two polarizations, and **K** is the matrix of the horizontal magnetic fields for the two polarizations. Then the electric and magnetic fields are related by

$$\mathbf{A}(\omega) = \mathbf{Z}(\omega).\mathbf{K}(\omega) \qquad 3.13$$

where **Z** is the impedance tensor. In the expanded version,

$$\begin{bmatrix} E_X^{(1)}(\omega) & E_X^{(2)}(\omega) \\ E_Y^{(1)}(\omega) & E_Y^{(2)}(\omega) \end{bmatrix} = \begin{bmatrix} Z_{XX}(\omega) & Z_{XY}(\omega) \\ Z_{YX}(\omega) & Z_{YY}(\omega) \end{bmatrix} \begin{bmatrix} H_X^{(1)}(\omega) & H_X^{(2)}(\omega) \\ H_Y^{(1)}(\omega) & H_Y^{(2)}(\omega) \end{bmatrix} \qquad 3.14$$

where superscripts 1 and 2 stand for the polarization numbers, the subscripts X and Y denote the horizontal Cartesian components. The impedance tensor is therefore given by

$$\mathbf{Z}(\omega) = \begin{bmatrix} Z_{XX}(\omega) & Z_{XY}(\omega) \\ Z_{YX}(\omega) & Z_{YY}(\omega) \end{bmatrix} = \begin{bmatrix} E_X^{(1)}(\omega) & E_X^{(2)}(\omega) \\ E_Y^{(1)}(\omega) & E_Y^{(2)}(\omega) \end{bmatrix} \begin{bmatrix} H_X^{(1)}(\omega) & H_X^{(2)}(\omega) \\ H_Y^{(1)}(\omega) & H_Y^{(2)}(\omega) \end{bmatrix}^{-1} \qquad 3.15$$

3.6. Earth Models in Magnetotellurics

3.6.1. One-Dimensional Earth Models

In a one-dimensional (1D) Earth, the resistivity, or conductivity, changes as a function of depth only (i.e., σ(z) or ρ(z)). In this case, the diagonal elements of the impedance tensor are zero, and the off-diagonal elements are equal in magnitude with opposite sign ($Z_{YX} = -Z_{XY}$, which all makes sense since one could rotate this situation around the vertical axis by any angle and the situation has not changed). The tensor takes the form (Swift, 1967; Vozoff, 1991; Simpson and Bahr, 2005)

$$\mathbf{Z}_{1D}(\omega) = \begin{bmatrix} 0 & Z_{XY}(\omega) \\ -Z_{XY}(\omega) & 0 \end{bmatrix} \qquad 3.16$$

3.6.2. Two-Dimensional Earth Models

Two-dimensional (2D) models of the Earth are generally defined by a strike direction in which conductivity and the source are constant. In the 2D case, it is the principle of conservation of charge (equation 3.7) playing a leading role in what happens at a discontinuity. The simple example in Figure 3.3 shows two structures having different conductivities (σ_1, σ_2) that are separated by a discontinuity. Conservation of charge across the discontinuity (vertical contact), where the conductivity changes, means that E_Y is discontinuous. In detail, one lateral component, which is assumed to be X, is aligned parallel to the strike direction, and all portions of the field remain to stay constant ($\partial/\partial X \equiv 0$). That is to say, assume that the X axis is the strike direction, and the $\partial/\partial X = 0$. In addition to this, Faraday's and Ampère's laws give the two sets of decoupled field equations. These equations can be written as:

$$\frac{\partial \mathbf{E}_X}{\partial Y} = \frac{\partial \mathbf{B}_Z}{\partial t} = i\omega \mathbf{B}_Z \qquad 3.17$$

$$\frac{\partial \mathbf{E}_X}{\partial z} = \frac{\partial \mathbf{B}_Y}{\partial t} = -i\omega \mathbf{B}_Y \qquad 3.18$$

$$\frac{\partial \mathbf{B}_Z}{\partial Y} - \frac{\partial \mathbf{B}_Y}{\partial z} = \mu\sigma \mathbf{E}_X \qquad 3.19$$

$$\frac{\partial \mathbf{B}_X}{\partial Y} = \mu\sigma \mathbf{E}_Z \qquad 3.20$$

$$-\frac{\partial \mathbf{B}_X}{\partial z} = \mu\sigma\mathbf{E}_Y \qquad 3.21$$

$$\frac{\partial \mathbf{E}_Z}{\partial Y} - \frac{\partial \mathbf{E}_Y}{\partial z} = i\omega\mathbf{B}_X \qquad 3.22$$

The first set of equations (from equation 3.17 to 3.19) define the transverse electric (TE) mode, which represents the currents flowing along the strike direction (Simpson and Bahr, 2005; Weidelt and Chave, 2012). The second set of equations (from 3.20 to 3.22) describes the transverse magnetic (TM) mode in which currents flow perpendicular to the strike direction (Simpson and Bahr, 2005). In general, the TE mode is used to determine deep conductors along with the strike direction, whilst the TM mode is better at imaging shallower resistive structures (Berdichevsky et al., 1998).

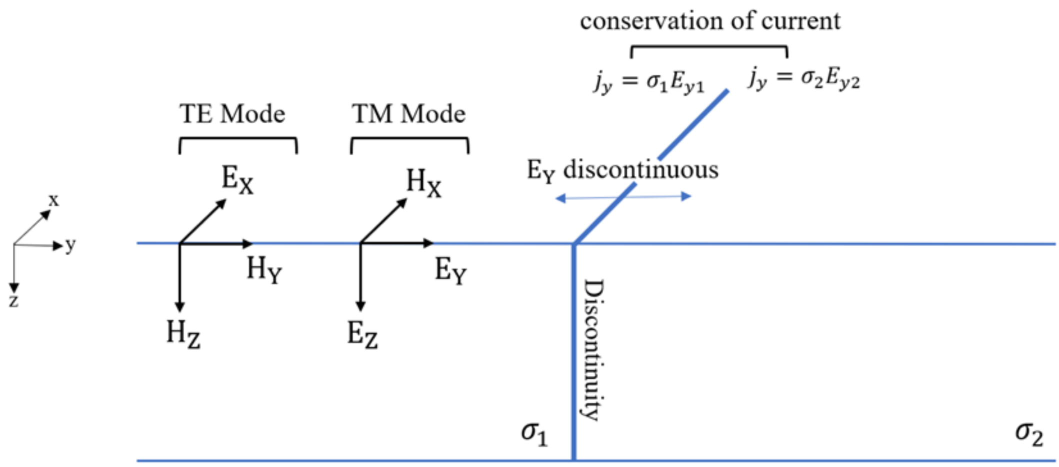

Figure 3.3: A basic 2D model example made up of two structures having different conductivities at a vertical contact. As a result of the conservation of charge at the discontinuity (vertical contact), EY is discontinuous. The x-direction is parallel to the strike in this example. The AMT or MT response decouples into two polarizations, one with the electric field aligned along strike (TE mode) and one with electric field aligned perpendicular to the strike (TM mode) (modified after Simpson and Bahr, 2005).

The impedance tensor for a 2D Earth is an off-diagonal tensor, and its off-diagonal elements are neither equal in magnitude, nor opposite in sign, but rather the tensor has the general form (assuming X and Yare indeed parallel to and perpendicular to the strike)

$$\mathbf{Z}_{2D}(\omega) = \begin{bmatrix} 0 & Z_{XY}(\omega) \\ Z_{YX}(\omega) & 0 \end{bmatrix} \tag{3.23}$$

In most 2D cases, the measurements are not carried out parallel and perpendicular to the strike direction since this direction is not known as a priori information. In these cases, the geoelectric strike can be determined with the help of several different approaches such as Swift's skew (Swift, 1967), Bahr's parameters (Bahr, 1988), the tensor decomposition of Groom and Bailey (1989), another tensor decomposition by McNeice and Jones (2001), and the phase tensor method of Caldwell et al. (2004). Having obtained the strike angle (θ), the MT impedance tensor can be rotated around the vertical axis (Marti, 2006). Moreover, the new X axis, which is now x′, is parallel to the geoelectric strike, and the impedance tensor of the new coordinate frame (x′, y′, Z) takes the form given by

$$\mathbf{Z}'_{2\mathrm{D}}(\omega) = R(\theta) \cdot \mathbf{Z}_{2\mathrm{D}}(\omega) \cdot R^T(\theta) \tag{3.24}$$

where prime indicates the new reference frame, R is the two-by-two clockwise rotation matrix, θ is the geoelectric strike, and ω is the frequency. The corresponding rotation matrix can be written as

$$R(\theta) = \begin{bmatrix} \cos(\theta) & \sin(\theta) \\ -\sin(\theta) & \cos(\theta) \end{bmatrix} \tag{3.25}$$

$R^T(\theta)$ is the transpose of this rotation matrix. In the new coordinate system, the TE and TM modes would be appropriately defined.

3.6.3. Three-Dimensional Earth Models

The three-dimensional (3D) Earth is the most general model for geoelectrical structure. In this case, the impedance elements are different from each other, and the tensor takes the form

$$\mathbf{Z}_{3D}(\omega) = \begin{bmatrix} Z_{XX}(\omega) & Z_{XY}(\omega) \\ Z_{YX}(\omega) & Z_{YY}(\omega) \end{bmatrix} \qquad 3.26$$

The data rotation along with the geoelectric strike direction is not needed, and the field decoupling into two modes is not possible (Marti, 2006).

3.7. Magnetic Transfer Functions

Magnetic transfer functions contain the information of the presence or absence of lateral variations in conductivity. Magnetic transfer functions are linear combinations of the horizontal and vertical magnetic field components (Vozoff, 1991; Simpson and Bahr, 2005). The mathematical representation of this function can be written as

$$H_z(\omega) = (\mathbf{T}_X(\omega) \;\; \mathbf{T}_Y(\omega)) \begin{pmatrix} H_X(\omega) \\ H_Y(\omega) \end{pmatrix} \qquad 3.27$$

where H_z is the vertical magnetic field, H_X and H_Y are horizontal components of the magnetic field, and $\mathbf{T}_X$ and $\mathbf{T}_Y$ are the complex magnetic field transfer functions. Tipper is the other common name for the magnetic transfer function. It can be used to show which side of a contact is more conductive. That is to say, near a boundary between a conductor and a resistive body, the near-surface current density parallel to strike will be higher on the conductive side, in which the tipper vectors point to the conductive side obeying the Parkinson convention (Vozoff, 1991; Simpson and Bahr, 2005).

Arrows have been commonly used for representing the separate real and imaginary parts of tippers in MT. Two conventions are widely followed to visualize the tippers; one of them is the Parkinson convention (Parkinson, 1959), in which the arrows point toward conductive zones, and the other one is the Wiese convention (Wiese, 1962), in which the arrows point toward resistive zones (Vozoff, 1991; Caldwell et al., 2004; Simpson and Bahr, 2005). Over the center of a conductive anomaly, the vertical magnetic field goes to zero (Vozoff, 1991; Simpson and Bahr, 2005).

For the 1D case, there is no localized tube of current in the ground, and the current flow is always as a sheet that is infinite in the X and Y directions. This means there is no vertical component of the magnetic field generated by the currents induced in the ground. In the 2D case, the tipper is not zero. The real and imaginary parts of both components align perpendicular to the geoelectric strike. The rotation of tipper can be done as

$$\mathbf{T}'_{2\mathrm{D}}(\omega) = R(\theta) \cdot \mathbf{T}_{2\mathrm{D}}(\omega) \tag{3.28}$$

where $R(\theta)$ is the rotation matrix shown in equation 3.25. In the 3D case, the tipper is not zero, and the rotation can no longer be performed.

3.8. Apparent Resistivity and Impedance Phase

One of the most frequently used parameters in the MT and AMT methods is the apparent resistivity (ρ_a). Cagniard (1953) came up with two significant assumptions to obtain apparent resistivity; firstly, the Earth should have horizontal layers, which should be homogeneous and isotropic, and the second one is the plane EM wave assumption. Taking these assumptions into consideration, Cagniard (1953) stated that resistivity could be determined as a function of depth if apparent resistivity is known (Vozoff et al., 1963). The apparent resistivity is given by

$$\rho_a = \frac{1}{\omega\mu_0}\left|\frac{\mathrm{E_X}}{\mathrm{H_Y}}\right|^2 \qquad 3.29$$

where ρ_a is apparent resistivity (Ωm), $\mathrm{E_X}$ (V m^{-1}) and $\mathrm{H_Y}$ (A m^{-1}) are the horizontal components of the electric and magnetic fields, respectively, μ_0 is the magnetic permeability of free space, and ω is the angular frequency. In particular, apparent resistivity can be treated as the average resistivity of the equivalent uniform layered medium (Cagniard, 1953; Simpson and Bahr, 2005).

Another widely used parameter is the impedance phase. The horizontal components of the electric and magnetic fields have a phase shift (Tikhonov, 1950; Kaufmann and Keller, 1981; Vozoff, 1991). Since the impedance tensor elements are complex quantities, the phase shift can be retrieved by taking imaginary and real parts into account. This phase shift can be represented as

$$\Phi_{\mathrm{ij}} = arctan\left(\frac{\mathrm{Im(Zij)}}{\mathrm{Re(Zij)}}\right) \qquad 3.30$$

where i and j indicate either x and y or y and x.

In the homogeneous half-space case, where the real and imaginary parts of the impedance tensor elements are equal in magnitude (namely, becoming frequency-independent), the apparent resistivity is the same as the resistivity of the half-space, and the impedance phase is 45°. In other cases, if the conductivity of the medium increases with depth, the impedance phase increases and becomes larger than 45° and vice versa (Kaufman and Keller, 1981; Vozoff, 1991; Simpson and Bahr, 2005).

3.9. Skin Depth

The EM field decays with depth exponentially in a uniformly conductive medium. Skin depth is where the EM field will have decreased to ≈ 37% (i.e., 1/e) of its amplitude at the surface (Chave and Jones, 2012; Bedrosian, 2007). The formula for skin depth in a uniform medium is given as

$$\delta(\omega) = \sqrt{\frac{2}{\omega\mu\sigma}} \qquad 3.31$$

Assuming the magnetic permeability is that of free space, equation (3.31) can be written as

$$\delta \cong 503\sqrt{\rho/f} \qquad 3.32$$

where δ is in metres, f is the frequency in Hz (or in s^{-1}), and ρ is the resistivity (Ωm). It can be inferred from equation (3.32) that EM fields attenuate faster in a conducting layer than in a resistive layer (Bedrosian, 2007; Chave and Jones, 2012).

3.10. Summary

The essential theoretical points behind the AMT method have been explained above. The classical assumptions of the MT method are valid for the AMT method as well. The AMT method is a passive method, which has a natural source. The frequency range of the method is approximately 10 – 10,000 Hz. Maxwell's equations and the constitutive relations are the main theoretical equations explaining the physical basis of the behaviour of the EM fields and their interactions with subsurface structure. In different cases, such as 1D, 2D, or 3D Earth's subsurface, the processes may vary. The diagonal elements of the impedance tensor take zero value while off-diagonals are equal to each other with a minus sign for a 1D Earth model. For the 2D case, the diagonals are still zero but the off-diagonals are not equal to each other. In the 3D case, all elements of the impedance tensor are different from each other. The apparent resistivity and phase are the most frequently used parameters in the MT method, and both of them can be calculated using the impedance tensor elements.

4 Forward Modelling and Inversion of AMT Data

4.1. Introduction

In most geophysical surveys, the modelling of the geophysical data is an essential part of the study. This step, in general, consists of two procedures: 1) forward modelling, and 2) inversion of the observed data. The former is based on creating a candidate model and obtaining the synthetic data for that model and the survey geometry of interest. The latter comprises the fitting of the observed and synthetic data using an automatic mathematical approach, such as the Gauss-Newton (GN) method. In the present study, the algorithm mentioned in Jahandari and Farquharson (2017) is used for the forward modelling and inversion of the AMT data-set. An unstructured mesh is used for discretizing the Earth model for the inverse problem and for discretizing the mathematics of the forward problem. That algorithm uses a minimum-structure approximation for minimization and unstructured grids for finite elements. In this chapter, mesh generation and the software used for model creation will be described, as this is a non-trivial issue for unstructured tetrahedral meshes. The theoretical backgrounds of the forward modelling and inversion of the AMT data will also be explained in detail. The sections below are ordered according to the sequence in which they are encountered while performing modelling and inversion of a data set.

4.2. 3D Model Creation Software: FacetModeller

In the present study, FacetModeller is used to create 3D models. It was introduced in Lelièvre et al. (2018) and is a Java-based program that provides the capability to create, manipulate and analyze 3D piecewise linear complexes (PLCs). A PLC is an organized way of describing a "box", and the "sides" and "top" and "bottom" of the box, except that it can be quite complicated and have all sorts of "alcoves" and corners and bits sticking out (see Figure 4.1.a). PLCs, which were first introduced in Miller et al. (1996), must satisfy two conditions: 1) an edge is a union of facets, and 2) if two different facets intersect each other, then this intersection is a union of facets (Si, 2015; Lelièvre et al., 2018). In the software, the term “node” stands for the vertices of the facets of a PLC, and the word “edge” means the connection between a pair of nodes (i.e., the line segment that ties two nodes together). Another critical requirement is the “quality” of the PLC of a surface. That is to say, higher mesh qualities might be needed to improve the accuracy of the calculations when performing numerical analyses based on finite-volume or finite-element methods. Therefore, to obtain higher mesh quality, the quality of the PLC should be satisfactorily high. This can be achieved by avoiding very small and large vertex angles (Lelièvre et al., 2018).

FacetModeller allows for the use of images as an input, for example, digitizing vertical cross-sections, interpolated horizontal depth sections, and geological maps. It enables surfaces in 3D to be defined by connecting nodes on the surface of a considered model (e.g., a patchwork of facets on the surface; Lelièvre et al., 2018). In the present study, 3D models have been created by following the steps of defining nodes on the depth sections and then linking those to create surfaces rather than using images as inputs. The graphical user interface (GUI) of Facetmodeller is presented in Figure 4.1.

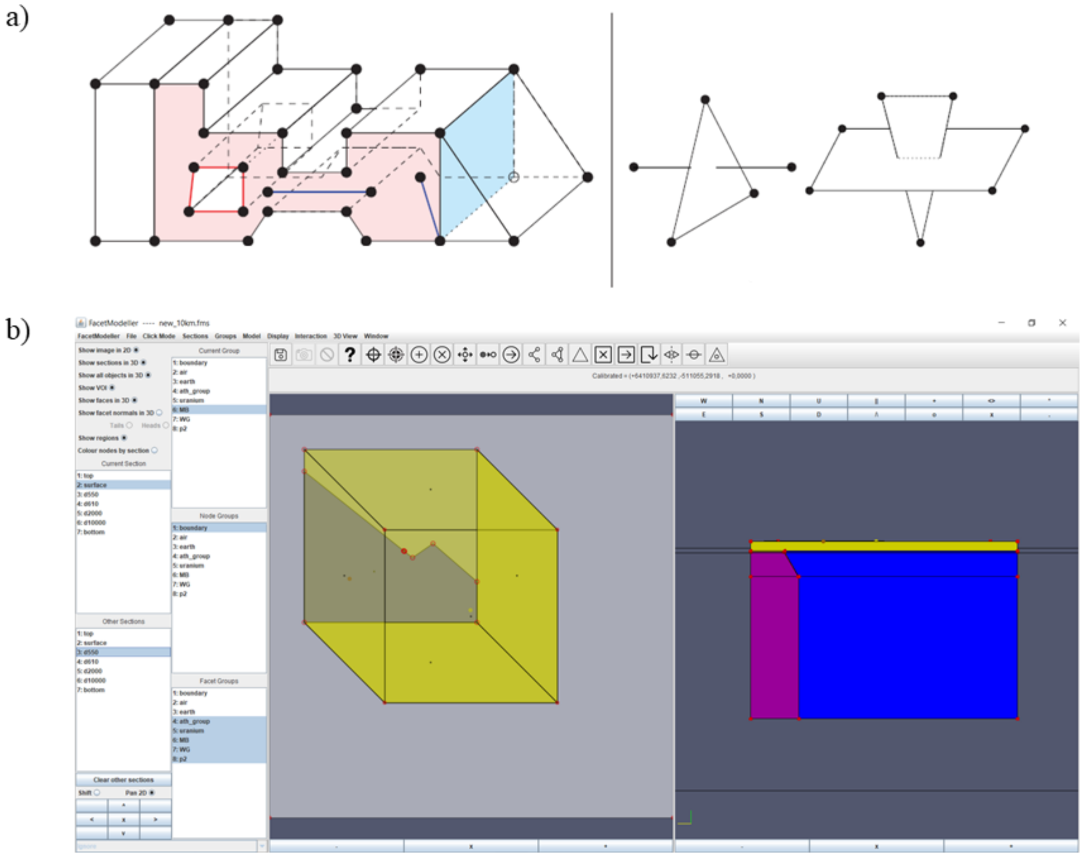

Figure 4.1: A) Left panel is an example of a 3D PLC. The pinkish side is a polygon, including a hole and the edges and vertices floating in it. The blue side is an example of an interior polygon. The second figure on the right shows non-PLCs (taken from Wi, 2015). B) a screenshot presenting the GUI of facetmodeller. The left side corresponds to the 2D horizontal depth sections, whereas the one on the right corresponds to the 3D view panel. Different colours indicate the different geological structures.

As shown in Figure 4.1, it is possible to define distinctive colours for different facet groups and node groups in the software. For example, in the view of FacetModeller shown in Figure 4.1, the blue colour corresponds to the Wollaston Group, purple indicates the Metamorphic Basement, and yellow is used for indicating the Athabasca Group (see Figure 2.2.b). The visualization is optional: the “3D view” panel can be used to see the corresponding model in 3D, together with working in 2D horizontal depth sections or vertical cross-sections.

Other functions such as adding nodes to exact coordinates directly, or removing them, joining nodes together to create facets, calibration of the depth or vertical sections are easy to perform no matter how complicated the model is. Lastly, various outputs are produced, e.g., polygon, node, or elements files, that are needed to generate meshes for a model and enable the visualization of the created models in other software such as Paraview.

4.3. Generation of the Tetrahedral Meshes (Tetrahedral and Voronoï Grids)

In the present study, the forward and inverse problem source codes are based on tetrahedral (Delaunay Triangulation) meshes. The meaning of the term “tetrahedral mesh” is a 3D unstructured grid cutting the corresponding 3D domain into pieces (Si, 2015; Jahandari and Farquharson, 2014). In more detail, suppose that Ω is a computational domain for any modelling. The 3D unstructured grids play a role in partitioning Ω into simplified structures just as nodes, triangles, segments, and tetrahedra (Lu, 2020). This partitioning is useful for complicated geometries, and it is able to coarsen or refine around a structure of interest (Si, 2015). A tetrahedron consists of four triangular faces and nodes, and six edges. Due to having four faces, each tetrahedron is surrounded by four different neighbouring tetrahedra. Voronoï cells (Dirichlet tessellation), which are arbitrary convex polyhedra, are dual grids used to create primary grids by connecting the circumcentres of primary cells that share the corresponding node (Jahandari, 2015). The most striking feature of the unstructured grids and Voronoï cells is being orthogonal to each other (Figure 4.2). In other words, the edges of the cells on one grid are perpendicular to the faces of the cells in the other grid (Jahandari, 2015).

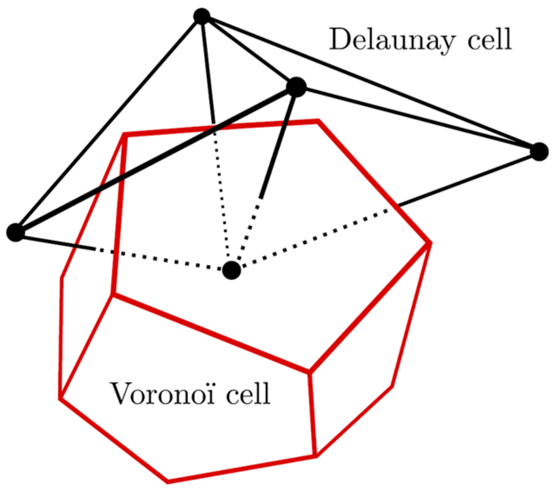

Figure 4.2: Tetrahedral (Delaunay cell, black) and Voronoï cells (red). The edges of the Delaunay cells meet at the center of a Voronoï cell. Moreover, the edges of the tetrahedra are orthogonal to the faces of the Voronoï cells (and vice versa). (modified after Jahandari and Farquharson, 2014; Lu, 2020.)

TetGen (Si, 2004) is used for the generation of the mesh in this study. This C++-based open-source program allows one to generate Delaunay and Voronoï grids. The Delaunay Triangulation quality can be controlled by checking the ratio of the length of the smallest edge to the radius of the circumsphere of the corresponding tetrahedron. Another critical issue with the quality is controlling the minimum internal dihedral angle of the tetrahedra. The fundamental point here is having tetrahedra that fill the full space or volume accurately – i.e., longer and narrower tetrahedra do not fill the space or volume. Since the mesh generation is Delaunay Triangulation, none of the vertices can be located in the circumsphere of any tetrahedra. This guarantees getting rid of skewed or flat tetrahedra. Moreover, all circumcentres of the tetrahedra are placed inside the meshed domain (Jahandari, 2015).

In the present study, generating a mesh is the last step before starting the calculation processes (i.e., forward problem and inversion). To achieve this, after creating the geological model in FacetModeller, the output (or ".poly" file) of this model is used as an input for generating the mesh utilizing TetGen. One of the advantages of using TetGen is that the refinement around observation points is advantageous for generating accurate data at higher frequencies. This provides getting more information at shallower depths. In contrast, it is almost impossible to perform this using rectilinear meshes. The total number of cells would rise when the refinements were done around the observation points using rectilinear meshes. The thing with rectilinear meshes is that any refinement around observation locations propagates all the way out to the boundaries of the computational domain, meaning there are lots of cells where there does not need to be lots of cells. For unstructured meshes, the refinement can be localized where it is needed, and the mesh coarsens outwards in all directions. Having lots of cells also increases the need for memory. Not only may it increase the demand in the amount of memory, but it also may increase the need for computing time. In contrast, unstructured tetrahedral grids require fewer computing nodes and computing time in this case. It is generally a more efficient means of discretizing a 3D computational domain.

Having generated the mesh with TetGen, the output files are used for computations. These files contain the connectivity information for the nodes to form edges, the relation of edges to create the faces, and the relation of faces generating cells. These files can be counted as two different faces, cell, node files, one neighbour, and an edge file (Jahandari, 2015). These files help to transfer information between these cells during calculations. An example of a mesh for a 3D model is shown in Figure 4.3. The next step is to start solving the forward or inverse problems.

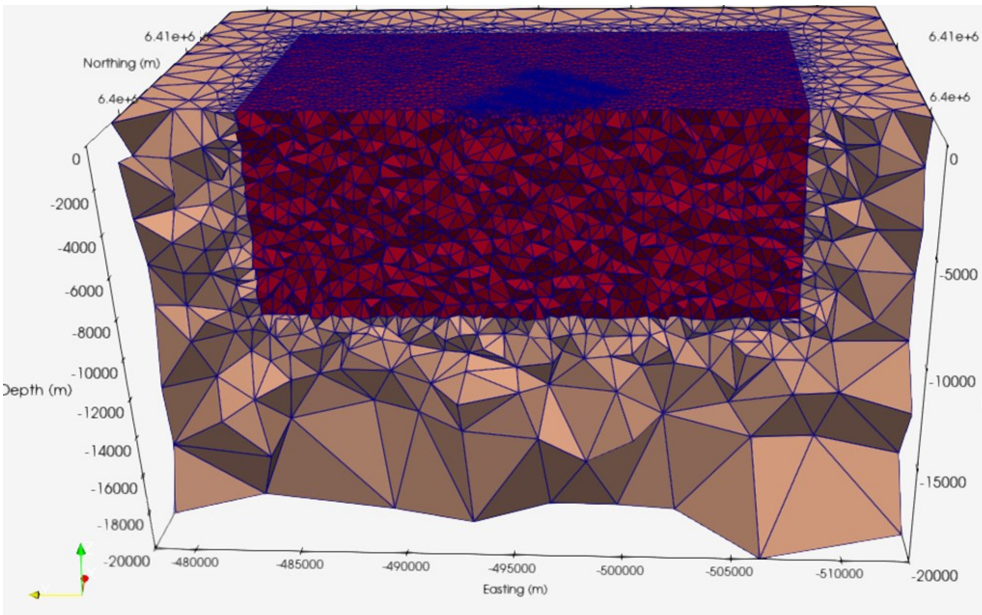

Figure 4.3: A view of an example unstructured tetrahedral mesh for a 3D model.

4.4. The Forward Problem

In this thesis, the solution of the forward AMT problem is sought with code introduced in Jahandari and Farquharson (2017). The code uses an edge-based finite-element (FE) method to solve the forward problem. In essence, this method is a divergence-free method in which the unknown electric field is defined at the edges of the elements (Jahandari and Farquharson, 2017). Furthermore, the approach satisfies the continuity of the tangential component of the electric field across the interfaces between cells (Jin, 2002; Farquharson and Miensopust, 2011; Jahandari and Farquharson, 2017).

The finite-element (FE) method is a numerical method widely used for solving partial differential equations and a group of boundary conditions. The general concept of the method is based on partitioning the corresponding domain into small subdomains, which are called finite elements. In the method, the distribution of the unknown quantity, e.g., electric field, is interpolated depending on the values at the edges or the nodes. For this, interpolation functions should be a set of polynomials, and, therefore, the accuracy of the solution depends upon the order of those. Then, the solution can be obtained after solving a system of linear equations. This system of equations would be formed by converting the differential equations and related boundary conditions into integro-differential equations in one of two ways, minimizing a functional or using weighted residuals, namely the Galerkin method (Polycarpou, 2006).

The solution of the FE method-based forward problem is achieved using the source-free version of the Helmholtz equation in the code mentioned in Jahandari and Farquharson (2017). This equation can be expressed as

$$\nabla \times \nabla \times \mathbf{E} + i\omega\mu_0\sigma\mathbf{E} = 0 \qquad 4.1$$

where E is the electric field, i denotes the imaginary unit, a time-dependence of e^{iwt} is supposed, ω is the angular frequency, μ_0 is the magnetic permeability of the free-space, and σ is the conductivity. For solving equation 4.1, the inhomogeneous Dirichlet boundary condition appropriate for a 1D earth model is used.

In the code, the partitioning of the corresponding domain in the forward problem is achieved using the Galerkin method (weighted residuals method). Mainly, the method consists of creating a residual function that gives the error between the two sides of equation 4.1 for an approximate electric field. Then, the residual is weighted by the basis functions, and it is set to zero and minimized to find an approximate solution (Jahandari and Farquharson, 2017). The weighted residual constructed for equation 4.1 can be written as

$$\mathbf{R} = \mathbf{N} \cdot (\nabla \times \nabla \times \tilde{\mathrm{E}} + i\omega\mu_0\sigma\tilde{\mathrm{E}}) \qquad 4.2$$

where Ẽ is the approximate electric field linked with the solutions along the edges and inside each tetrahedral cell by

$$\mathbf{E} = \sum_{\mathrm{u}=1}^{6} \mathbf{N}_{\mathrm{u}}\tilde{\mathrm{E}}_{\mathrm{u}} \qquad 4.3$$

where $\mathbf{N}_{\mathrm{u}}$ stands for the first-order vector basis functions that are associated with the edges.

Substituting equation 4.3 into equation 4.2, and integrating over the domain *Ω* and equating to zero yields

$$\sum_{q=1}^{ma} \tilde{\mathrm{E}}_{\mathrm{q}} \int (\boldsymbol{\nabla} \times \mathbf{N_m}) \cdot (\boldsymbol{\nabla} \times \mathbf{N_q}) d\Omega + i\omega\mu_0 \sum_{q=1}^{ma} \tilde{\mathrm{E}}_{\mathrm{q}} \int \sigma \mathbf{N_m} \cdot \mathbf{N_q} d\Omega = 0 \qquad 4.4$$

where *ma* is the number of the edges in the mesh and m=1,2,…, *ma*. Since the basis functions take values different from zero only inside their specific elements, equation 4.4 can be written in terms of volume *V* of each element:

$$\sum_{q=1}^{6} \tilde{\mathrm{E}}_{\mathrm{q}} \int (\boldsymbol{\nabla} \times \mathbf{N_m}) \cdot (\boldsymbol{\nabla} \times \mathbf{N_q}) d\Omega + i\omega\mu_0 \sum_{q=1}^{6} \tilde{\mathrm{E}}_{\mathrm{q}} \int \sigma \mathbf{N_m} \cdot \mathbf{N_q} d\Omega = 0 \qquad 4.5$$

by noting that *ma* in equation 4.4 turns into 6 in equation 4.5. This step gives the system of equations, which can be written as

$$\mathbf{KE} = \mathbf{b} \qquad 4.6$$

where b denotes the boundary values, E stands for the approximate total electric field values along the edges, and K is the coefficient matrix. The real-valued form can be expressed as

$$\begin{pmatrix} \boldsymbol{A} & -\boldsymbol{B} \\ -\boldsymbol{B} & -\boldsymbol{A} \end{pmatrix} \begin{pmatrix} \mathbf{E_{re}} \\ -\mathbf{E_{im}} \end{pmatrix} = \begin{pmatrix} \mathbf{b_{im}} \\ -\mathbf{b_{re}} \end{pmatrix} \qquad 4.7$$

where **A** and **B** are highly sparse matrices. To keep the symmetry of the complex system in equation 4.6, the second rows of **K** and **b** are multiplied by minus one in equation 4.7. MUMPS, a sparse direct solver introduced in Amestoy et al. (2006), is used for solving the system, and impedance and magnetic transfer functions can be obtained for each station in the model (Jahandari and Farquharson, 2017).

4.5. The Inverse Problem

The minimum-structure inversion procedure is used in the algorithm mentioned in Jahandari and Farquharson (2017). In addition to the minimum-structure approach, an iterative model-space Gauss-Newton (GN) algorithm is used for the optimization. This iterative solver is active at every step of GN, and it requires the sensitivity matrix-vector products. The calculation of this product is satisfied using pseudo-forward modelling. The main advantage of using this procedure is that it avoids the need to form the Hessian and Jacobian matrices explicitly and thus results in less computation time and memory.

The main idea behind the forward problem can be expressed by the equation below

$$\mathbf{d} = \mathrm{F}(\mathbf{m}) \tag{4.8}$$

where F is the forward operator, d is the calculated data vector with the size of *N*, and m is the model vector having the size of *M*. Here, F defines the non-linear relation in the EM theory. Because the inverse of F does not exist in general, then the direct solution of equation 4.8 to obtain m is not possible. For this reason, an inverse problem is generally formulated in which the solution minimizes an objective function. This objective function primarily involves a measure of data misfit (Jahandari and Farquharson, 2017).

In the minimum-structure inversion approach, the computational domain is partitioned into elements that are piecewise constant with respect to conductivity. In this scenario, the inversion targets finding a solution model that sufficiently reproduces the observed data d^t while keeping the model as simple as possible. The solution is obtained by minimizing an objective function, Φ, which is the sum of measures of data misfit, ϕ_d, and model structure, ϕ_m (Jahandari and Farquharson, 2017). The minimization process is iterative because of the non-linear relationship in equation 4.8. This relation can be formulated for the *n*th iteration as

$$\Phi^n = \phi_d^n + \phi_m^n \tag{4.9}$$

and the data misfit can be written as

$$\phi_d^n = \|\mathbf{W}_d(\boldsymbol{d}^t - \boldsymbol{d}^n)\|^2 \tag{4.10}$$

which is the presentation of the l_2-norm. In equation 4.10, W_d is the diagonal matrix whose elements are the reciprocals of the standard deviations of the noise in the observed data:

$$\boldsymbol{W}_d = diag\{1/s_1, 1/s_2, \ldots, 1/s_i,\}, \quad i=1, 2, \ldots, N, \tag{4.11}$$

and d^n is the current calculated data, which is linked to the data for the previous iteration, which can be expanded as

$$\boldsymbol{d}^n = \boldsymbol{d}^{n-1} + \delta\boldsymbol{d}^n. \tag{4.12}$$

The second term on the right-hand side is the data perturbation. Because F (equation 4.8) is linearized, this term can be linked to the model perturbation parameter, δm^n, using the Jacobian or sensitivity matrix

$$\delta\boldsymbol{d}^n = \mathbf{J}^{n-1} \cdot \delta\boldsymbol{m}^n \tag{4.13}$$

and δm^n is used to update the model

$$\boldsymbol{m}^n = \boldsymbol{m}^{n-1} + \lambda\delta\boldsymbol{m}^n. \tag{4.14}$$

where λ stands for the step length. This approach is implemented in the code by Mitra Kangazian to guarantee that the objective function is decreased. The parameter λ is consecutively reduced by half from its initial value if needed during calculations (Farquharson and Oldenburg, 2004). That can be formulated as

$$\phi_d^n(\lambda) + \beta^n\phi_m^n(\lambda) < \phi_d^{n-1}(\lambda) + \beta^n\phi_m^{n-1}(\lambda) \tag{4.15}$$

and it is called the damped GN method.

The model-structure term consists of two parameters, the model smallness and the model roughness, ϕ_s^n and ϕ_r^n, respectively. The relation between these can be written as

$$\phi_m^n = \beta^n(\alpha_s\phi_s^n + \alpha_r\phi_r^n) \tag{4.16}$$

where α_s and α_r are constant scalars and β^n regularizes the inversion by adjusting the relative importance of model structure (ϕ_m) and data misfit (ϕ_d) (Jahandari and Farquharson, 2017). The regularization parameter, β^n, follows a cooling strategy in which it starts from a high value in the first iteration and decreases linearly by a constant factor of

$$\beta^n = c\beta^{n-1} \tag{4.17}$$

where c is the cooling parameter. The value of β^n is kept constant once the target misfit value is reached (Farquharson, 2008; Jahandari and Farquharson, 2017).

The model roughness term (ϕ_r^n) means the roughness of the current model m^n which can be written in the form

$$\phi_r^n = \|\mathbf{W}_\mathrm{r}\, \boldsymbol{m}^n\|^2 \qquad 4.18$$

where $\mathrm{W_r}$ is the first-order finite-difference (FD) matrix, and it acts on the neighbouring tetrahedra centroids in the active mesh zone of the corresponding model (Lelièvre and Farquharson, 2013; Jahandari and Farquharson, 2017).

The model smallness parameter (ϕ_s^n) is a measure of how close the model at the *n*-th iteration (m^n) is to the reference model (m^n). The relation can be written as

$$\phi_r^n = \left\|\mathbf{W}_\mathrm{s}(\, \boldsymbol{m}^n - \, \boldsymbol{m}^f)\right\|^2. \qquad 4.19$$

In the equation above, $\mathrm{W_s}$ is the weighting matrix controlling this closeness throughout the active cells in the mesh (Jahandari and Farquharson, 2017).

For the GN method, the derivation is achieved by taking the derivative of the objective function at the *n*-th iteration (Φ^n) with respect to δm^n and equating to zero. The expanded form is

$$\frac{\partial \phi_d^n}{\delta \boldsymbol{m}^n} + \beta^n \alpha_s \,\frac{\partial \phi_s^n}{\partial \delta \boldsymbol{m}^n} + \,\beta^n \alpha_r \frac{\partial \phi_r^n}{\partial \delta \boldsymbol{m}^n} = 0. \qquad 4.20$$

In terms of matrix notation, the partial derivatives above can be written as

$$\frac{\partial \phi_d^n}{\delta \boldsymbol{m}^n} = -2\, \mathbf{J}^{n-1^T}\, \mathbf{W}_\mathrm{d}^\mathrm{T} \mathbf{W}_\mathrm{d}\, (\boldsymbol{d}^t - \boldsymbol{d}^{n-1} - \mathbf{J}^{n-1} \delta \boldsymbol{m}^n) \qquad 4.21$$

$$\frac{\partial \phi_s^n}{\partial \delta \boldsymbol{m}^n} = 2\, \mathbf{W}_\mathrm{s}^\mathrm{T} \mathbf{W}_\mathrm{s}\, (\boldsymbol{m}^{n-1} + \delta \boldsymbol{m}^n - \boldsymbol{m}^f) \qquad 4.22$$

$$\frac{\partial \phi_r^n}{\partial \delta \boldsymbol{m}^n} = 2\, \mathbf{W}_{\mathrm{r}}^{\mathrm{T}} \mathbf{W}_{\mathrm{r}}\, (\boldsymbol{m}^{n-1} + \delta \boldsymbol{m}^n) \qquad 4.23$$

and substituting equations 4.20 to 4.22 into 4.19, and re-arranging it gives

$$\begin{aligned} &\left\{ \mathbf{J}^{n-1^T}\, \mathbf{W}_{\mathrm{d}}^{\mathrm{T}} \mathbf{W}_{\mathrm{d}}\, \mathbf{J}^{n-1} + \beta^n \alpha_s \mathbf{W}_{\mathrm{s}}^{\mathrm{T}} \mathbf{W}_{\mathrm{s}} + \beta^n \alpha_r \mathbf{W}_{\mathrm{r}}^{\mathrm{T}} \mathbf{W}_{\mathrm{r}} \right\} \delta \boldsymbol{m}^n \\ &= \mathbf{J}^{n-1^T}\, \mathbf{W}_{\mathrm{d}}^{\mathrm{T}} \mathbf{W}_{\mathrm{d}}\, (\boldsymbol{d}^t - \boldsymbol{d}^{n-1}) + \beta^n \alpha_s \mathbf{W}_{\mathrm{s}}^{\mathrm{T}} \mathbf{W}_{\mathrm{s}}\, (\boldsymbol{m}^f - \boldsymbol{m}^{n-1}) \\ &\quad - \beta^n \alpha_r \mathbf{W}_{\mathrm{r}}^{\mathrm{T}} \mathbf{W}_{\mathrm{r}}\, \boldsymbol{m}^{n-1} \end{aligned} \qquad 4.24$$

where the left-hand side of the equation represents an approximation of the Hessian matrix, which distinguishes the Gauss-Newton approach from the full Newton approach, and the right-hand side is the vector of the gradient of the objective function (Φ^{n}).

The solution of the matrix equation shown in equation 4.24 is achieved by using GMRES, an iterative solver from SPARSKIT (Saad, 1990) that uses a dual-threshold incomplete LU factorization at every GN iteration. The advantage of using SPARSKIT is that it provides better convergence (Jahandari and Farquharson, 2017). Also, the direct solver MUMPS (Amestoy et al. 2006) is used at each iteration for the LU factorization of K (see equation 4.7) at all frequencies for forward problems and pseudo-forward problems to compute the product of the Jacobian with a vector (Jahandari and Farquharson, 2017).

4.6. Summary

In this chapter, the fundamental theories behind the forward modelling and the inversion of the AMT data are explained. Furthermore, the modelling software and the mesh generation open-source code are introduced.

The forward modelling consists of creating a geological model and calculation of the AMT data mathematically. In contrast, inversion is a mathematical way of estimating model parameters. Several techniques can be used for inversions, such as the steepest descent or the GN method. In this study, the inversion code is based on minimum-structure inversion. Although rectilinear grids are widely used in the inversion, the unstructured tetrahedral grids are used in the present study.

5 Results

5.1. Introduction

In this chapter, the details of the modelling and inversion done on the McArthur River AMT data-set will be explained. Additionally, the apparent resistivity and phase fit of the measured and the calculated data will be examined. For the initial forward modelling, as mentioned previously, the synthetic model of the study area was created using FacetModeller (Lelièvre et al., 2018), and meshes were generated with the help of TetGen (Si, 2015). This includes creating a simple model that is not fully representative of the McArthur River area and comparing the observed and calculated data. For the inversion step, the creation of the model follows the same procedures as in the forward modelling except for considering the geological structures, i.e., unconstrained inversion. The following sections explain the details of the forward modelling and present the plots of the measured data.

5.2. Collected AMT Data and Plots

5.2.1. Collected AMT Data

As mentioned in Chapter 2, previous studies have revealed that a method for imaging deeper parts of the McArthur River mine area was required to delineate the P2 Fault, which dominates the mineralization system in the area. AMT data were collected in 2001 and 2002 by Geosystem Canada Inc. within the scope of the EXTECH-IV (EXploration Science and TECHnology) Project (Craven et al., 2007; Tuncer, 2007).

Previous EXTECH projects had been carried out for other mineral research. In detail, the EXTECH-I and EXTECH-II projects were launched in order to investigate massive sulphide ore bodies in Manitoba and New Brunswick (Tuncer, 2007) in Canada. The third EXTECH project was launched in the Northwest Territories in Canada for gold investigation. The EXTECH-IV Project was undertaken to try to determine the uranium mineralization in the Athabasca Basin. Surveys for the project were mainly carried out in the McArthur river mine area (Tuncer, 2007).

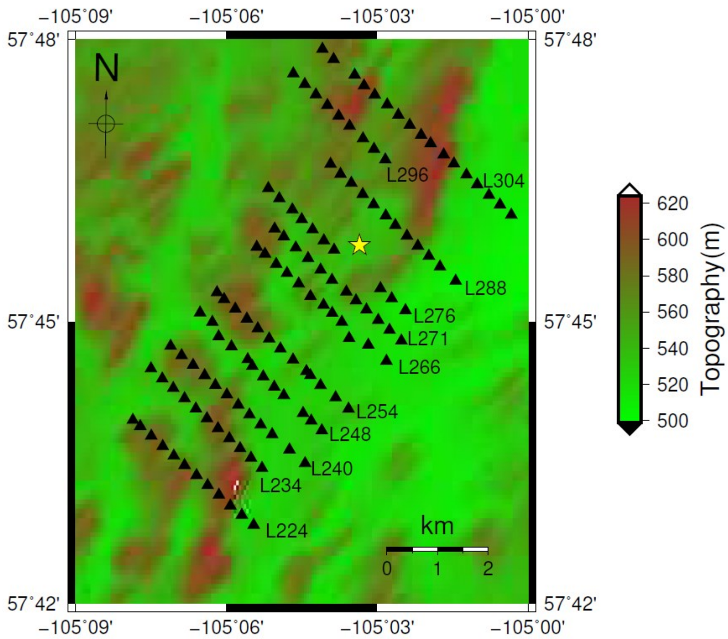

Figure 5.1: A topography map of the study area. (Topography data was downloaded from the Canada Digital Elevation Map website.) Black triangles indicate the AMT sounding locations. The yellow star shows the approximate location of the McArthur River mine.

The 2002 AMT data-set comprised 132 stations on 11 almost parallel profiles crossing the P2 Fault perpendicularly (Figure 5.1). Details of the stations (e.g., latitude, longitude, station numbers, and station codes) and another map that shows the stations with their identifying codes are presented in Appendix A. For the data collection, Metronix AMT systems (24-bit ADU-06 acquisition systems) were used. The magnetic fields were measured with sensors of Geosystem Canada Inc. and BF-6 and BF-10 induction coils produced by Electro-Magnetic Instruments (Craven et al., 2007). The profiles were located approximately 800 metres from each other, and the distance between each station is about 300 metres. The length of electric field dipoles was about 50 metres. AMT data coverage in the survey area was designed to allow a fully 3D analysis. The time-series data were recorded with sampling rates of 40,960, 4096 and 256 Hz (Craven et al., 2007). Usable AMT data were obtained over the frequency range of 10,200 – 3 Hz (Craven et al., 2007). To reduce the bias arising from EM noise, the coherent time-series segments were automatically selected for robust analysis. An iterative re-weighting scheme was used to provide a robust estimate of the apparent resistivities and phases (Larsen et al., 1996).

5.2.2. Plots: Apparent Resistivity and Phase (TE & TM Only)

AMT data were available in the form of impedances and in the standard NS-WE coordinate system. The apparent resistivity and phase values of the collected AMT data were calculated for frequencies between 10^4 Hz and 3.812 Hz. In this sub-section, the results of these calculations are presented as plots of apparent resistivity (in log scale) and phase versus logarithmic periods. The data were rotated into the geoelectric strike direction (which was stated in Tuncer et al., 2006) as N45°E after decomposition; see equations 3.25 and 3.26 for rotation). The apparent resistivity and phase plots for the TE-TM modes for profiles L224, L254, L276 and L304 are presented in Figures 5.2 to 5.5, respectively. Plots for the other profiles can be found in Appendix B. The white gaps in all graphs indicate the data is missing – probably related to the AMT dead band – for the corresponding frequency.

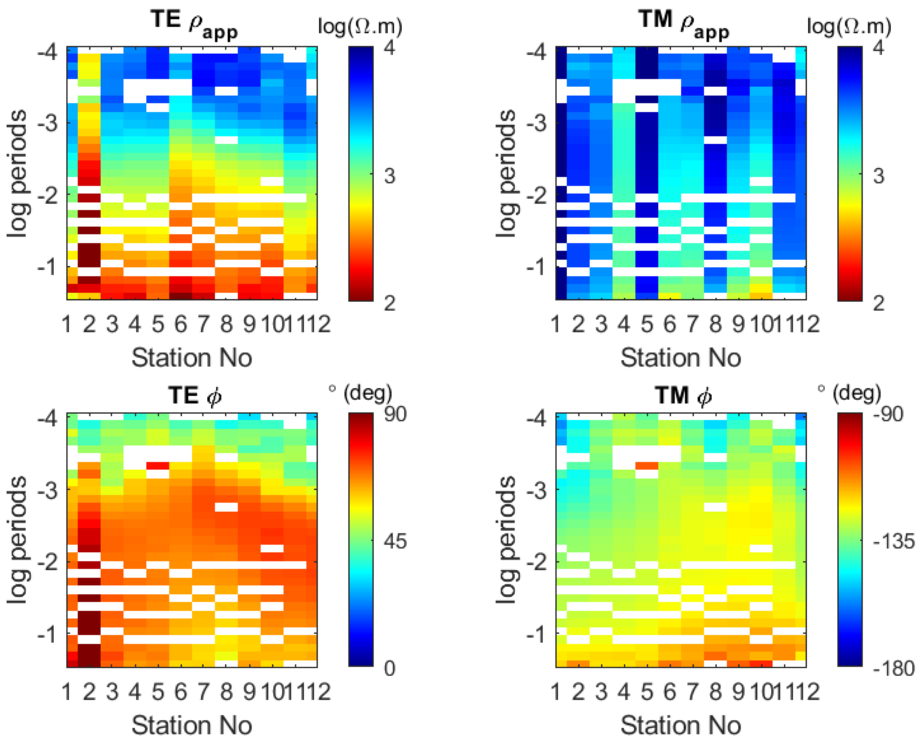

Figure 5.2: Plots of apparent resistivity and phase for profile L224. The left panel corresponds to the TE mode, and the right panels correspond to the TM mode.

In Figure 5.2, the apparent resistivity and phase plots of profile L224 are given for TE and TM modes. At the NW part of profile L224 (the left side of the panels in Figure 5.2), especially in the TE mode plots, high resistivity values at the first station and very low resistivity values around the second station can be observed. The reason for this might be problems in measuring the AMT data, such as static shift. The conductive response of the graphitic fault can be observed around the 6th, 7th and the 8th stations in the TE-mode apparent resistivity graph (red colours, i.e., low resistivities, from middle to long periods).

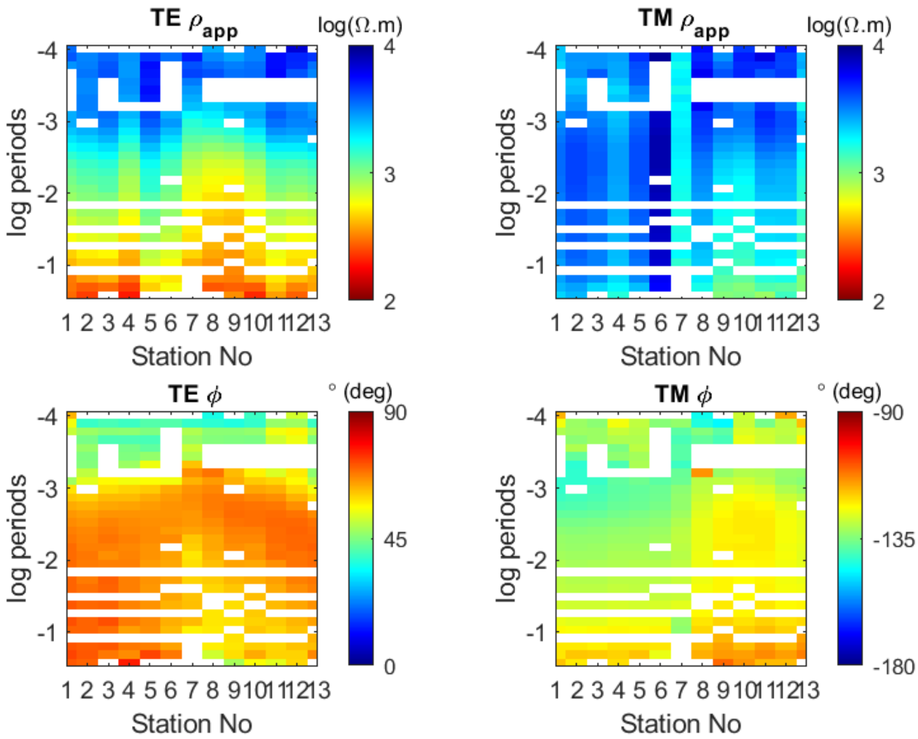

Figure 5.3: Plots of apparent resistivity and phase for profile L254. The left panels correspond to the TE-mode, and the right panels correspond to the TM-mode.

In Figure 5.3, the apparent resistivity and phase plots for profile L254 are given. The low resistivity peak, which might possibly be the response of the conductive graphitic fault, can be observed between stations 7 and 9 in the TE-mode apparent resistivity graph.

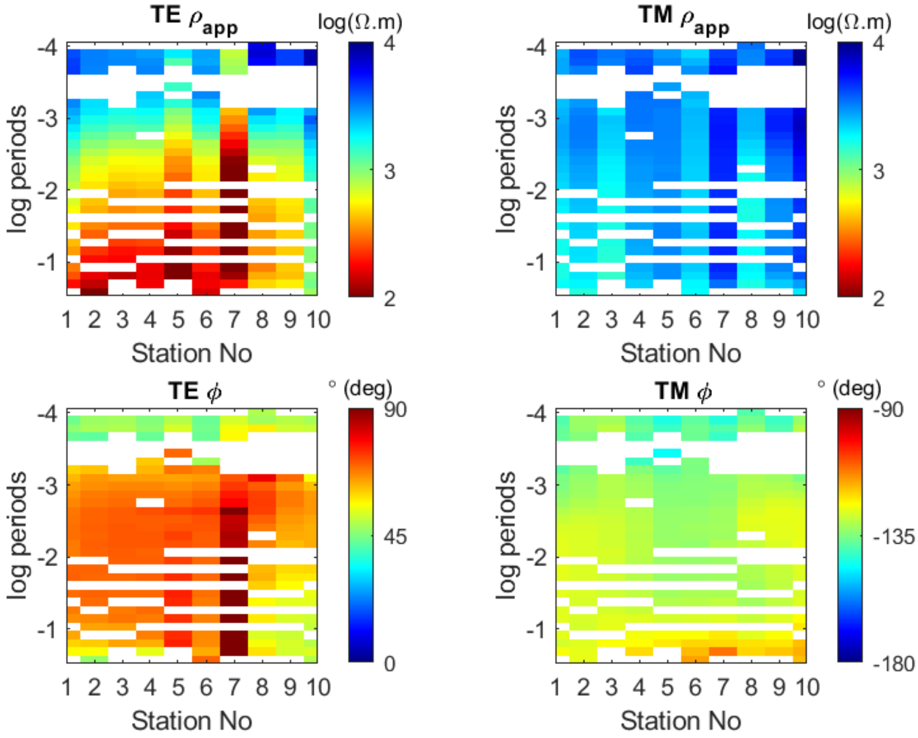

Figure 5.4: Plots of apparent resistivity and phase for profile L276. The left panels correspond to the TE mode, and the right panels correspond to the TM mode

Figure 5.4 shows the apparent resistivity and phase graphs of profile L276. For this profile, it is hard to identify any response of the graphitic fault. However, considering the trend of low resistivity values, the lowest values for the apparent resistivity are centred around the 7th station.

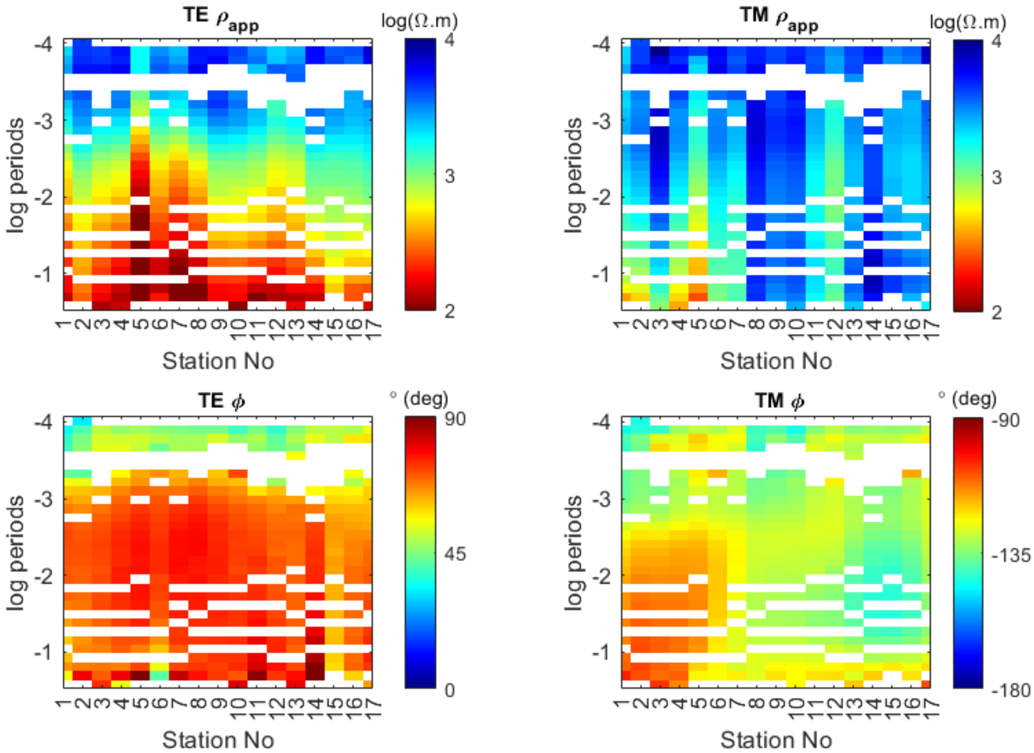

Figure 5.5: Plots of apparent resistivity and phase for profile L304. The left panels correspond to the TE mode, and the right panels correspond to the TM-mode.

According to the TE-mode plots of profile L304, presented in Figure 5.5, the possible location of the P2 Fault might be around the 4th and 5th to 7th stations. This response in the TE-mode plot might be evidence that the fault has shifted to the northwestern side of the study area or has another main branch to the southwest of the mining camp.

To conclude, all apparent resistivity and phase plots, and the induction arrow map presented in Tuncer et al. (2006), show consistent results regarding the fault location. The combination of these sources of information and what is known from previous studies (Chapter 2) is used to create a geological model that is used as the basis for forward modelling the AMT data. Details of the model and results are presented in the following section (Section 5.3).

5.3. Forward Model and Results

5.3.1. Forward Model

In this sub-section, the details of the earth model for forward modelling and the AMT responses computed for it are presented. To create a proper model of the McArthur River area, the first step was representing the schematic cross-section of the area (Figure 5.6). FacetModeller was used for constructing a 3D geological model of the study area.

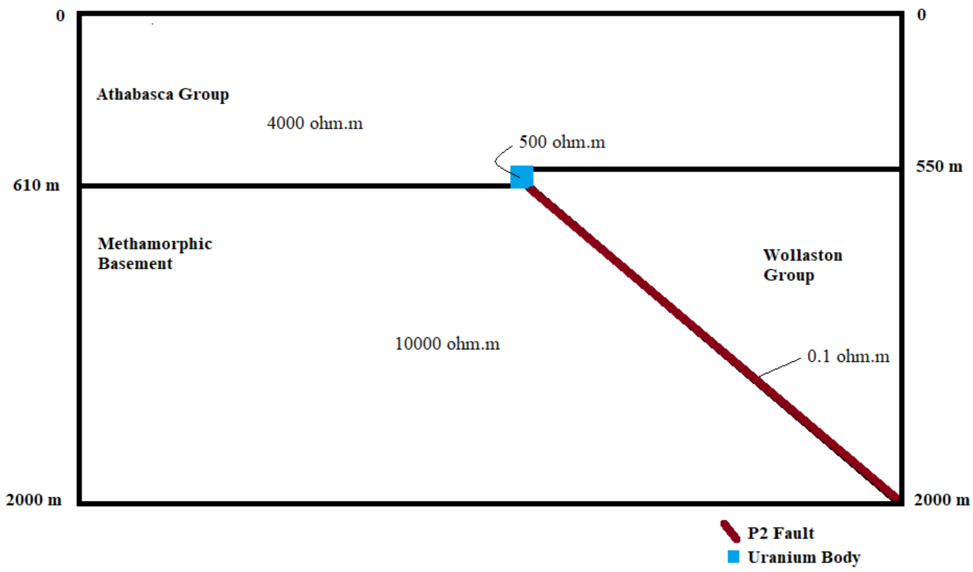

Figure 5.6: Schematic cross-section of the study area. (Modified from Tuncer et al., 2006; Tuncer, 2007; Farquharson and Craven, 2009.)

In the present study, the fundamental aim of the forward modelling was obtaining the geophysical response of the P2 Fault rather than the uranium body, although the uranium ore-body is embedded in the model. Because the main target of the study was delineating the graphitic fault in the area, the branches of the P2 Fault are modelled following the induction arrow (tipper) map presented in Tuncer et al. (2006). In essence, the reversals of these arrows indicate the variation in the conductivity. Therefore, these reversals are thought to be the fault indicators in the present study. The original version of the induction arrow map and the one showing the reversal locations, which are also assumed to be possible fault locations, are presented in Figure 5.7.

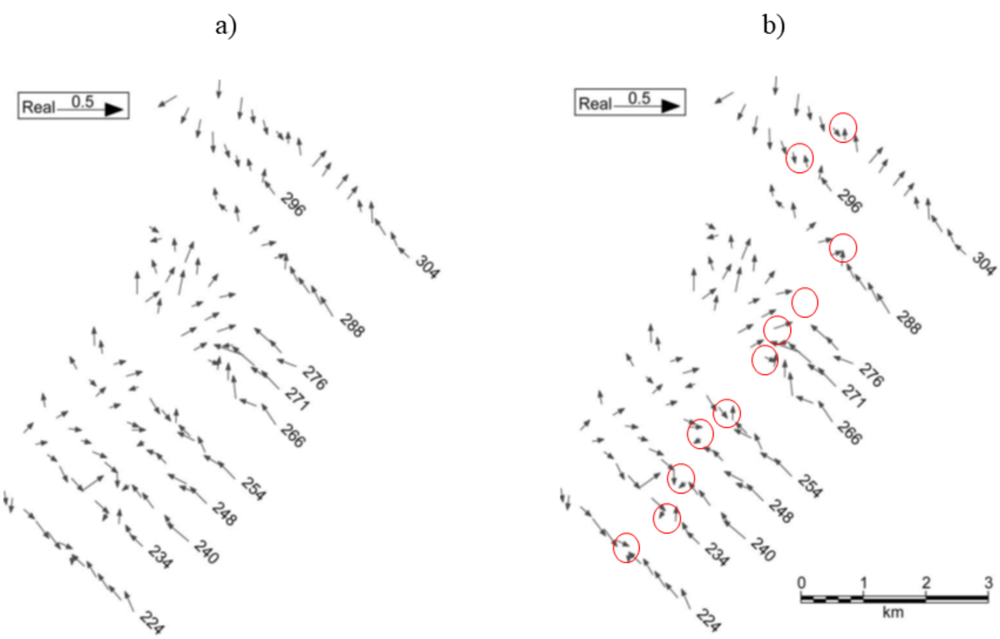

Figure 5.7: Induction arrow maps of the study area (modified from Tuncer et al., 2006). a) Induction arrow map of the measured data at 100 Hz. b)The same map with red circles showing the reversals indicating the possible location of the graphitic fault (P2 Fault).

The geological model (e.g., forward model) mentioned above consists of different geological structures. These geological structures are embedded in the homogeneous half-space following the previous studies. Views of the models are presented from different perspectives in Figure 5.8. Because of the requirements of the modelling scheme, the total vertical extent of the computational domain (from the top of the air layer to the bottom of the earth layer) was 40 km, and its extents in both Northing and Easting directions were 35 km for the half-space (see Figure 5.8.a). The P2 Fault aligns approximately N45E°, having a dip between 45°-65° to the southeast, according to the technical report published by Cameco Corporation in 2018. In the forward model, the dip of the fault was assumed to be 60 degrees. A conductivity of 10^{-8} S/m was used as the conductivity value for the air layer, and 10^{-2} S/m was used for the homogeneous half-space (earth) conductivity. For the geological units near the surface, the overburden layer was not considered because its thickness caused an unnecessarily large number of cells in the mesh. That is to say, the top portion of the model was assumed to be the Athabasca Group layer having a uniform resistivity (or conductivity) value (see Figure 5.6). The next step was creating tetrahedral grids with the help of TetGen (Si, 2015).

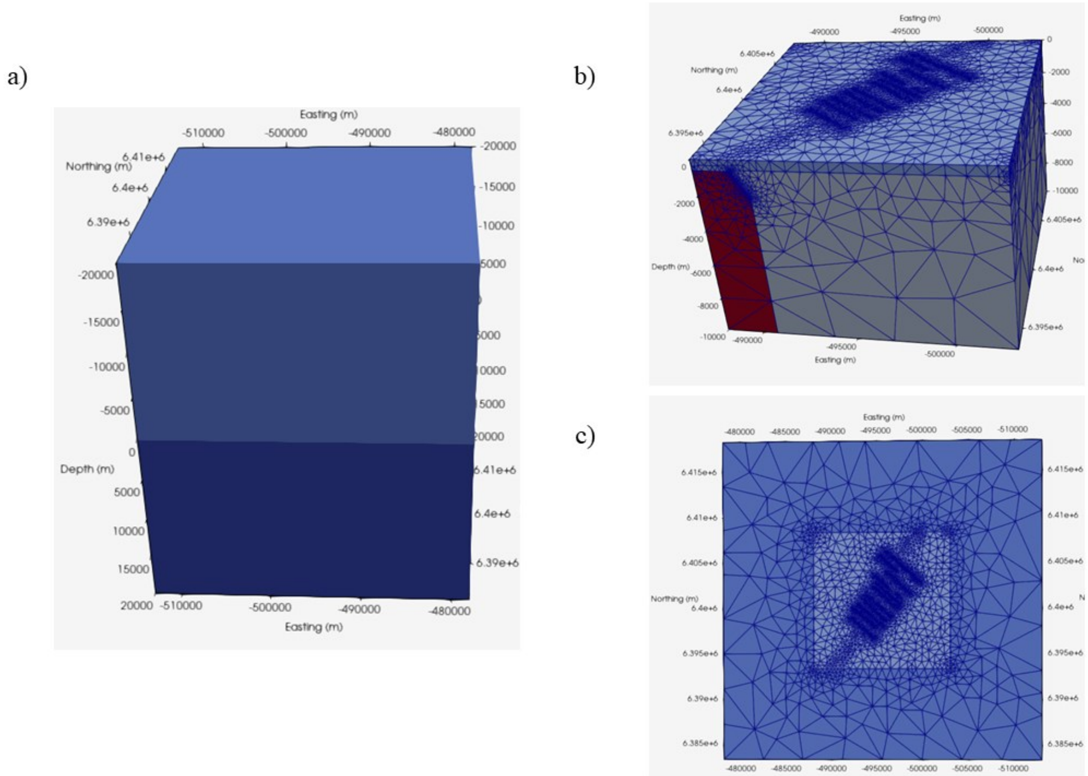

Figure 5.8: Different views of the forward model. a) The model with the outer shell, in which the dark blue portion corresponds to the homogeneous half-space (earth), and the lighter blue part corresponds to the air layer. b) The area of interest of the model, where refinements at the top indicate the AMT sounding locations, and the refinement on the front side corresponds to the P2 Fault. c) Horizontal slice through the mesh and model at the earth-air interface.

In Figure 5.8.b, the triangles on the surface correspond to the edges of the tetrahedra in the unstructured tetrahedral mesh. On the top of the model, refinements indicate the AMT sounding points. On the front side, the dip of the fault can be observed, and the alignment of the two possible branches of the P2 Fault can be followed at the surface. Figure 5.8.c is the cut of the model shown in Figure 5.8.a at the

Earth's surface (the boundary between the light and dark blue in Figure 5.8.a), which shows the Earth's surface (from above) in the area of interest.

A transparent view of the area of interest is shown in Figure 5.9. In this figure, the inner part of the model from the top-view is demonstrated using the "wireframe" option of Paraview. The lighter blue triangles in Figure 5.9 belong to the Athabasca layer – the transparent one – and the AMT sounding points on the top of it. The darker blue triangles belong to the P2 Fault (the one tessellated with dark blue triangles), Wollaston Group (right-hand side of the model view) and the metamorphic basement (the part with burgundy colour; see Figure 5.6).

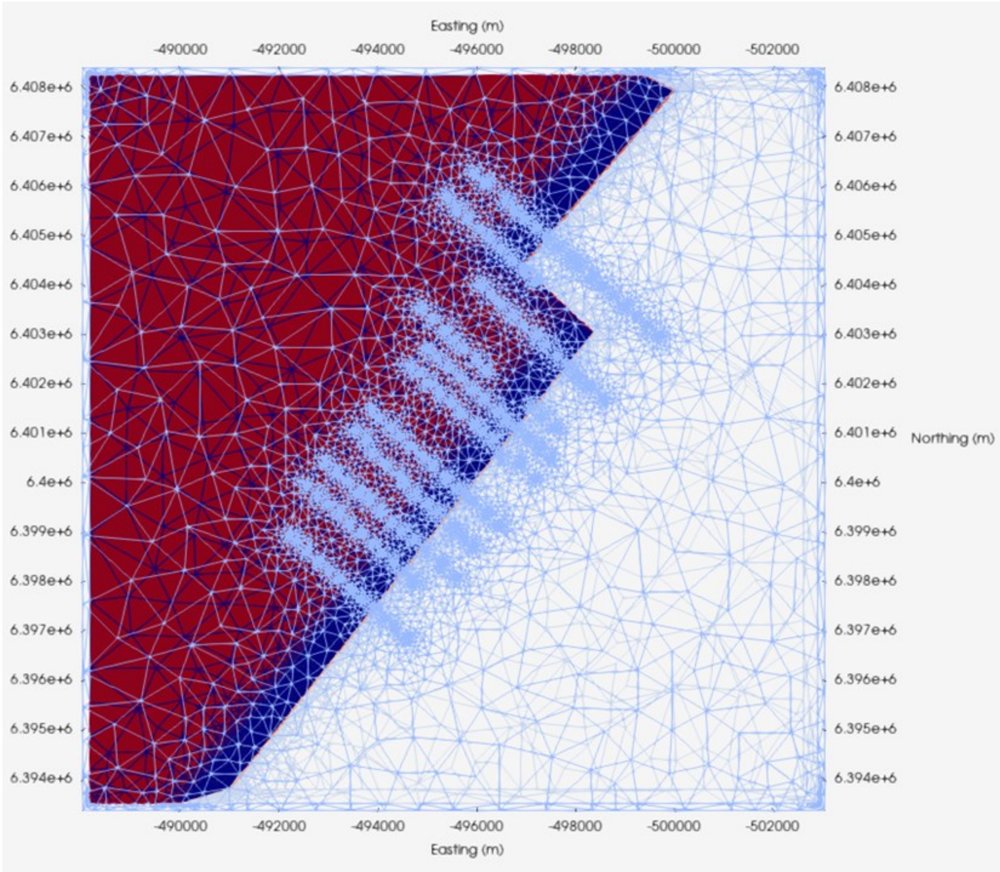

Figure 5.9: A transparent view of the area of interest. The lighter meshes belong to the Athabasca layer and the refinements around the AMT sounding points. The darker meshes belong to structures located below this layer.

For the forward modelling, if the fault zone is extended down to the full depth of the volume of interest, the total number of cells becomes large and the memory required by the forward modelling problematic. This issue directly affects the memory use during calculations and hence calculation time. Because of this reason, the P2 Fault is truncated at a depth of 2 km, whereas the area of interest (Figure 5.8.b) extends to a depth of 10 km. The area of interest extends 15 km in both Easting and Northing directions. The total number of mesh tetrahedra for the volume of interest is 353,015. It is 448,585 for the whole model presented in Figure 5.8.a. As mentioned in Chapter 4, the forward modelling code mentioned in Jahandari and Farquharson (2017) is used for forward calculation. The calculation time on a node with 16 GB of RAM in Torngat, which is a cluster including some computing nodes and those nodes include several CPUs for geophysical studies, for one frequency was approximately 25 minutes for this model.

5.3.2. Results of Forward Modelling: Apparent Resistivity and Phase Plots (TE-TM Only)

The apparent resistivity and phase values from the forward modelling were calculated from the computed impedances for 31 frequencies between 10^3 Hz and 3.812 Hz. The frequency list is presented in Table 5.1. For the modelling, the most common frequencies across the stations were used as much as possible. As in the plots of the measured AMT data, the results of these calculations are presented as the plots of apparent resistivity (in log scale) and phase versus logarithmic periods. The electric and magnetic field values were computed in the NS-WE coordinate system and the impedances first calculated in this coordinate system. Then, the impedances were rotated as mentioned in the theory chapter (see equations 3.25, 3.26). After rotating the impedances to the geoelectric strike direction (N45°E), the apparent resistivity and phase plots for the TE and TM modes were calculated. These apparent resistivities and phases for profiles L224, L254, L276 and L304 are presented in Figures 5.10 to 5.13, respectively. Plots of the other profiles can be found in Appendix B.

Table 5.1: List of frequencies used for the forward modelling

Number	Frequency (Hz)	Number	Frequency (Hz)	Number	Frequency (Hz)
1	10240.0	11	336.00	21	41.000
2	7680.0	12	244.00	22	32.750
3	5120.0	13	177.00	23	31.000
4	3840.0	14	128.00	24	22.250
5	2560.0	15	97.000	25	21.000
6	1920.0	16	81.000	26	15.120
7	1280.0	17	71.000	27	11.000
8	960.00	18	61.000	28	10.250
9	640.00	19	51.000	29	6.9370
10	464.00	20	48.250	30	4.8750
				31	3.8120

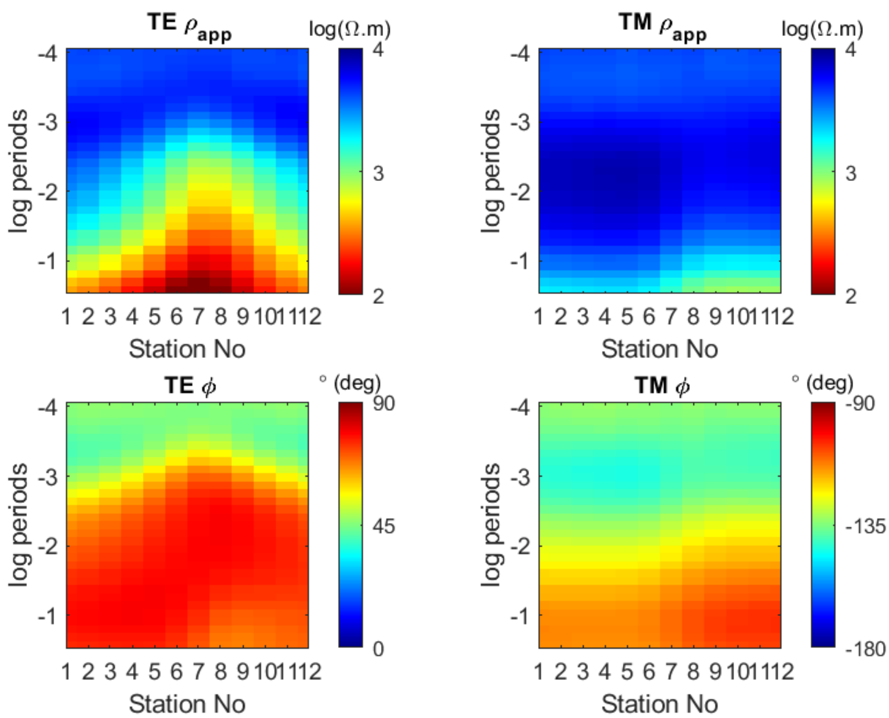

Figure 5.10: Plots of calculated apparent resistivity and phase for profile L224 over the model in Figures 5.8 and 5.9. The left panels correspond to the TE mode, and the right panels correspond to the TM mode.

In Figure 5.10, the apparent resistivity and phase plots of the forward modelled data along profile L224 are demonstrated for TE and TM modes. As expected, the conductive response of the graphitic fault can be observed between stations 6 to 10 in the apparent resistivity graph of the TE mode.

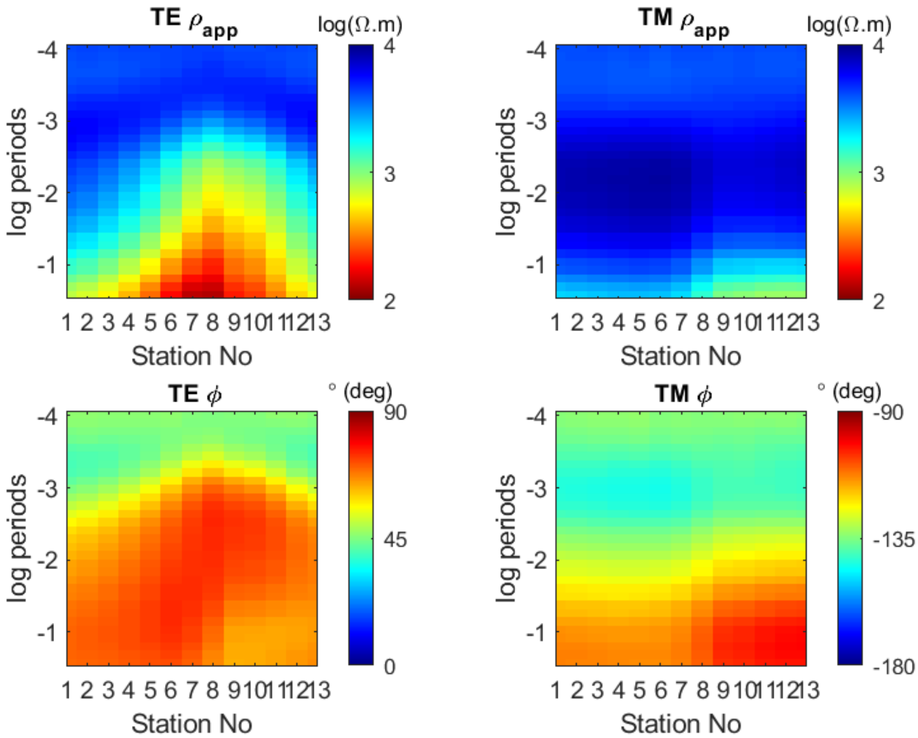

Figure 5.11: Plots of calculated apparent resistivity and phase for profile L254 over the model in Figures 5.8 and 5.9. The left panels correspond to the TE mode, and the right panels correspond to the TM mode.

In Figure 5.11, the apparent resistivity and phase plots of the forward modelled data along profile L254 are demonstrated for the TE and TM modes. The low resistivity peak between stations 7 and 9 in the apparent resistivity graph of the TE mode indicates the P2 Fault.

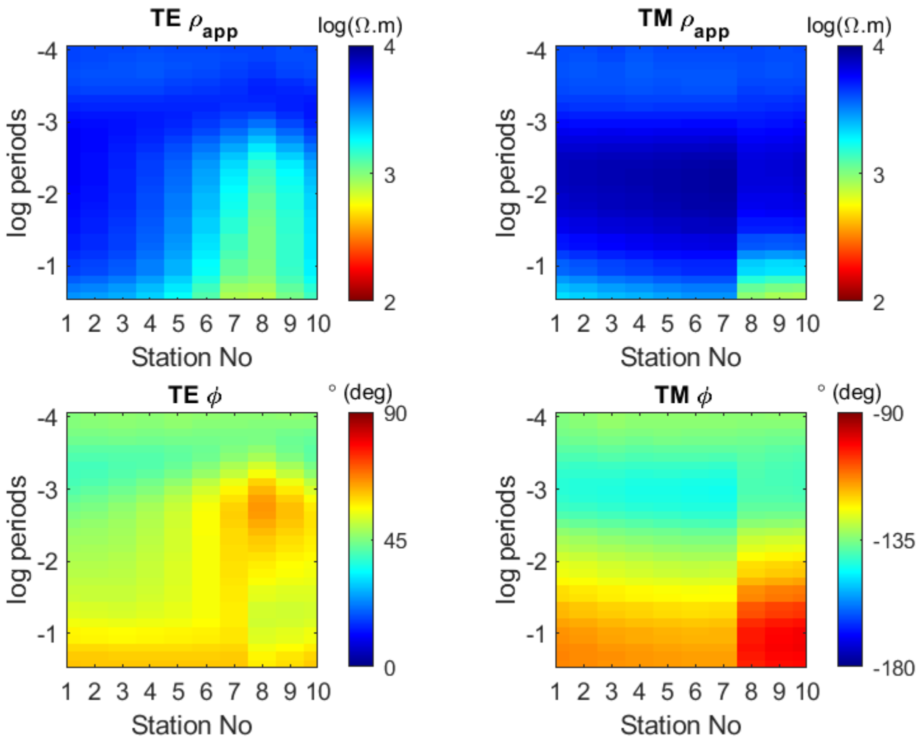

Figure 5.12: Plots of calculated apparent resistivity and phase for profile L276 over the model in Figures 5.8 and 5.9. The left panels correspond to the TE mode, and the right panels correspond to the TM mode.

Figure 5.12 shows the apparent resistivity and phase graphs of the synthetic data for profile L276 for the TE and TM modes. For this profile, the low resistivity values are concentrated around the 7th and 8th stations. The movement of the low apparent resistivity values towards the right-hand sides of these plots makes sense given the location of the fault in the model. In the TE-mode window of Figure 5.12, the data for stations 7–10 look different from the others. This is related to the station coverage, i.e., the gap between stations in Figures 5.1 and 5.9. Similarly, the effect of the gap between the sixth and the seventh stations of the profile L276 can be observed in the TM-mode apparent resistivities after the seventh station.

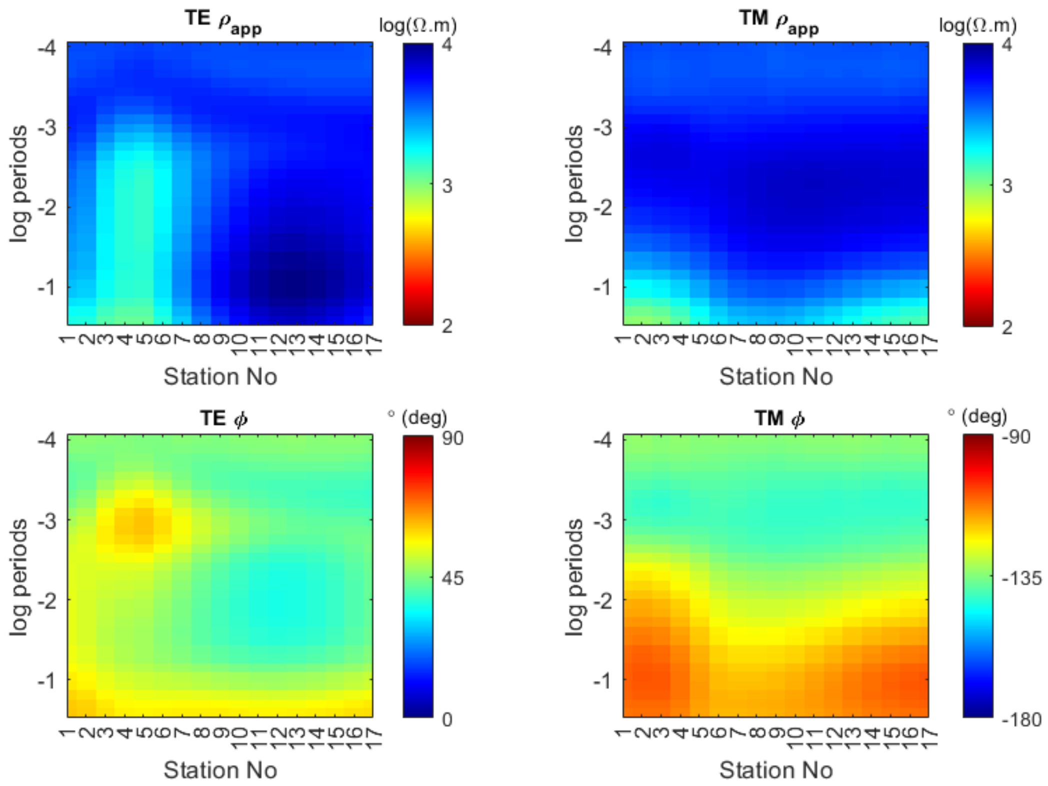

Figure 5.13: Plots of calculated apparent resistivity and phase for profile L304 over the model in Figures 5.8 and 5.9. The left panels correspond to the TE mode, and the right panels correspond to the TM mode.

According to the TE mode plots of the synthetic data for profile L304 presented in Figure 5.13, the apparent resistivities have the lowest values between the 3rd and the 7th stations. Moreover, a phase anomaly has occurred at middle-to-short periods for these stations. These greater apparent conductivities, and the elevated phases, are indications that the fault has shifted to the northwestern side of the study area (after profile L276, see Figure 5.1).

To conclude, the representative geological features, which are also main geoelectric structures of the McArthur River area, were considered for the forward modelling. Then, the responses, apparent resistivities and phases, were calculated. The plots presented in this sub-section show these responses with respect to the periods. Responses in these figures indicate the anomalies created by the dipping P2 Fault in the created model.

5.4. Comparison of Collected Data and the Forward Model Results

The forward model of the study area was built considering the geological features presented in previous studies, such as Tuncer et al. (2006) and Farquharson and Craven (2009). For instance, the alignment of the graphitic fault (P2 Fault) was determined from the induction arrow map presented in Tuncer et al. (2006). Moreover, the schematic cross-section of the subsurface (see Figure 5.1) was created following the cross-section presented in Tuncer et al. (2006) and Farquharson and Craven (2009). It is clear that there is an approximately 50 m step at the bottom of the Athabasca Group from the northwestern and southeastern sides of the fault in the geological model. This step has resulted from the upward movement of the footwall (southeastern block) relative to the northwestern block. As mentioned above, these geological features are considered in the forward model. However, the Athabasca Group is considered one thick layer starting from the surface and extending to a depth of 550 m on the northwestern side of the model and 610 m on the southeastern side.

Plots of the measured data (Figures 5.2 to 5.5) and the results of the forward modelling show consistent results. For instance, the TE and TM mode plots of L224 and L254 show a good agreement on the graphitic fault's possible location. In the phase plots for the TE and TM modes, the general variation of the phase values with respect to the periods is consistent with those in the measured data plots. Although it is not a definitive way of interpreting the geological structure for every AMT-sounding example, the likely place can be interpreted by seeking the dominant low resistivity responses in the apparent resistivity. The consistency between the apparent resistivities and phase values of the forward-modelled and measured data is also good for the profiles L276 and L304. For the same profiles, variations of the phase values, both for the TE and TM modes, also show good consistency with the measured data.

Besides other geological structures in the forward model, the uranium body is added to the model between profiles L276 and L288. However, the response of the uranium body could not be observed either on the measured data or the forward-modelled data. The occurrence of the uranium body might be sought on the plots of profile L276, which is the closest one to the uranium body; it is hard to distinguish its effect on the apparent resistivity and phase plots. The reason for having no uranium body effect on the measured and the forward model plots is that the stations or profiles do not recover the uranium body satisfactorily since the mining camp activity creates an EM noise affecting the AMT data. As a result of this, profiles in the study area have not been located close enough for imaging the uranium body.

In addition to the apparent resistivity and phase plots, the induction arrows for the forward-modelled data were also plotted. In Figure 5.14, the induction arrow map for the forward-modelling results presented in Tuncer et al. (2006) and the equivalent induction arrow map for the forward-modelled data computed in this study are plotted in the same figure for comparison. (The induction arrow plots for the real data are shown in Figures 5.8 and 5.9.)

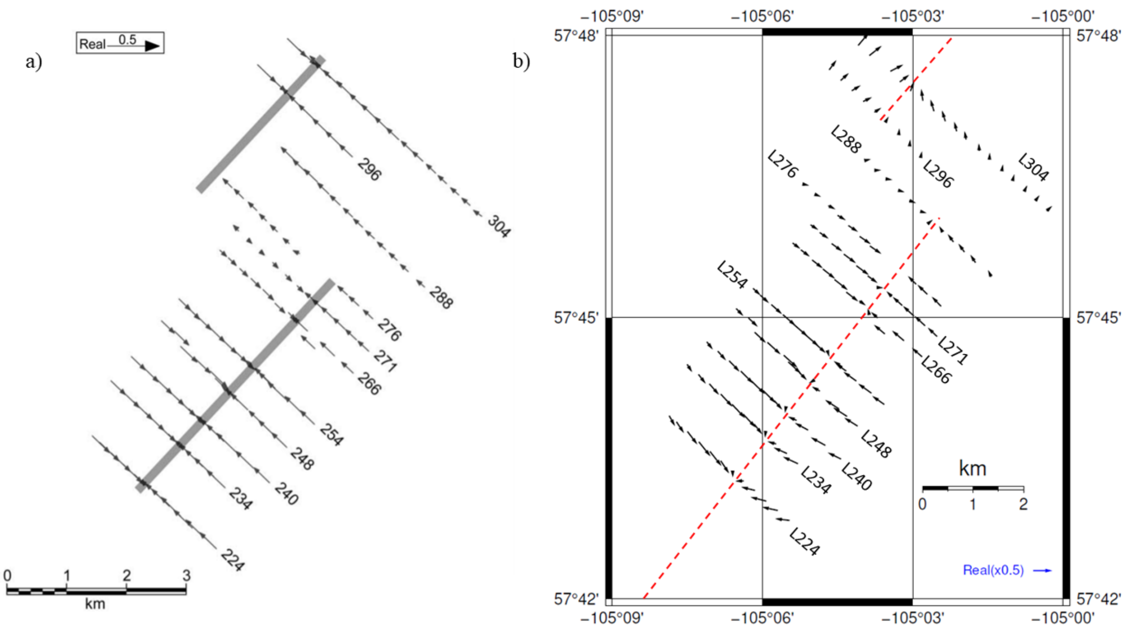

Figure 5.14: a) Synthetic induction arrow map at 100 Hz presented in Tuncer et al. (2006). Grey rectangles indicate the location of the top of the graphitic conductor (P2 Fault). b) Synthetic induction arrow map at 128 Hz (the closest frequency to 100 Hz) in the present study. The red dashed line shows the two segments of the P2 fault in the model considered here.

The synthetic induction arrows for 128 Hz (the closest of the frequencies considered here to 100 Hz) are plotted on Figure 5.14 following the Parkinson convention, in which tips of induction arrows point towards conductive bodies. It can be seen from Figure 5.14 that the two induction arrow maps show slight differences, which is expected due to the differences in the extensions of the graphitic conductors. (In the model presented in Tuncer et al., 2006, the conductor dips steeply to the depth of 2 km, in this study it dips with 60 degrees to the same depth.) It can be inferred from the map presented in Tuncer et al. (2006) that segments of the fault have been truncated around the first and last profiles of the sounding array. However, in the present study, both segments of the P2 Fault are extended to the northeastern and southwestern ends of the model. This is the reason why the induction arrows for the present study show slightly different directions at profiles L224 (very slight difference), L288, L296 and L304 compared to the induction arrows on the map presented in Tuncer et al. (2006). The induction arrows in the remaining profiles point directly to the graphitic conductor, as is the case for the map of Tuncer et al. (2006).

Lastly, the TE and TM mode results shown in Figures 5.2 to 5.5 and from 5.10 to 5.13 show good agreement. In addition to these figures, the ones in the appendices (for all the other profiles) are also similarly consistent. The induction arrow maps show that the response of the graphitic conductor is clear. In the following sections, results of inverting both the forward-modelled data and the real data are given and assessed.

5.5. Inversion Model Details and Results for the Forward-Modelled Data

5.5.1. Introduction

In this sub-section, the details and results of the synthetic data inversion will be presented. The main target for inverting the synthetic data in addition to the inversion of the real data was to understand the behaviour of the code presented in Jahandari and Farquharson (2017), which has been updated by Mitra Kangazian. This inversion enabled the model constructed by the inversion of the synthetic data to be assessed. Once the synthetic data were inverted, the inversion procedure was applied to the real AMT data.

5.5.2. Inversion Model Details

The spatial dimensions of the model created for the inversion procedure were 85×85×60 km in the Northing, Easting and vertical directions. The model consists of four different zones: air layer, the volume of interest, padding zone 1 and padding zone 2 (Figure 5.15). The volume of interest is embedded in the first padding zone, and the starting model can be considered as a homogeneous half-space (earth) layer.

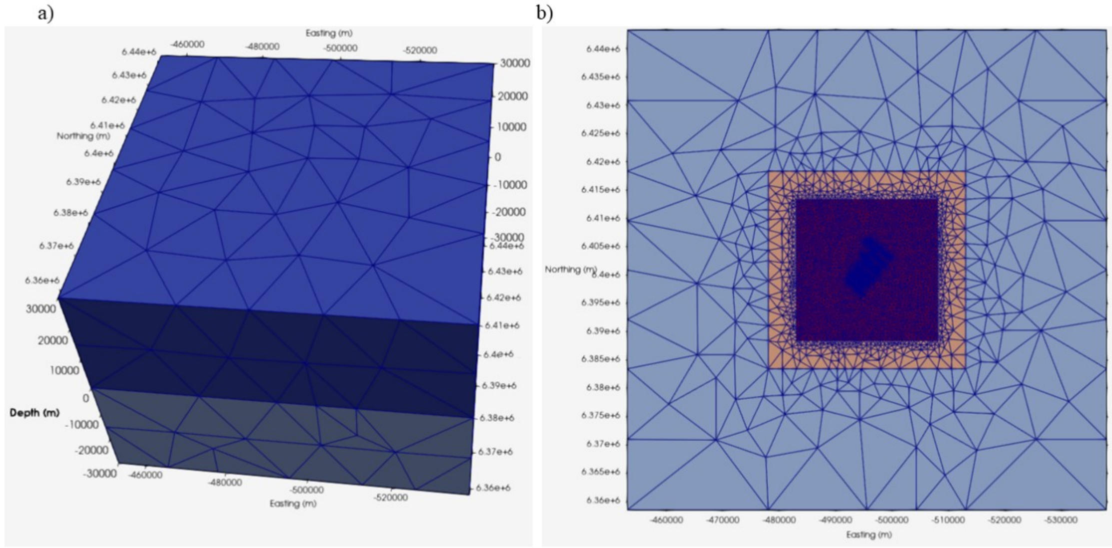

Figure 5.15: The mesh used for the inversion of the synthetic data. a) Outer shell of the model. The darker layer corresponds to the air, and the lighter one indicates the second padding zone. b) Top view of the ground-surface cut of the model. The outer lighter part belongs to the second padding zone, the pinkish beige part is the first padding zone (homogeneous half-space /earth), and the inner burgundy area is the area of interest. Concentrated refinements in the area of interest indicate the AMT sounding locations.

In Figure 5.15.a, the outer shell of the model is presented. The inner part of the model is shown in panel b of the same figure. In both panels, the blue triangles correspond to the unstructured grids. The total number of mesh tetrahedra was 351,372. The mesh was refined in the area of interest in order to have a higher resolution for the solution. Another refinement was applied for the AMT sounding locations (Figure 5.16).

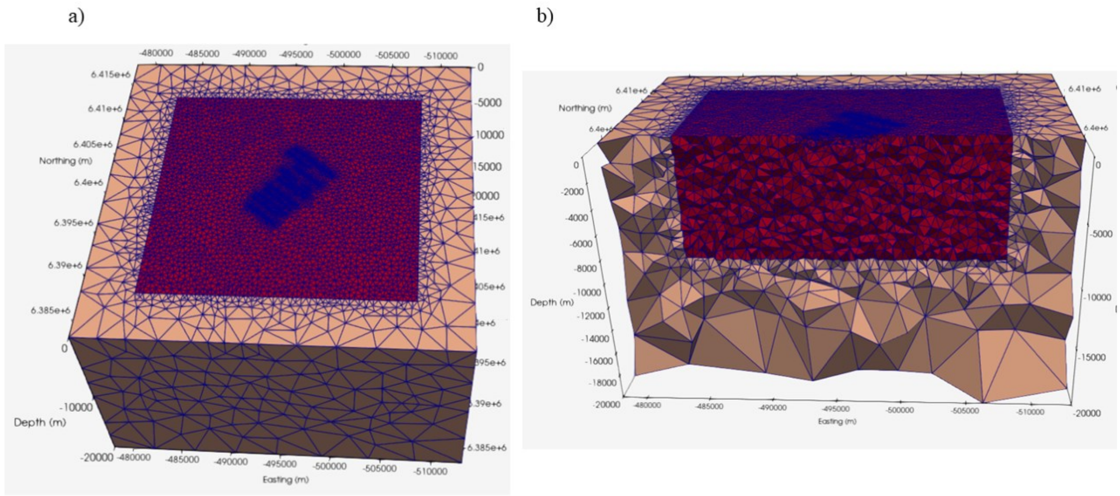

Figure 5.16: The first padding region and the area of interest of the mesh shown in Figure 5.15. a) The burgundy area is the area of interest, and b) is a vertical clipped section through the part of the mesh shown in panel a.

In Figure 5.16, detailed views of the area of interest are presented. The dimensions of the area of interest (burgundy area) are 25×25×10 km in east-west, north-south and vertical directions. The area of interest is also called “the active zone”, where the conductivities of the cells are sought in the inversion. The pinkish beige part corresponds to the earth layer (padding zone 1), which extends 20 km in the vertical direction. In contrast to the burgundy area, this padding zone extends five more kilometres in the east-west and north-south directions. These dimensions were considered to diminish any possible boundary effects. The Earth-air interface is taken to be flat since the topography does not change dramatically in the study area (see Figure 5.1).

5.5.3. Inversion Results for the Synthetic Data

Results of inverting the forward-modelled data discussed in Section 5.4 are presented in this sub-section. Data at ten frequencies were considered: 5120, 1280, 640, 336, 128, 81, 41, 15.12, 6.937, 3.812 Hz. Only impedance tensor elements were considered as the data to invert. That is to say, the magnetic transfer function data were not considered for this inversion. The total number of data for these ten frequencies is 10,560. Gaussian noise with zero mean and standard deviations of two percent was added to the synthetic data. The code introduced in Jahandari and Farquharson (2017) was used for the inversion and run until the target misfit was reached. The final data misfit for the solution was 10,559.21, corresponding to a normalized misfit equal to 0.99 (10559.21/10560). For Gaussian data errors the standard-deviation-normalized misfit should of course be chi-squared distributed, and since the expectation value of chi-squared for large data number is approximately equal to n, the misfit should also be close to the number of data n. This number satisfied the mentioned relationship.

For the inversion of the synthetic data, the initial and reference models were the same, corresponding to a homogeneous half-space of 10^{-2} S/m (and an air layer of 10^{-8} S/m). The inversion code allows the user to choose the cooling schedule. For this inversion, the starting value of the trade-off parameter was picked as 1E+3, with the trade-off parameter levelling off once it reached 2.5E-3. Until levelling off, the cooling parameter was 0.9. The levelling-off of the trade-off parameter is an attempt to get to the value of the trade-off parameter that is going to result in the misfit we want.

Figure 5.17 shows the variations of the trade-off parameter, model smallness and roughness parameters, the data misfit and the objective function for the given cooling parameter (which was 0.9 in this inversion). As can be seen from the figure, the data misfit and the overall objective function decrease smoothly and steadily while the model parameters show an increase iteration by iteration. The main idea behind these curves is their steady, stable progression. This means that excessive structure has not been introduced into the model too early in the iterative process and that by the end of the iterative procedure, the inversion has converged to the solution of the optimization problem.

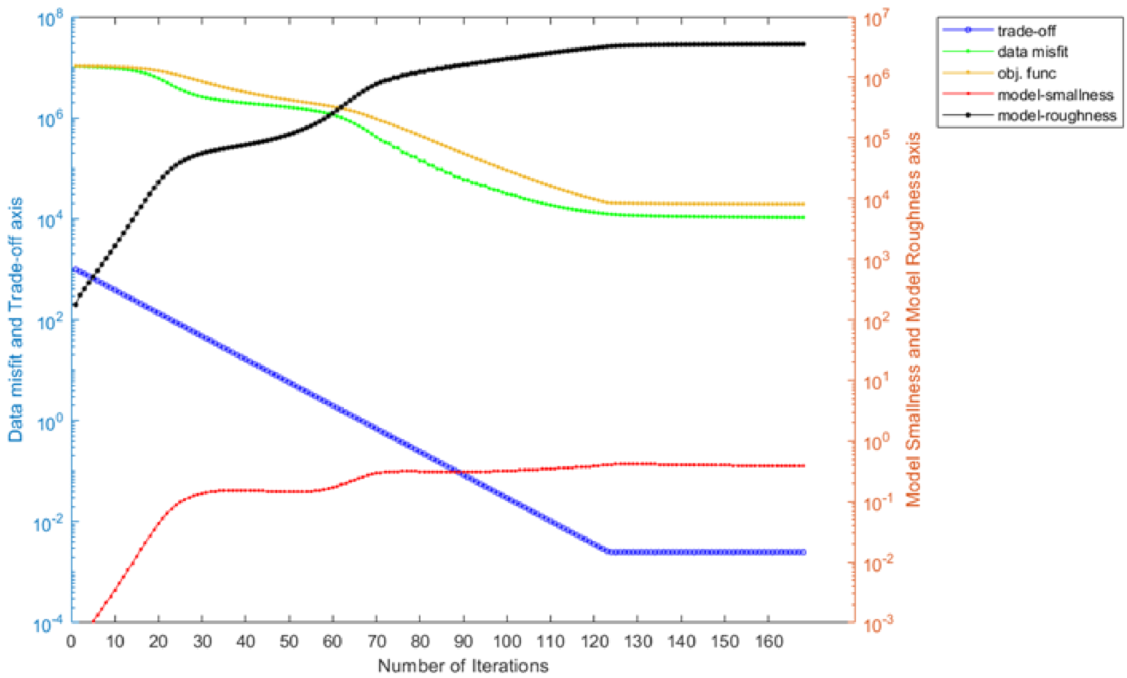

Figure 5.17: Convergence curves for the synthetic data inversion. The curves correspond to the data misfit, objective function and model parameter variations with respect to iterations for the given cooling parameter (0.9). The left vertical axis is for the data parameters, and the right vertical axis is for the model parameters.

Plots of the noisy synthetic data going into the inversion and the calculated impedance data for the model constructed by the inversion are presented in Figure 5.18 for an arbitrarily selected station. In these plots, the data are normalized by the square root of the angular frequency to remove the intrinsic trend with frequency present in the impedances, and to give a meaningful curve similar to apparent resistivity curves. The equivalent plots for the other stations can be found in Appendix C. The graphs are plotted considering the data at all the frequencies used in the inversion. The error bars in the plots indicate the standard deviation of the noise added to the data. In general, the calculated data show a satisfactory agreement with the synthetic data at all stations.

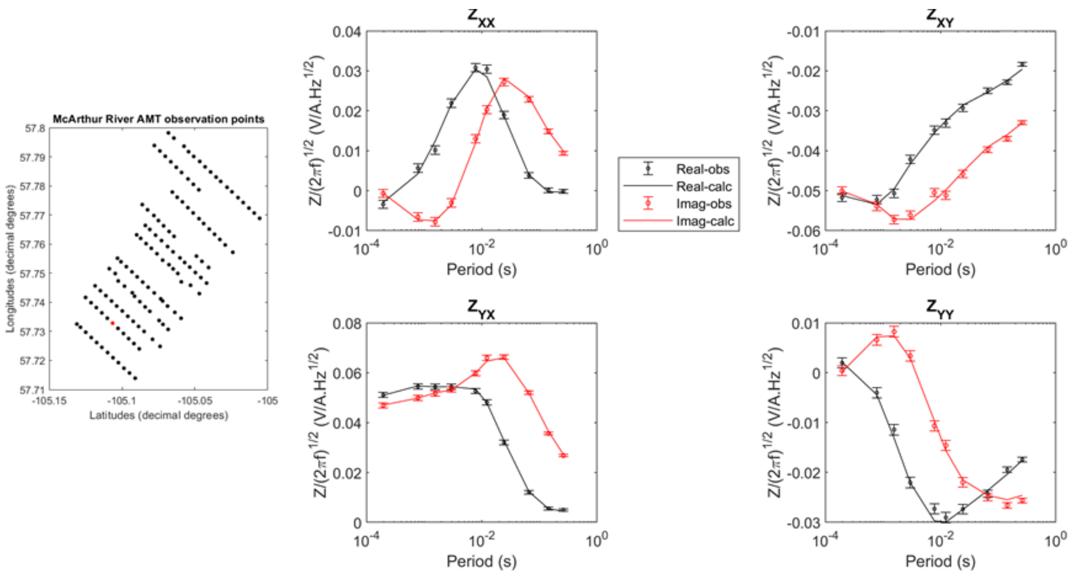

Figure 5.18: Data-fit curves of the impedance, in NS-EW coordinate system, data at ten frequencies for station 13 (the red dot on the left-hand side). Error bars indicate the standard deviation of the noise added to the synthetic data. The lines show the calculated data for the final inversion model. Black and red colours indicate the real and imaginary parts of the impedance data.

In Figure 5.19, the fits in terms of the apparent resistivity and phase values are shown for the TE and TM modes in addition to the impedance plots presented in Figure 5.18. The corresponding curves for the other stations can be found in Appendix C. These graphs are also plotted considering the data with respect to all periods used in the inversion. Reassuringly, the data, when viewed in terms of apparent resistivities and phases also show a good agreement.

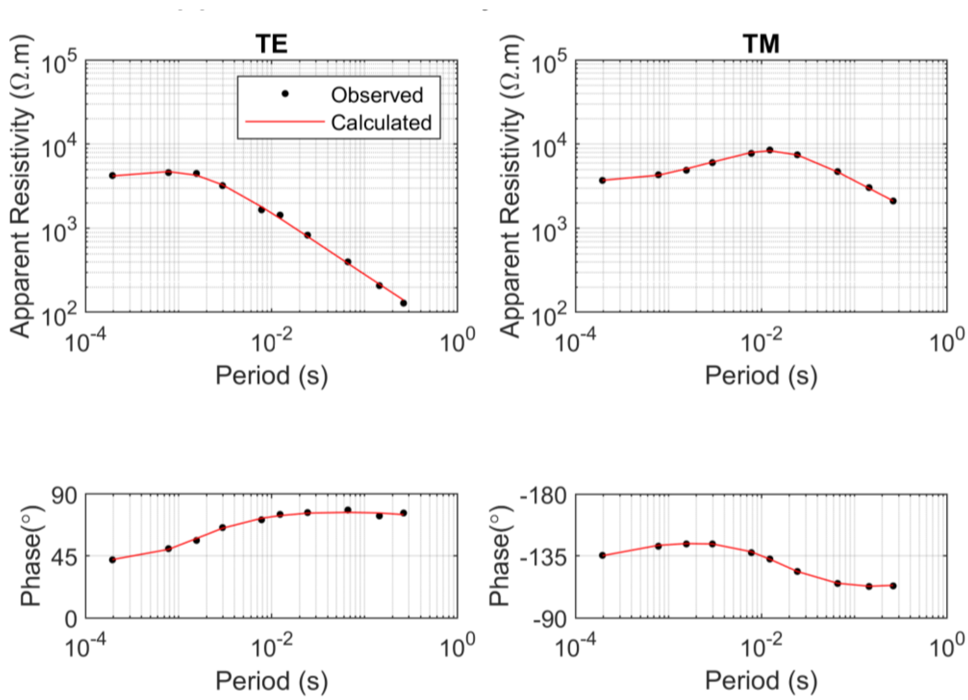

Figure 5.19: Data-fit curves in terms of apparent resistivity and phase at ten frequencies for station 13 (see Figure 5.18 for the station location). Lines indicated calculated data for the final model. The dots indicate the (noisy) synthetic data going into the inversion. Black and red colours indicate real and imaginary parts.

Vertical cross-sections through the final inversion model along every profile are shown in Figure 5.20. The maximum depth of the cross-sections is 2 km. (The depths of the active zone and padding zones are not shown.) For this inversion, it took almost 30 minutes to solve one iteration, and the total time to finish the inversion was approximately 85 hours.

In all cross-sections presented in Figure 5.20, conductive regions are present at the locations of the P2 Fault in the true model. The small, shallow, somewhat conductive bodies might be artifacts because of the noise in the data or a consequence of a lower frequency than ideal for imaging the near-surface. However, the resolution of the solution and the replication of the synthetic P2 Fault is satisfactory; the conductor seems to be a blob in the minimum structure inversions instead of a thinner conductive fault zone – the dip of the fault is observable in almost all vertical cross-sections. Given these results, observing a clear indication of the P2 fault is expected from the real data inversions.

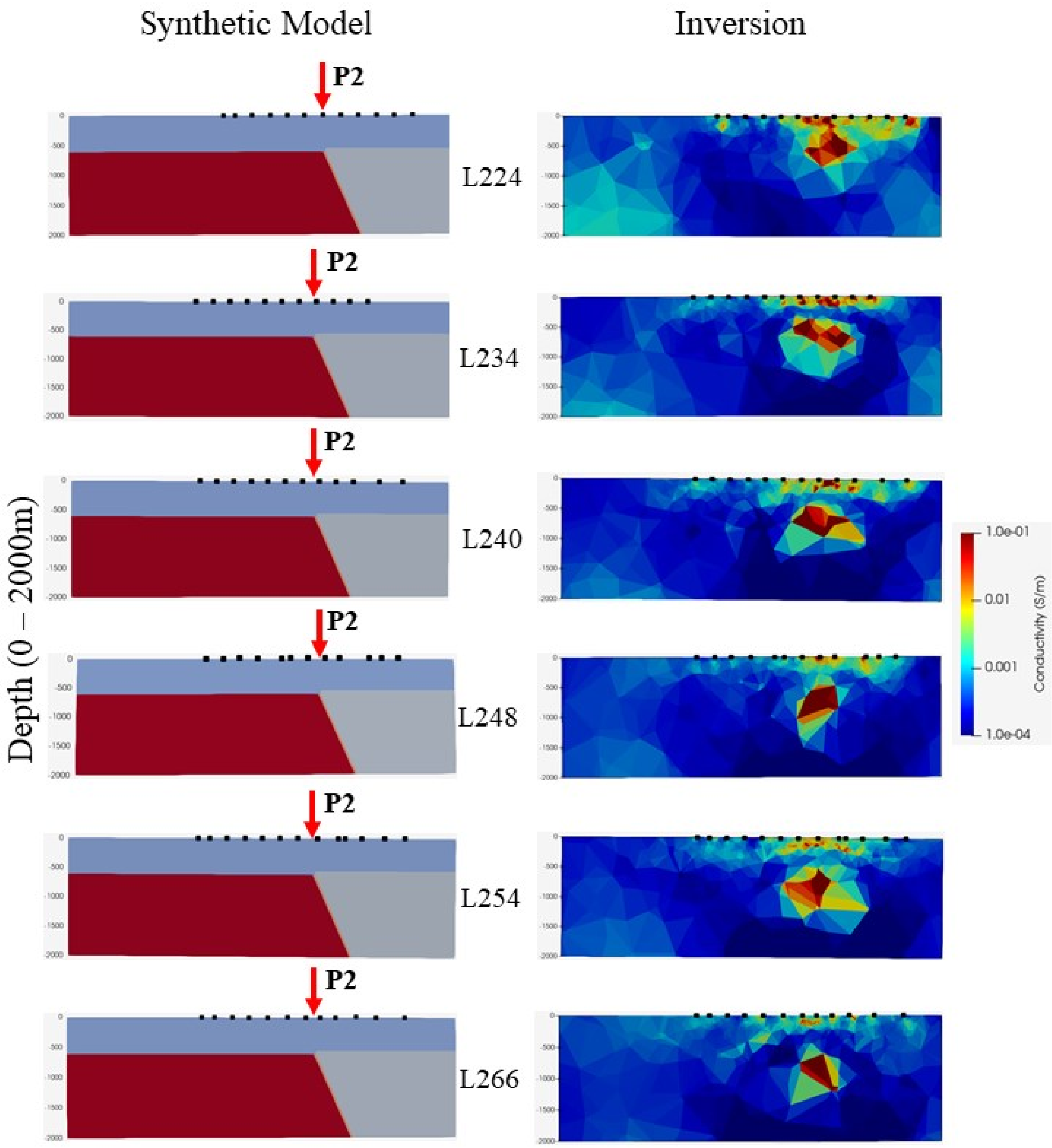

Figure 5.20: Left panel shows the vertical cross-sections of the synthetic model, and the right panel shows the final inversion model for the synthetic data (first 6 profiles). Black dots show the AMT-sounding locations in both panels. The red arrows indicate the P2 Fault in the synthetic model.

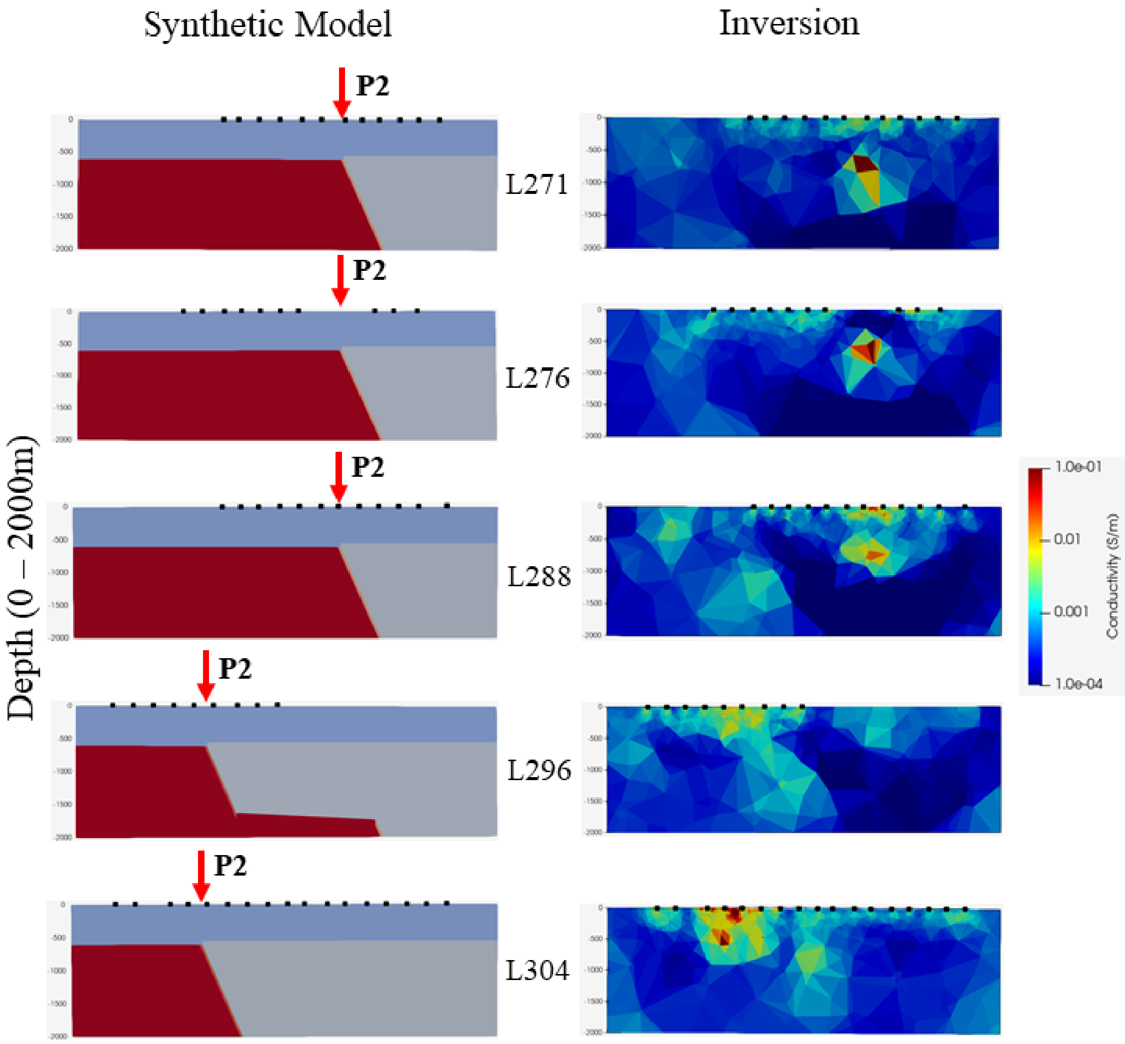

Figure 5.21: Figure 5.20 continued (last five profiles). The left panel shows the vertical cross-sections of the synthetic model, and the right panel shows the final inversion model for the synthetic data. Black dots show the AMT-sounding locations in both panels. The red arrows indicate the P2 Fault in the synthetic model.

Horizontal slices from the final inversion model are shown in Figure 5.21. These slices represents four different depths from top to bottom. As can be seen from the figure, SW-NE oriented responses can only be observed on the surface slice. The slices of deeper parts (Z=500,750, and 1000) involve only the response of the graphitic conductor.

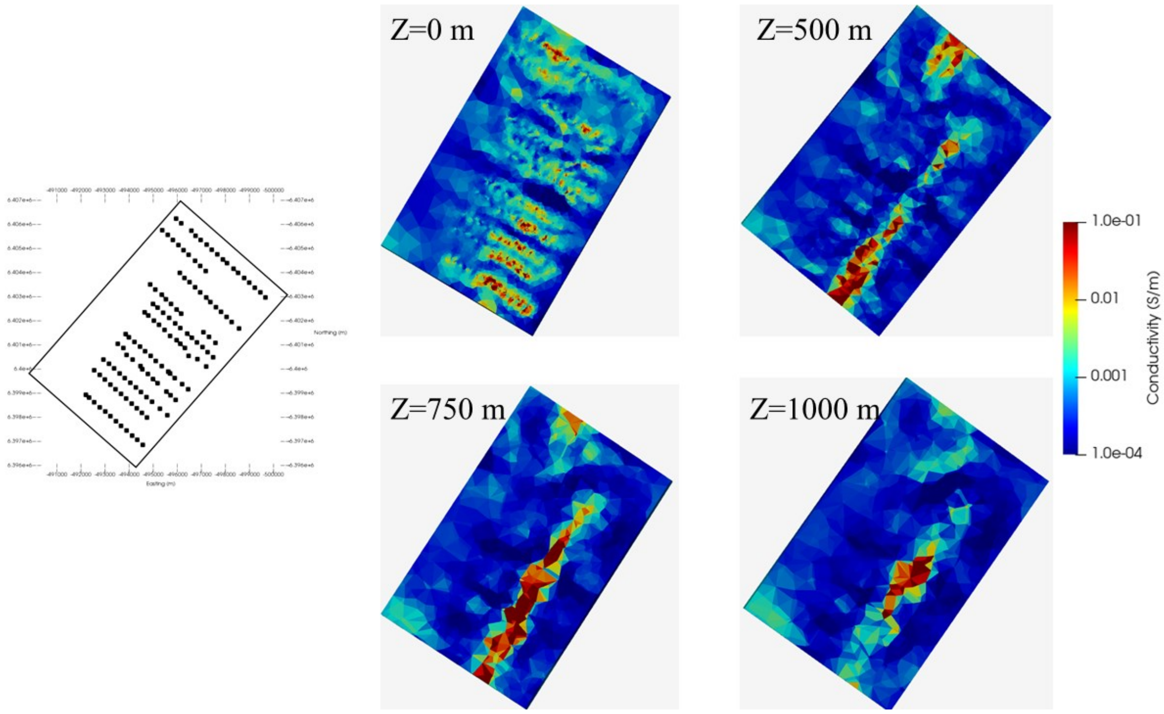

Figure 5.22: Horizontal slices from final inversion model of the synthetic data. The leftmost panel shows the field orientation where black dots show the observation points and the black rectangle shows the other four panels' boundaries.

5.6. Inversion of the Real AMT Data

The mesh used for the inversion of the real AMT data set was the same as for the inversion of the synthetic data set (see Figures 5.16 and 5.17). As in the synthetic-data inversion, the air-earth interference was assumed to be flat. The real data set was inverted, considering different types and levels of noise. In particular, the variances in the ".edi" files – the original data files containing the final processed impedances – were considered for one inversion, and in two other inversions, 3 and 5 percent noise levels were considered. Because the measurement errors are not known, the different noise levels were used to see how the data differs. The details of these three inversions are explained in the following sub-sections.

5.6.1. Inversion Results for the Real AMT Data

In the present study – as mentioned above – three different cases are considered for inverting the real AMT data set. In previous studies, various assumptions about the noise in the data have been considered while inverting the same real data set. This led to different models being constructed by the inversions. Because of this, three different noise scenarios were tested. These noise scenarios comprised using the variances in the ".edi" files as the (squares of) the measurement uncertainties, and using 3% and 5% noise levels.

For the inversion of the real data-set, 20 frequencies were considered (Table 5.2). Higher and lower frequencies were added to the data, and number of middle frequencies were increased compared to the synthetic data inversion. Mostly, the medium frequencies were picked with respect to the skin depth issue in order to have a better resolution of the graphitic conductor. Also, high and low frequencies were added to help to image the bottom parts (around the basement) and the near-surface parts of the model better than previous studies because the meshes used (i.e., rectilinear meshes) could not provide a good resolution near the surface. The consistencies or differences in the inversion results for the three different noise scenarios will be discussed later in the discussion sub-section. Also, the results will be compared to the inversion results of the previous studies.

Table 5.2: The twenty frequencies considered in all inversions of the real data-set.

Number	Frequency (Hz)	Number	Frequency (Hz)
1	7680.0	11	81.0
2	5120.0	12	61.0
3	3840.0	13	41.0
4	1280.0	14	22.25
5	640.0	15	15.12
6	464.0	16	11.0
7	336.0	17	6.937
8	177.00	18	4.875
9	128.00	19	3.812
10	97.00	20	2.563

5.6.1.1 Inversion with Variances

For this inversion, the variances in the ".edi" files were considered as estimates of the variances (i.e., squares of the standard deviations) of the noise in the data. As for all inversions in this thesis, only the impedance tensor elements in the NS-EW coordinate system were considered as data to invert. In theory, the variances do reflect the true error level associated with the data, at least the error derived from the spectral analysis. However, observations suggest variances estimated for robust remote-referenced data do often underestimate the true error level (e.g., as suggested by comparing the jumps between adjacent period estimates with the size of the variances). The estimated variances will also not account for geological noise, galvanic distortion, and other aspects excluded from the inversion model – it was not really known what the target misfit should be. In the real data inversions of this study, the trade-off parameter was not decreased any further once the decrease in the data misfit and objective function start to slow down (as explained in subheading 5.5.3). The plots of observed and calculated data were checked to see if the data fit is looking okay.

As for the synthetic data presented in the previous section, the initial and reference models for the real data inversions consisted of a homogeneous half-space of 10^{-2} S/m (and an air layer of 10^{-8} S/m). For this inversion, the starting value of the trade-off parameter was picked as 1E+3, which was the same as for the synthetic data inversion. However, in contrast to the synthetic data inversion, the trade-off parameter was levelled off at 1E-2. Until this value of the trade-off parameter, the cooling parameter was 0.9.

Figure 5.23 presents the behaviour of the trade-off parameter, the model smallness and roughness parameters, the data misfit and the objective function as functions of iteration. The data parameters decrease while the model parameters show an increase iteration by iteration and show a slightly decreasing trend after the levelling off of the trade-off parameter. The inversion run is assumed to have completed its mission when the data objective function has reached a stable asymptote value. For this inversion, the final data misfit was 137,747.13, whereas the total number of data was 21,120, meaning the data misfit is six times larger than the total number of data – in other words, the misfit is equivalent to individual data misfits being six times larger than the estimated standard deviation. However, this is not a problem in the case of real data inversion because the actual error levels are not known during real data collection. If the trade-off parameter is decreased to a lower value before levelling off, then the data misfit does not decrease too much, and a lot of structure starts to build up in the model. This is the point considered in this study.

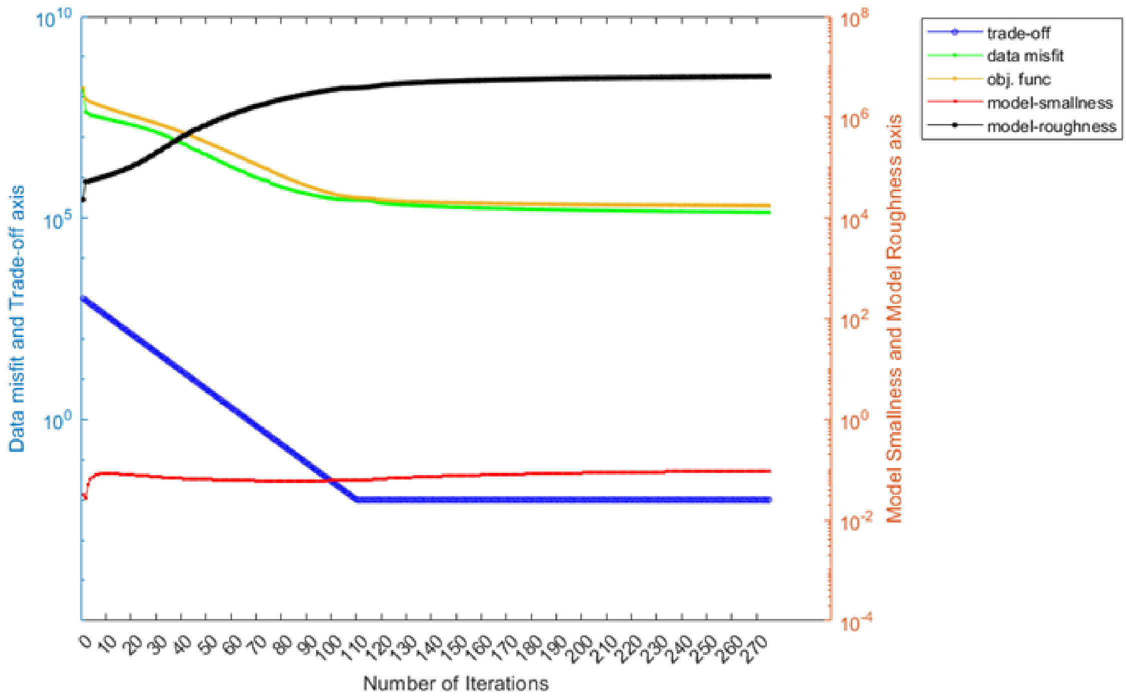

Figure 5.23: Convergence curves for the real-data inversion using variances to give estimates of the data uncertainties. The cooling parameter was equal to 0.9, shown by the slope of the blue curve. The left vertical axis belongs to the data parameters, and the right vertical axis is for the model parameters.

The data-fit plots for the inversion using the variances to give the measurement uncertainties are presented in Figures 5.24 and 5.25 for an arbitrarily selected station. These plots show the data in two different forms. In Figure 5.24, the impedance data normalized by the square root of the angular frequency are plotted with respect to the period. The error bars in Figure 5.24 indicate the measurement uncertainties used in the inversion, which were equal to the square roots of the variances provided with the data.

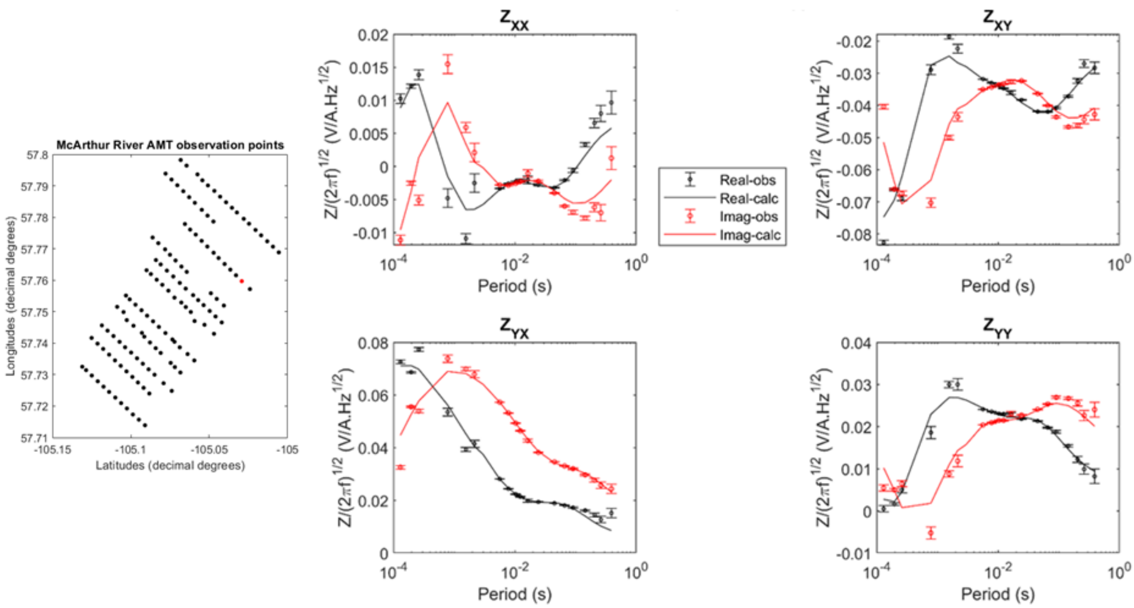

Figure 5.24: Data-fit plots for the impedance data in the NS-EW coordinate system for the 20 frequencies of station 105 (the red dot in the window on the left-hand side). Error bars indicate the uncertainties assigned to the data (equal to the square roots of the variances provided with the data). Lines indicate the calculated data. Black and red colours correspond to the real and imaginary parts respectively of the impedance data.

In Figure 5.25, the apparent resistivity and phase values are shown for the TE and TM modes. The graphs for the other stations can be found in Appendix D. These graphs are plotted considering the data with respect to all periods used in the inversion. The calculated data for the result of the inversion shows a satisfactory agreement with the collected data at all stations in both forms of the data.

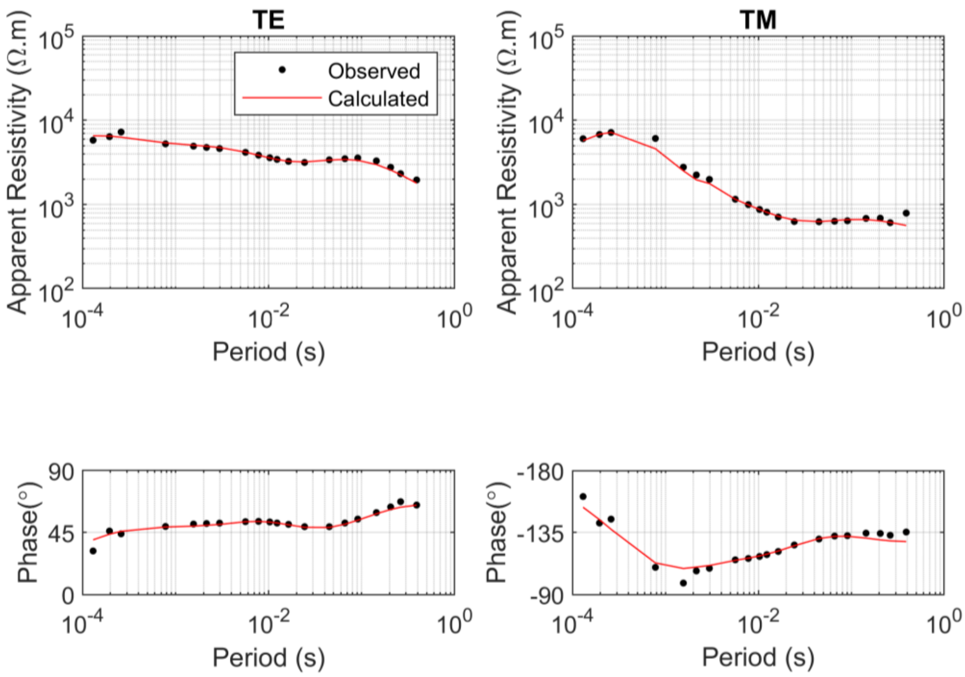

Figure 5.25: Data-fit curves in terms of the apparent resistivity and phase values for the TE and TM modes (with respect to the geoelectric strike) for station 105. (See Figure 5.24 for station location.) Black dots indicate the observed data, whereas the red lines indicate the calculated data for the inversion result (the inversion using the variances to give the measurement uncertainties).

In all the cross-sections presented in Figure 5.26, the conductive response associated with the P2 Fault can be observed (highlighted with ellipses). Up to the profile L266, the background seems more resistive than the background of the remaining profiles, 0.001 S/m and lower compared to mostly above 0.001 S/m (from L271 to L304). Some conductivity extremities are observed in the vertical cross-sections. For instance, a conductive body at the southeastern end of profile L304 is present. Moreover, another conductive extremity can be observed around the northwestern end of the profile L224 (just beneath the observation points – not the left-hand side of the observation points). On the cross-sections for the profiles L296 and L304, the conductive effect of the second segment of the conductive fault is visible. However, it is not clear if the conductive response at the northeastern end of profile L288 is associated with the graphitic conductor.

The vertical cross-sections through the final inversion model along every profile are shown in Figure 5.26. The maximum depth of the cross-sections is 2 km. For this inversion, it took almost 65 minutes (it is an average value with some iterations that took longer and some shorter) to solve one iteration until levelling off the trade-off parameter, then it took nearly 45 minutes per iteration after applying the levelling-off procedure. The total time to finish the inversion was approximately 145 hours.

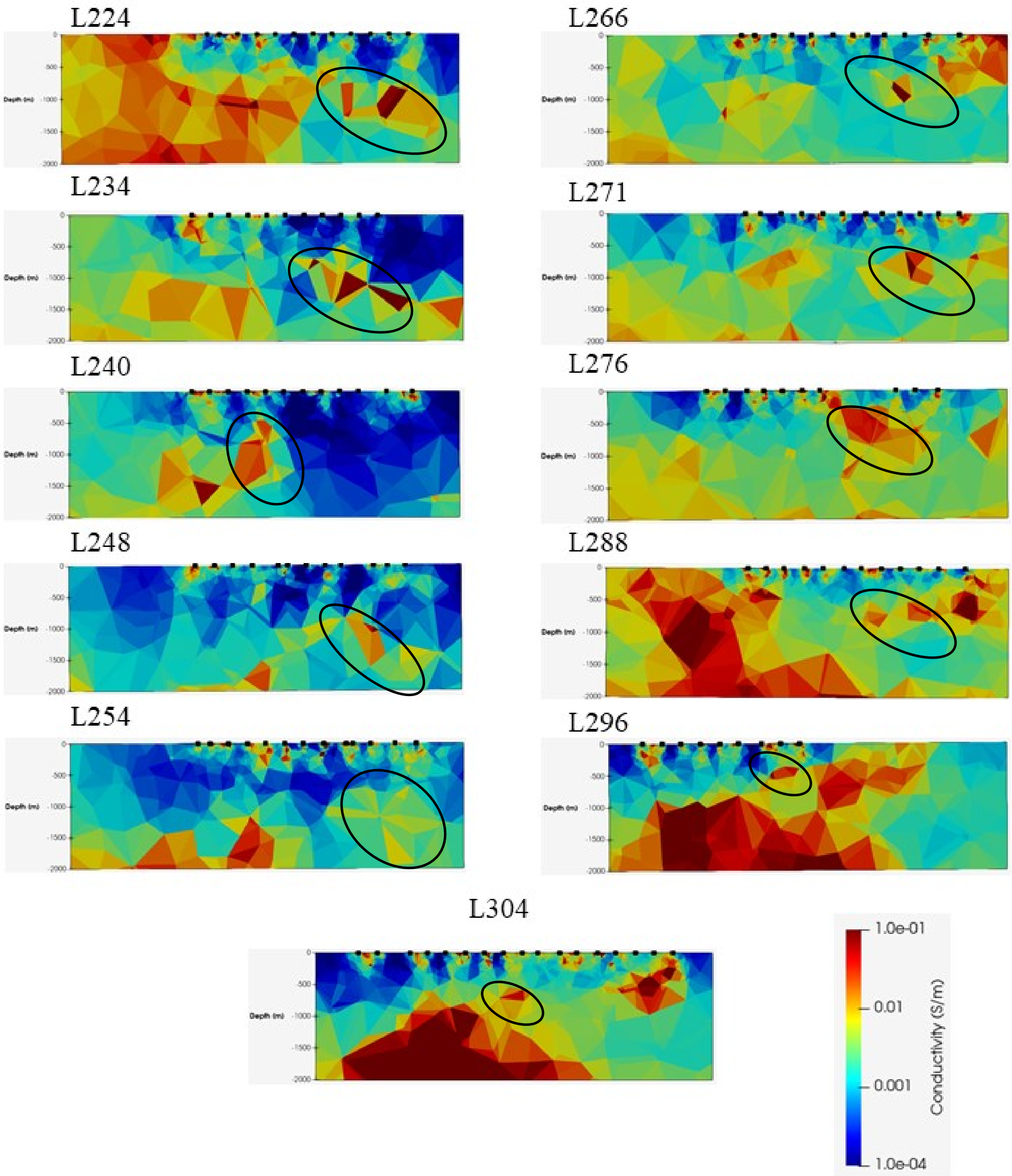

Figure 5.26: Vertical cross-sections of the final inversion model for the inversion of the real data-set using the variances for estimates of uncertainties. Black dots show the AMT-sounding locations. Ellipses show the appearance of the P2 Fault.

5.6.1.2 Inversion with 3% Measurement Uncertainties

For this inversion, uncertainties of 3% were considered to see how the general features of the final inversion model will be affected. As for all inversions in the present study, only the impedance tensor elements were considered as the data to invert. 3% of the average absolute values of all impedance tensor elements were calculated at a particular frequency. This means that the measurement uncertainties associated with the diagonal elements, in particular, are not too small.

As for the first inversion of the real data explained above, the initial and reference models were both a homogeneous half-space of 10^{-2} S/m. Similar to both the inversion of the synthetic data and the first inversion of the real data, the initial value of the trade-off parameter was 1E+3 for this inversion, and it was levelled off at 1E-2. The cooling parameter was again 0.9 until levelling off of the trade-off parameter.

Figure 5.27 presents the behaviour of the trade-off parameter, the model smallness and roughness parameters, the data misfit and the objective function as functions of iteration for this inversion. The data parameters decrease while the model parameters show an increase iteration-by-iteration and then show a slightly decreasing trend after the levelling off of the trade-off parameter. The inversion run was assumed to have completed its task when the objective function had reached a stable value. For this inversion, the data misfit was 144,741.13, whereas the total number of data is 21,120, which means that the data misfit is seven times larger than the total number of data. As for the previous real-data inversion, this is not a problem in the case of real data inversion because the actual error levels are not known during real data collection (as explained in detail in the first paragraph in subsection 5.6.1.1).

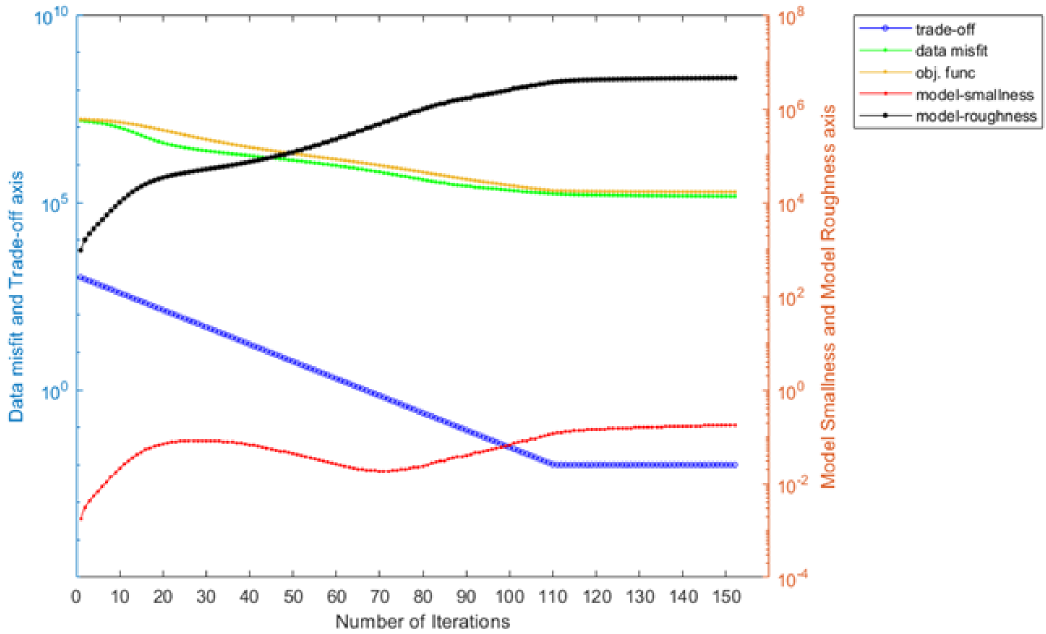

Figure 5.27: Convergence curves for the real data inversion with 3% uncertainties. This graph shows the data and model parameter variations with respect to iteration for the given cooling parameter (0.9). The left vertical axis belongs to the data parameters, and the right vertical axis is for the model parameters.

The data-fit curves of the inversion with 3% uncertainties are presented in Figures 5.28 and 5.29 for an arbitrarily selected station. These plots are generated for the two different data types. In Figure 5.28, the impedance data (normalized by the square root of the angular frequency) are shown. In Figure 5.29, the apparent resistivity and phase values are shown for TE and TM modes. Fit curves for the other stations can be found in Appendix E. These graphs are plotted considering the data with respect to all periods used in the inversion. The error bars in Figure 5.28 indicate the noise added to the data. The data-fit plots in Figures 5.28 and 5.29 revealed that the results of the inversion with 3% uncertainties are smoother than the previous one. Moreover, the calculated data in both Figure 5.28 and 5.29 are closer to the observed ones (error bars). These improvements in data-fit plots indicate a better agreement of the calculated and observed data.

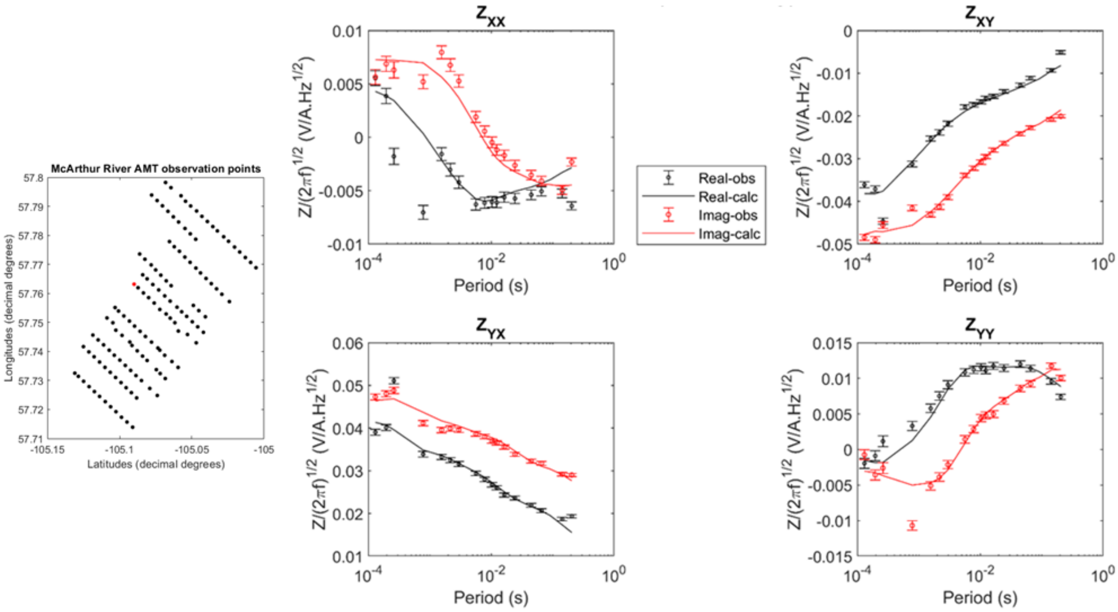

Figure 5.28: Data-fit curves of the impedance data, in the NS-EW coordinate system, for the 20 frequencies of station 70 (for the station location, see the red dot in the window on the left-hand side). The error bars indicate the uncertainties assigned to the data (3%). The lines show the calculated data. Black and red colours indicate the real and imaginary parts of the impedance data.

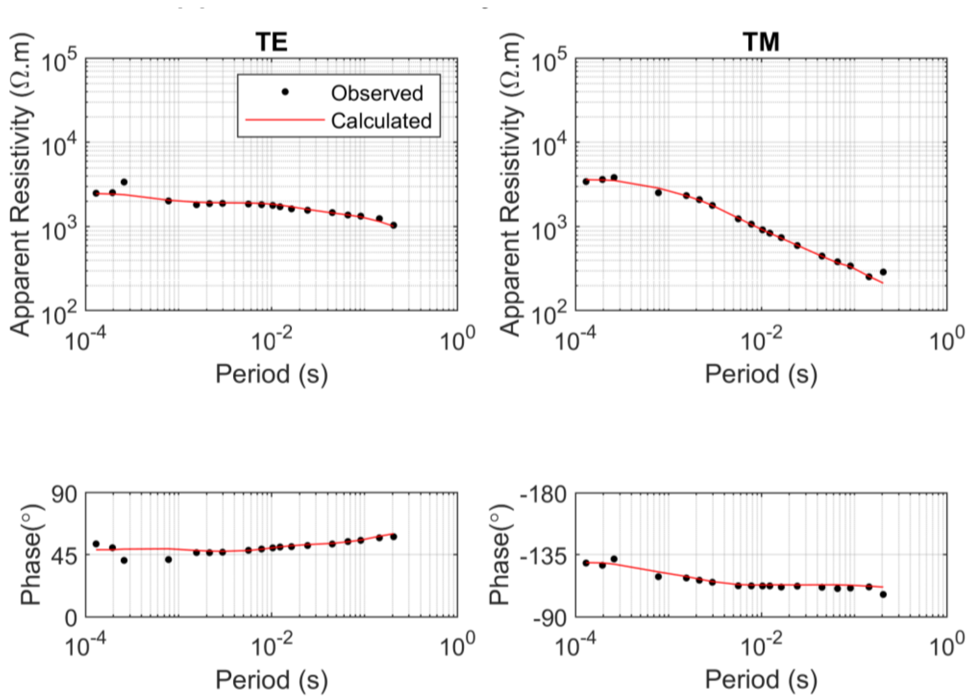

Figure 5.29: Fit curves of apparent resistivity and phase values for TE and TM modes of station 70. (See Figure 5.28 for the station location.) Black dots indicate the observed data, whereas the red line stands for the results of inversion with the variances as error floors.

The vertical cross-sections through the final inversion model along every profile are shown in Figure 5.30. For this inversion, it took almost 66 minutes to solve one iteration until levelling off the trade-off parameter, and then it took nearly 42 minutes per iteration after applying the levelling-off procedure. The total time to finish the inversion was approximately 143 hours.

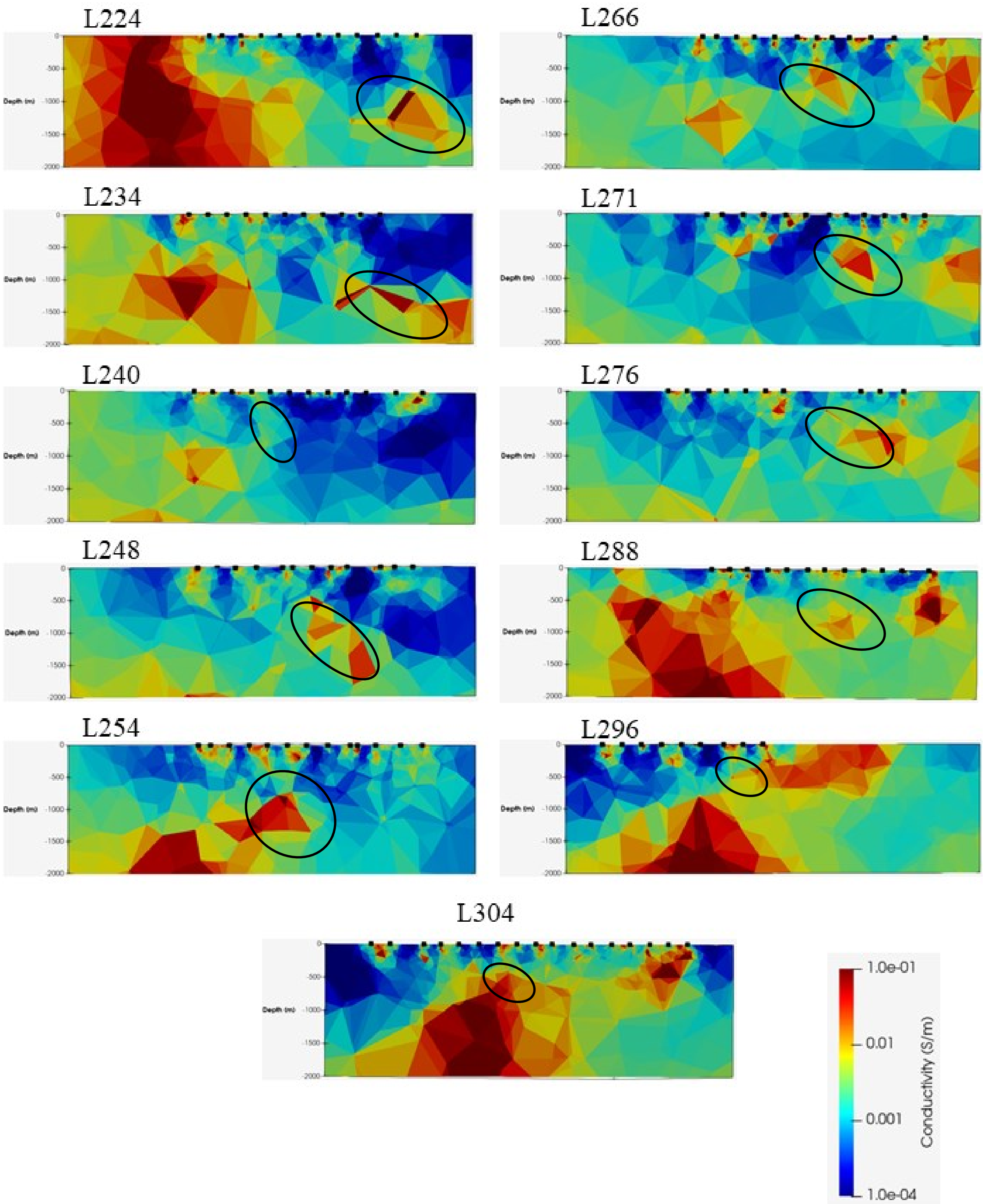

Figure 5.30: Vertical cross-sections of the final inversion model for the inversion with 3% uncertainties. Black dots show the AMT-sounding locations. Ellipses show the response of the P2 Fault.

In all the cross-sections presented in Figure 5.30, the conductive response associated with the P2 Fault can be observed – ellipses show the possible response of the P2 Fault. The locations of the ellipses are also coinciding with the induction arrow reversals. The common conductive structures are not really changed by using different measurement uncertainties; however, this inversion result is smoother than the results of the inversion using the variances provided with the data (and which were generated from the data processing). Moreover, the links between some conductors are more apparent in these inversion results. For instance, the connection between the more significant (at the bottom center) and smaller (at the southeastern end of the profile) conductors in L304 is visible. These connections are also visible for L254, L288, and L296, the same as for L304. The backgrounds are more resistive south of profile L266 than the background of the remaining profiles (from L271 to L304). Except for the points explained here, the interpretations made for the previous inversion of the real data are still valid for the results of this inversion.

5.6.1.3 Inversion with 5% Uncertainties

For this inversion, uncertainties of 5% were considered to check the effect of the uncertainty level on the data. For this, at a certain frequency, 5% of the average absolute values of all elements of the impedance tensor were calculated. As for all other inversions in the present study, only the impedance tensor elements were inverted. As in the previous inversions presented above, it is accepted that the solution has been reached when the objective function begins to decrease only slowly. The trade-off parameter was levelled off, and further iterations were done to reach convergence.

As for the other inversion examples above, the initial and reference models were the same, consisting of a homogeneous half-space of 10^{-2} S/m. Similar to the previous inversion, the initial trade-off parameter was 1E+3, then levelled off at 1E-2. The cooling parameter was again 0.9 until levelling off of the trade-off parameter.

In Figure 5.31, the variation of the trade-off parameter, the model smallness and roughness parameters, the data misfit and the objective function for the given cooling parameter are shown. The model parameters rise while the data parameters go down iteration-by-iteration, with the data parameters showing a slightly decreasing trend after levelling off of the trade-off parameter. As for the previous examples, the calculation is assumed to have completed its duty when the objective function has reached a stable value and is no longer changing. For this inversion, the data misfit was 65,201.39, whereas the total number of data is 21,120, and thus the data misfit is three times larger than the total number of data. This makes sense as the uncertainties are (approximately) twice the size they were for the previous inversion, and it reached the same solution with the previous one.

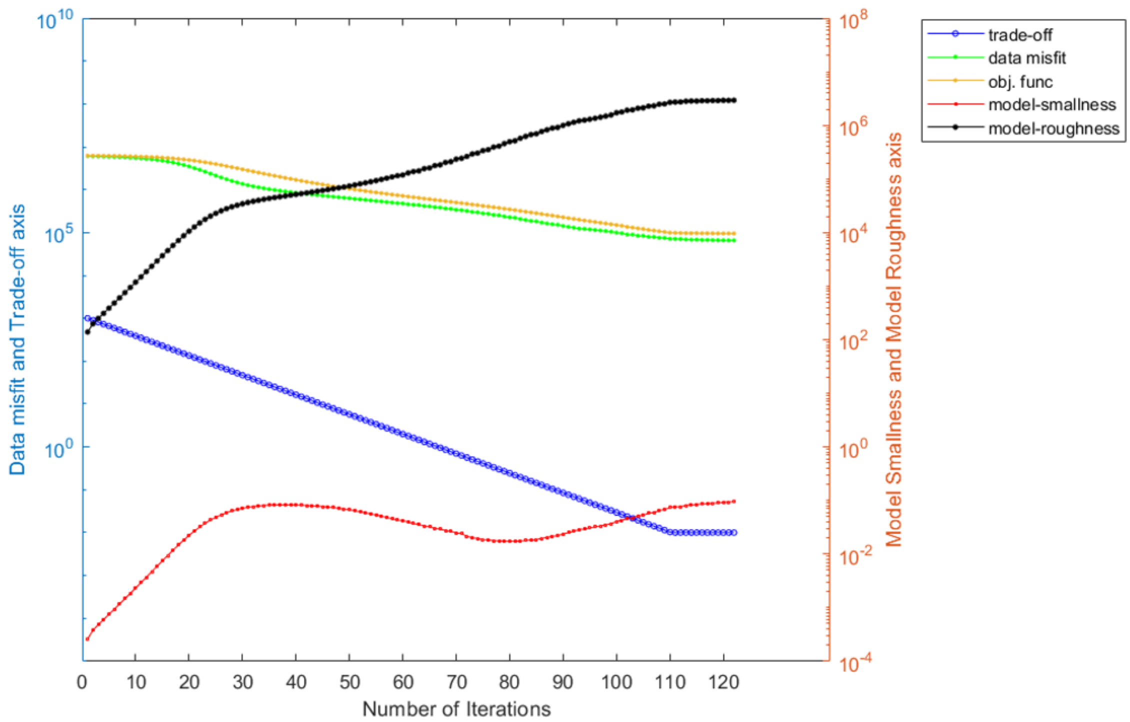

Figure 5.31: Convergence curves for the real data inversion with 5% uncertainties. The graph shows the data and model parameter variations with respect to iterations for the given cooling parameter (0.9). The left vertical axis belongs to the data parameters, and the right vertical axis is for the model parameters.

As for the previous inversion results, the data-fit plots are presented in Figures 5.32 and 5.33 for an arbitrarily selected station. In Figure 5.32, the impedance data are normalized by the square root of the angular frequency and presented with respect to periods. Although the error bars are larger than they are for the 3% inversion, the data-fit plots show that lines are pretty much the same as for the 3% inversion.

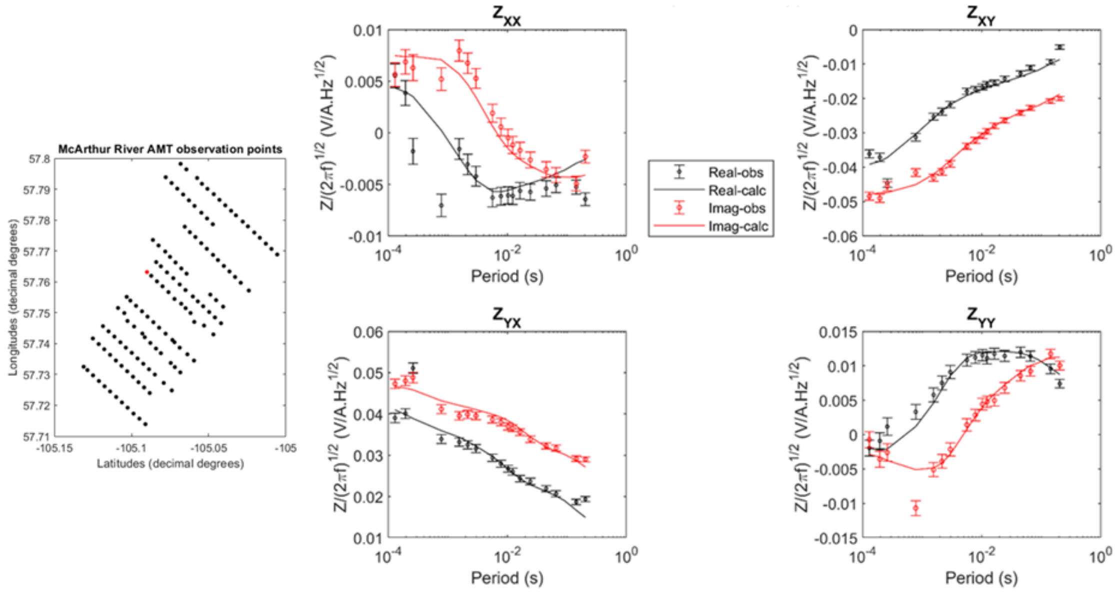

Figure 5.32: Data-fit curves of the impedance data – in NS-EW coordinate system – for 20 frequencies of station 70 (station location presented as the red dot on the left-hand side window) for the inversion with 5% uncertainties. Lines indicate the calculated data. Black and red colours indicate the real and imaginary parts of the impedance data.

In Figure 5.33, the fits are shown for the apparent resistivity and phase values of the TE and TM modes. Data fit plots for the other stations can be found in Appendix F. These graphs are plotted considering the data with respect to all periods used in the inversion.

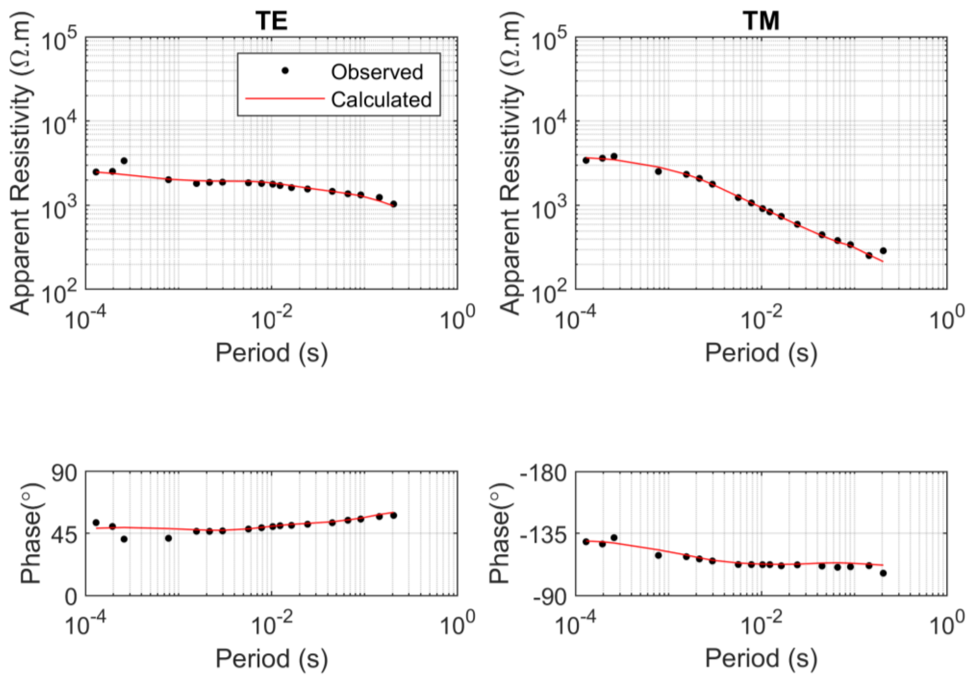

Figure 5.33: Data-fit curves shown in terms of apparent resistivity and phase values for TE and TM modes of station 70 – see Figure 5.32 for the station location. Black dots indicate the observed data, whereas the red lines stand for the results of the inversion.

The vertical cross-sections through the final inversion model along every profile are shown in Figure 5.34. For this inversion, it took almost 66 minutes to solve one iteration until levelling off the trade-off parameter, and then nearly 42 minutes per iteration after applying the levelling-off procedure. The total time to finish the inversion was approximately 143 hours.

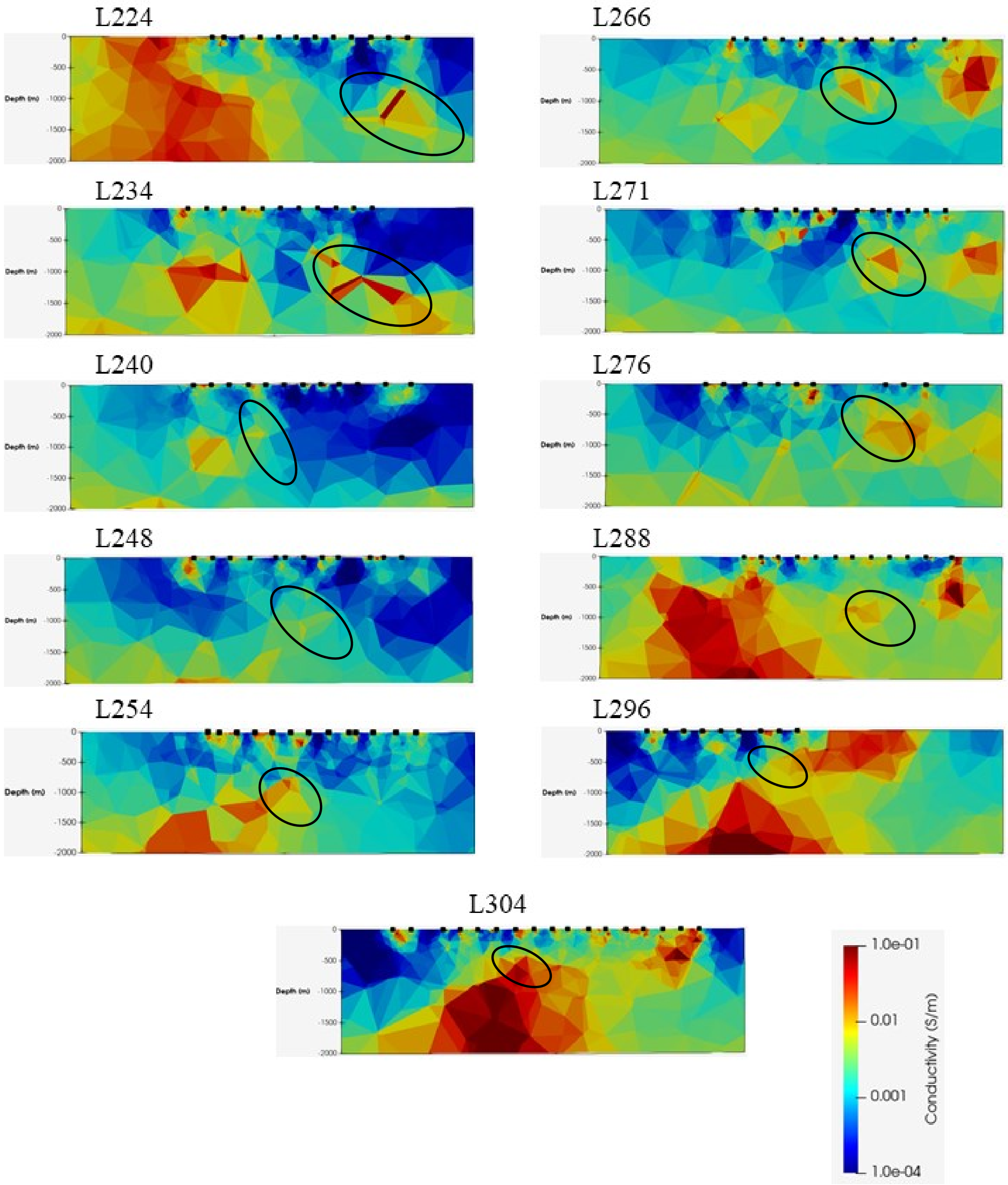

Figure 5.34: Vertical cross-sections of the final inversion model for the inversion with 5% uncertainties. Black dots show the AMT-sounding locations. Ellipses show the response of the P2 Fault.

In all vertical cross-sections shown in Figure 5.34, the conductive response associated with the P2 Fault can be observed (ellipses at every vertical cross-section). Figure 5.34 shows that using 5% uncertainties has yielded the smoothest inversion results compared to the others above. Here the term “smoothest” indicates that it is obvious that the connections between the main conductive features are more visible than those in previous inversion results. In general, this means that the model is more or less similar to the result for the 3% inversion. Except for this detail, the interpretations made on the previous inversion are still valid for the results of this inversion. For instance, the connection between the more significant (at the bottom center) and smaller (at the southeastern end of the profile) conductors in L304 is smoother than ever. Likely, the links between main features at L254, L288 and L296 became clearer. For the backgrounds, they still seem to be more resistive up to the profile L266 than the ones seen from L271 to L304.

5.7. Summary

In this chapter, forward-modelling and inversion attempts were presented. For the modelling of the McArthur River area, the collected AMT data-set were used for investigation of the features that presumably are due to the P2 Fault. Then, a model that is representative of the general geology of the area was constructed. The P2 Fault was embedded in the model considering the interpretations made in the earlier studies. The next step was computing AMT data for this model and comparing the results with the observed data. The comparison revealed that the correspondence was decent, particularly what is presumably the P2 fault signature. After that, the synthetic data-set was inverted with the code introduced in Jahandari and Farquharson (2017). Inverting the synthetic data set allowed me to get an appreciation for what the inversion can do. For instance, the variation of the features in the model were observed iteration-by-iteration and the levelling off of the trade-off parameter was the vital part. Having a smooth convergence curve graph was another vital part of the inversion. The last step was inverting the real AMT data-set and seeing the conductive features. This scheme was repeated for different uncertainty levels. Although the model smoothness changed by the different uncertainties, the locations of the main conductive features were not affected. Using different uncertainties had an impact on the links between conductors. The P2 Fault has a blobby (smeared-out) feature in the model, and it was in the right location (according to the information presented in previous studies) and at the right depth (beneath the sandstone layer and unconformity zone, and approximately starting at a depth of 500 m and extending down to nearly 2km at some profiles).

6 Discussion and Conclusion

6.1. Discussion

Craven et al. (2006) summarize the results from a number of different studies that inverted the McArthur River AMT data-set. The details of these previous studies are presented in Table 6.1. The vertical cross-sections presented in Craven et al. (2006), which are reproduced in Figure 6.1, are used for comparing the results of this study with those from the previous ones.

Table 6.1: Summary of the previous inversion studies of the McArthur River AMT data set.

Performed by	Algorithm	Data	Dimensionality	Mesh	Error Floors	Static Shift Incorporated
Tuncer	Rodi & Macike, 2001	TE TM Apparent Resistivities, Phases and Tipper	2D	-	20%, 5%, and 0.025	YES
Siripunvaraporn	Siripunvaraporn et al. 2005	Real & Imaginary parts of the off diagonal impedances	3D	56X56X33 aligned with survey lines	5%	NO
Mackie	Mackie et al. 2001	ln(Zxy) & ln(Zyx), Zxx & Zyy, Tipper	3D	56X44X79 aligned with survey lines	5% 20% 0.02	YES
Farquharson	Farquharson et al. 2002	Real & Imaginary parts of all impedances	3D	60X70X40 in N-S and E-W direction	Variances in ".edi" files	NO

The previous inversions have been conducted by different researchers using different algorithms. The 2D inversion results presented in Tuncer et al. (2006) were obtained using the algorithm introduced in Rodi & Mackie (2001). For this inversion, the TE and TM mode apparent resistivities, phases and magnetic transfer functions were the data that were inverted. The error floors were 20% for the apparent resistivities, 5% for the phase values, and lastly 0.025 for the magnetic transfer function data. Values of static shift at each station were solved for during the inversion as well as the conductivity model.

Unlike the 2D inversion, a 3D inversion was performed using the algorithm introduced in Siripunvaraporn et al. (2005). Real and imaginary parts of the off-diagonal elements of the impedance tensor were used for the inversion, and the error floor was 5%. Static shift was not taken into account. The mesh was aligned with the survey lines, and had 56×56×30 cells.

Another 3D inversion was performed using the algorithm introduced in Mackie et al. (2001). In this inversion, the natural logarithm of the off-diagonal elements and the diagonal elements of the impedance tensor were used for inversion. In addition to the impedance elements, the magnetic transfer functions were also included in the inversion. The static shift was also taken into account. For this inversion, the error floors were 5% for the logarithmic impedance elements, 20% for the diagonal elements of the impedance tensor, and 0.02 for the magnetic transfer function data. The mesh was aligned with the survey lines, and was generated with 56×44×79 cells.

The results presented in Farquharson and Craven (2009) used the algorithm introduced in Farquharson et al. (2002). All elements of the impedance tensor were used for the inversion, but the magnetic transfer functions were not considered. The static shift was not taken into consideration. For this inversion, the variances estimated from the data processing were accepted as the (squares of the) measurement uncertainties.

The impedances were kept in the NS-EW coordinate system The mesh was aligned with the N-S and E-W directions, and it had 60×70×40 cells.

As a comparison, the techniques and theoretical background of the inversion procedure used in the present study are closer to the approach described in Farquharson & Craven (2009). On the other hand, the type of mesh is different from all the previous studies. In the present study, unstructured tetrahedral grids were used as the mesh, whereas the others mentioned above all used rectilinear grids. As in Farquharson and Craven (2009), the computational domain was aligned with the N-S and E-W directions. The impedances were in the NS-EW coordinate system. In contrast to the inversions performed by Tuncer and Mackie, the static shift was not considered in the present study. As for the measurement uncertainties, three different strategies were tested for the inversions in the present study. These were: 1) the square roots of the variances estimated from the processing, 2) 3% measurement uncertainties, and 3) 5% measurement uncertainties.

The variation of the data misfit with each frequency can be found in Table 6.2. It can be inferred from the table that the data misfit values took highest values at lower (≤15.12 Hz) and higher frequencies (≥ 177 Hz) for the inversions with 3% and 5% uncertainties. However, it reached the lowest values around the middle frequencies (between 15.12 Hz and 177 Hz). In contrast, for the inversion with variances as uncertainties, the data misfit has the lowest values at frequencies 2.563, and 3.812 Hz. There is no significant increasing or decreasing trend of the data misfit for this inversion.

Table 6.2: Data misfit values for each frequencies for the inversion with variances as uncertainties, 3% uncertainties, and 5% uncertainties.

Frequencies (Hz)	Data Misfits for Inversions		
	Variances as uncertainties	3% uncertainties	5% uncertainties
2.563	427.84	13911	6358.3
3.812	877.29	16449	7359.3
4.875	2942.7	18492	8155.1
6.937	14650	8486.7	4346.9
11	7269.5	3261.6	1595.7
15.12	11837	4109.2	1999.8
22.25	9499.8	1681	826.94
41	5513.1	2008.7	1041.8
61	1445.5	1624.6	810.17
81	2200.5	1365.4	747.62
97	3702.2	1101	683
128	4760.1	1199	708.19
177	10905	1632.5	906.15
336	6892.4	1950.8	1110.4
464	9369.8	3626.7	1819.3
640	1888.8	7227.7	3087.1
1280	1473.7	23708	9776.6
3840	6636	18206	7469.6
5120	20927	8114.8	3210.4
7680	14529	6585.3	3189

The results of the previous inversions mentioned above have been presented as vertical cross-sections and birds-eye views for different depths in Craven et al. (2006). The vertical cross-sections shown in this study and in the previous ones are presented in Figure 6.1. The birds-eye view comparisons can be found in Figure 6.2.

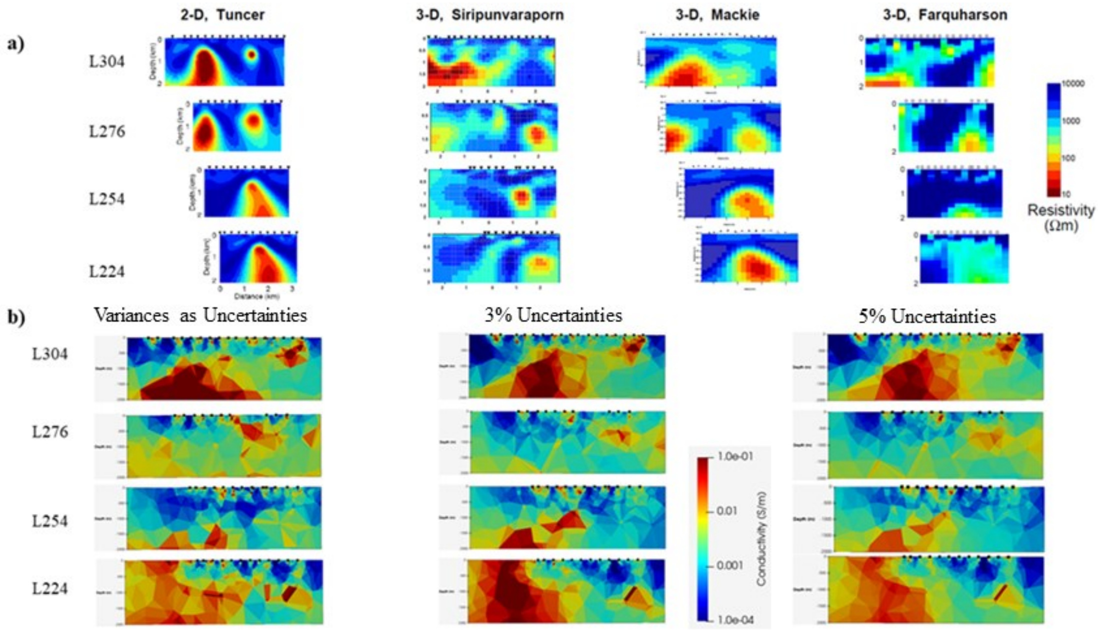

Figure 6.1: Comparison of the inversion results for the McArthur River AMT data-set. a) Results from previous studies (modified from Craven et al., 2006). b) Results of the three different inversion attempts in the present study.

Figure 6.1.a demonstrates the different inversion results obtained by the various researchers. Although the same data-set was used for these inversions, the results are not one-by-one consistent. The colour bars of Figure 6.1.b and Figure 6.1.a are the same, with red indicating high conductivity (low resistivity) and blue indicating low conductivity (high resistivity). In Figure 6.1.b, the consistency for the P2 Fault is acceptable compared to the previous studies – presented in Figure 6.1.a. However, conductivity extremities at the northwestern ends of profiles L224 and L254 are not observed in the vertical cross-sections of the previous studies. The appearance of the conductivity extremity at the northwestern end of profile L304 is the most common feature for all inversions.

Comparing the horizontal slices presented in Craven et al. (2007) with those from this study it is clear that they are not close to each other (see Figure 6.2). Horizontal slices from the previous AMT studies are presented in Figure 6.2.a, and horizontal slices from the inversions conducted in this study are shown in Figure 6.2.b. It is clear from the panels of Figure 6.2 that results of this study and the previous ones do not present the similar conductive body appearances. One of the reasons for the differences is the mesh orientation. All of the previous inversions, except for the one done by Farquharson, were done with the mesh aligned along the geoelectric strike. However, the orientation of the mesh used in this study and in the inversion conducted by Farquharson were in the NS-EW coordinate system. The code used in this study is not able to enhance smoothing the in a particular chosen direction, for example the strike direction of N45°E. Another reason responsible for the differences in results is using the default minimum-structure inversion. In more detail, the distances between stations along the lines are less than the distances between lines. The default minimum-structure inversion puts blobs under the profiles. Therefore, the data have blobby features instead of having elongated 2D-ish features. In Figure Figure 6.2.b, SE-NW oriented features could be observed dominantly rather than the expected SW-NE oriented graphitic conductor. This problem seems to be an example of the problems mentioned in Tietze and Ritter (2013) and Miensopust (2017). In order to understand the behaviour of the responses, the final inversion model of the synthetic data was checked in a similar way in Figure 6.2.b. The model cuts at the same depths as in the figure below showed that only surface slice has SE-NW aligned features, which means they are totally artefacts. The slices of the deeper parts only showed SW-NE aligned graphitic conductor. The reason of SE-NW aligned responses mostly because of the inappropriate station spacing along the lines. They are further apart between lines but much more closer along the lines.

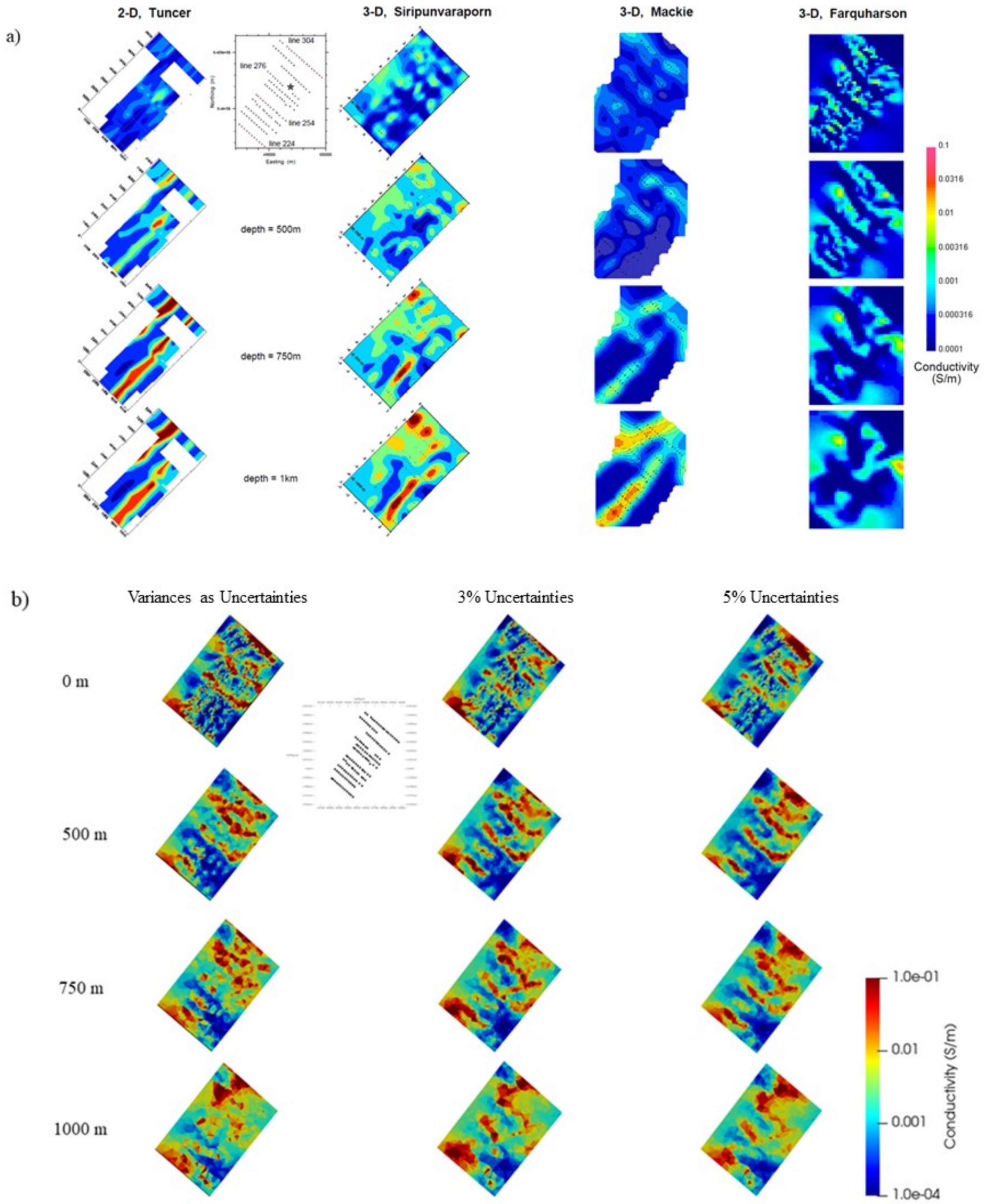

Figure 6.2: a) Horizontal slices from previous AMT inversion studies (modified from Craven et al., 2007). b) Horizontal slices from different inversions conducted in this study.

From the geological point of view, the vertical cross-sections of the inversions might provide a better understanding of the fluid flow mechanism in the study area. For example, the vertical cross-sections presented in Figures 5.22, 5.26, and 5.30 show that a resistive feature is observed at the top of the major conductive units. This feature can be observed clearly in the panels of Figure 5.30, which shows the results of the inversion with the 5% uncertainties. The resistive feature might be the resistive halo due to the silicification and egress type (Figure 2.2.c) hydrothermal fluid flow. The hypotesized resistive feature (or halo) effect is visible in vertical cross-sections of L224, L234, L240, L248, and L254. The fluid flow mechanism might be ingress type around the remaining profiles (i.e., L266, L271, L276, L288, L296) because a significant resistive feature is not observed at these profiles. The horizontal slices mentioned above show that the conductive features are getting more pronounced at the northern end of the study area. The different fluid flow mechanisms might be responsible for the increase in the conductivity after profile L254, around the profile L266.

A possible halo just above the graphitic conductor and in the unconformity zone at L224 has previously been discussed by Tuncer et al. (2006). In Figure 6.3, as a visual explanation to the paragraph just above, the vertical cross-section of the inversion with the 5% uncertainties is compared to the corresponding cross-section from Tuncer et al. (2006). The cross-section at the bottom belongs to this study, and the one on top is modified from Tuncer et al. (2006). According to the figure, a resistive halo is imaged above the graphitic conductor.

a)

b)

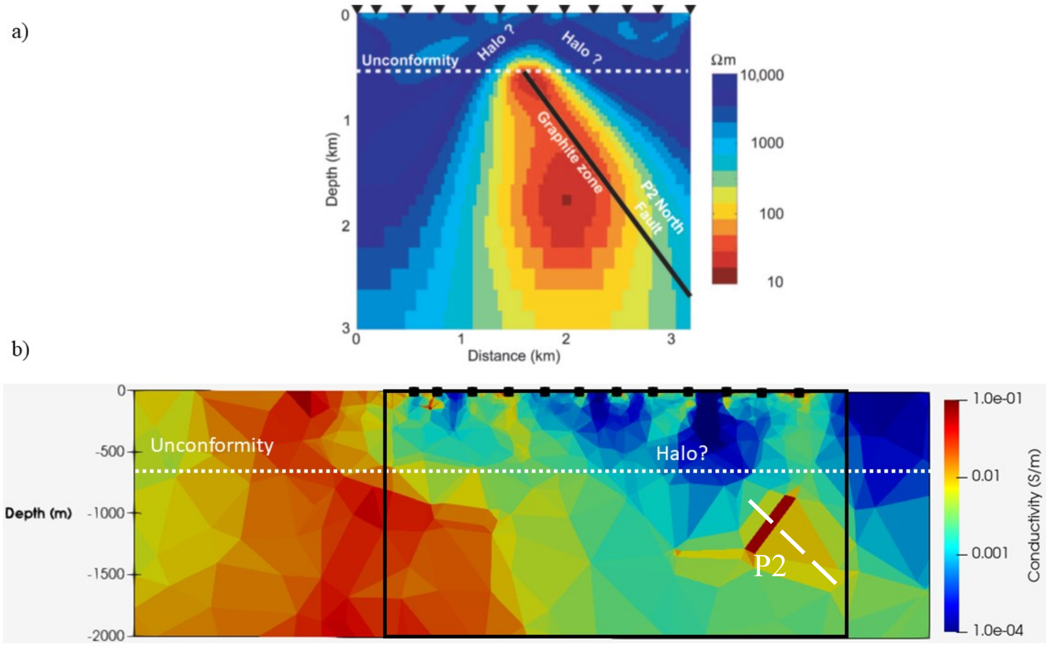

Figure 6.3: Comparison of the vertical cross-section of L224. a) Vertical cross-section modified from Tuncer et al. (2006). b) Resulting vertical cross-section of the inversion with the 5% uncertainties for L224. The small white dashes indicate the depth of unconformity zone and the larger white dashed line indicates the response of the P2 Fault.

6.2. Conclusion

In the present study, 3D inversions were carried out of the Audio-Frequency Magnetotelluric (AMT) data-set that was acquired in the McArthur River mine area of the Athabasca Basin over the graphitic P2 Fault. In the McArthur River area numerous surveys have been carried out to understand the U deposition mechanism and understand the regional and district scale geology. These surveys have revealed that the P2 Fault is a graphitic conductor and plays a vital role for the uranium mineralization. However, these surveys could not be successful for imaging its deeper parts and the AMT method, which is able to see conductive features at these depths, was conducted.

In the study area, the AMT data were collected at 132 stations in 11 lines aligned perpendicular to the P2 Fault. In the present study, the algorithm mentioned in Jahandari and Farquharson (2017) was used for the forward modelling and inversion of the AMT data-set. The mentioned algorithm uses a minimum-structure approach for the inversions and unstructured tetrahedral meshes to parameterize the conductivity model. Using unstructured grids is advantageous compared to structured grids because the latter typically requires more cells than the former for the same level of discretization.

Based on the models and interpretations of the previous studies, a model was built as being representative of the area. To create a geologically representative model, the response of the P2 Fault was investigated using the collected AMT data-set. Having the AMT data calculated for this model, the next step was comparing the results with the observed data. Results of the comparison showed that the signature of the P2 Fault is satisfactory. However, there is no better representation of the graphitic fault than the others presented previously. The synthetic data-set was inverted with the code mentioned in Jahandari and Farquharson (2017) to become familiar with the minimum-structure inversion procedure. For the real data, three different inversions were conducted for three different uncertainty levels. Results of these inversions showed that the main features, i.e., the P2 Fault, were not affected by changing the uncertainties. However, the links between the main conductive features were getting better and the conductivity extremities near some profiles were started to vanish for the inversions with different uncertainties. In terms of location and depth of the P2 Fault, seeing that it was not affected by changing the uncertainties was satisfactory.

In the present study, four inversions were conducted. The first one was the synthetic data inversion, and three others were the real data inversions with different uncertainties, i.e, measurement variances as uncertainties, 3% uncertainties and 5% uncertainties. The synthetic data inversion was a practice step for the real data inversion and the fundamental work procedure of the inversion code was learned at this step. It seems that the geological model is a good representative of the study area. The induction arrows clearly showed the location of the fault. Additionally, the artefacts were observed at the surface layer only. The other top-view slices having depths at 500, 750, and 1000 m has only response of the SW-NE oriented graphitic conductor. The (square roots of the) measurement variances were used as uncertainties for the first real data inversion. The data-fit curves were very sharp and the conductivity changes in the vertical conductivity cross-sections were not smooth. The results of inversion with the 3% uncertainties had better smooth data-fit curves and vertical conductivity cross-sections. In these cross-sections, the links between the main conductive features became visible. The smoothest results were obtained from the inversion with 5% uncertainties. The conductivity extremities near the starts and the ends of the profiles became weaker – but this does not mean that they can be neglectable, they are still visible – and the connections between the conductive bodies became stronger. The data-fit curves of this inversion were very close to the ones for 3% inversion except for the sizes of the error-bars. Because of having smoothest clearer results, it seems that the results of inversion with 5% uncertainties are the best.

References

Amestoy, P.R., Guermouche, A., L'Excellent, J.Y. and Pralet, S., 2006, "Hybrid scheduling for the parallel solution of linear systems". Parallel computing, 32(2), pp.136-156.

Bahr, K., 1988, "Interpretation of the Magnetotelluric Impedance Tensor: Regional Induction and Local Telluric Distortion", J. Geophys., Vol. 62, pp. 119-127.

Bedrosian, P., 2007, "MT + Integrating Magnetotellurics to Determine Earth Structure, Composition and Processes", Surveys in Geophysics, Vol. 28, pp. 121-167.

Berdichevsky, M.N., V.I. Dmitriev, and E.E. Pozdnjakova, 1998, "On Two-Dimensional Interpretation of Magnetotelluric Soundings", Geophys. J. Int., Vol. 133, pp. 585606.

Bray, L., Murdock G., M., Renaud, Alain, D. "McArthur River Project Northern Saskatchewan, Canada": National Instrument 43- 101 Technical Report. 2018, Cameco Corporation.

Cagniard, L., 1953, "Basic Theory of the Magnetotelluric Method in Geophysical Prospecting", Geophysics, Vol. 18, pp. 605-635.

Caldwell, T. G., H. M., Bibby & C. Brown, 2004, "The magnetotelluric phase tensor", Geophysical Journal International, Vol. 158(2), pp. 457-469.

Campbell, J. E., Shieves, R. B. K. and Klassen R. A., 2002, "Integrated field investigations of airborne radiometric spectral domains, NEA-IAEA test area, eastern Athabasca Basin: A preliminary report, Summary of Investigations 2002", v2, Saskatchewan Geological Survey, Saskatchewan Industry Resources, Miscellaneous Report 2002-4.2, Paper D-2.

Canadian Digital Elevation Model (CDEM). [computer file]. Ottawa, ON: Natural Resources Canada. (2015).

Card, C. D., D. Pana, R. A. Stern and N. Rayner, 2007. New insights into the geological history of the basement rocks to the southern Athabasca Basin, Saskatchewan and Alberta, in Jefferson, C.W., and Delaney, G., eds., EXTECH IV: Geology and Uranium EXploration TECHnology of theProterozoic Athabasca Basin, Saskatchewan and Alberta: Geological Survey of Canada, Bulletin 588 (also Saskatchewan Geological Society, Special Publication 18; Geological Association of Canada, Mineral Deposits Division, Special Publication 4).

Chave, A. D., & A. G., Jones, 2012, "The magnetotelluric method: Theory and practice", Cambridge University Press.

Craven, J. A., C. G. Farquharson, R. L. Mackie, W. Siripunvaraporn, V. Tuncer and M. J. Unsworth, 2006. A comparison of two- and three-dimensional modelling of audiomagnetotelluric data collected at the world's richest uranium mine, Saskatchewan, Canada, 18th International Workshop on Electromagnetic Induction in the Earth, El Vendrell, Spain.

Craven, J. A., G. McNeice, B. Powell, R. Koch, I. R. Annesley, G. Wood, C. J. Mwenifumbo, M. Unsworth and W. Xiao, 2007. Audio-magnetotelluric studies at the McArthur River mining camp and Shea Creek area, northern Saskatchewan, in Jefferson, C.W., and Delaney, G., eds., EXTECH IV: Geology and Uranium EXploration TECHnology of the Proterozoic Athabasca Basin, Saskatchewan and Alberta: Geological Survey of

Canada, Bulletin 588 (also Saskatchewan Geological Society, Special Publication 17; Geological Association of Canada, Mineral Deposits Division, Special Publication 4).

Cristall, J., and D. Brisbin, 2006, Geological sources of VTEM responses along the Collins Bay Fault, Athabasca Basin: Proceedings of the Giant Uranium Deposits Short Course, PDAC.

Dahlkamp, F.J., 1978, "Geological appraisal of the Key Lake U-Ni deposits, northern Saskatchewan, Economic Geology", 73, 1430-1449.

Darijani, M., 2019, "Investigating modelling and inversion techniques for overburden stripping for uranium exploration in the Athabasca Basin, Canada", Doctoral dissertation, Memorial University of Newfoundland.

Darijani, M., Farquharson, C.G. and Lelièvre, P.G., 2021, "Joint and constrained inversion of magnetic and gravity data: A case history from the McArthur River area, Canada". Geophysics, 86(2), pp.B79-B95.

Ferguson, I.J., Jones, A.G. and Chave, A.D., 2012, "Case histories and geological applications. In The magnetotelluric method: theory and practice". Cambridge University Press.

Farquharson, C.G., Oldenburg, D.W., Haber, E. and Shekhtman, R., 2002, "An algorithm for the three-dimensional inversion of magnetotelluric data". In SEG Technical Program Expanded Abstracts 2002 (pp. 649-652). Society of Exploration Geophysicists.

Farquharson, C.G., and Oldenburg, D.W., 2004, “A comparison of automatic techniques for estimating the regularization parameter in nonlinear inverse problems”, Geophysical Journal International, 156, 411–425.

Farquharson, C. G., and J. A. Craven, 2009, “Three-dimensional inversion of magnetotelluric data for mineral exploration: An example from the McArthur River uranium deposit, Saskatchewan, Canada”: Journal of Applied Geophysics, 68, no. 4, 450–458, doi: 10.1016/j.jappgeo.2008 .02.002.

Farquharson, C.G. and Miensopust, M.P., 2011, “Three-dimensional finite-element modelling of magnetotelluric data with a divergence correction”. Journal of Applied Geophysics, 75(4), pp.699-710.

Garcia, X. and Jones, A.G., 2002, “Atmospheric sources for audio-magnetotelluric (AMT) sounding”. Geophysics, 67(2), pp.448-458.

Garcia, X. and Jones, A.G., 2008, “Robust processing of magnetotelluric data in the AMT dead band using the continuous wavelet transform”. Geophysics, 73(6), pp.F223-F234.

Grant, F.S., Guilford, J.P. and West, G.F., 1965, “Interpretation theory in applied geophysics”. New York: McGraw-Hill.

Griffiths, D. J., 1999, “Introduction to Electrodynamics”, third edition: Prentice-Hall inc.

Groom, R.W., and, R.C. Bailey, 1989, “Decomposition of Magnetotelluric Impedance Tensor in the Presence of Local Three-Dimensional Galvanic Distortion”, J. Geophys. Res., Vol. 94, pp. 1913-1925.

Györfi, I., Hajnal, Z., White, D.J., Takács, E., Reilkoff, B., Annesley, I.R., Powell, B., and Koch, R., 2007, High-resolution seismic survey from the McArthur River region: contributions to mapping the complex P2 uranium ore zone, Athabasca Basin, Saskatchewan, in Jefferson, C.W., and Delaney, G., eds., EXTECH IV: Geology and Uranium EXploration TECHnology of the Proterozoic Athabasca Basin, Saskatchewan and Alberta: Geological Survey of Canada, Bulletin 588, (also Geological Association of Canada, Mineral Deposits Division, Special Publication 4; Saskatchewan Geological Society, Special Publication 18), p. 397-412.

Hajnal, Z., E. Takács, D. J. White, I. Györfi, B. Powell, and R. Koch, 2007, Regional seismic signature of the basement and crust beneath the McArthur River mine district, Athabasca Basin, Saskatchewan, in C. W. Jefferson, and G. Delaney, eds., EXTECH IV: Geology and uranium exploration technology of the Proterozoic Athabasca Basin; Saskatchewan and Alberta: Geological Survey of Canada, Bulletin, 588, 389–396.

Irvine, R. and Witherly, K., 2006, "Advances in airborne EM acquisition and processing for uranium exploration in the Athabasca Basin, Canada", SEG/New Orleans 76th Annual Meeting.

Jahandari, H., and Farquharson, C.G., 2014, "A finite-volume solution to the geophysical electromagnetic forward problem using unstructured grids". Geophysics 79, E287–E302.

Jahandari, H., 2015, "Three-dimensional numerical modelling of gravity and electromagnetic data using unstructured tetrahedral grids", PhD thesis, Memorial University of Newfoundland, St. John's, NL, Canada, 183 p.

Jahandari, H., and Farquharson, C.G., 2017, “3-D minimum-structure inversion of magnetotelluric data using the finite-element method and tetrahedral grids”. Geophysical Journal International, 211(2), pp.1189-1205.

Jefferson, C. W., D. J. Thomas, S. S. Gandhi, P. Ramaekers, G. Delaney, D. Brisbin, C. Cutts, P. Portella and R. A. Olson, 2007. Unconformity associated uranium deposits, in Jefferson, C.W., and Delaney, G., eds., EXTECH IV: Geology and Uranium EXploration TECHnology of the Proterozoic Athabasca Basin, Saskatchewan and Alberta: Geological Survey of Canada, Bulletin 588 (also Saskatchewan Geological Society, Special Publication 18; Geological Association of Canada, Mineral Deposits Division, Special Publication 4).

Jin, J., 2002, The finite element method in electromagnetics, 2nd ed.: John Wiley & Sons Inc.

Kaufman, A. A., and G.V. Keller, 1981, “The magnetotelluric sounding method, methods in geochemistry and geophysics”, Elsevier scientific publishing company.

Knipping, H.D., 1974, “The concepts of supergene versus hypogene emplacement of uranium at Rabbit Lake, Saskatchewan, Canada”, in Formation of Uranium Deposits, International Atomic Energy Agency, Vienna, p. 531-548.

Larsen, J., R. L. Mackie, A. Manzella, A. Fiordelisi and S. Rieven, 1996, “Robust smooth magnetotelluric transfer functions”, Geophysical Journal International, 124, 801 – 819.

Lelièvre, P., Carter-McAuslan, A., Farquharson, C. and Hurich, C., 2012, “Unified geophysical and geological 3D Earth models”. The Leading Edge, 31(3), pp.322-328.

Lelièvre, P.G. and Farquharson, C.G., 2013, “Gradient and smoothness regularization operators for geophysical inversion on unstructured meshes”. Geophysical Journal International, 195(1), pp.330-341.

Lelièvre, P.G., Carter-McAuslan, A.E., Dunham, M.W., Jones, D.J., Nalepa, M., Squires, C.L., Tycholiz, C.J., Vallee, M.A. and Farquharson, C.G., 2018, “FacetModeller: Software for manual creation, manipulation and analysis of 3D surface-based models”. SoftwareX, 7, pp.41-46.

Long, D. G. F., 2007, “Topographic influences on the sedimentology of the Manitou Falls Formation, eastern Athabasca Basin, Saskatchewan; in Jefferson, C.W., and Delaney, G., eds., EXTECH IV: Geology and Uranium EXploration TECHnology of the Proterozoic Athabasca Basin, Saskatchewan and Alberta”: Geological Survey of Canada, Bulletin 588 (also Saskatchewan Geological Society, Special Publication 18; Geological Association of Canada, Mineral Deposits Division, Special Publication 4).

Lu, X., 2020, “Three-dimensional finite-volume time-domain modeling of graphitic fault zones in the Athabasca Basin using unstructured grids”, Doctoral dissertation, Memorial University of Newfoundland.

Mackie, R. L., W. Rodi and M. D. Watts, 2001,” 3-D magnetotelluric inversion for resource exploration”: Extended Abstracts, SEG/San Antonio 75th Annual Meeting.

Marlatt, J., McGill, B., Matthews, R., Sopuck, V., and Pollock, G., 1992, “The discovery of the McArthur River uranium deposit, Saskatchewan, Canada, new developments in uranium exploration, resources, production and demand“, International Atomic Energy

Agency - Nuclear Energy Agency of the OECD, Vienna, 26-29 August, 1991, Technical Committee Meeting, Proceedings, IAEA TECDOC-650, p. 118-127.

Martí, A., 2006. “A Magnetotelluric Investigation of Geoelectrical Dimensionality and Study of the Central Betic Crustal Structure”. Dissertation, Department de Geodinmica i Geofsica, Universitat de Barcelona.

Matthews, R., Koch, R., Leppin, M., Powell, B., and Sopuck, V., 1997, Advances in integrated exploration for unconformity uranium deposits in Western Canada; in Proceedings of Exploration 97: Fourth Decennial International Conference on Mineral Exploration, (ed.) A.G. Gubins; GEO F/X, 993-1001, 1068 p.

McGill, B.D., Marlatt, J.L., Matthews, R.B., Sopuck, V.J., Homeniuk, L.A., and Hubregtse, J.J., 1993, “The P2 North uranium deposit Saskatchewan, Canada”, Exploration Mining Geology, v. 2, p. 321–331.

McNeice, G.W., and A.G., Jones, 2001, “Multisite, Multifrequency Tensor Decomposition of Magnetotelluric Data”, Geophysics, Vol. 66, pp. 158-173.

Miensopust. M.P., “Multidimensional Magnetotellurics: A 2D Study and a 3D Approach to Simultaneously Invert for Resistivity Structure and Distortion Parameters”, PhD thesis, NUI Galway, 2010.

Miensopust, M.P., 2017. Application of 3-D electromagnetic inversion in practice: challenges, pitfalls and solution approaches. Surveys in Geophysics, 38(5), pp.869-933.

Miller, G.L., Talmor, D., Teng, S.H., Walkington, N. and Wang, H., 1996. "Control volume meshes using sphere packing: Generation, refinement and coarsening", p.47-61.

Milsom, J., 1989. "Field Geophysics", John Wiley & Sons, New York.

Mwenifumbo, C.J., Percival, J.B., Bernius, G., Elliott, B., Jefferson, C.W., Wasyliuk, K., and Drever, G., 2007, "Comparison of geophysical, mineralogical and stratigraphic attributes in drill holes MAC 218 and RL 88, McArthur River uranium camp, Athabasca Basin, Saskatchewan", in Jefferson, C.W., and Delaney, G., eds., EXTECH IV: Geology and Uranium EXploration TECHnology of the Proterozoic Athabasca Basin, Saskatchewan and Alberta: Geological Survey of Canada, Bulletin 588, (also Geological Association of Canada, Mineral Deposits Division, Special Publication 4; Saskatchewan Geological Society, Special Publication 18) p. 507-520.

Palacky, G.J., 1988, "Resistivity characteristics of geologic targets". Electromagnetic methods in applied geophysics, 1, pp.53-129.

Parkinson, W.D., 1962, "The Influence of Continents and Oceans on Geomagnetic Variations", The Geophysical Journal of the Royal Astronomical Society, Vol. 6, pp. 411-449.

Polycarpou, A.C., 2005, "Introduction to the finite element method in electromagnetics. Synthesis Lectures on Computational Electromagnetics", 1(1), pp.1-126.

Portella, P. and Annesley, I.R., 2000, "Paleoproterozoic thermotectonic evolution of the eastern sub-Athabasca basement, northern Saskatchewan: Integrated geophysical and geological data". Summary of Investigations, 2, pp.2000-4.

Ramaekers, P., 1990, “Geology of the Athabasca Group (Helikian) in northern Saskatchewan; Saskatchewan Geological Survey”, Report 195, 49 p.

Ramaekers, P., Jefferson, C.W., Yeo, G.M., Collier, B., Long, D.G.F., Catuneanu, O., Bernier, S., Kupsch, B., Post, R., Drever, G., McHardy, S., Jiricka, D., Cutts, C., and Wheatley, K., 2007, Revised geological map and stratigraphy of the Athabasca Group, Saskatchewan and Alberta, in Jefferson, C.W., and Delaney, G., eds., EXTECH IV: Geology and Uranium EXploration TECHnology of the Proterozoic Athabasca Basin, Saskatchewan and Alberta: Geological Survey of Canada, Bulletin 588, (also Geological Association of Canada, Mineral Deposits Division, Special Publication 4; Saskatchewan Geological Society, Special Publication 18) p. 155-192.

Ruzicka, V., 1996, Unconformity associated uranium, Geology of Canada, 8, 197 – 210.

Rodi, W., and Mackie R.L., 2001, “Nonlinear conjugate gradients algorithm for 2D magnetotelluric inversion”, Geophysics, 66(1):174–187.

Si, H., 2015, ”TetGen, a Delaunay-Based Quality Tetrahedral Mesh Generator". ACM Trans. on Mathematical Software”, 41 (2), Article 11 (February 2015), 36 pages. DOI=10.1145/2629697 http://doi.acm.org/10.1145/2629697.

Simpson, F., and K. Bahr, 2005, “Practical Magnetotellurics”, Cambridge University Press.

Siripunvaraporn, W., Egbert, G., Lenbury, Y. and Uyeshima, M., 2005, “Three-dimensional magnetotelluric inversion: data-space method”, Physics of the Earth and planetary interiors", 150(1-3), pp.3-14.

Smith, Richard S., and Lemieux, 2009, “Examples showing characteristics of the megatem airborne electromagnetic system”, ASEG Extended Abstracts, 2009:1, 1-10, DOI: 10.1071/ASEG2009ab050

Strangway, D.W., Swift Jr, C.M. and Holmer, R.C., 1973, “The application of audio-frequency magnetotellurics (AMT) to mineral exploration”. Geophysics, 38(6), pp.1159-1175. Interiors. 150, 3 – 14.

Swift C. M., 1967, “A Magnetotelluric Investigation of an Electrical Conductivity Anomaly in the South-Western United States”, Ph.D. Thesis, M.I.T.

Telford, W. M., L. P. Geldart and R. E. Sheriff, 1990, “Applied Geophysics”. Cambridge University Press, Cambridge, UK.

Thomas, D.J., Jefferson, C.W., Yeo, G.M., Card, C., and Sopuck, V., 2002, “Introduction; in Field Trip A1. The Eastern Athabasca Basin and its Uranium Deposits”, (ed.) N. Andrade, G. Breton, C.W. Jefferson, D.J. Thomas, G. Tourigny, S. Wilson, and G.M. Yeo; Geological Association of Canada–Mineralogical Association of Canada Guidebook, Saskatoon, Saskatchewan, p. 1–22.

Thomas, M. D. and McHardy, S., 2007. “Magnetic insights into basement geology in the area of McArthur River uranium deposit, Athabasca Basin, Saskatchewan”, in Jefferson, C.W. and Delaney, G., eds., EXTECH IV: Geology and Uranium Exploration TECHnology of the Proterozoic Athabasca Basin, Saskatchewan and Alberta: Geological Survey of Canada, Bulletin 588 (also Saskatchewan Geological Society, Special Publication 18; Geological Association of Canada, Mineral Deposits

Division,Special Publication 4).

Thomas, M.D., and Wood, G., 2007. “Geological significance of gravity anomalies in the area of McArthur River uranium deposit, Athabasca Basin, Saskatchewan”; in EXTECH IV: Geology and Uranium EXploration TECHnology of the Proterozoic Athabasca Basin, Saskatchewan and Alberta, (ed.) C.W. Jefferson and G. Delaney; Geological Survey of Canada, Bulletin 588, p. 441–464.

Tietze, K. and Ritter, O., 2013. Three-dimensional magnetotelluric inversion in practice—the electrical conductivity structure of the San Andreas Fault in Central California. Geophysical Journal International, 195(1), pp.130-147.

Tikhonov, A.N., 1950, “On Determining Electrical Characteristics of the Deep Layers of the Earth’s Crust”, Doklady, Vol. 73, pp. 281-285.

Tuncer, V., M. J. Unsworth, W. Siripunvaraporn and J. A. Craven, 2006a, “Exploration for unconformity type uranium deposits with audio-magnetotelluric data: A case study from the McArthur River Mine, Saskatchewan (Canada)”, Geophysics, 71 (6), B201 – B209.

Tuncer, V., 2007, “Exploration for unconformity type uranium deposits with audiomagnetotellurics data: A case study from the McArthur River Mine, Saskatchewan, Canada”, M.Sc. Thesis, University of Alberta.

Vozoff, K., Hasegawa, H. and Ellis, R.M., 1963. “Results and limitations of magnetotelluric surveys in simple geologic situations”. Geophysics, 28(5), pp.778-792.

Vozoff, K., 1991, “The Magnetotelluric Method”, in Nabighian, M. N., Ed., Electromagnetic Methods in Applied Geophysics: SEG., 2B, 641-711.

Ward, Stanley H., and Hohmann, G. W., 1988, “Electromagnetic Theory for Geophysical Applications”, Electromagnetic Methods in Applied Geophysics, Vol. 1, pp. 130311.

Weidelt, P., and Chave, A. D., Chapter 2: “The theoretical basis for electromafnetic induction (The Magnetotelluric Method Theory and practice)”. Cambridge University Press, 1st edition, 2012.

Wessel, P., Smith, W. H. F., Scharroo, R., Luis, J., and Wobbe, F., Generic Mapping Tools: Improved Version Released, EOS Trans. AGU, 94(45), p. 409–410, 2013. doi:10.1002/2013EO450001.

White, D. J., Z. Hajnal, B. Roberts, I. Gyorfi, B. Reilkoff, B. Bellefleur, C. Mueller, S. Woelz, C. J. Mwenifumbo, E. Takacs, D. R. Schmitt, D. Brisbin, C. W. Jefferson, R. Koch, B. Powell and I. Annesley, 2007, “Seismic methods for uranium exploration; an overview of EXTECH IV seismic studies at the McArthur River mining camp, Athabasca Basin, Saskatchewan”; in Jefferson, C.W., and Delaney, G., eds., EXTECH IV: Geology and Uranium EXploration TECHnology of the Proterozoic Athabasca Basin, Saskatchewan and Alberta: Geological Survey of Canada, Bulletin 588.

Wiese, H., 1962, “Geomagnetische tiefentellurik, Geophys”. Pura. Appl., 52, 83 – 103.

Witherly, K., Irvine, R. and Morrison, E., 2004, “The Geotech VTEM time domain helicopter EM system. ASEG Extended Abstracts”, 2004(1), pp.1-4.

Wood, G., and Thomas, M.D., 2002, “Modeling of high-resolution gravity data near the McArthur River uranium deposit, Athabasca Basin”, Summary of Investigations 2002, v2, Saskatchewan Geological Survey, Saskatchewan Industry Resources, Miscellaneous Report 2002-4.2, Paper D-16.

Zonge, K.L. and Hughes, L.J., 1991, “Controlled source audio-frequency magnetotellurics”, In Electromagnetic Methods in Applied Geophysics: Volume 2, Application, Parts A and B (pp. 713-810). Society of Exploration Geophysicists.

Appendix A – Station Names

The AMT sounding stations in the study area are listed in the table below with station numbers, names, latitudes, longitudes and elevations. In Figure A.1, the map of the study area with the station names is presented.

Table A.1: Station list of the AMT soundings in the study area.

Station Number	Station Name	Latitude	Longitude	Elevation
1	22401S	57.726182972	-105.117469250	529.250
2	22402N	57.727886111	-105.121151778	583.470
3	22404S	57.724506556	-105.113887889	551.970
4	22405N	57.729723806	-105.124935833	554.300
5	22407S	57.722731556	-105.109920444	566.300
6	22408N	57.731435778	-105.128585528	556.930
7	22410N	57.732520111	-105.131041028	514.380
8	22410S	57.720947222	-105.106238722	548.450
9	22413S	57.719261639	-105.102507306	575.450
10	22416S	57.717342444	-105.098725222	586.960
11	22419S	57.715692611	-105.094910694	509.960
12	22422S	57.713925972	-105.090978722	498.210
13	23401S	57.732812611	-105.106458222	564.100
14	23402N	57.734534083	-105.110140944	516.100
15	23404S	57.731037139	-105.102809250	584.500
16	23405N	57.736363139	-105.113891556	523.600
17	23407S	57.729279639	-105.099043167	590.000
18	23408N	57.738183083	-105.117659278	518.200

19	23410S	57.727512861	-105.095478917	552.300
20	23411N	57.739859333	-105.121292556	522.700
21	23413S	57.725808889	-105.091864778	531.100
22	23414N	57.741652139	-105.125044167	515.800
23	23416S	57.724006056	-105.088217194	515.100
24	24001S	57.737021694	-105.099870444	550.300
25	24002N	57.738698306	-105.103687528	536.600
26	24004S	57.735201222	-105.096086944	500.650
27	24005N	57.740428944	-105.107219611	536.600
28	24007S	57.733470389	-105.092387972	511.800
29	24008N	57.742266972	-105.111088278	536.600
30	24010S	57.731694556	-105.088672472	511.530
31	24011N	57.743979194	-105.114872944	536.600
32	24013S	57.729981556	-105.084856750	506.100
33	24014N	57.745646528	-105.118523444	549.600
34	24017S	57.727263667	-105.079108306	548.390
35	24020S	57.724841583	-105.073915361	548.390
36	24801N	57.743260639	-105.092950444	521.410
37	24801S	57.742076083	-105.091435722	530.020
38	24804S	57.740228306	-105.087803194	519.330
39	24805N	57.745538056	-105.098348500	507.740
40	24807S	57.738398417	-105.084137472	516.850
41	24808N	57.747331139	-105.102603500	522.040
42	24809S	57.736900444	-105.080959917	509.340
43	24811N	57.749889361	-105.104677194	524.110
44	24814N	57.751547639	-105.108764611	511.670
45	24814S	57.733742611	-105.074588444	516.760
46	24817S	57.732396833	-105.071898944	498.310
47	24820S	57.730683167	-105.068386167	513.750
48	25400N	57.746939389	-105.085837194	527.110

49	25403N	57.748733222	-105.089621361	555.840
50	25403S	57.745163361	-105.082120639	518.130
51	25406N	57.750464194	-105.093220944	571.510
52	25407S	57.743216889	-105.077916972	523.250
53	25409N	57.752239778	-105.097073000	579.210
54	25410S	57.741180556	-105.073478417	513.210
55	25411S	57.740453750	-105.072166861	489.860
56	25412N	57.753934528	-105.100774000	574.500
57	25414N	57.755136250	-105.103146500	556.030
58	25414S	57.738677139	-105.068804333	516.150
59	25417S	57.736533000	-105.063795667	516.150
60	25420S	57.734514083	-105.059509889	519.220
61	26600N	57.754461556	-105.072161167	537.950
62	26603N	57.756682389	-105.076063972	532.620
63	26603S	57.752914528	-105.067789667	513.300
64	26606N	57.758548306	-105.079916028	923.440
65	26606S	57.751478861	-105.064947639	504.630
66	26609N	57.760162778	-105.083515861	830.700
67	26609S	57.749899611	-105.061735972	515.500
68	26612N	57.761956722	-105.087234083	830.700
69	26612S	57.747035417	-105.059328861	514.680
70	26614N	57.763176389	-105.089976444	830.700
71	26615S	57.745843583	-105.052977167	510.580
72	26620S	57.742980639	-105.046942861	31.150
73	27101N	57.759147667	-105.068792806	538.910
74	27102S	57.757335250	-105.065008556	519.940
75	27105N	57.761193278	-105.072947639	536.040
76	27105S	57.755244750	-105.060249639	547.300
77	27108N	57.763059194	-105.077001694	520.570
78	27108S	57.753683333	-105.057037889	522.260

79	27111N	57.765023806	-105.080972389	545.480
80	27111S	57.752086000	-105.053574333	506.410
81	27114N	57.766400611	-105.084009278	631.850
82	27114S	57.750228278	-105.049657111	502.550
83	27117S	57.748487111	-105.045925222	509.970
84	27120S	57.746584250	-105.041975139	563.470
85	27602N	57.762662056	-105.064312250	513.430
86	27605N	57.764331000	-105.067693417	539.770
87	27608N	57.766278056	-105.071462000	530.230
88	27610S	57.755860417	-105.048925500	548.190
89	27611N	57.768090389	-105.075045806	528.220
90	27613S	57.754065361	-105.045193000	505.930
91	27614N	57.769813111	-105.078142306	526.180
92	27616S	57.751956083	-105.040620472	496.770
93	27617N	57.771786444	-105.082466806	526.180
94	27620N	57.773571500	-105.086118917	532.420
95	28801S	57.768723611	-105.047161139	521.640
96	28802N	57.770707111	-105.051198083	515.340
97	28804S	57.767054056	-105.043999028	545.230
98	28805N	57.772520000	-105.054814944	545.840
99	28807S	57.765151111	-105.040147861	554.550
100	28808N	57.774512361	-105.058583750	537.050
101	28810S	57.763364750	-105.036515694	543.550
102	28811N	57.776082556	-105.062167333	571.730
103	28813S	57.761578278	-105.032867083	507.500
104	28814N	57.777868333	-105.065482583	541.560
105	28816S	57.759701889	-105.029201944	505.600
106	28819S	57.757170000	-105.023974000	492.220
107	29606N	57.778657861	-105.047308583	529.970
108	29609N	57.780524722	-105.051060639	545.000

109	29612N	57.782373528	-105.054712167	551.560
110	29615N	57.784599083	-105.059171833	572.970
111	29618N	57.786375833	-105.062790417	586.770
112	29621N	57.788278139	-105.066527333	572.620
113	29624N	57.790171333	-105.070331861	549.010
114	29627N	57.792001583	-105.074018944	532.280
115	29630N	57.793876583	-105.077824250	512.630
116	30401N	57.781527889	-105.032313500	574.640
117	30402S	57.779525917	-105.027940083	588.780
118	30404N	57.783009111	-105.035459333	573.720
119	30405S	57.777945750	-105.024559417	555.750
120	30407N	57.784768528	-105.039227917	561.030
121	30408S	57.775970389	-105.020405444	492.960
122	30410N	57.786545750	-105.043013722	552.680
123	30411S	57.774264306	-105.016840472	494.570
124	30413N	57.788394778	-105.046682250	545.930
125	30414S	57.772369528	-105.012939528	487.750
126	30416N	57.790117778	-105.050805083	572.780
127	30417S	57.770672194	-105.009274389	494.980
128	30419N	57.791742083	-105.054356306	576.070
129	30420S	57.768858028	-105.005542333	489.010
130	30422N	57.793635944	-105.057470944	541.260
131	30426N	57.796426056	-105.064456417	568.650
132	30430N	57.798211556	-105.068194222	558.140

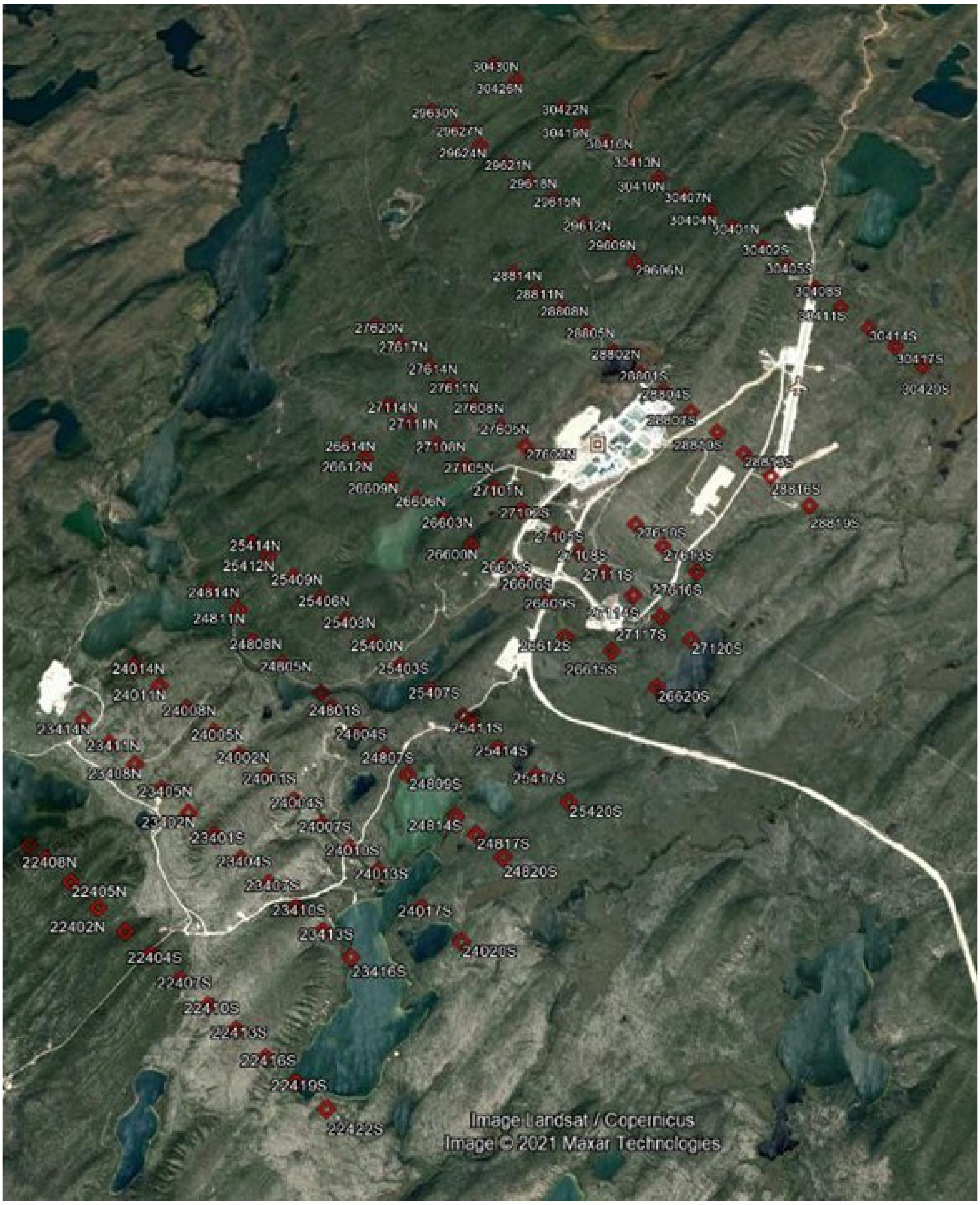

Figure A.1: Map of station locations with station names from Google Earth. (Latitude and longitude information was downloaded from https://ftp.maps.canada.ca/pub/nrcan_rncan/vector/gsc_sem/extech-IV_MT/mcarthur.txt.)

Appendix B – Apparent Resistivities and Phases From Measured Data and Synthetic Data (TE-TM only)

B.1 Apparent Resistivities and Phases From Mesured Data

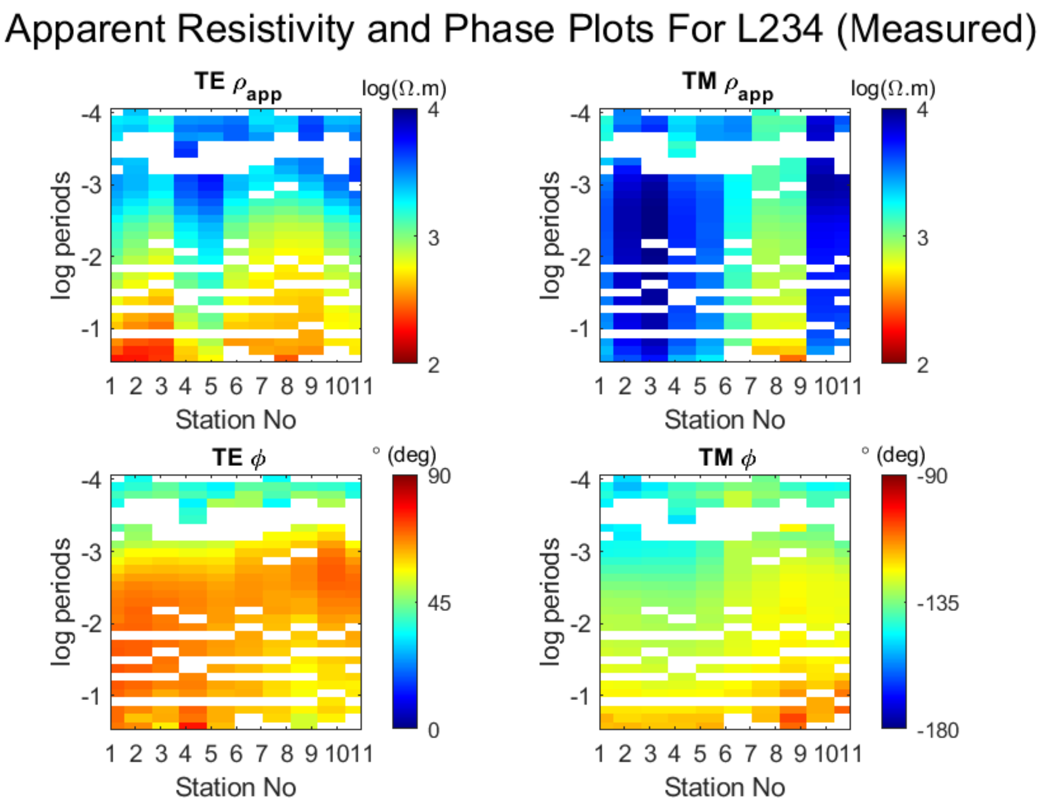

Apparent Resistivity and Phase Plots For L240 (Measured)

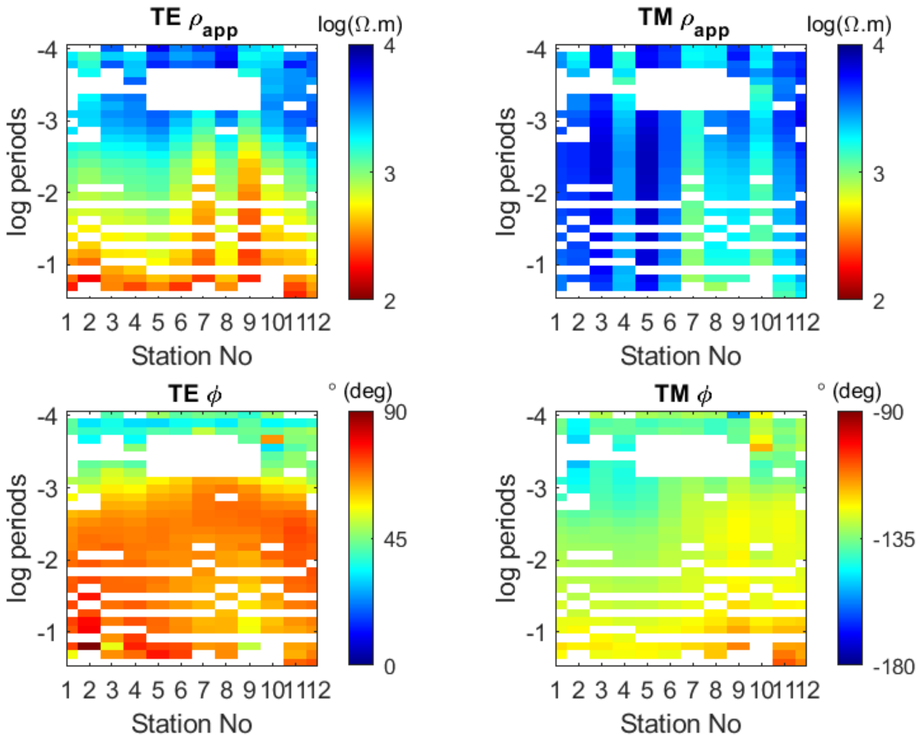

Apparent Resistivity and Phase Plots For L248 (Measured)

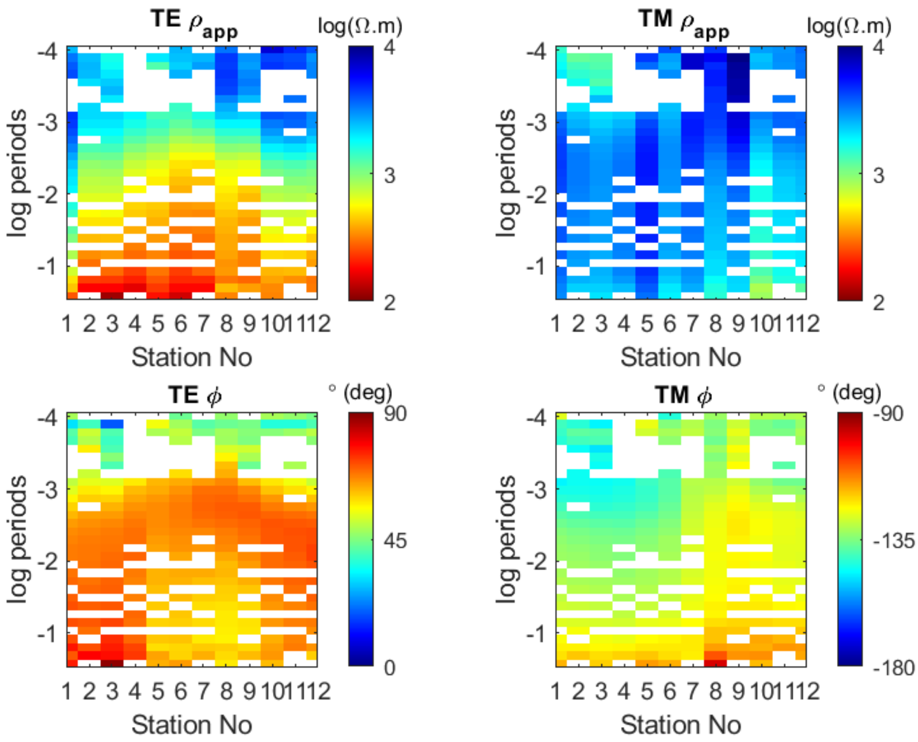

Apparent Resistivity and Phase Plots For L266 (Measured)

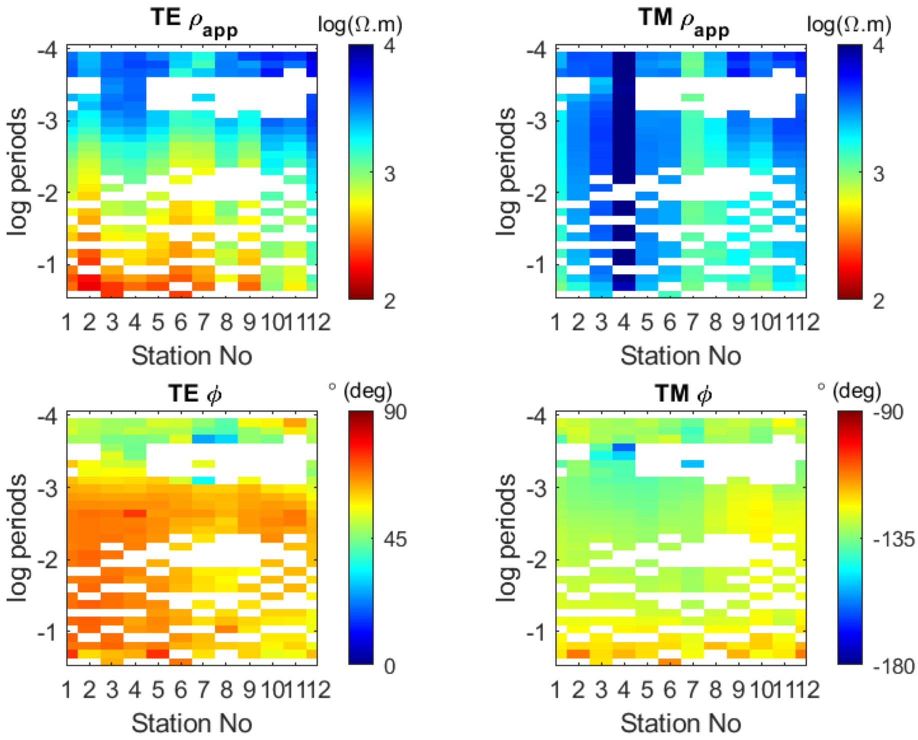

Apparent Resistivity and Phase Plots For L271 (Measured)

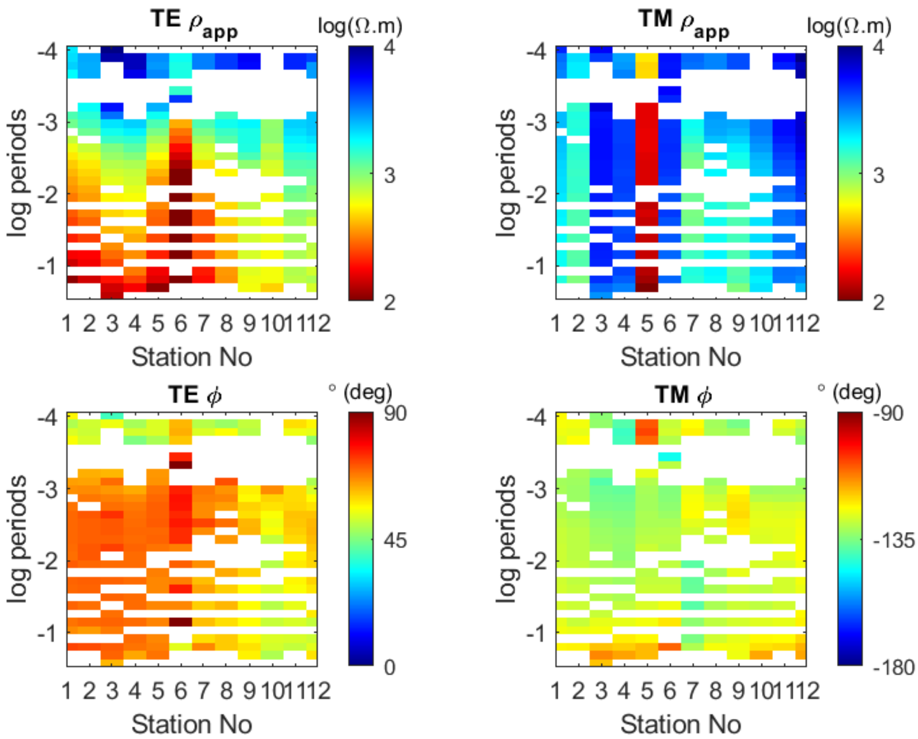

Apparent Resistivity and Phase Plots For L288 (Measured)

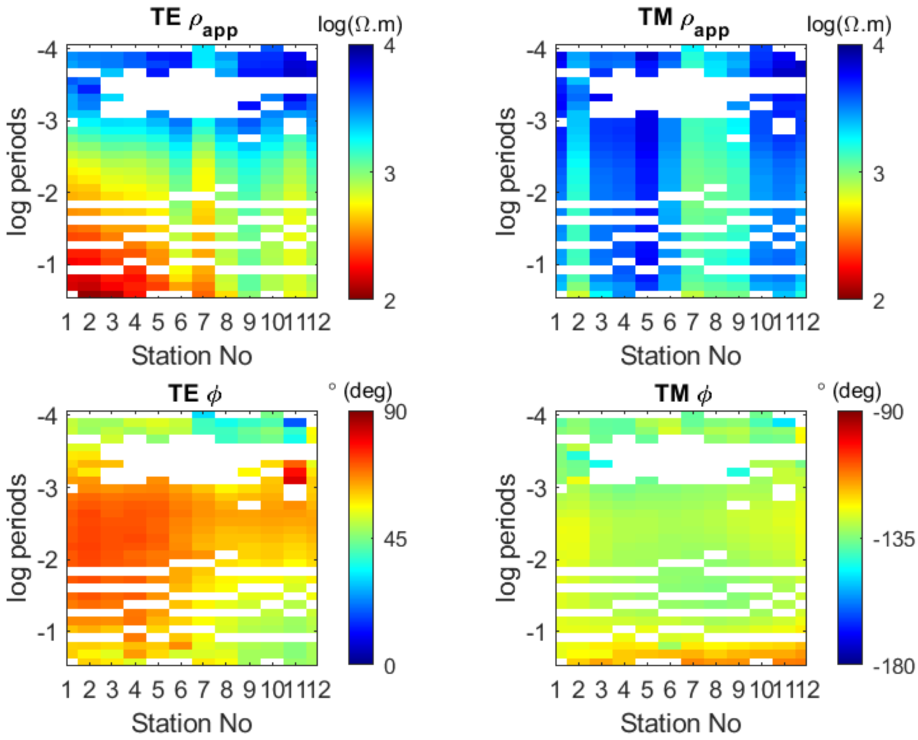

Apparent Resistivity and Phase Plots For L296 (Measured)

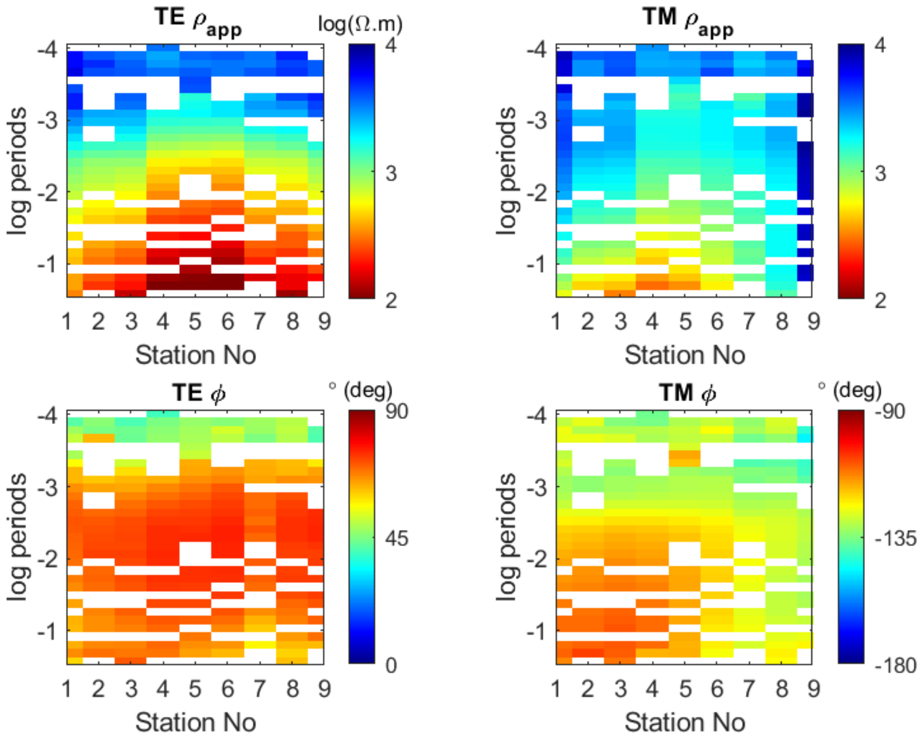

B.2 Apparent Resistivities and Phases From Synthetic Data

Apparent Resistivity and Phase Plots For L234 (Synthetic Data)

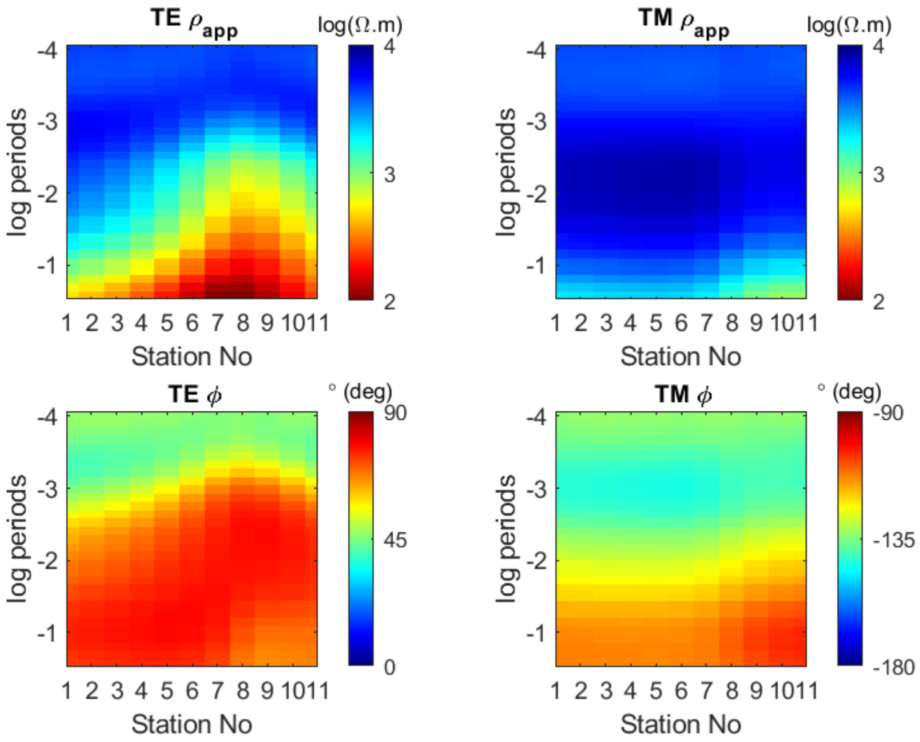

Apparent Resistivity and Phase Plots For L240 (Synthetic Data)

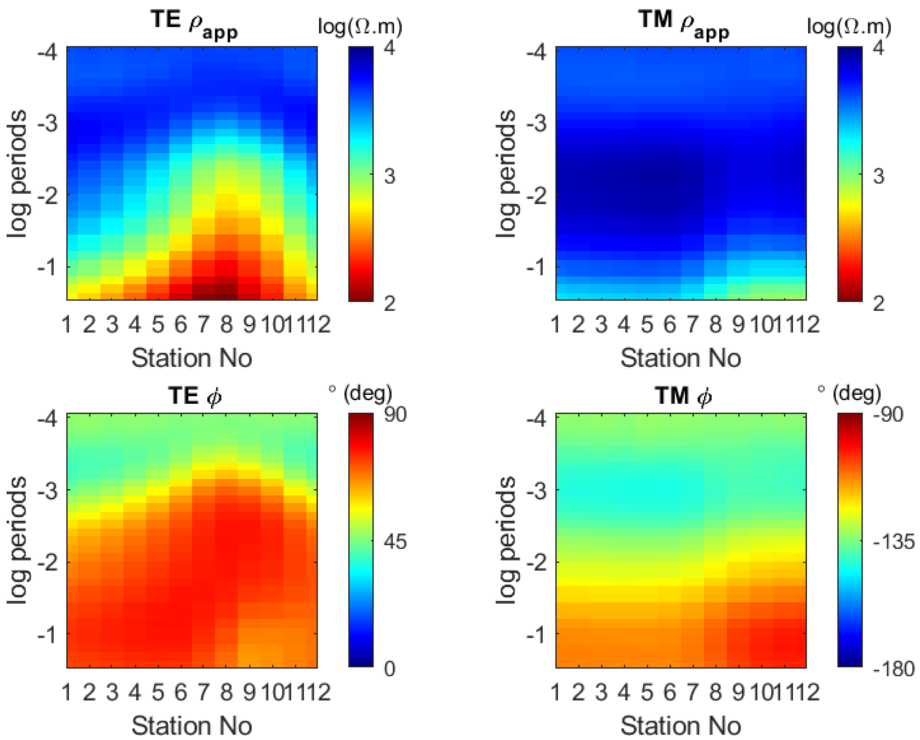

Apparent Resistivity and Phase Plots For L248 (Synthetic Data)

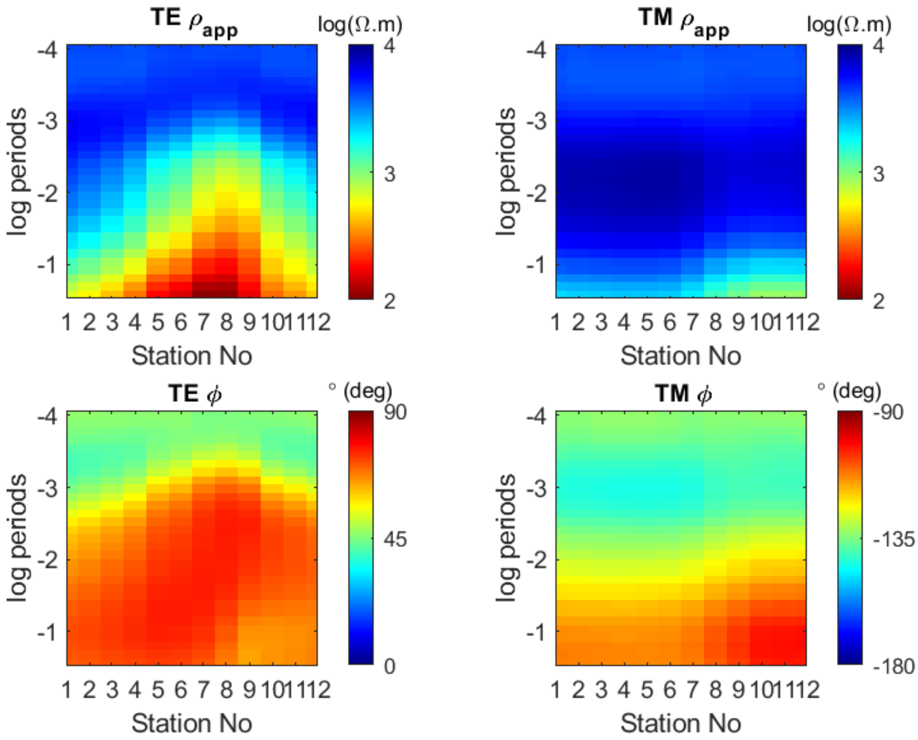

Apparent Resistivity and Phase Plots For L266 (Synthetic Data)

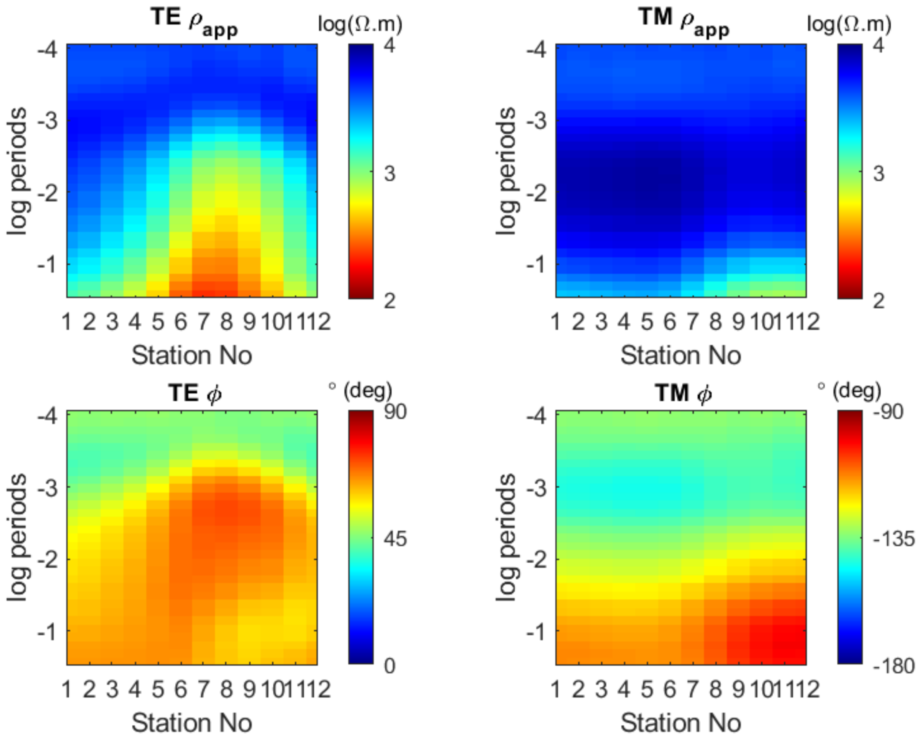

Apparent Resistivity and Phase Plots For L271 (Synthetic Data)

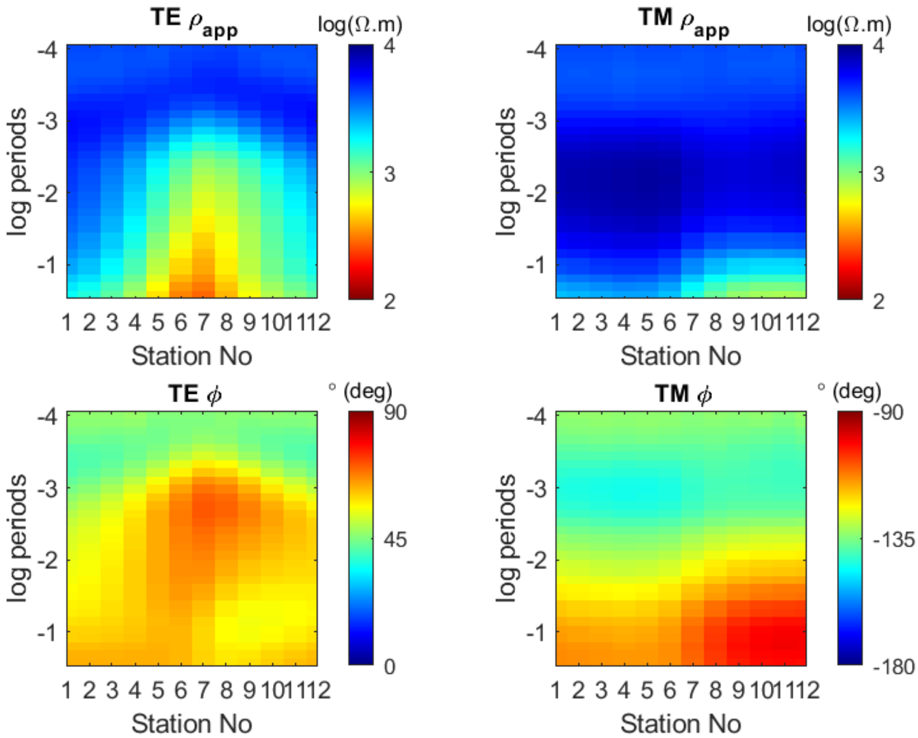

Apparent Resistivity and Phase Plots For L276 (Synthetic Data)

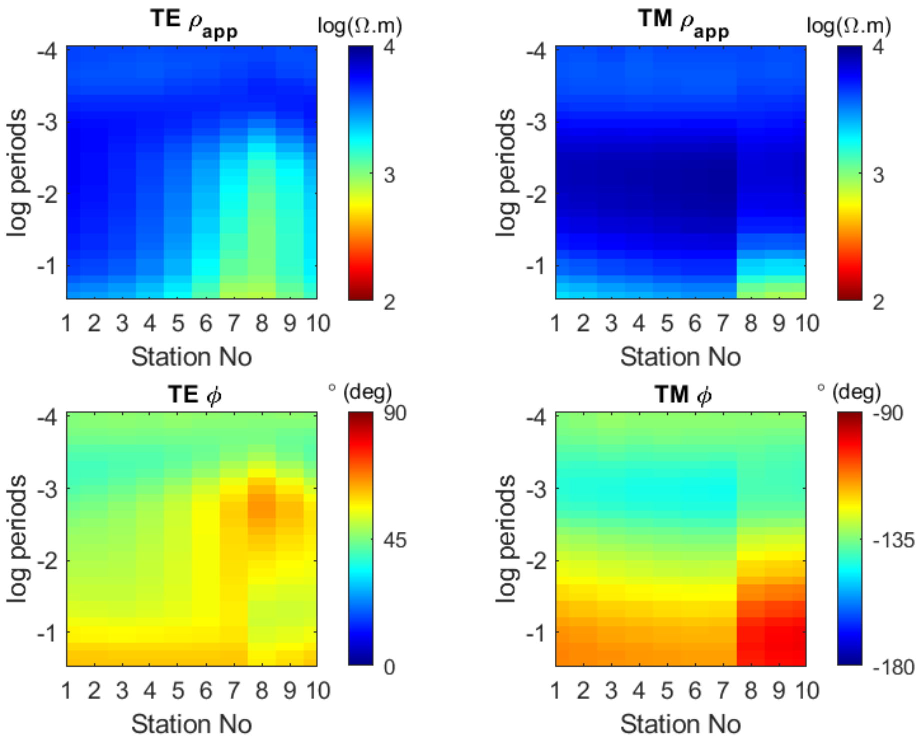

Apparent Resistivity and Phase Plots For L288 (Synthetic Data)

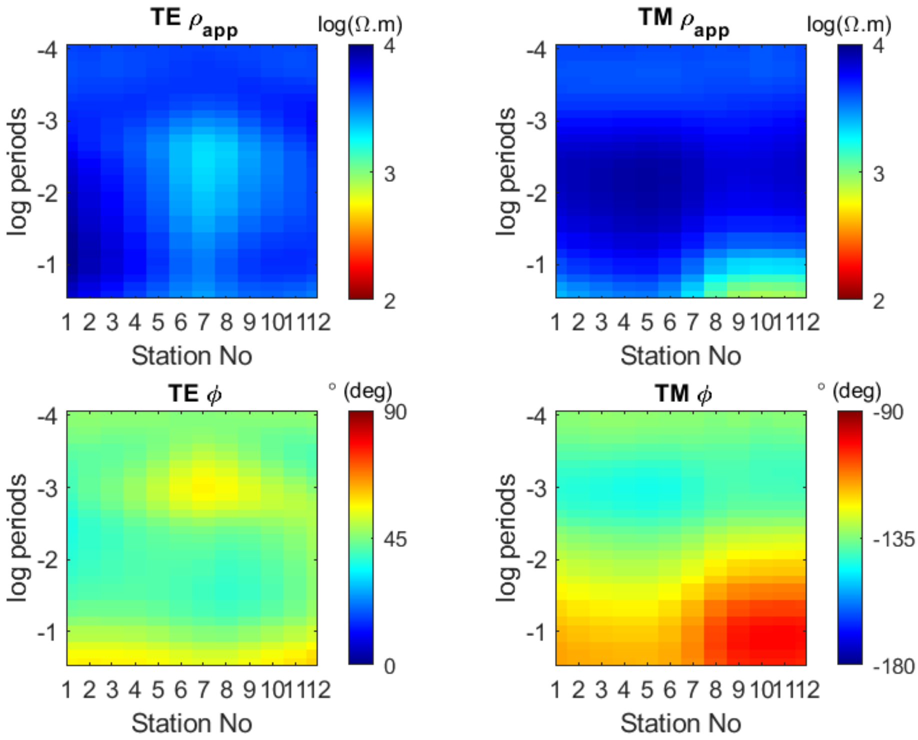

Apparent Resistivity and Phase Plots For L296 (Synthetic Data)

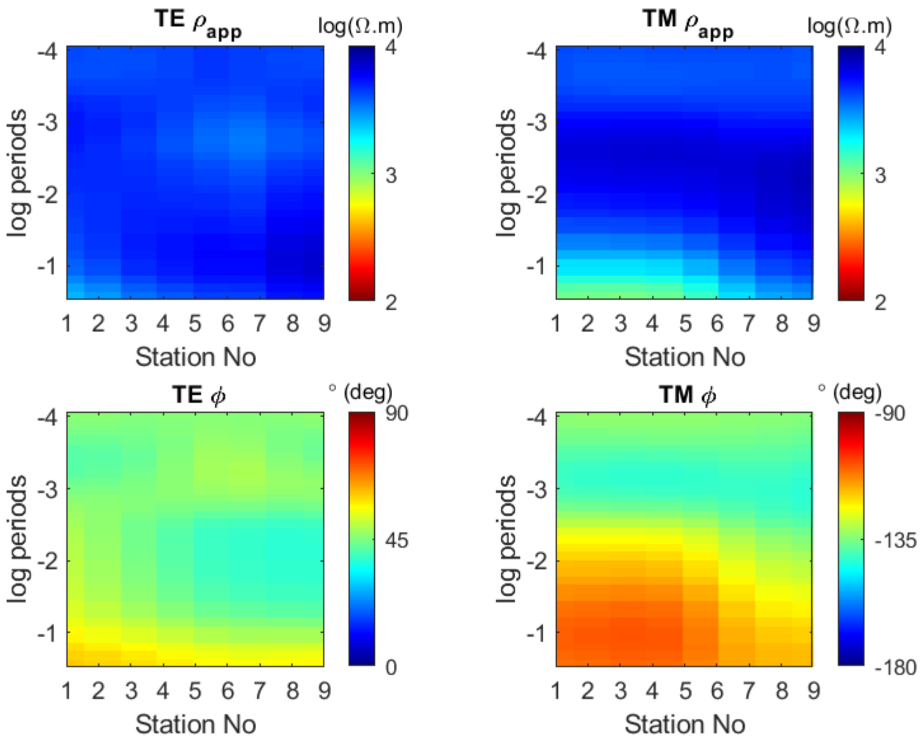

Appendix C – Fit Plots of Impedances, Apparent Resistivities and Phases for Inversion of the Synthetic Data

C.1. Fit Plots of Impedances

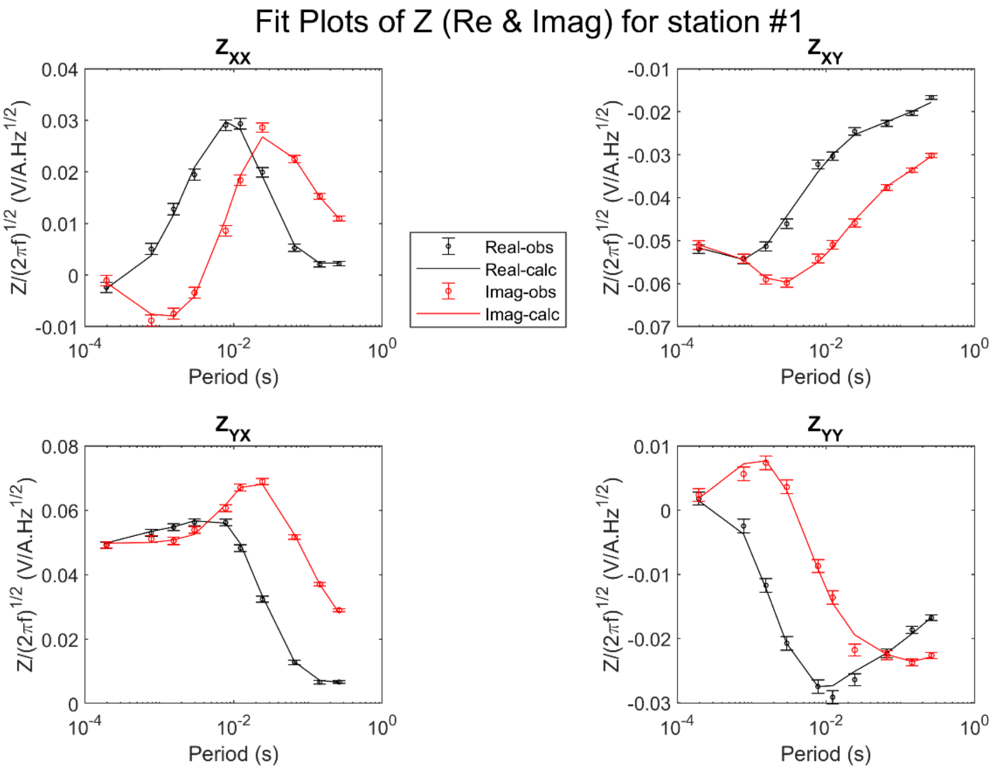

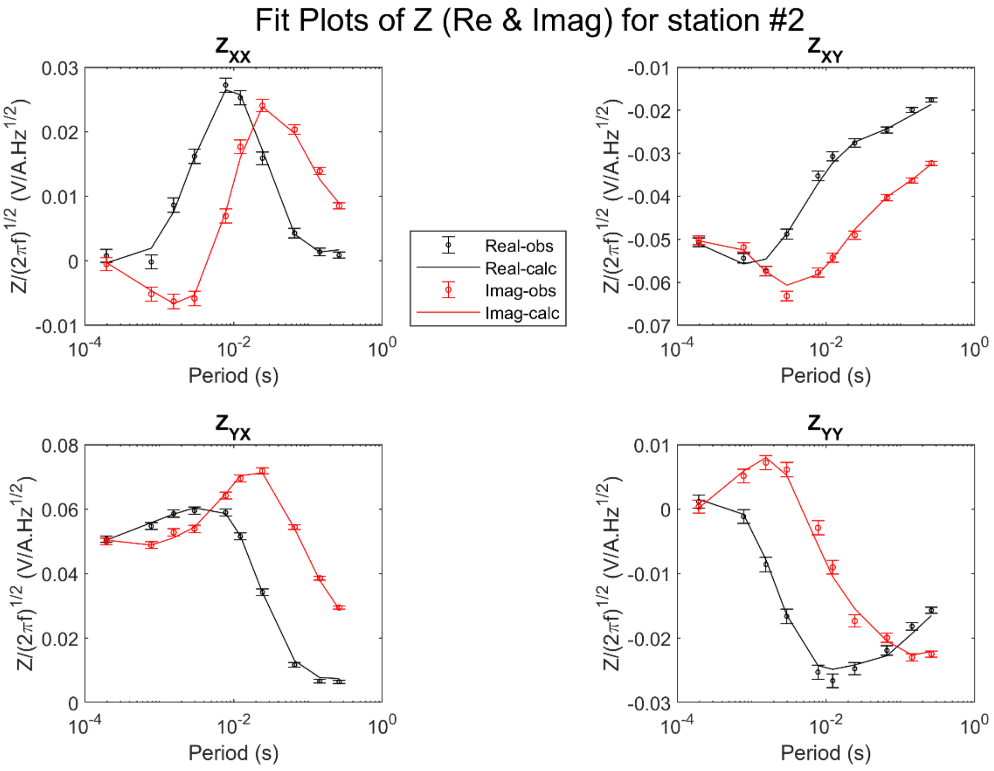
Fit Plots of Z (Re & Imag) for station #2
Z_{XX}
Z_{XY}
Z_{YX}
Z_{YY}
$Z/(2\pi f)^{1/2}$ (V/A.Hz$^{1/2}$)
Period (s)
Real-obs
Real-calc
Imag-obs
Imag-calc

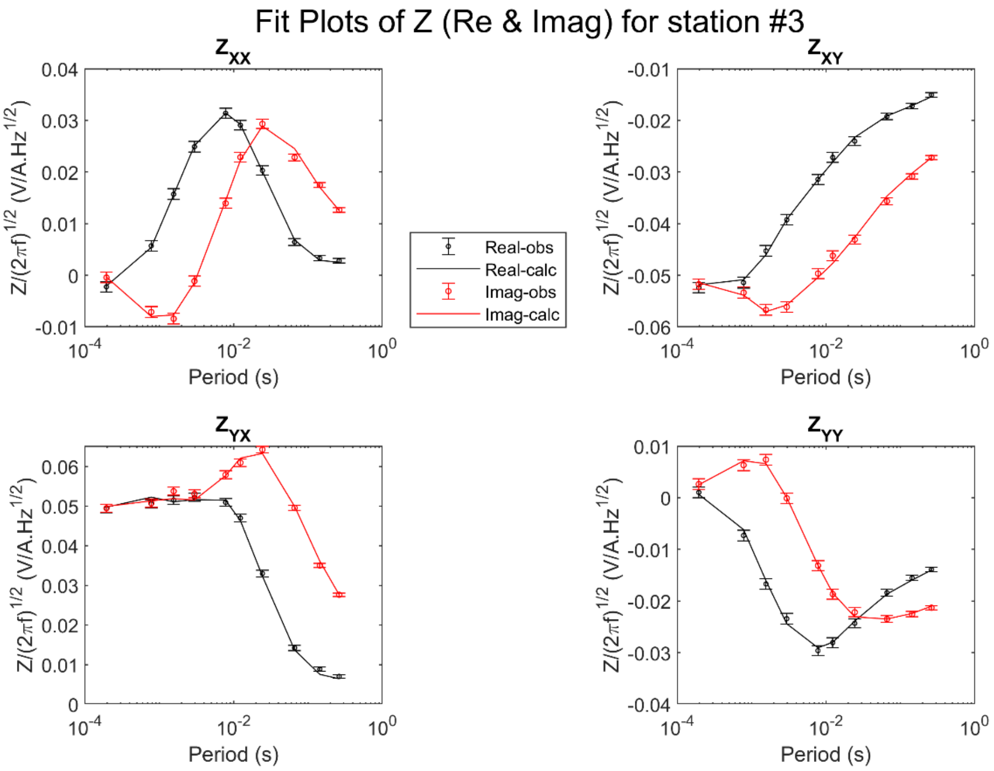
Fit Plots of Z (Re & Imag) for station #3
Z_{XX}
Z_{XY}
Z_{YX}
Z_{YY}
$Z/(2\pi f)^{1/2}$ (V/A.Hz$^{1/2}$)
Period (s)
Real-obs
Real-calc
Imag-obs
Imag-calc

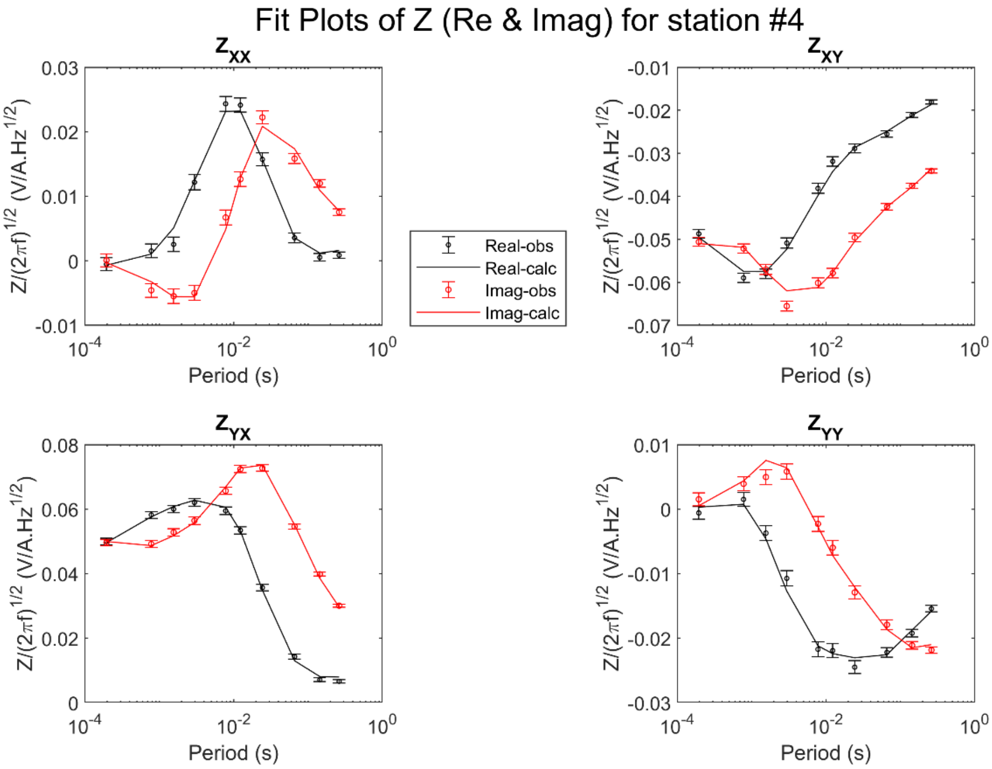
Fit Plots of Z (Re & Imag) for station #4
Z_XX
Z_XY
Z_YX
Z_YY
Z/(2πf)^1/2 (V/A.Hz^1/2)
Period (s)
Real-obs
Real-calc
Imag-obs
Imag-calc

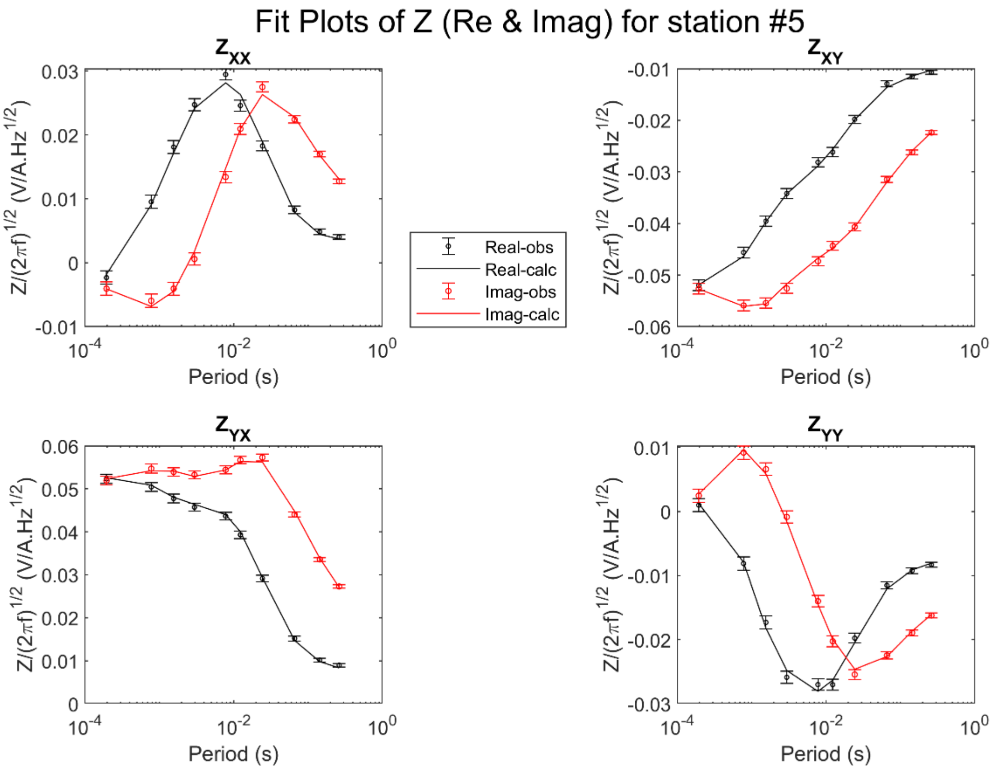
Fit Plots of Z (Re & Imag) for station #5
Z_XX
Z_XY
Z_YX
Z_YY
Z/(2πf)^1/2 (V/A.Hz^1/2)
Period (s)
Real-obs
Real-calc
Imag-obs
Imag-calc

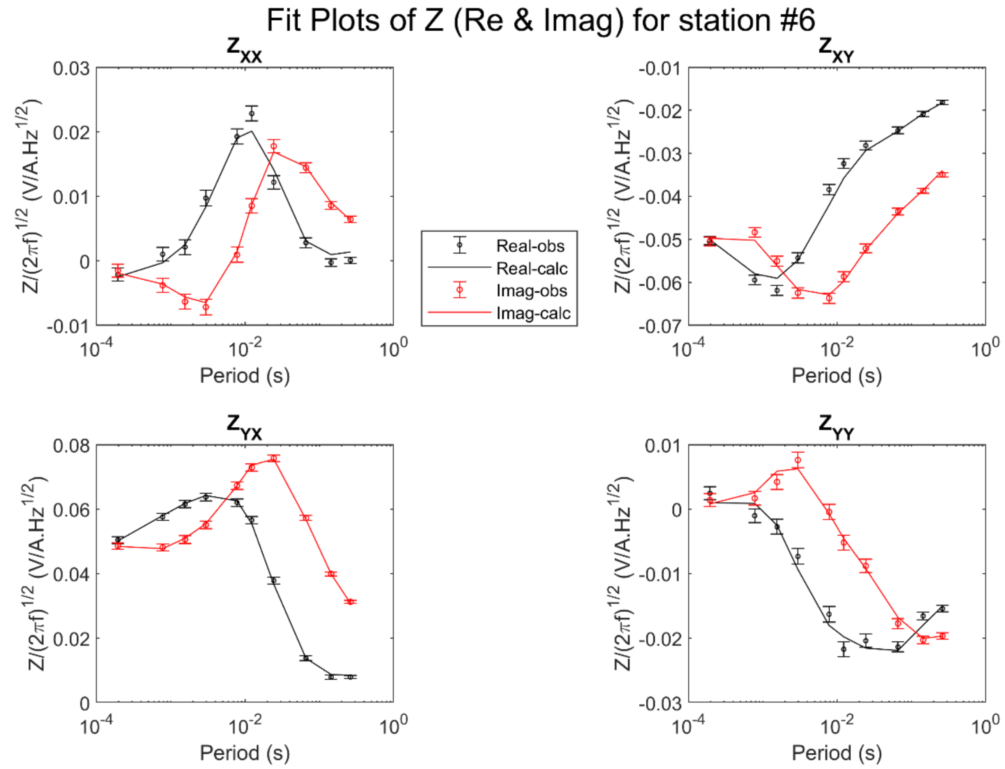
Fit Plots of Z (Re & Imag) for station #6
Z_XX
Z_XY
Z_YX
Z_YY
Z/(2πf)^1/2 (V/A.Hz^1/2)
Period (s)
Real-obs
Real-calc
Imag-obs
Imag-calc

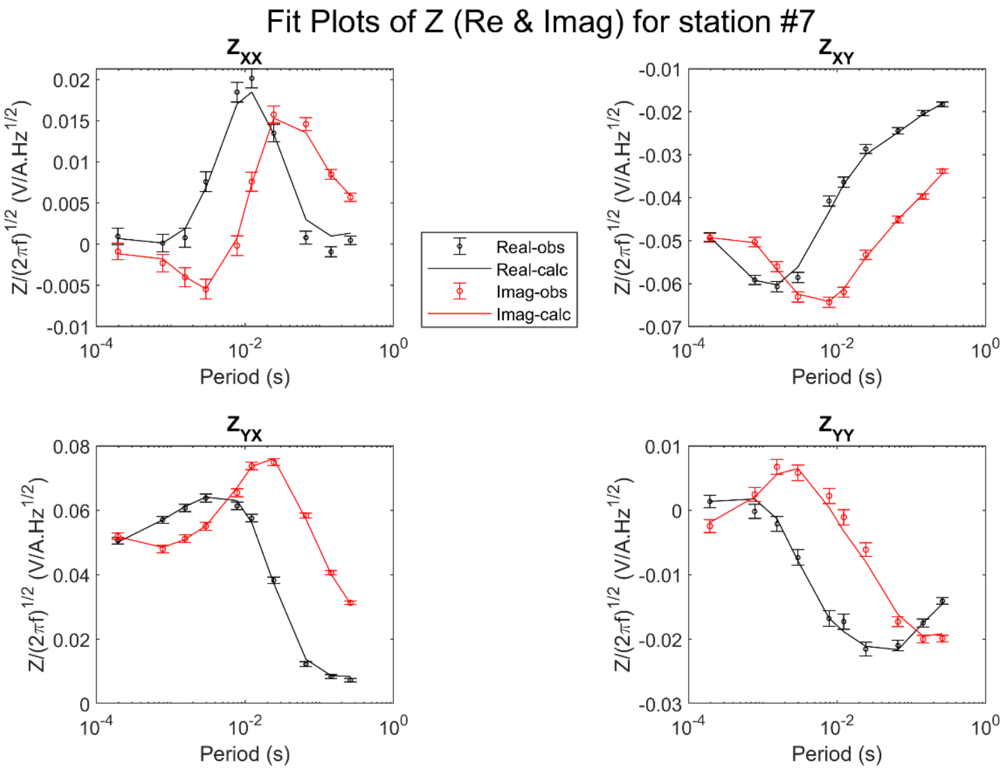
Fit Plots of Z (Re & Imag) for station #7
Z_XX
Z_XY
Z_YX
Z_YY
Z/(2πf)^1/2 (V/A.Hz^1/2)
Period (s)
Real-obs
Real-calc
Imag-obs
Imag-calc

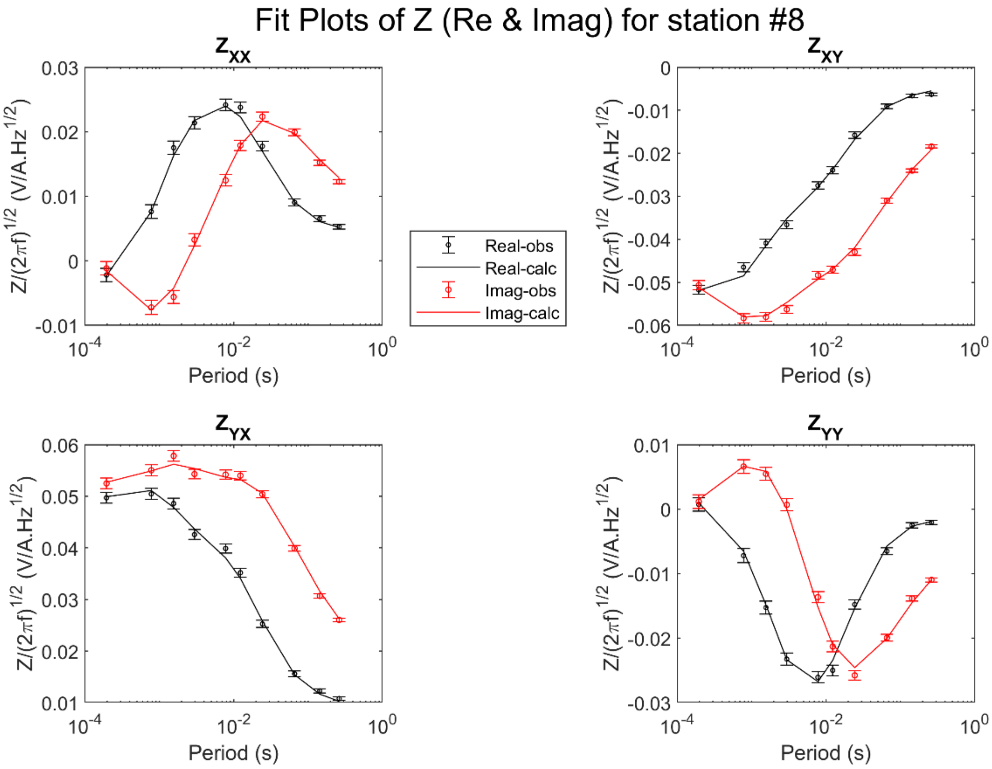
Fit Plots of Z (Re & Imag) for station #8
Z_{XX}
Z_{XY}
Z_{YX}
Z_{YY}
Real-obs
Real-calc
Imag-obs
Imag-calc
Period (s)
$Z/(2\pi f)^{1/2}$ (V/A.Hz$^{1/2}$)

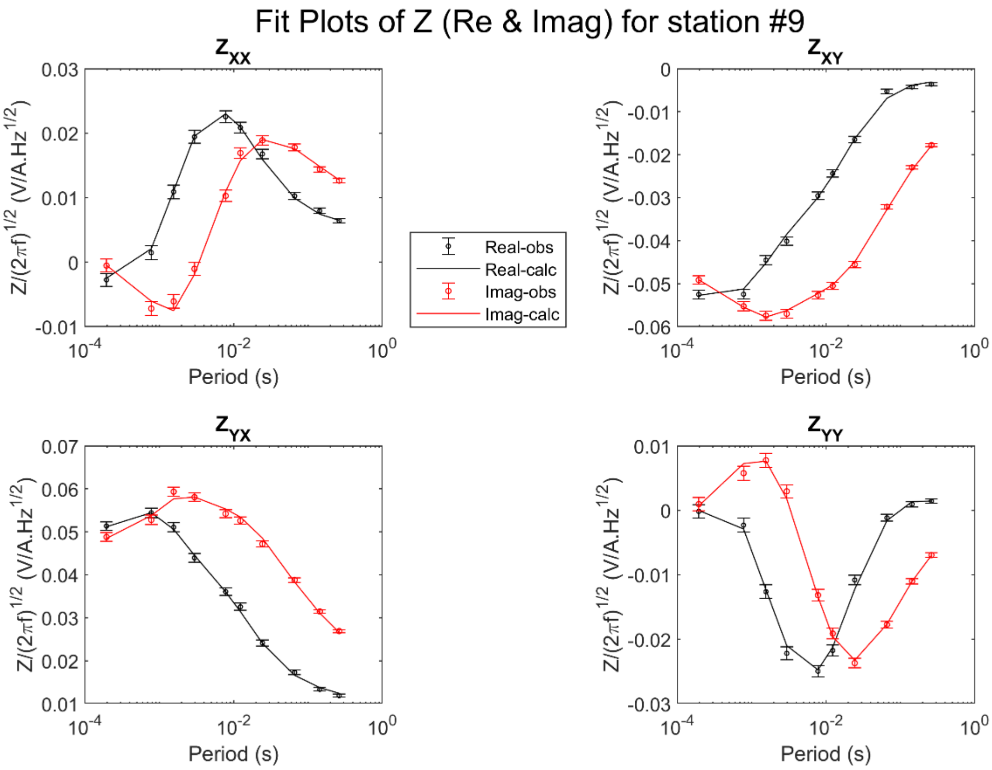
Fit Plots of Z (Re & Imag) for station #9
Z_{XX}
Z_{XY}
Z_{YX}
Z_{YY}
Real-obs
Real-calc
Imag-obs
Imag-calc
Period (s)
$Z/(2\pi f)^{1/2}$ (V/A.Hz$^{1/2}$)

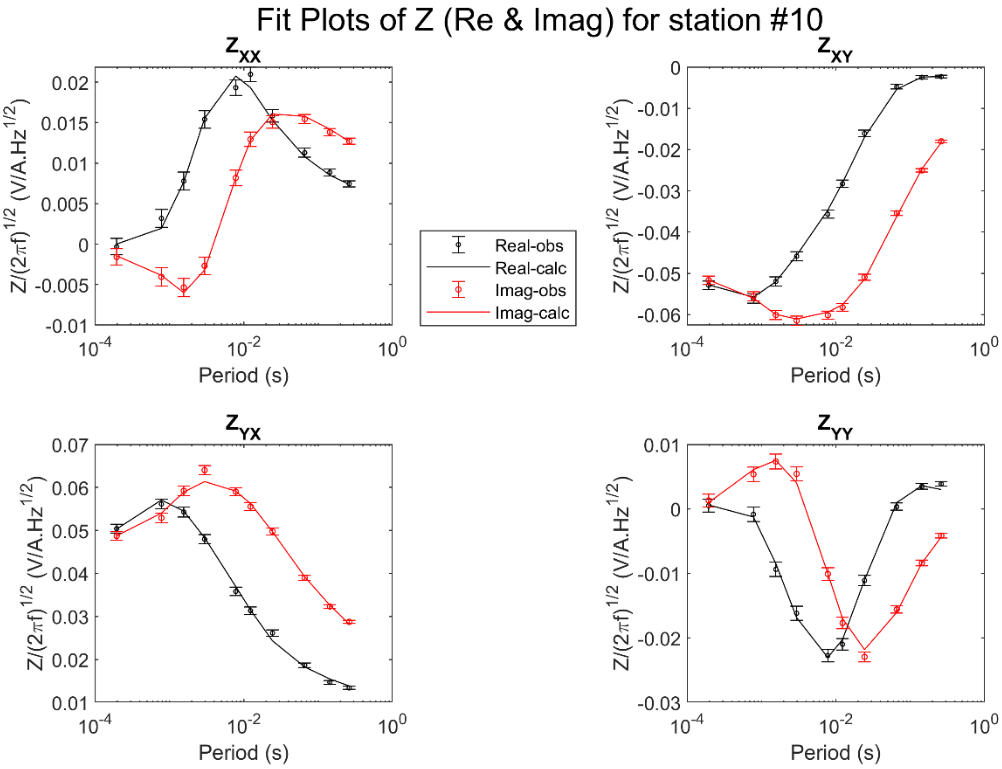
Fit Plots of Z (Re & Imag) for station #10
Z_{XX}
Z_{XY}
Z_{YX}
Z_{YY}
$Z/(2\pi f)^{1/2}$ (V/A.Hz$^{1/2}$)
Period (s)
Real-obs
Real-calc
Imag-obs
Imag-calc

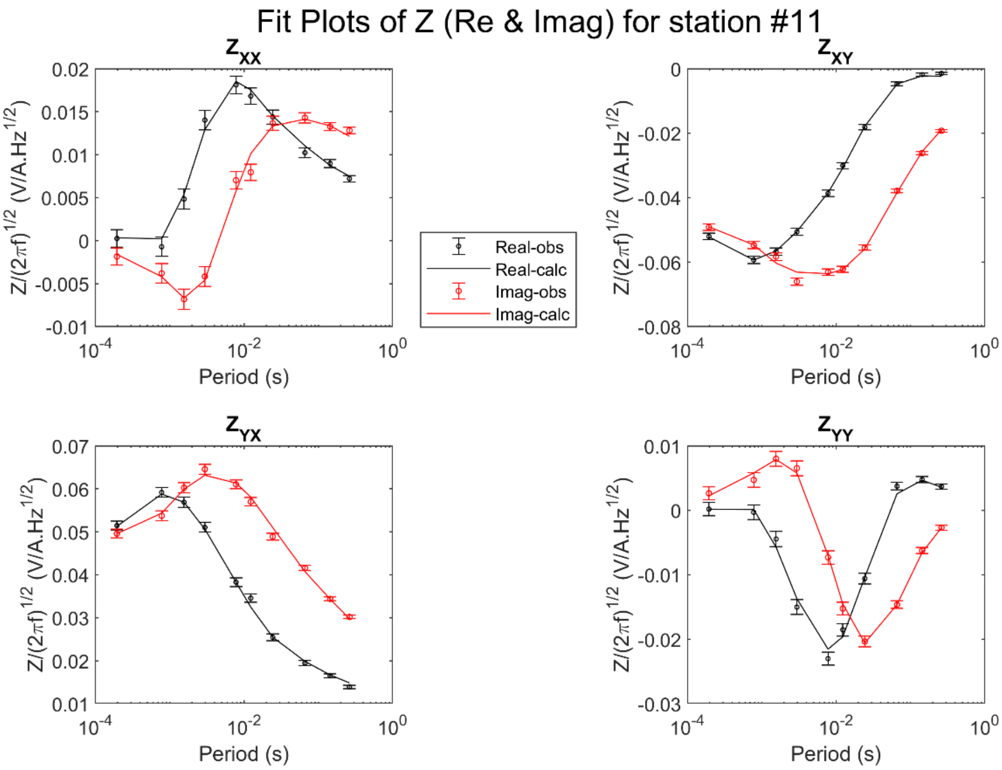
Fit Plots of Z (Re & Imag) for station #11
Z_{XX}
Z_{XY}
Z_{YX}
Z_{YY}
$Z/(2\pi f)^{1/2}$ (V/A.Hz$^{1/2}$)
Period (s)
Real-obs
Real-calc
Imag-obs
Imag-calc

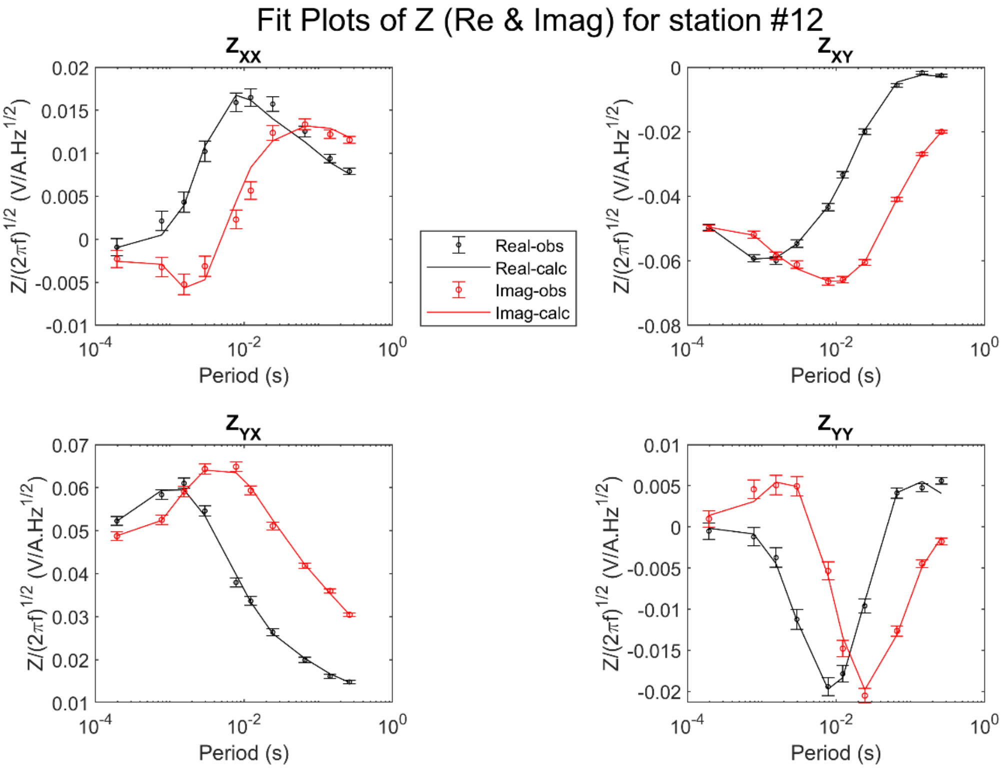
Fit Plots of Z (Re & Imag) for station #12
Z_XX
Z_XY
Z_YX
Z_YY
Z/(2πf)^1/2 (V/A.Hz^1/2)
Period (s)
Real-obs
Real-calc
Imag-obs
Imag-calc

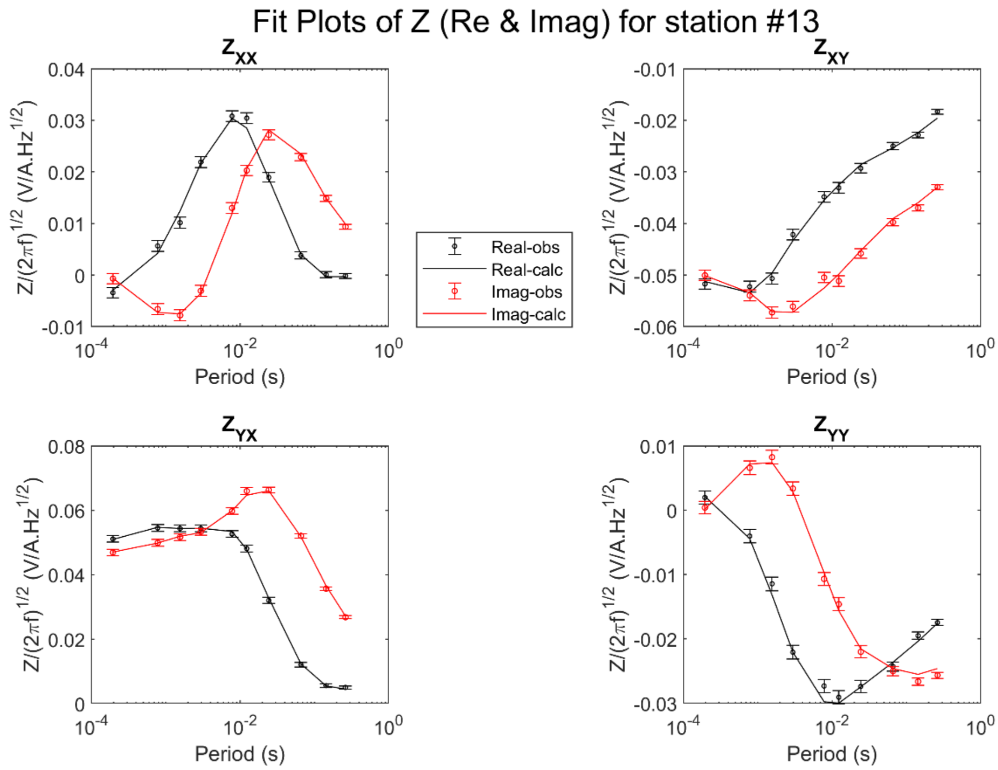
Fit Plots of Z (Re & Imag) for station #13
Z_XX
Z_XY
Z_YX
Z_YY
Z/(2πf)^1/2 (V/A.Hz^1/2)
Period (s)
Real-obs
Real-calc
Imag-obs
Imag-calc

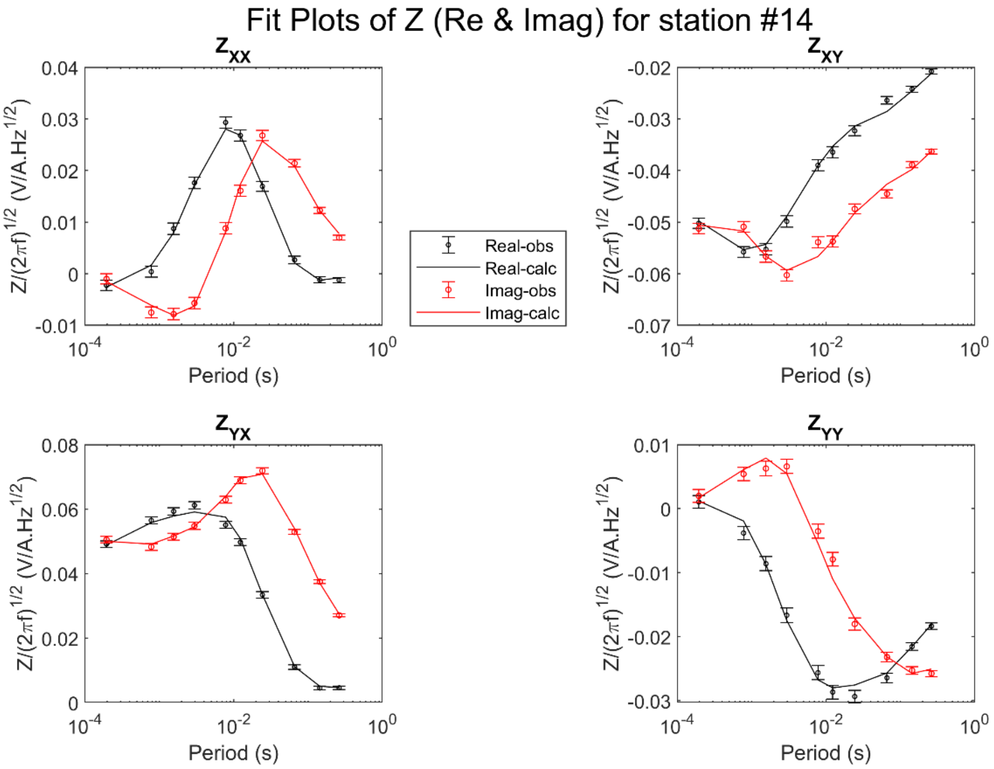
Fit Plots of Z (Re & Imag) for station #14
Z_XX
Z_XY
Z_YX
Z_YY
Z/(2πf)^1/2 (V/A.Hz^1/2)
Period (s)
Real-obs
Real-calc
Imag-obs
Imag-calc

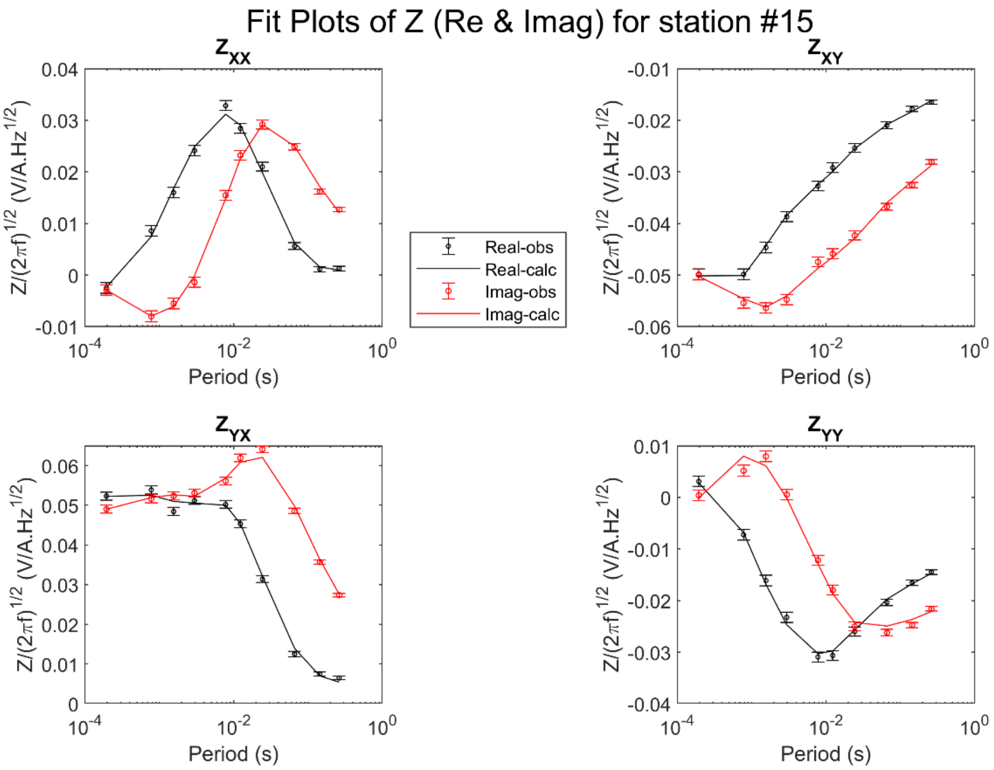
Fit Plots of Z (Re & Imag) for station #15
Z_XX
Z_XY
Z_YX
Z_YY
Z/(2πf)^1/2 (V/A.Hz^1/2)
Period (s)
Real-obs
Real-calc
Imag-obs
Imag-calc

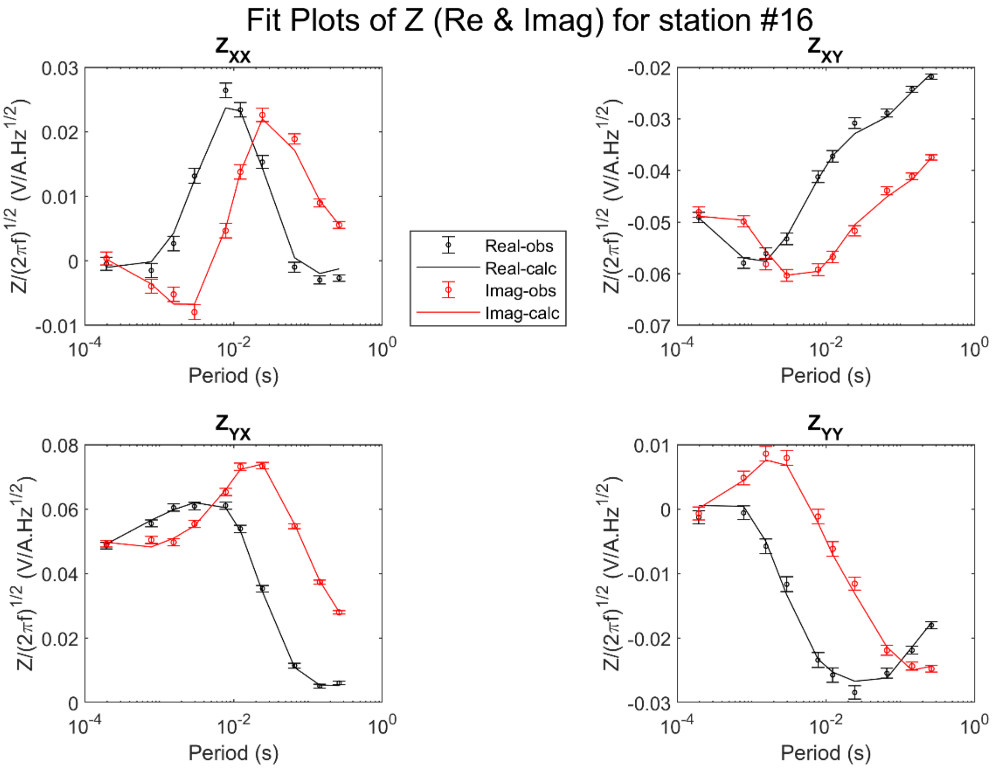
Fit Plots of Z (Re & Imag) for station #16
Z_{XX}
Z_{XY}
Z_{YX}
Z_{YY}
$Z/(2\pi f)^{1/2}$ (V/A.Hz$^{1/2}$)
Period (s)
Real-obs
Real-calc
Imag-obs
Imag-calc

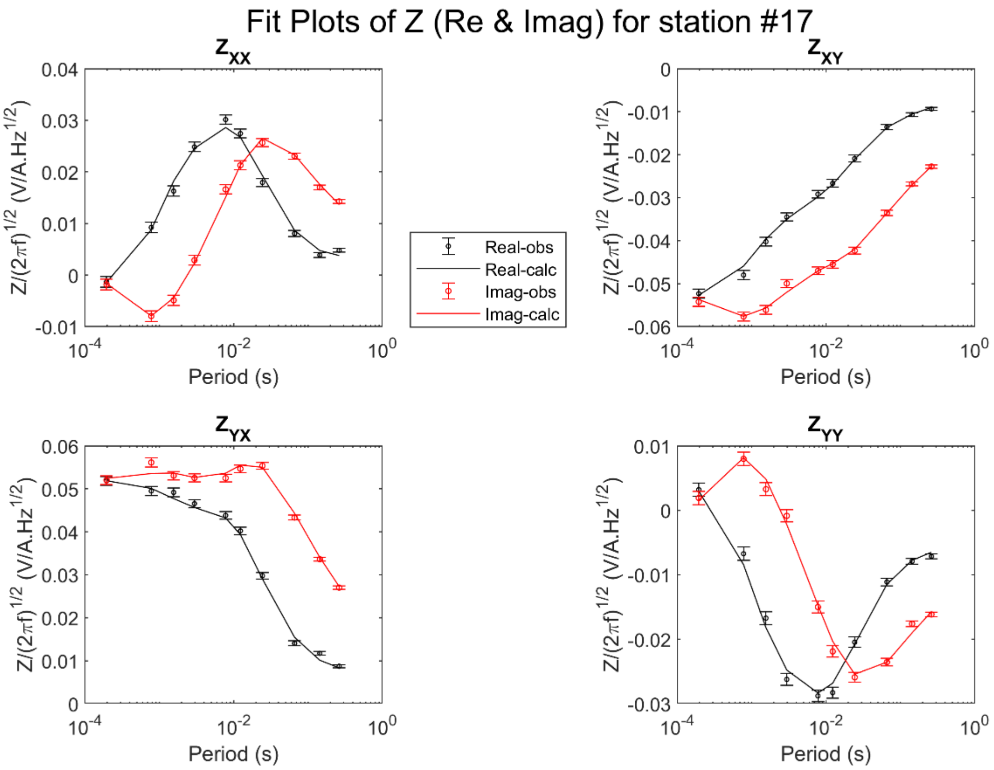
Fit Plots of Z (Re & Imag) for station #17
Z_{XX}
Z_{XY}
Z_{YX}
Z_{YY}
$Z/(2\pi f)^{1/2}$ (V/A.Hz$^{1/2}$)
Period (s)
Real-obs
Real-calc
Imag-obs
Imag-calc

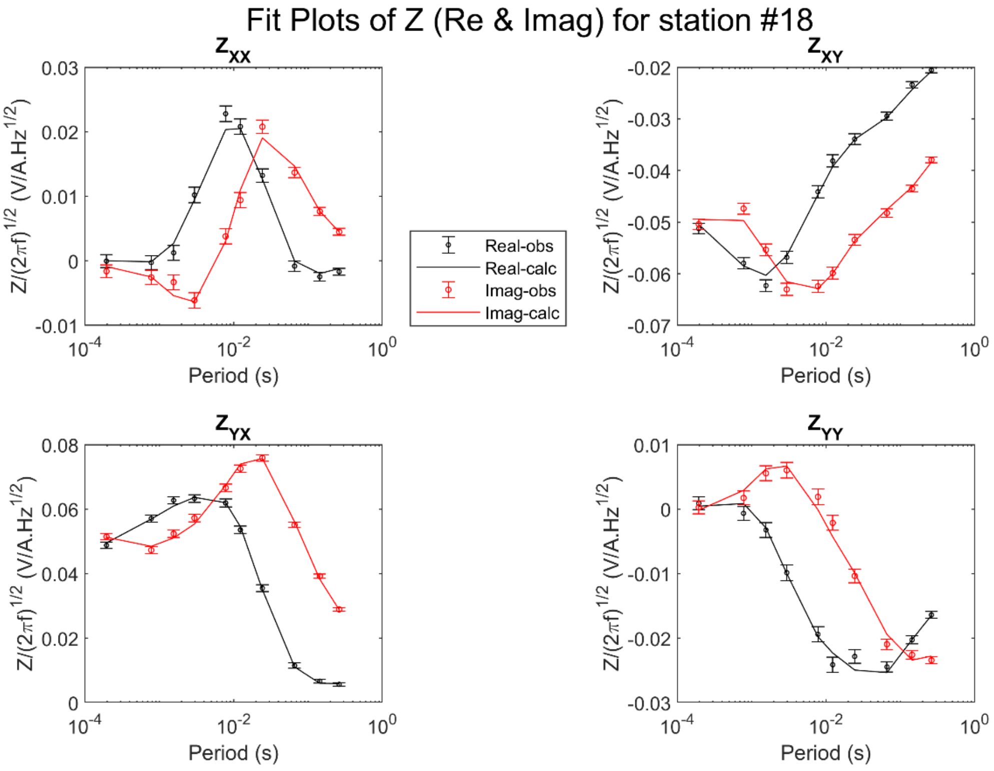
Fit Plots of Z (Re & Imag) for station #18
Z_{XX}
Z_{XY}
Z_{YX}
Z_{YY}
$Z/(2\pi f)^{1/2}$ (V/A.Hz$^{1/2}$)
Period (s)
Real-obs
Real-calc
Imag-obs
Imag-calc

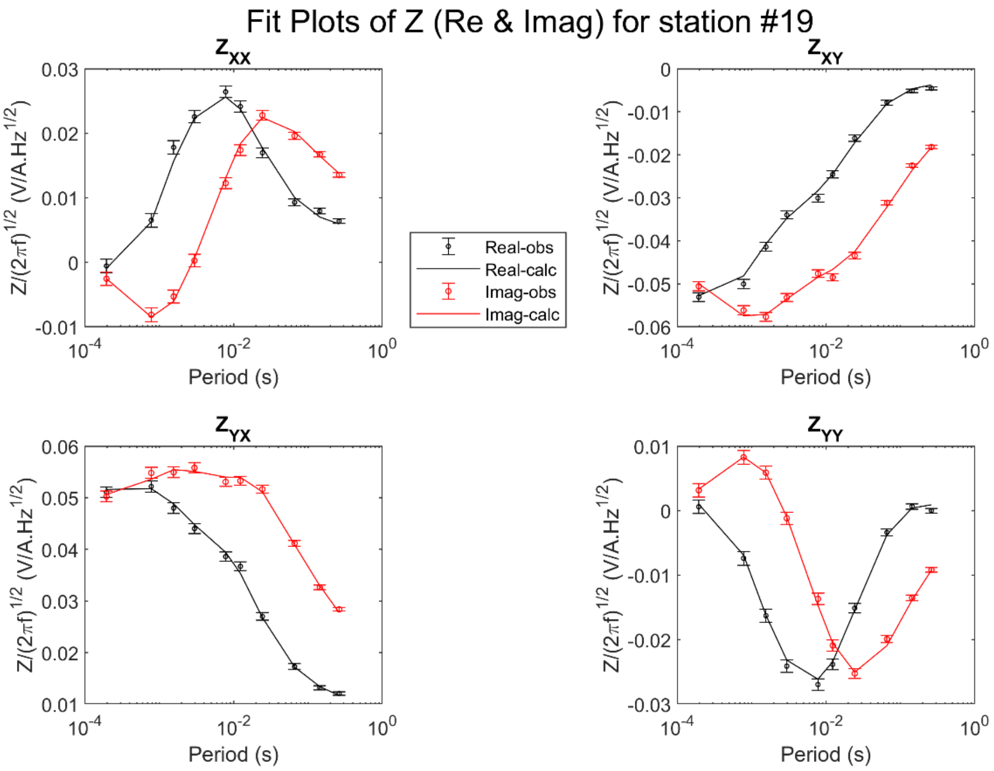
Fit Plots of Z (Re & Imag) for station #19
Z_{XX}
Z_{XY}
Z_{YX}
Z_{YY}
$Z/(2\pi f)^{1/2}$ (V/A.Hz$^{1/2}$)
Period (s)
Real-obs
Real-calc
Imag-obs
Imag-calc

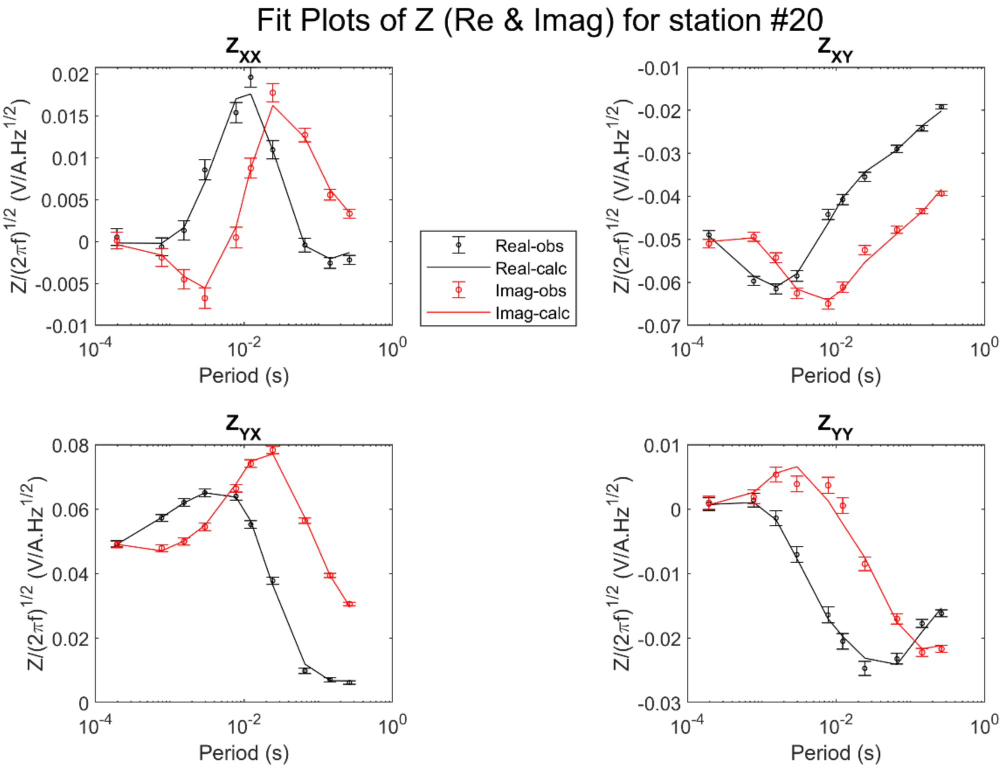
Fit Plots of Z (Re & Imag) for station #20
Z_{XX}
Z_{XY}
Z_{YX}
Z_{YY}
$Z/(2\pi f)^{1/2}$ (V/A.Hz$^{1/2}$)
Period (s)
Real-obs
Real-calc
Imag-obs
Imag-calc

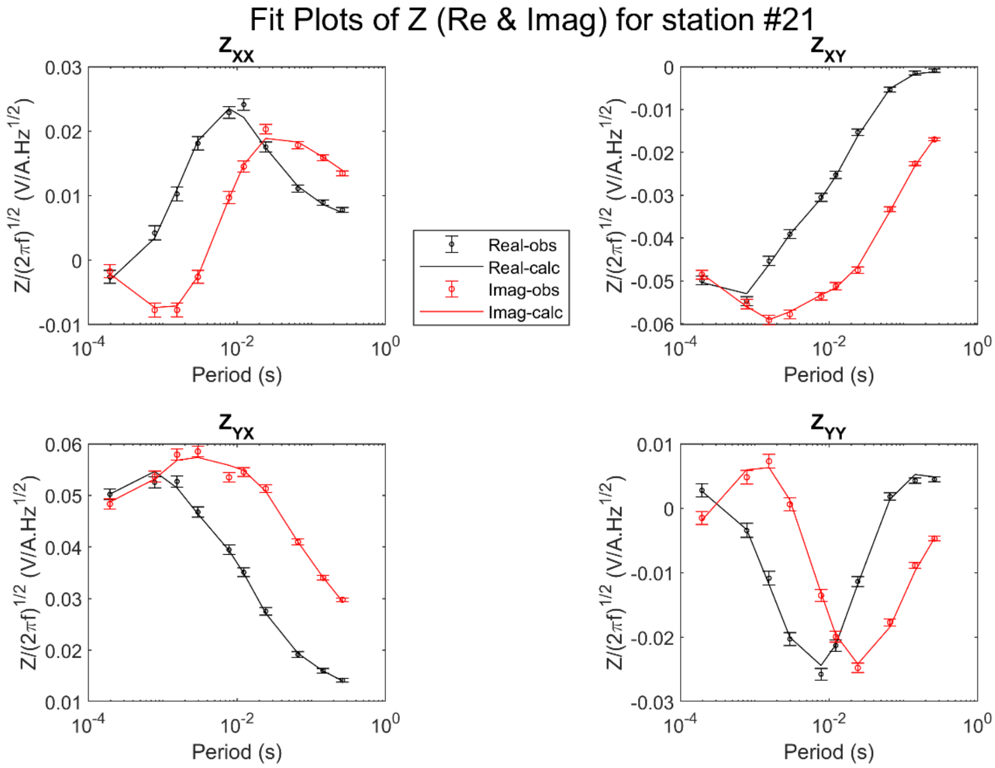
Fit Plots of Z (Re & Imag) for station #21
Z_{XX}
Z_{XY}
Z_{YX}
Z_{YY}
$Z/(2\pi f)^{1/2}$ (V/A.Hz$^{1/2}$)
Period (s)
Real-obs
Real-calc
Imag-obs
Imag-calc

Fit Plots of Z (Re & Imag) for station #22

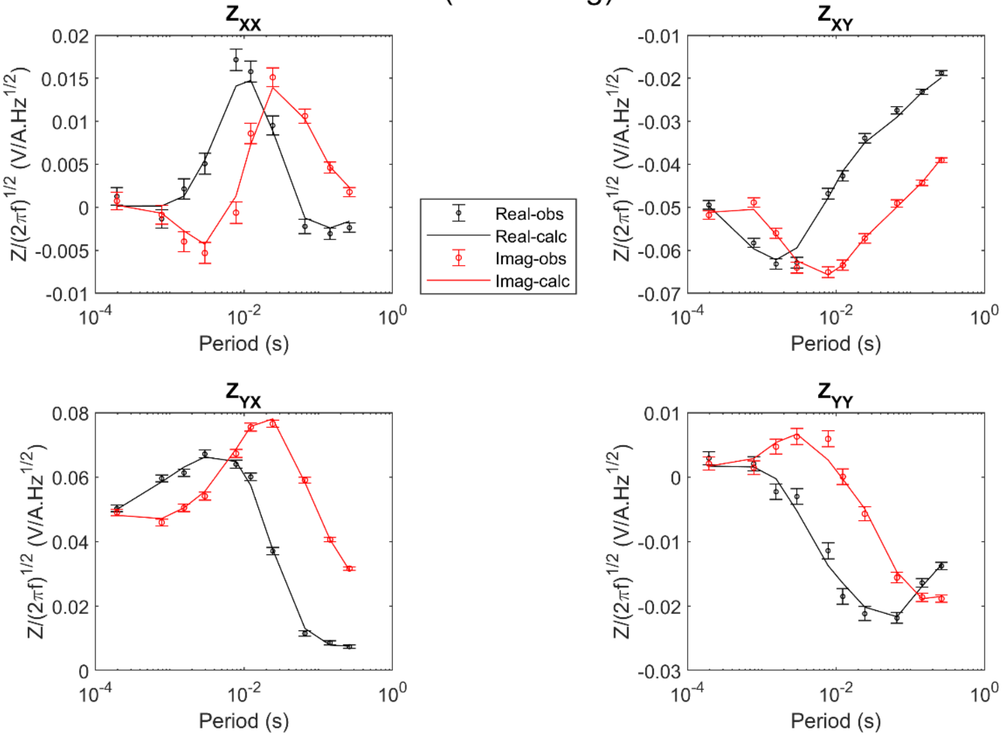

Fit Plots of Z (Re & Imag) for station #23

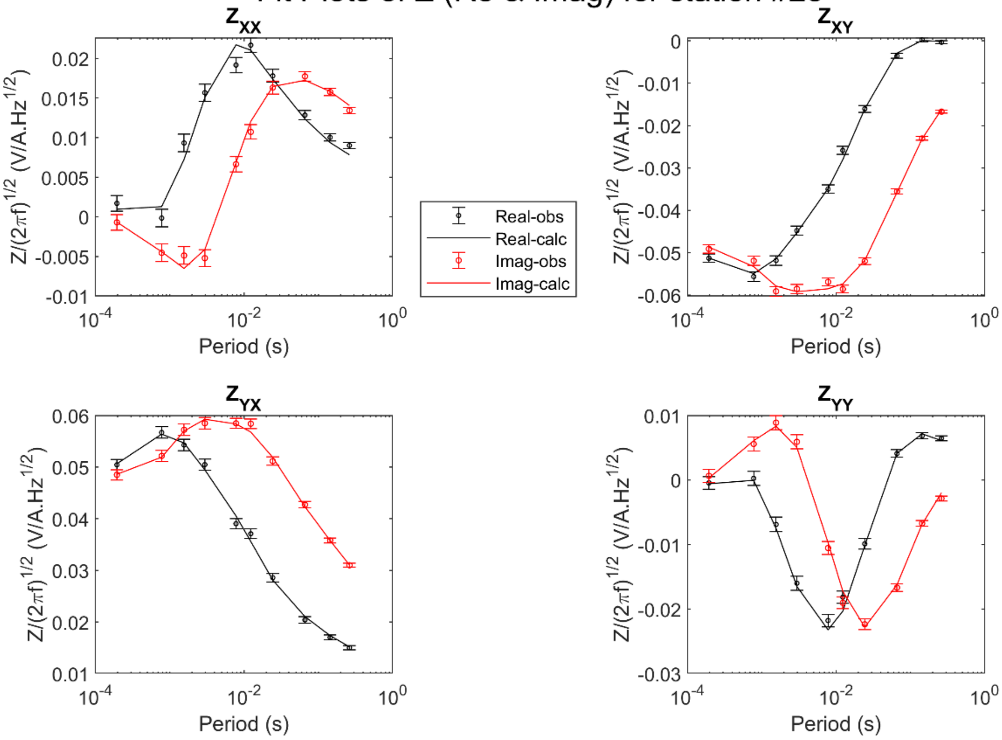

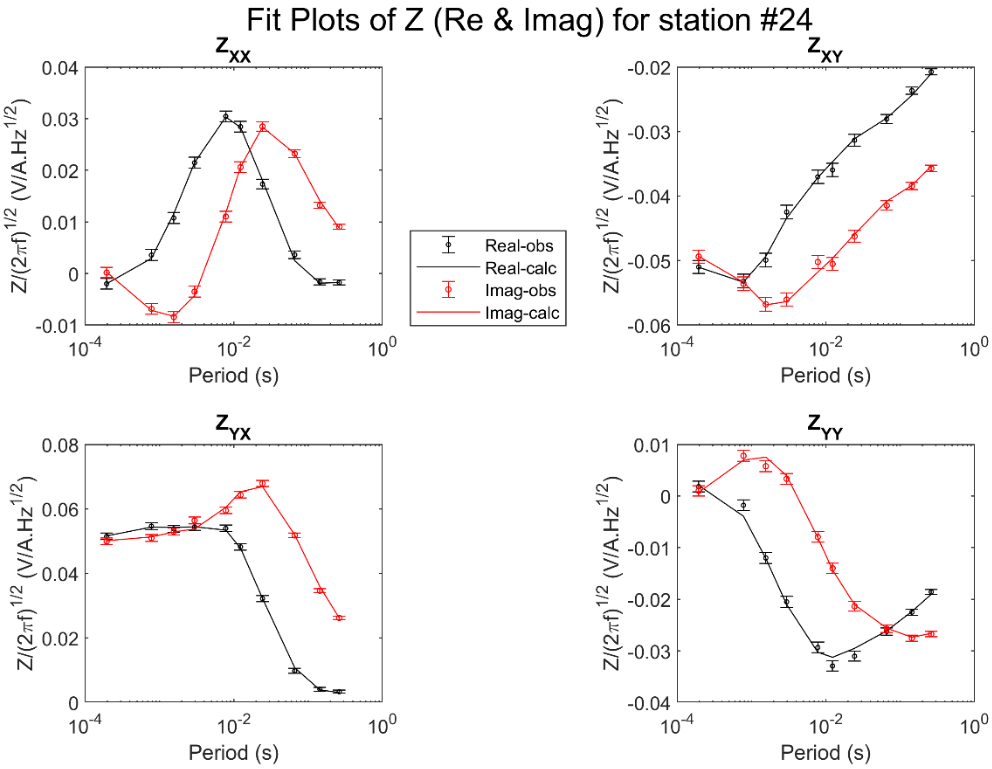
Fit Plots of Z (Re & Imag) for station #24
Z_XX
Z_XY
Z_YX
Z_YY
Z/(2πf)^1/2 (V/A.Hz^1/2)
Period (s)
Real-obs
Real-calc
Imag-obs
Imag-calc

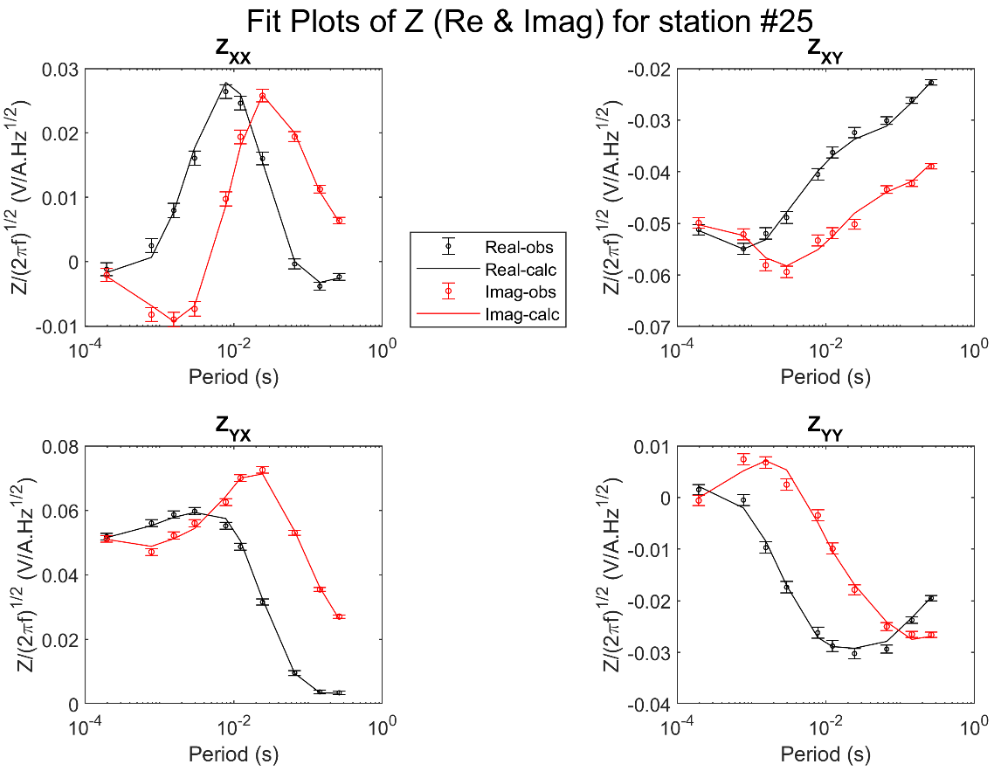
Fit Plots of Z (Re & Imag) for station #25
Z_XX
Z_XY
Z_YX
Z_YY
Z/(2πf)^1/2 (V/A.Hz^1/2)
Period (s)
Real-obs
Real-calc
Imag-obs
Imag-calc

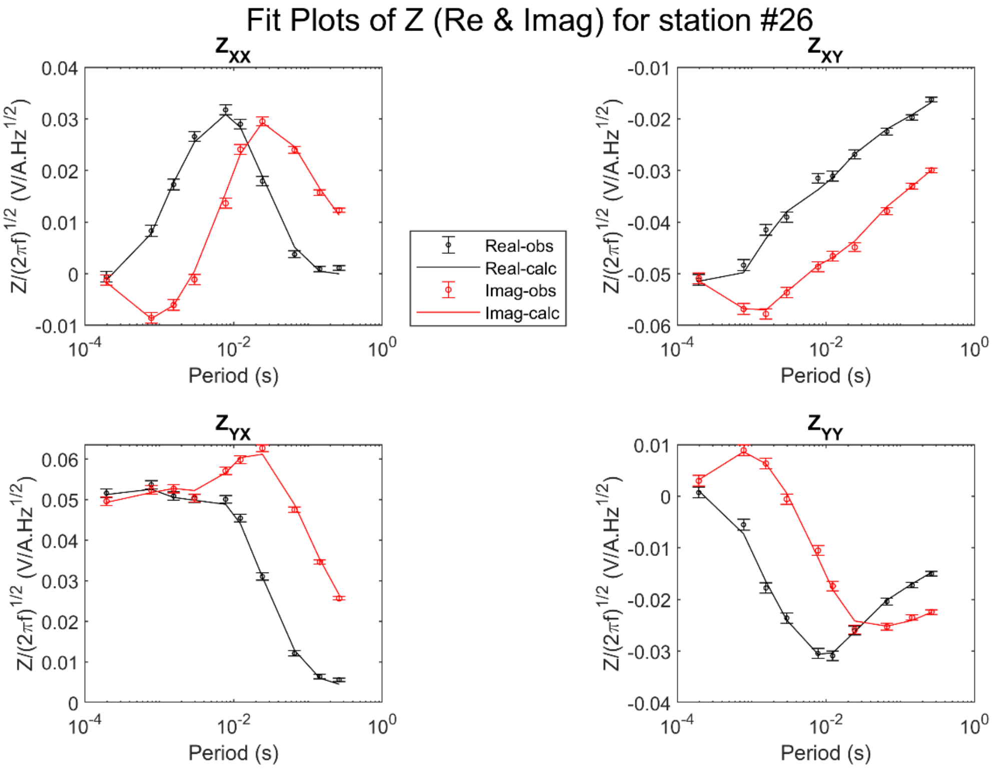
Fit Plots of Z (Re & Imag) for station #26
Z_XX
Z_XY
Z_YX
Z_YY
Z/(2πf)^1/2 (V/A.Hz^1/2)
Period (s)
Real-obs
Real-calc
Imag-obs
Imag-calc

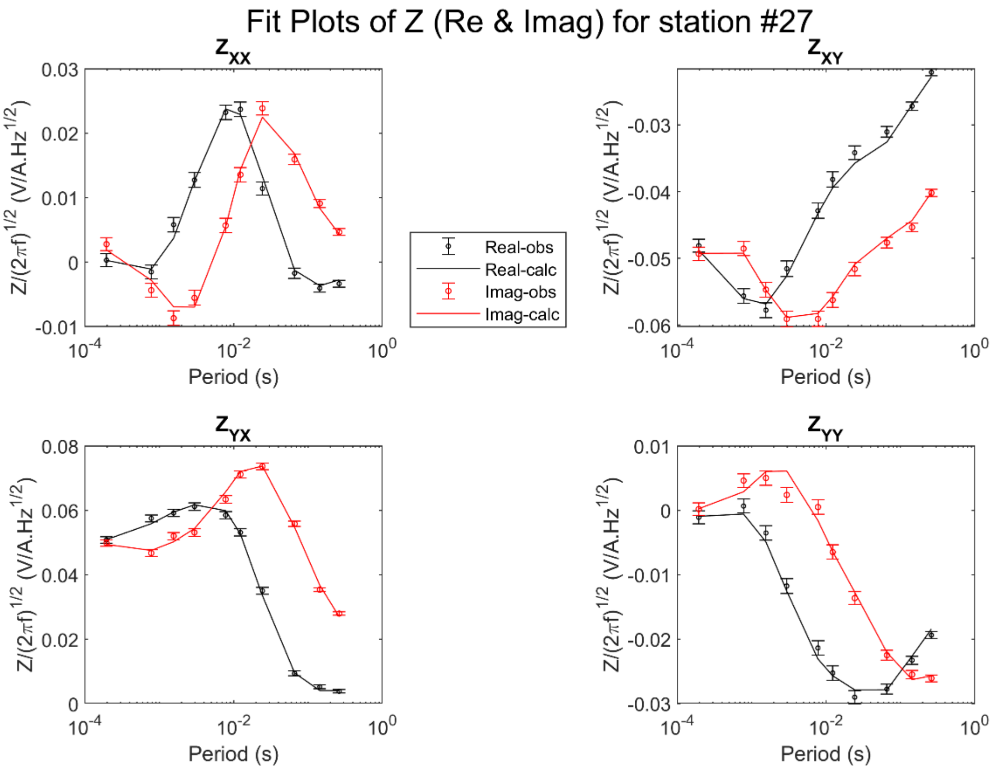
Fit Plots of Z (Re & Imag) for station #27
Z_XX
Z_XY
Z_YX
Z_YY
Z/(2πf)^1/2 (V/A.Hz^1/2)
Period (s)
Real-obs
Real-calc
Imag-obs
Imag-calc

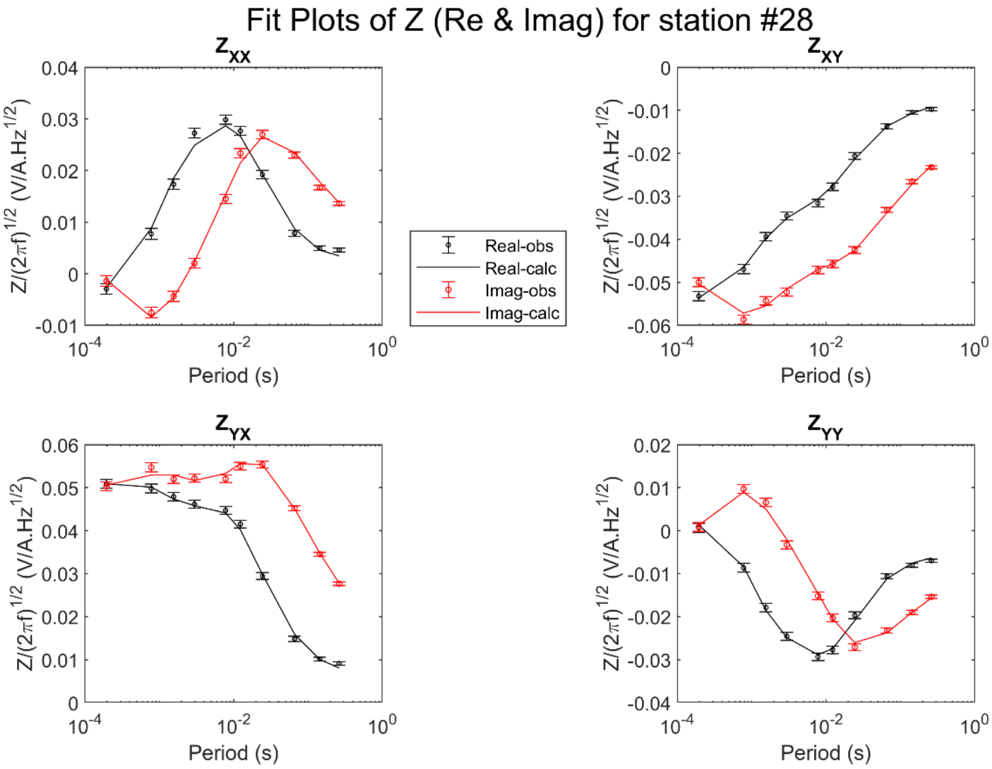

Fit Plots of Z (Re & Imag) for station #28
Z_{XX}
Z_{XY}
Z_{YX}
Z_{YY}
Real-obs
Real-calc
Imag-obs
Imag-calc
$Z/(2\pi f)^{1/2}$ (V/A.Hz$^{1/2}$)
Period (s)

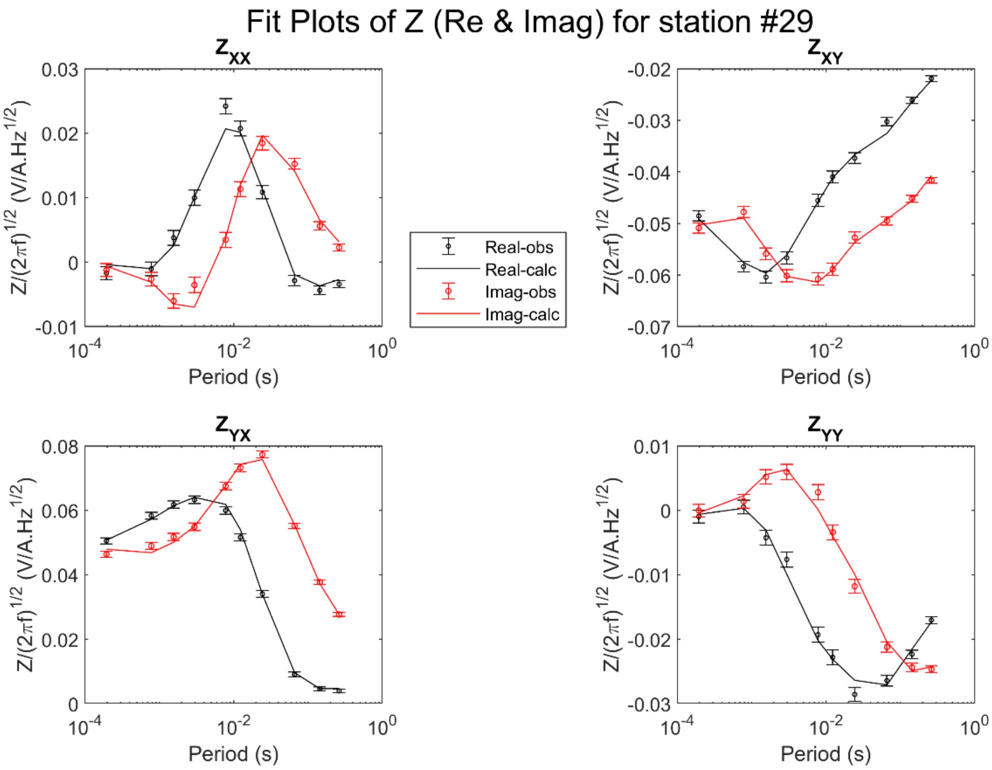

Fit Plots of Z (Re & Imag) for station #29
Z_{XX}
Z_{XY}
Z_{YX}
Z_{YY}
Real-obs
Real-calc
Imag-obs
Imag-calc
$Z/(2\pi f)^{1/2}$ (V/A.Hz$^{1/2}$)
Period (s)

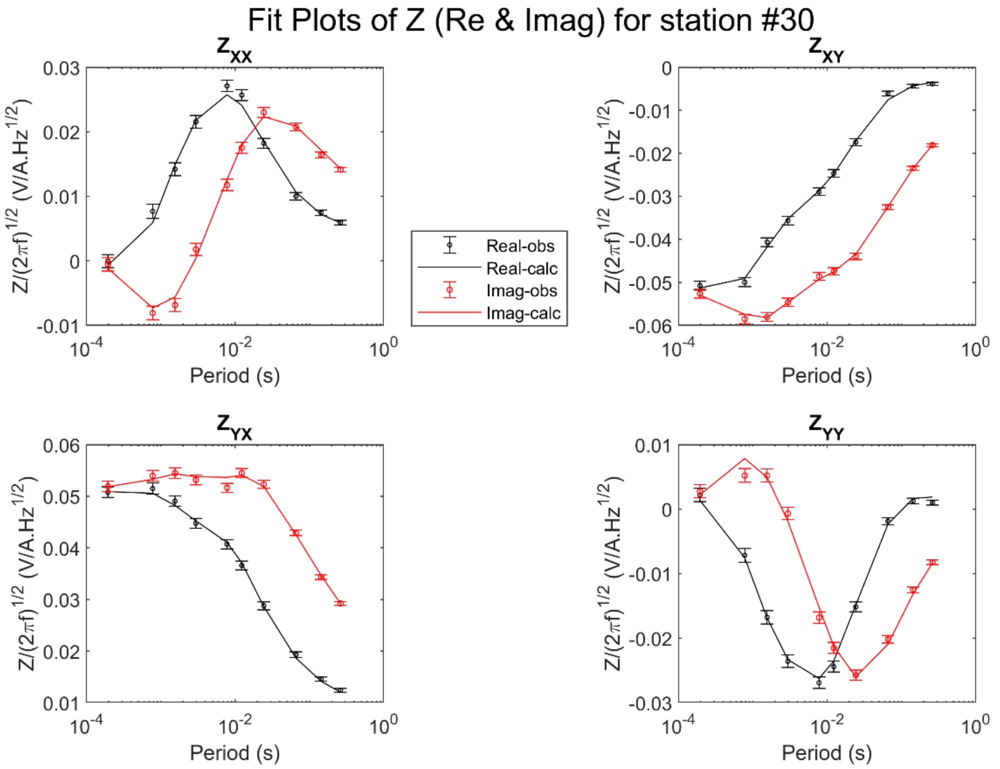
Fit Plots of Z (Re & Imag) for station #30
Z_XX
Z_XY
Z_YX
Z_YY
Z/(2πf)^1/2 (V/A.Hz^1/2)
Period (s)
Real-obs
Real-calc
Imag-obs
Imag-calc

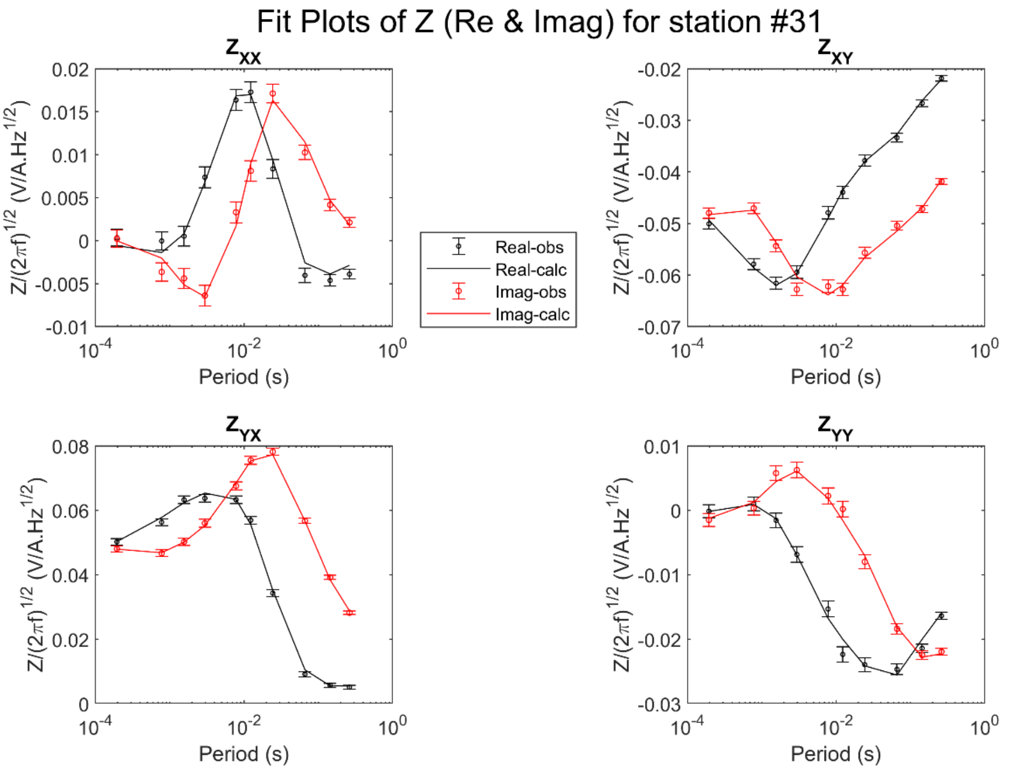
Fit Plots of Z (Re & Imag) for station #31
Z_XX
Z_XY
Z_YX
Z_YY
Z/(2πf)^1/2 (V/A.Hz^1/2)
Period (s)
Real-obs
Real-calc
Imag-obs
Imag-calc

Fit Plots of Z (Re & Imag) for station #32

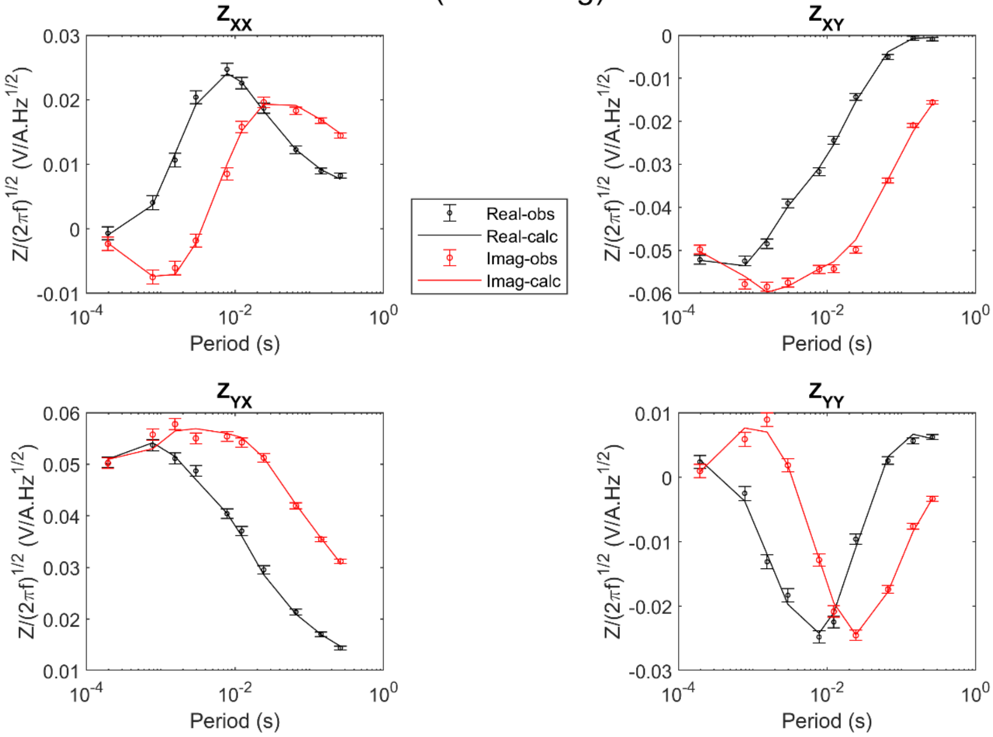

Fit Plots of Z (Re & Imag) for station #33

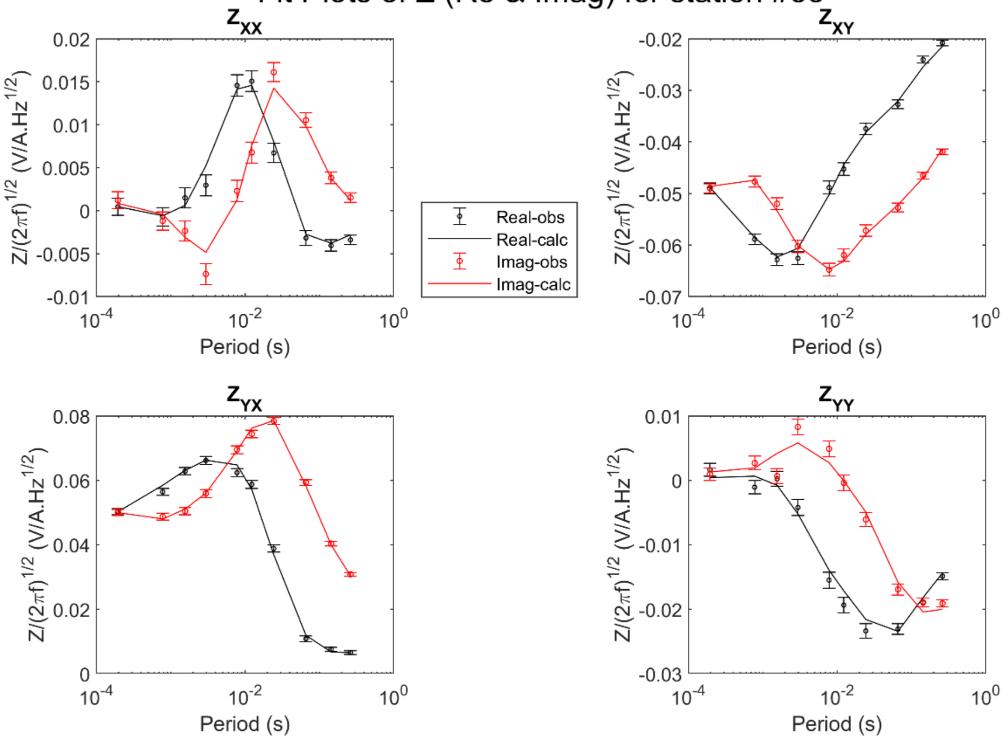

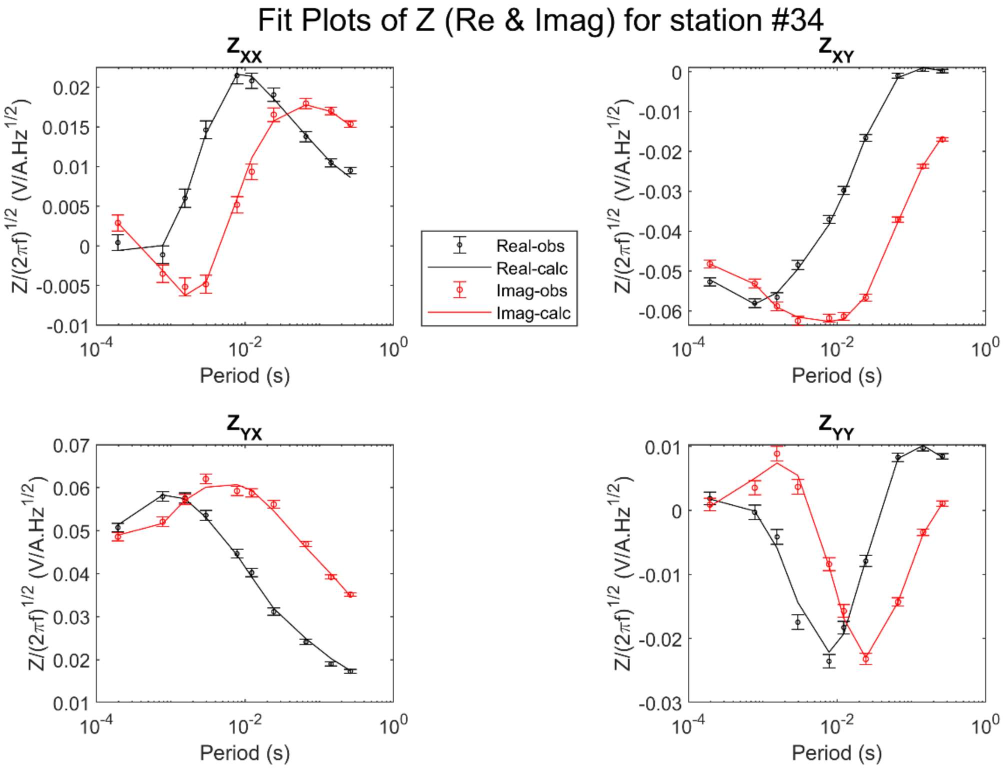
Fit Plots of Z (Re & Imag) for station #34
Z_{XX}
Z_{XY}
Z_{YX}
Z_{YY}
Real-obs
Real-calc
Imag-obs
Imag-calc
$Z/(2\pi f)^{1/2}$ (V/A.Hz$^{1/2}$)
Period (s)

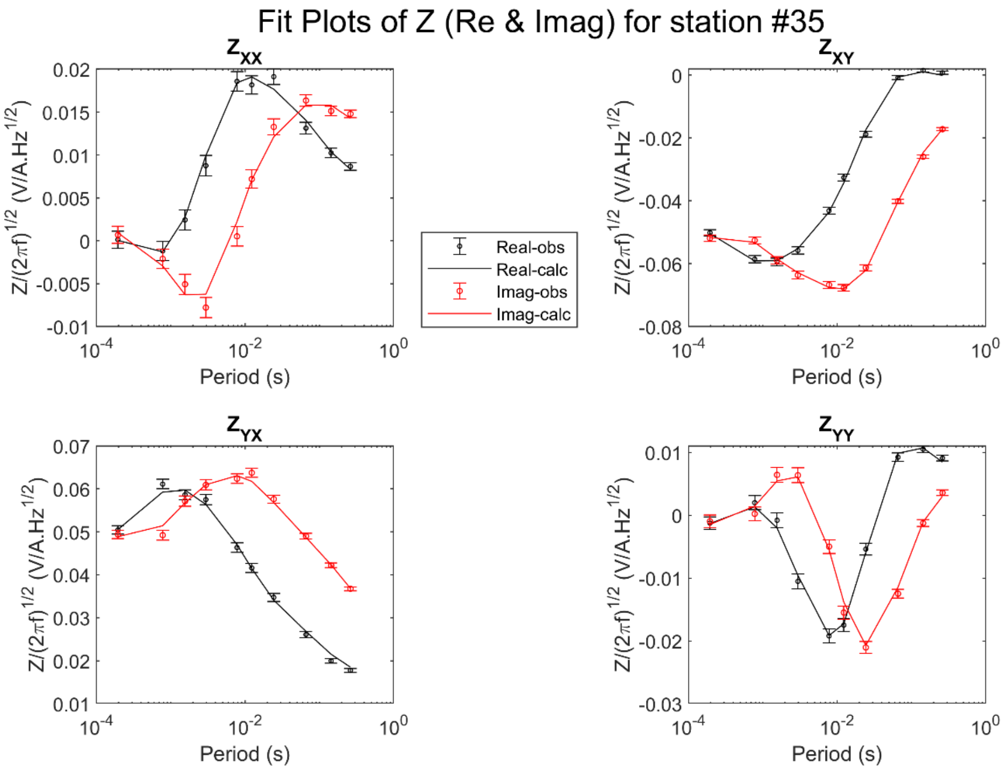
Fit Plots of Z (Re & Imag) for station #35
Z_{XX}
Z_{XY}
Z_{YX}
Z_{YY}
Real-obs
Real-calc
Imag-obs
Imag-calc
$Z/(2\pi f)^{1/2}$ (V/A.Hz$^{1/2}$)
Period (s)

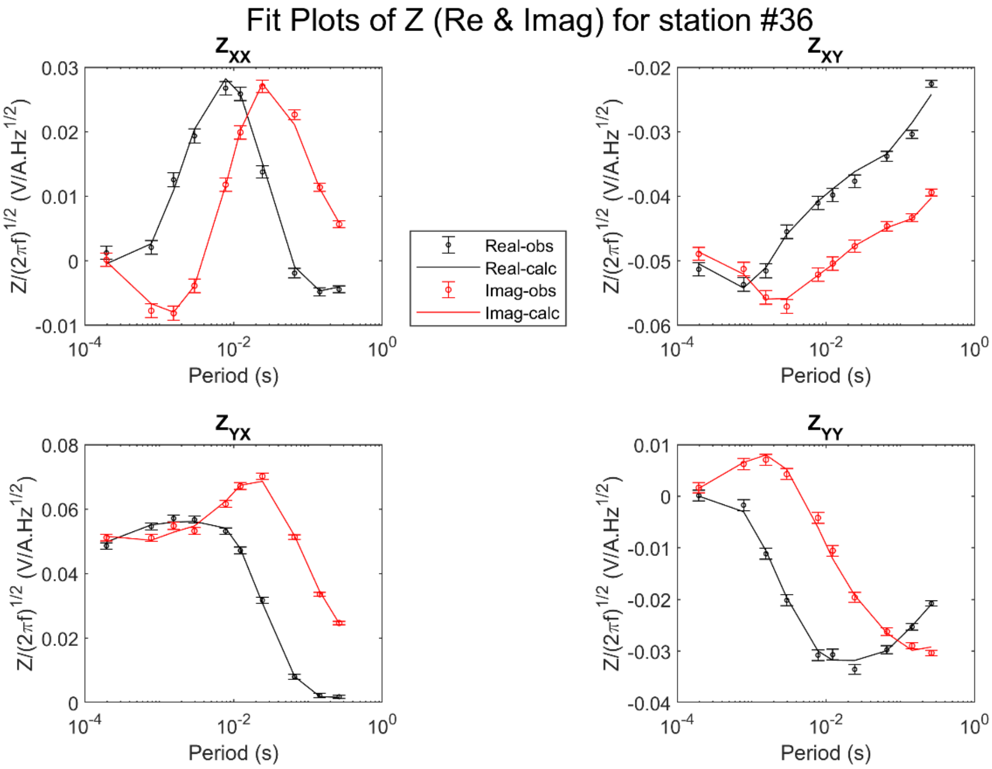
Fit Plots of Z (Re & Imag) for station #36
Z_XX
Z_XY
Z_YX
Z_YY
Z/(2πf)^1/2 (V/A.Hz^1/2)
Period (s)
Real-obs
Real-calc
Imag-obs
Imag-calc

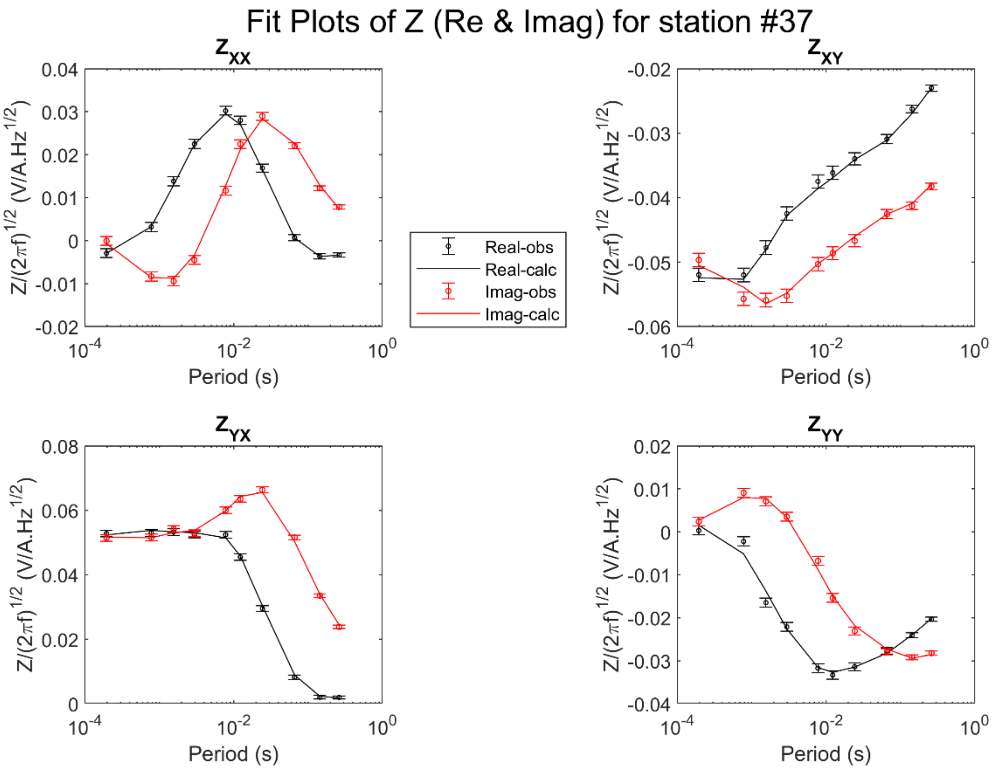
Fit Plots of Z (Re & Imag) for station #37
Z_XX
Z_XY
Z_YX
Z_YY
Z/(2πf)^1/2 (V/A.Hz^1/2)
Period (s)
Real-obs
Real-calc
Imag-obs
Imag-calc

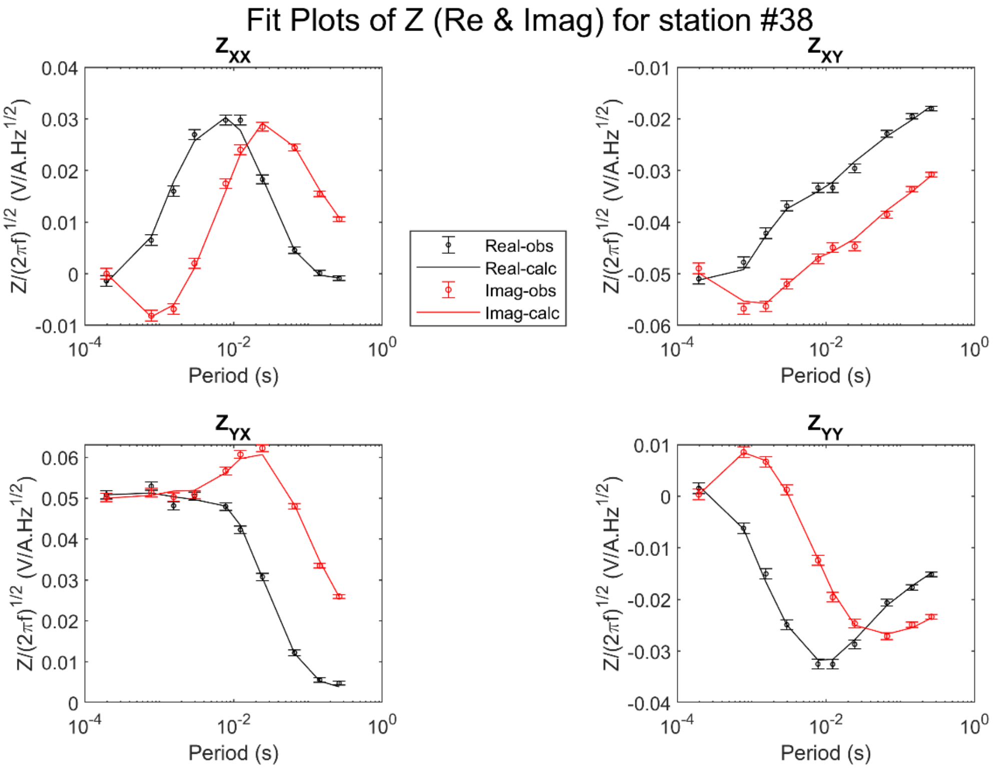

Fit Plots of Z (Re & Imag) for station #38
Z_{XX}
Z_{XY}
Z_{YX}
Z_{YY}
$Z/(2\pi f)^{1/2}$ (V/A.Hz$^{1/2}$)
Period (s)
Real-obs
Real-calc
Imag-obs
Imag-calc

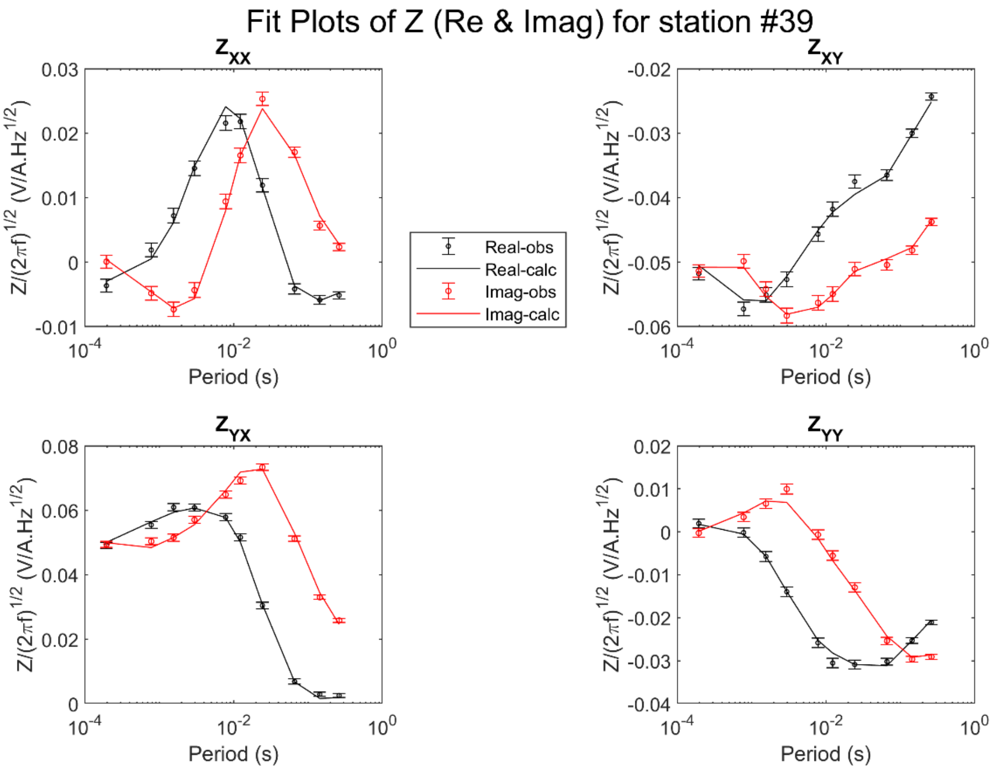

Fit Plots of Z (Re & Imag) for station #39
Z_{XX}
Z_{XY}
Z_{YX}
Z_{YY}
$Z/(2\pi f)^{1/2}$ (V/A.Hz$^{1/2}$)
Period (s)
Real-obs
Real-calc
Imag-obs
Imag-calc

Fit Plots of Z (Re & Imag) for station #40

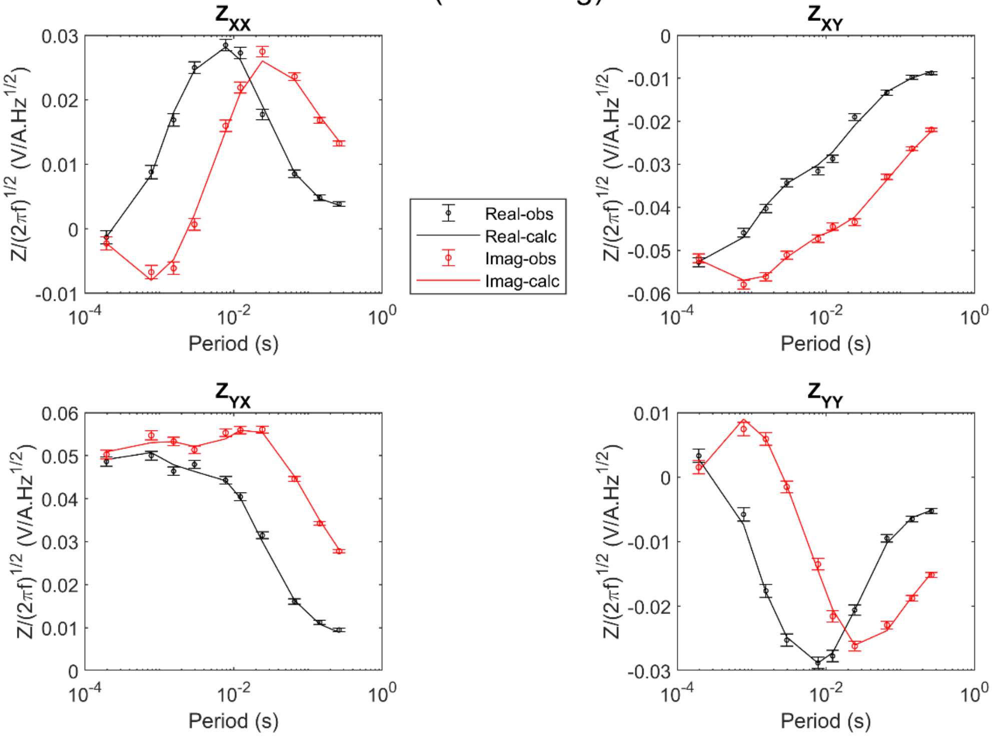

Fit Plots of Z (Re & Imag) for station #41

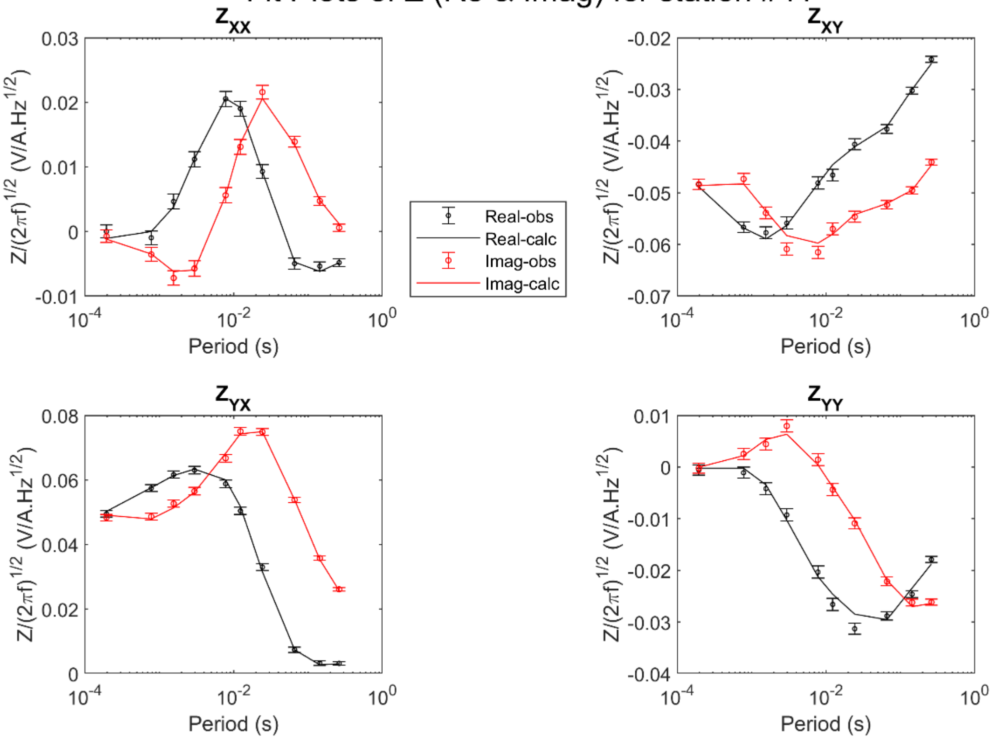

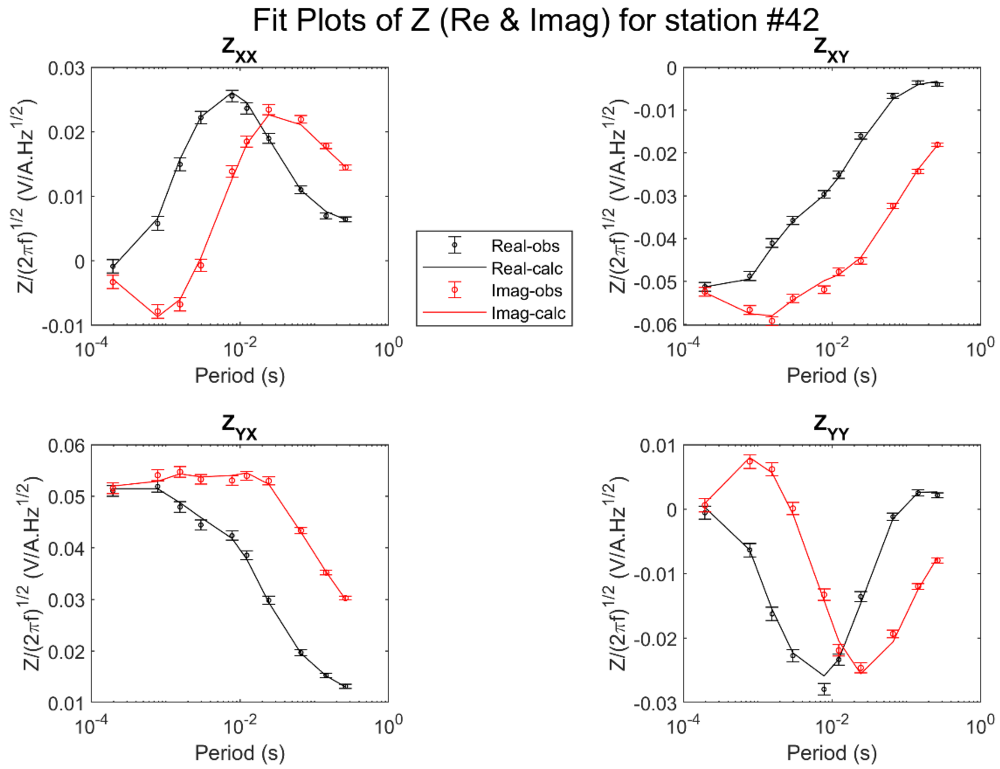
Fit Plots of Z (Re & Imag) for station #42
Z_{XX}
Z_{XY}
Z_{YX}
Z_{YY}
$Z/(2\pi f)^{1/2}$ (V/A.Hz$^{1/2}$)
Period (s)
Real-obs
Real-calc
Imag-obs
Imag-calc

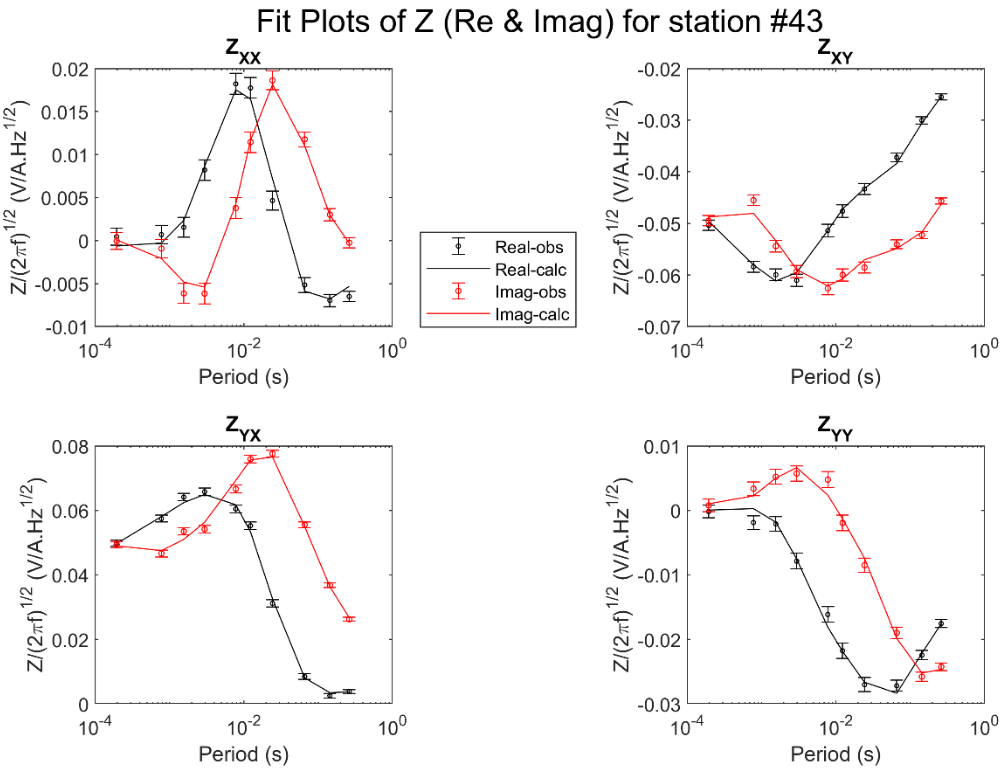
Fit Plots of Z (Re & Imag) for station #43
Z_{XX}
Z_{XY}
Z_{YX}
Z_{YY}
$Z/(2\pi f)^{1/2}$ (V/A.Hz$^{1/2}$)
Period (s)
Real-obs
Real-calc
Imag-obs
Imag-calc

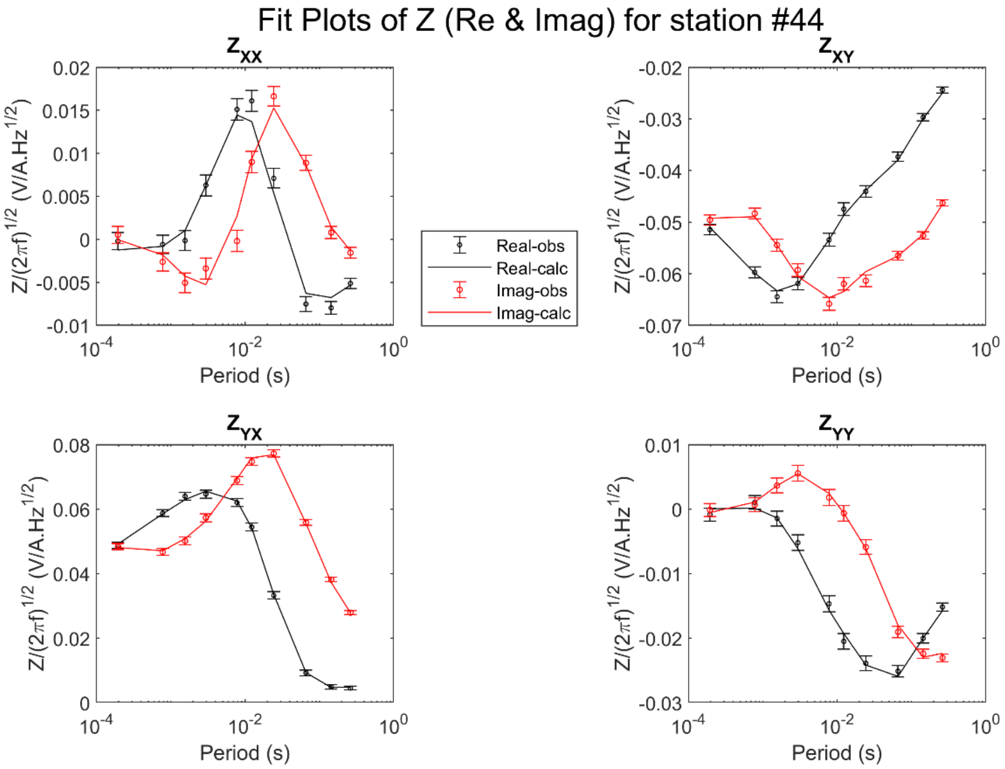
Fit Plots of Z (Re & Imag) for station #44
Z_{XX}
Z_{XY}
Z_{YX}
Z_{YY}
$Z/(2\pi f)^{1/2}$ (V/A.Hz$^{1/2}$)
Period (s)
Real-obs
Real-calc
Imag-obs
Imag-calc

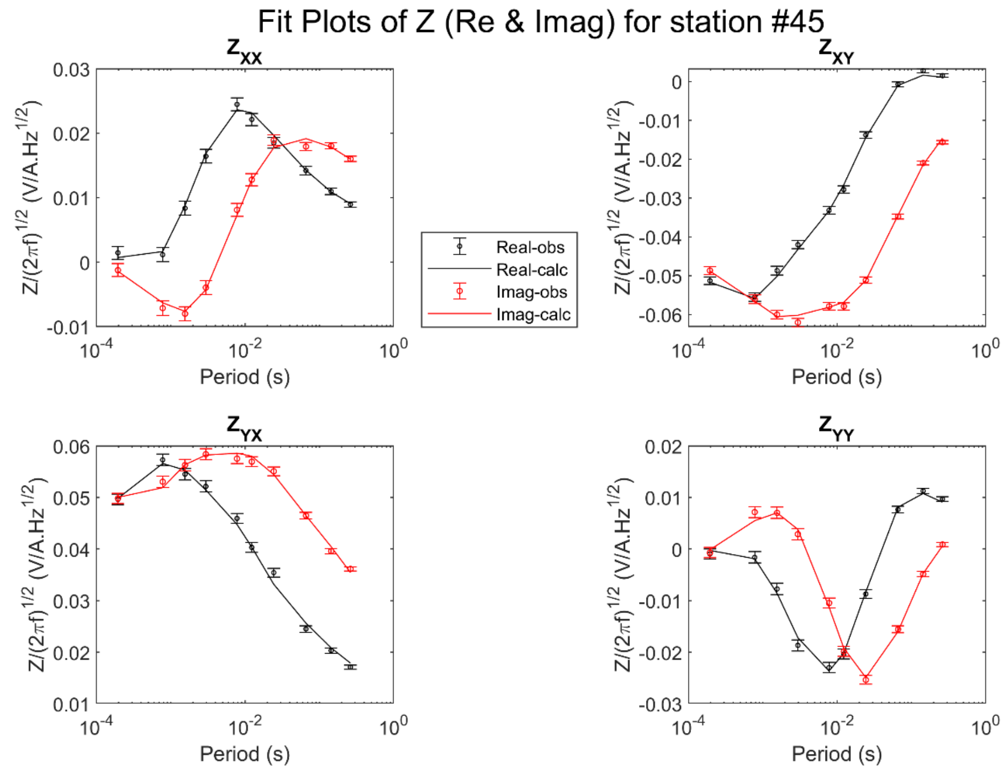
Fit Plots of Z (Re & Imag) for station #45
Z_{XX}
Z_{XY}
Z_{YX}
Z_{YY}
$Z/(2\pi f)^{1/2}$ (V/A.Hz$^{1/2}$)
Period (s)
Real-obs
Real-calc
Imag-obs
Imag-calc

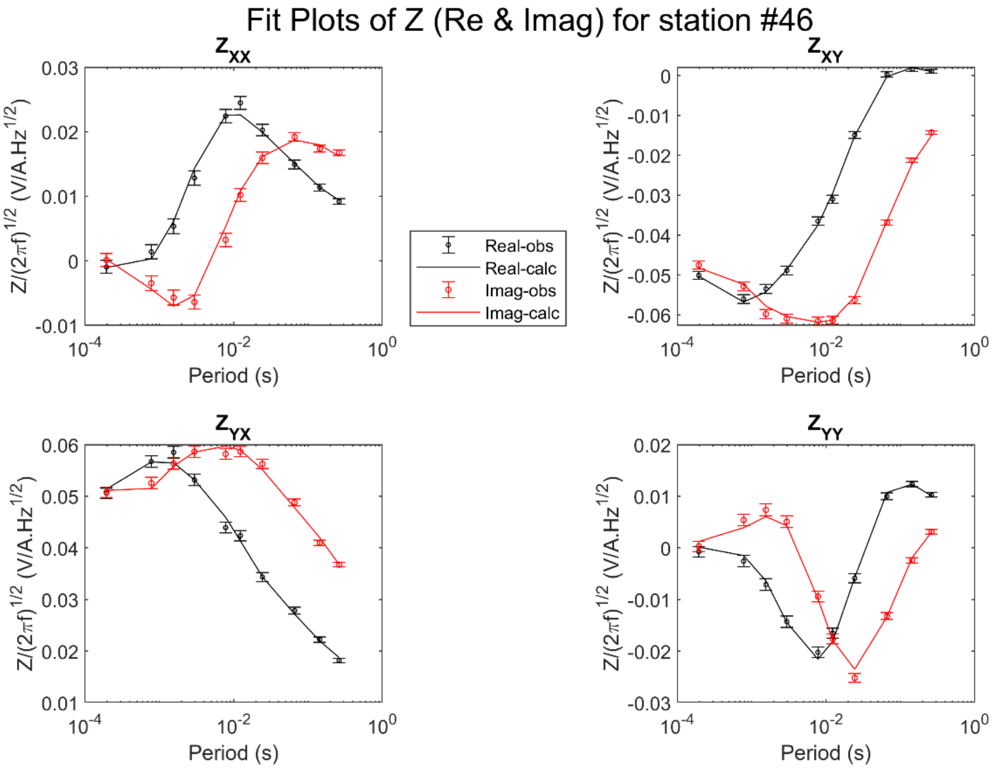
Fit Plots of Z (Re & Imag) for station #46
ZXX
ZXY
ZYX
ZYY
Z/(2πf)^1/2 (V/A.Hz^1/2)
Period (s)
Real-obs
Real-calc
Imag-obs
Imag-calc

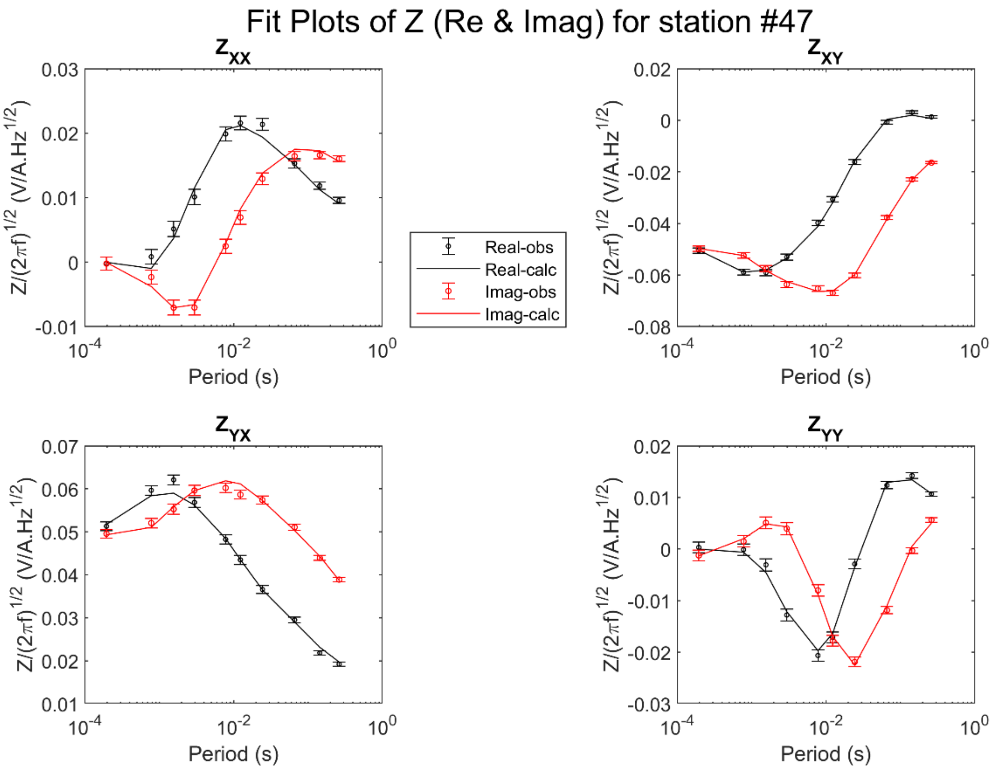
Fit Plots of Z (Re & Imag) for station #47
ZXX
ZXY
ZYX
ZYY
Z/(2πf)^1/2 (V/A.Hz^1/2)
Period (s)
Real-obs
Real-calc
Imag-obs
Imag-calc

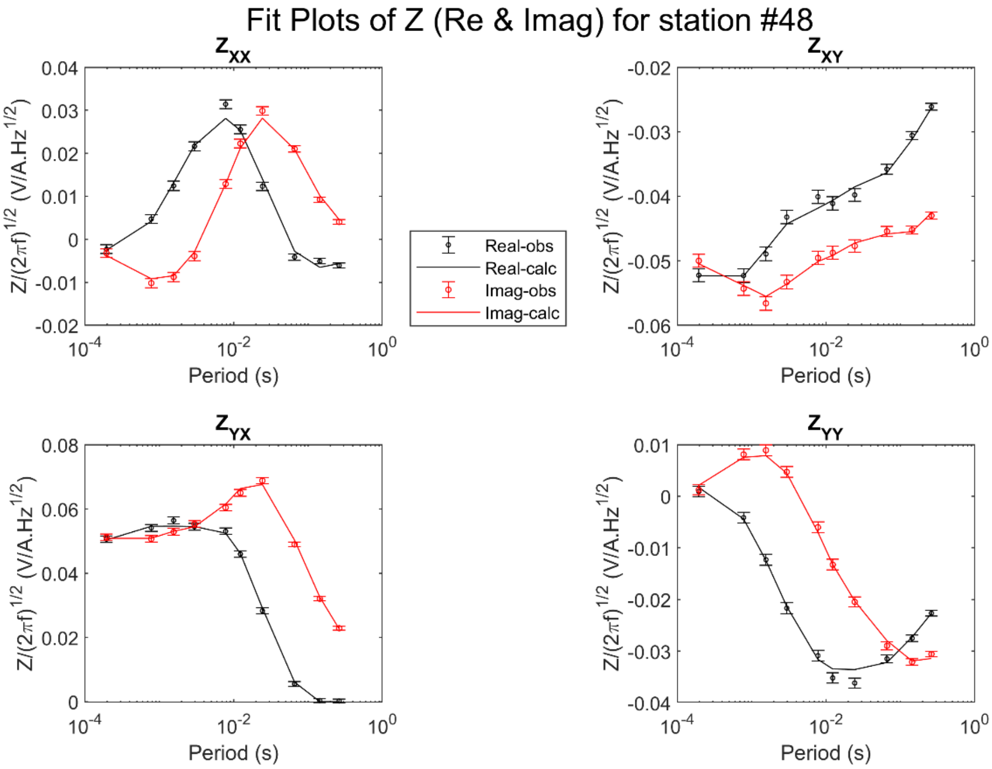
Fit Plots of Z (Re & Imag) for station #48
Z_{XX}
Z_{XY}
Z_{YX}
Z_{YY}
$Z/(2\pi f)^{1/2}$ (V/A.Hz$^{1/2}$)
Period (s)
Real-obs
Real-calc
Imag-obs
Imag-calc

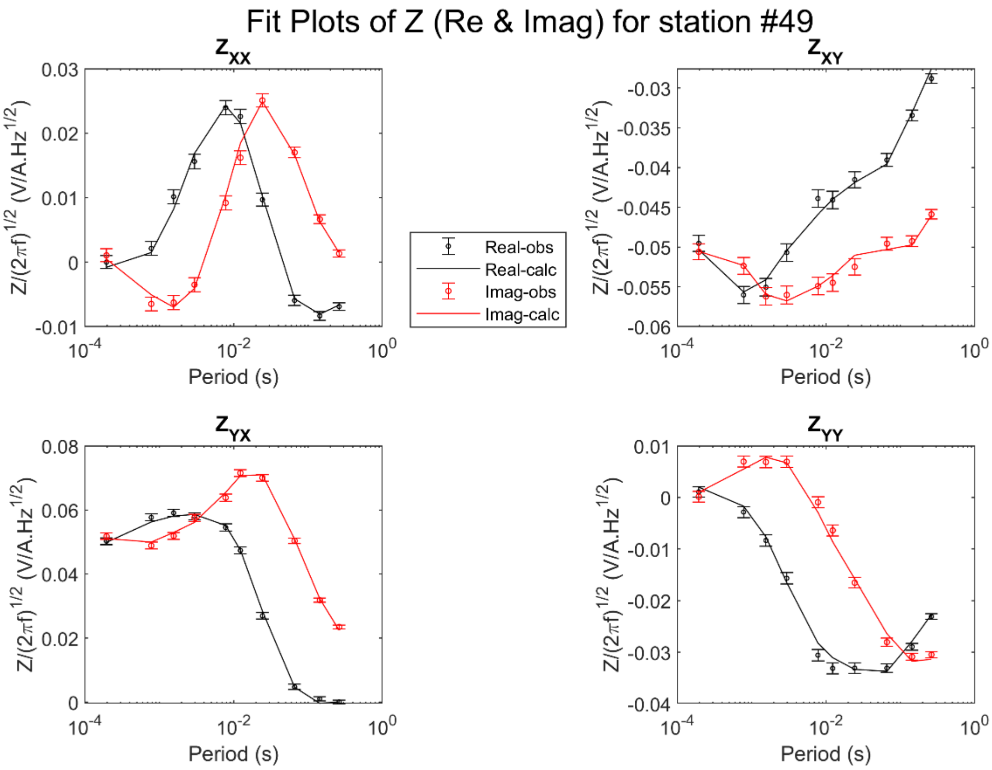
Fit Plots of Z (Re & Imag) for station #49
Z_{XX}
Z_{XY}
Z_{YX}
Z_{YY}
$Z/(2\pi f)^{1/2}$ (V/A.Hz$^{1/2}$)
Period (s)
Real-obs
Real-calc
Imag-obs
Imag-calc

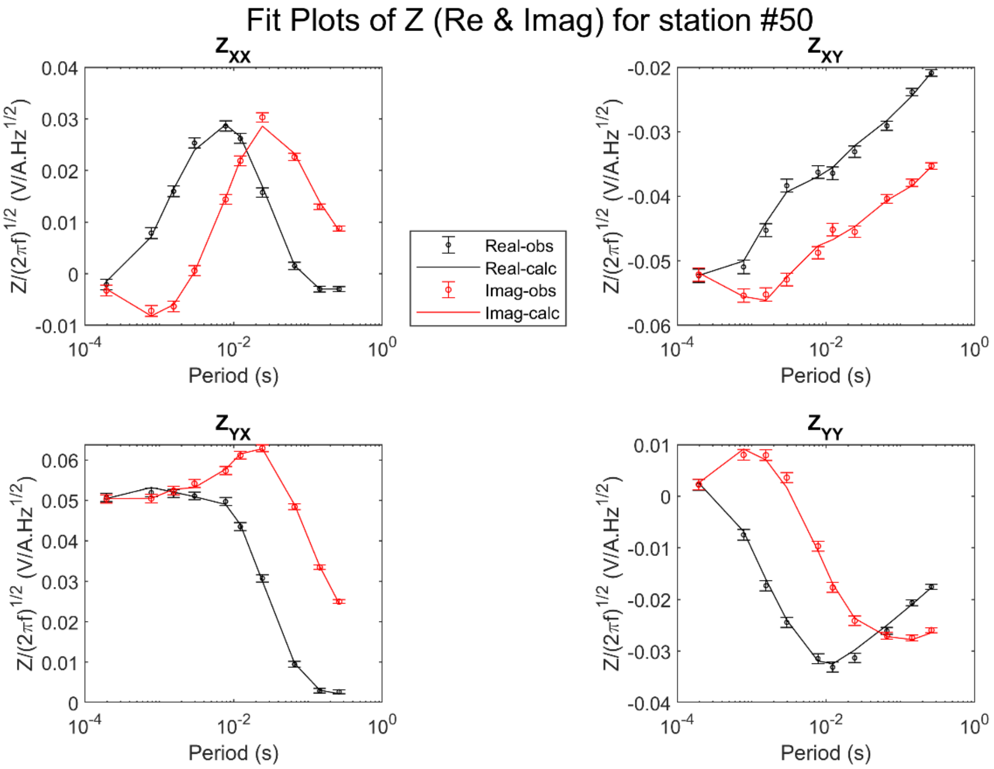
Fit Plots of Z (Re & Imag) for station #50
ZXX
ZXY
ZYX
ZYY
Z/(2πf)^1/2 (V/A.Hz^1/2)
Period (s)
Real-obs
Real-calc
Imag-obs
Imag-calc

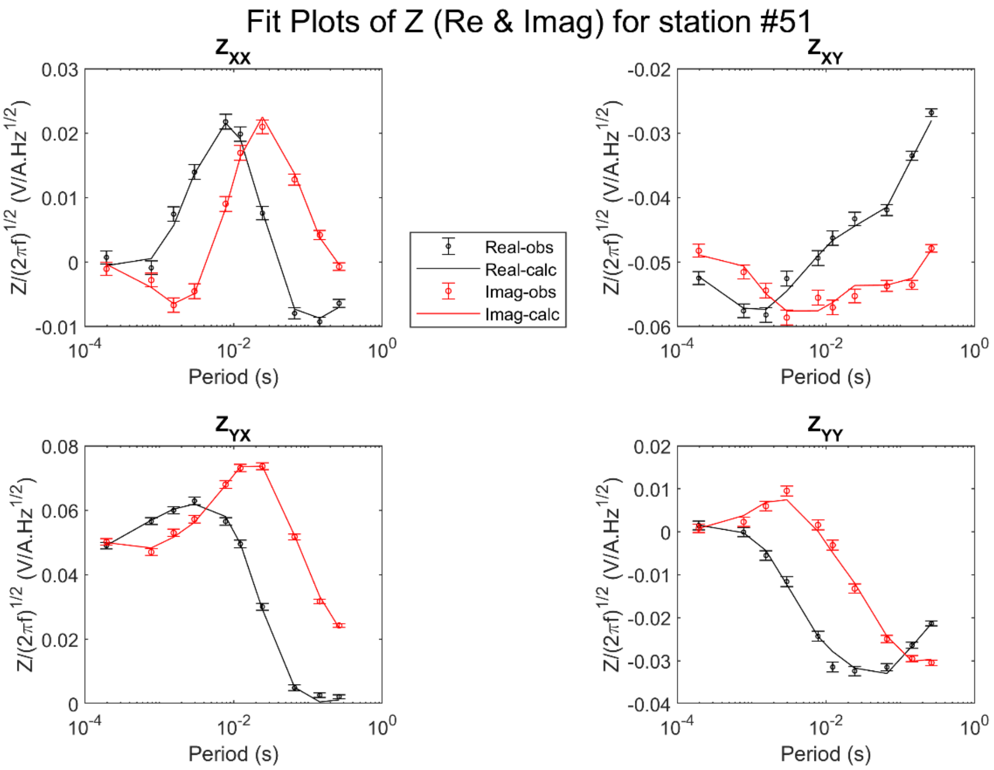
Fit Plots of Z (Re & Imag) for station #51
ZXX
ZXY
ZYX
ZYY
Z/(2πf)^1/2 (V/A.Hz^1/2)
Period (s)
Real-obs
Real-calc
Imag-obs
Imag-calc

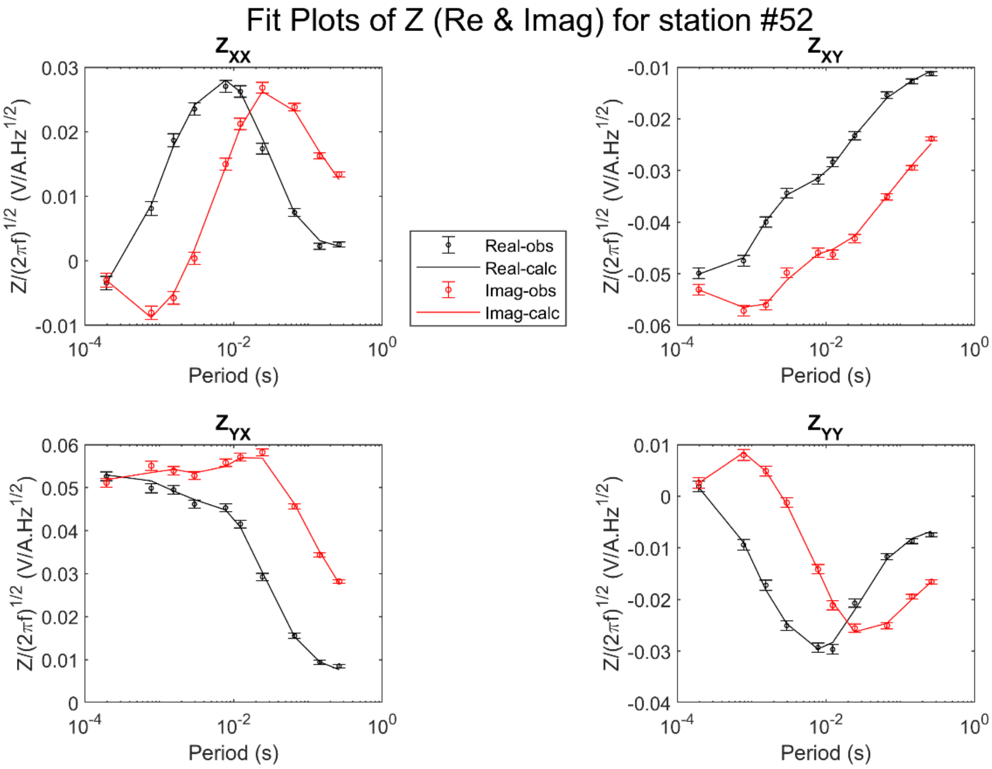

Fit Plots of Z (Re & Imag) for station #52
Z_XX
Z_XY
Z_YX
Z_YY
Z/(2πf)^1/2 (V/A.Hz^1/2)
Period (s)
Real-obs
Real-calc
Imag-obs
Imag-calc

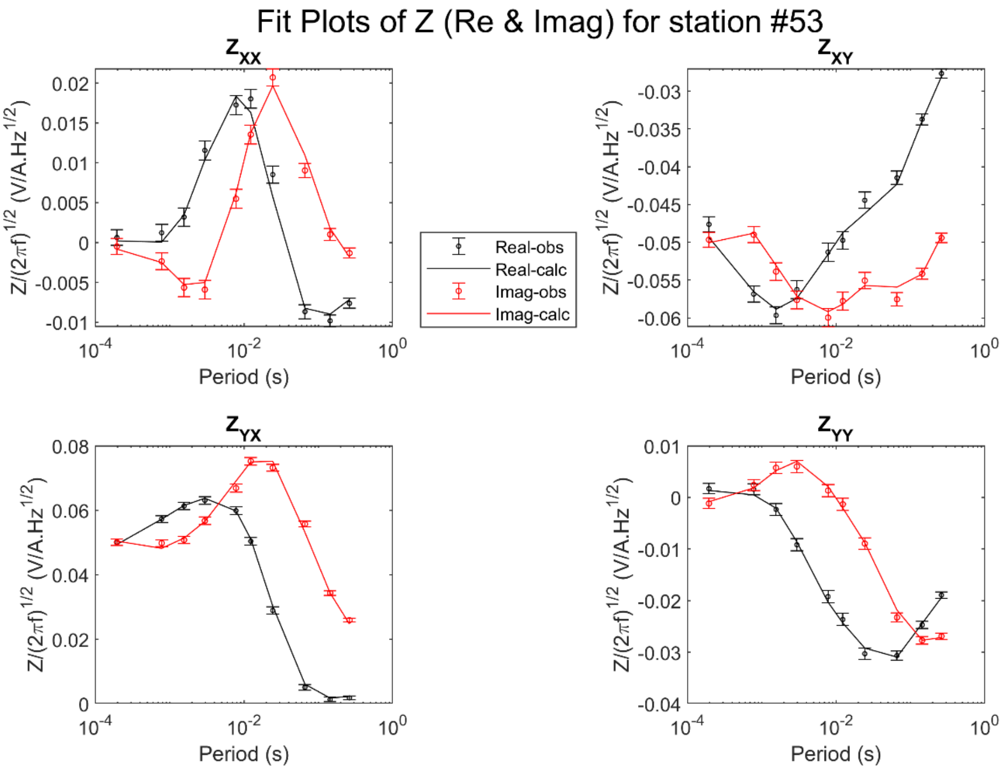

Fit Plots of Z (Re & Imag) for station #53
Z_XX
Z_XY
Z_YX
Z_YY
Z/(2πf)^1/2 (V/A.Hz^1/2)
Period (s)
Real-obs
Real-calc
Imag-obs
Imag-calc

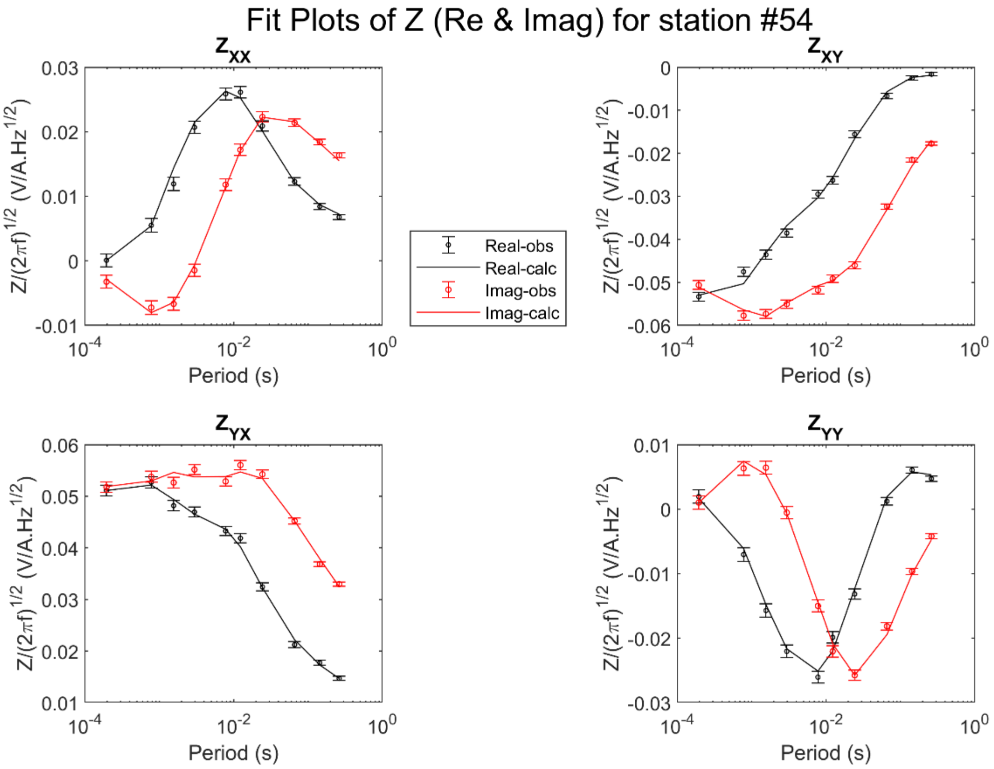
Fit Plots of Z (Re & Imag) for station #54
Z_XX
Z_XY
Z_YX
Z_YY
Z/(2πf)^1/2 (V/A.Hz^1/2)
Period (s)
Real-obs
Real-calc
Imag-obs
Imag-calc

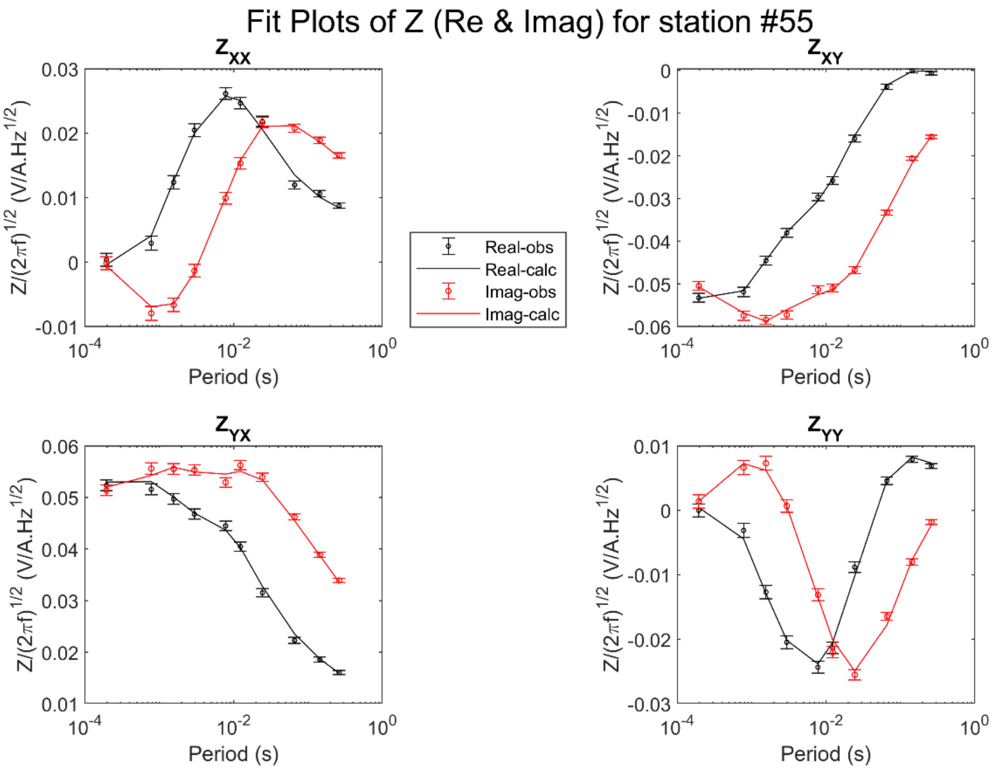
Fit Plots of Z (Re & Imag) for station #55
Z_XX
Z_XY
Z_YX
Z_YY
Z/(2πf)^1/2 (V/A.Hz^1/2)
Period (s)
Real-obs
Real-calc
Imag-obs
Imag-calc

Fit Plots of Z (Re & Imag) for station #56

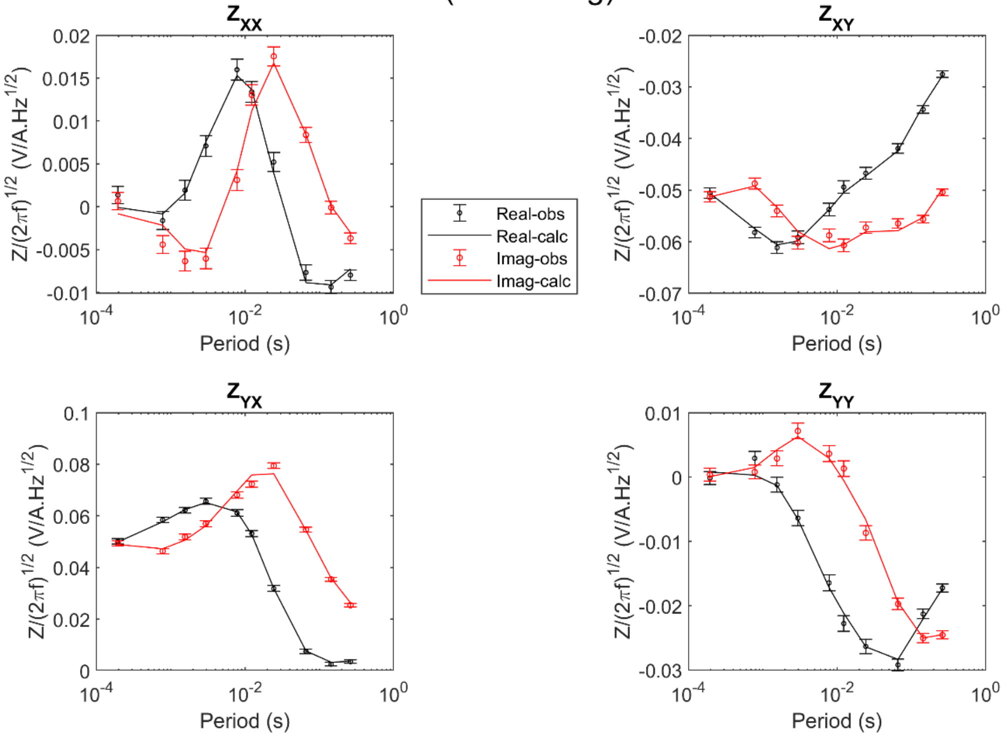

Fit Plots of Z (Re & Imag) for station #57

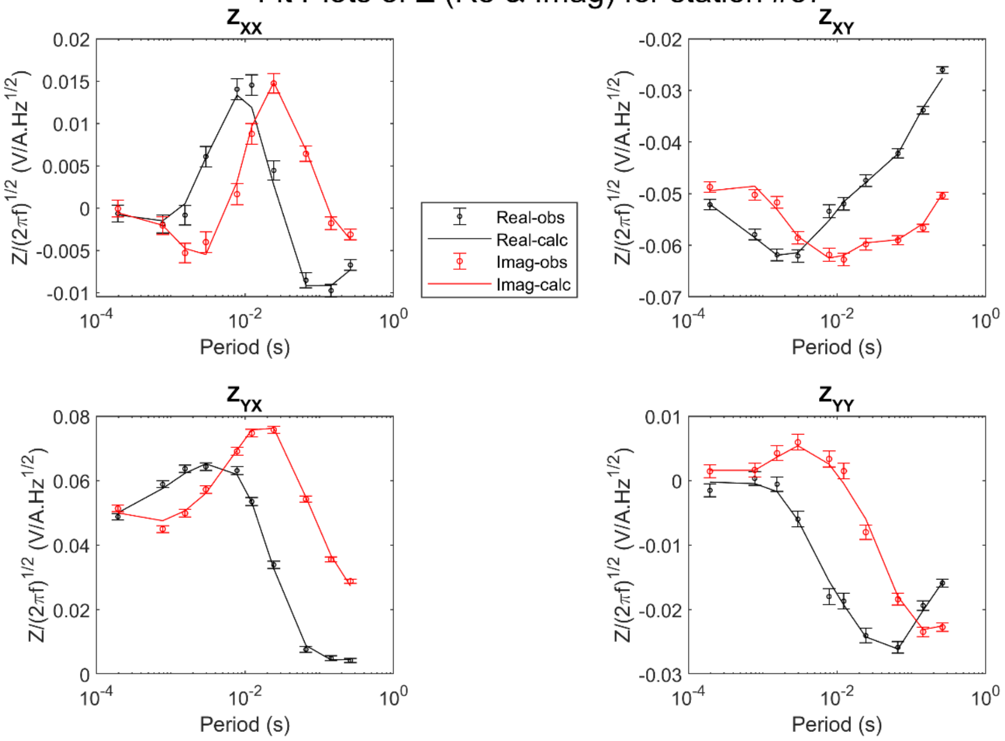

Fit Plots of Z (Re & Imag) for station #58

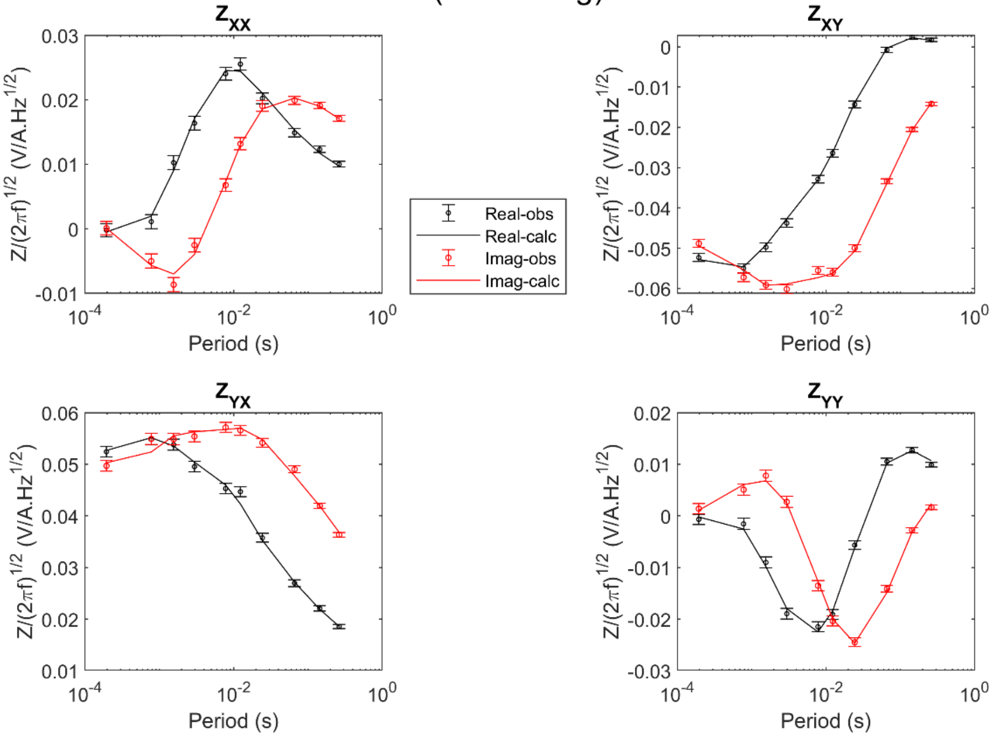

Fit Plots of Z (Re & Imag) for station #59

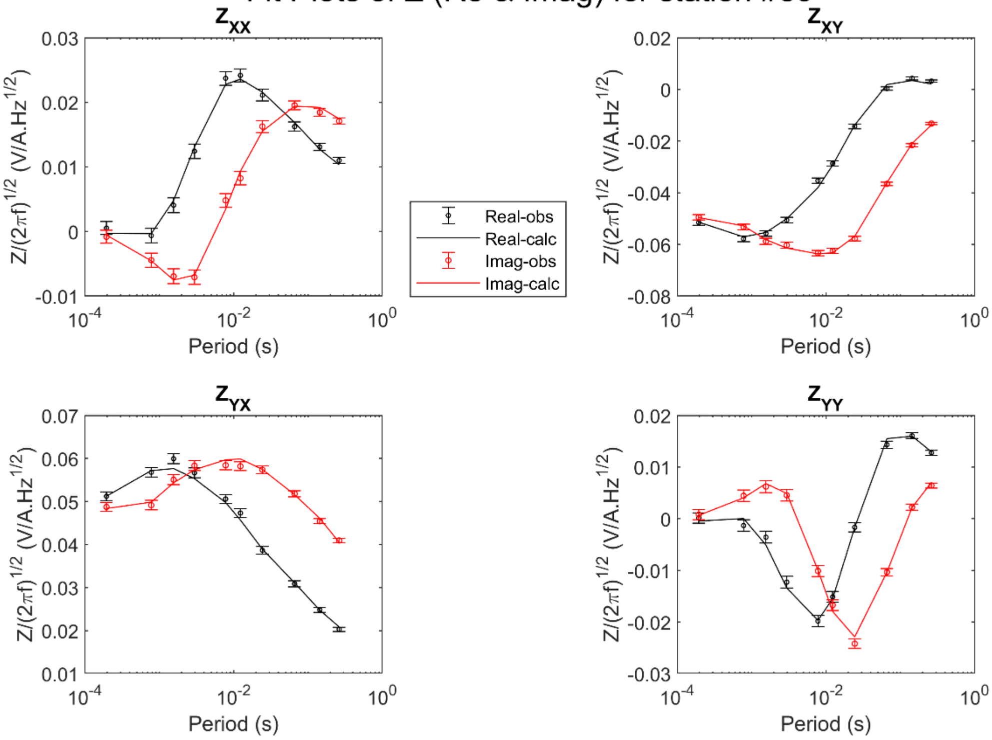

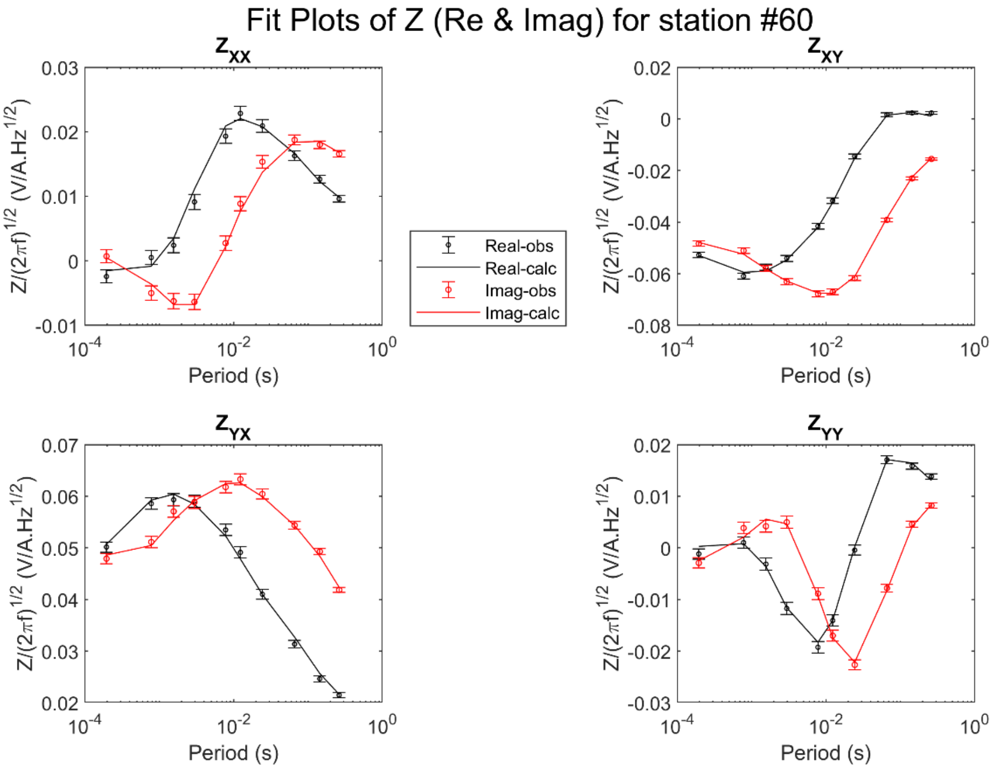

Fit Plots of Z (Re & Imag) for station #60
Z_XX
Z_XY
Z_YX
Z_YY
Z/(2πf)^1/2 (V/A.Hz^1/2)
Period (s)
Real-obs
Real-calc
Imag-obs
Imag-calc

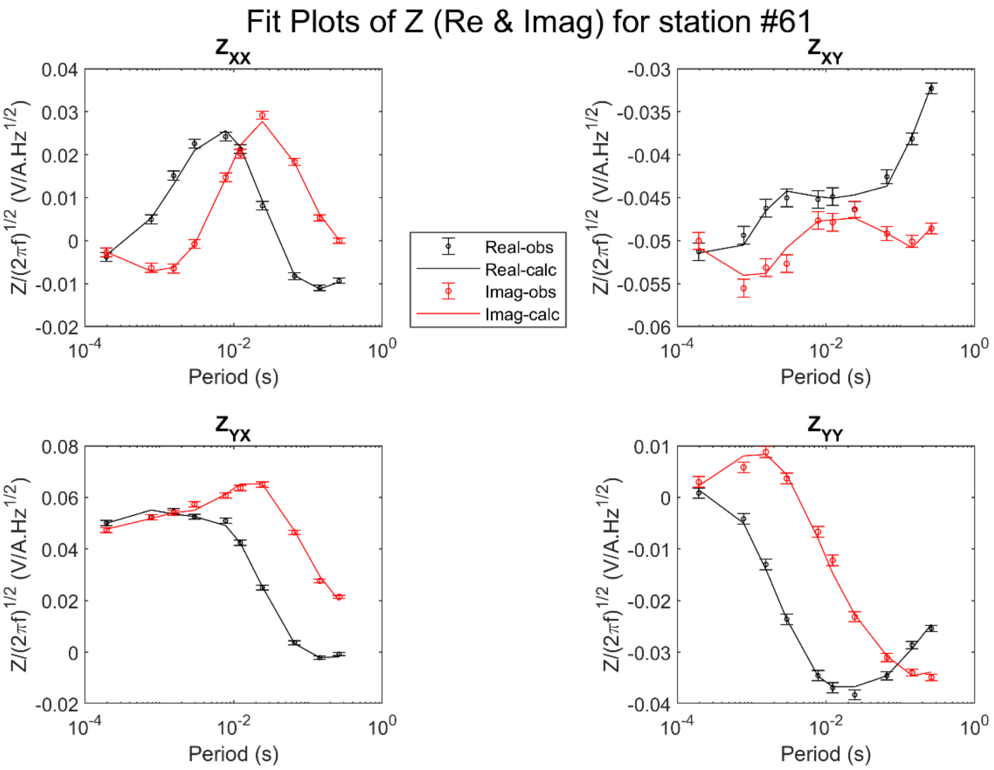

Fit Plots of Z (Re & Imag) for station #61
Z_XX
Z_XY
Z_YX
Z_YY
Z/(2πf)^1/2 (V/A.Hz^1/2)
Period (s)
Real-obs
Real-calc
Imag-obs
Imag-calc

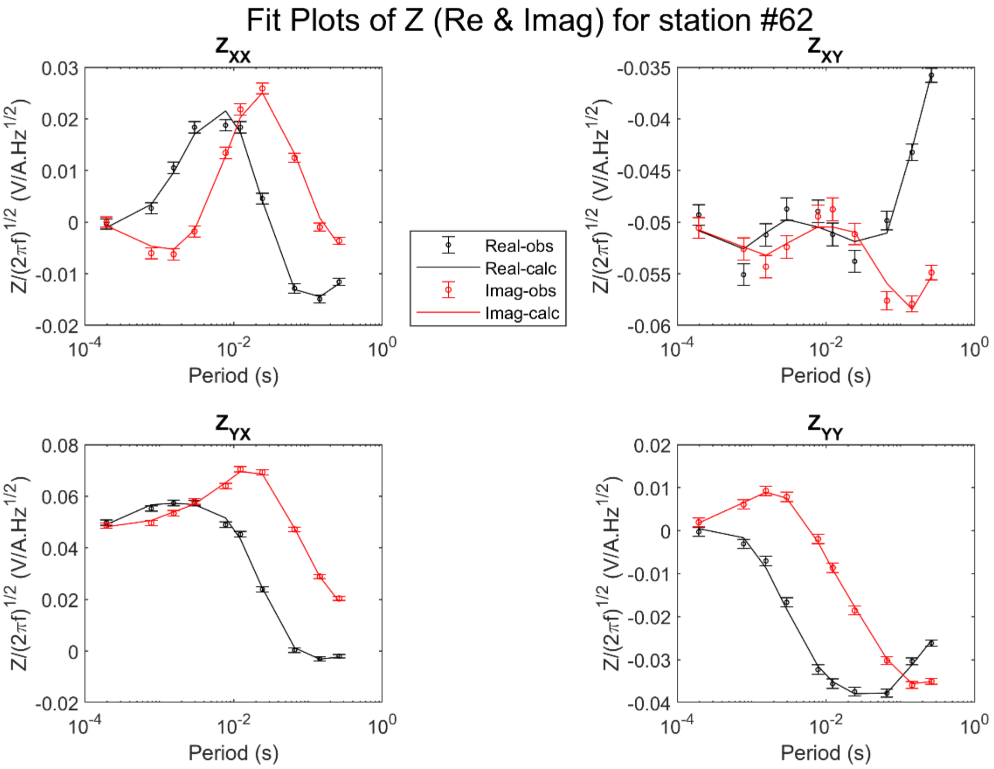
Fit Plots of Z (Re & Imag) for station #62
Z_XX
Z_XY
Z_YX
Z_YY
Z/(2πf)^1/2 (V/A.Hz^1/2)
Period (s)
Real-obs
Real-calc
Imag-obs
Imag-calc

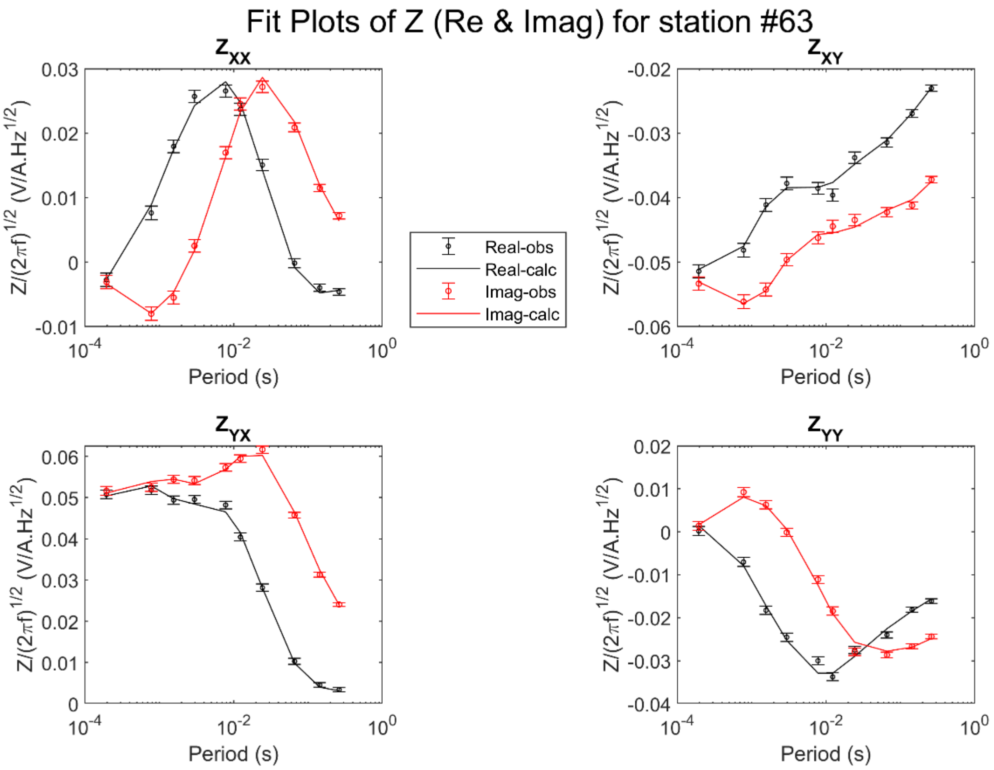
Fit Plots of Z (Re & Imag) for station #63
Z_XX
Z_XY
Z_YX
Z_YY
Z/(2πf)^1/2 (V/A.Hz^1/2)
Period (s)
Real-obs
Real-calc
Imag-obs
Imag-calc

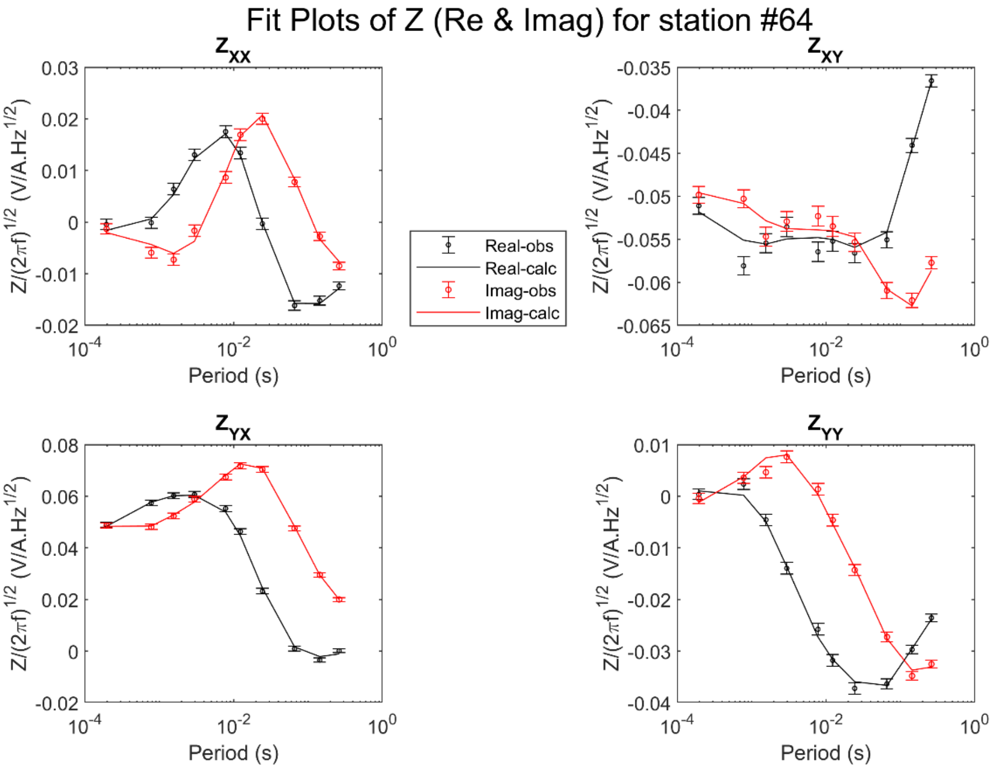
Fit Plots of Z (Re & Imag) for station #64
Z_XX
Z_XY
Z_YX
Z_YY
Z/(2πf)^1/2 (V/A.Hz^1/2)
Period (s)
Real-obs
Real-calc
Imag-obs
Imag-calc

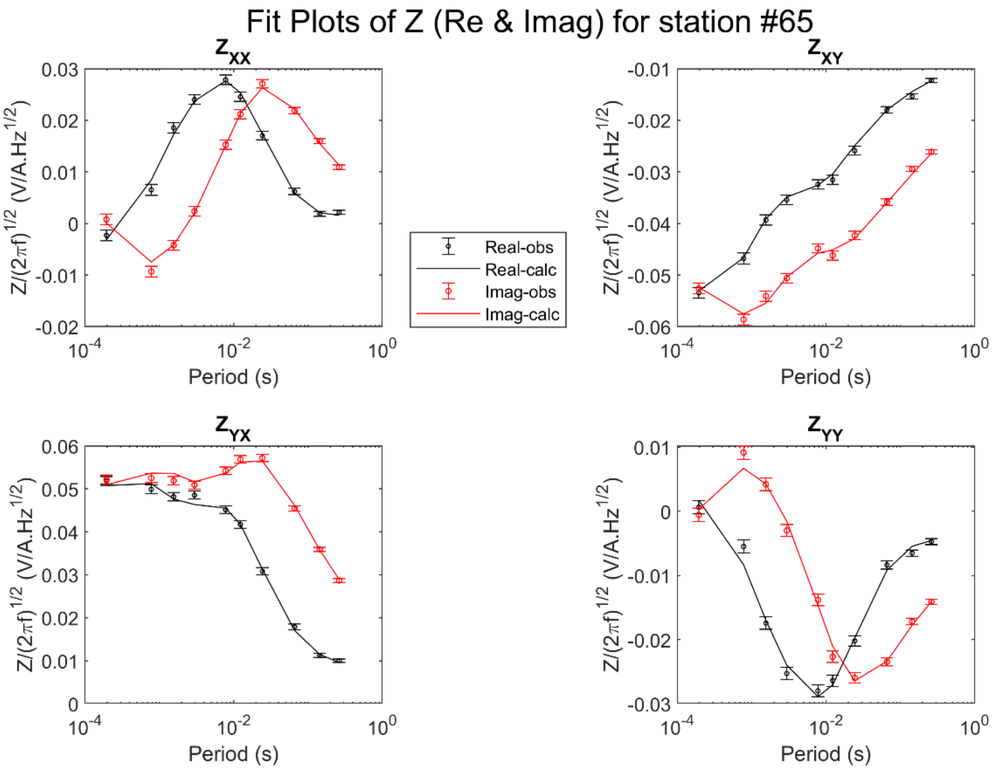
Fit Plots of Z (Re & Imag) for station #65
Z_XX
Z_XY
Z_YX
Z_YY
Z/(2πf)^1/2 (V/A.Hz^1/2)
Period (s)
Real-obs
Real-calc
Imag-obs
Imag-calc

Fit Plots of Z (Re & Imag) for station #66

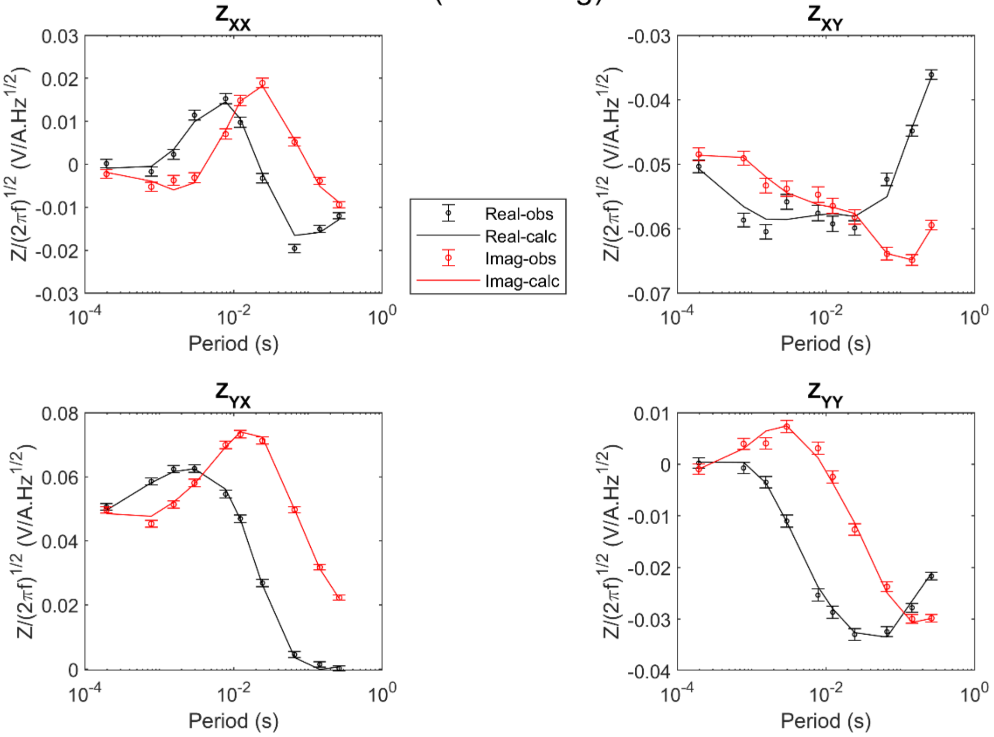

Fit Plots of Z (Re & Imag) for station #67

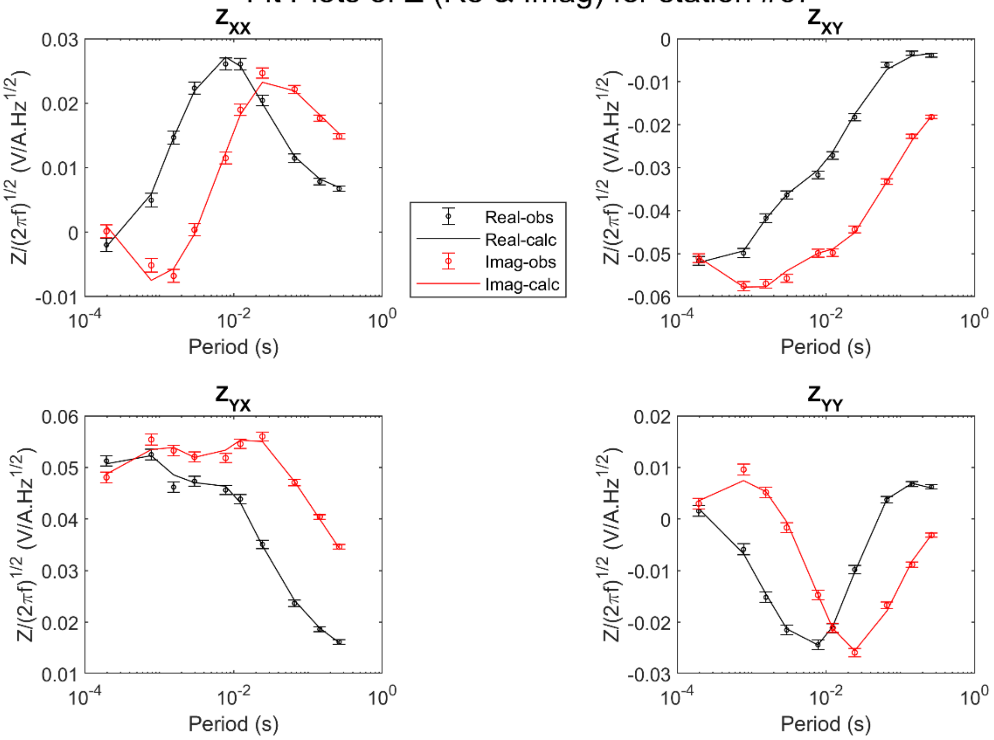

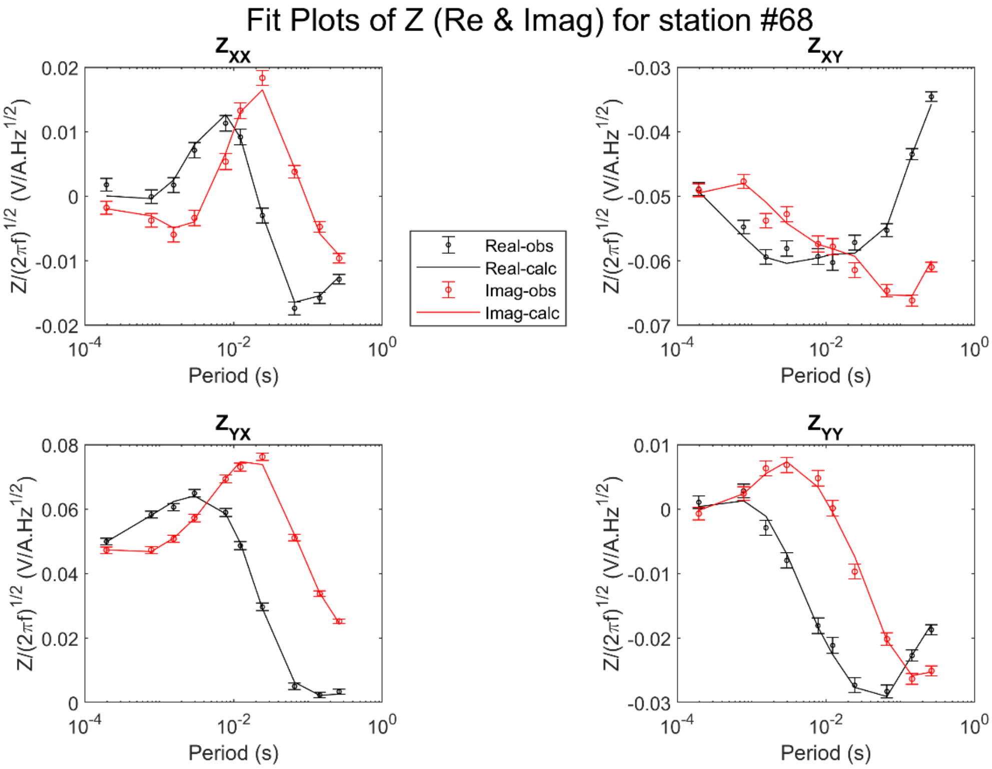
Fit Plots of Z (Re & Imag) for station #68
Z_XX
Z_XY
Z_YX
Z_YY
Z/(2πf)^1/2 (V/A.Hz^1/2)
Period (s)
Real-obs
Real-calc
Imag-obs
Imag-calc

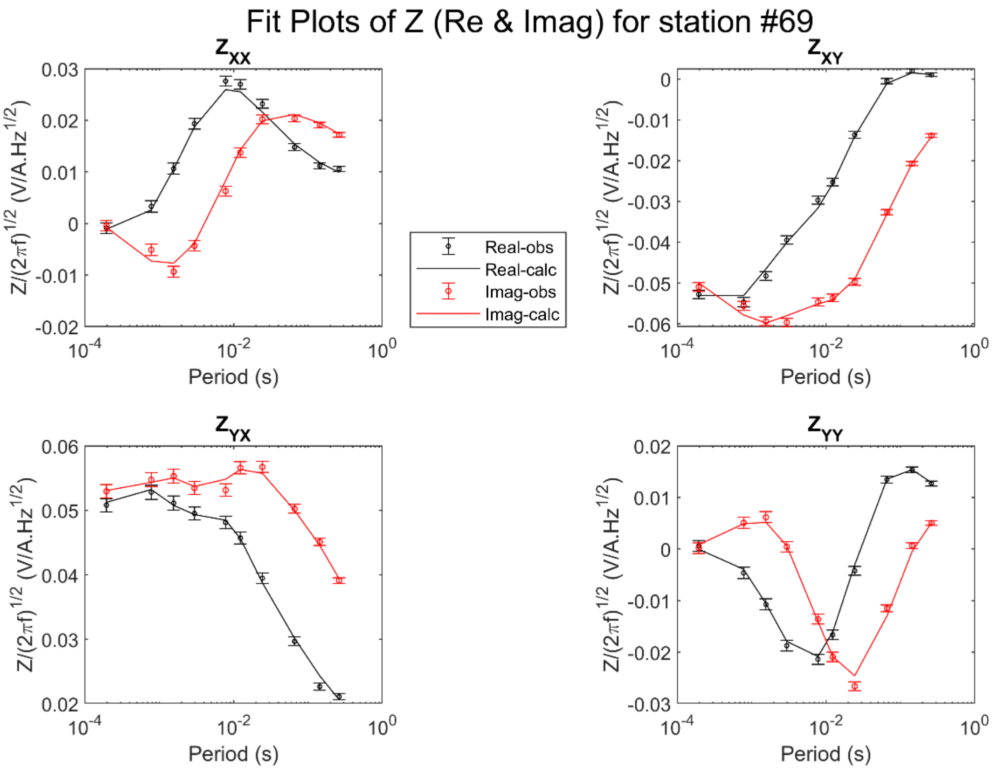
Fit Plots of Z (Re & Imag) for station #69
Z_XX
Z_XY
Z_YX
Z_YY
Z/(2πf)^1/2 (V/A.Hz^1/2)
Period (s)
Real-obs
Real-calc
Imag-obs
Imag-calc

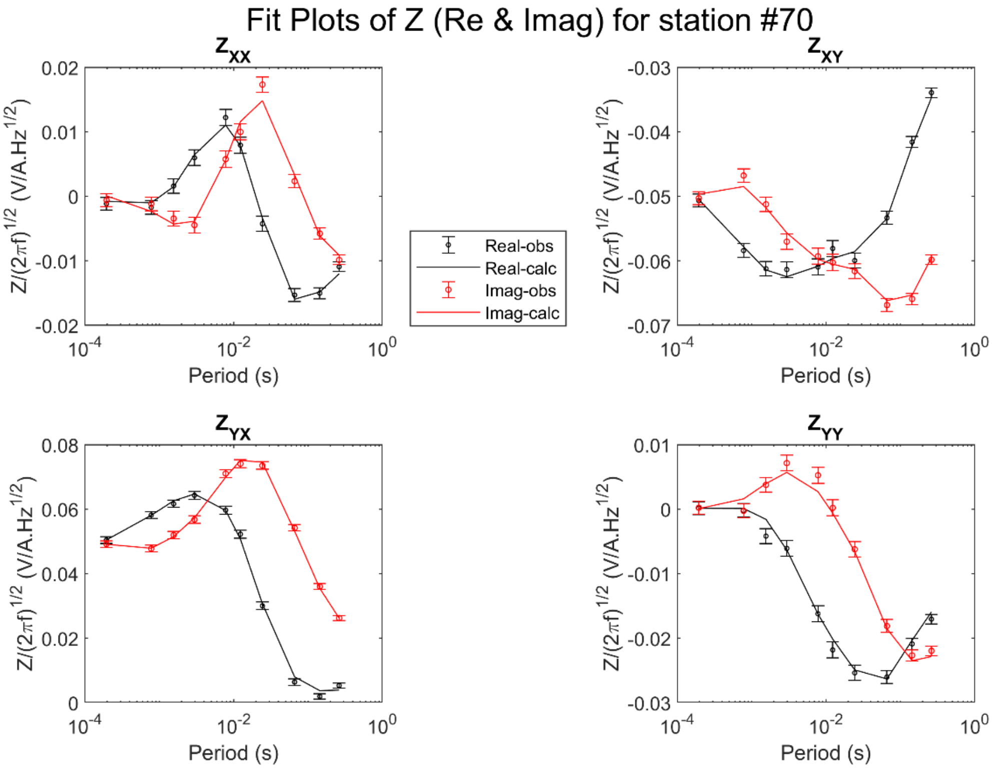
Fit Plots of Z (Re & Imag) for station #70
Z_{XX}
Z_{XY}
Z_{YX}
Z_{YY}
$Z/(2\pi f)^{1/2}$ (V/A.Hz$^{1/2}$)
Period (s)
Real-obs
Real-calc
Imag-obs
Imag-calc

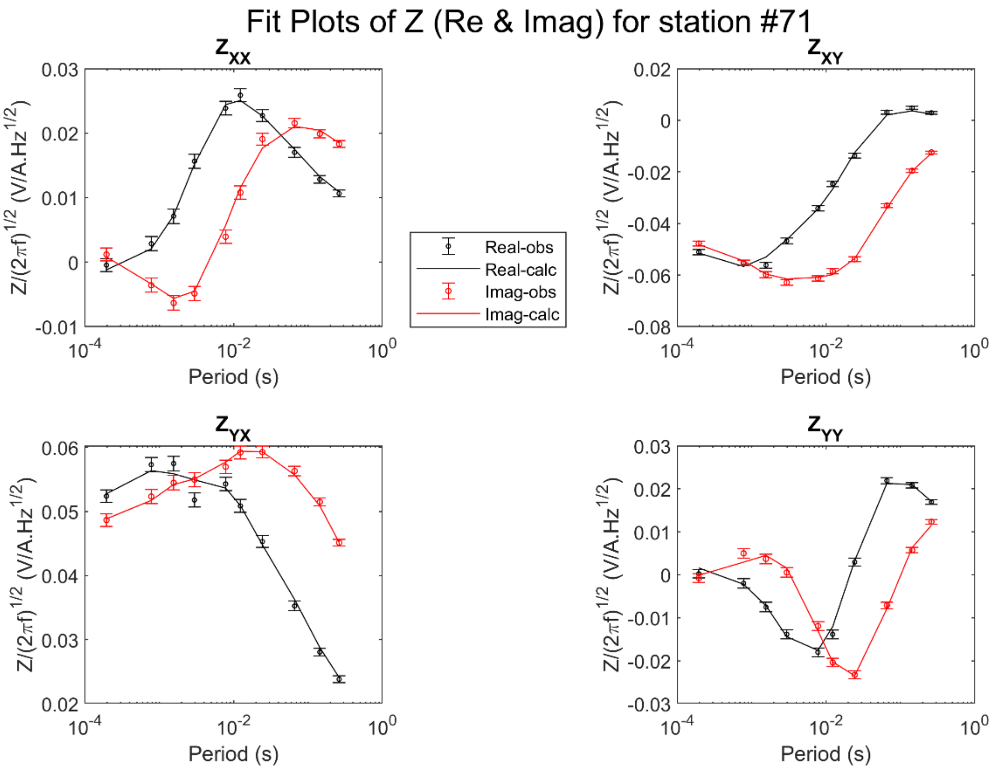
Fit Plots of Z (Re & Imag) for station #71
Z_{XX}
Z_{XY}
Z_{YX}
Z_{YY}
$Z/(2\pi f)^{1/2}$ (V/A.Hz$^{1/2}$)
Period (s)
Real-obs
Real-calc
Imag-obs
Imag-calc

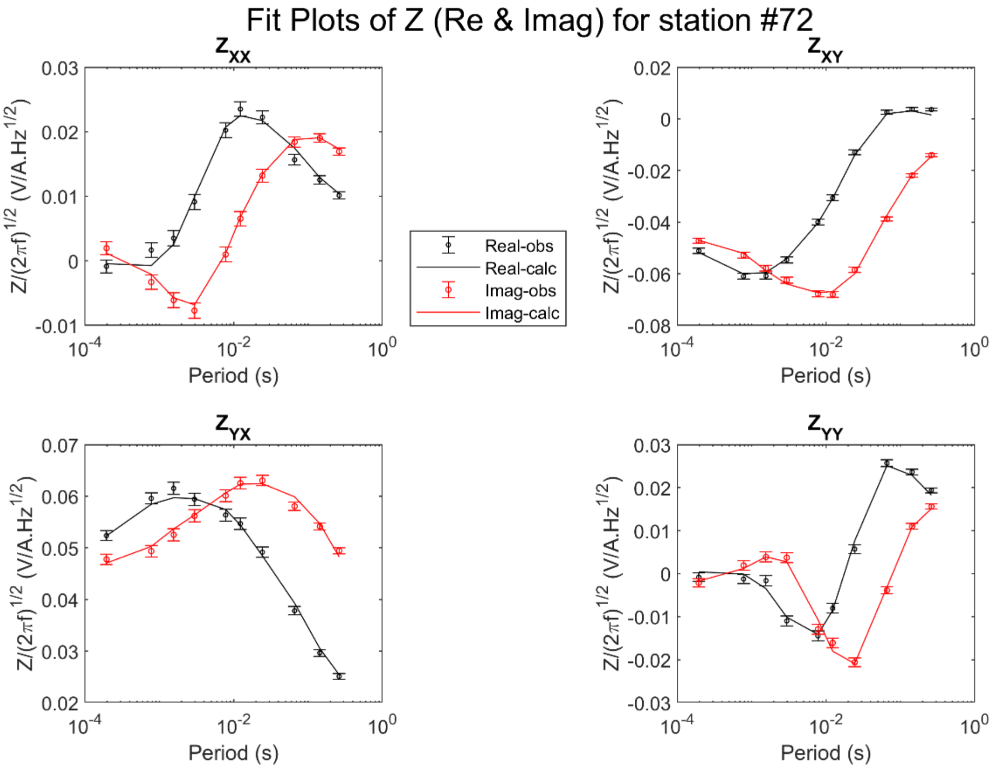
Fit Plots of Z (Re & Imag) for station #72
ZXX
ZXY
ZYX
ZYY
Z/(2πf)1/2 (V/A.Hz1/2)
Period (s)
Real-obs
Real-calc
Imag-obs
Imag-calc

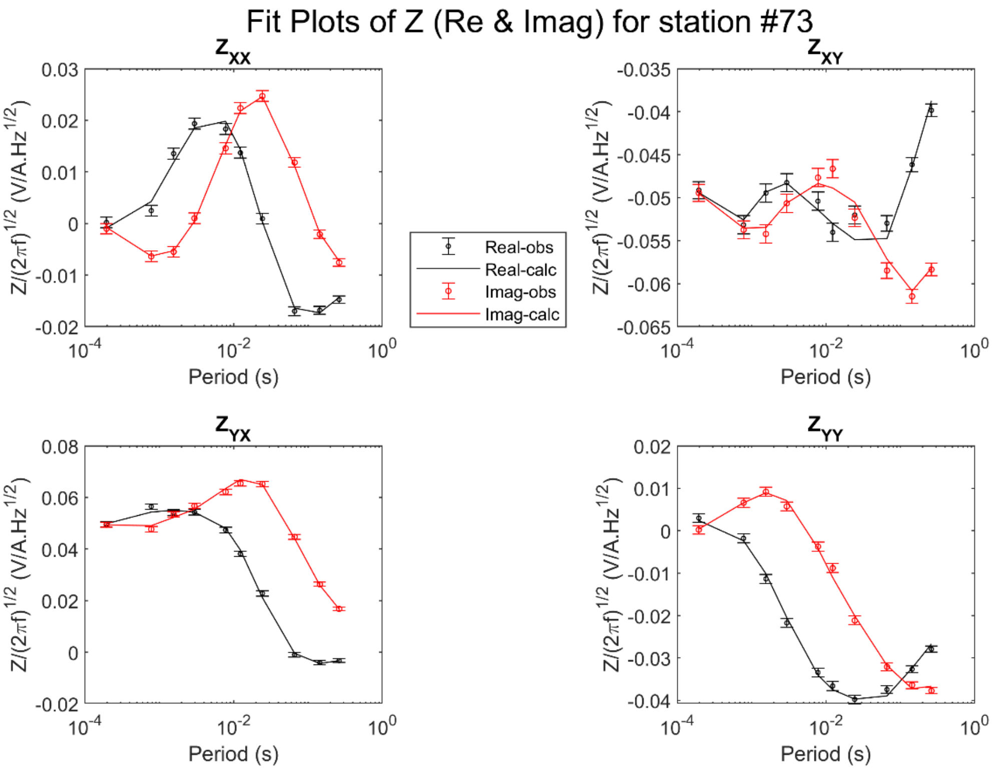
Fit Plots of Z (Re & Imag) for station #73
ZXX
ZXY
ZYX
ZYY
Z/(2πf)1/2 (V/A.Hz1/2)
Period (s)
Real-obs
Real-calc
Imag-obs
Imag-calc

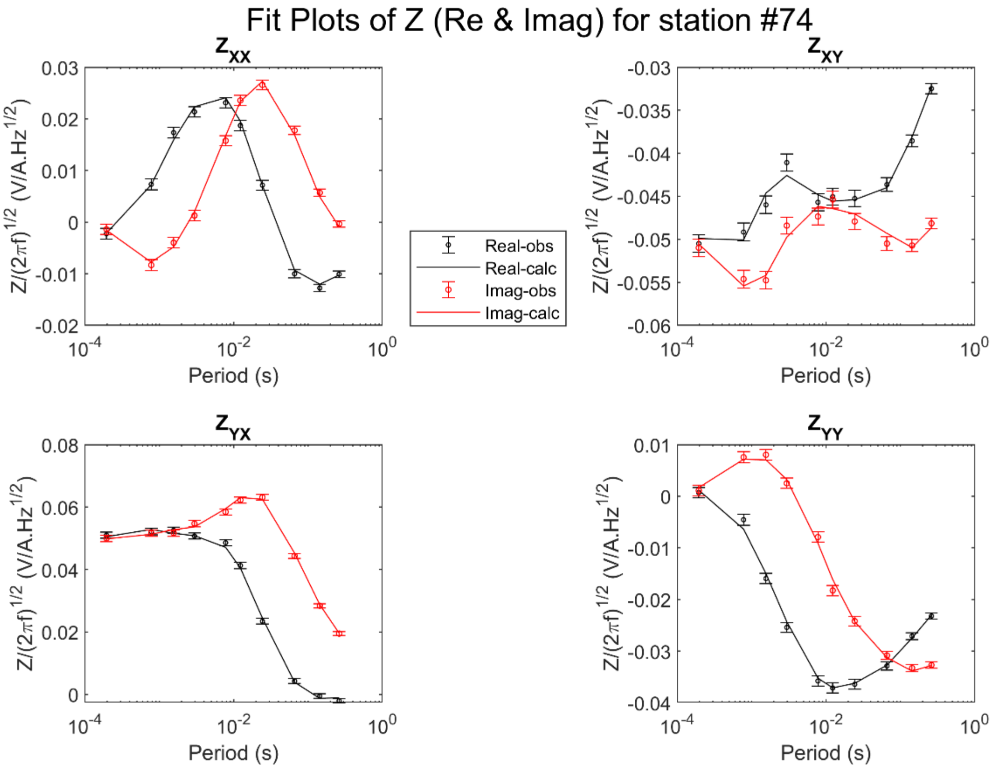
Fit Plots of Z (Re & Imag) for station #74
Z_XX
Z_XY
Z_YX
Z_YY
Z/(2πf)^1/2 (V/A.Hz^1/2)
Period (s)
Real-obs
Real-calc
Imag-obs
Imag-calc

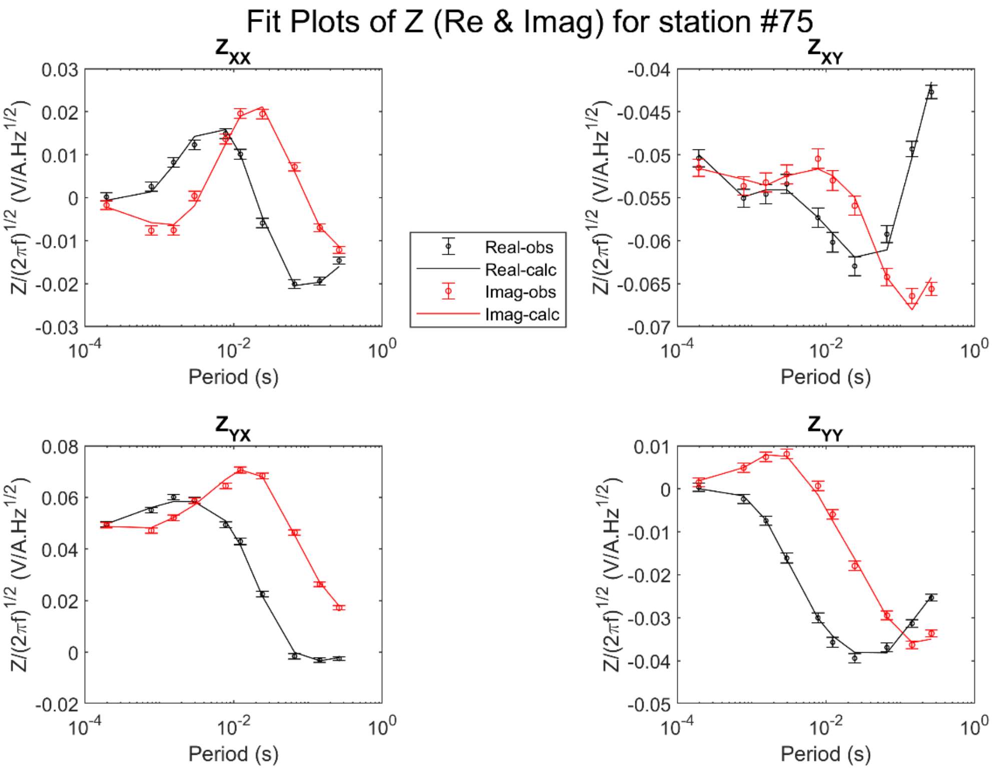
Fit Plots of Z (Re & Imag) for station #75
Z_XX
Z_XY
Z_YX
Z_YY
Z/(2πf)^1/2 (V/A.Hz^1/2)
Period (s)
Real-obs
Real-calc
Imag-obs
Imag-calc

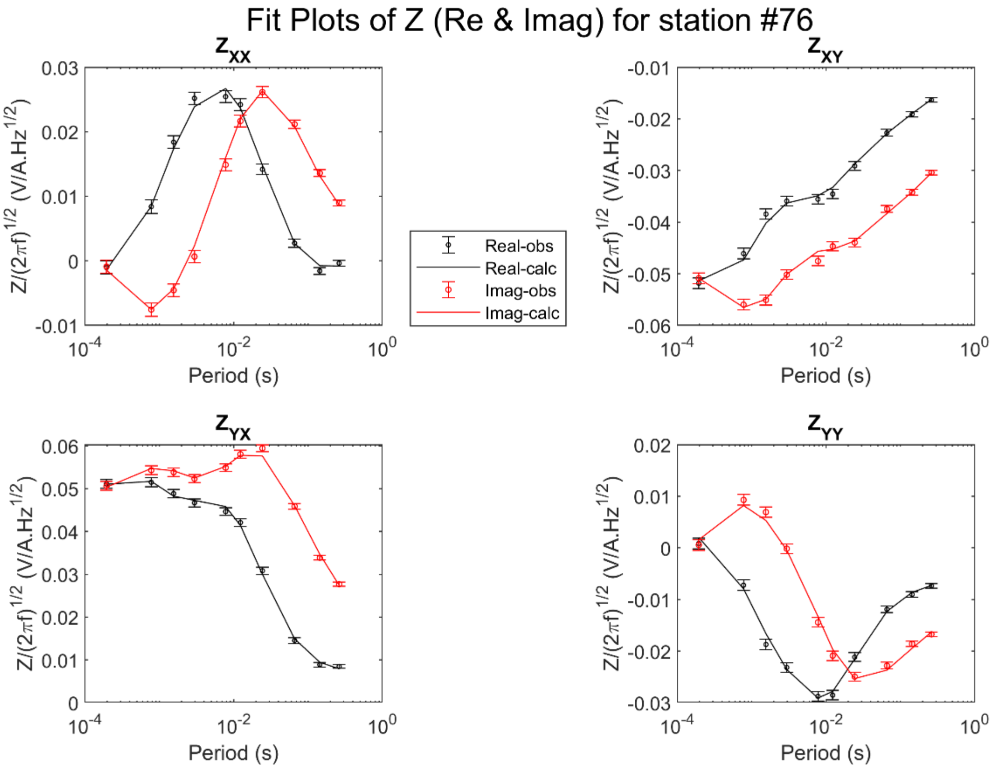
Fit Plots of Z (Re & Imag) for station #76
ZXX
ZXY
ZYX
ZYY
Z/(2πf)^1/2 (V/A.Hz^1/2)
Period (s)
Real-obs
Real-calc
Imag-obs
Imag-calc

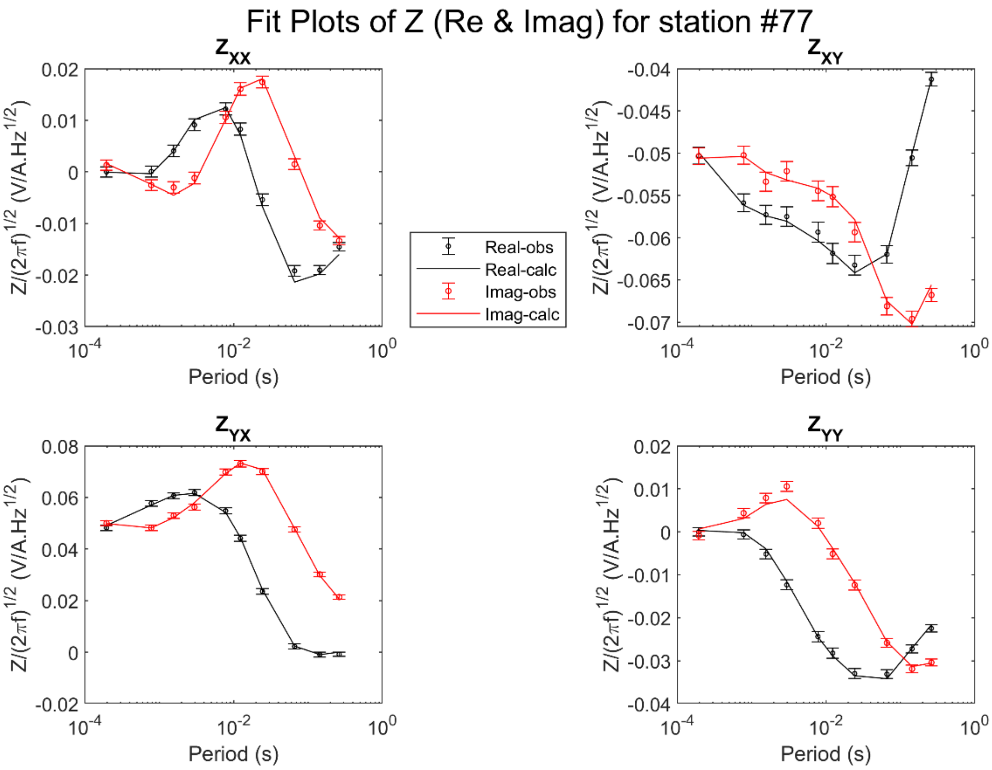
Fit Plots of Z (Re & Imag) for station #77
ZXX
ZXY
ZYX
ZYY
Z/(2πf)^1/2 (V/A.Hz^1/2)
Period (s)
Real-obs
Real-calc
Imag-obs
Imag-calc

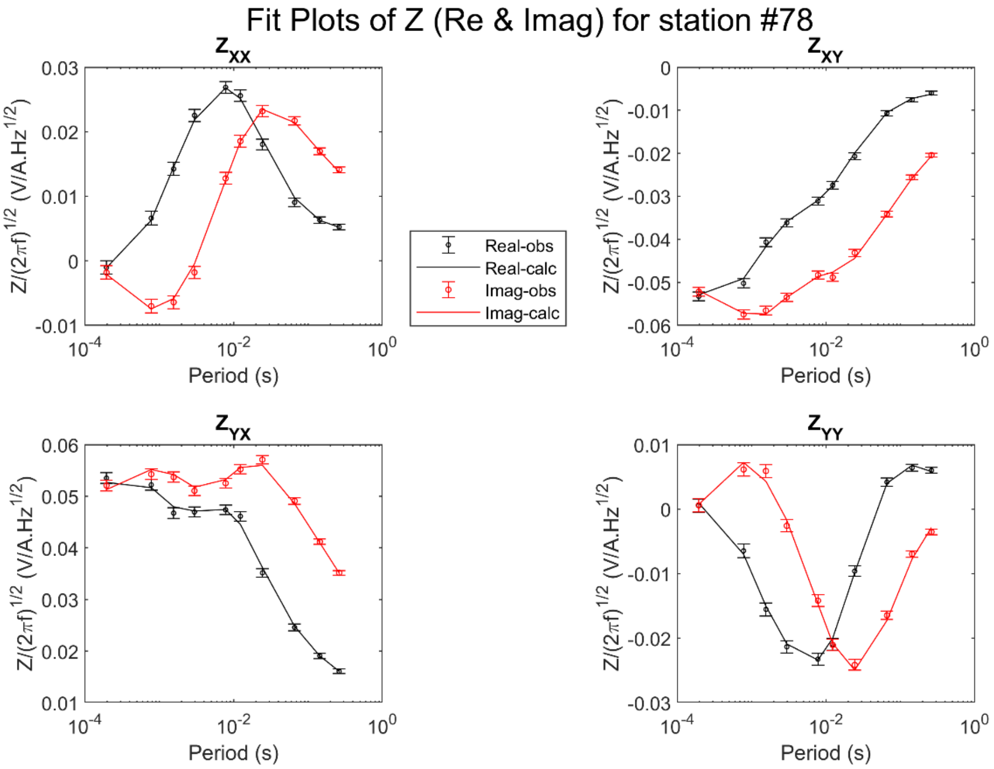
Fit Plots of Z (Re & Imag) for station #78
Z_{XX}
Z_{XY}
Z_{YX}
Z_{YY}
$Z/(2\pi f)^{1/2}$ (V/A.Hz$^{1/2}$)
Period (s)
Real-obs
Real-calc
Imag-obs
Imag-calc

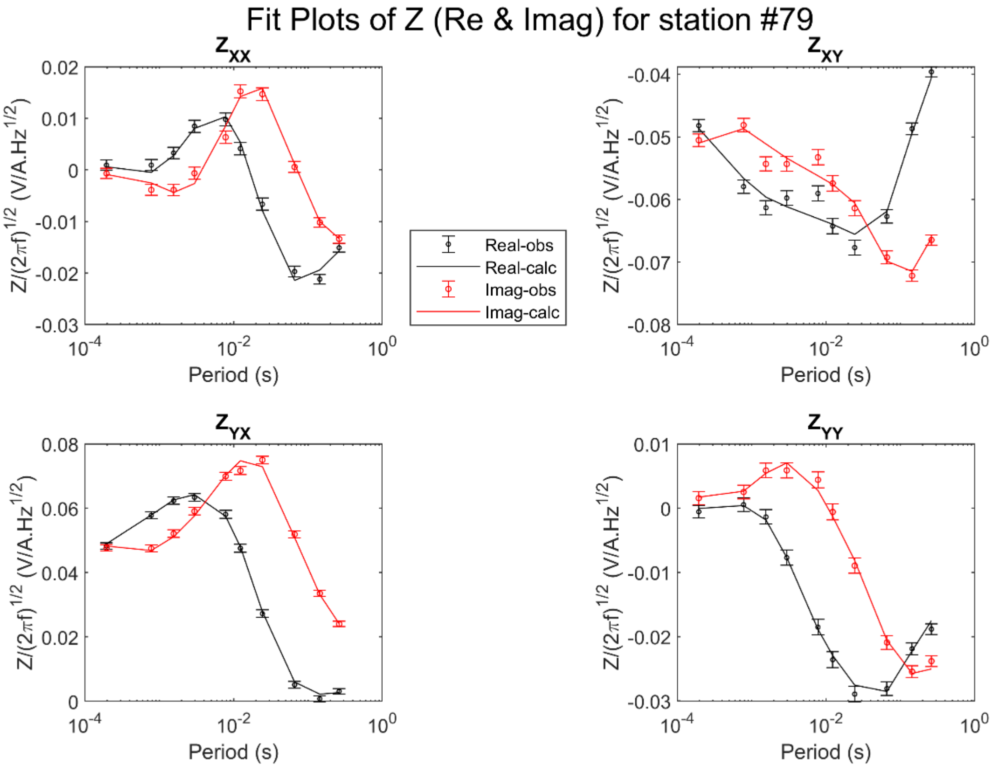
Fit Plots of Z (Re & Imag) for station #79
Z_{XX}
Z_{XY}
Z_{YX}
Z_{YY}
$Z/(2\pi f)^{1/2}$ (V/A.Hz$^{1/2}$)
Period (s)
Real-obs
Real-calc
Imag-obs
Imag-calc

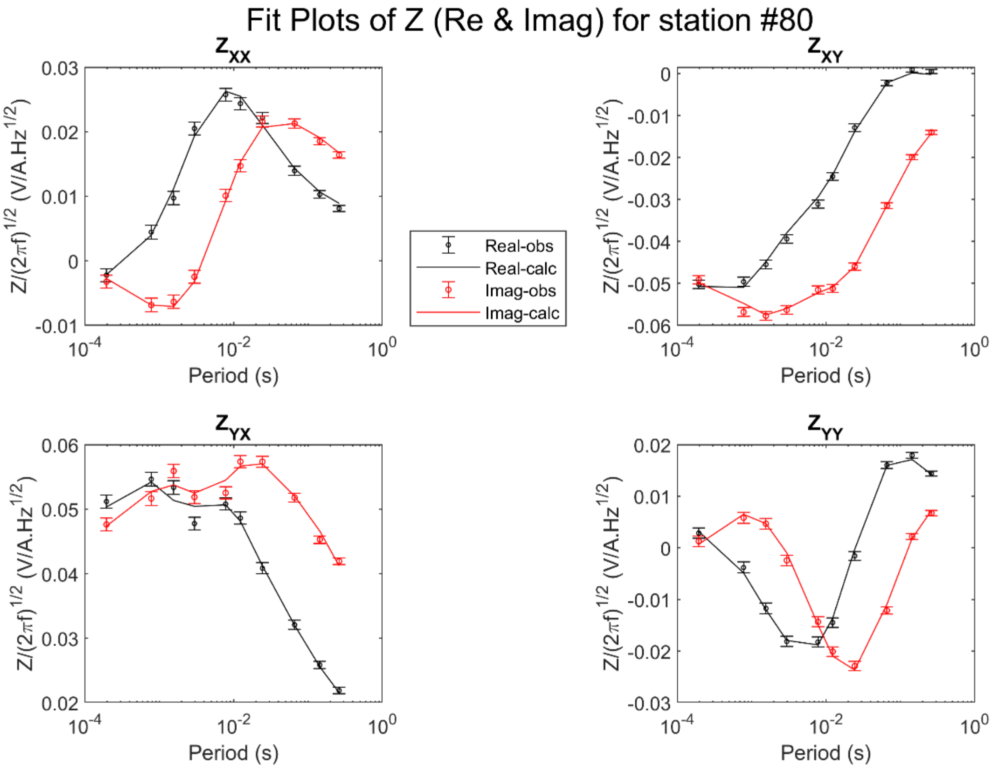

Fit Plots of Z (Re & Imag) for station #80
Z_XX
Z_XY
Z_YX
Z_YY
Z/(2πf)^1/2 (V/A.Hz^1/2)
Period (s)
Real-obs
Real-calc
Imag-obs
Imag-calc

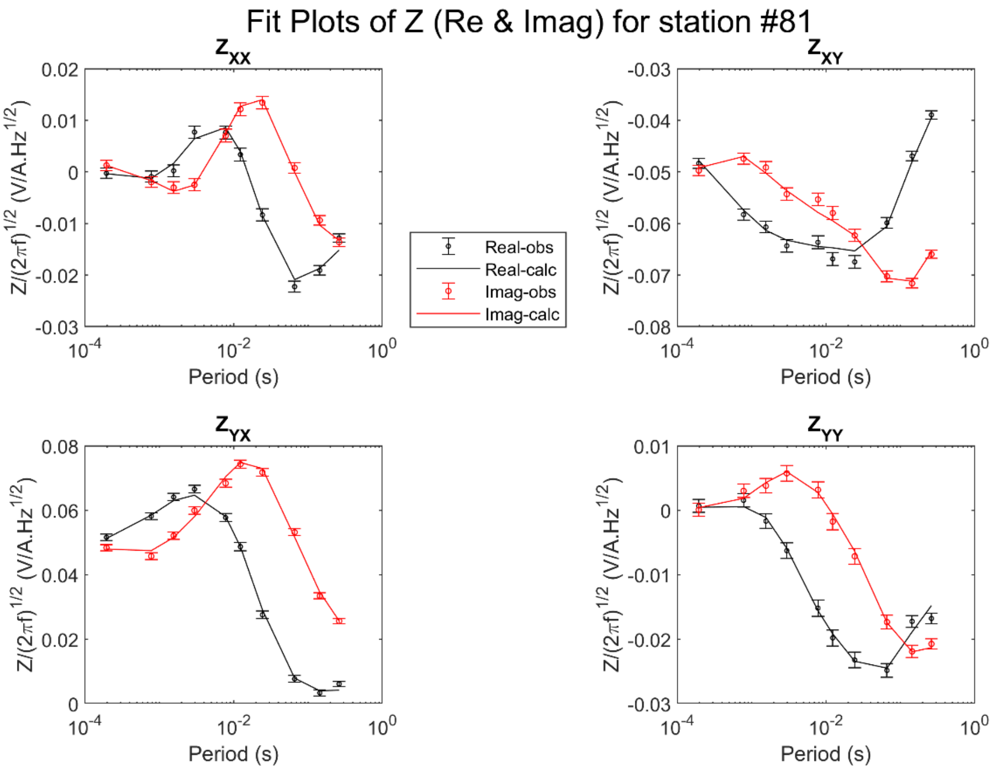

Fit Plots of Z (Re & Imag) for station #81
Z_XX
Z_XY
Z_YX
Z_YY
Z/(2πf)^1/2 (V/A.Hz^1/2)
Period (s)
Real-obs
Real-calc
Imag-obs
Imag-calc

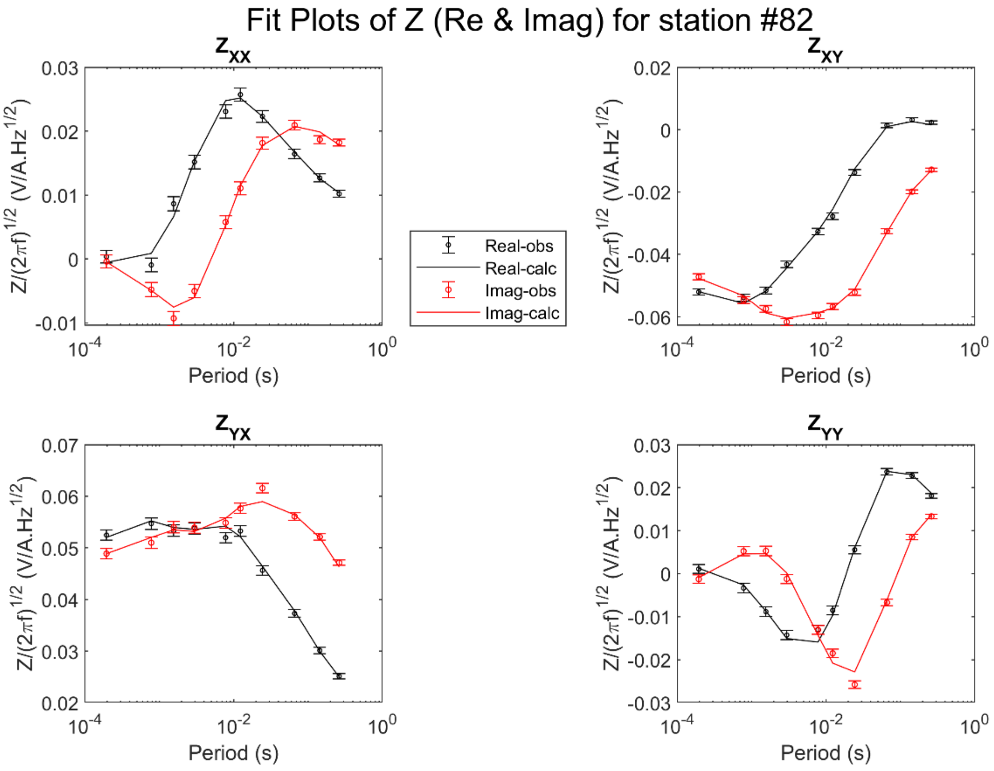
Fit Plots of Z (Re & Imag) for station #82
Z_XX
Z_XY
Z_YX
Z_YY
Z/(2πf)^1/2 (V/A.Hz^1/2)
Period (s)
Real-obs
Real-calc
Imag-obs
Imag-calc

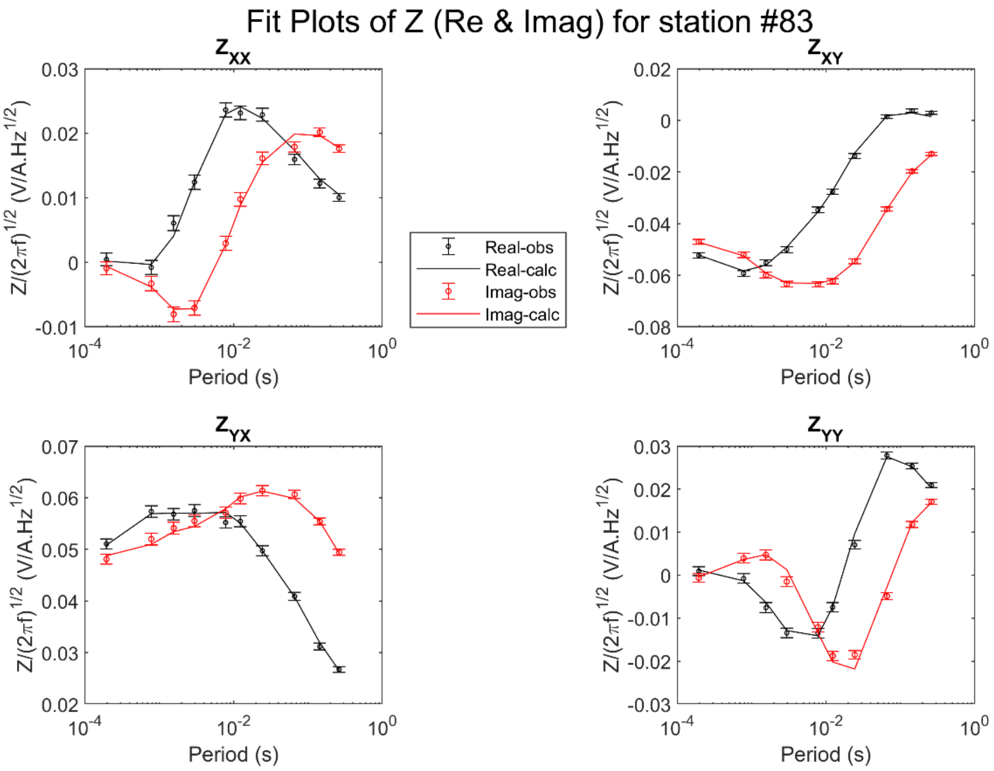
Fit Plots of Z (Re & Imag) for station #83
Z_XX
Z_XY
Z_YX
Z_YY
Z/(2πf)^1/2 (V/A.Hz^1/2)
Period (s)
Real-obs
Real-calc
Imag-obs
Imag-calc

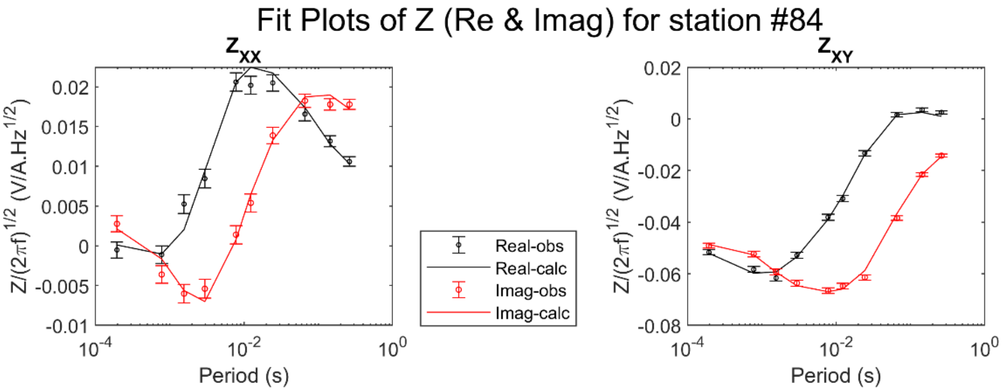
Fit Plots of Z (Re & Imag) for station #84
Z_XX
Z_XY
Z_YX
Z_YY
Z/(2πf)^1/2 (V/A.Hz^1/2)
Period (s)
Real-obs
Real-calc
Imag-obs
Imag-calc

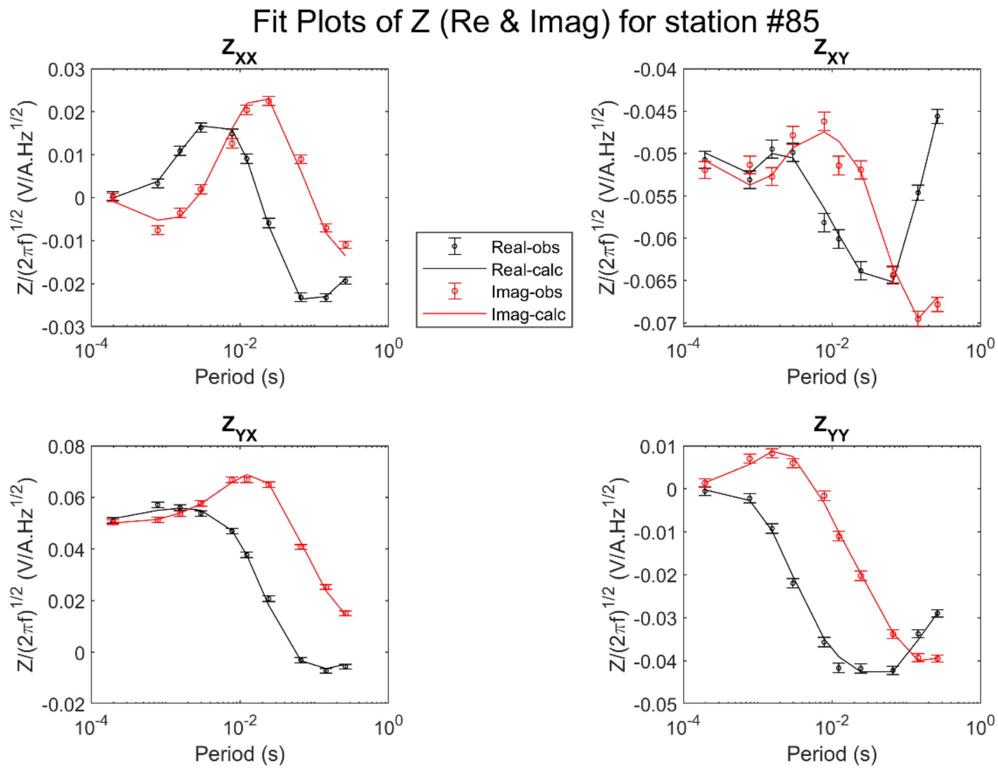
Fit Plots of Z (Re & Imag) for station #85
Z_XX
Z_XY
Z_YX
Z_YY
Z/(2πf)^1/2 (V/A.Hz^1/2)
Period (s)
Real-obs
Real-calc
Imag-obs
Imag-calc

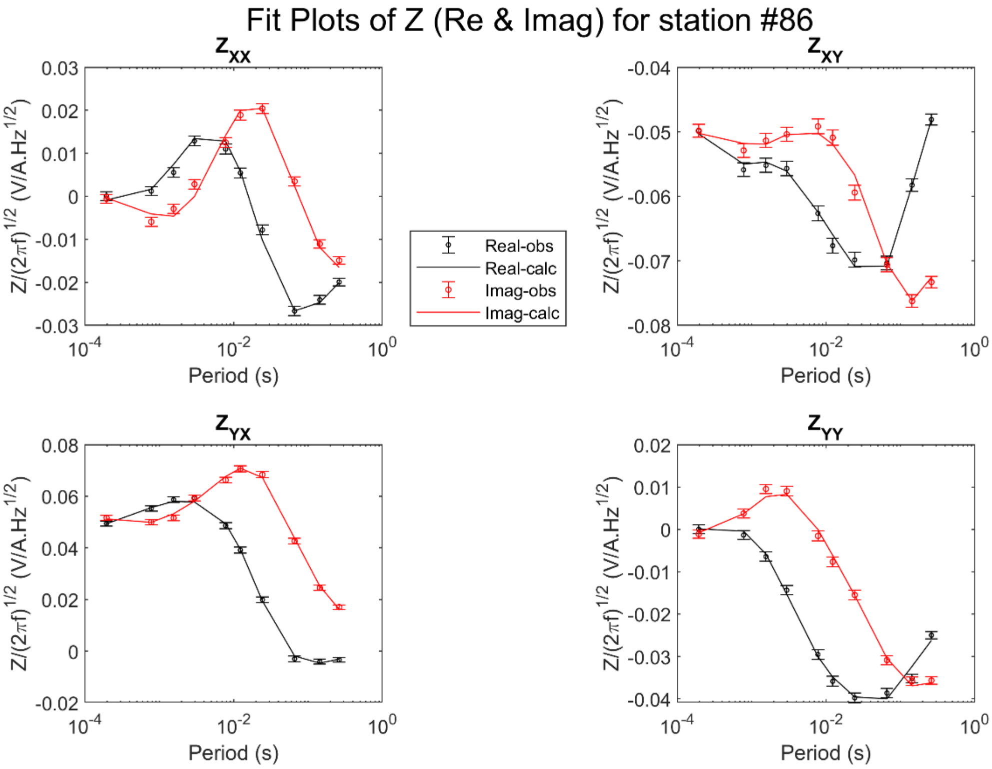

Fit Plots of Z (Re & Imag) for station #86
Z_XX
Z_XY
Z_YX
Z_YY
Z/(2πf)^1/2 (V/A.Hz^1/2)
Period (s)
Real-obs
Real-calc
Imag-obs
Imag-calc

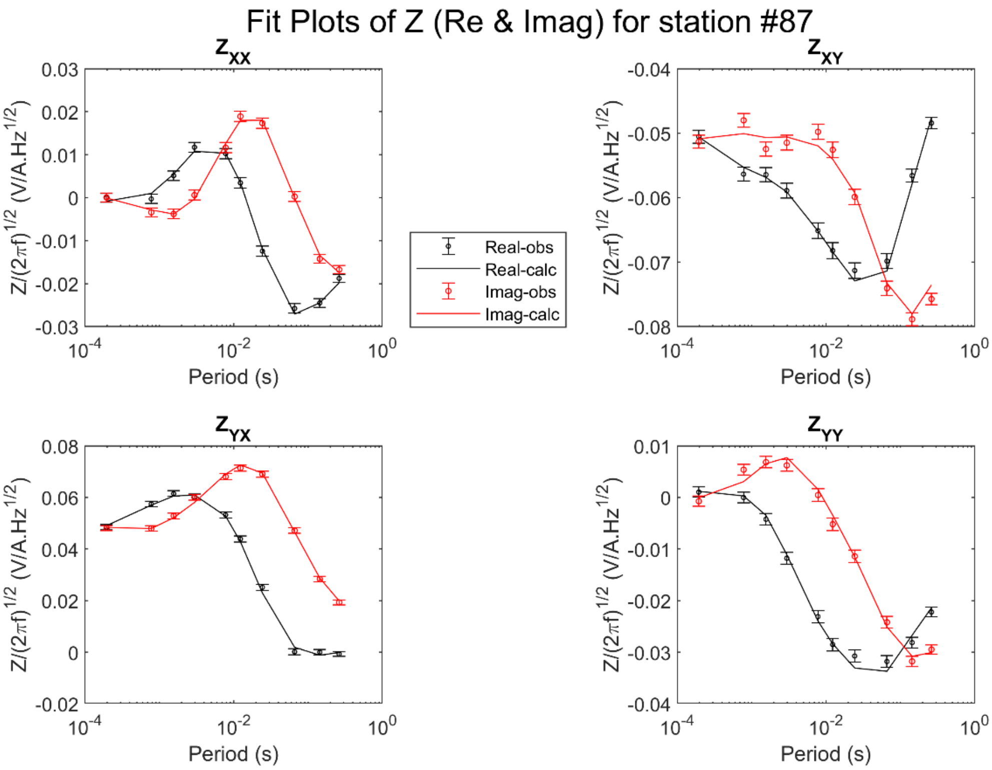

Fit Plots of Z (Re & Imag) for station #87
Z_XX
Z_XY
Z_YX
Z_YY
Z/(2πf)^1/2 (V/A.Hz^1/2)
Period (s)
Real-obs
Real-calc
Imag-obs
Imag-calc

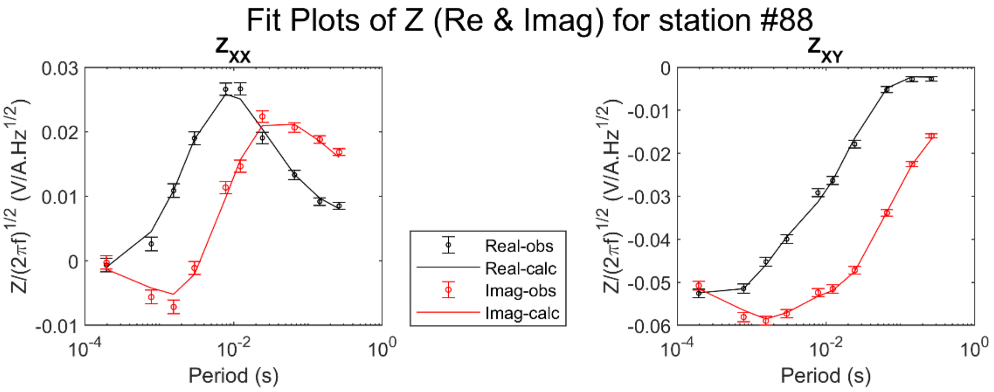
Fit Plots of Z (Re & Imag) for station #88
Z_{XX}
Z_{XY}
Z_{YX}
Z_{YY}
$Z/(2\pi f)^{1/2}$ (V/A.Hz$^{1/2}$)
Period (s)
Real-obs
Real-calc
Imag-obs
Imag-calc

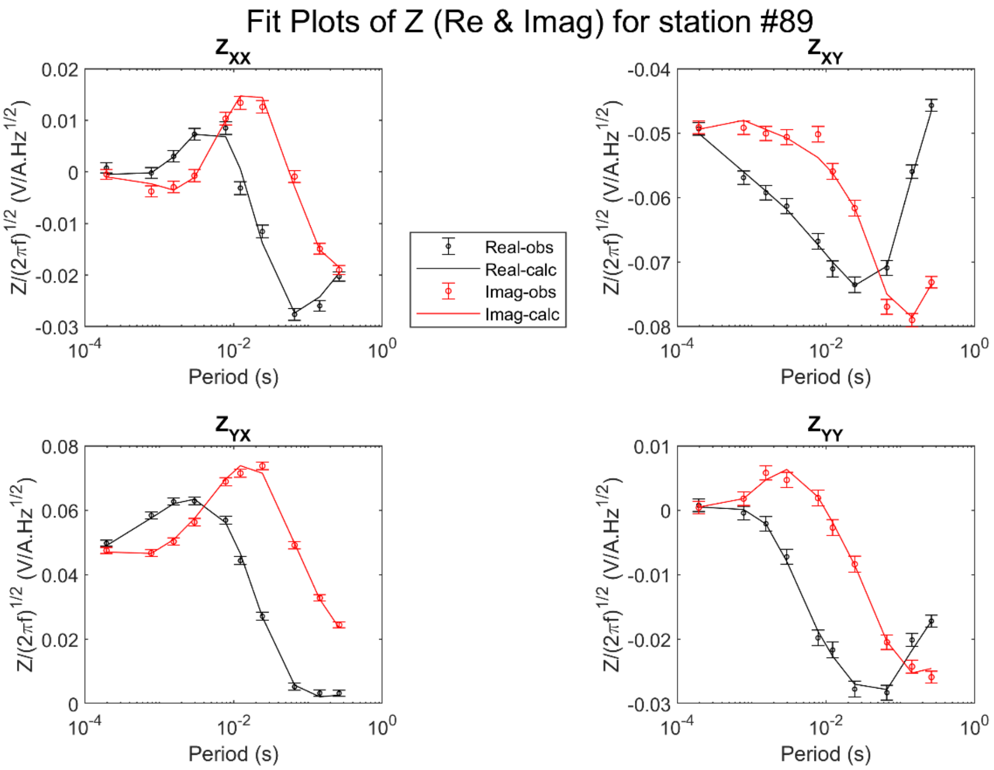
Fit Plots of Z (Re & Imag) for station #89
Z_{XX}
Z_{XY}
Z_{YX}
Z_{YY}
$Z/(2\pi f)^{1/2}$ (V/A.Hz$^{1/2}$)
Period (s)
Real-obs
Real-calc
Imag-obs
Imag-calc

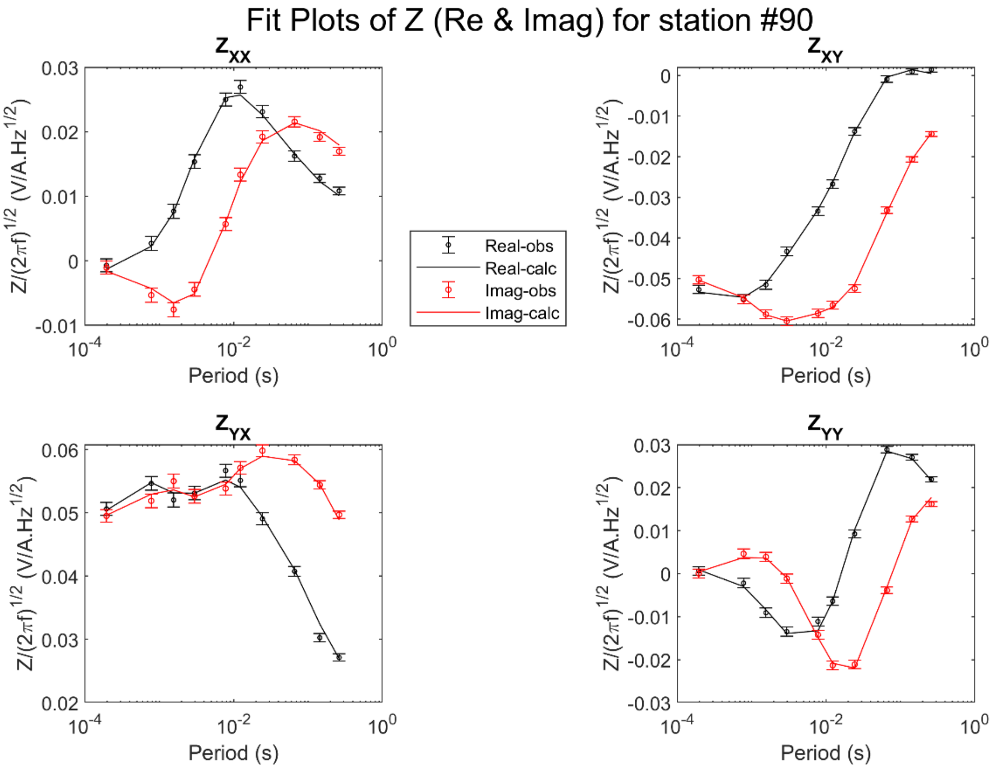
Fit Plots of Z (Re & Imag) for station #90
Z_XX
Z_XY
Z_YX
Z_YY
Z/(2πf)^1/2 (V/A.Hz^1/2)
Period (s)
Real-obs
Real-calc
Imag-obs
Imag-calc

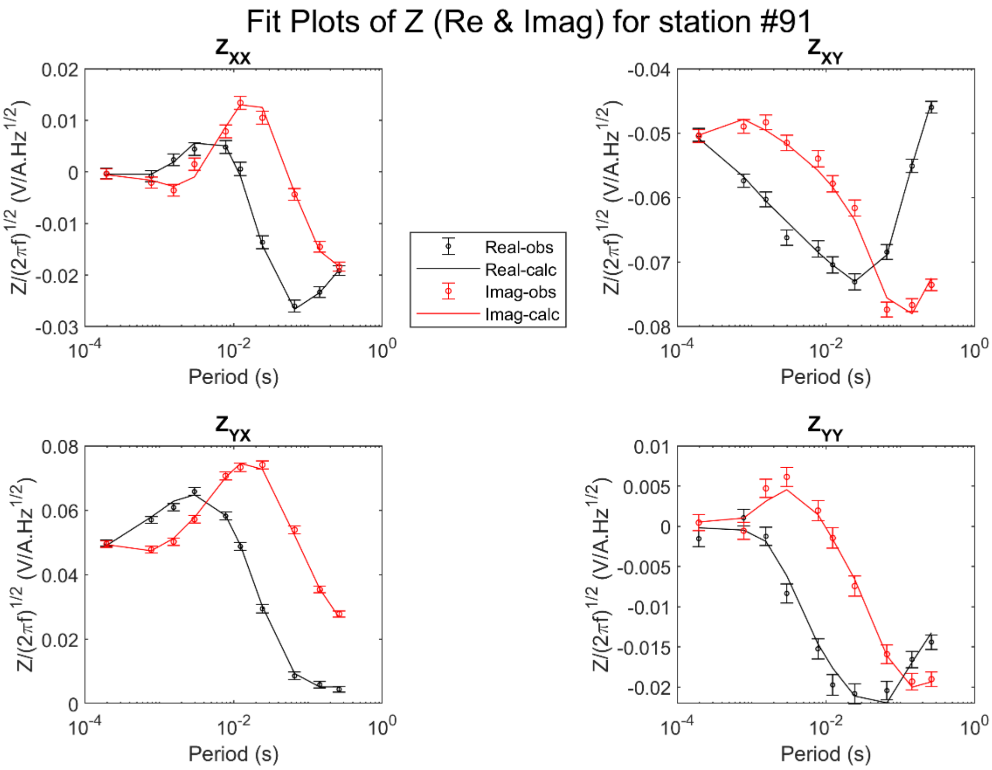
Fit Plots of Z (Re & Imag) for station #91
Z_XX
Z_XY
Z_YX
Z_YY
Z/(2πf)^1/2 (V/A.Hz^1/2)
Period (s)
Real-obs
Real-calc
Imag-obs
Imag-calc

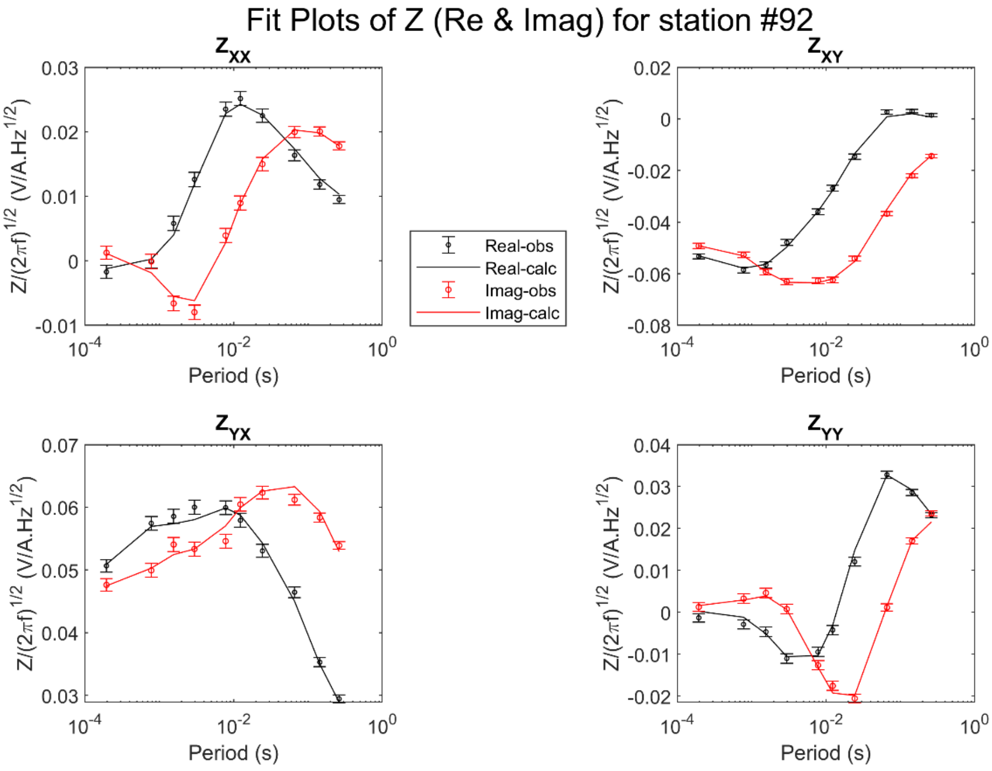
Fit Plots of Z (Re & Imag) for station #92
Z_{XX}
Z_{XY}
Z_{YX}
Z_{YY}
$Z/(2\pi f)^{1/2}$ (V/A.Hz$^{1/2}$)
Period (s)
Real-obs
Real-calc
Imag-obs
Imag-calc

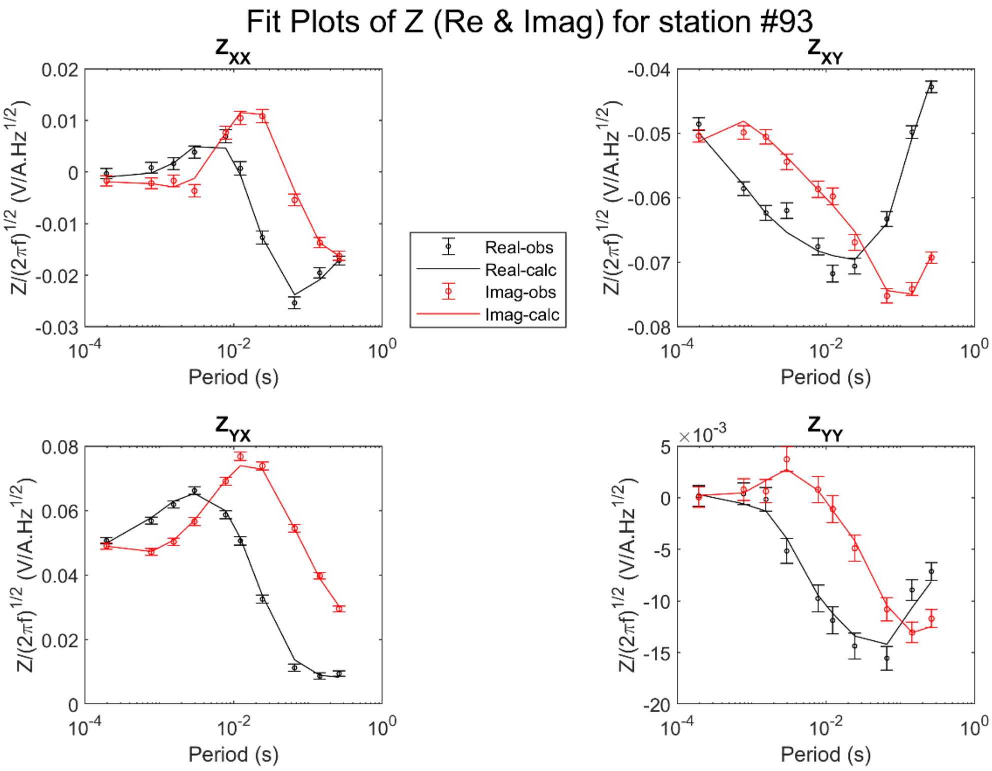
Fit Plots of Z (Re & Imag) for station #93
Z_{XX}
Z_{XY}
Z_{YX}
Z_{YY}
$Z/(2\pi f)^{1/2}$ (V/A.Hz$^{1/2}$)
Period (s)
$\times 10^{-3}$
Real-obs
Real-calc
Imag-obs
Imag-calc

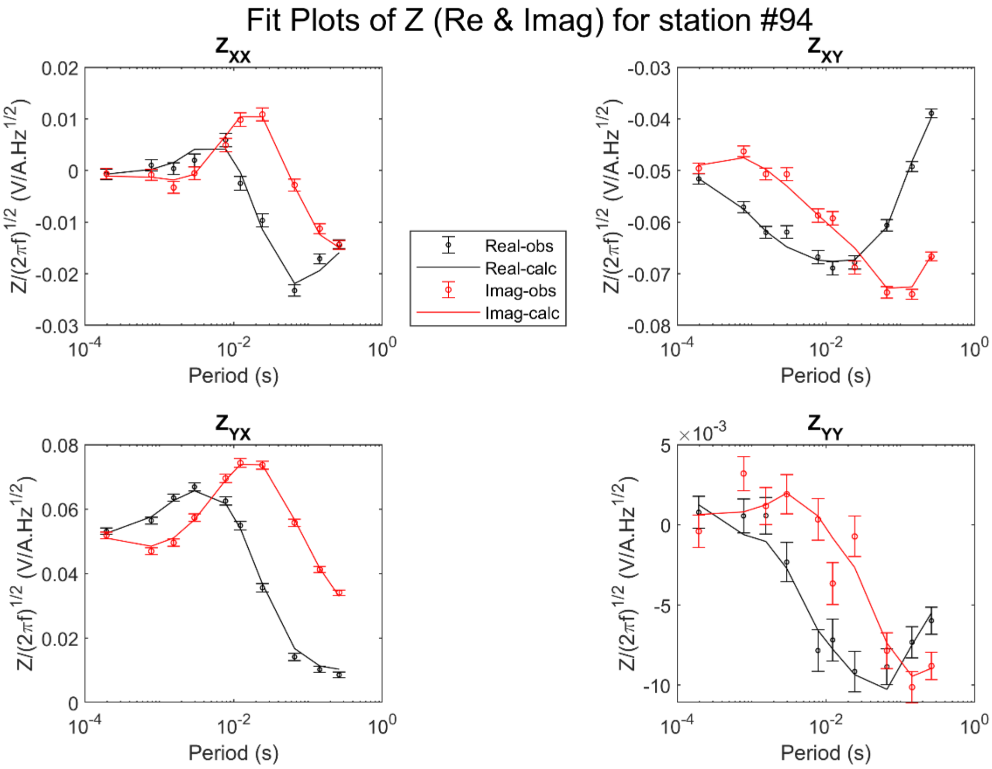
Fit Plots of Z (Re & Imag) for station #94
Z XX
Z XY
Z YX
Z YY
Z/(2πf)1/2 (V/A.Hz 1/2)
Period (s)
Real-obs
Real-calc
Imag-obs
Imag-calc
×10-3

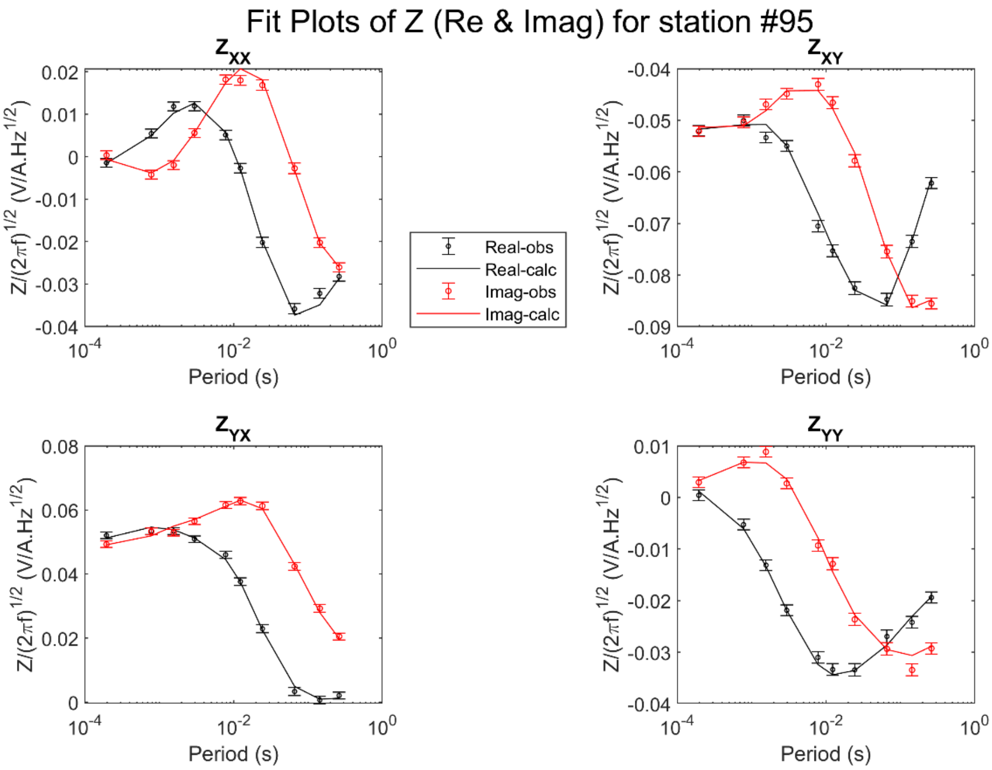
Fit Plots of Z (Re & Imag) for station #95
Z XX
Z XY
Z YX
Z YY
Z/(2πf)1/2 (V/A.Hz 1/2)
Period (s)
Real-obs
Real-calc
Imag-obs
Imag-calc

Fit Plots of Z (Re & Imag) for station #96

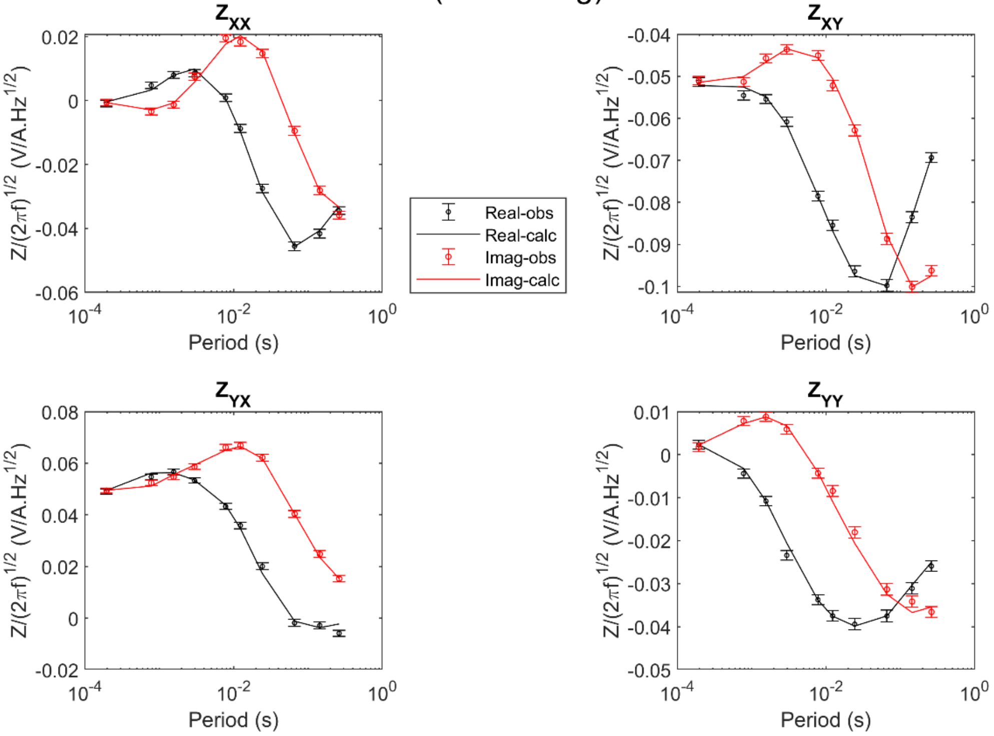

Fit Plots of Z (Re & Imag) for station #97

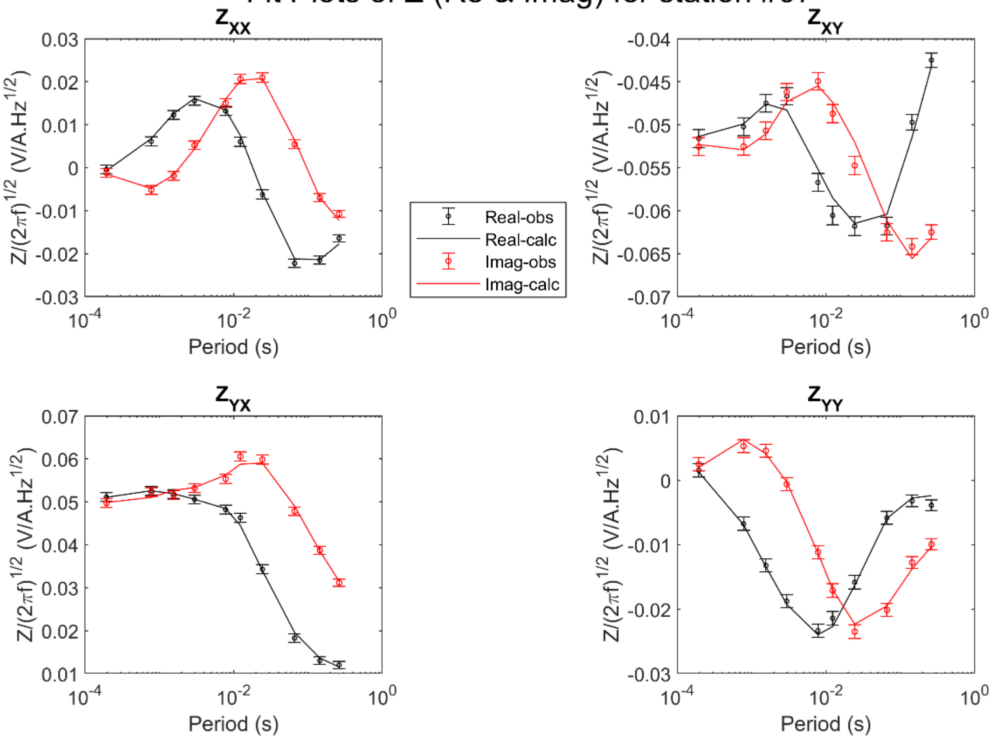

Fit Plots of Z (Re & Imag) for station #98

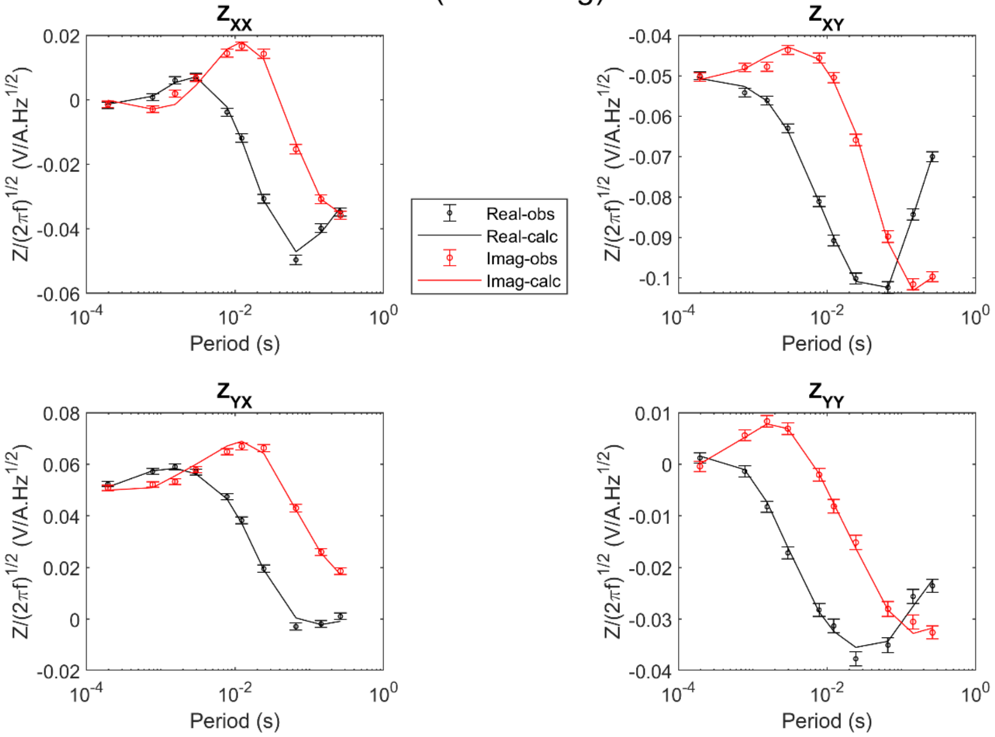

Fit Plots of Z (Re & Imag) for station #99

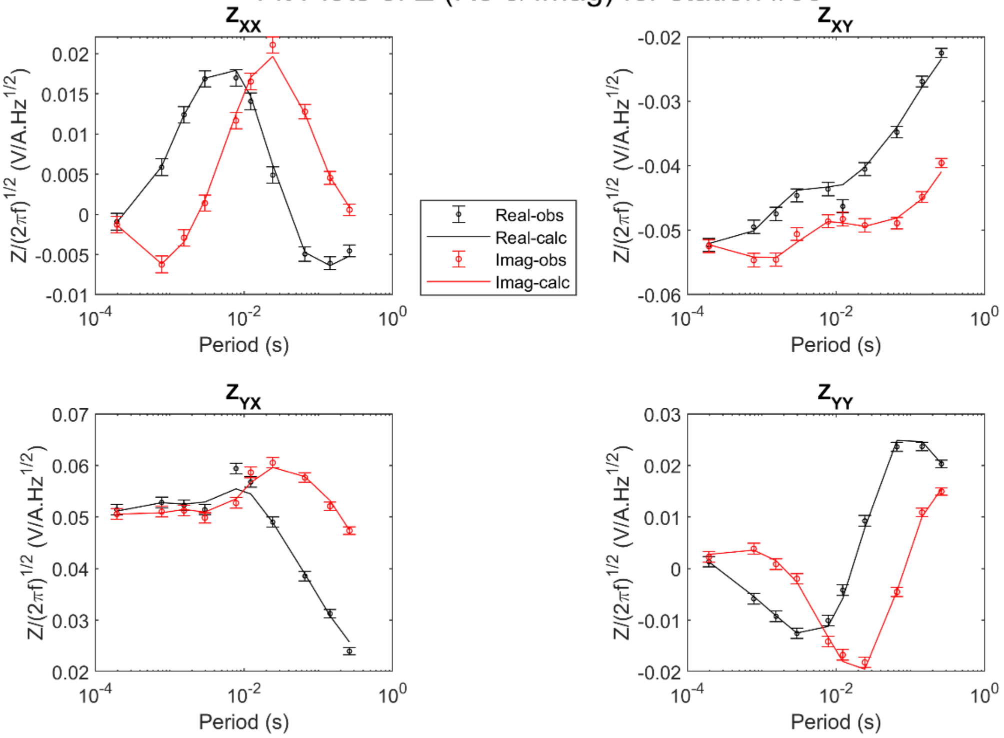

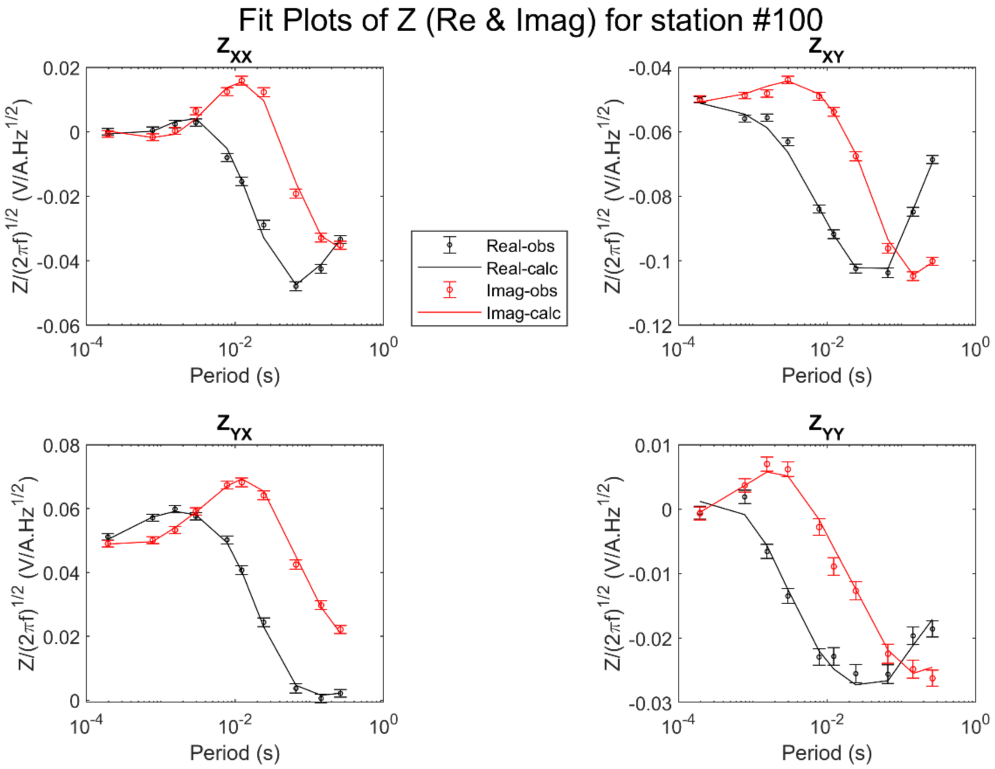
Fit Plots of Z (Re & Imag) for station #100
Z_XX
Z_XY
Z_YX
Z_YY
Real-obs
Real-calc
Imag-obs
Imag-calc
Z/(2πf)^1/2 (V/A.Hz^1/2)
Period (s)

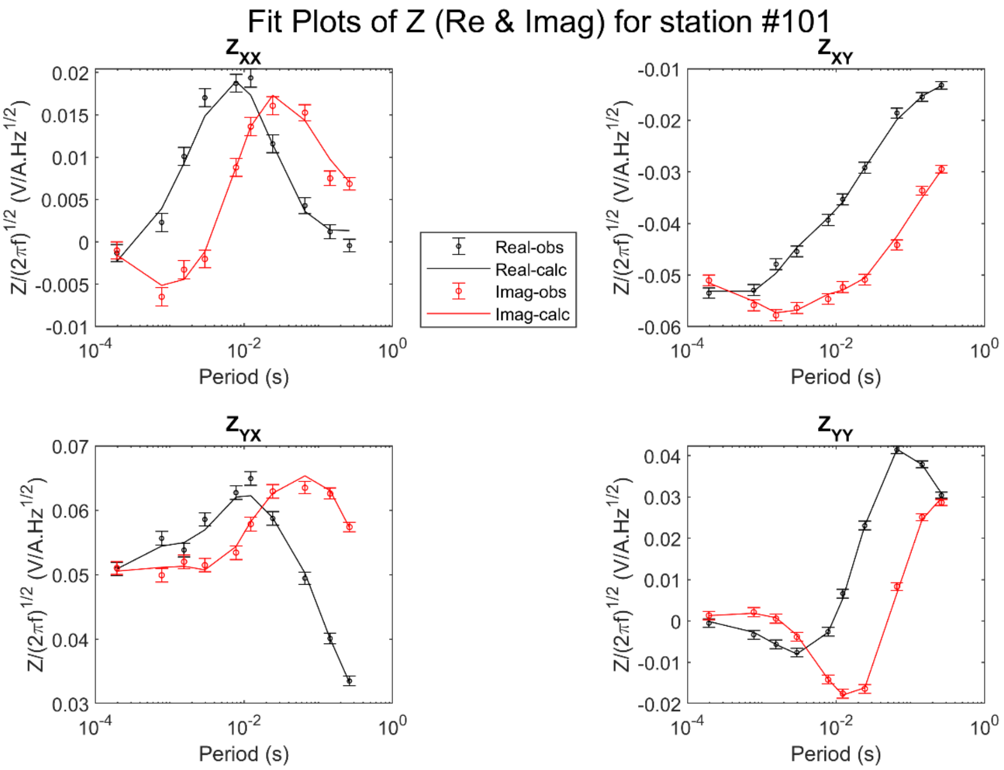
Fit Plots of Z (Re & Imag) for station #101
Z_XX
Z_XY
Z_YX
Z_YY
Real-obs
Real-calc
Imag-obs
Imag-calc
Z/(2πf)^1/2 (V/A.Hz^1/2)
Period (s)

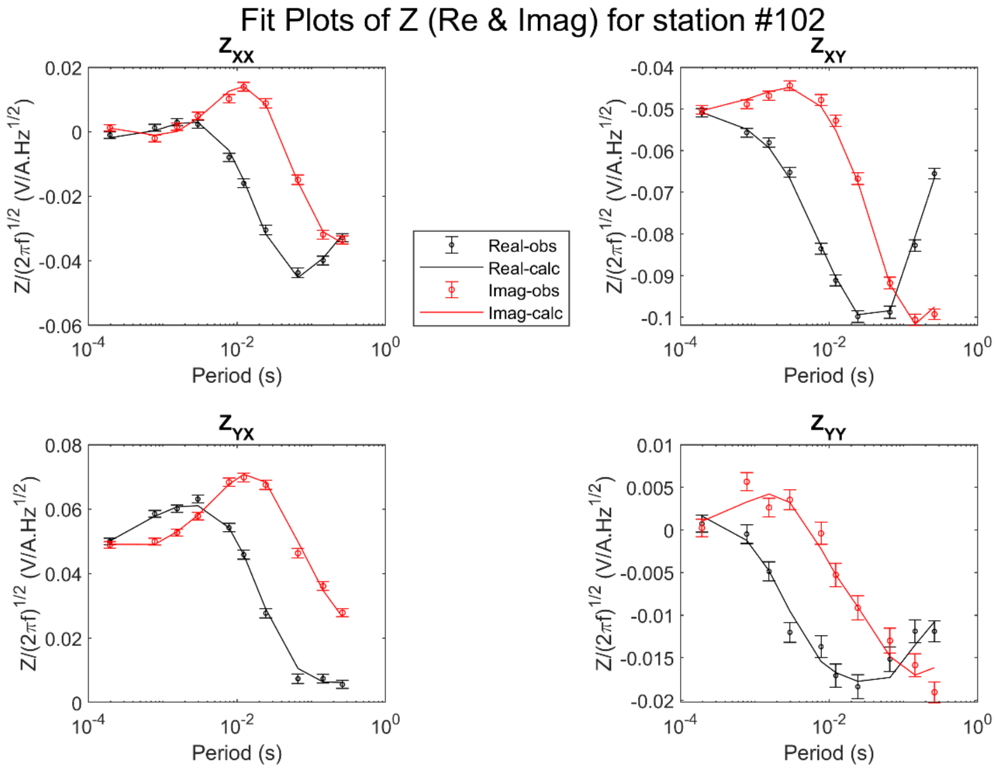
Fit Plots of Z (Re & Imag) for station #102
Z_{XX}
Z_{XY}
Z_{YX}
Z_{YY}
$Z/(2\pi f)^{1/2}$ (V/A.Hz$^{1/2}$)
Period (s)
Real-obs
Real-calc
Imag-obs
Imag-calc

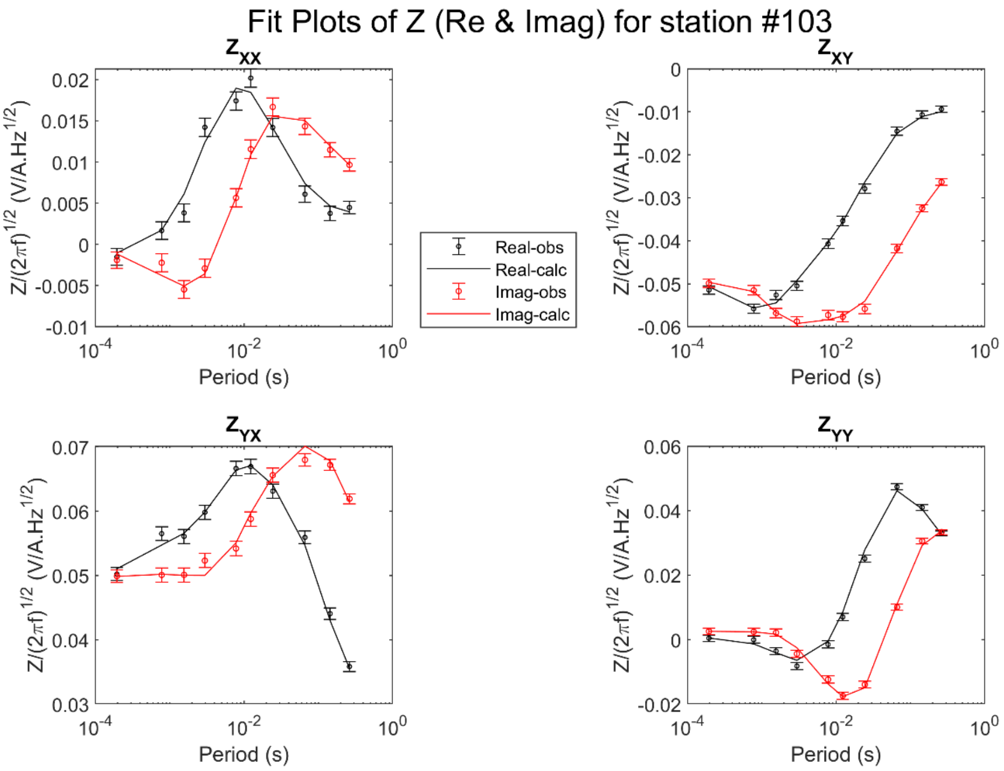
Fit Plots of Z (Re & Imag) for station #103
Z_{XX}
Z_{XY}
Z_{YX}
Z_{YY}
$Z/(2\pi f)^{1/2}$ (V/A.Hz$^{1/2}$)
Period (s)
Real-obs
Real-calc
Imag-obs
Imag-calc

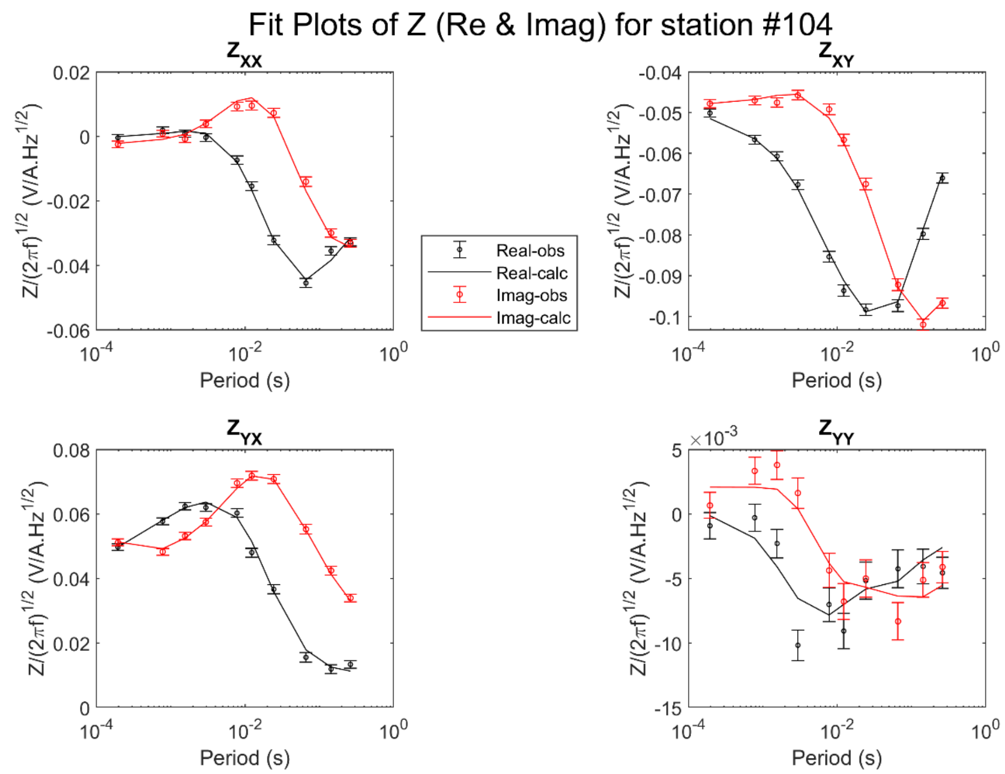
Fit Plots of Z (Re & Imag) for station #104
Z XX
Z XY
Z YX
Z YY
Z/(2πf)^1/2 (V/A.Hz^1/2)
Period (s)
×10^-3
Real-obs
Real-calc
Imag-obs
Imag-calc

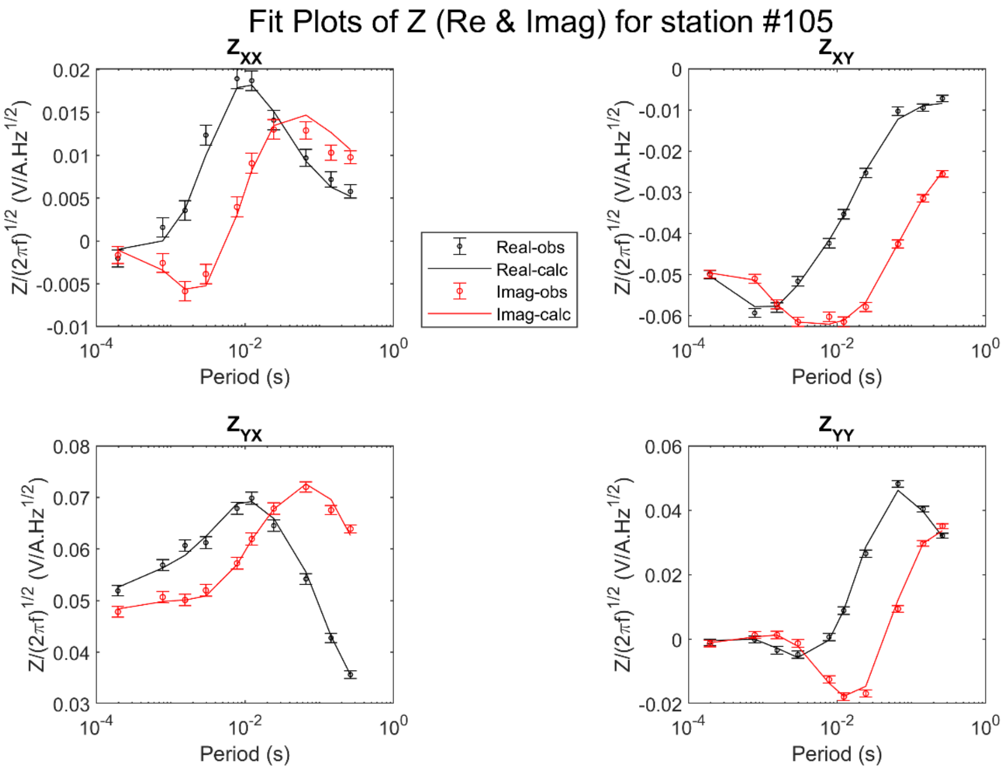
Fit Plots of Z (Re & Imag) for station #105
Z XX
Z XY
Z YX
Z YY
Z/(2πf)^1/2 (V/A.Hz^1/2)
Period (s)
Real-obs
Real-calc
Imag-obs
Imag-calc

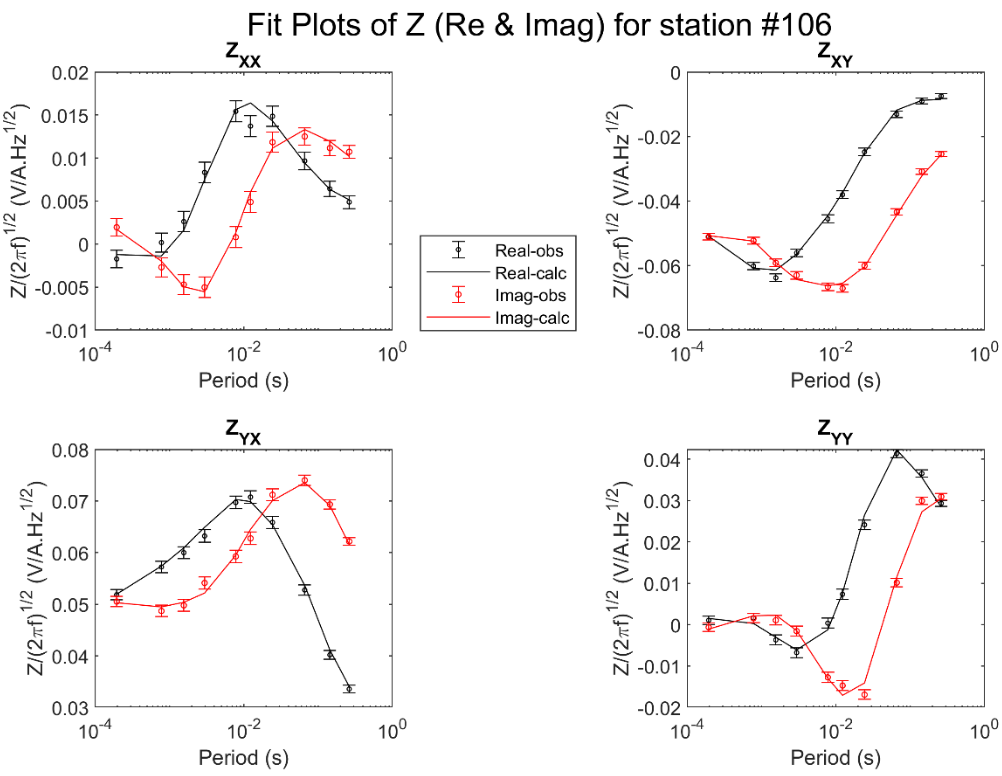
Fit Plots of Z (Re & Imag) for station #106
Z_XX
Z_XY
Z_YX
Z_YY
Real-obs
Real-calc
Imag-obs
Imag-calc
Z/(2πf)^1/2 (V/A.Hz^1/2)
Period (s)

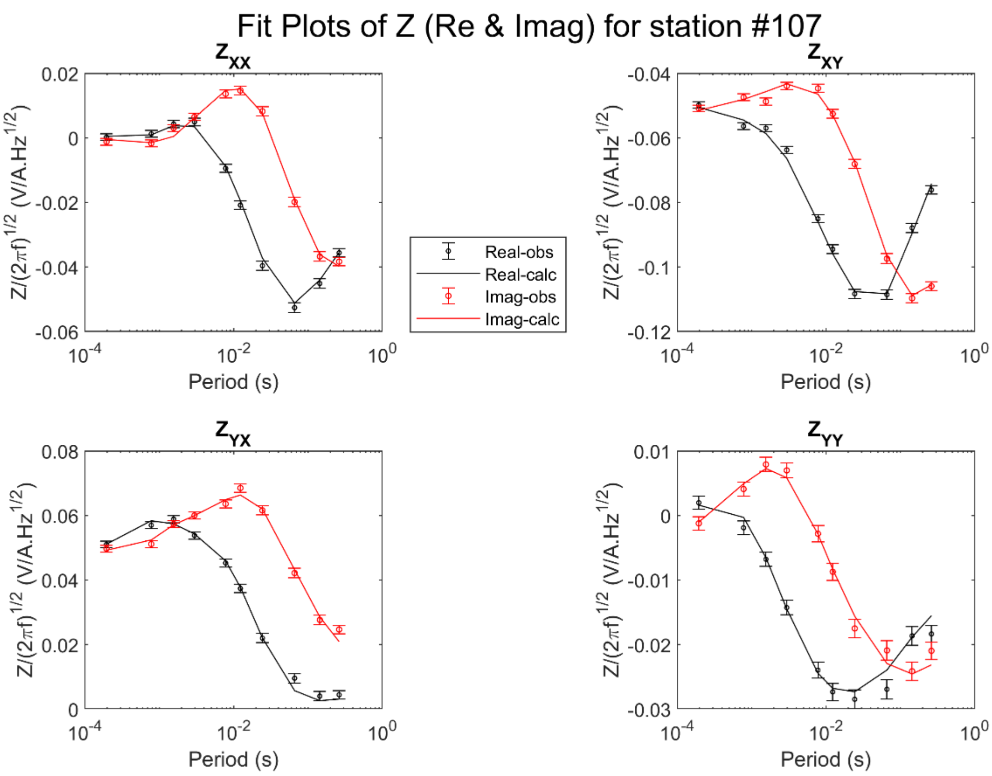
Fit Plots of Z (Re & Imag) for station #107
Z_XX
Z_XY
Z_YX
Z_YY
Real-obs
Real-calc
Imag-obs
Imag-calc
Z/(2πf)^1/2 (V/A.Hz^1/2)
Period (s)

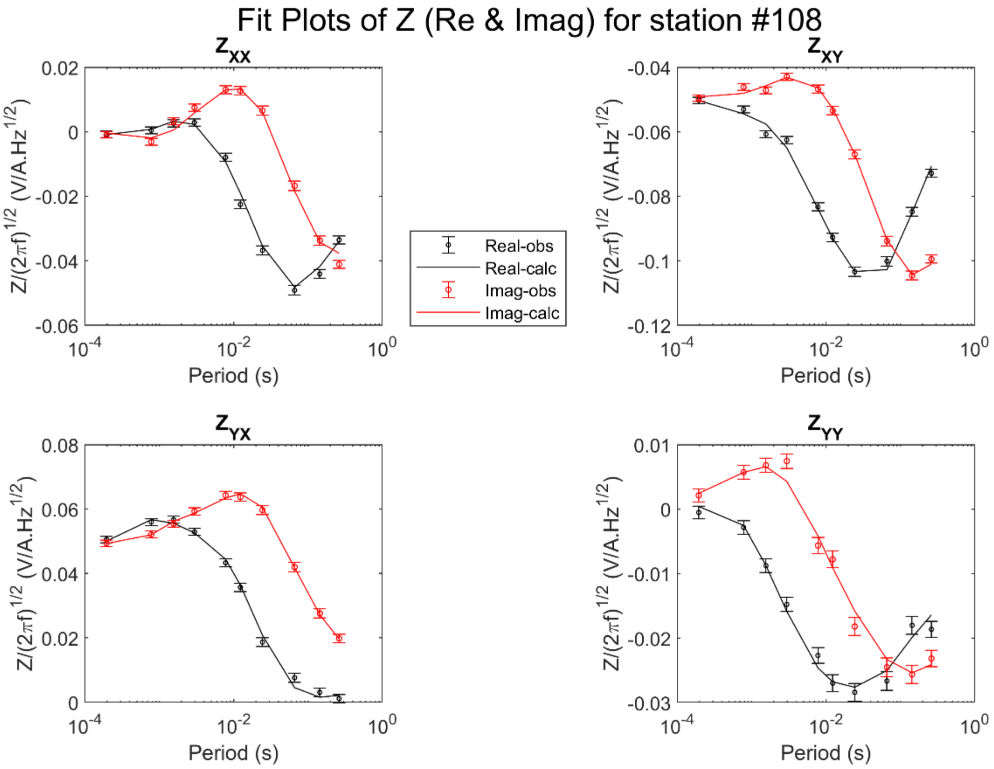

Fit Plots of Z (Re & Imag) for station #108
Z_XX
Z_XY
Z_YX
Z_YY
Z/(2πf)^1/2 (V/A.Hz^1/2)
Period (s)
Real-obs
Real-calc
Imag-obs
Imag-calc

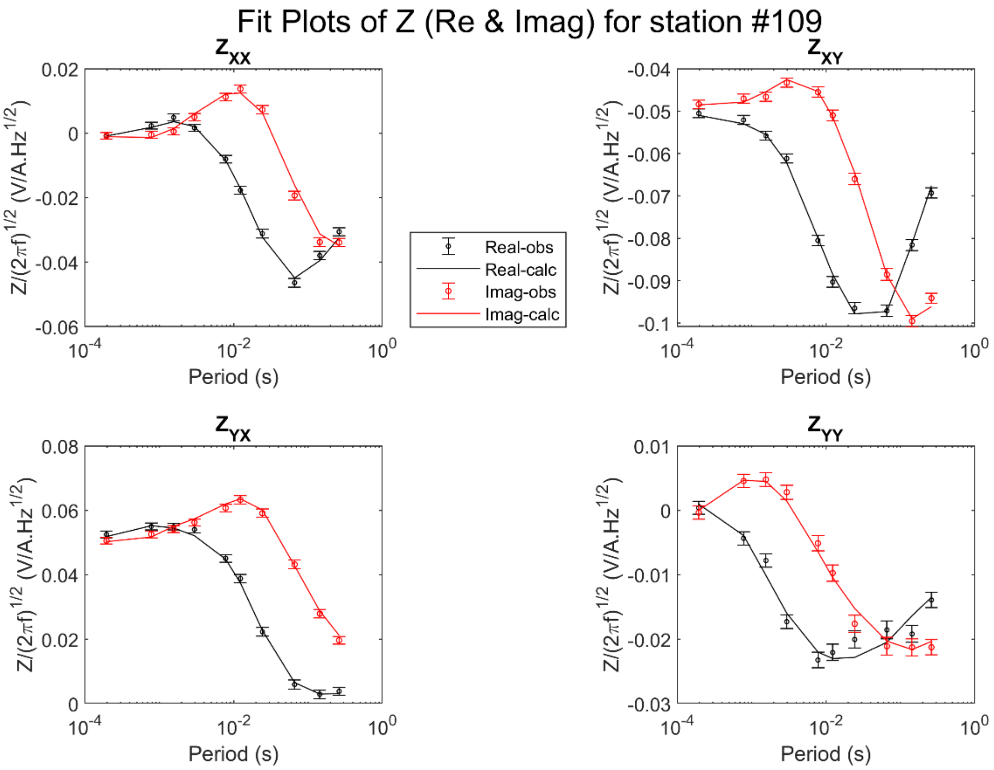

Fit Plots of Z (Re & Imag) for station #109
Z_XX
Z_XY
Z_YX
Z_YY
Z/(2πf)^1/2 (V/A.Hz^1/2)
Period (s)
Real-obs
Real-calc
Imag-obs
Imag-calc

Fit Plots of Z (Re & Imag) for station #110

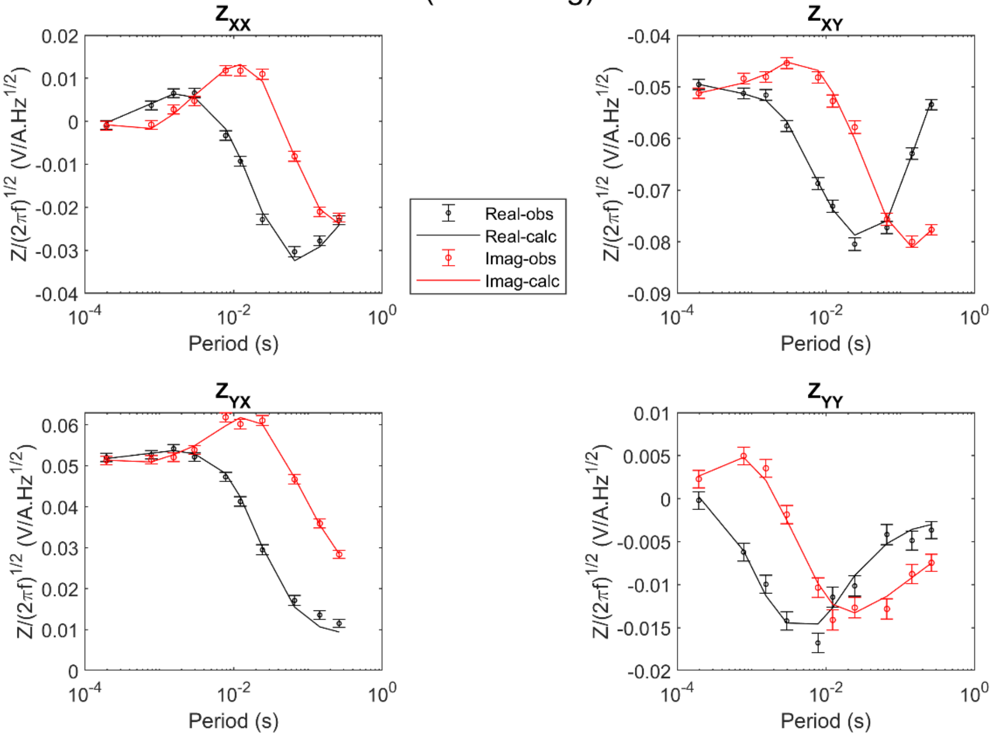

Fit Plots of Z (Re & Imag) for station #111

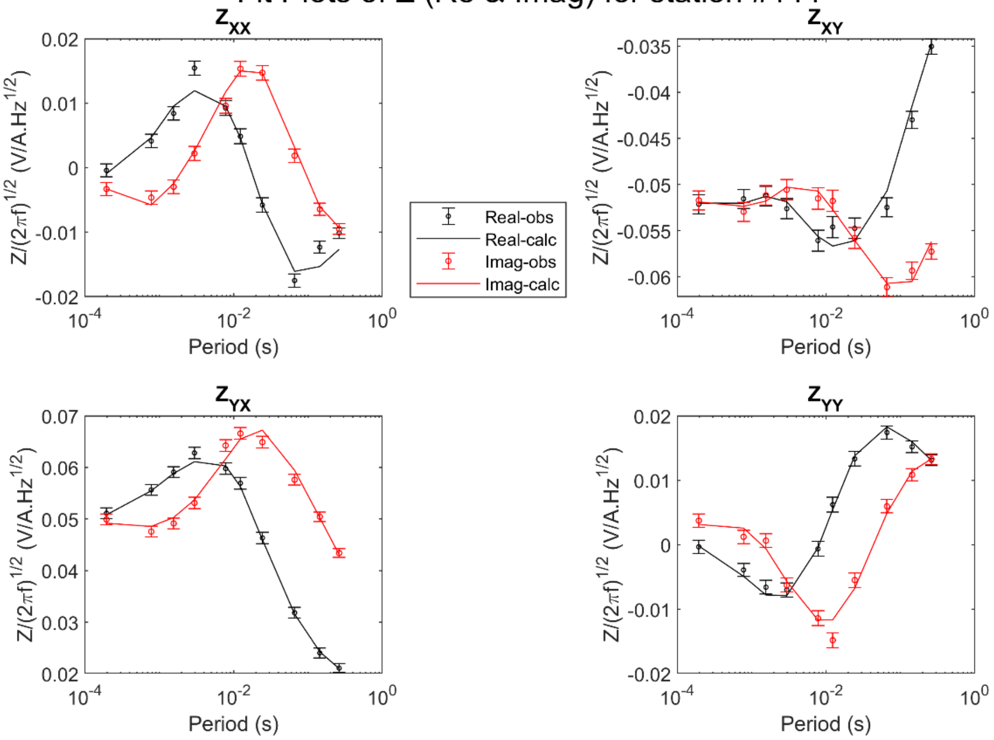

Fit Plots of Z (Re & Imag) for station #112

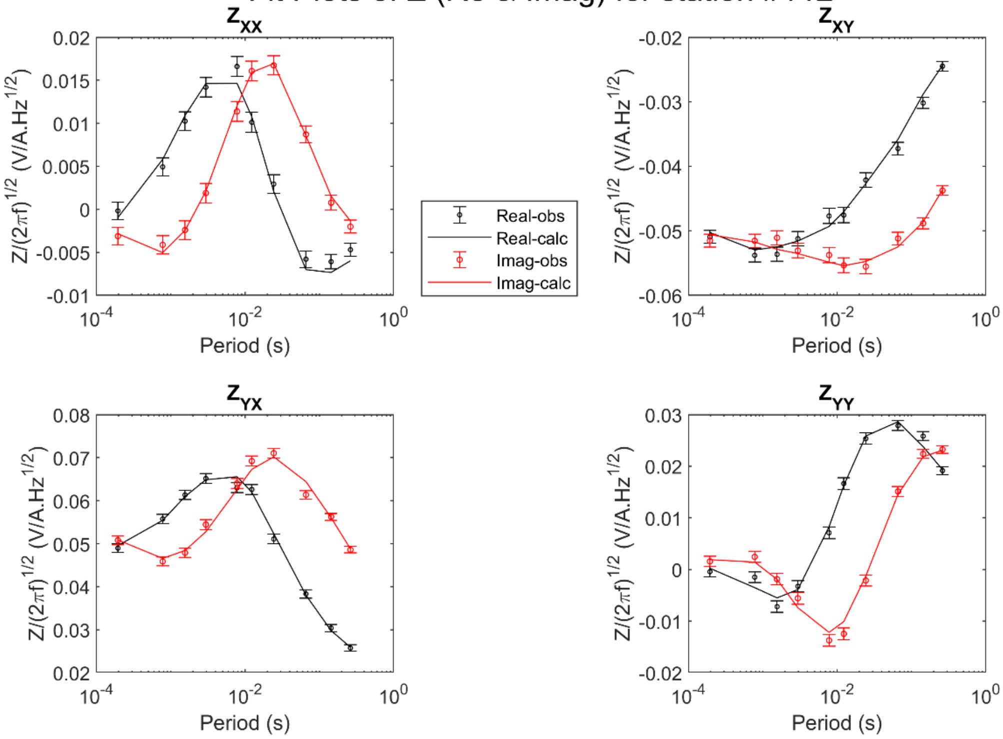

Fit Plots of Z (Re & Imag) for station #113

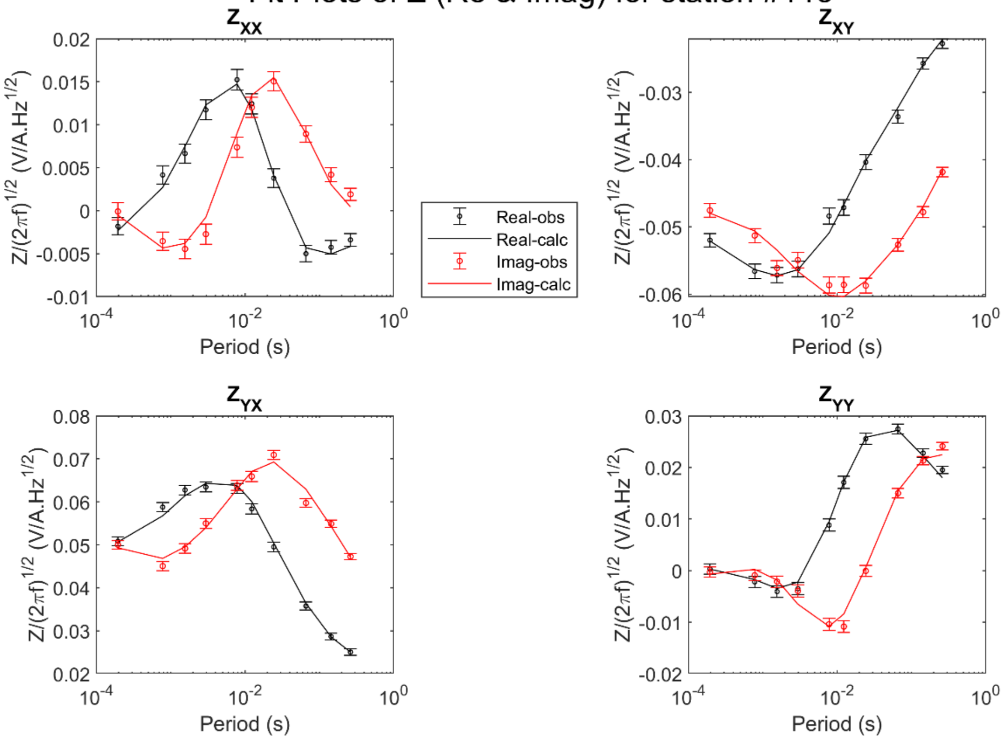

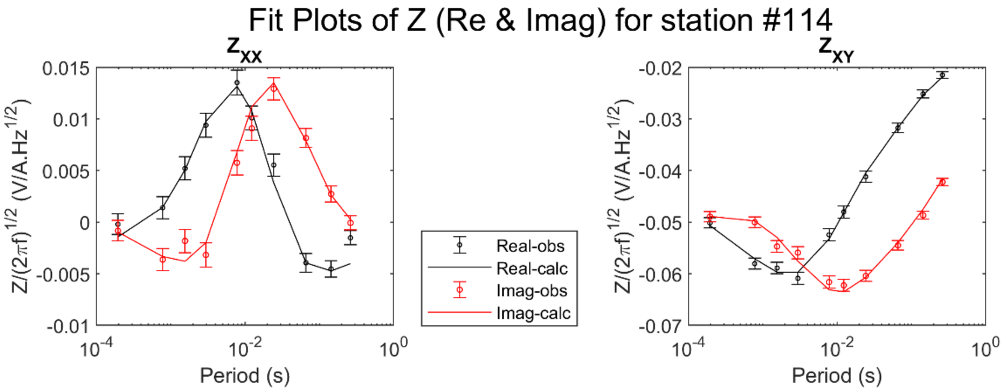
Fit Plots of Z (Re & Imag) for station #114
Z_XX
Z_XY
Z_YX
Z_YY
Z/(2πf)^1/2 (V/A.Hz^1/2)
Period (s)
Real-obs
Real-calc
Imag-obs
Imag-calc

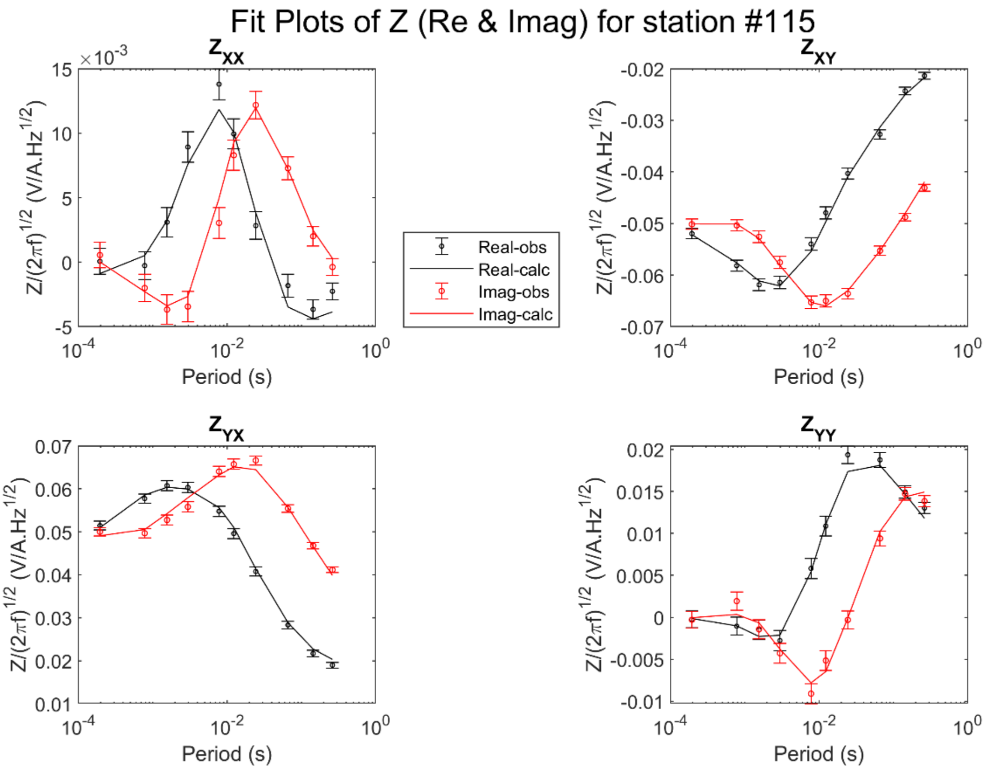
Fit Plots of Z (Re & Imag) for station #115
Z_XX
Z_XY
Z_YX
Z_YY
×10^-3
Z/(2πf)^1/2 (V/A.Hz^1/2)
Period (s)
Real-obs
Real-calc
Imag-obs
Imag-calc

Fit Plots of Z (Re & Imag) for station #116

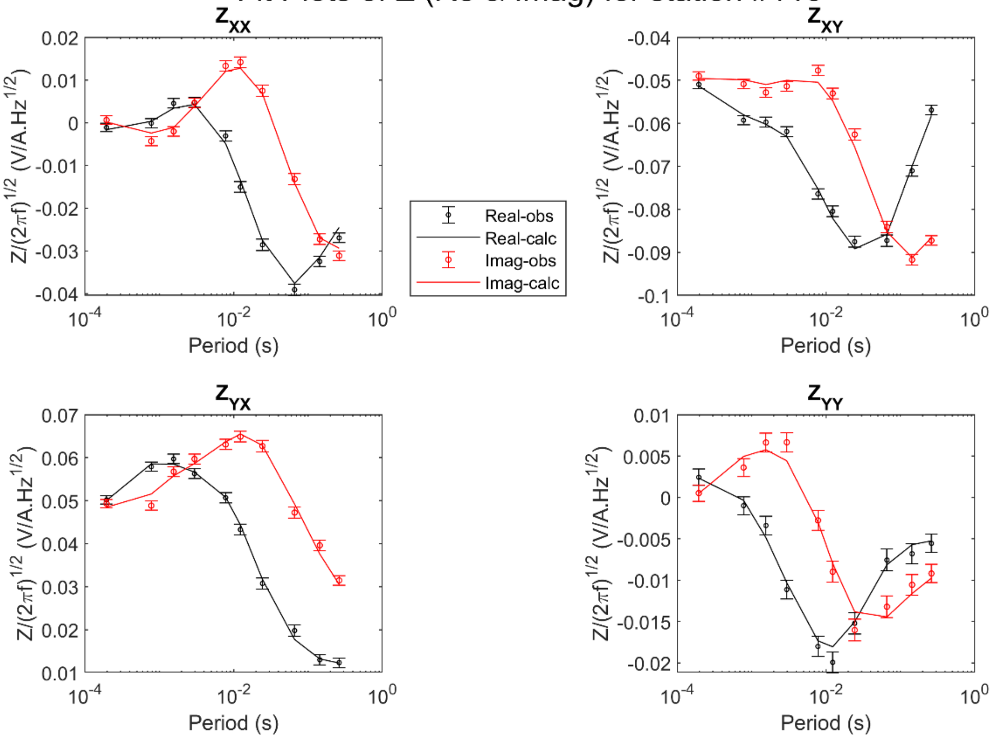

Fit Plots of Z (Re & Imag) for station #117

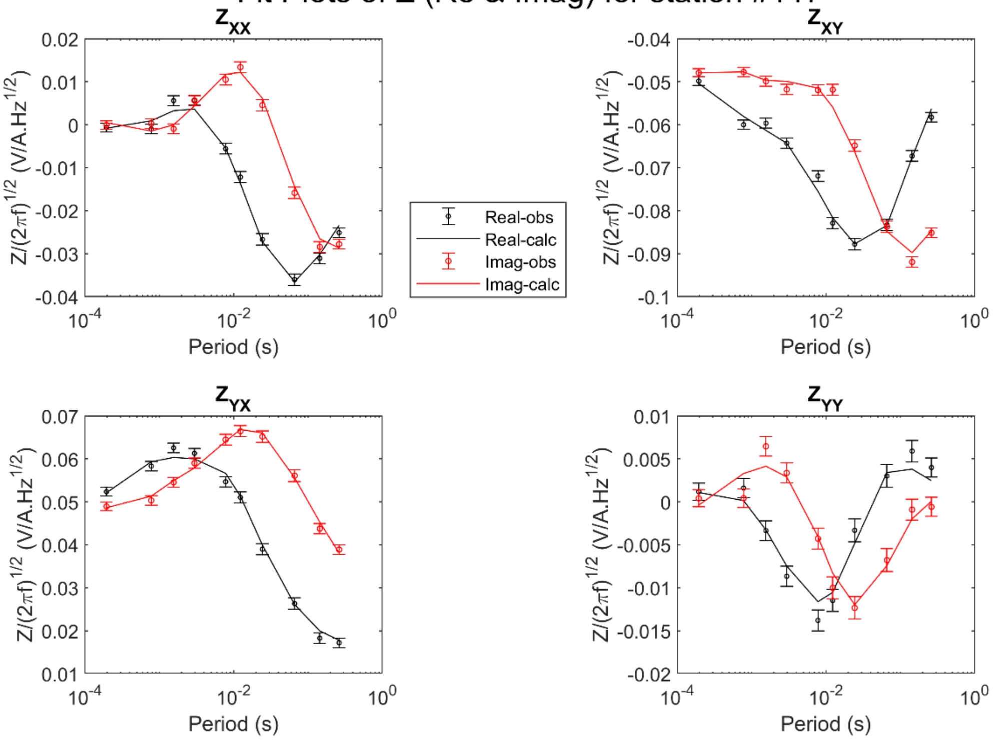

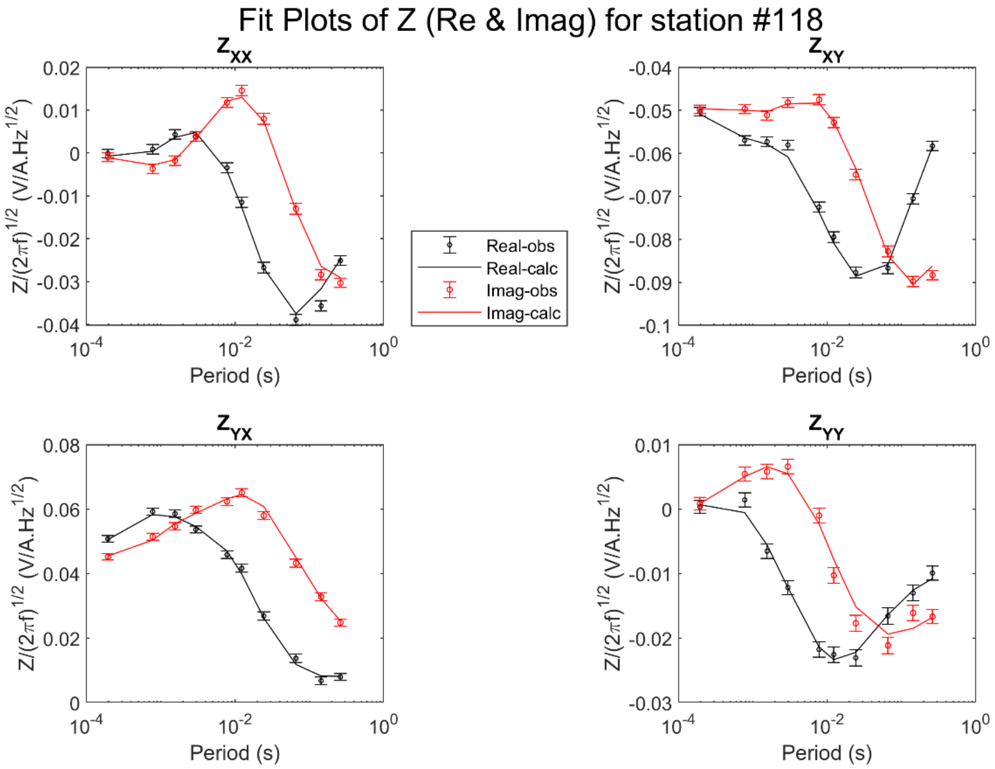
Fit Plots of Z (Re & Imag) for station #118
Z_XX
Z_XY
Z_YX
Z_YY
Z/(2πf)^1/2 (V/A.Hz^1/2)
Period (s)
Real-obs
Real-calc
Imag-obs
Imag-calc

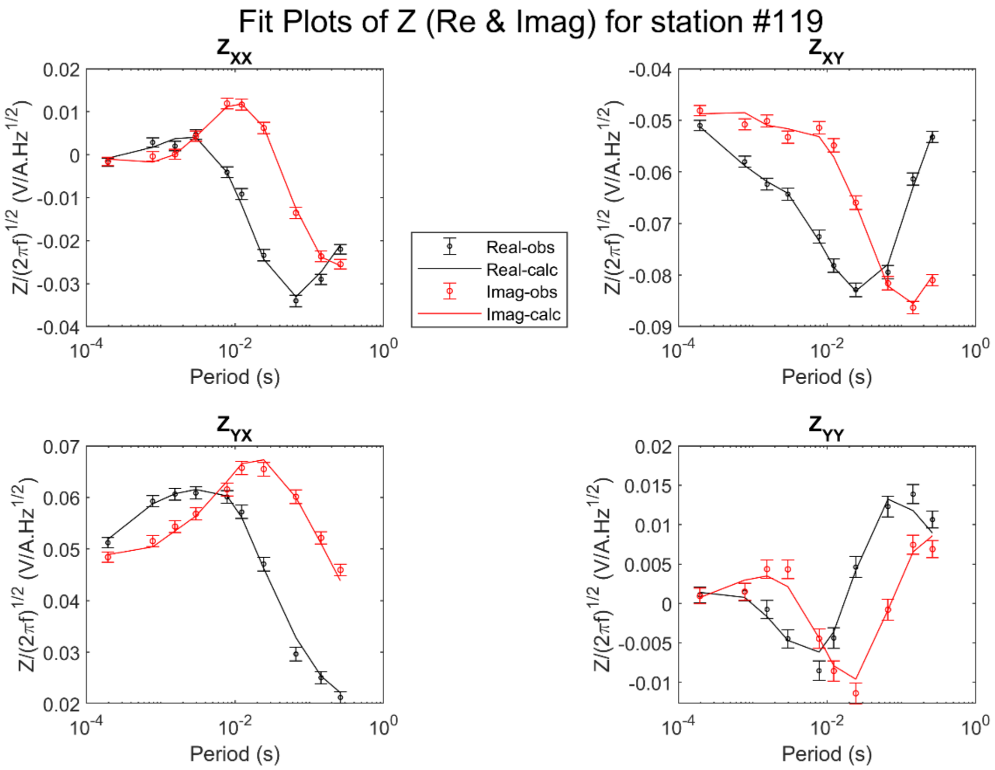
Fit Plots of Z (Re & Imag) for station #119
Z_XX
Z_XY
Z_YX
Z_YY
Z/(2πf)^1/2 (V/A.Hz^1/2)
Period (s)
Real-obs
Real-calc
Imag-obs
Imag-calc

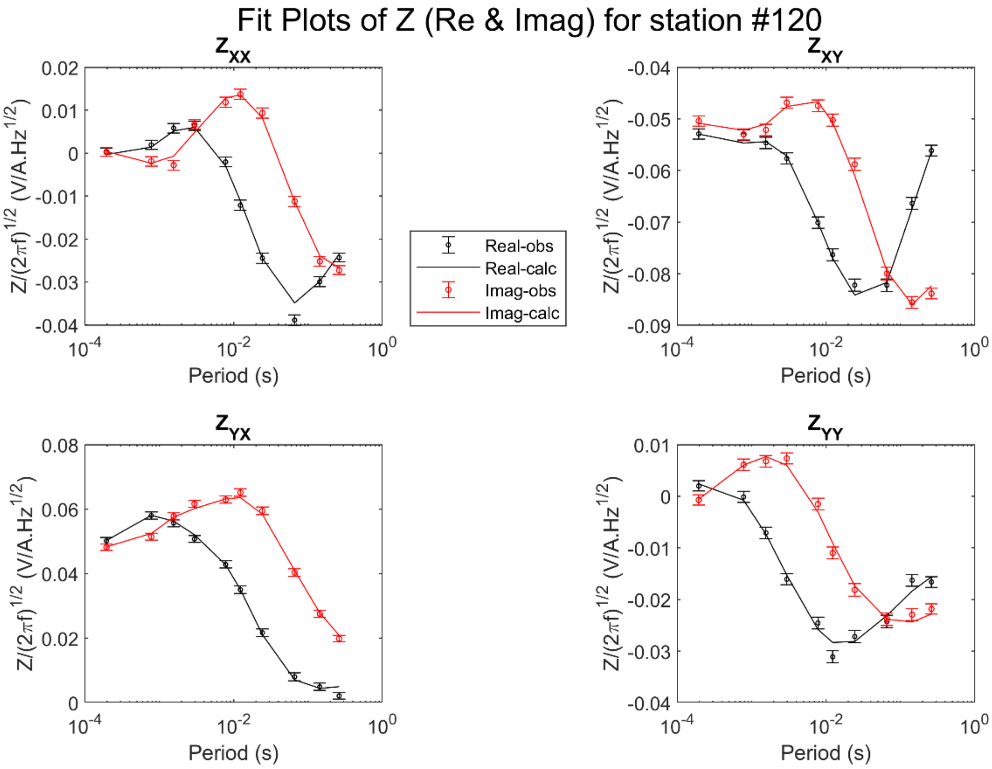
Fit Plots of Z (Re & Imag) for station #120
Z_XX
Z_XY
Z_YX
Z_YY
Z/(2πf)^1/2 (V/A.Hz^1/2)
Period (s)
Real-obs
Real-calc
Imag-obs
Imag-calc

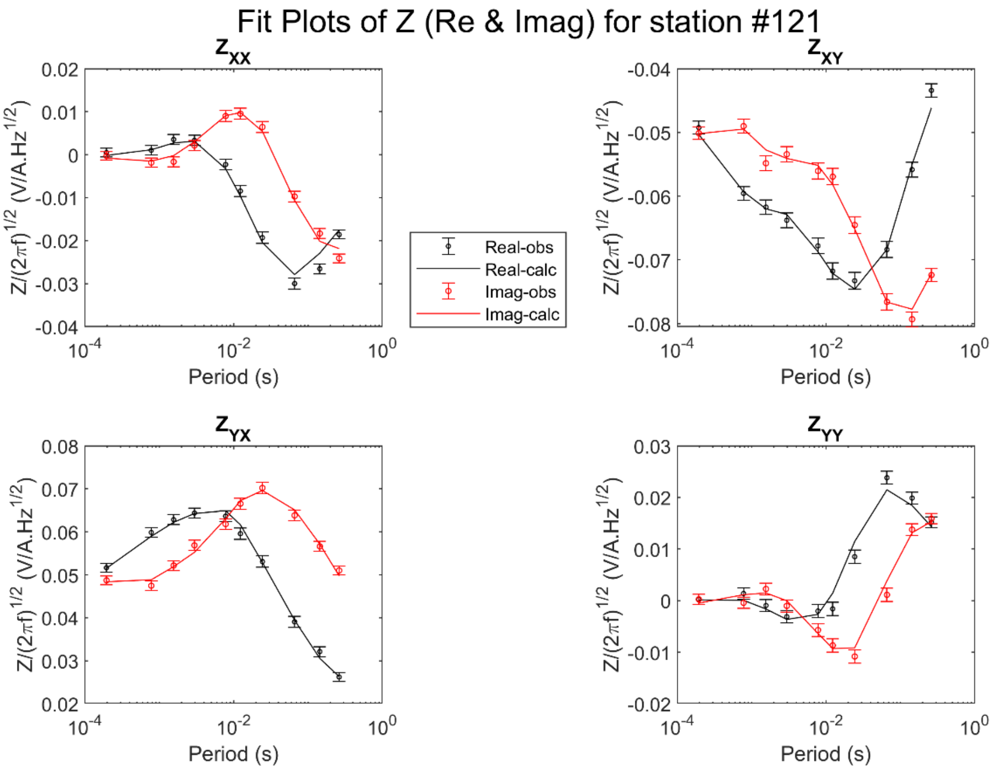
Fit Plots of Z (Re & Imag) for station #121
Z_XX
Z_XY
Z_YX
Z_YY
Z/(2πf)^1/2 (V/A.Hz^1/2)
Period (s)
Real-obs
Real-calc
Imag-obs
Imag-calc

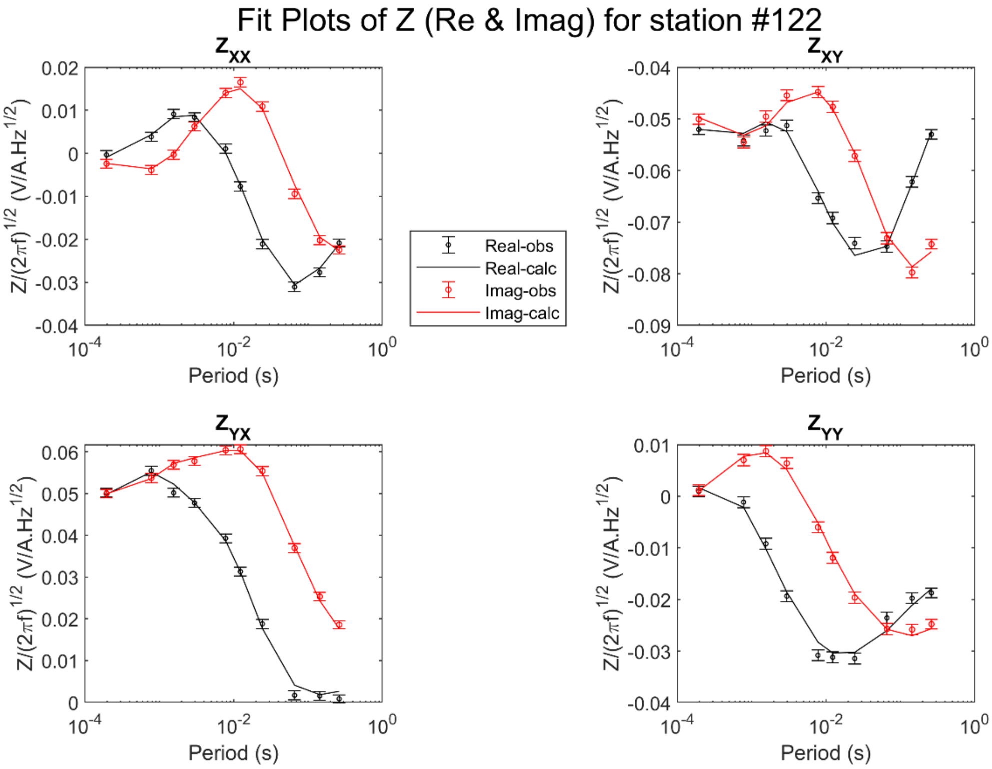
Fit Plots of Z (Re & Imag) for station #122
Z_{XX}
Z_{XY}
Z_{YX}
Z_{YY}
$Z/(2\pi f)^{1/2}$ (V/A.Hz$^{1/2}$)
Period (s)
Real-obs
Real-calc
Imag-obs
Imag-calc

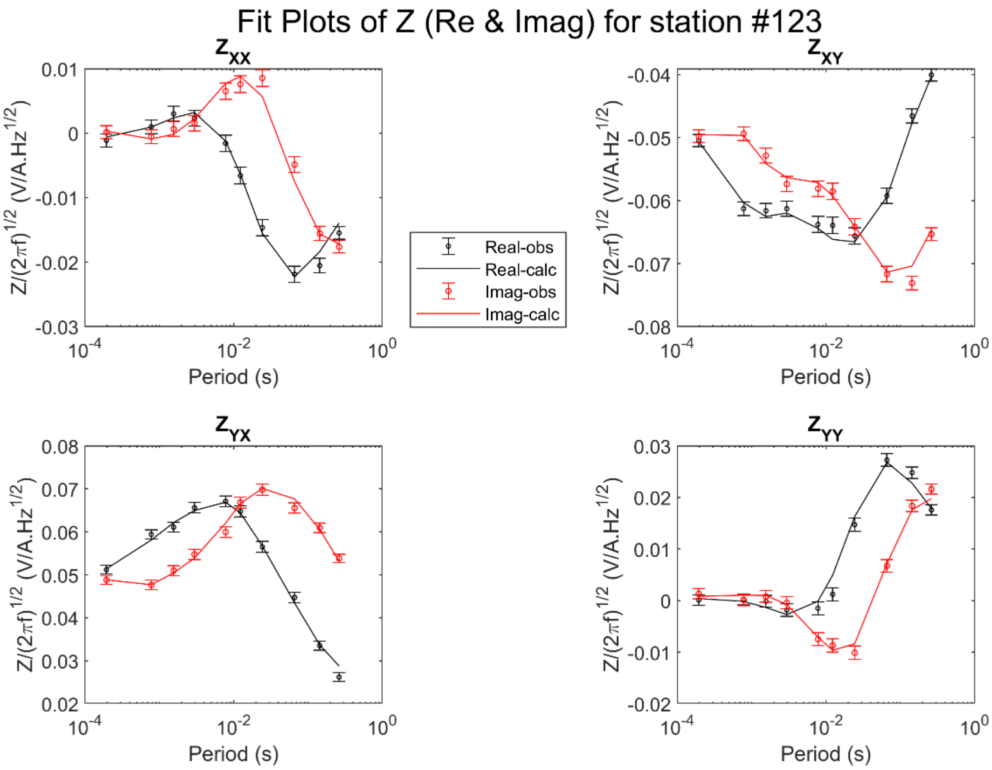
Fit Plots of Z (Re & Imag) for station #123
Z_{XX}
Z_{XY}
Z_{YX}
Z_{YY}
$Z/(2\pi f)^{1/2}$ (V/A.Hz$^{1/2}$)
Period (s)
Real-obs
Real-calc
Imag-obs
Imag-calc

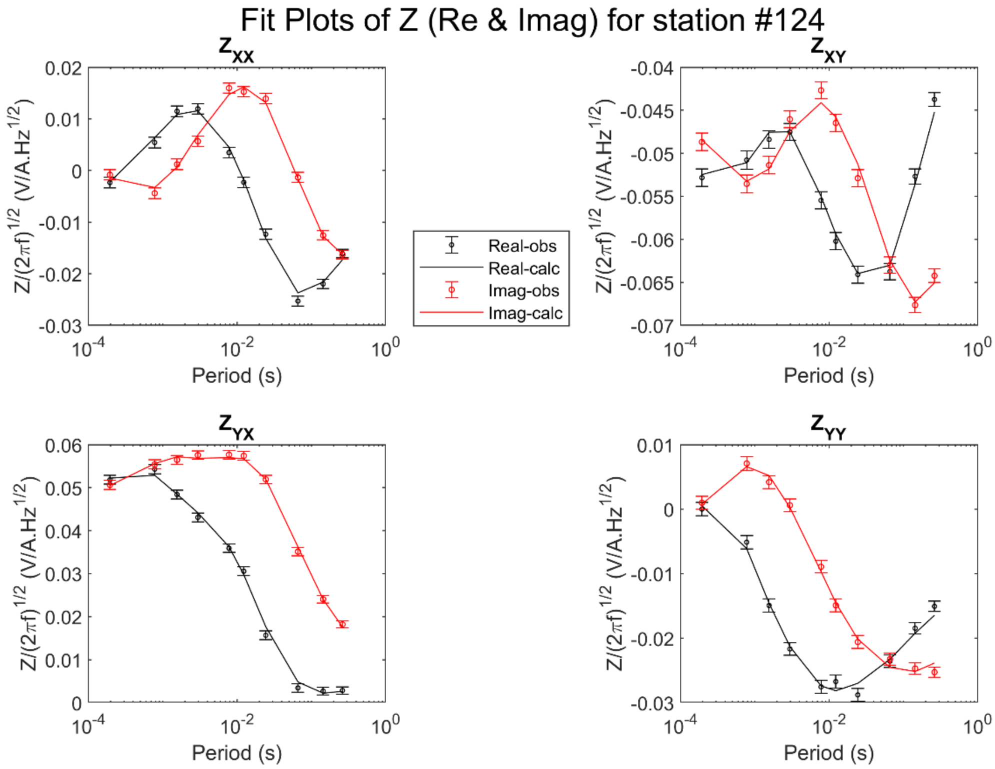
Fit Plots of Z (Re & Imag) for station #124
Z_XX
Z_XY
Z_YX
Z_YY
Z/(2πf)^1/2 (V/A.Hz^1/2)
Period (s)
Real-obs
Real-calc
Imag-obs
Imag-calc

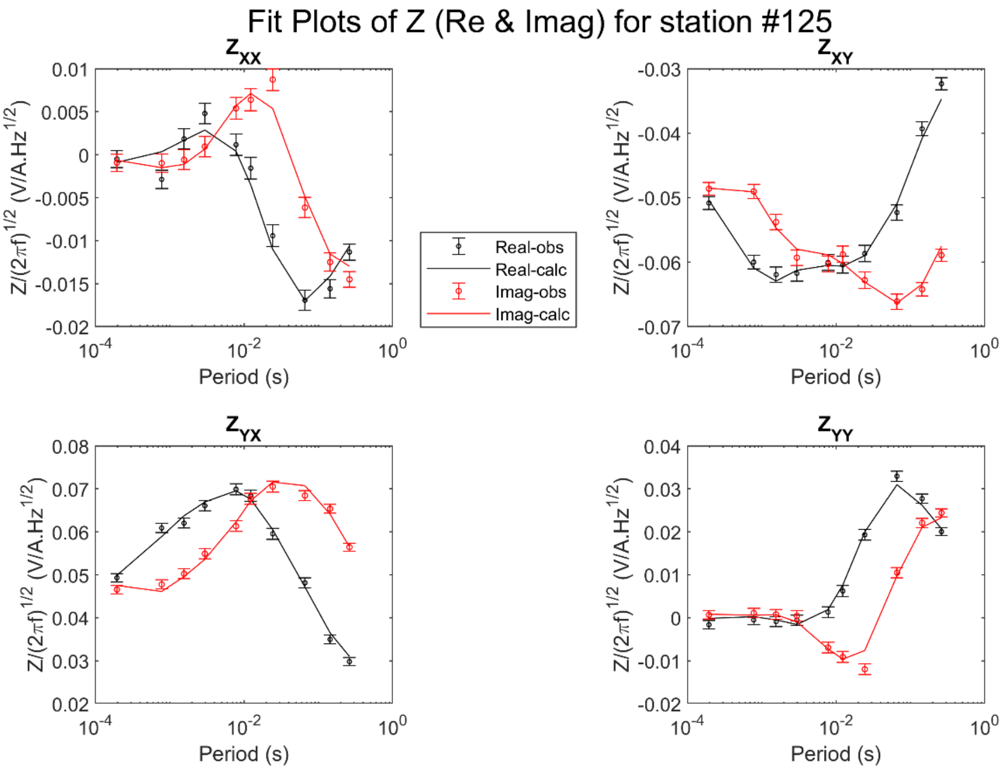
Fit Plots of Z (Re & Imag) for station #125
Z_XX
Z_XY
Z_YX
Z_YY
Z/(2πf)^1/2 (V/A.Hz^1/2)
Period (s)
Real-obs
Real-calc
Imag-obs
Imag-calc

Fit Plots of Z (Re & Imag) for station #126

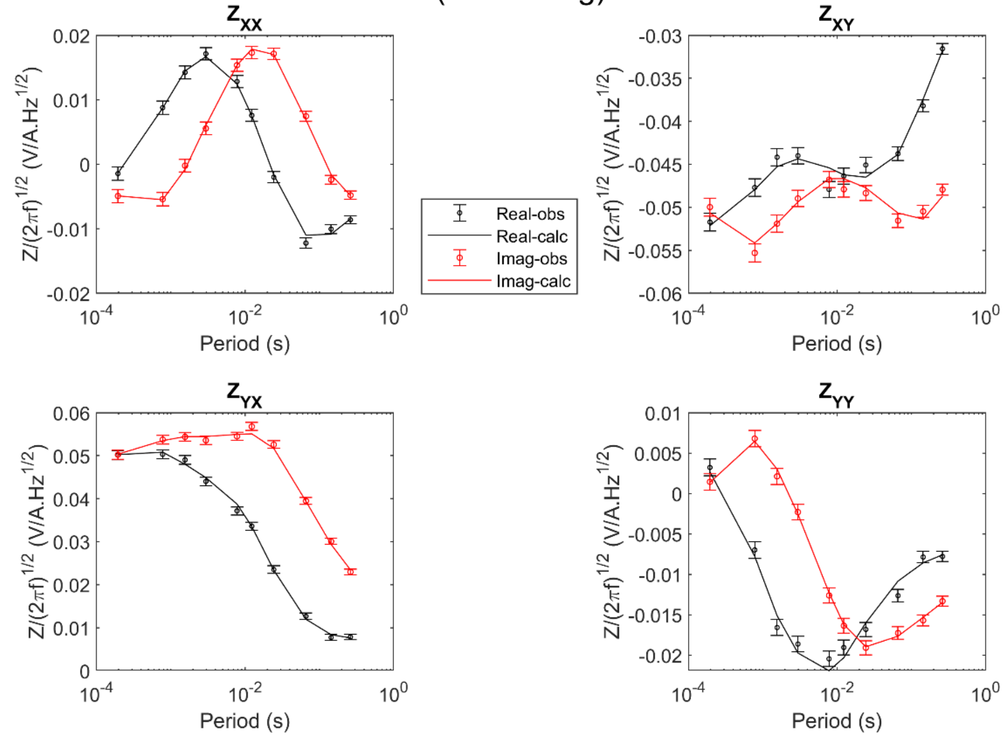

Fit Plots of Z (Re & Imag) for station #127

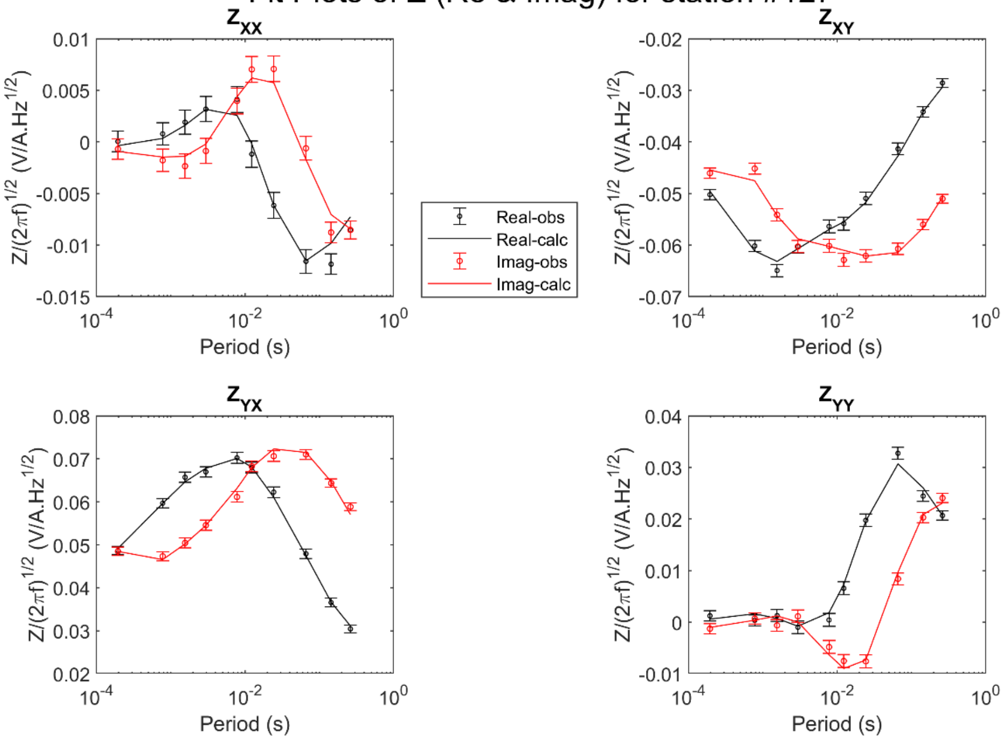

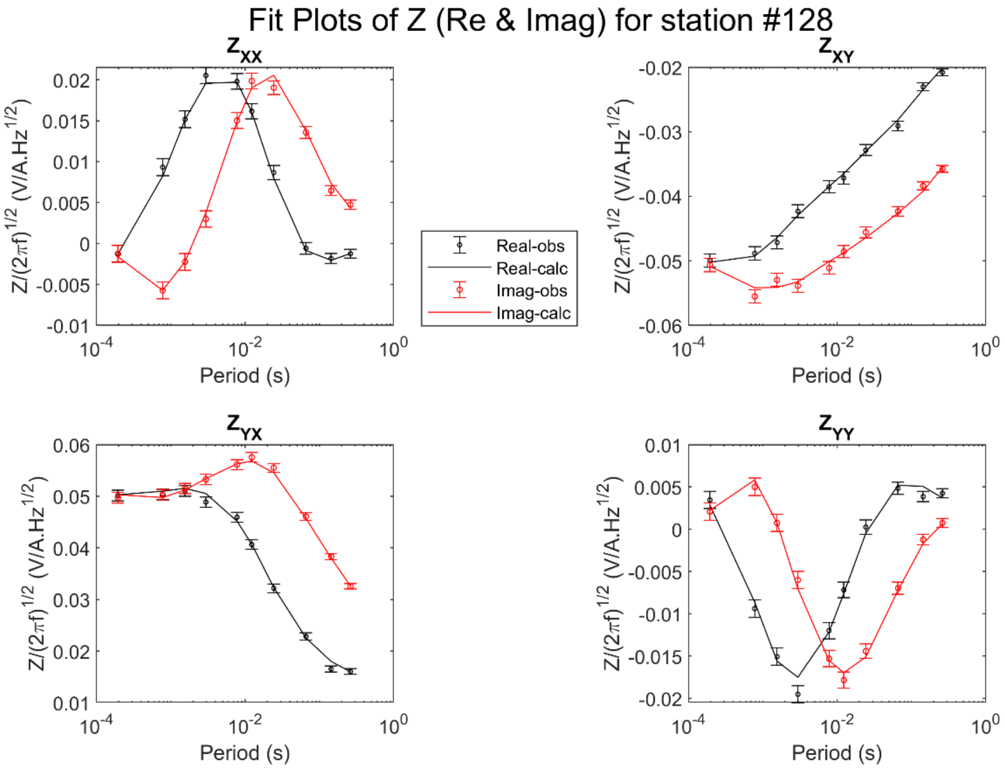
Fit Plots of Z (Re & Imag) for station #128
Z_{XX}
Z_{XY}
Z_{YX}
Z_{YY}
$Z/(2\pi f)^{1/2}$ (V/A.Hz$^{1/2}$)
Period (s)
Real-obs
Real-calc
Imag-obs
Imag-calc

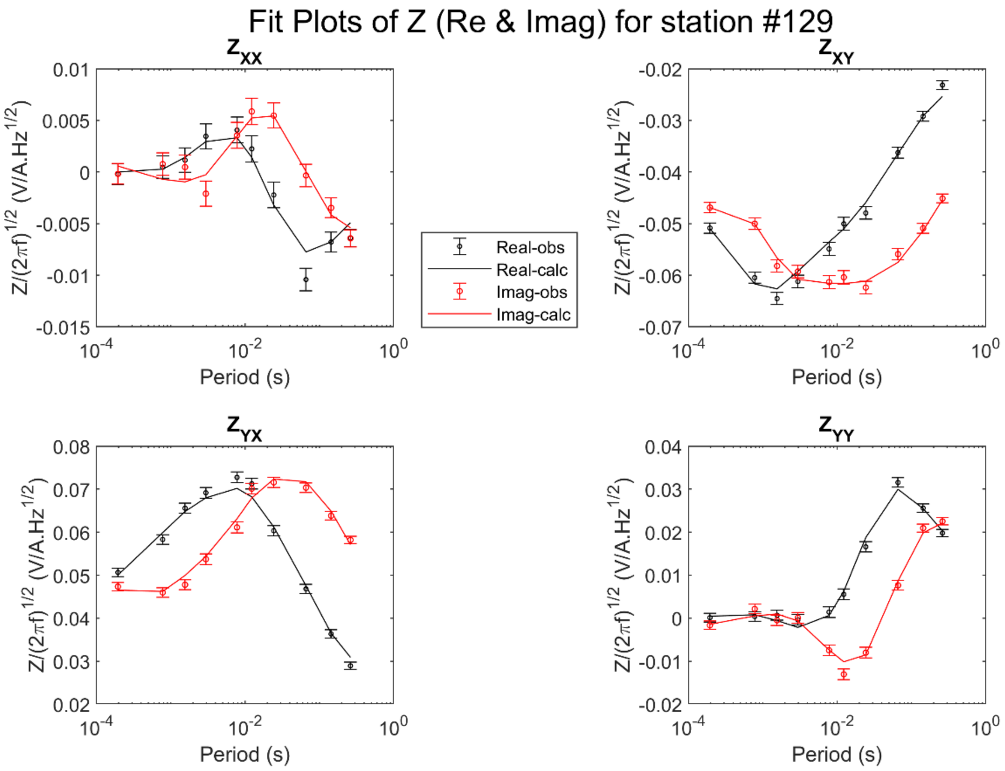
Fit Plots of Z (Re & Imag) for station #129
Z_{XX}
Z_{XY}
Z_{YX}
Z_{YY}
$Z/(2\pi f)^{1/2}$ (V/A.Hz$^{1/2}$)
Period (s)
Real-obs
Real-calc
Imag-obs
Imag-calc

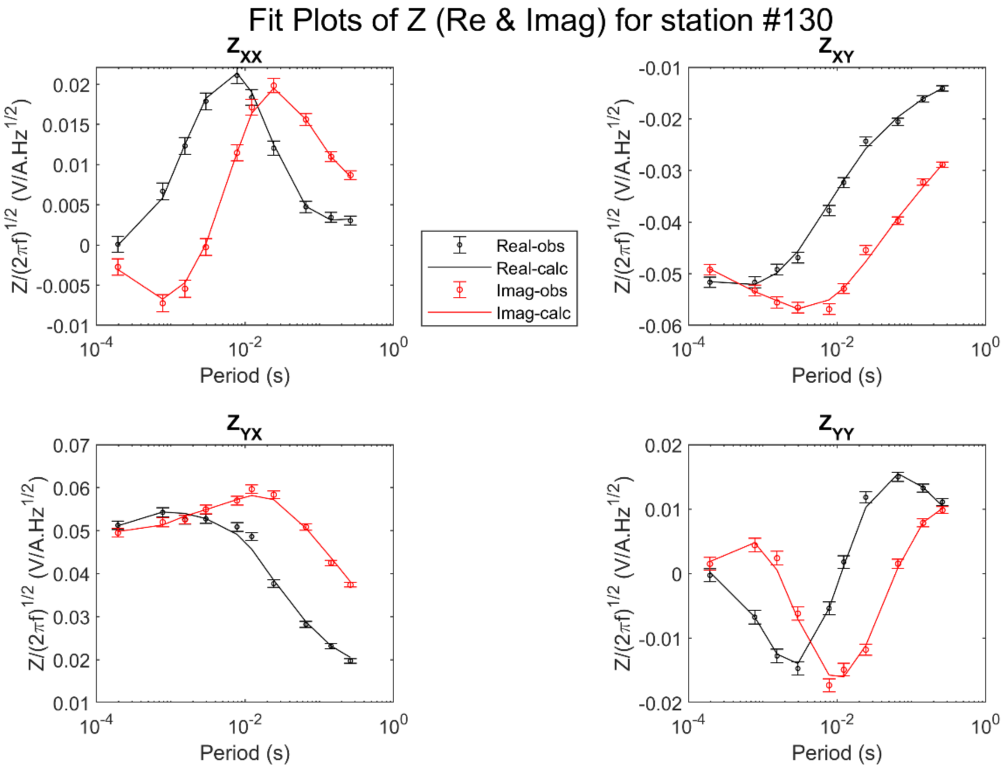
Fit Plots of Z (Re & Imag) for station #130
Z_{XX}
Z_{XY}
Z_{YX}
Z_{YY}
$Z/(2\pi f)^{1/2}$ (V/A.Hz$^{1/2}$)
Period (s)
Real-obs
Real-calc
Imag-obs
Imag-calc

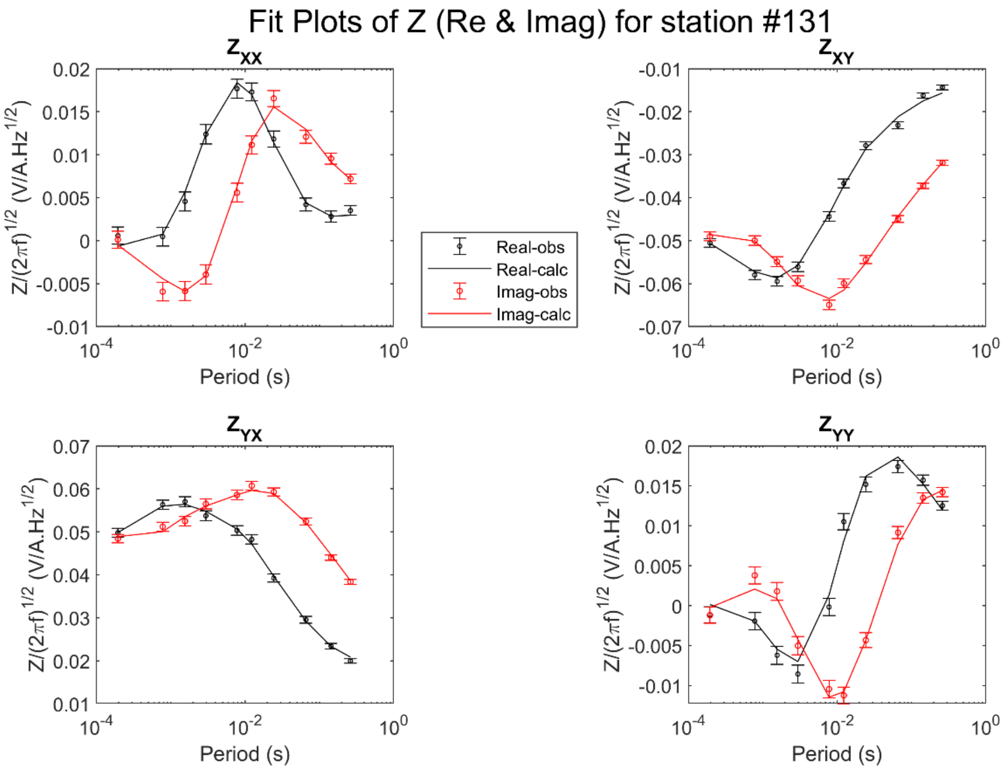
Fit Plots of Z (Re & Imag) for station #131
Z_{XX}
Z_{XY}
Z_{YX}
Z_{YY}
$Z/(2\pi f)^{1/2}$ (V/A.Hz$^{1/2}$)
Period (s)
Real-obs
Real-calc
Imag-obs
Imag-calc

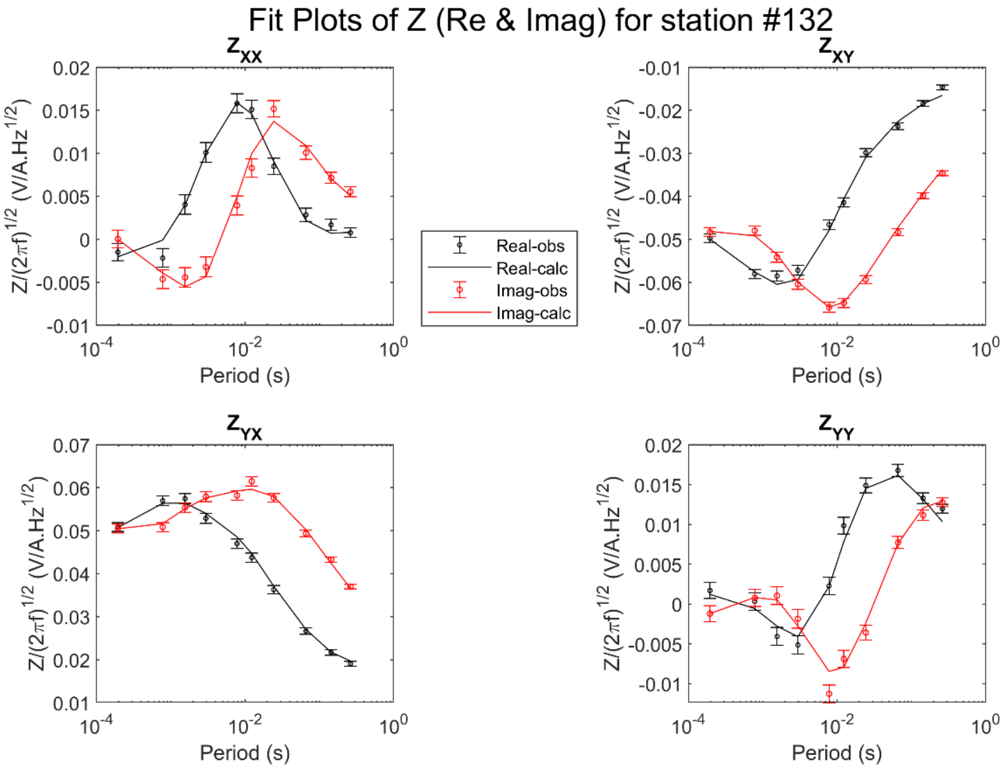

Fit Plots of Z (Re & Imag) for station #132
Z_XX
Z_XY
Z_YX
Z_YY
Z/(2πf)^1/2 (V/A.Hz^1/2)
Period (s)
Real-obs
Real-calc
Imag-obs
Imag-calc

C.2 Fits of Apparent Resistivities and Phases

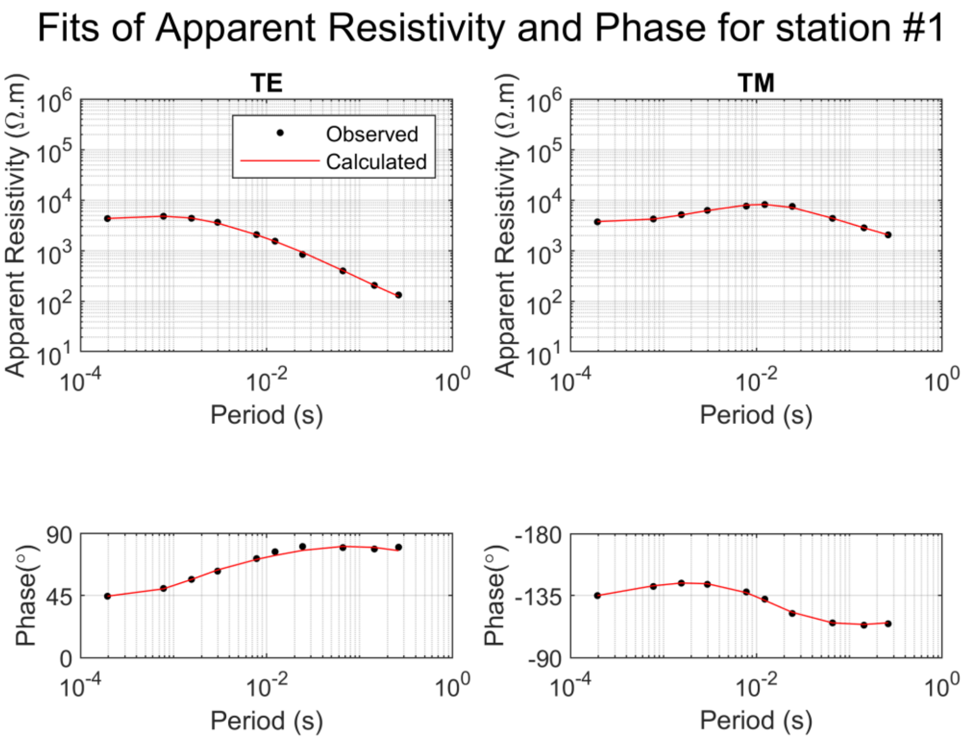

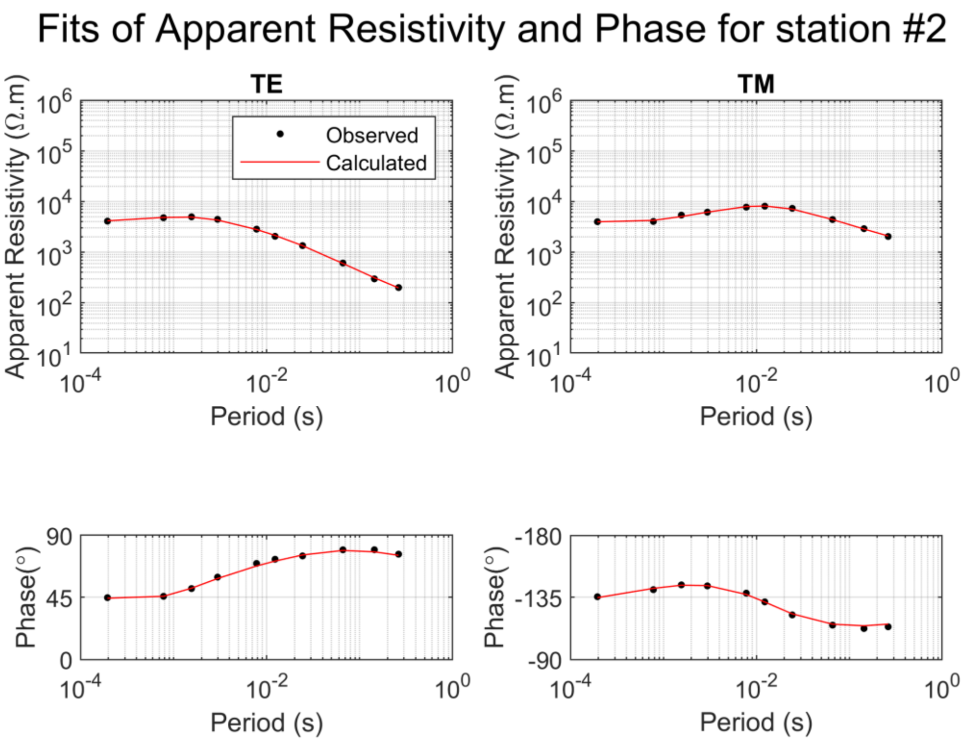

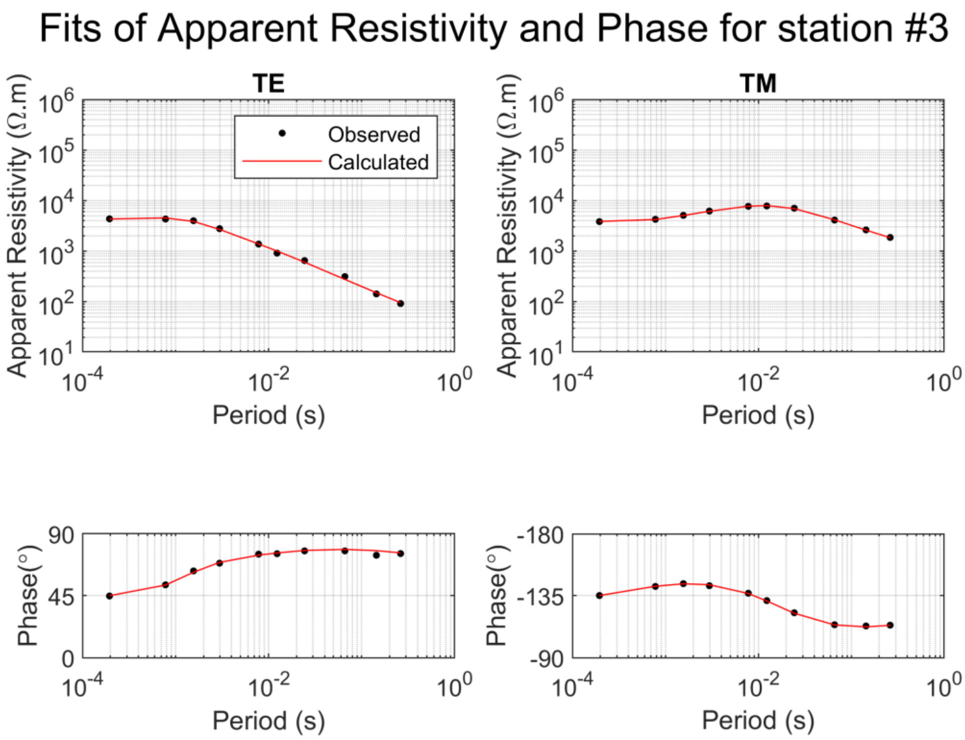

Fits of Apparent Resistivity and Phase for station #3
TE
TM
Observed
Calculated
Apparent Resistivity (Ω.m)
Phase(°)
Period (s)

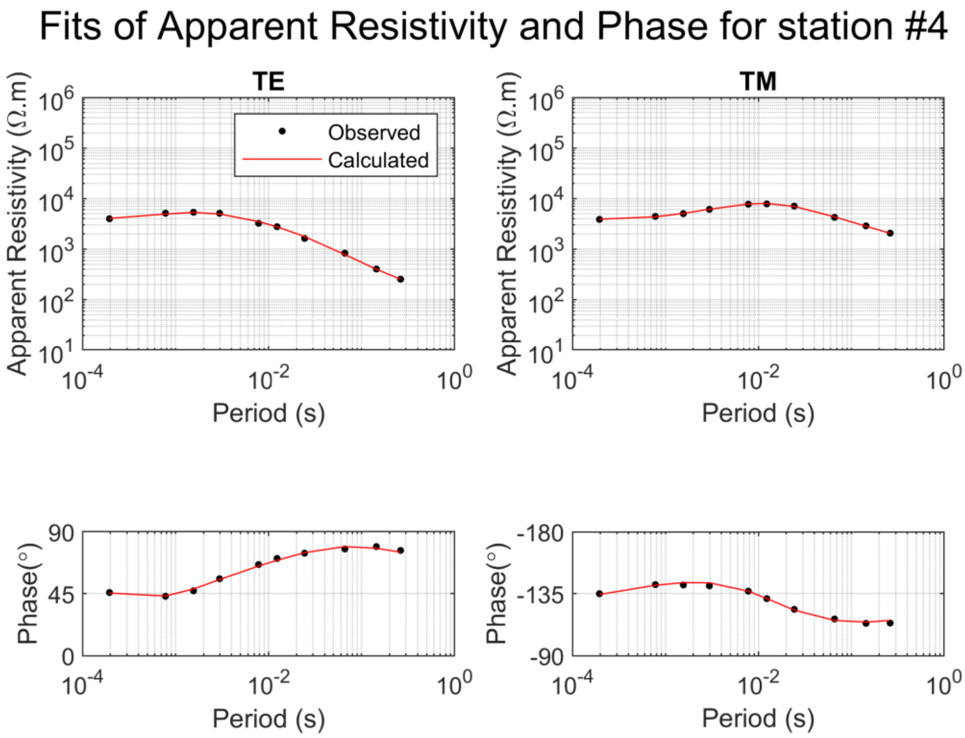

Fits of Apparent Resistivity and Phase for station #4
TE
TM
Observed
Calculated
Apparent Resistivity (Ω.m)
Phase(°)
Period (s)

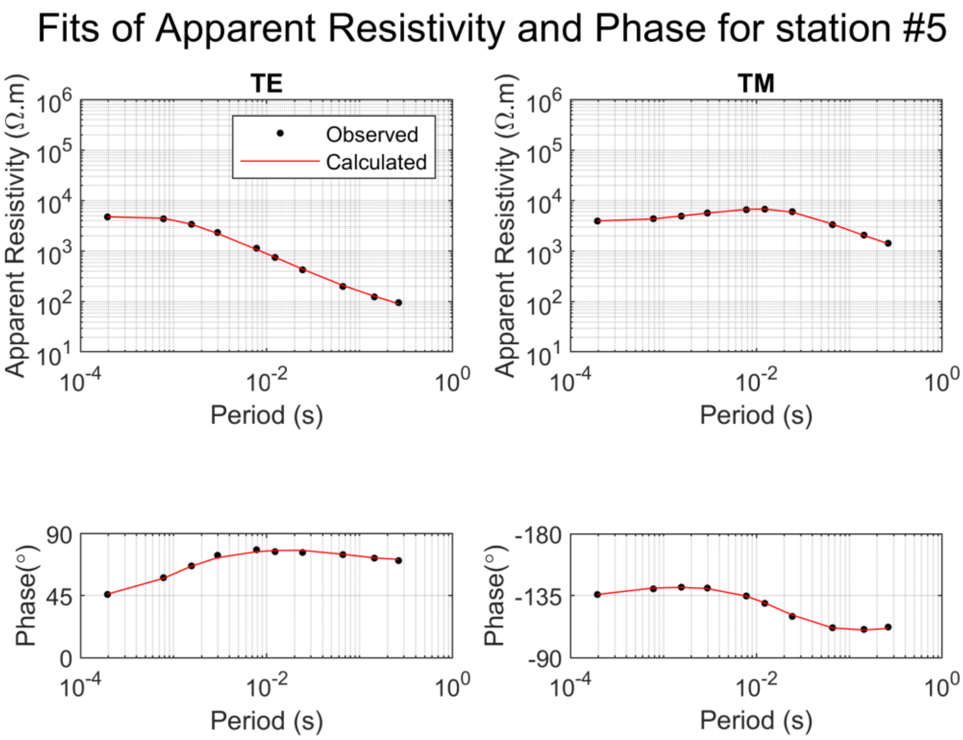
Fits of Apparent Resistivity and Phase for station #5
TE
TM
Observed
Calculated
Apparent Resistivity (Ω.m)
Phase(°)
Period (s)

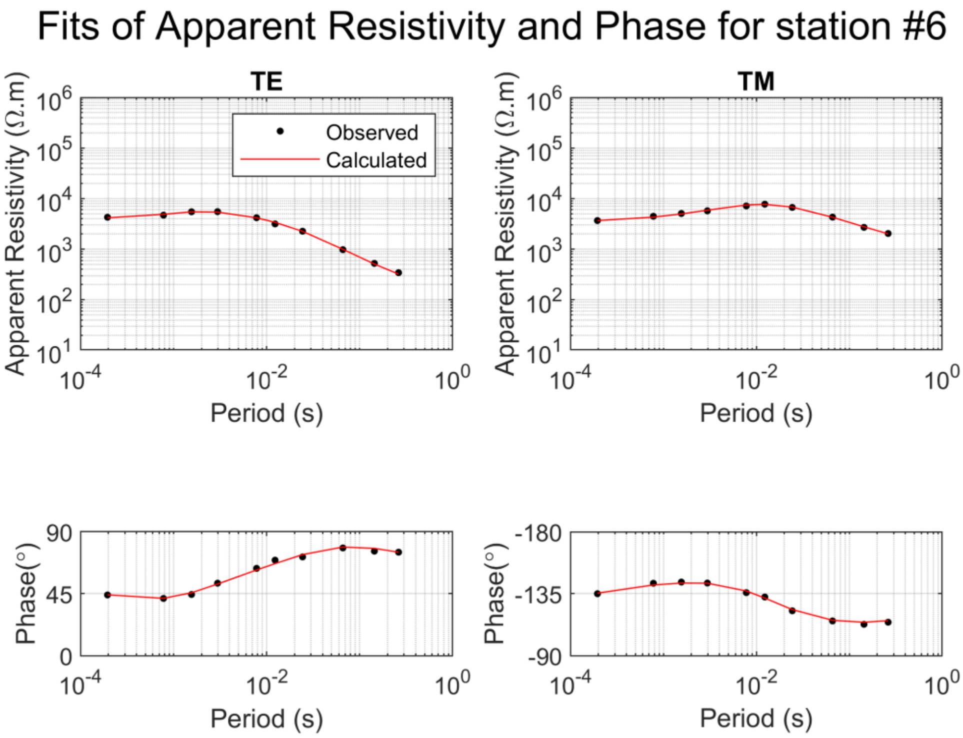
Fits of Apparent Resistivity and Phase for station #6
TE
TM
Observed
Calculated
Apparent Resistivity (Ω.m)
Phase(°)
Period (s)

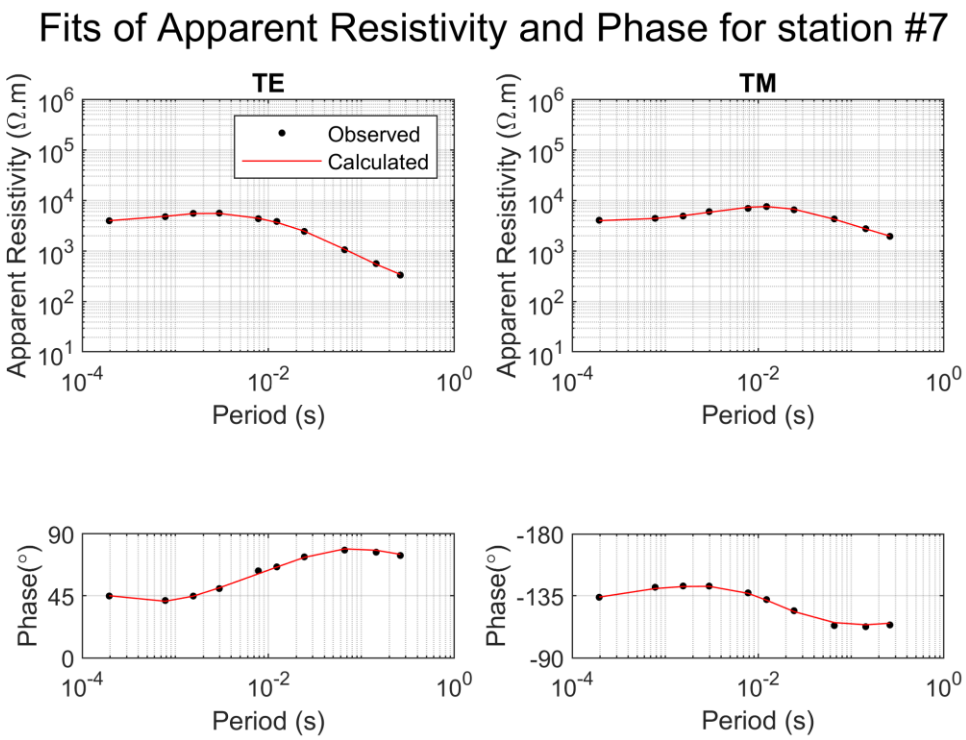
Fits of Apparent Resistivity and Phase for station #7
TE
TM
Observed
Calculated
Apparent Resistivity (Ω.m)
Phase(°)
Period (s)

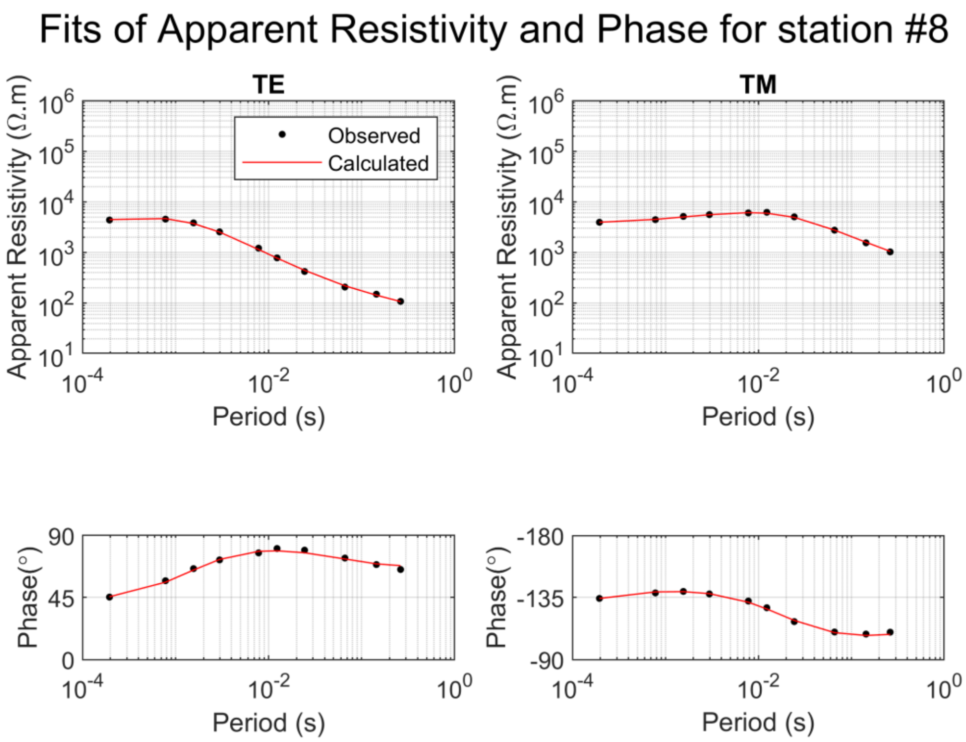
Fits of Apparent Resistivity and Phase for station #8
TE
TM
Observed
Calculated
Apparent Resistivity (Ω.m)
Phase(°)
Period (s)

Fits of Apparent Resistivity and Phase for station #9

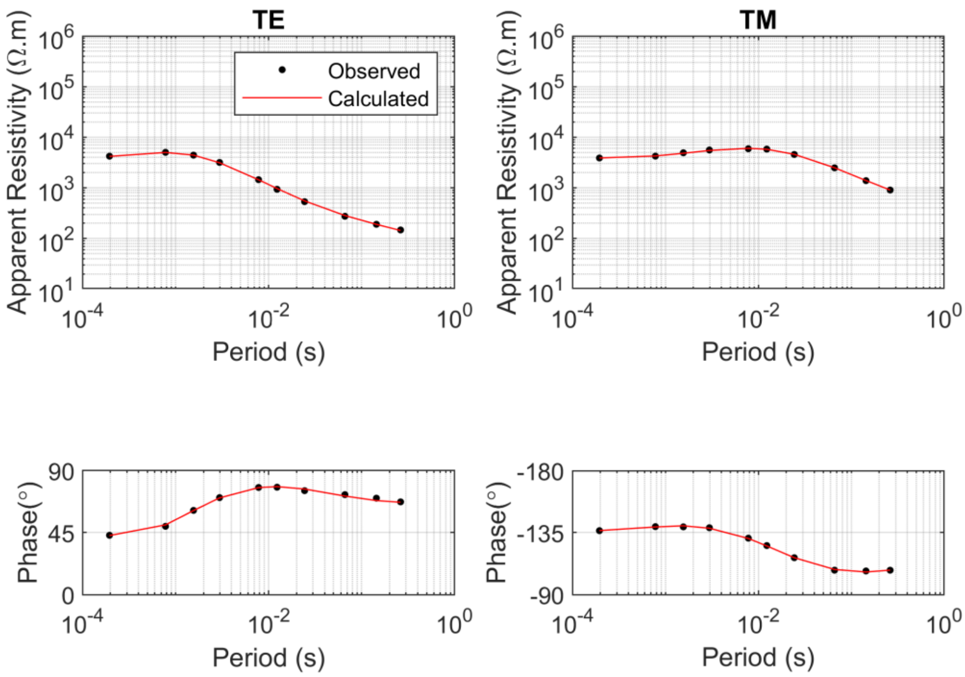

Fits of Apparent Resistivity and Phase for station #10

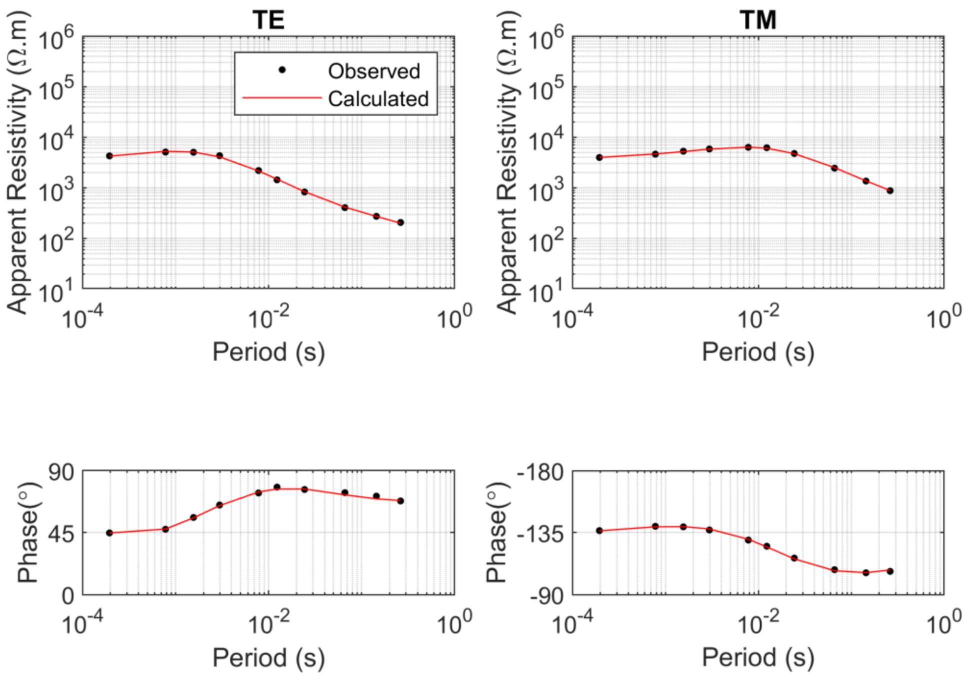

Fits of Apparent Resistivity and Phase for station #11

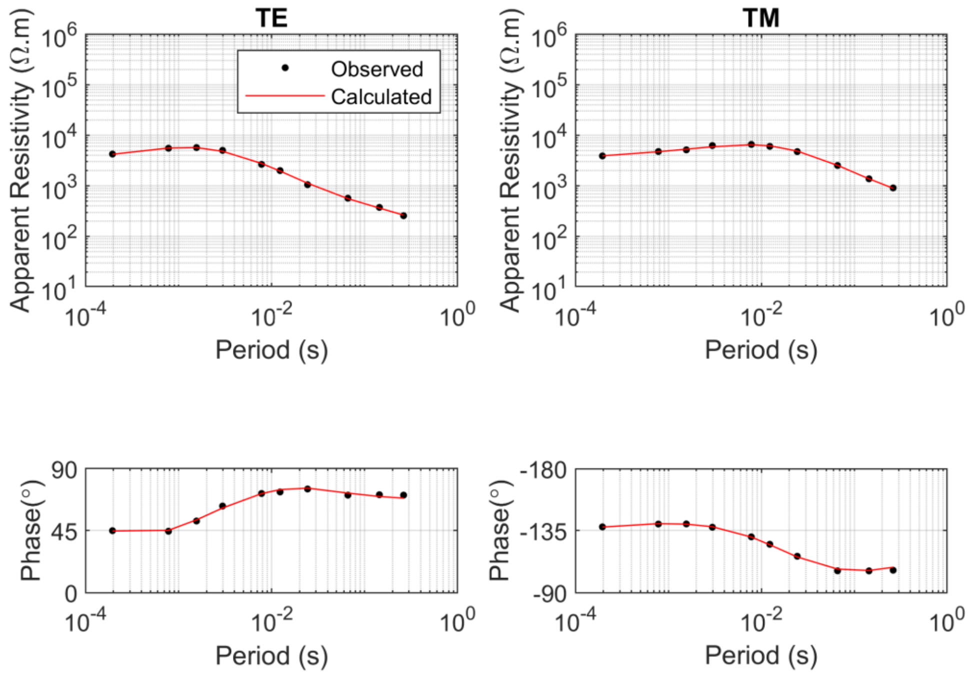

Fits of Apparent Resistivity and Phase for station #12

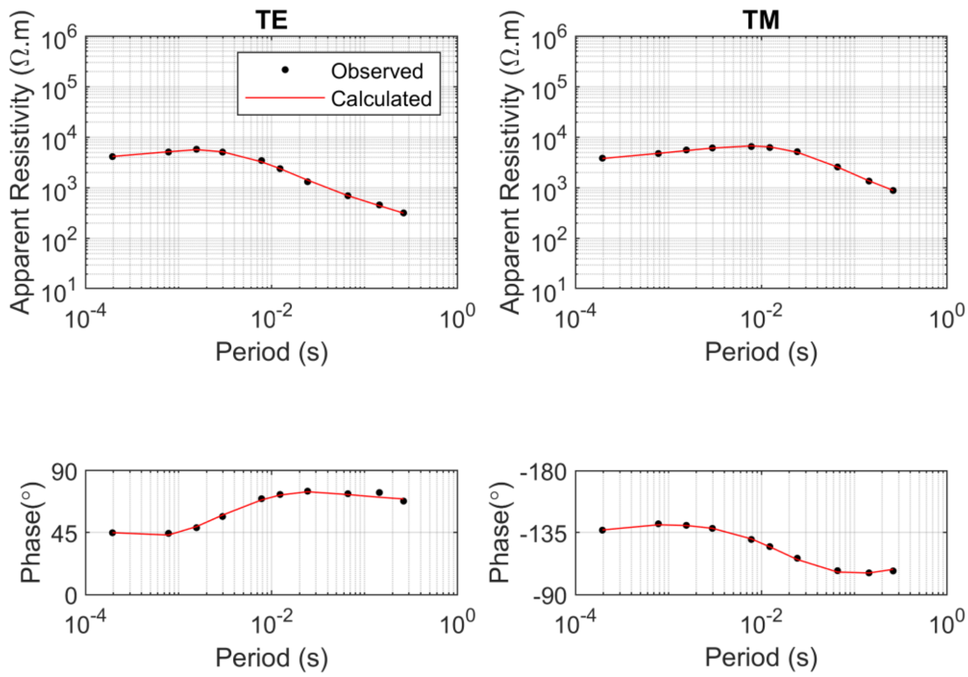

Fits of Apparent Resistivity and Phase for station #13

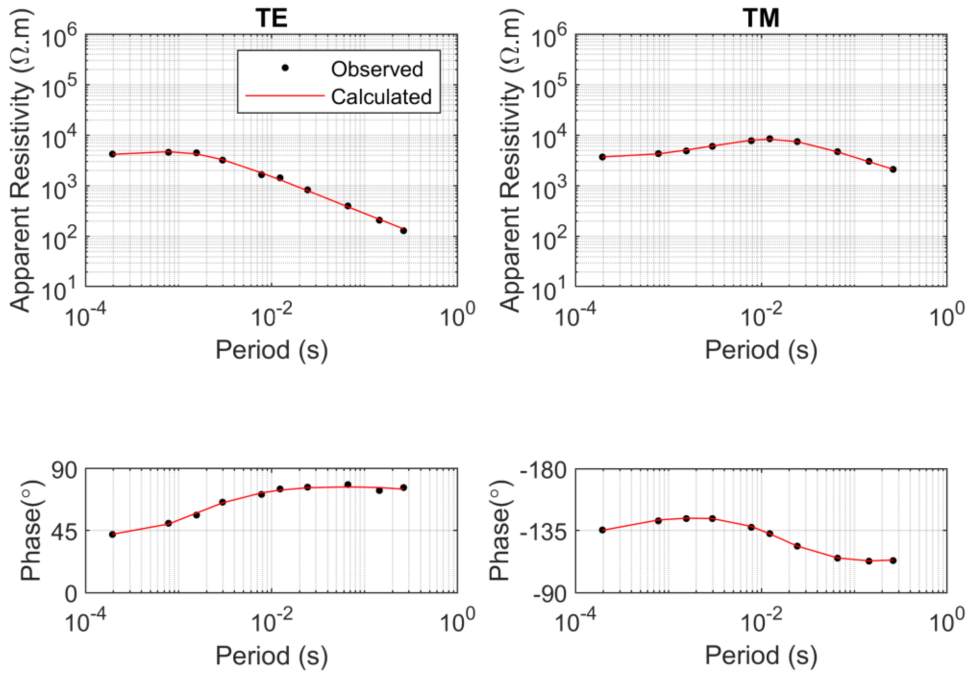

Fits of Apparent Resistivity and Phase for station #14

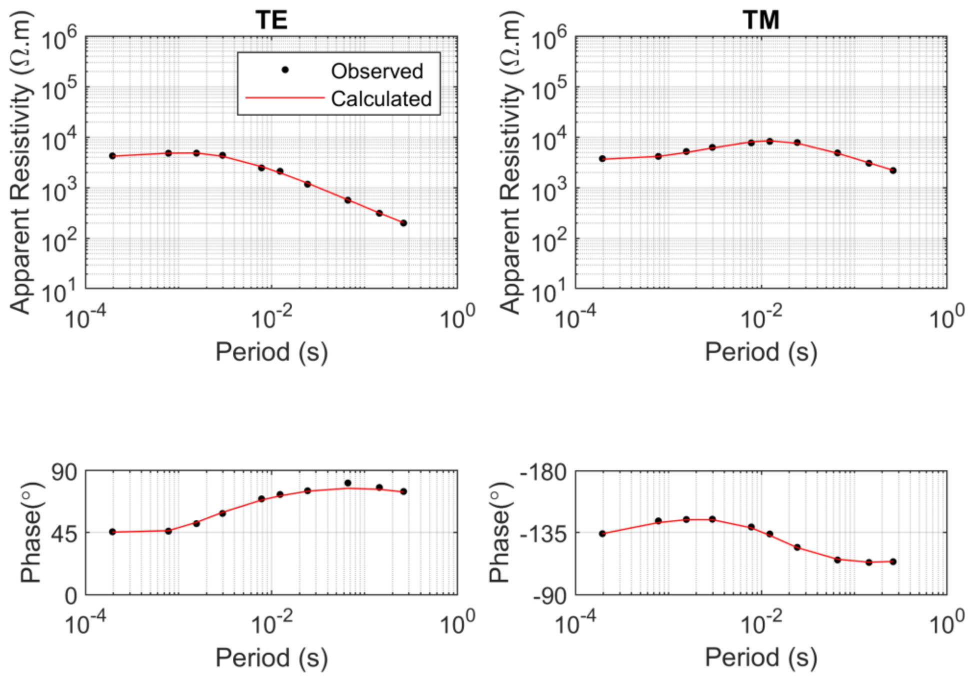

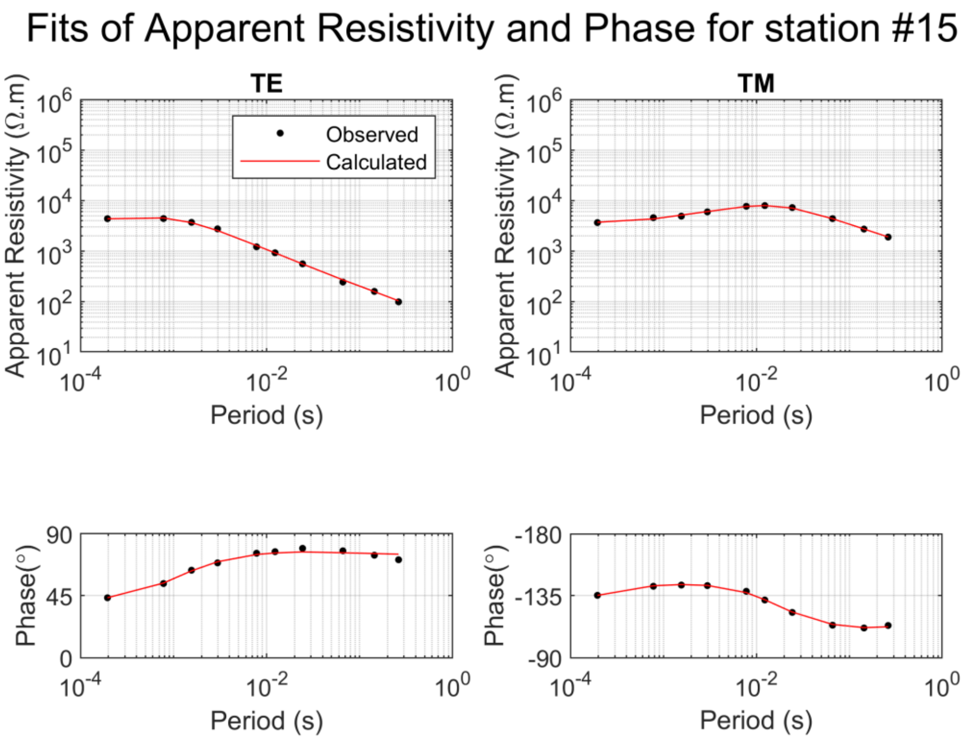
Fits of Apparent Resistivity and Phase for station #15
TE
TM
Observed
Calculated
Apparent Resistivity (Ω.m)
Phase(°)
Period (s)

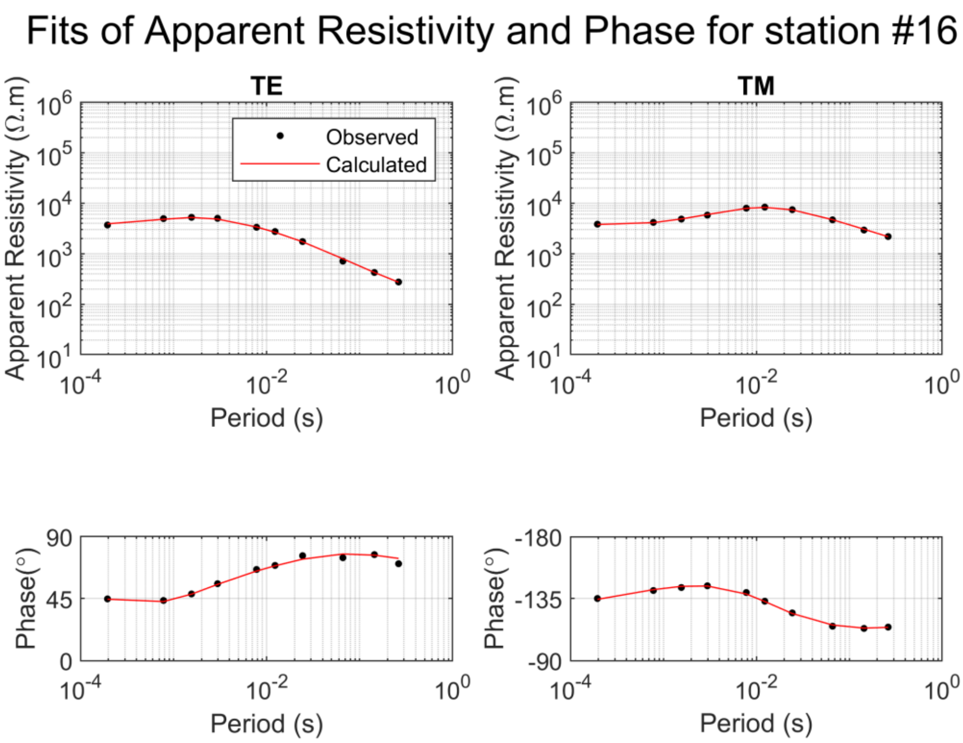
Fits of Apparent Resistivity and Phase for station #16
TE
TM
Observed
Calculated
Apparent Resistivity (Ω.m)
Phase(°)
Period (s)

Fits of Apparent Resistivity and Phase for station #17

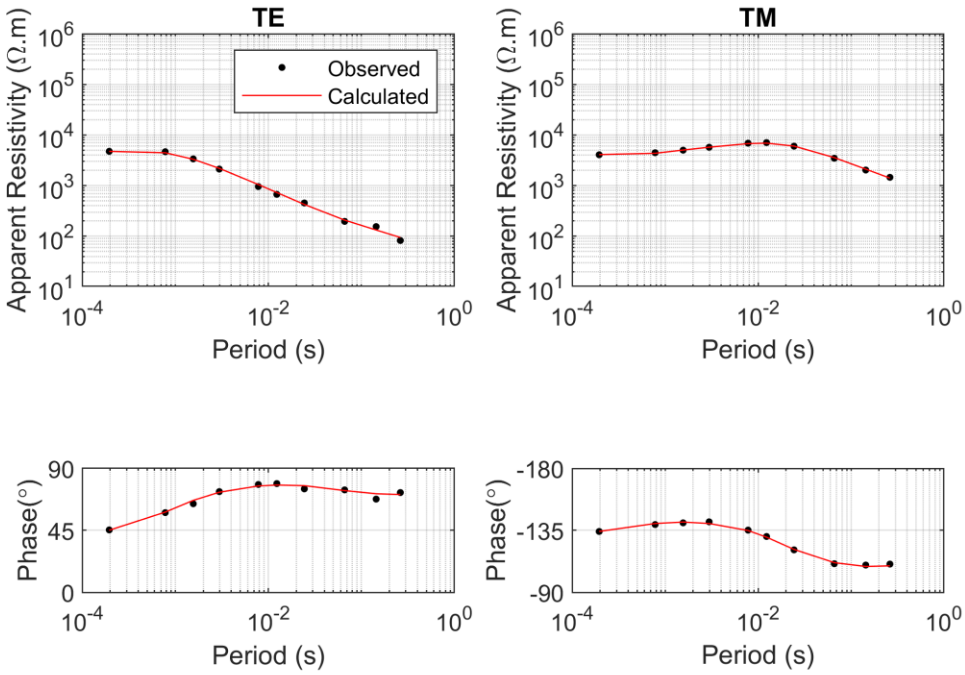

Fits of Apparent Resistivity and Phase for station #18

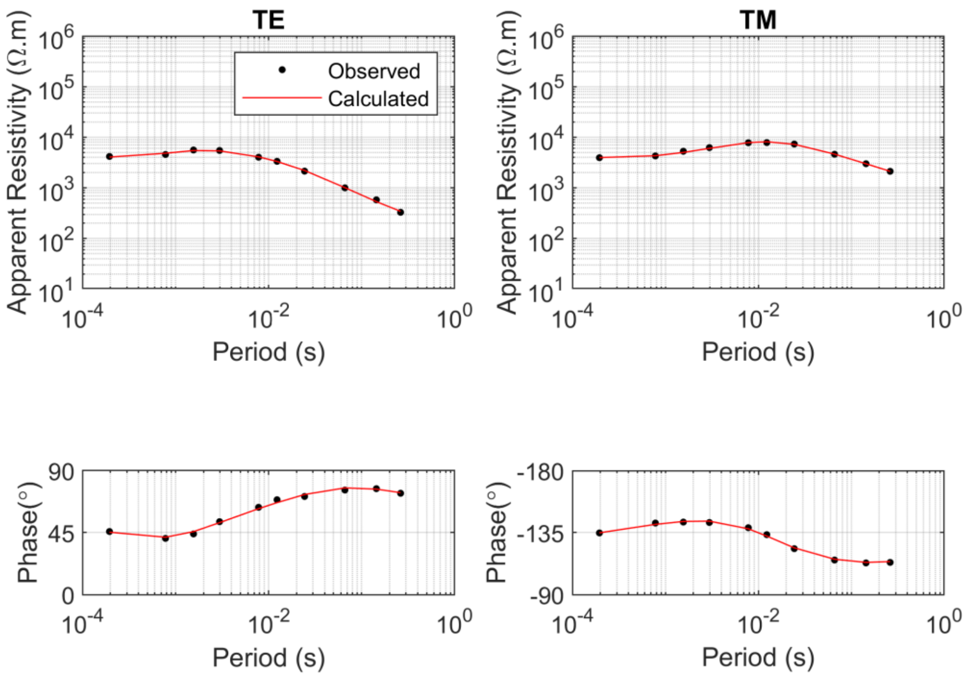

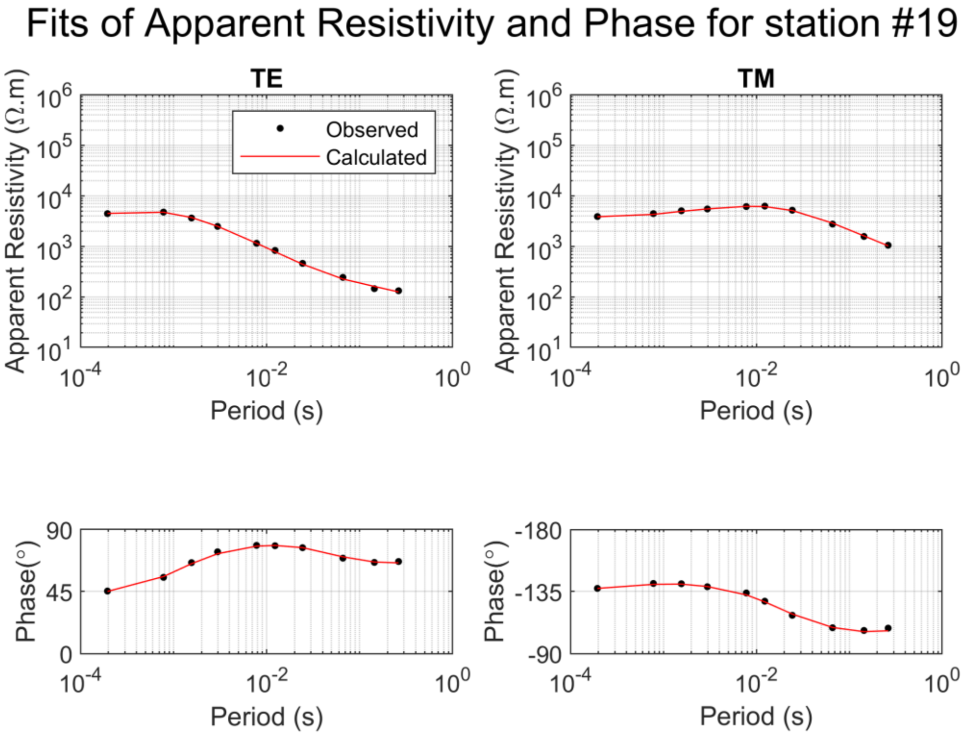
Fits of Apparent Resistivity and Phase for station #19
TE
TM
Observed
Calculated
Apparent Resistivity (Ω.m)
Phase(°)
Period (s)

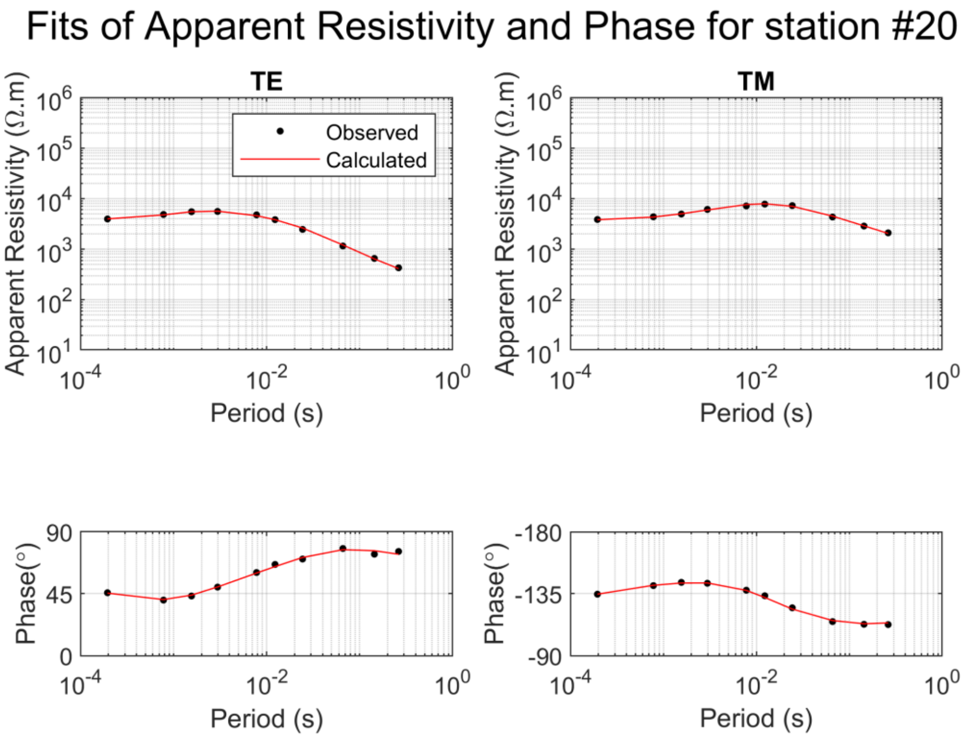
Fits of Apparent Resistivity and Phase for station #20
TE
TM
Observed
Calculated
Apparent Resistivity (Ω.m)
Phase(°)
Period (s)

Fits of Apparent Resistivity and Phase for station #21

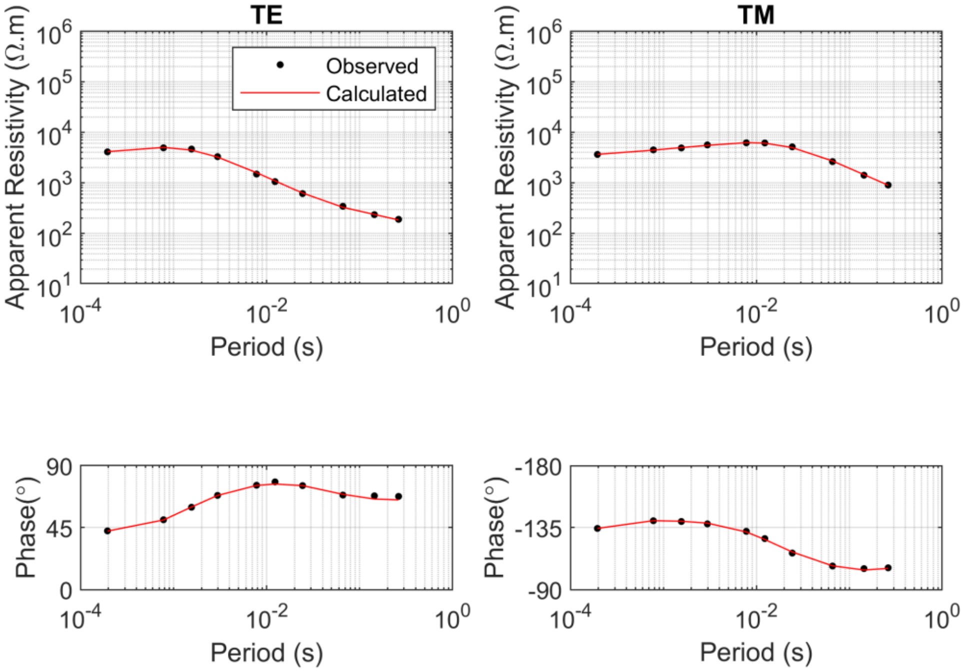

Fits of Apparent Resistivity and Phase for station #22

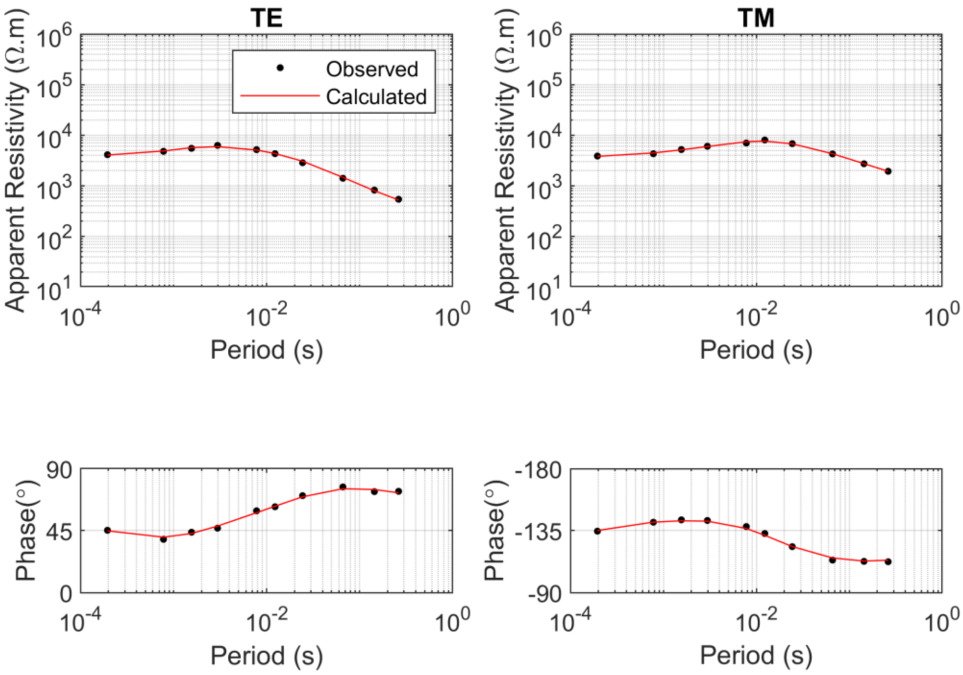

Fits of Apparent Resistivity and Phase for station #23

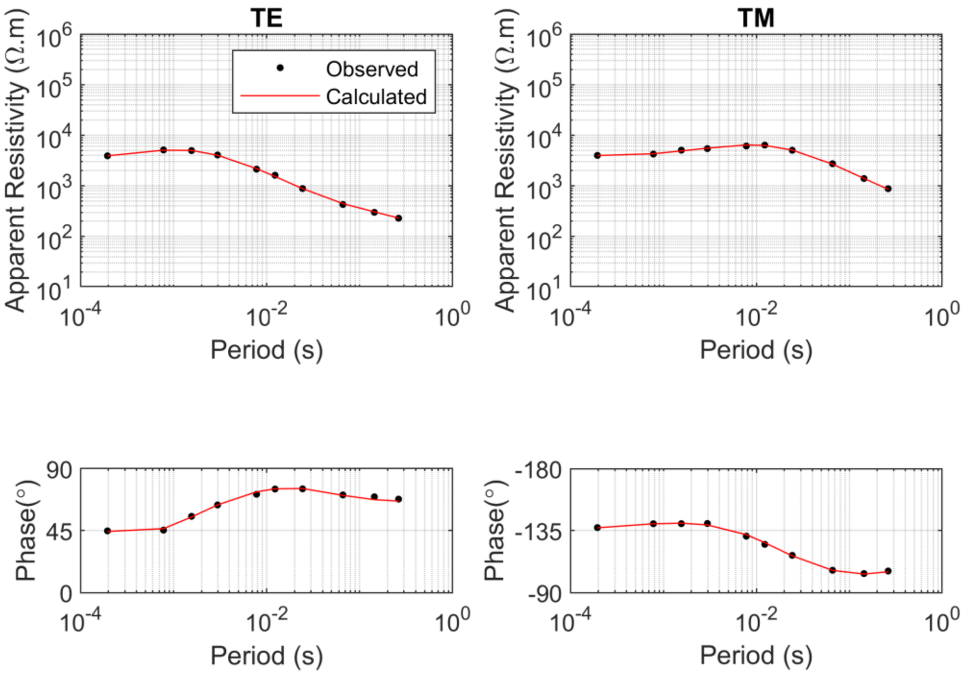

Fits of Apparent Resistivity and Phase for station #24

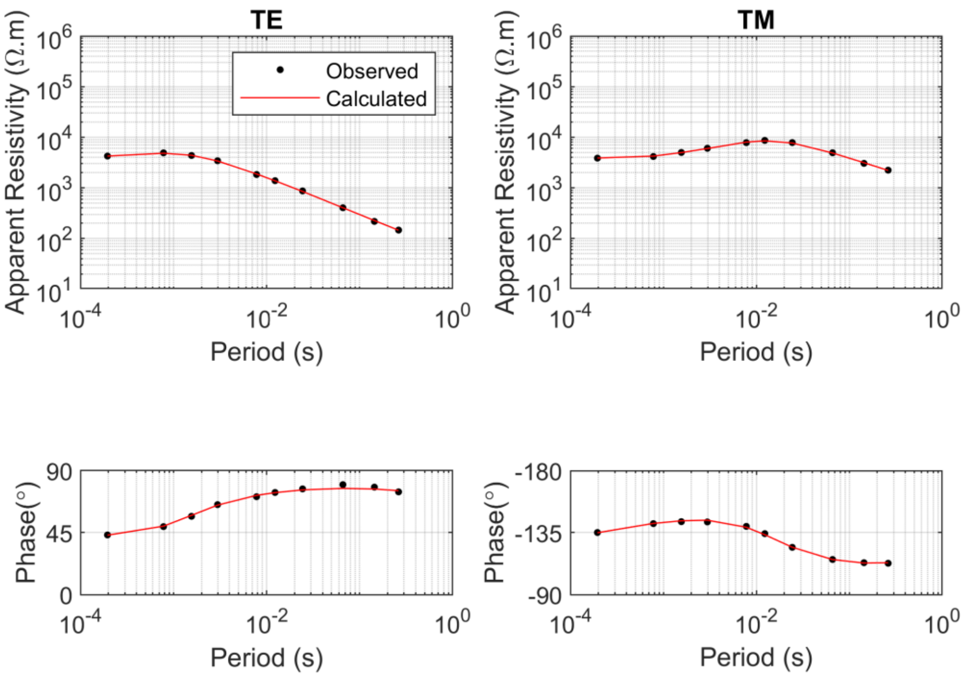

Fits of Apparent Resistivity and Phase for station #25

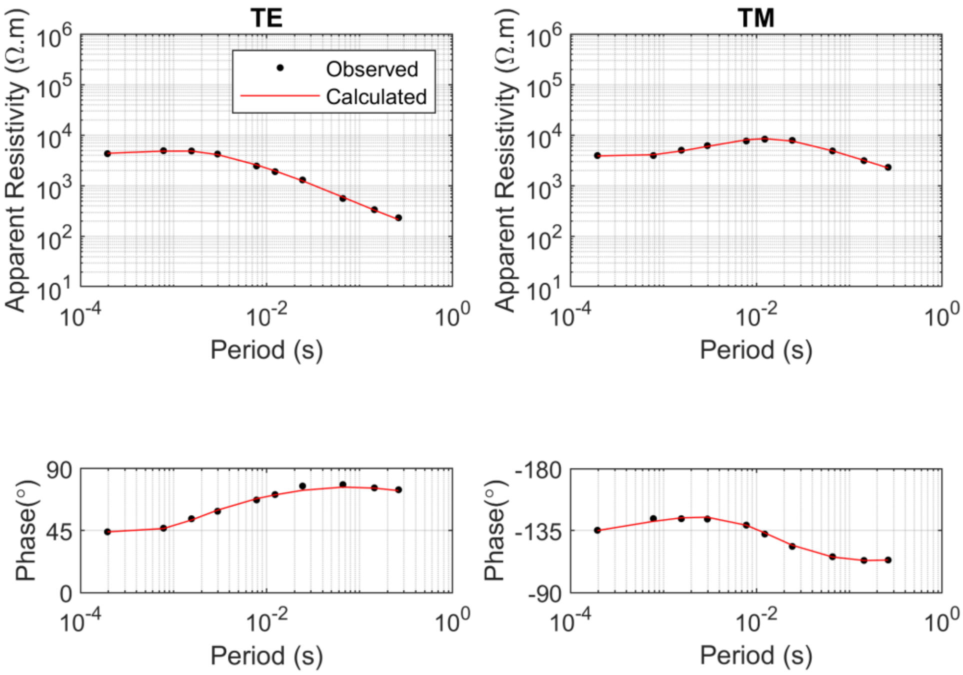

Fits of Apparent Resistivity and Phase for station #26

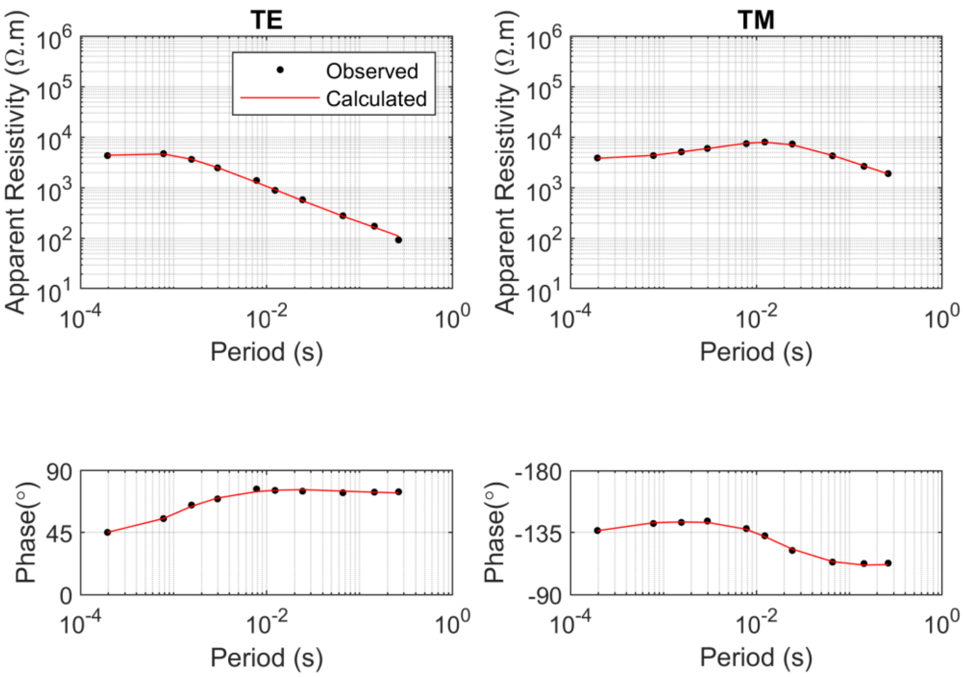

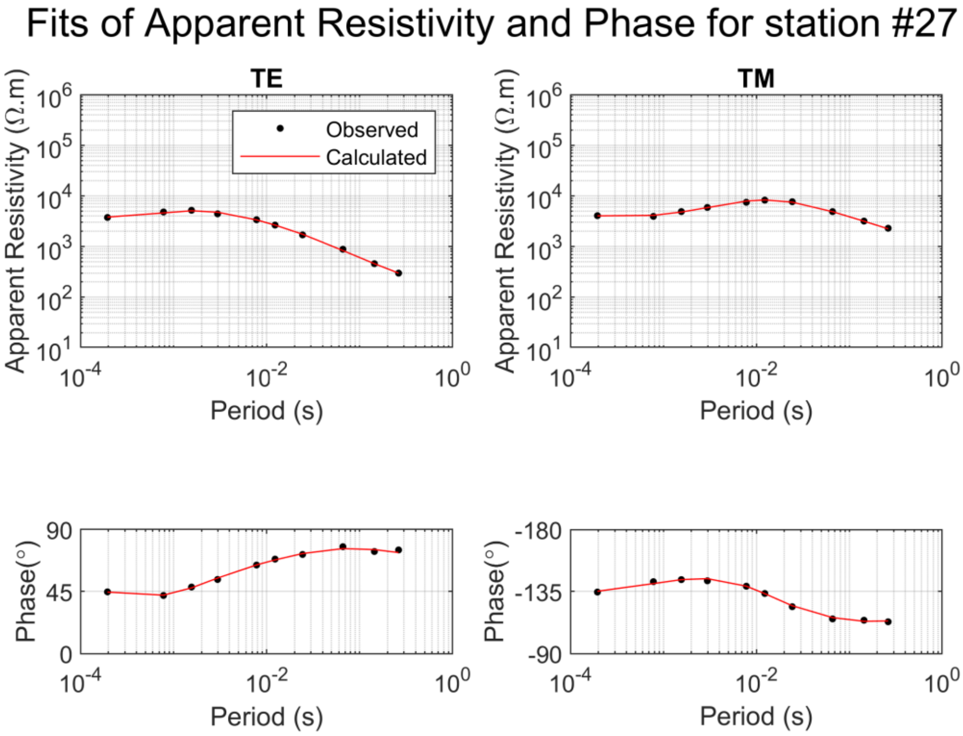
Fits of Apparent Resistivity and Phase for station #27
TE
TM
Observed
Calculated
Apparent Resistivity (Ω.m)
Phase(°)
Period (s)

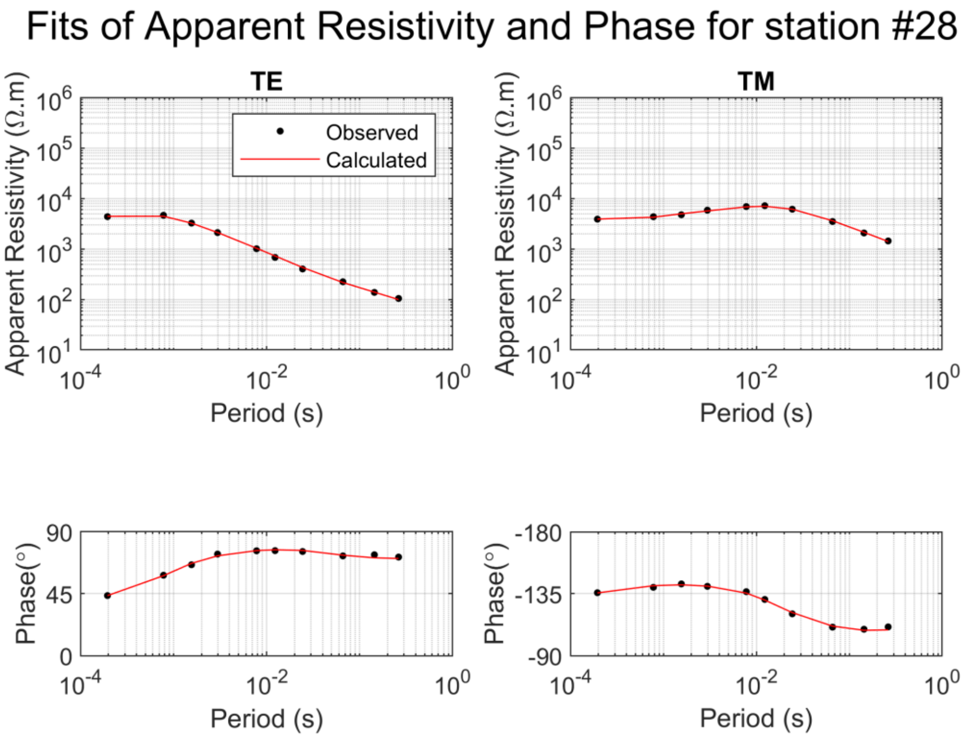
Fits of Apparent Resistivity and Phase for station #28
TE
TM
Observed
Calculated
Apparent Resistivity (Ω.m)
Phase(°)
Period (s)

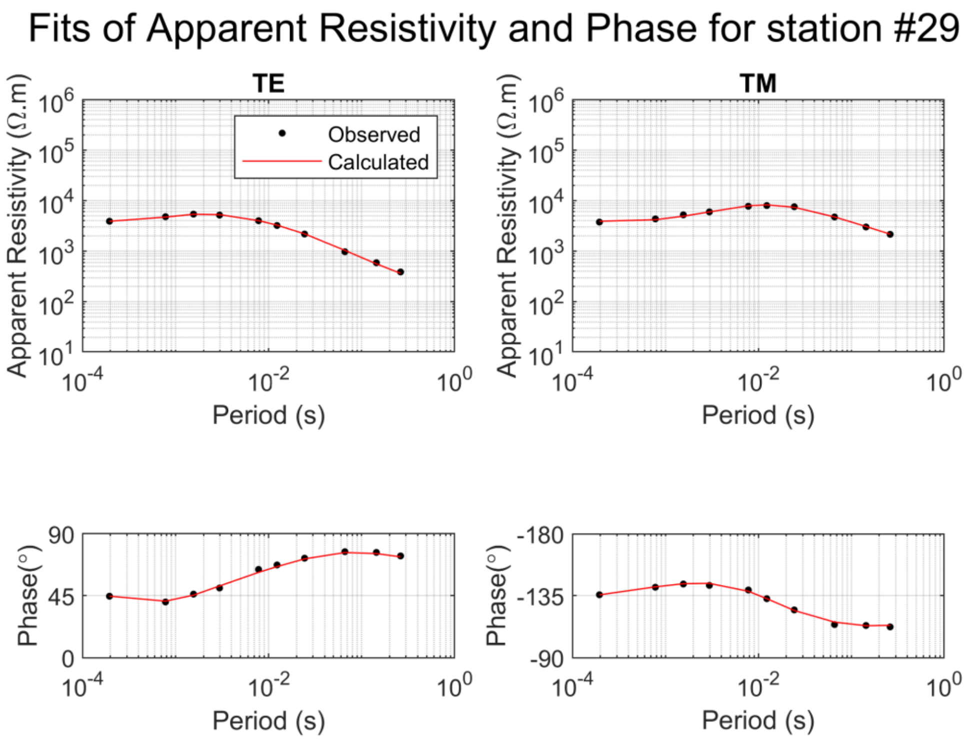
Fits of Apparent Resistivity and Phase for station #29
TE
TM
Observed
Calculated
Apparent Resistivity (Ω.m)
Period (s)
Phase(°)

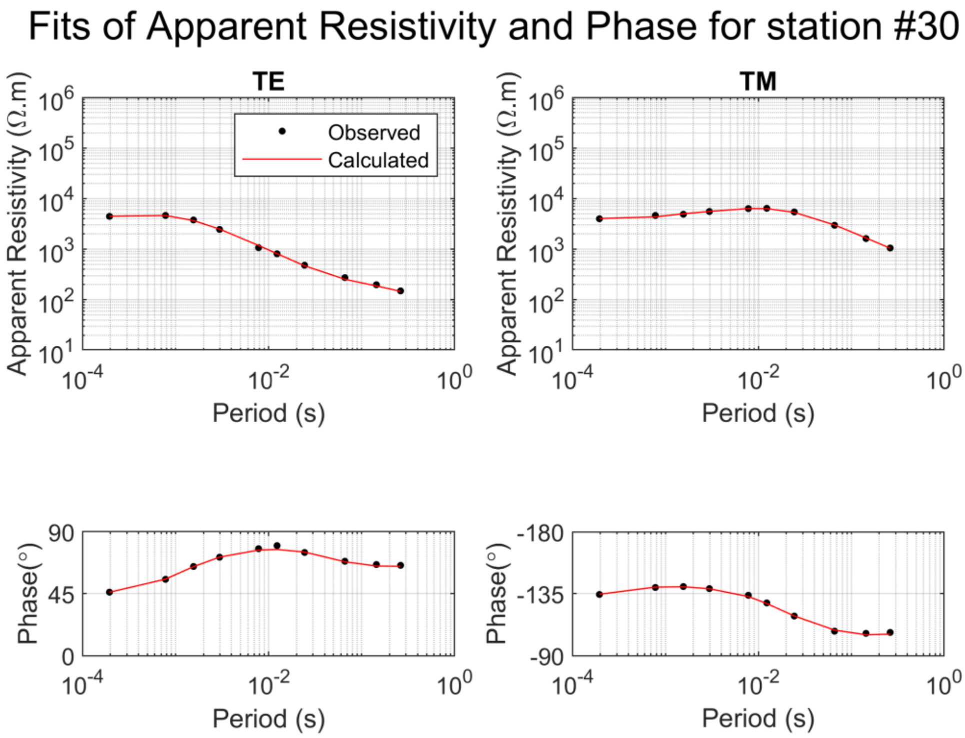
Fits of Apparent Resistivity and Phase for station #30
TE
TM
Observed
Calculated
Apparent Resistivity (Ω.m)
Period (s)
Phase(°)

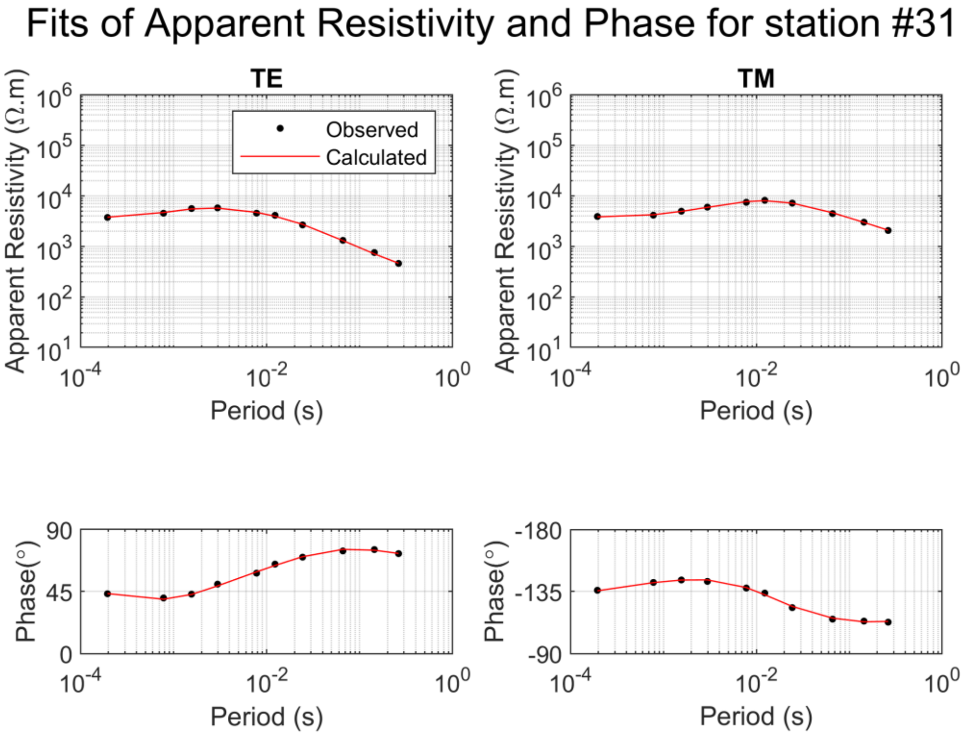
Fits of Apparent Resistivity and Phase for station #31
TE
TM
Observed
Calculated
Apparent Resistivity (Ω.m)
Phase(°)
Period (s)

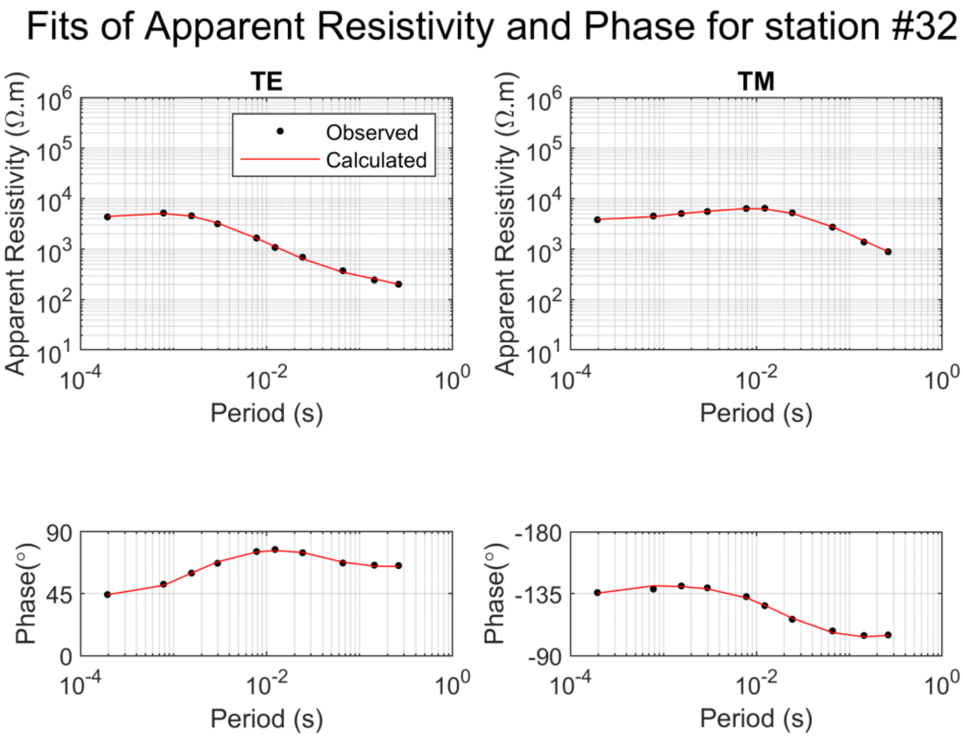
Fits of Apparent Resistivity and Phase for station #32
TE
TM
Observed
Calculated
Apparent Resistivity (Ω.m)
Phase(°)
Period (s)

Fits of Apparent Resistivity and Phase for station #33

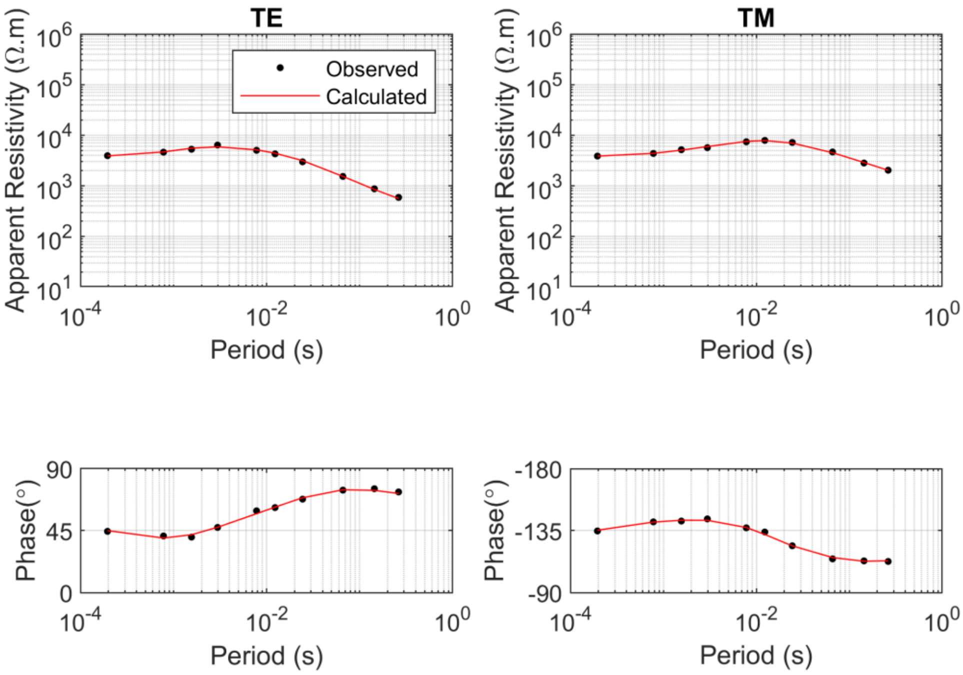

Fits of Apparent Resistivity and Phase for station #34

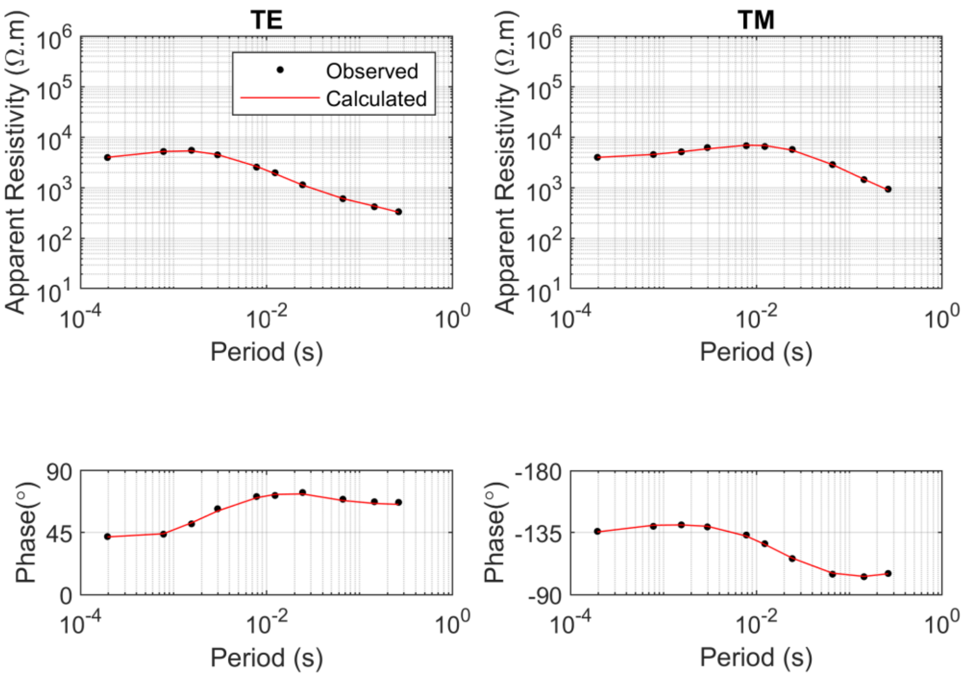

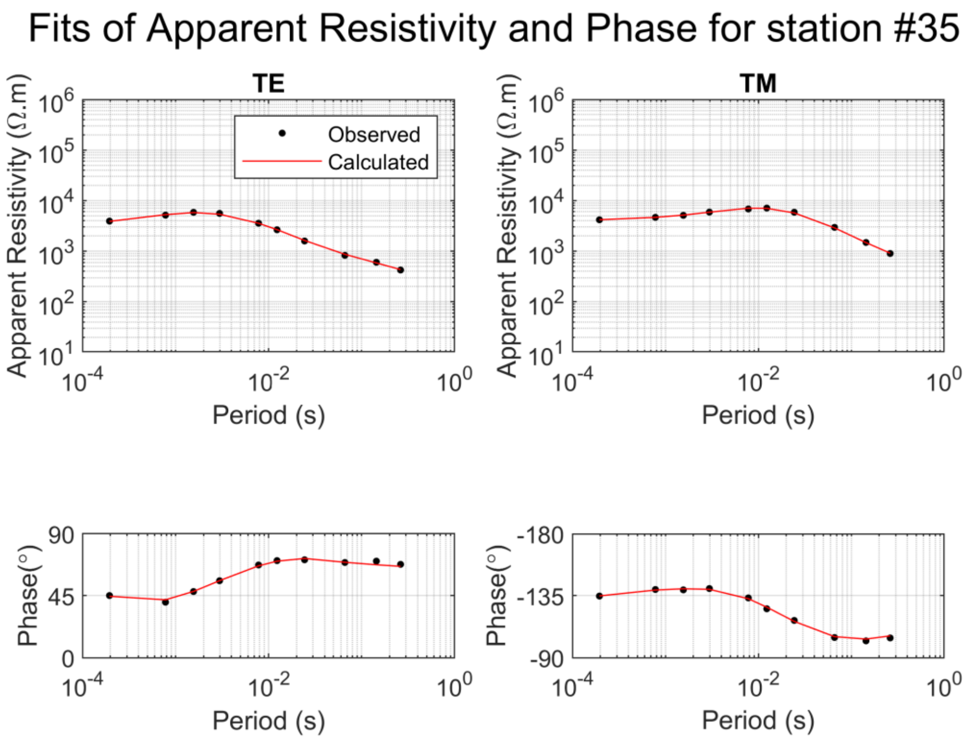
Fits of Apparent Resistivity and Phase for station #35
TE
TM
Observed
Calculated
Apparent Resistivity (Ω.m)
Period (s)
Phase(°)
10^6
10^5
10^4
10^3
10^2
10^1
10^-4
10^-2
10^0
90
45
0
-180
-135
-90

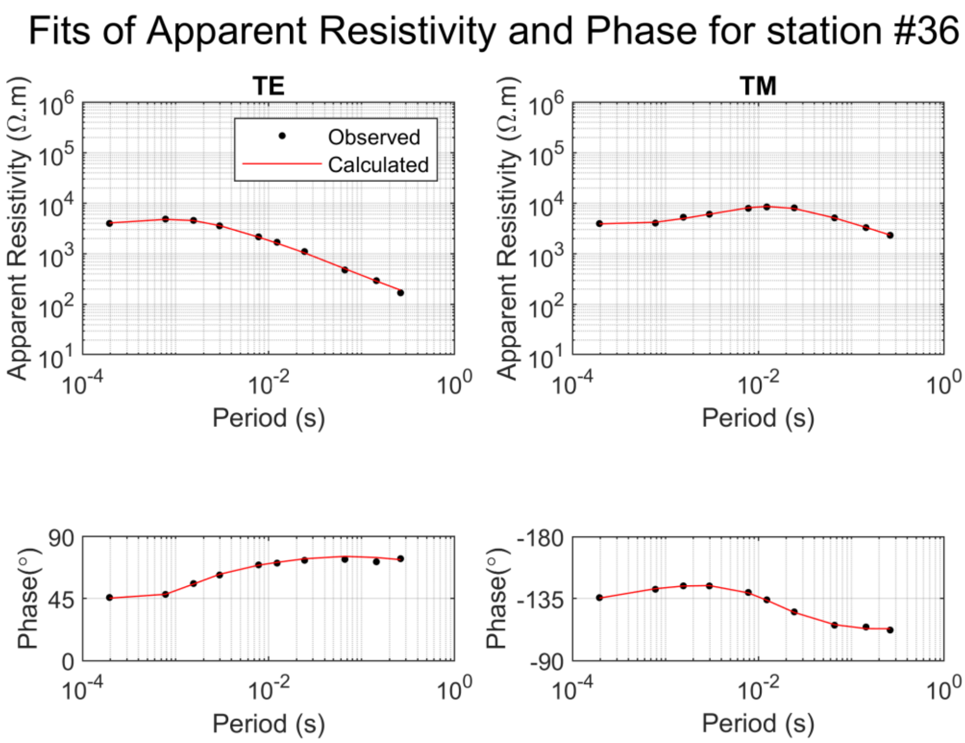
Fits of Apparent Resistivity and Phase for station #36
TE
TM
Observed
Calculated
Apparent Resistivity (Ω.m)
Period (s)
Phase(°)
10^6
10^5
10^4
10^3
10^2
10^1
10^-4
10^-2
10^0
90
45
0
-180
-135
-90

Fits of Apparent Resistivity and Phase for station #37

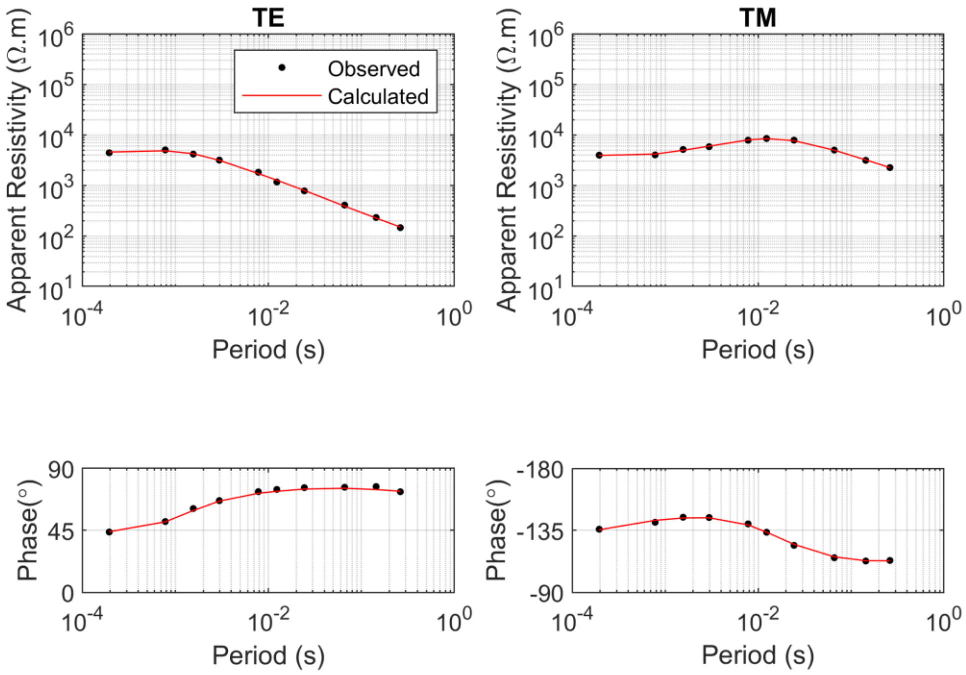

Fits of Apparent Resistivity and Phase for station #38

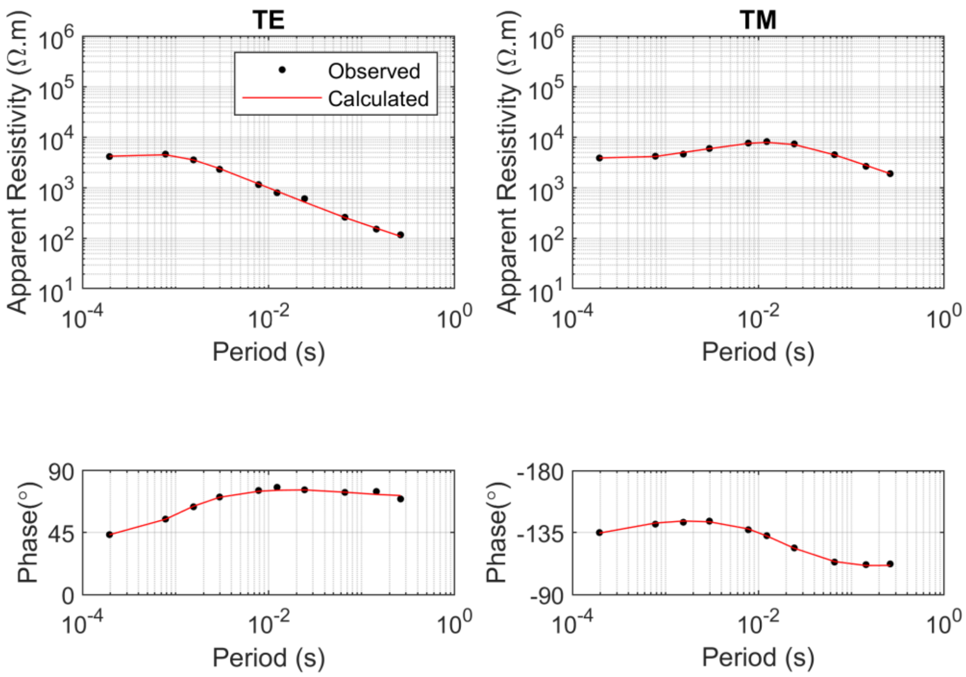

Fits of Apparent Resistivity and Phase for station #39

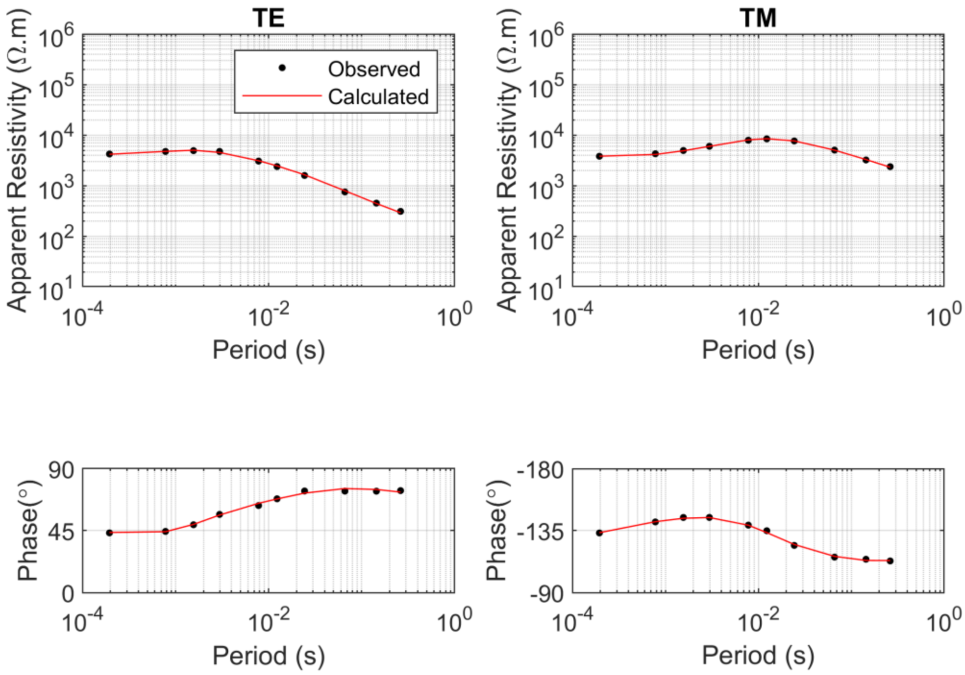

Fits of Apparent Resistivity and Phase for station #40

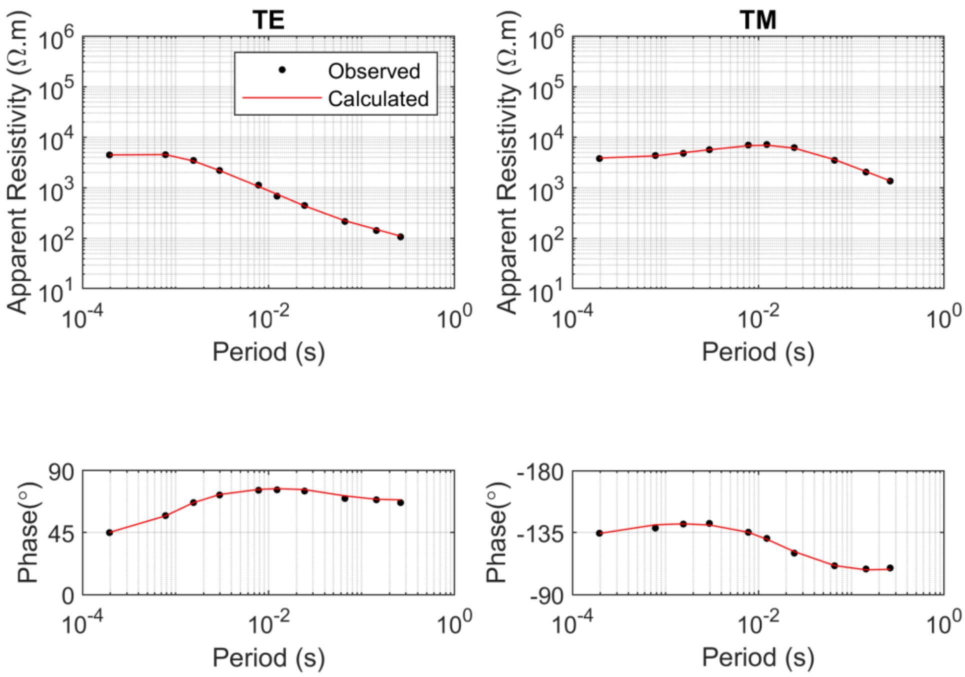

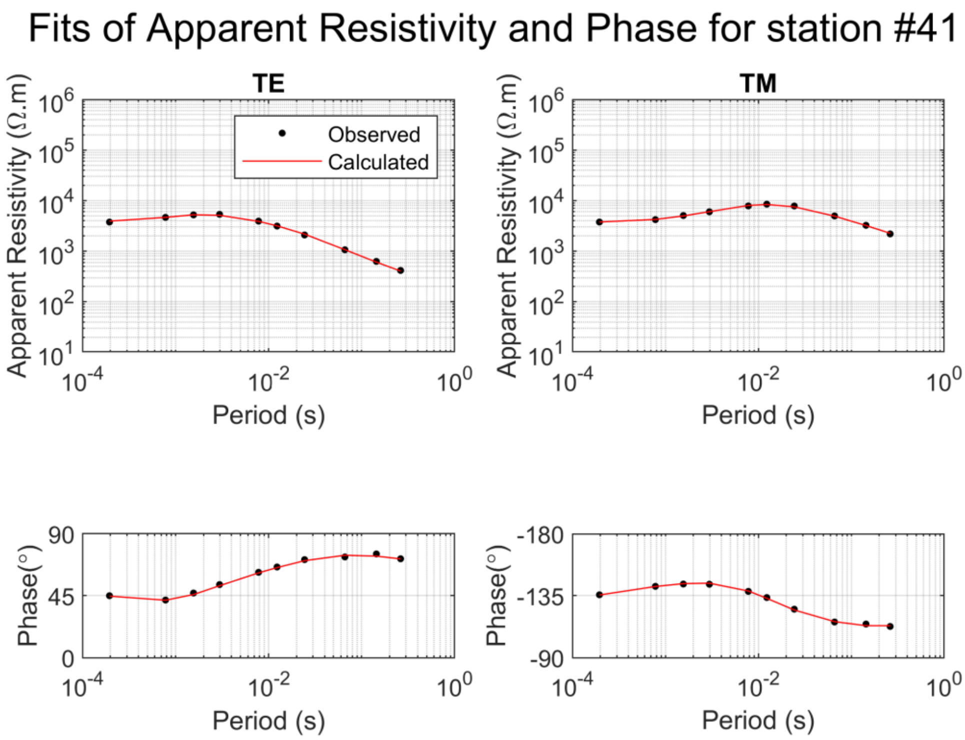
Fits of Apparent Resistivity and Phase for station #41
TE
TM
Observed
Calculated
Apparent Resistivity (Ω.m)
Phase(°)
Period (s)

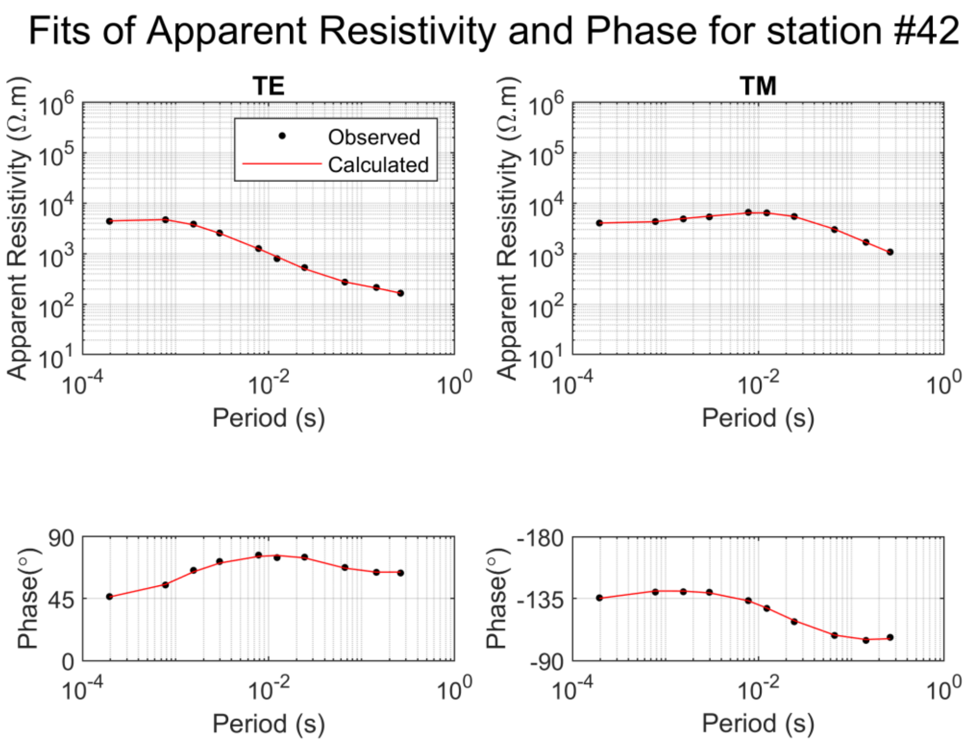
Fits of Apparent Resistivity and Phase for station #42
TE
TM
Observed
Calculated
Apparent Resistivity (Ω.m)
Phase(°)
Period (s)

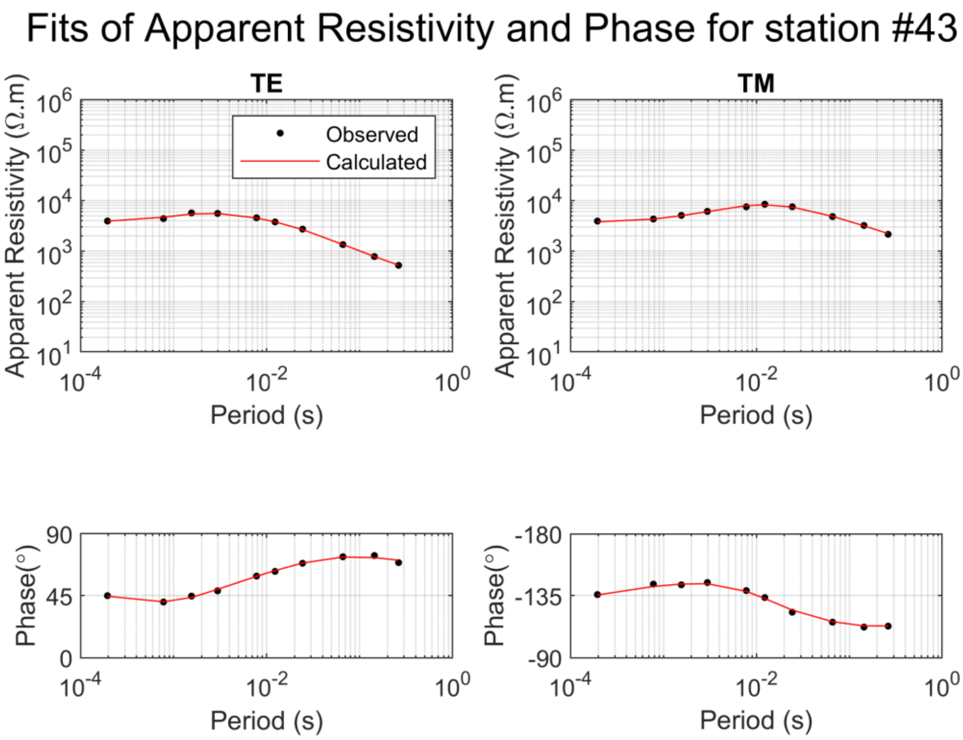
Fits of Apparent Resistivity and Phase for station #43
TE
TM
Observed
Calculated
Apparent Resistivity (Ω.m)
Period (s)
Phase(°)

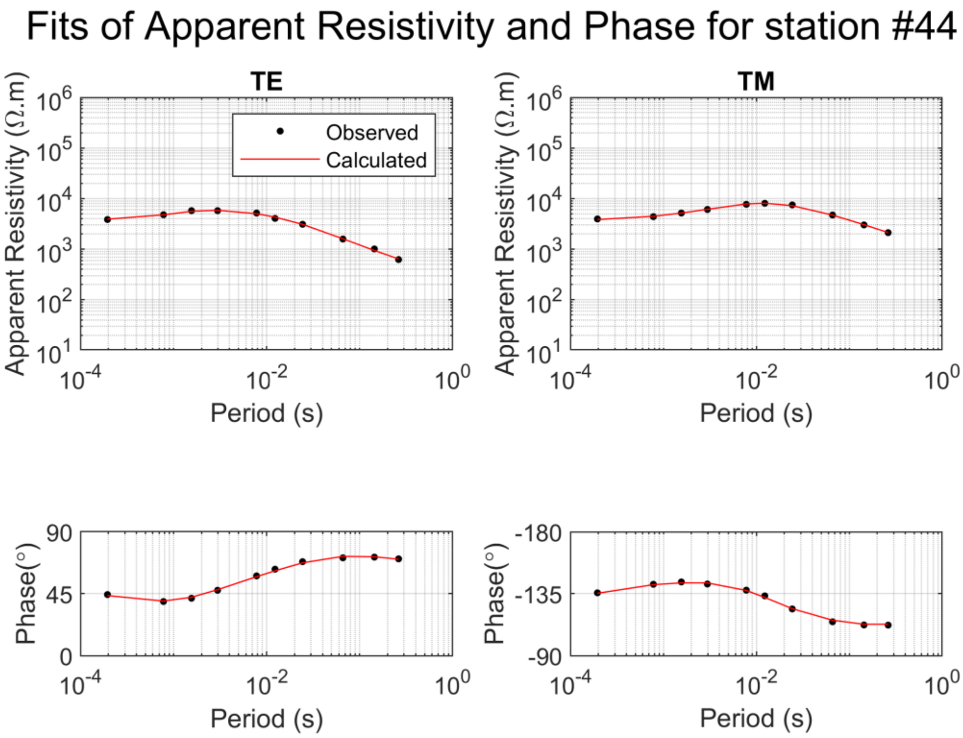
Fits of Apparent Resistivity and Phase for station #44
TE
TM
Observed
Calculated
Apparent Resistivity (Ω.m)
Period (s)
Phase(°)

Fits of Apparent Resistivity and Phase for station #45

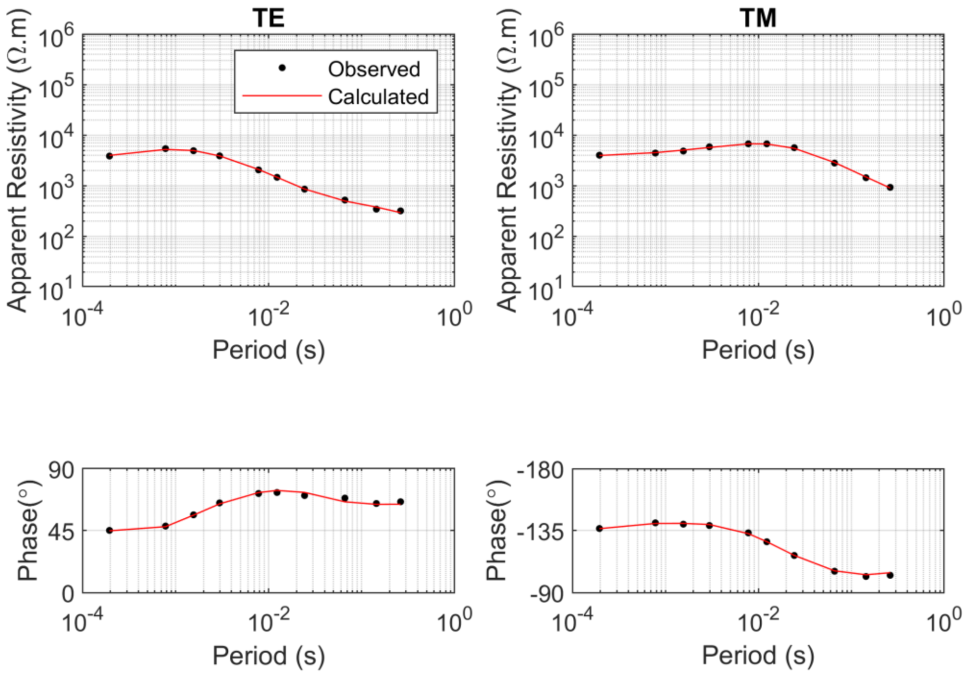

Fits of Apparent Resistivity and Phase for station #46

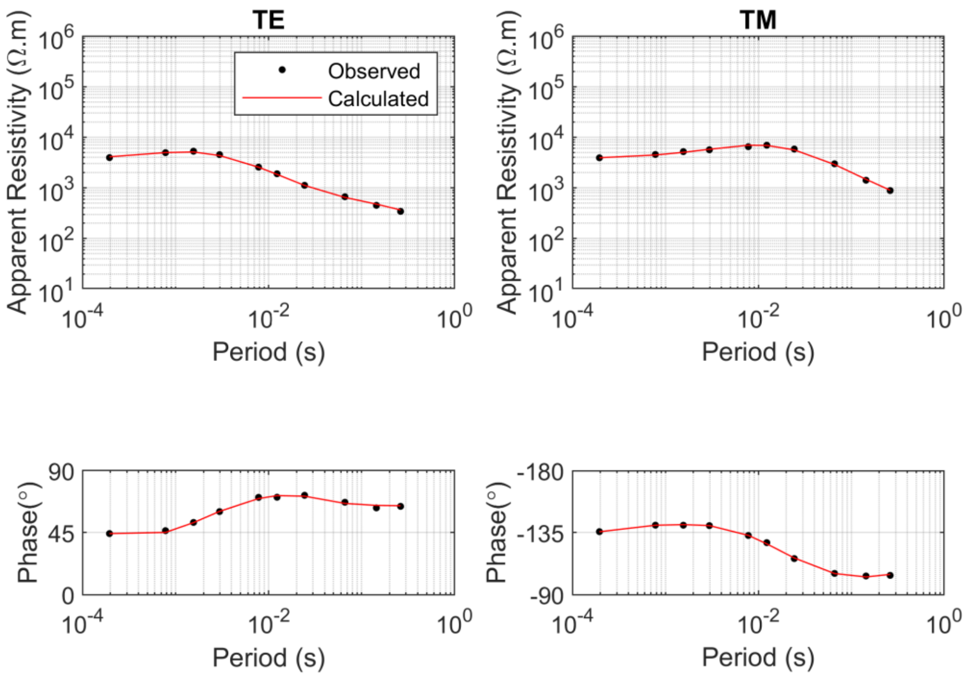

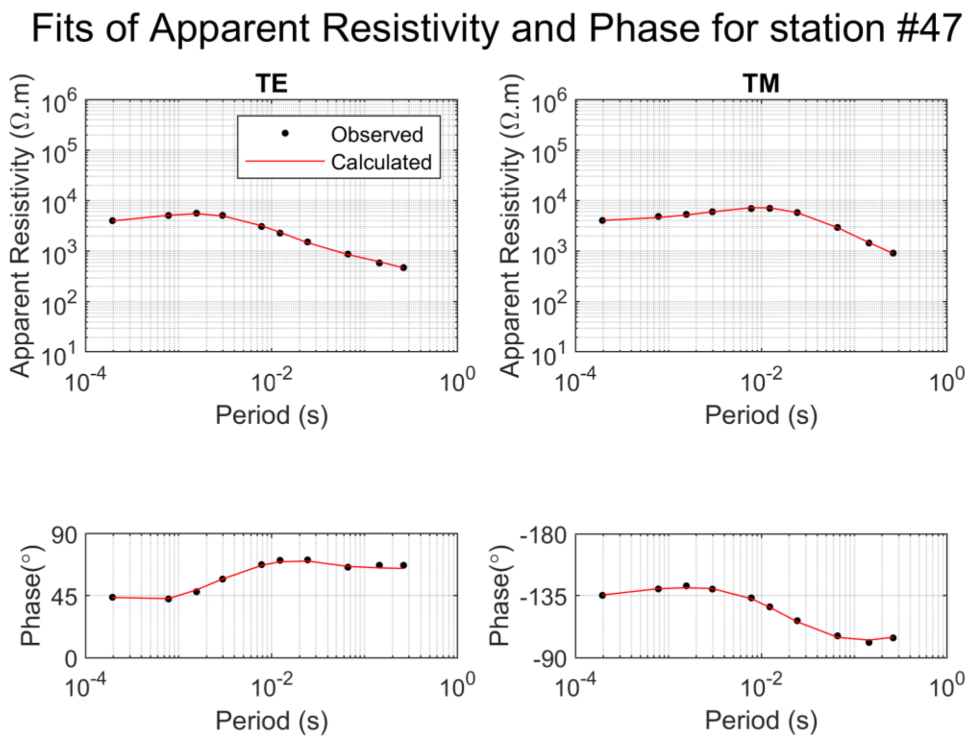
Fits of Apparent Resistivity and Phase for station #47
TE
TM
Observed
Calculated
Apparent Resistivity (Ω.m)
Phase(°)
Period (s)

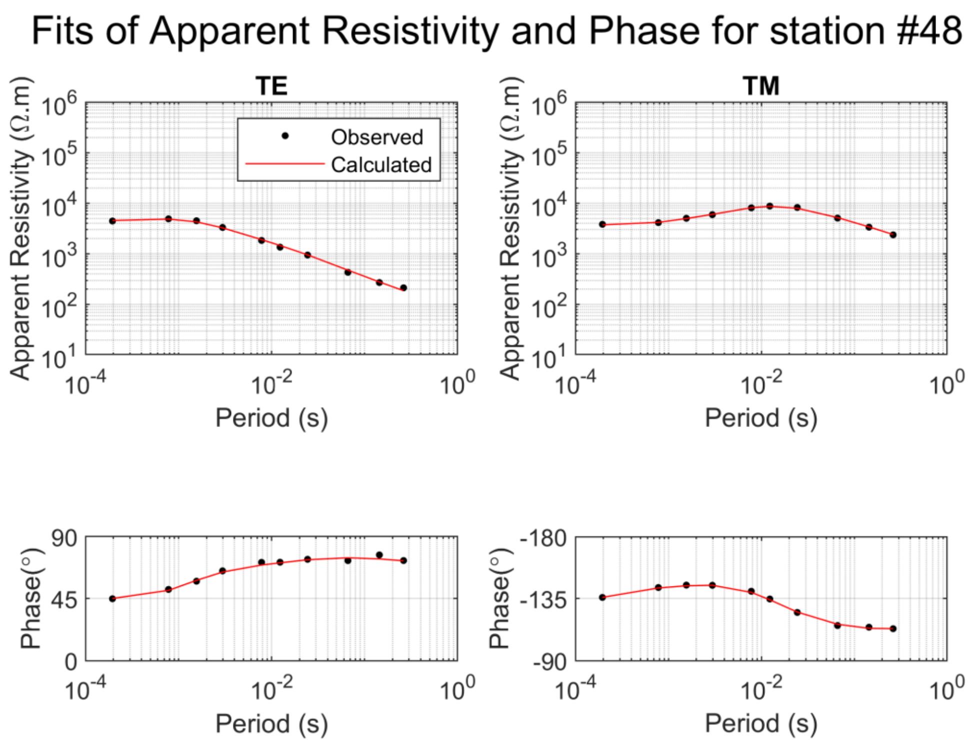
Fits of Apparent Resistivity and Phase for station #48
TE
TM
Observed
Calculated
Apparent Resistivity (Ω.m)
Phase(°)
Period (s)

Fits of Apparent Resistivity and Phase for station #49

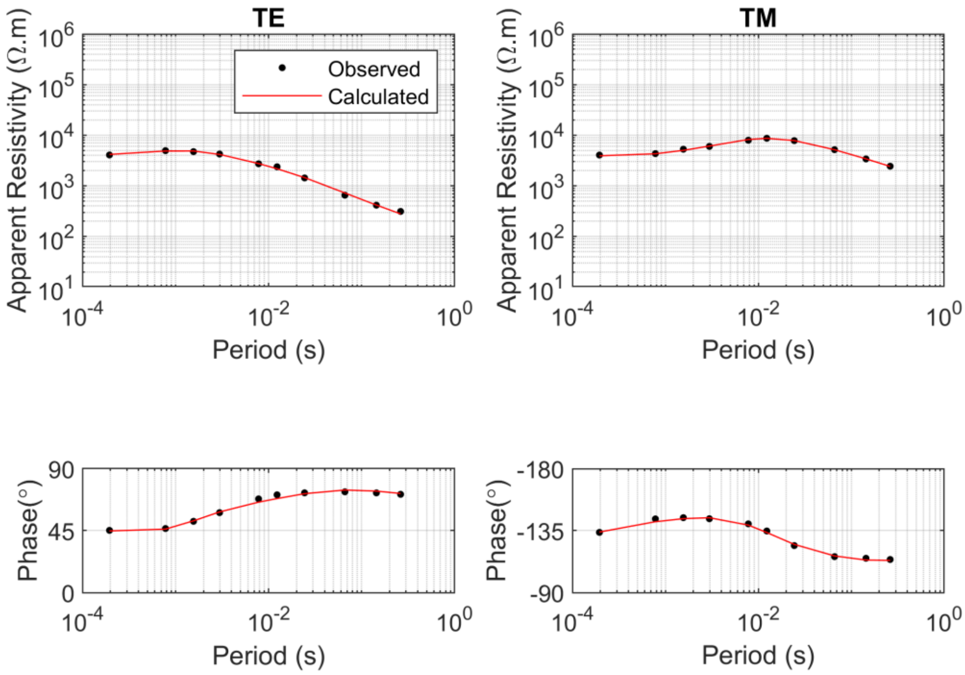

Fits of Apparent Resistivity and Phase for station #50

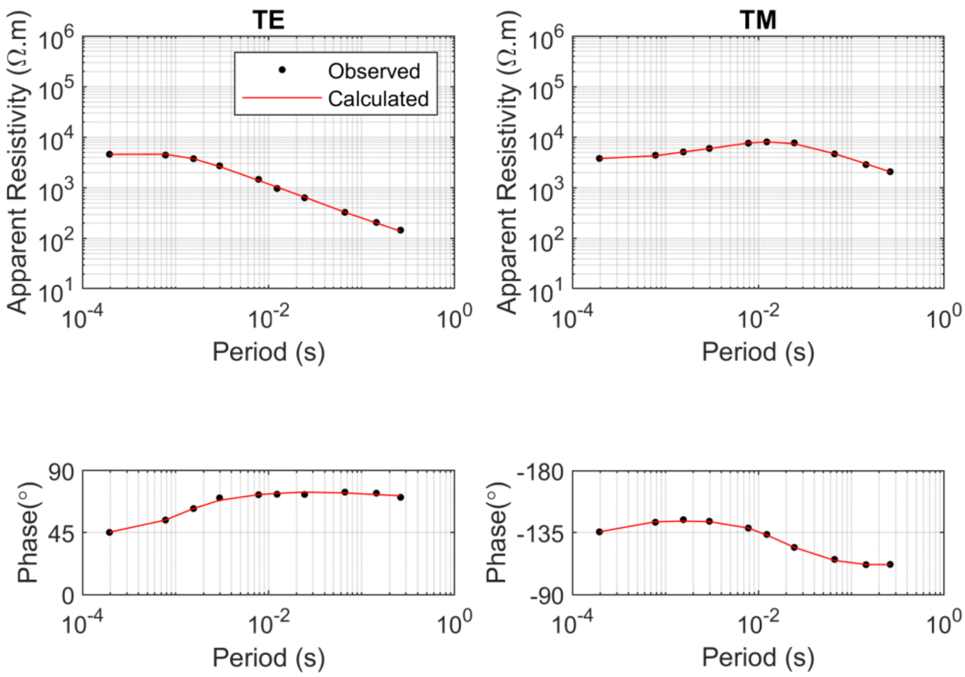

Fits of Apparent Resistivity and Phase for station #51

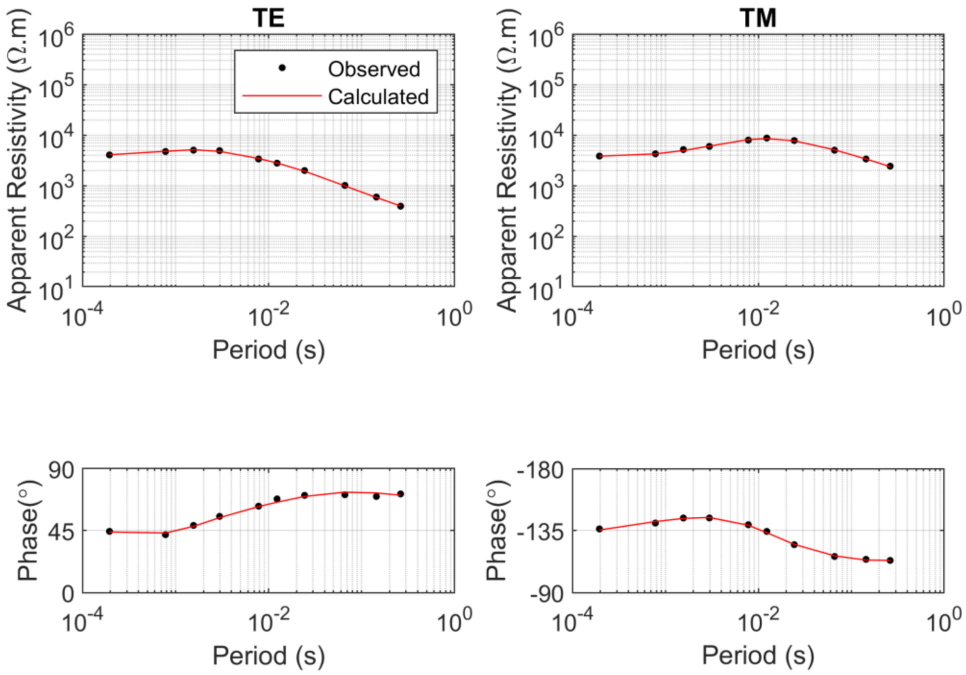

Fits of Apparent Resistivity and Phase for station #52

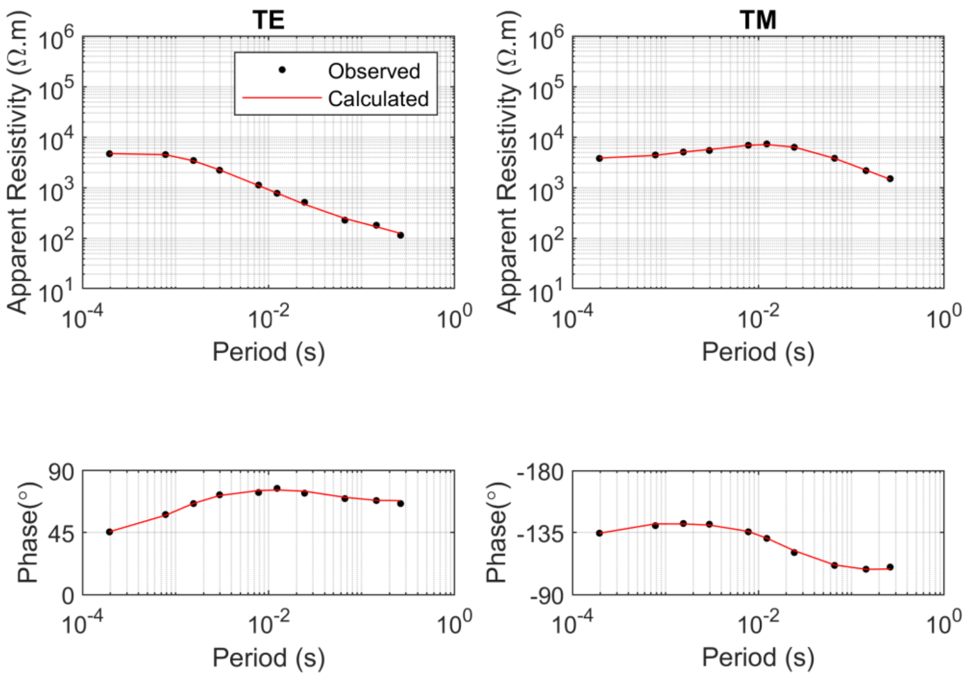

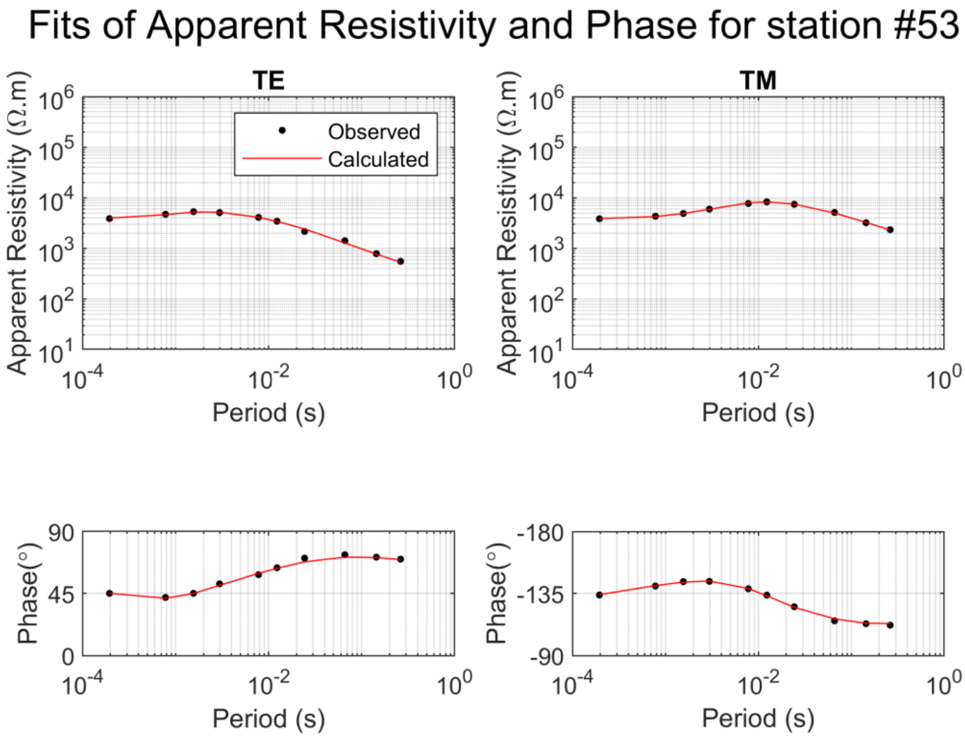
Fits of Apparent Resistivity and Phase for station #53
TE
TM
Observed
Calculated
Apparent Resistivity (Ω.m)
Phase(°)
Period (s)

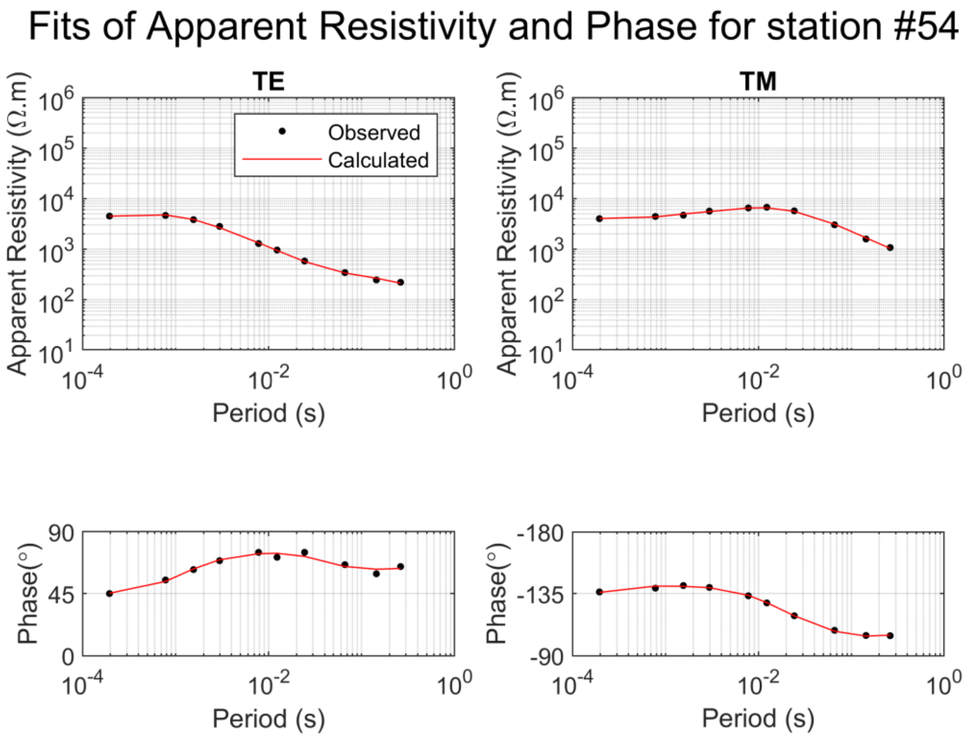
Fits of Apparent Resistivity and Phase for station #54
TE
TM
Observed
Calculated
Apparent Resistivity (Ω.m)
Phase(°)
Period (s)

Fits of Apparent Resistivity and Phase for station #55

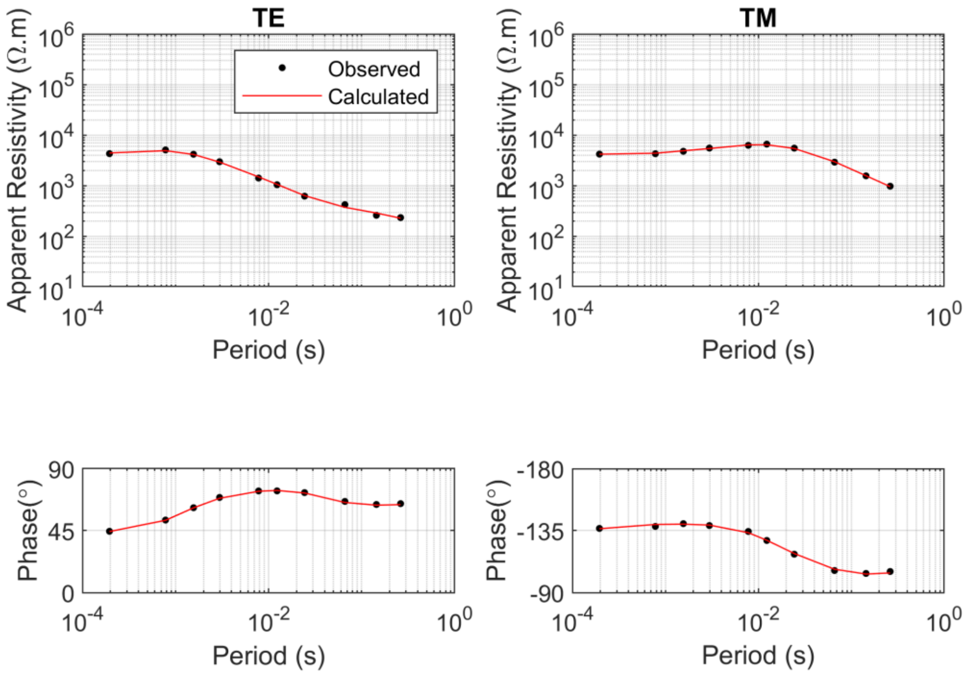

Fits of Apparent Resistivity and Phase for station #56

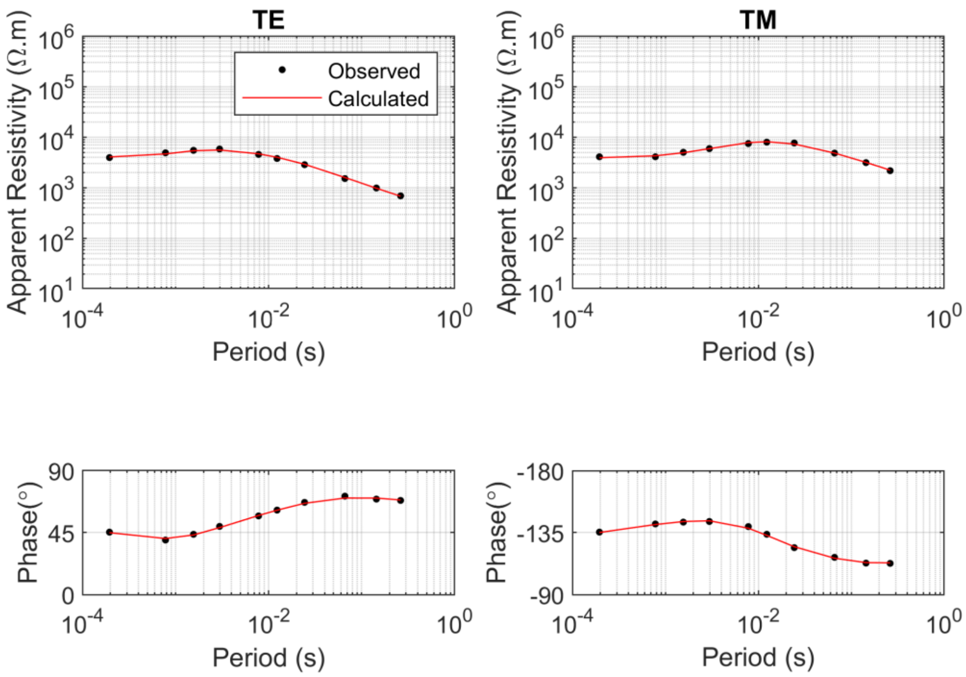

Fits of Apparent Resistivity and Phase for station #57

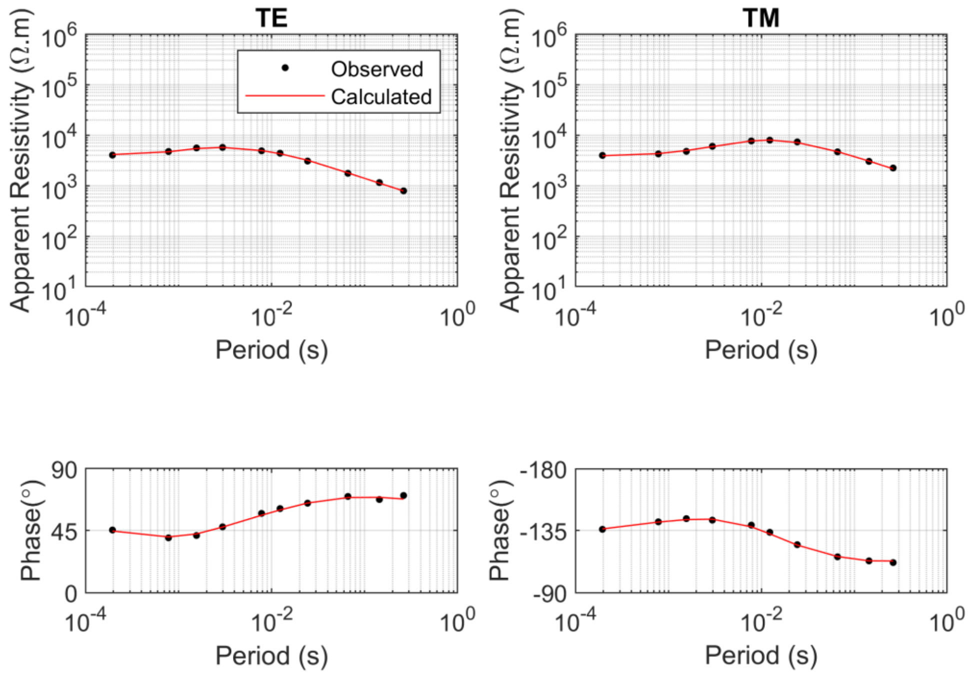

Fits of Apparent Resistivity and Phase for station #58

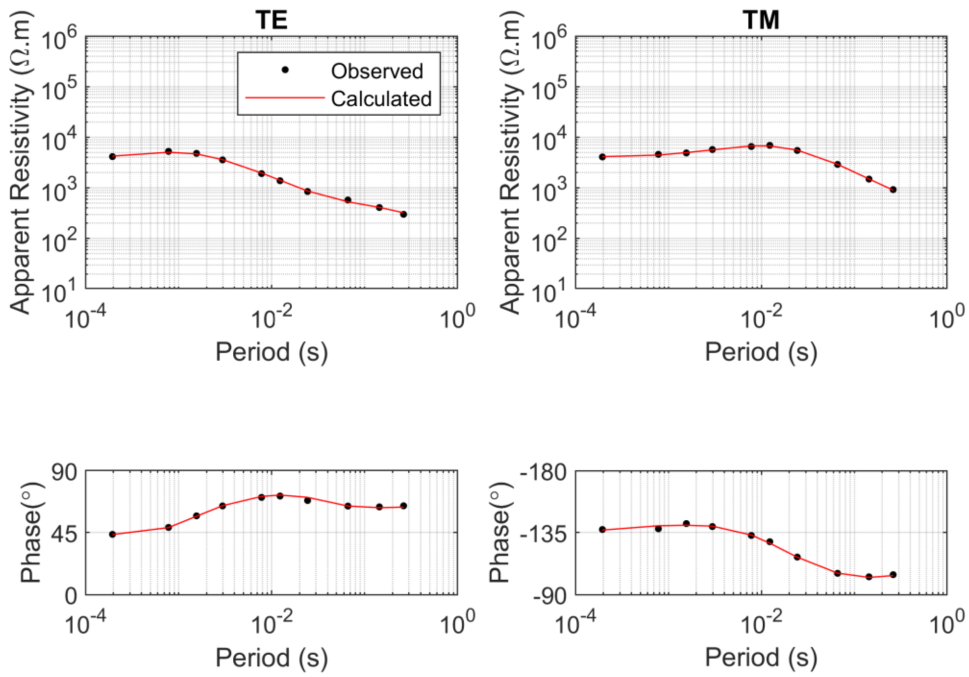

Fits of Apparent Resistivity and Phase for station #59

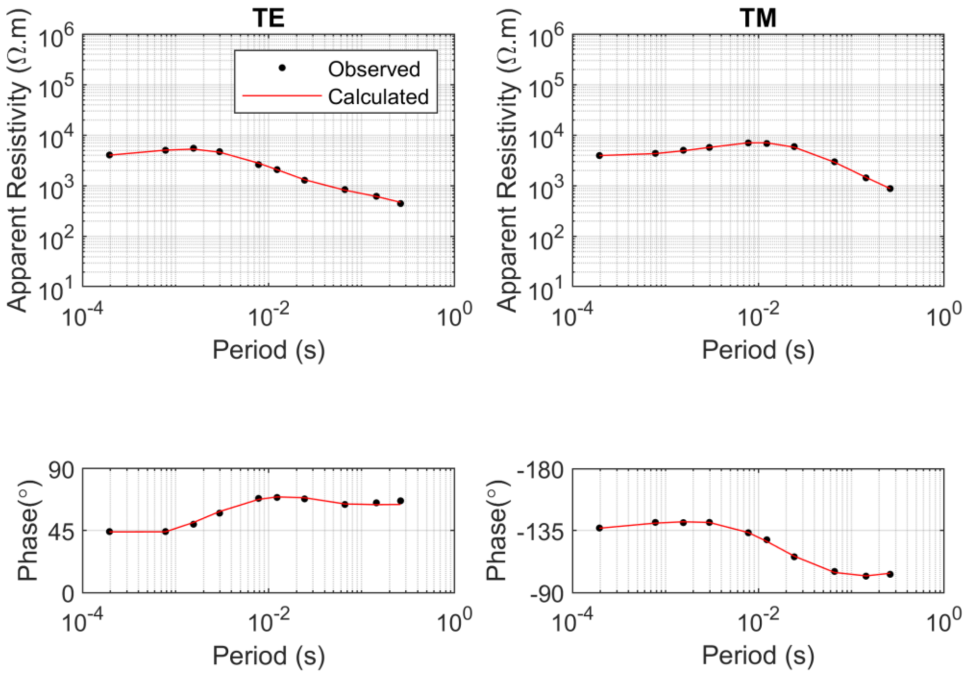

Fits of Apparent Resistivity and Phase for station #60

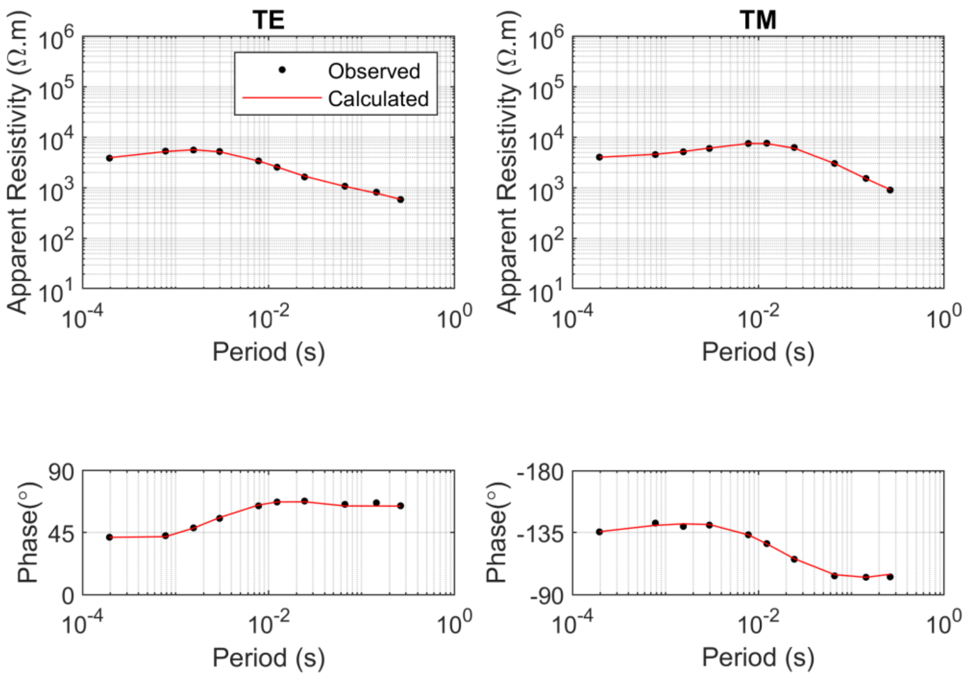

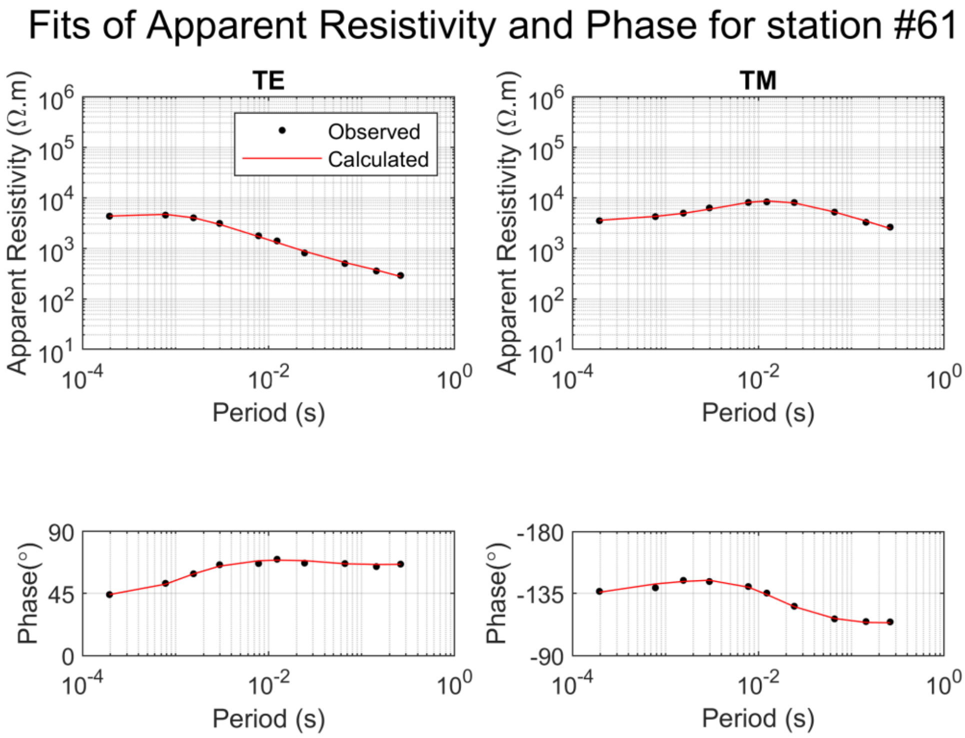
Fits of Apparent Resistivity and Phase for station #61
TE
TM
Observed
Calculated
Apparent Resistivity (Ω.m)
Period (s)
Phase(°)

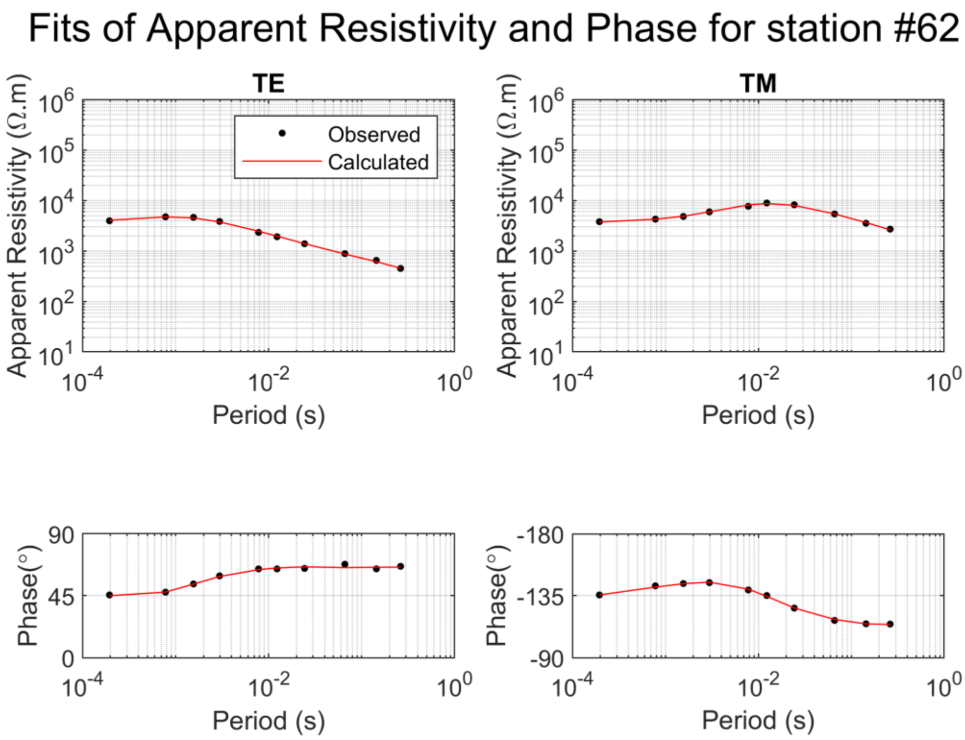
Fits of Apparent Resistivity and Phase for station #62
TE
TM
Observed
Calculated
Apparent Resistivity (Ω.m)
Period (s)
Phase(°)

Fits of Apparent Resistivity and Phase for station #63

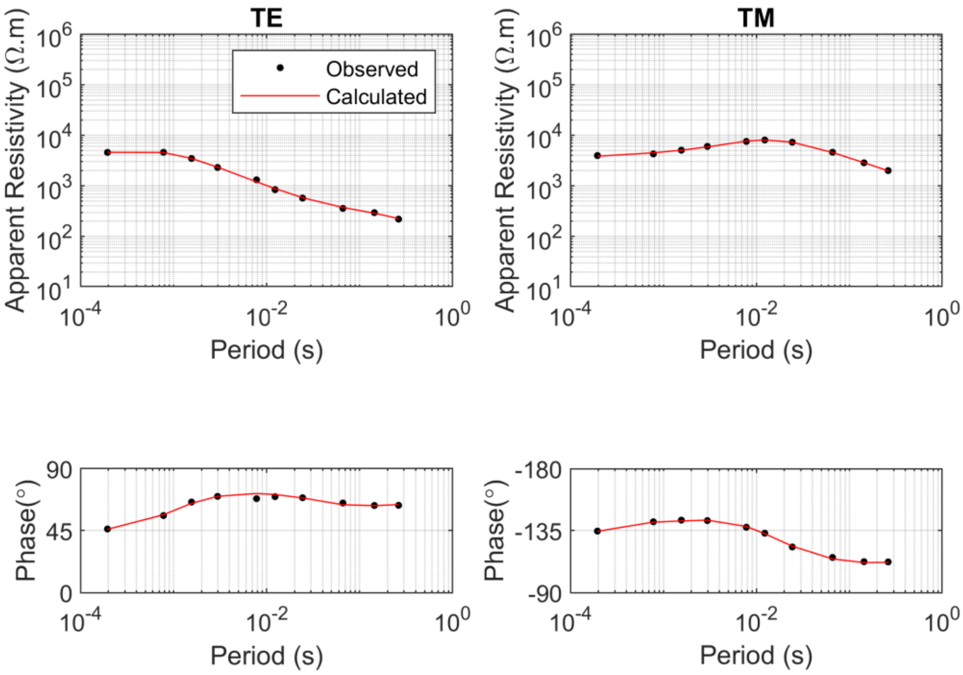

Fits of Apparent Resistivity and Phase for station #64

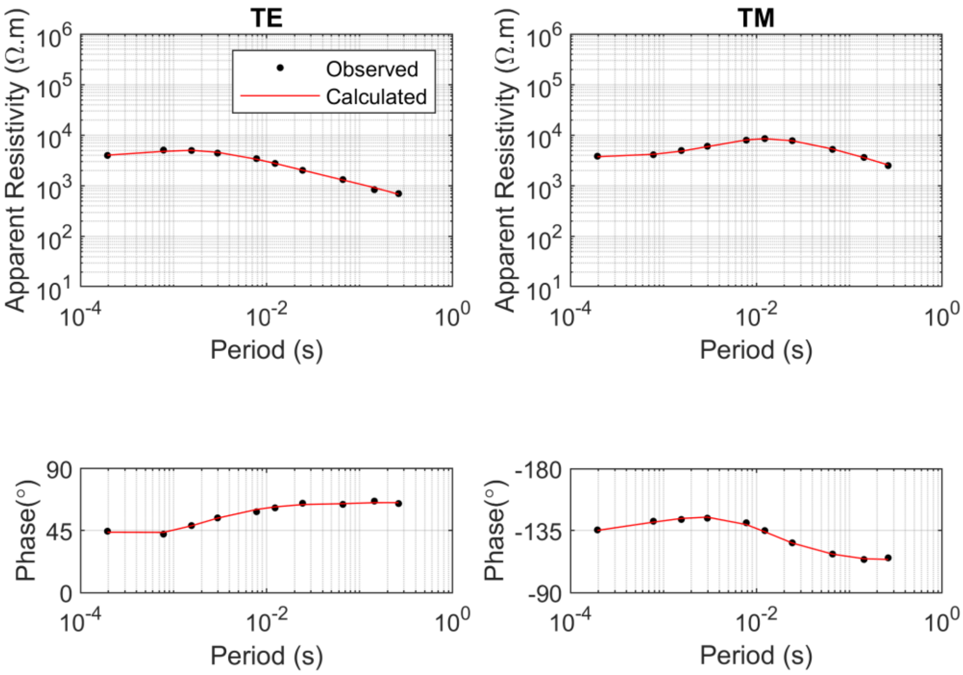

Fits of Apparent Resistivity and Phase for station #65

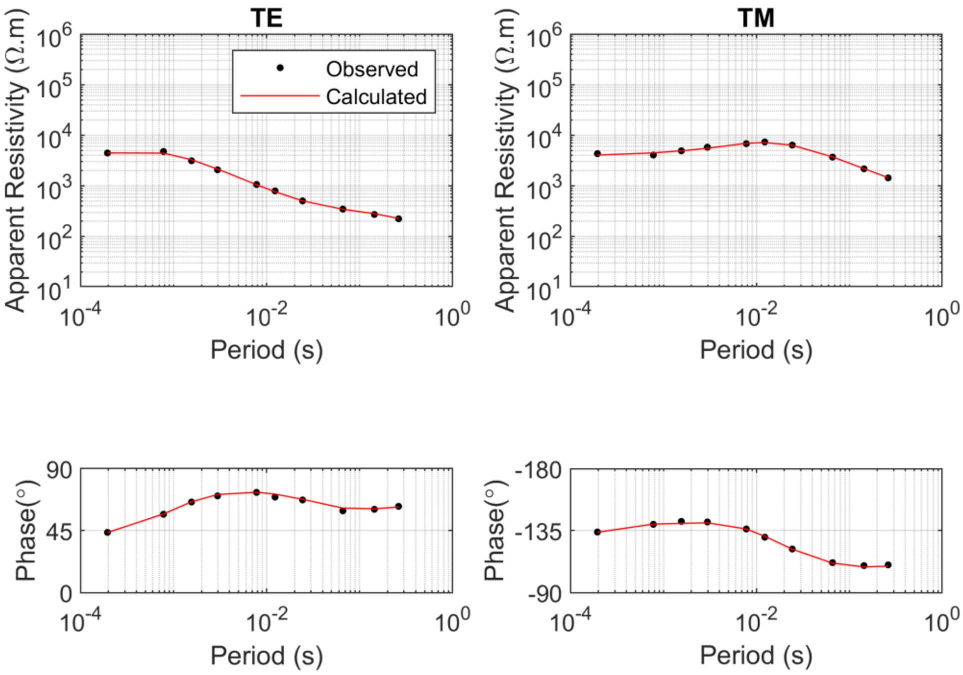

Fits of Apparent Resistivity and Phase for station #66

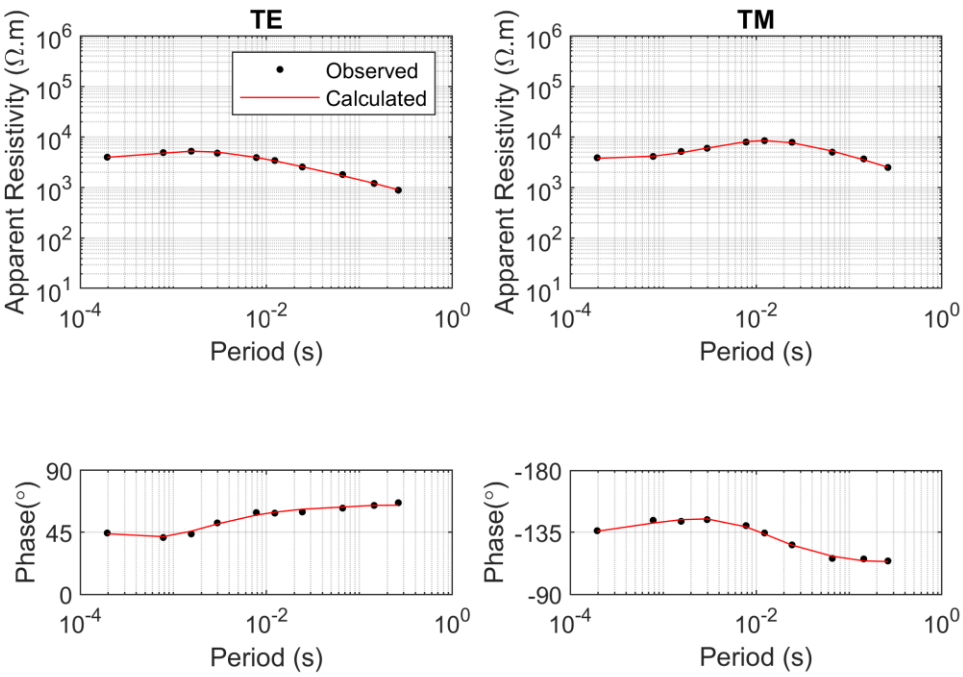

Fits of Apparent Resistivity and Phase for station #67

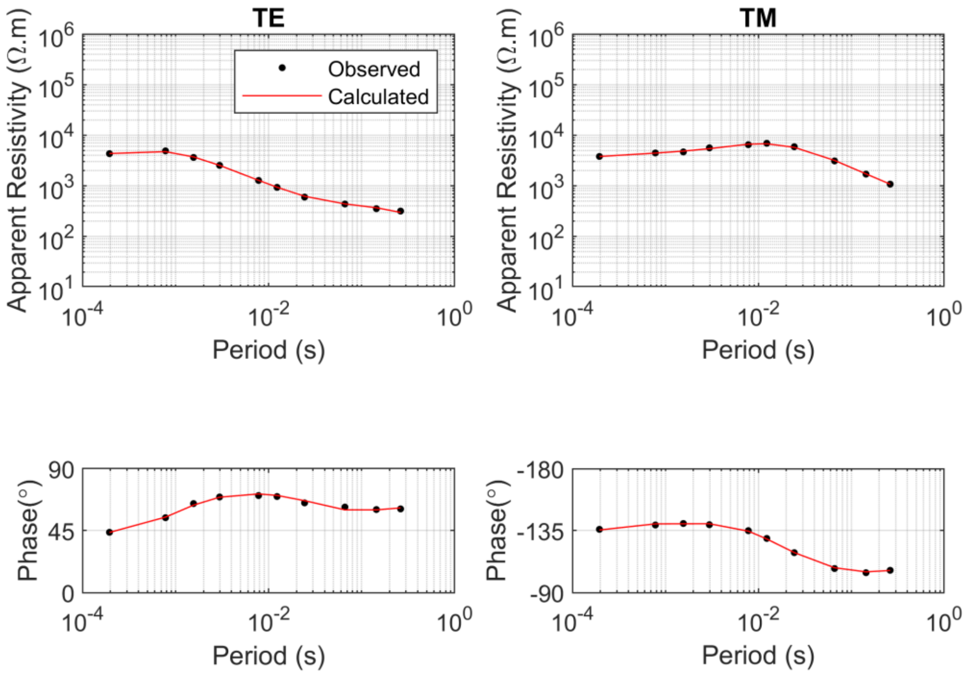

Fits of Apparent Resistivity and Phase for station #68

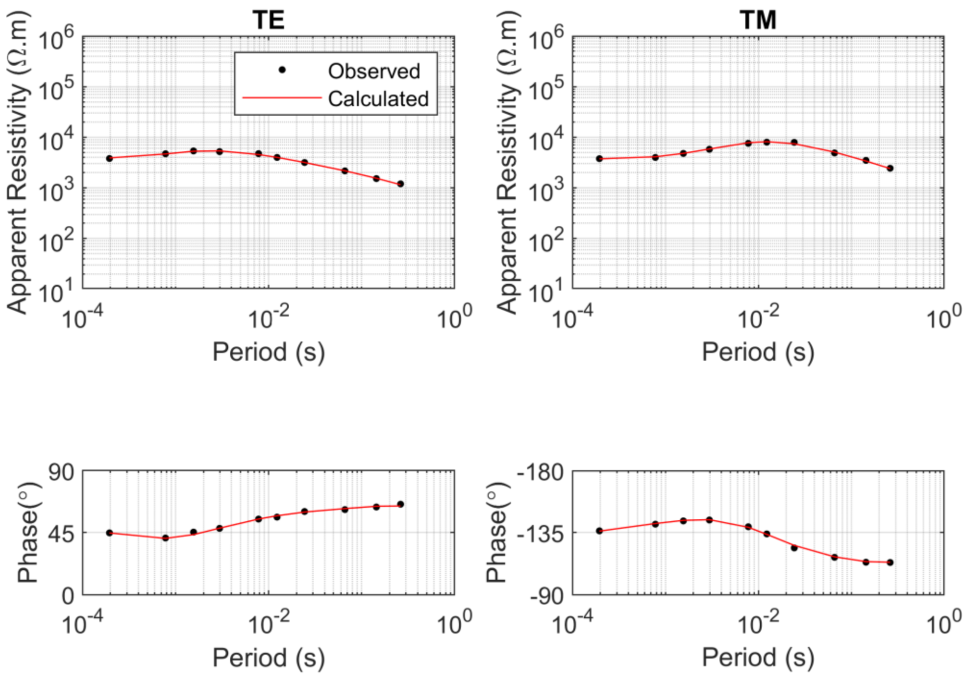

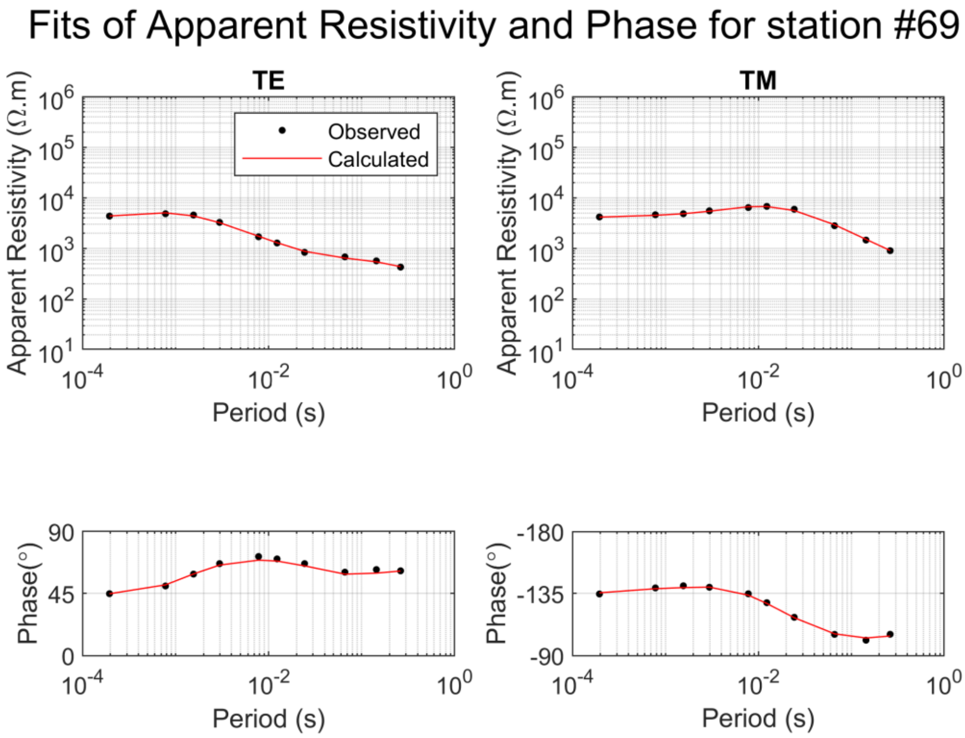
Fits of Apparent Resistivity and Phase for station #69
TE
TM
Observed
Calculated
Apparent Resistivity (Ω.m)
Phase(°)
Period (s)

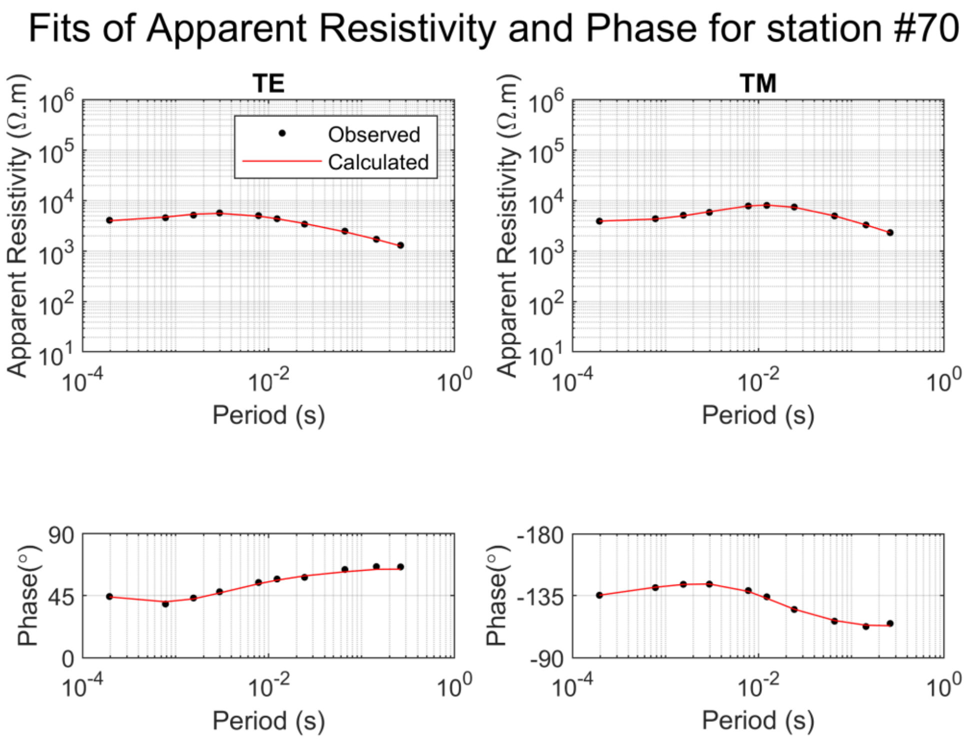
Fits of Apparent Resistivity and Phase for station #70
TE
TM
Observed
Calculated
Apparent Resistivity (Ω.m)
Phase(°)
Period (s)

Fits of Apparent Resistivity and Phase for station #71

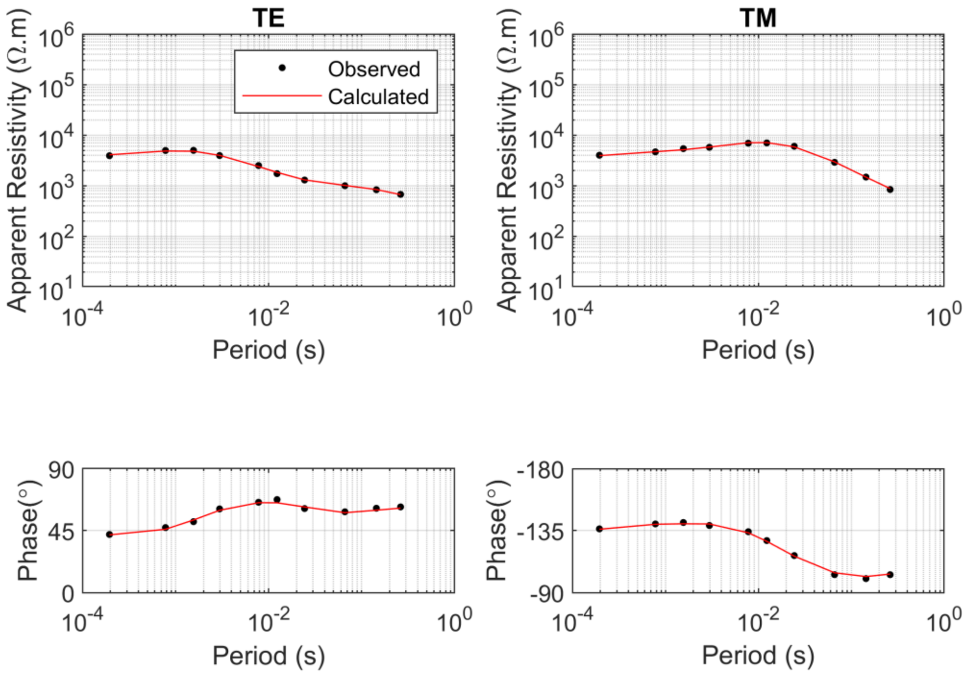

Fits of Apparent Resistivity and Phase for station #72

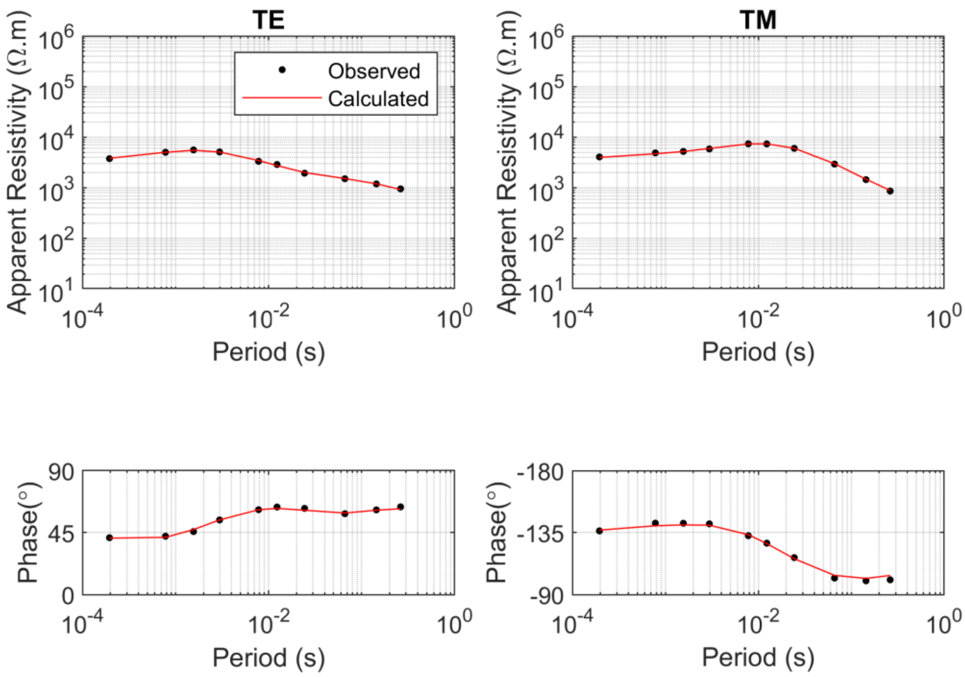

Fits of Apparent Resistivity and Phase for station #73

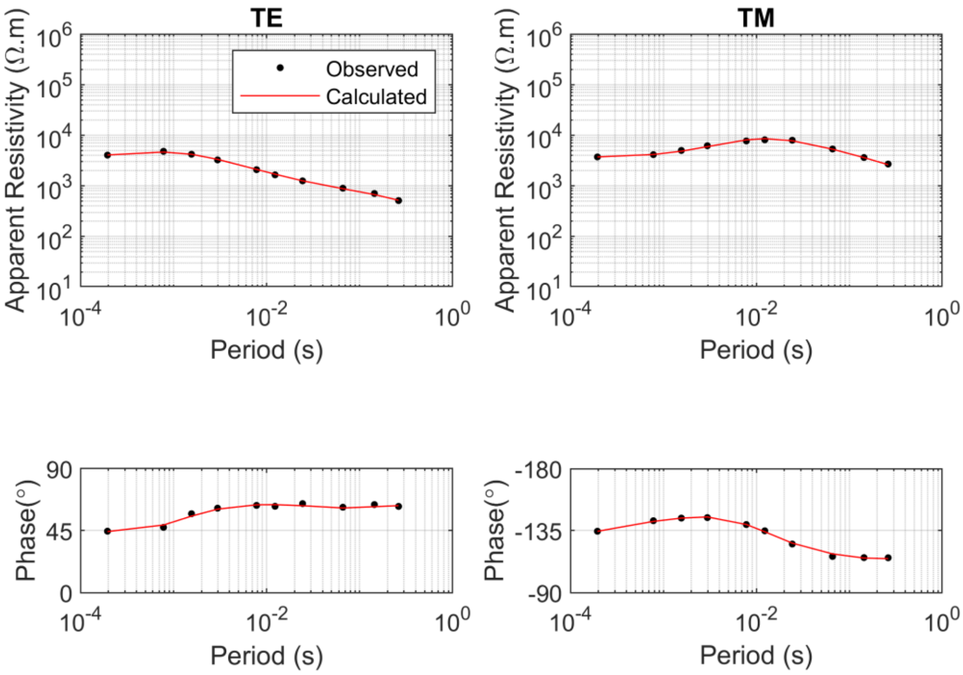

Fits of Apparent Resistivity and Phase for station #74

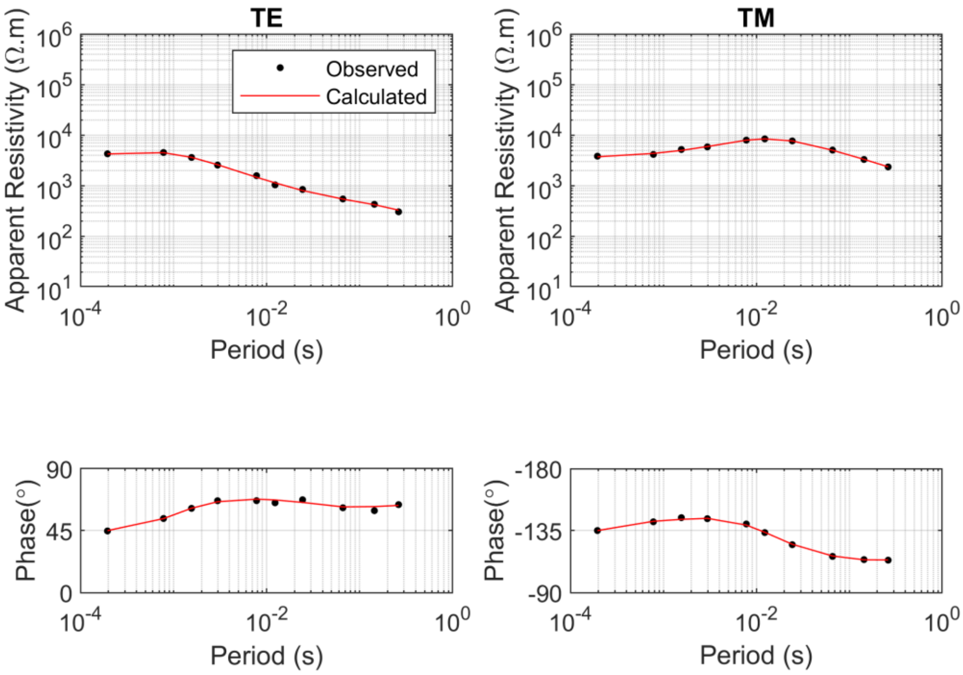

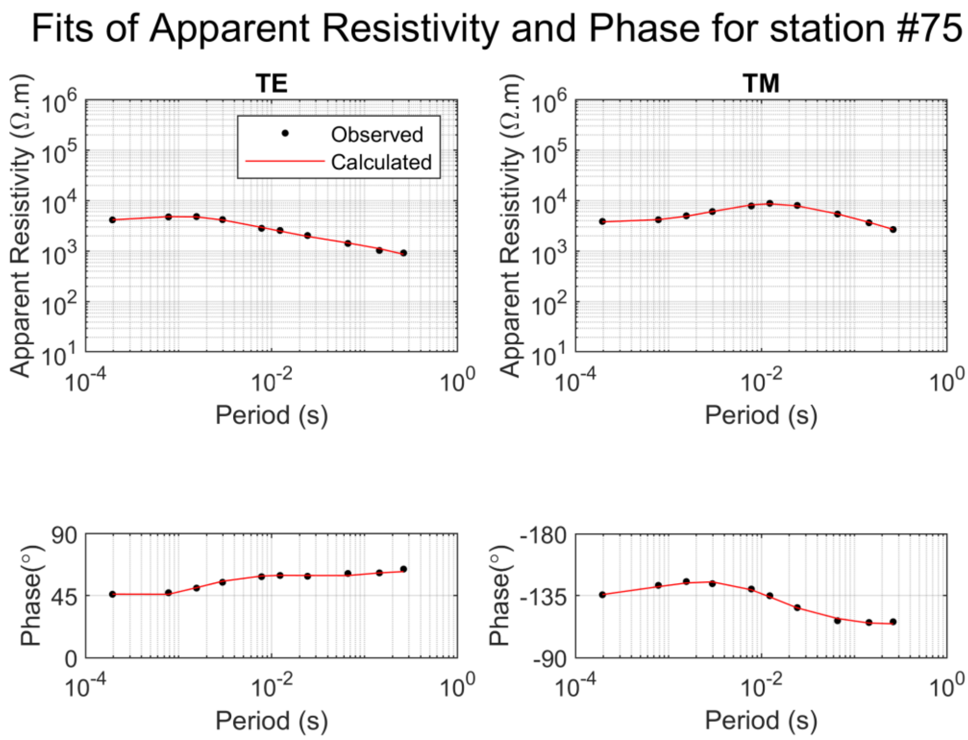
Fits of Apparent Resistivity and Phase for station #75
TE
TM
Observed
Calculated
Apparent Resistivity (Ω.m)
Phase(°)
Period (s)
90
45
0
-180
-135
-90

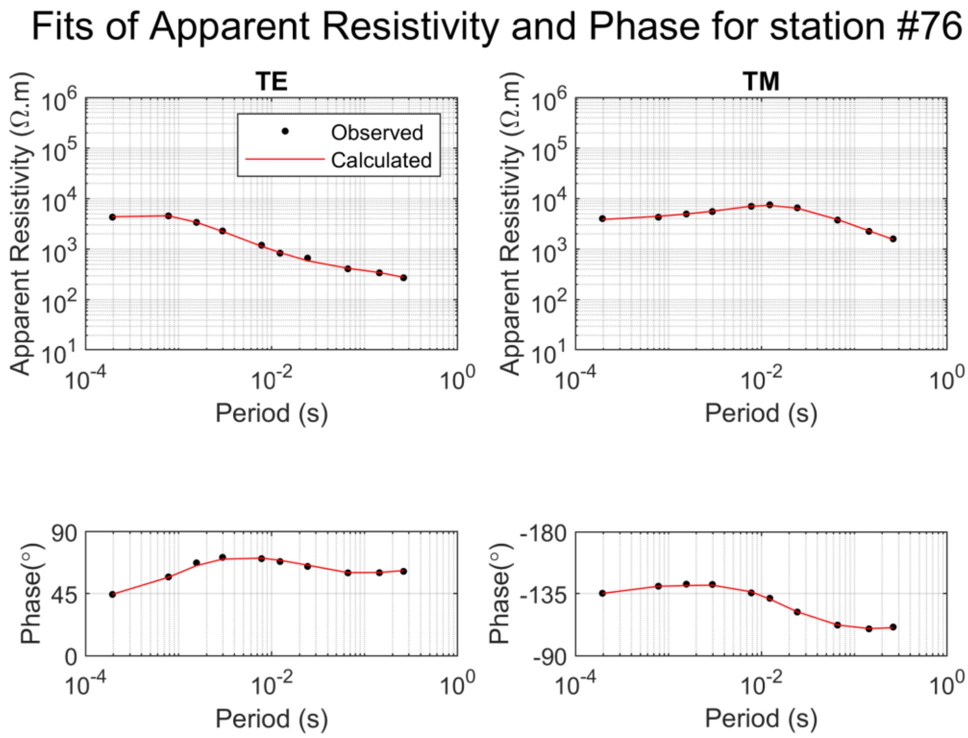
Fits of Apparent Resistivity and Phase for station #76
TE
TM
Observed
Calculated
Apparent Resistivity (Ω.m)
Phase(°)
Period (s)
90
45
0
-180
-135
-90

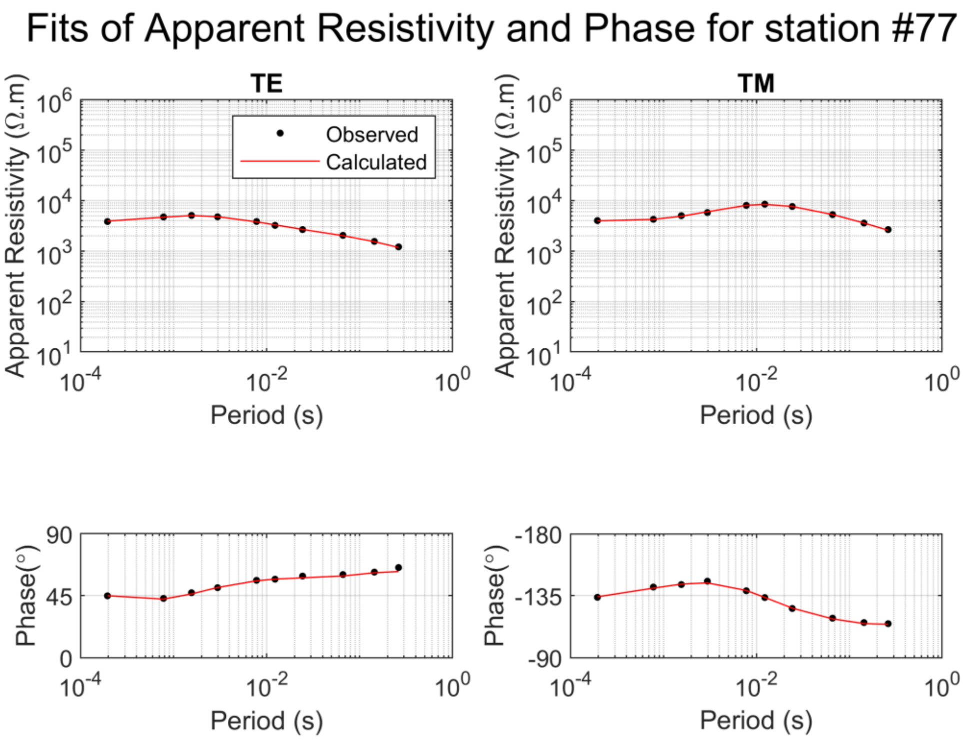
Fits of Apparent Resistivity and Phase for station #77
TE
TM
Observed
Calculated
Apparent Resistivity (Ω.m)
Period (s)
Phase(°)

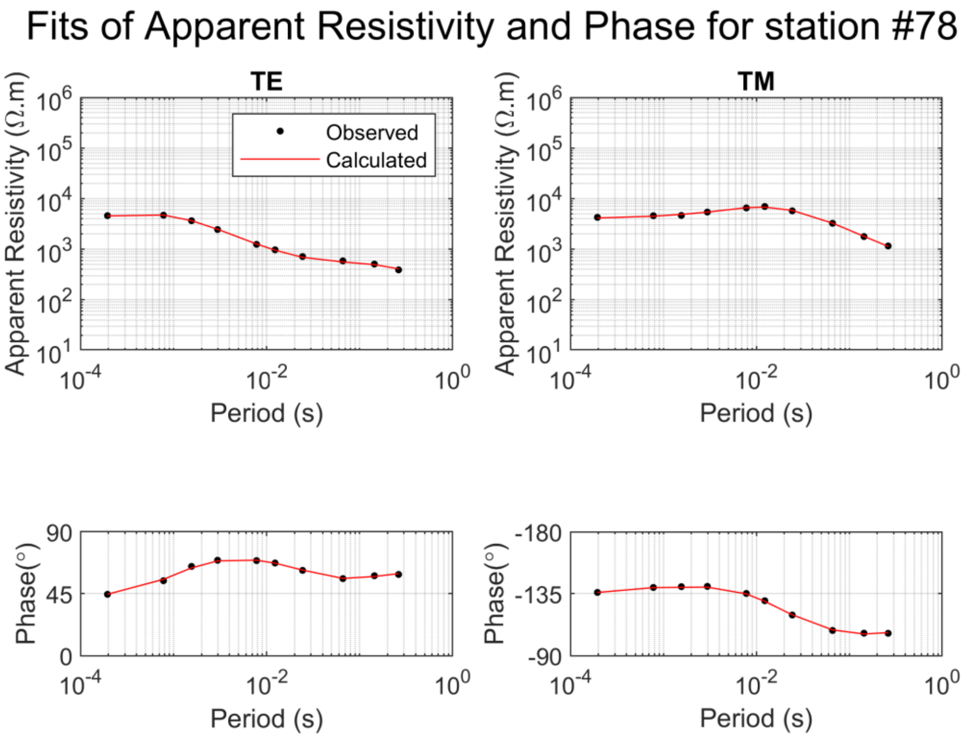
Fits of Apparent Resistivity and Phase for station #78
TE
TM
Observed
Calculated
Apparent Resistivity (Ω.m)
Period (s)
Phase(°)

Fits of Apparent Resistivity and Phase for station #79

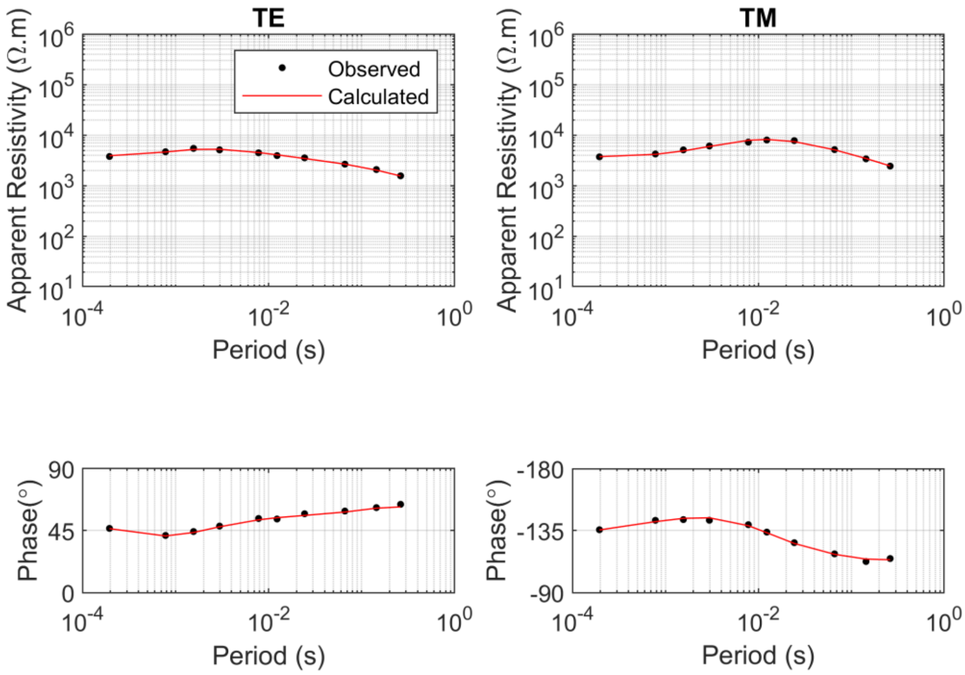

Fits of Apparent Resistivity and Phase for station #80

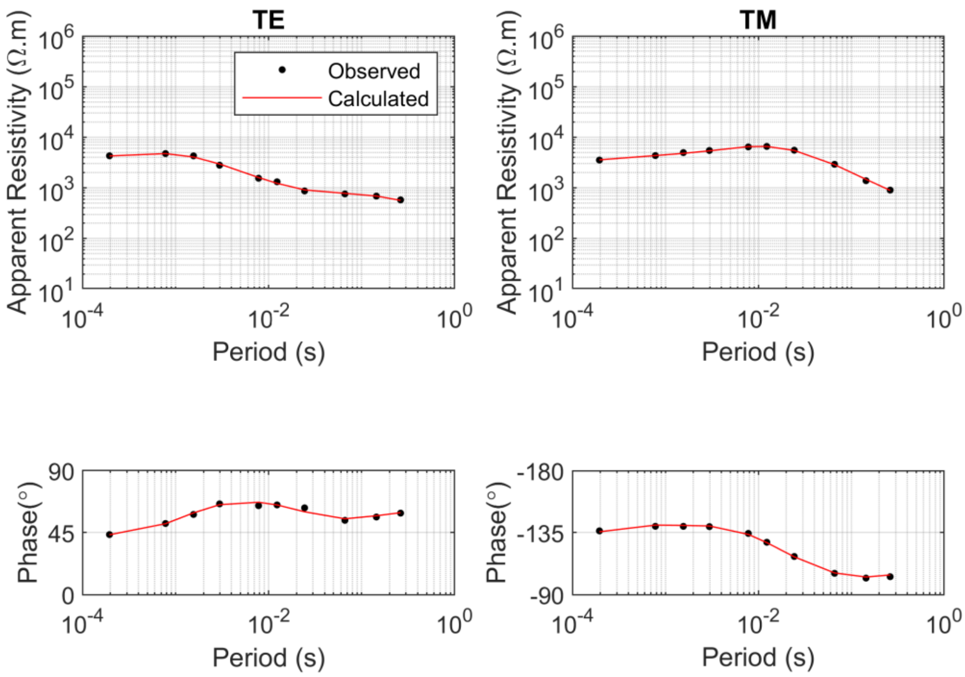

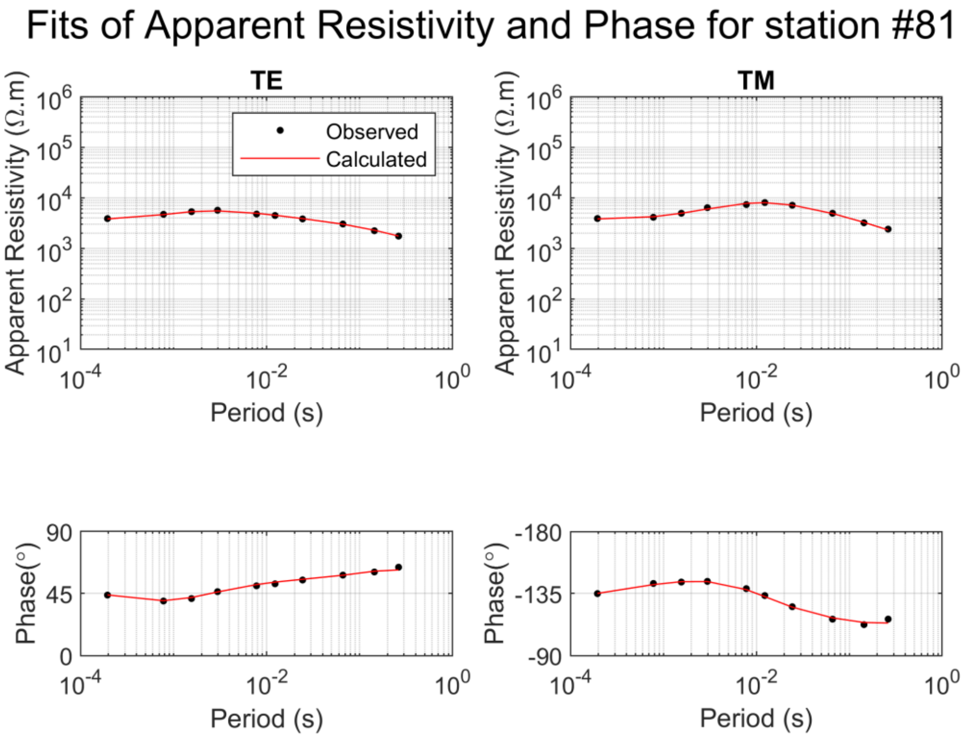
Fits of Apparent Resistivity and Phase for station #81
TE
TM
Observed
Calculated
Apparent Resistivity (Ω.m)
Period (s)
Phase(°)
10^{1} 10^{2} 10^{3} 10^{4} 10^{5} 10^{6}
10^{-4} 10^{-2} 10^{0}
0 45 90
-90 -135 -180

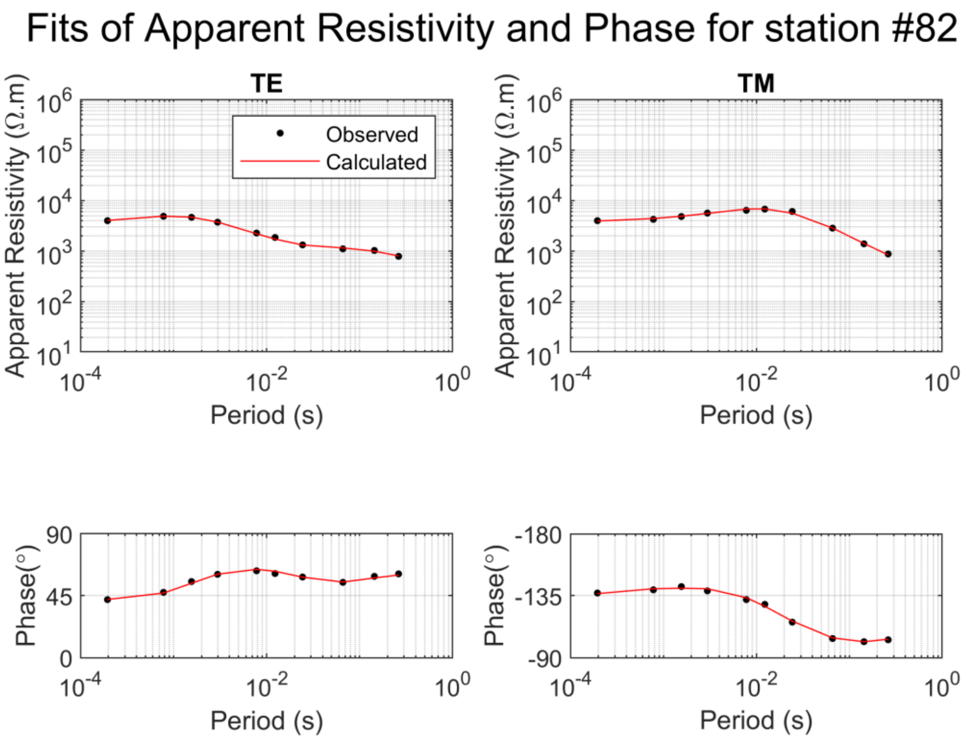
Fits of Apparent Resistivity and Phase for station #82
TE
TM
Observed
Calculated
Apparent Resistivity (Ω.m)
Period (s)
Phase(°)
10^{1} 10^{2} 10^{3} 10^{4} 10^{5} 10^{6}
10^{-4} 10^{-2} 10^{0}
0 45 90
-90 -135 -180

Fits of Apparent Resistivity and Phase for station #83

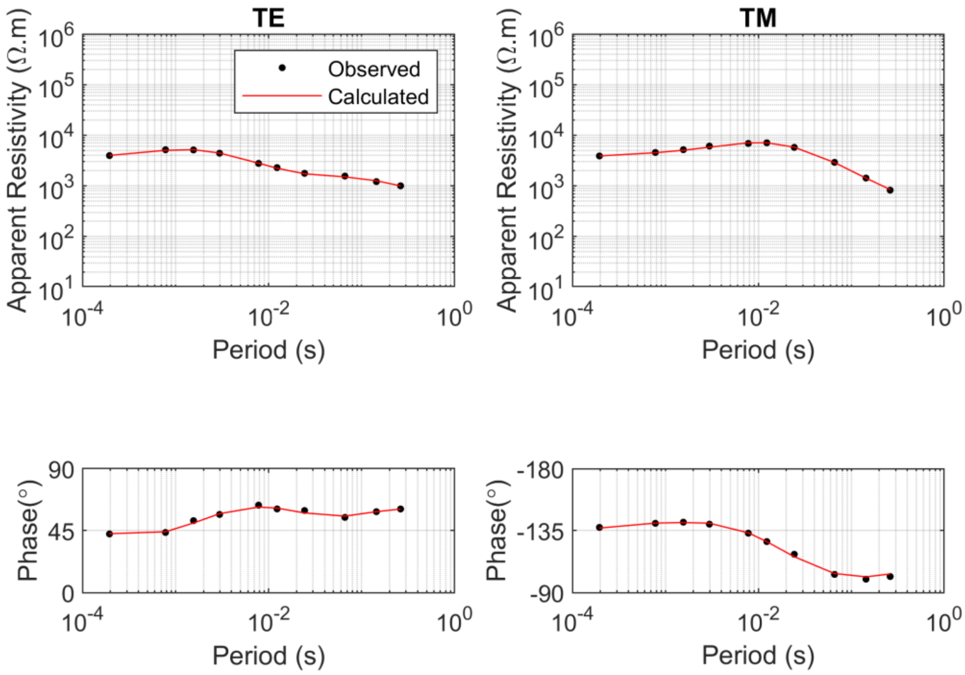

Fits of Apparent Resistivity and Phase for station #84

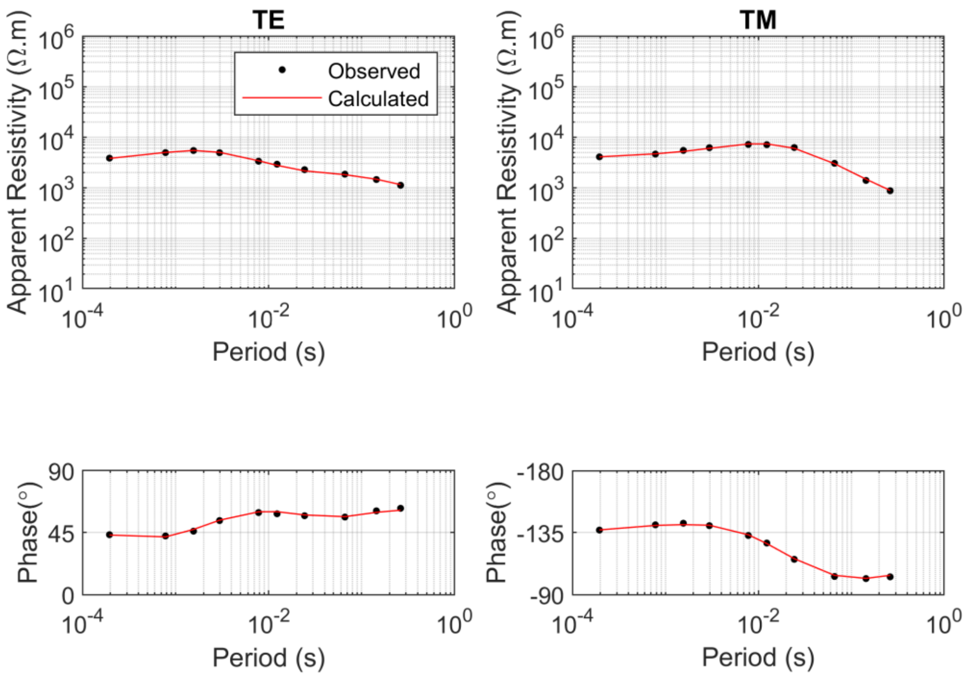

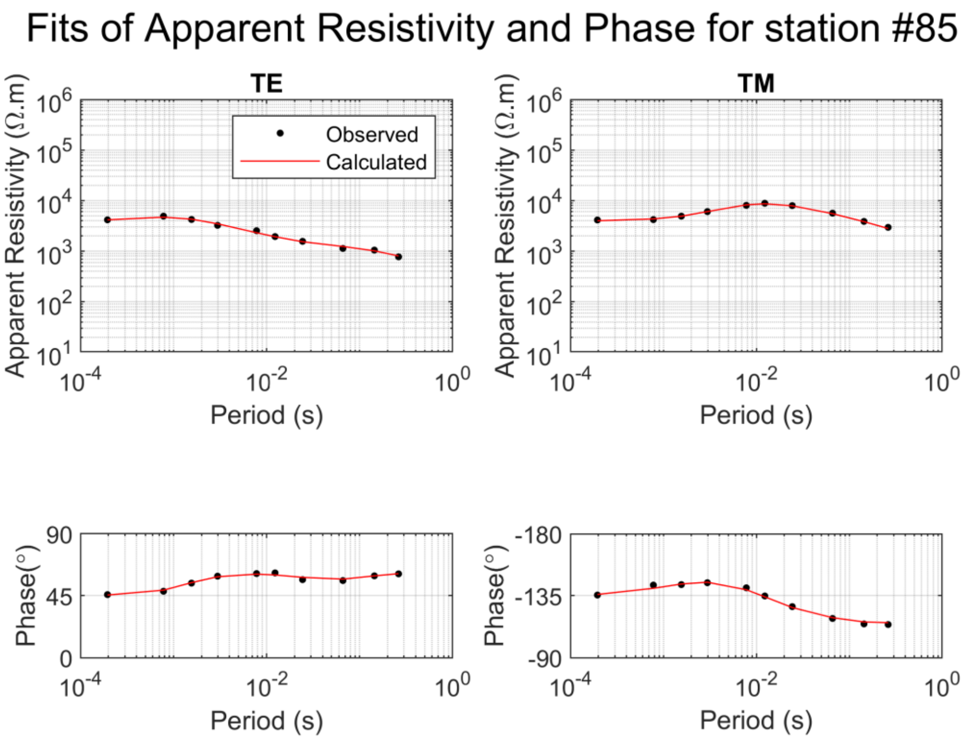

Fits of Apparent Resistivity and Phase for station #85
TE
TM
Observed
Calculated
Apparent Resistivity (Ω.m)
Period (s)
Phase(°)

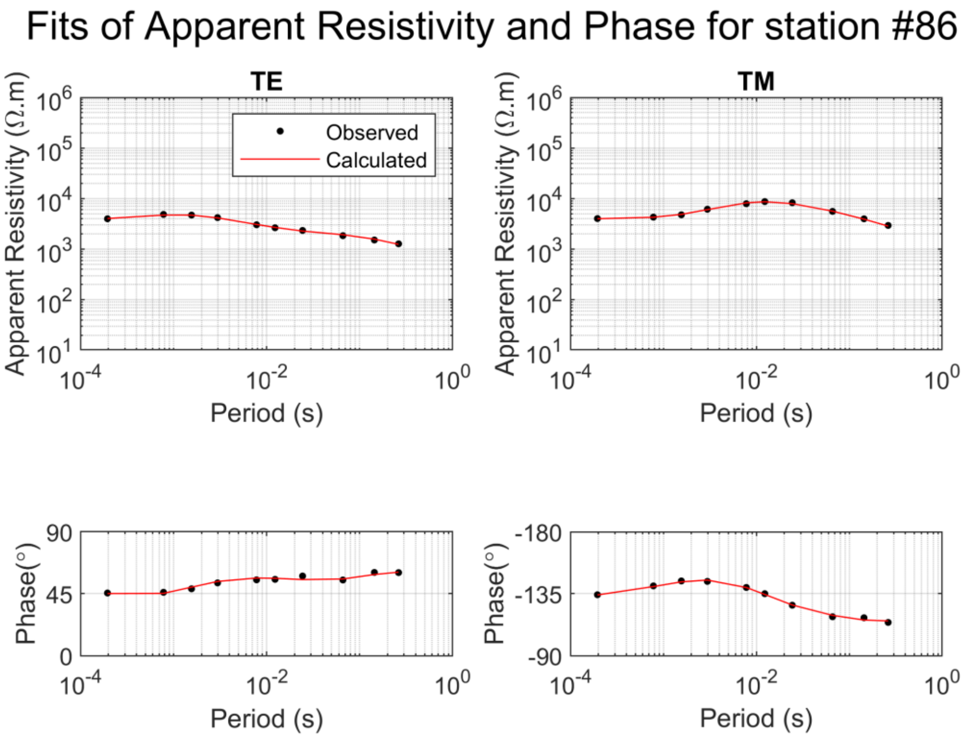

Fits of Apparent Resistivity and Phase for station #86
TE
TM
Observed
Calculated
Apparent Resistivity (Ω.m)
Period (s)
Phase(°)

Fits of Apparent Resistivity and Phase for station #87

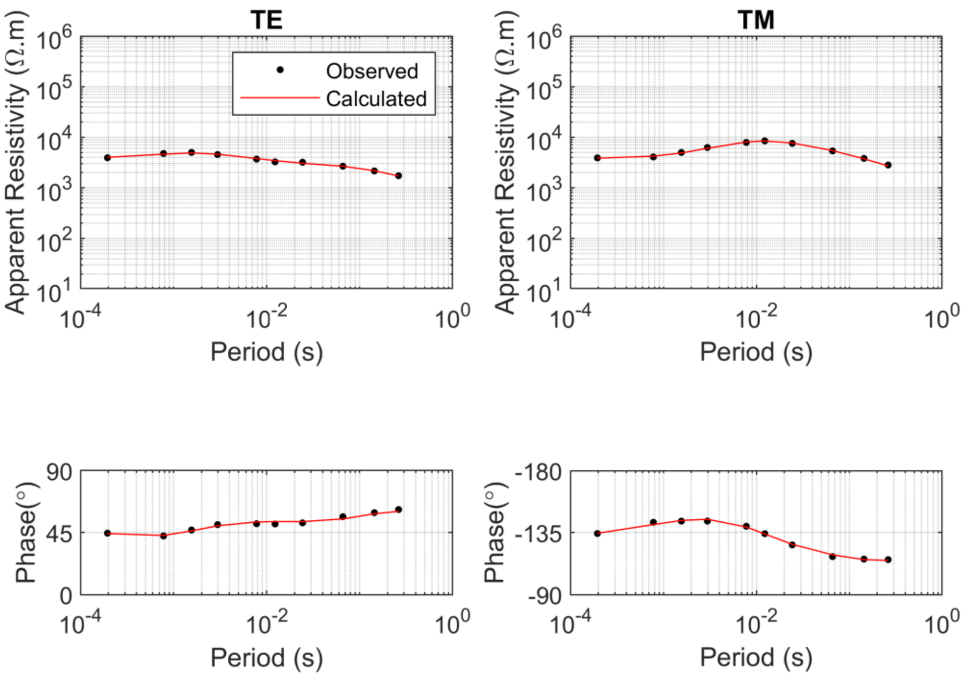

Fits of Apparent Resistivity and Phase for station #88

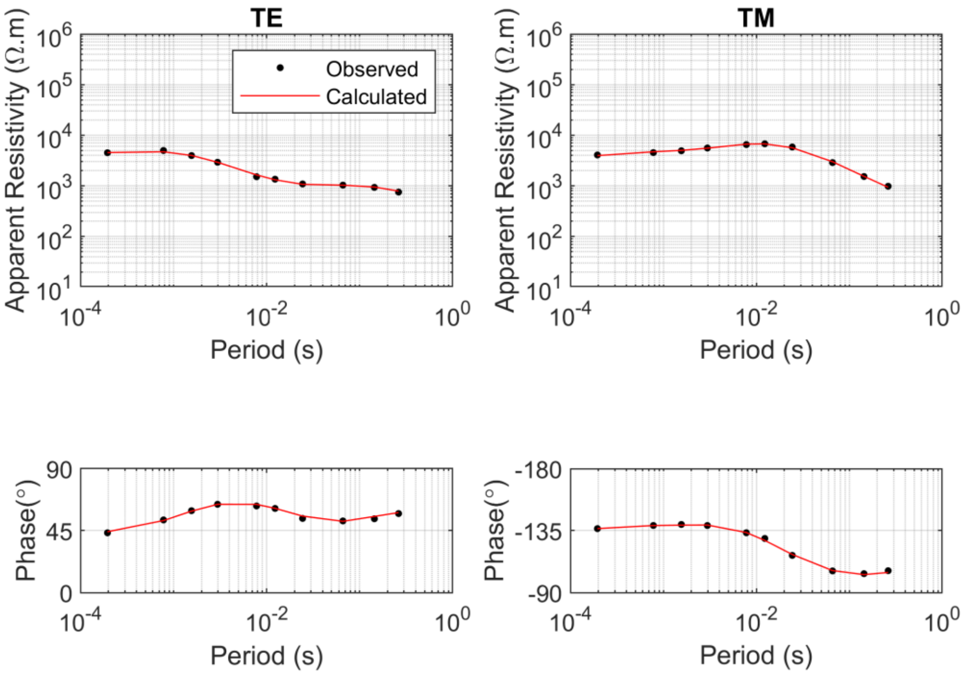

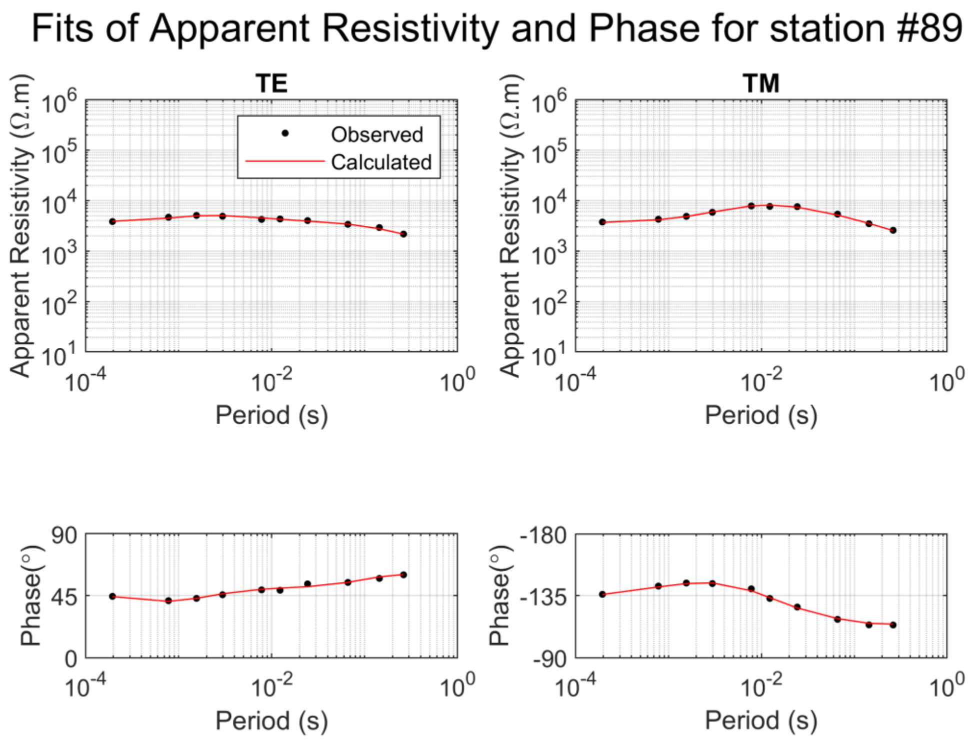

Fits of Apparent Resistivity and Phase for station #89
TE
TM
Observed
Calculated
Apparent Resistivity (Ω.m)
Period (s)
Phase(°)
10^{6}
10^{5}
10^{4}
10^{3}
10^{2}
10^{1}
10^{-4}
10^{-2}
10^{0}
90
45
0
-180
-135
-90

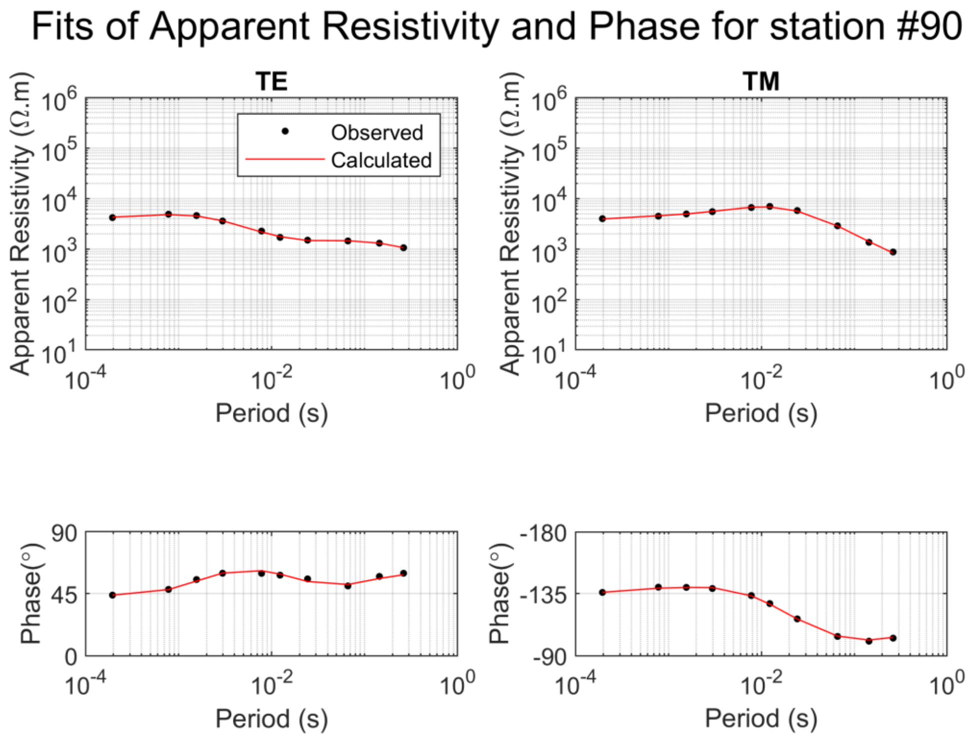

Fits of Apparent Resistivity and Phase for station #90
TE
TM
Observed
Calculated
Apparent Resistivity (Ω.m)
Period (s)
Phase(°)
10^{6}
10^{5}
10^{4}
10^{3}
10^{2}
10^{1}
10^{-4}
10^{-2}
10^{0}
90
45
0
-180
-135
-90

Fits of Apparent Resistivity and Phase for station #91

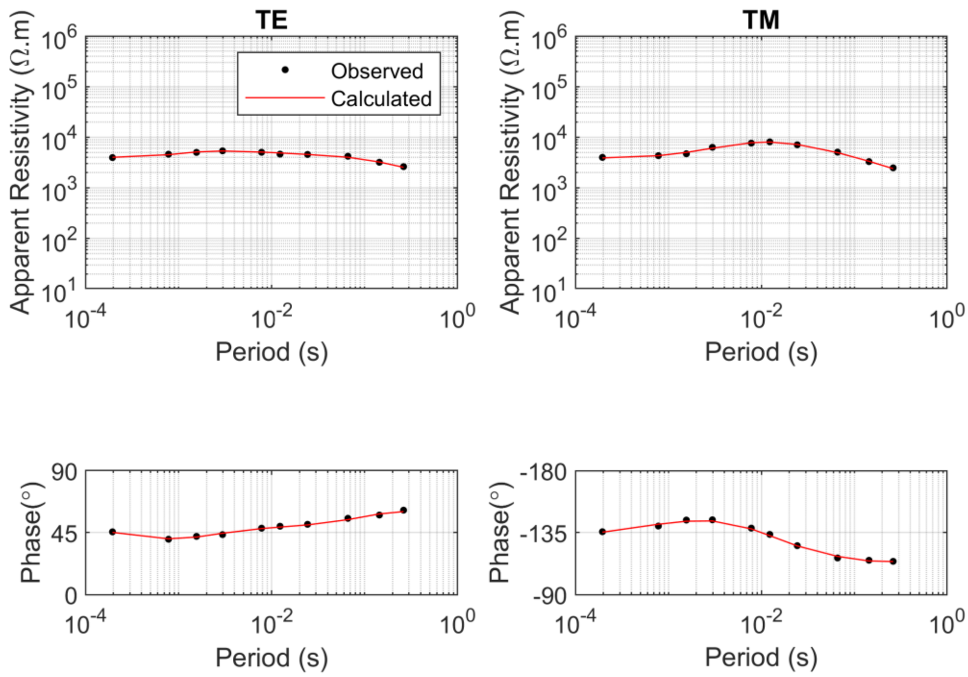

Fits of Apparent Resistivity and Phase for station #92

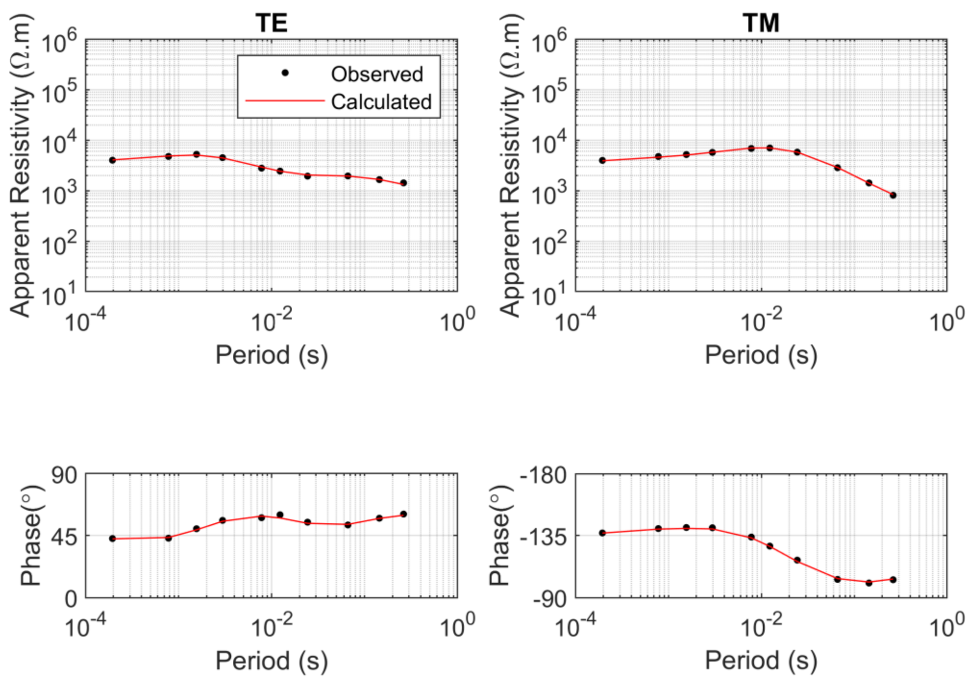

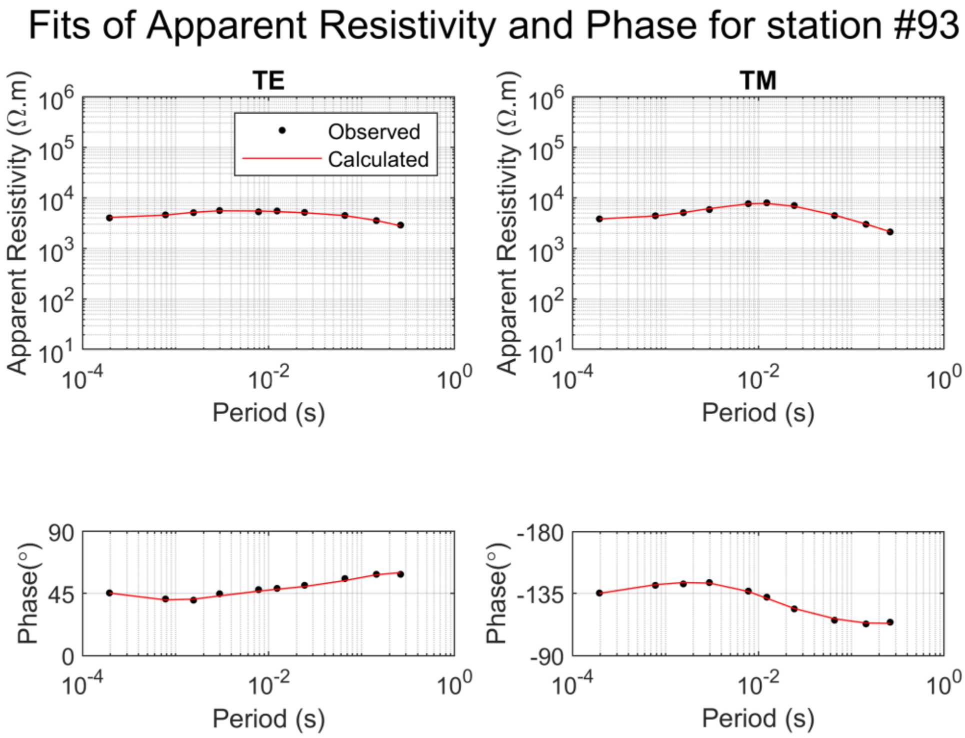
Fits of Apparent Resistivity and Phase for station #93
TE
TM
Observed
Calculated
Apparent Resistivity (Ω.m)
Phase(°)
Period (s)
90
45
0
-180
-135
-90

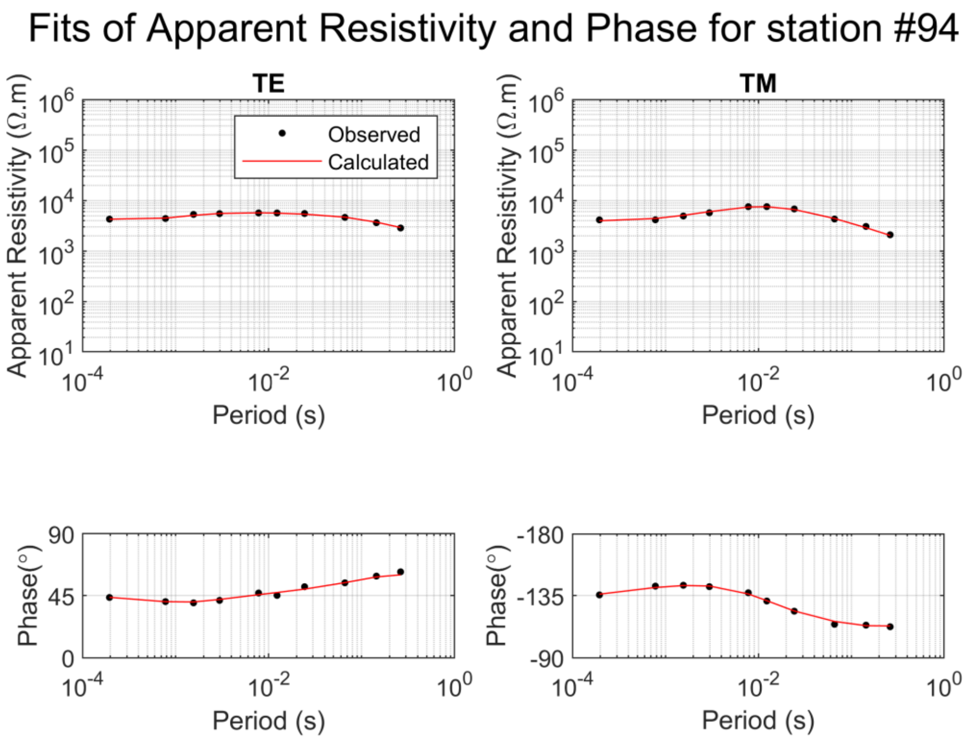
Fits of Apparent Resistivity and Phase for station #94
TE
TM
Observed
Calculated
Apparent Resistivity (Ω.m)
Phase(°)
Period (s)
90
45
0
-180
-135
-90

Fits of Apparent Resistivity and Phase for station #95

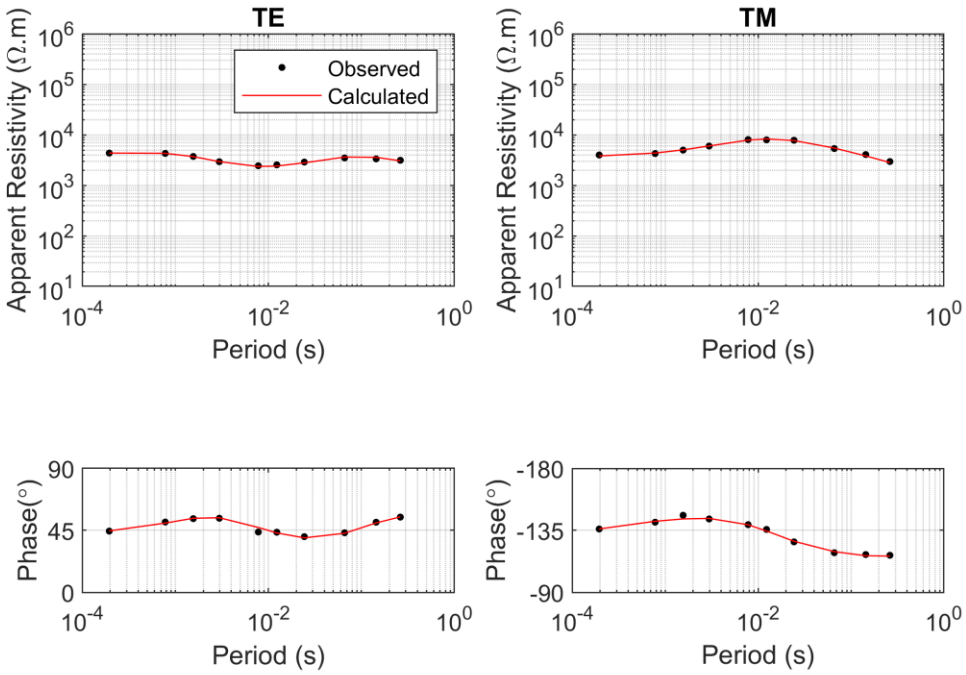

Fits of Apparent Resistivity and Phase for station #96

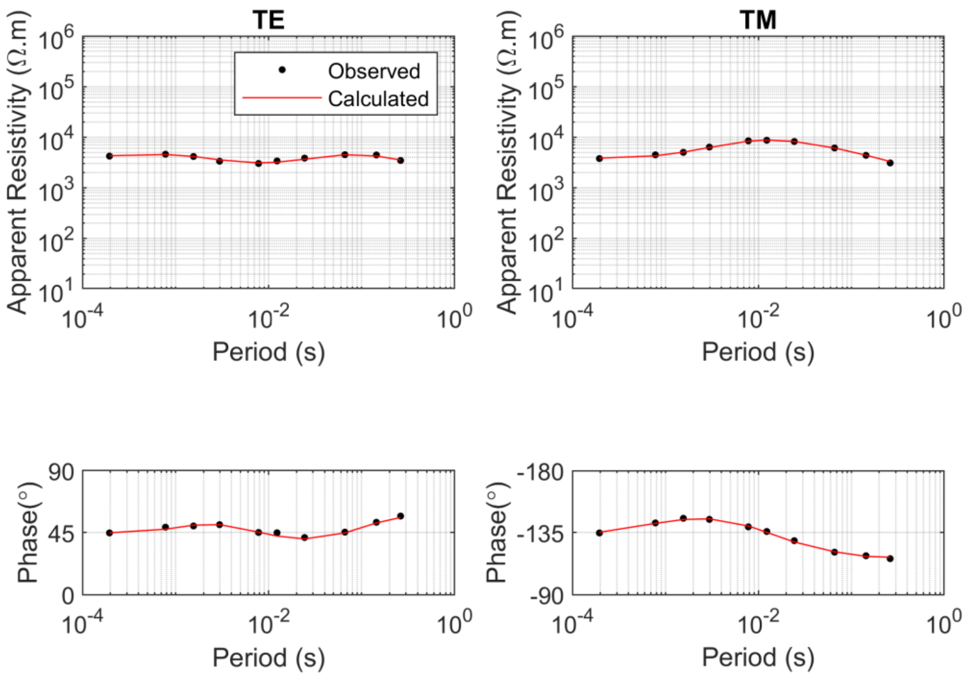

Fits of Apparent Resistivity and Phase for station #97

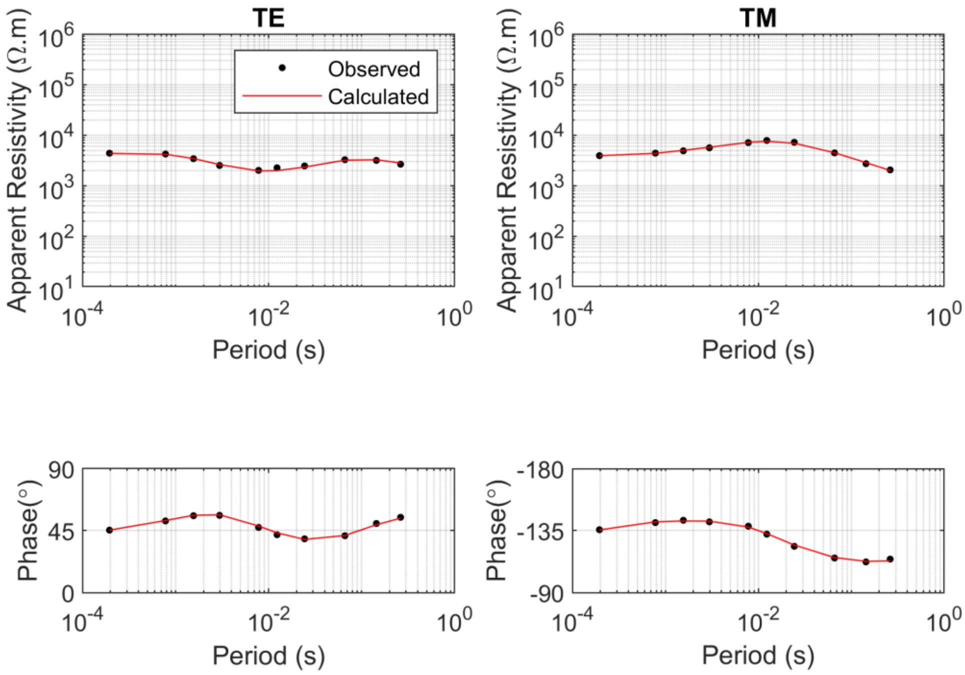

Fits of Apparent Resistivity and Phase for station #98

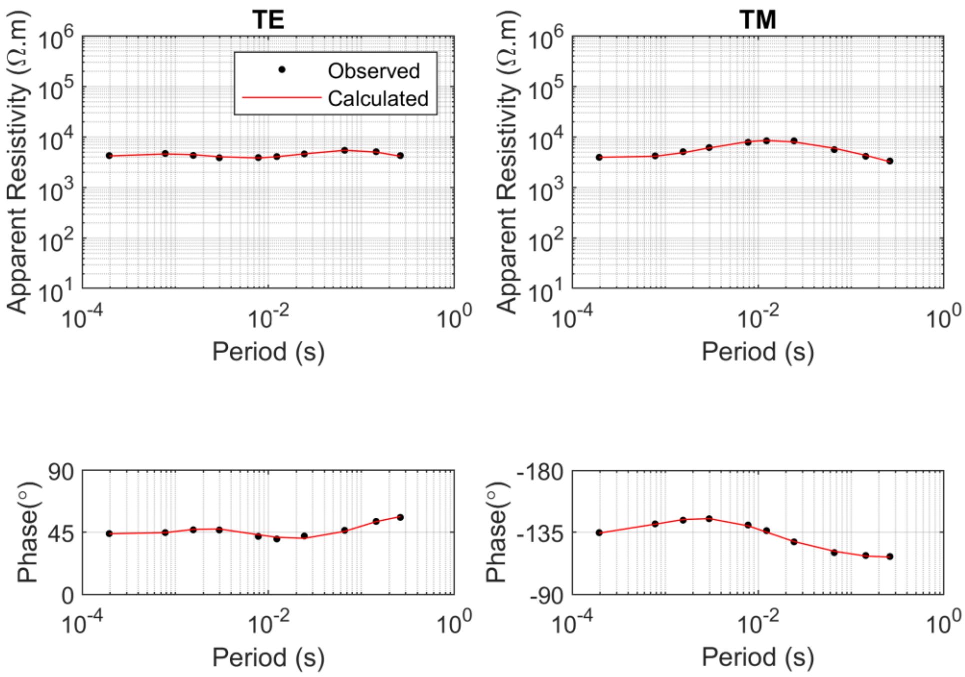

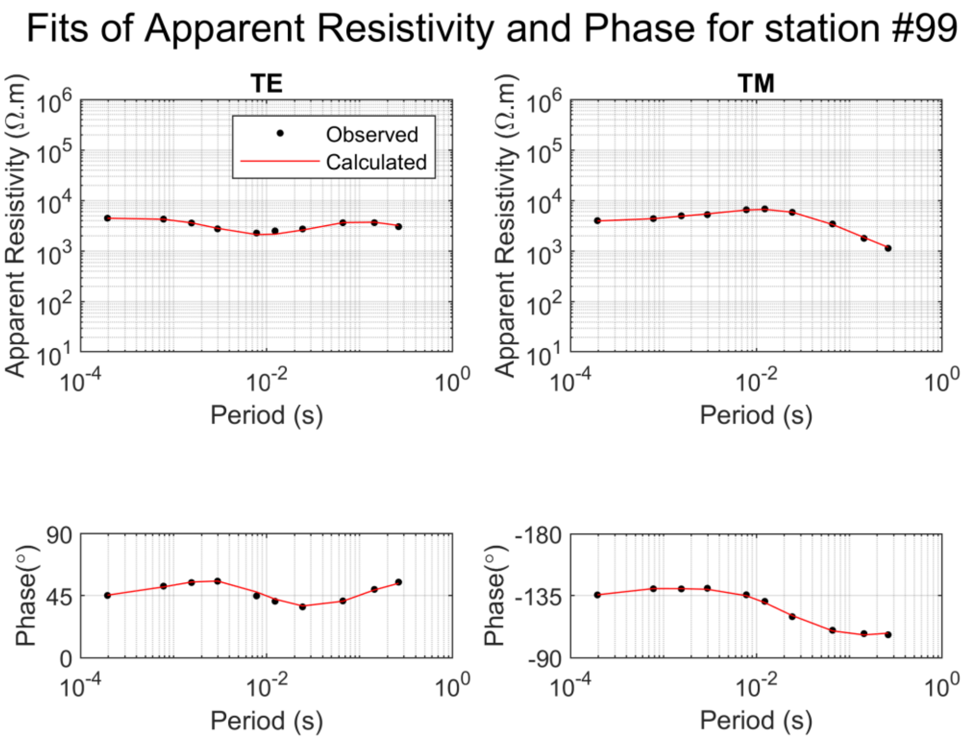
Fits of Apparent Resistivity and Phase for station #99
TE
TM
Observed
Calculated
Apparent Resistivity (Ω.m)
Period (s)
Phase(°)

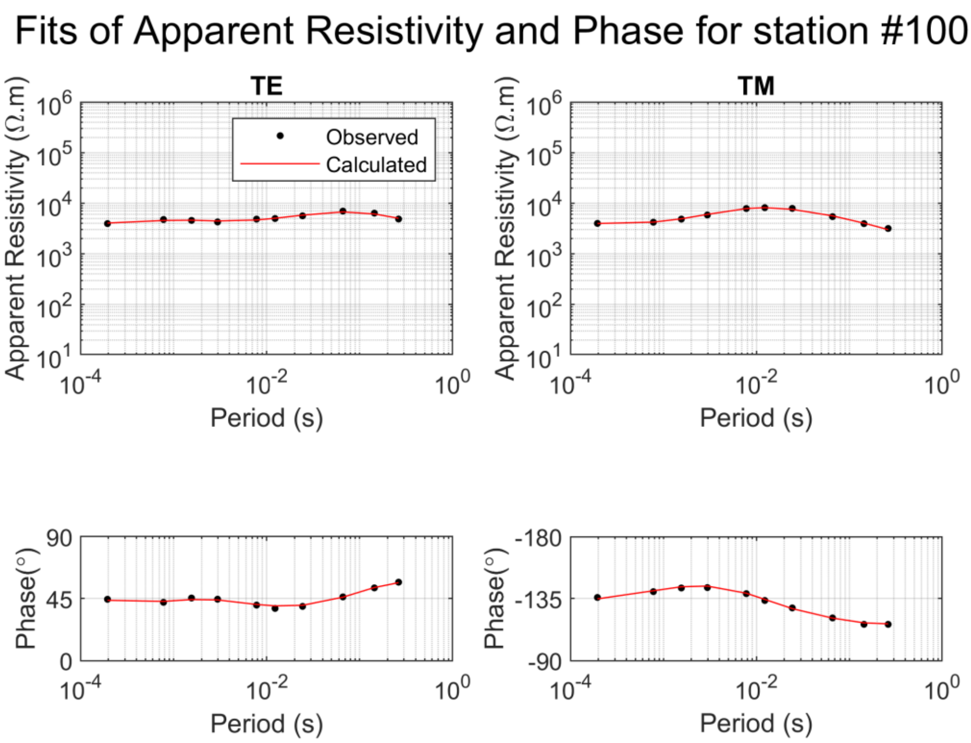
Fits of Apparent Resistivity and Phase for station #100
TE
TM
Observed
Calculated
Apparent Resistivity (Ω.m)
Period (s)
Phase(°)

Fits of Apparent Resistivity and Phase for station #101

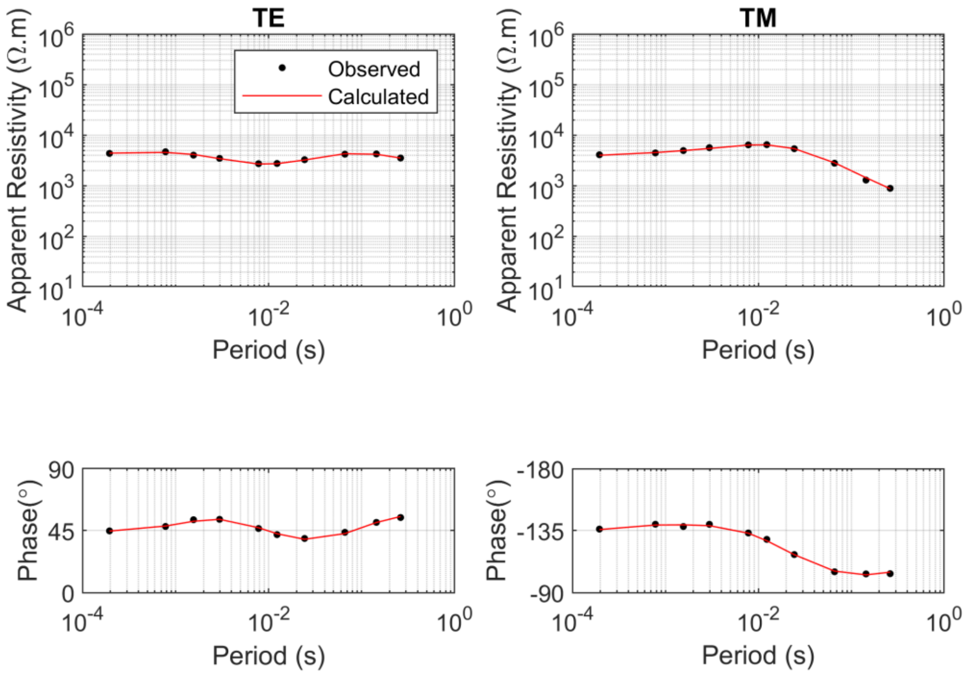

Fits of Apparent Resistivity and Phase for station #102

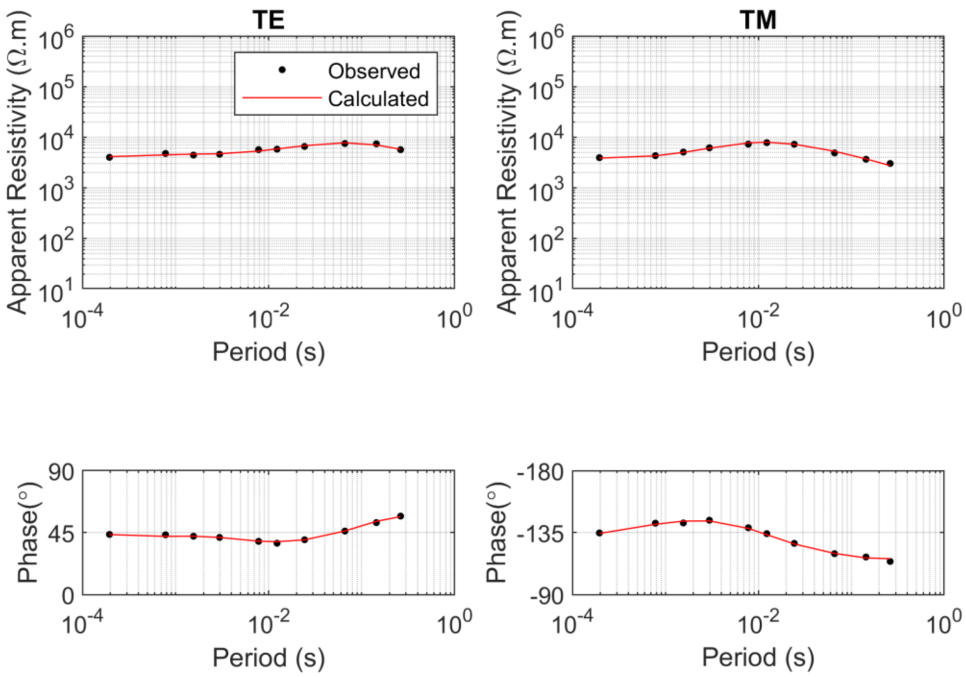

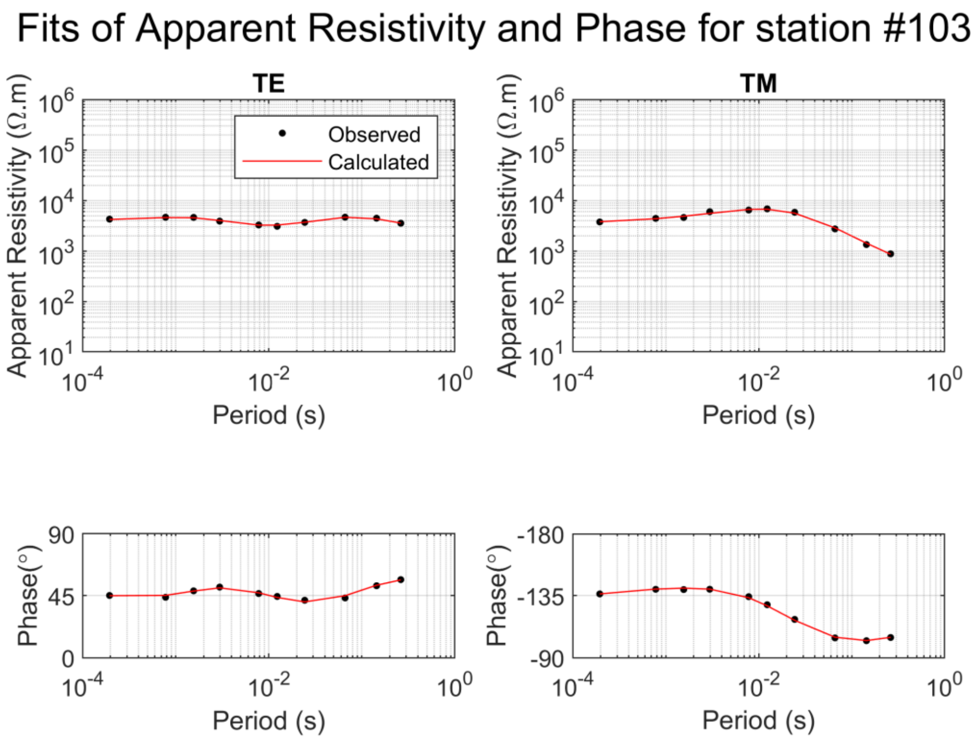
Fits of Apparent Resistivity and Phase for station #103
TE
TM
Observed
Calculated
Apparent Resistivity (Ω.m)
Period (s)
Phase(°)

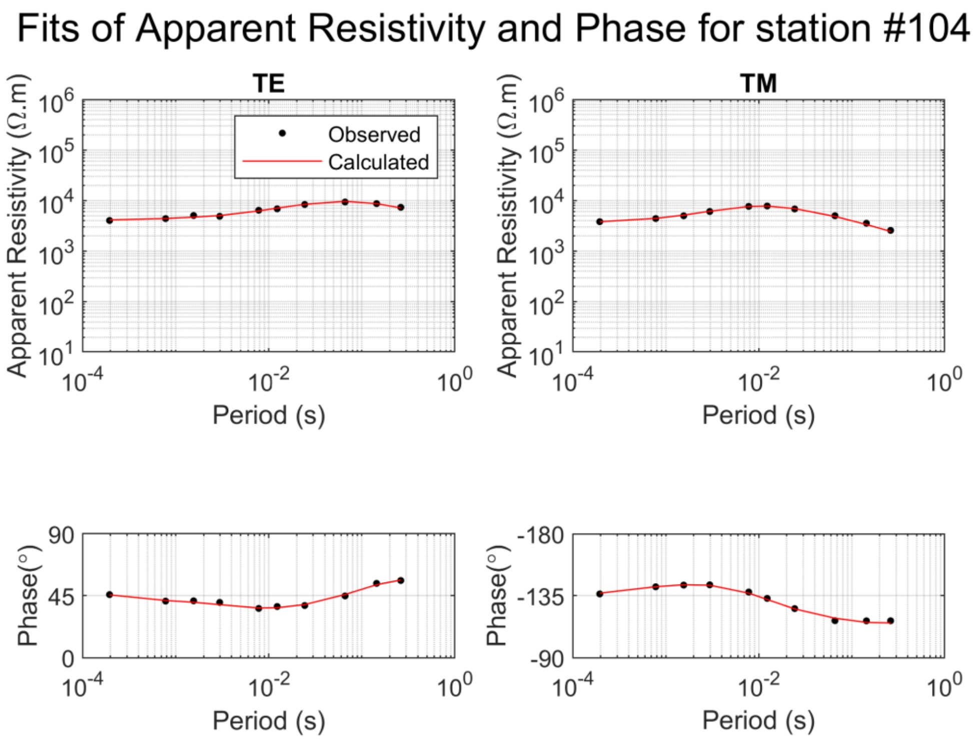
Fits of Apparent Resistivity and Phase for station #104
TE
TM
Observed
Calculated
Apparent Resistivity (Ω.m)
Period (s)
Phase(°)

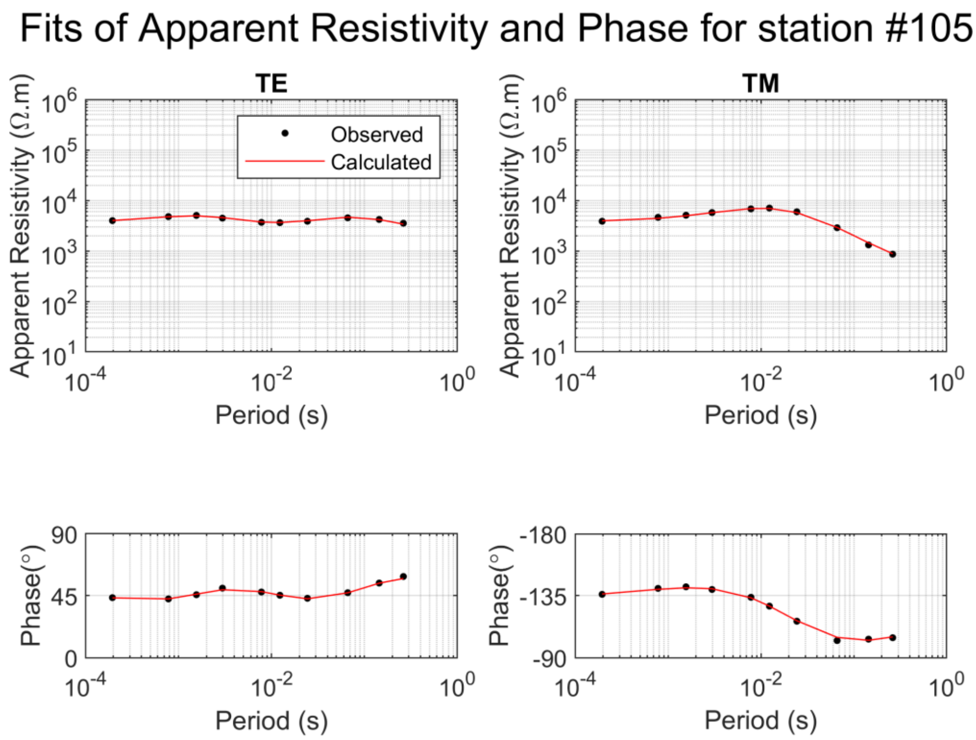
Fits of Apparent Resistivity and Phase for station #105
TE
TM
Observed
Calculated
Apparent Resistivity (Ω.m)
Phase(°)
Period (s)

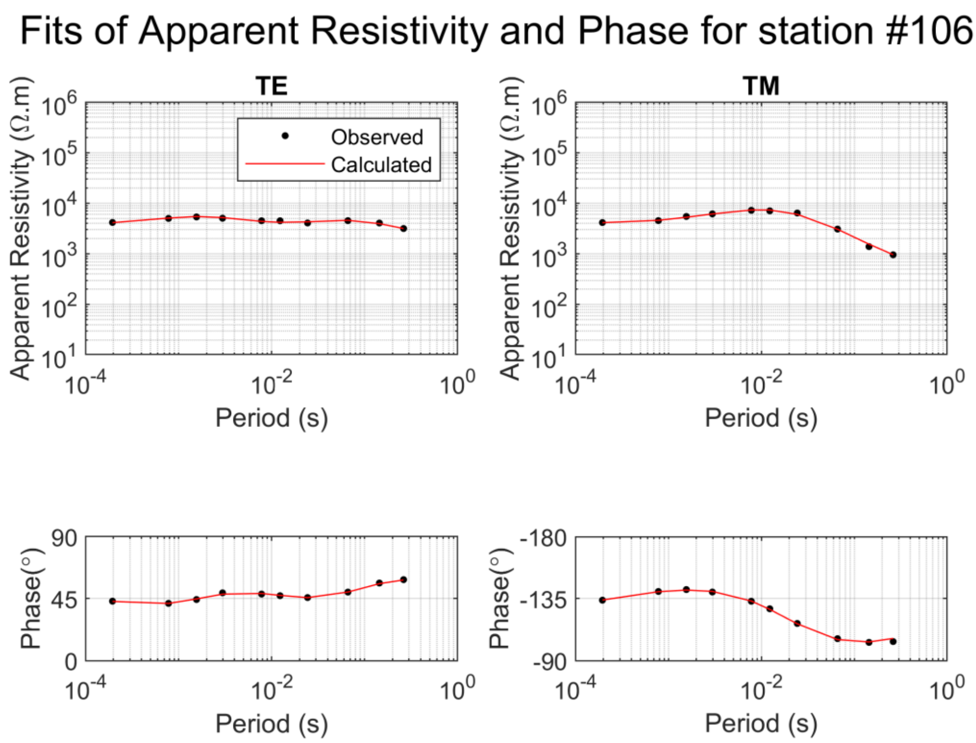
Fits of Apparent Resistivity and Phase for station #106
TE
TM
Observed
Calculated
Apparent Resistivity (Ω.m)
Phase(°)
Period (s)

Fits of Apparent Resistivity and Phase for station #107

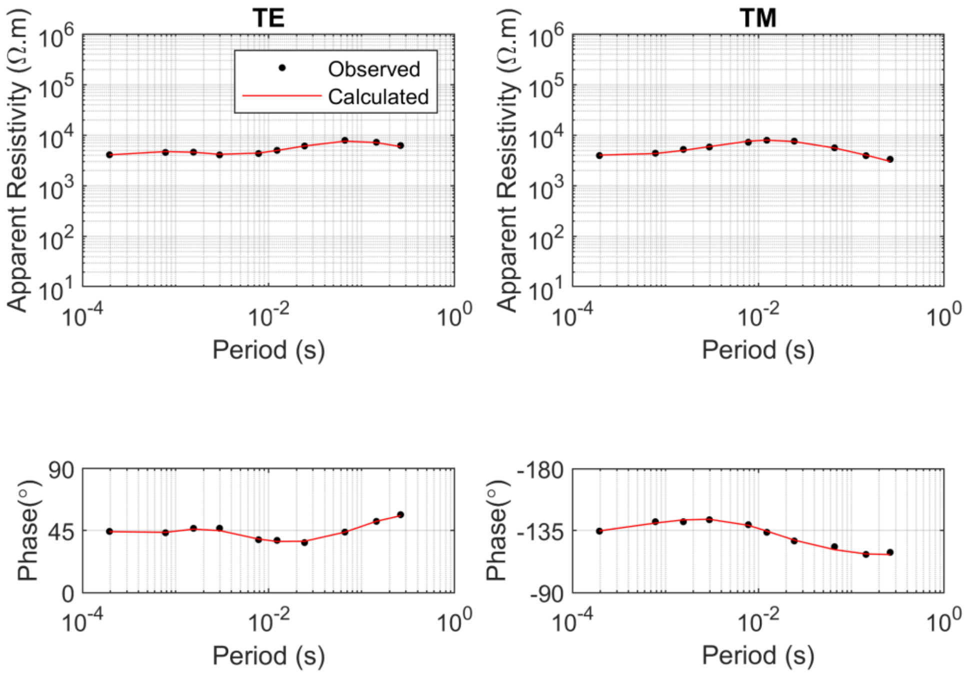

Fits of Apparent Resistivity and Phase for station #108

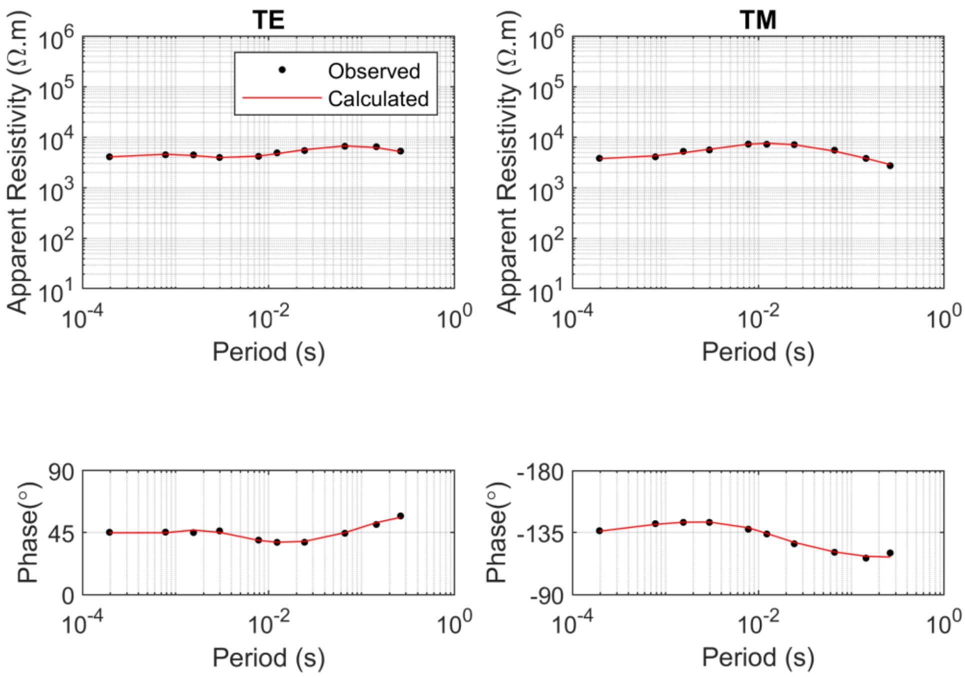

Fits of Apparent Resistivity and Phase for station #109

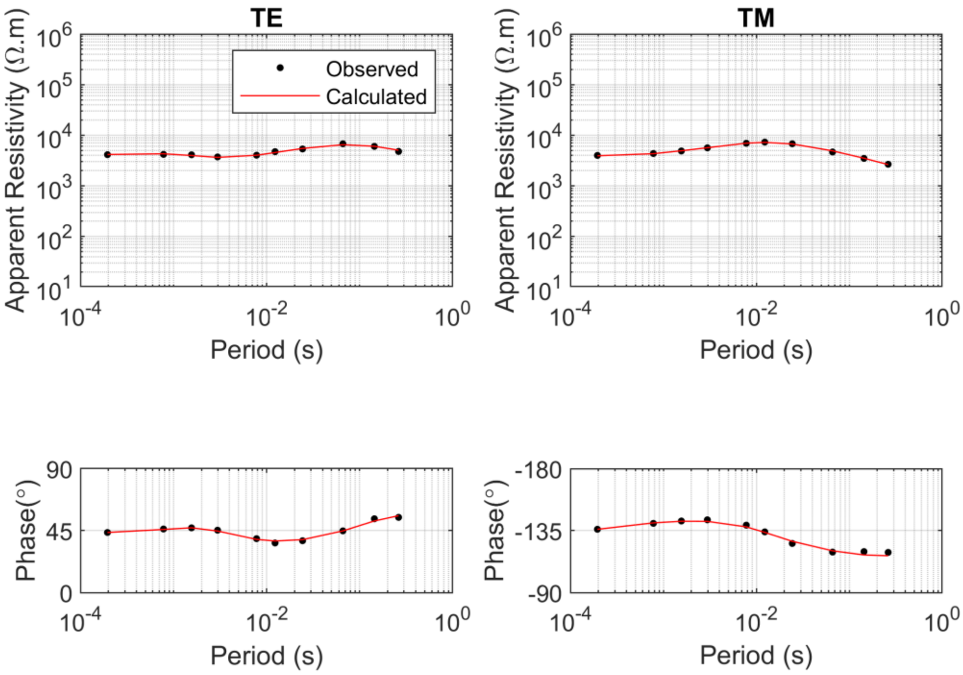

Fits of Apparent Resistivity and Phase for station #110

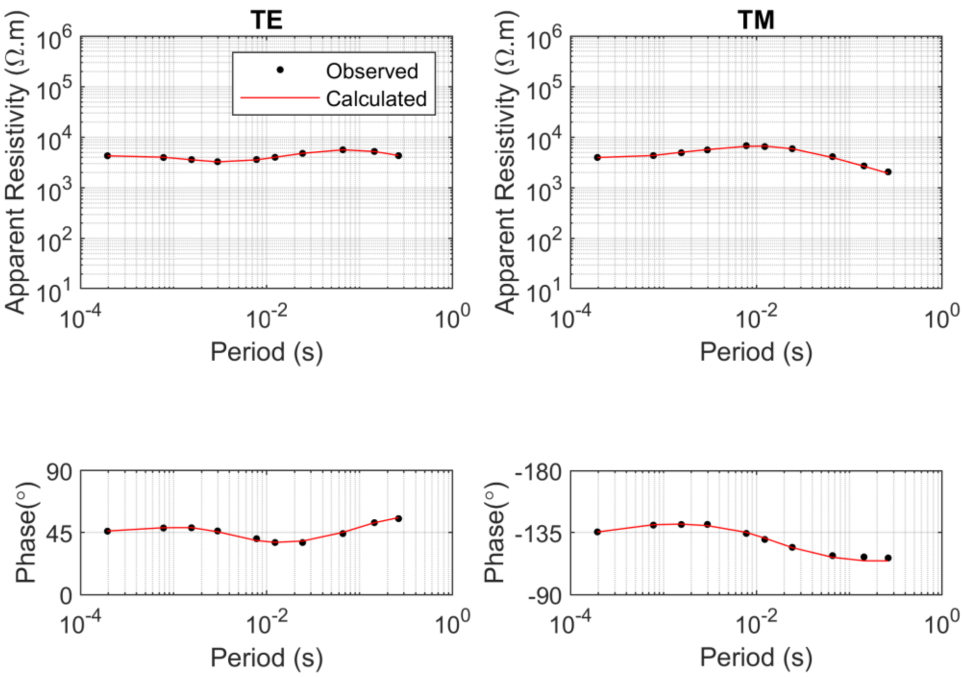

Fits of Apparent Resistivity and Phase for station #111

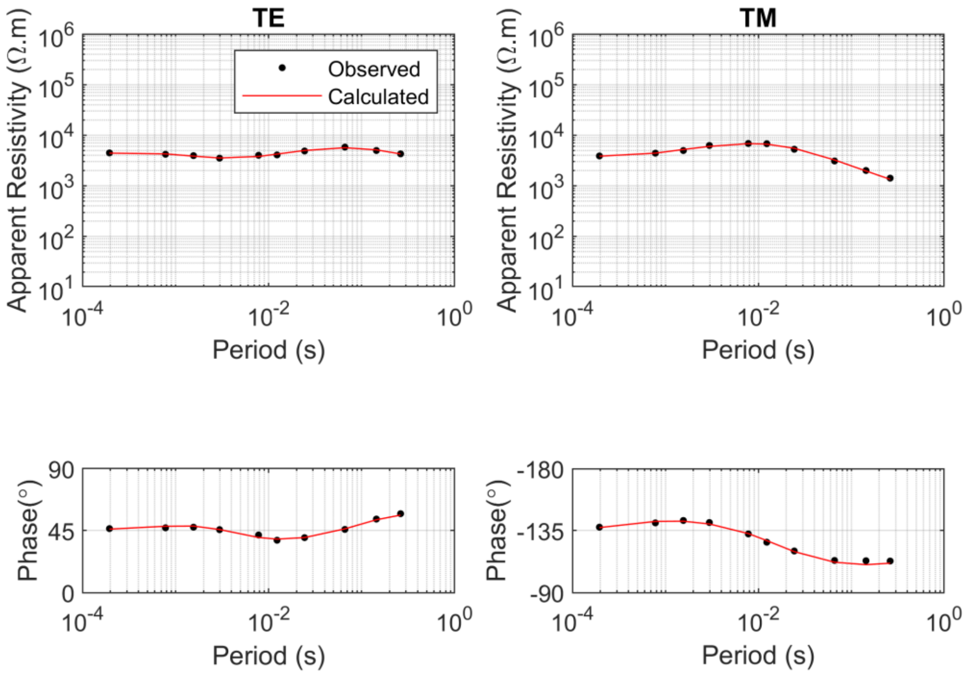

Fits of Apparent Resistivity and Phase for station #112

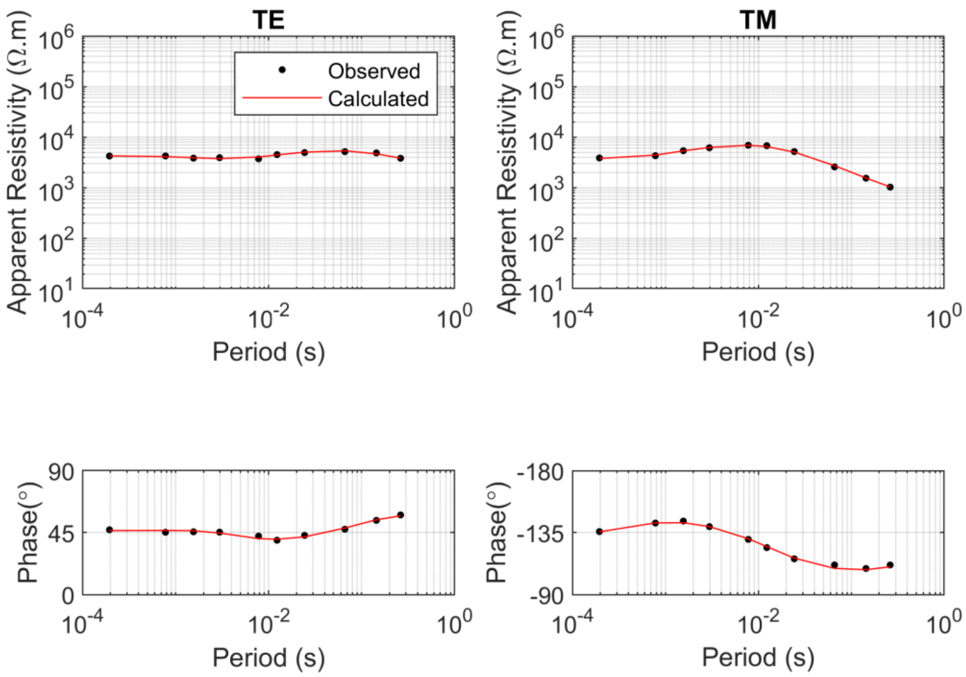

Fits of Apparent Resistivity and Phase for station #113

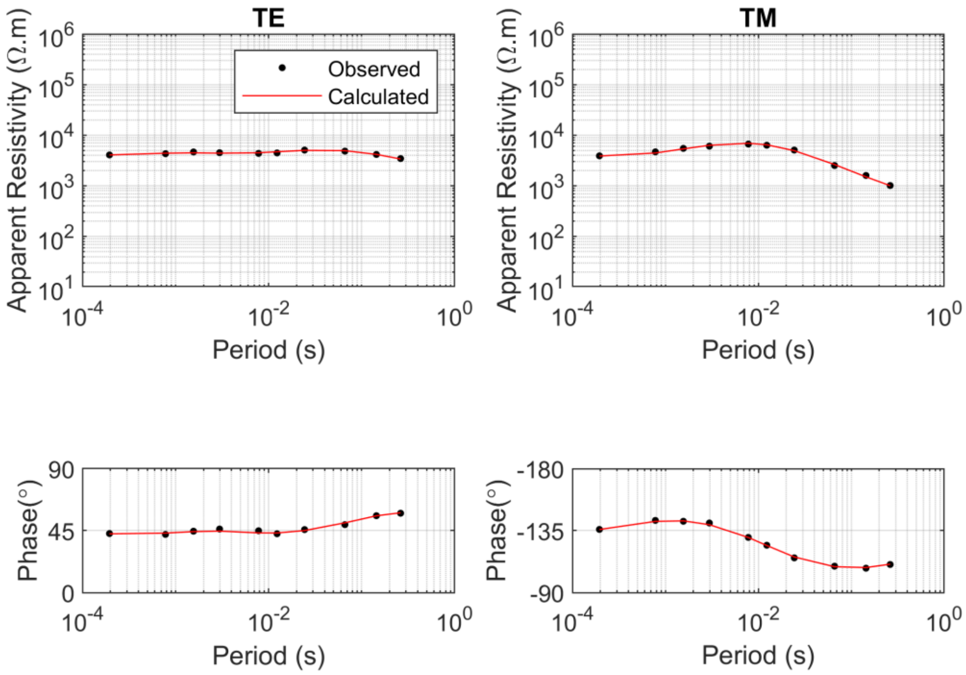

Fits of Apparent Resistivity and Phase for station #114

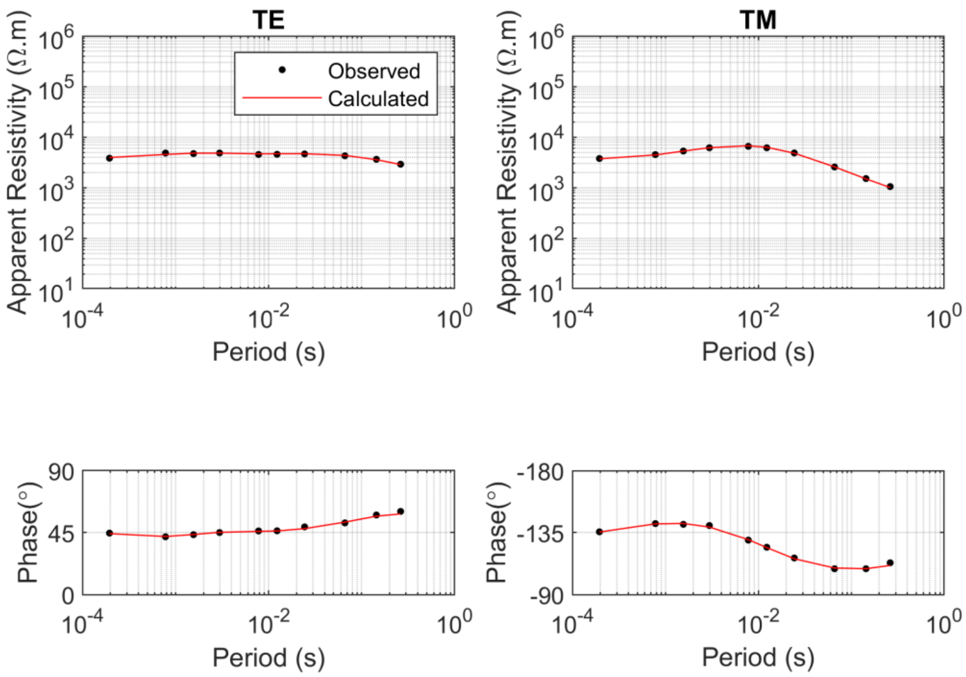

Fits of Apparent Resistivity and Phase for station #115

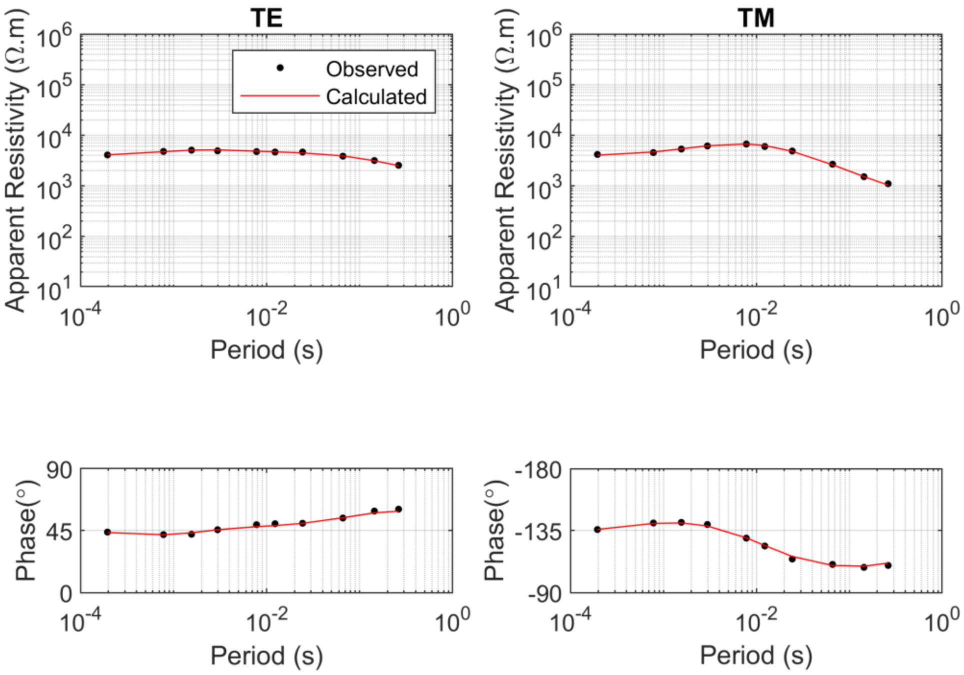

Fits of Apparent Resistivity and Phase for station #116

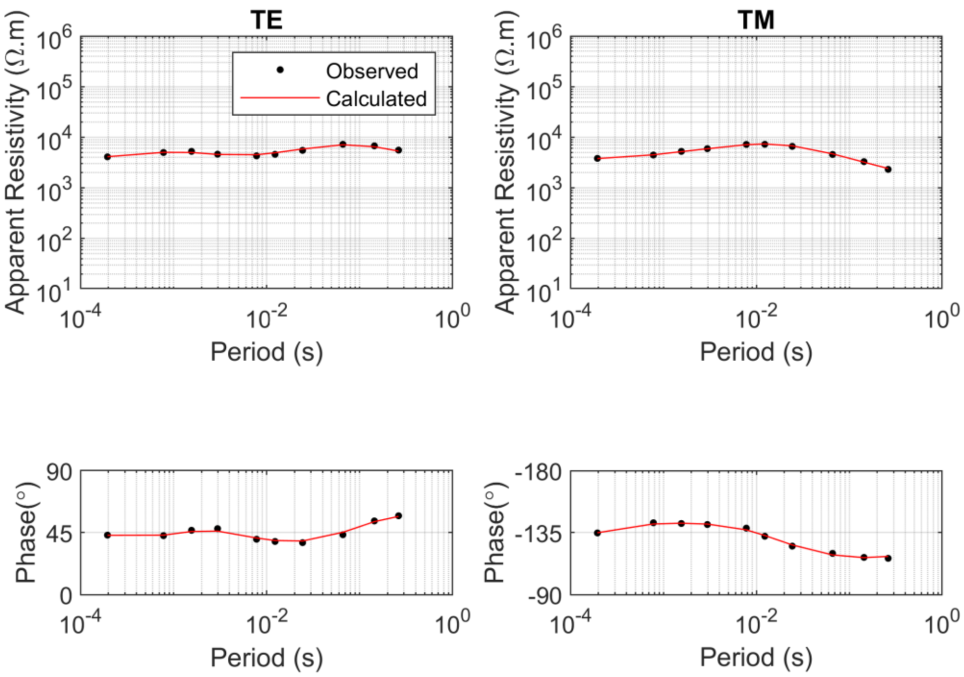

Fits of Apparent Resistivity and Phase for station #117

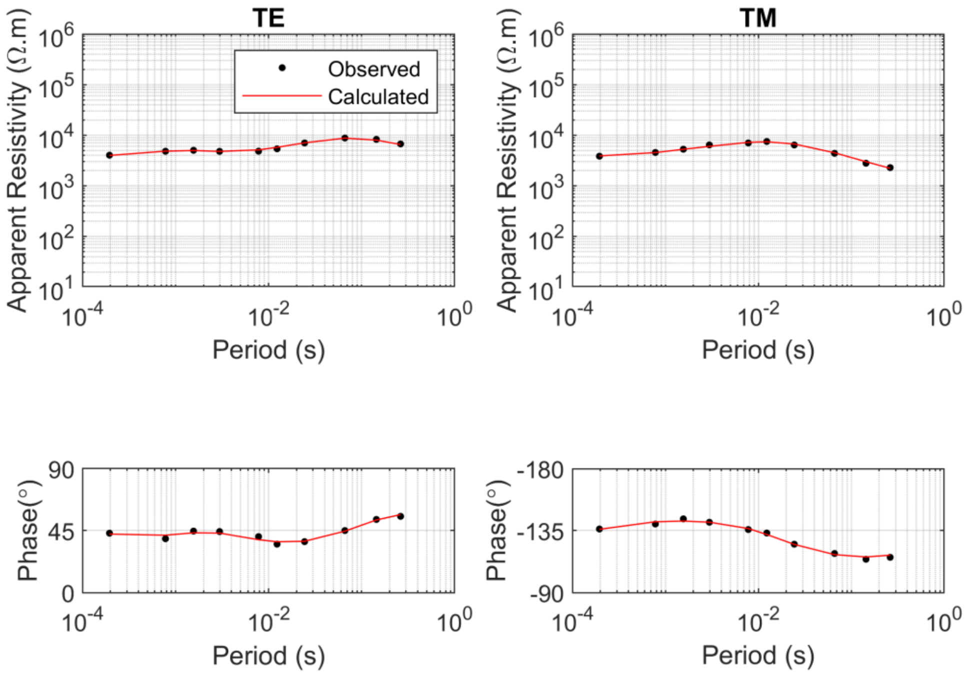

Fits of Apparent Resistivity and Phase for station #118

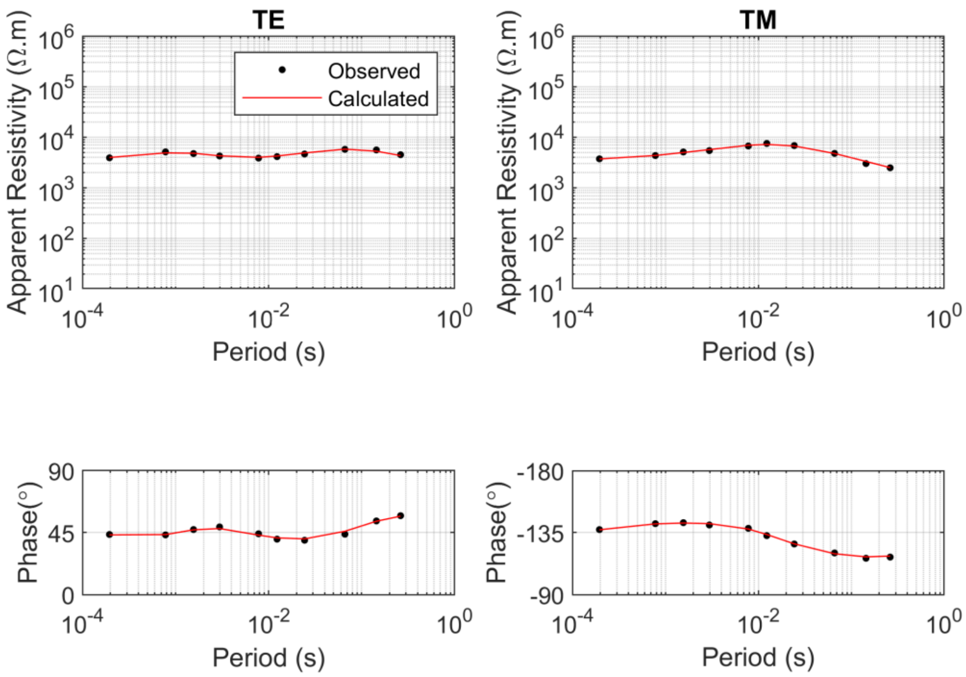

Fits of Apparent Resistivity and Phase for station #119

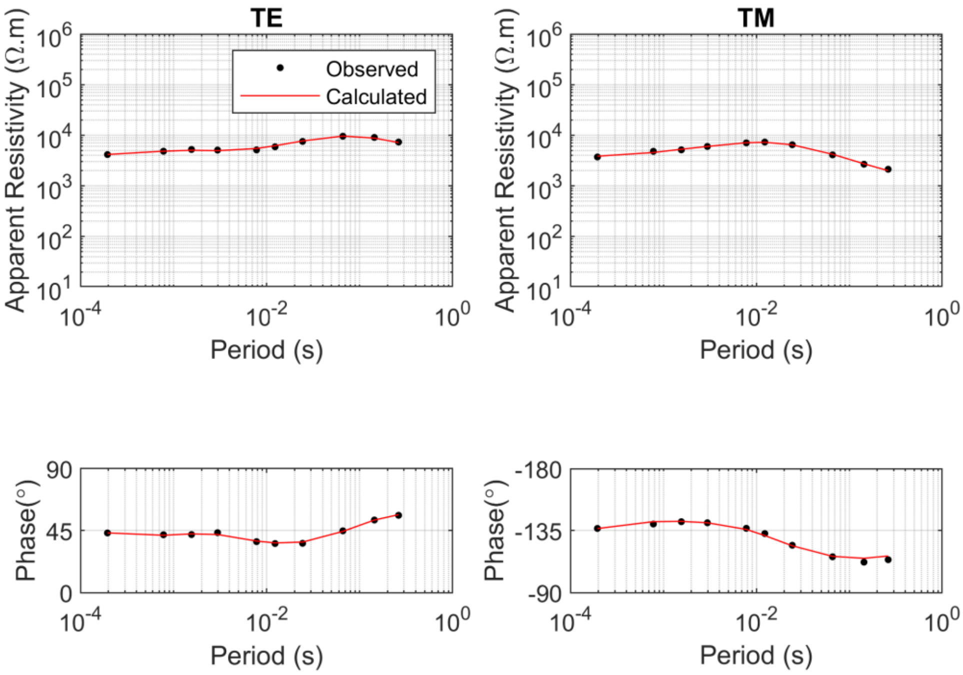

Fits of Apparent Resistivity and Phase for station #120

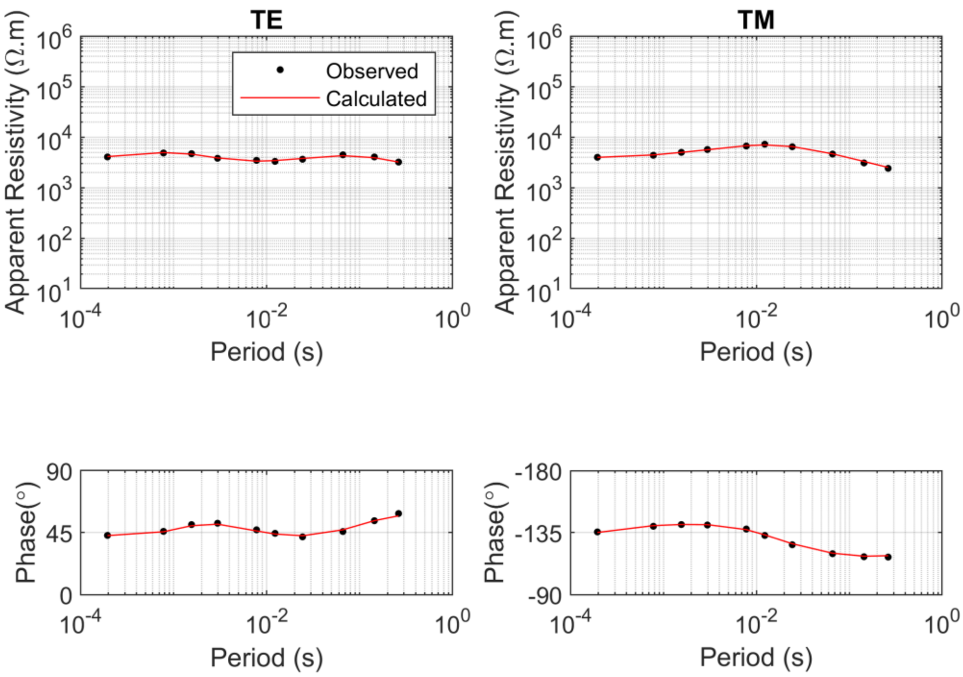

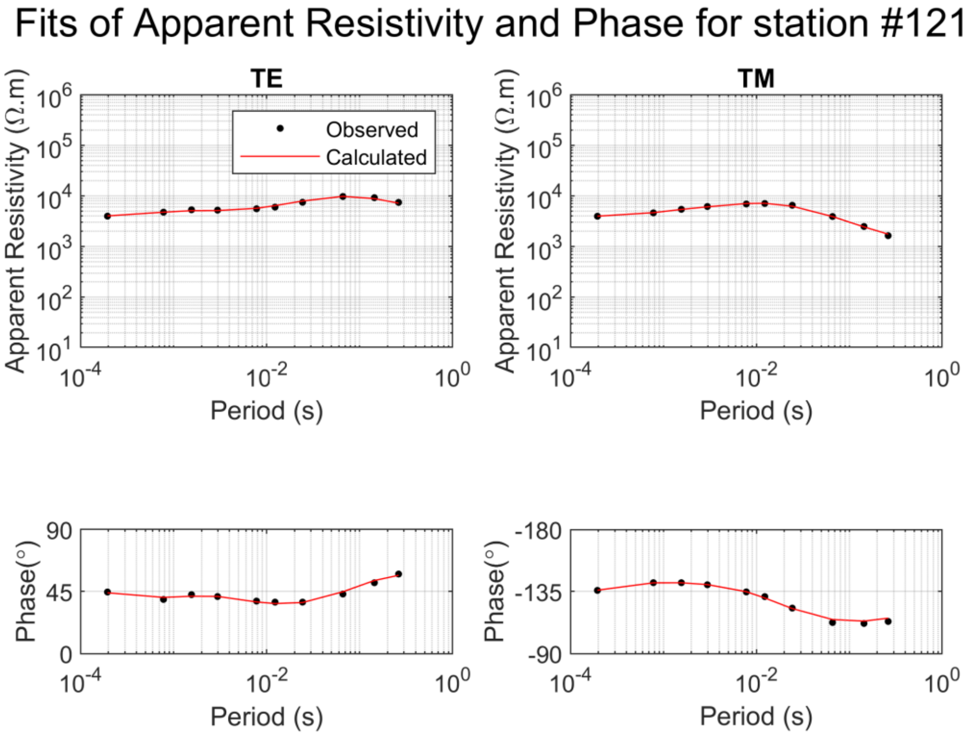
Fits of Apparent Resistivity and Phase for station #121
TE
TM
Observed
Calculated
Apparent Resistivity (Ω.m)
Period (s)
Phase(°)

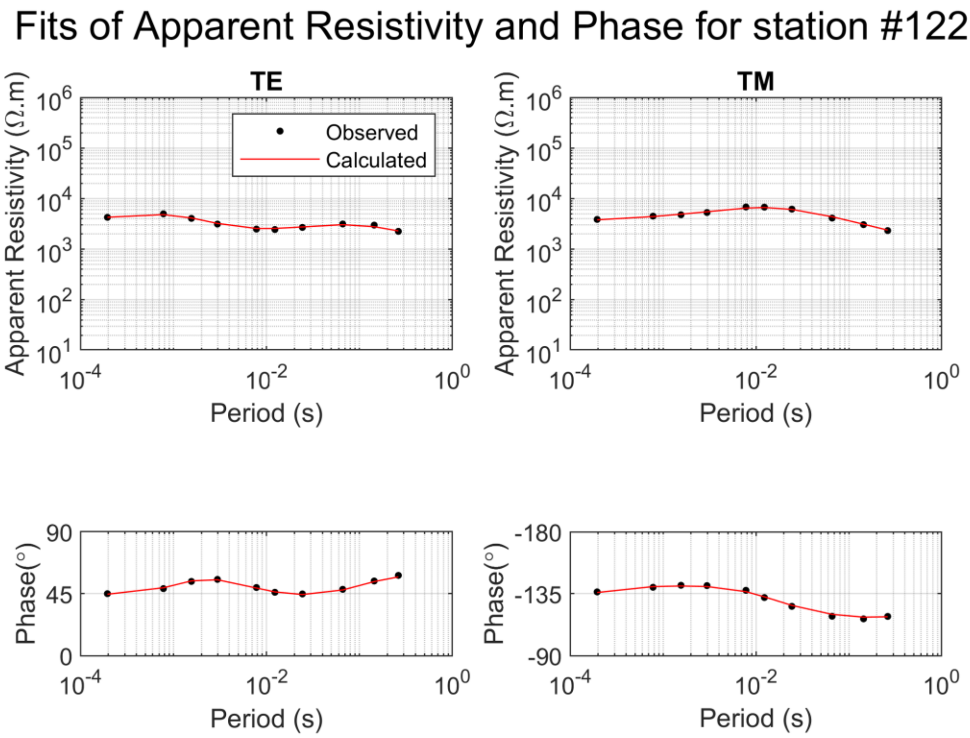
Fits of Apparent Resistivity and Phase for station #122
TE
TM
Observed
Calculated
Apparent Resistivity (Ω.m)
Period (s)
Phase(°)

Fits of Apparent Resistivity and Phase for station #123

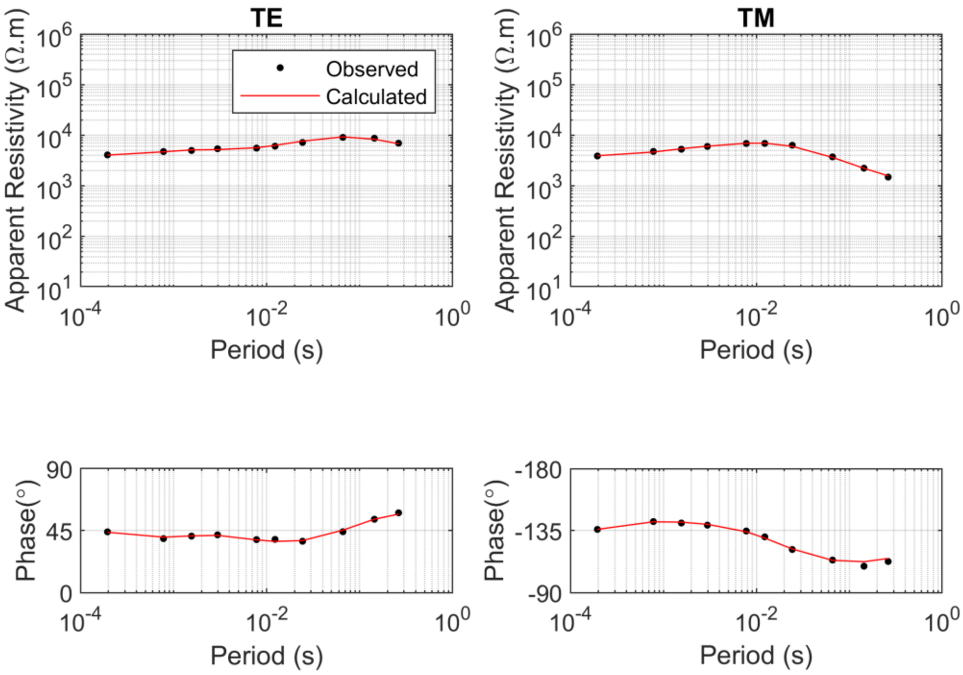

Fits of Apparent Resistivity and Phase for station #124

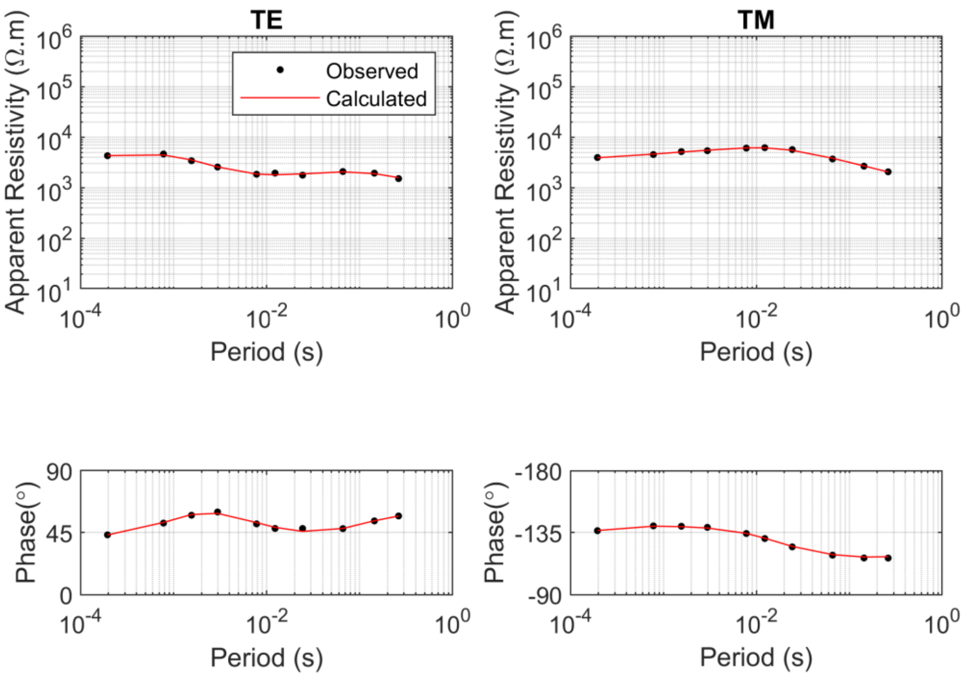

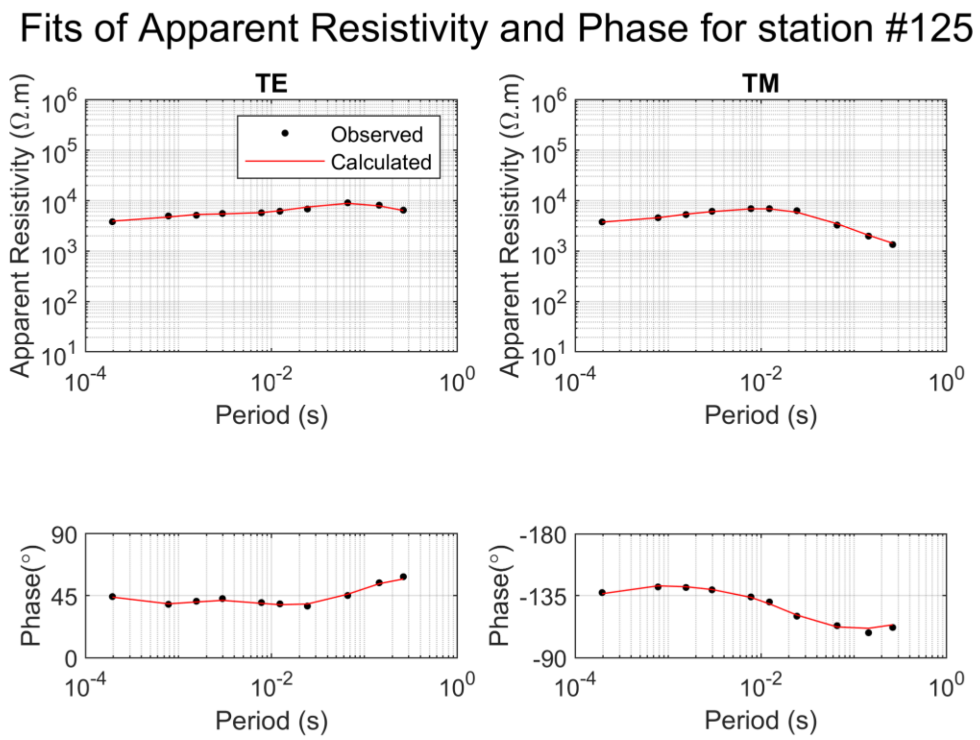
Fits of Apparent Resistivity and Phase for station #125
TE
TM
Observed
Calculated
Apparent Resistivity (Ω.m)
Phase(°)
Period (s)

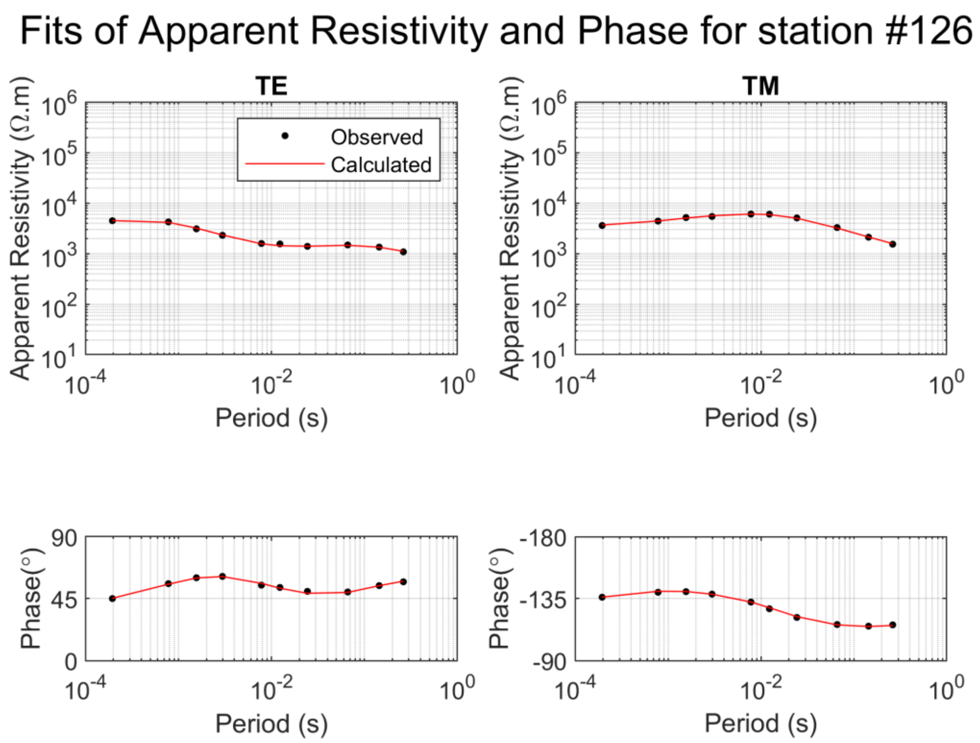
Fits of Apparent Resistivity and Phase for station #126
TE
TM
Observed
Calculated
Apparent Resistivity (Ω.m)
Phase(°)
Period (s)

Fits of Apparent Resistivity and Phase for station #127

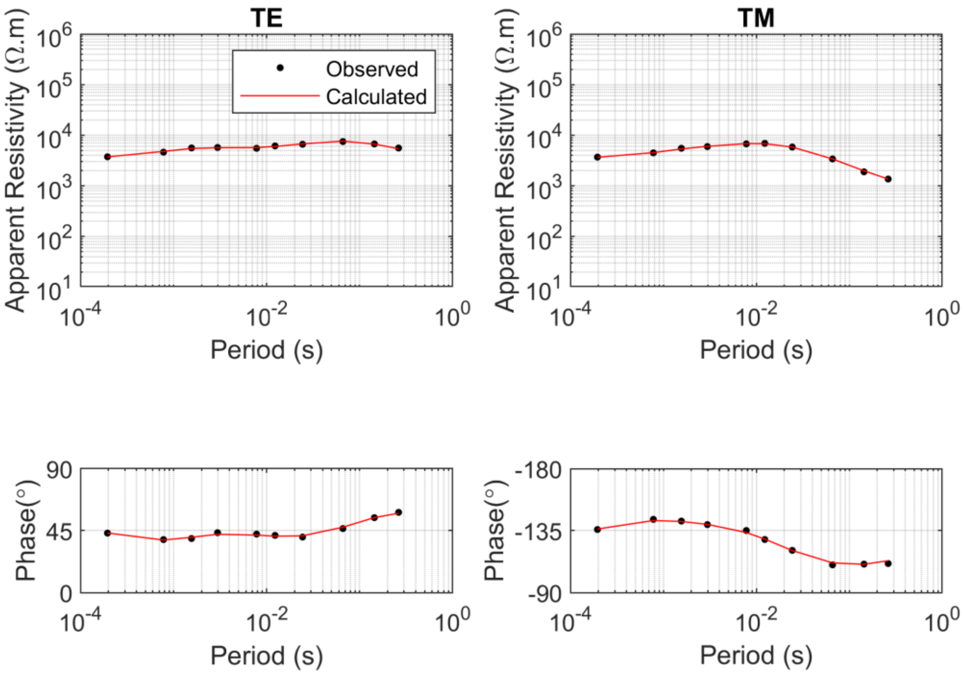

Fits of Apparent Resistivity and Phase for station #128

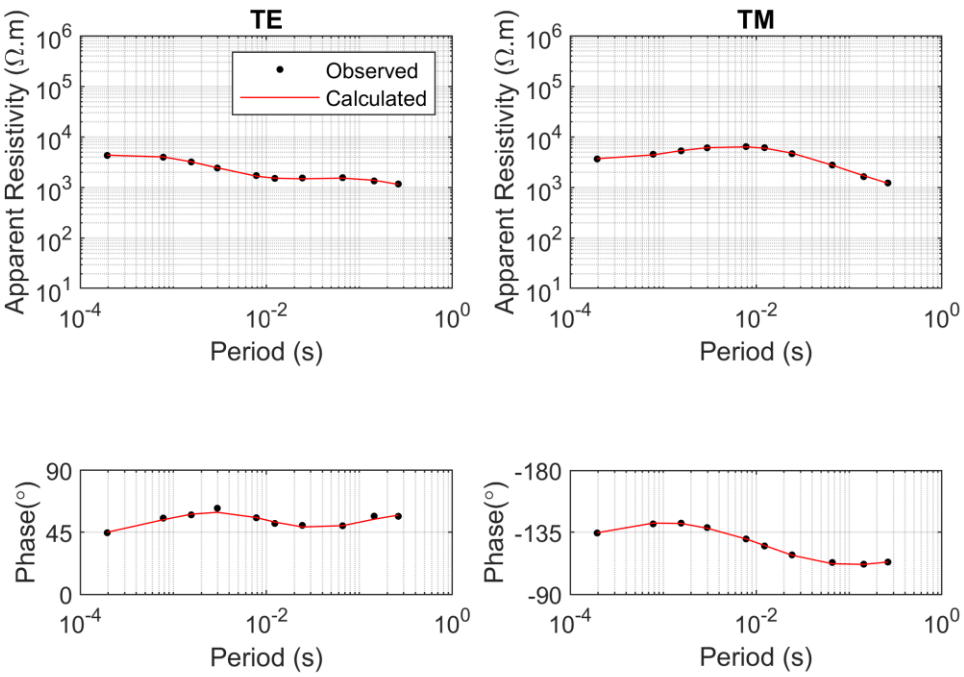

Fits of Apparent Resistivity and Phase for station #129

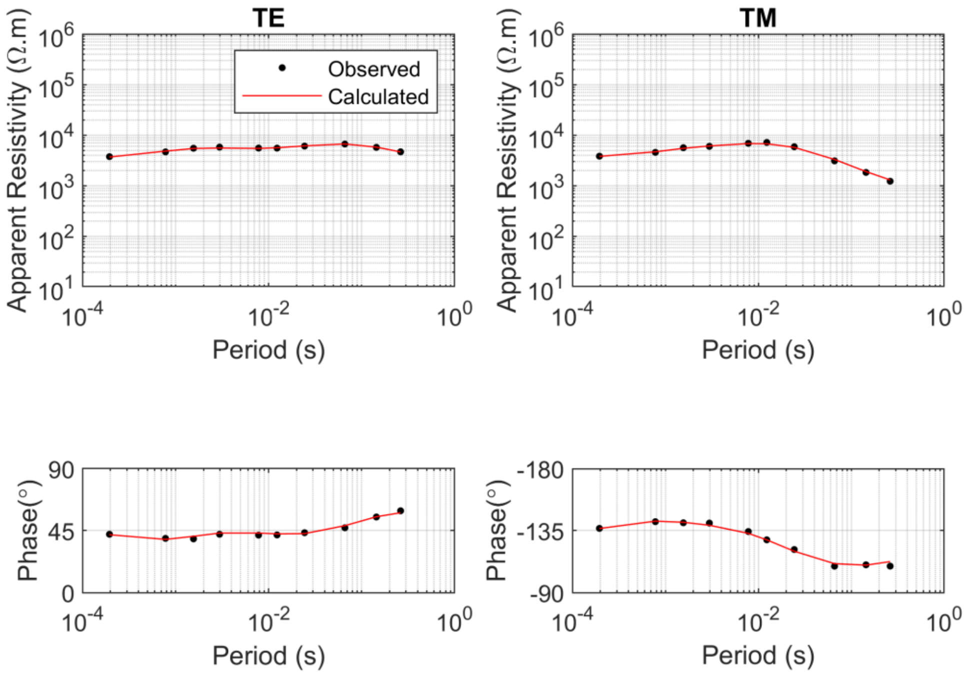

Fits of Apparent Resistivity and Phase for station #130

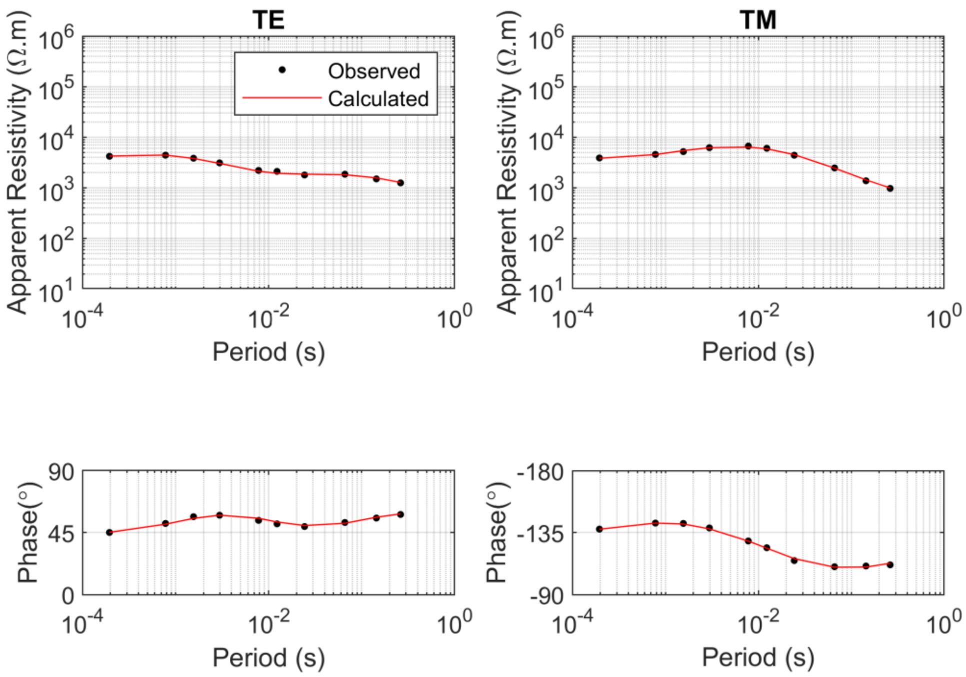

Fits of Apparent Resistivity and Phase for station #131

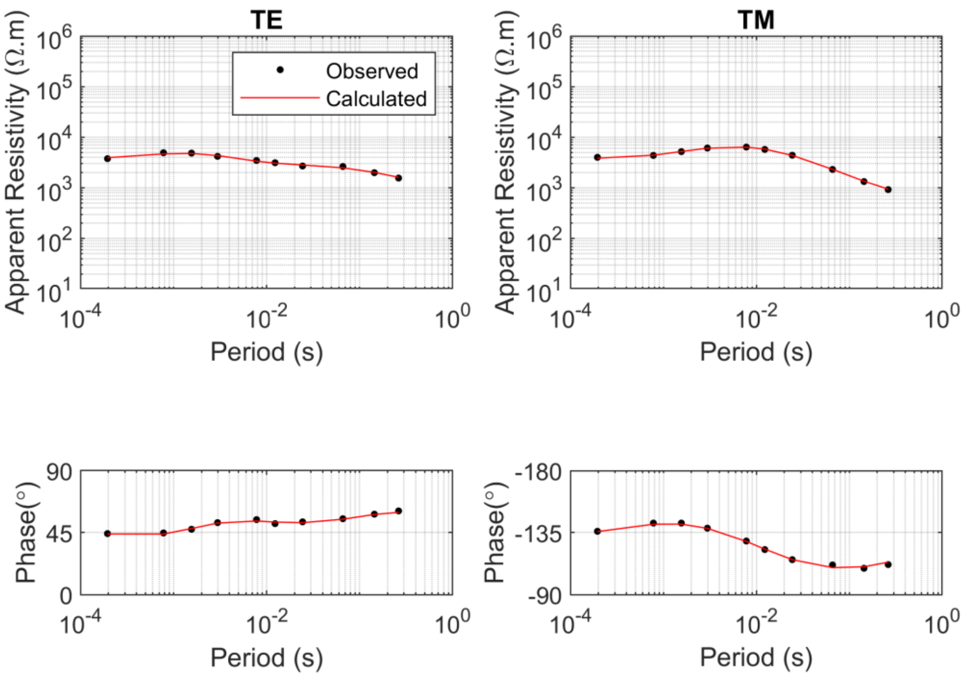

Fits of Apparent Resistivity and Phase for station #132

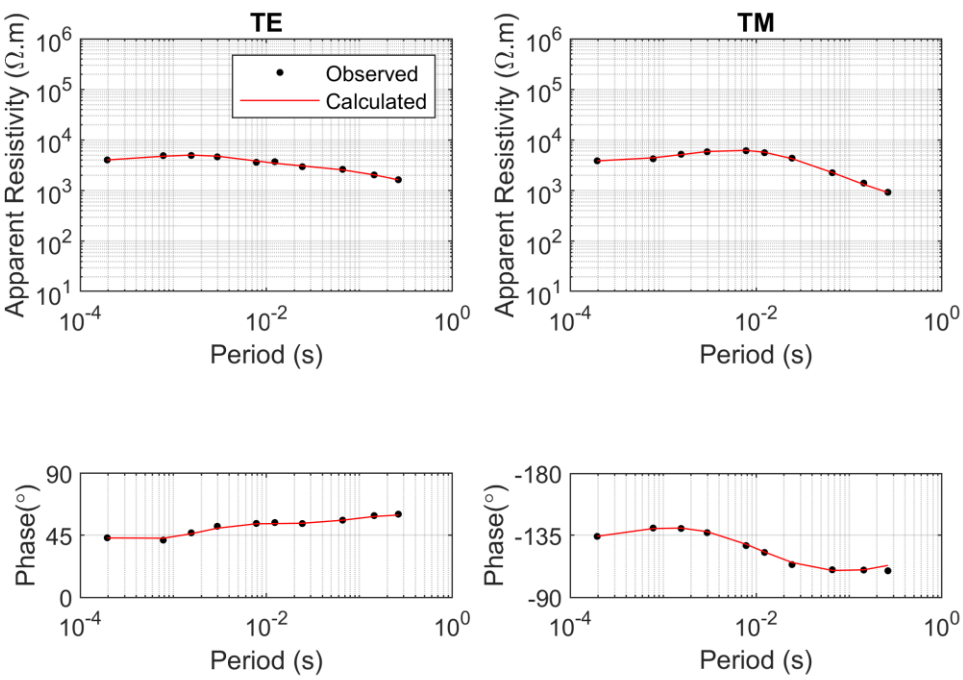

Appendix D – Fit Plots of Impedances, Apparent Resistivities and Phases for Inversion with Variances

D.1. Fit Plots of Impedances

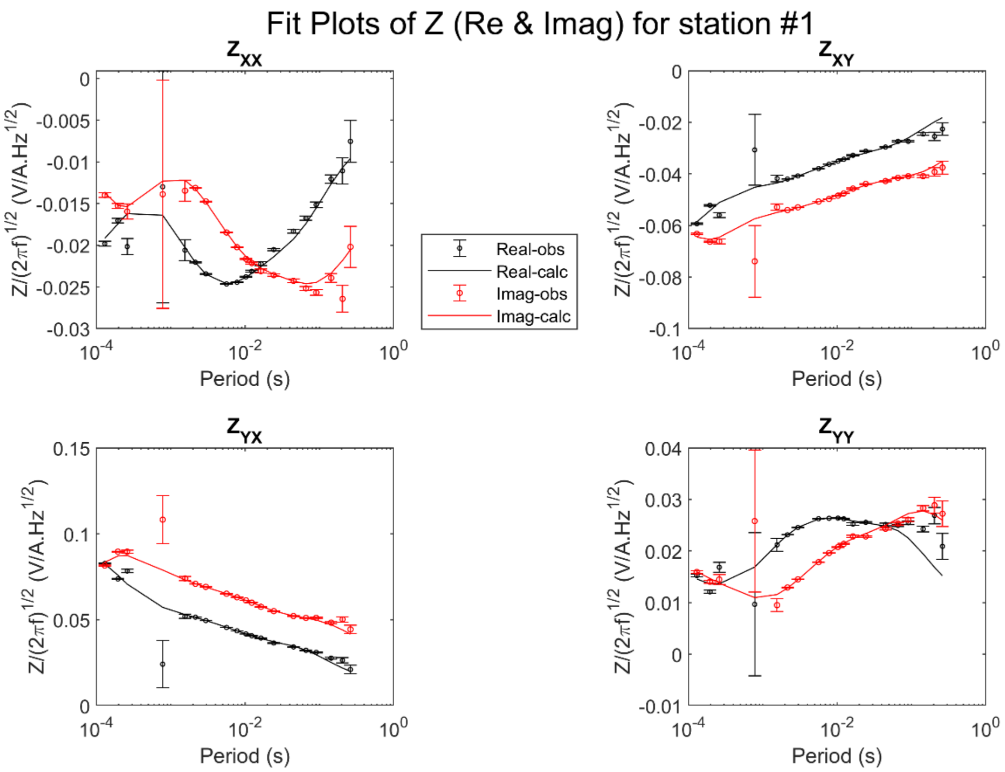

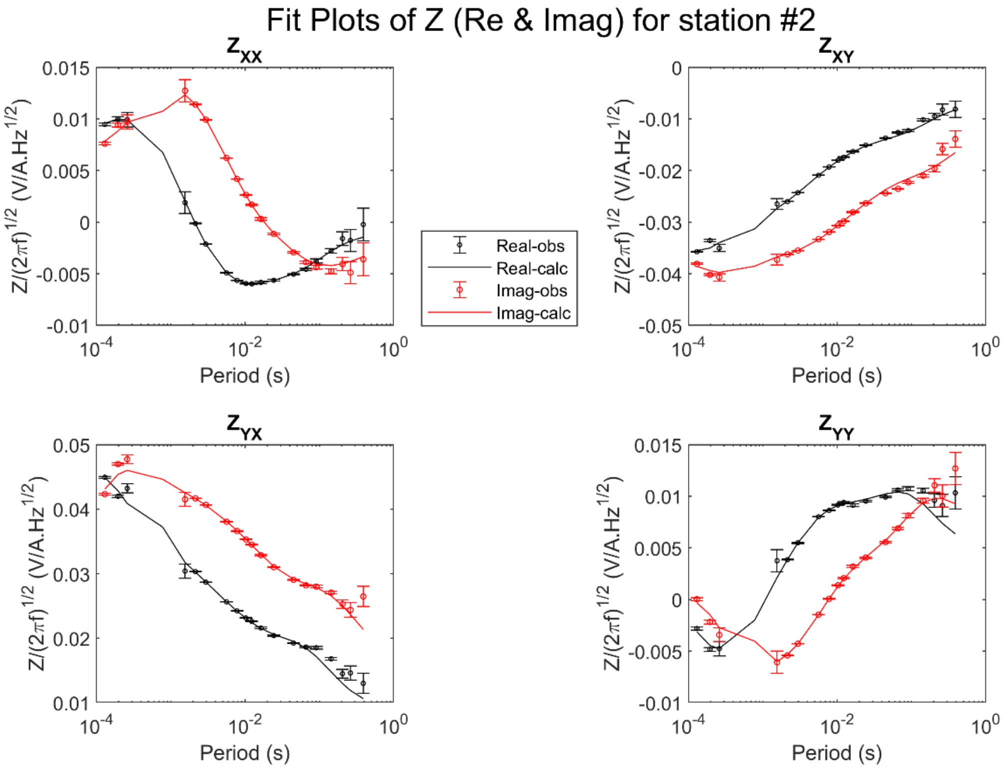

Fit Plots of Z (Re & Imag) for station #2
Z_XX
Z_XY
Z_YX
Z_YY
Z/(2πf)^1/2 (V/A.Hz^1/2)
Period (s)
Real-obs
Real-calc
Imag-obs
Imag-calc

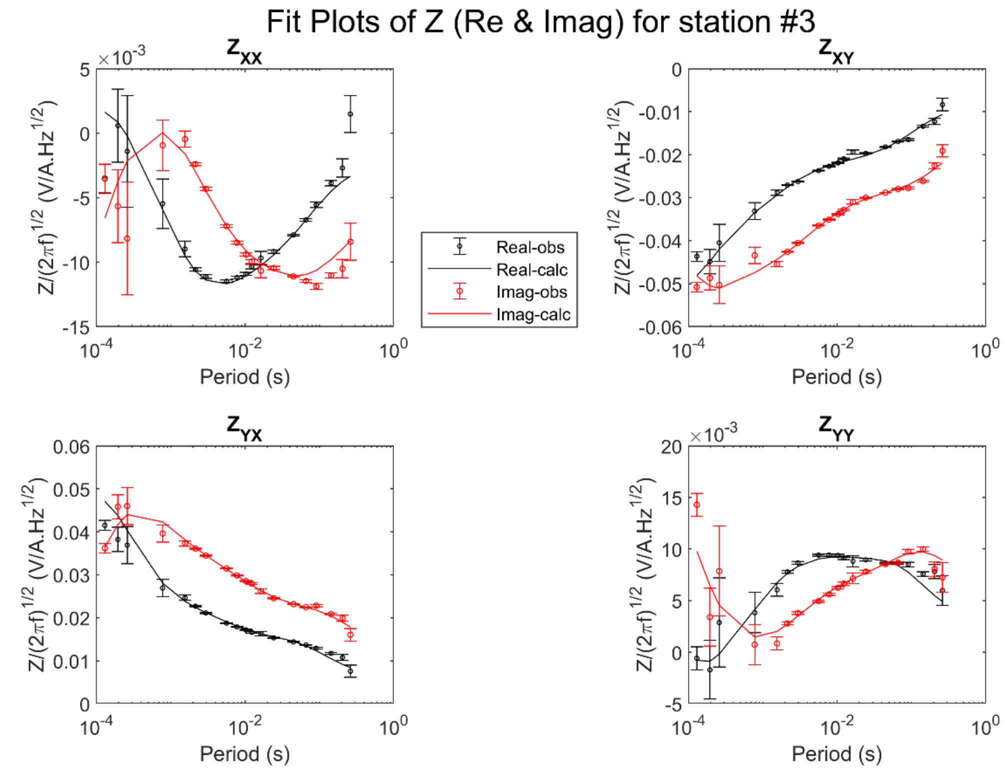

Fit Plots of Z (Re & Imag) for station #3
Z_XX
Z_XY
Z_YX
Z_YY
×10^-3
Z/(2πf)^1/2 (V/A.Hz^1/2)
Period (s)
Real-obs
Real-calc
Imag-obs
Imag-calc

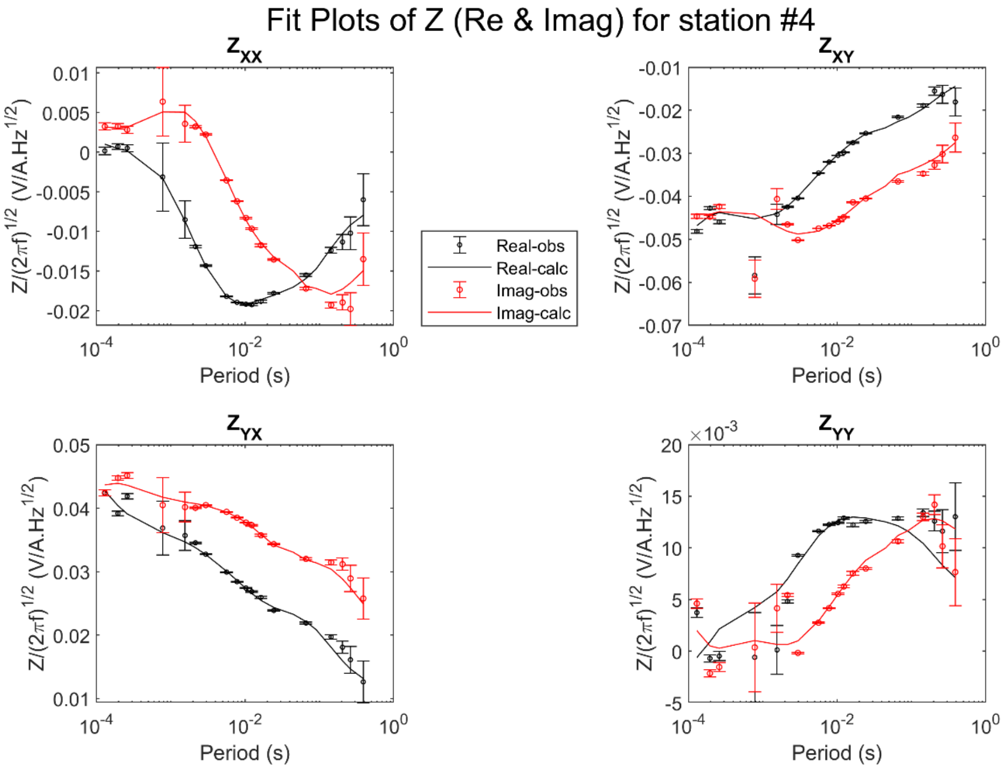

Fit Plots of Z (Re & Imag) for station #4
Z_{XX}
Z_{XY}
Z_{YX}
Z_{YY}
Real-obs
Real-calc
Imag-obs
Imag-calc
Period (s)
$Z/(2\pi f)^{1/2}$ (V/A.Hz$^{1/2}$)

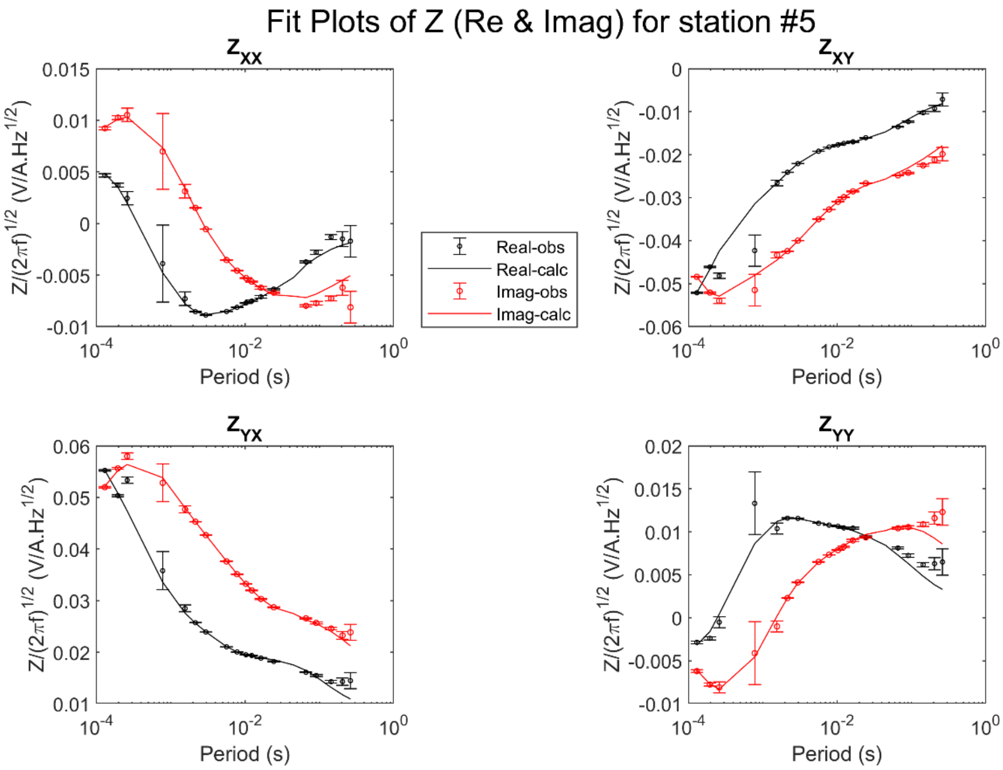

Fit Plots of Z (Re & Imag) for station #5
Z_{XX}
Z_{XY}
Z_{YX}
Z_{YY}
Real-obs
Real-calc
Imag-obs
Imag-calc
Period (s)
$Z/(2\pi f)^{1/2}$ (V/A.Hz$^{1/2}$)

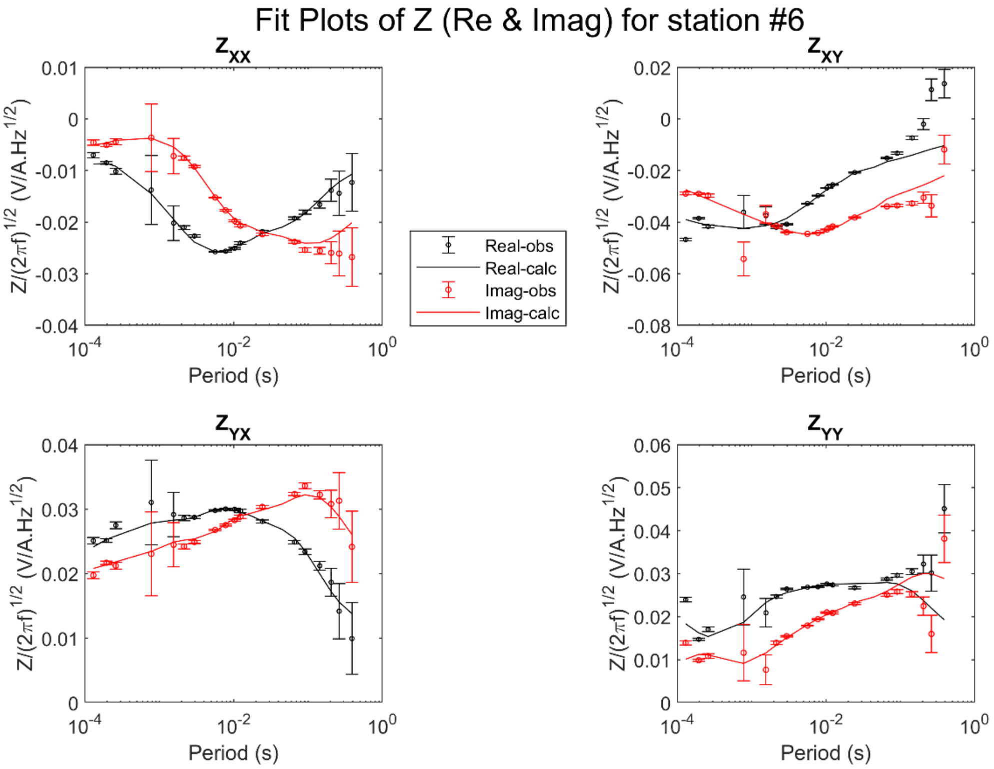
Fit Plots of Z (Re & Imag) for station #6
Z_{XX}
Z_{XY}
Z_{YX}
Z_{YY}
Real-obs
Real-calc
Imag-obs
Imag-calc
$Z/(2\pi f)^{1/2}$ (V/A.Hz$^{1/2}$)
Period (s)

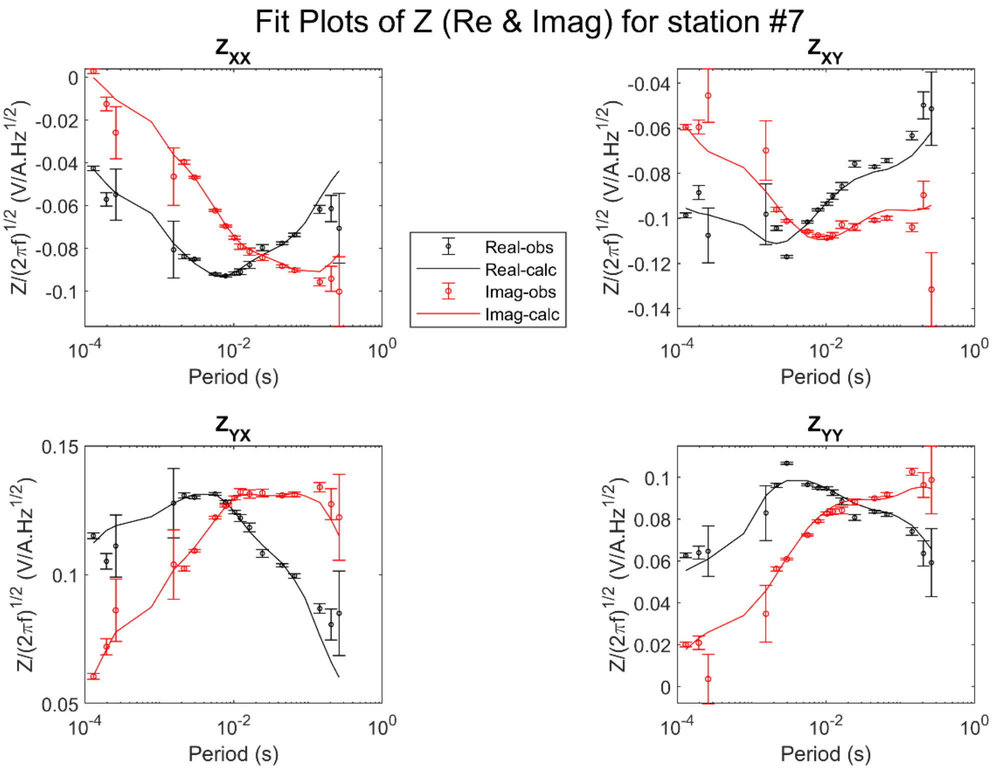
Fit Plots of Z (Re & Imag) for station #7
Z_{XX}
Z_{XY}
Z_{YX}
Z_{YY}
Real-obs
Real-calc
Imag-obs
Imag-calc
$Z/(2\pi f)^{1/2}$ (V/A.Hz$^{1/2}$)
Period (s)

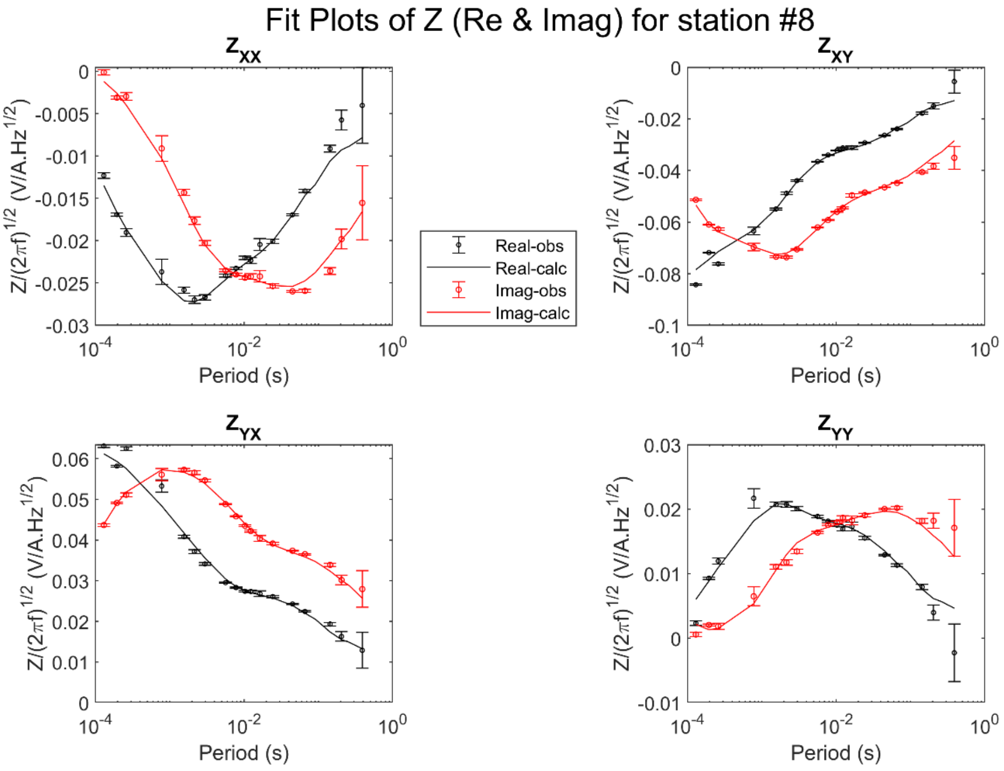

Fit Plots of Z (Re & Imag) for station #8
Z_XX
Z_XY
Z_YX
Z_YY
Z/(2πf)^1/2 (V/A.Hz^1/2)
Period (s)
Real-obs
Real-calc
Imag-obs
Imag-calc

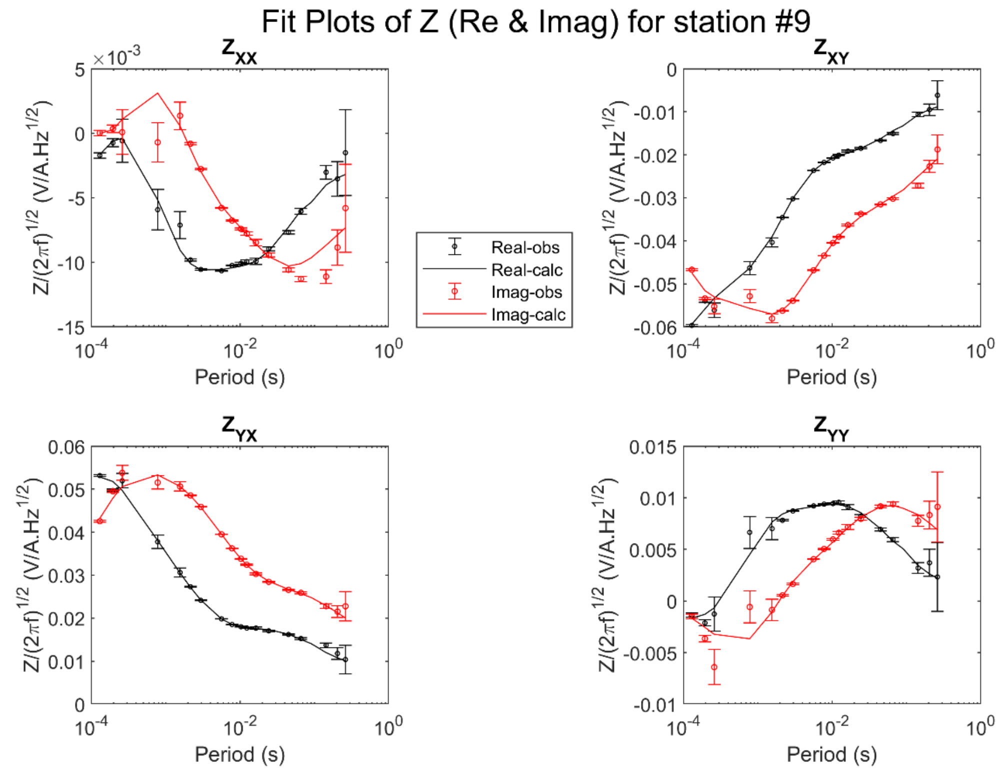

Fit Plots of Z (Re & Imag) for station #9
Z_XX
Z_XY
Z_YX
Z_YY
×10^-3
Z/(2πf)^1/2 (V/A.Hz^1/2)
Period (s)
Real-obs
Real-calc
Imag-obs
Imag-calc

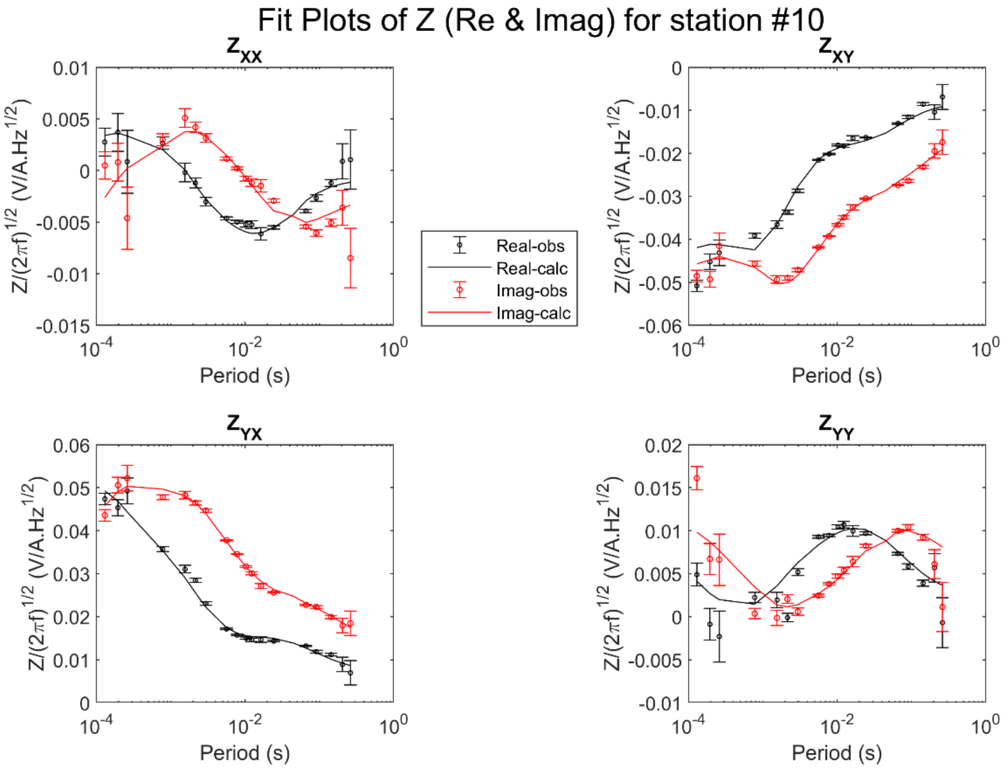
Fit Plots of Z (Re & Imag) for station #10
Z XX
Z XY
Z YX
Z YY
Z/(2πf)^1/2 (V/A.Hz^1/2)
Period (s)
Real-obs
Real-calc
Imag-obs
Imag-calc

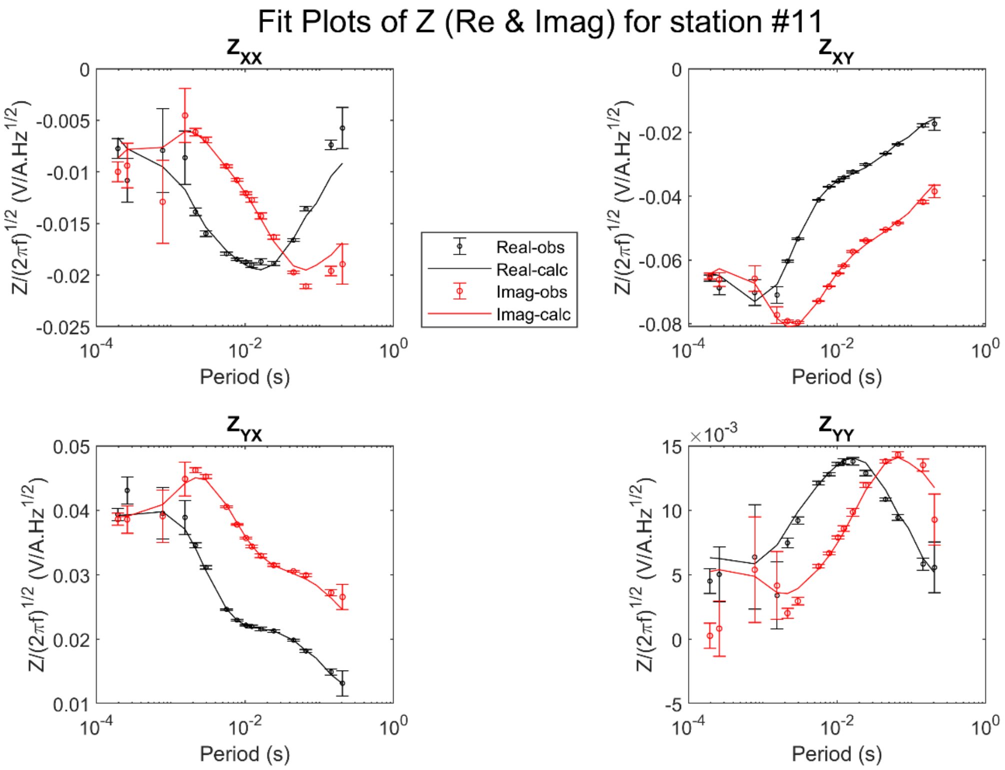
Fit Plots of Z (Re & Imag) for station #11
Z XX
Z XY
Z YX
Z YY
Z/(2πf)^1/2 (V/A.Hz^1/2)
Period (s)
Real-obs
Real-calc
Imag-obs
Imag-calc

Fit Plots of Z (Re & Imag) for station #12

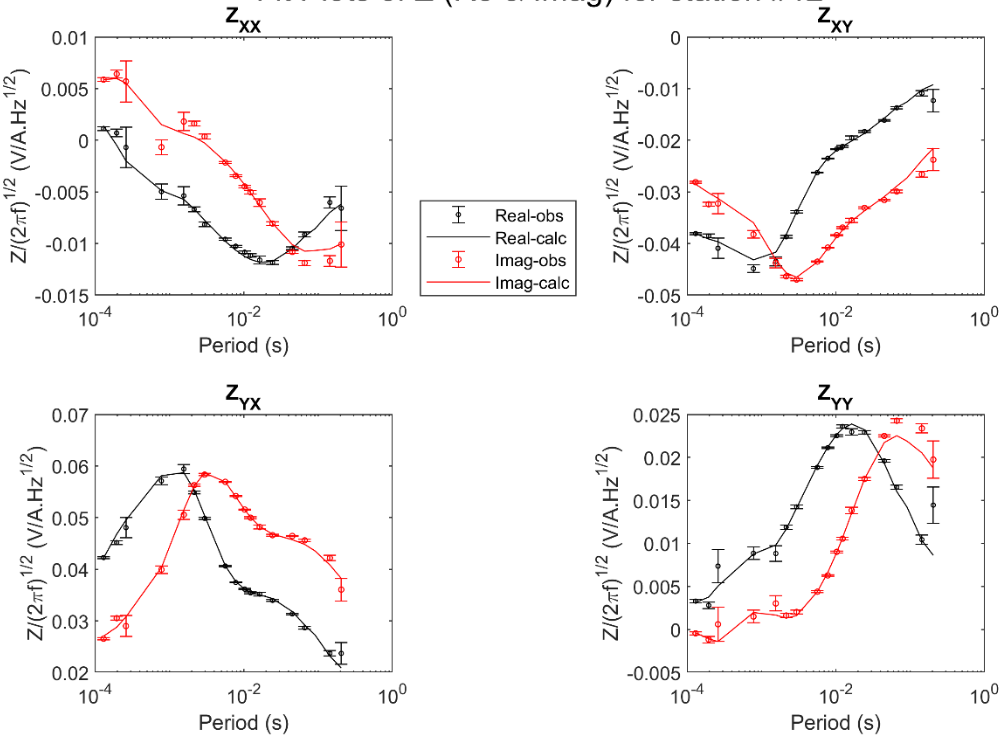

Fit Plots of Z (Re & Imag) for station #13

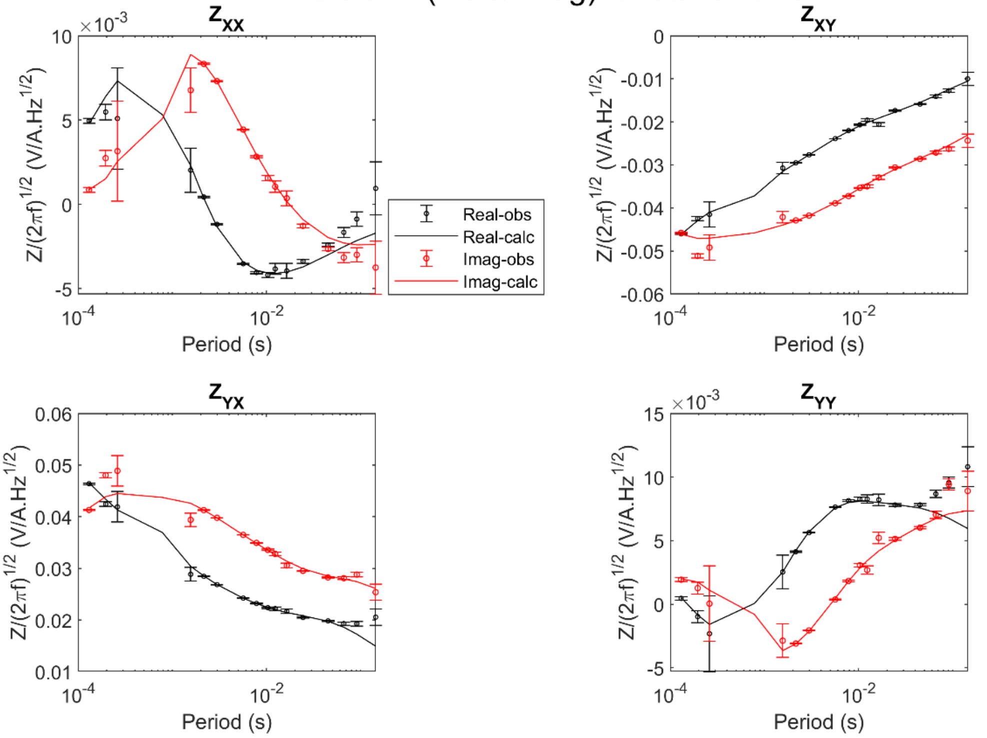

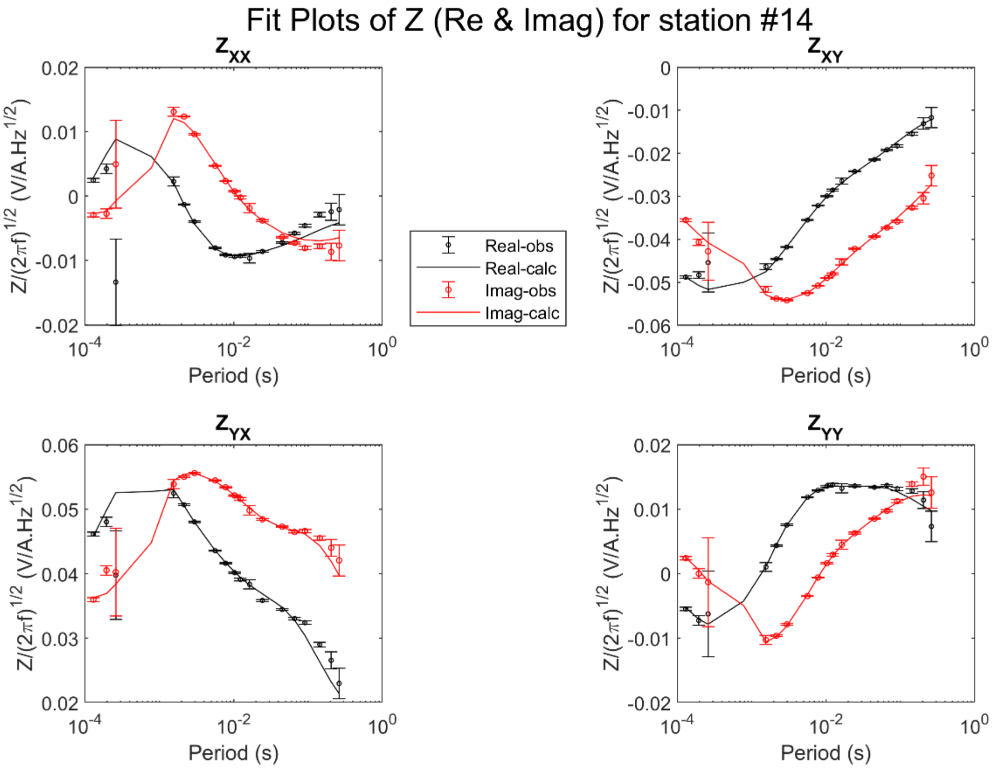
Fit Plots of Z (Re & Imag) for station #14
Z_XX
Z_XY
Z_YX
Z_YY
Z/(2πf)^1/2 (V/A.Hz^1/2)
Period (s)
Real-obs
Real-calc
Imag-obs
Imag-calc

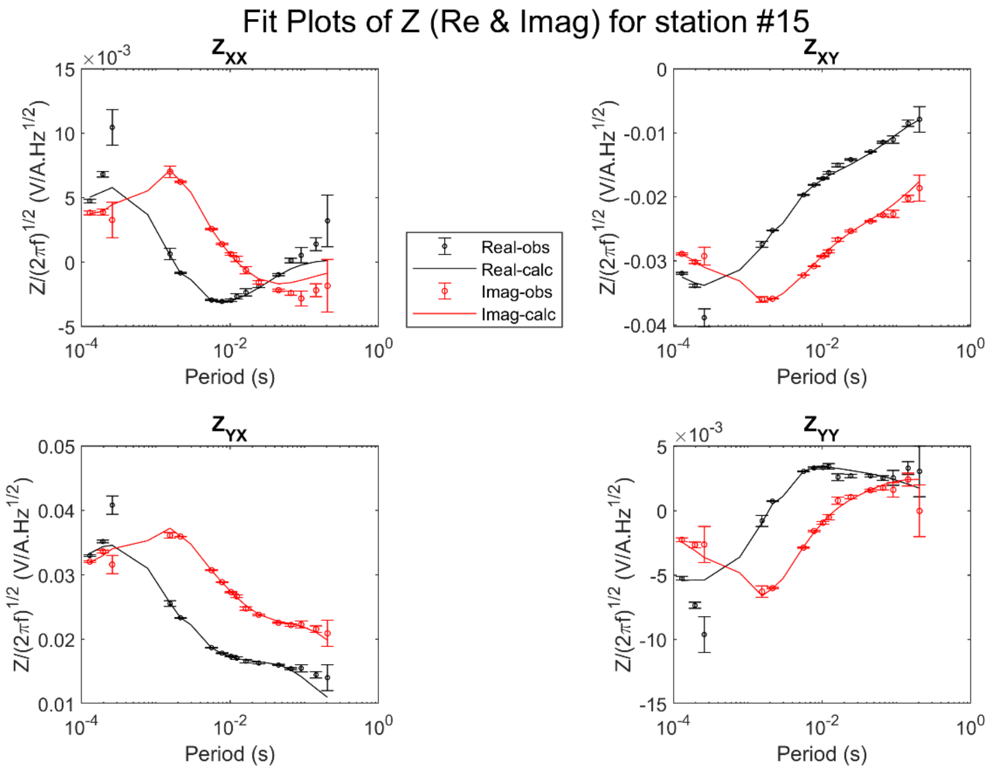
Fit Plots of Z (Re & Imag) for station #15
Z_XX
Z_XY
Z_YX
Z_YY
×10^-3
Z/(2πf)^1/2 (V/A.Hz^1/2)
Period (s)
Real-obs
Real-calc
Imag-obs
Imag-calc

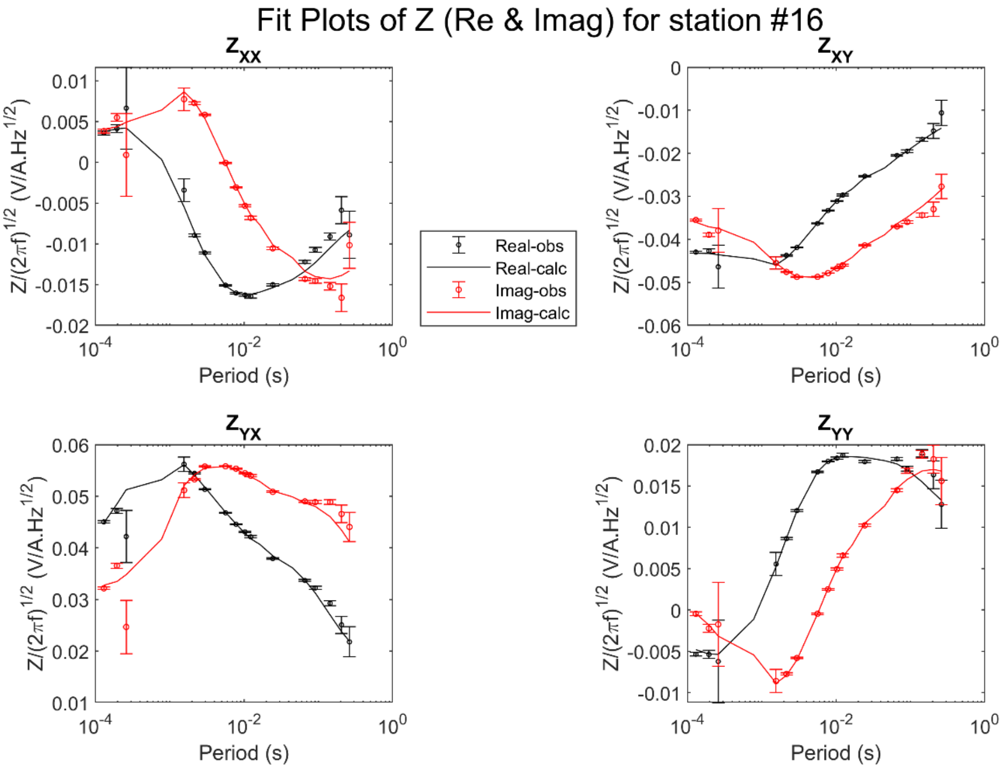
Fit Plots of Z (Re & Imag) for station #16
Z_XX
Z_XY
Z_YX
Z_YY
Z/(2πf)^1/2 (V/A.Hz^1/2)
Period (s)
Real-obs
Real-calc
Imag-obs
Imag-calc

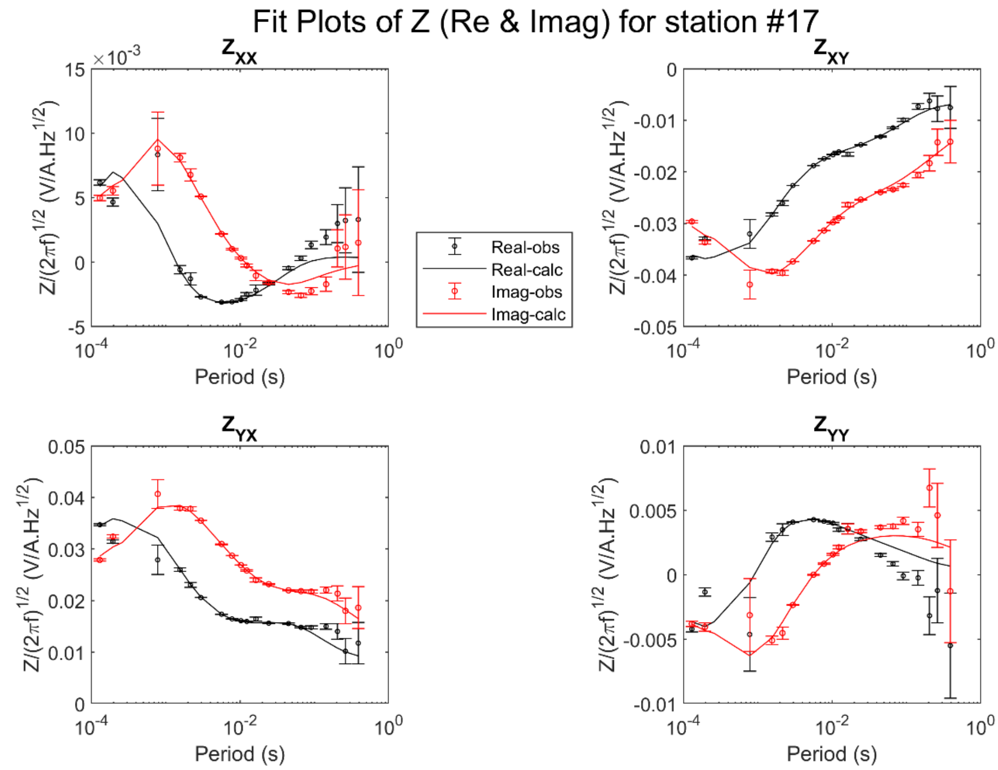
Fit Plots of Z (Re & Imag) for station #17
Z_XX
Z_XY
Z_YX
Z_YY
Z/(2πf)^1/2 (V/A.Hz^1/2)
Period (s)
Real-obs
Real-calc
Imag-obs
Imag-calc

Fit Plots of Z (Re & Imag) for station #18

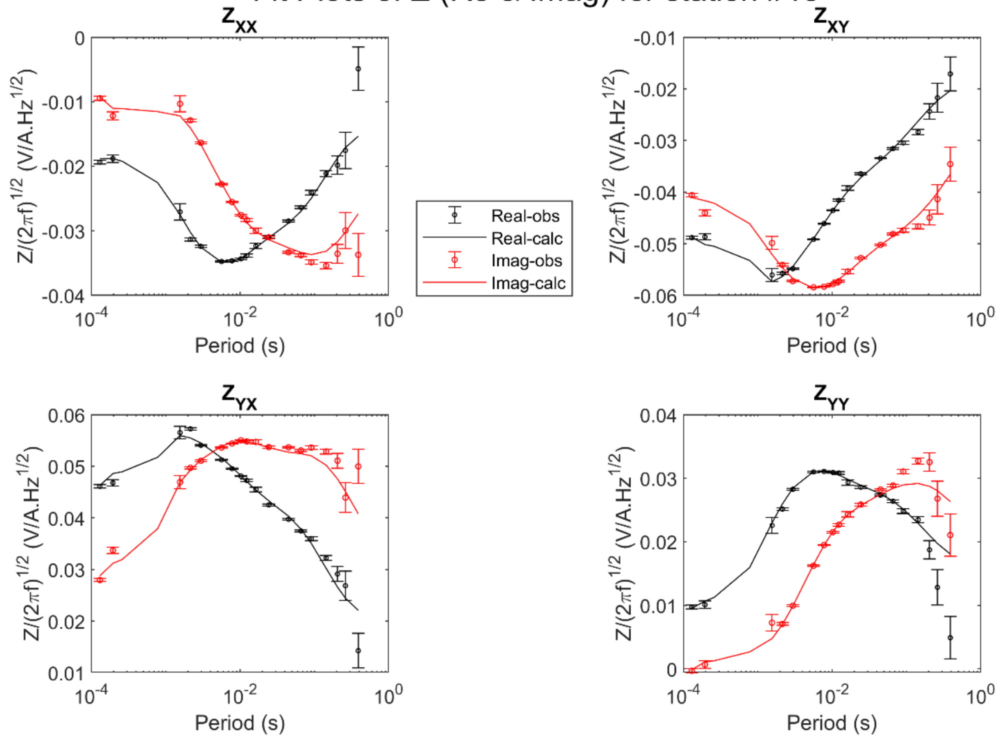

Fit Plots of Z (Re & Imag) for station #19

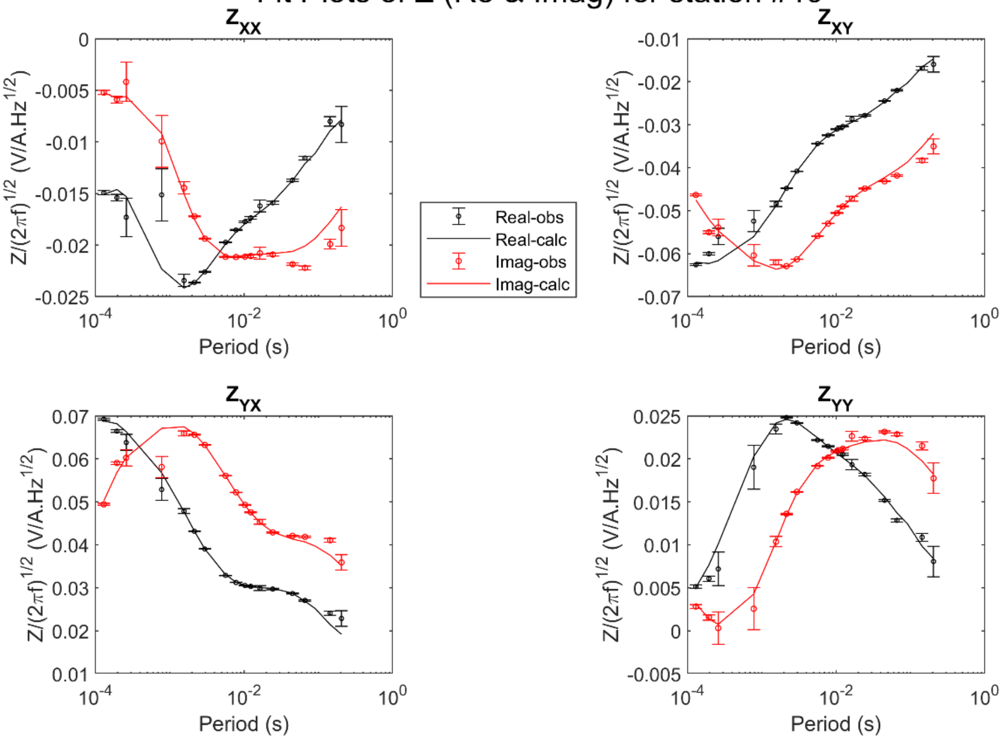

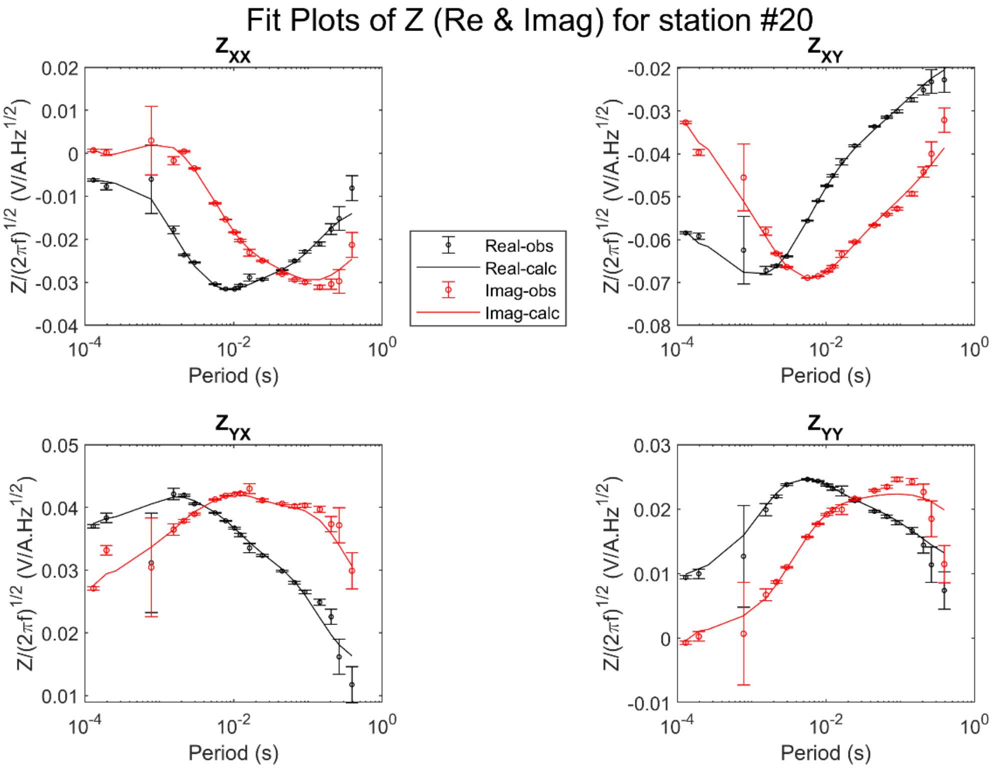

Fit Plots of Z (Re & Imag) for station #20
Z_{XX}
Z_{XY}
Z_{YX}
Z_{YY}
$Z/(2\pi f)^{1/2}$ (V/A.Hz$^{1/2}$)
Period (s)
Real-obs
Real-calc
Imag-obs
Imag-calc

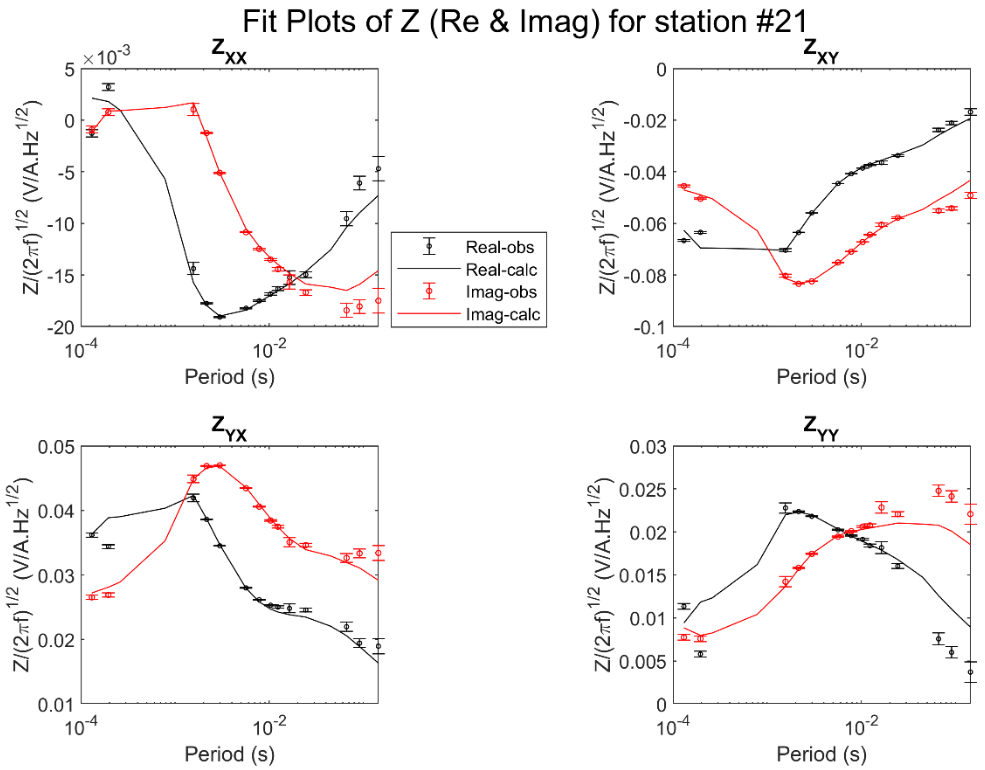

Fit Plots of Z (Re & Imag) for station #21
Z_{XX}
Z_{XY}
Z_{YX}
Z_{YY}
$\times 10^{-3}$
$Z/(2\pi f)^{1/2}$ (V/A.Hz$^{1/2}$)
Period (s)
Real-obs
Real-calc
Imag-obs
Imag-calc

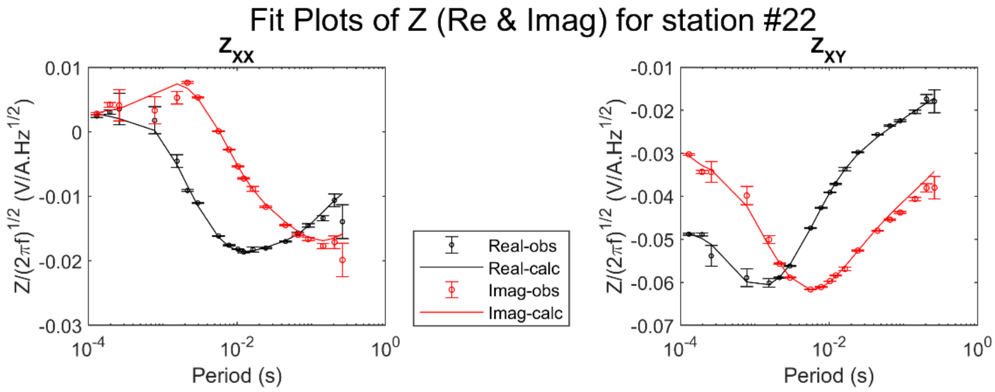
Fit Plots of Z (Re & Imag) for station #22
Z_XX
Z_XY
Z_YX
Z_YY
Z/(2πf)^1/2 (V/A.Hz^1/2)
Period (s)
Real-obs
Real-calc
Imag-obs
Imag-calc

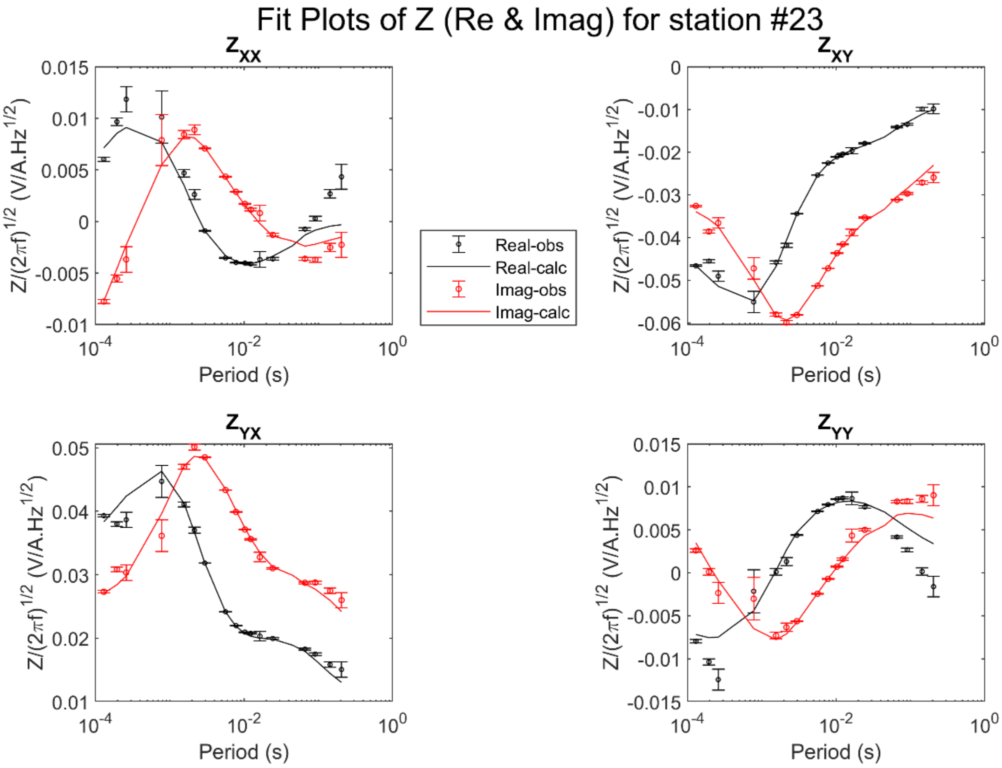
Fit Plots of Z (Re & Imag) for station #23
Z_XX
Z_XY
Z_YX
Z_YY
Z/(2πf)^1/2 (V/A.Hz^1/2)
Period (s)
Real-obs
Real-calc
Imag-obs
Imag-calc

Fit Plots of Z (Re & Imag) for station #24

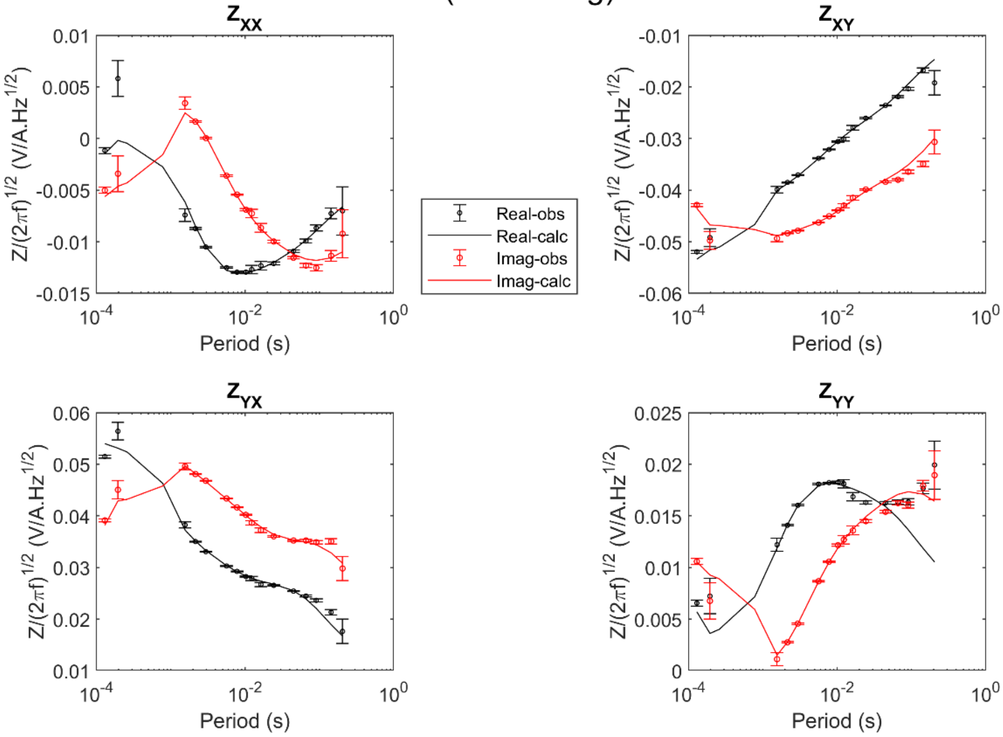

Fit Plots of Z (Re & Imag) for station #25

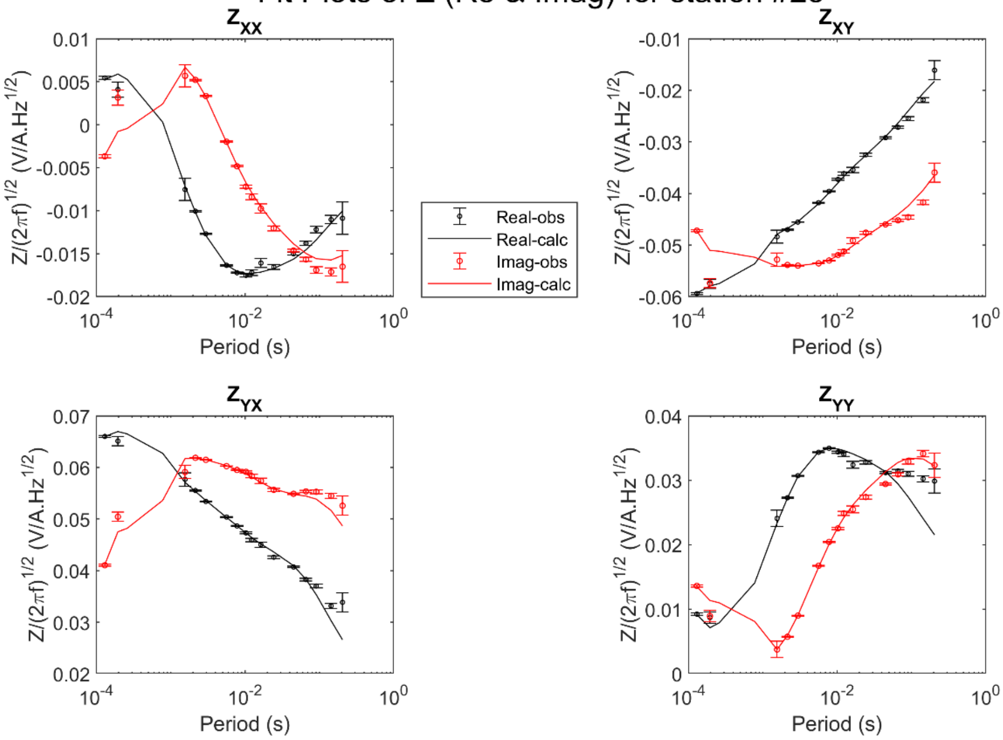

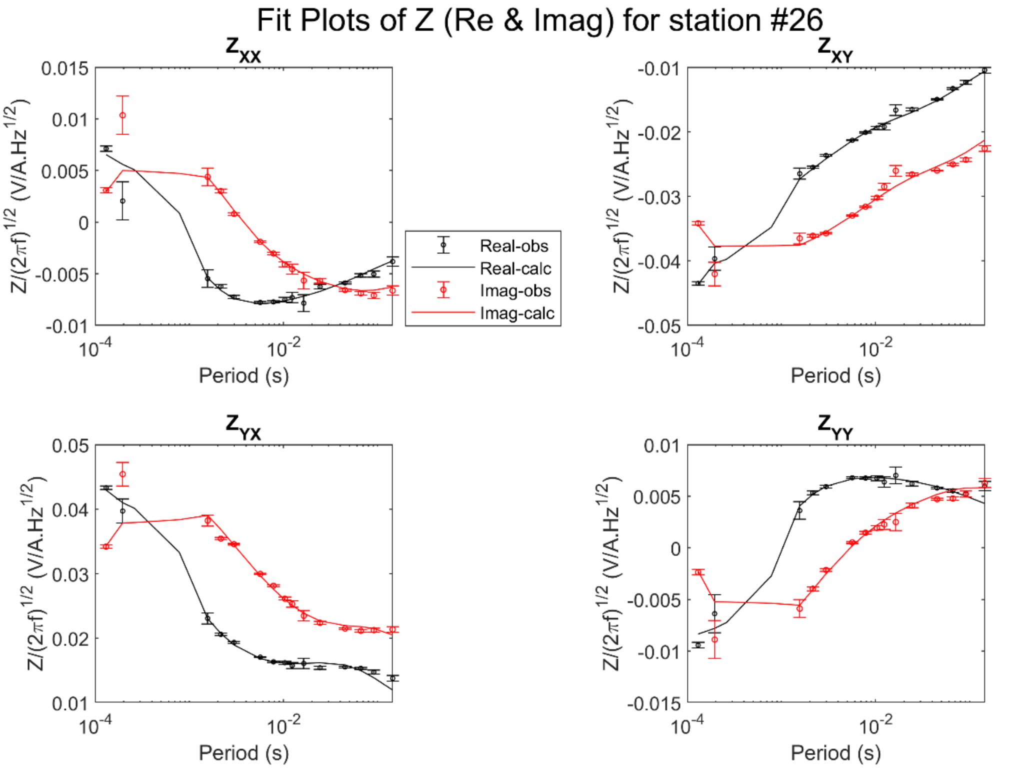
Fit Plots of Z (Re & Imag) for station #26
ZXX
ZXY
ZYX
ZYY
Z/(2πf)^1/2 (V/A.Hz^1/2)
Period (s)
Real-obs
Real-calc
Imag-obs
Imag-calc

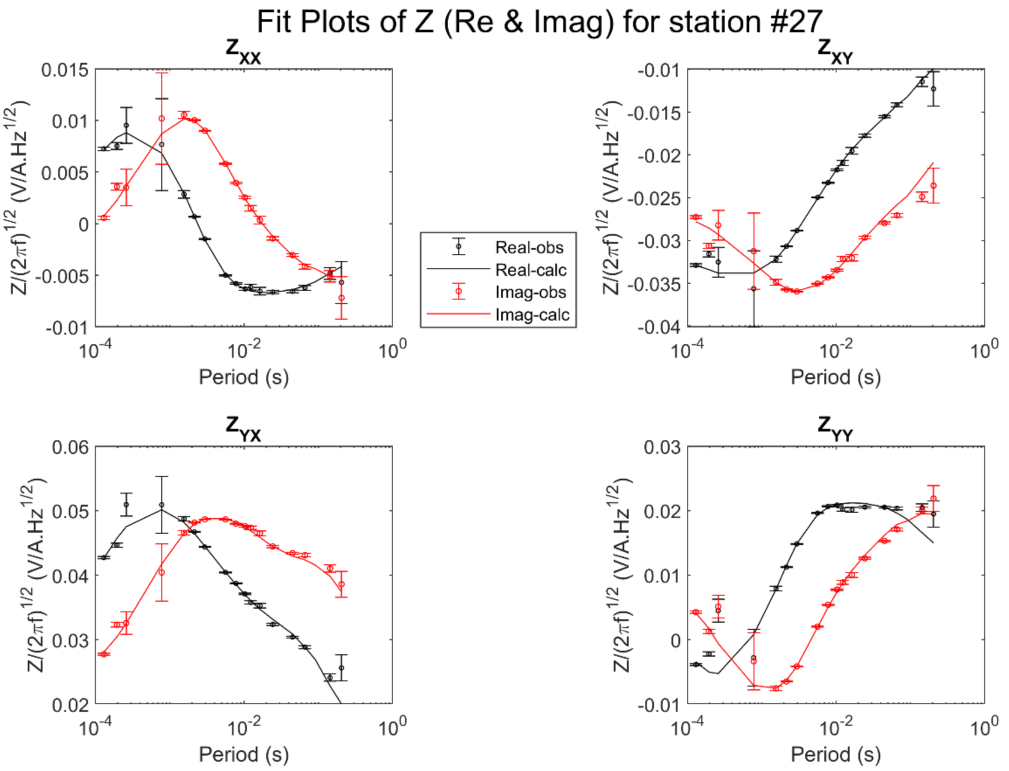
Fit Plots of Z (Re & Imag) for station #27
ZXX
ZXY
ZYX
ZYY
Z/(2πf)^1/2 (V/A.Hz^1/2)
Period (s)
Real-obs
Real-calc
Imag-obs
Imag-calc

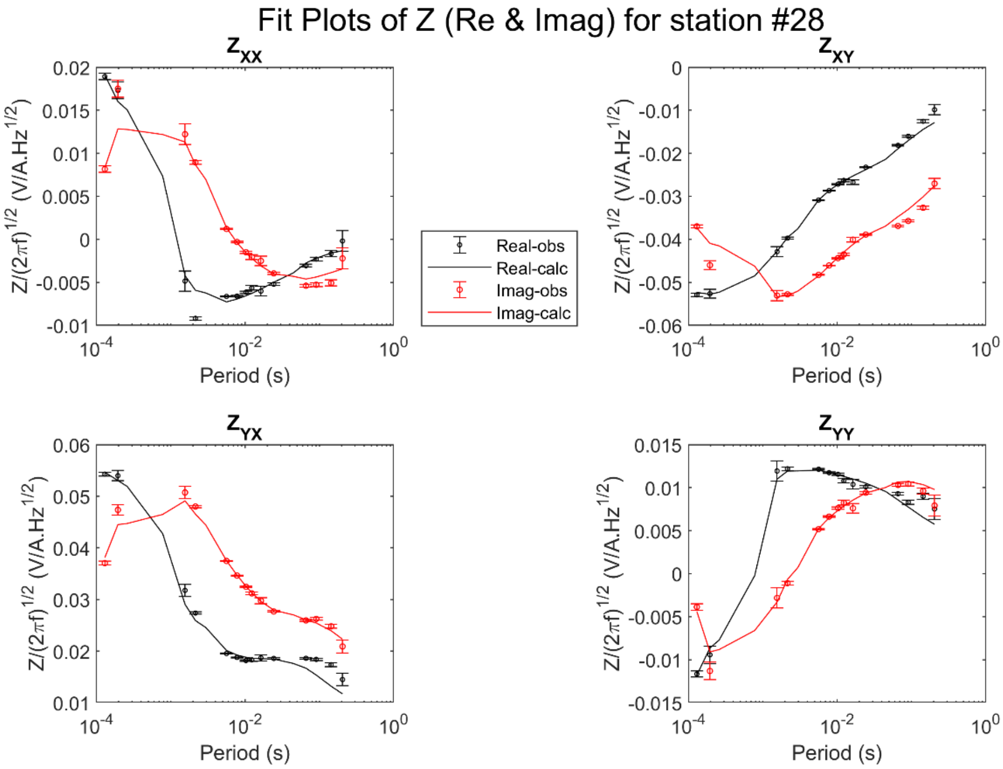
Fit Plots of Z (Re & Imag) for station #28
Z_{XX}
Z_{XY}
Z_{YX}
Z_{YY}
$Z/(2\pi f)^{1/2}$ (V/A.Hz$^{1/2}$)
Period (s)
Real-obs
Real-calc
Imag-obs
Imag-calc

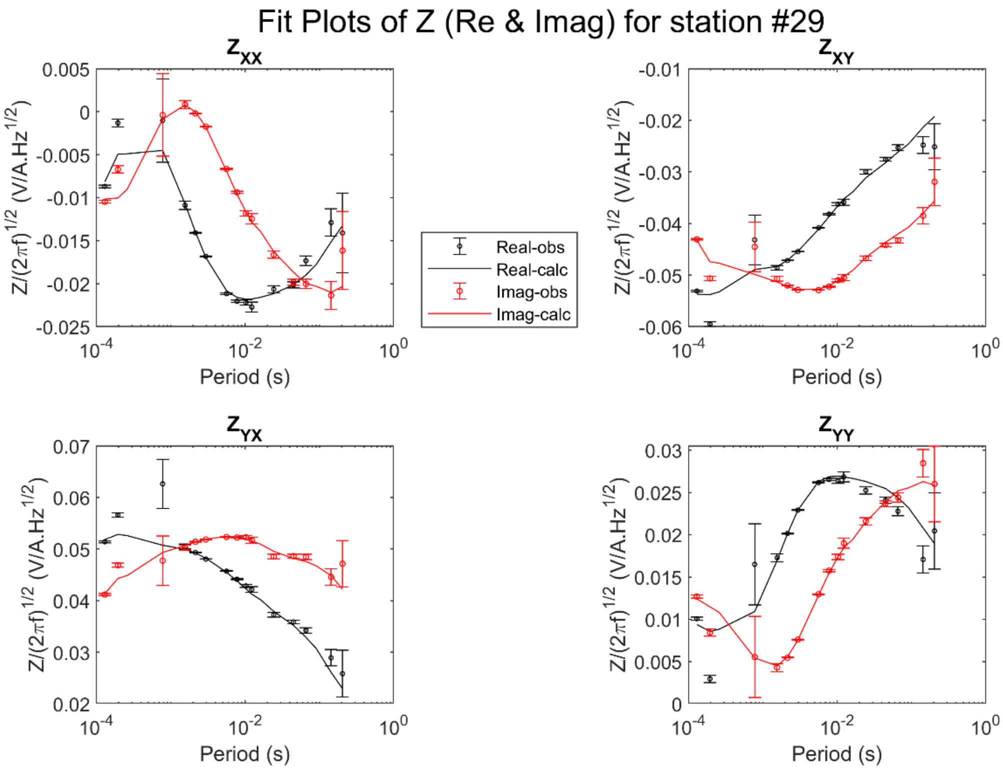
Fit Plots of Z (Re & Imag) for station #29
Z_{XX}
Z_{XY}
Z_{YX}
Z_{YY}
$Z/(2\pi f)^{1/2}$ (V/A.Hz$^{1/2}$)
Period (s)
Real-obs
Real-calc
Imag-obs
Imag-calc

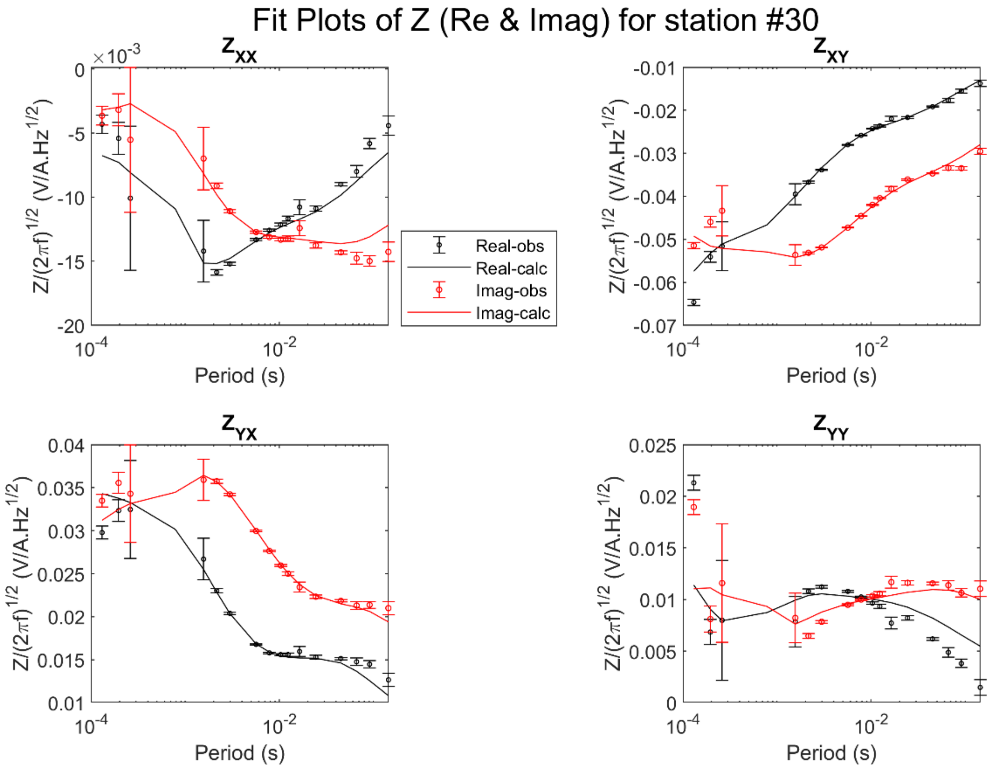
Fit Plots of Z (Re & Imag) for station #30
Z_XX
Z_XY
Z_YX
Z_YY
Z/(2πf)^1/2 (V/A.Hz^1/2)
Period (s)
Real-obs
Real-calc
Imag-obs
Imag-calc

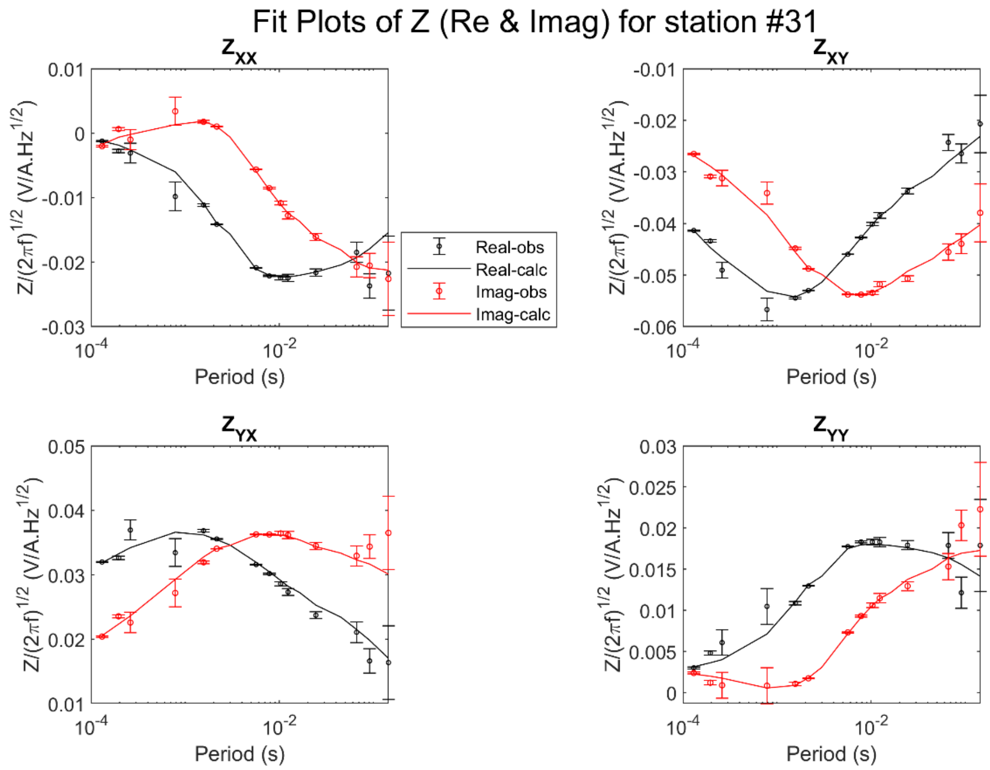
Fit Plots of Z (Re & Imag) for station #31
Z_XX
Z_XY
Z_YX
Z_YY
Z/(2πf)^1/2 (V/A.Hz^1/2)
Period (s)
Real-obs
Real-calc
Imag-obs
Imag-calc

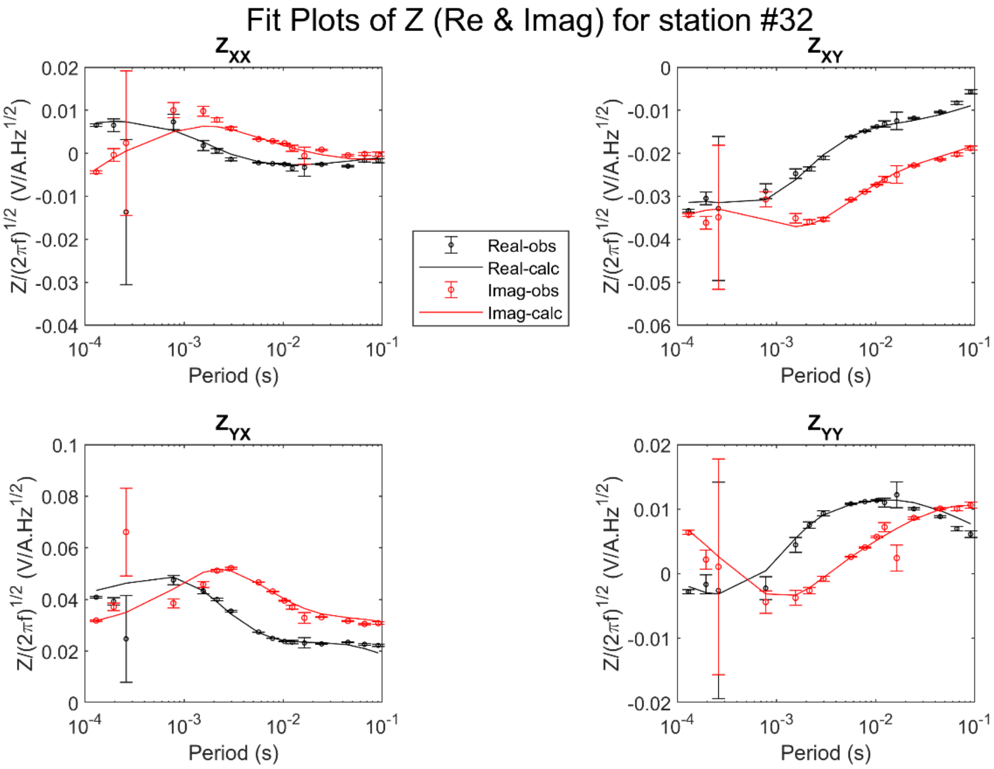
Fit Plots of Z (Re & Imag) for station #32
Z_{XX}
Z_{XY}
Z_{YX}
Z_{YY}
Real-obs
Real-calc
Imag-obs
Imag-calc
$Z/(2\pi f)^{1/2}$ (V/A.Hz$^{1/2}$)
Period (s)

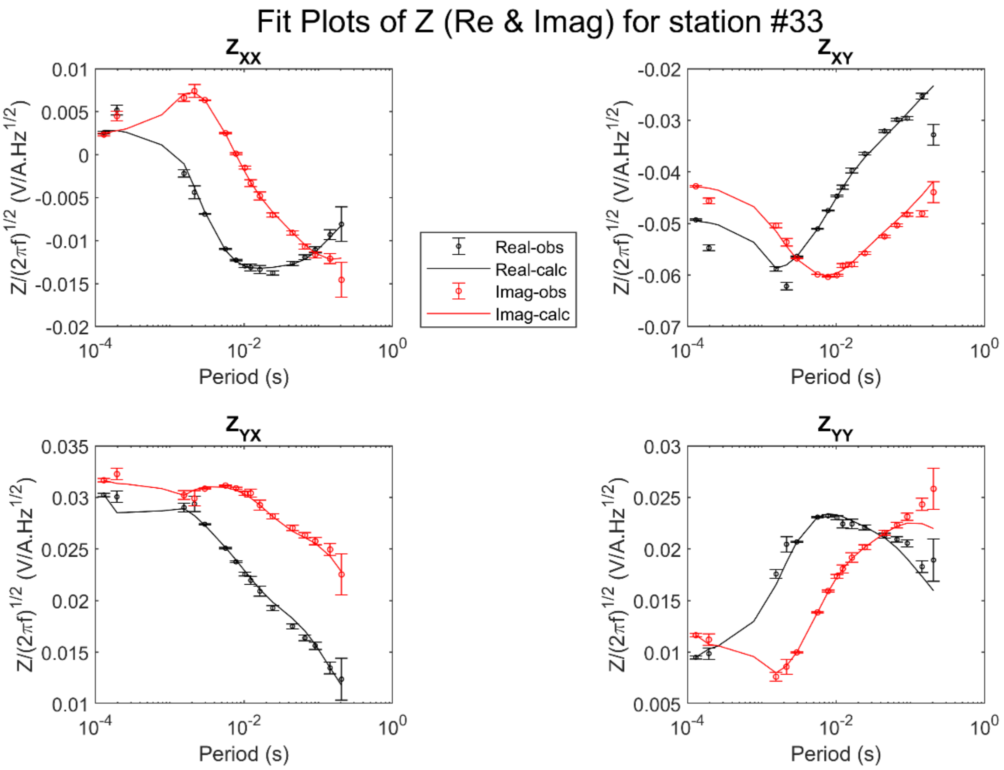
Fit Plots of Z (Re & Imag) for station #33
Z_{XX}
Z_{XY}
Z_{YX}
Z_{YY}
Real-obs
Real-calc
Imag-obs
Imag-calc
$Z/(2\pi f)^{1/2}$ (V/A.Hz$^{1/2}$)
Period (s)

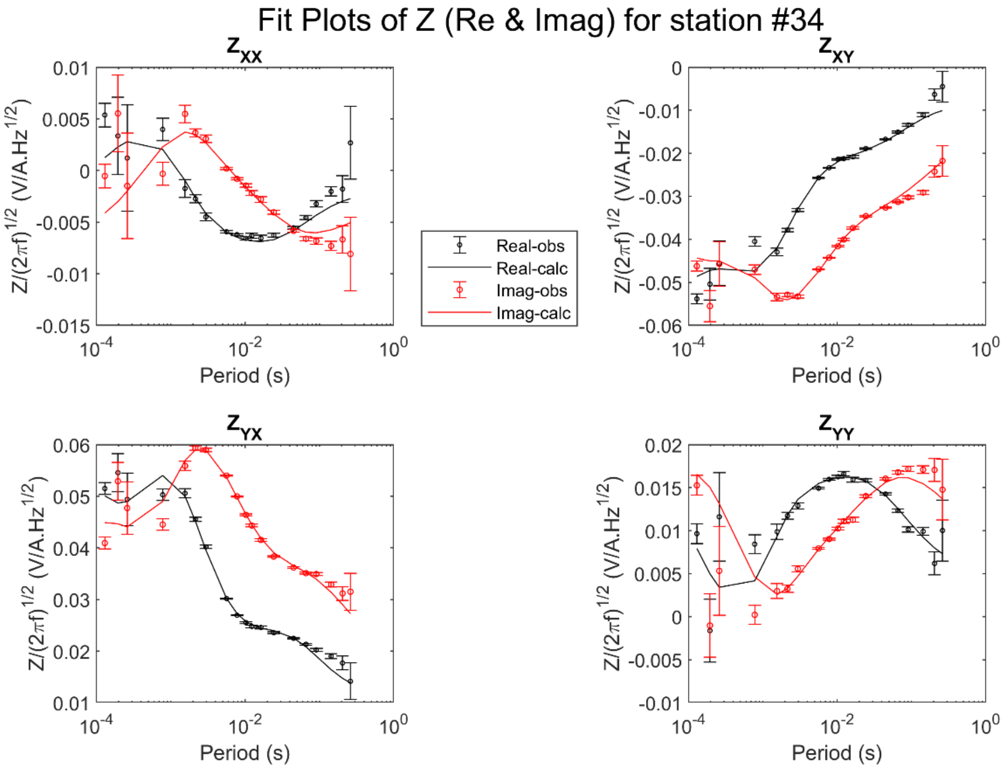
Fit Plots of Z (Re & Imag) for station #34
Z XX
Z XY
Z YX
Z YY
Z/(2πf)^1/2 (V/A.Hz^1/2)
Period (s)
Real-obs
Real-calc
Imag-obs
Imag-calc

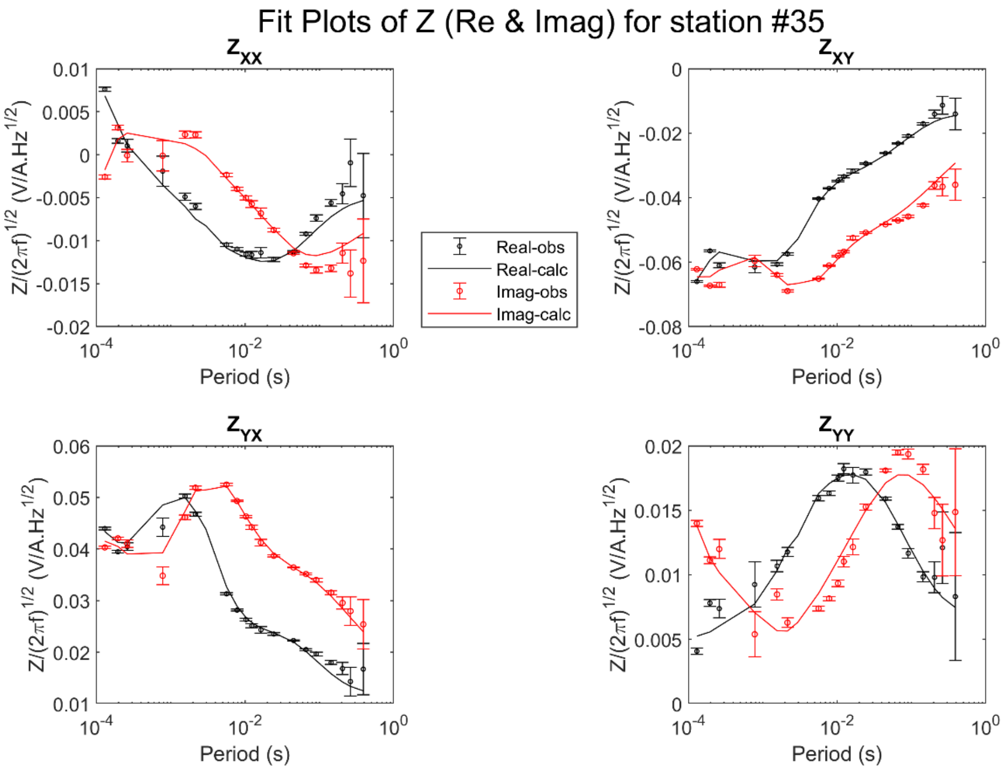
Fit Plots of Z (Re & Imag) for station #35
Z XX
Z XY
Z YX
Z YY
Z/(2πf)^1/2 (V/A.Hz^1/2)
Period (s)
Real-obs
Real-calc
Imag-obs
Imag-calc

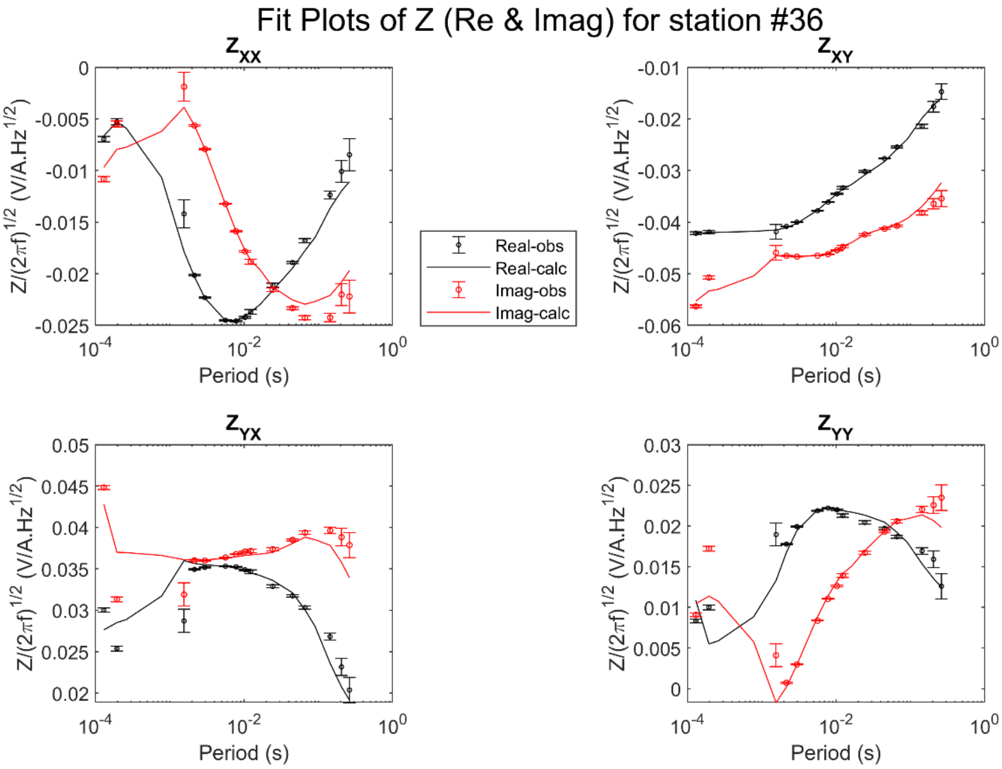
Fit Plots of Z (Re & Imag) for station #36
Z_{XX}
Z_{XY}
Z_{YX}
Z_{YY}
$Z/(2\pi f)^{1/2}$ (V/A.Hz$^{1/2}$)
Period (s)
Real-obs
Real-calc
Imag-obs
Imag-calc

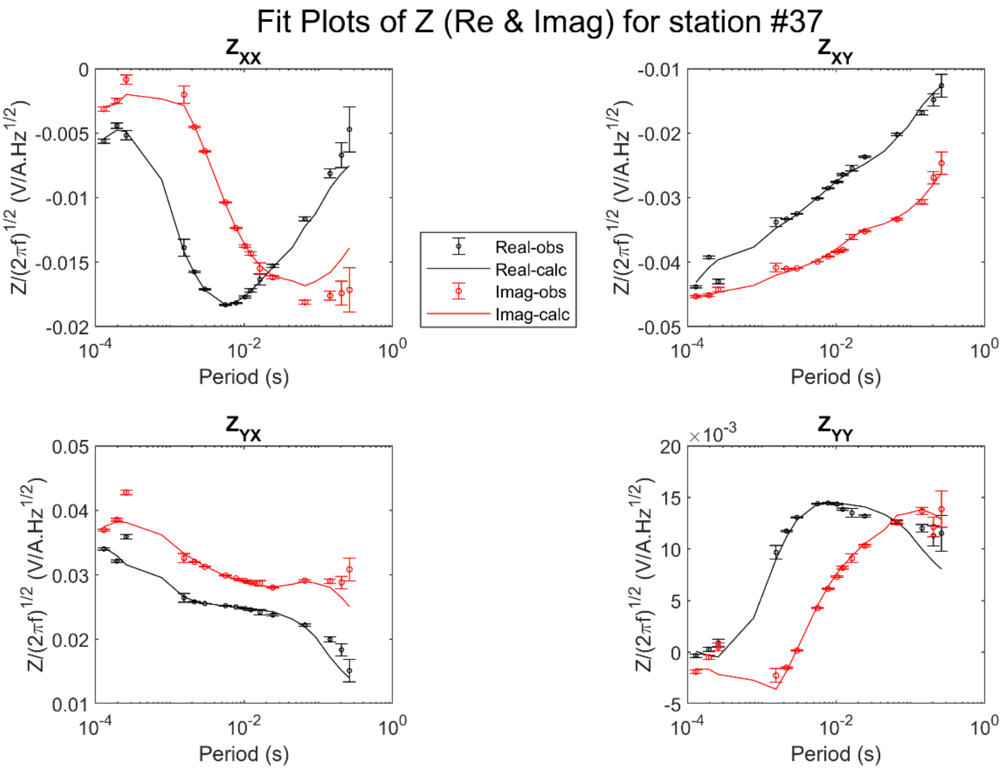
Fit Plots of Z (Re & Imag) for station #37
Z_{XX}
Z_{XY}
Z_{YX}
Z_{YY}
$Z/(2\pi f)^{1/2}$ (V/A.Hz$^{1/2}$)
Period (s)
$\times 10^{-3}$
Real-obs
Real-calc
Imag-obs
Imag-calc

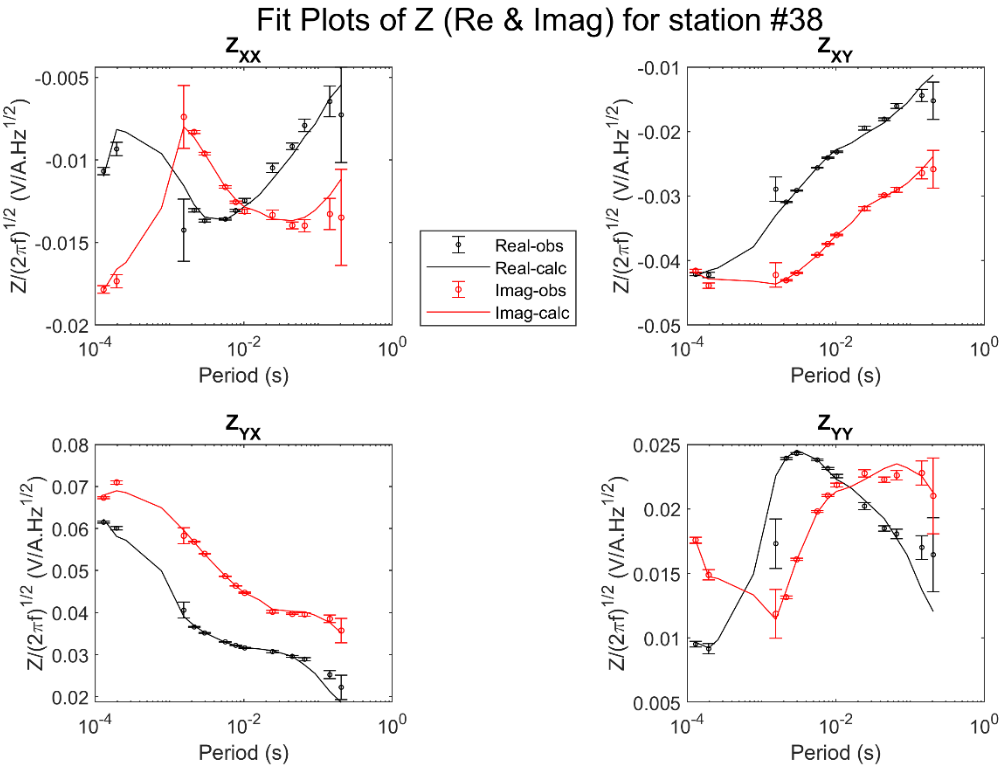
Fit Plots of Z (Re & Imag) for station #38
Z_XX
Z_XY
Z_YX
Z_YY
Z/(2πf)^1/2 (V/A.Hz^1/2)
Period (s)
Real-obs
Real-calc
Imag-obs
Imag-calc

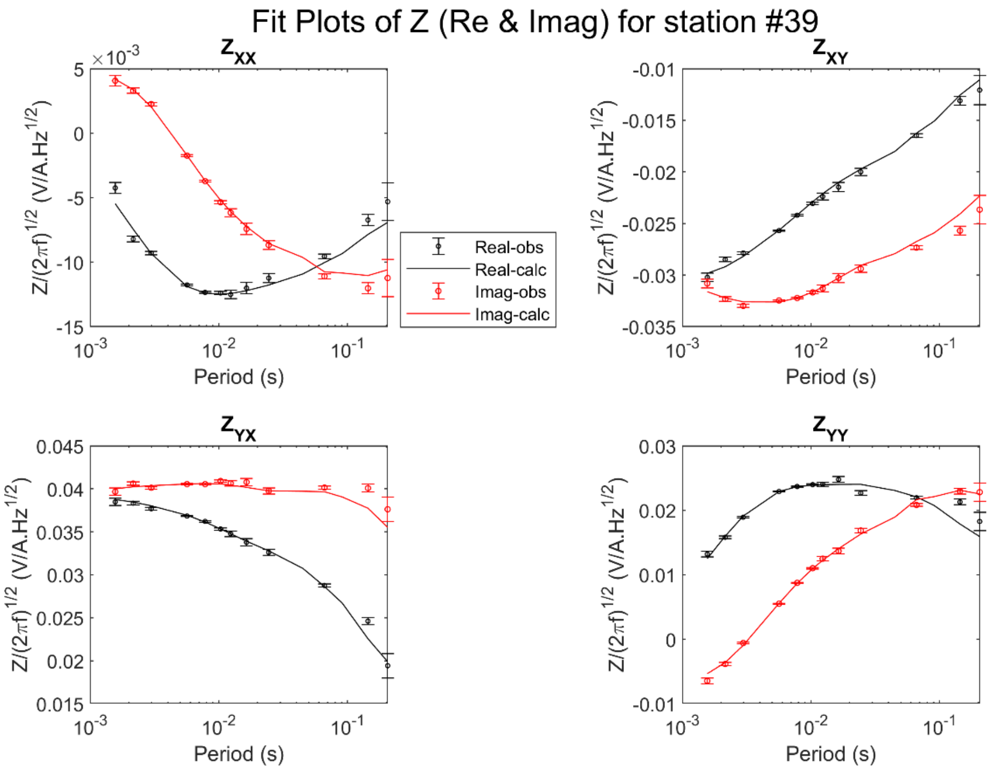
Fit Plots of Z (Re & Imag) for station #39
Z_XX
Z_XY
Z_YX
Z_YY
Z/(2πf)^1/2 (V/A.Hz^1/2)
Period (s)
Real-obs
Real-calc
Imag-obs
Imag-calc

Fit Plots of Z (Re & Imag) for station #40

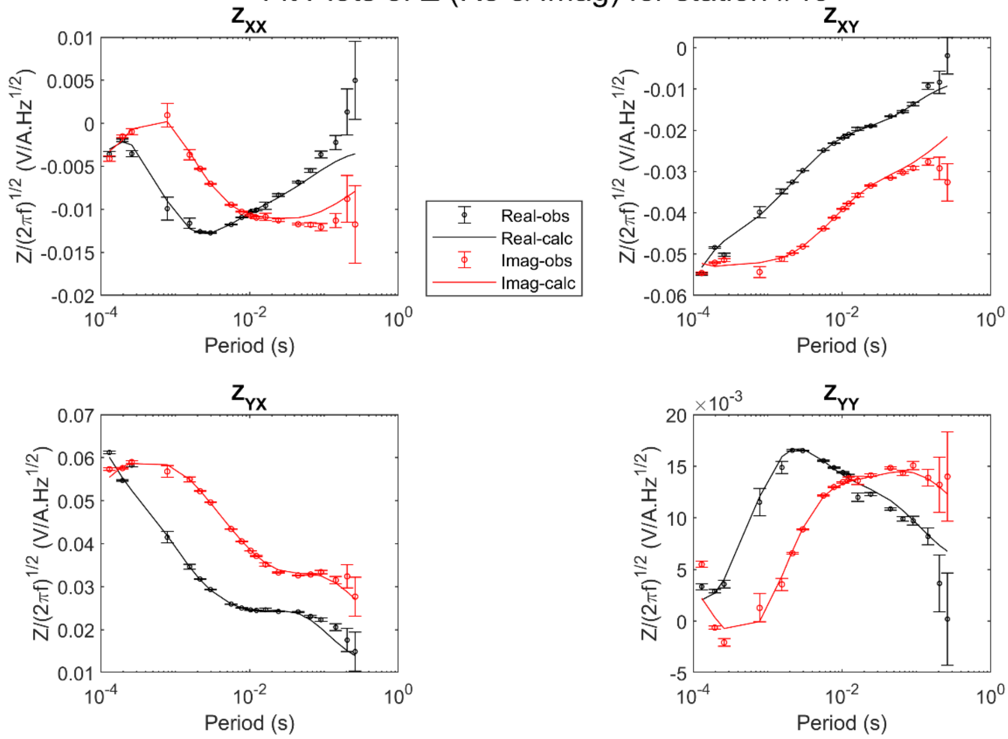

Fit Plots of Z (Re & Imag) for station #41

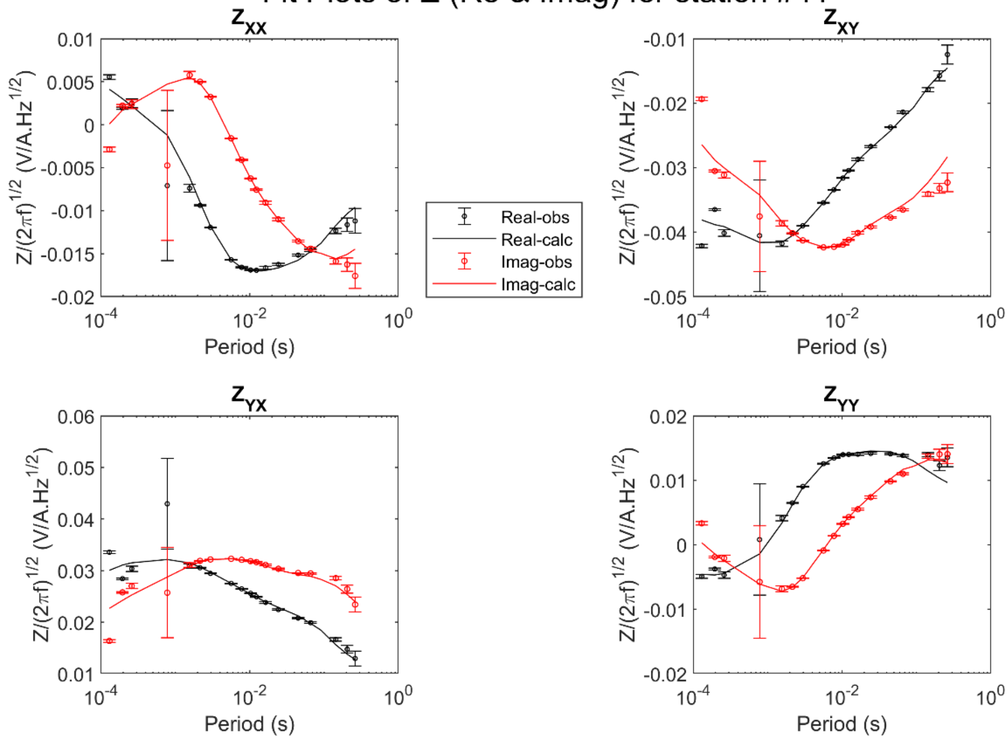

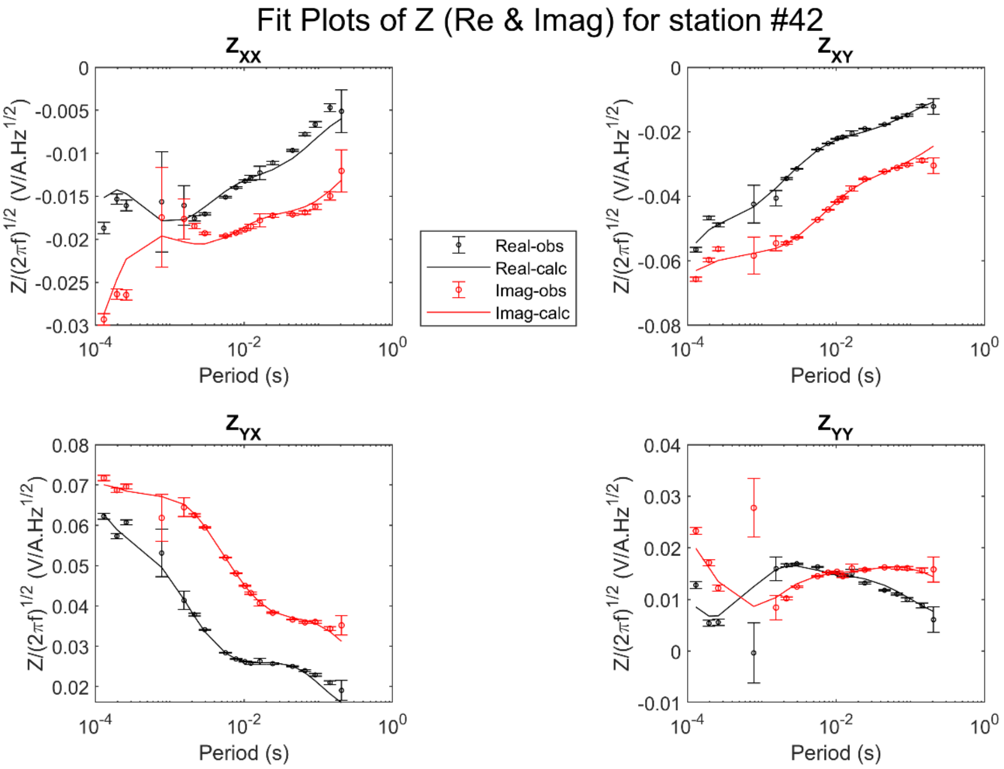
Fit Plots of Z (Re & Imag) for station #42
Z_XX
Z_XY
Z_YX
Z_YY
Z/(2πf)^1/2 (V/A.Hz^1/2)
Period (s)
Real-obs
Real-calc
Imag-obs
Imag-calc

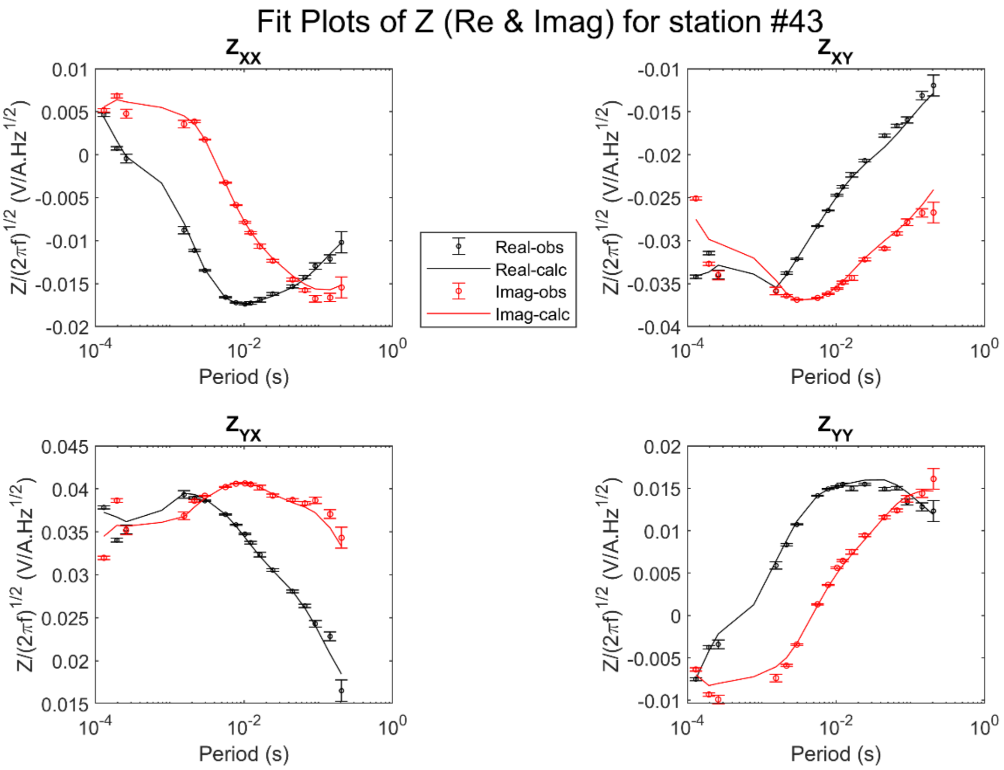
Fit Plots of Z (Re & Imag) for station #43
Z_XX
Z_XY
Z_YX
Z_YY
Z/(2πf)^1/2 (V/A.Hz^1/2)
Period (s)
Real-obs
Real-calc
Imag-obs
Imag-calc

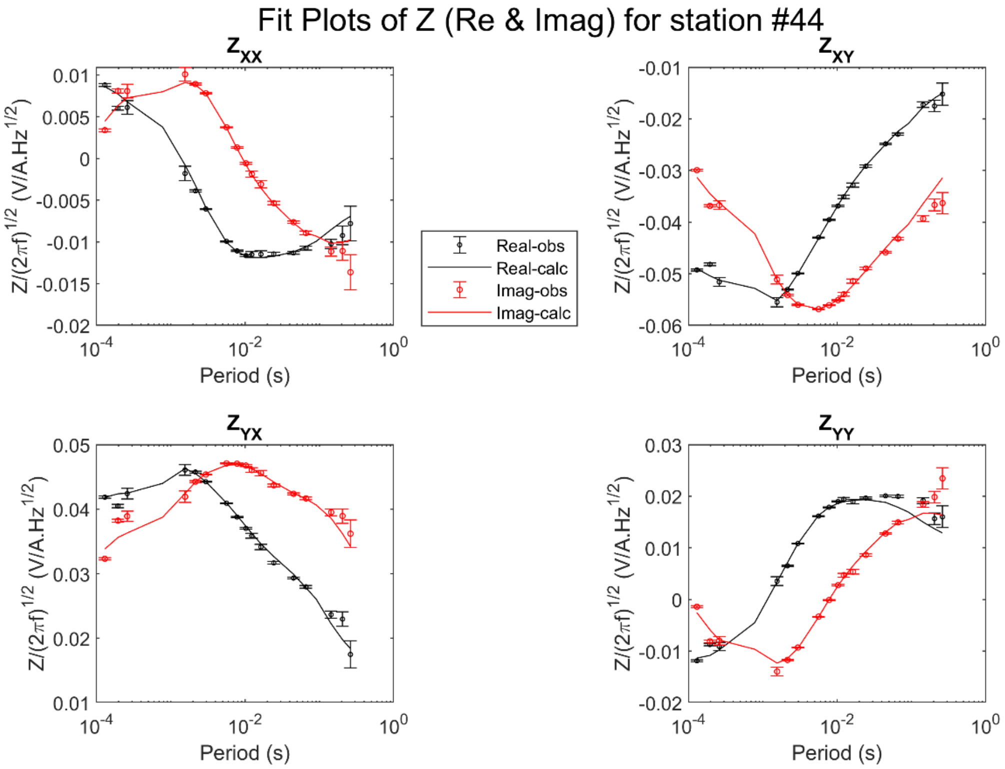
Fit Plots of Z (Re & Imag) for station #44
Z_XX
Z_XY
Z_YX
Z_YY
Z/(2πf)^1/2 (V/A.Hz^1/2)
Period (s)
Real-obs
Real-calc
Imag-obs
Imag-calc

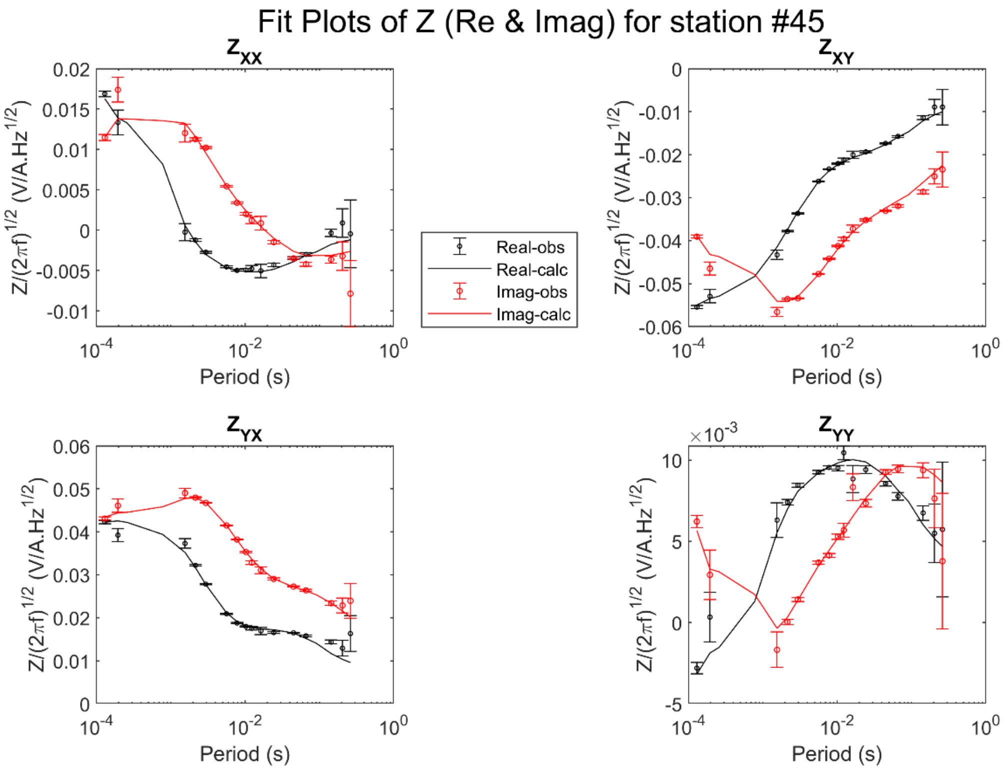
Fit Plots of Z (Re & Imag) for station #45
Z_XX
Z_XY
Z_YX
Z_YY
Z/(2πf)^1/2 (V/A.Hz^1/2)
Period (s)
Real-obs
Real-calc
Imag-obs
Imag-calc

Fit Plots of Z (Re & Imag) for station #46

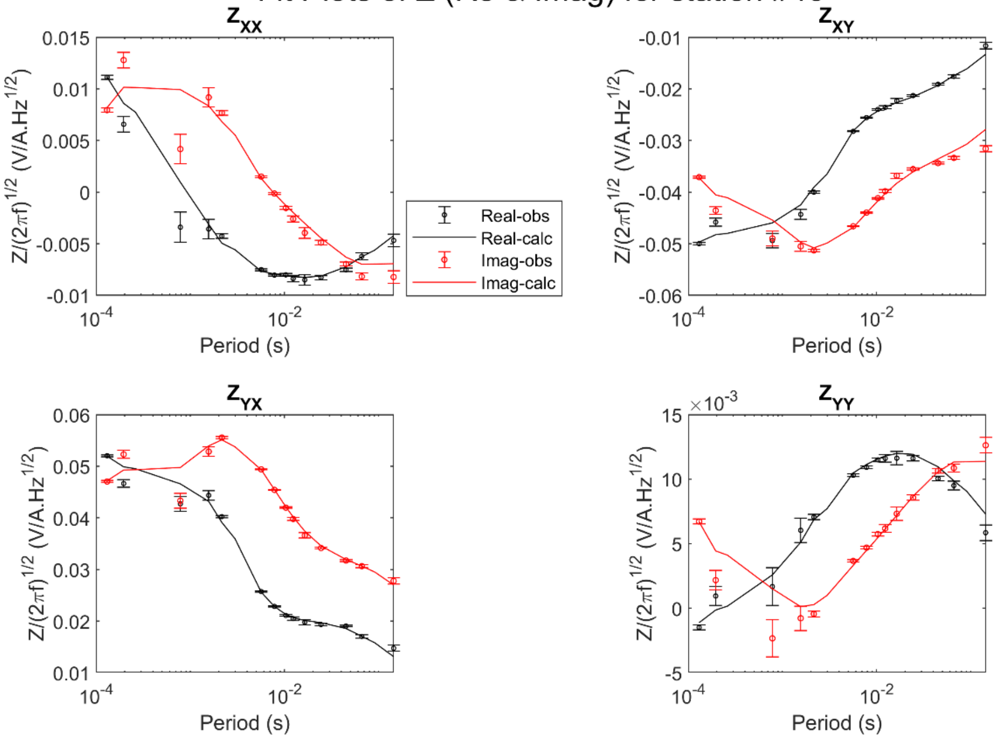

Fit Plots of Z (Re & Imag) for station #47

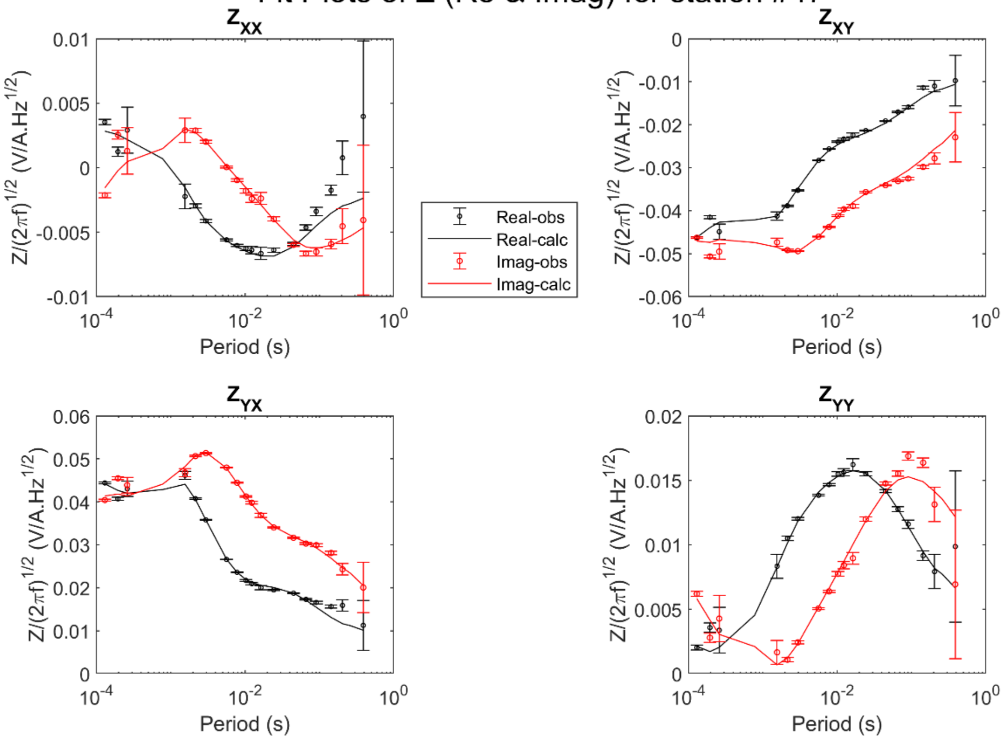

Fit Plots of Z (Re & Imag) for station #48

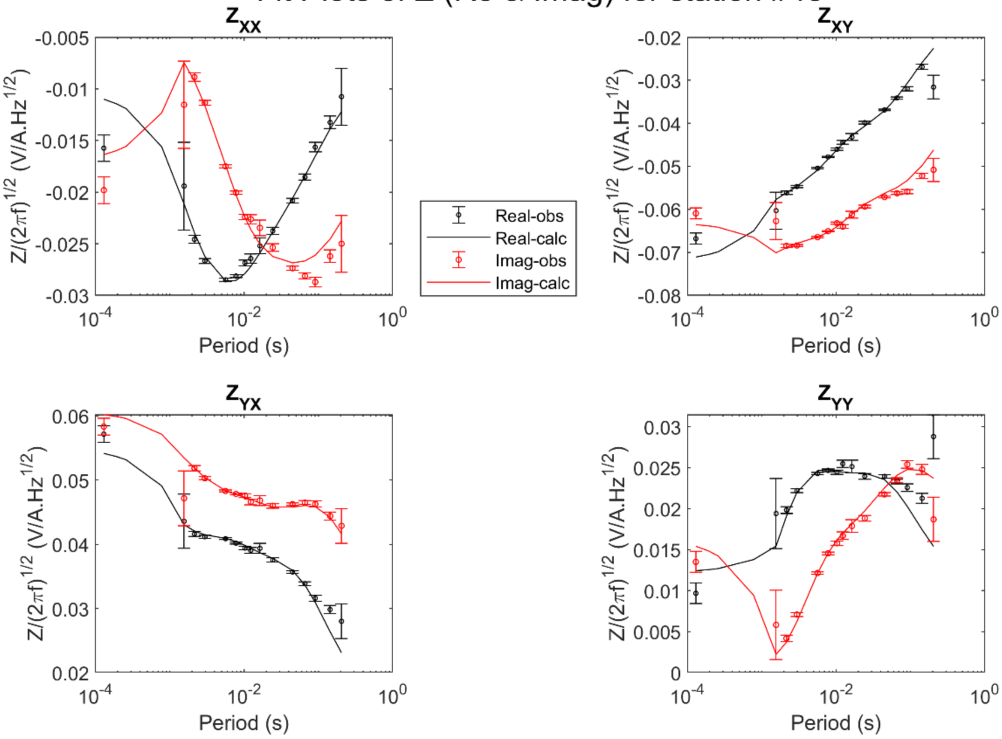

Fit Plots of Z (Re & Imag) for station #49

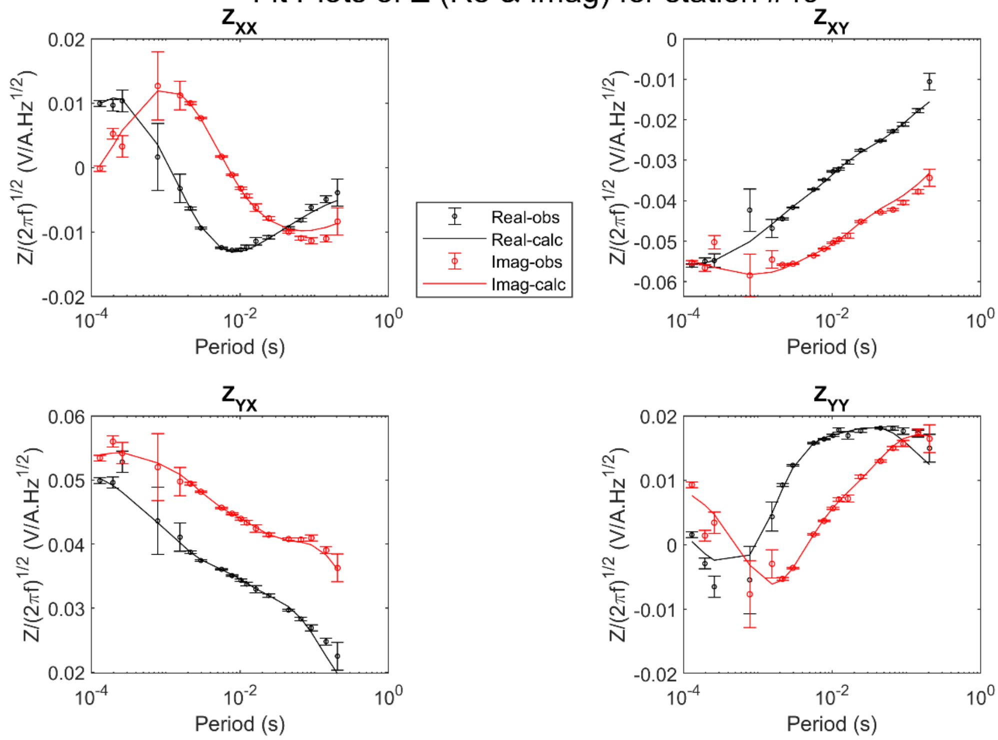

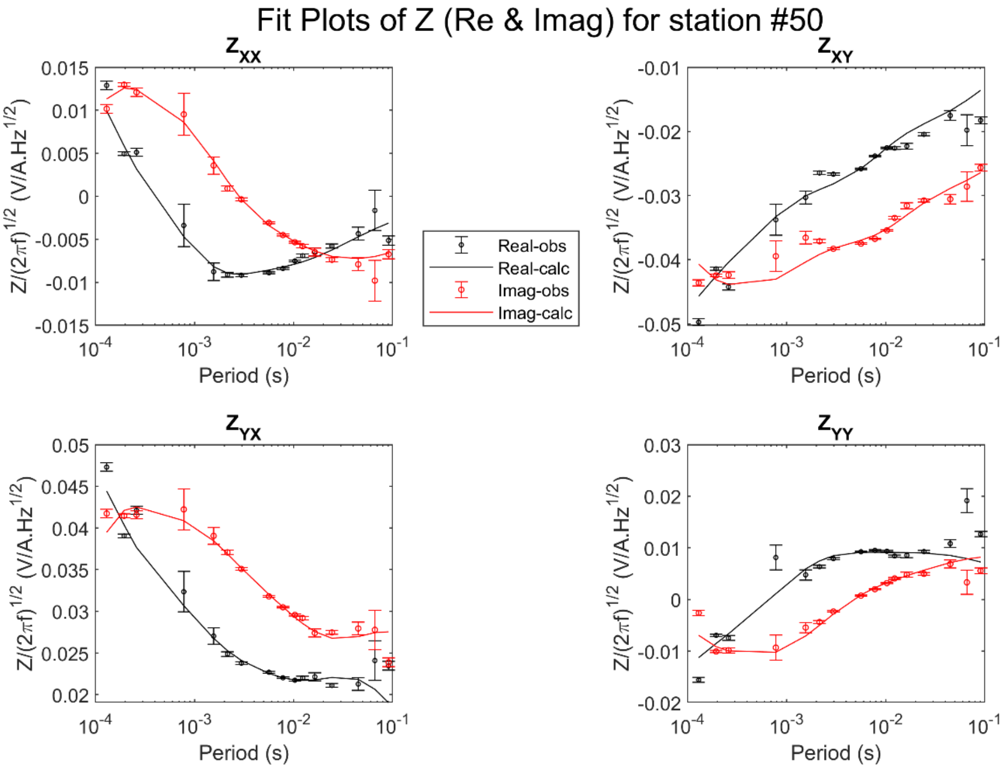
Fit Plots of Z (Re & Imag) for station #50
Z_XX
Z_XY
Z_YX
Z_YY
Z/(2πf)^1/2 (V/A.Hz^1/2)
Period (s)
Real-obs
Real-calc
Imag-obs
Imag-calc

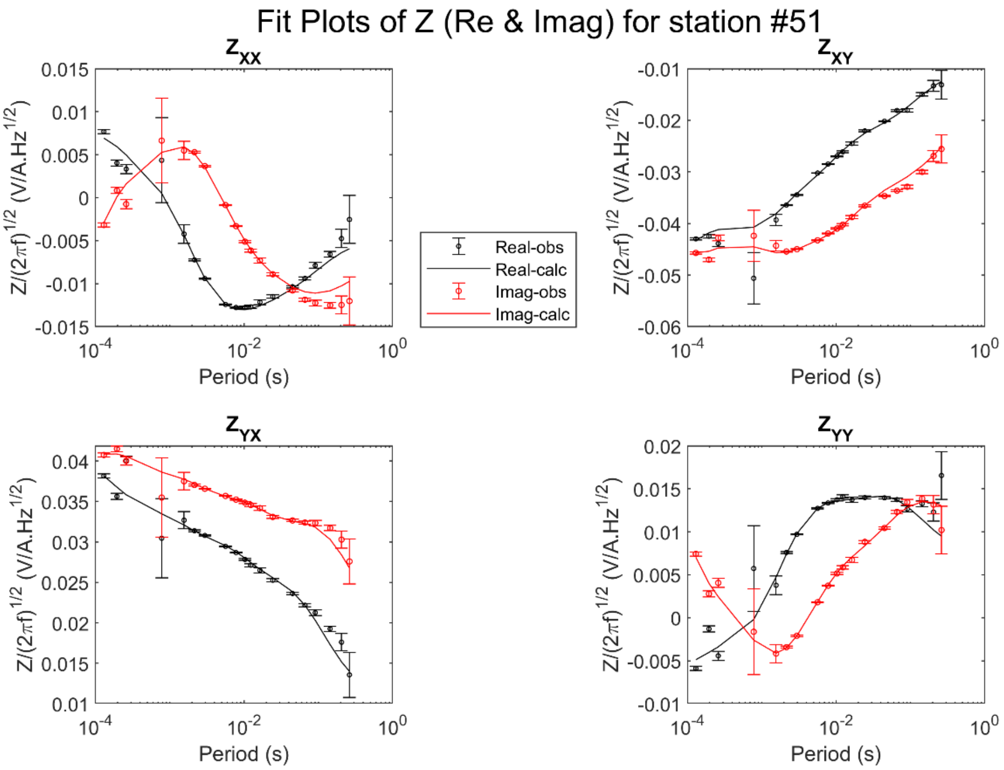
Fit Plots of Z (Re & Imag) for station #51
Z_XX
Z_XY
Z_YX
Z_YY
Z/(2πf)^1/2 (V/A.Hz^1/2)
Period (s)
Real-obs
Real-calc
Imag-obs
Imag-calc

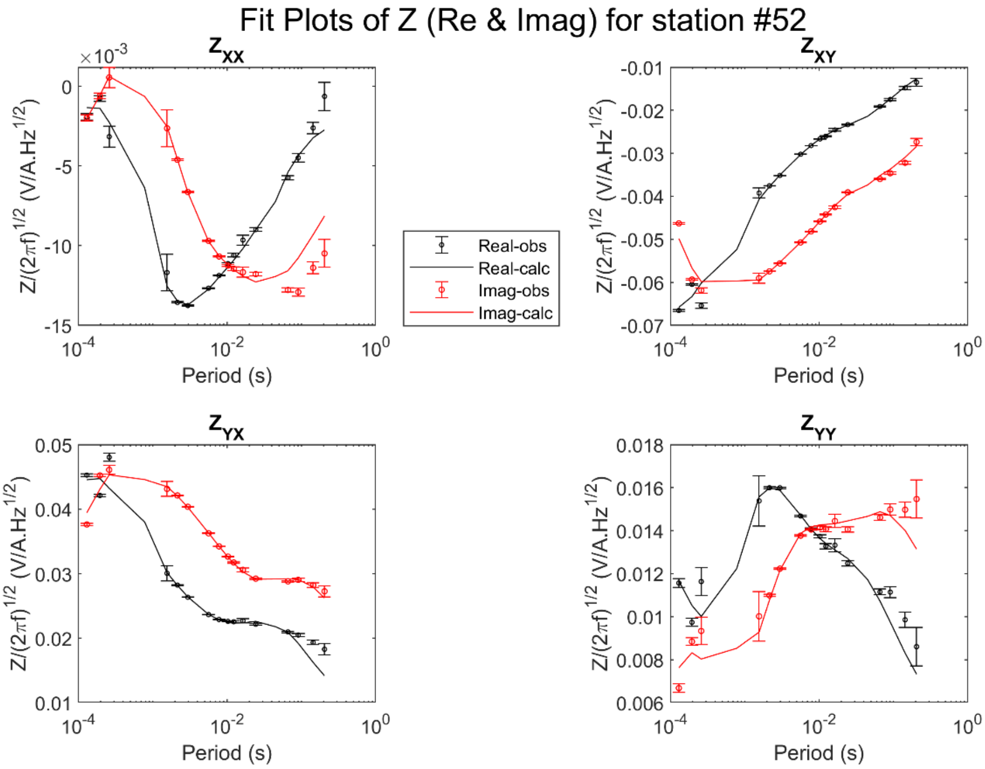
Fit Plots of Z (Re & Imag) for station #52
Z_{XX}
Z_{XY}
Z_{YX}
Z_{YY}
$\times 10^{-3}$
$Z/(2\pi f)^{1/2}$ (V/A.Hz$^{1/2}$)
Period (s)
Real-obs
Real-calc
Imag-obs
Imag-calc

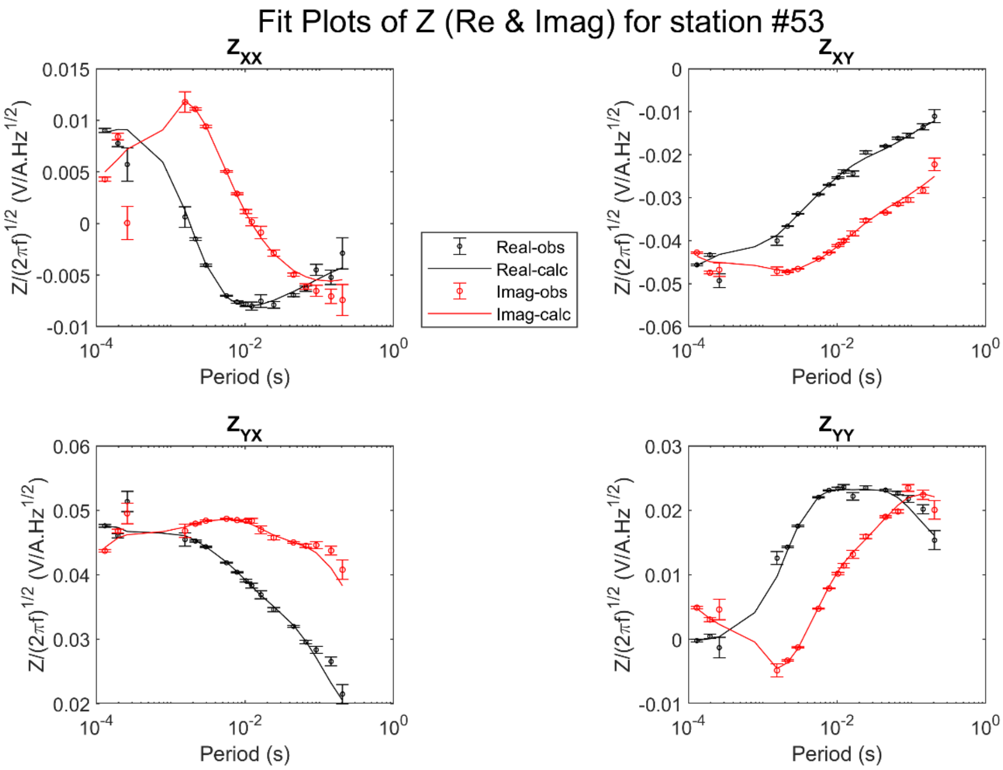
Fit Plots of Z (Re & Imag) for station #53
Z_{XX}
Z_{XY}
Z_{YX}
Z_{YY}
$Z/(2\pi f)^{1/2}$ (V/A.Hz$^{1/2}$)
Period (s)
Real-obs
Real-calc
Imag-obs
Imag-calc

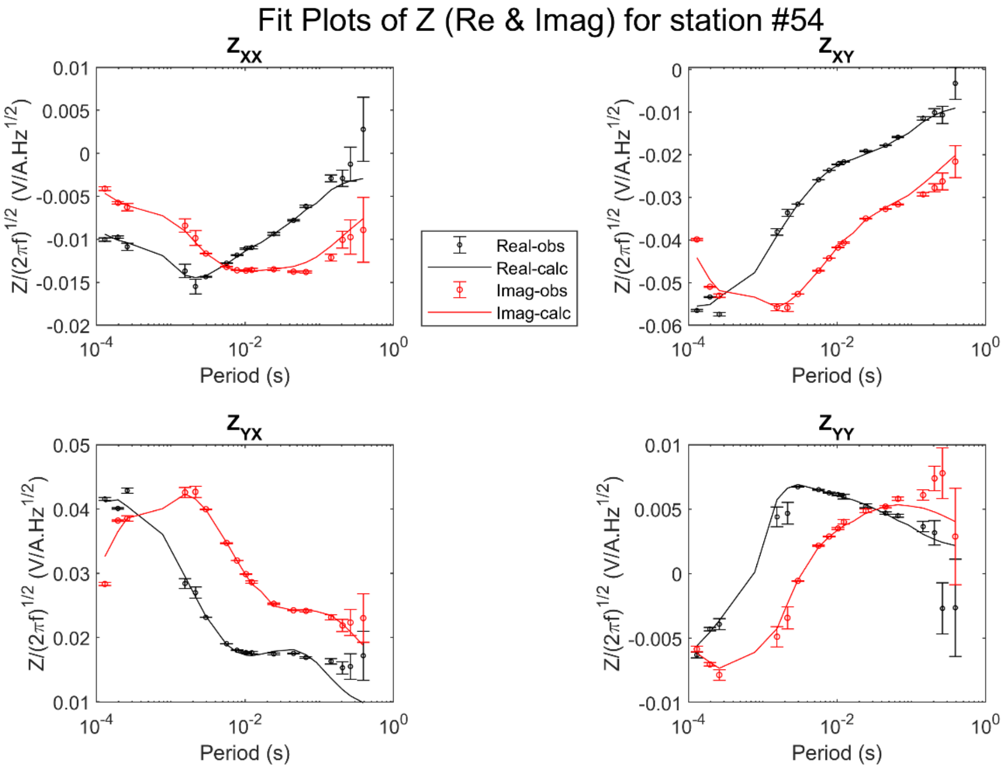
Fit Plots of Z (Re & Imag) for station #54
Z_{XX}
Z_{XY}
Z_{YX}
Z_{YY}
$Z/(2\pi f)^{1/2}$ (V/A.Hz$^{1/2}$)
Period (s)
Real-obs
Real-calc
Imag-obs
Imag-calc

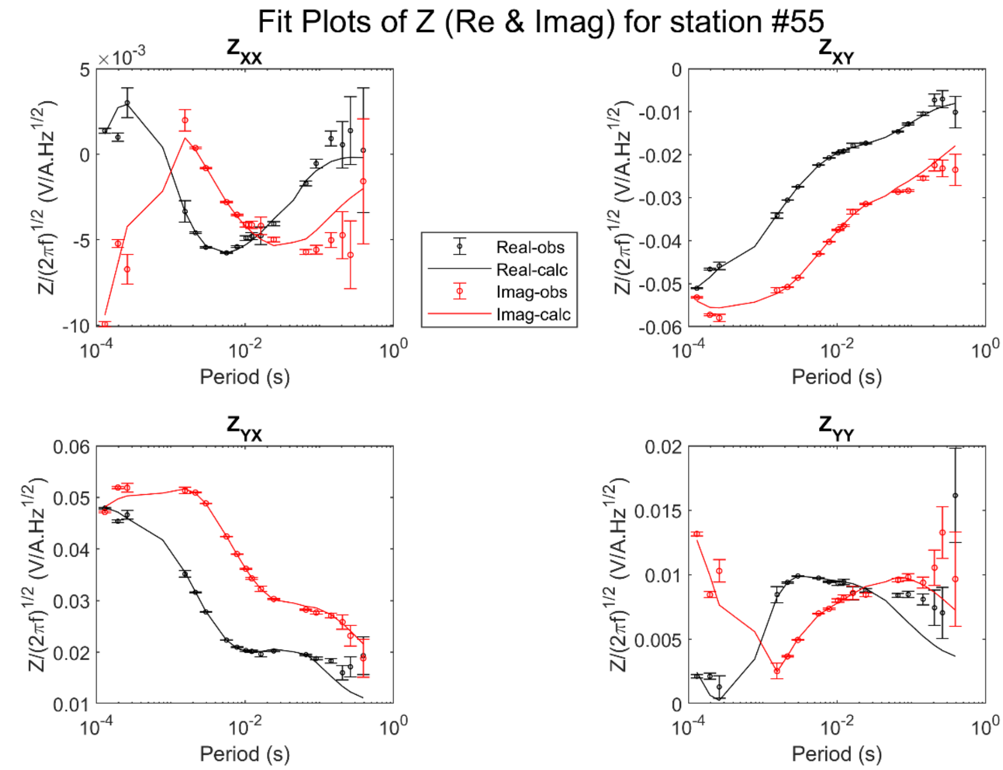
Fit Plots of Z (Re & Imag) for station #55
Z_{XX}
Z_{XY}
Z_{YX}
Z_{YY}
$\times 10^{-3}$
$Z/(2\pi f)^{1/2}$ (V/A.Hz$^{1/2}$)
Period (s)
Real-obs
Real-calc
Imag-obs
Imag-calc

Fit Plots of Z (Re & Imag) for station #56

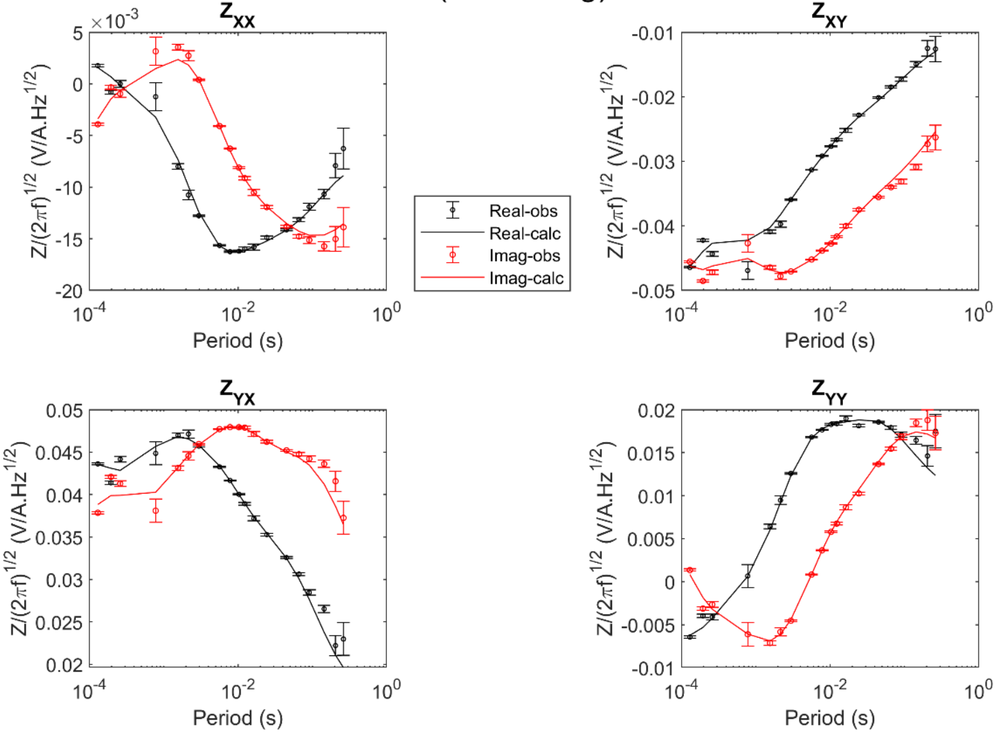

Fit Plots of Z (Re & Imag) for station #57

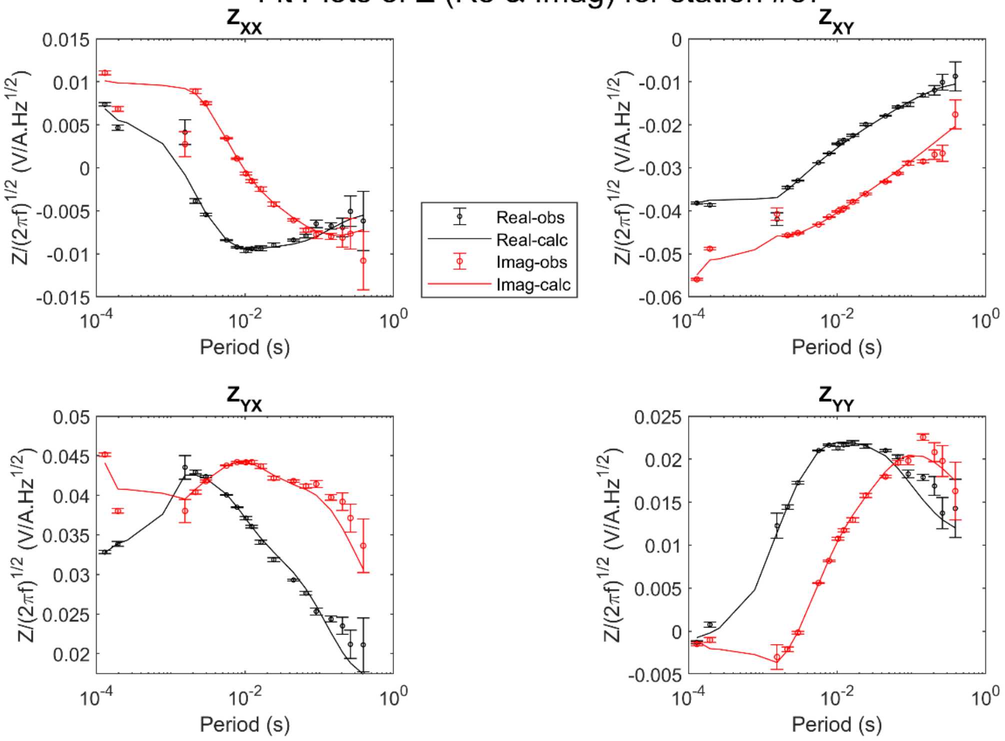

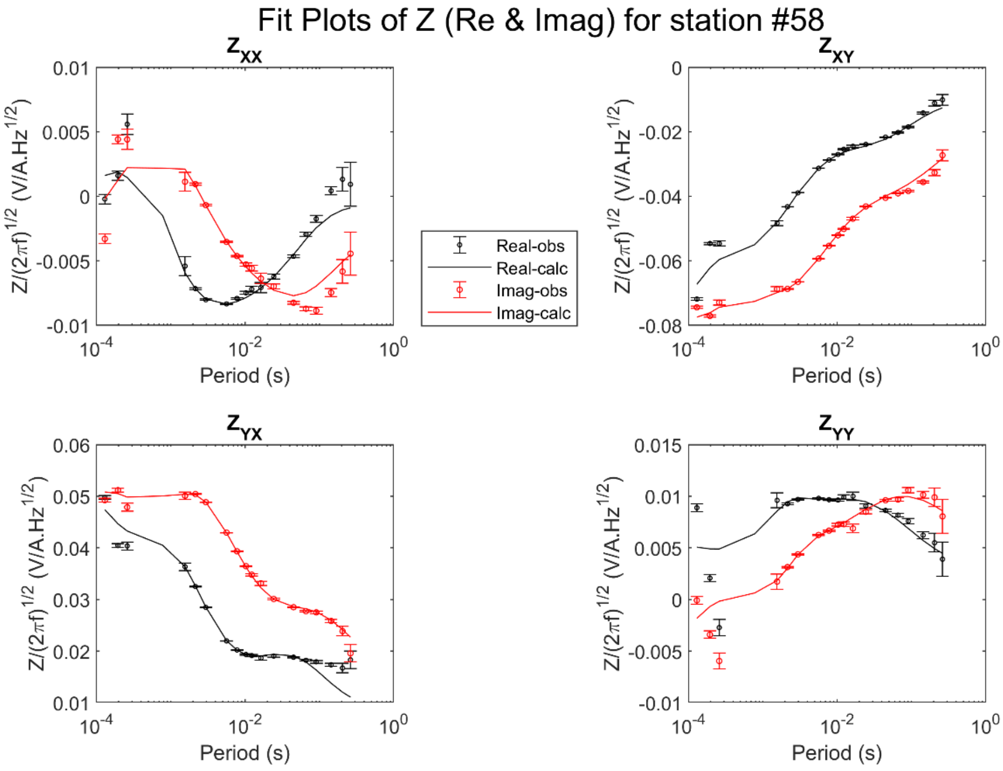
Fit Plots of Z (Re & Imag) for station #58
Z_XX
Z_XY
Z_YX
Z_YY
Z/(2πf)^1/2 (V/A.Hz^1/2)
Period (s)
Real-obs
Real-calc
Imag-obs
Imag-calc

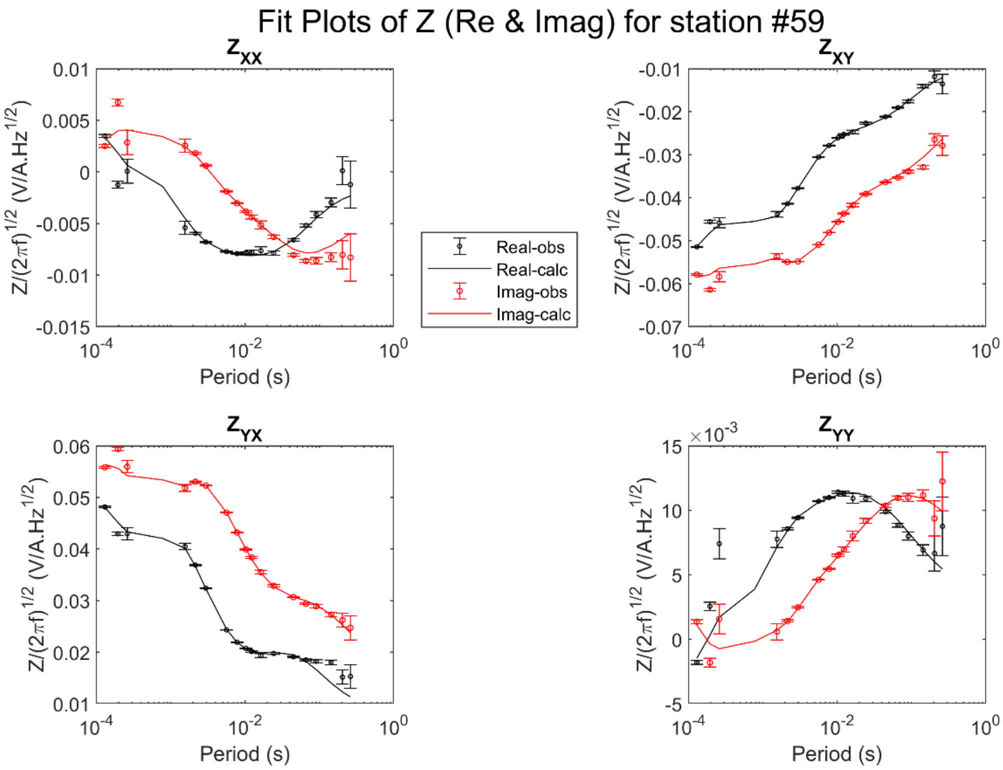
Fit Plots of Z (Re & Imag) for station #59
Z_XX
Z_XY
Z_YX
Z_YY
×10^-3
Z/(2πf)^1/2 (V/A.Hz^1/2)
Period (s)
Real-obs
Real-calc
Imag-obs
Imag-calc

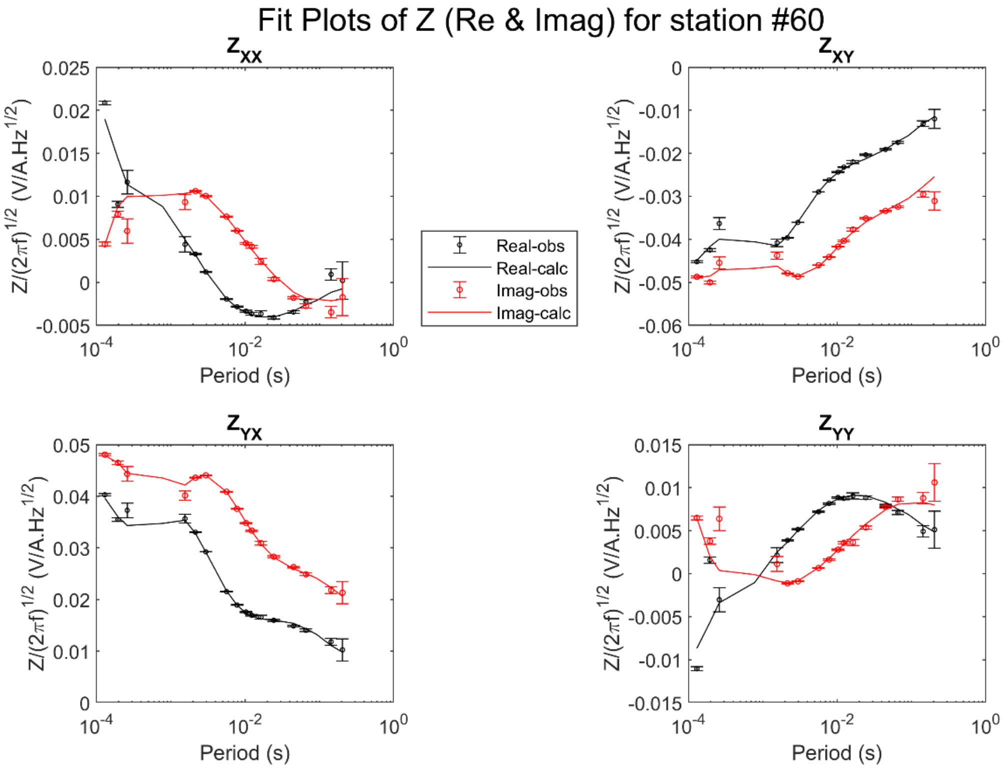
Fit Plots of Z (Re & Imag) for station #60
Z_XX
Z_XY
Z_YX
Z_YY
Z/(2πf)^1/2 (V/A.Hz^1/2)
Period (s)
Real-obs
Real-calc
Imag-obs
Imag-calc

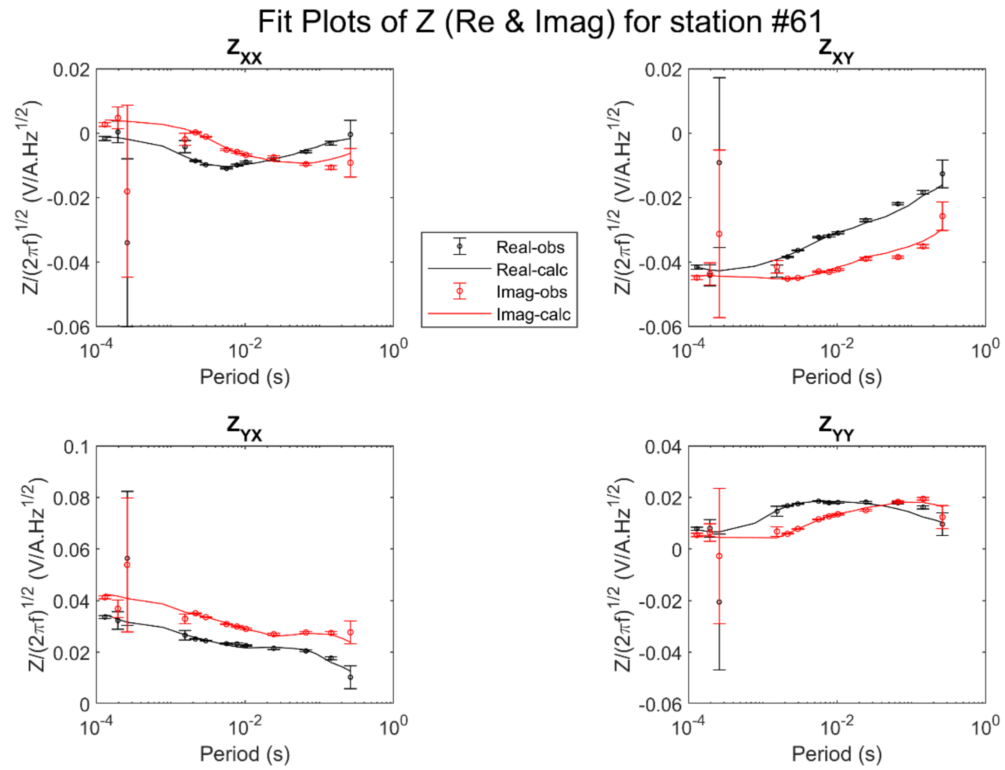
Fit Plots of Z (Re & Imag) for station #61
Z_XX
Z_XY
Z_YX
Z_YY
Z/(2πf)^1/2 (V/A.Hz^1/2)
Period (s)
Real-obs
Real-calc
Imag-obs
Imag-calc

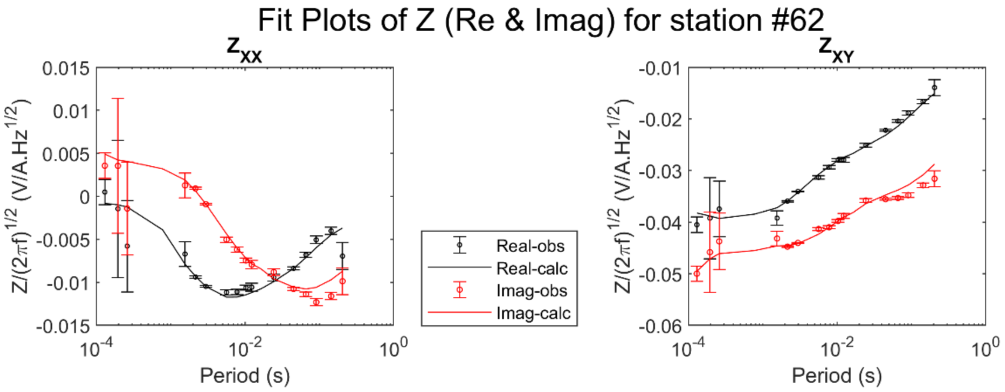

Fit Plots of Z (Re & Imag) for station #62
ZXX
ZXY
ZYX
ZYY
Z/(2πf)^1/2 (V/A.Hz^1/2)
Period (s)
Real-obs
Real-calc
Imag-obs
Imag-calc

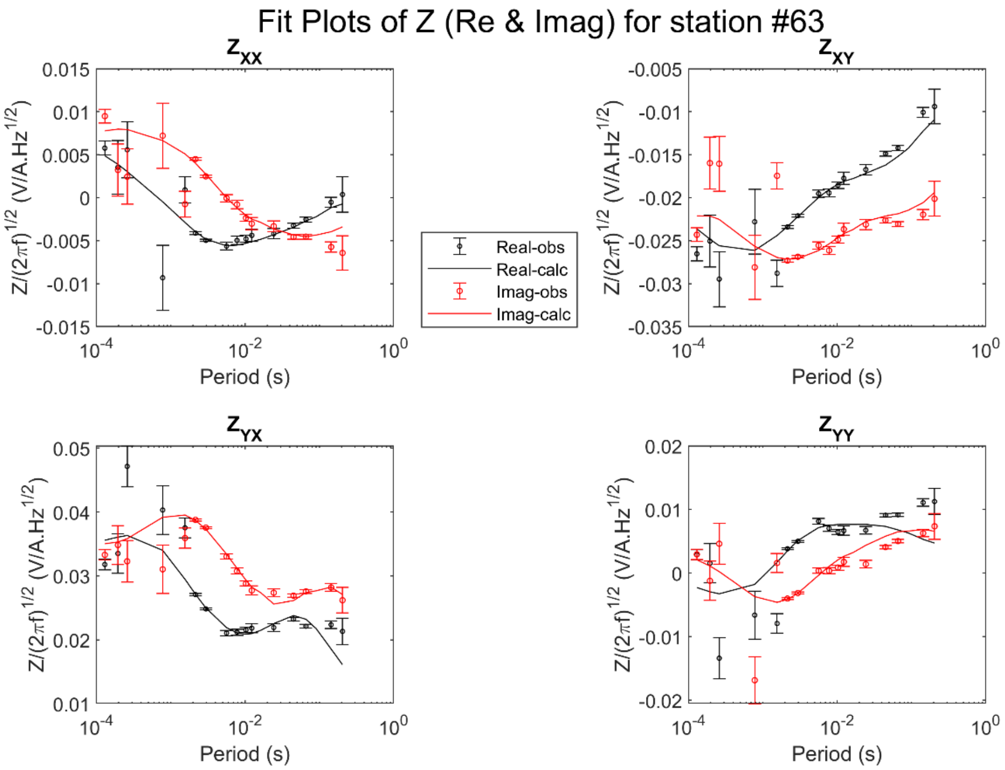

Fit Plots of Z (Re & Imag) for station #63
ZXX
ZXY
ZYX
ZYY
Z/(2πf)^1/2 (V/A.Hz^1/2)
Period (s)
Real-obs
Real-calc
Imag-obs
Imag-calc

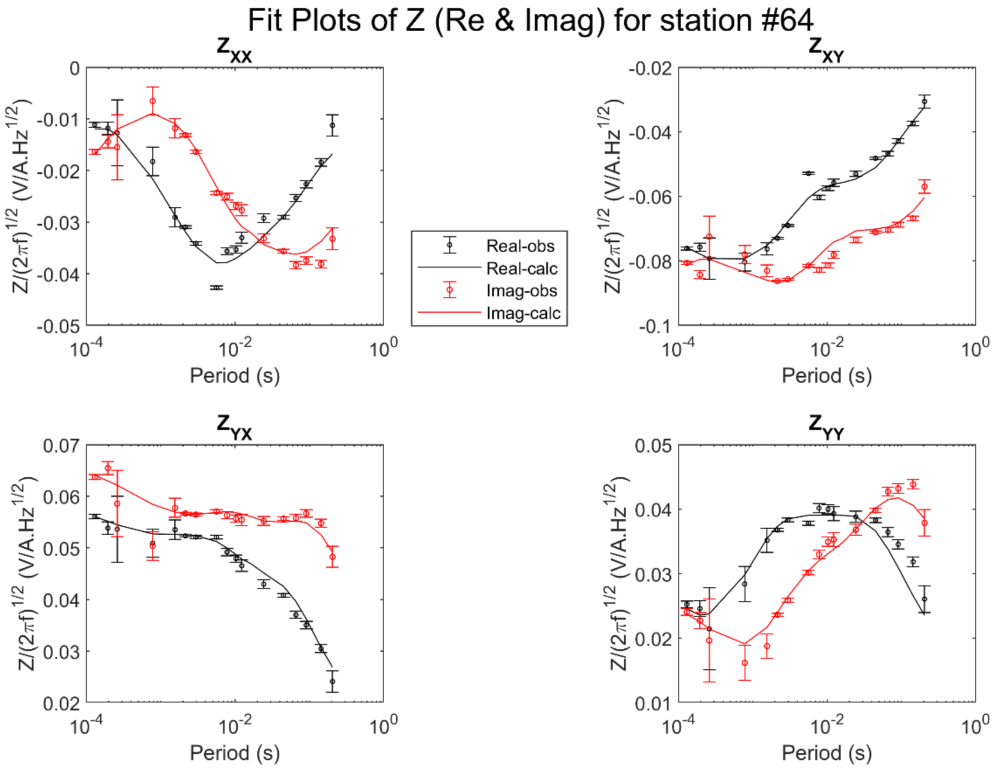
Fit Plots of Z (Re & Imag) for station #64
Z_XX
Z_XY
Z_YX
Z_YY
Real-obs
Real-calc
Imag-obs
Imag-calc
Z/(2πf)^1/2 (V/A.Hz^1/2)
Period (s)

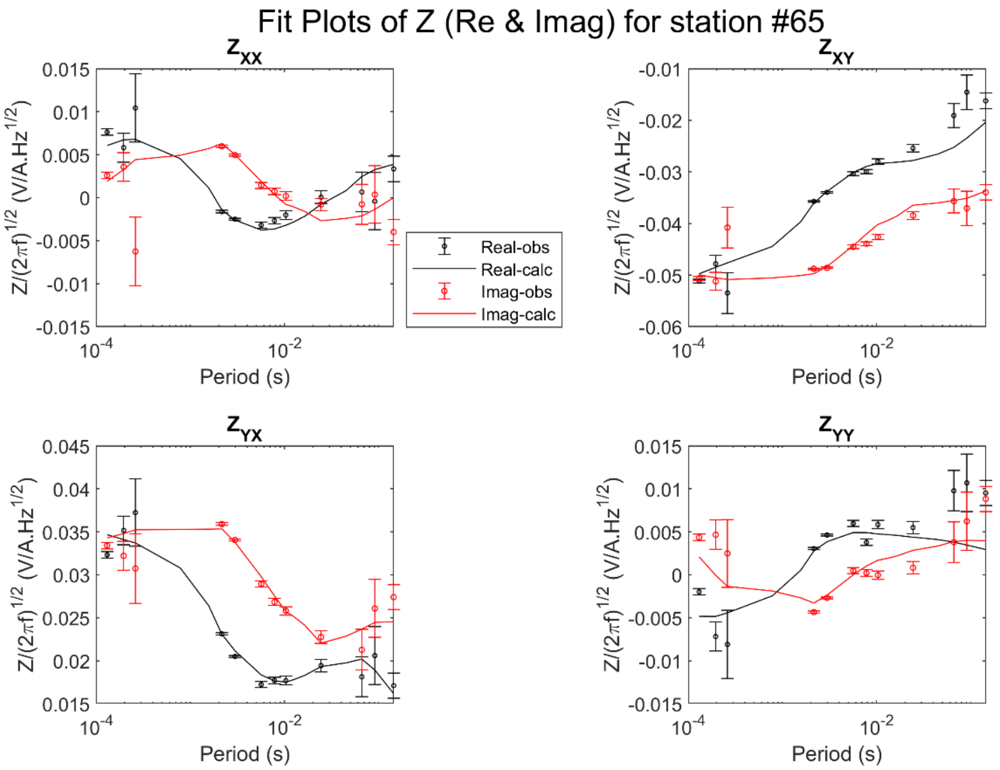
Fit Plots of Z (Re & Imag) for station #65
Z_XX
Z_XY
Z_YX
Z_YY
Real-obs
Real-calc
Imag-obs
Imag-calc
Z/(2πf)^1/2 (V/A.Hz^1/2)
Period (s)

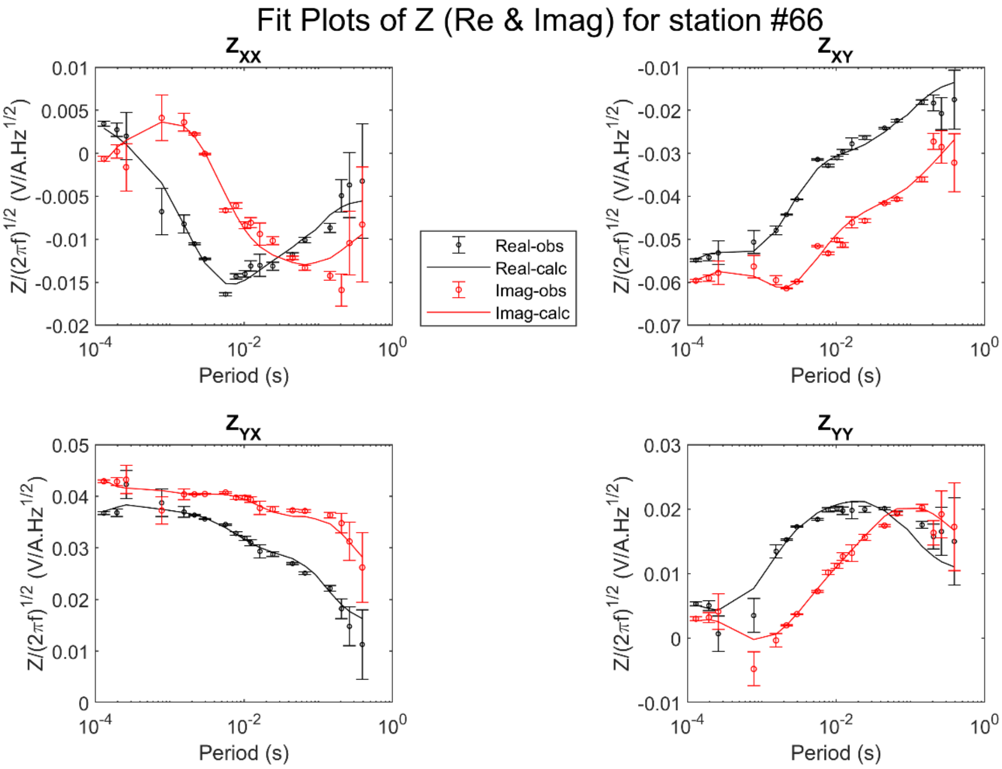
Fit Plots of Z (Re & Imag) for station #66
Z_{XX}
Z_{XY}
Z_{YX}
Z_{YY}
$Z/(2\pi f)^{1/2}$ (V/A.Hz$^{1/2}$)
Period (s)
Real-obs
Real-calc
Imag-obs
Imag-calc

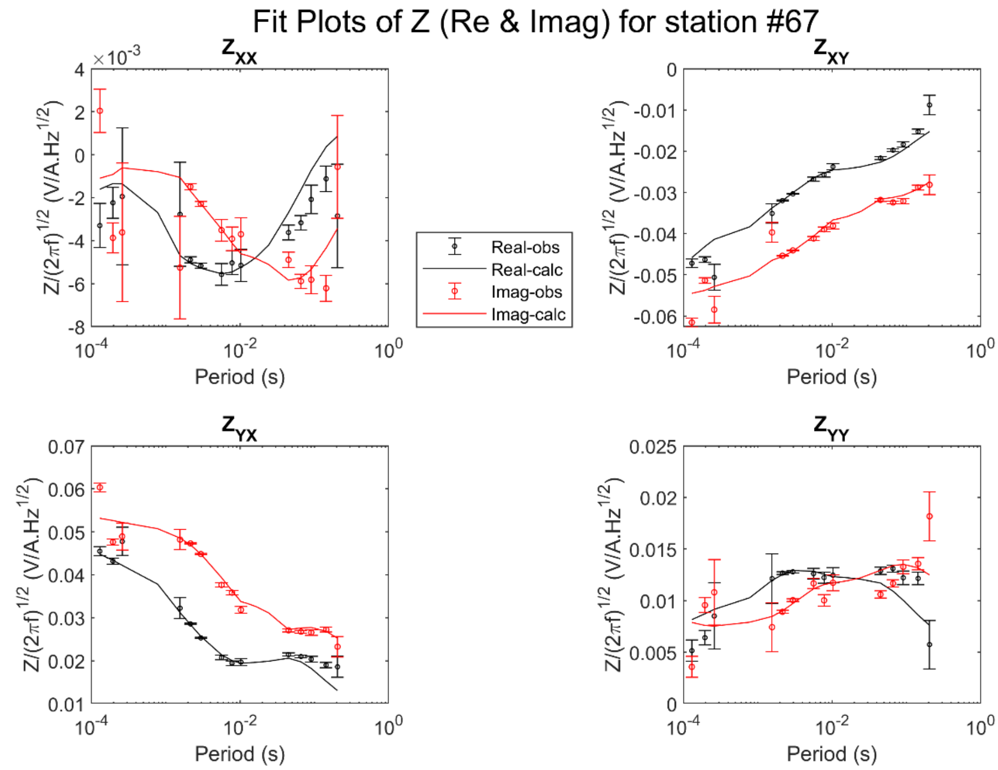
Fit Plots of Z (Re & Imag) for station #67
Z_{XX}
Z_{XY}
Z_{YX}
Z_{YY}
$\times 10^{-3}$
$Z/(2\pi f)^{1/2}$ (V/A.Hz$^{1/2}$)
Period (s)
Real-obs
Real-calc
Imag-obs
Imag-calc

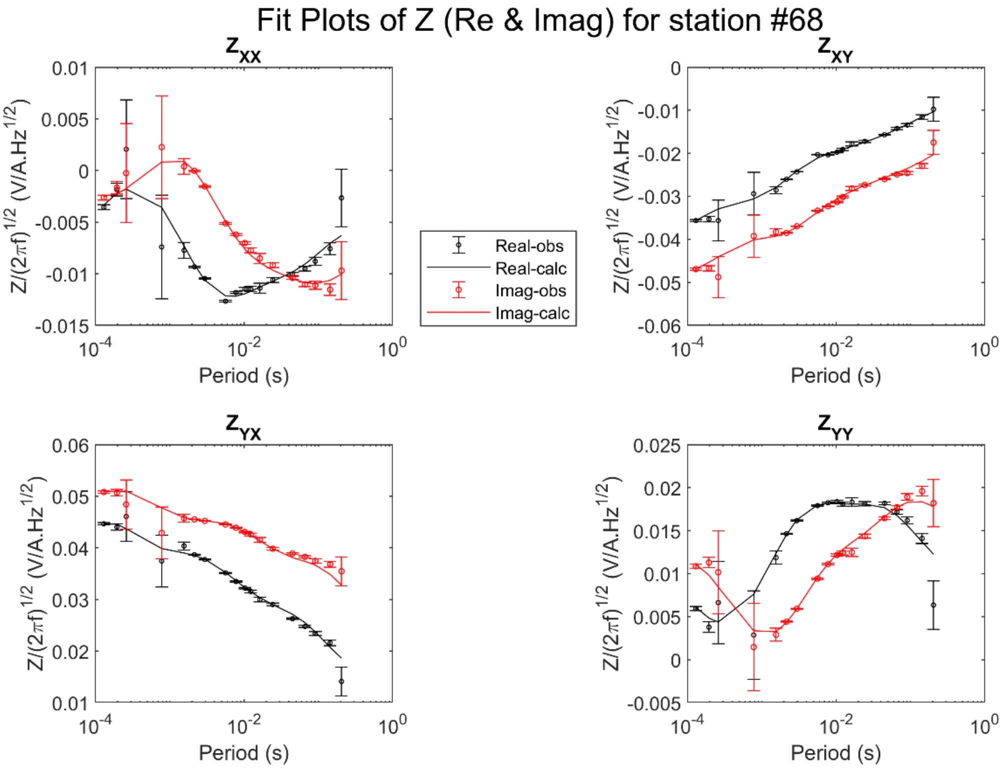

Fit Plots of Z (Re & Imag) for station #68
Z_XX
Z_XY
Z_YX
Z_YY
Z/(2πf)^1/2 (V/A.Hz^1/2)
Period (s)
Real-obs
Real-calc
Imag-obs
Imag-calc

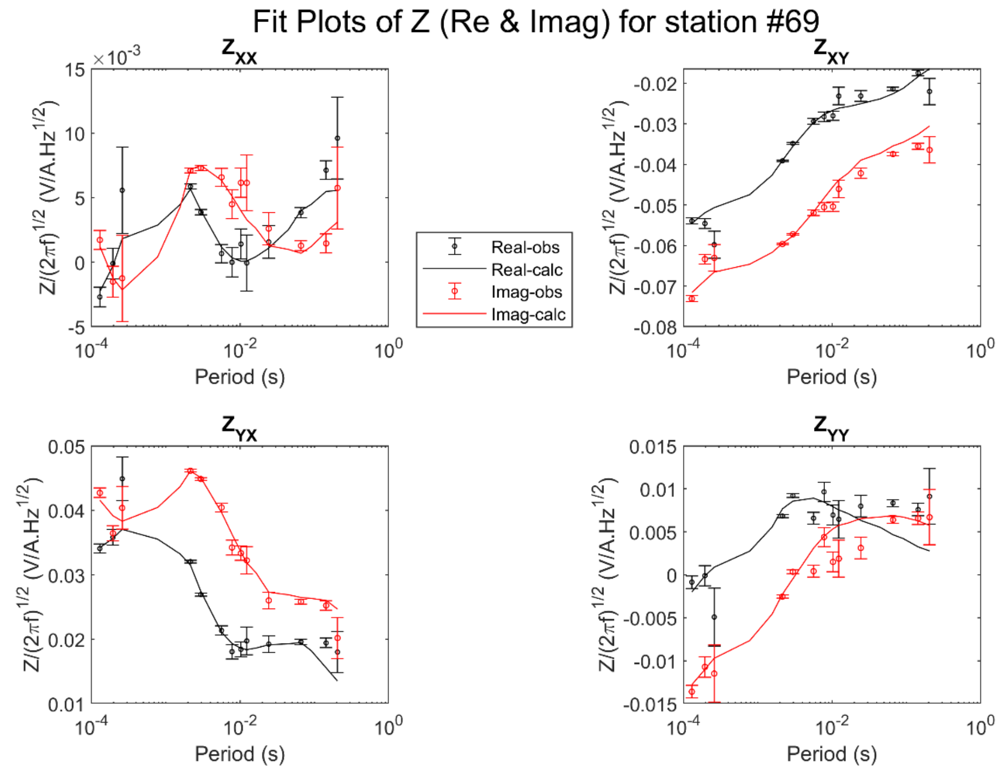

Fit Plots of Z (Re & Imag) for station #69
Z_XX
Z_XY
Z_YX
Z_YY
Z/(2πf)^1/2 (V/A.Hz^1/2)
Period (s)
Real-obs
Real-calc
Imag-obs
Imag-calc

Fit Plots of Z (Re & Imag) for station #70

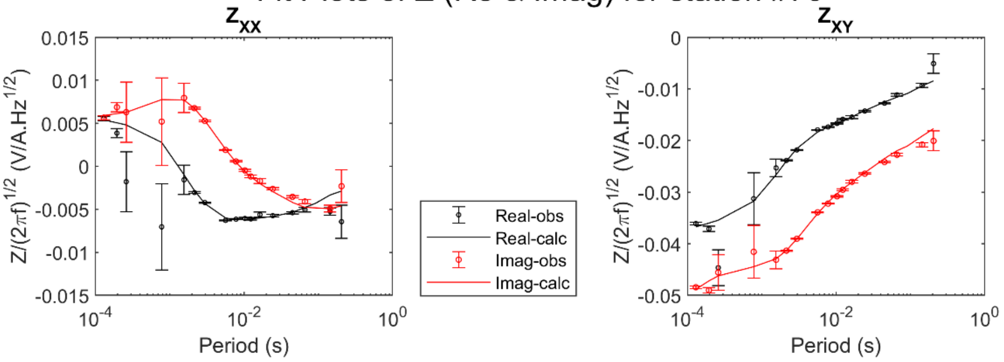

Fit Plots of Z (Re & Imag) for station #71

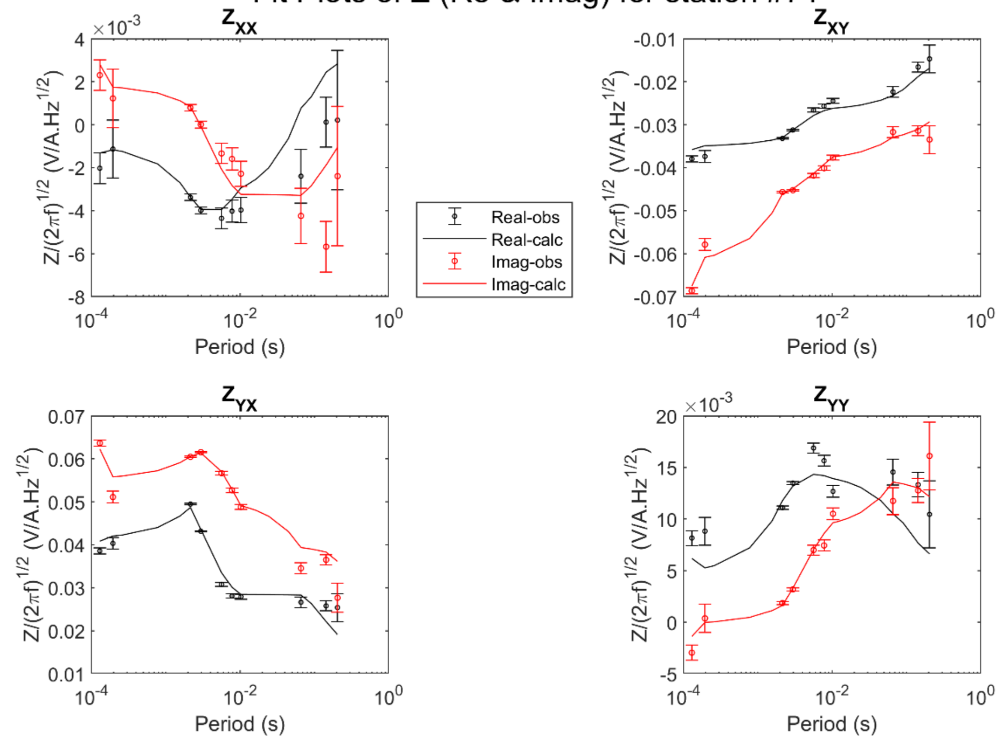

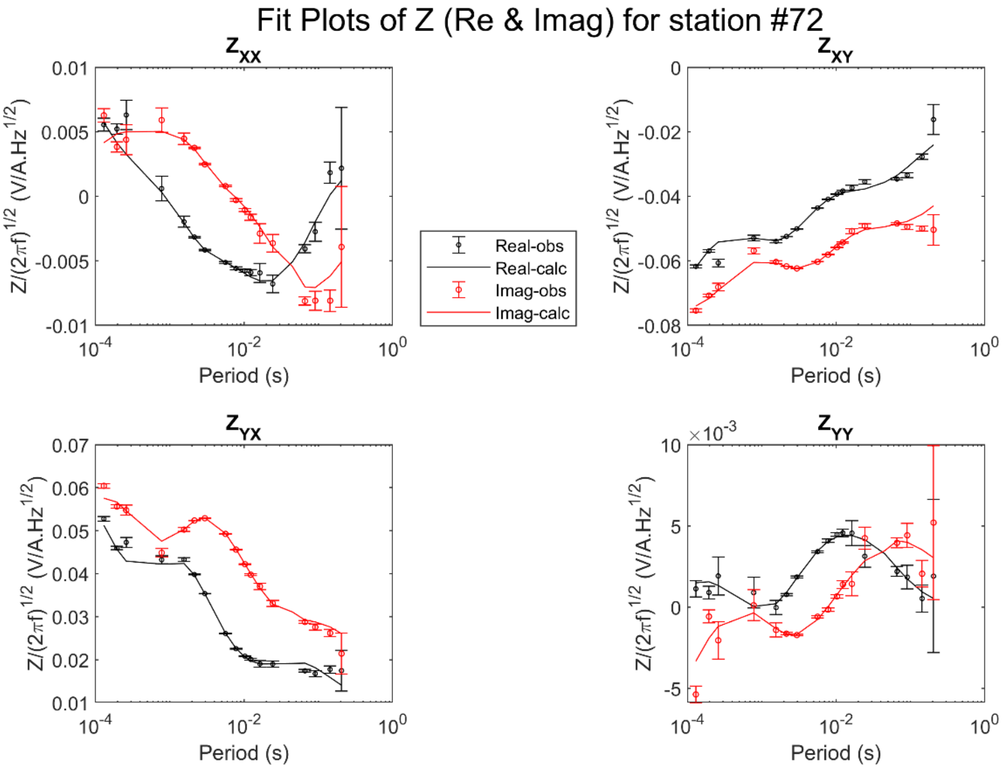
Fit Plots of Z (Re & Imag) for station #72
Z_{XX}
Z_{XY}
Z_{YX}
Z_{YY}
$Z/(2\pi f)^{1/2}$ (V/A.Hz$^{1/2}$)
Period (s)
Real-obs
Real-calc
Imag-obs
Imag-calc
$\times 10^{-3}$

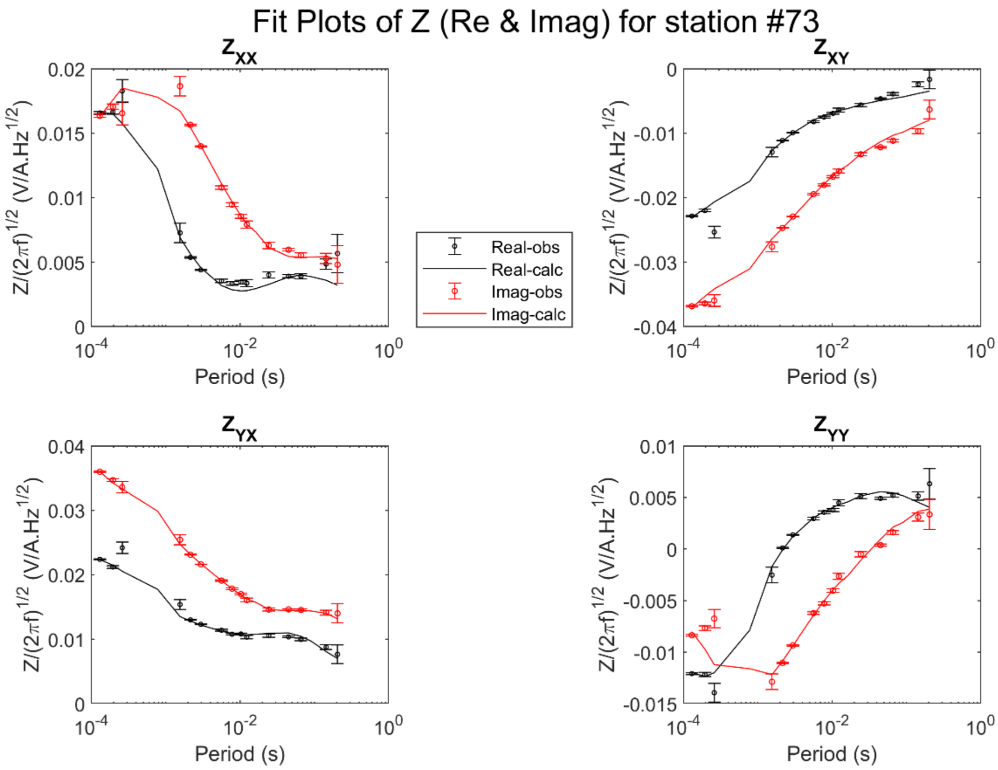
Fit Plots of Z (Re & Imag) for station #73
Z_{XX}
Z_{XY}
Z_{YX}
Z_{YY}
$Z/(2\pi f)^{1/2}$ (V/A.Hz$^{1/2}$)
Period (s)
Real-obs
Real-calc
Imag-obs
Imag-calc

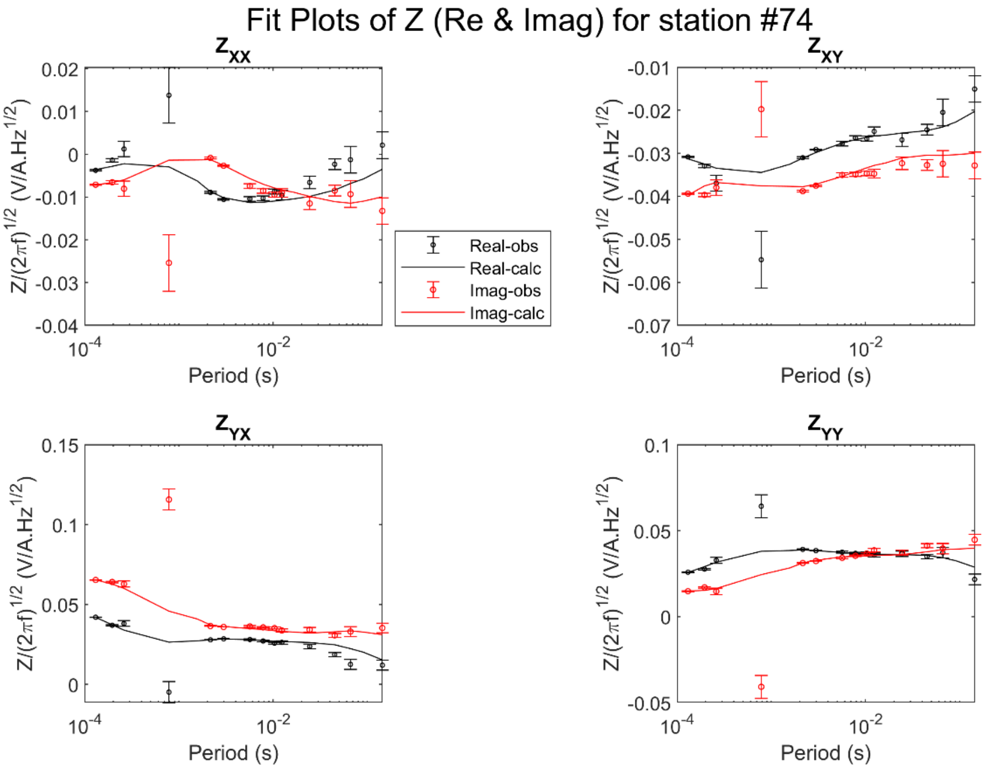
Fit Plots of Z (Re & Imag) for station #74
Z_XX
Z_XY
Z_YX
Z_YY
Z/(2πf)^1/2 (V/A.Hz^1/2)
Period (s)
Real-obs
Real-calc
Imag-obs
Imag-calc

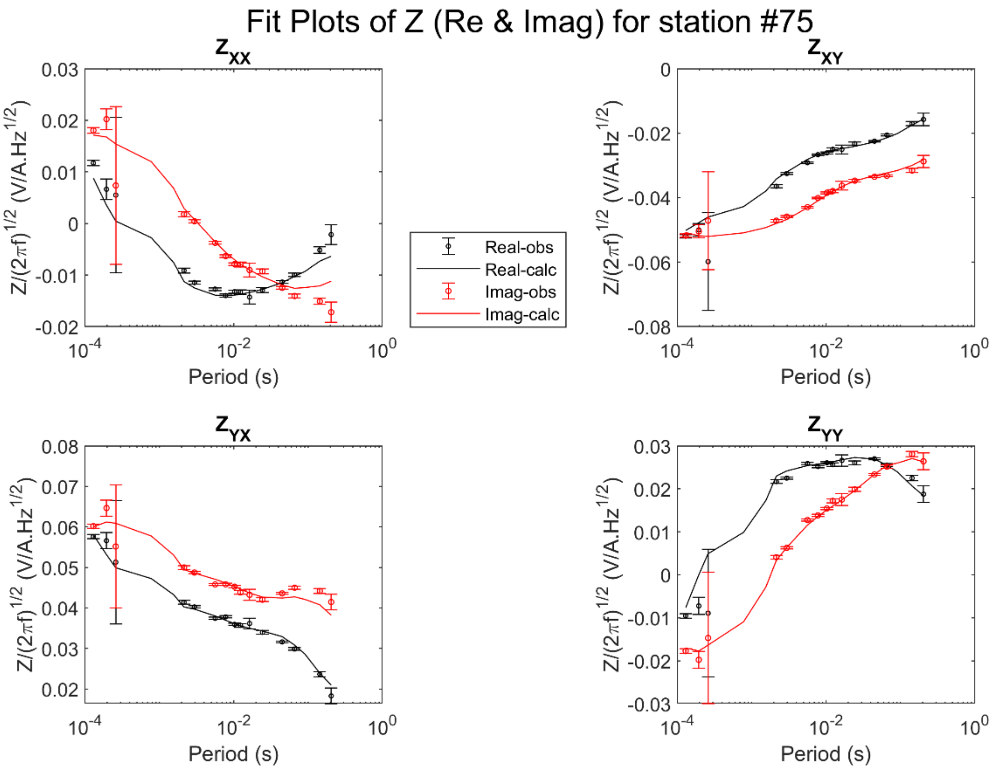
Fit Plots of Z (Re & Imag) for station #75
Z_XX
Z_XY
Z_YX
Z_YY
Z/(2πf)^1/2 (V/A.Hz^1/2)
Period (s)
Real-obs
Real-calc
Imag-obs
Imag-calc

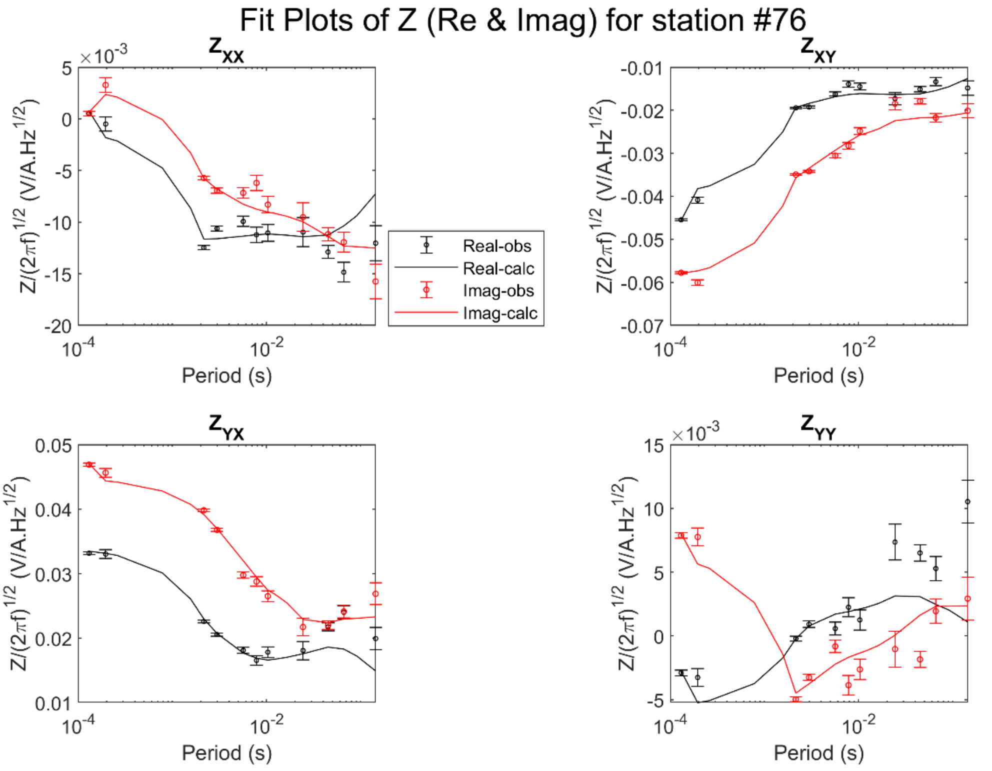
Fit Plots of Z (Re & Imag) for station #76
Z_XX
Z_XY
Z_YX
Z_YY
Z/(2πf)^1/2 (V/A.Hz^1/2)
Period (s)
Real-obs
Real-calc
Imag-obs
Imag-calc

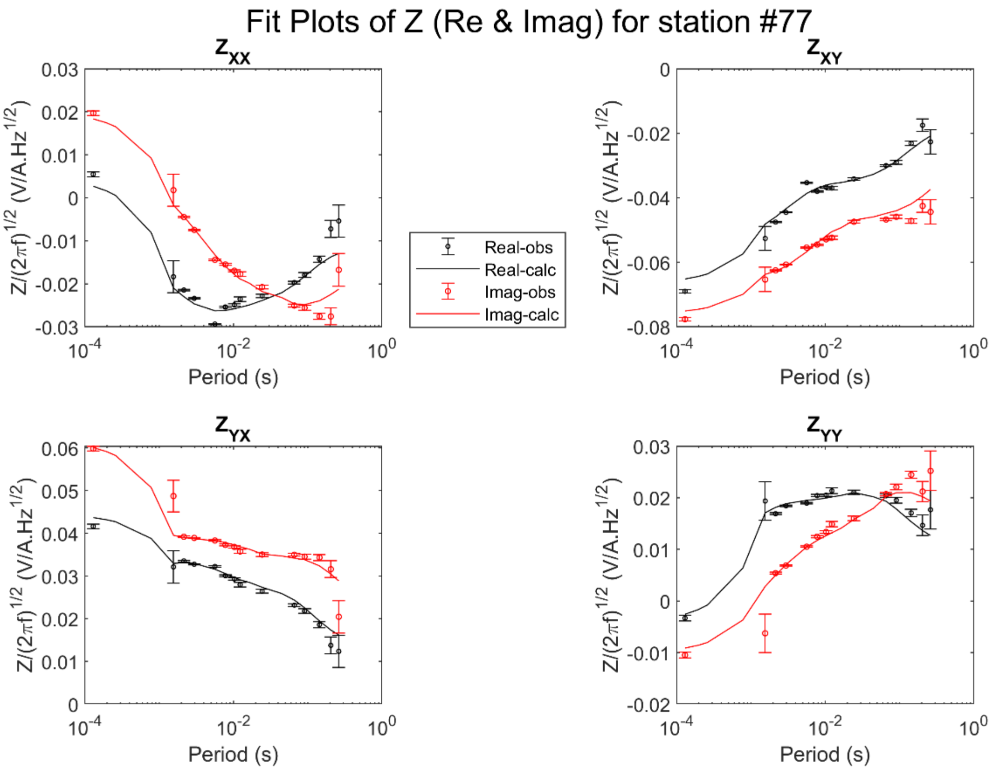
Fit Plots of Z (Re & Imag) for station #77
Z_XX
Z_XY
Z_YX
Z_YY
Z/(2πf)^1/2 (V/A.Hz^1/2)
Period (s)
Real-obs
Real-calc
Imag-obs
Imag-calc

Fit Plots of Z (Re & Imag) for station #78

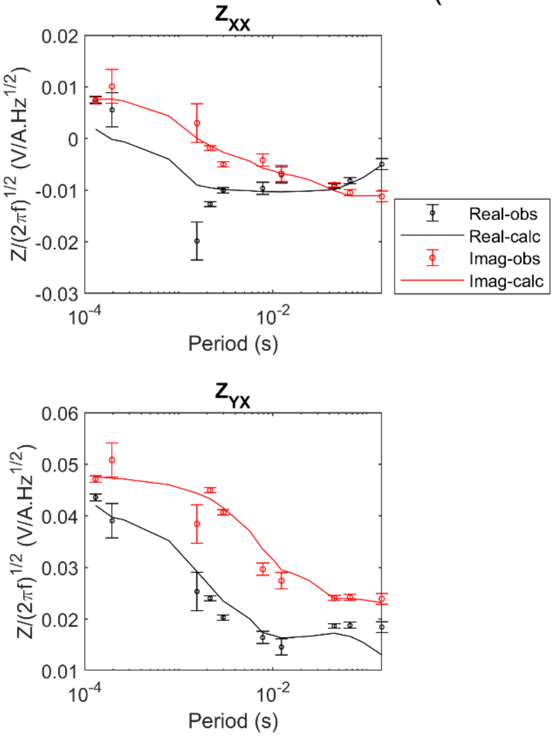

Fit Plots of Z (Re & Imag) for station #79

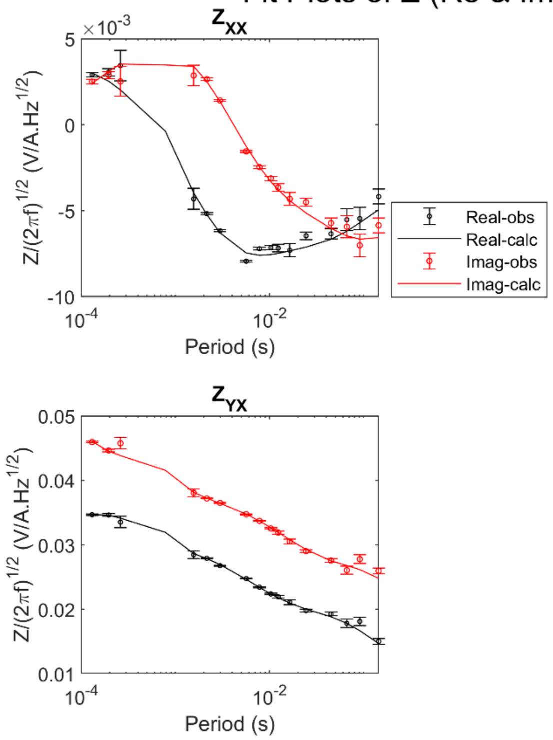

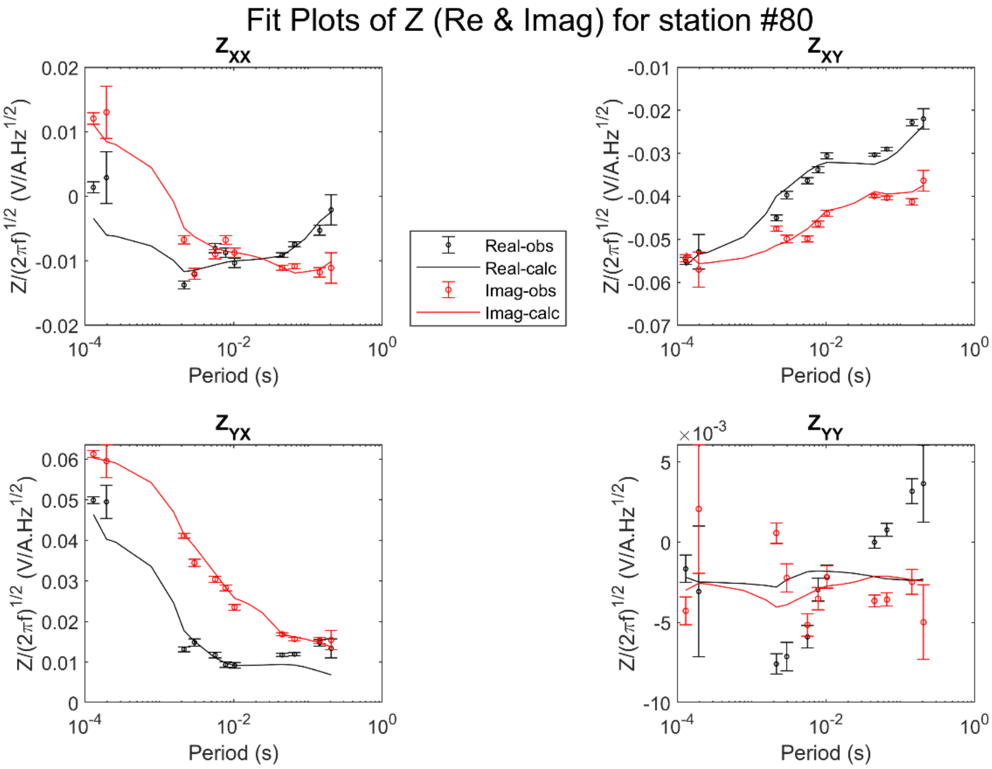
Fit Plots of Z (Re & Imag) for station #80
Z_XX
Z_XY
Z_YX
Z_YY
Z/(2πf)^1/2 (V/A.Hz^1/2)
Period (s)
Real-obs
Real-calc
Imag-obs
Imag-calc

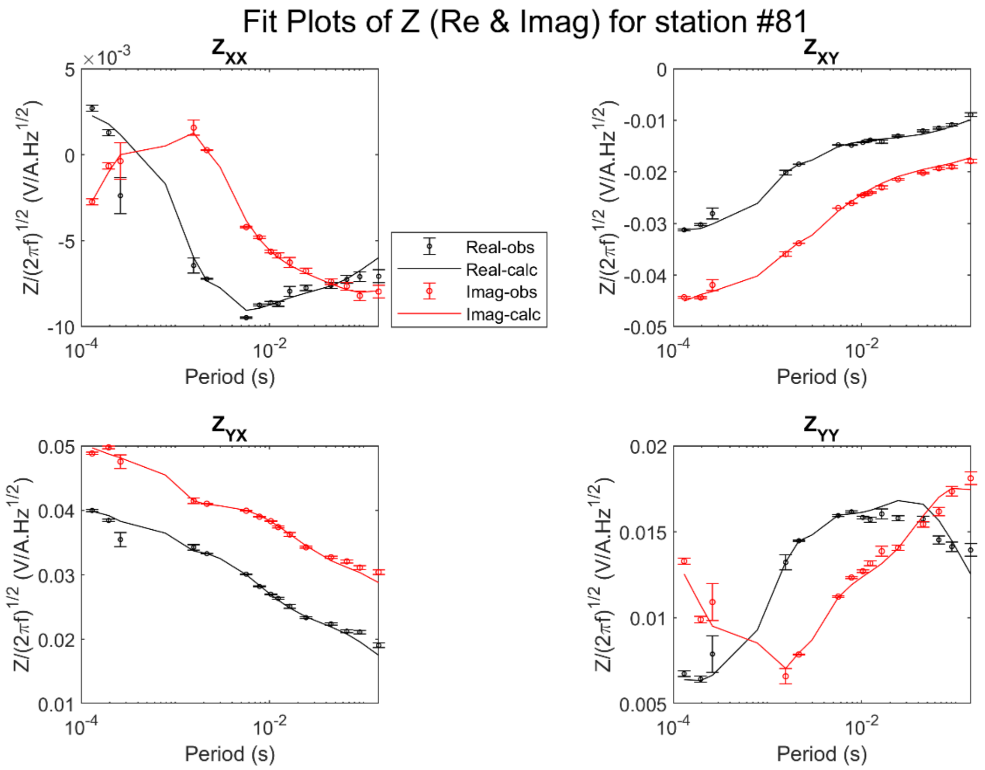
Fit Plots of Z (Re & Imag) for station #81
Z_XX
Z_XY
Z_YX
Z_YY
Z/(2πf)^1/2 (V/A.Hz^1/2)
Period (s)
Real-obs
Real-calc
Imag-obs
Imag-calc

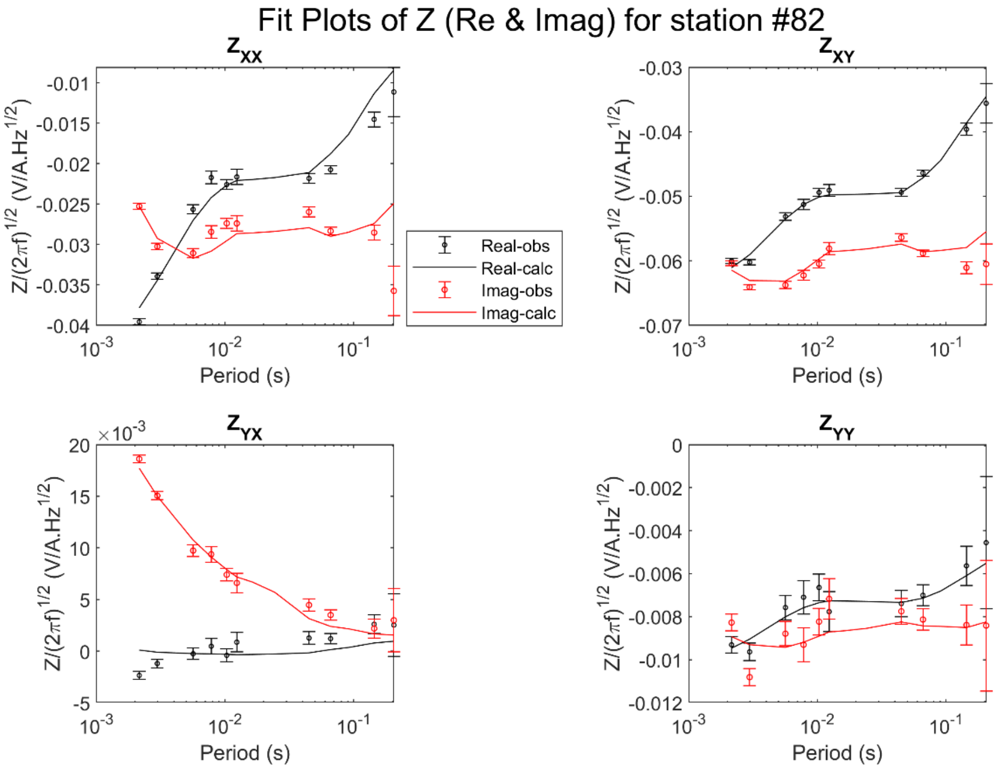
Fit Plots of Z (Re & Imag) for station #82
Z_XX
Z_XY
Z_YX
Z_YY
Z/(2πf)^1/2 (V/A.Hz^1/2)
Period (s)
Real-obs
Real-calc
Imag-obs
Imag-calc

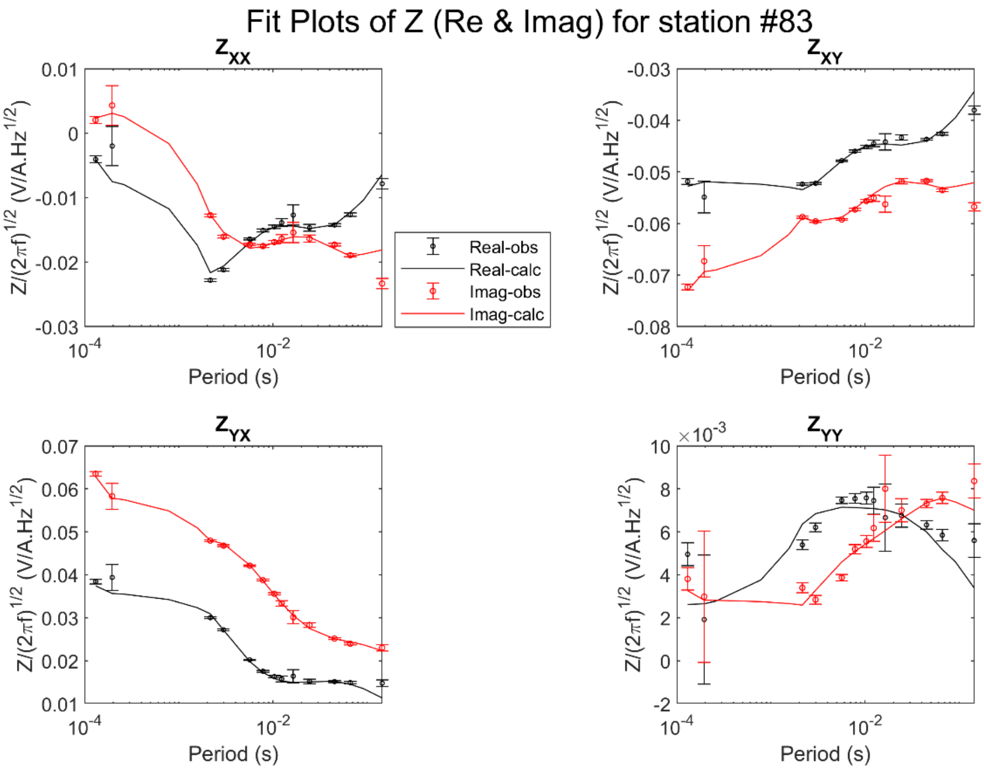
Fit Plots of Z (Re & Imag) for station #83
Z_XX
Z_XY
Z_YX
Z_YY
Z/(2πf)^1/2 (V/A.Hz^1/2)
Period (s)
Real-obs
Real-calc
Imag-obs
Imag-calc

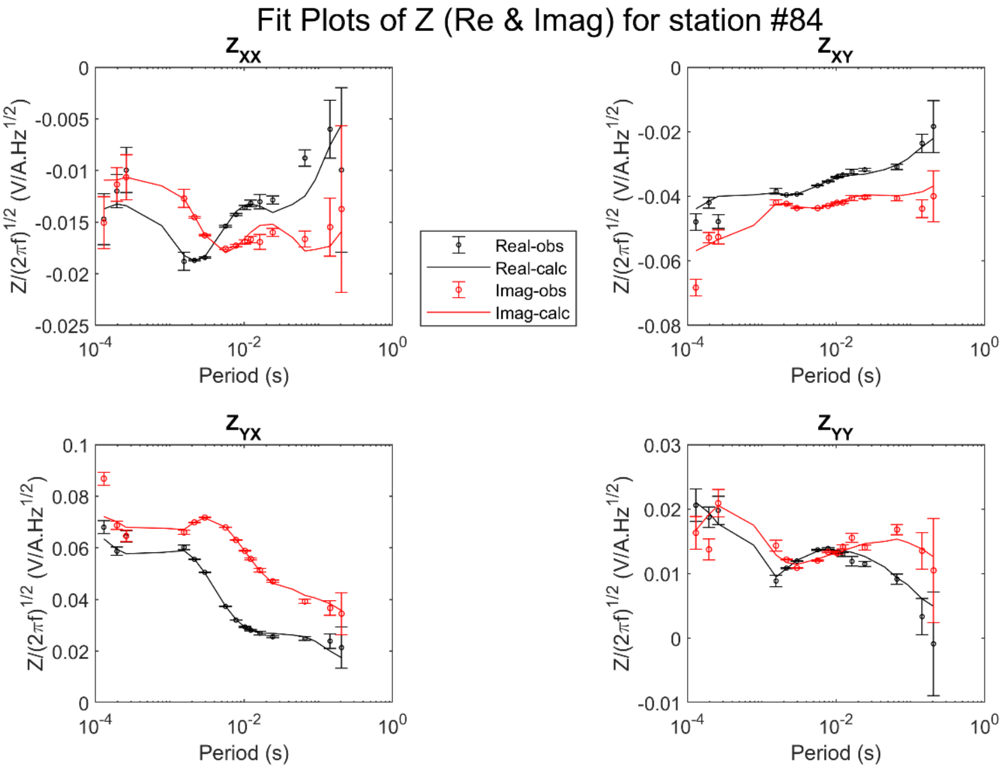
Fit Plots of Z (Re & Imag) for station #84
Z_{XX}
Z_{XY}
Z_{YX}
Z_{YY}
Real-obs
Real-calc
Imag-obs
Imag-calc
$Z/(2\pi f)^{1/2}$ (V/A.Hz$^{1/2}$)
Period (s)

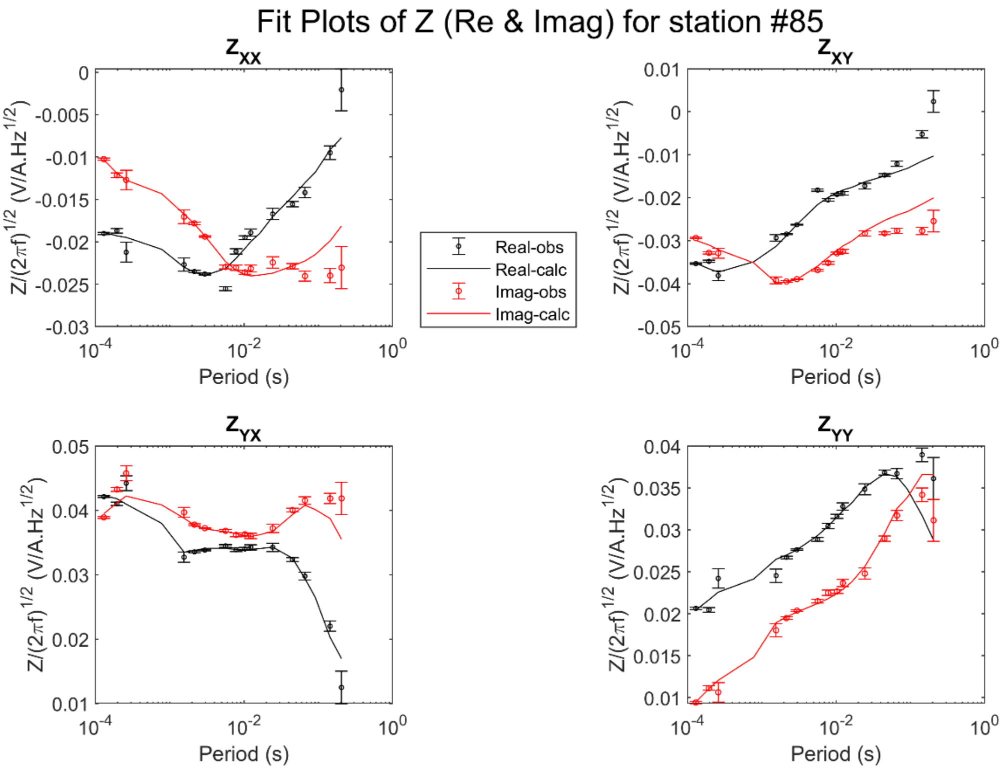
Fit Plots of Z (Re & Imag) for station #85
Z_{XX}
Z_{XY}
Z_{YX}
Z_{YY}
Real-obs
Real-calc
Imag-obs
Imag-calc
$Z/(2\pi f)^{1/2}$ (V/A.Hz$^{1/2}$)
Period (s)

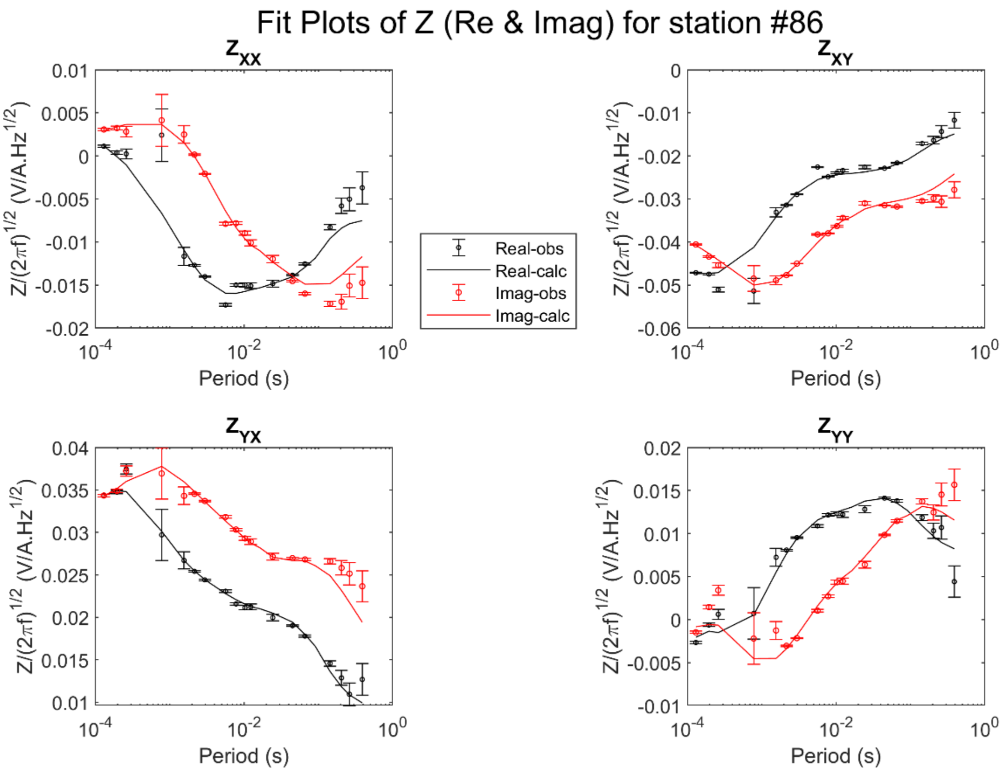
Fit Plots of Z (Re & Imag) for station #86
Z_{XX}
Z_{XY}
Z_{YX}
Z_{YY}
$Z/(2\pi f)^{1/2}$ (V/A.Hz$^{1/2}$)
Period (s)
Real-obs
Real-calc
Imag-obs
Imag-calc

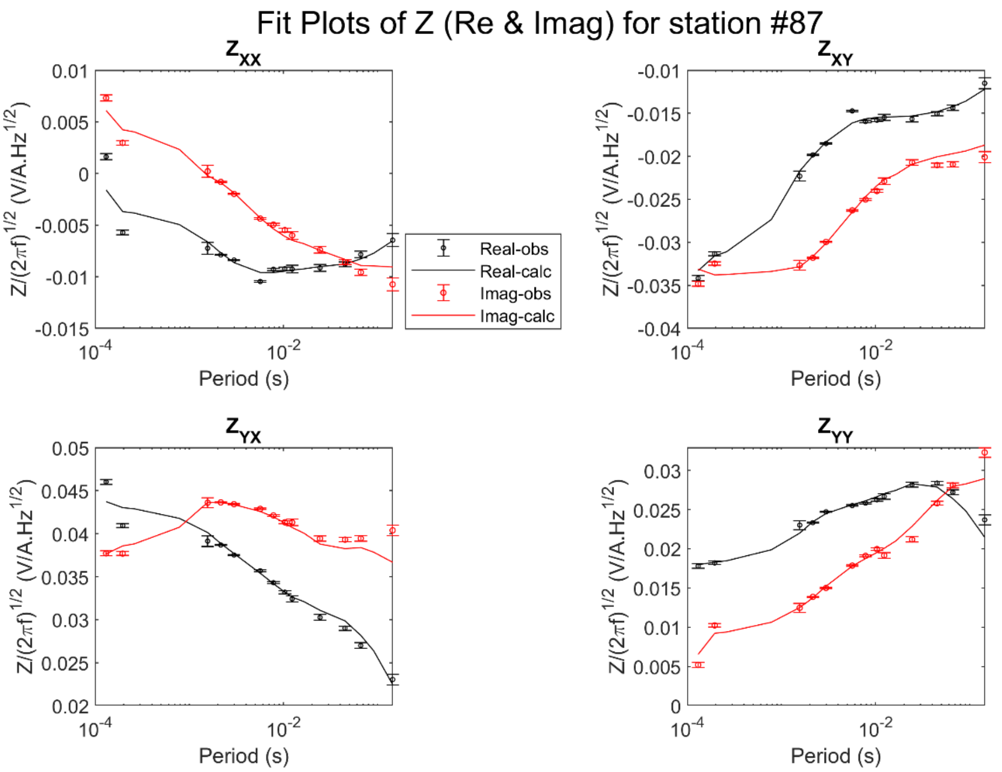
Fit Plots of Z (Re & Imag) for station #87
Z_{XX}
Z_{XY}
Z_{YX}
Z_{YY}
$Z/(2\pi f)^{1/2}$ (V/A.Hz$^{1/2}$)
Period (s)
Real-obs
Real-calc
Imag-obs
Imag-calc

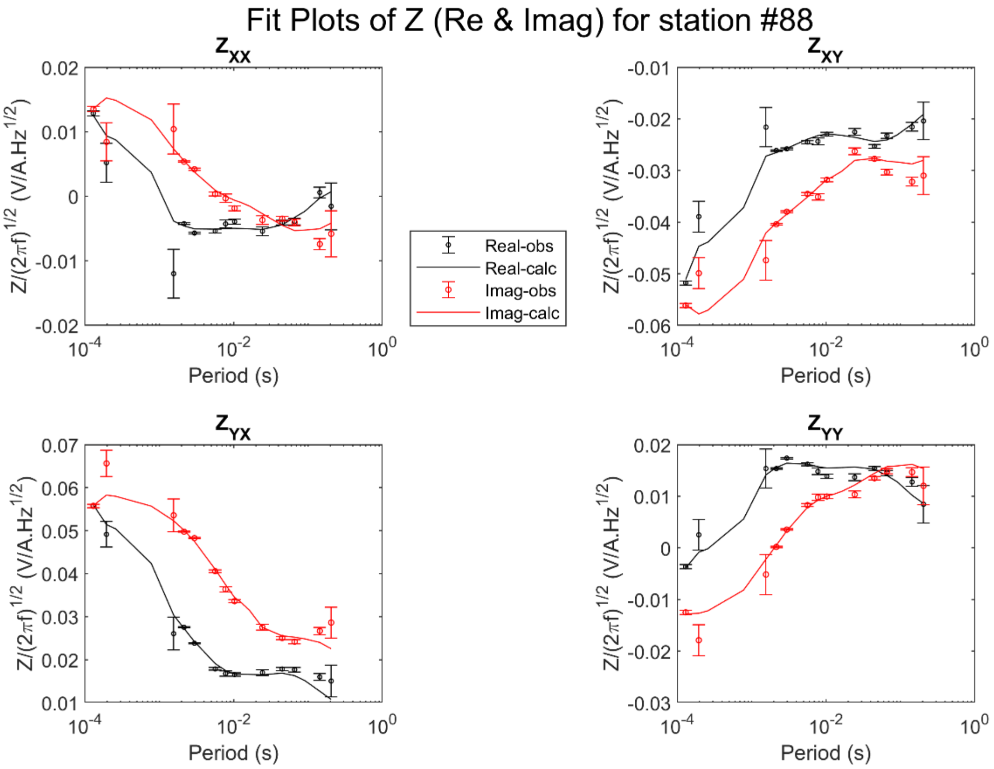
Fit Plots of Z (Re & Imag) for station #88
Z_{XX}
Z_{XY}
Z_{YX}
Z_{YY}
$Z/(2\pi f)^{1/2}$ (V/A.Hz$^{1/2}$)
Period (s)
Real-obs
Real-calc
Imag-obs
Imag-calc

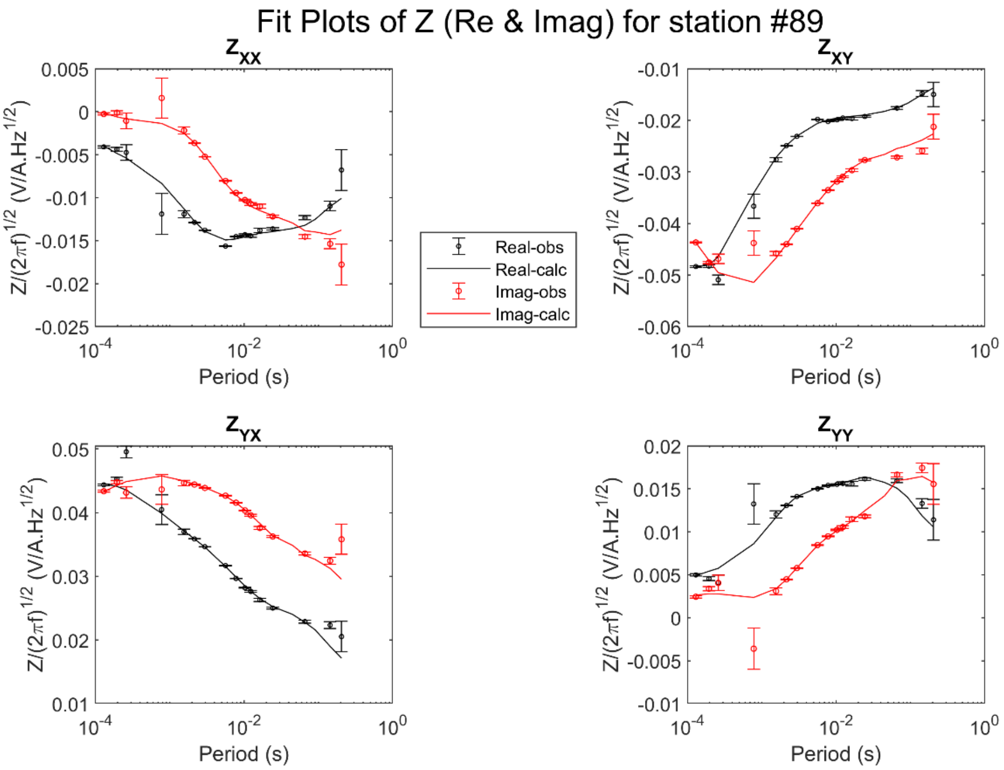
Fit Plots of Z (Re & Imag) for station #89
Z_{XX}
Z_{XY}
Z_{YX}
Z_{YY}
$Z/(2\pi f)^{1/2}$ (V/A.Hz$^{1/2}$)
Period (s)
Real-obs
Real-calc
Imag-obs
Imag-calc

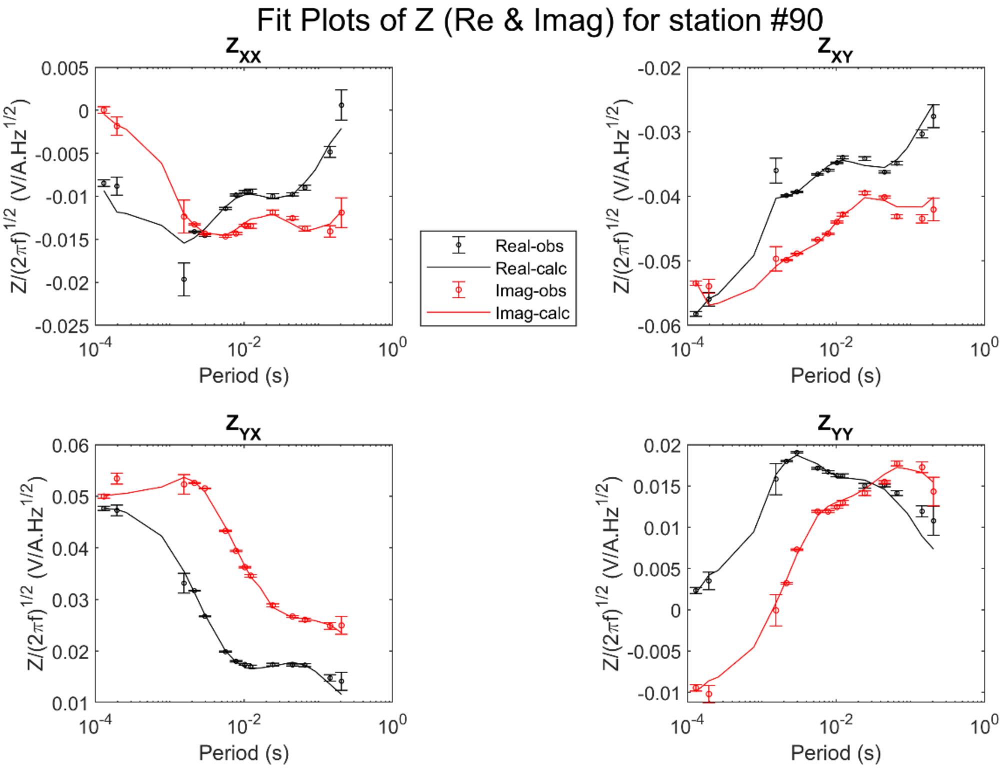
Fit Plots of Z (Re & Imag) for station #90
Z_{XX}
Z_{XY}
Z_{YX}
Z_{YY}
Real-obs
Real-calc
Imag-obs
Imag-calc
$Z/(2\pi f)^{1/2}$ (V/A.Hz$^{1/2}$)
Period (s)

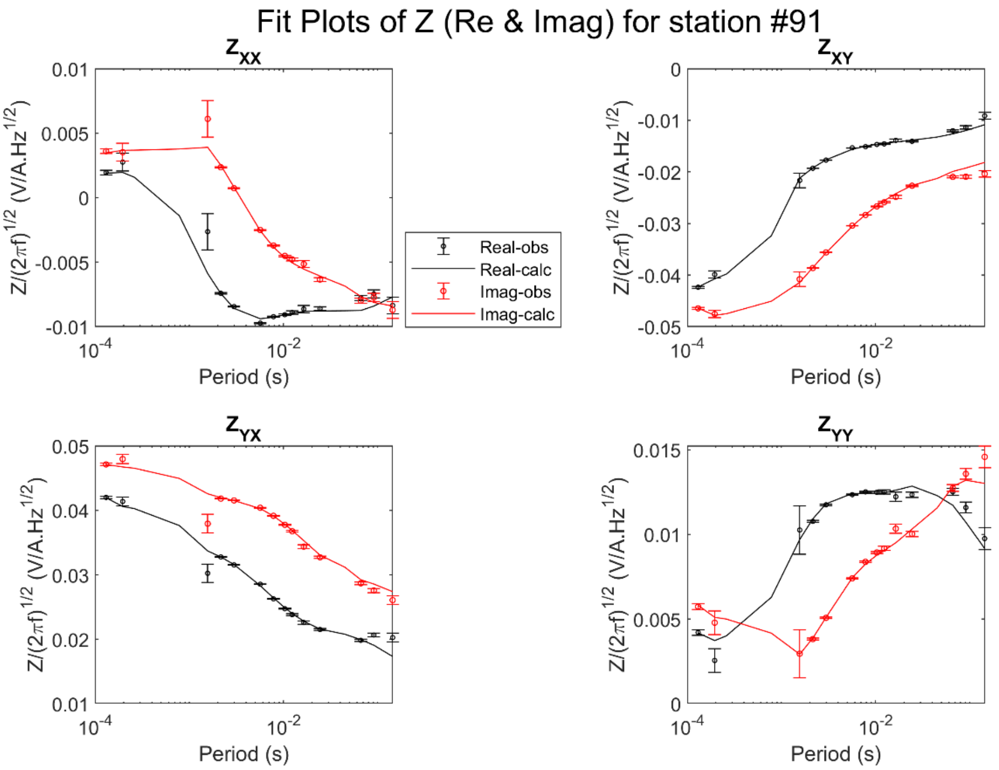
Fit Plots of Z (Re & Imag) for station #91
Z_{XX}
Z_{XY}
Z_{YX}
Z_{YY}
Real-obs
Real-calc
Imag-obs
Imag-calc
$Z/(2\pi f)^{1/2}$ (V/A.Hz$^{1/2}$)
Period (s)

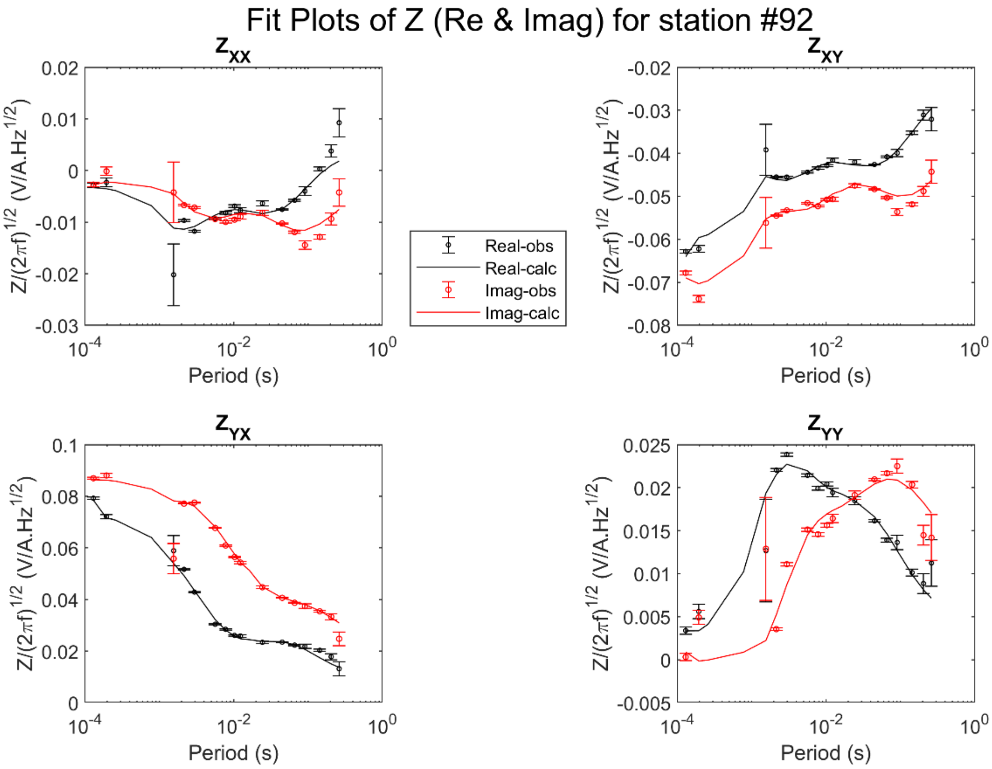
Fit Plots of Z (Re & Imag) for station #92
Z_{XX}
Z_{XY}
Z_{YX}
Z_{YY}
$Z/(2\pi f)^{1/2}$ (V/A.Hz$^{1/2}$)
Period (s)
Real-obs
Real-calc
Imag-obs
Imag-calc

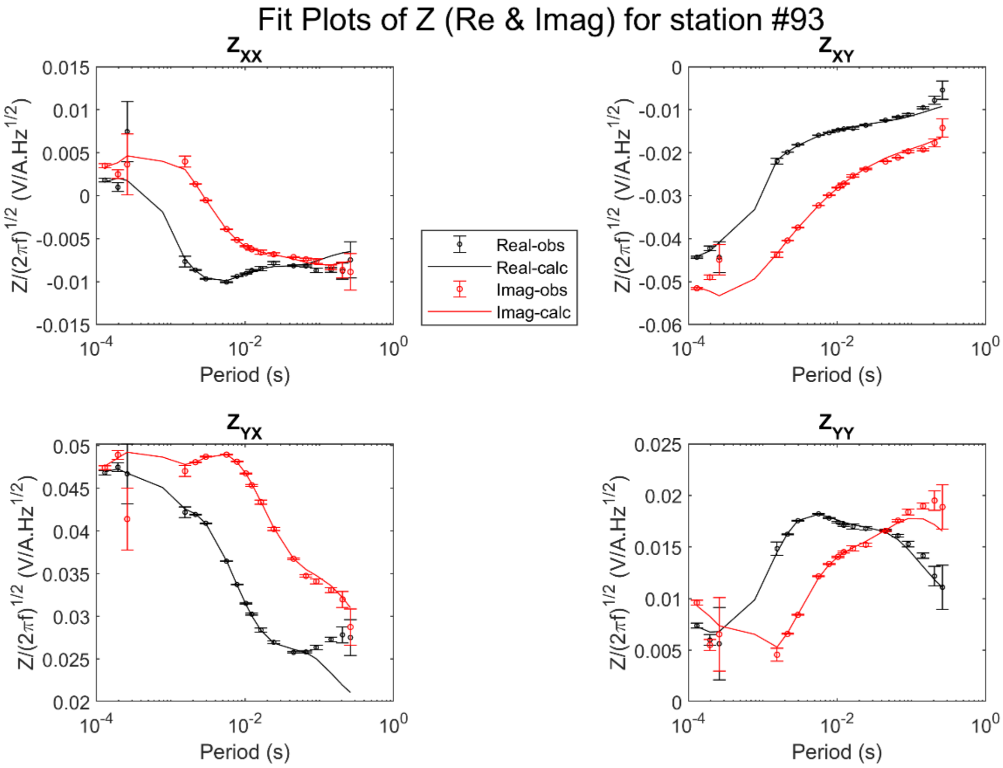
Fit Plots of Z (Re & Imag) for station #93
Z_{XX}
Z_{XY}
Z_{YX}
Z_{YY}
$Z/(2\pi f)^{1/2}$ (V/A.Hz$^{1/2}$)
Period (s)
Real-obs
Real-calc
Imag-obs
Imag-calc

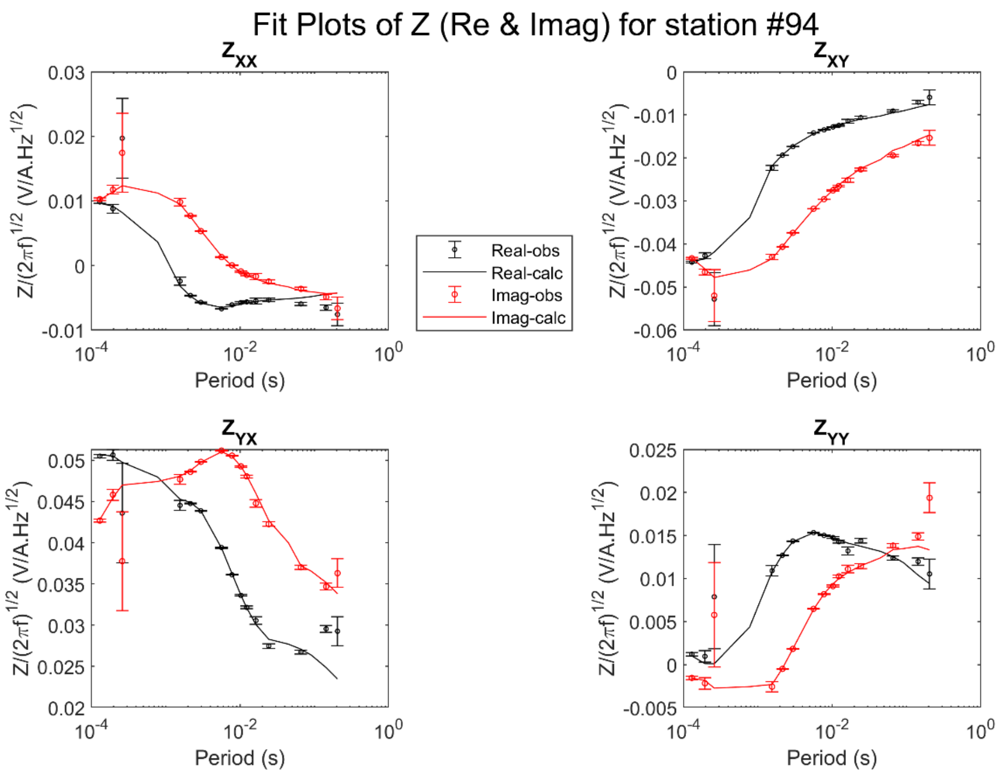

Fit Plots of Z (Re & Imag) for station #94
Z_XX
Z_XY
Z_YX
Z_YY
Z/(2πf)^1/2 (V/A.Hz^1/2)
Period (s)
Real-obs
Real-calc
Imag-obs
Imag-calc

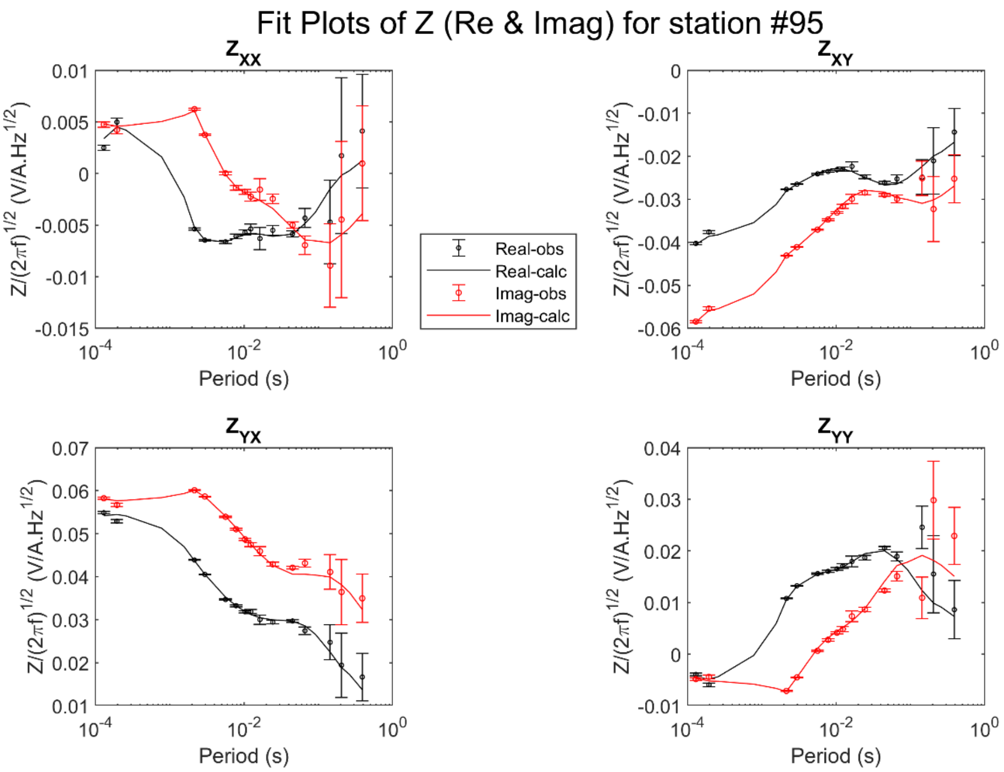

Fit Plots of Z (Re & Imag) for station #95
Z_XX
Z_XY
Z_YX
Z_YY
Z/(2πf)^1/2 (V/A.Hz^1/2)
Period (s)
Real-obs
Real-calc
Imag-obs
Imag-calc

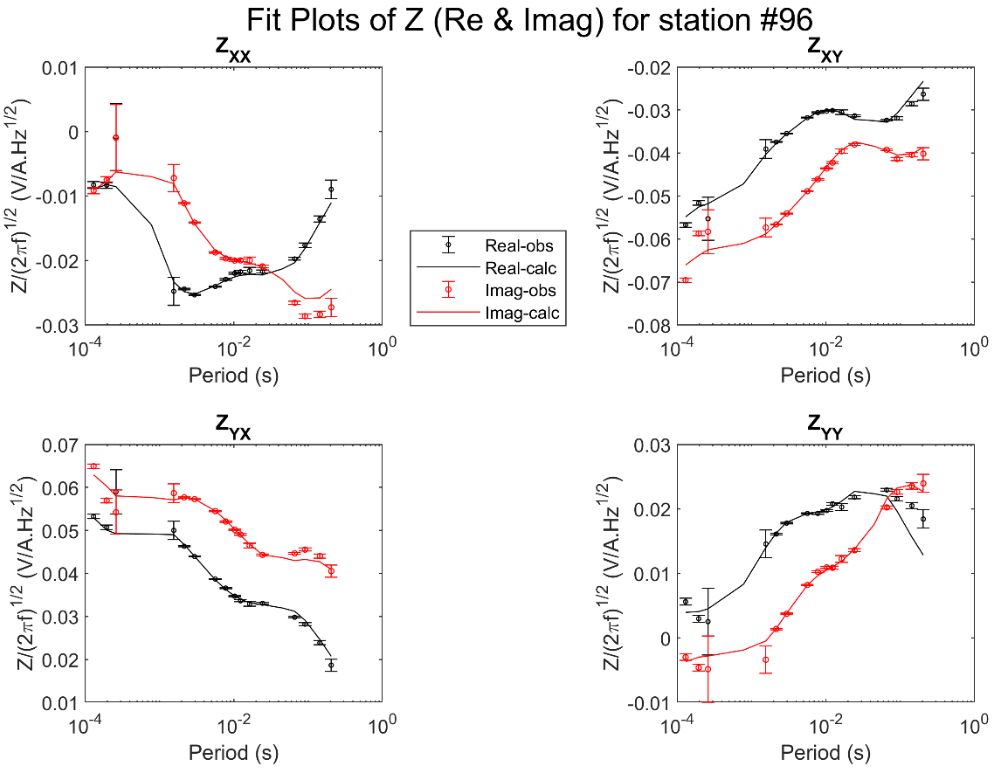
Fit Plots of Z (Re & Imag) for station #96
Z_{XX}
Z_{XY}
Z_{YX}
Z_{YY}
Real-obs
Real-calc
Imag-obs
Imag-calc
$Z/(2\pi f)^{1/2}$ (V/A.Hz$^{1/2}$)
Period (s)

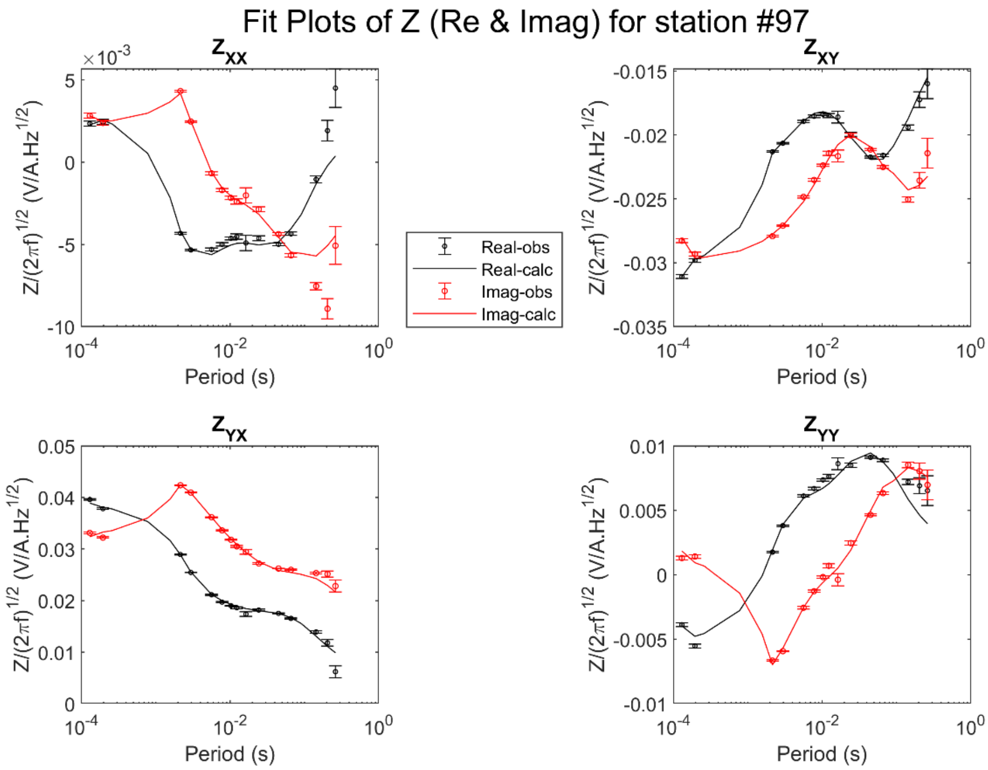
Fit Plots of Z (Re & Imag) for station #97
Z_{XX}
Z_{XY}
Z_{YX}
Z_{YY}
Real-obs
Real-calc
Imag-obs
Imag-calc
$Z/(2\pi f)^{1/2}$ (V/A.Hz$^{1/2}$)
Period (s)

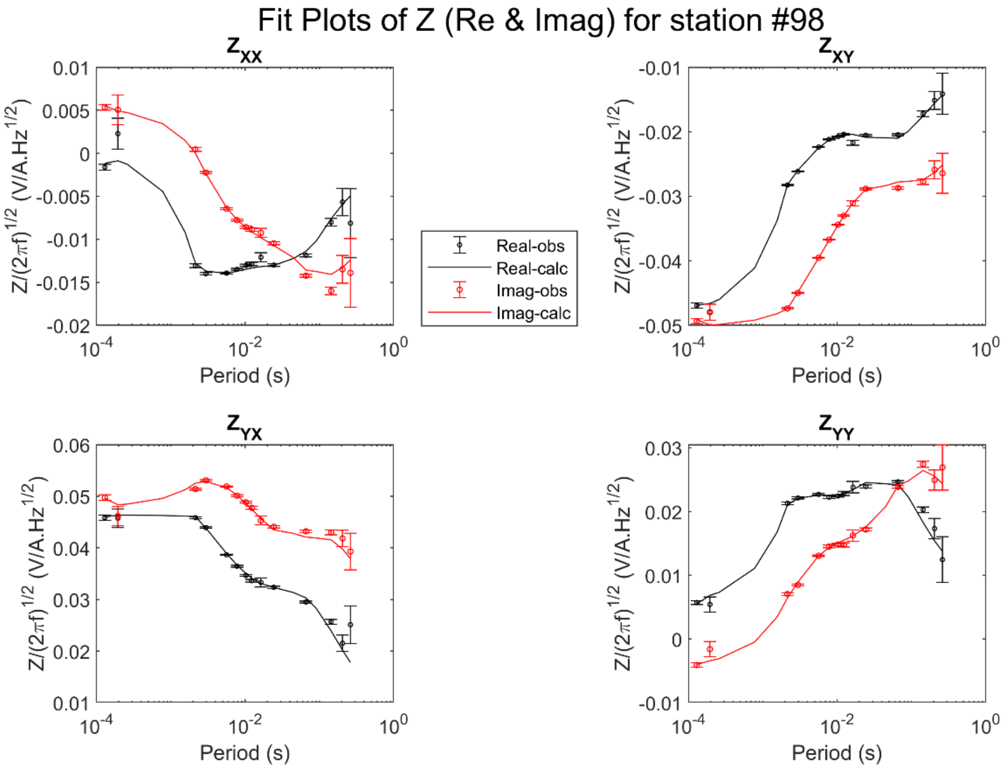
Fit Plots of Z (Re & Imag) for station #98
Z_XX
Z_XY
Z_YX
Z_YY
Z/(2πf)^1/2 (V/A.Hz^1/2)
Period (s)
Real-obs
Real-calc
Imag-obs
Imag-calc

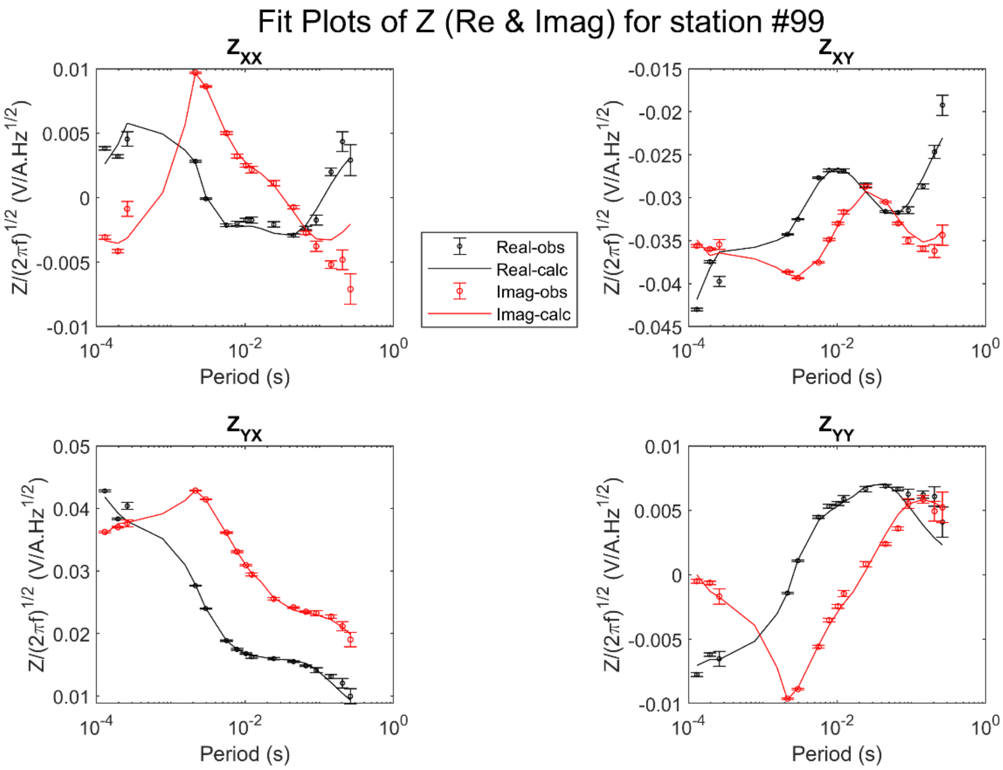
Fit Plots of Z (Re & Imag) for station #99
Z_XX
Z_XY
Z_YX
Z_YY
Z/(2πf)^1/2 (V/A.Hz^1/2)
Period (s)
Real-obs
Real-calc
Imag-obs
Imag-calc

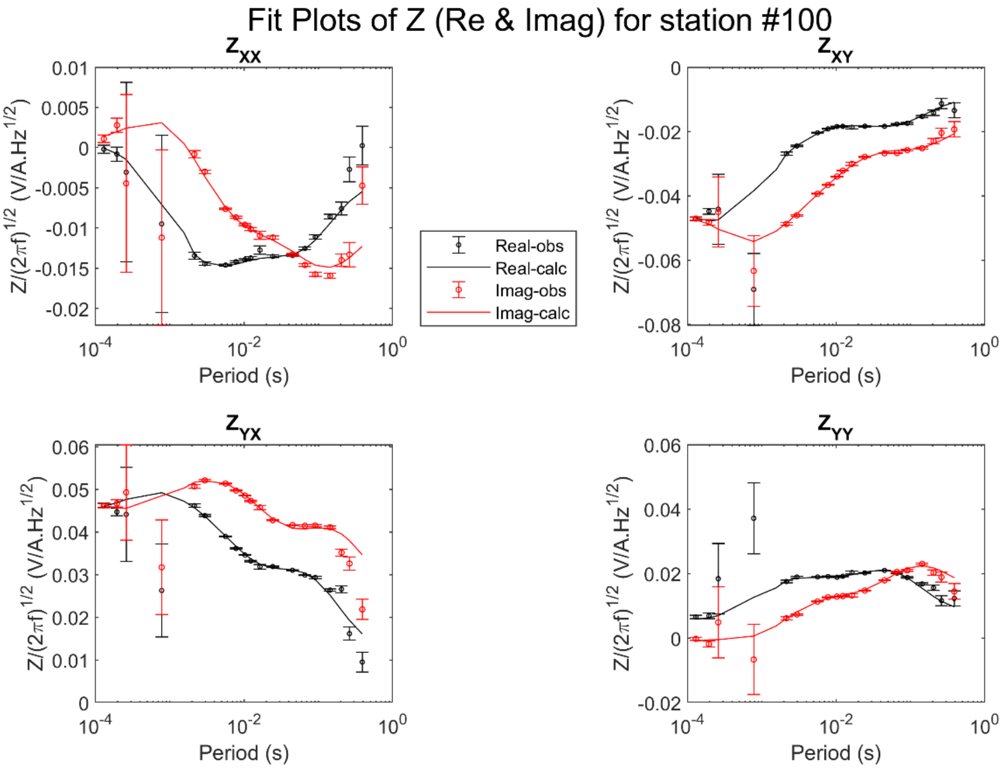
Fit Plots of Z (Re & Imag) for station #100
Z_XX
Z_XY
Z_YX
Z_YY
Z/(2πf)^1/2 (V/A.Hz^1/2)
Period (s)
Real-obs
Real-calc
Imag-obs
Imag-calc

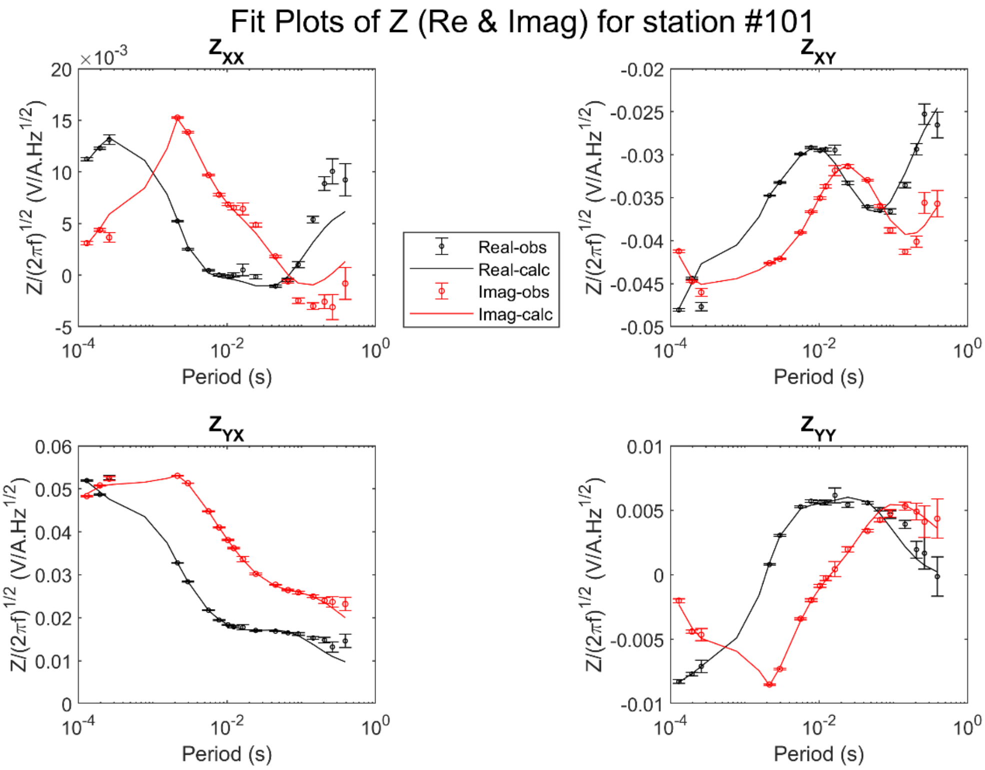
Fit Plots of Z (Re & Imag) for station #101
Z_XX
Z_XY
Z_YX
Z_YY
×10^-3
Z/(2πf)^1/2 (V/A.Hz^1/2)
Period (s)
Real-obs
Real-calc
Imag-obs
Imag-calc

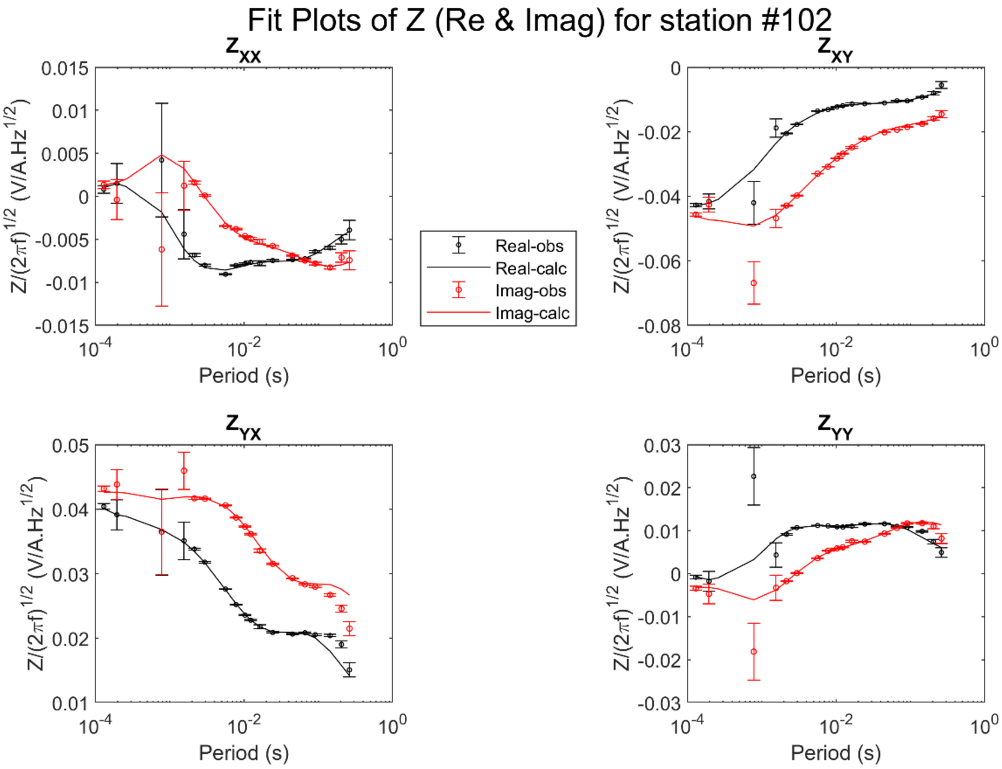
Fit Plots of Z (Re & Imag) for station #102
Z_XX
Z_XY
Z_YX
Z_YY
Z/(2πf)^1/2 (V/A.Hz^1/2)
Period (s)
Real-obs
Real-calc
Imag-obs
Imag-calc

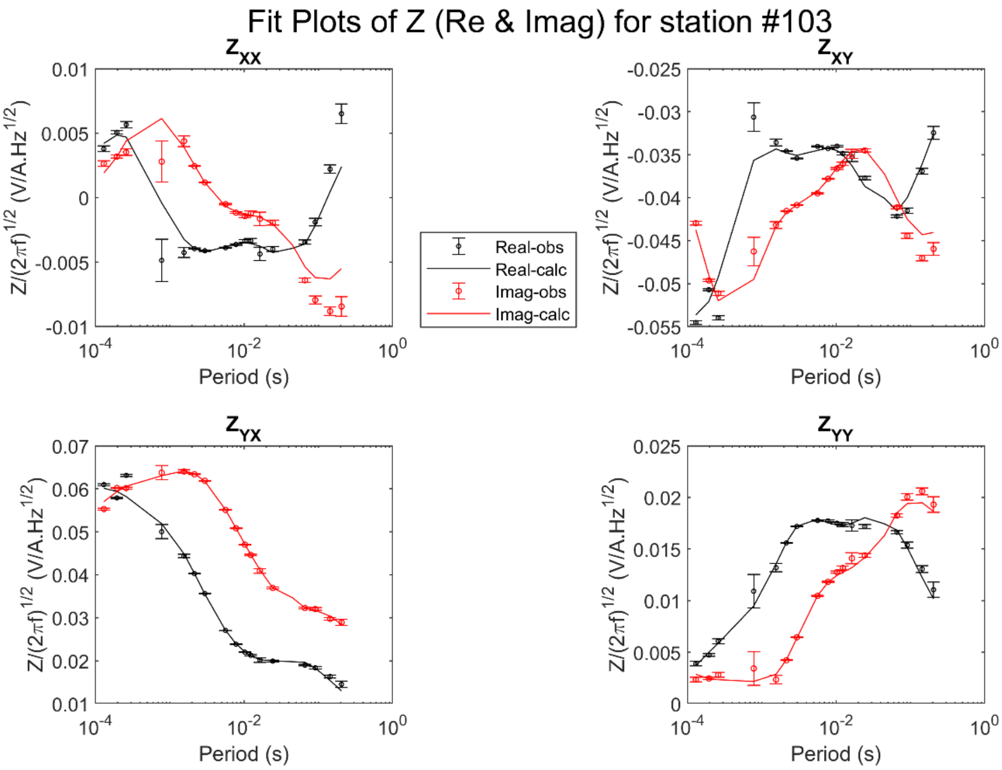
Fit Plots of Z (Re & Imag) for station #103
Z_XX
Z_XY
Z_YX
Z_YY
Z/(2πf)^1/2 (V/A.Hz^1/2)
Period (s)
Real-obs
Real-calc
Imag-obs
Imag-calc

Fit Plots of Z (Re & Imag) for station #104

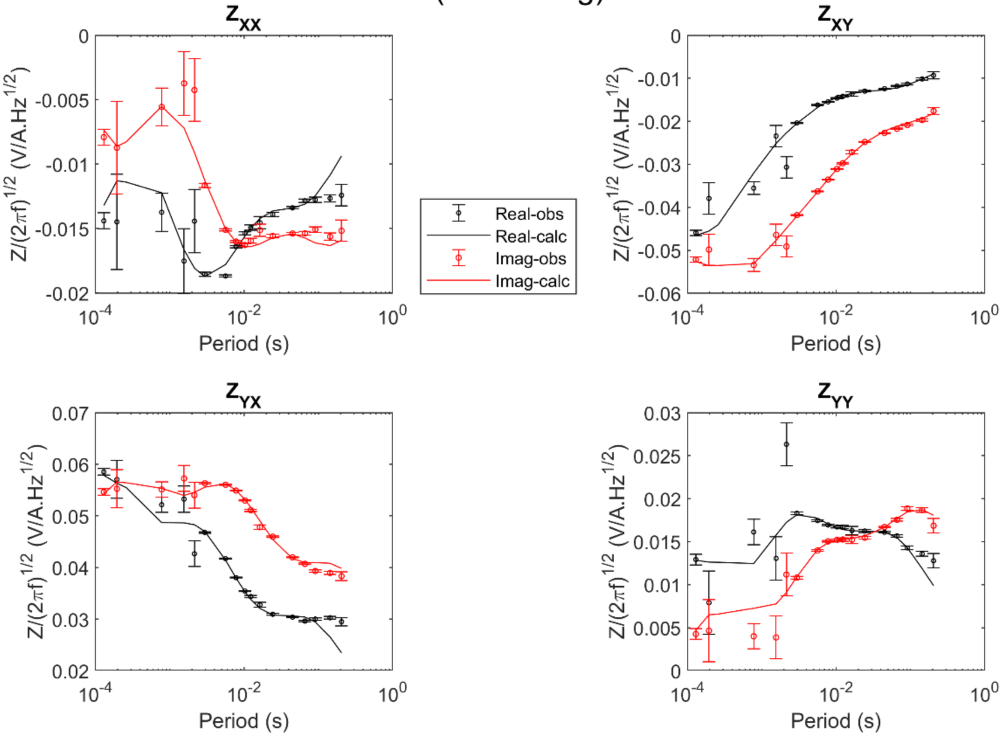

Fit Plots of Z (Re & Imag) for station #105

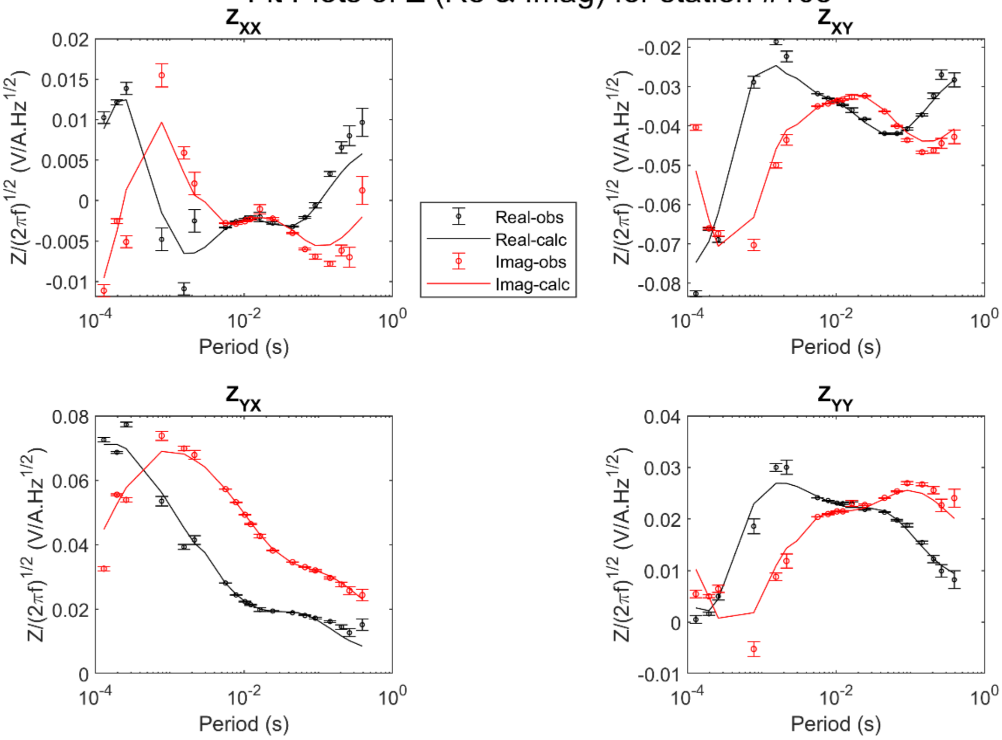

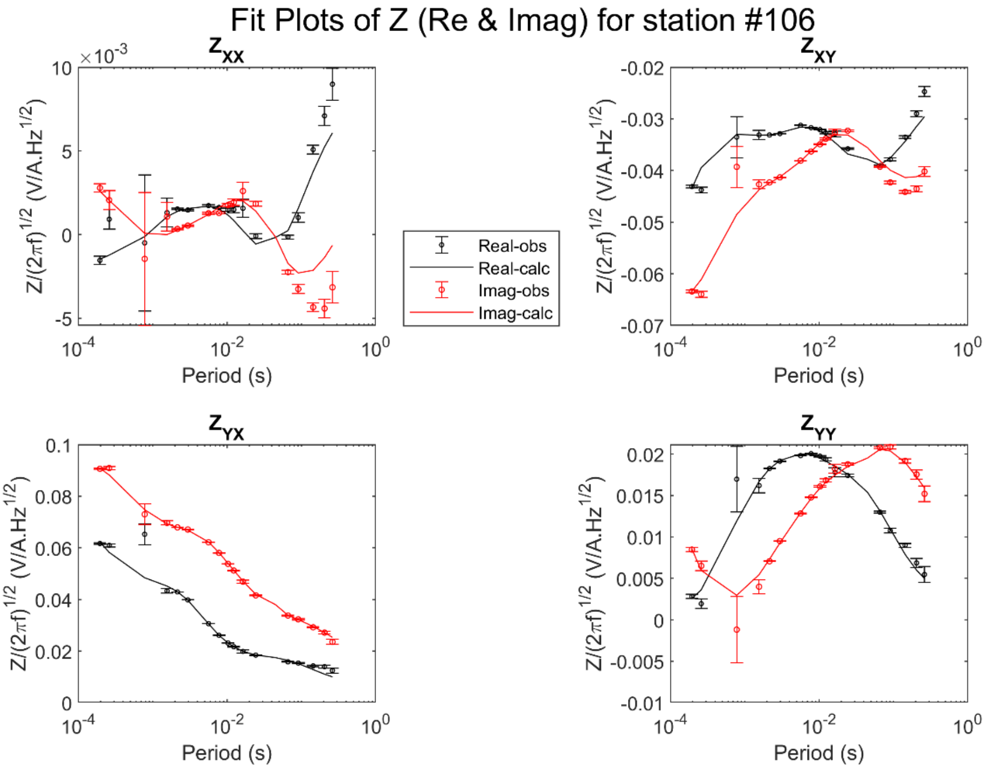

Fit Plots of Z (Re & Imag) for station #106
Z_XX
Z_XY
Z_YX
Z_YY
Z/(2πf)^1/2 (V/A.Hz^1/2)
Period (s)
Real-obs
Real-calc
Imag-obs
Imag-calc

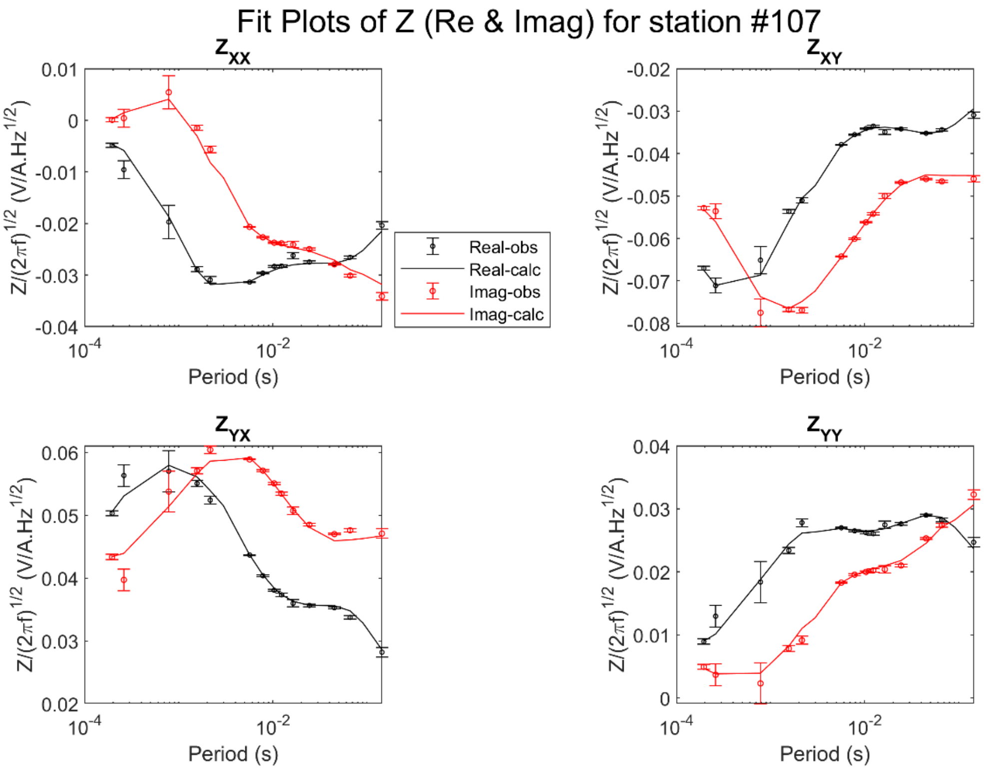

Fit Plots of Z (Re & Imag) for station #107
Z_XX
Z_XY
Z_YX
Z_YY
Z/(2πf)^1/2 (V/A.Hz^1/2)
Period (s)
Real-obs
Real-calc
Imag-obs
Imag-calc

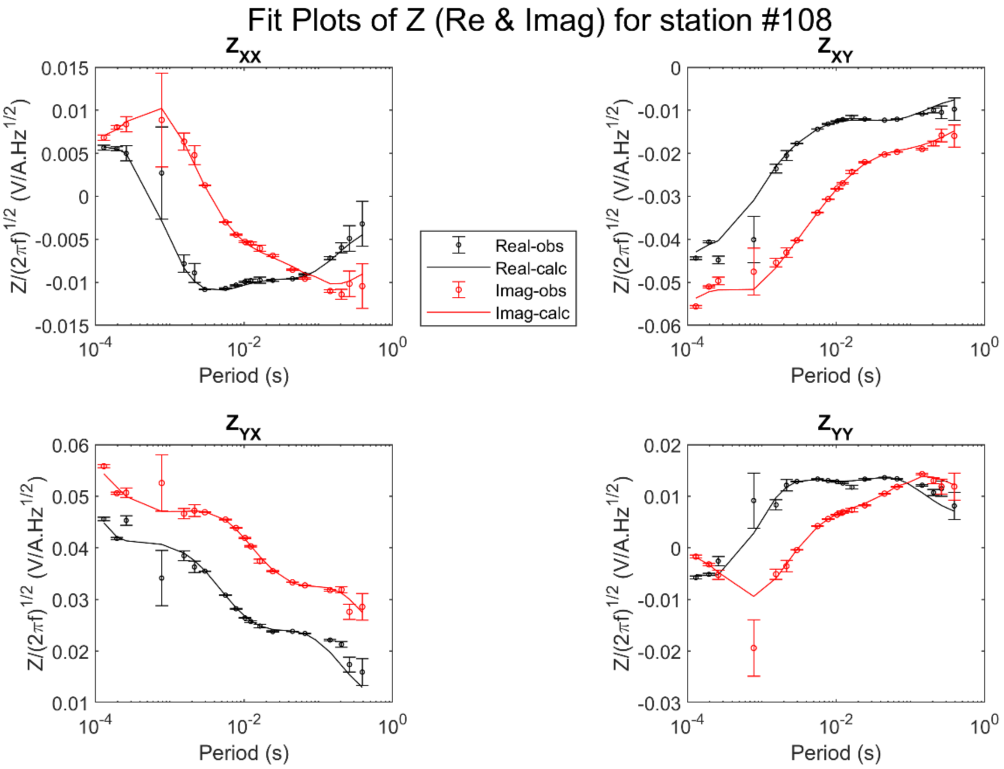
Fit Plots of Z (Re & Imag) for station #108
ZXX
ZXY
ZYX
ZYY
Z/(2πf)1/2 (V/A.Hz1/2)
Period (s)
Real-obs
Real-calc
Imag-obs
Imag-calc

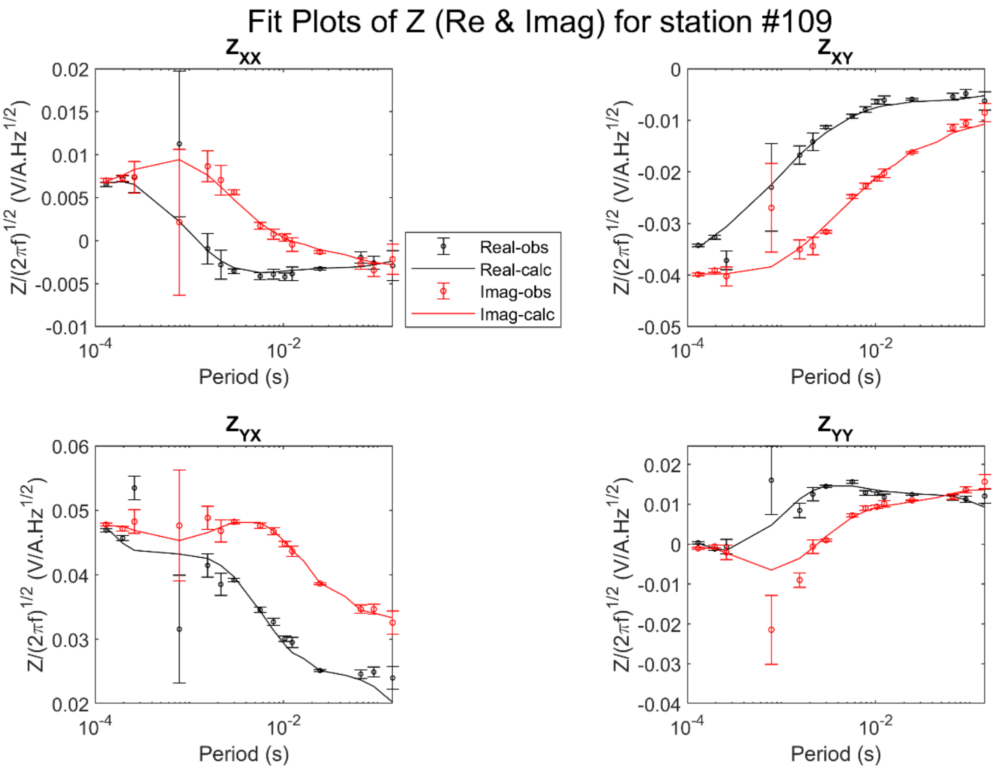
Fit Plots of Z (Re & Imag) for station #109
ZXX
ZXY
ZYX
ZYY
Z/(2πf)1/2 (V/A.Hz1/2)
Period (s)
Real-obs
Real-calc
Imag-obs
Imag-calc

Fit Plots of Z (Re & Imag) for station #110

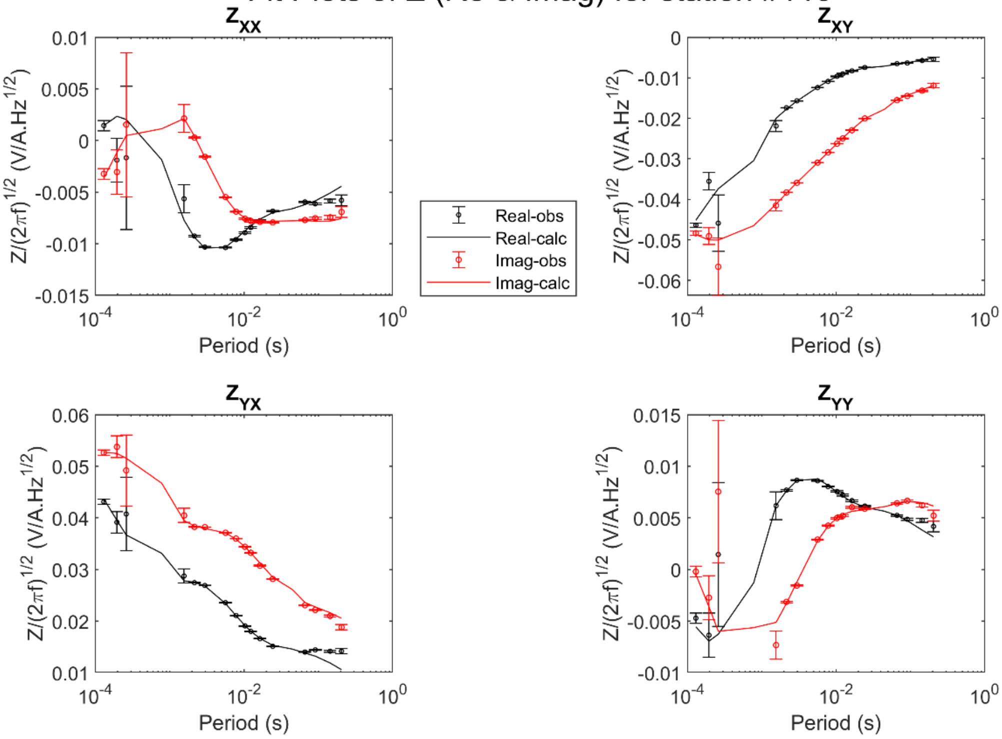

Fit Plots of Z (Re & Imag) for station #111

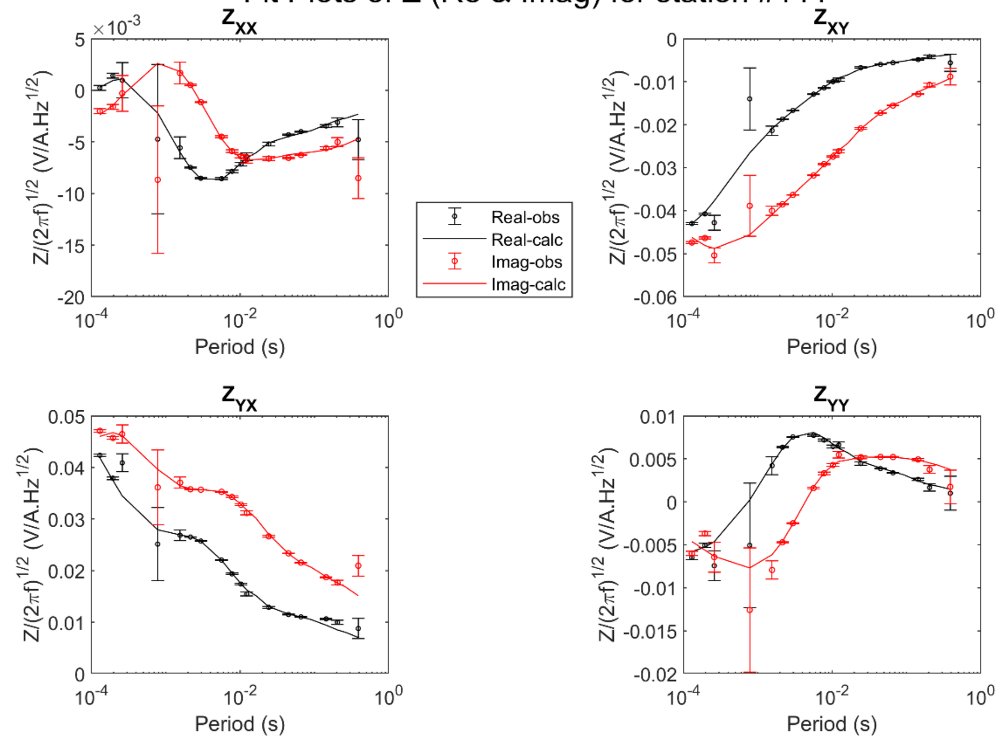

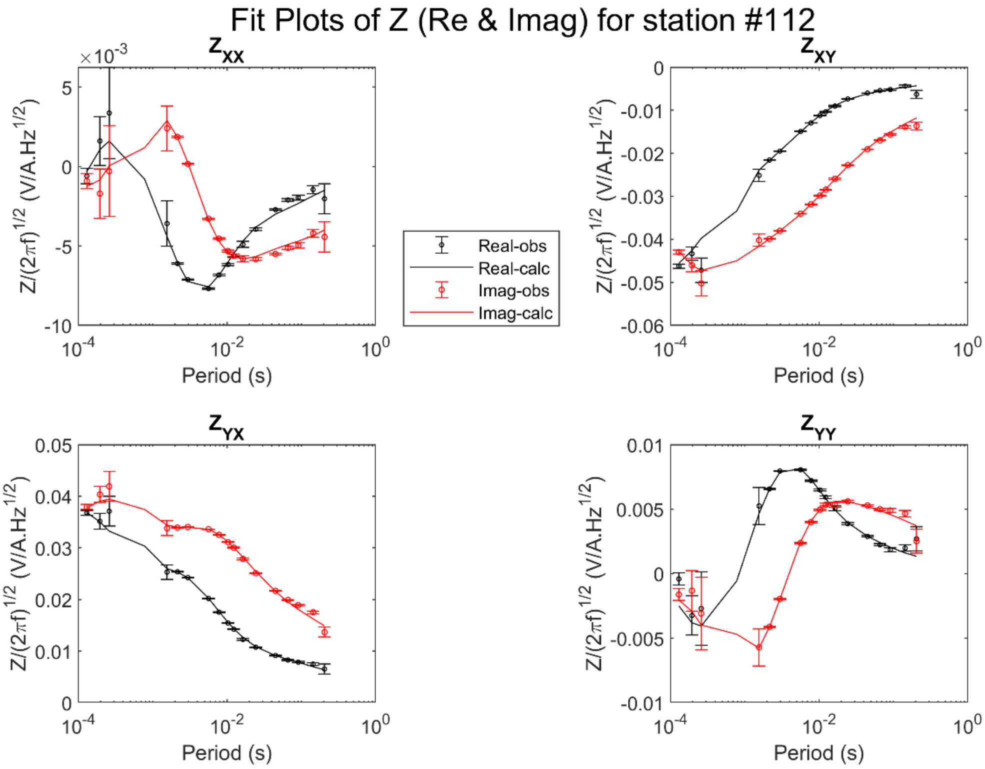
Fit Plots of Z (Re & Imag) for station #112
Z_XX
Z_XY
Z_YX
Z_YY
Z/(2πf)^1/2 (V/A.Hz^1/2)
Period (s)
Real-obs
Real-calc
Imag-obs
Imag-calc

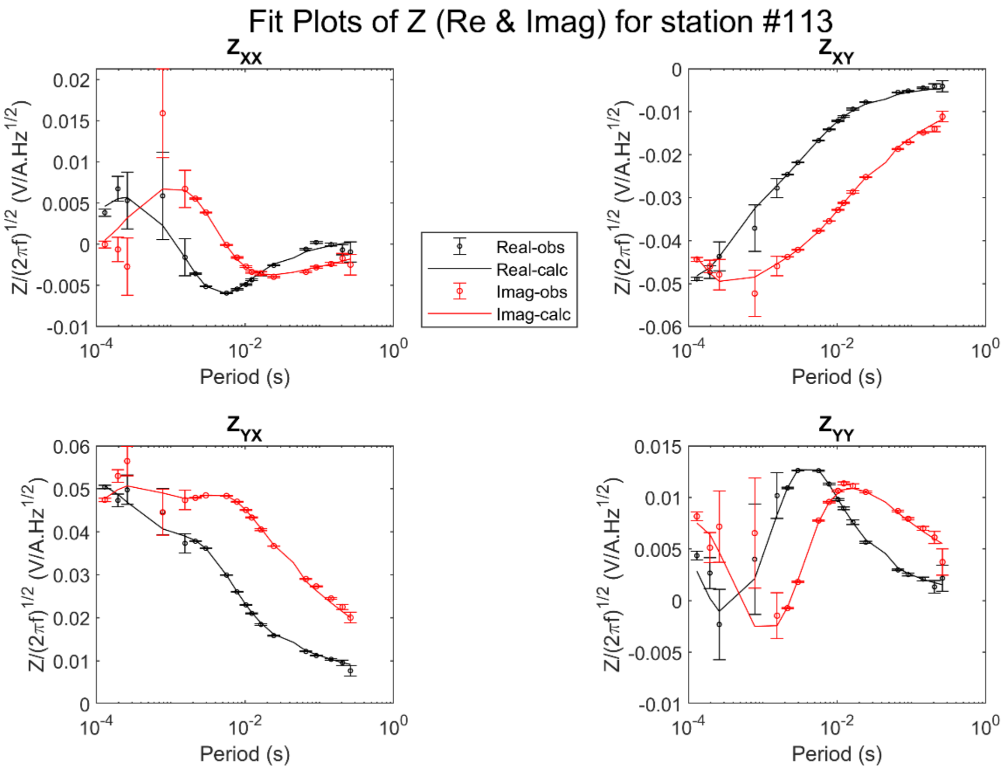
Fit Plots of Z (Re & Imag) for station #113
Z_XX
Z_XY
Z_YX
Z_YY
Z/(2πf)^1/2 (V/A.Hz^1/2)
Period (s)
Real-obs
Real-calc
Imag-obs
Imag-calc

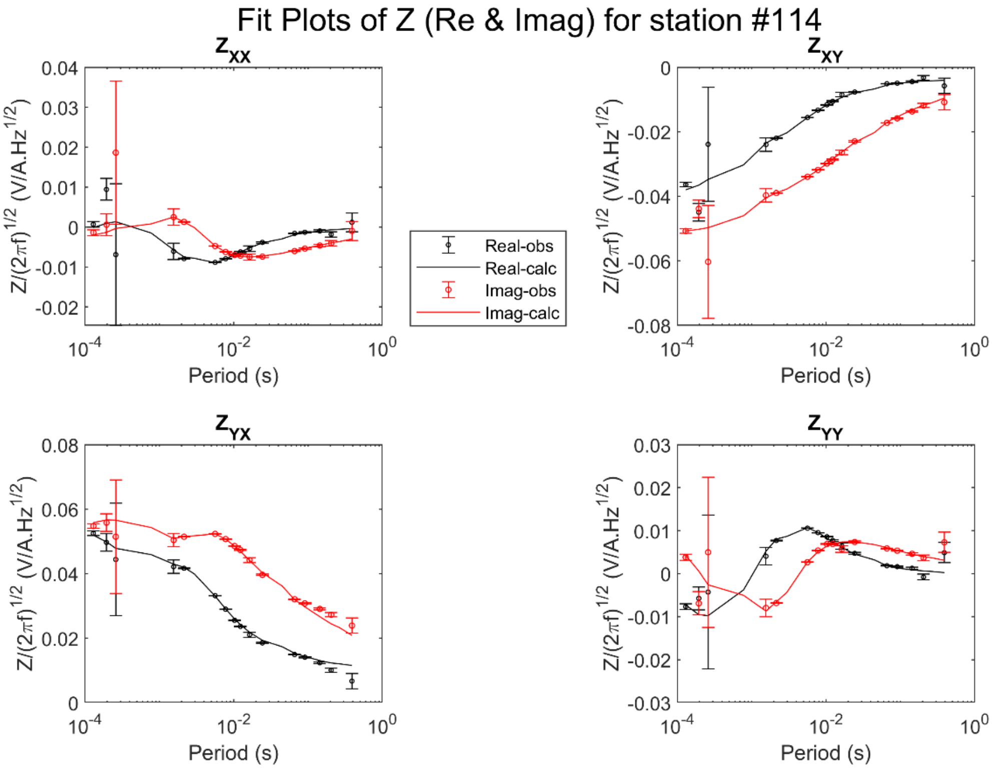

Fit Plots of Z (Re & Imag) for station #114
Z_XX
Z_XY
Z_YX
Z_YY
Z/(2πf)^1/2 (V/A.Hz^1/2)
Period (s)
Real-obs
Real-calc
Imag-obs
Imag-calc

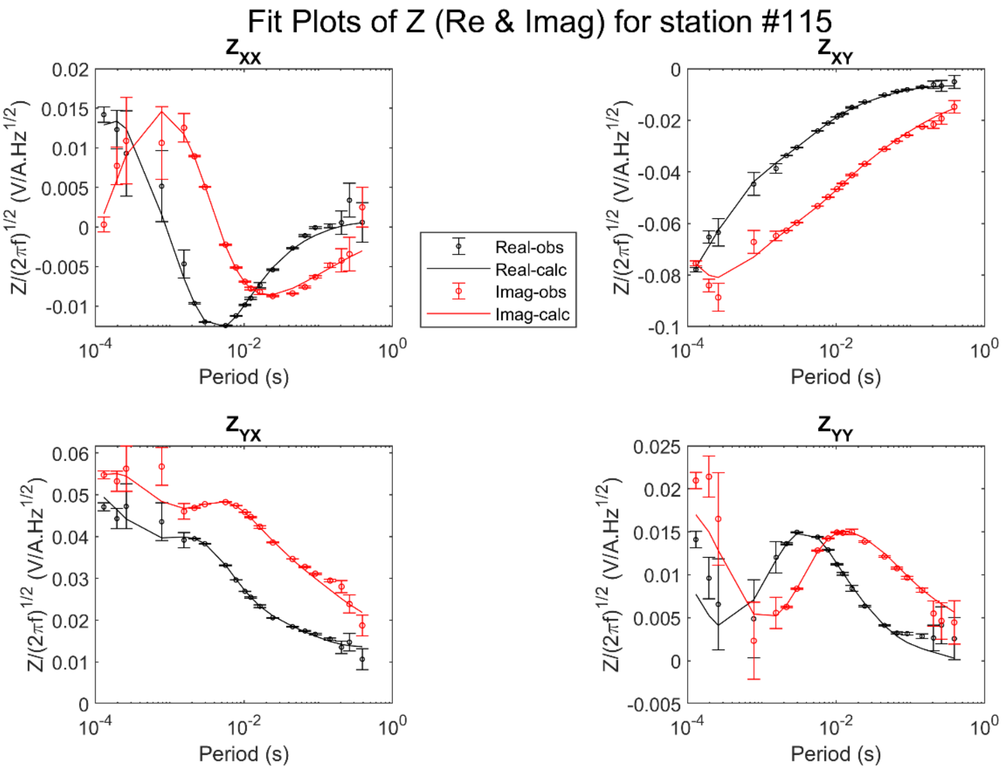

Fit Plots of Z (Re & Imag) for station #115
Z_XX
Z_XY
Z_YX
Z_YY
Z/(2πf)^1/2 (V/A.Hz^1/2)
Period (s)
Real-obs
Real-calc
Imag-obs
Imag-calc

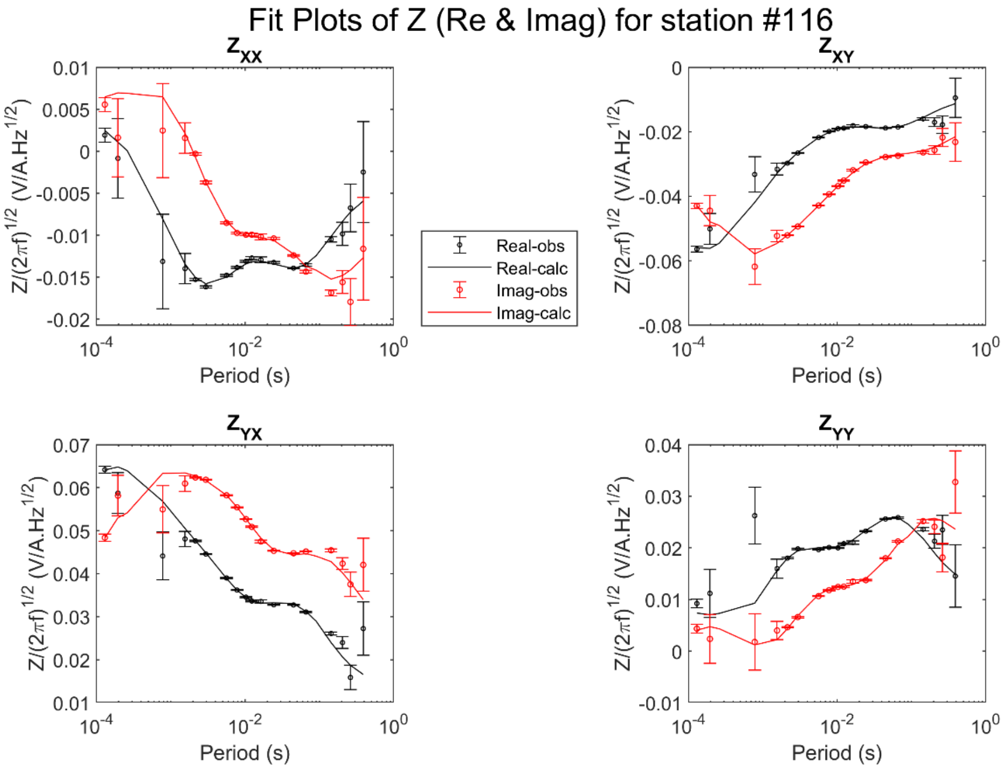
Fit Plots of Z (Re & Imag) for station #116
Z_XX
Z_XY
Z_YX
Z_YY
Z/(2πf)^1/2 (V/A.Hz^1/2)
Period (s)
Real-obs
Real-calc
Imag-obs
Imag-calc

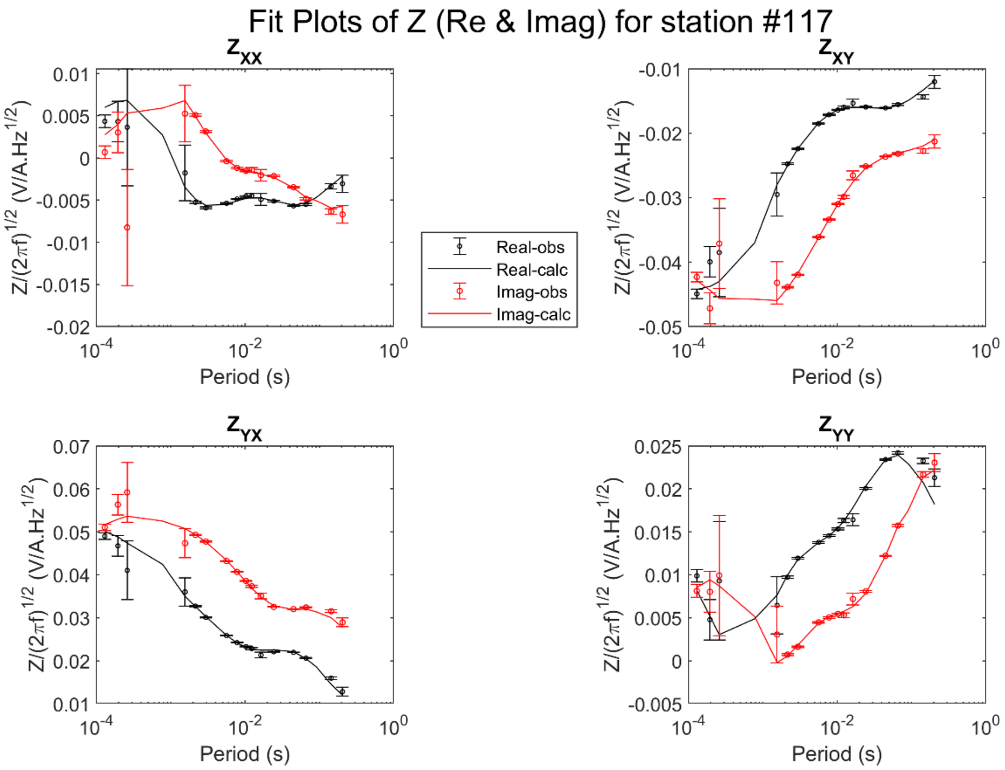
Fit Plots of Z (Re & Imag) for station #117
Z_XX
Z_XY
Z_YX
Z_YY
Z/(2πf)^1/2 (V/A.Hz^1/2)
Period (s)
Real-obs
Real-calc
Imag-obs
Imag-calc

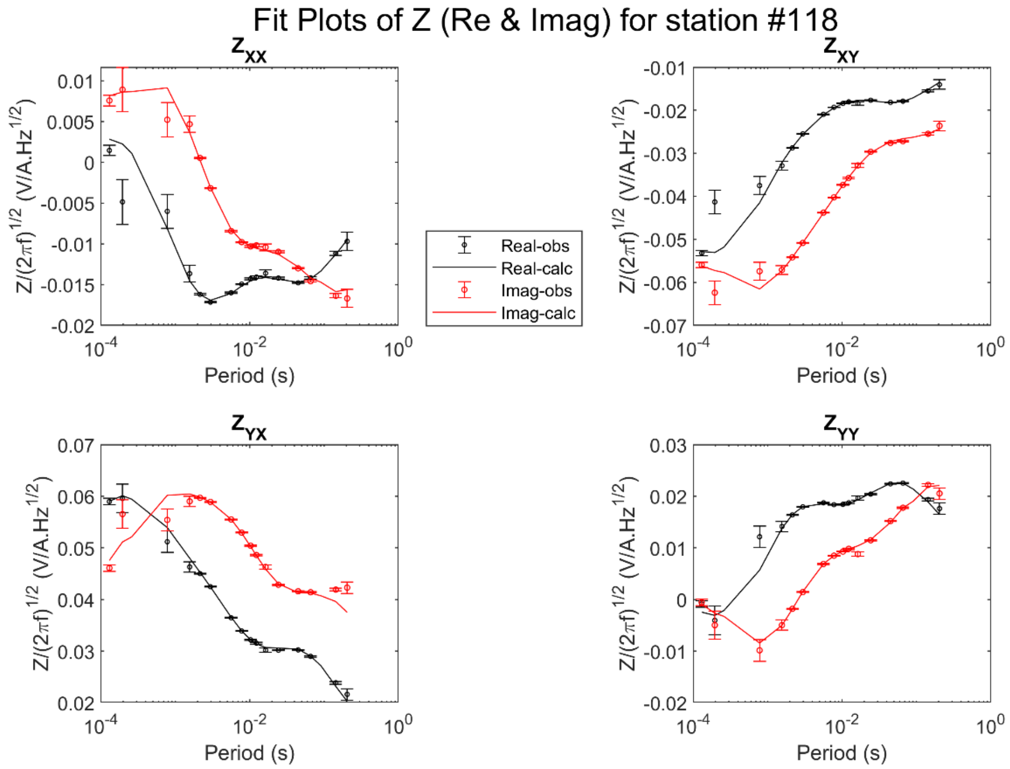
Fit Plots of Z (Re & Imag) for station #118
Z_{XX}
Z_{XY}
Z_{YX}
Z_{YY}
$Z/(2\pi f)^{1/2}$ (V/A.Hz$^{1/2}$)
Period (s)
Real-obs
Real-calc
Imag-obs
Imag-calc

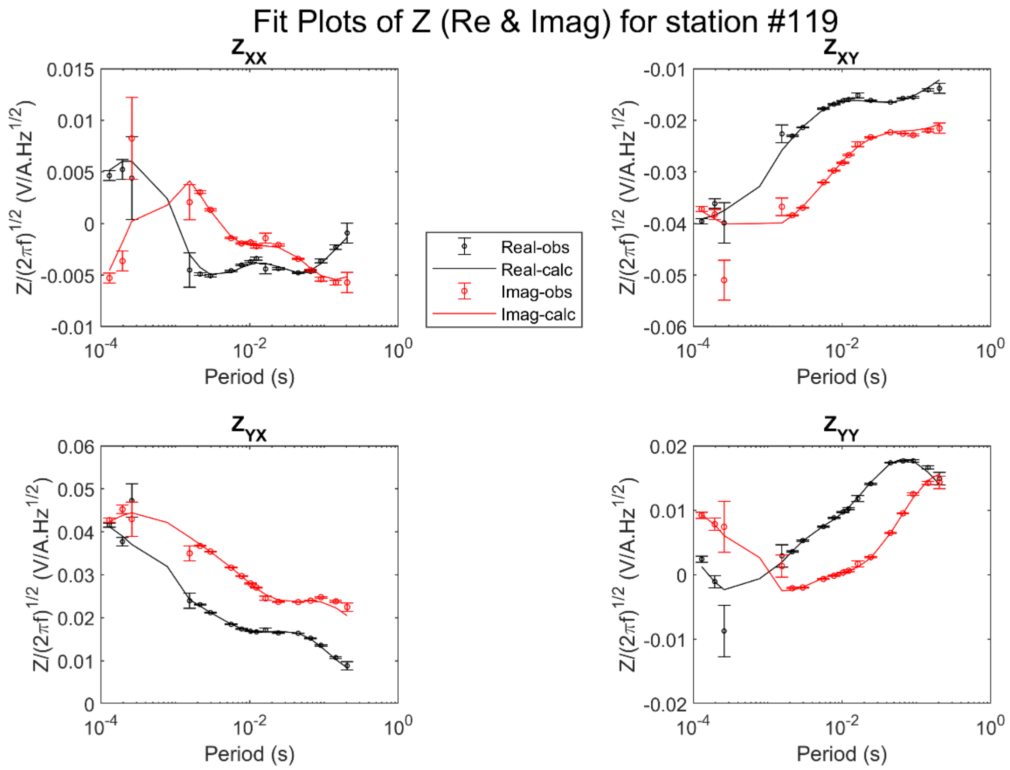
Fit Plots of Z (Re & Imag) for station #119
Z_{XX}
Z_{XY}
Z_{YX}
Z_{YY}
$Z/(2\pi f)^{1/2}$ (V/A.Hz$^{1/2}$)
Period (s)
Real-obs
Real-calc
Imag-obs
Imag-calc

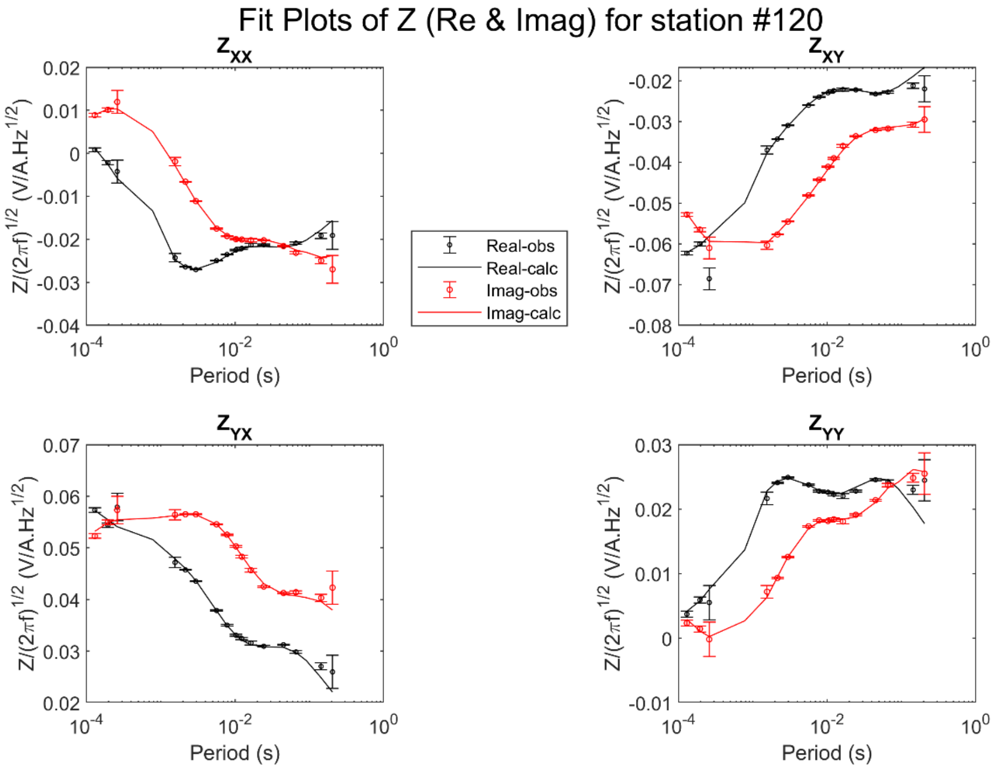
Fit Plots of Z (Re & Imag) for station #120
Z_{XX}
Z_{XY}
Z_{YX}
Z_{YY}
Real-obs
Real-calc
Imag-obs
Imag-calc
$Z/(2\pi f)^{1/2}$ (V/A.Hz$^{1/2}$)
Period (s)

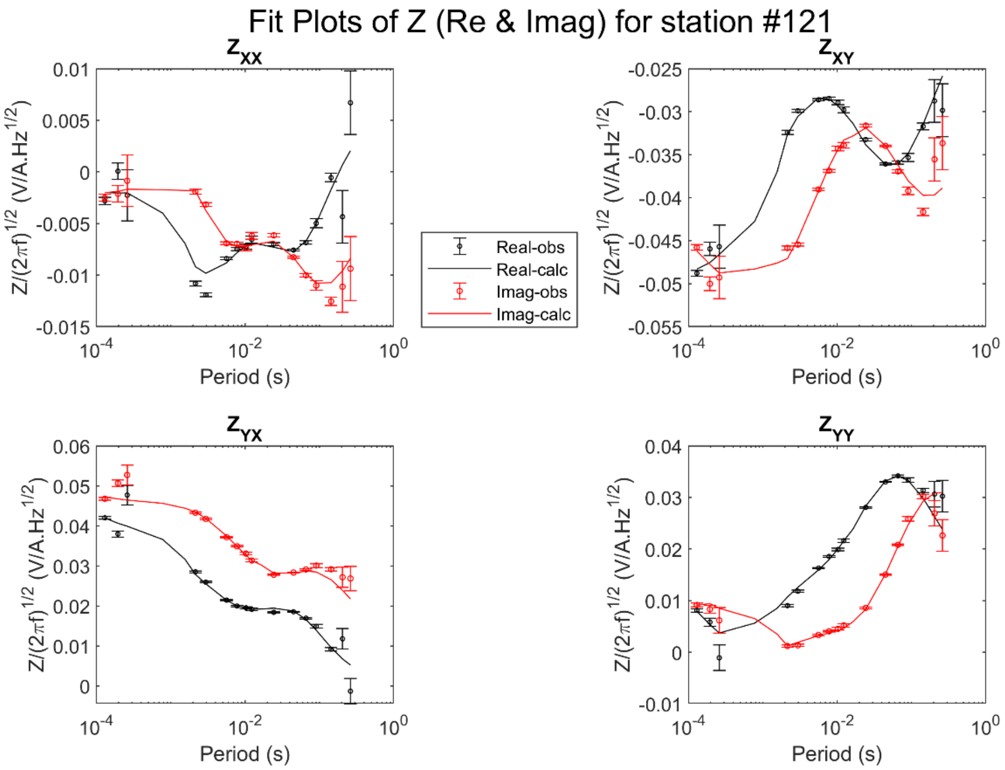
Fit Plots of Z (Re & Imag) for station #121
Z_{XX}
Z_{XY}
Z_{YX}
Z_{YY}
Real-obs
Real-calc
Imag-obs
Imag-calc
$Z/(2\pi f)^{1/2}$ (V/A.Hz$^{1/2}$)
Period (s)

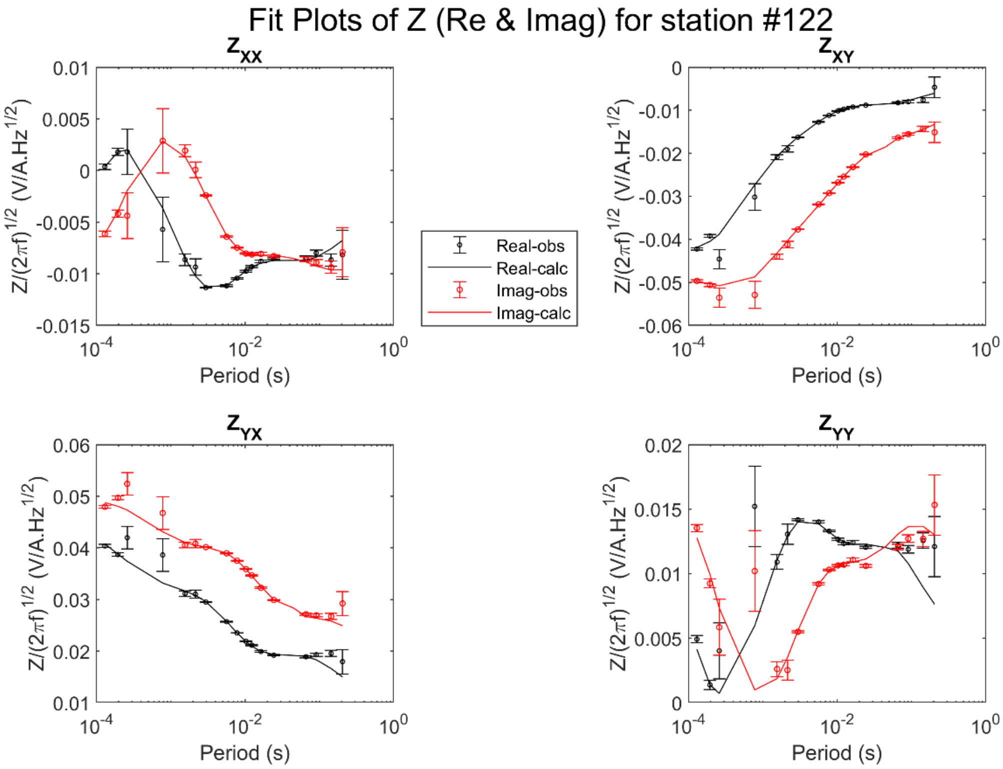
Fit Plots of Z (Re & Imag) for station #122
Z_XX
Z_XY
Z_YX
Z_YY
Real-obs
Real-calc
Imag-obs
Imag-calc
Period (s)
Z/(2πf)^1/2 (V/A.Hz^1/2)

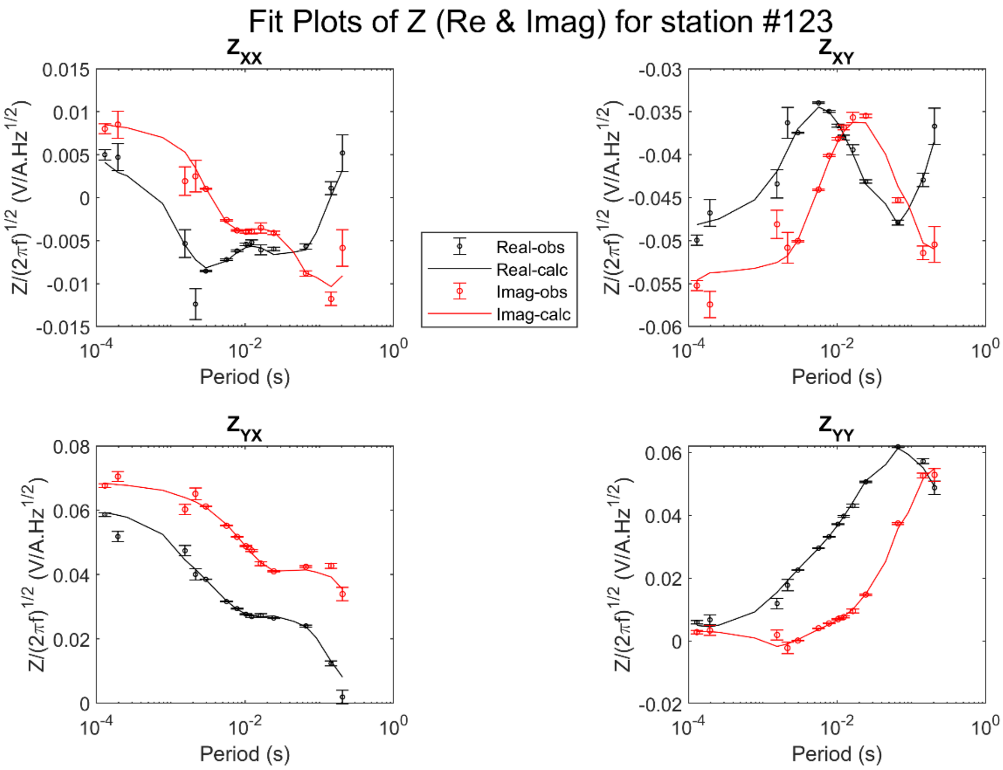
Fit Plots of Z (Re & Imag) for station #123
Z_XX
Z_XY
Z_YX
Z_YY
Real-obs
Real-calc
Imag-obs
Imag-calc
Period (s)
Z/(2πf)^1/2 (V/A.Hz^1/2)

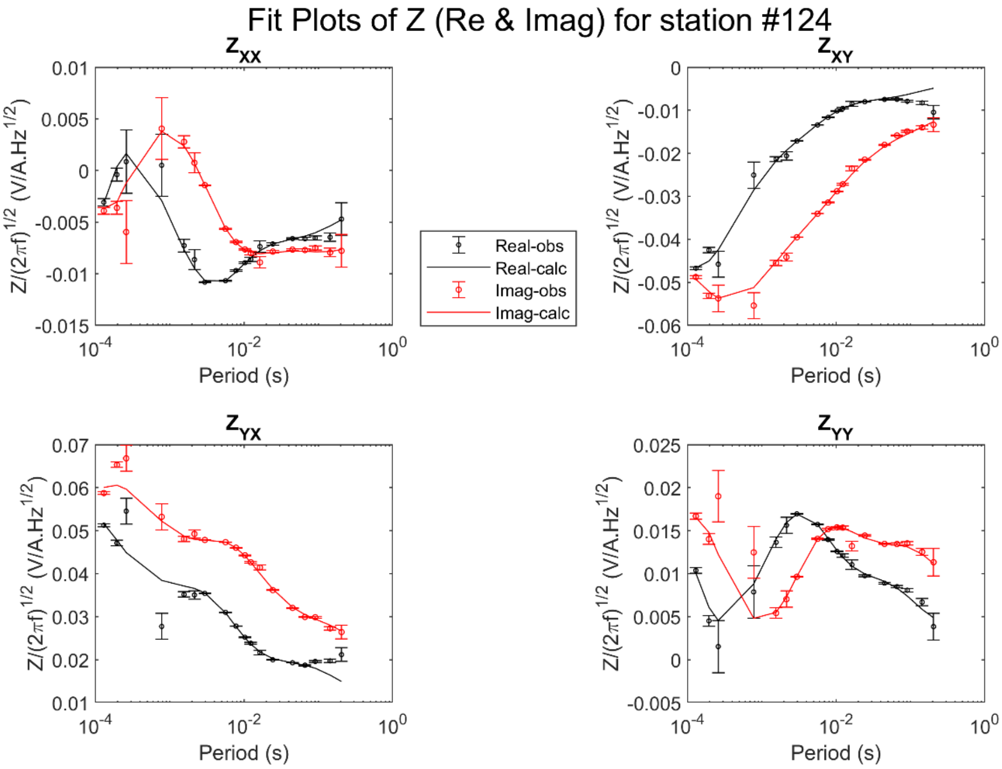
Fit Plots of Z (Re & Imag) for station #124
Z_{XX}
Z_{XY}
Z_{YX}
Z_{YY}
$Z/(2\pi f)^{1/2}$ (V/A.Hz$^{1/2}$)
Period (s)
Real-obs
Real-calc
Imag-obs
Imag-calc

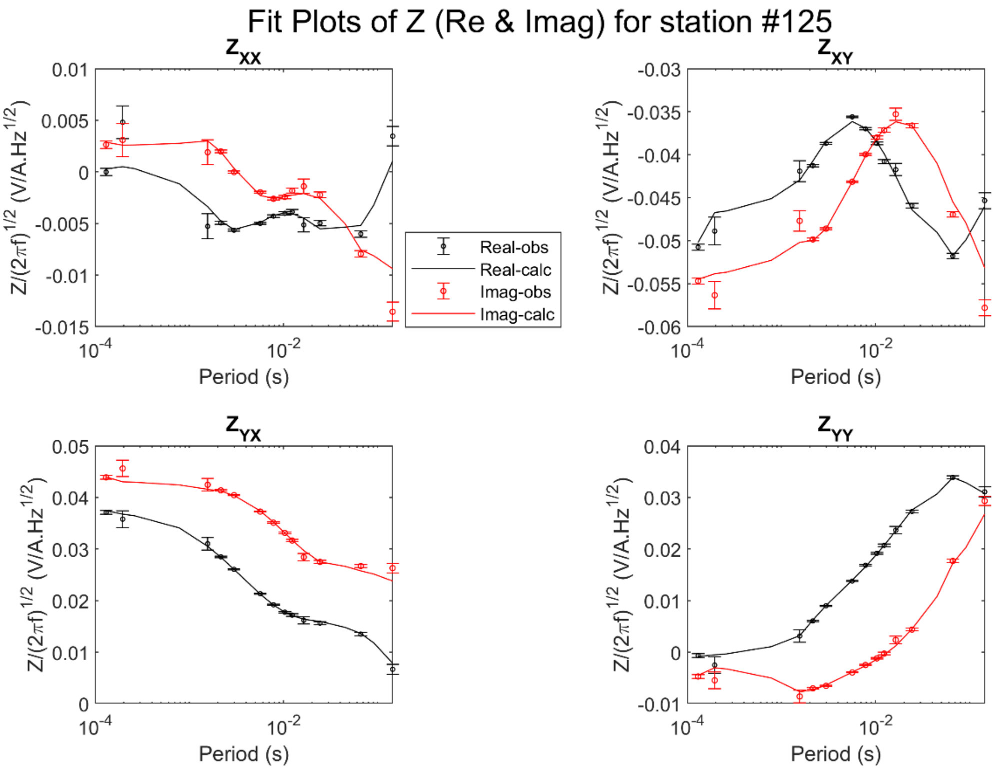
Fit Plots of Z (Re & Imag) for station #125
Z_{XX}
Z_{XY}
Z_{YX}
Z_{YY}
$Z/(2\pi f)^{1/2}$ (V/A.Hz$^{1/2}$)
Period (s)
Real-obs
Real-calc
Imag-obs
Imag-calc

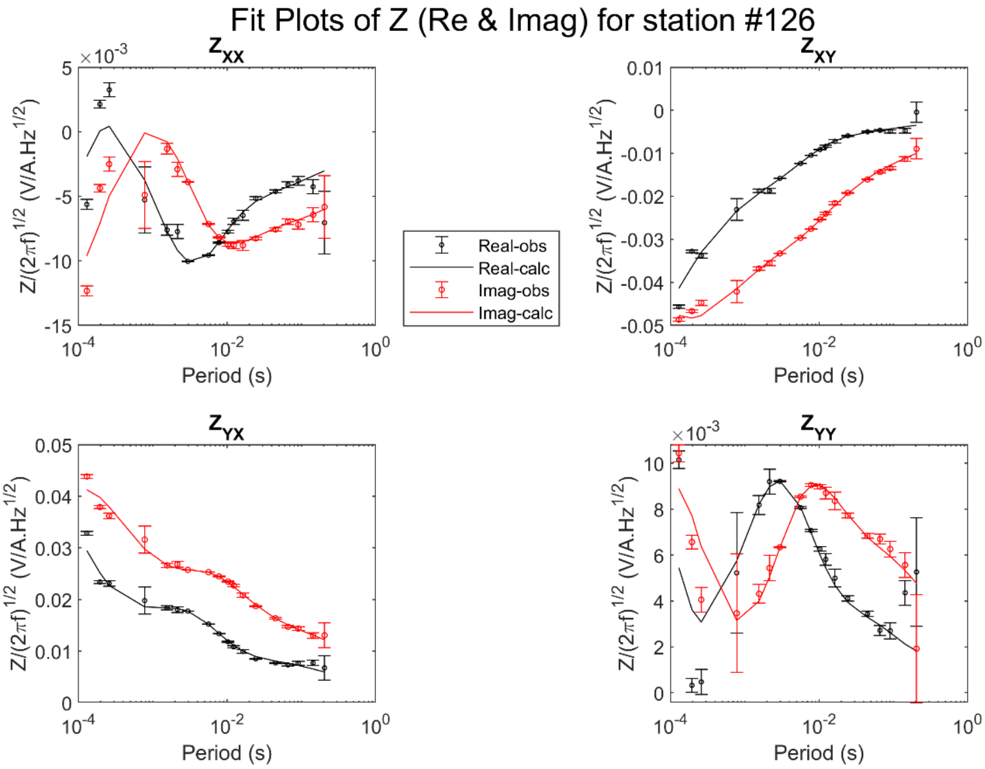
Fit Plots of Z (Re & Imag) for station #126
Z_XX
Z_XY
Z_YX
Z_YY
Z/(2πf)^1/2 (V/A.Hz^1/2)
Period (s)
Real-obs
Real-calc
Imag-obs
Imag-calc

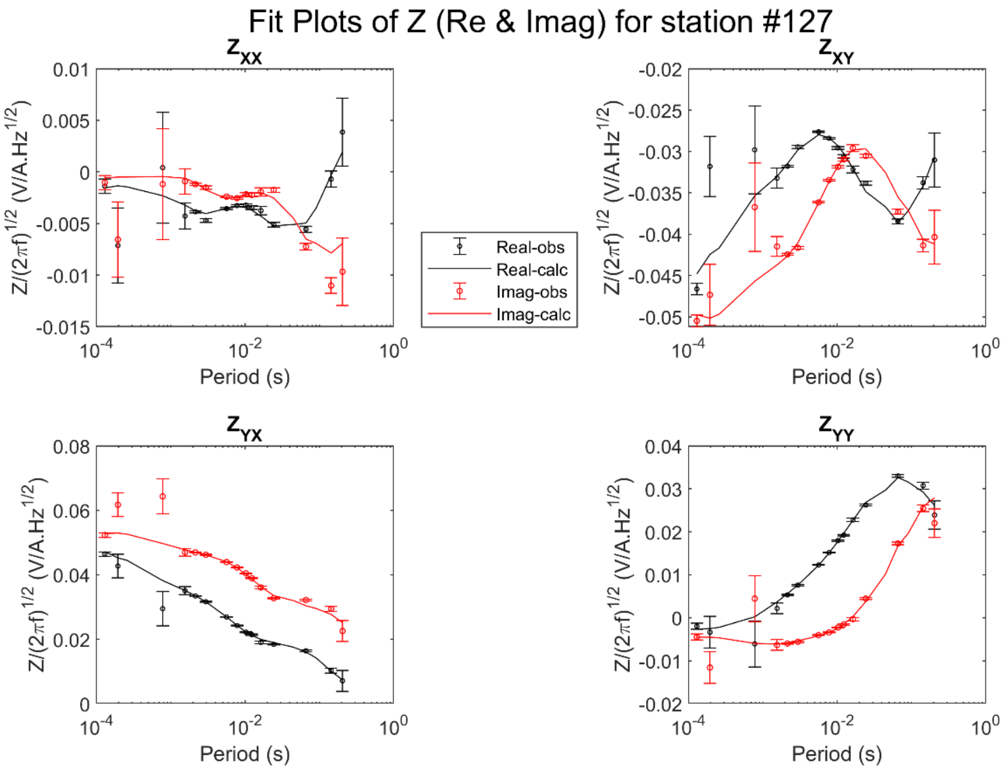
Fit Plots of Z (Re & Imag) for station #127
Z_XX
Z_XY
Z_YX
Z_YY
Z/(2πf)^1/2 (V/A.Hz^1/2)
Period (s)
Real-obs
Real-calc
Imag-obs
Imag-calc

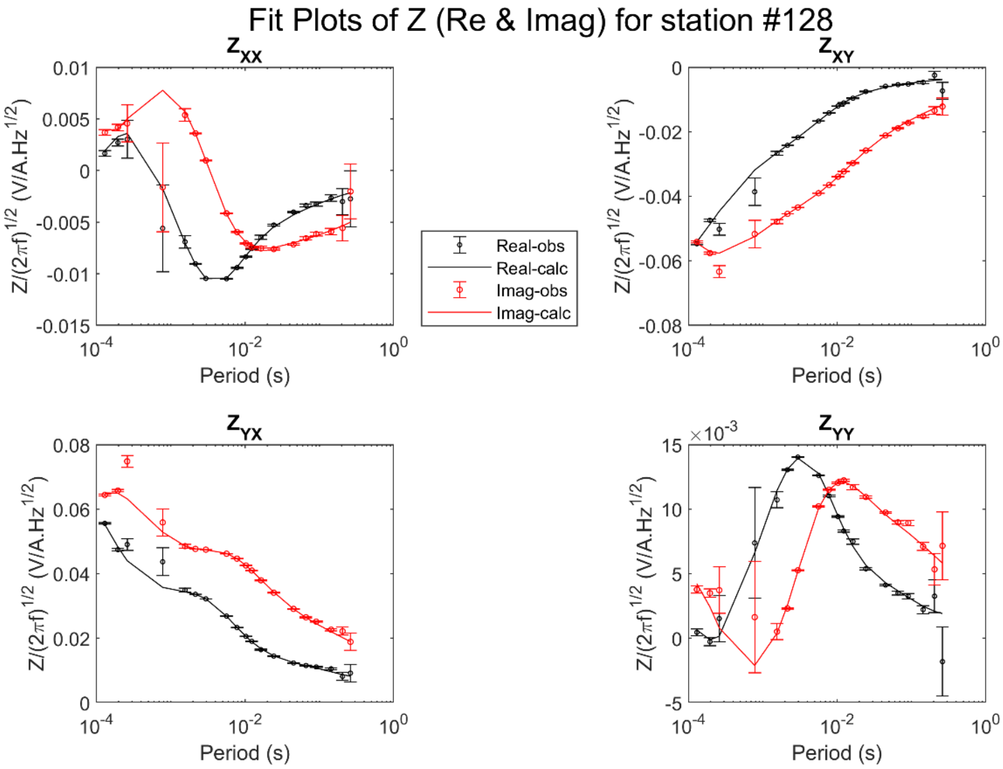

Fit Plots of Z (Re & Imag) for station #128
Z_XX
Z_XY
Z_YX
Z_YY
Real-obs
Real-calc
Imag-obs
Imag-calc
Z/(2πf)^1/2 (V/A.Hz^1/2)
Period (s)

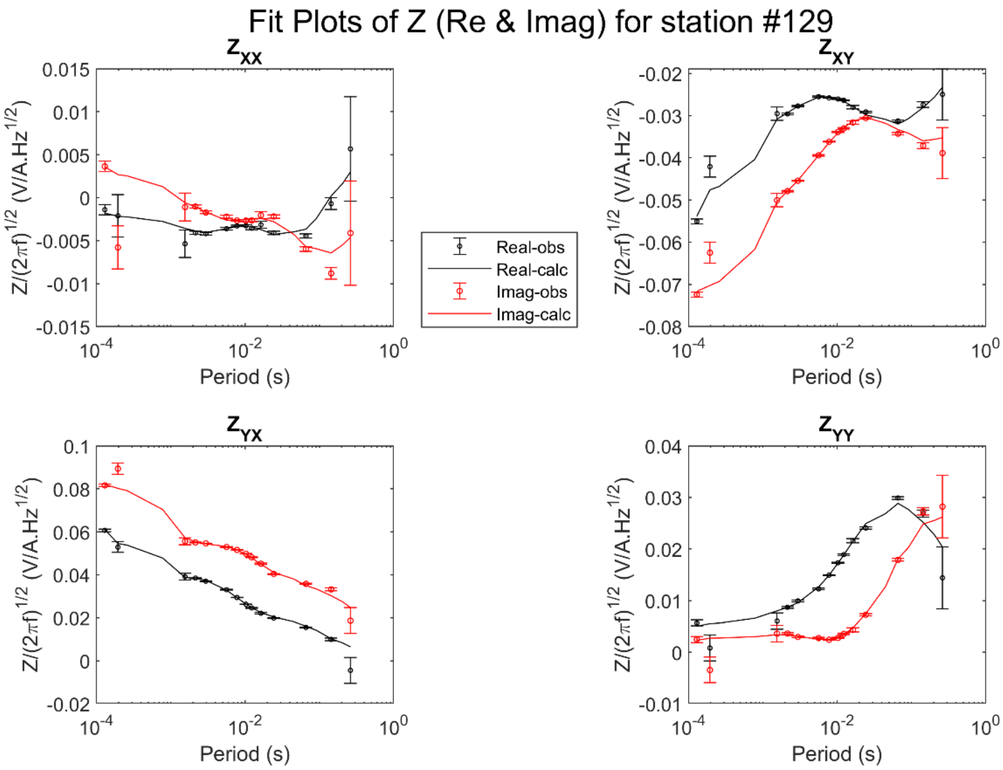

Fit Plots of Z (Re & Imag) for station #129
Z_XX
Z_XY
Z_YX
Z_YY
Real-obs
Real-calc
Imag-obs
Imag-calc
Z/(2πf)^1/2 (V/A.Hz^1/2)
Period (s)

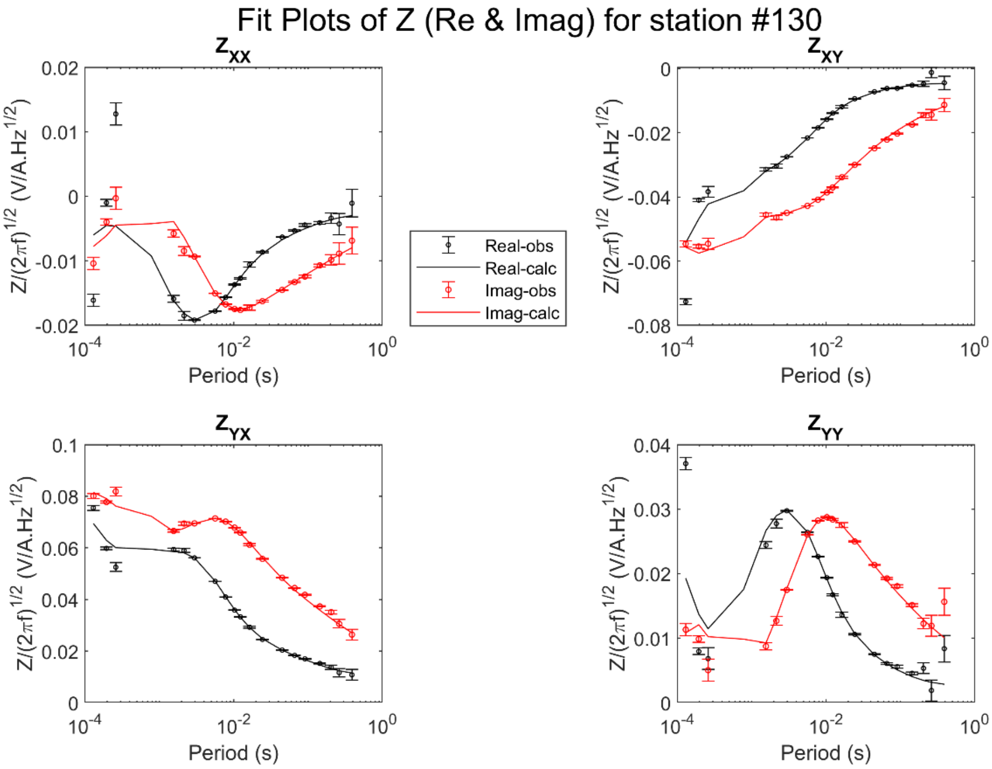
Fit Plots of Z (Re & Imag) for station #130
Z_XX
Z_XY
Z_YX
Z_YY
Z/(2πf)^1/2 (V/A.Hz^1/2)
Period (s)
Real-obs
Real-calc
Imag-obs
Imag-calc

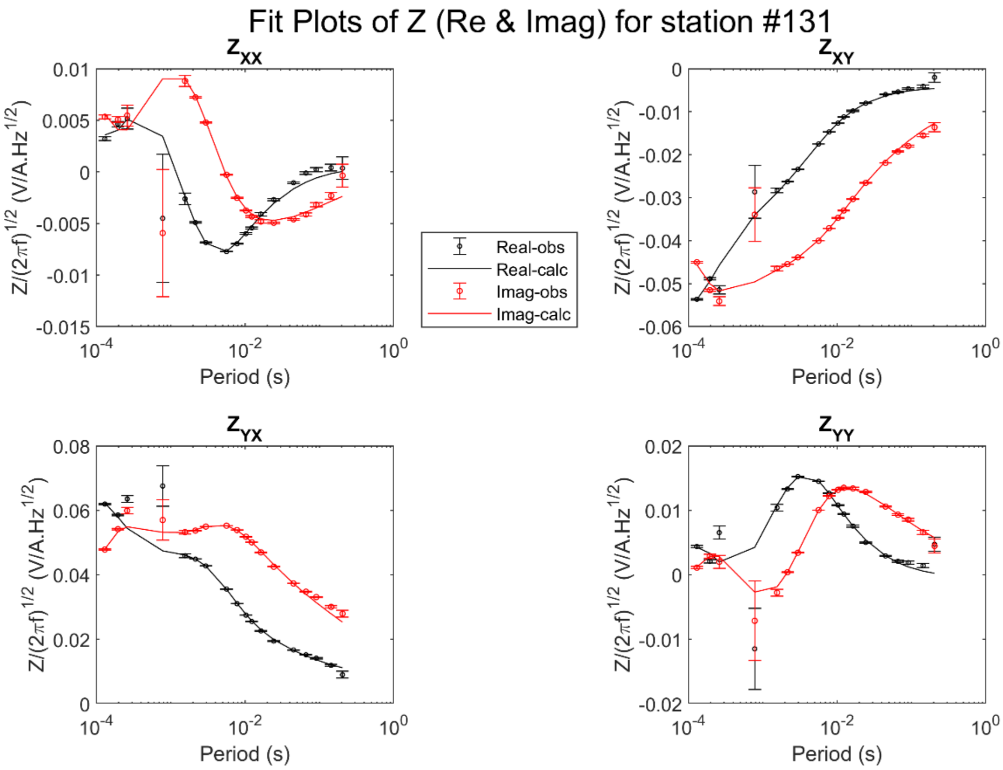
Fit Plots of Z (Re & Imag) for station #131
Z_XX
Z_XY
Z_YX
Z_YY
Z/(2πf)^1/2 (V/A.Hz^1/2)
Period (s)
Real-obs
Real-calc
Imag-obs
Imag-calc

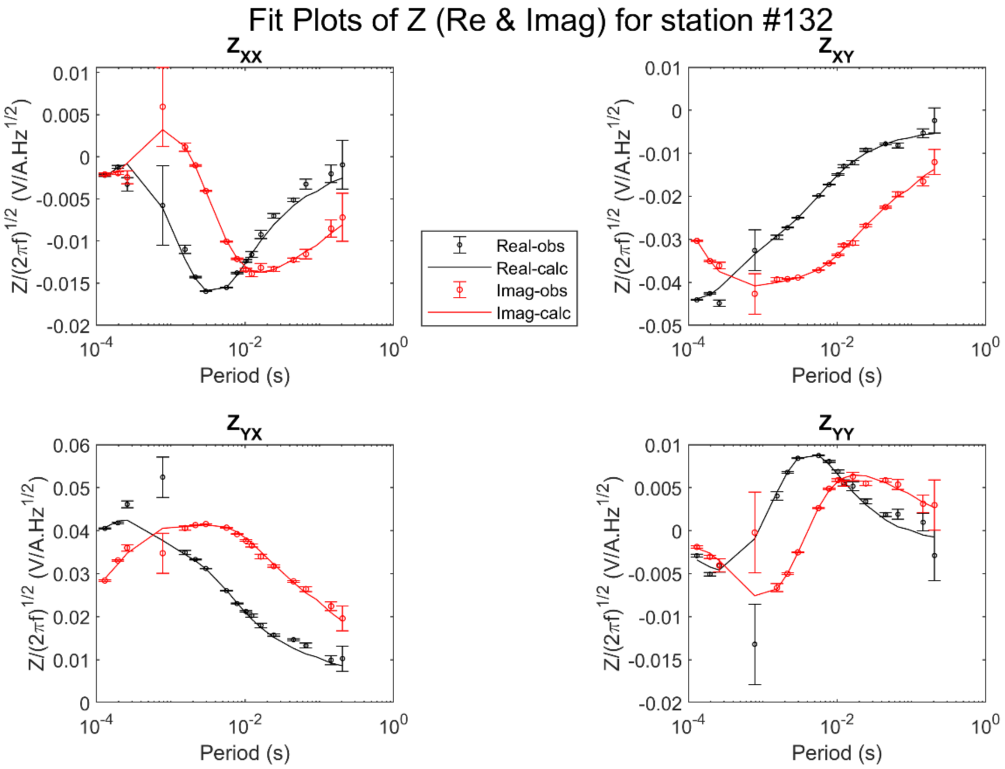

Fit Plots of Z (Re & Imag) for station #132
Z_{XX}
Z_{XY}
Z_{YX}
Z_{YY}
Real-obs
Real-calc
Imag-obs
Imag-calc
Period (s)
$Z/(2\pi f)^{1/2}$ (V/A.Hz$^{1/2}$)

D.2. Fit Plots of Apparent Resistivities and Phases

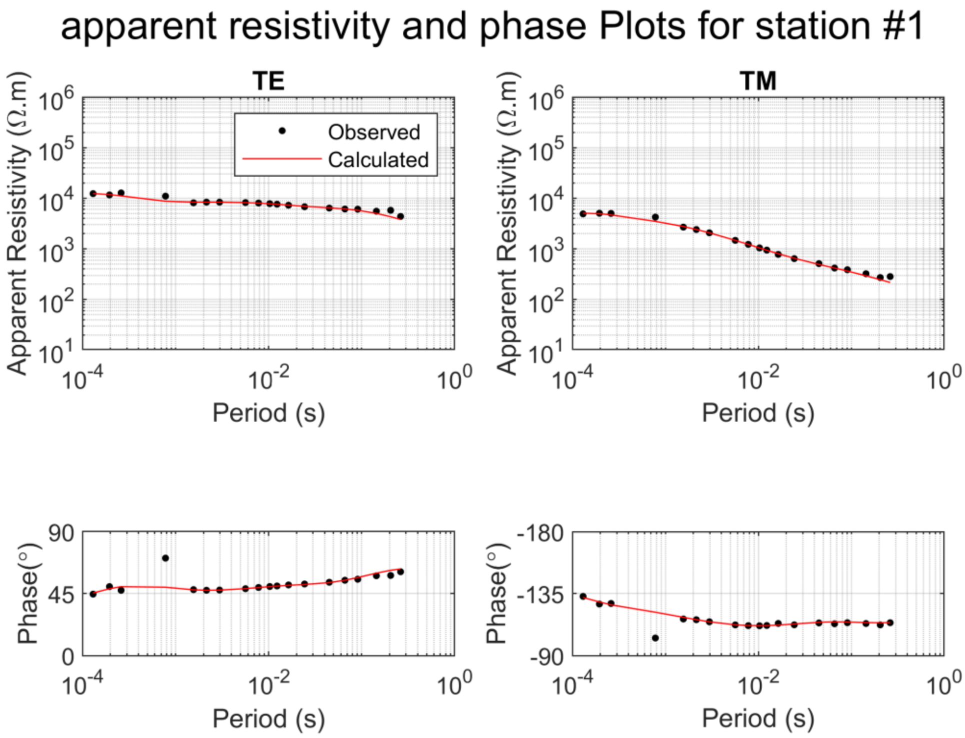

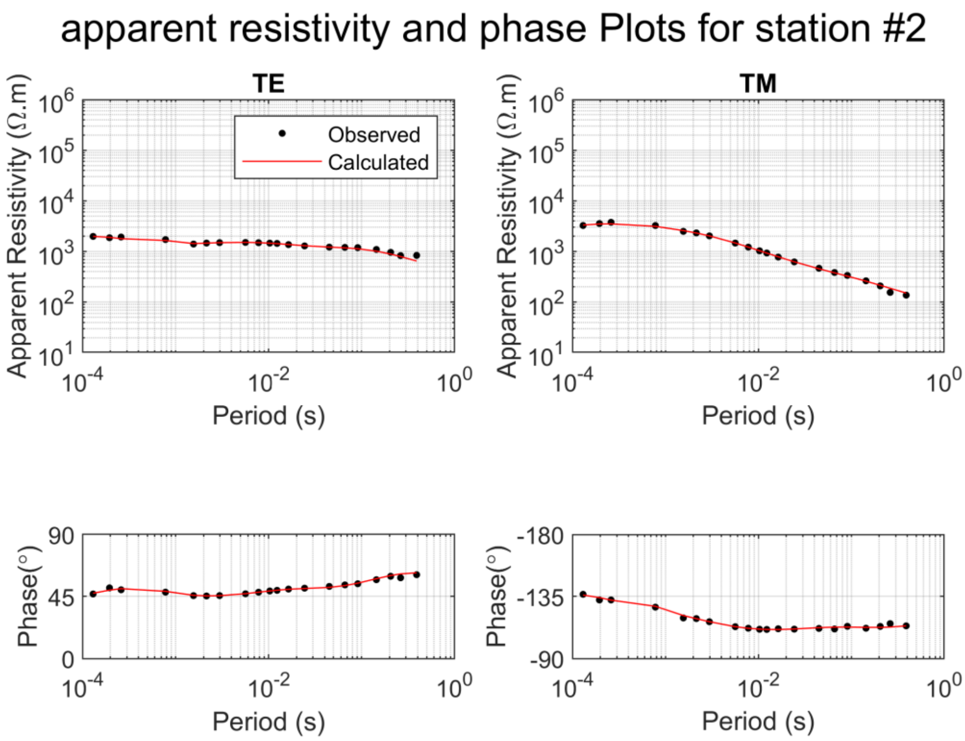

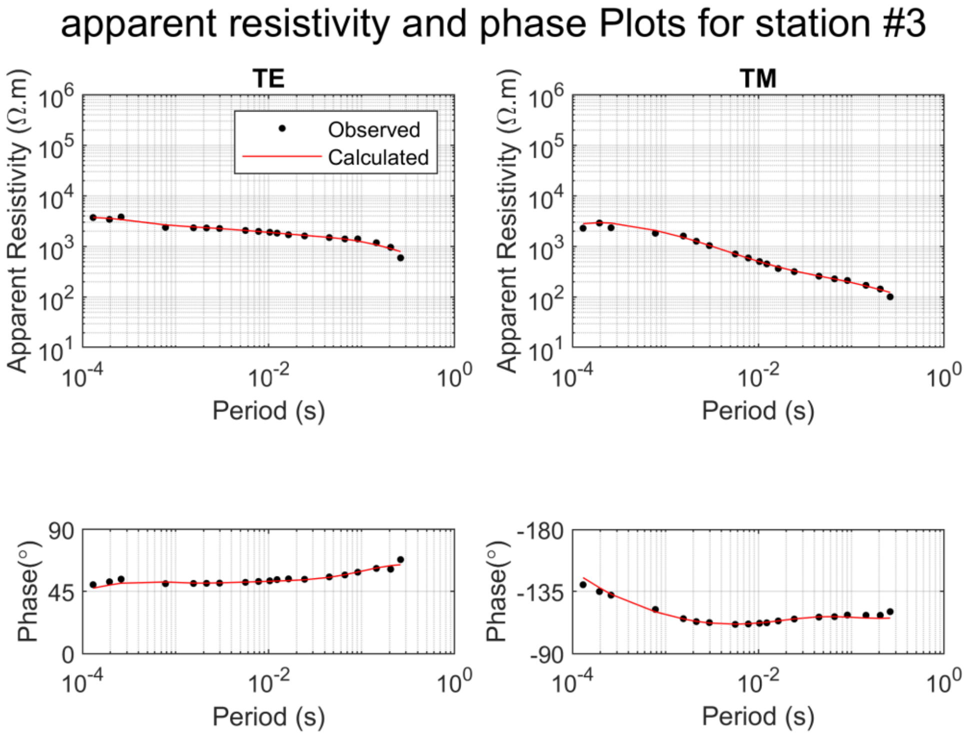
apparent resistivity and phase Plots for station #3
TE
TM
Observed
Calculated
Apparent Resistivity (Ω.m)
Period (s)
Phase(°)

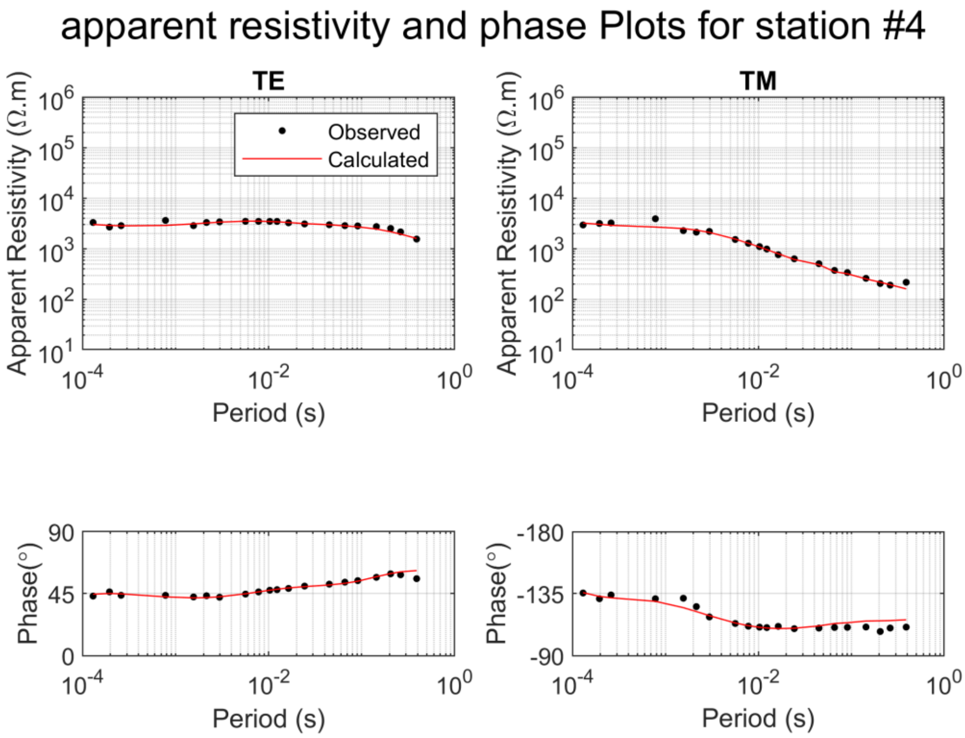
apparent resistivity and phase Plots for station #4
TE
TM
Observed
Calculated
Apparent Resistivity (Ω.m)
Period (s)
Phase(°)

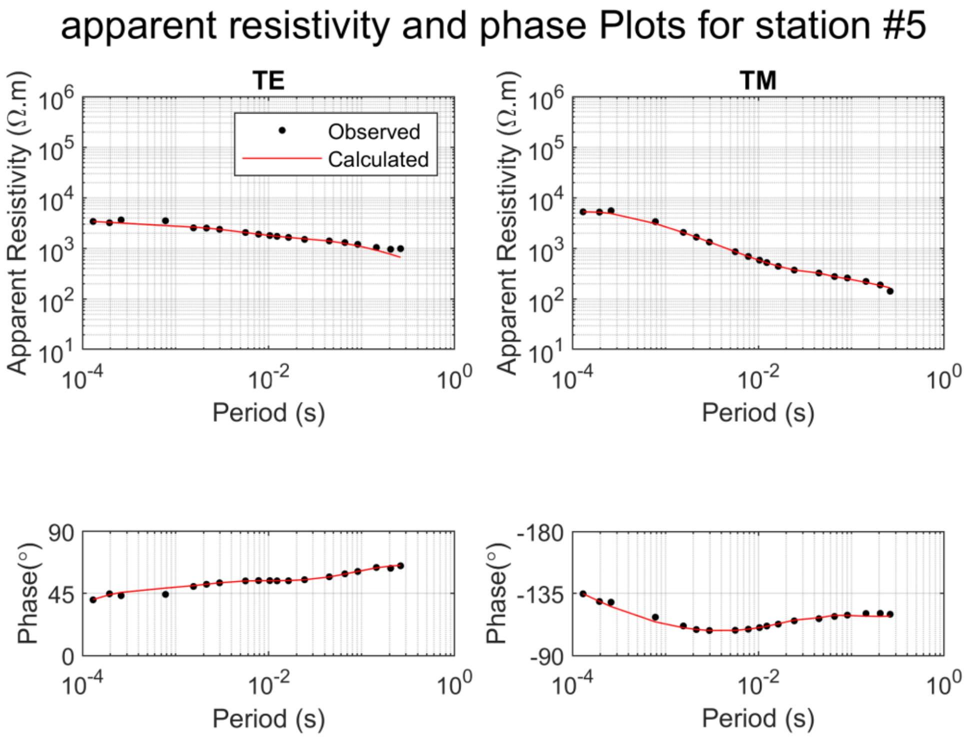
apparent resistivity and phase Plots for station #5
TE
TM
Observed
Calculated
Apparent Resistivity (Ω.m)
Period (s)
Phase(°)

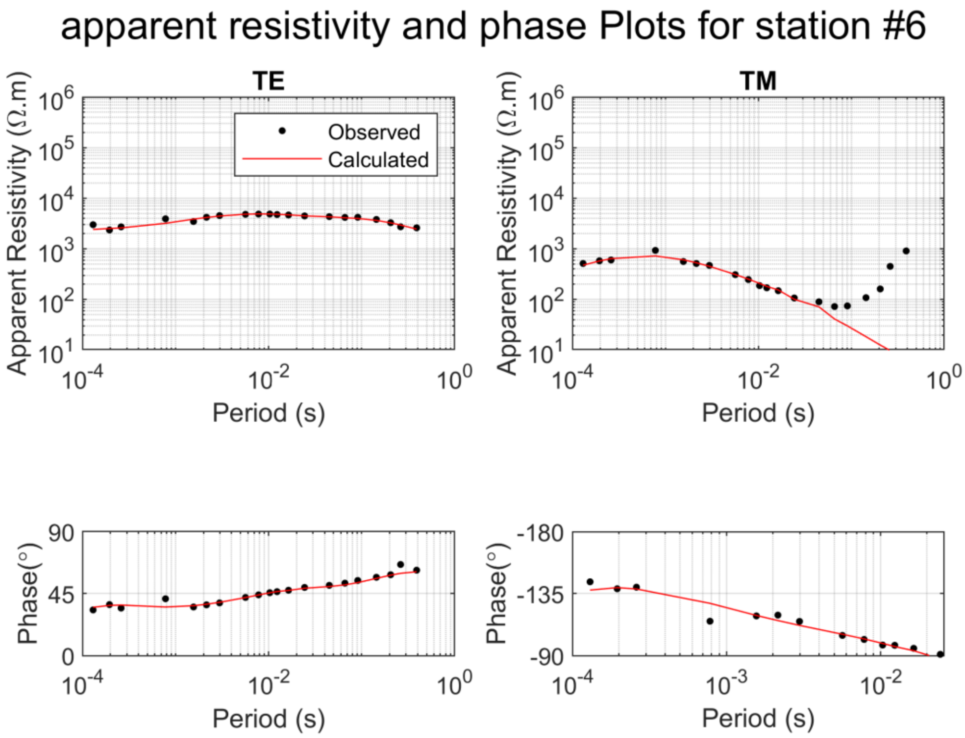
apparent resistivity and phase Plots for station #6
TE
TM
Observed
Calculated
Apparent Resistivity (Ω.m)
Period (s)
Phase(°)

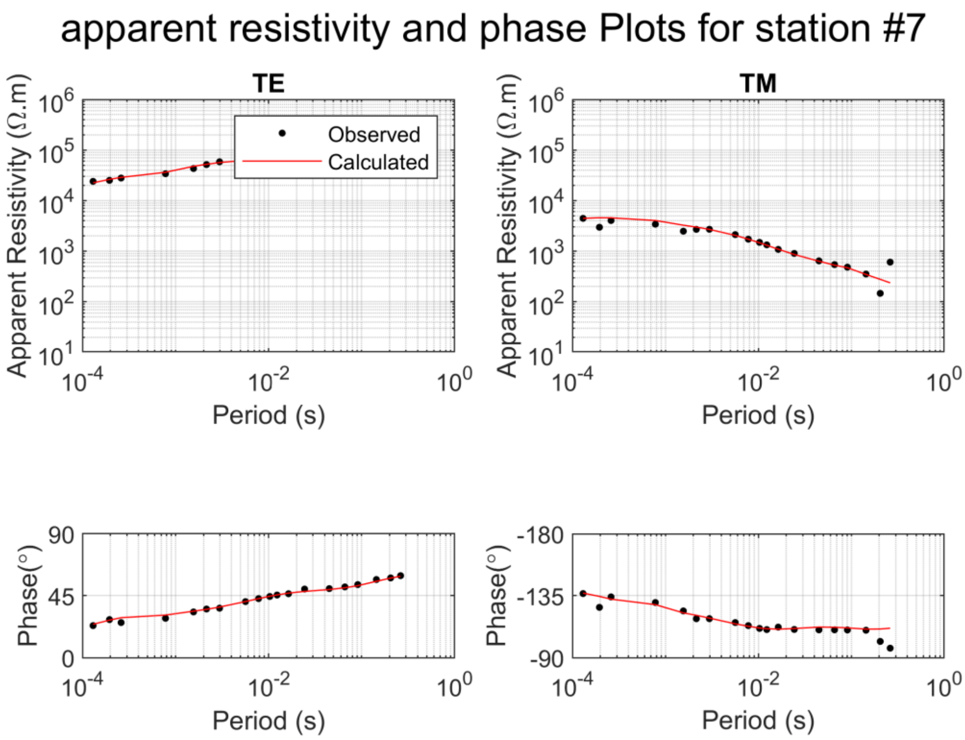
apparent resistivity and phase Plots for station #7
TE
TM
Apparent Resistivity (Ω.m)
Observed
Calculated
Period (s)
Phase(°)

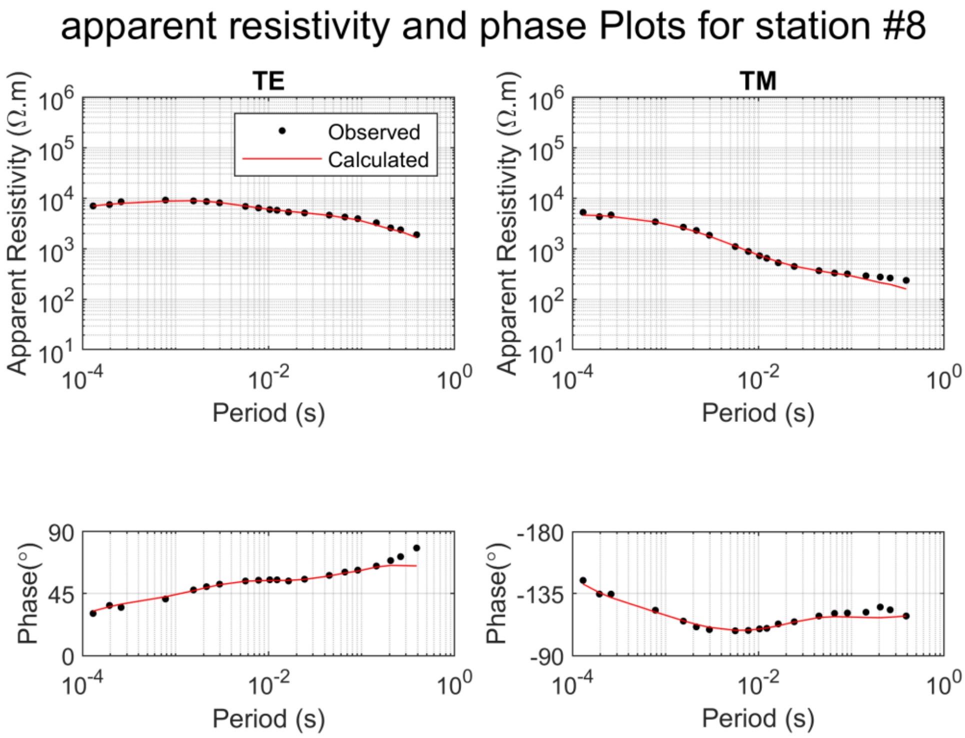
apparent resistivity and phase Plots for station #8
TE
TM
Apparent Resistivity (Ω.m)
Observed
Calculated
Period (s)
Phase(°)

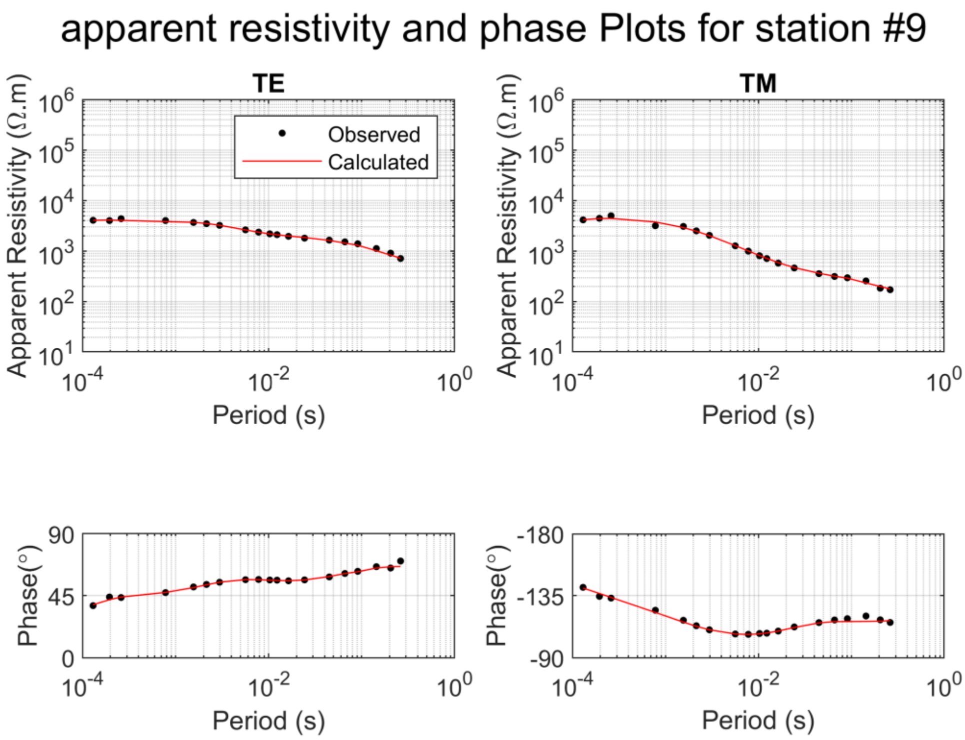
apparent resistivity and phase Plots for station #9
TE
TM
Observed
Calculated
Apparent Resistivity (Ω.m)
Phase(°)
Period (s)

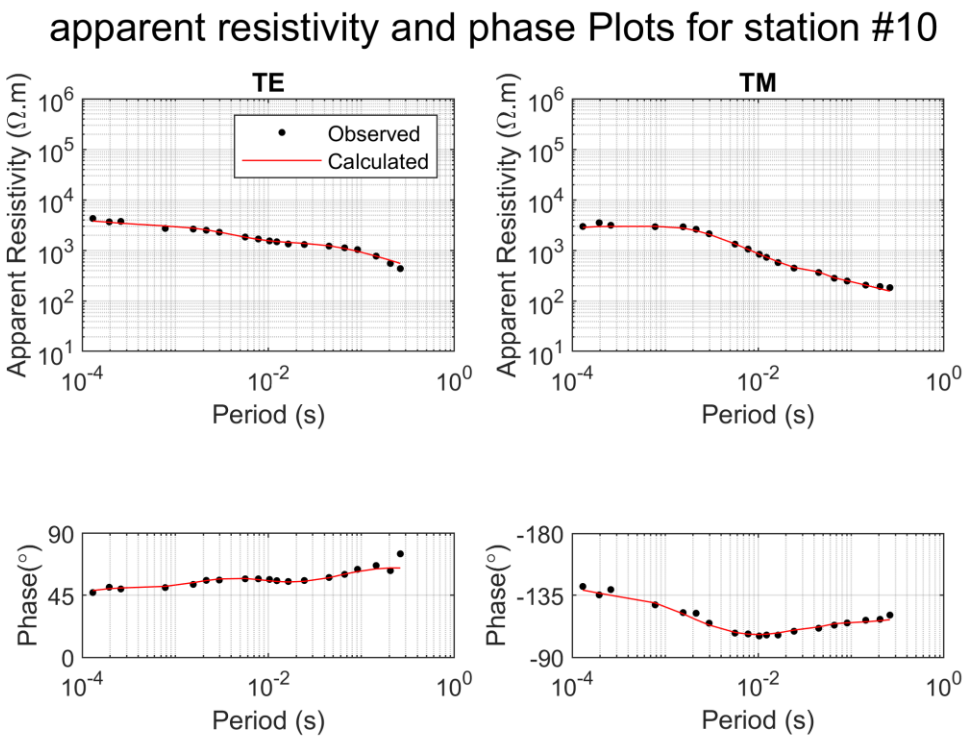
apparent resistivity and phase Plots for station #10
TE
TM
Observed
Calculated
Apparent Resistivity (Ω.m)
Phase(°)
Period (s)

apparent resistivity and phase Plots for station #11

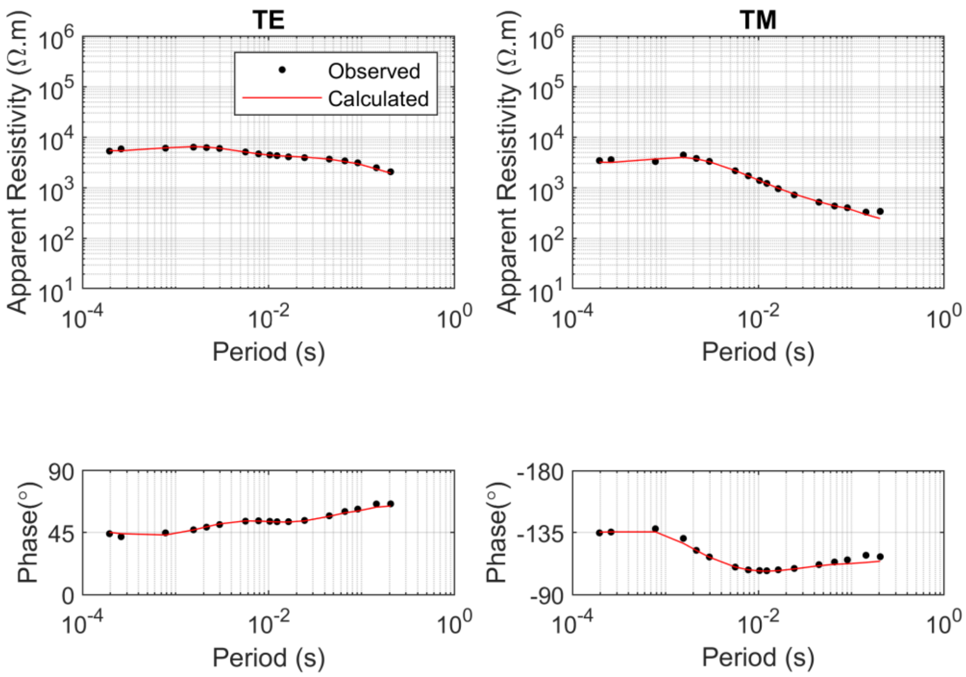

apparent resistivity and phase Plots for station #12

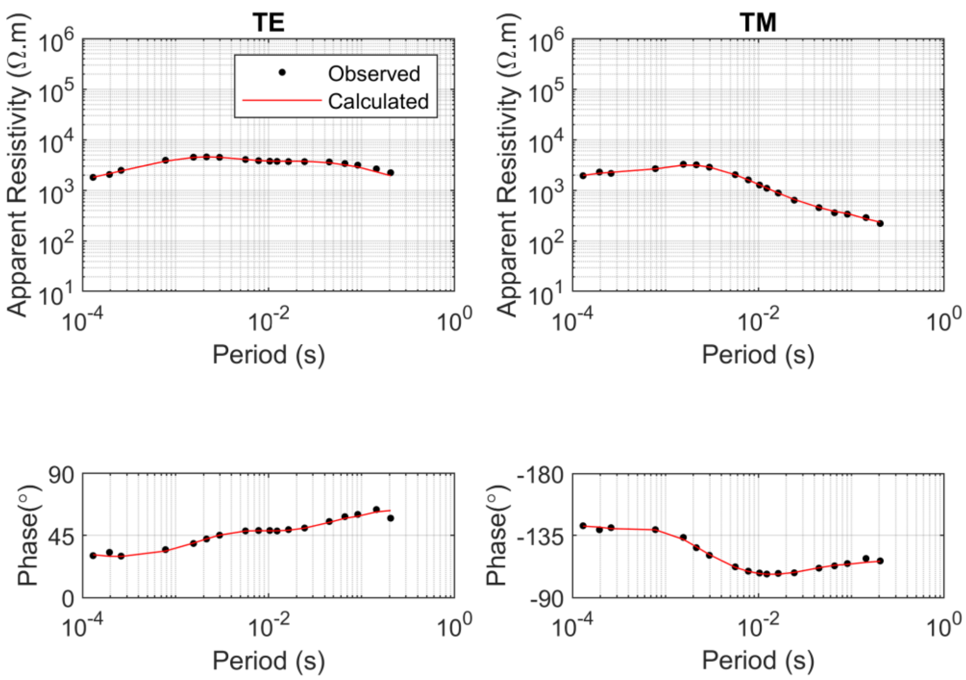

apparent resistivity and phase Plots for station #13

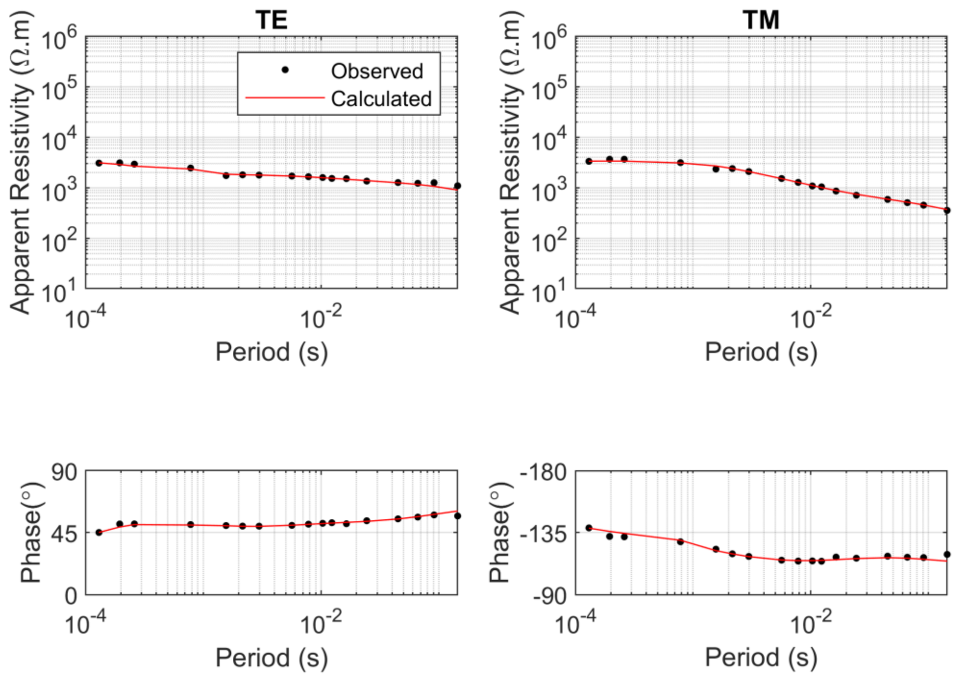

apparent resistivity and phase Plots for station #14

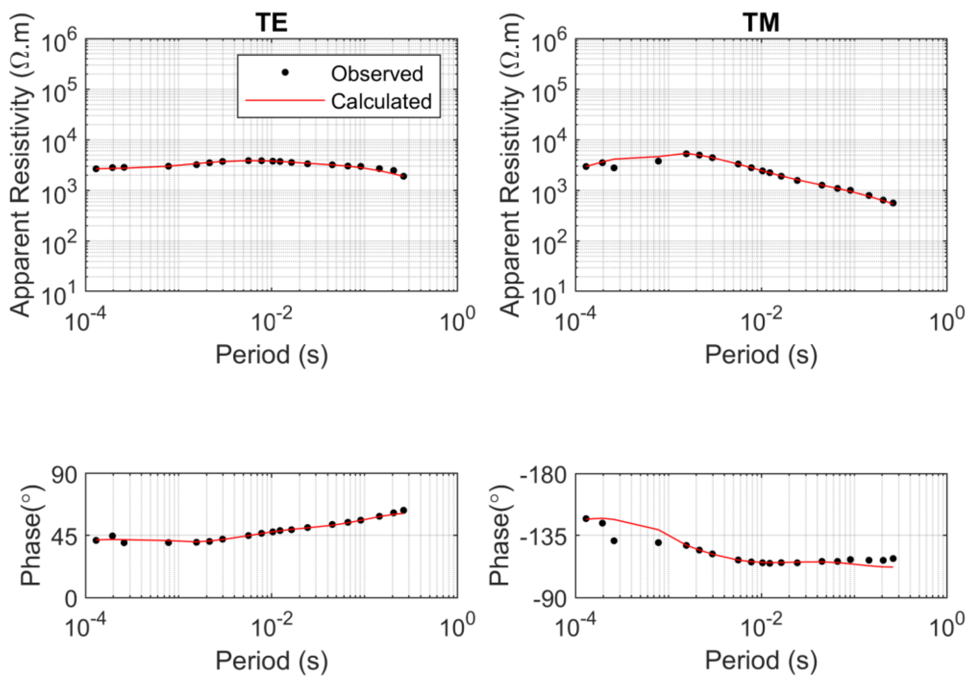

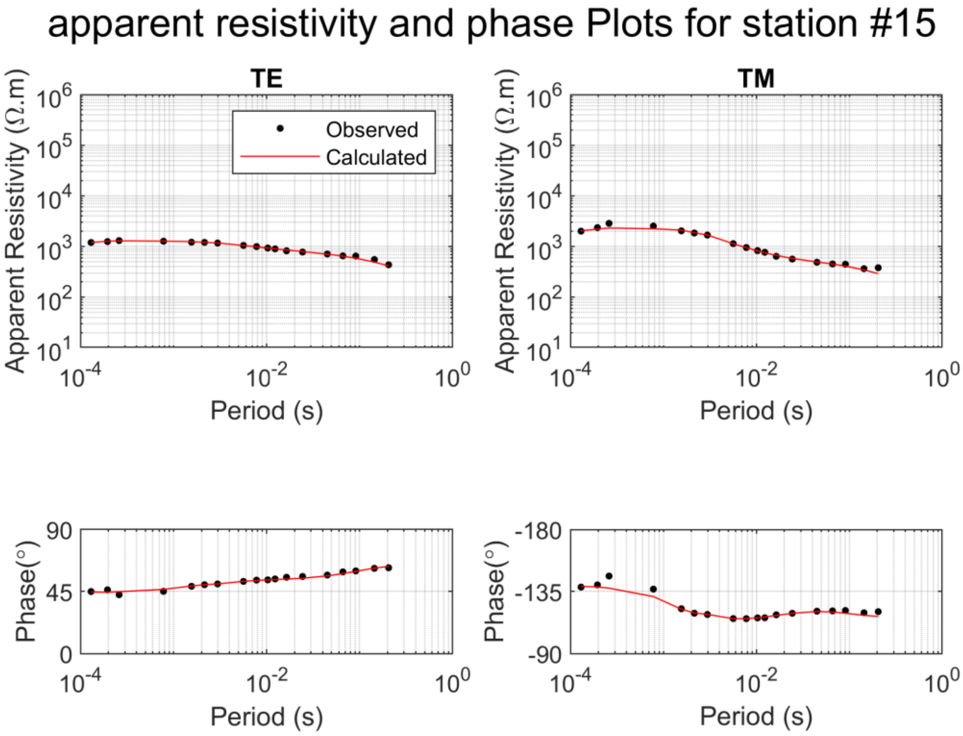
apparent resistivity and phase Plots for station #15
TE
TM
Observed
Calculated
Apparent Resistivity (Ω.m)
Period (s)
Phase(°)

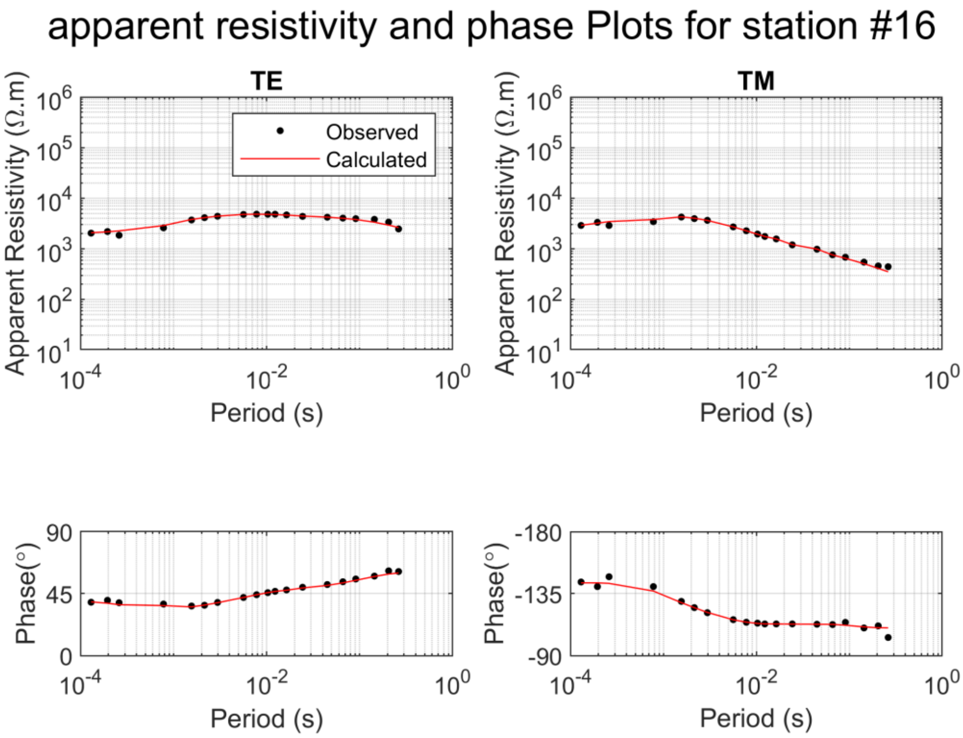
apparent resistivity and phase Plots for station #16
TE
TM
Observed
Calculated
Apparent Resistivity (Ω.m)
Period (s)
Phase(°)

apparent resistivity and phase Plots for station #17

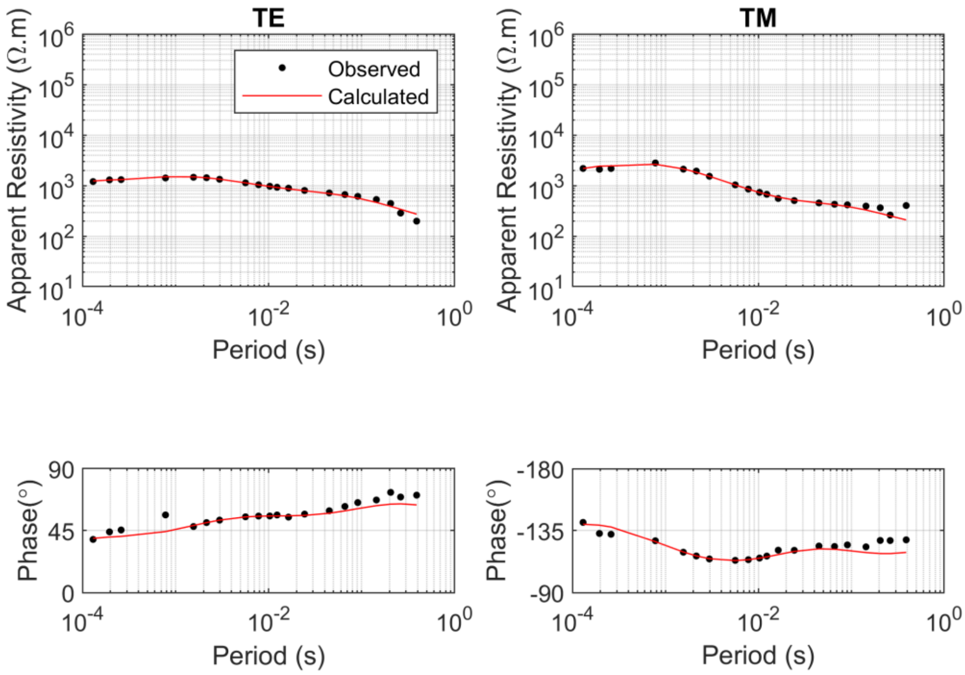

apparent resistivity and phase Plots for station #18

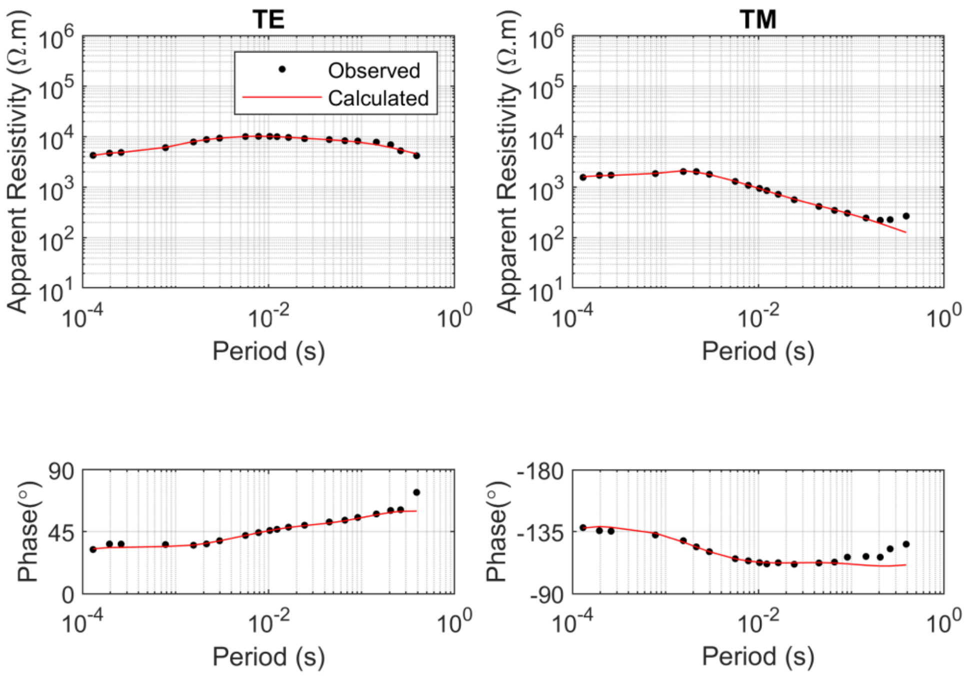

apparent resistivity and phase Plots for station #19

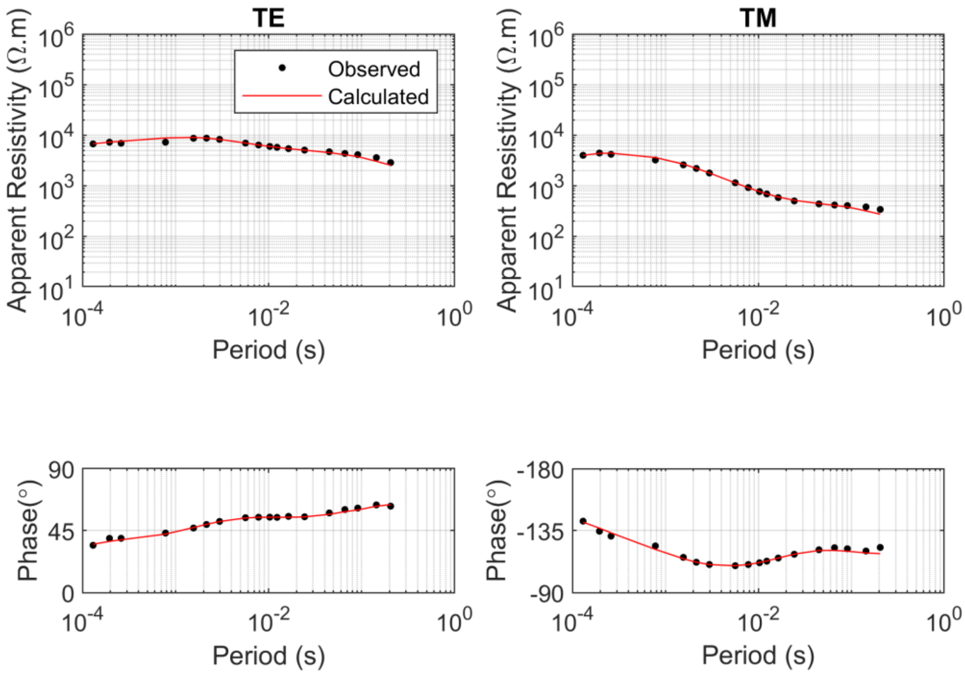

apparent resistivity and phase Plots for station #20

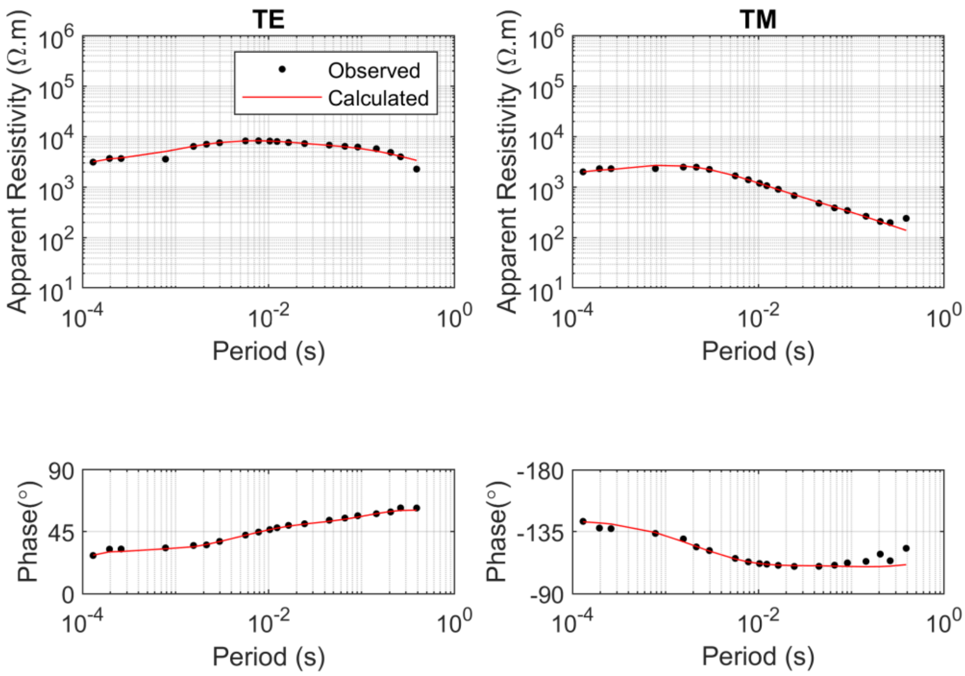

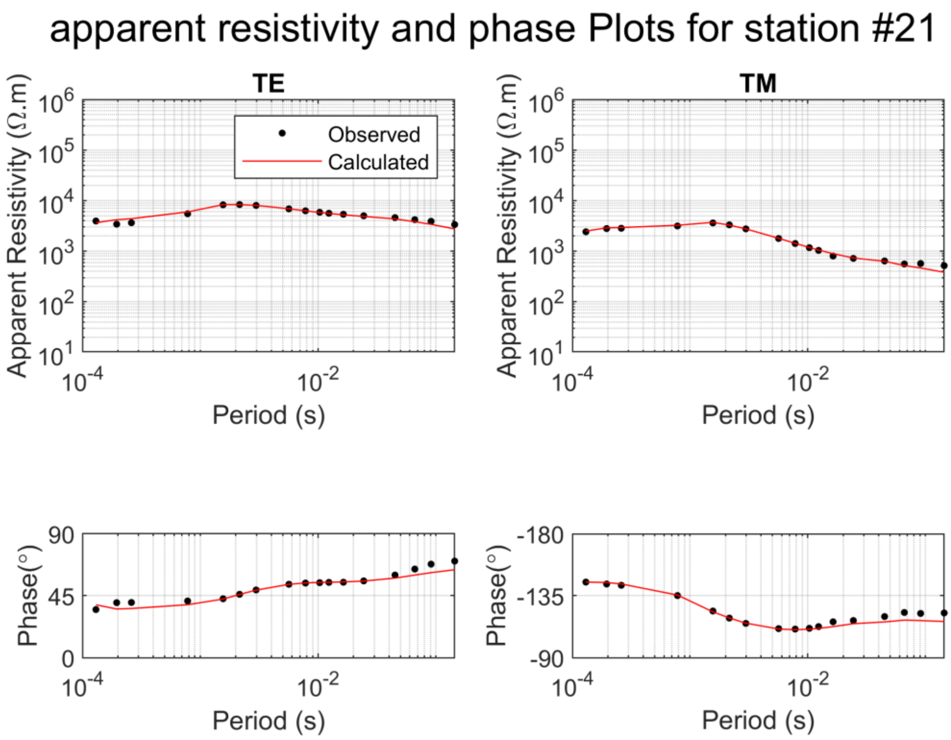
apparent resistivity and phase Plots for station #21
TE
TM
Observed
Calculated
Apparent Resistivity (Ω.m)
Period (s)
Phase(°)
10^{6}
10^{5}
10^{4}
10^{3}
10^{2}
10^{1}
10^{-4}
10^{-2}
90
45
0
-180
-135
-90

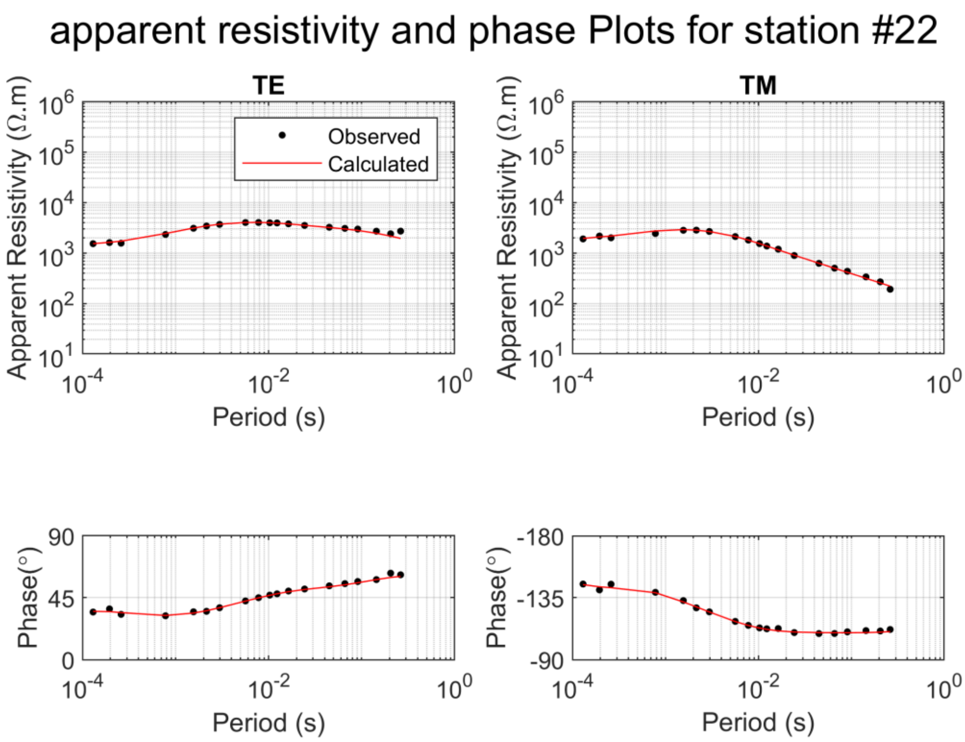
apparent resistivity and phase Plots for station #22
TE
TM
Observed
Calculated
Apparent Resistivity (Ω.m)
Period (s)
Phase(°)
10^{6}
10^{5}
10^{4}
10^{3}
10^{2}
10^{1}
10^{-4}
10^{-2}
10^{0}
90
45
0
-180
-135
-90

apparent resistivity and phase Plots for station #23

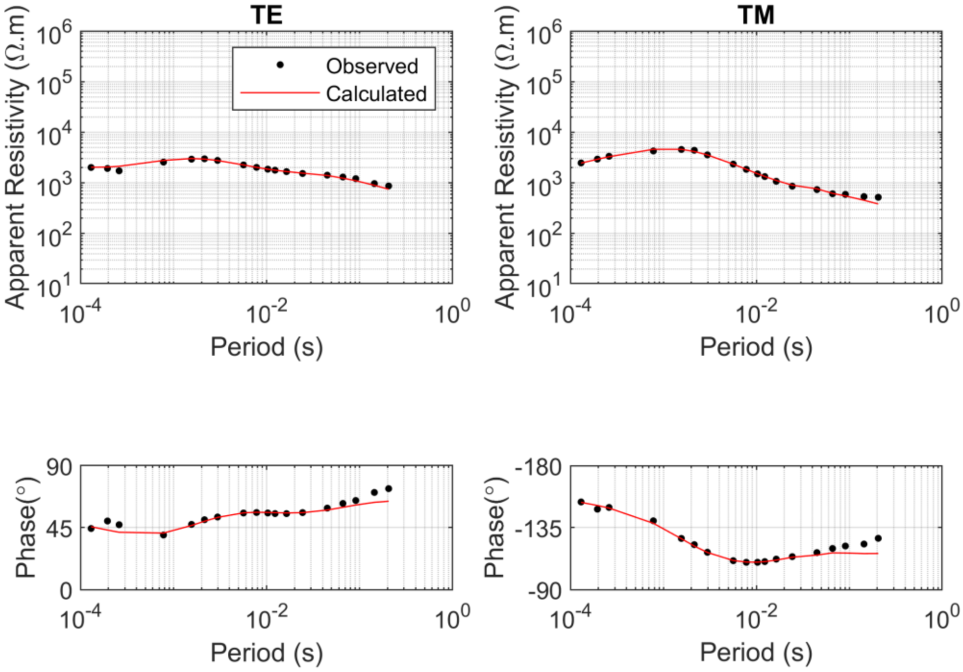

apparent resistivity and phase Plots for station #24

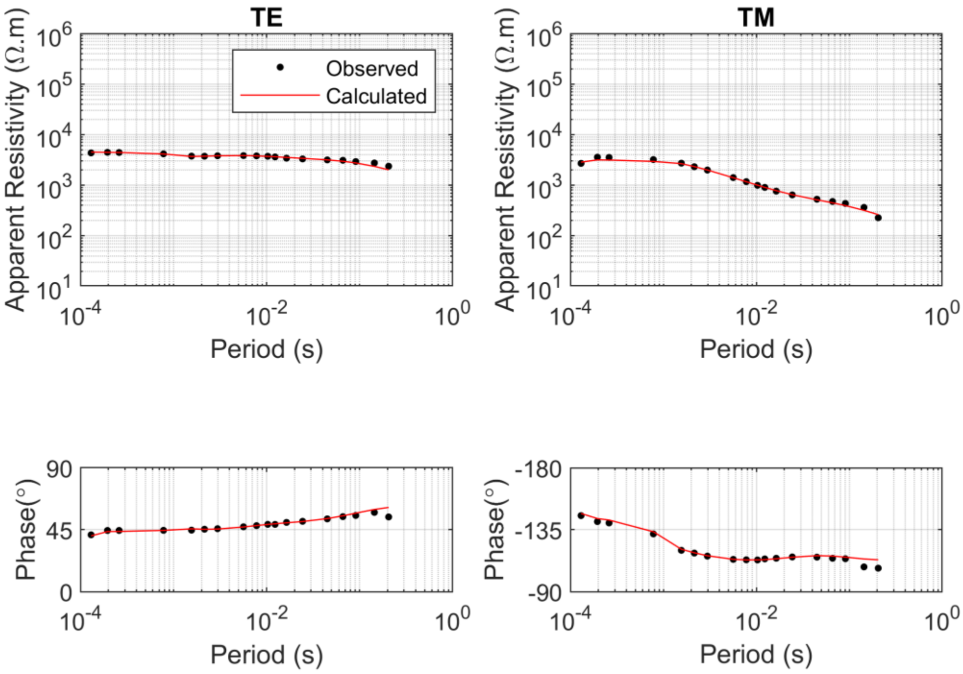

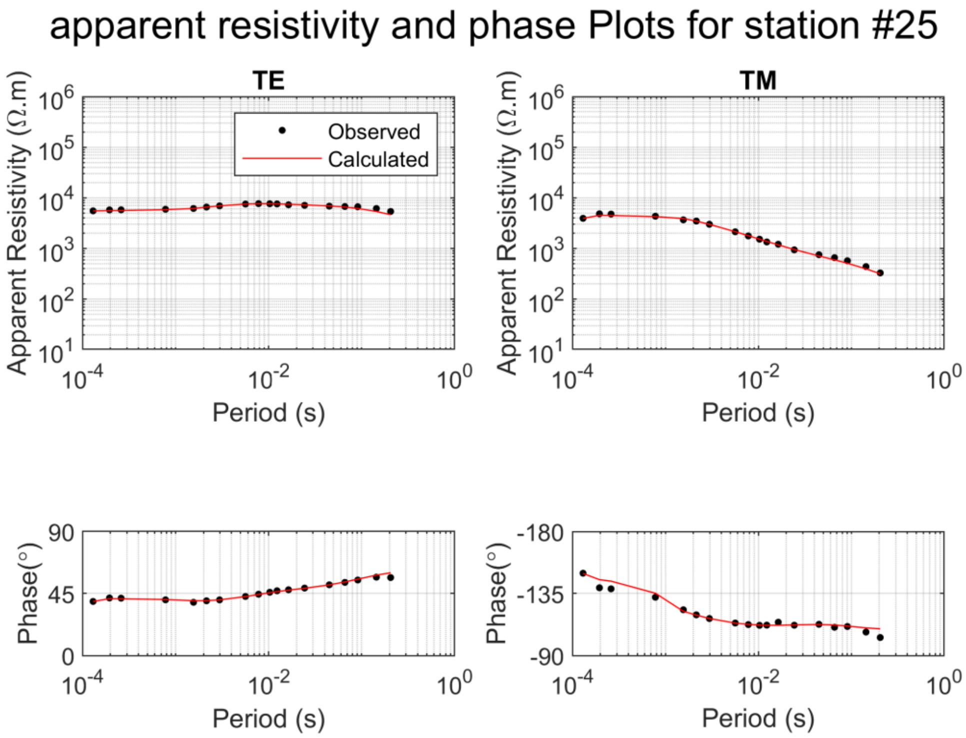
apparent resistivity and phase Plots for station #25
TE
TM
Observed
Calculated
Apparent Resistivity (Ω.m)
Phase(°)
Period (s)

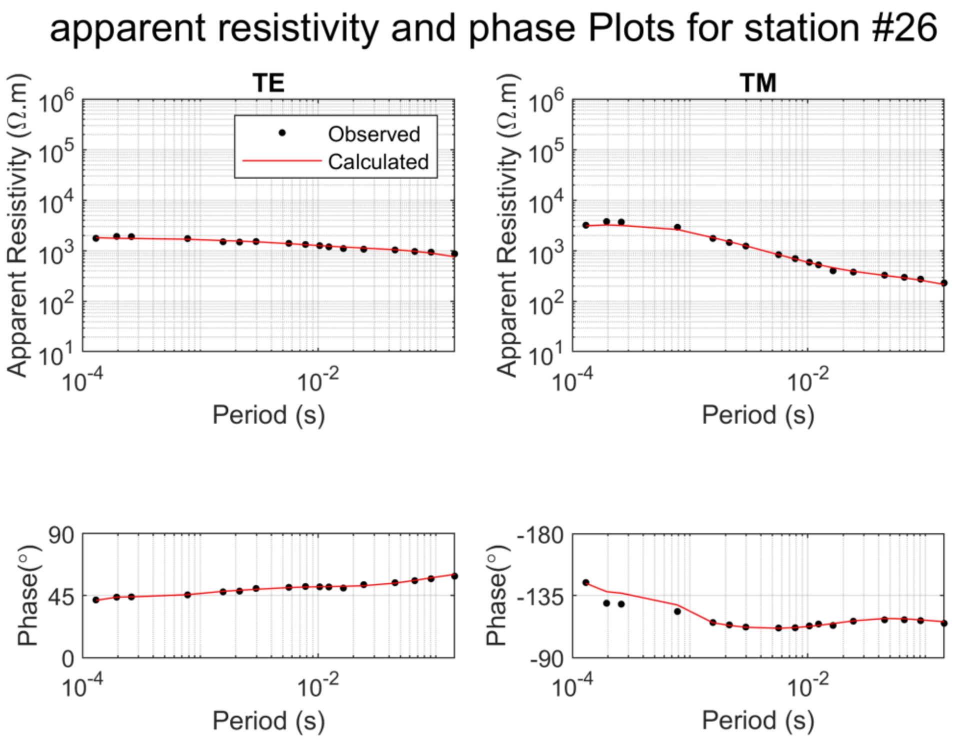
apparent resistivity and phase Plots for station #26
TE
TM
Observed
Calculated
Apparent Resistivity (Ω.m)
Phase(°)
Period (s)

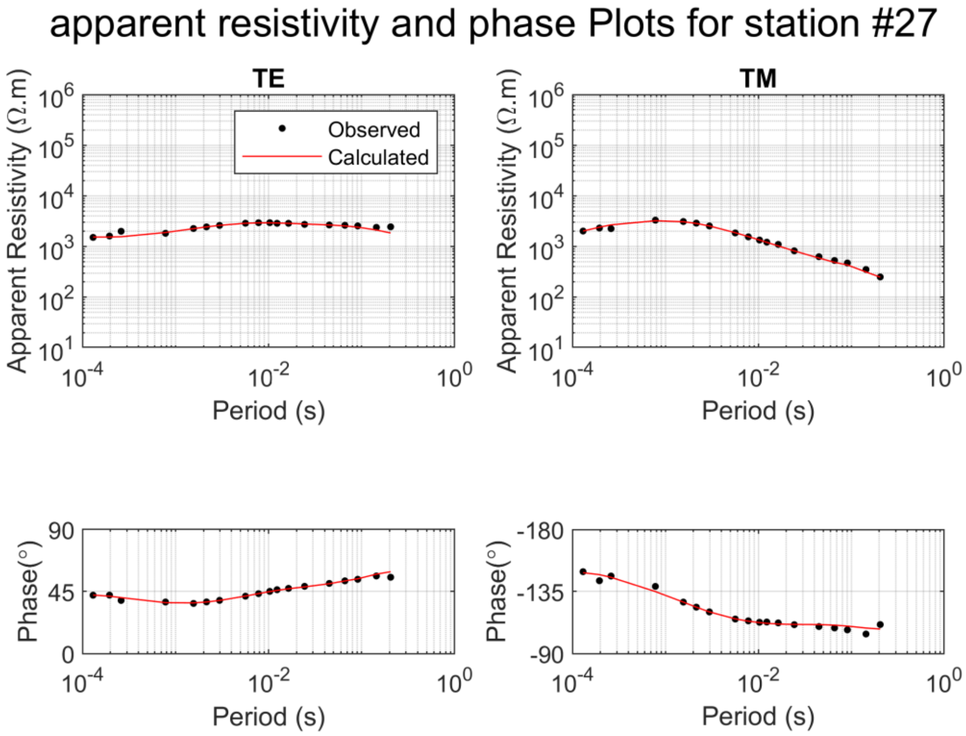
apparent resistivity and phase Plots for station #27
TE
TM
Observed
Calculated
Apparent Resistivity (Ω.m)
Period (s)
Phase(°)

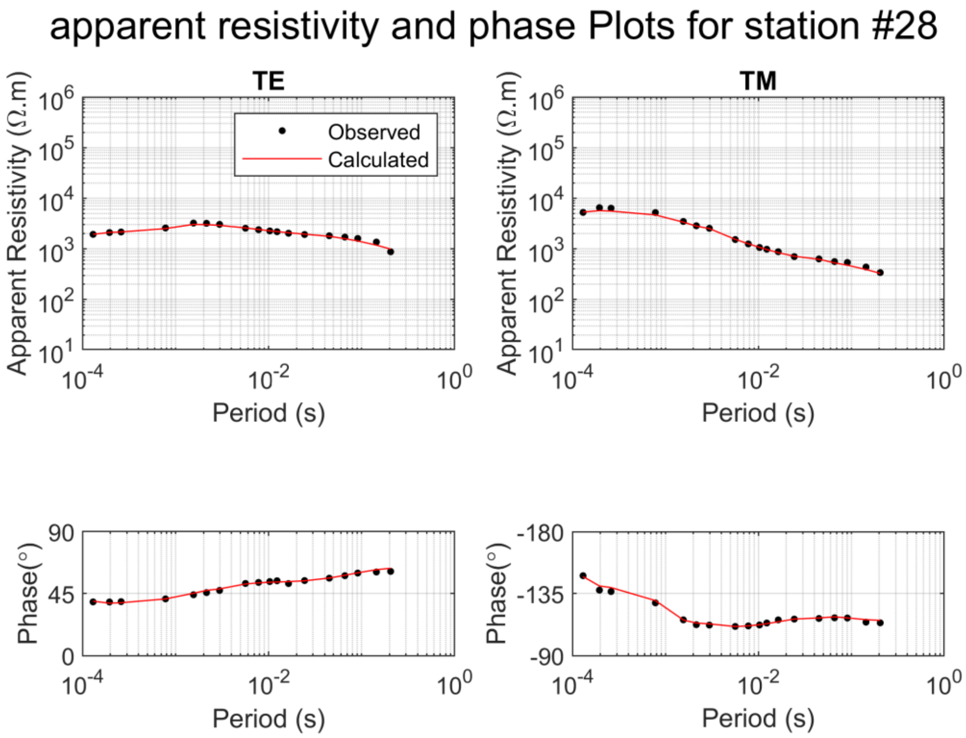
apparent resistivity and phase Plots for station #28
TE
TM
Observed
Calculated
Apparent Resistivity (Ω.m)
Period (s)
Phase(°)

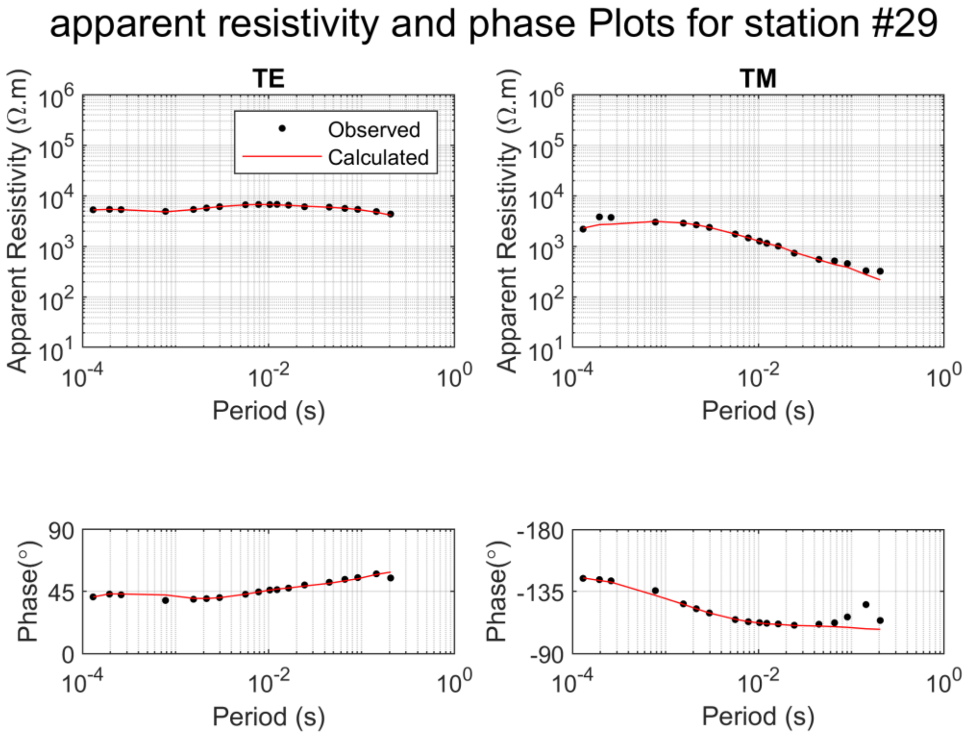
apparent resistivity and phase Plots for station #29
TE
TM
Observed
Calculated
Apparent Resistivity (Ω.m)
Phase(°)
Period (s)

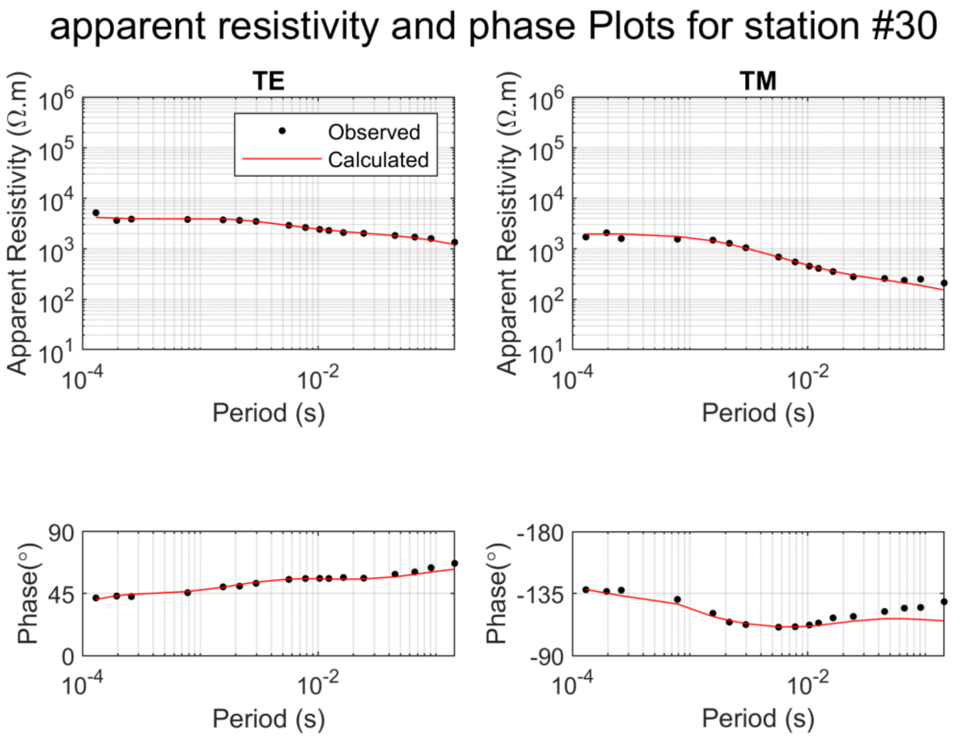
apparent resistivity and phase Plots for station #30
TE
TM
Observed
Calculated
Apparent Resistivity (Ω.m)
Phase(°)
Period (s)

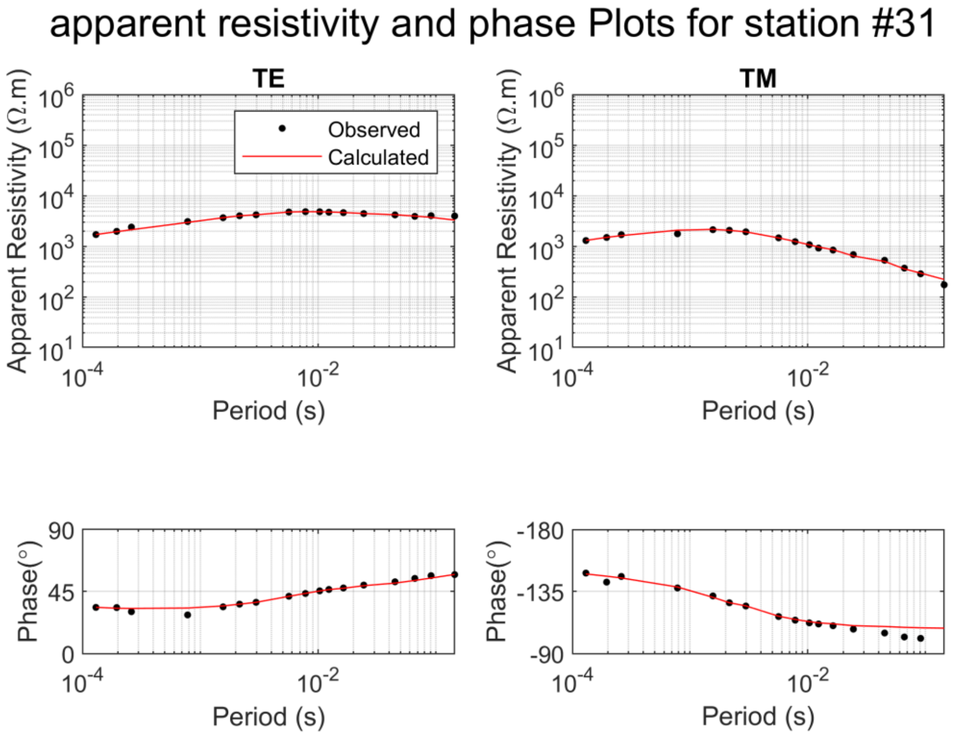
apparent resistivity and phase Plots for station #31
TE
TM
Observed
Calculated
Apparent Resistivity (Ω.m)
Period (s)
Phase(°)

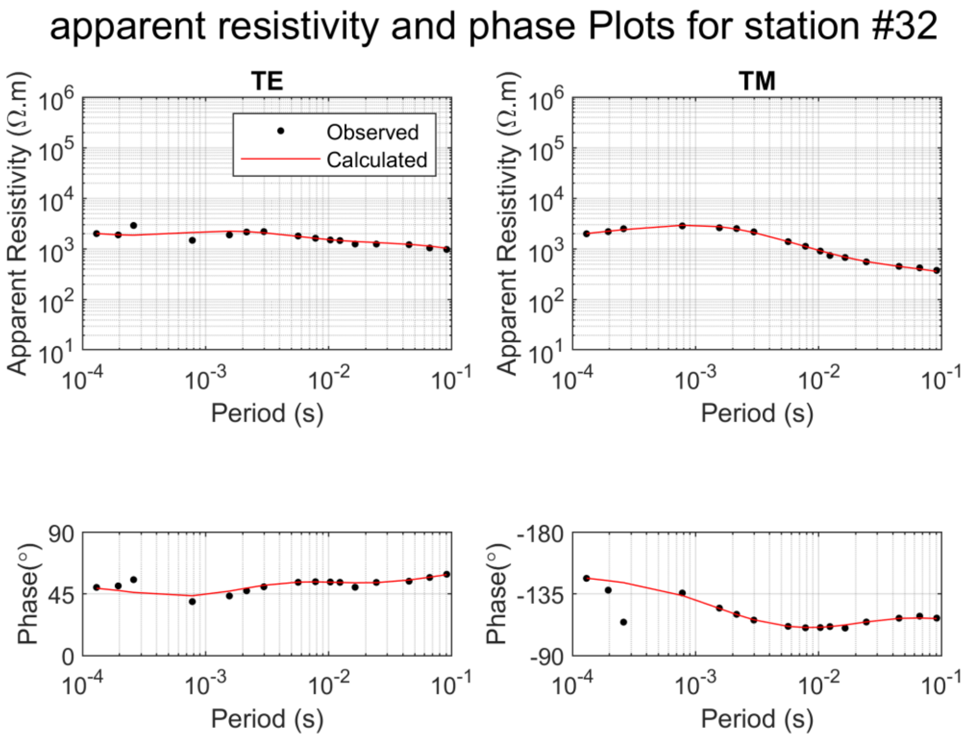
apparent resistivity and phase Plots for station #32
TE
TM
Observed
Calculated
Apparent Resistivity (Ω.m)
Period (s)
Phase(°)

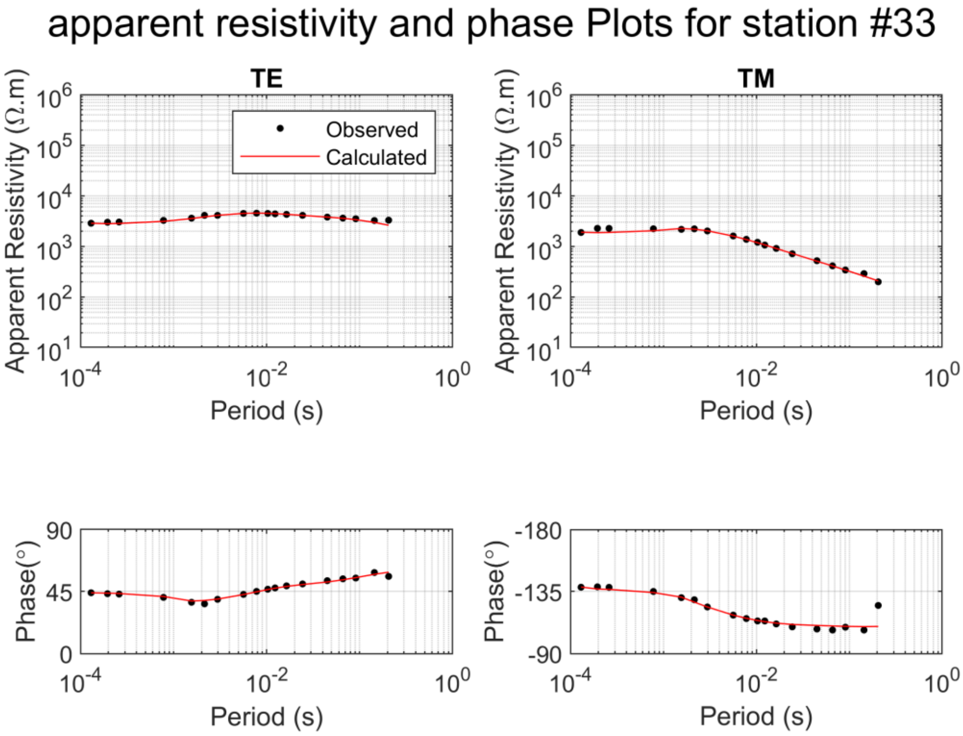
apparent resistivity and phase Plots for station #33
TE
TM
Observed
Calculated
Apparent Resistivity (Ω.m)
Phase(°)
Period (s)

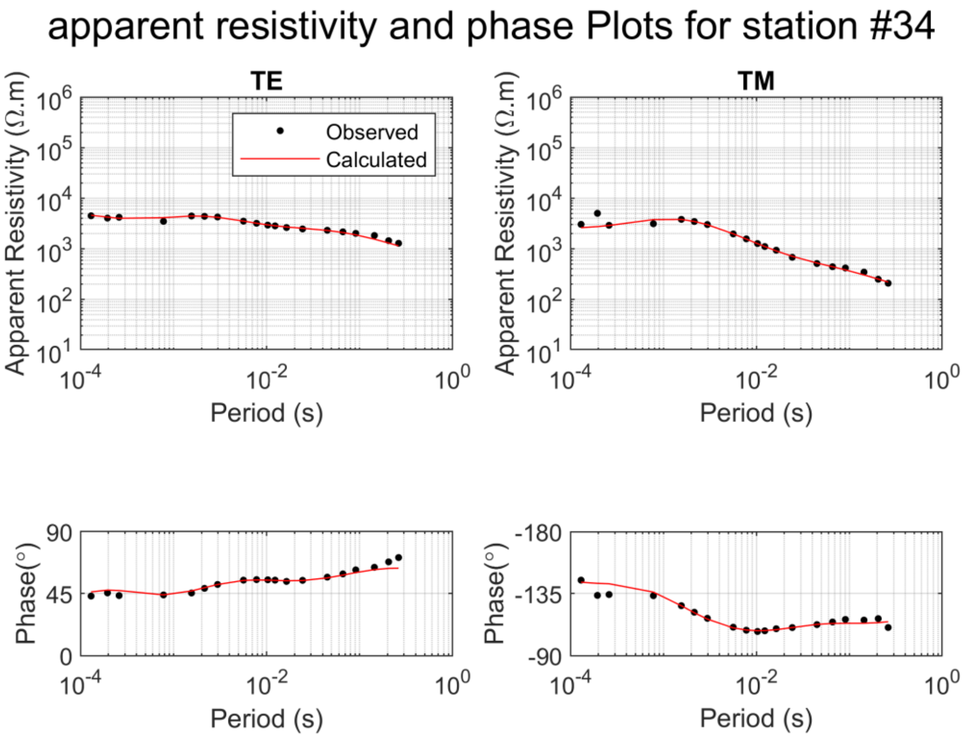
apparent resistivity and phase Plots for station #34
TE
TM
Observed
Calculated
Apparent Resistivity (Ω.m)
Phase(°)
Period (s)

apparent resistivity and phase Plots for station #35

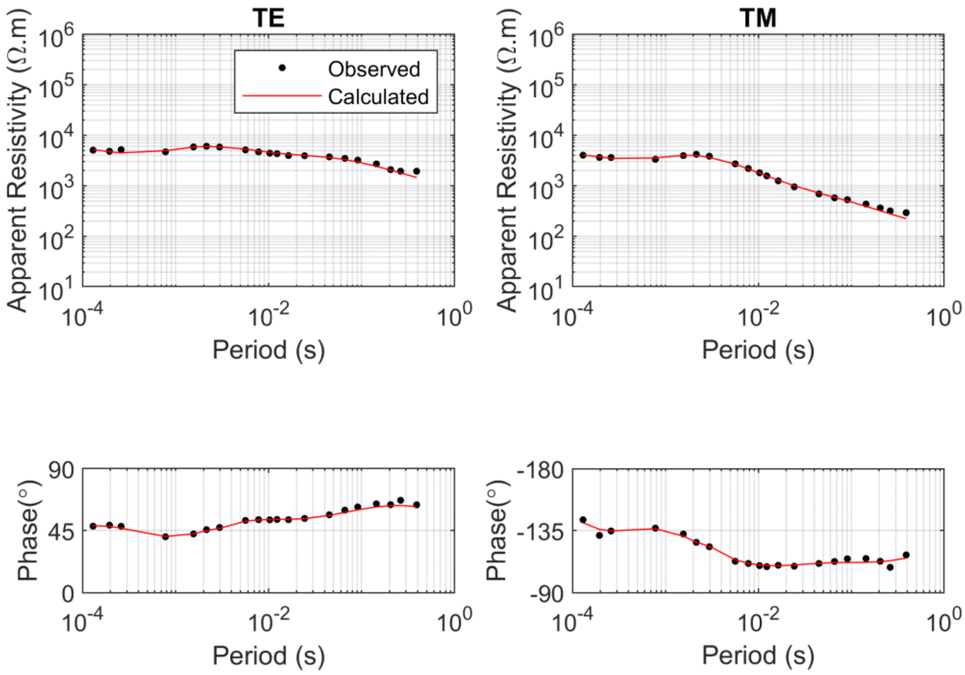

apparent resistivity and phase Plots for station #36

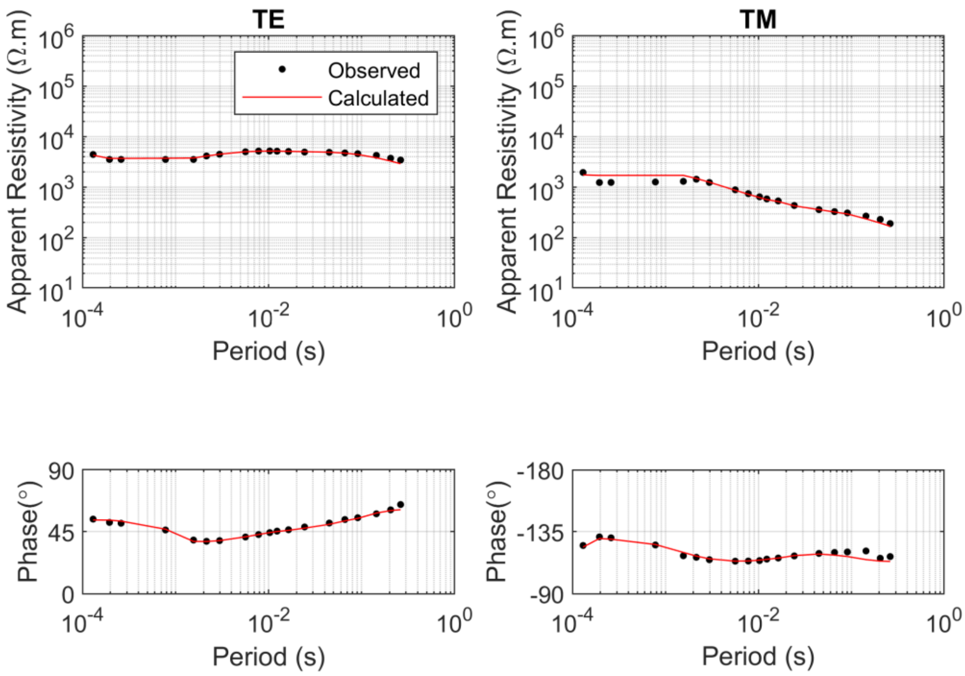

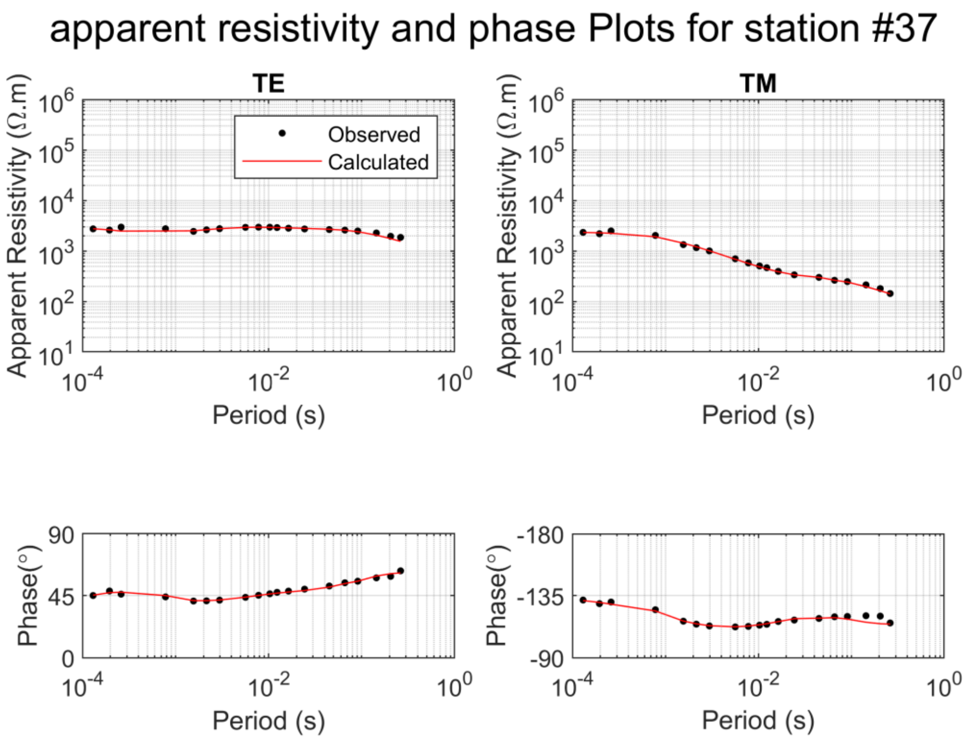
apparent resistivity and phase Plots for station #37
TE
TM
Observed
Calculated
Apparent Resistivity (Ω.m)
Phase(°)
Period (s)

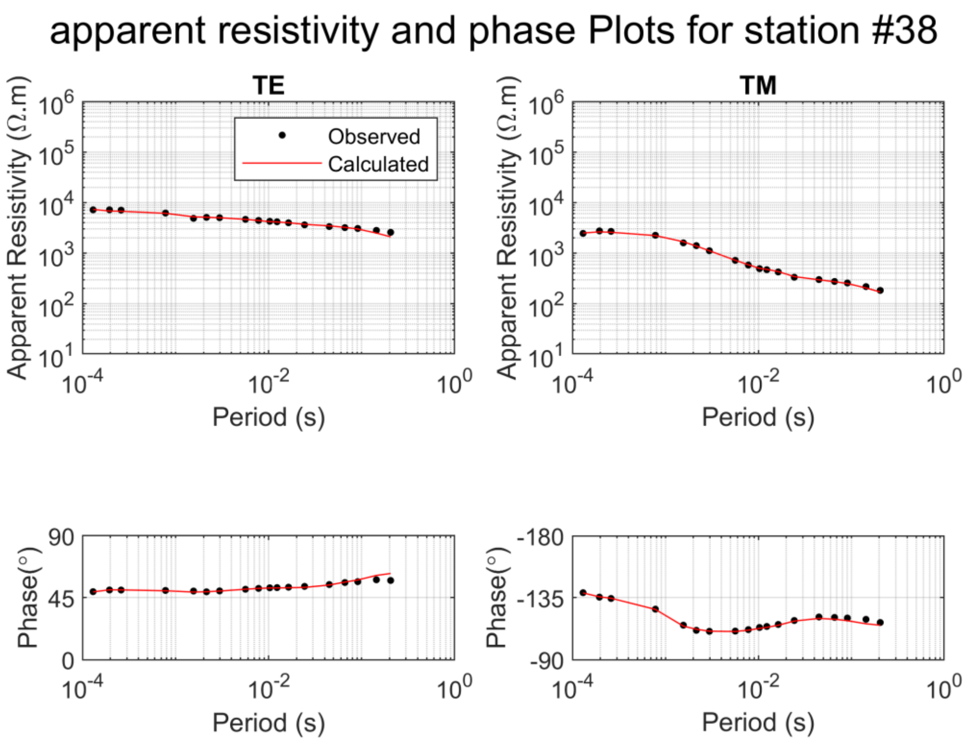
apparent resistivity and phase Plots for station #38
TE
TM
Observed
Calculated
Apparent Resistivity (Ω.m)
Phase(°)
Period (s)

apparent resistivity and phase Plots for station #39

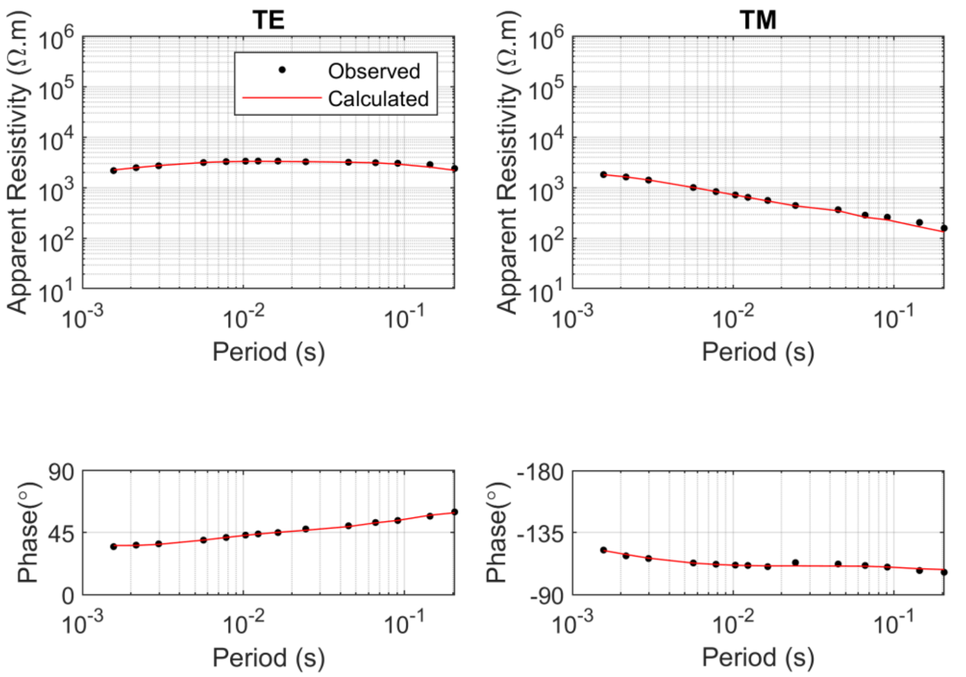

apparent resistivity and phase Plots for station #40

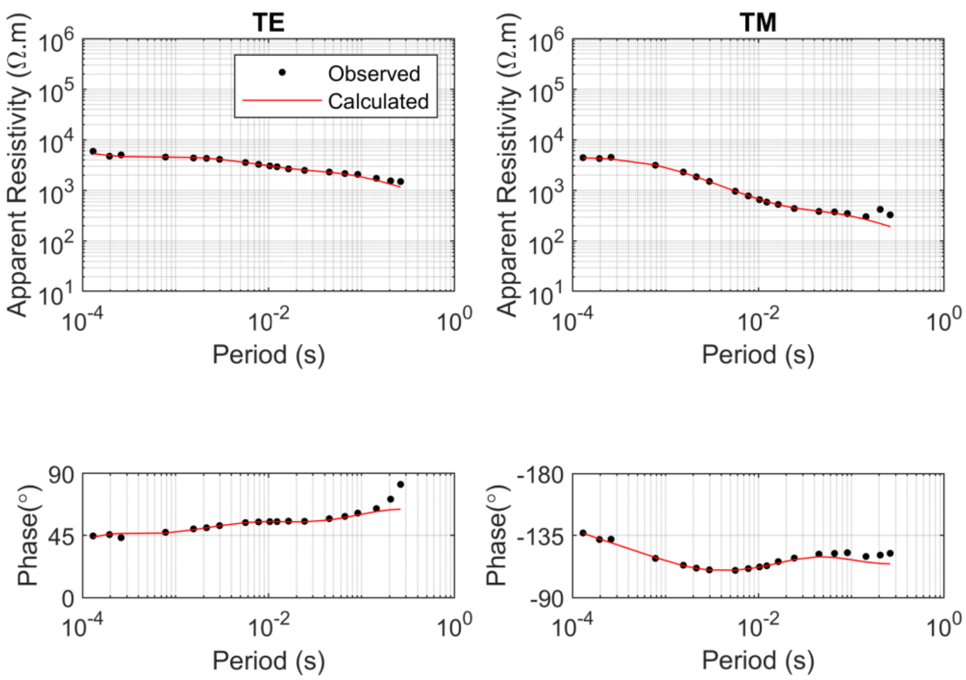

apparent resistivity and phase Plots for station #41

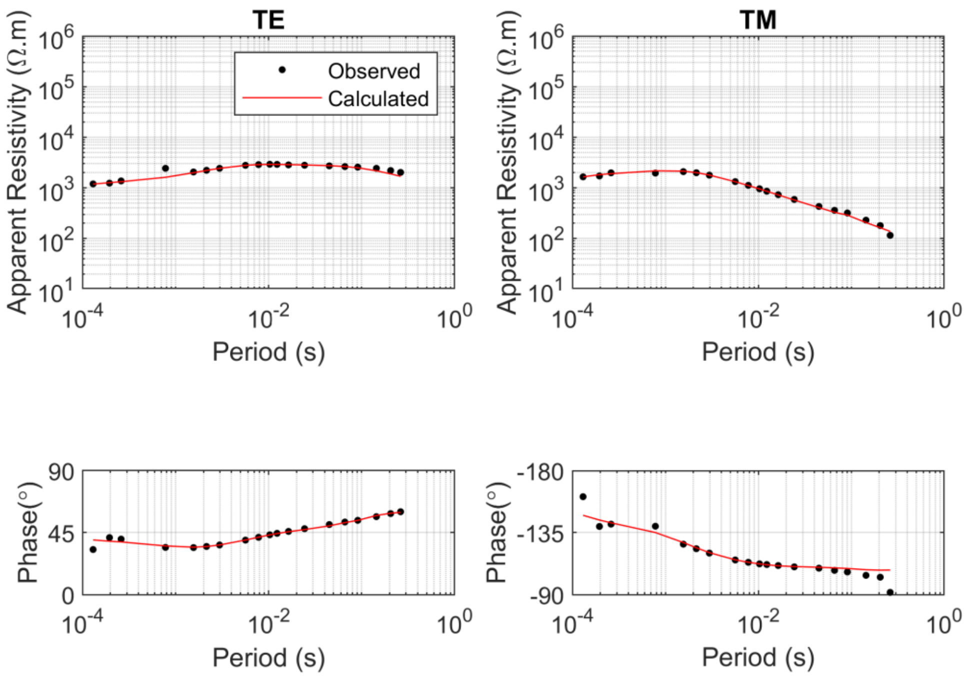

apparent resistivity and phase Plots for station #42

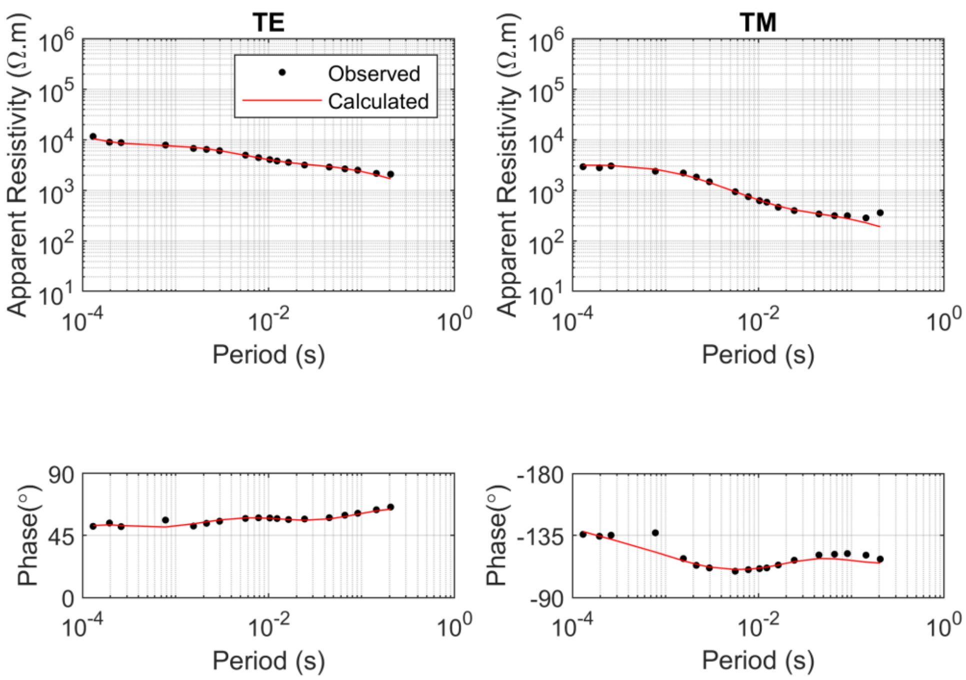

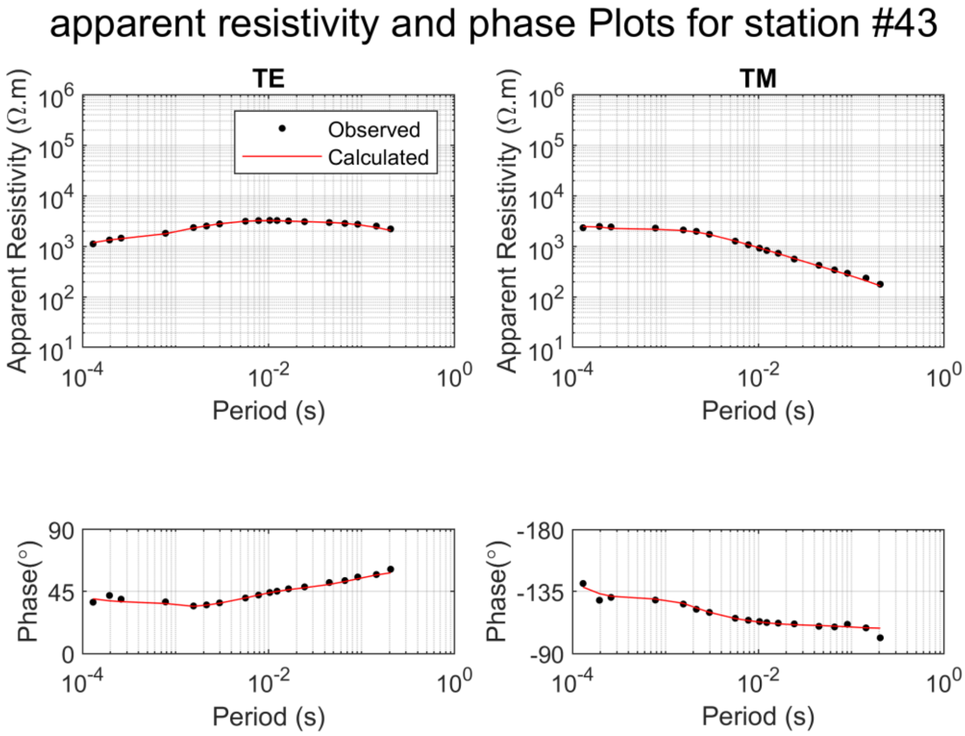
apparent resistivity and phase Plots for station #43
TE
TM
Observed
Calculated
Apparent Resistivity (Ω.m)
Phase(°)
Period (s)

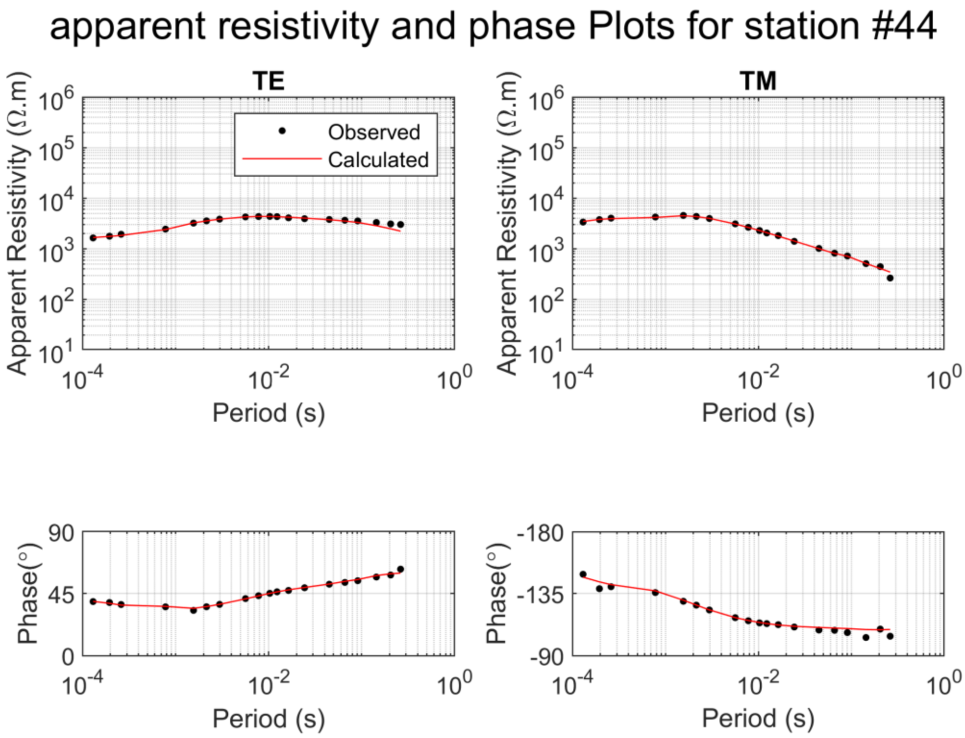
apparent resistivity and phase Plots for station #44
TE
TM
Observed
Calculated
Apparent Resistivity (Ω.m)
Phase(°)
Period (s)

apparent resistivity and phase Plots for station #45

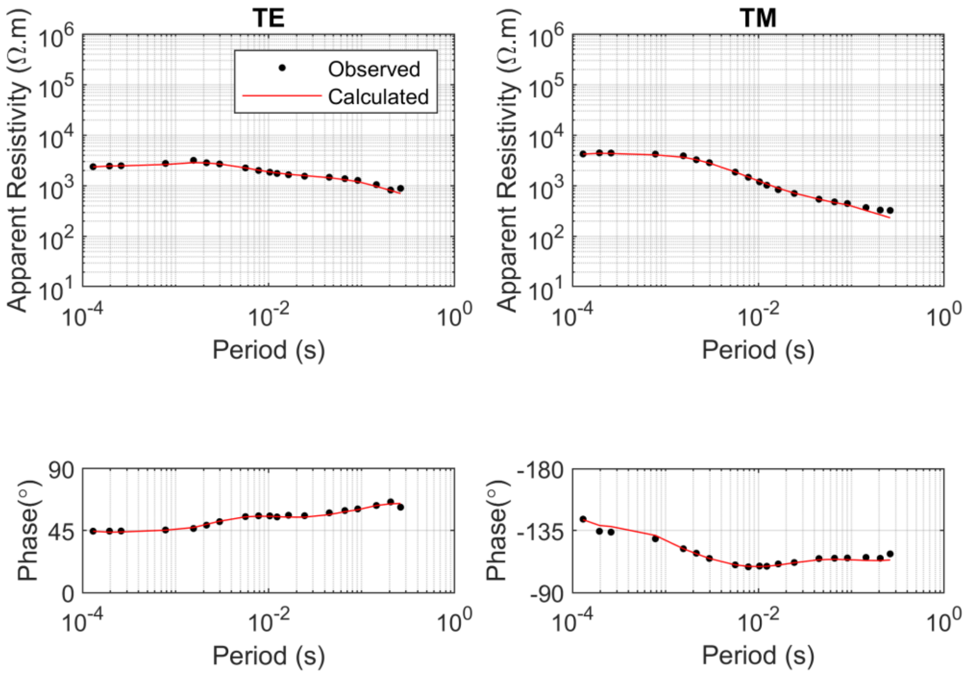

apparent resistivity and phase Plots for station #46

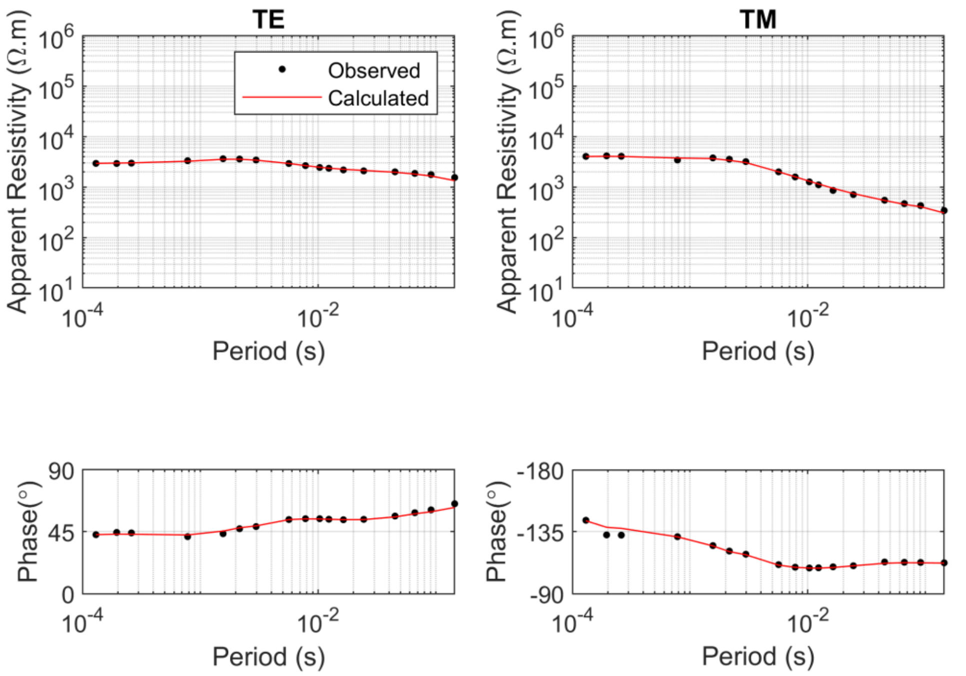

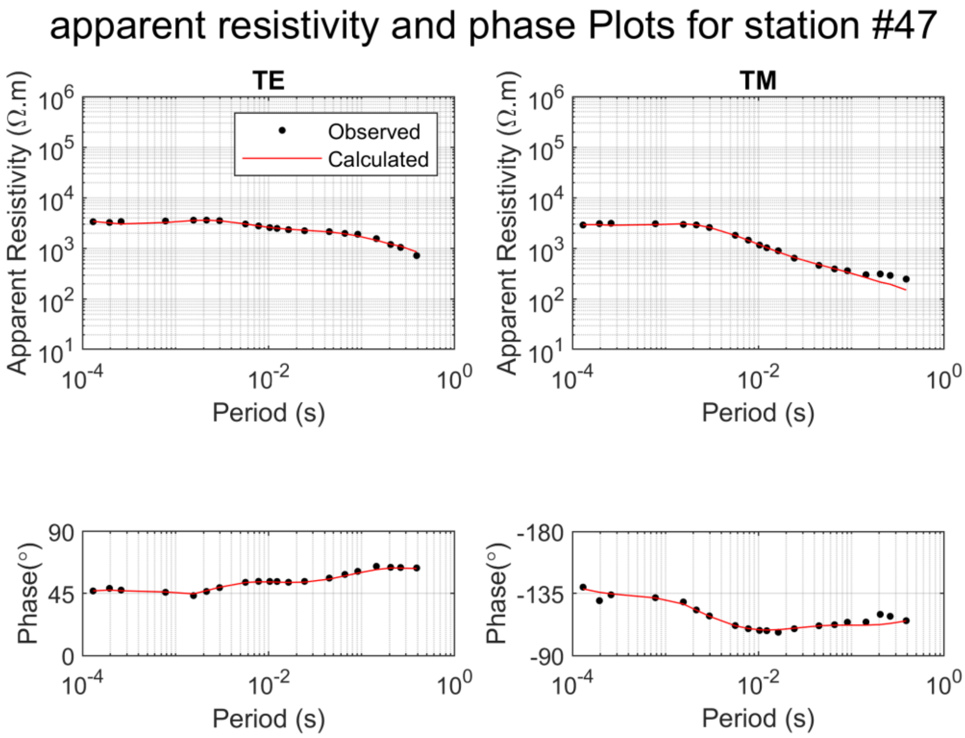
apparent resistivity and phase Plots for station #47
TE
TM
Observed
Calculated
Apparent Resistivity (Ω.m)
Period (s)
Phase(°)
90
45
0
-180
-135
-90

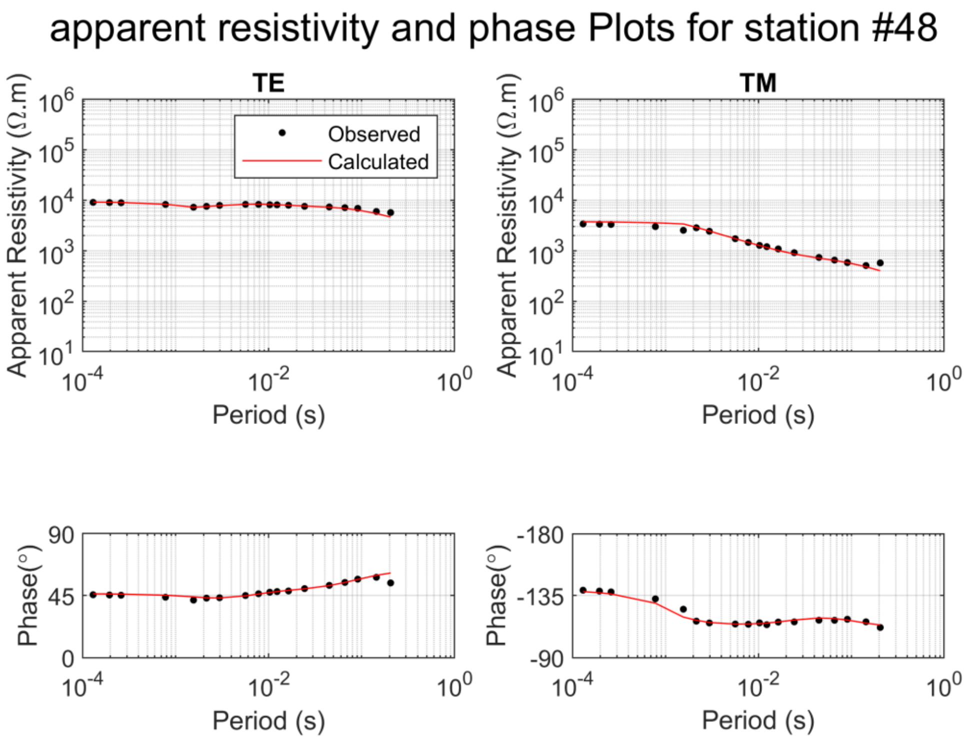
apparent resistivity and phase Plots for station #48
TE
TM
Observed
Calculated
Apparent Resistivity (Ω.m)
Period (s)
Phase(°)
90
45
0
-180
-135
-90

apparent resistivity and phase Plots for station #49

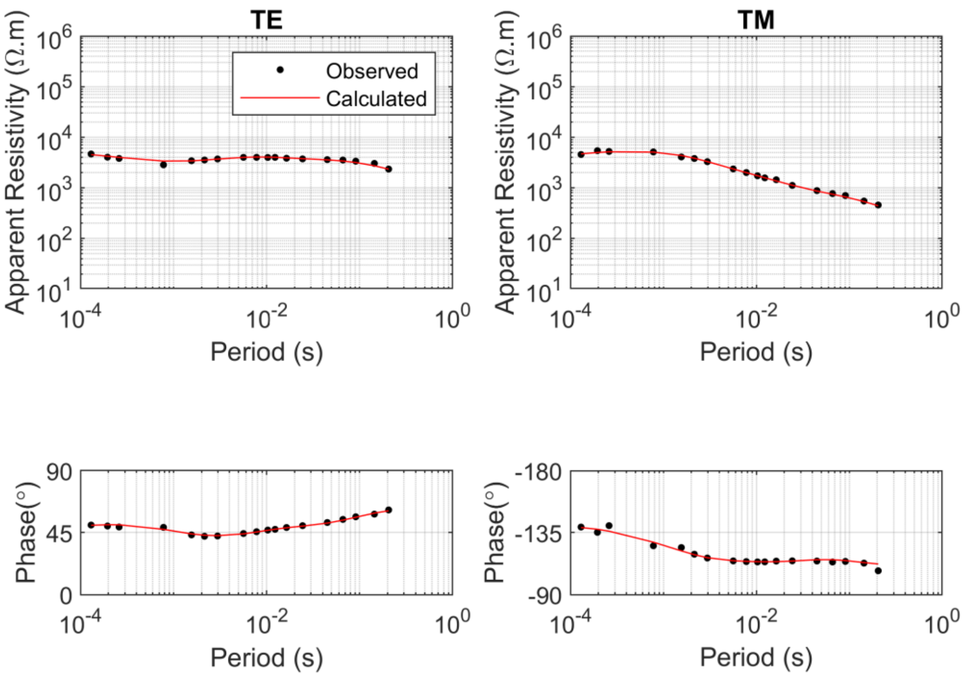

apparent resistivity and phase Plots for station #50

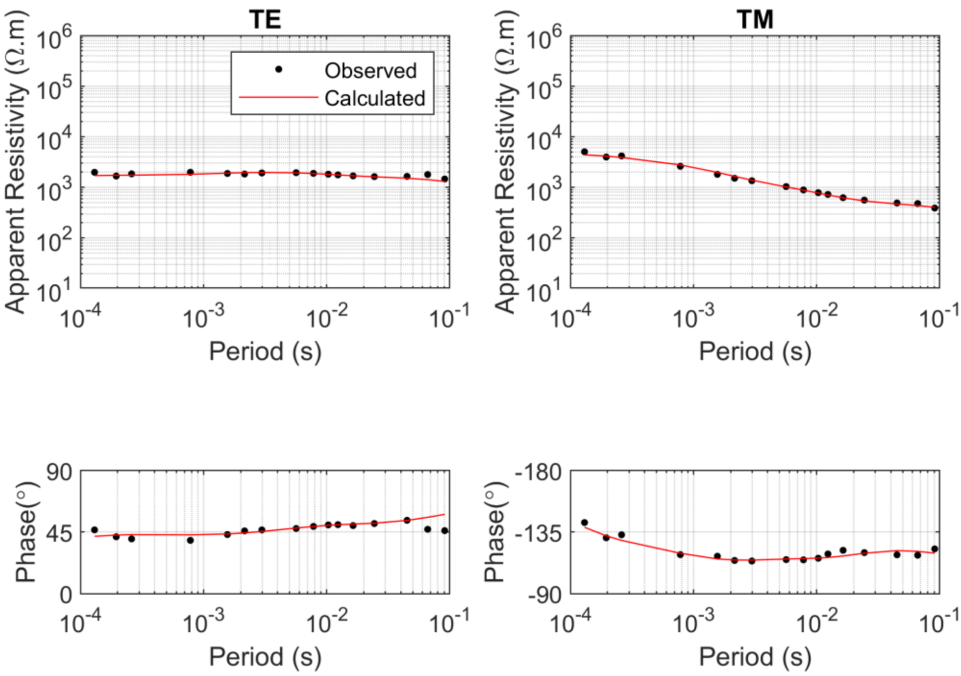

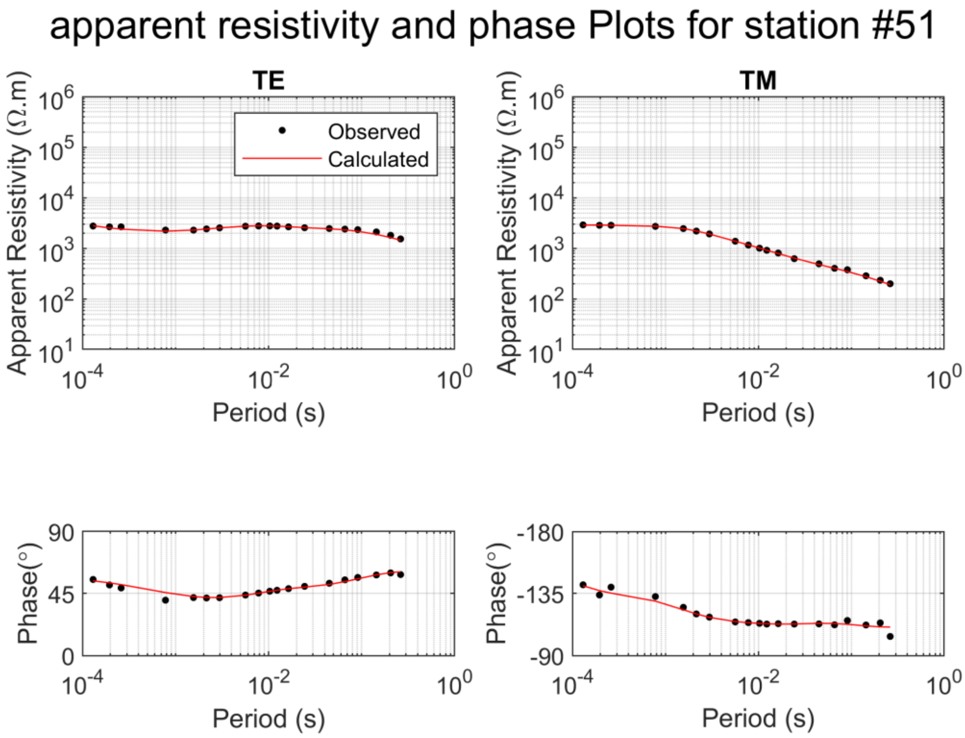
apparent resistivity and phase Plots for station #51
TE
TM
Observed
Calculated
Apparent Resistivity (Ω.m)
Period (s)
Phase(°)

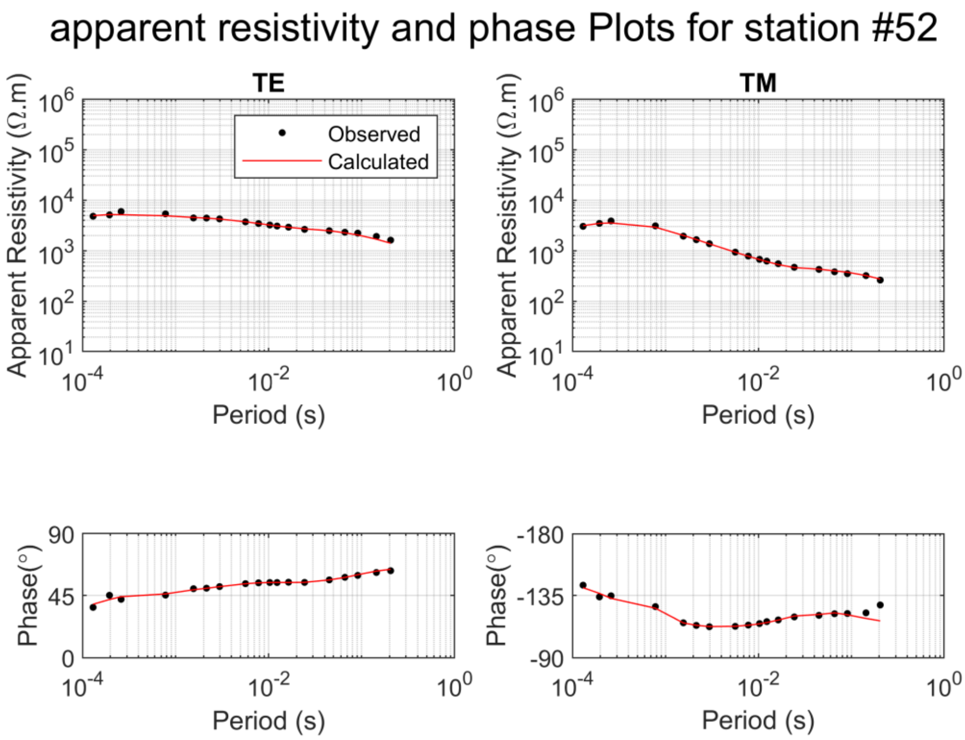
apparent resistivity and phase Plots for station #52
TE
TM
Observed
Calculated
Apparent Resistivity (Ω.m)
Period (s)
Phase(°)

apparent resistivity and phase Plots for station #53

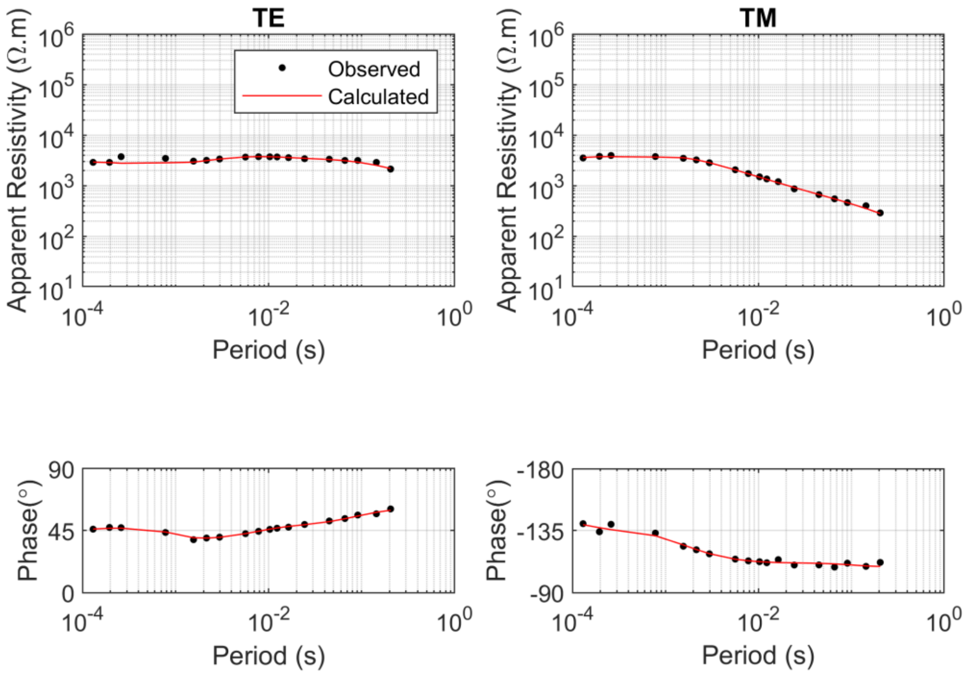

apparent resistivity and phase Plots for station #54

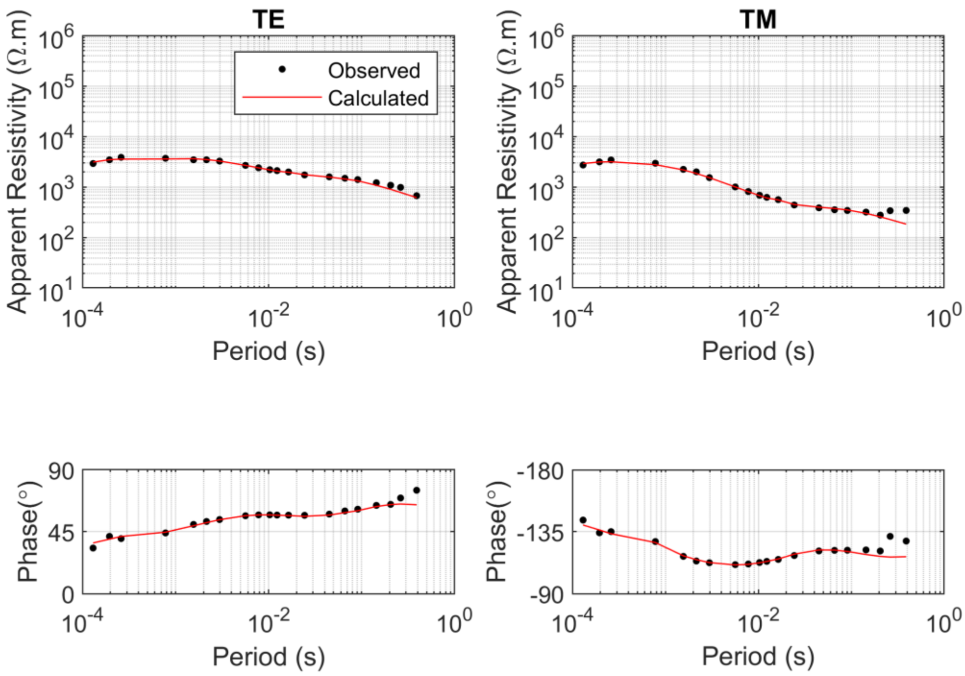

apparent resistivity and phase Plots for station #55

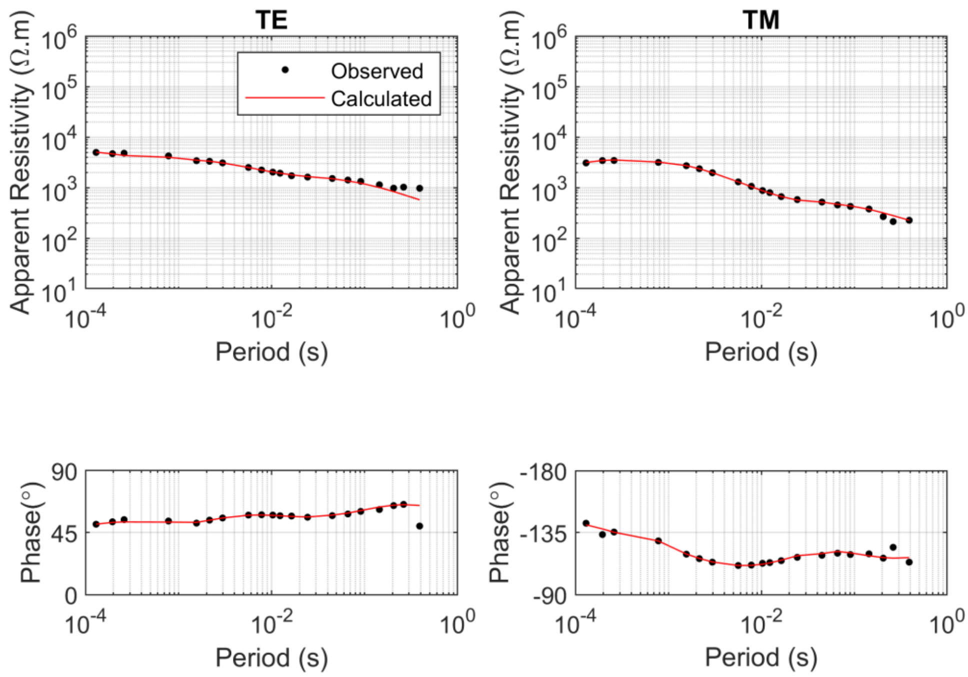

apparent resistivity and phase Plots for station #56

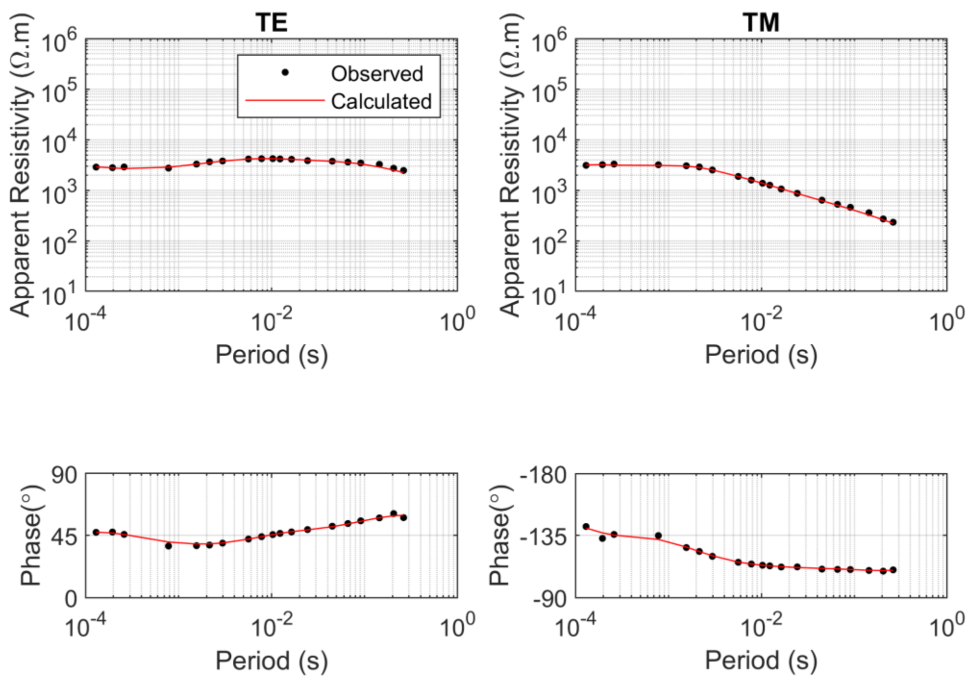

apparent resistivity and phase Plots for station #57

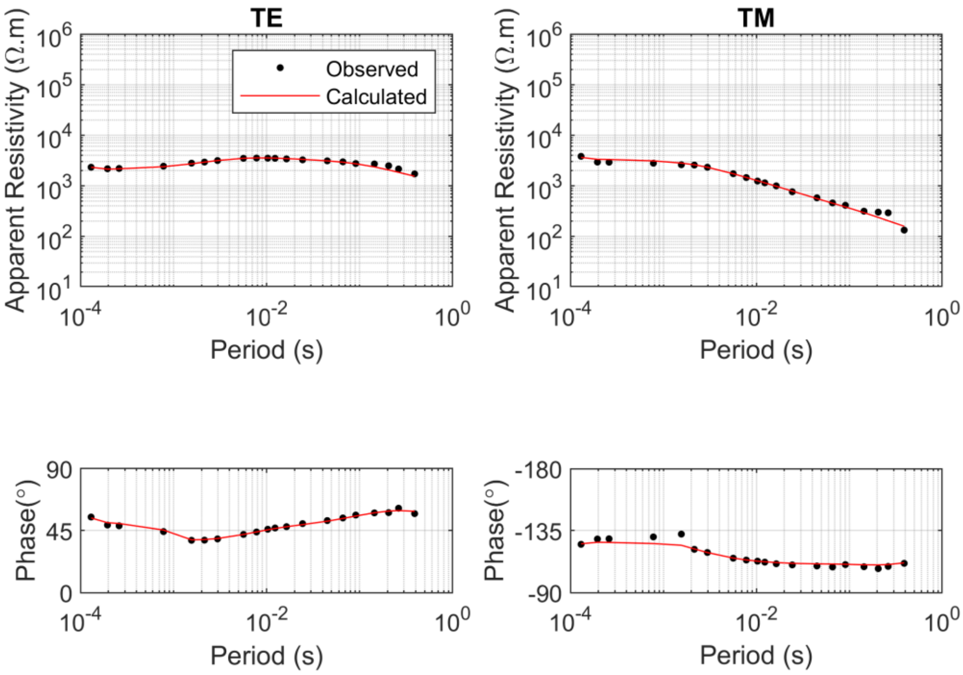

apparent resistivity and phase Plots for station #58

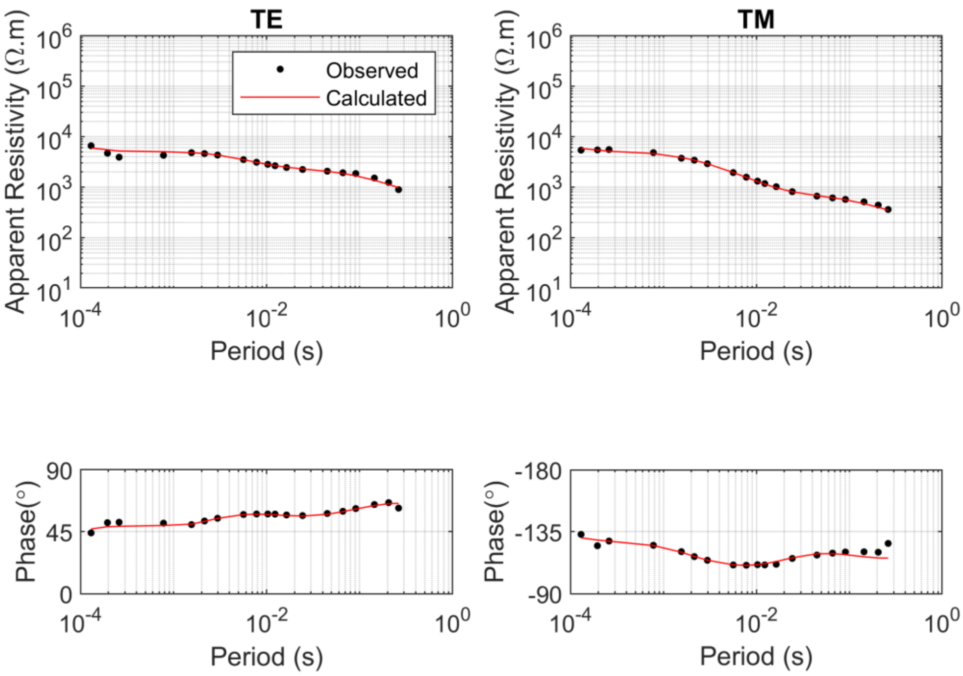

apparent resistivity and phase Plots for station #59

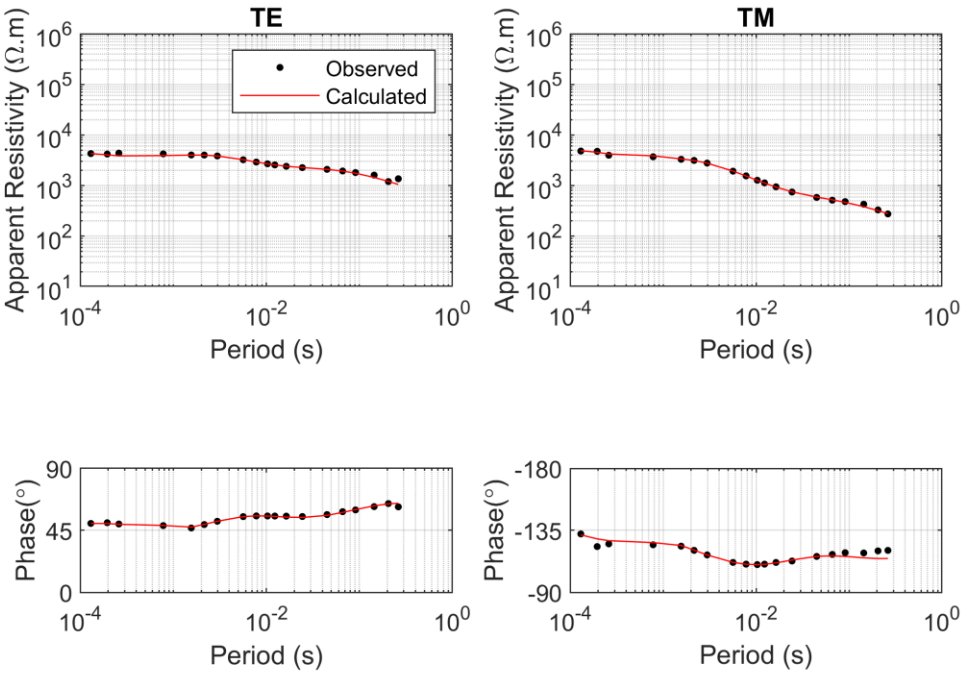

apparent resistivity and phase Plots for station #60

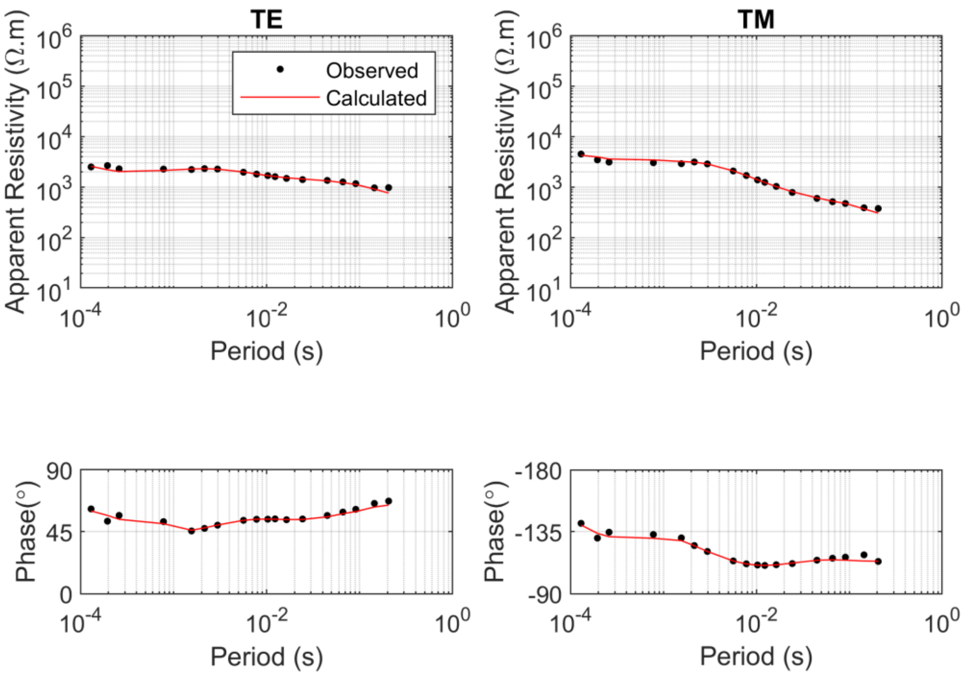

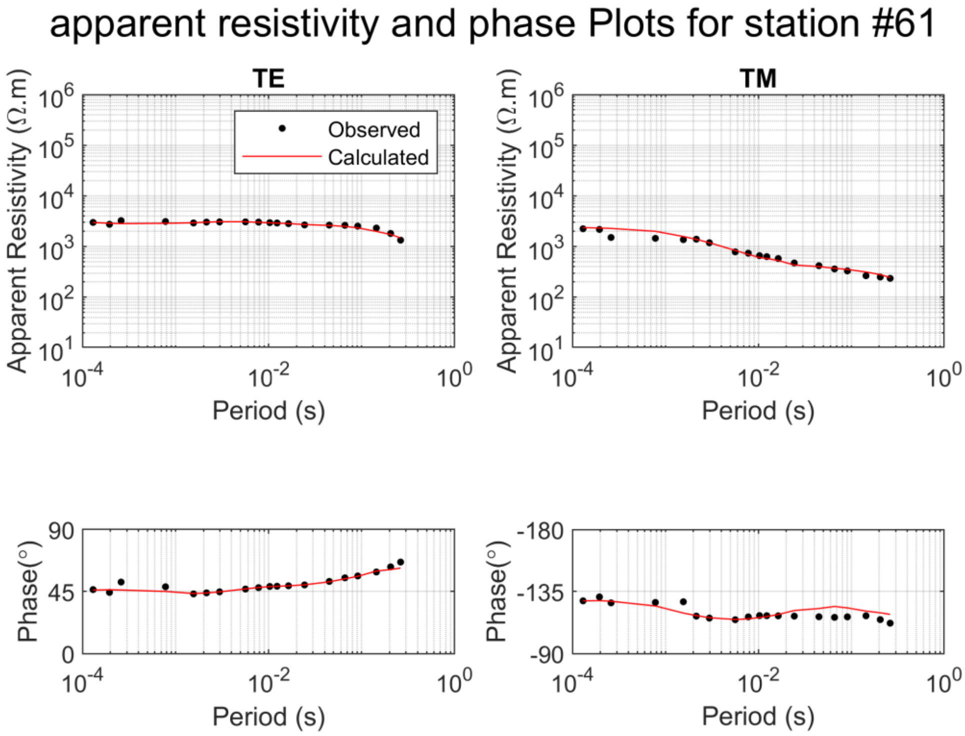
apparent resistivity and phase Plots for station #61
TE
TM
Observed
Calculated
Apparent Resistivity (Ω.m)
Phase(°)
Period (s)

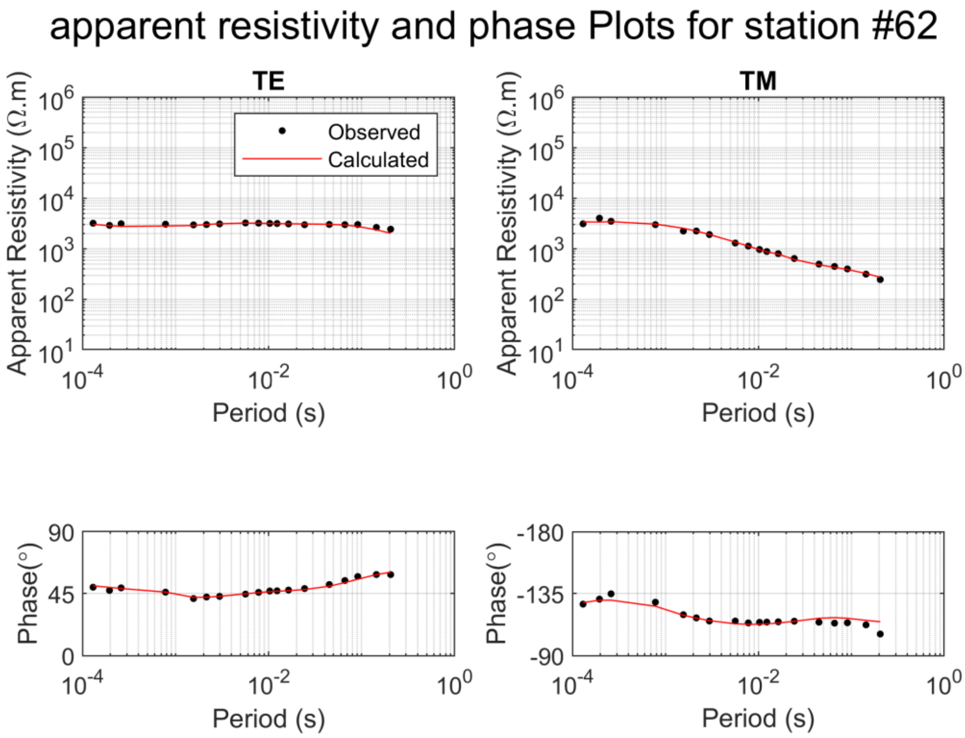
apparent resistivity and phase Plots for station #62
TE
TM
Observed
Calculated
Apparent Resistivity (Ω.m)
Phase(°)
Period (s)

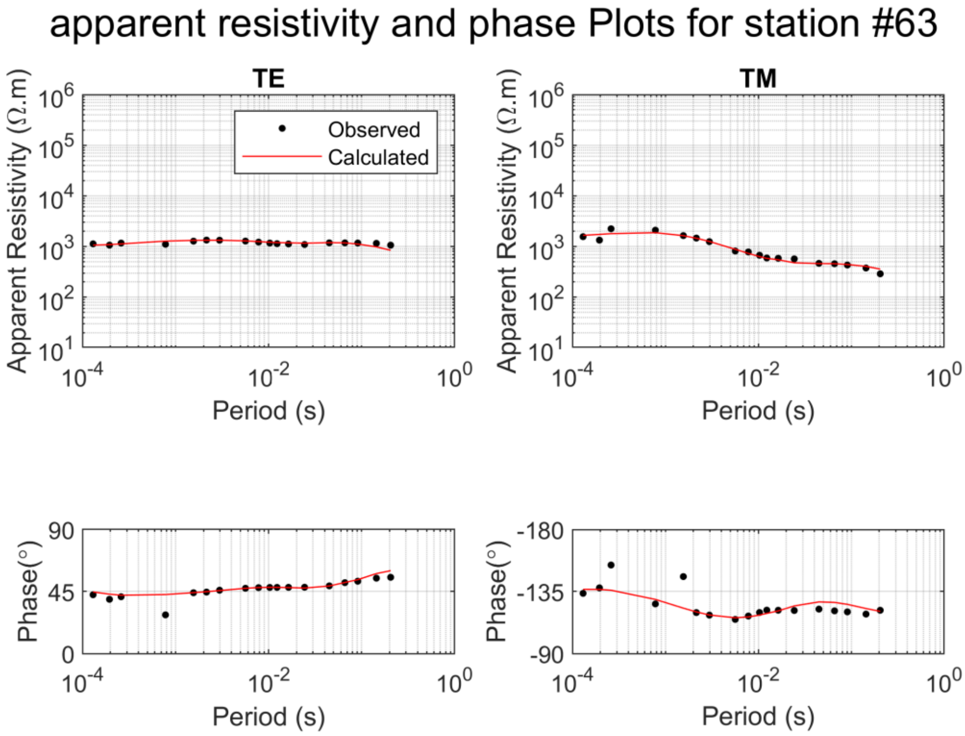
apparent resistivity and phase Plots for station #63
TE
TM
Observed
Calculated
Apparent Resistivity (Ω.m)
Period (s)
Phase(°)

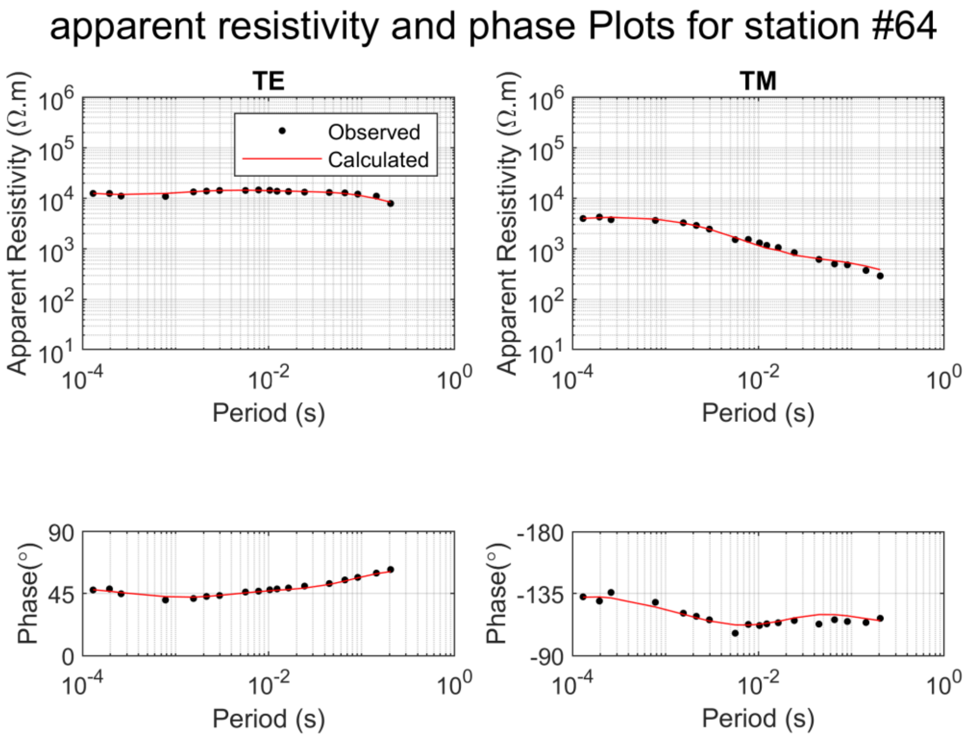
apparent resistivity and phase Plots for station #64
TE
TM
Observed
Calculated
Apparent Resistivity (Ω.m)
Period (s)
Phase(°)

apparent resistivity and phase Plots for station #65

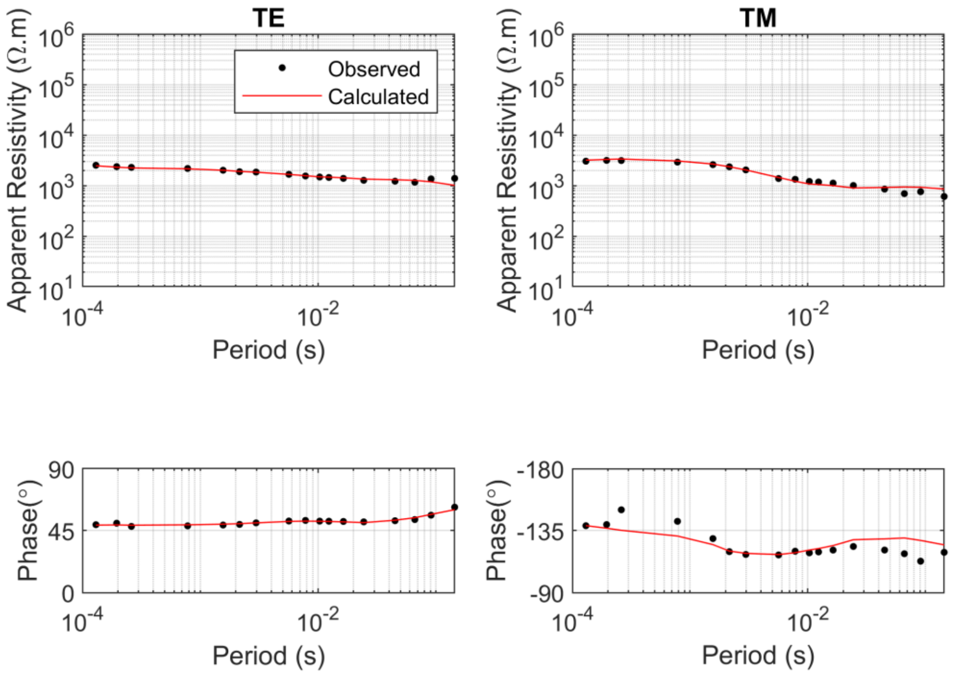

apparent resistivity and phase Plots for station #66

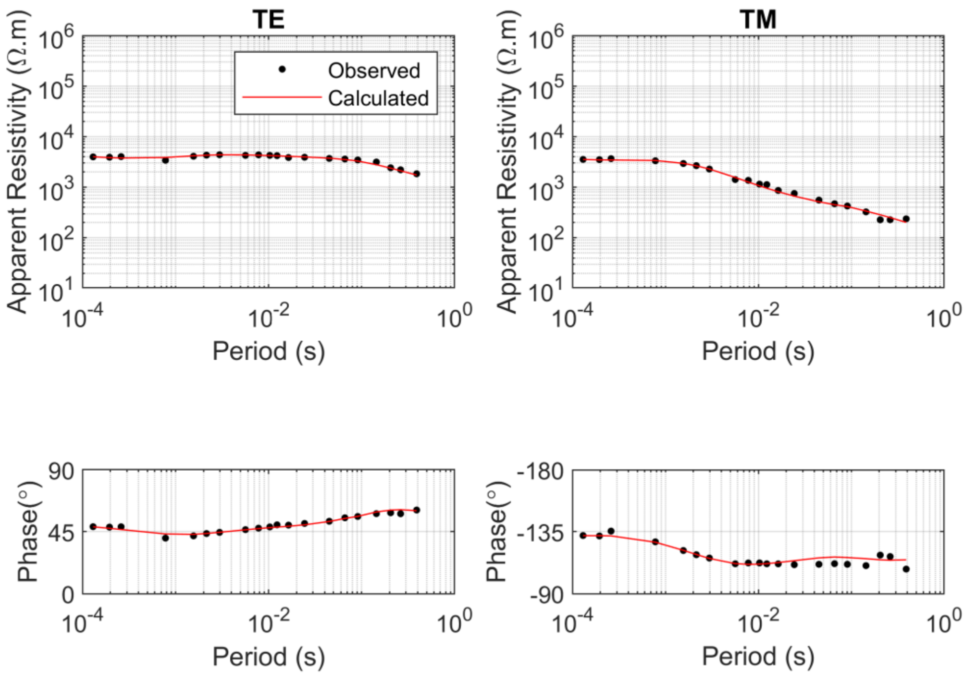

apparent resistivity and phase Plots for station #67

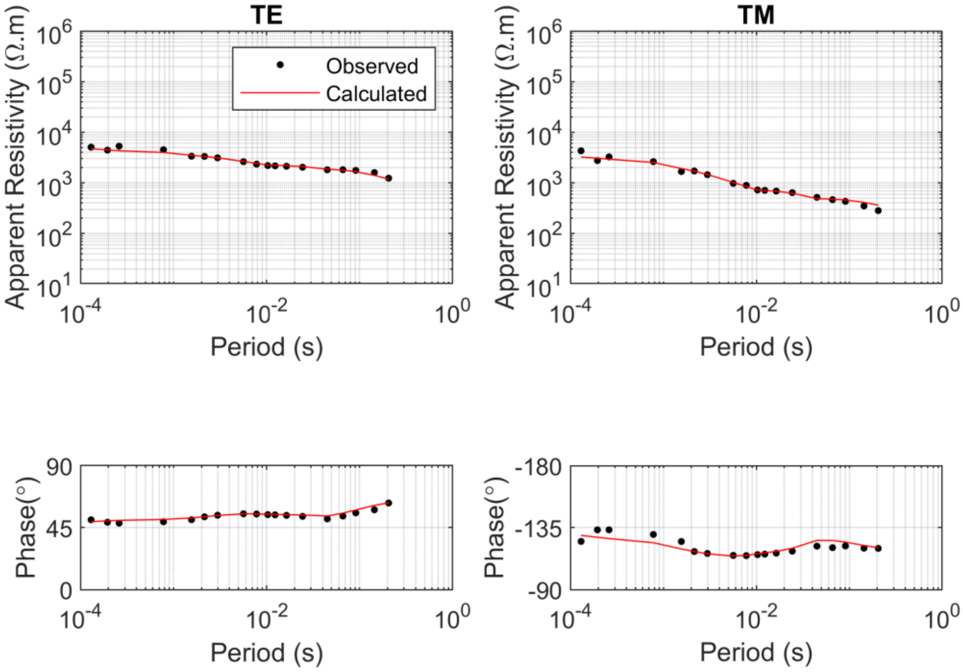

apparent resistivity and phase Plots for station #68

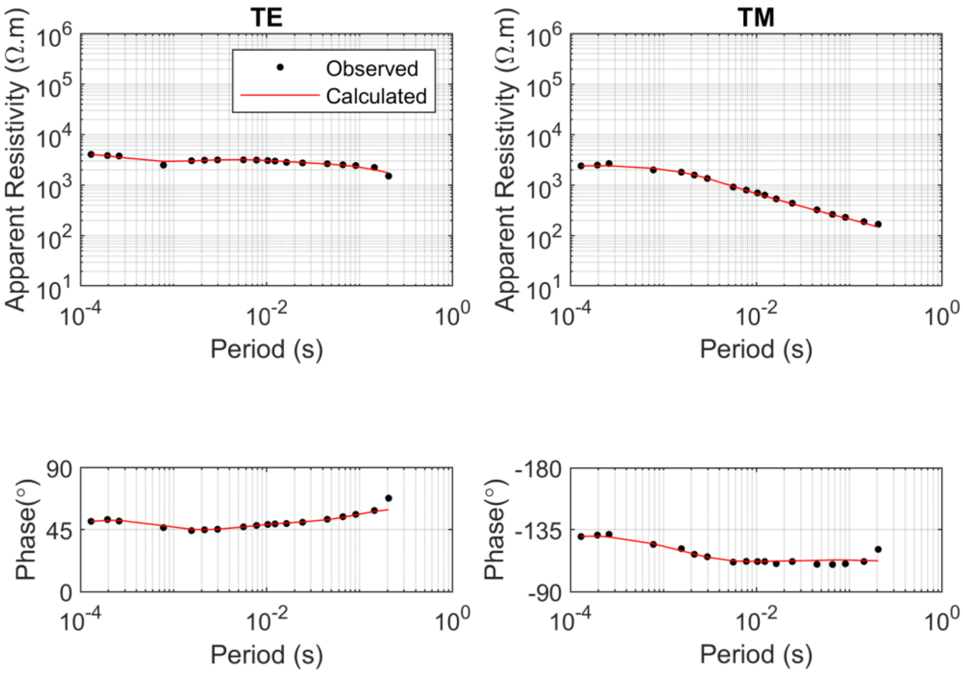

apparent resistivity and phase Plots for station #69

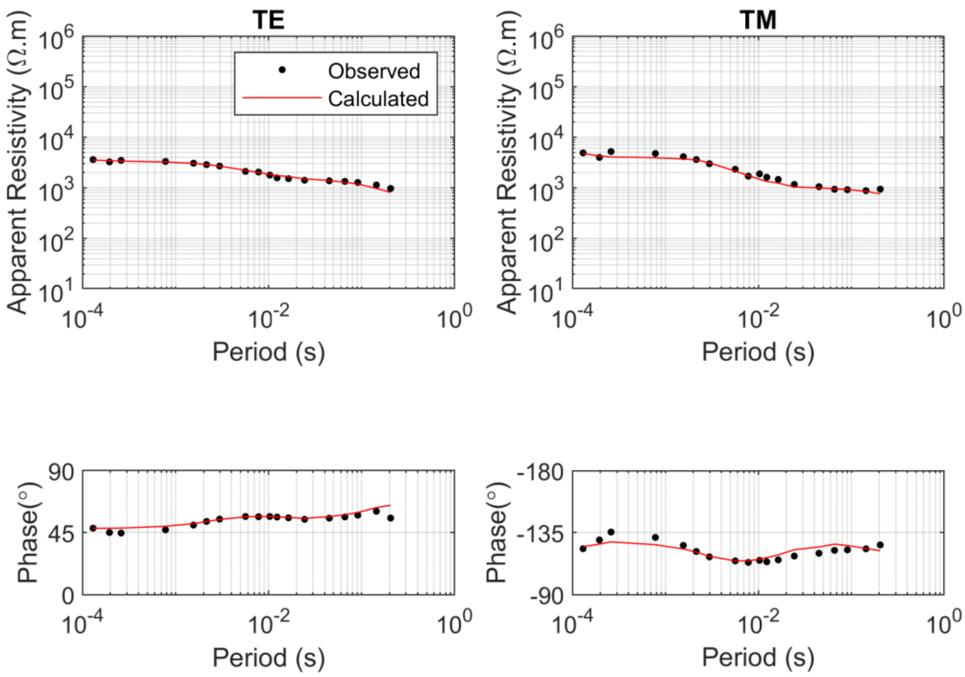

apparent resistivity and phase Plots for station #70

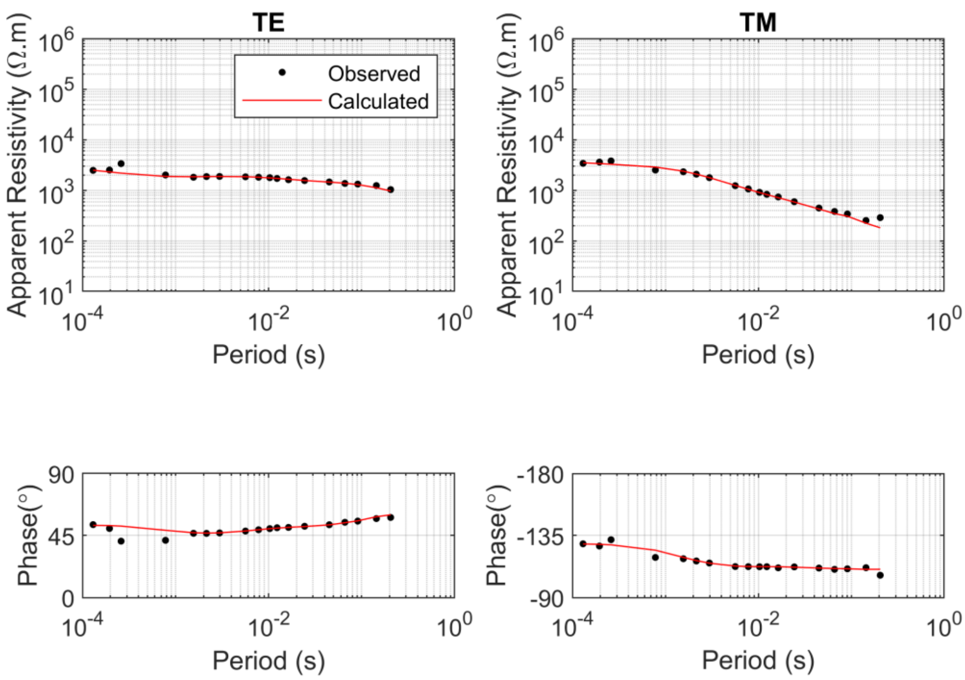

apparent resistivity and phase Plots for station #71

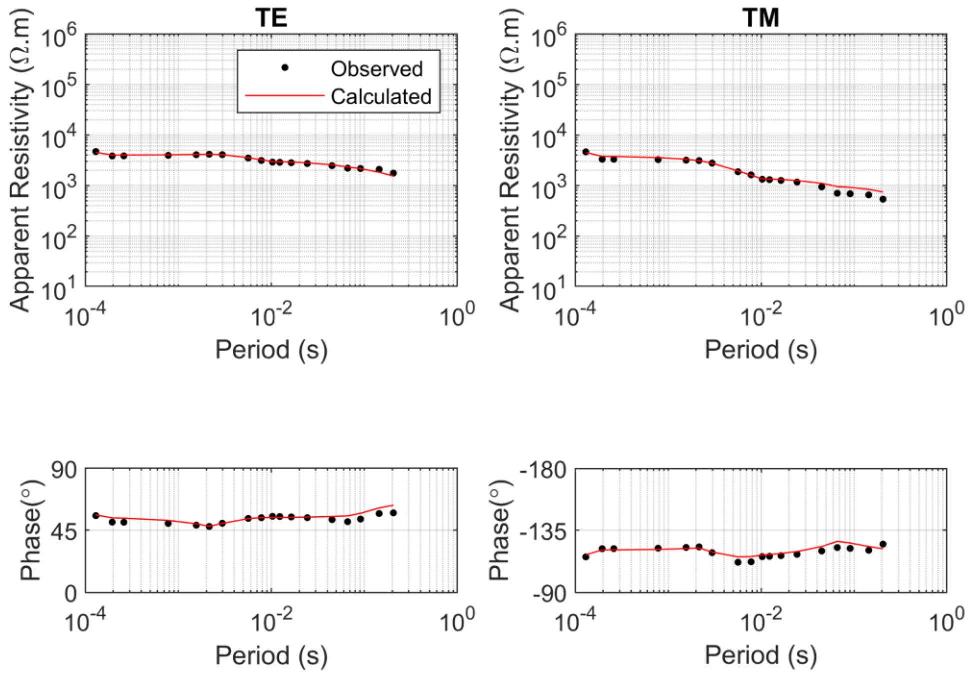

apparent resistivity and phase Plots for station #72

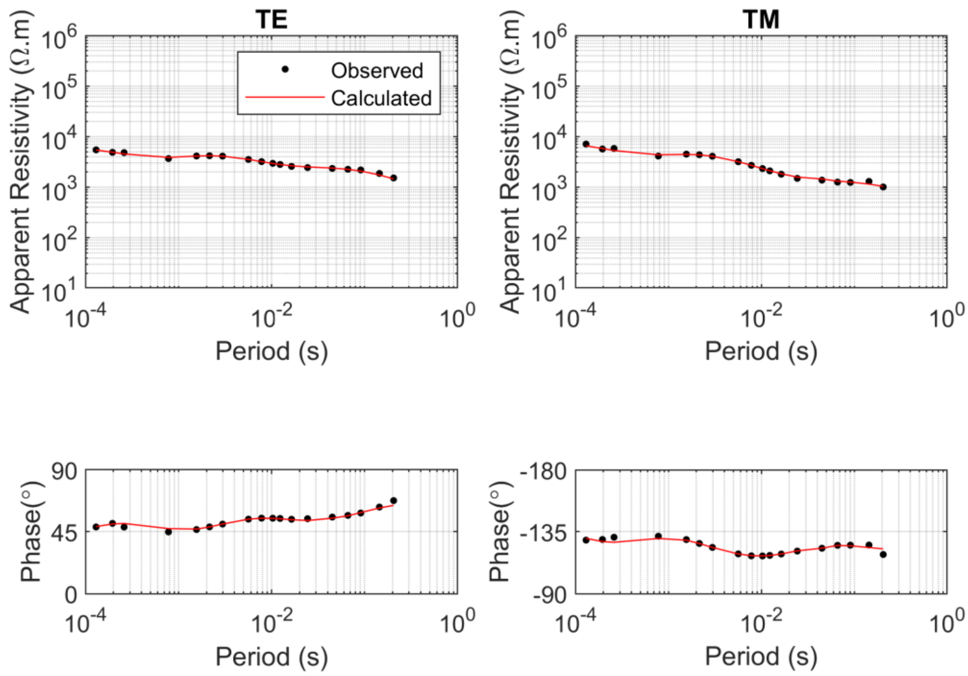

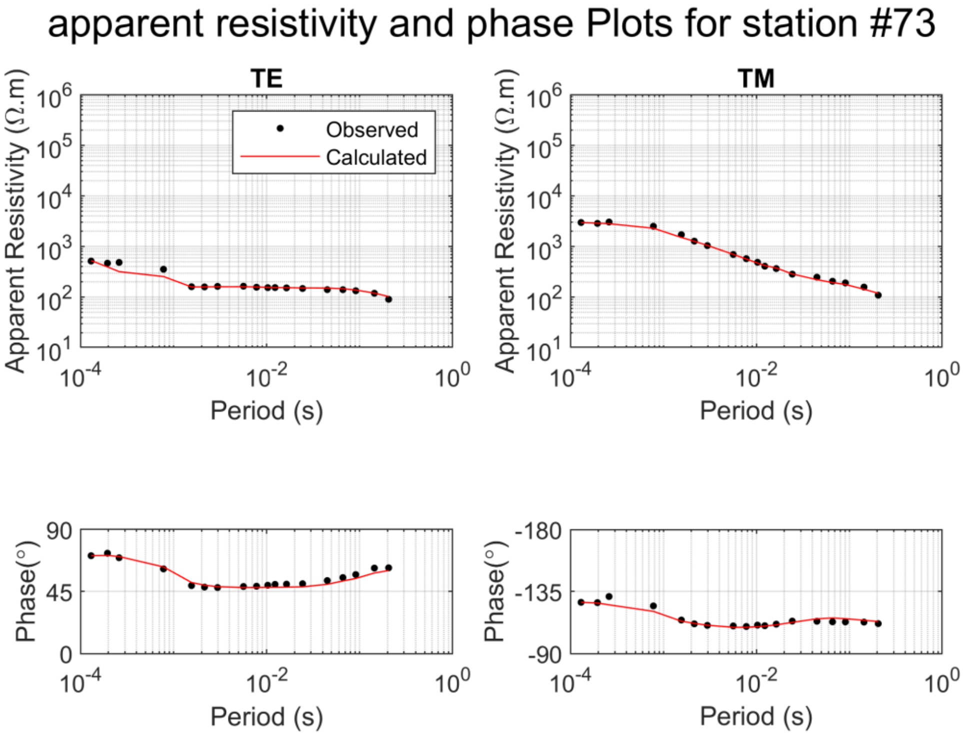
apparent resistivity and phase Plots for station #73
TE
TM
Observed
Calculated
Apparent Resistivity (Ω.m)
Period (s)
Phase(°)

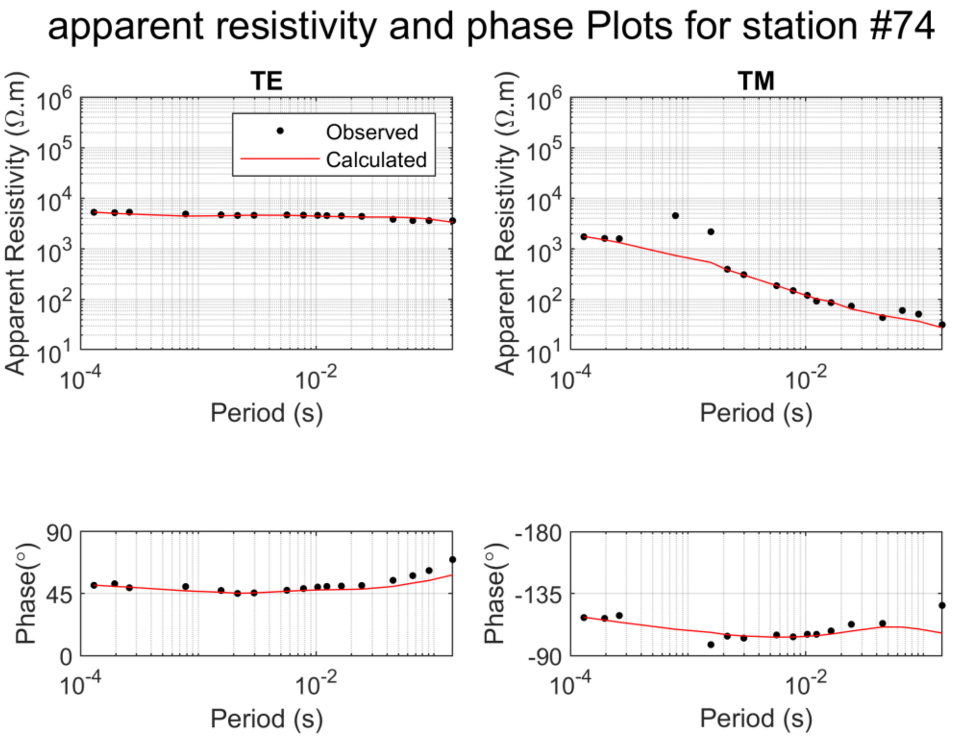
apparent resistivity and phase Plots for station #74
TE
TM
Observed
Calculated
Apparent Resistivity (Ω.m)
Period (s)
Phase(°)

apparent resistivity and phase Plots for station #75

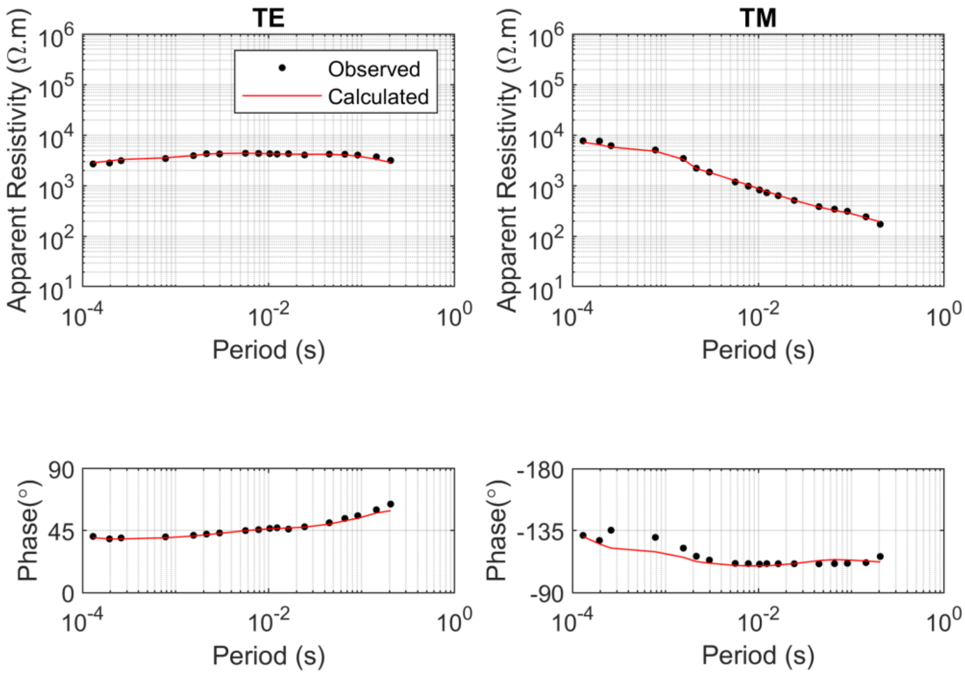

apparent resistivity and phase Plots for station #76

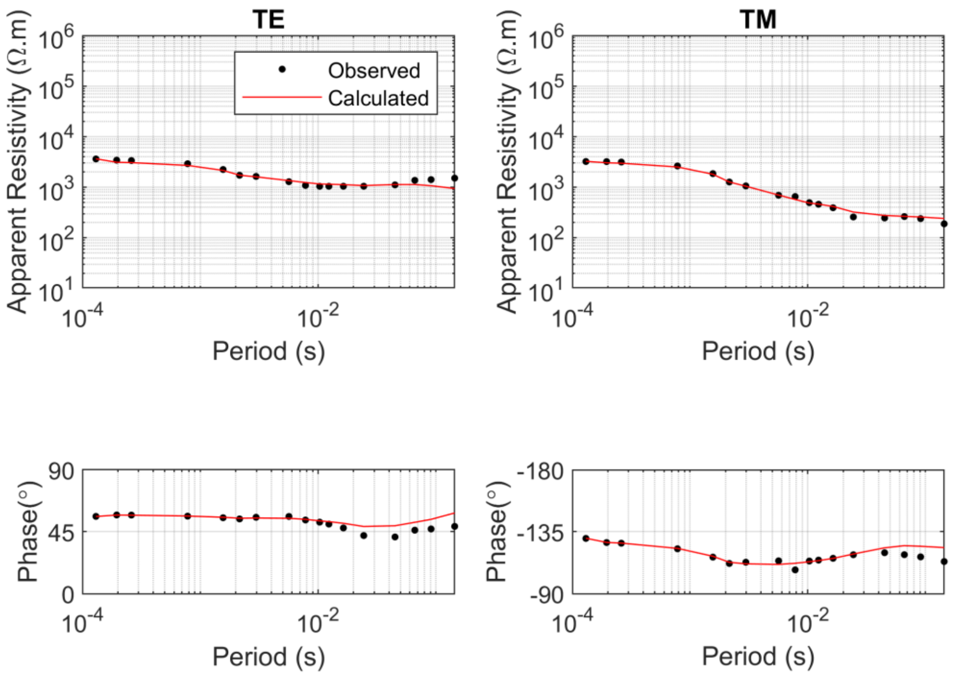

apparent resistivity and phase Plots for station #77

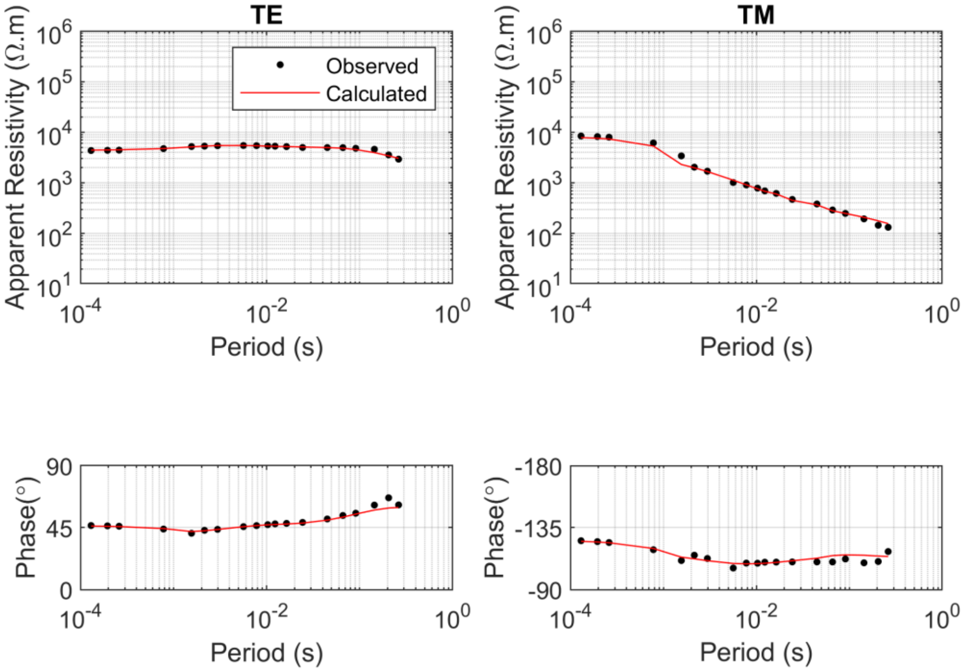

apparent resistivity and phase Plots for station #78

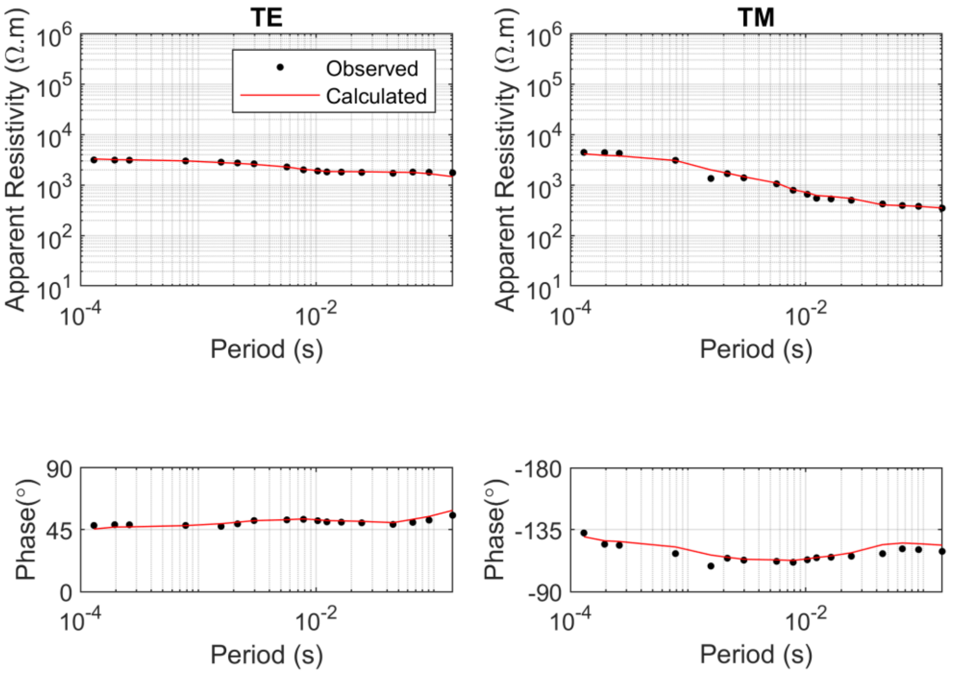

apparent resistivity and phase Plots for station #79

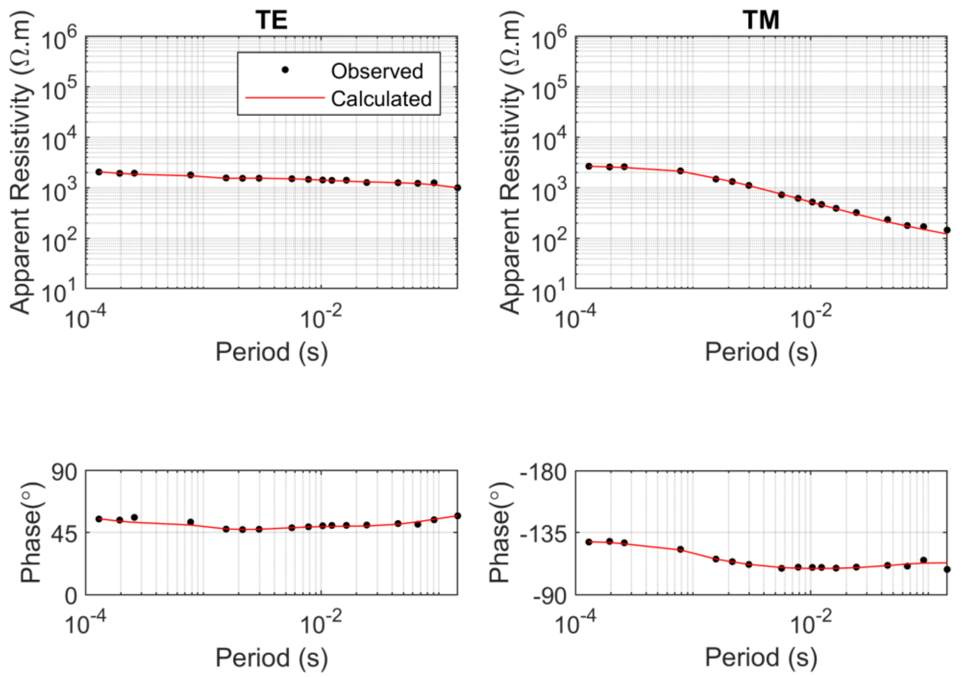

apparent resistivity and phase Plots for station #80

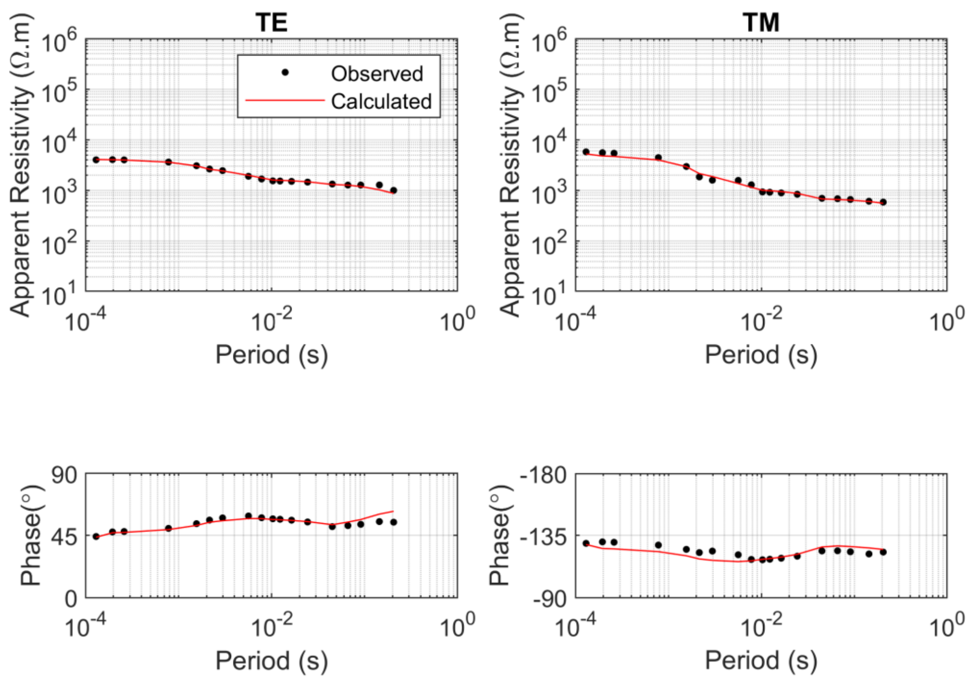

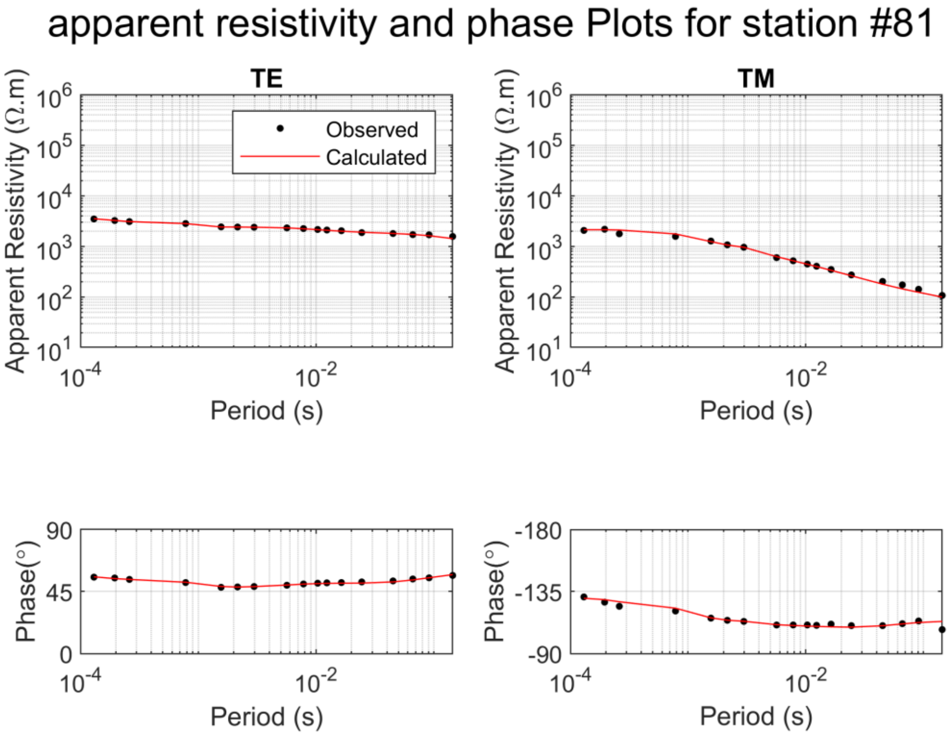
apparent resistivity and phase Plots for station #81
TE
TM
Observed
Calculated
Apparent Resistivity (Ω.m)
Phase(°)
Period (s)

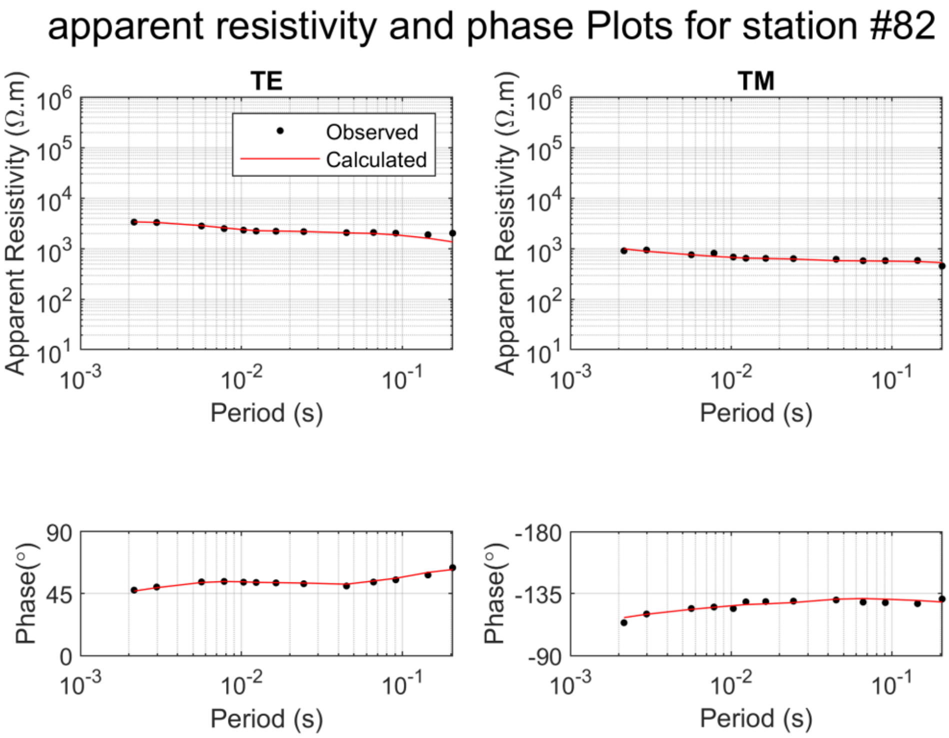
apparent resistivity and phase Plots for station #82
TE
TM
Observed
Calculated
Apparent Resistivity (Ω.m)
Phase(°)
Period (s)

apparent resistivity and phase Plots for station #83

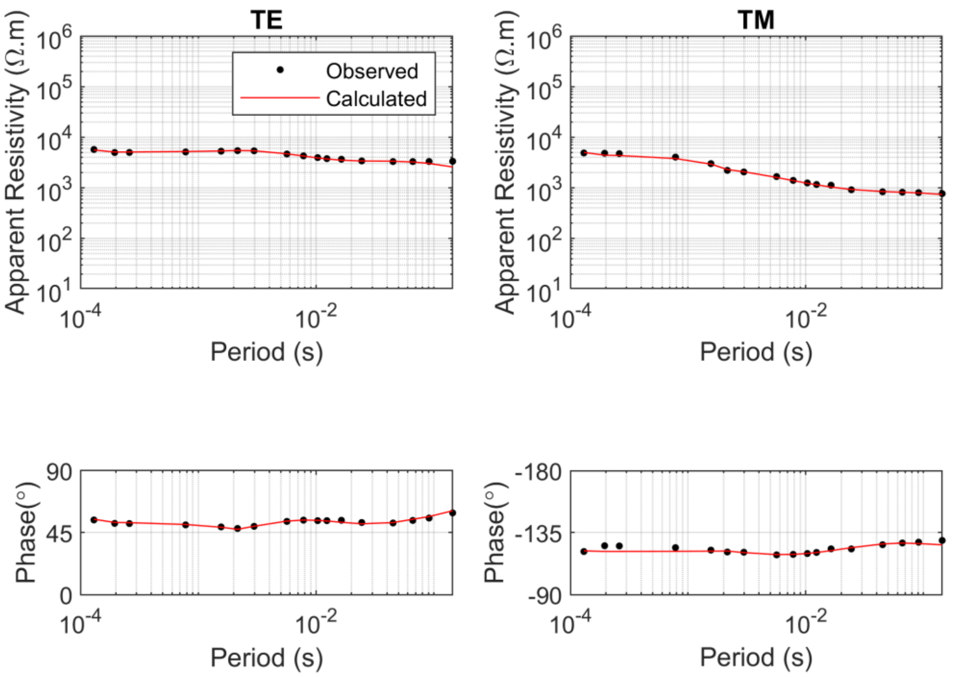

apparent resistivity and phase Plots for station #84

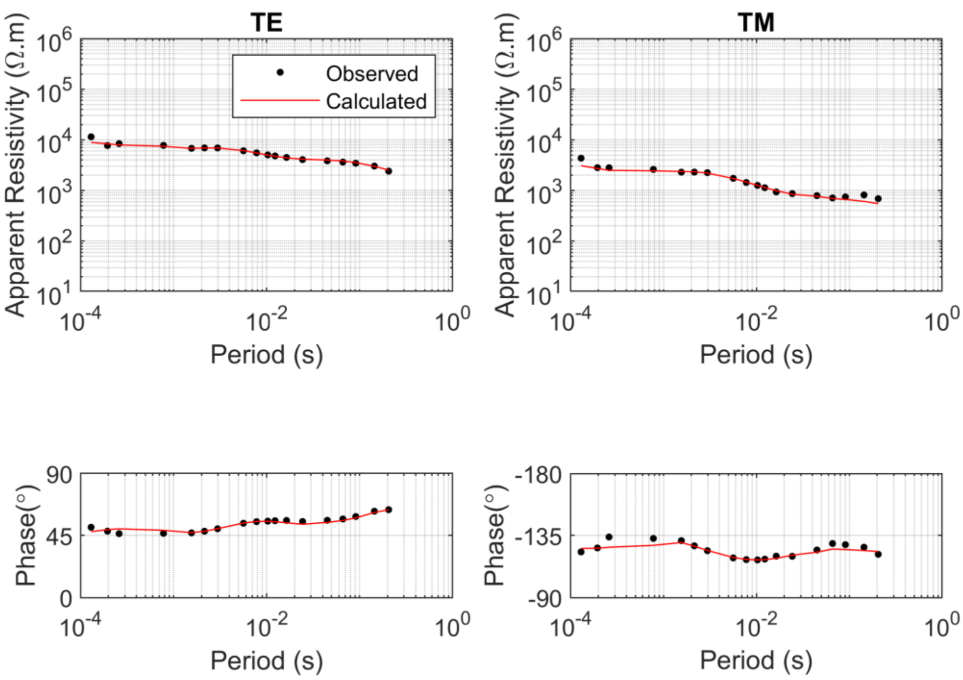

apparent resistivity and phase Plots for station #85

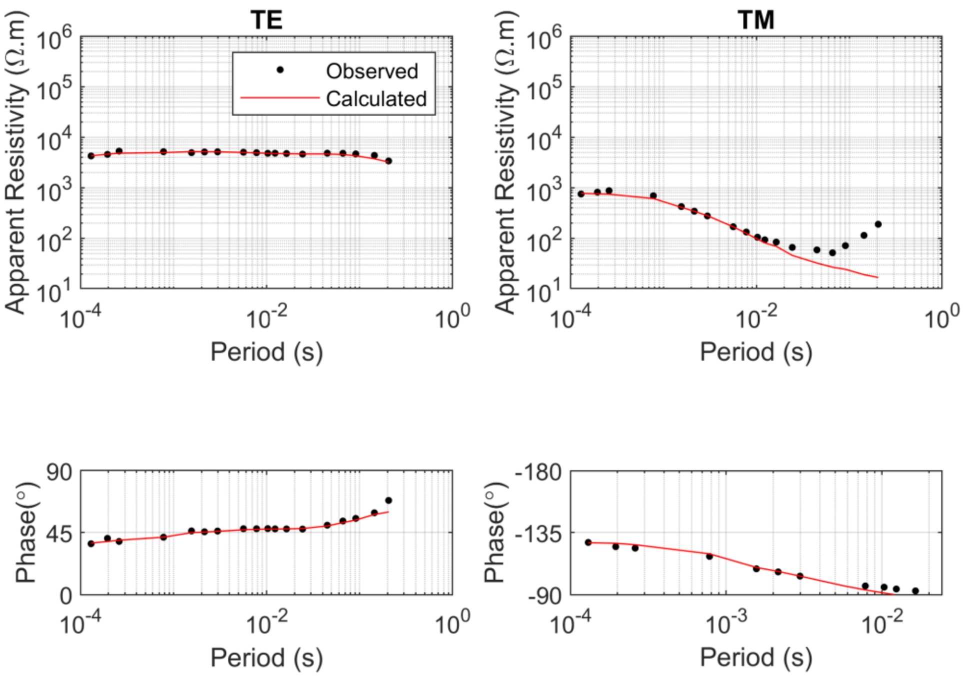

apparent resistivity and phase Plots for station #86

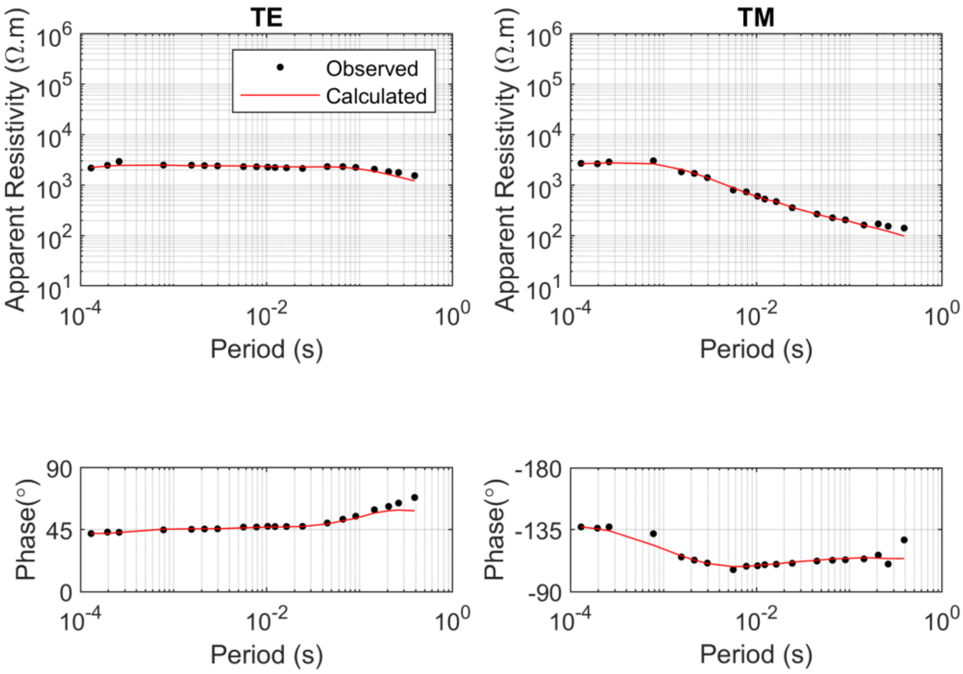

apparent resistivity and phase Plots for station #87

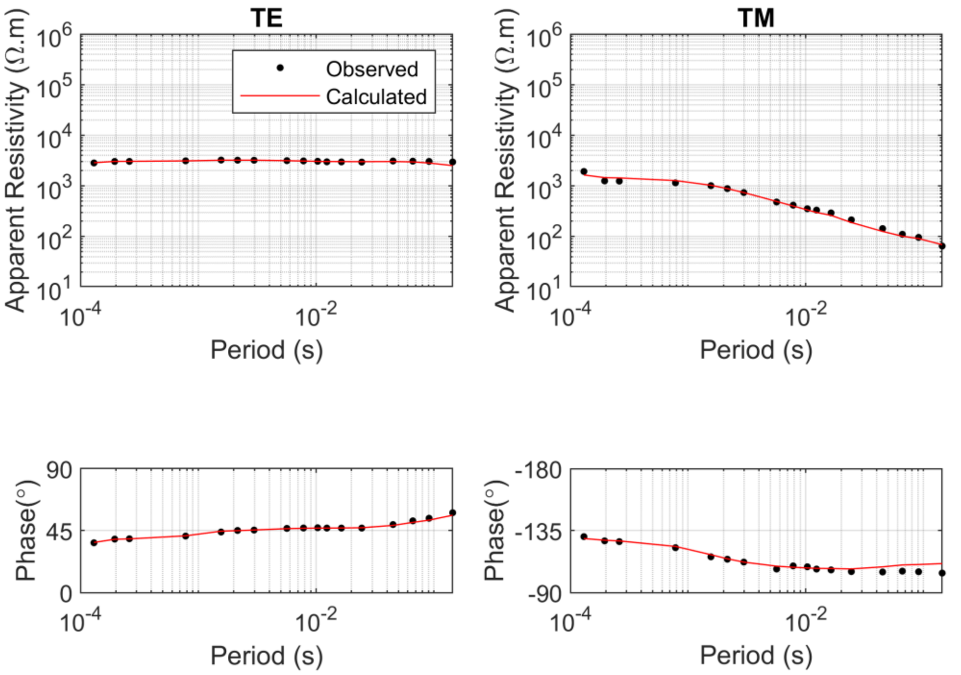

apparent resistivity and phase Plots for station #88

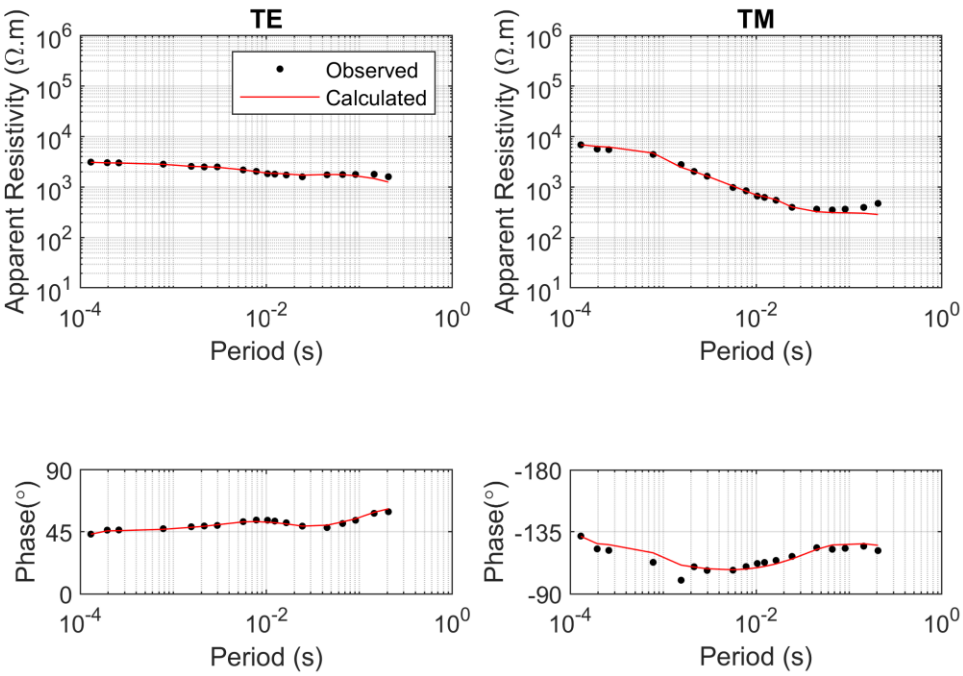

apparent resistivity and phase Plots for station #89

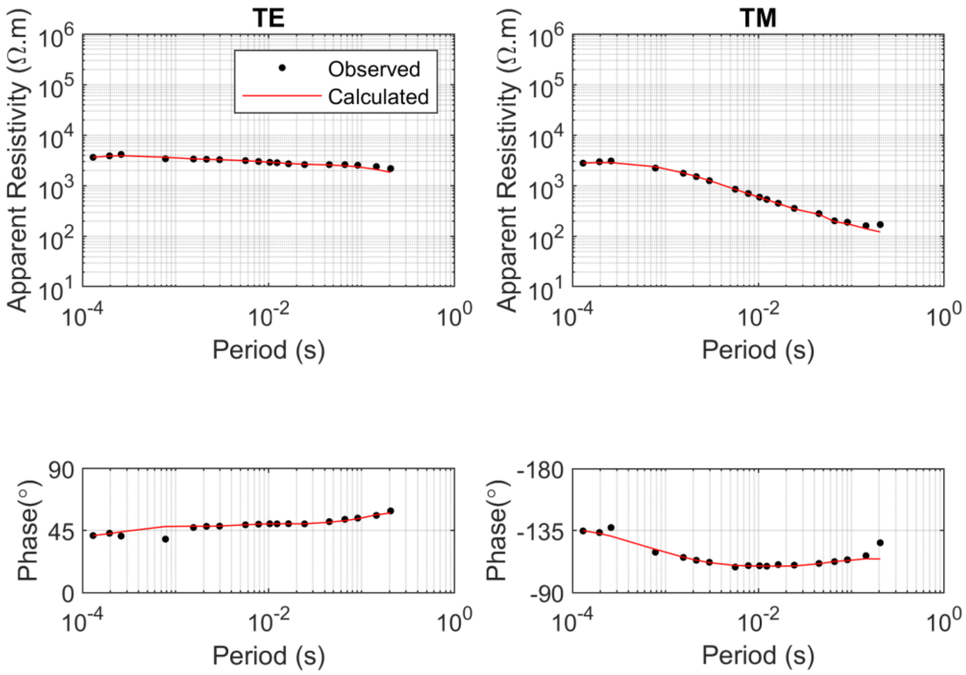

apparent resistivity and phase Plots for station #90

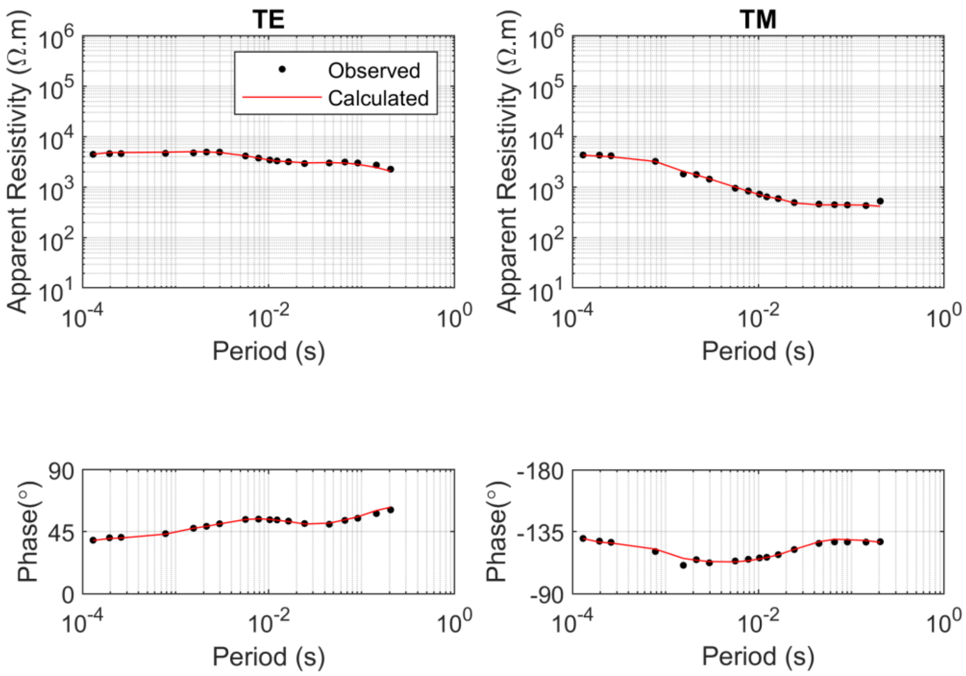

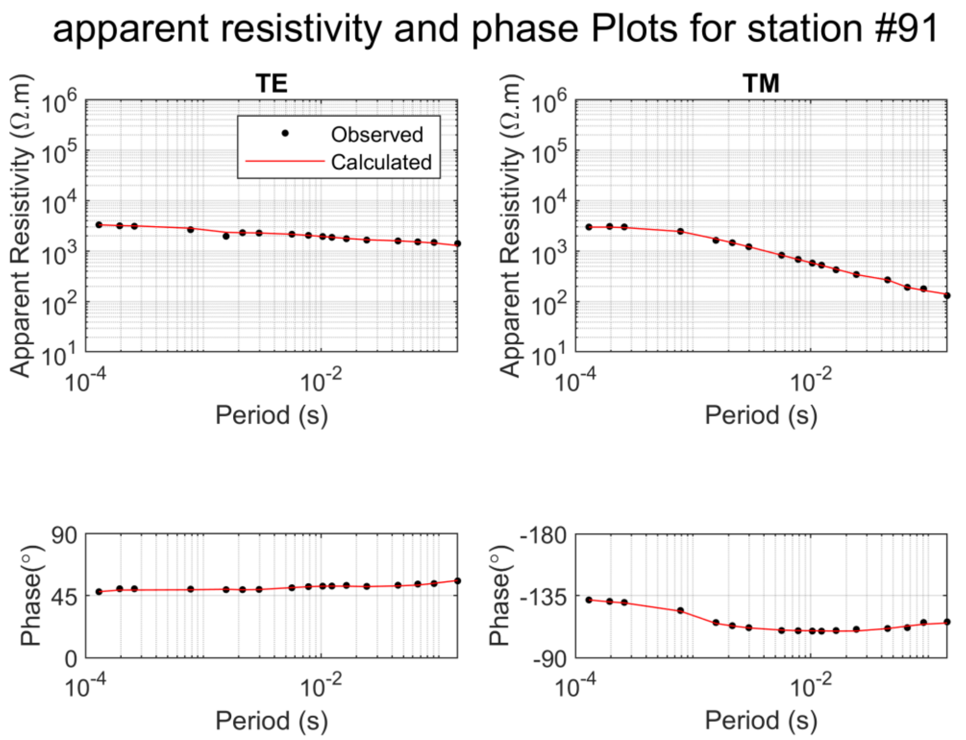

apparent resistivity and phase Plots for station #91
TE
TM
Observed
Calculated
Apparent Resistivity (Ω.m)
Phase(°)
Period (s)

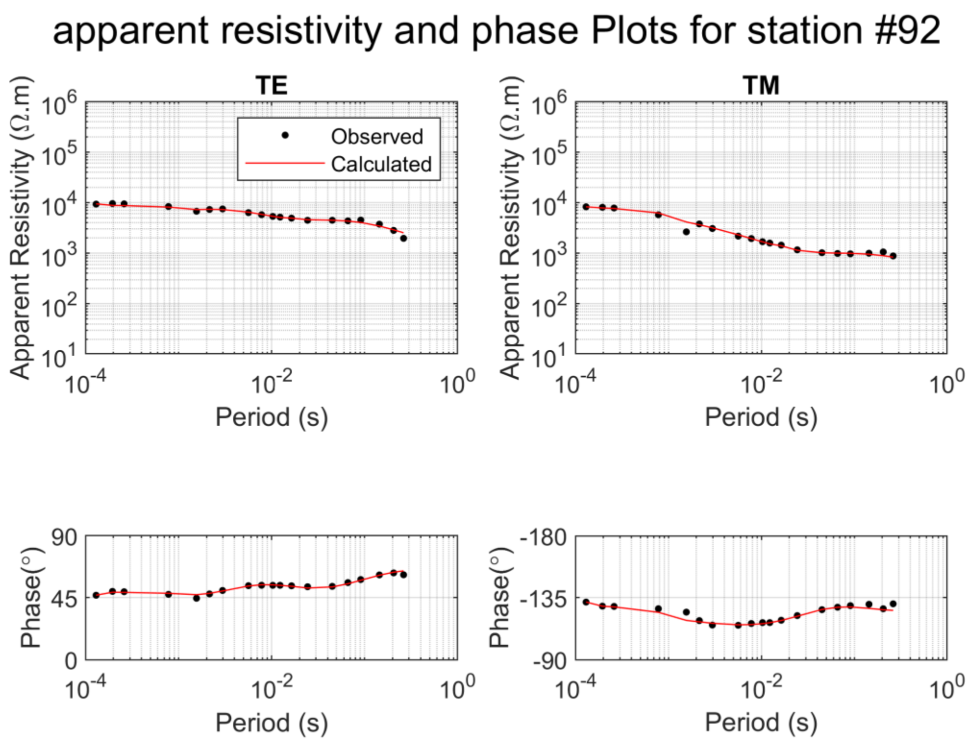

apparent resistivity and phase Plots for station #92
TE
TM
Observed
Calculated
Apparent Resistivity (Ω.m)
Phase(°)
Period (s)

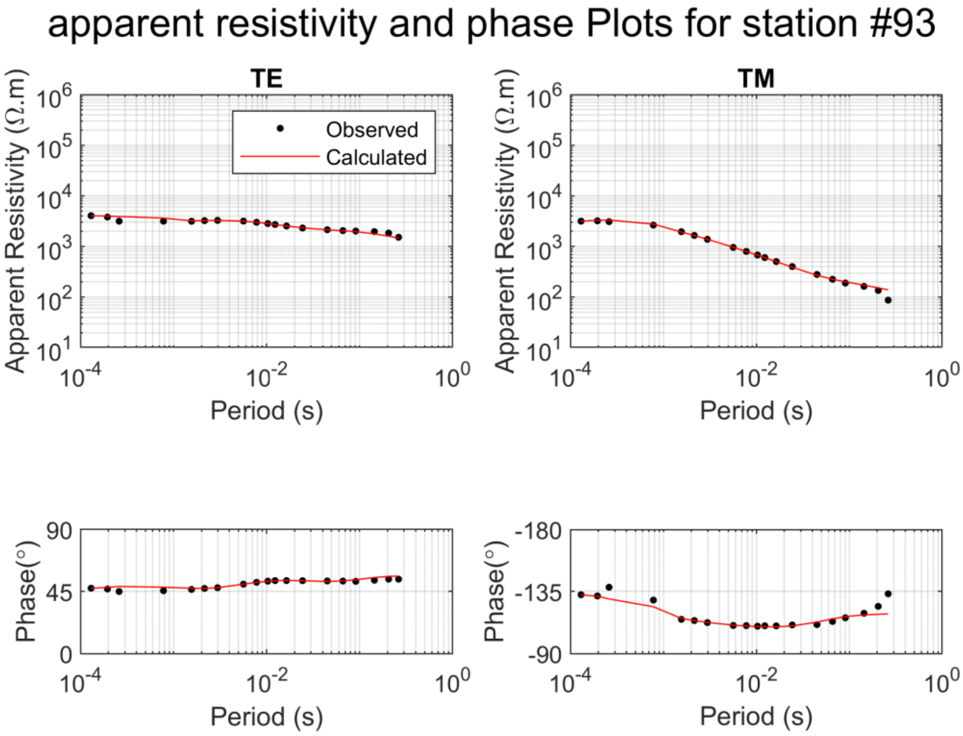
apparent resistivity and phase Plots for station #93
TE
TM
Observed
Calculated
Apparent Resistivity (Ω.m)
Phase(°)
Period (s)

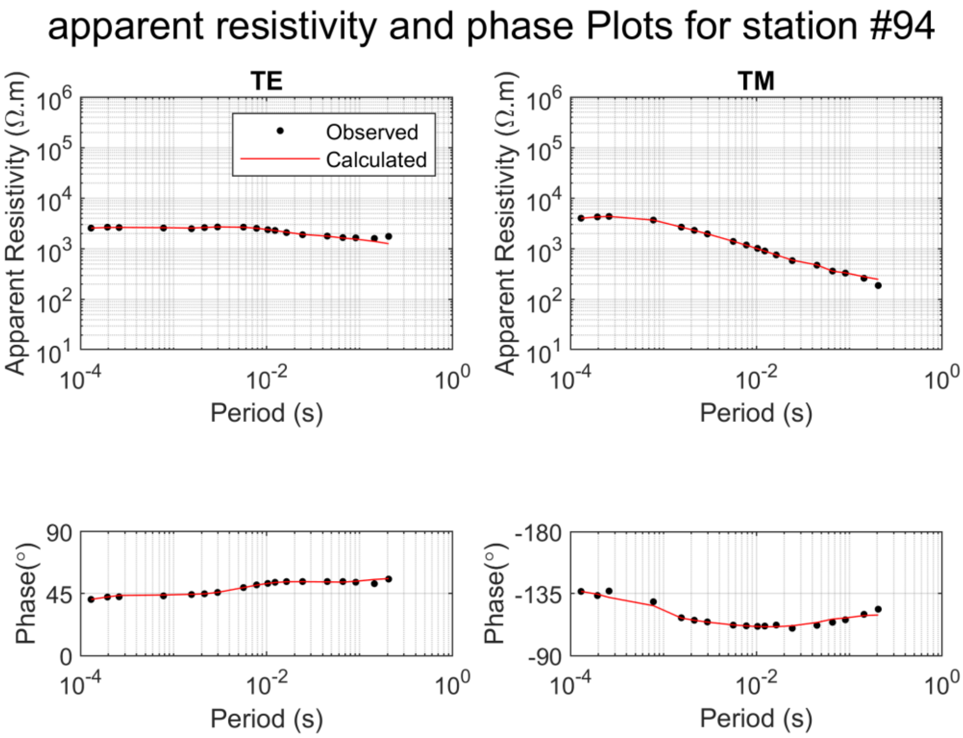
apparent resistivity and phase Plots for station #94
TE
TM
Observed
Calculated
Apparent Resistivity (Ω.m)
Phase(°)
Period (s)

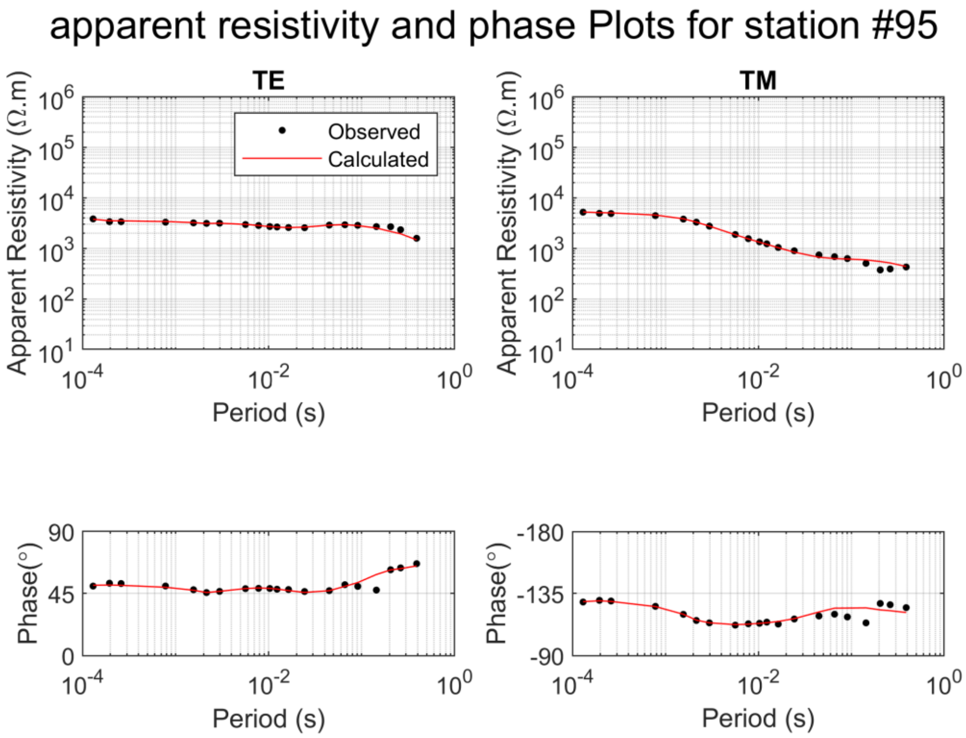
apparent resistivity and phase Plots for station #95
TE
TM
Observed
Calculated
Apparent Resistivity (Ω.m)
Period (s)
Phase(°)

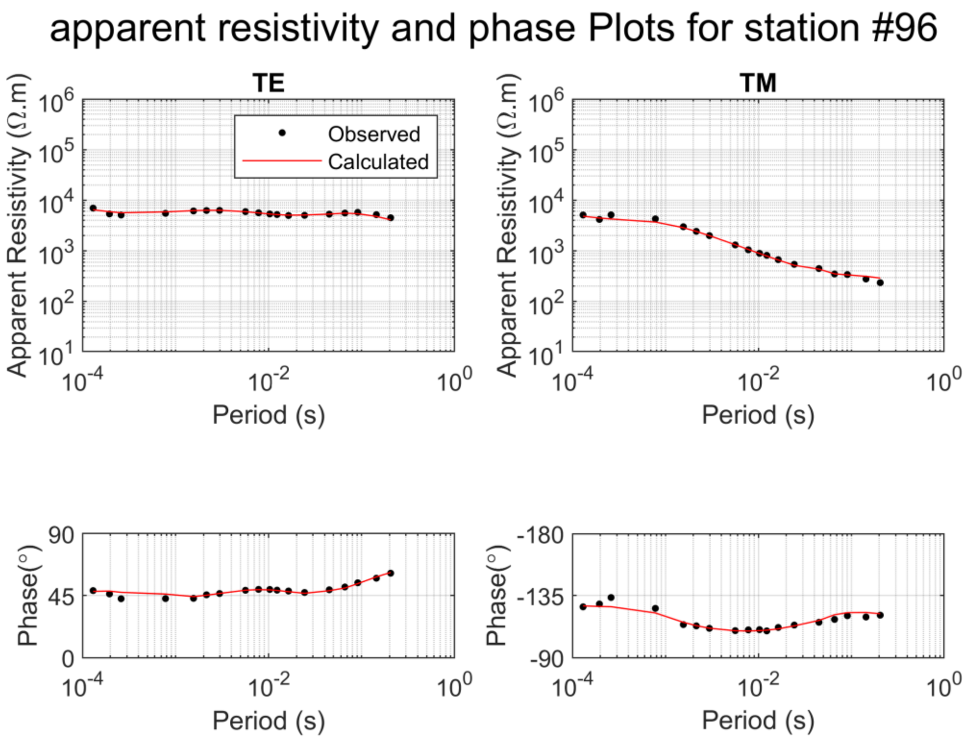
apparent resistivity and phase Plots for station #96
TE
TM
Observed
Calculated
Apparent Resistivity (Ω.m)
Period (s)
Phase(°)

apparent resistivity and phase Plots for station #97

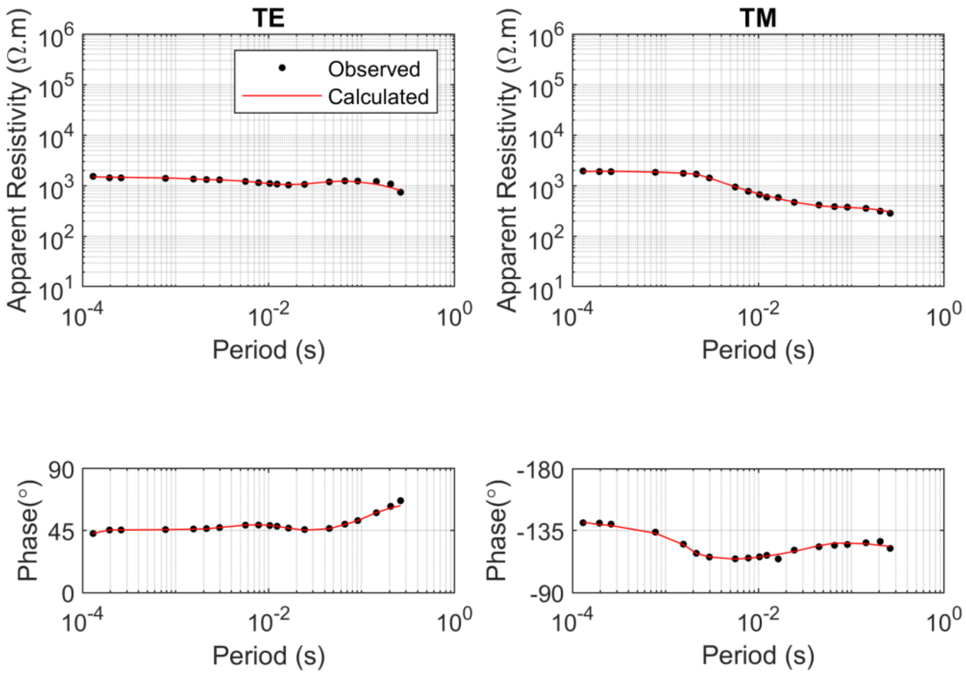

apparent resistivity and phase Plots for station #98

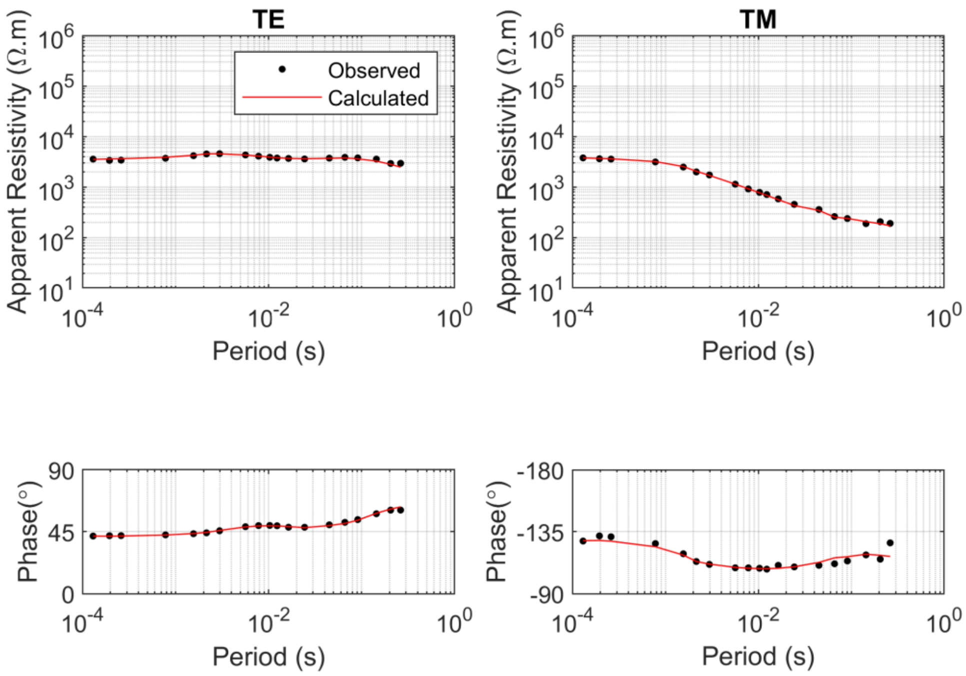

apparent resistivity and phase Plots for station #99

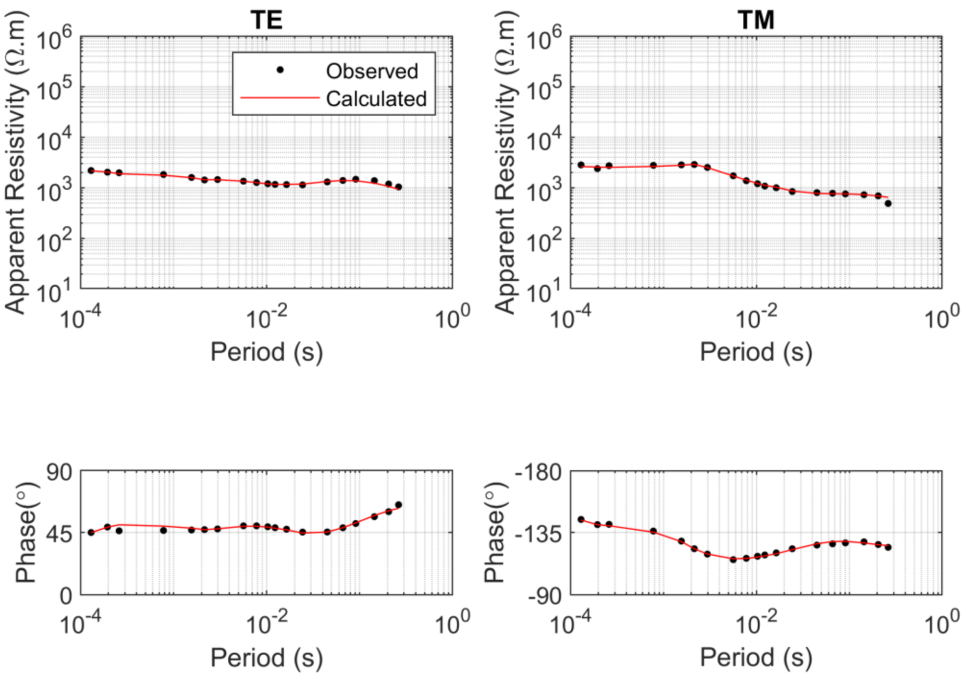

apparent resistivity and phase Plots for station #100

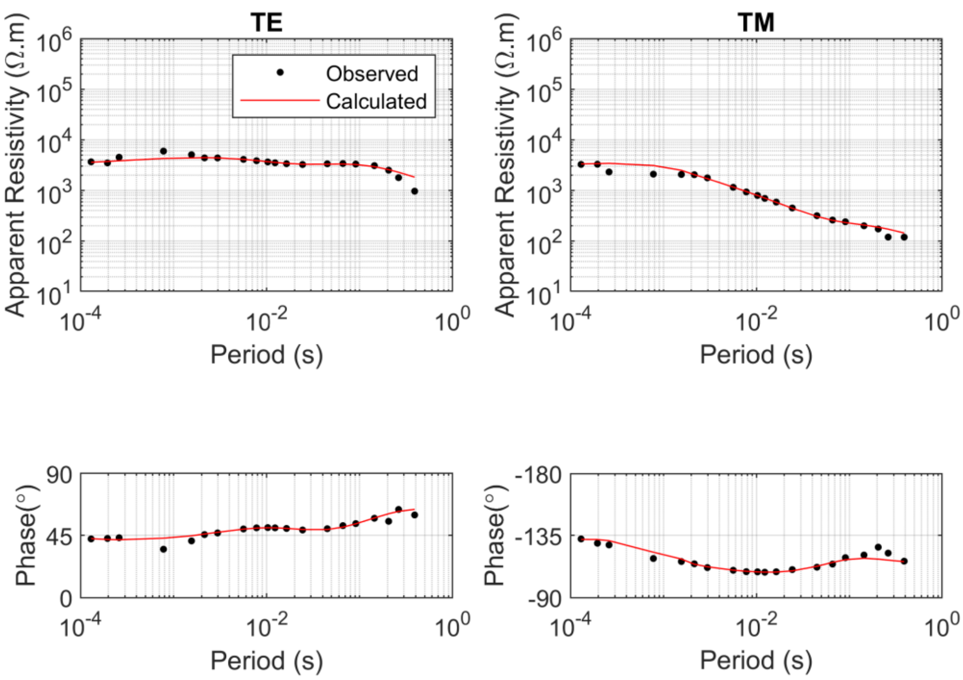

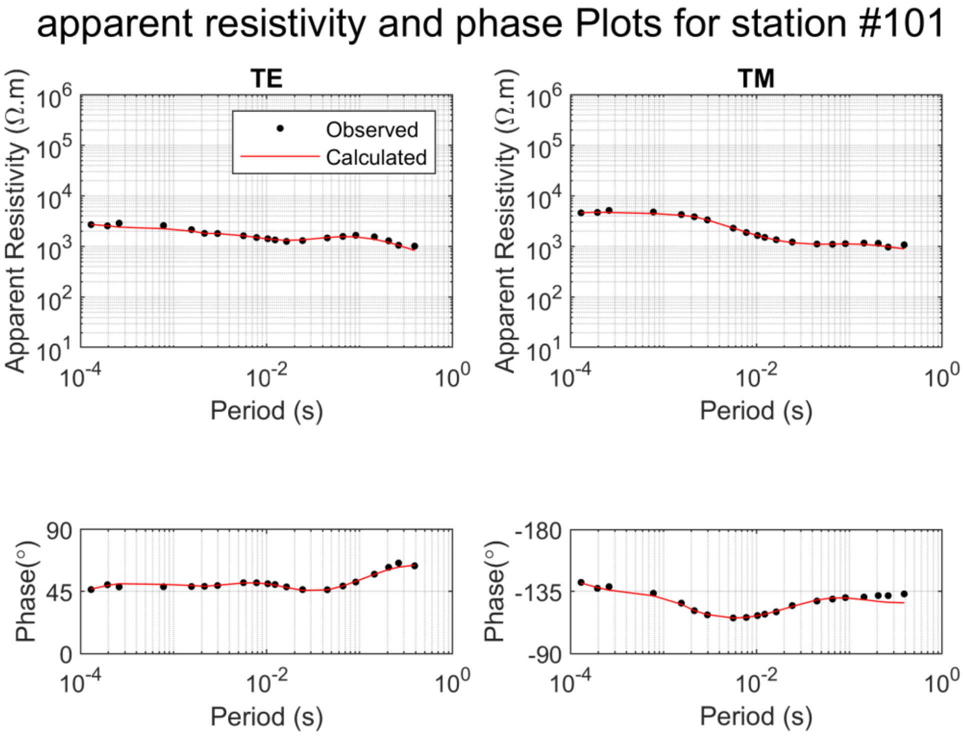
apparent resistivity and phase Plots for station #101
TE
TM
Observed
Calculated
Apparent Resistivity (Ω.m)
Period (s)
Phase(°)

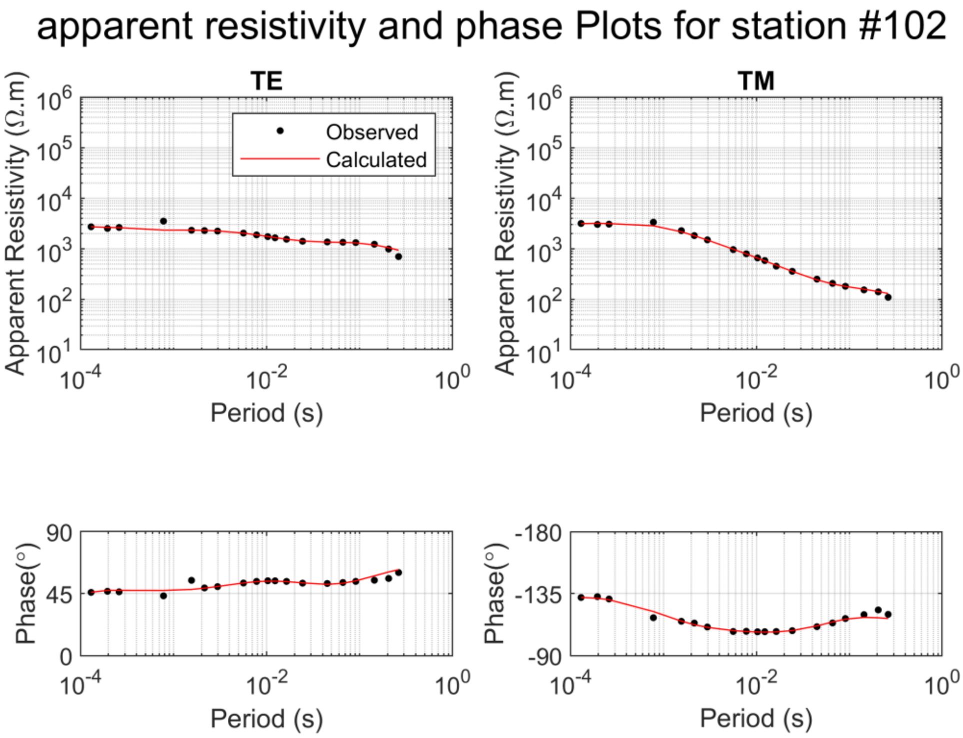
apparent resistivity and phase Plots for station #102
TE
TM
Observed
Calculated
Apparent Resistivity (Ω.m)
Period (s)
Phase(°)

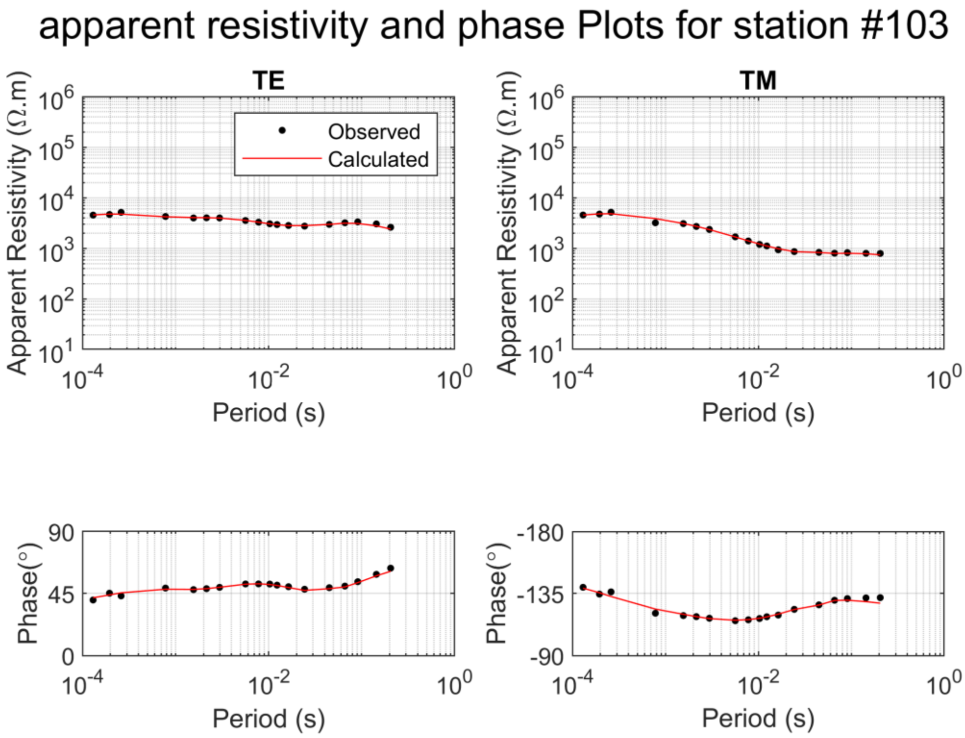
apparent resistivity and phase Plots for station #103
TE
TM
Observed
Calculated
Apparent Resistivity (Ω.m)
Period (s)
Phase(°)

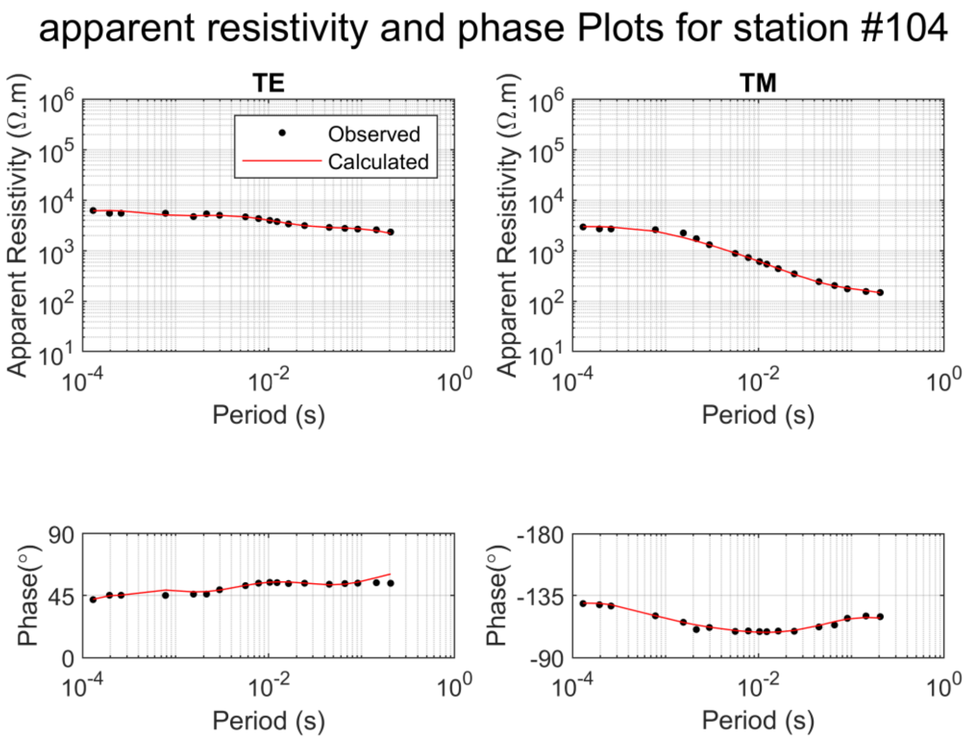
apparent resistivity and phase Plots for station #104
TE
TM
Observed
Calculated
Apparent Resistivity (Ω.m)
Period (s)
Phase(°)

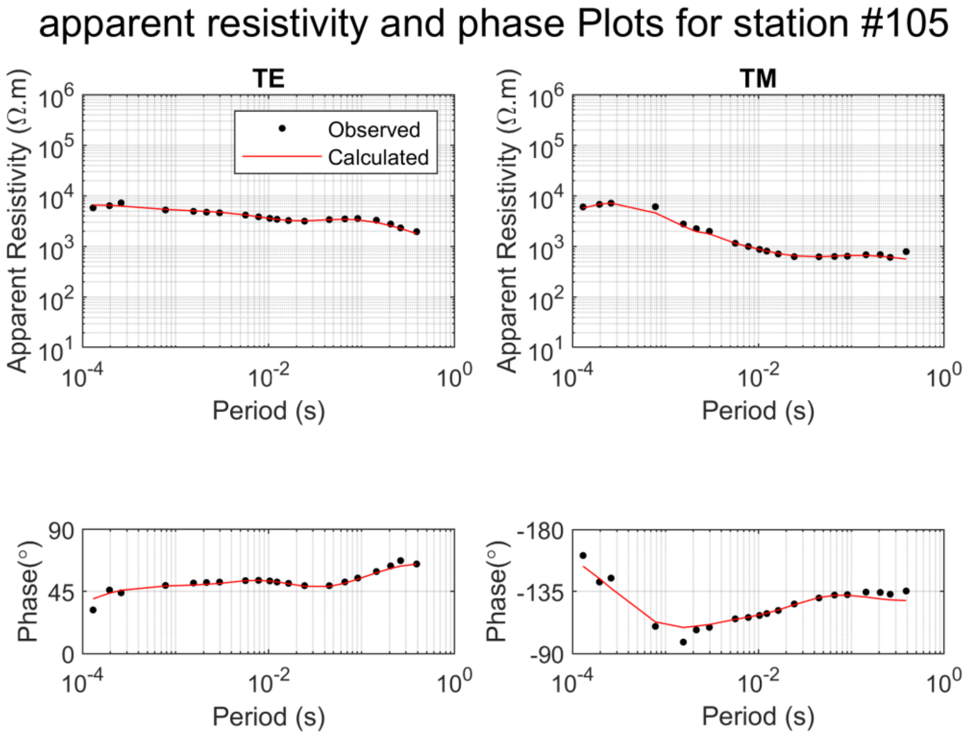
apparent resistivity and phase Plots for station #105
TE
TM
Observed
Calculated
Apparent Resistivity (Ω.m)
Phase(°)
Period (s)
90
45
0
-180
-135
-90

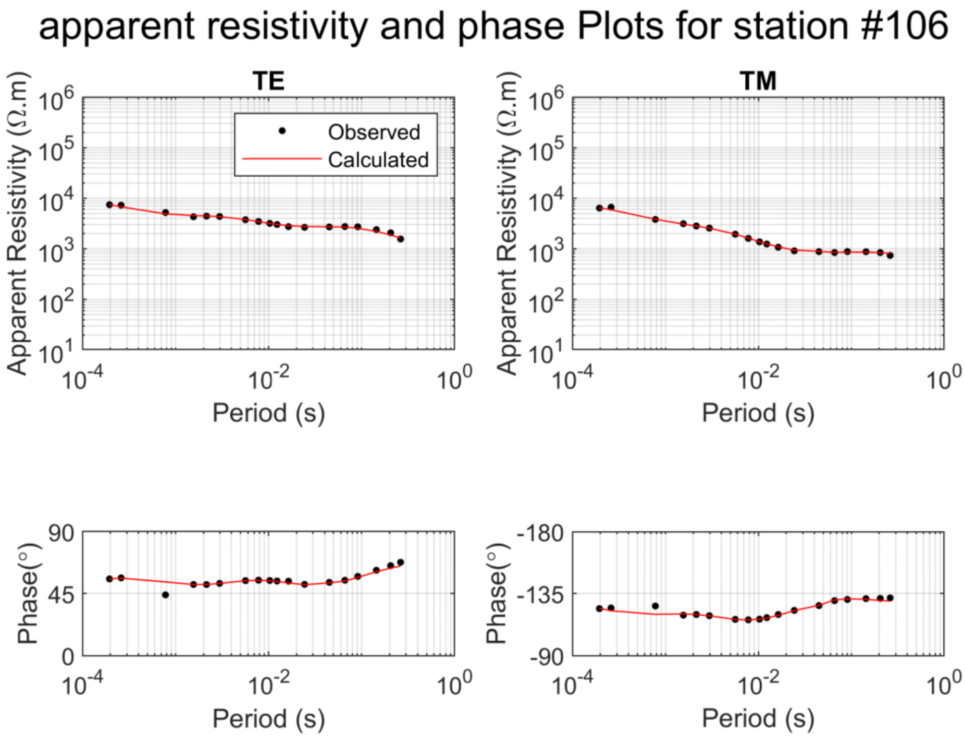
apparent resistivity and phase Plots for station #106
TE
TM
Observed
Calculated
Apparent Resistivity (Ω.m)
Phase(°)
Period (s)
90
45
0
-180
-135
-90

apparent resistivity and phase Plots for station #107

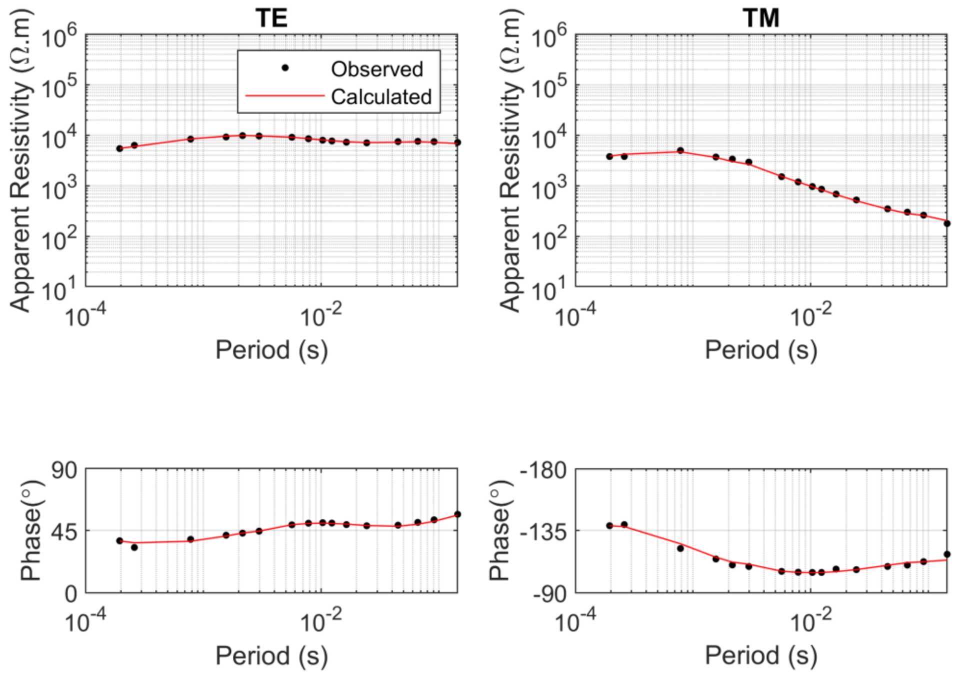

apparent resistivity and phase Plots for station #108

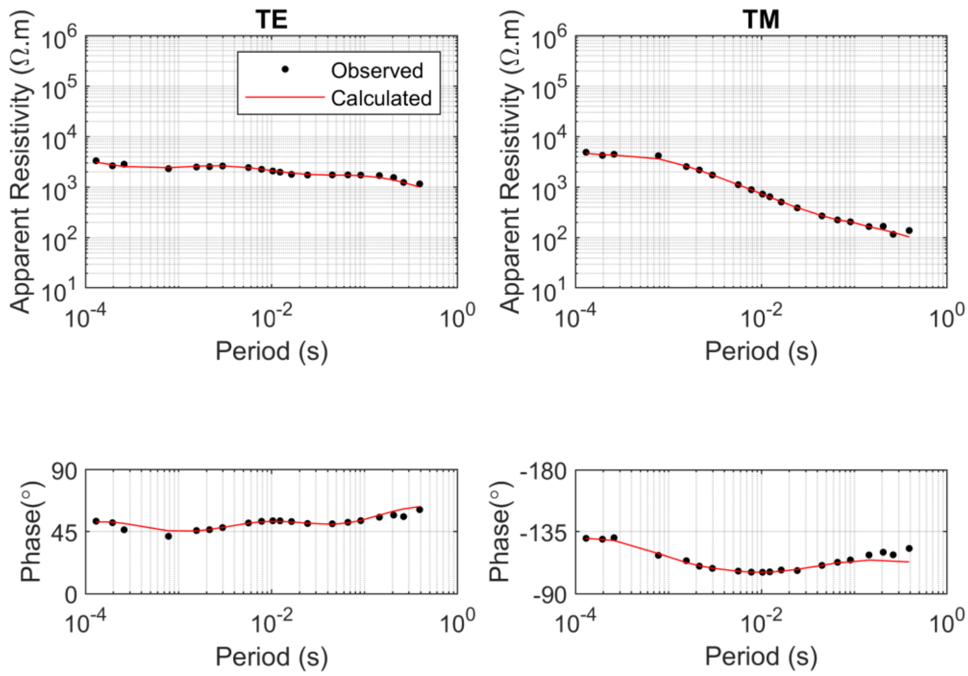

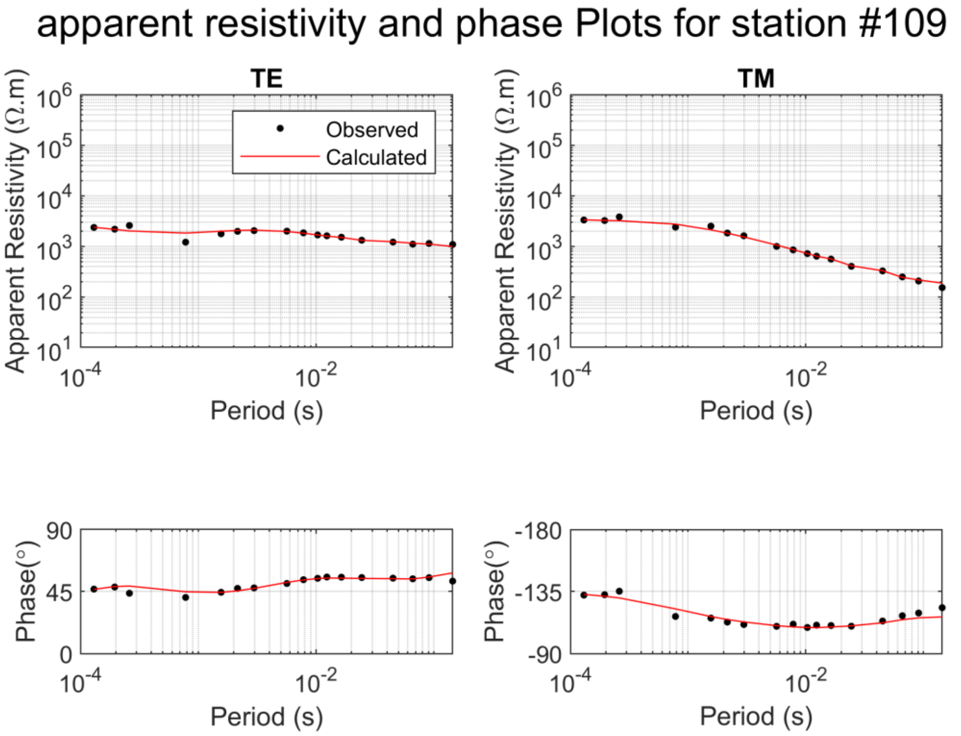
apparent resistivity and phase Plots for station #109
TE
TM
Observed
Calculated
Apparent Resistivity (Ω.m)
Phase(°)
Period (s)

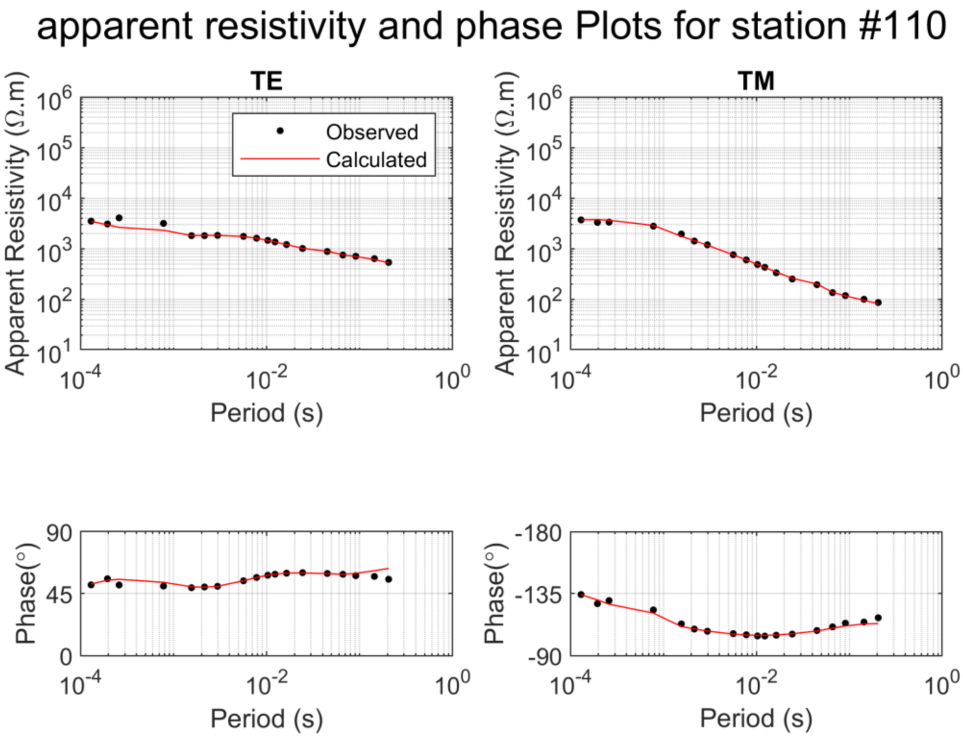
apparent resistivity and phase Plots for station #110
TE
TM
Observed
Calculated
Apparent Resistivity (Ω.m)
Phase(°)
Period (s)

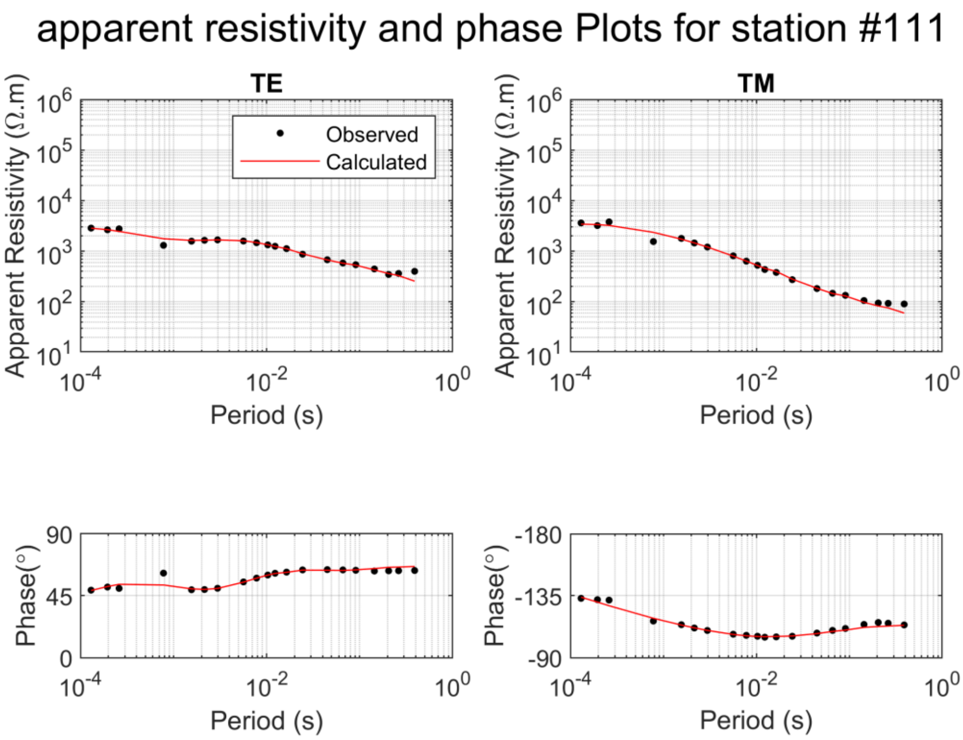

apparent resistivity and phase Plots for station #111
TE
TM
Observed
Calculated
Apparent Resistivity (Ω.m)
Period (s)
Phase(°)

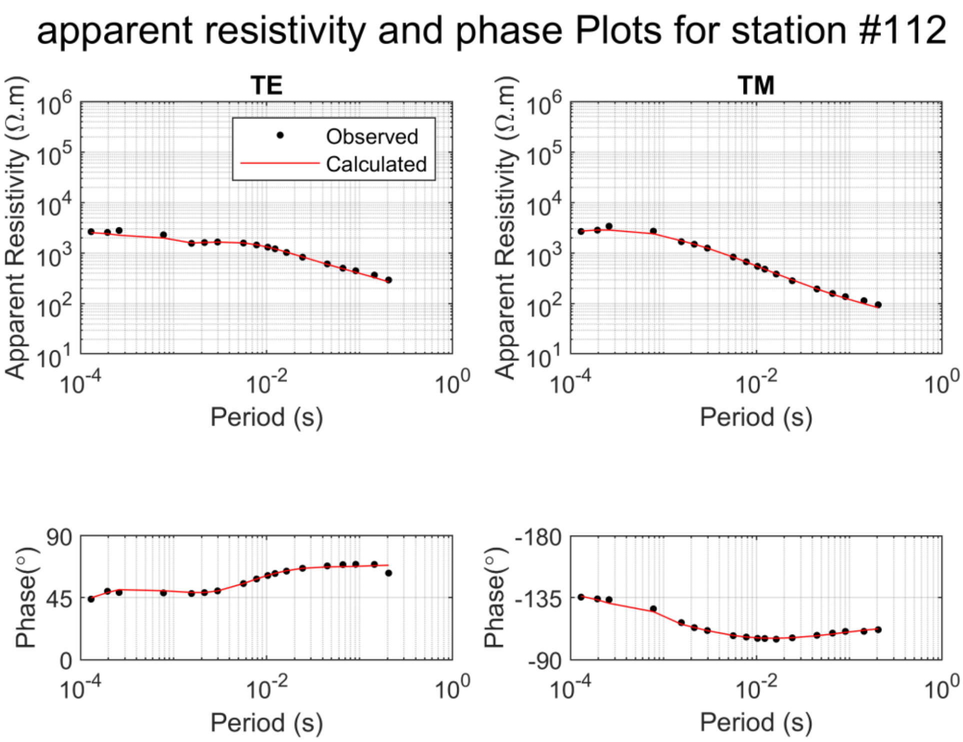

apparent resistivity and phase Plots for station #112
TE
TM
Observed
Calculated
Apparent Resistivity (Ω.m)
Period (s)
Phase(°)

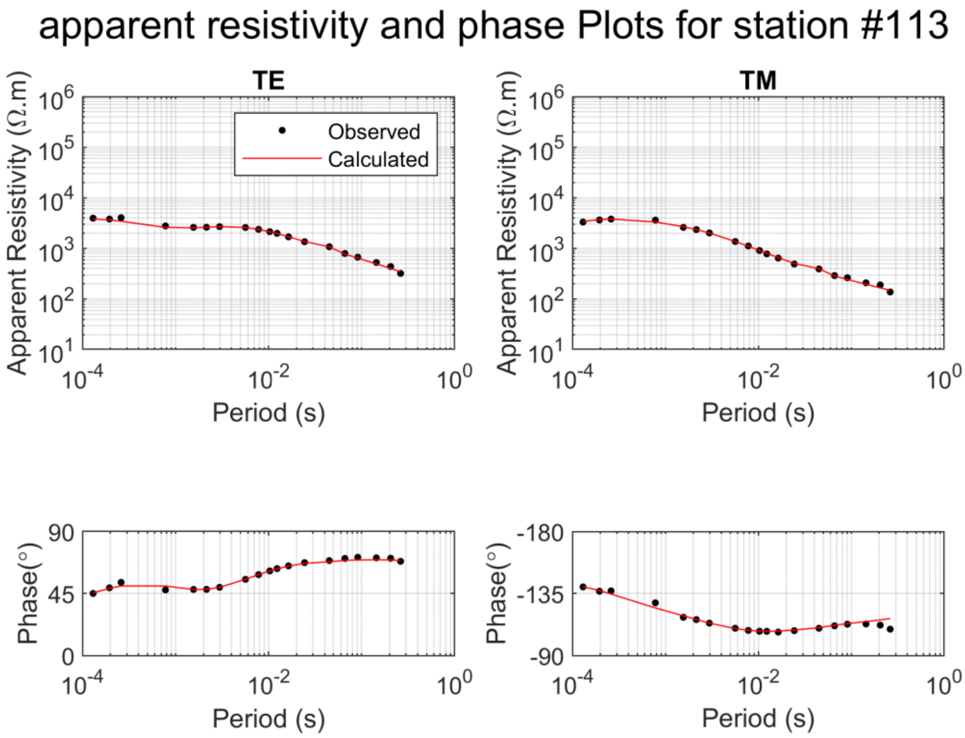
apparent resistivity and phase Plots for station #113
TE
TM
Observed
Calculated
Apparent Resistivity (Ω.m)
Period (s)
Phase(°)
10^6
10^5
10^4
10^3
10^2
10^1
10^-4
10^-2
10^0
90
45
0
-180
-135
-90

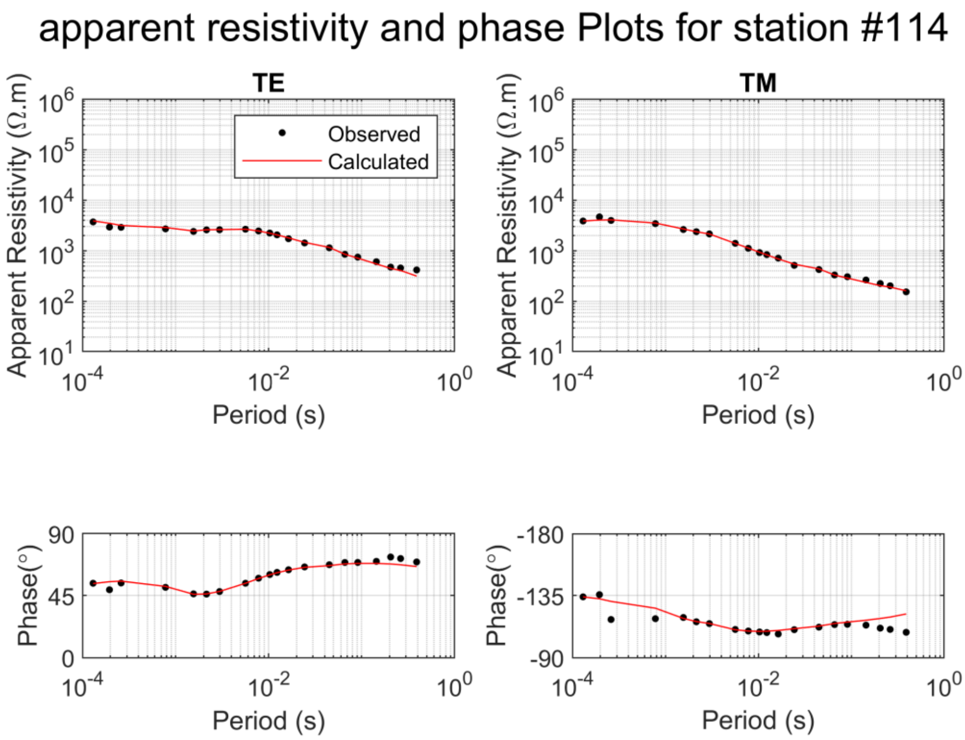
apparent resistivity and phase Plots for station #114
TE
TM
Observed
Calculated
Apparent Resistivity (Ω.m)
Period (s)
Phase(°)
10^6
10^5
10^4
10^3
10^2
10^1
10^-4
10^-2
10^0
90
45
0
-180
-135
-90

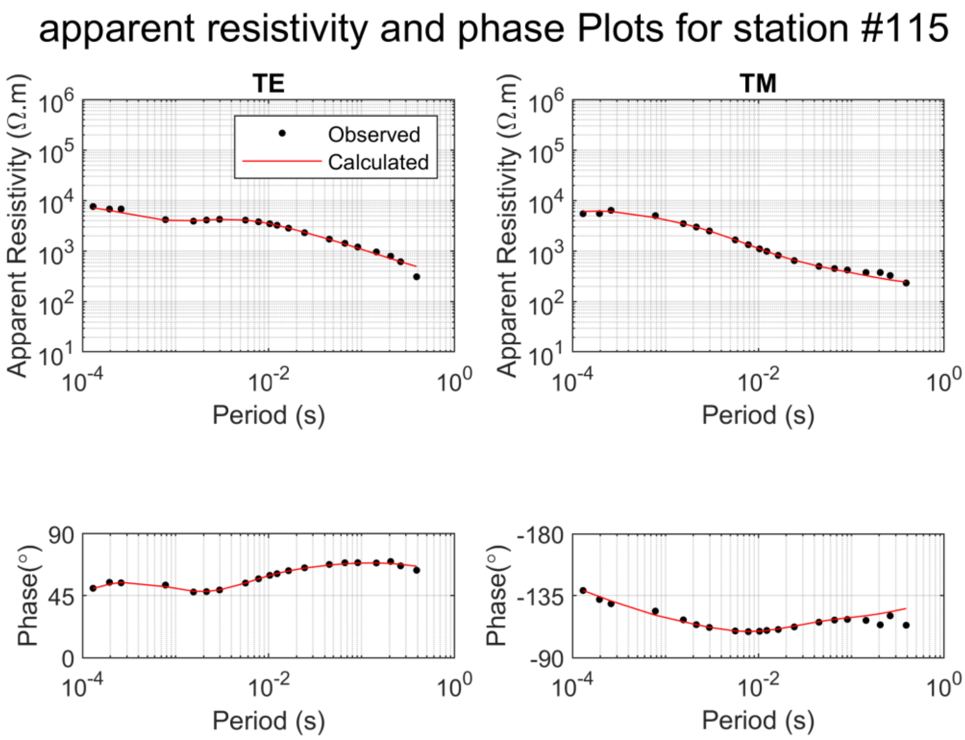
apparent resistivity and phase Plots for station #115
TE
TM
Observed
Calculated
Apparent Resistivity (Ω.m)
Period (s)
Phase(°)

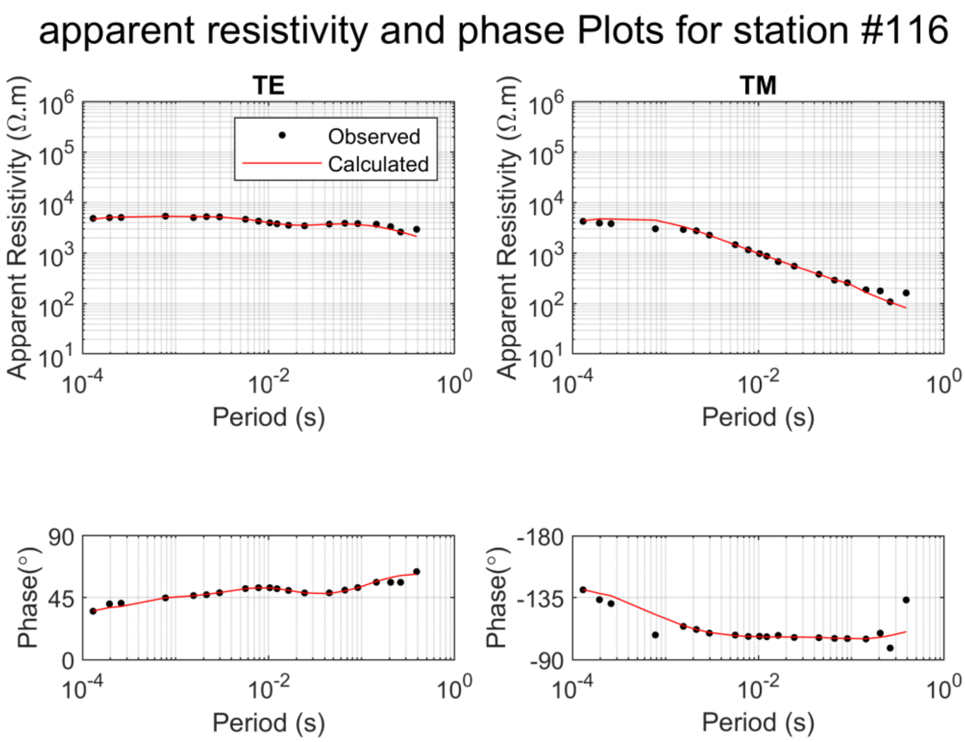
apparent resistivity and phase Plots for station #116
TE
TM
Observed
Calculated
Apparent Resistivity (Ω.m)
Period (s)
Phase(°)

apparent resistivity and phase Plots for station #117

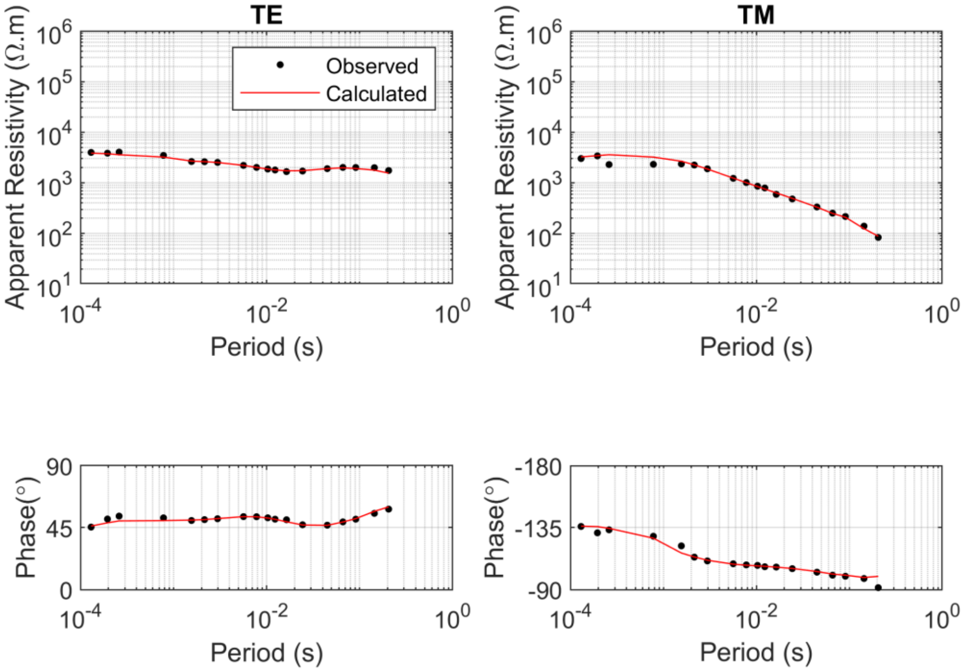

apparent resistivity and phase Plots for station #118

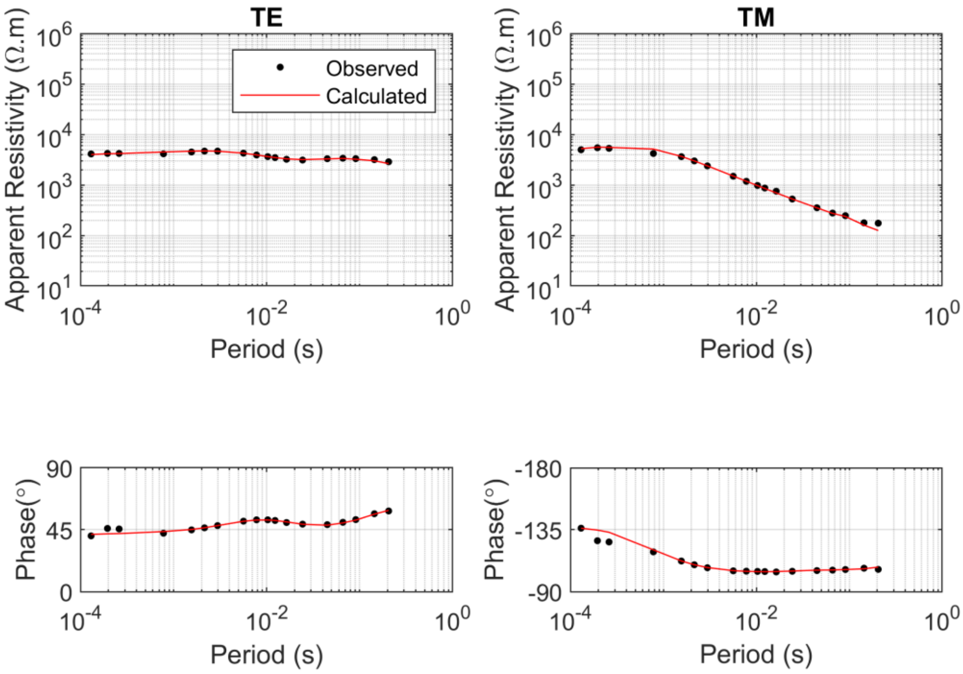

apparent resistivity and phase Plots for station #119

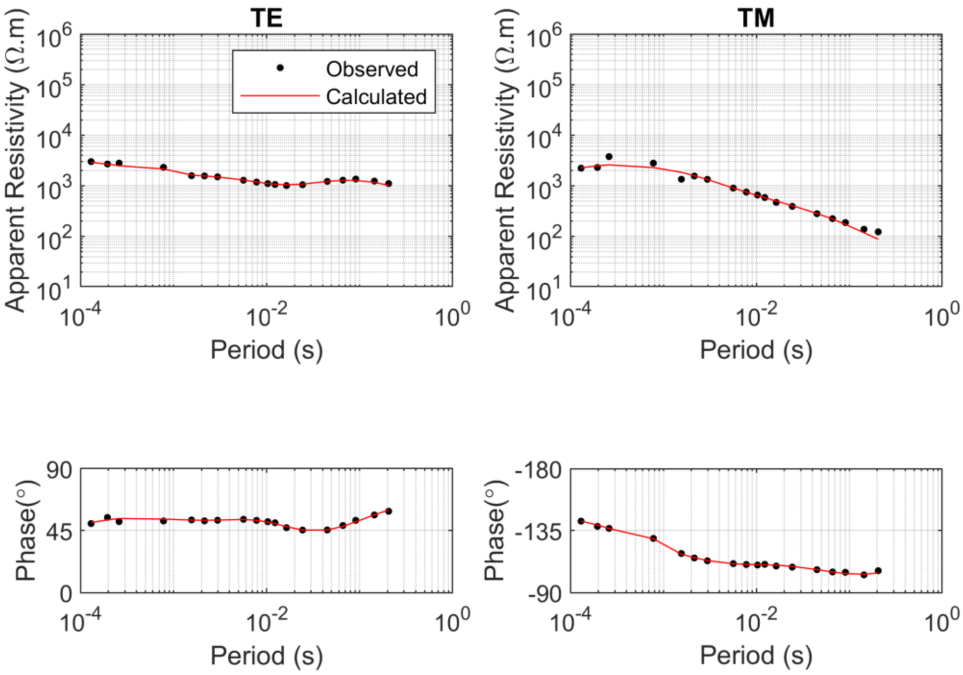

apparent resistivity and phase Plots for station #120

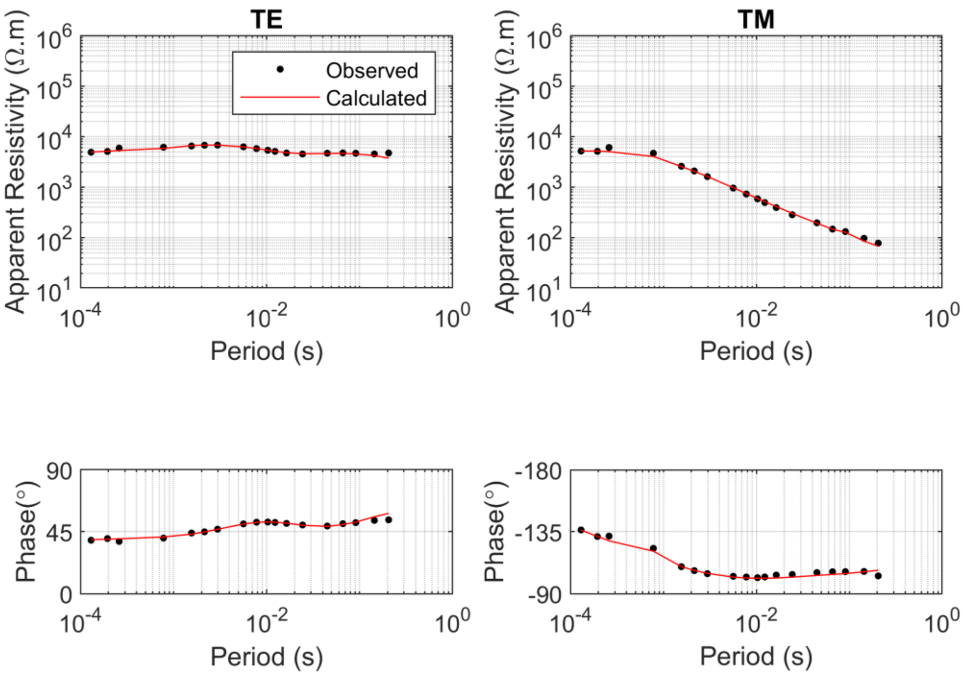

apparent resistivity and phase Plots for station #121

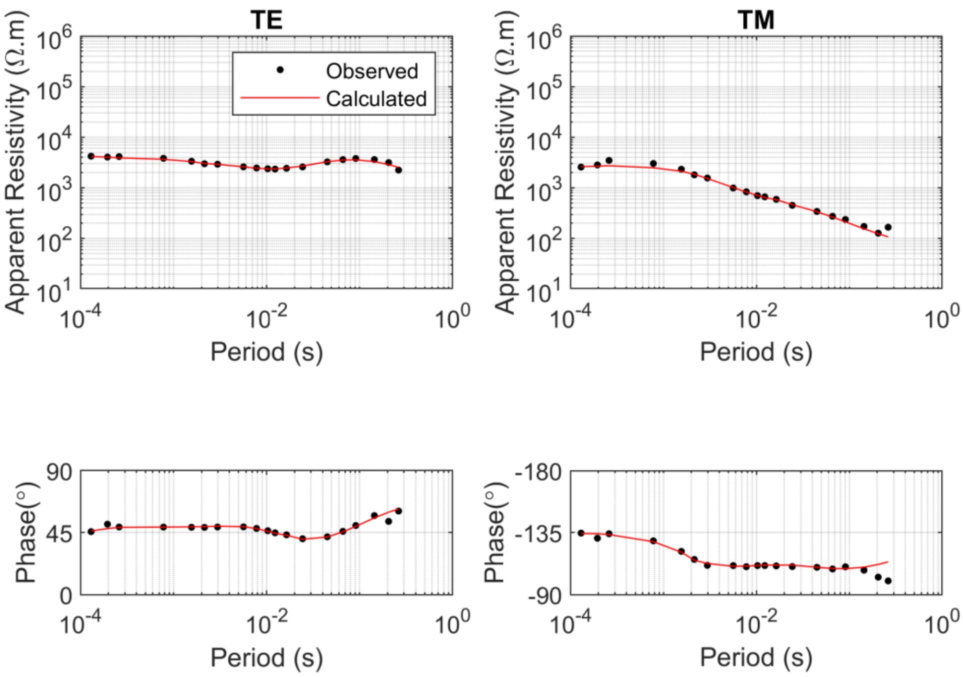

apparent resistivity and phase Plots for station #122

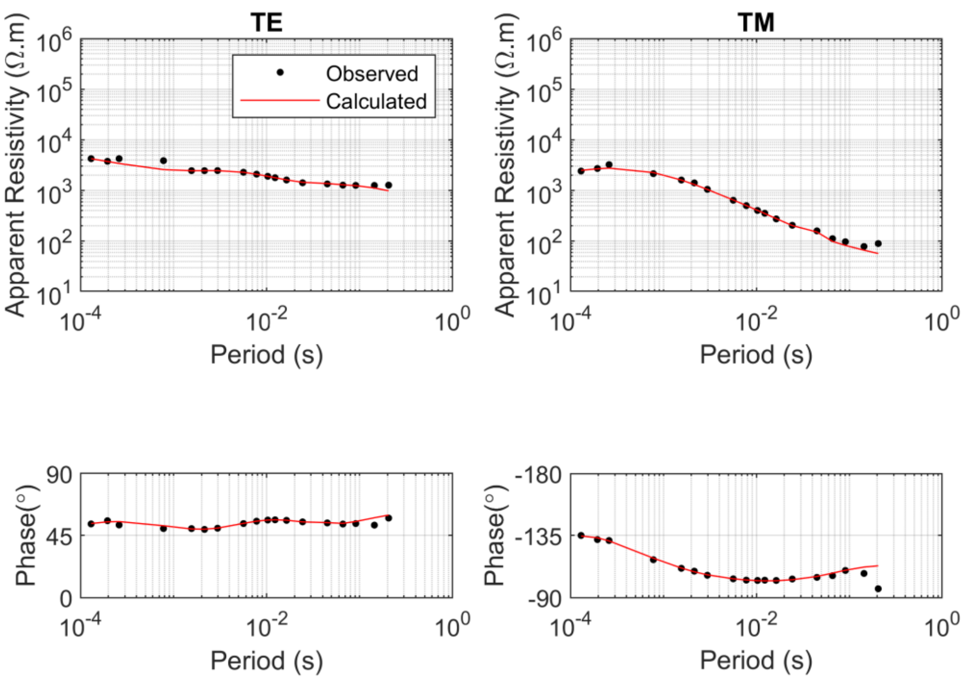

apparent resistivity and phase Plots for station #123

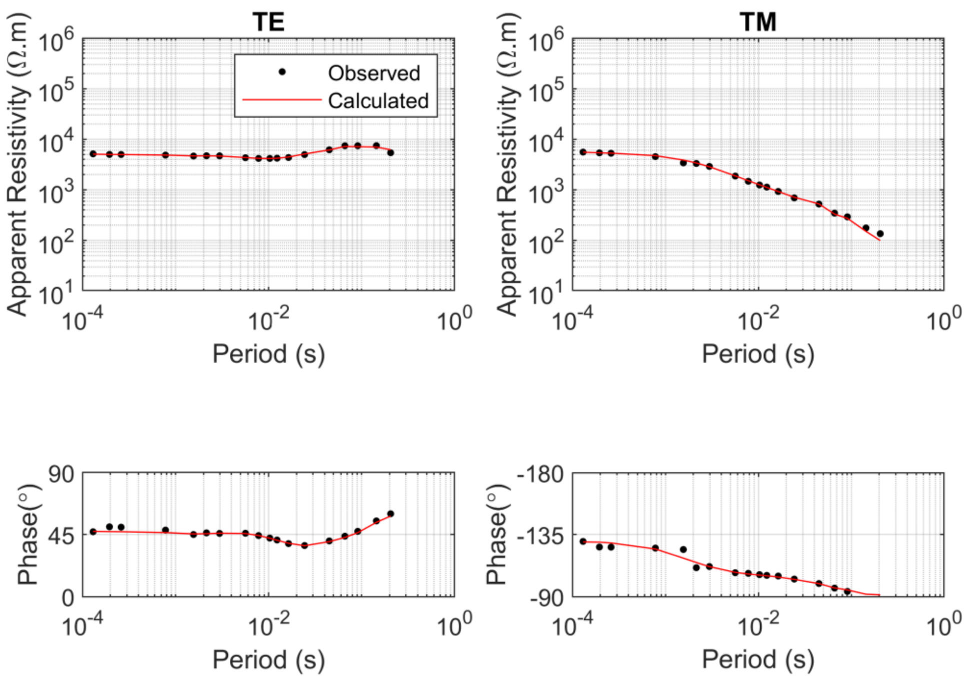

apparent resistivity and phase Plots for station #124

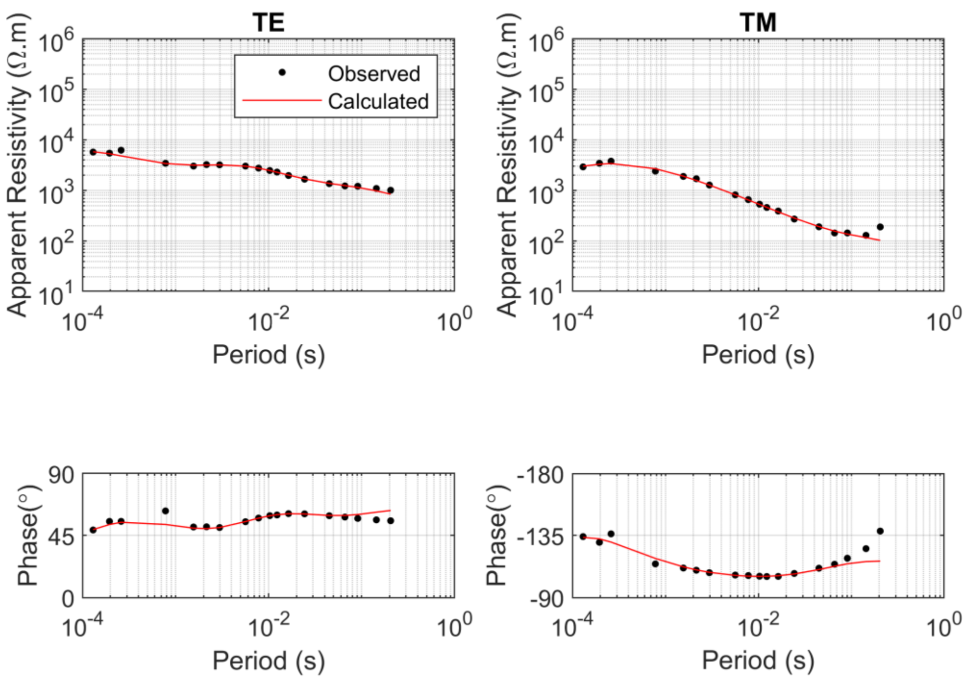

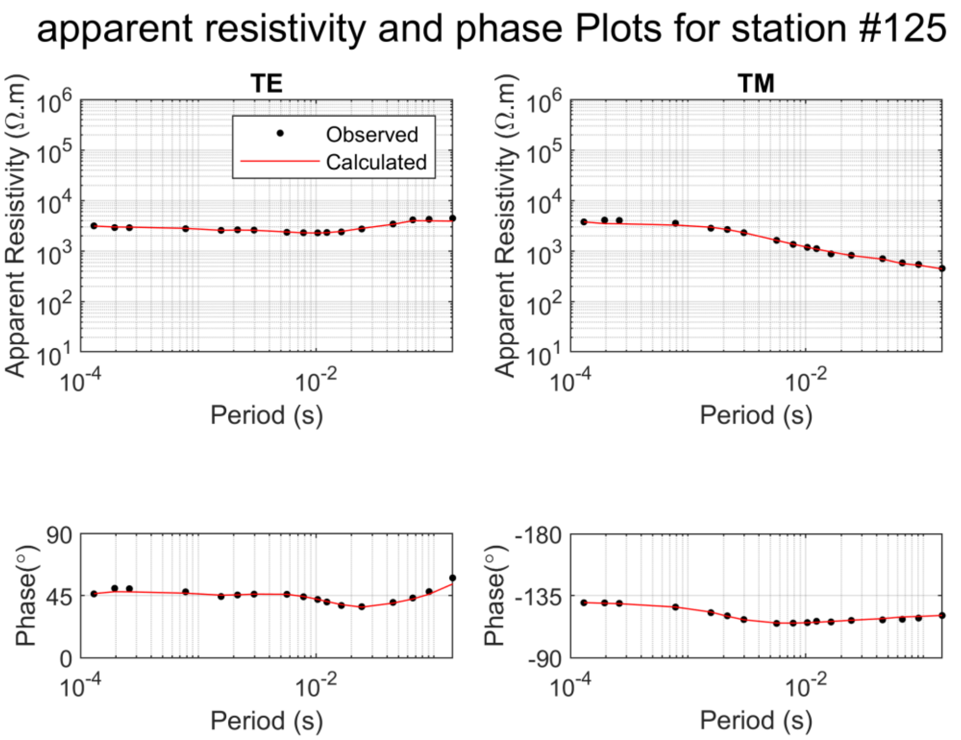
apparent resistivity and phase Plots for station #125
TE
TM
Observed
Calculated
Apparent Resistivity (Ω.m)
Period (s)
Phase(°)

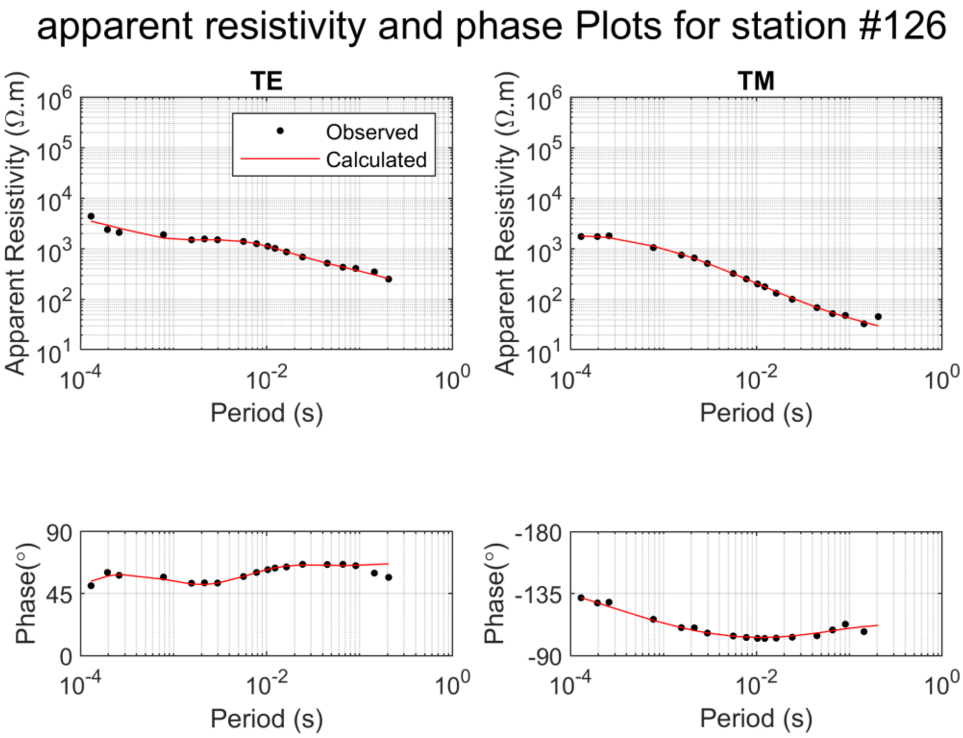
apparent resistivity and phase Plots for station #126
TE
TM
Observed
Calculated
Apparent Resistivity (Ω.m)
Period (s)
Phase(°)

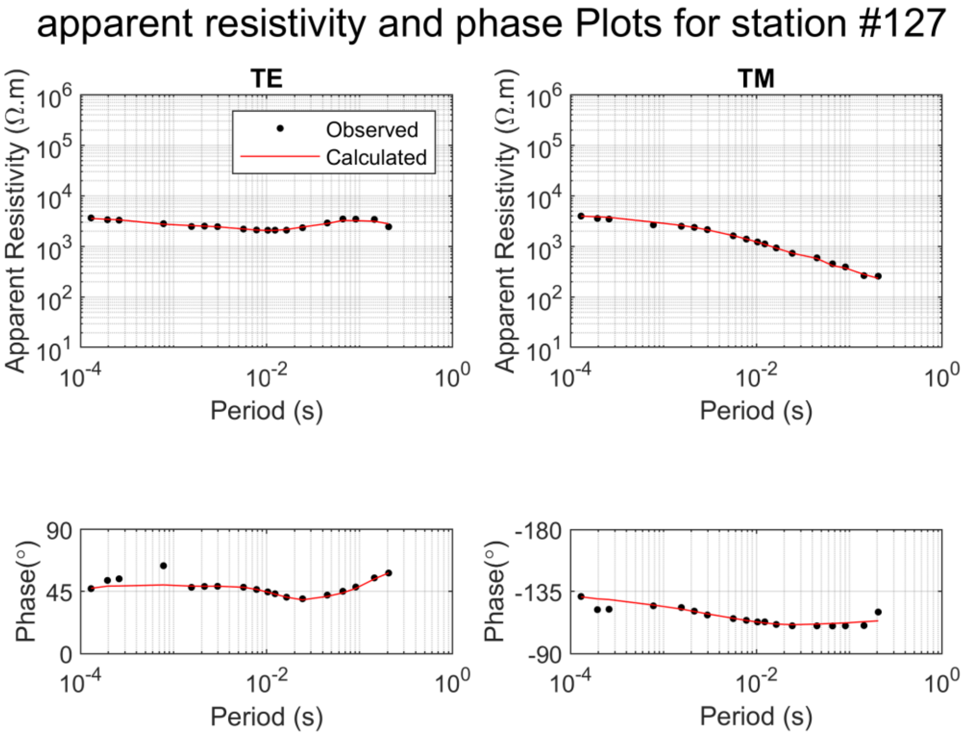
apparent resistivity and phase Plots for station #127
TE
TM
Observed
Calculated
Apparent Resistivity (Ω.m)
Period (s)
Phase(°)

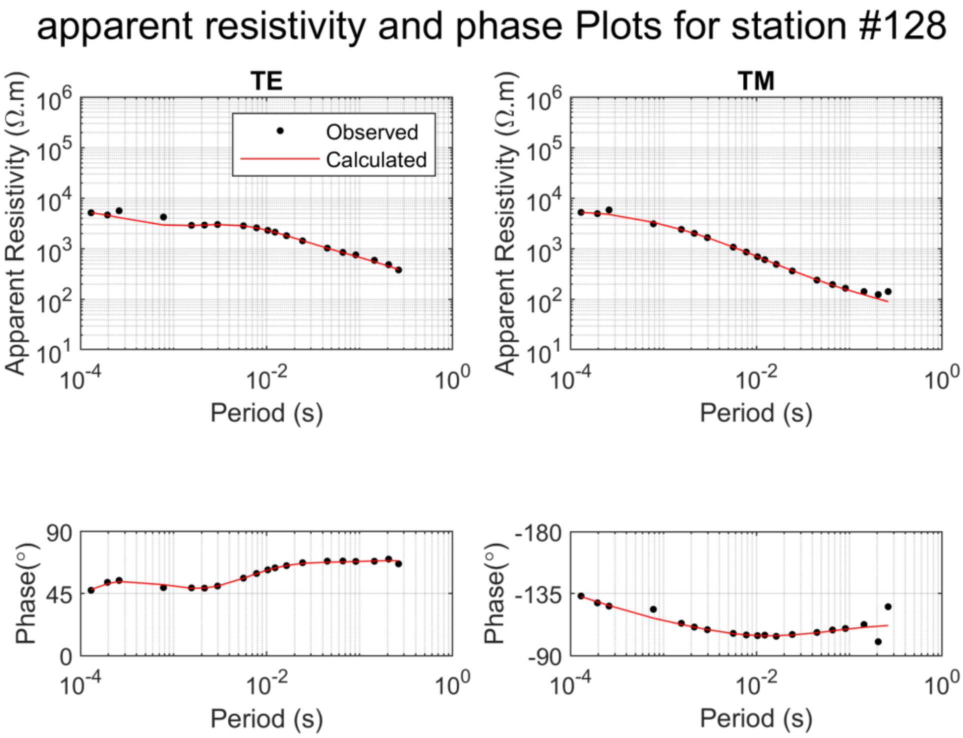
apparent resistivity and phase Plots for station #128
TE
TM
Observed
Calculated
Apparent Resistivity (Ω.m)
Period (s)
Phase(°)

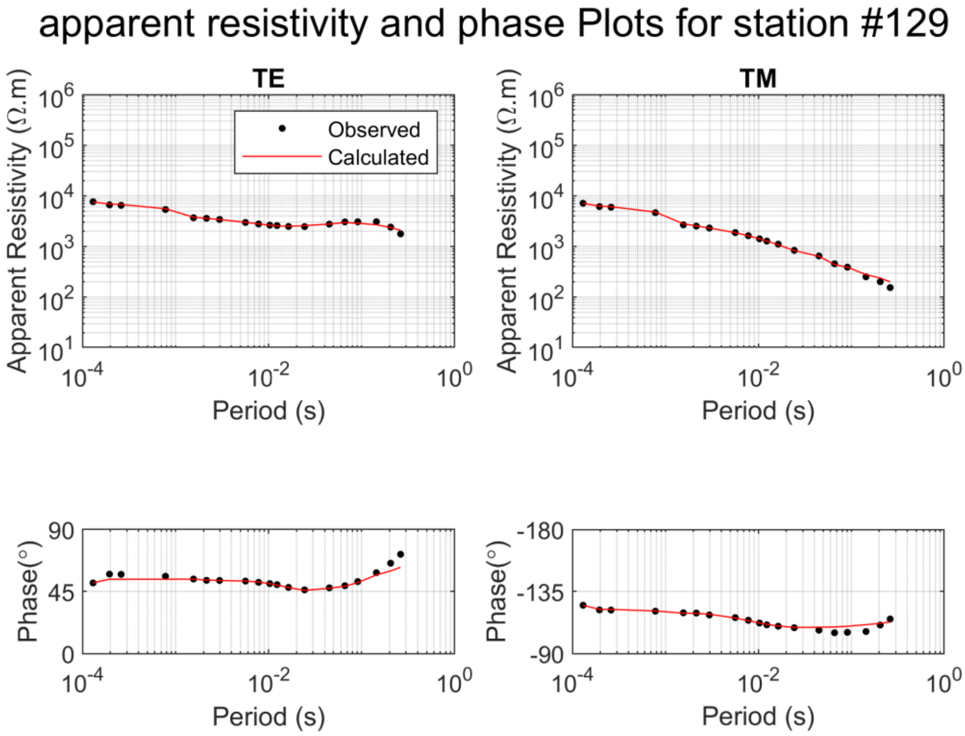
apparent resistivity and phase Plots for station #129
TE
TM
Observed
Calculated
Apparent Resistivity (Ω.m)
Phase(°)
Period (s)

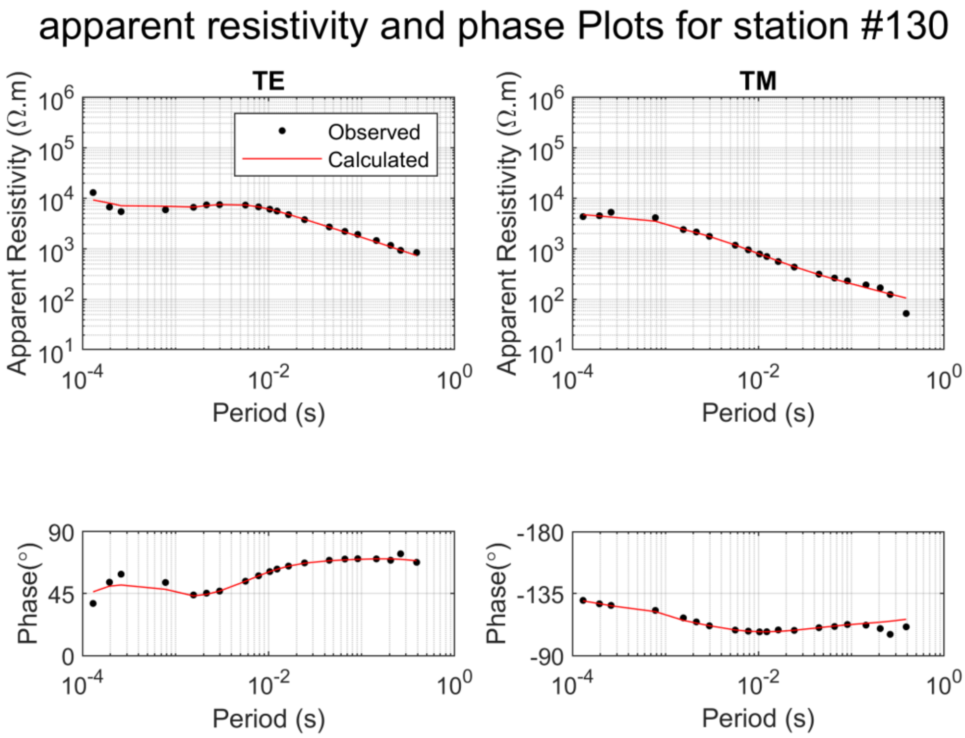
apparent resistivity and phase Plots for station #130
TE
TM
Observed
Calculated
Apparent Resistivity (Ω.m)
Phase(°)
Period (s)

apparent resistivity and phase Plots for station #131

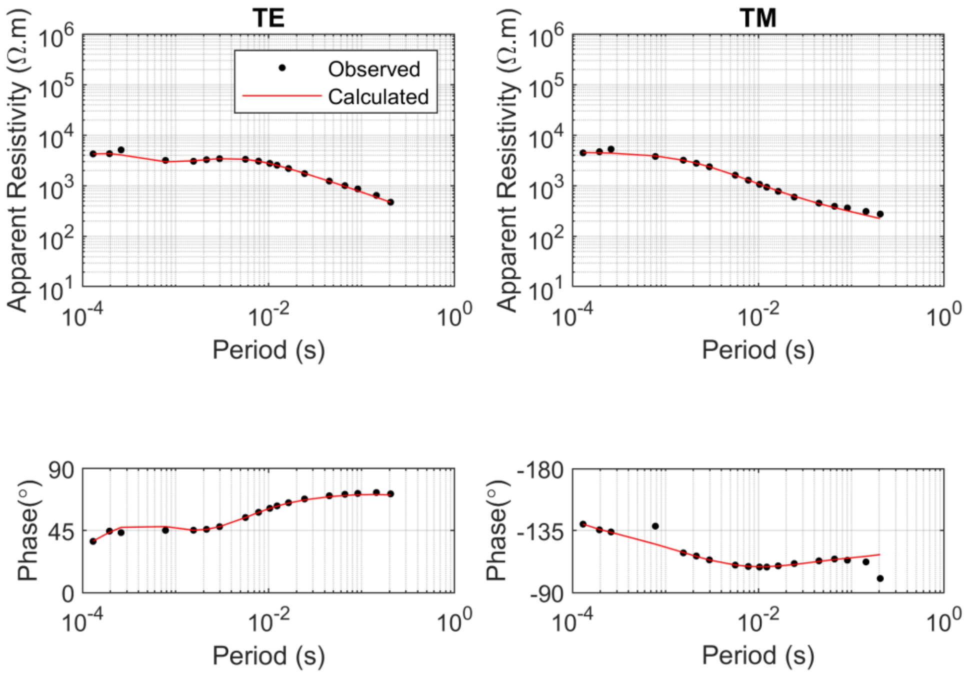

apparent resistivity and phase Plots for station #132

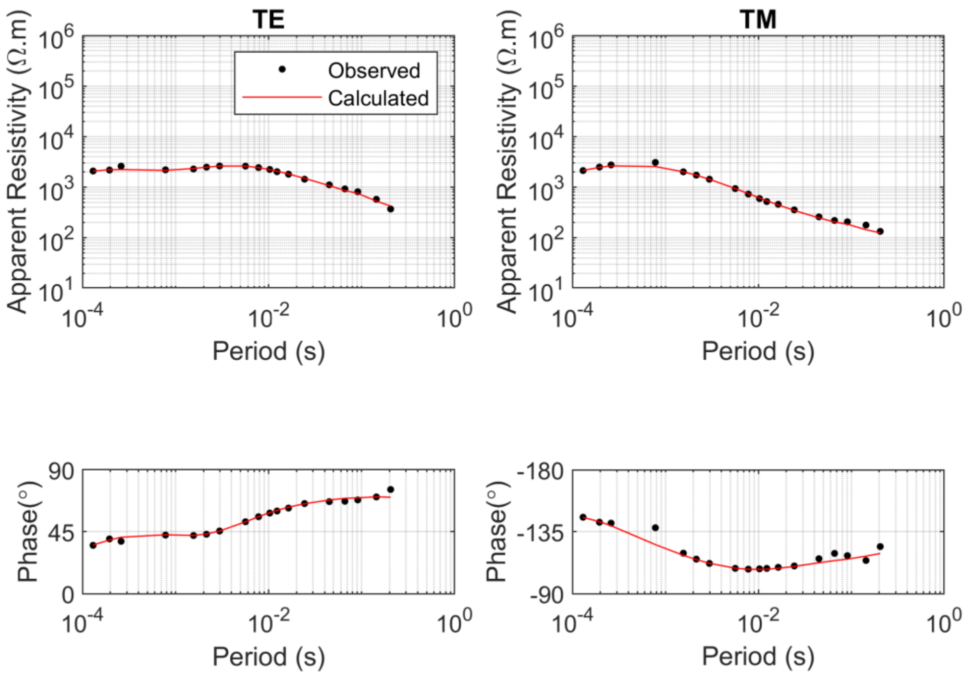

Appendix E – Fit Plots of Impedances, Apparent Resistivities and Phases for Inversion with 3% Uncertainties

E.1. Fit Plots of Impedances

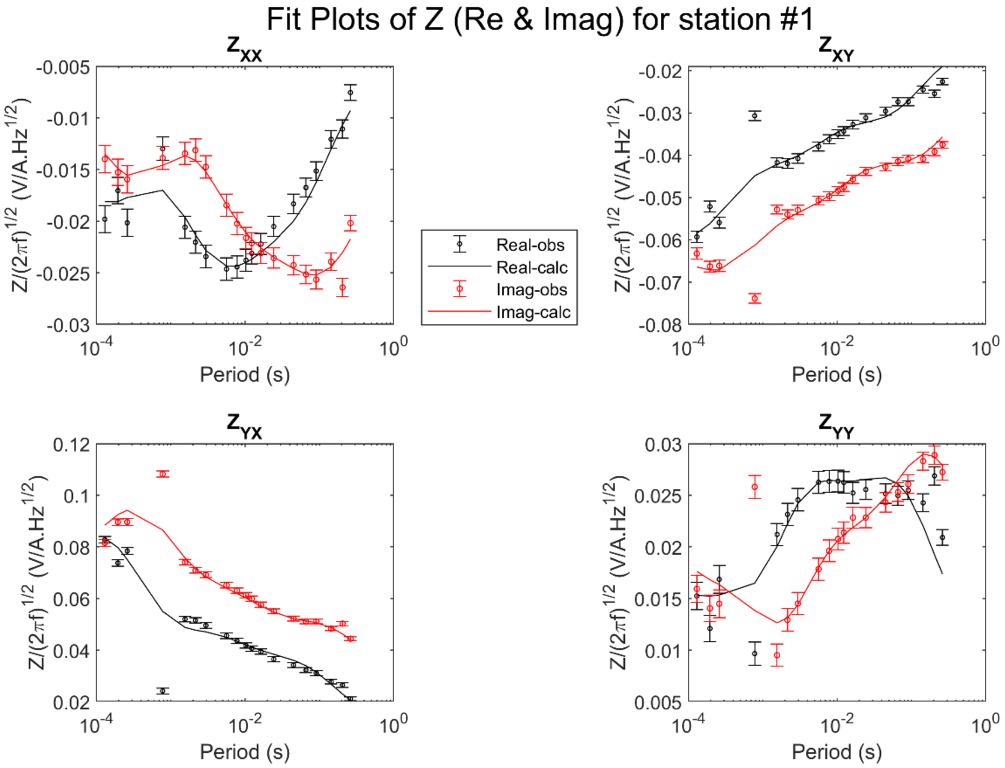

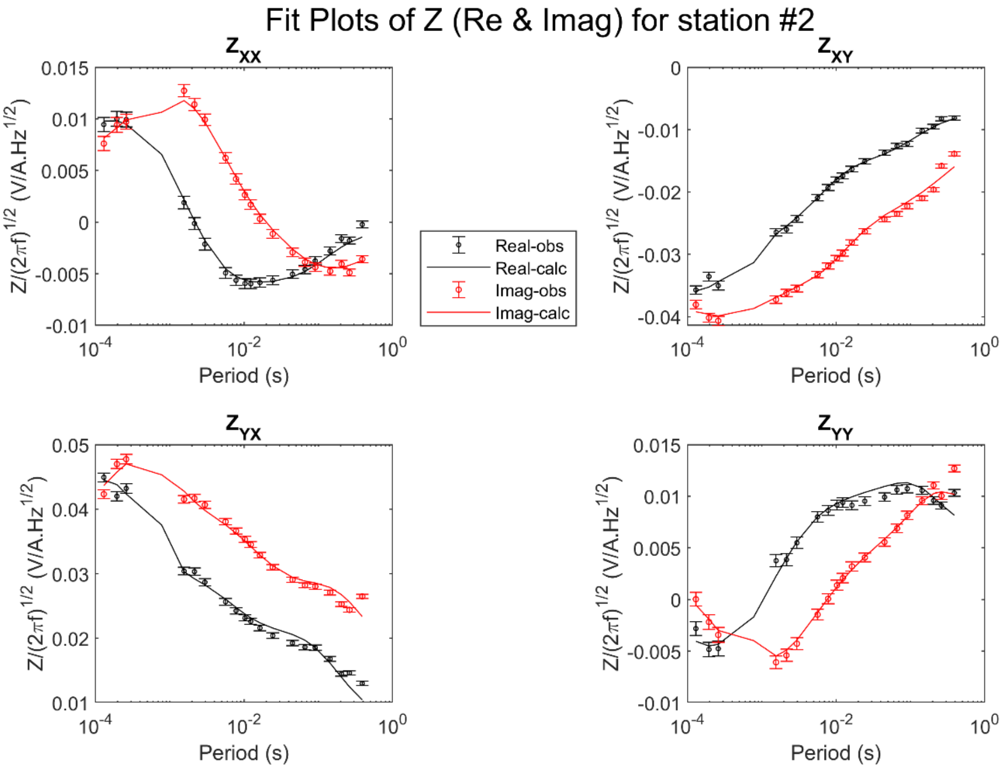
Fit Plots of Z (Re & Imag) for station #2
Z_{XX}
Z_{XY}
Z_{YX}
Z_{YY}
$Z/(2\pi f)^{1/2}$ (V/A.Hz$^{1/2}$)
Period (s)
Real-obs
Real-calc
Imag-obs
Imag-calc

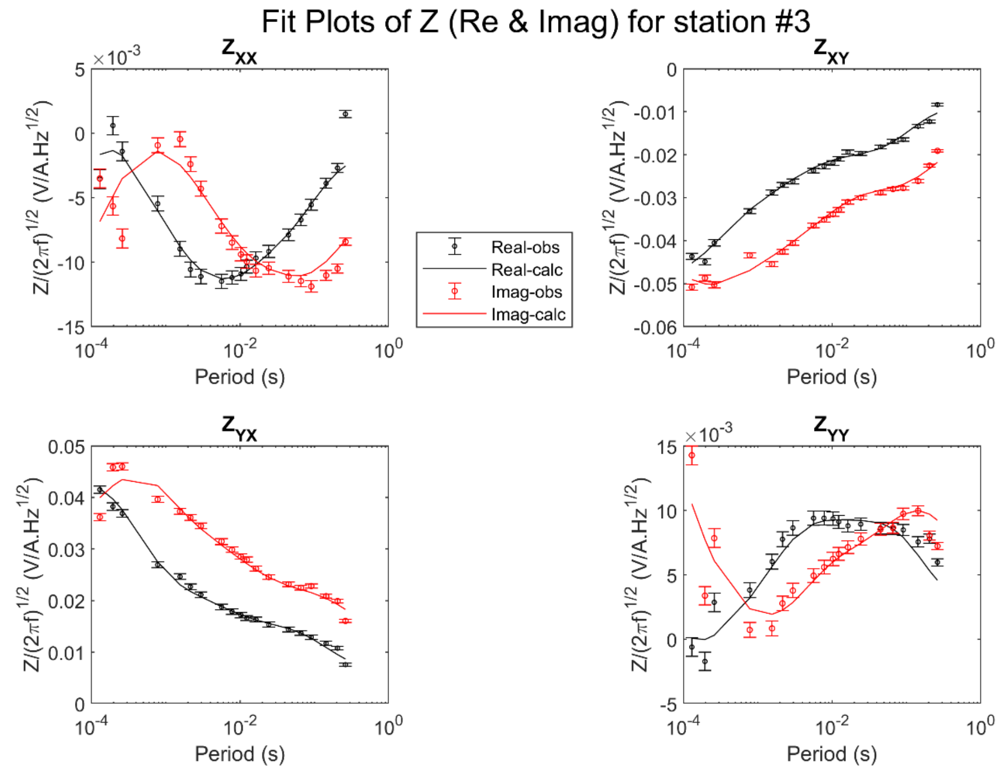
Fit Plots of Z (Re & Imag) for station #3
Z_{XX}
Z_{XY}
Z_{YX}
Z_{YY}
$\times 10^{-3}$
$Z/(2\pi f)^{1/2}$ (V/A.Hz$^{1/2}$)
Period (s)
Real-obs
Real-calc
Imag-obs
Imag-calc

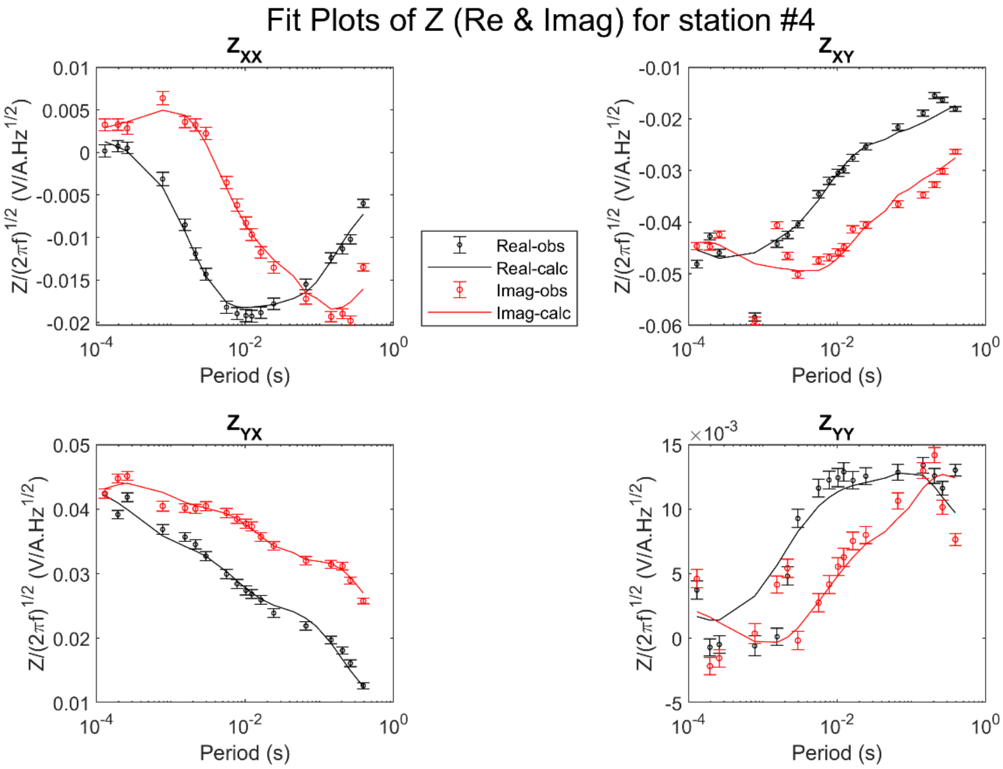
Fit Plots of Z (Re & Imag) for station #4
Z_{XX}
Z_{XY}
Z_{YX}
Z_{YY}
$Z/(2\pi f)^{1/2}$ (V/A.Hz$^{1/2}$)
Period (s)
Real-obs
Real-calc
Imag-obs
Imag-calc
$\times 10^{-3}$

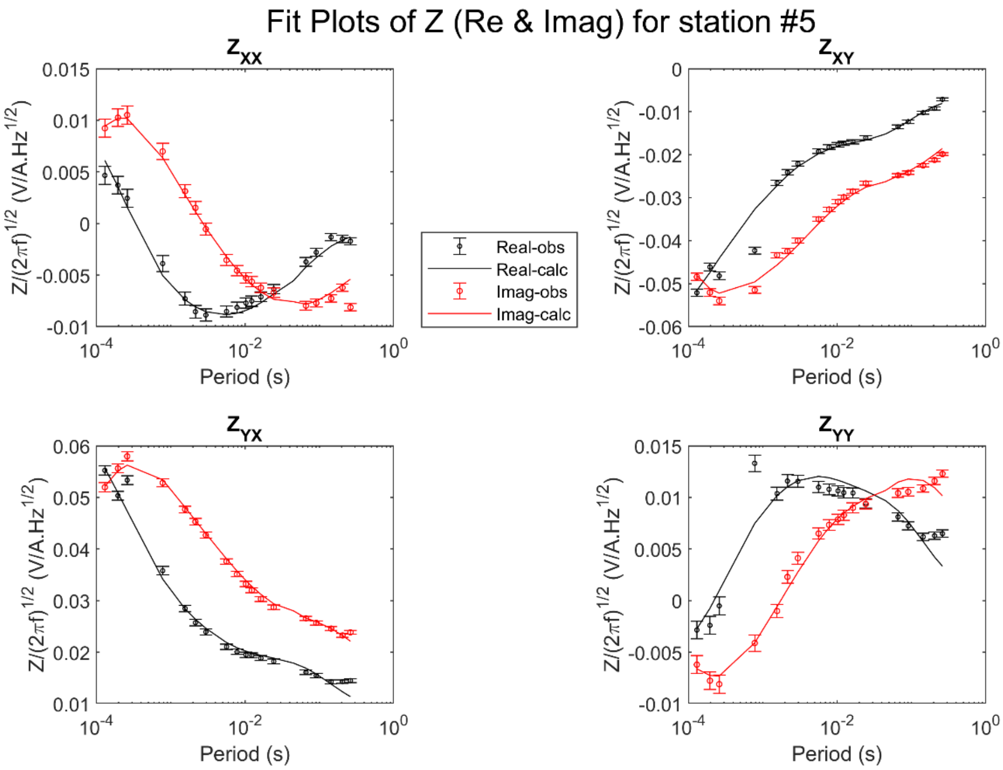
Fit Plots of Z (Re & Imag) for station #5
Z_{XX}
Z_{XY}
Z_{YX}
Z_{YY}
$Z/(2\pi f)^{1/2}$ (V/A.Hz$^{1/2}$)
Period (s)
Real-obs
Real-calc
Imag-obs
Imag-calc

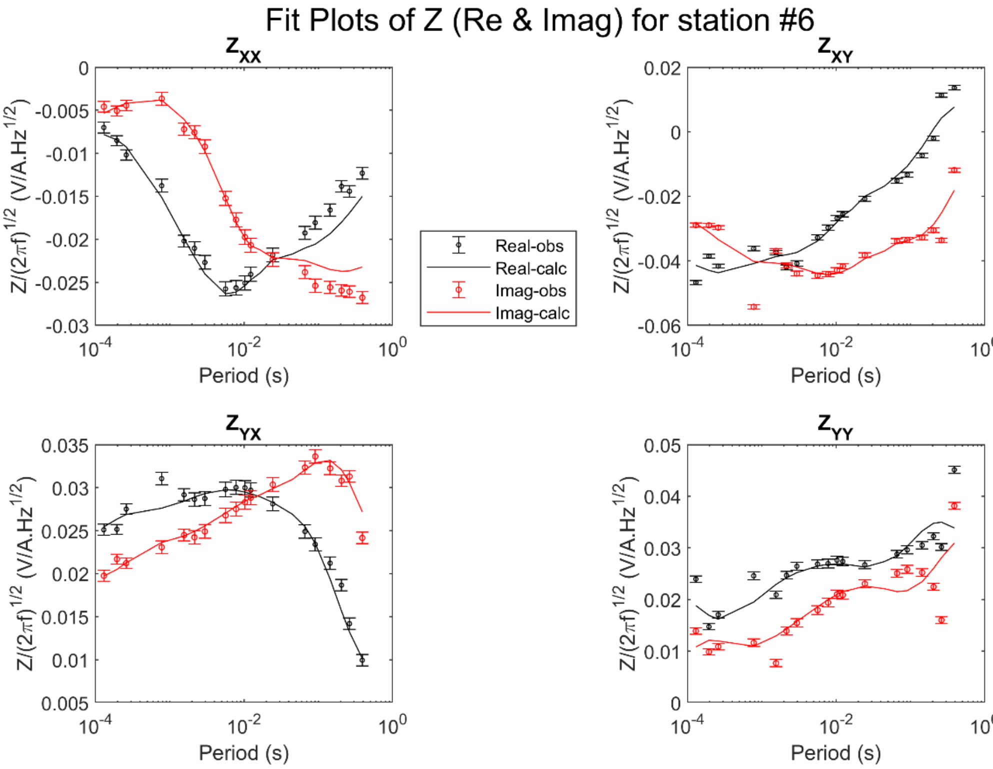
Fit Plots of Z (Re & Imag) for station #6
Z_{XX}
Z_{XY}
Z_{YX}
Z_{YY}
$Z/(2\pi f)^{1/2}$ (V/A.Hz$^{1/2}$)
Period (s)
Real-obs
Real-calc
Imag-obs
Imag-calc

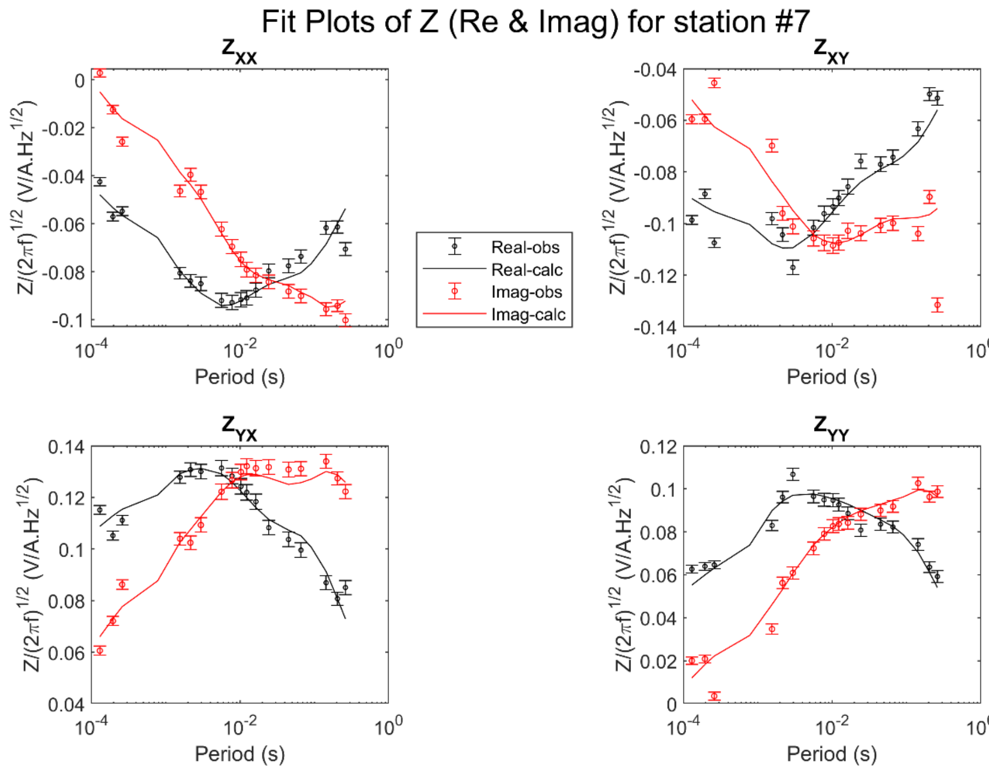
Fit Plots of Z (Re & Imag) for station #7
Z_{XX}
Z_{XY}
Z_{YX}
Z_{YY}
$Z/(2\pi f)^{1/2}$ (V/A.Hz$^{1/2}$)
Period (s)
Real-obs
Real-calc
Imag-obs
Imag-calc

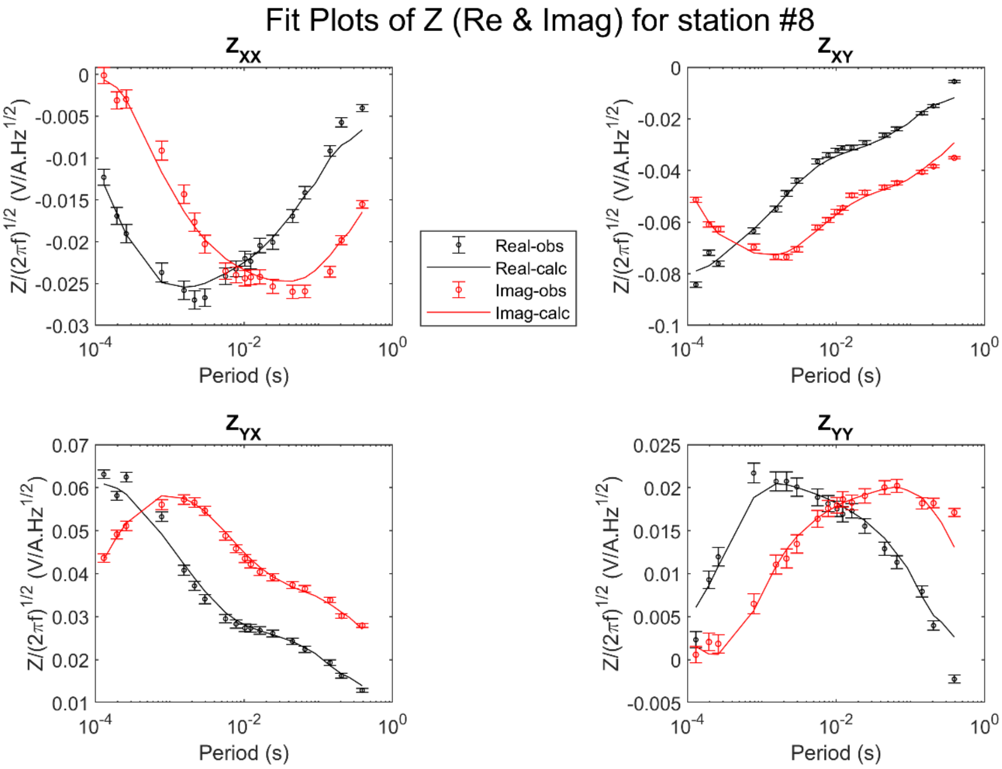
Fit Plots of Z (Re & Imag) for station #8
Z_XX
Z_XY
Z_YX
Z_YY
Z/(2πf)^1/2 (V/A.Hz^1/2)
Period (s)
Real-obs
Real-calc
Imag-obs
Imag-calc

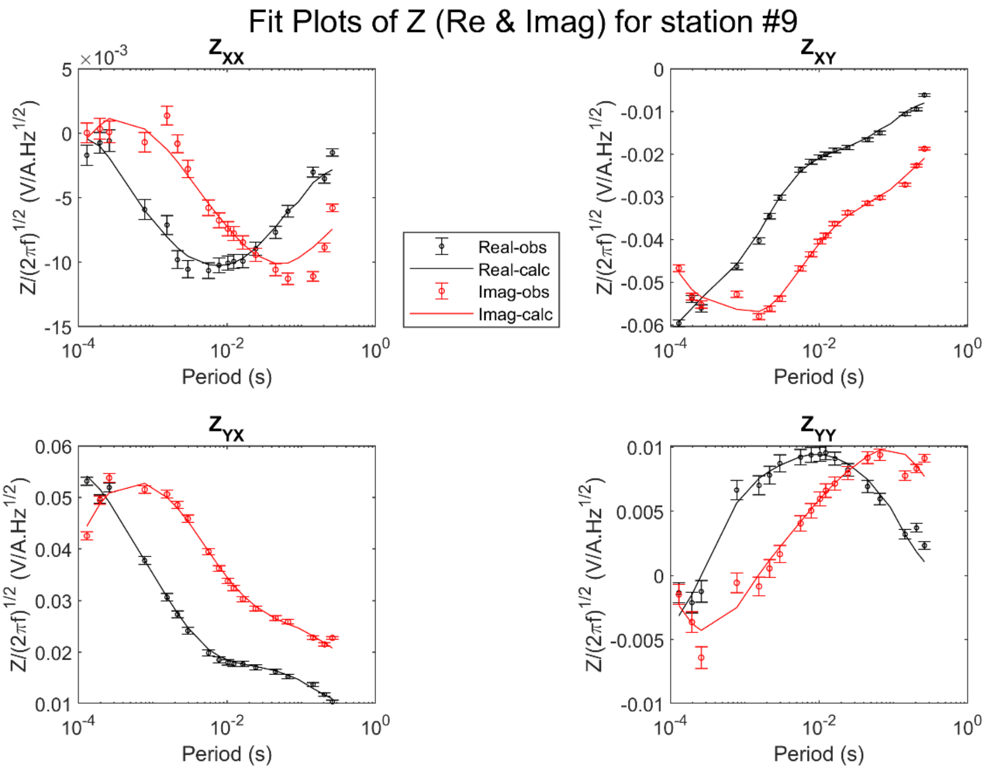
Fit Plots of Z (Re & Imag) for station #9
Z_XX
Z_XY
Z_YX
Z_YY
×10^-3
Z/(2πf)^1/2 (V/A.Hz^1/2)
Period (s)
Real-obs
Real-calc
Imag-obs
Imag-calc

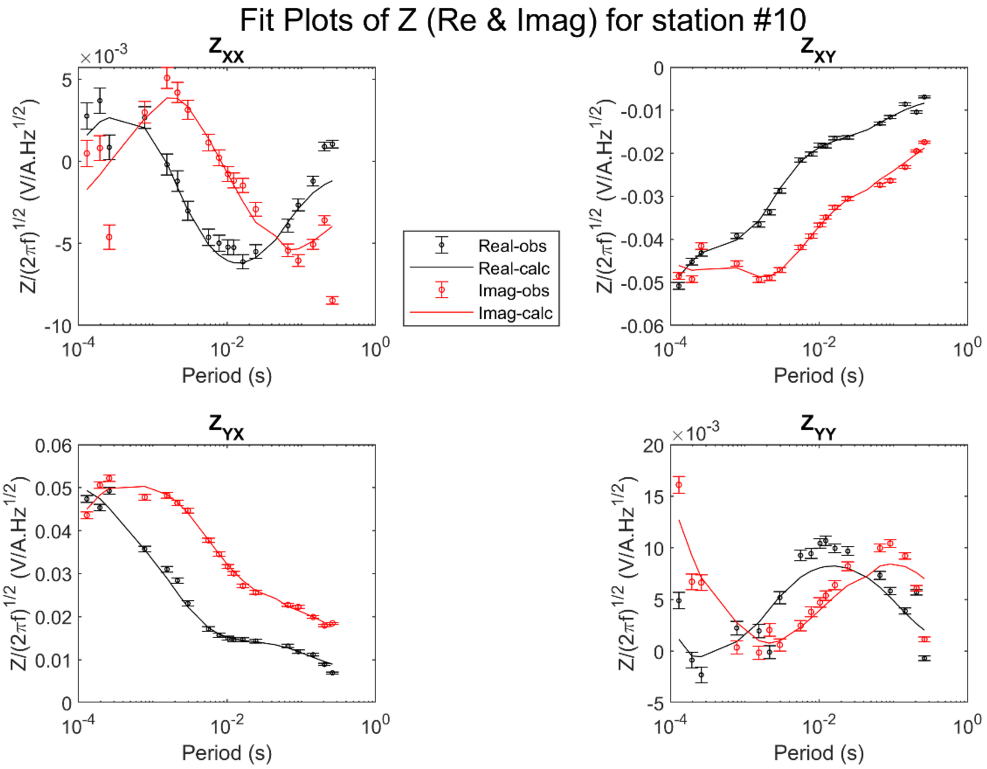
Fit Plots of Z (Re & Imag) for station #10
Z_XX
Z_XY
Z_YX
Z_YY
Z/(2πf)^1/2 (V/A.Hz^1/2)
Period (s)
Real-obs
Real-calc
Imag-obs
Imag-calc

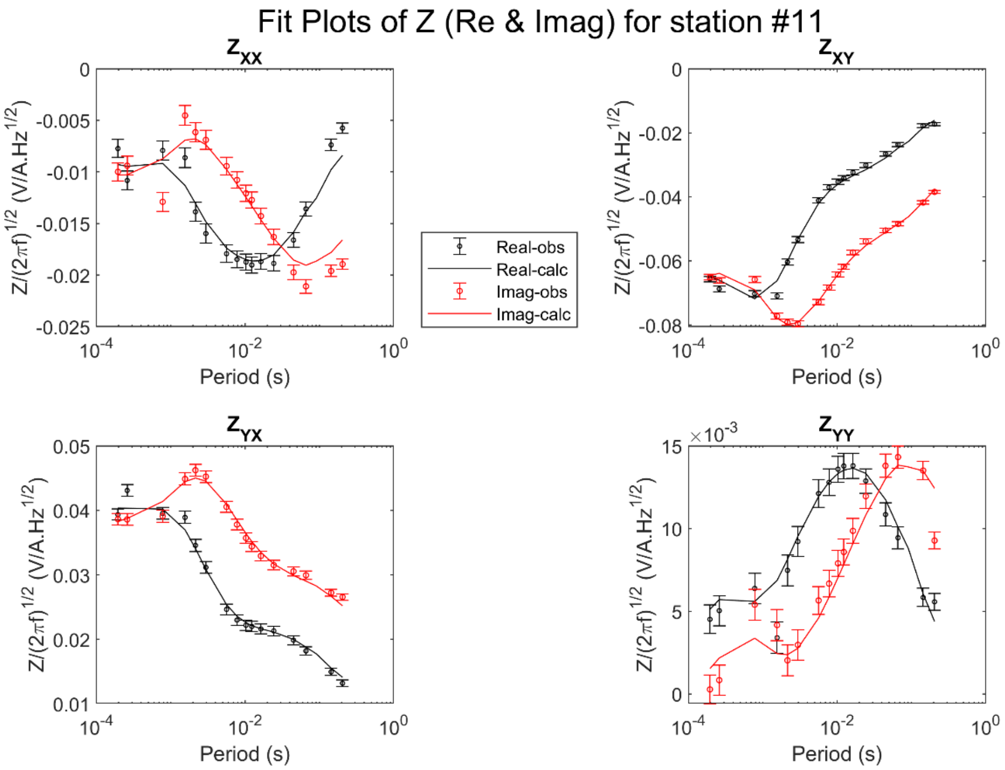
Fit Plots of Z (Re & Imag) for station #11
Z_XX
Z_XY
Z_YX
Z_YY
Z/(2πf)^1/2 (V/A.Hz^1/2)
Period (s)
Real-obs
Real-calc
Imag-obs
Imag-calc

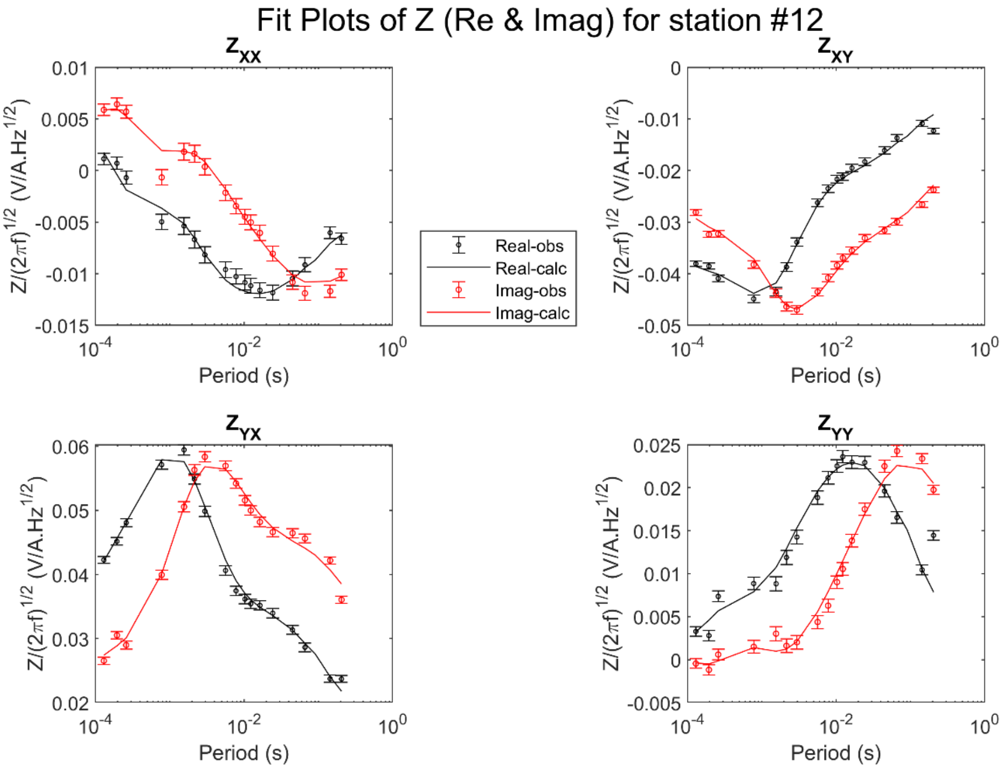

Fit Plots of Z (Re & Imag) for station #12
Z_{XX}
Z_{XY}
Z_{YX}
Z_{YY}
$Z/(2\pi f)^{1/2}$ (V/A.Hz$^{1/2}$)
Period (s)
Real-obs
Real-calc
Imag-obs
Imag-calc

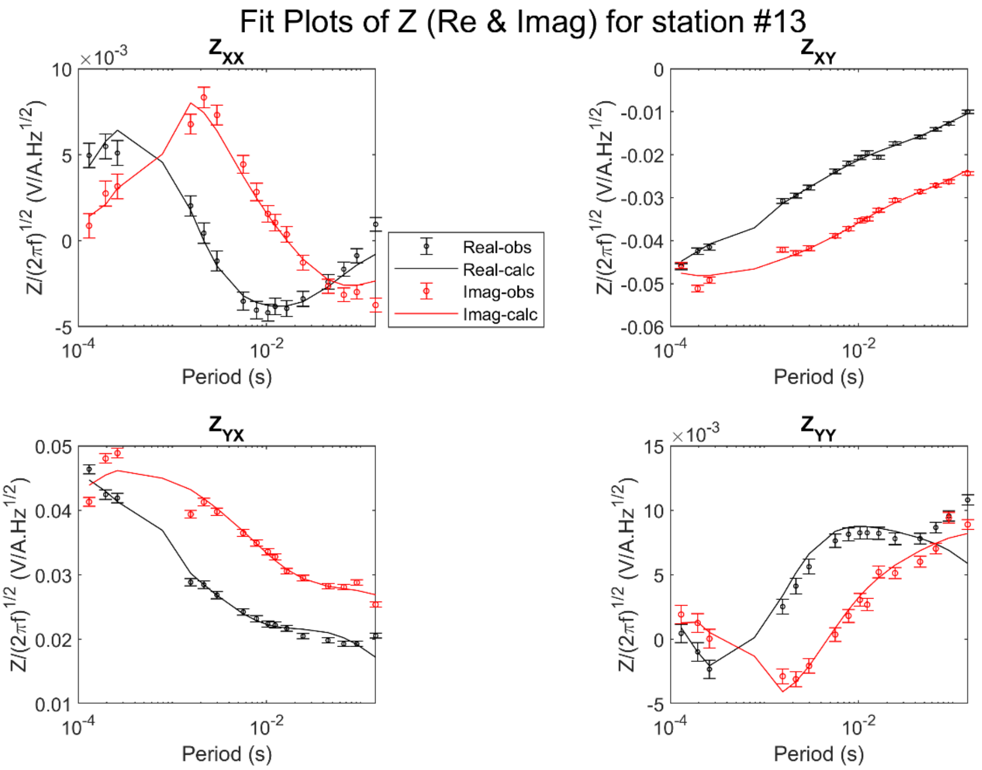

Fit Plots of Z (Re & Imag) for station #13
Z_{XX}
Z_{XY}
Z_{YX}
Z_{YY}
$\times 10^{-3}$
$Z/(2\pi f)^{1/2}$ (V/A.Hz$^{1/2}$)
Period (s)
Real-obs
Real-calc
Imag-obs
Imag-calc

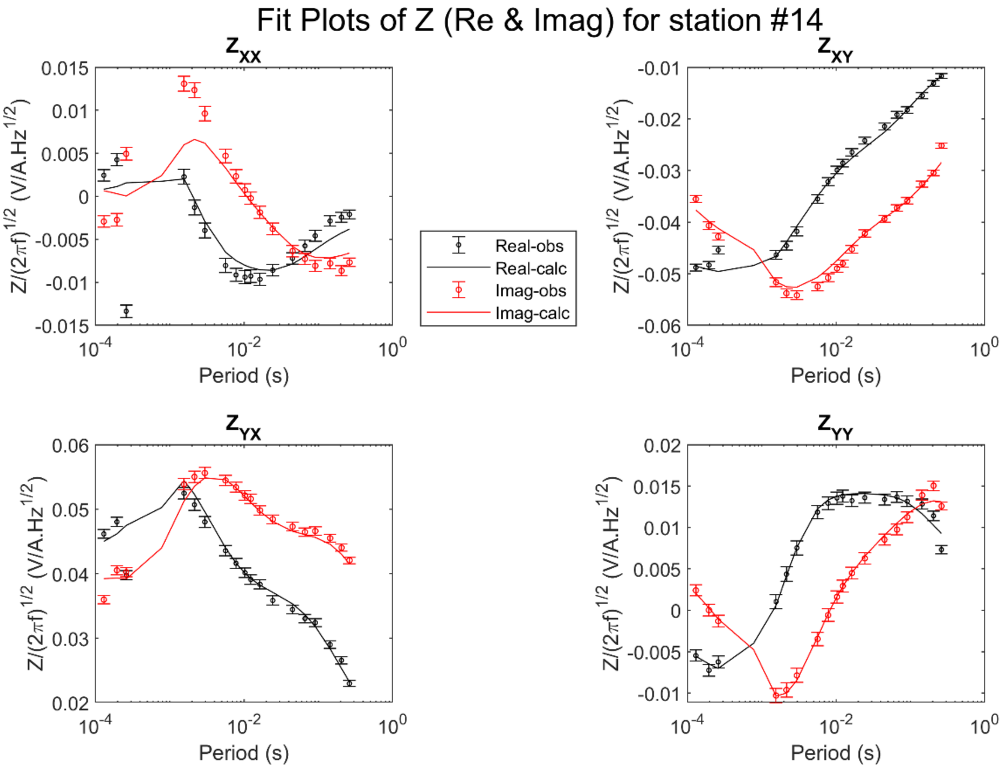

Fit Plots of Z (Re & Imag) for station #14
Z_{XX}
Z_{XY}
Z_{YX}
Z_{YY}
$Z/(2\pi f)^{1/2}$ (V/A.Hz$^{1/2}$)
Period (s)
Real-obs
Real-calc
Imag-obs
Imag-calc

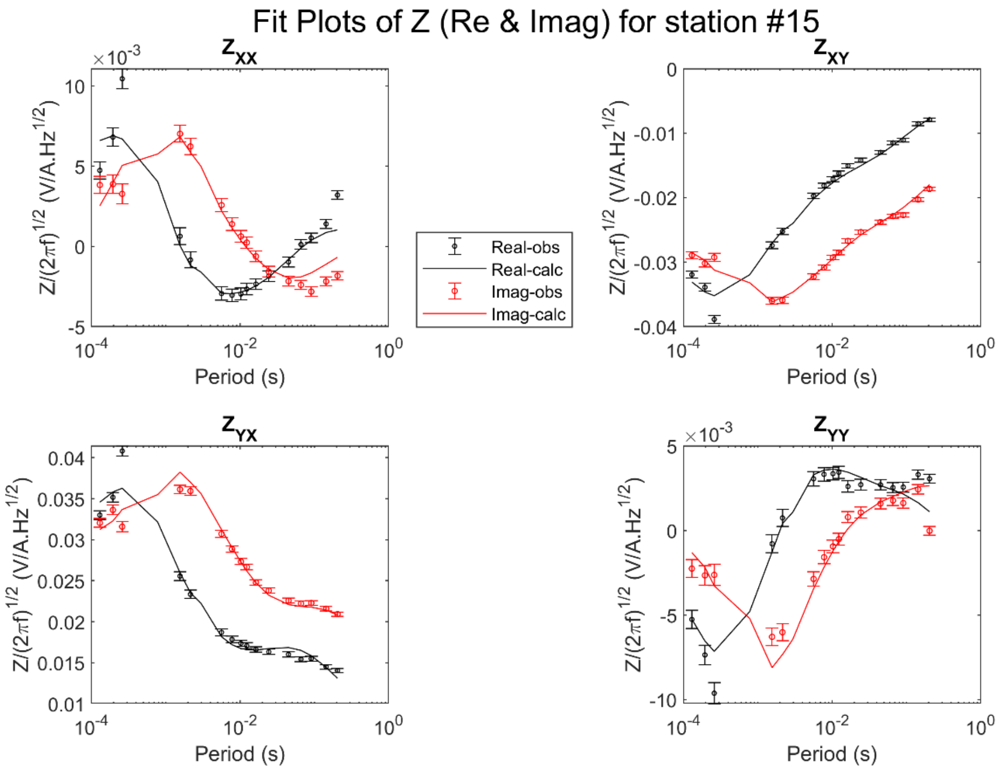

Fit Plots of Z (Re & Imag) for station #15
Z_{XX}
Z_{XY}
Z_{YX}
Z_{YY}
$\times 10^{-3}$
$Z/(2\pi f)^{1/2}$ (V/A.Hz$^{1/2}$)
Period (s)
Real-obs
Real-calc
Imag-obs
Imag-calc

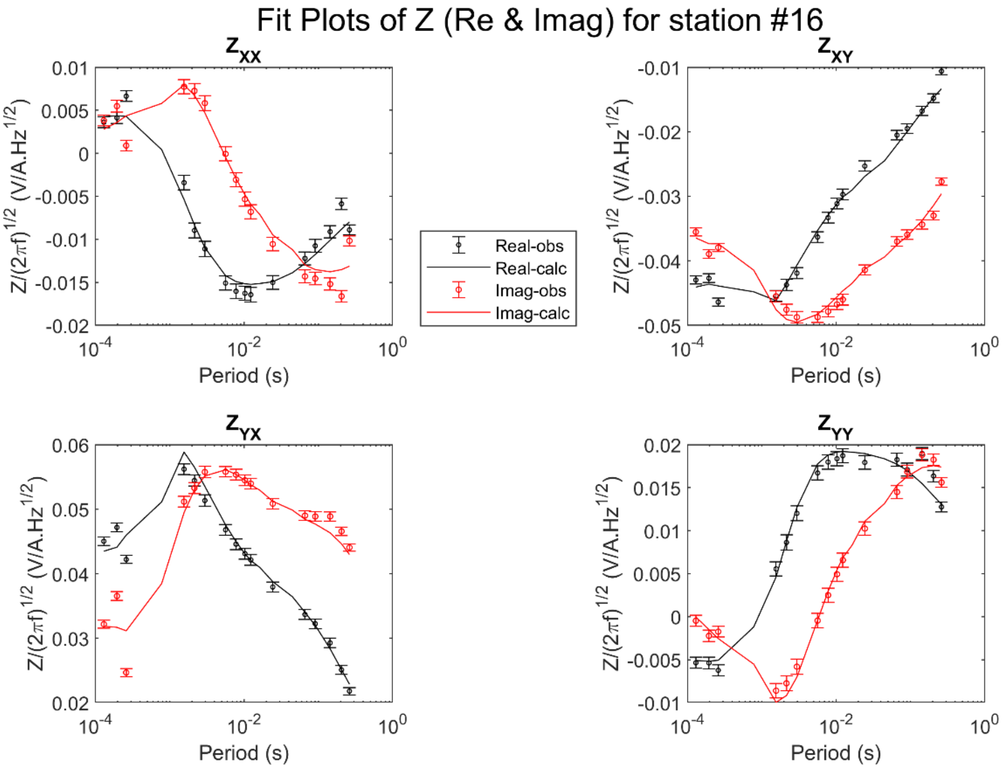
Fit Plots of Z (Re & Imag) for station #16
Z_XX
Z_XY
Z_YX
Z_YY
Z/(2πf)^1/2 (V/A.Hz^1/2)
Period (s)
Real-obs
Real-calc
Imag-obs
Imag-calc

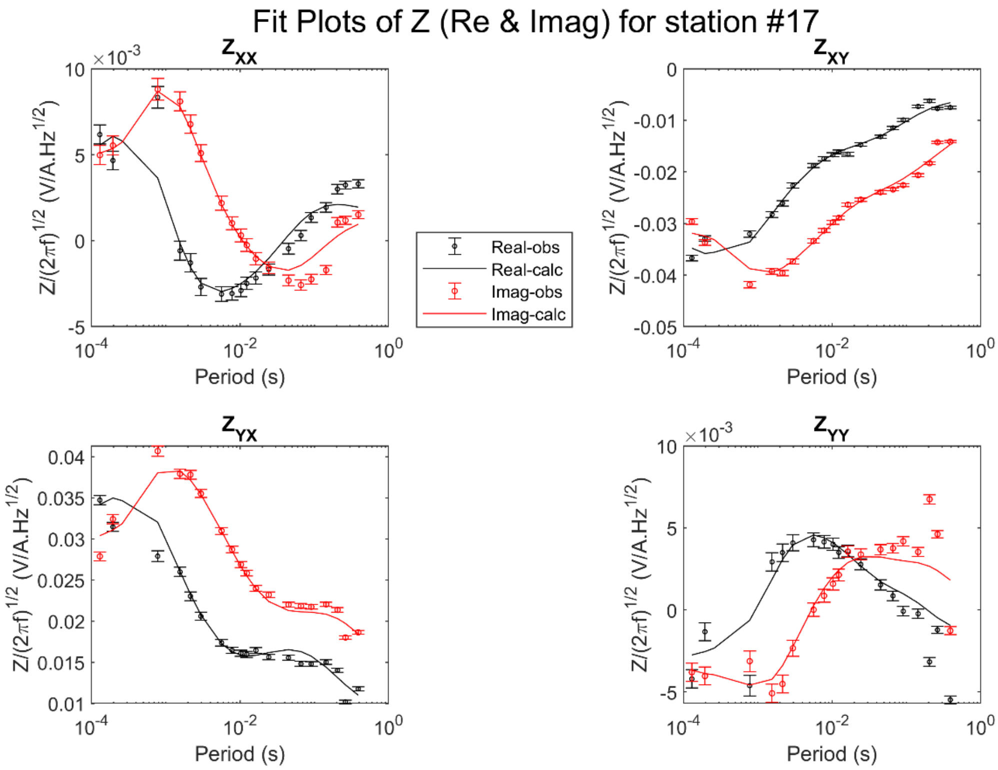
Fit Plots of Z (Re & Imag) for station #17
Z_XX
Z_XY
Z_YX
Z_YY
×10^-3
Z/(2πf)^1/2 (V/A.Hz^1/2)
Period (s)
Real-obs
Real-calc
Imag-obs
Imag-calc

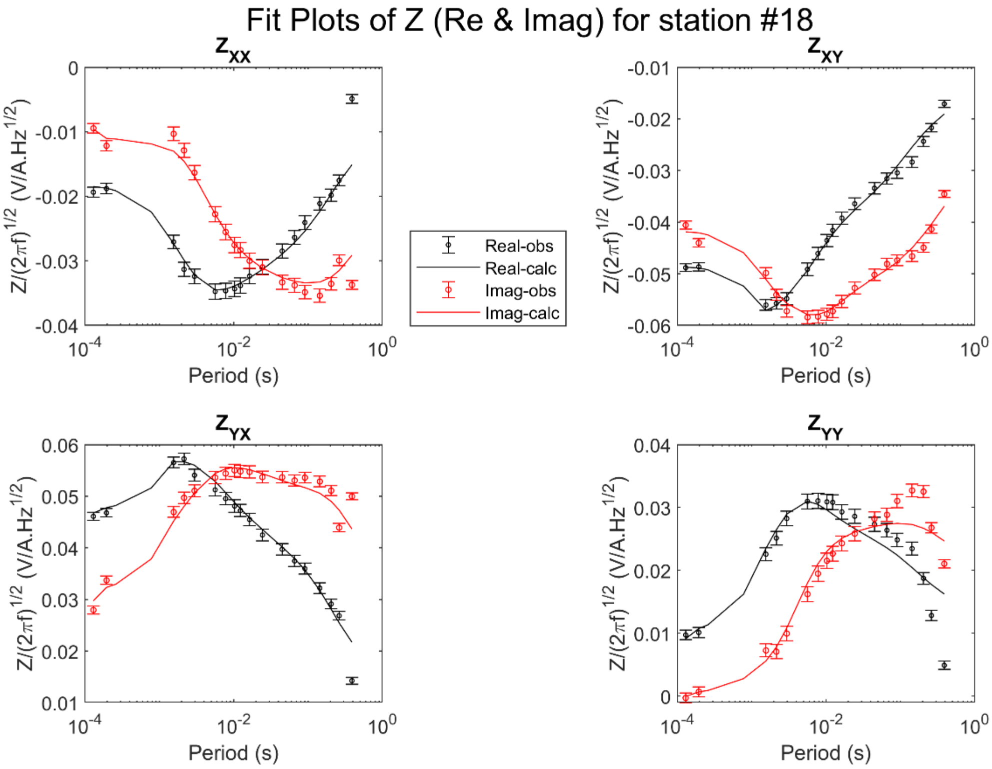
Fit Plots of Z (Re & Imag) for station #18
Z_{XX}
Z_{XY}
Z_{YX}
Z_{YY}
$Z/(2\pi f)^{1/2}$ (V/A.Hz$^{1/2}$)
Period (s)
Real-obs
Real-calc
Imag-obs
Imag-calc

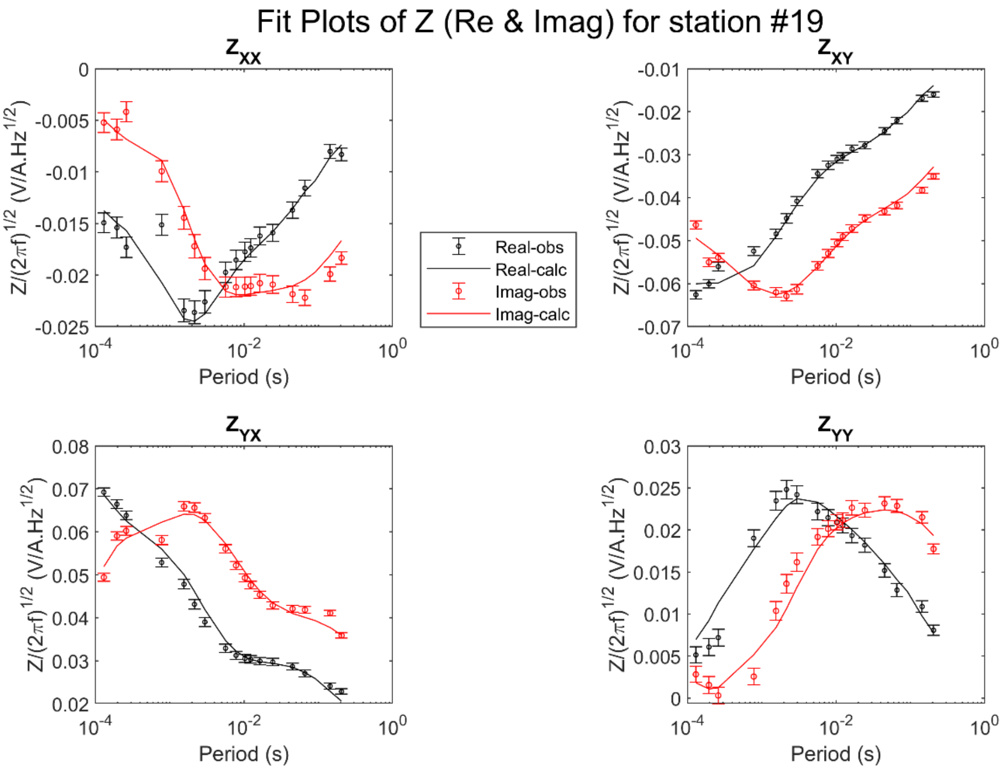
Fit Plots of Z (Re & Imag) for station #19
Z_{XX}
Z_{XY}
Z_{YX}
Z_{YY}
$Z/(2\pi f)^{1/2}$ (V/A.Hz$^{1/2}$)
Period (s)
Real-obs
Real-calc
Imag-obs
Imag-calc

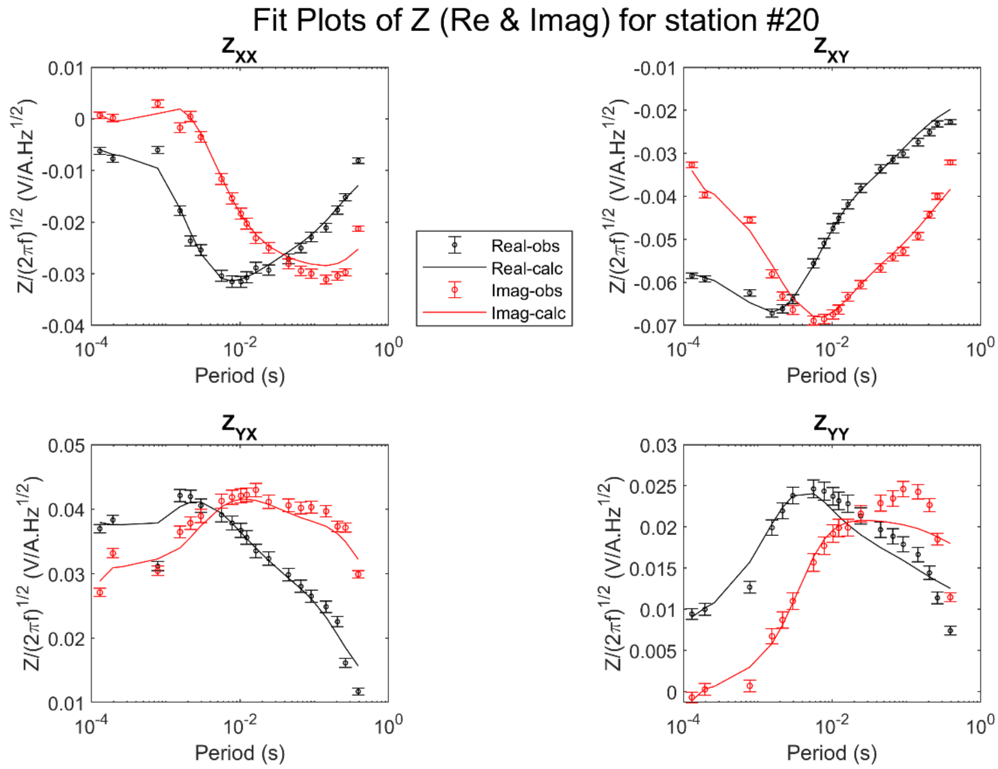
Fit Plots of Z (Re & Imag) for station #20
Z_XX
Z_XY
Z_YX
Z_YY
Z/(2πf)^1/2 (V/A.Hz^1/2)
Period (s)
Real-obs
Real-calc
Imag-obs
Imag-calc

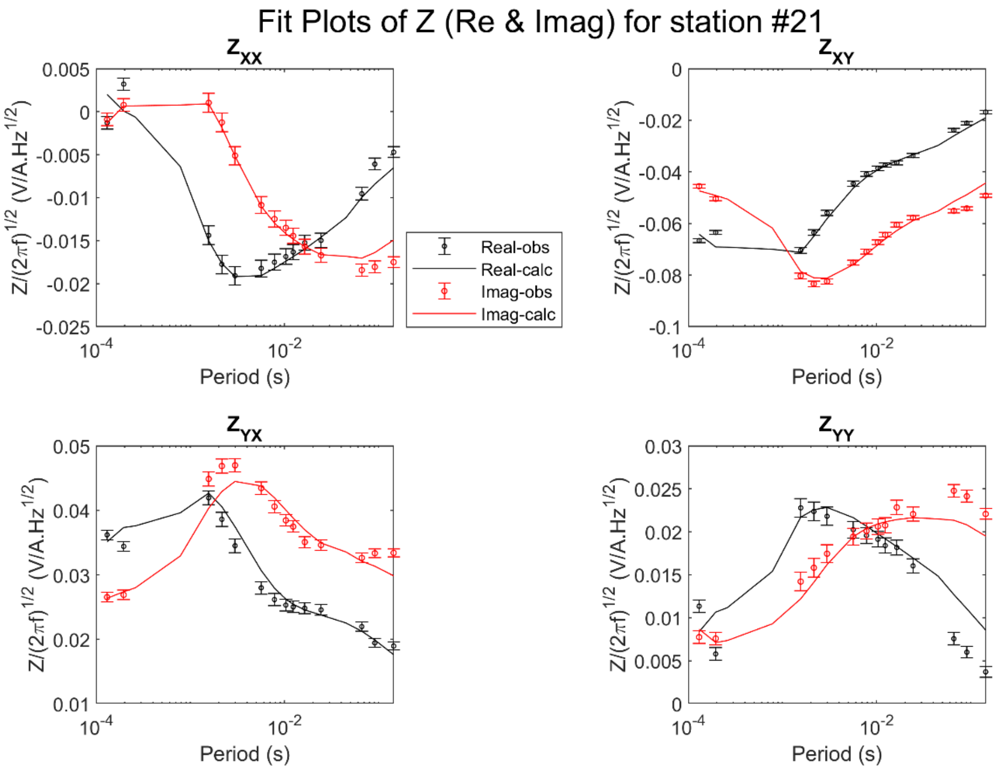
Fit Plots of Z (Re & Imag) for station #21
Z_XX
Z_XY
Z_YX
Z_YY
Z/(2πf)^1/2 (V/A.Hz^1/2)
Period (s)
Real-obs
Real-calc
Imag-obs
Imag-calc

Fit Plots of Z (Re & Imag) for station #22

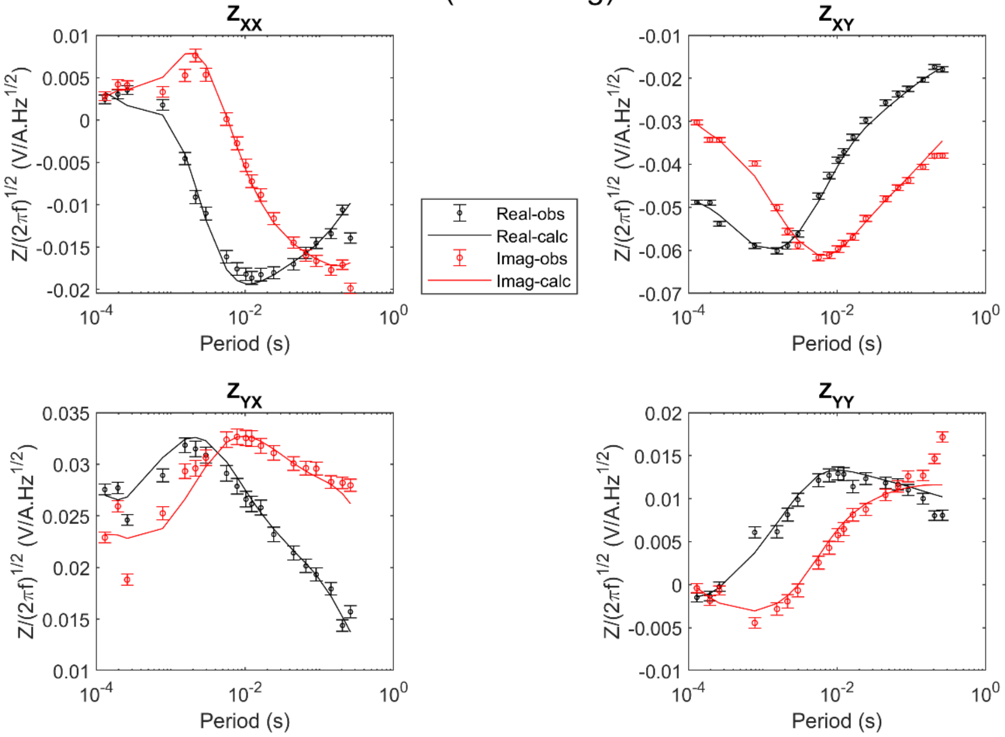

Fit Plots of Z (Re & Imag) for station #23

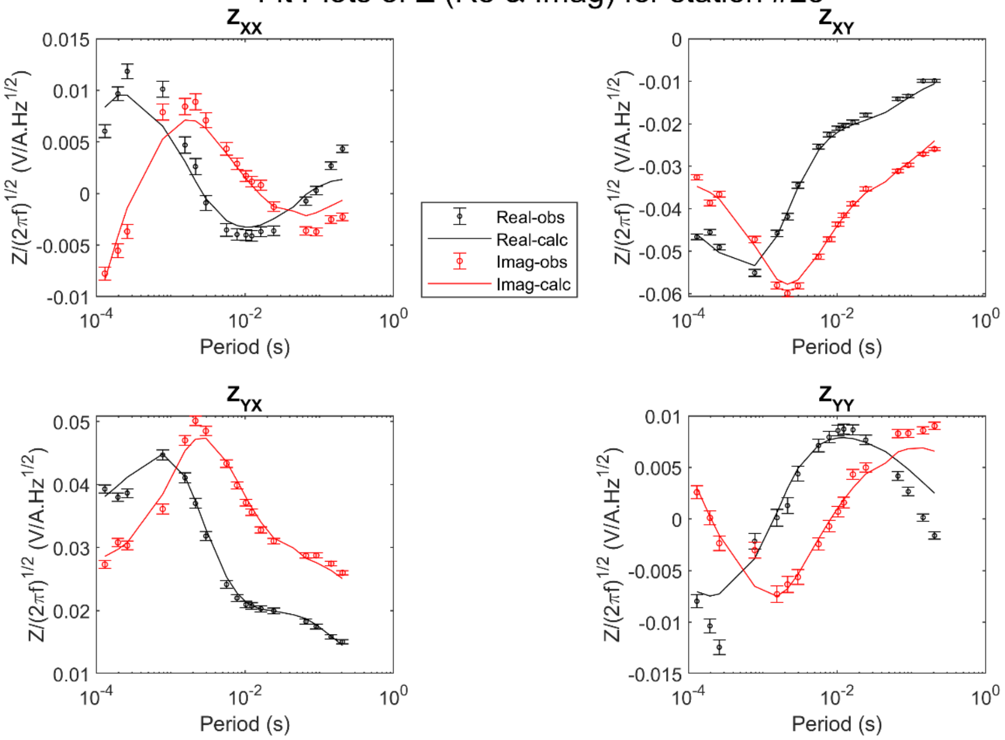

Fit Plots of Z (Re & Imag) for station #24

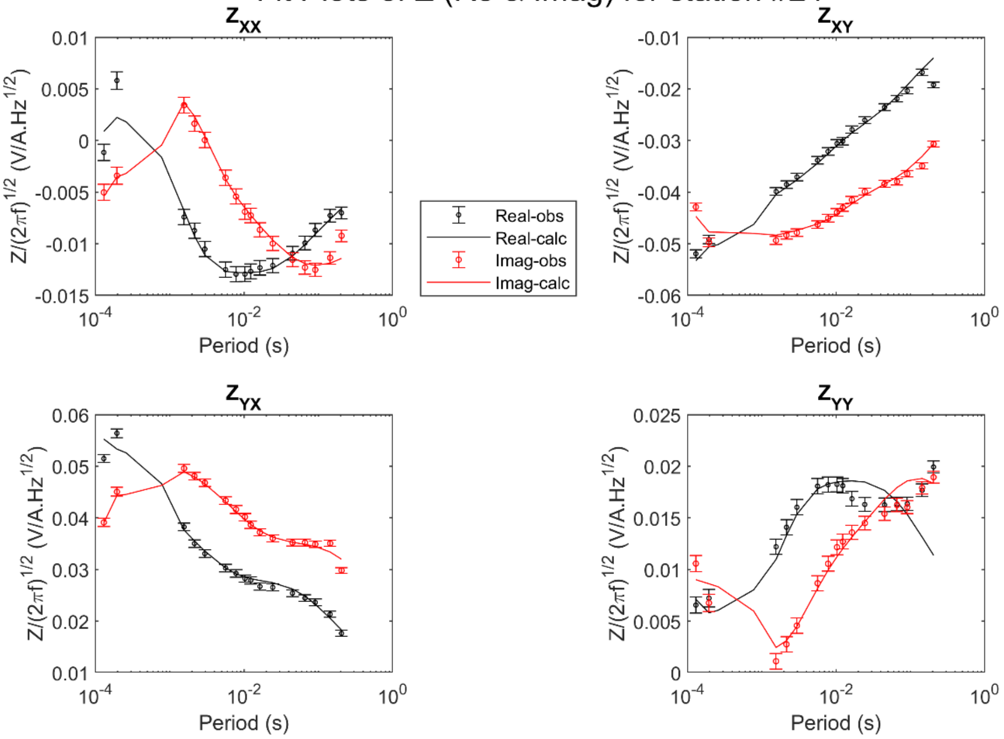

Fit Plots of Z (Re & Imag) for station #25

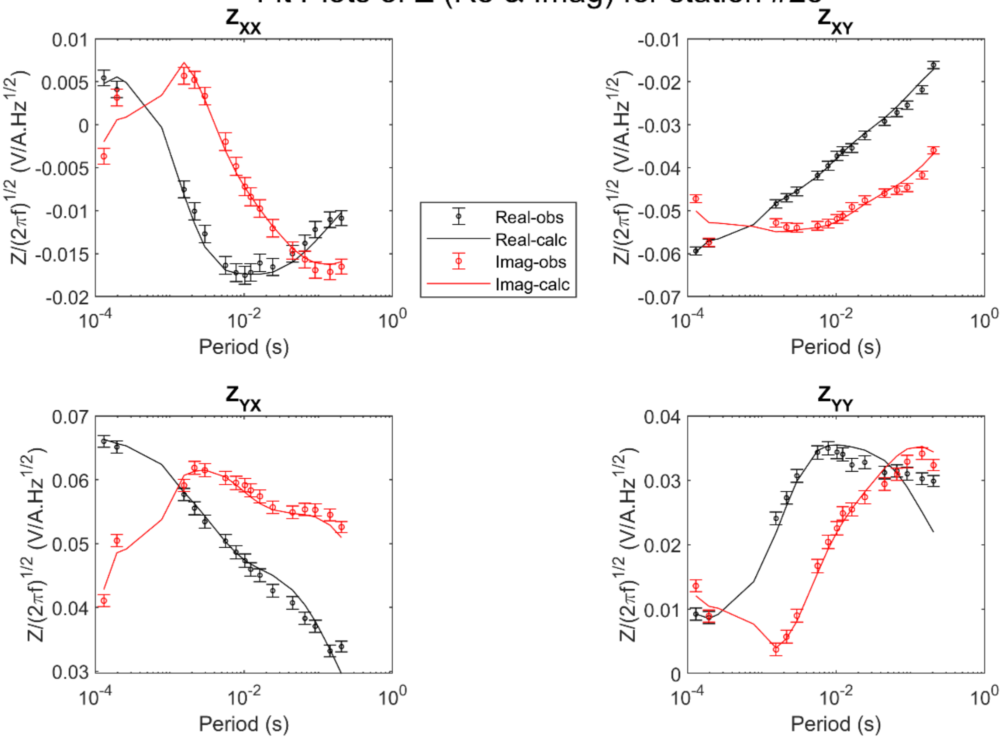

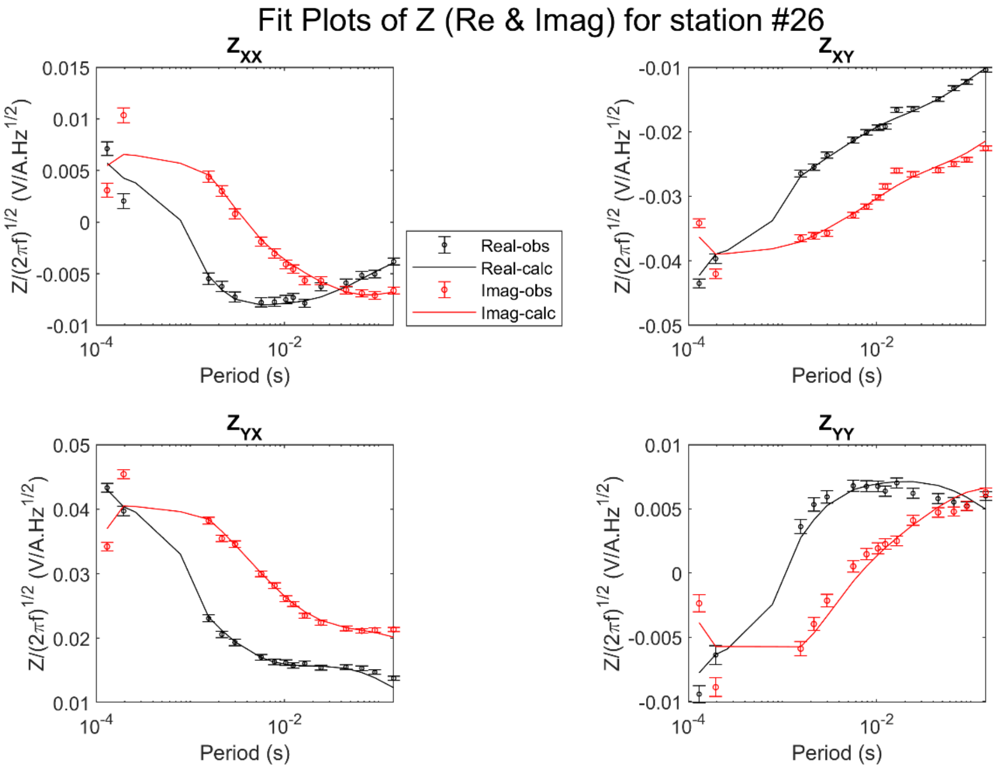

Fit Plots of Z (Re & Imag) for station #26
Z_XX
Z_XY
Z_YX
Z_YY
Z/(2πf)^1/2 (V/A.Hz^1/2)
Period (s)
Real-obs
Real-calc
Imag-obs
Imag-calc

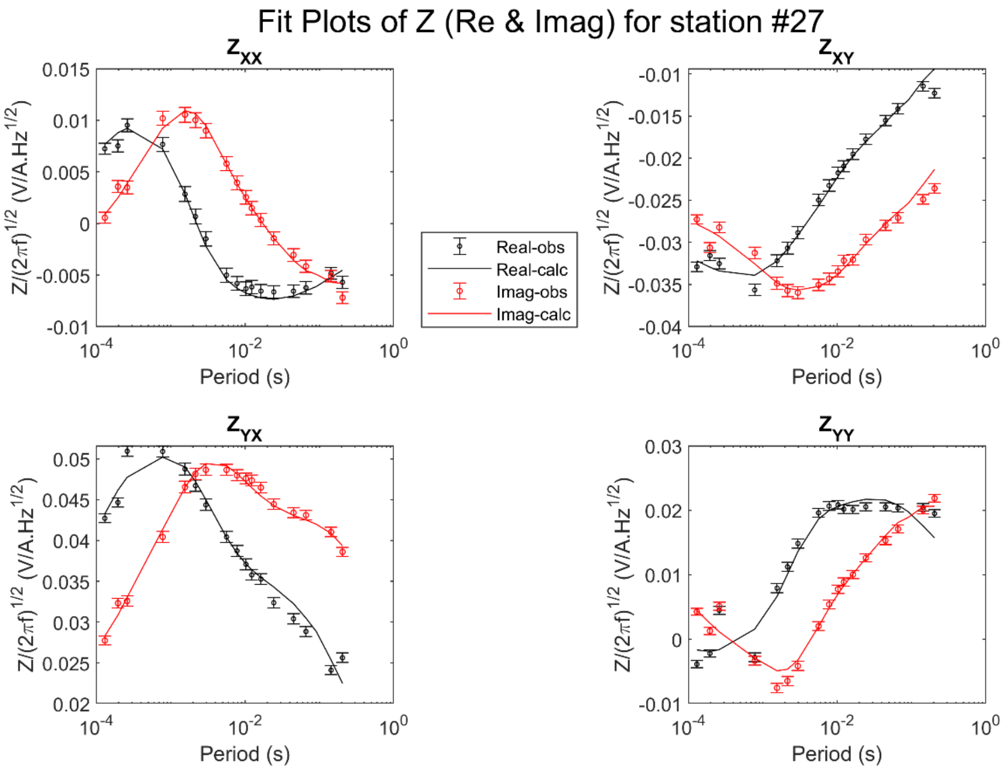

Fit Plots of Z (Re & Imag) for station #27
Z_XX
Z_XY
Z_YX
Z_YY
Z/(2πf)^1/2 (V/A.Hz^1/2)
Period (s)
Real-obs
Real-calc
Imag-obs
Imag-calc

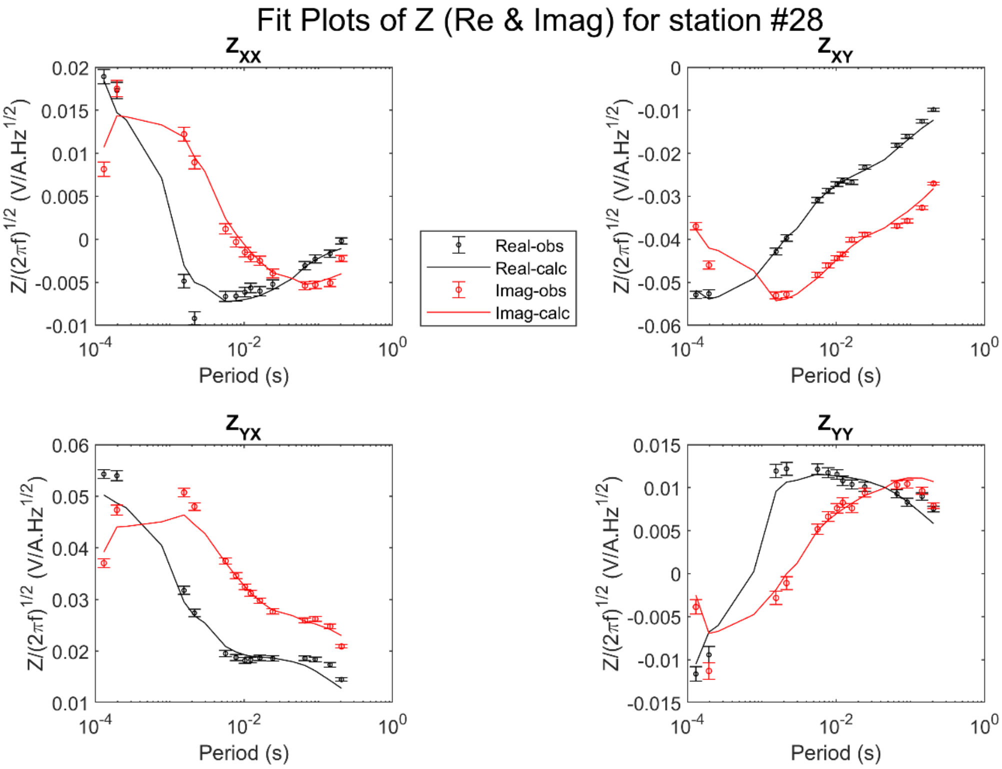
Fit Plots of Z (Re & Imag) for station #28
Z_XX
Z_XY
Z_YX
Z_YY
Z/(2πf)^1/2 (V/A.Hz^1/2)
Period (s)
Real-obs
Real-calc
Imag-obs
Imag-calc

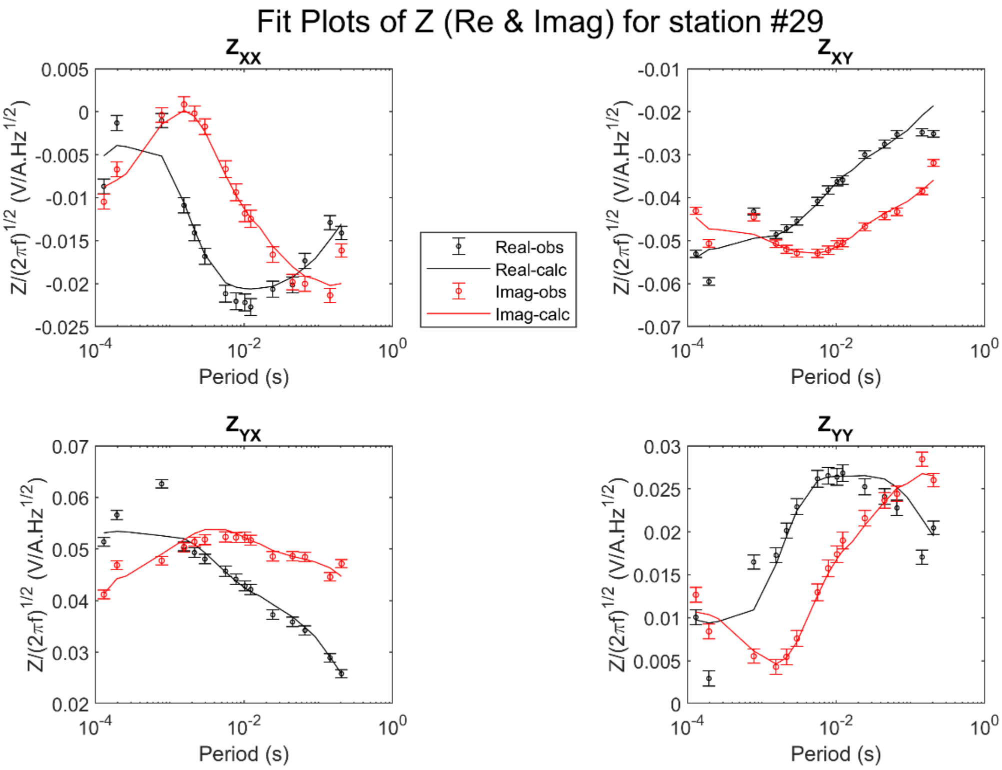
Fit Plots of Z (Re & Imag) for station #29
Z_XX
Z_XY
Z_YX
Z_YY
Z/(2πf)^1/2 (V/A.Hz^1/2)
Period (s)
Real-obs
Real-calc
Imag-obs
Imag-calc

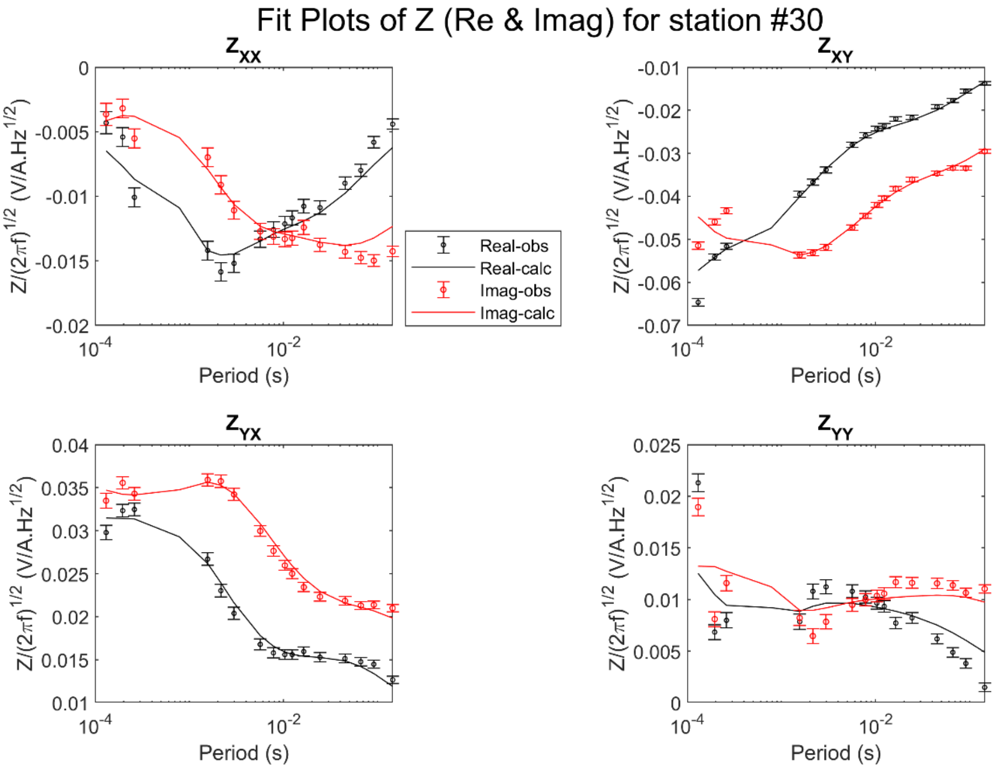
Fit Plots of Z (Re & Imag) for station #30
Z_{XX}
Z_{XY}
Z_{YX}
Z_{YY}
$Z/(2\pi f)^{1/2}$ (V/A.Hz$^{1/2}$)
Period (s)
Real-obs
Real-calc
Imag-obs
Imag-calc

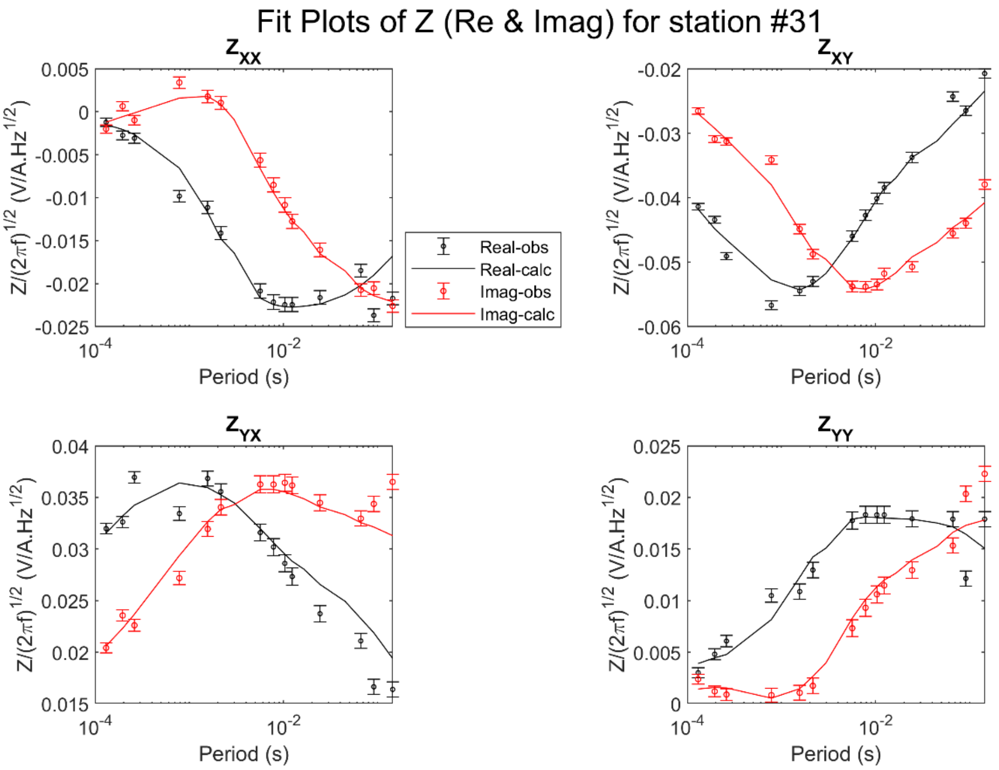
Fit Plots of Z (Re & Imag) for station #31
Z_{XX}
Z_{XY}
Z_{YX}
Z_{YY}
$Z/(2\pi f)^{1/2}$ (V/A.Hz$^{1/2}$)
Period (s)
Real-obs
Real-calc
Imag-obs
Imag-calc

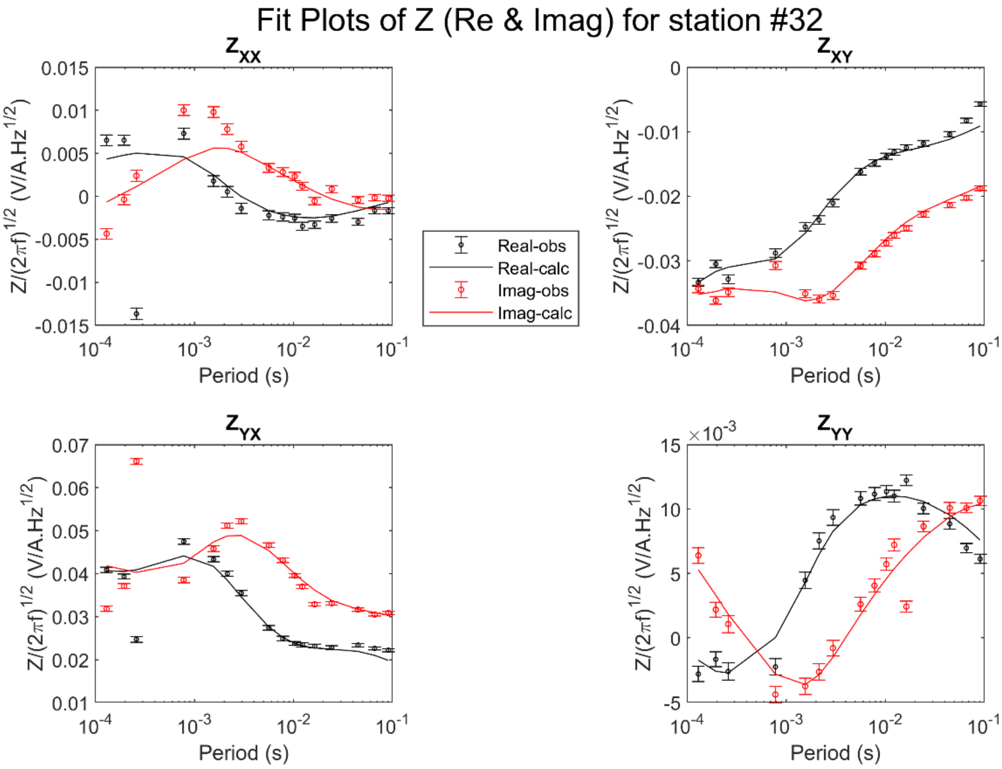
Fit Plots of Z (Re & Imag) for station #32
Z_{XX}
Z_{XY}
Z_{YX}
Z_{YY}
Real-obs
Real-calc
Imag-obs
Imag-calc
$Z/(2\pi f)^{1/2}$ (V/A.Hz$^{1/2}$)
Period (s)

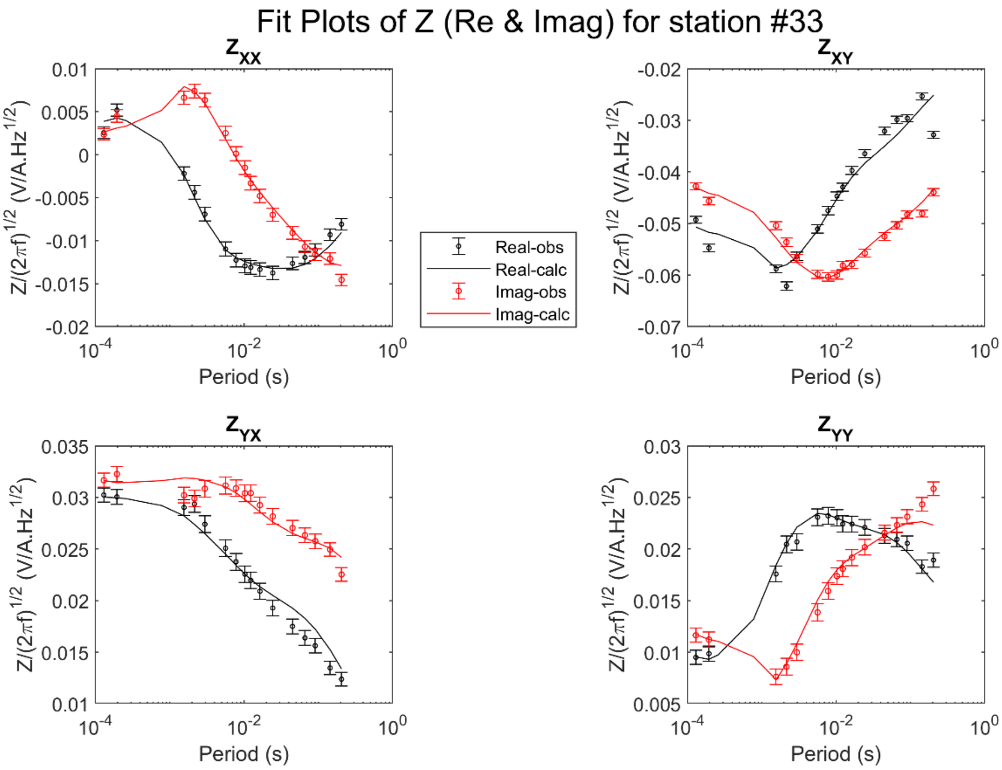
Fit Plots of Z (Re & Imag) for station #33
Z_{XX}
Z_{XY}
Z_{YX}
Z_{YY}
Real-obs
Real-calc
Imag-obs
Imag-calc
$Z/(2\pi f)^{1/2}$ (V/A.Hz$^{1/2}$)
Period (s)

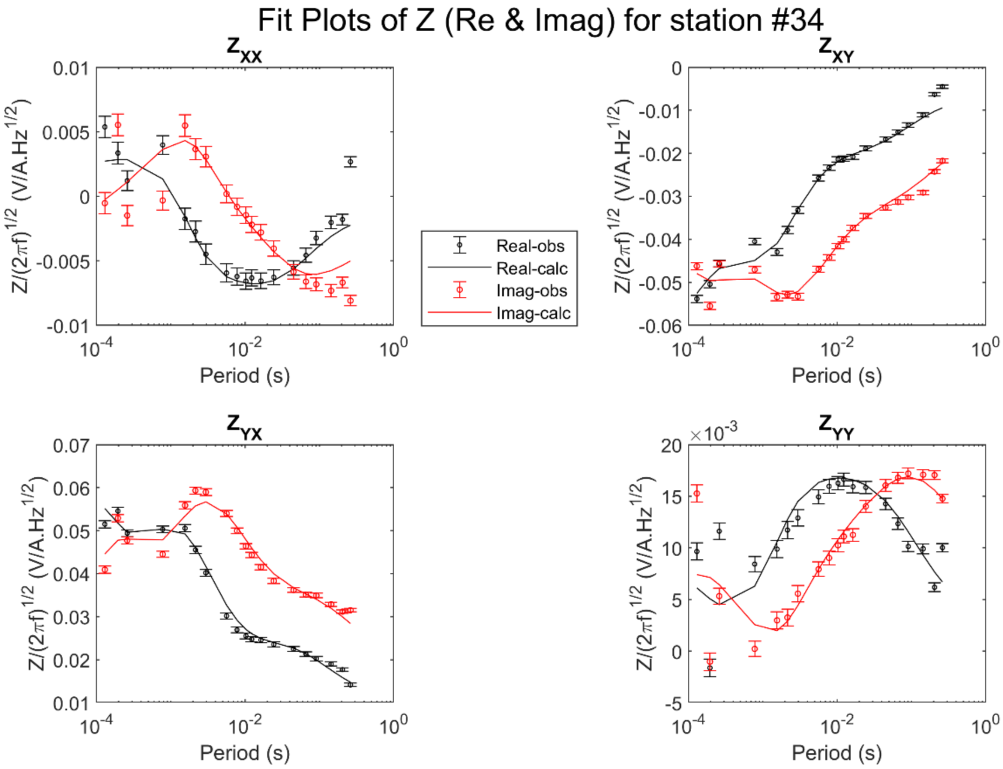
Fit Plots of Z (Re & Imag) for station #34
Z_{XX}
Z_{XY}
Z_{YX}
Z_{YY}
$Z/(2\pi f)^{1/2}$ (V/A.Hz$^{1/2}$)
Period (s)
Real-obs
Real-calc
Imag-obs
Imag-calc
$\times 10^{-3}$

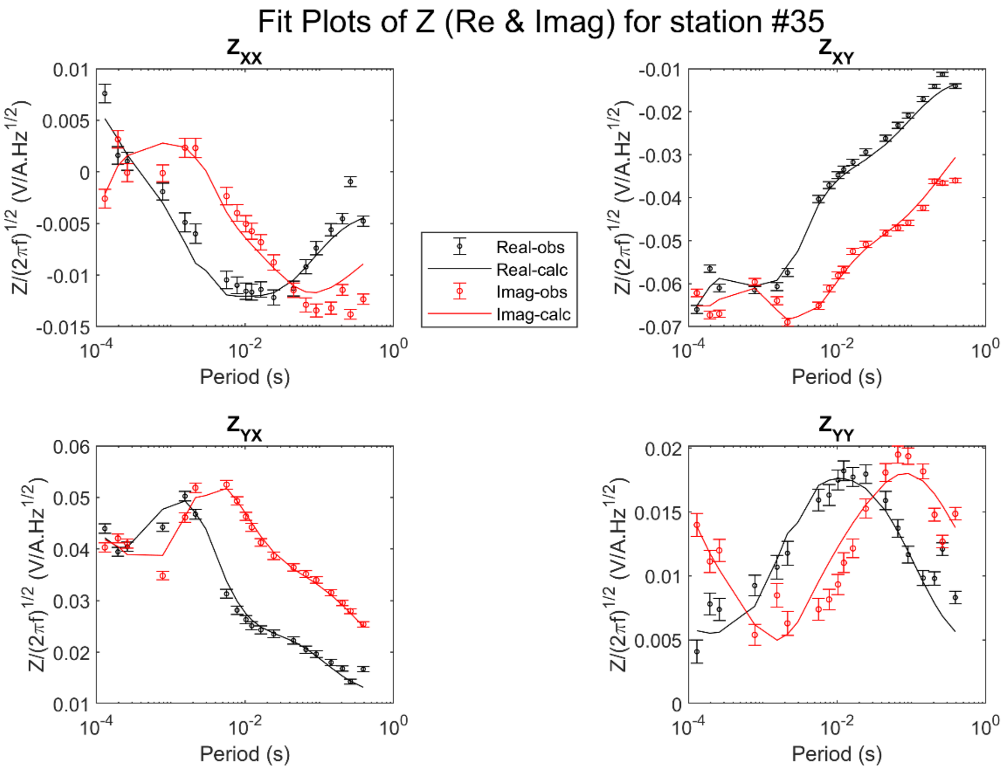
Fit Plots of Z (Re & Imag) for station #35
Z_{XX}
Z_{XY}
Z_{YX}
Z_{YY}
$Z/(2\pi f)^{1/2}$ (V/A.Hz$^{1/2}$)
Period (s)
Real-obs
Real-calc
Imag-obs
Imag-calc

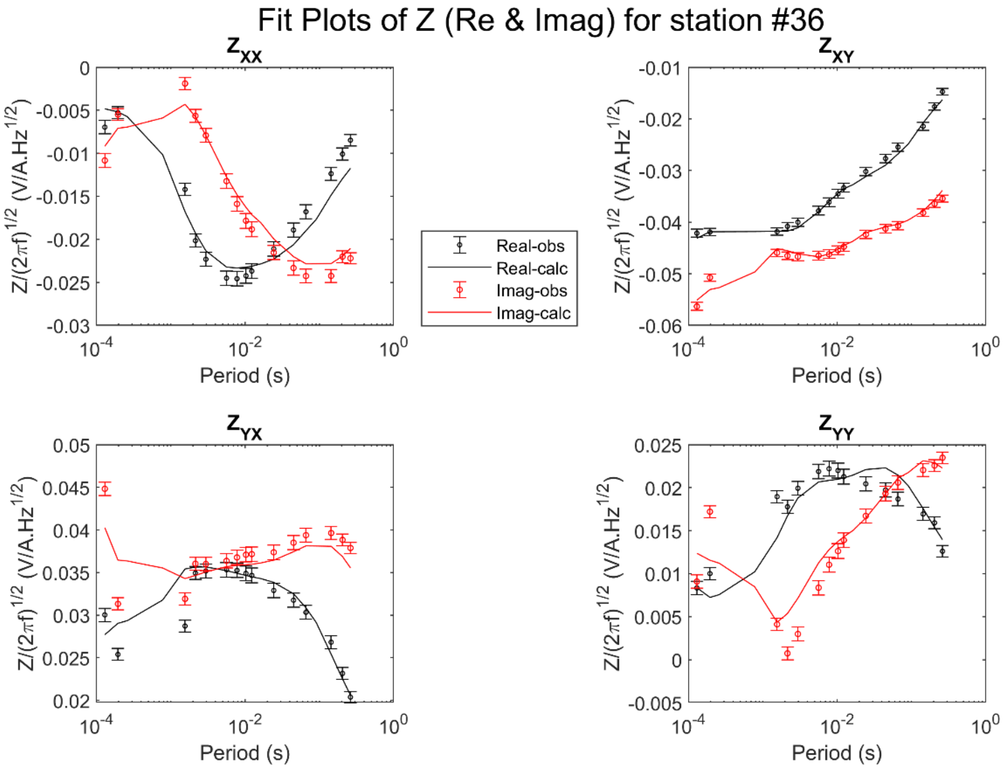
Fit Plots of Z (Re & Imag) for station #36
Z_XX
Z_XY
Z_YX
Z_YY
Z/(2πf)^1/2 (V/A.Hz^1/2)
Period (s)
Real-obs
Real-calc
Imag-obs
Imag-calc

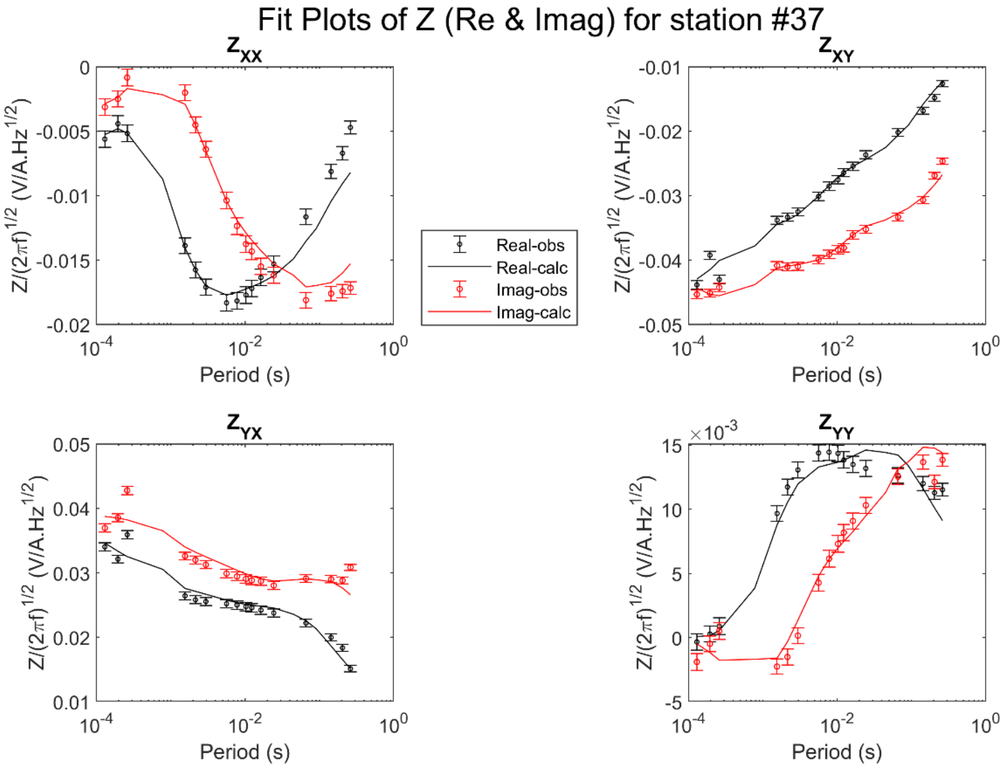
Fit Plots of Z (Re & Imag) for station #37
Z_XX
Z_XY
Z_YX
Z_YY
×10^-3
Z/(2πf)^1/2 (V/A.Hz^1/2)
Period (s)
Real-obs
Real-calc
Imag-obs
Imag-calc

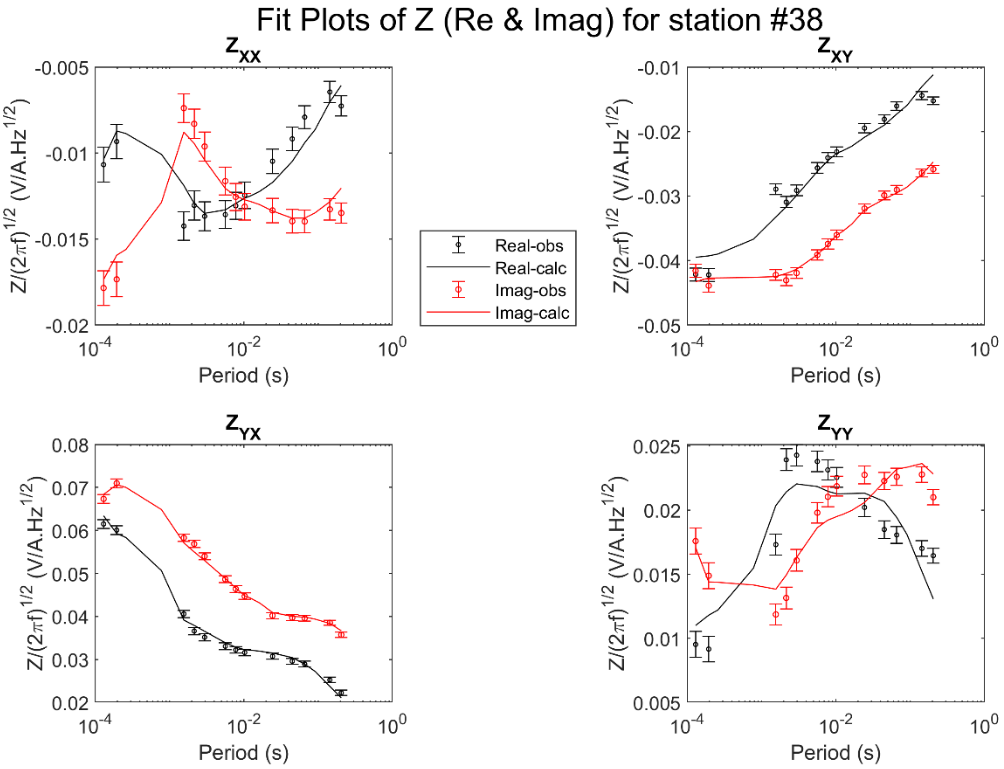
Fit Plots of Z (Re & Imag) for station #38
Z_XX
Z_XY
Z_YX
Z_YY
Z/(2πf)^1/2 (V/A.Hz^1/2)
Period (s)
Real-obs
Real-calc
Imag-obs
Imag-calc

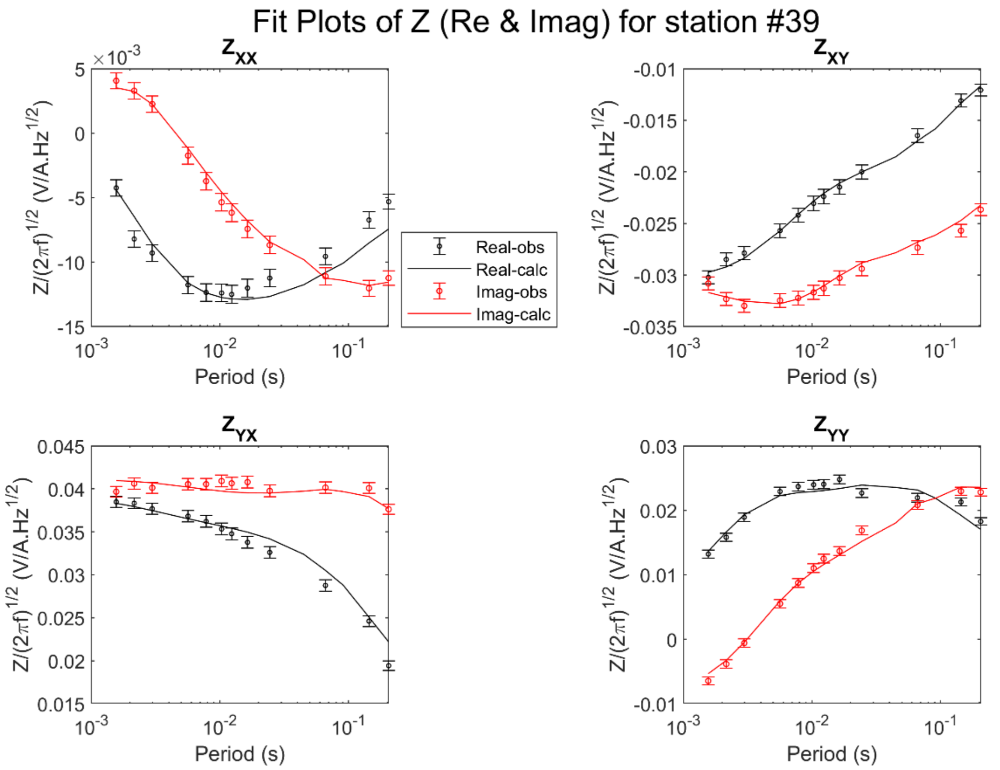
Fit Plots of Z (Re & Imag) for station #39
Z_XX
Z_XY
Z_YX
Z_YY
×10^-3
Z/(2πf)^1/2 (V/A.Hz^1/2)
Period (s)
Real-obs
Real-calc
Imag-obs
Imag-calc

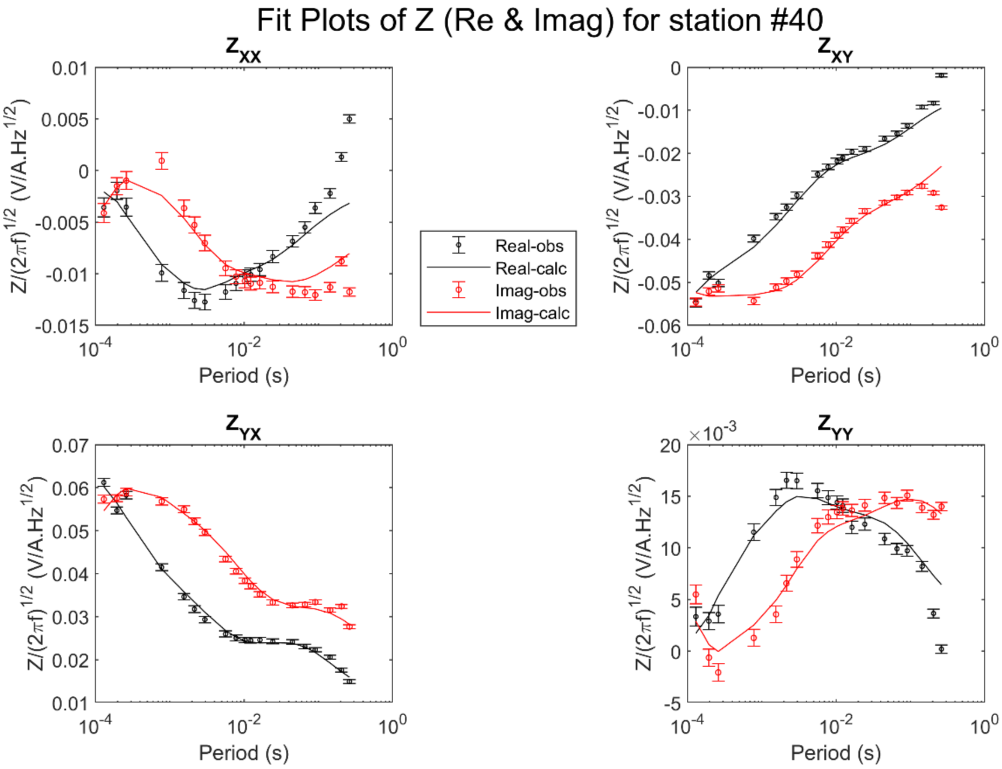

Fit Plots of Z (Re & Imag) for station #40
Z_{XX}
Z_{XY}
Z_{YX}
Z_{YY}
$\times 10^{-3}$
$Z/(2\pi f)^{1/2}$ (V/A.Hz$^{1/2}$)
Period (s)
Real-obs
Real-calc
Imag-obs
Imag-calc

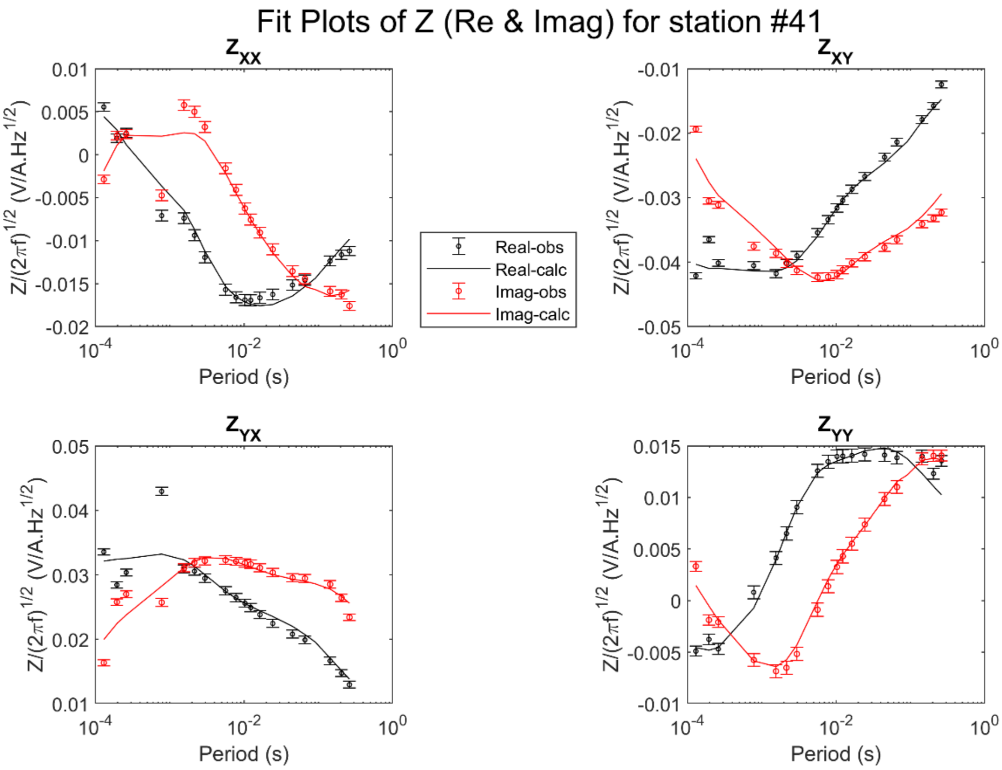

Fit Plots of Z (Re & Imag) for station #41
Z_{XX}
Z_{XY}
Z_{YX}
Z_{YY}
$Z/(2\pi f)^{1/2}$ (V/A.Hz$^{1/2}$)
Period (s)
Real-obs
Real-calc
Imag-obs
Imag-calc

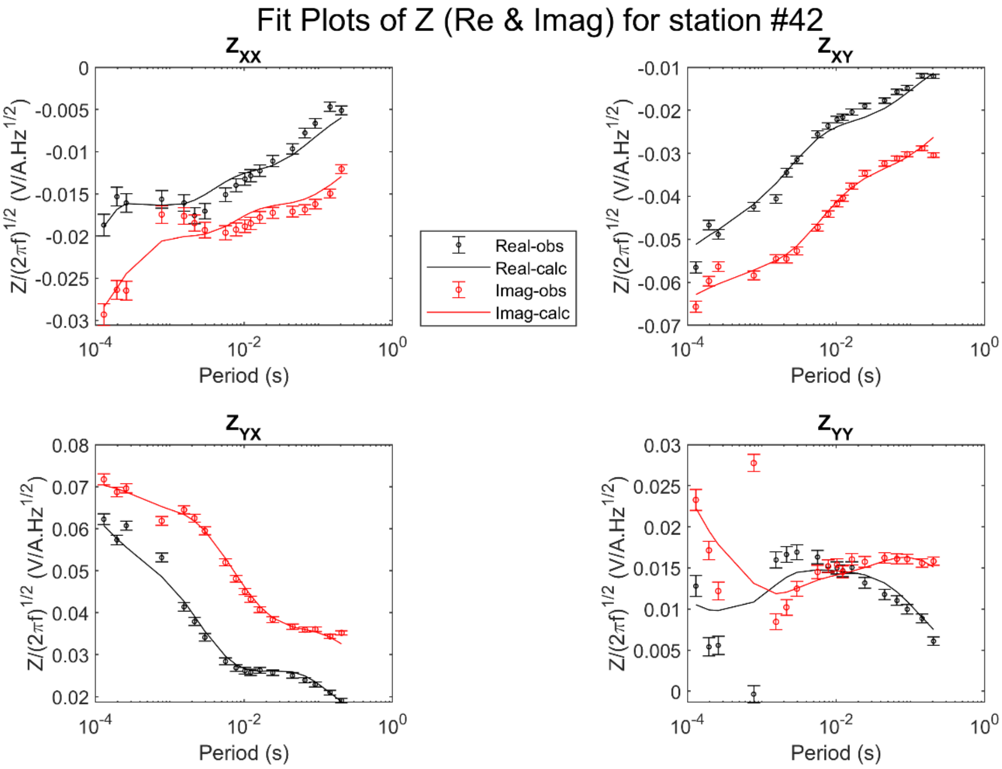

Fit Plots of Z (Re & Imag) for station #42
Z_XX
Z_XY
Z_YX
Z_YY
Z/(2πf)^1/2 (V/A.Hz^1/2)
Period (s)
Real-obs
Real-calc
Imag-obs
Imag-calc

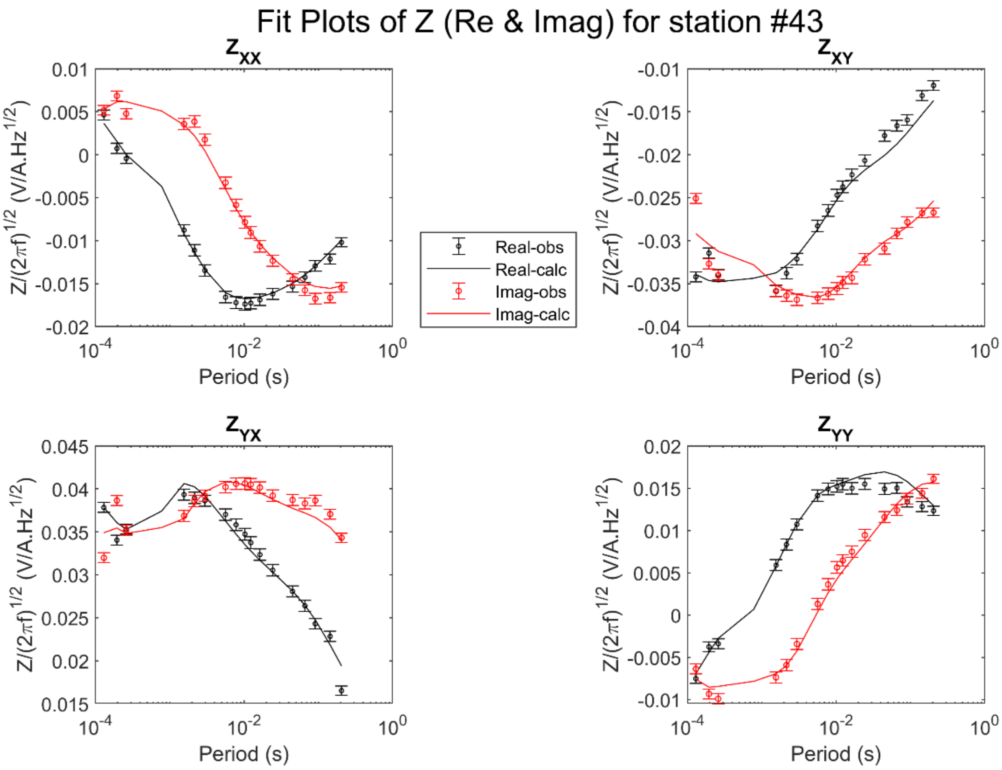

Fit Plots of Z (Re & Imag) for station #43
Z_XX
Z_XY
Z_YX
Z_YY
Z/(2πf)^1/2 (V/A.Hz^1/2)
Period (s)
Real-obs
Real-calc
Imag-obs
Imag-calc

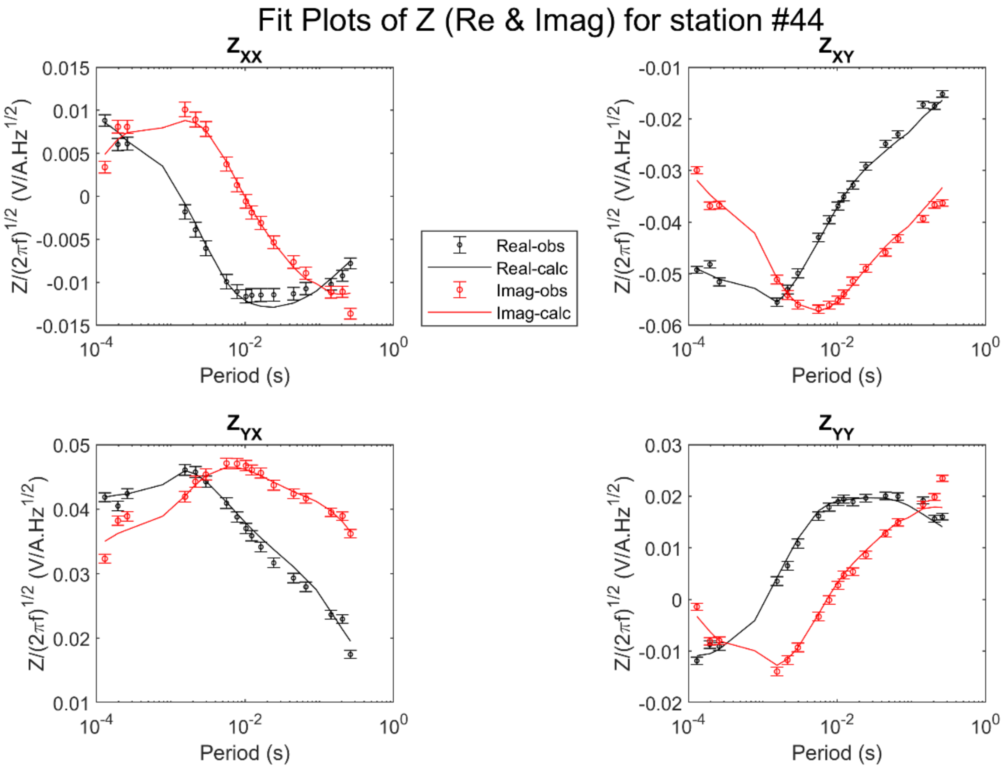

Fit Plots of Z (Re & Imag) for station #44
Z_XX
Z_XY
Z_YX
Z_YY
Z/(2πf)^1/2 (V/A.Hz^1/2)
Period (s)
Real-obs
Real-calc
Imag-obs
Imag-calc

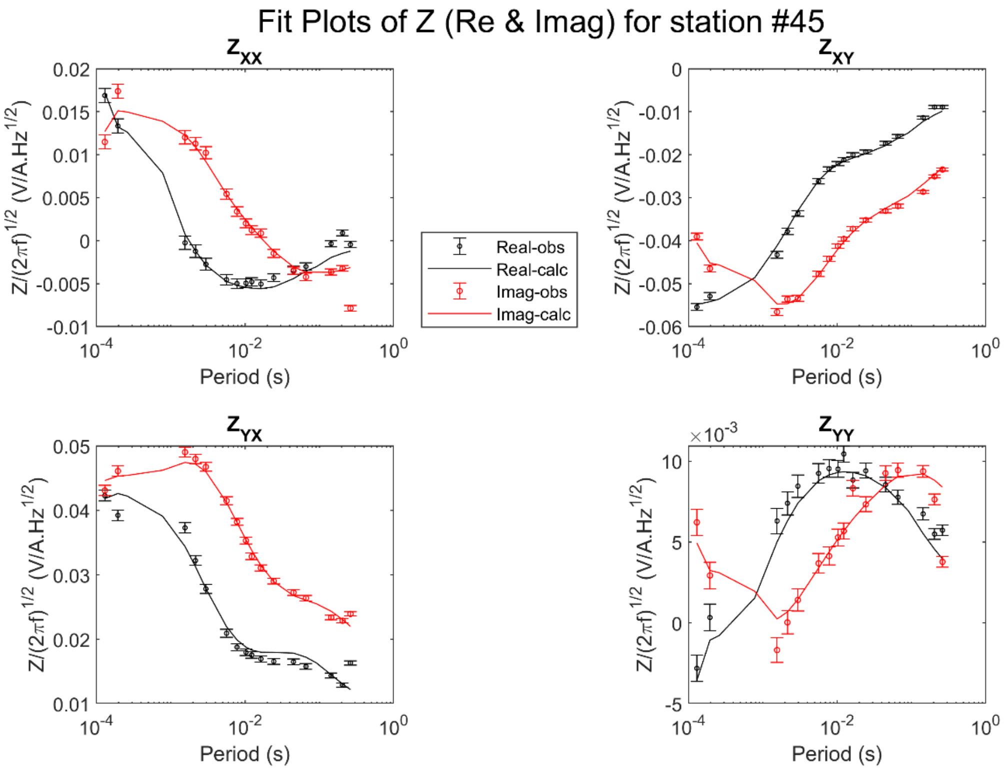

Fit Plots of Z (Re & Imag) for station #45
Z_XX
Z_XY
Z_YX
Z_YY
Z/(2πf)^1/2 (V/A.Hz^1/2)
Period (s)
Real-obs
Real-calc
Imag-obs
Imag-calc

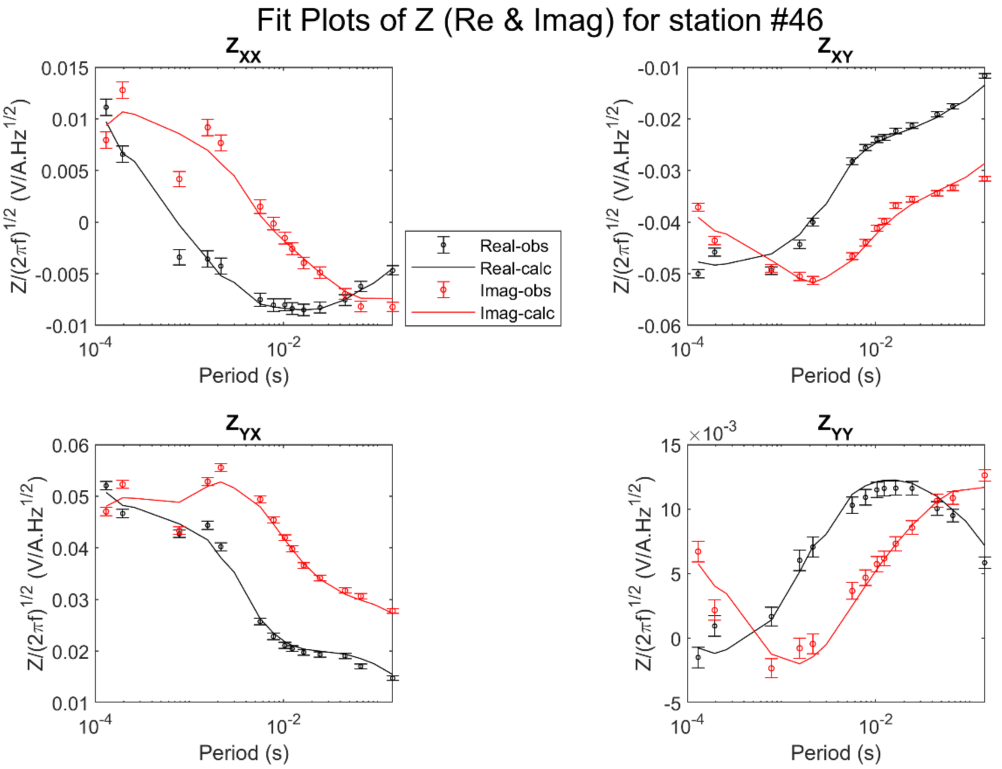
Fit Plots of Z (Re & Imag) for station #46
Z_XX
Z_XY
Z_YX
Z_YY
Z/(2πf)^{1/2} (V/A.Hz^{1/2})
Period (s)
Real-obs
Real-calc
Imag-obs
Imag-calc
×10^{-3}

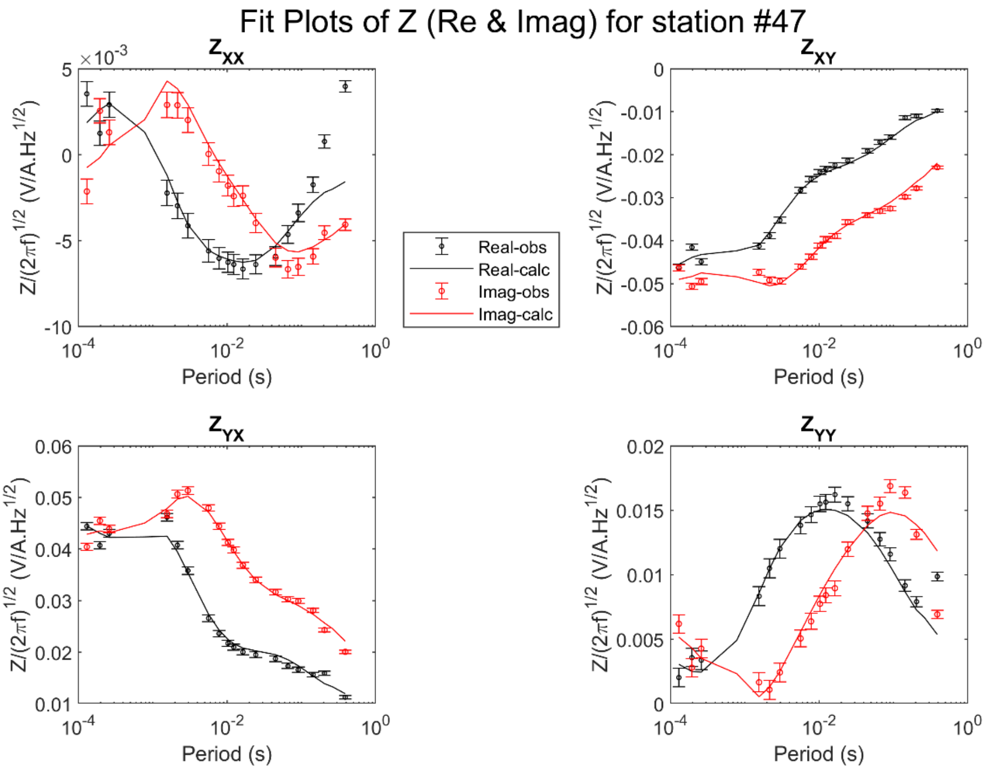
Fit Plots of Z (Re & Imag) for station #47
Z_XX
Z_XY
Z_YX
Z_YY
Z/(2πf)^{1/2} (V/A.Hz^{1/2})
Period (s)
Real-obs
Real-calc
Imag-obs
Imag-calc
×10^{-3}

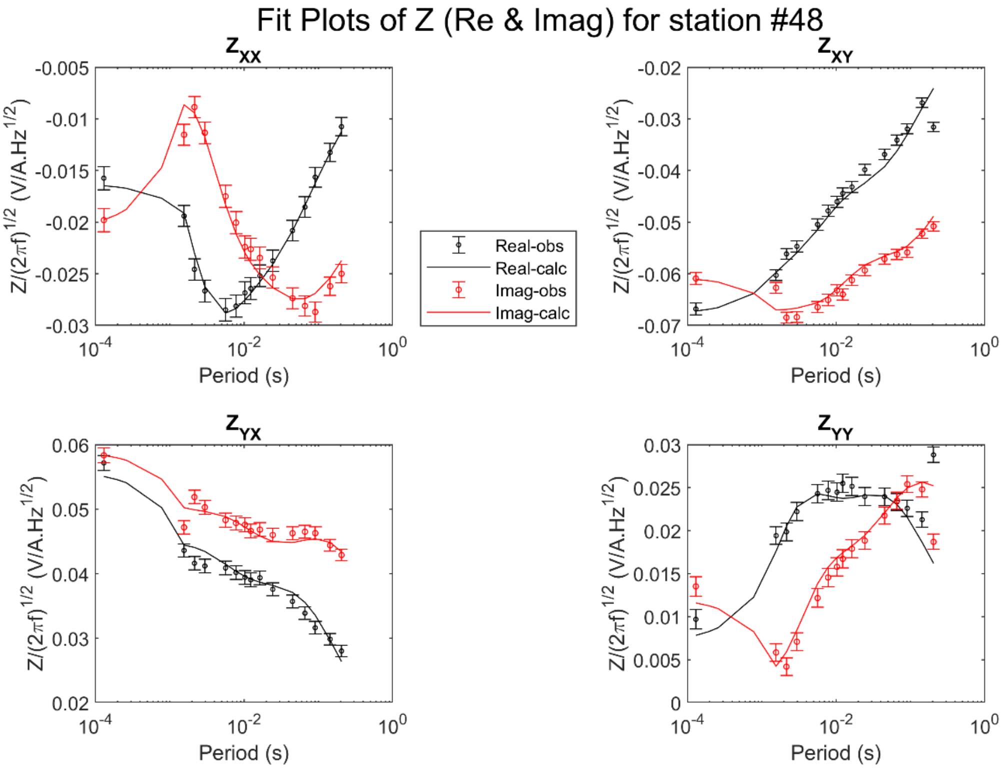
Fit Plots of Z (Re & Imag) for station #48
Z_{XX}
Z_{XY}
Z_{YX}
Z_{YY}
$Z/(2\pi f)^{1/2}$ (V/A.Hz$^{1/2}$)
Period (s)
Real-obs
Real-calc
Imag-obs
Imag-calc

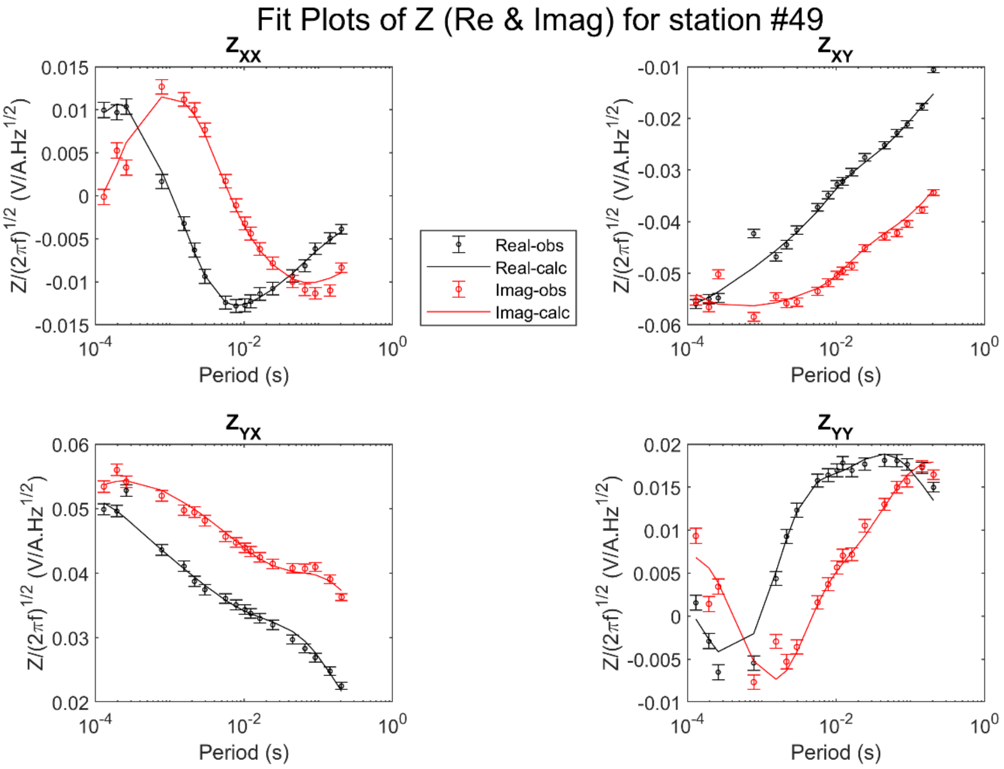
Fit Plots of Z (Re & Imag) for station #49
Z_{XX}
Z_{XY}
Z_{YX}
Z_{YY}
$Z/(2\pi f)^{1/2}$ (V/A.Hz$^{1/2}$)
Period (s)
Real-obs
Real-calc
Imag-obs
Imag-calc

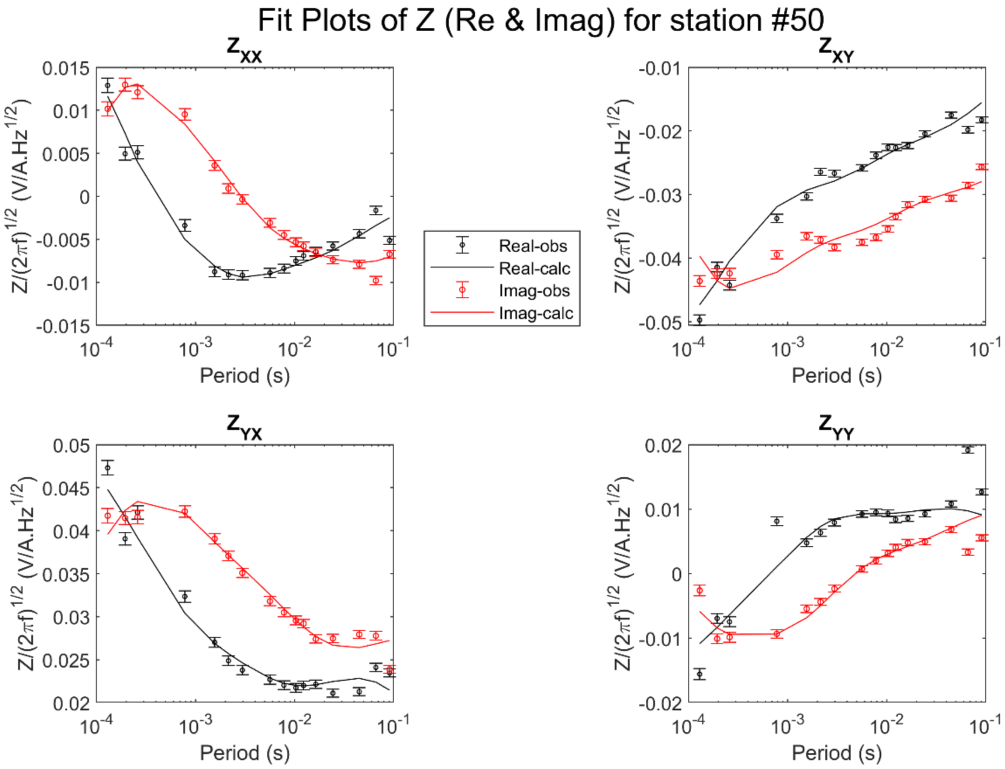
Fit Plots of Z (Re & Imag) for station #50
Z_XX
Z_XY
Z_YX
Z_YY
Z/(2πf)^1/2 (V/A.Hz^1/2)
Period (s)
Real-obs
Real-calc
Imag-obs
Imag-calc

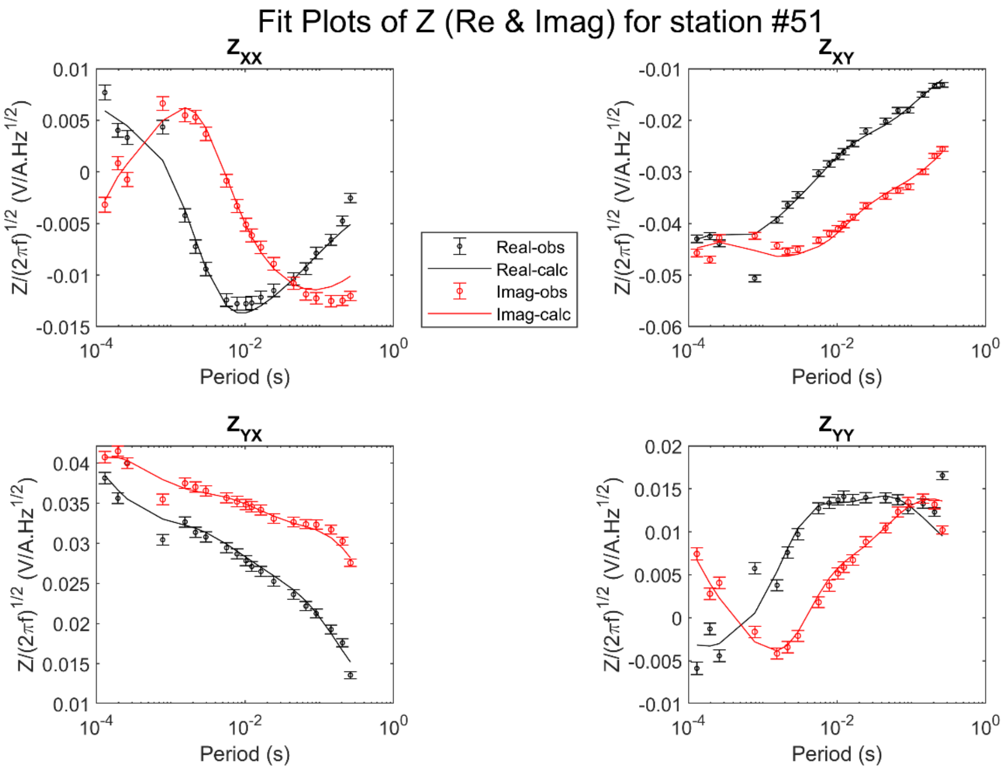
Fit Plots of Z (Re & Imag) for station #51
Z_XX
Z_XY
Z_YX
Z_YY
Z/(2πf)^1/2 (V/A.Hz^1/2)
Period (s)
Real-obs
Real-calc
Imag-obs
Imag-calc

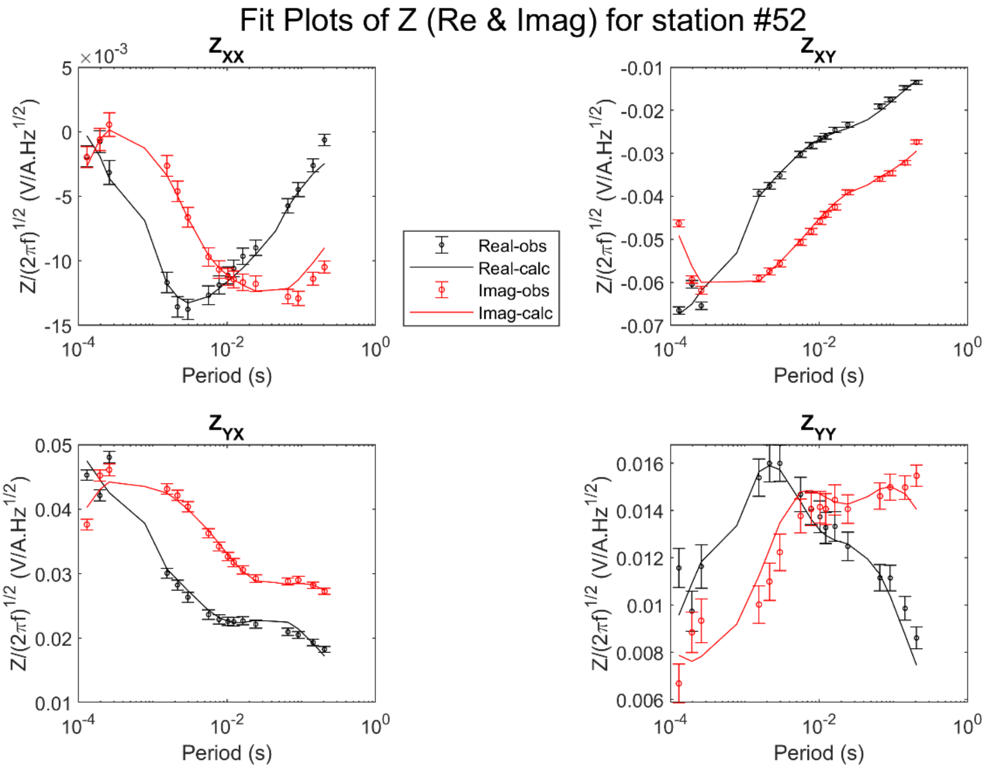
Fit Plots of Z (Re & Imag) for station #52
Z_XX
Z_XY
Z_YX
Z_YY
Z/(2πf)^1/2 (V/A.Hz^1/2)
Period (s)
Real-obs
Real-calc
Imag-obs
Imag-calc

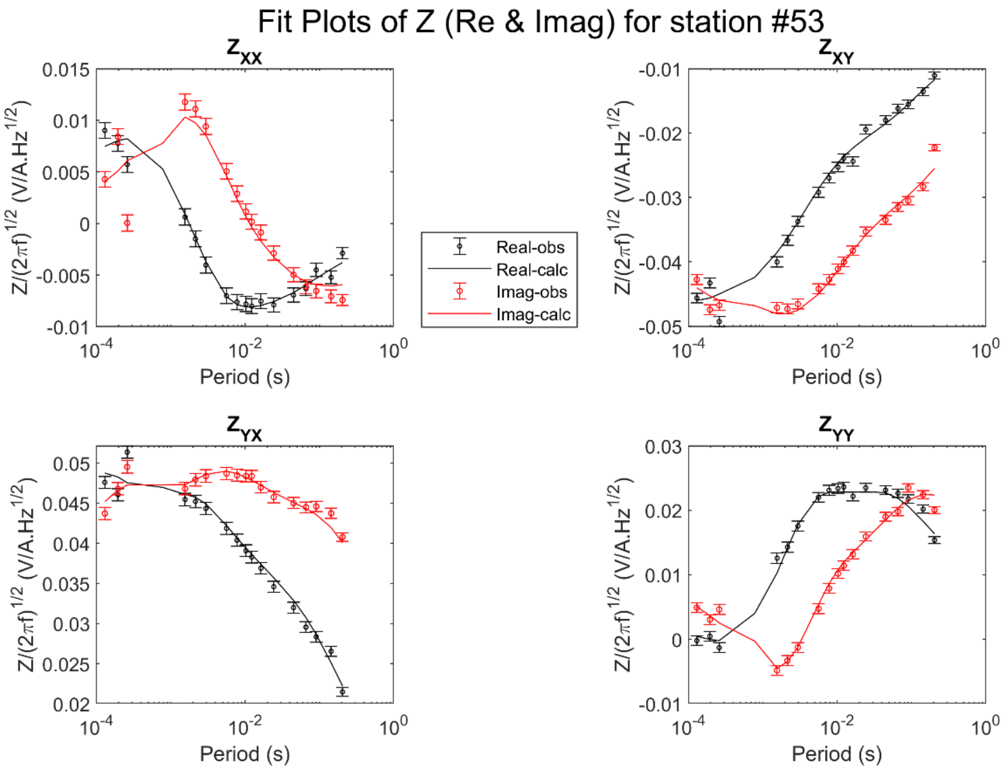
Fit Plots of Z (Re & Imag) for station #53
Z_XX
Z_XY
Z_YX
Z_YY
Z/(2πf)^1/2 (V/A.Hz^1/2)
Period (s)
Real-obs
Real-calc
Imag-obs
Imag-calc

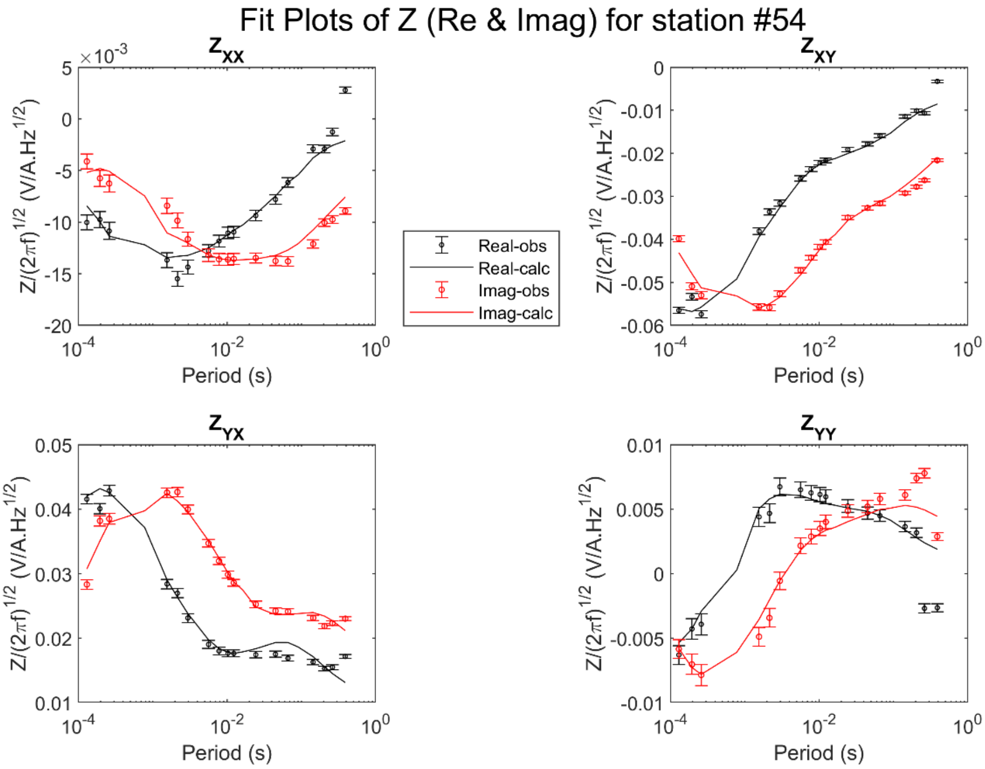
Fit Plots of Z (Re & Imag) for station #54
Z_{XX}
Z_{XY}
Z_{YX}
Z_{YY}
$Z/(2\pi f)^{1/2}$ (V/A.Hz$^{1/2}$)
Period (s)
Real-obs
Real-calc
Imag-obs
Imag-calc

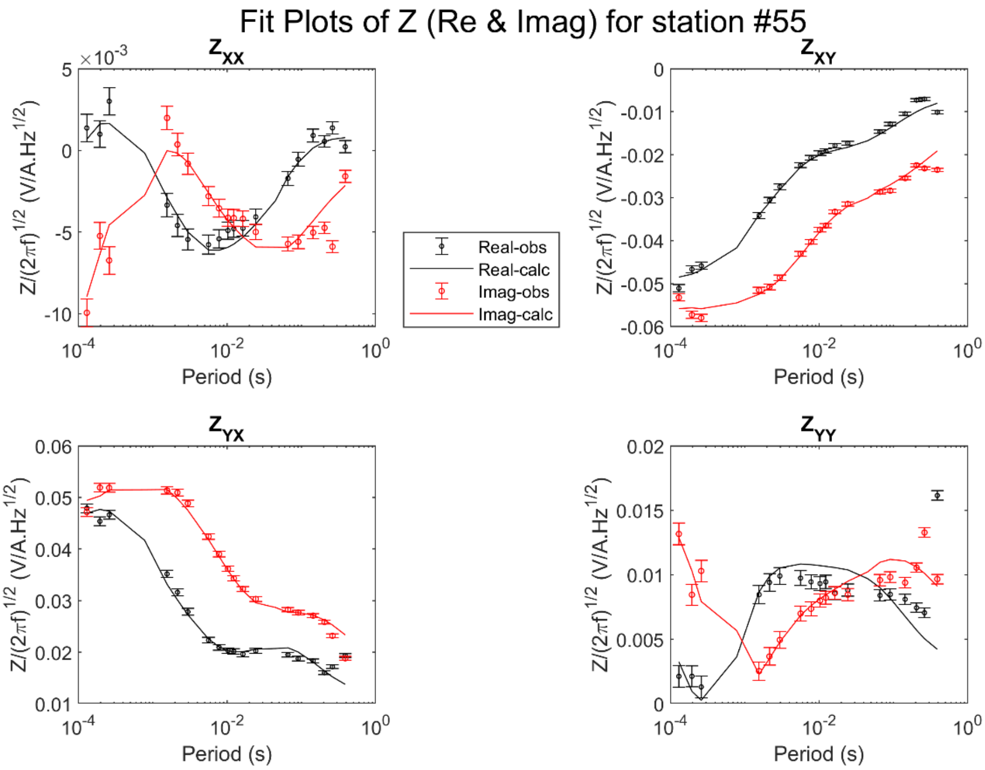
Fit Plots of Z (Re & Imag) for station #55
Z_{XX}
Z_{XY}
Z_{YX}
Z_{YY}
$Z/(2\pi f)^{1/2}$ (V/A.Hz$^{1/2}$)
Period (s)
Real-obs
Real-calc
Imag-obs
Imag-calc

Fit Plots of Z (Re & Imag) for station #56

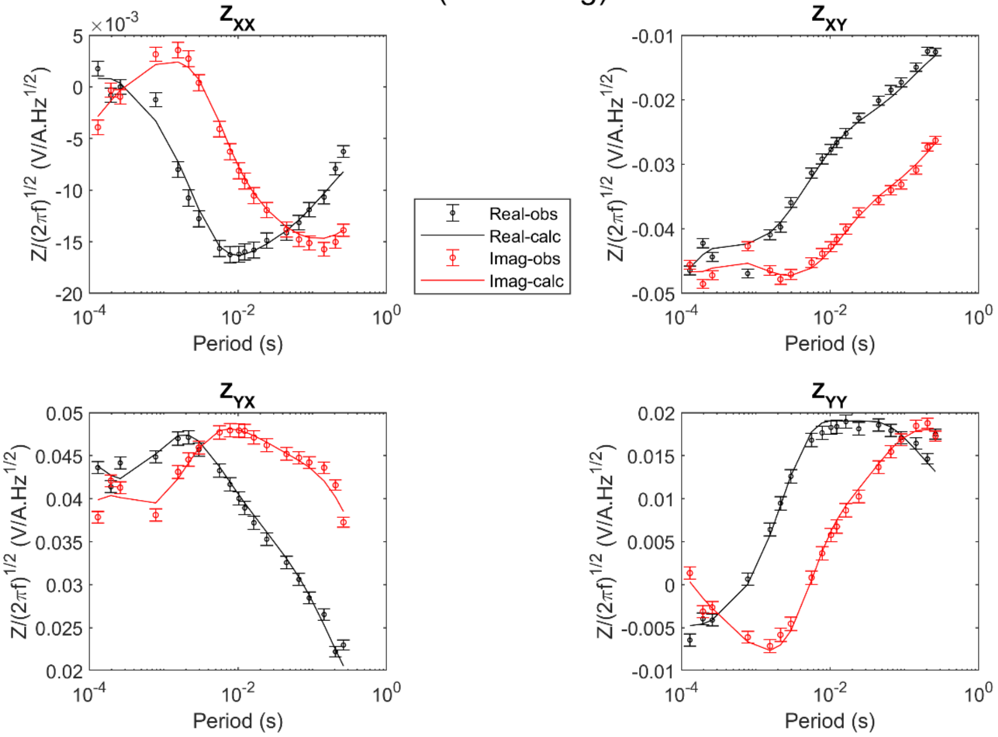

Fit Plots of Z (Re & Imag) for station #57

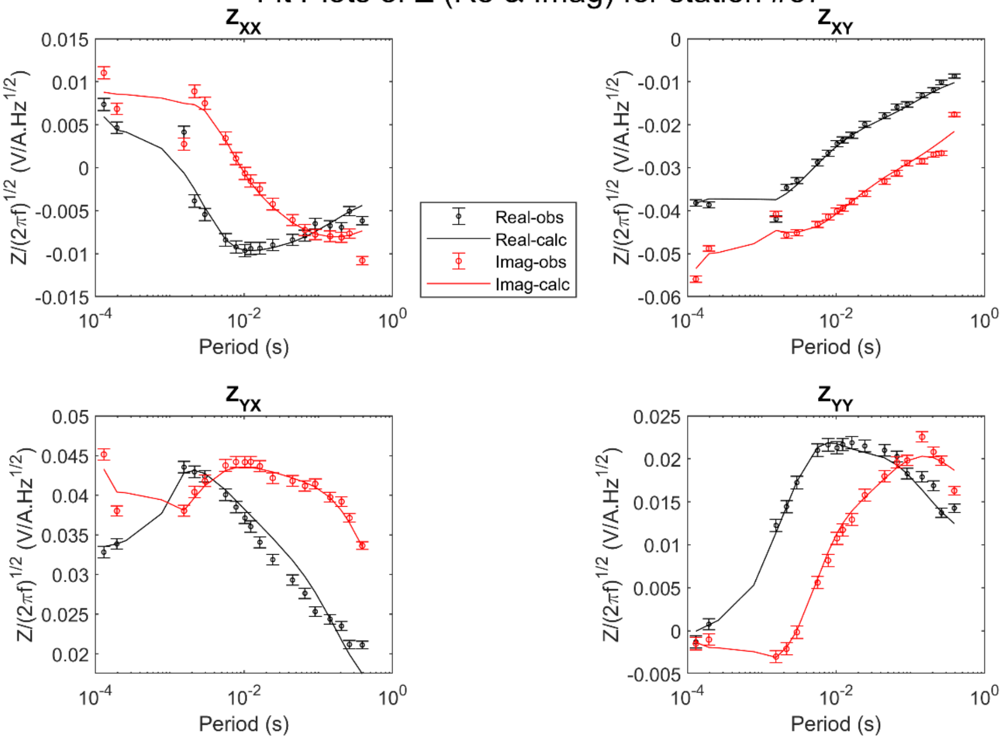

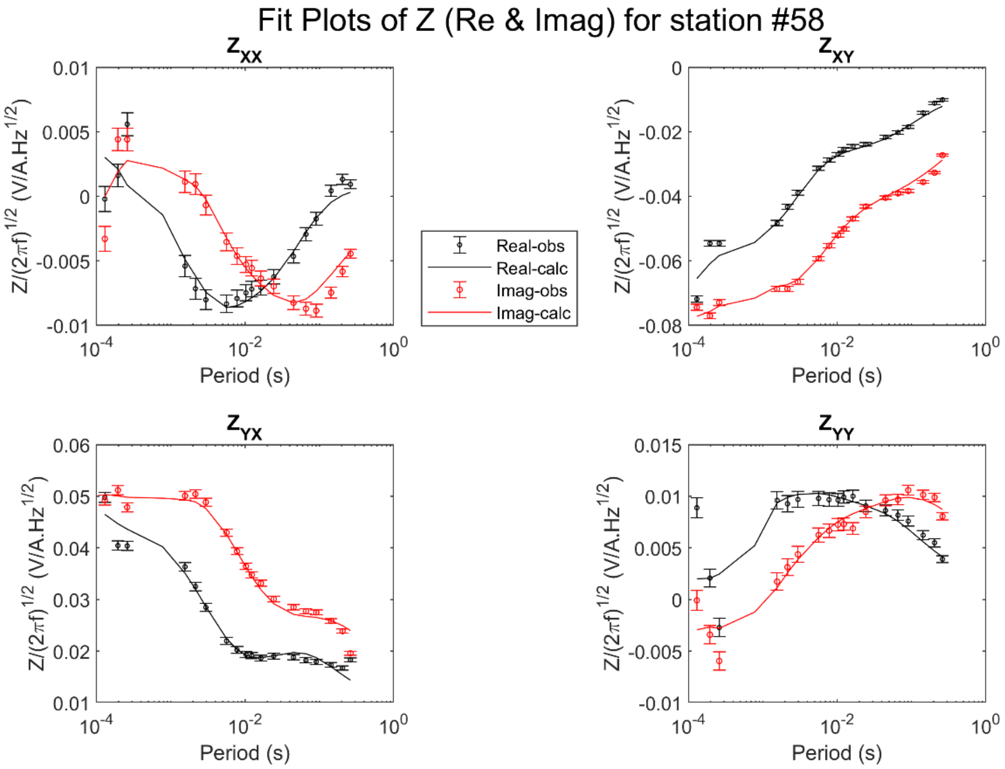
Fit Plots of Z (Re & Imag) for station #58
Z_{XX}
Z_{XY}
Z_{YX}
Z_{YY}
Real-obs
Real-calc
Imag-obs
Imag-calc
$Z/(2\pi f)^{1/2}$ (V/A.Hz$^{1/2}$)
Period (s)

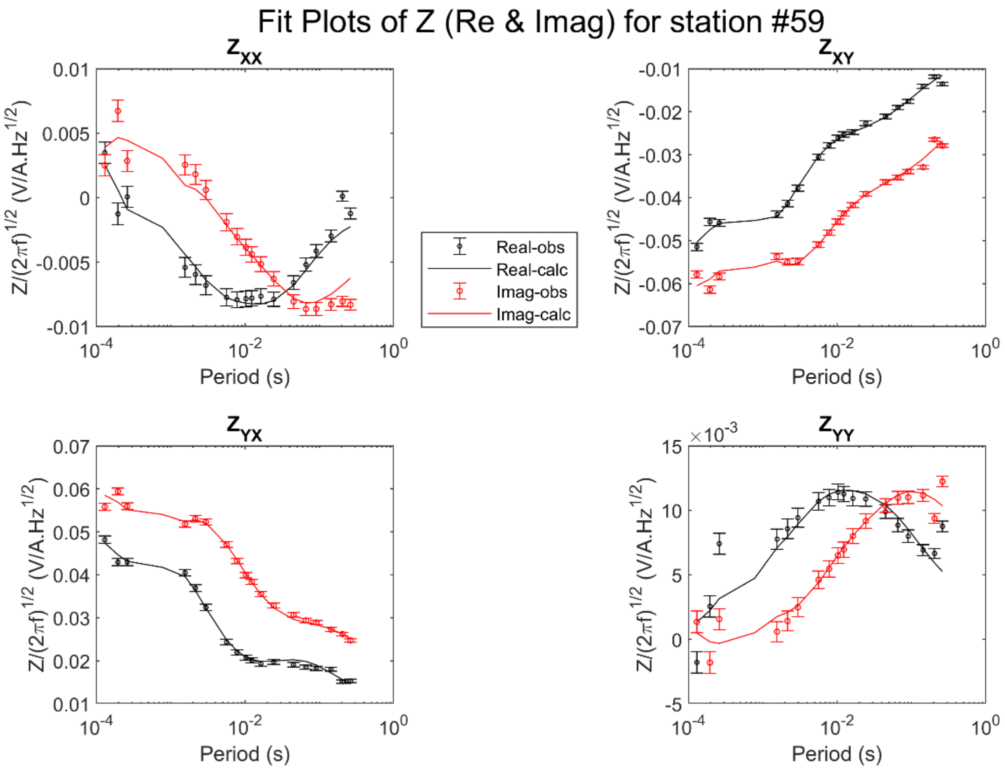
Fit Plots of Z (Re & Imag) for station #59
Z_{XX}
Z_{XY}
Z_{YX}
Z_{YY}
Real-obs
Real-calc
Imag-obs
Imag-calc
$Z/(2\pi f)^{1/2}$ (V/A.Hz$^{1/2}$)
Period (s)

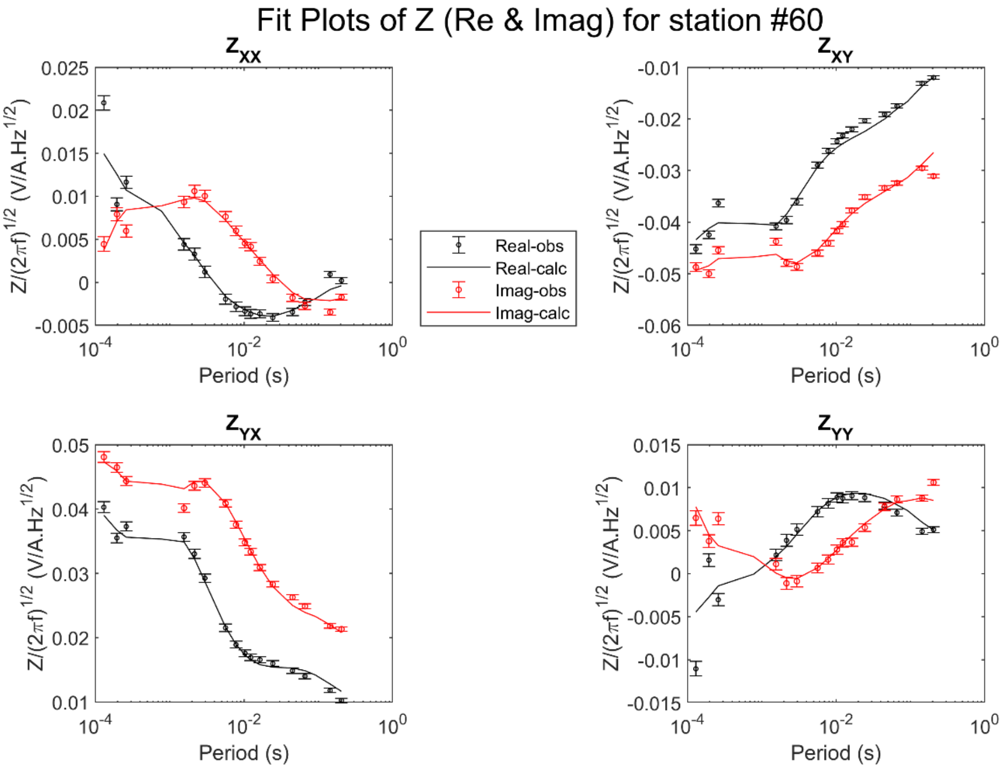
Fit Plots of Z (Re & Imag) for station #60
Z_XX
Z_XY
Z_YX
Z_YY
Z/(2πf)^1/2 (V/A.Hz^1/2)
Period (s)
Real-obs
Real-calc
Imag-obs
Imag-calc

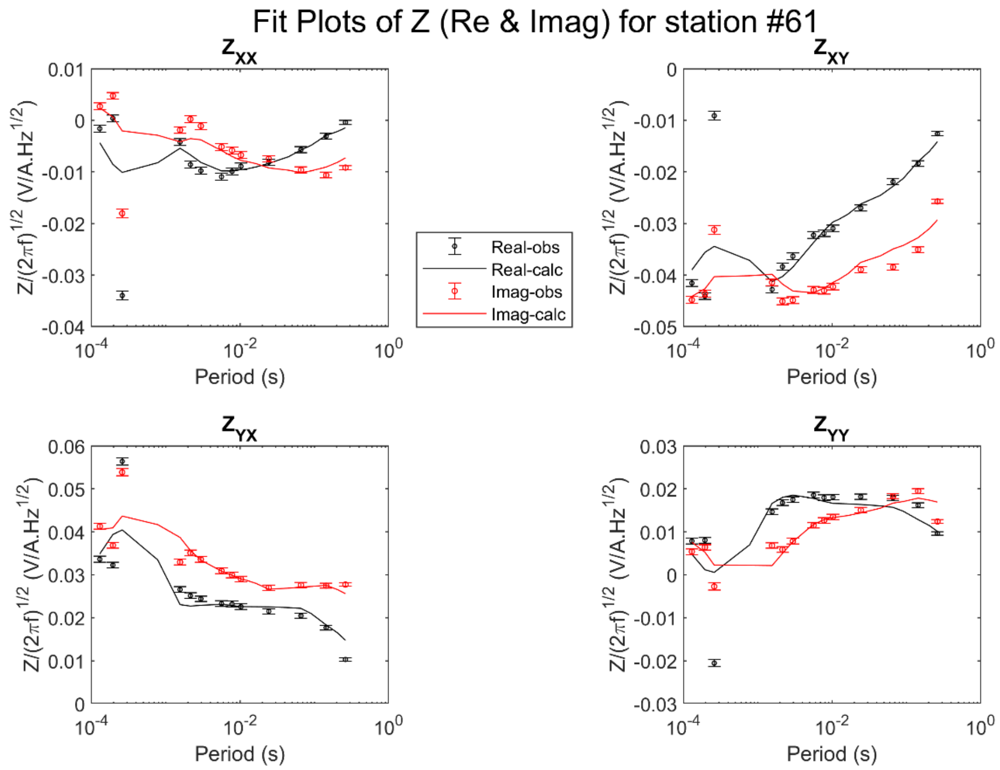
Fit Plots of Z (Re & Imag) for station #61
Z_XX
Z_XY
Z_YX
Z_YY
Z/(2πf)^1/2 (V/A.Hz^1/2)
Period (s)
Real-obs
Real-calc
Imag-obs
Imag-calc

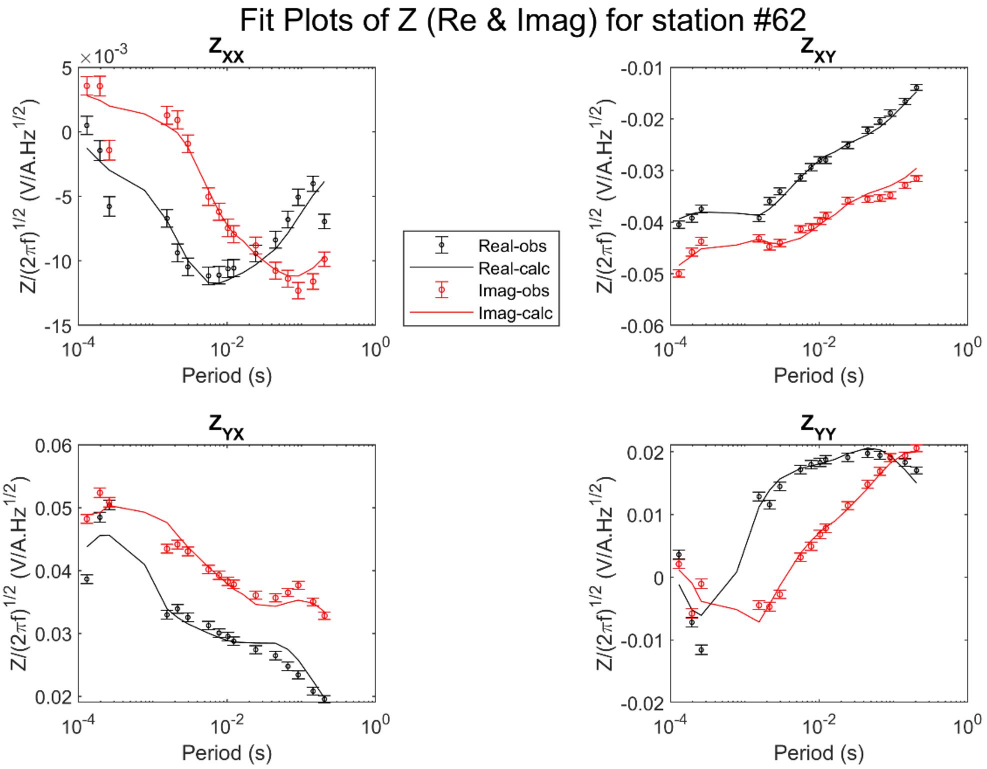
Fit Plots of Z (Re & Imag) for station #62
Z_XX
Z_XY
Z_YX
Z_YY
Z/(2πf)^1/2 (V/A.Hz^1/2)
Period (s)
Real-obs
Real-calc
Imag-obs
Imag-calc

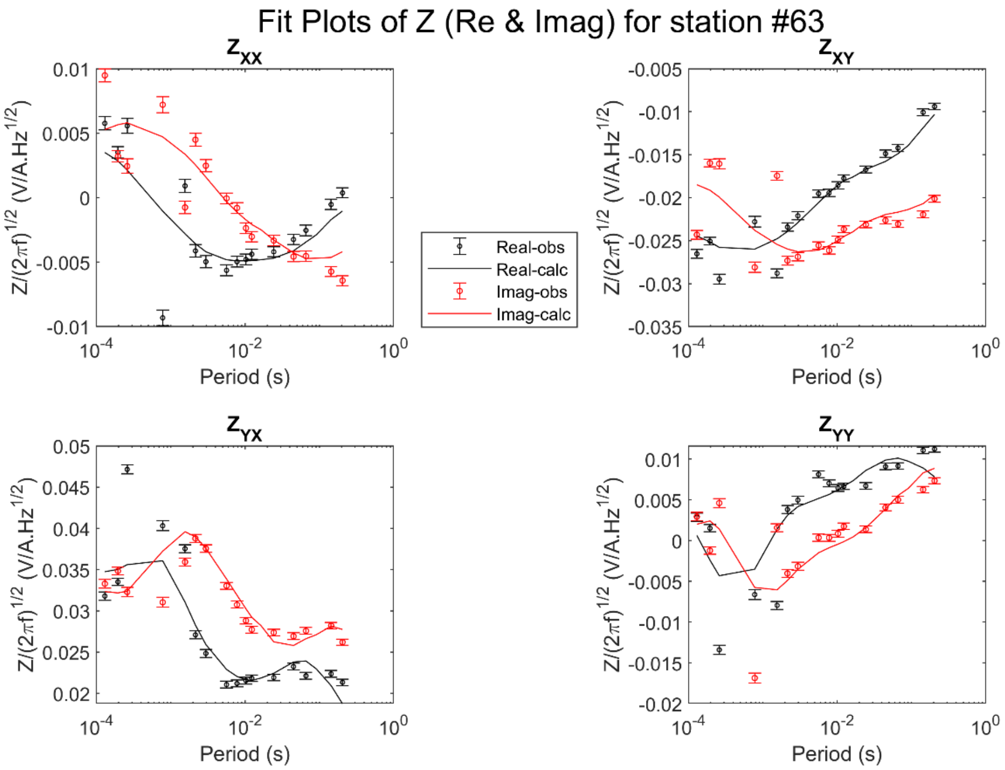
Fit Plots of Z (Re & Imag) for station #63
Z_XX
Z_XY
Z_YX
Z_YY
Z/(2πf)^1/2 (V/A.Hz^1/2)
Period (s)
Real-obs
Real-calc
Imag-obs
Imag-calc

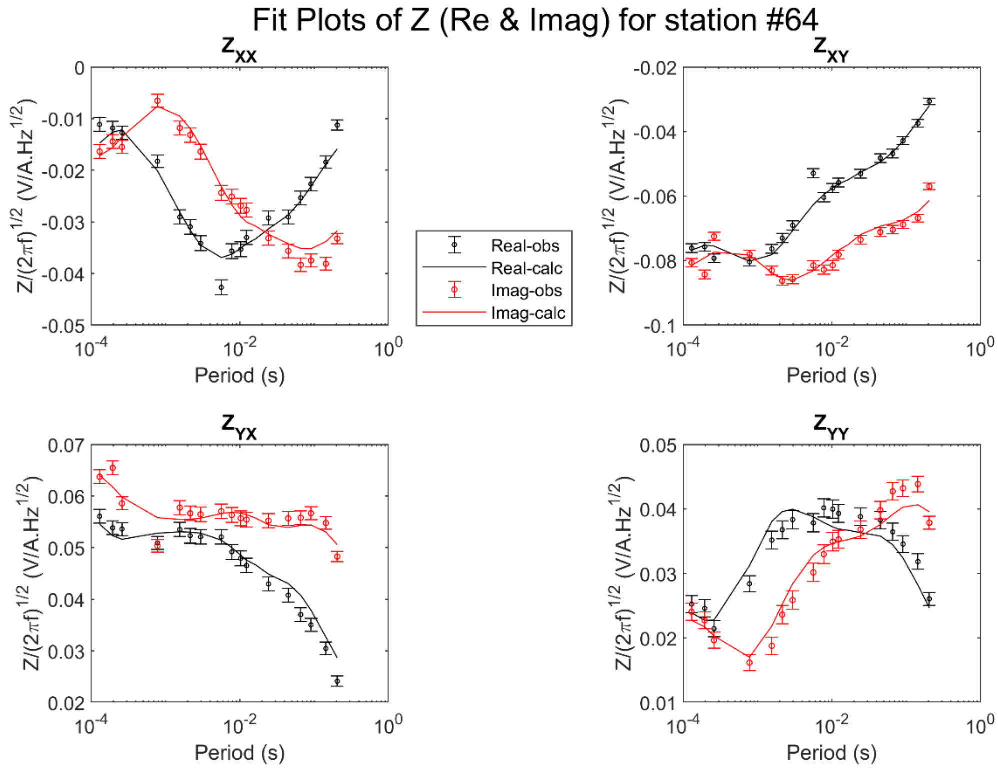
Fit Plots of Z (Re & Imag) for station #64
Z_{XX}
Z_{XY}
Z_{YX}
Z_{YY}
$Z/(2\pi f)^{1/2}$ (V/A.Hz$^{1/2}$)
Period (s)
Real-obs
Real-calc
Imag-obs
Imag-calc

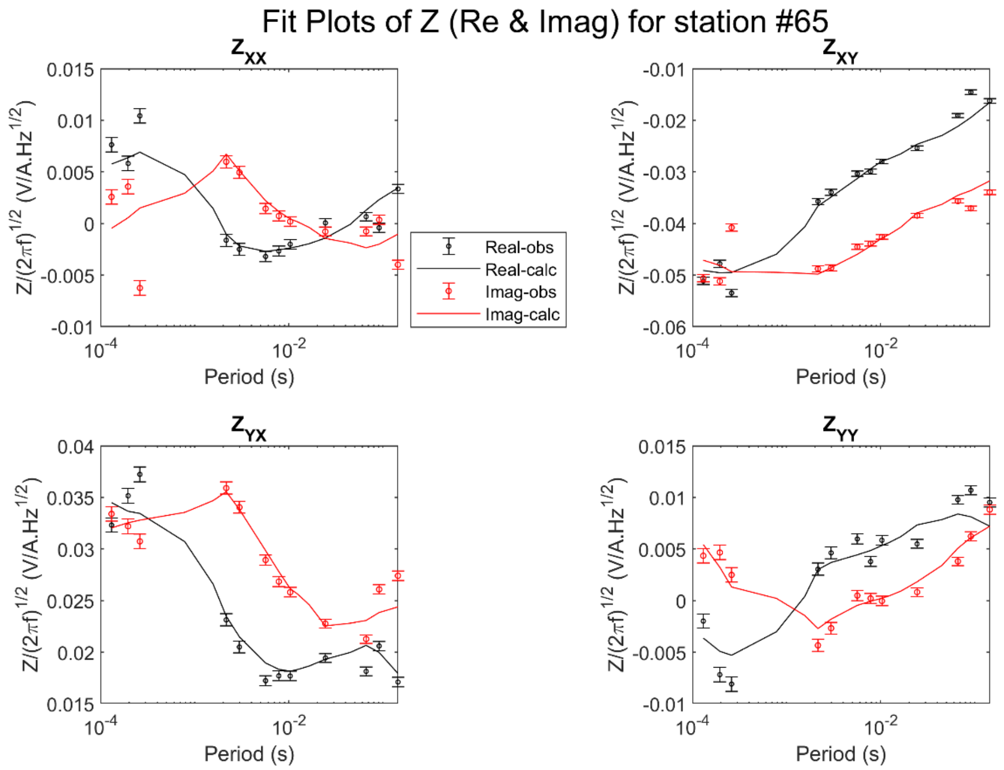
Fit Plots of Z (Re & Imag) for station #65
Z_{XX}
Z_{XY}
Z_{YX}
Z_{YY}
$Z/(2\pi f)^{1/2}$ (V/A.Hz$^{1/2}$)
Period (s)
Real-obs
Real-calc
Imag-obs
Imag-calc

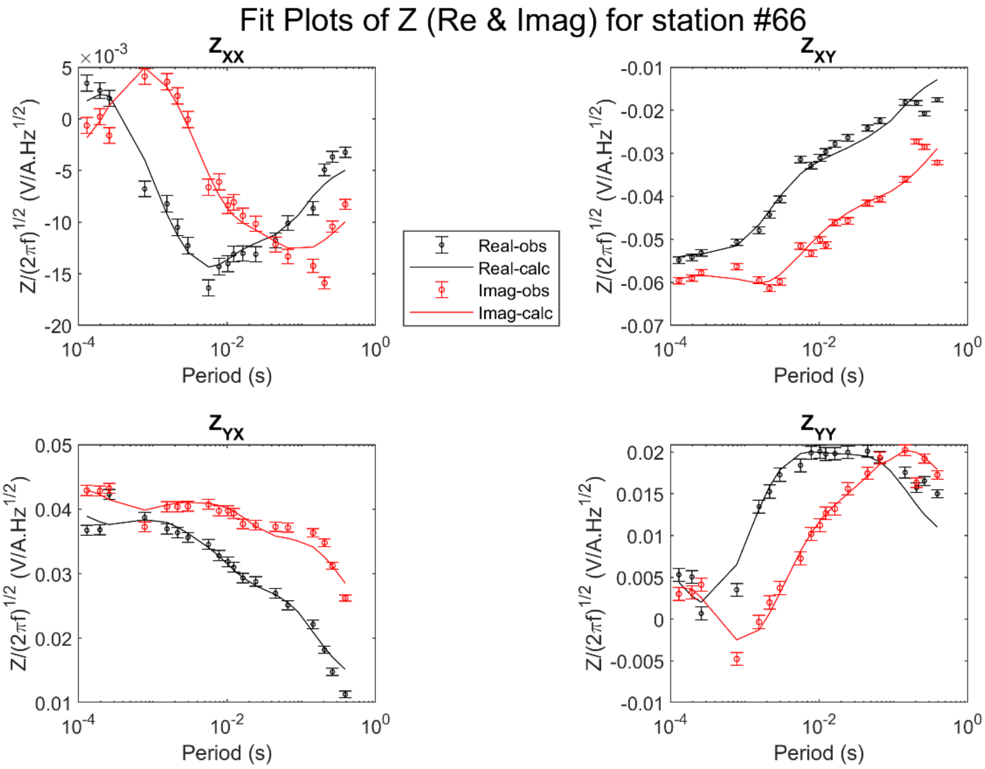
Fit Plots of Z (Re & Imag) for station #66
Z_XX
Z_XY
Z_YX
Z_YY
Z/(2πf)^1/2 (V/A.Hz^1/2)
Period (s)
Real-obs
Real-calc
Imag-obs
Imag-calc

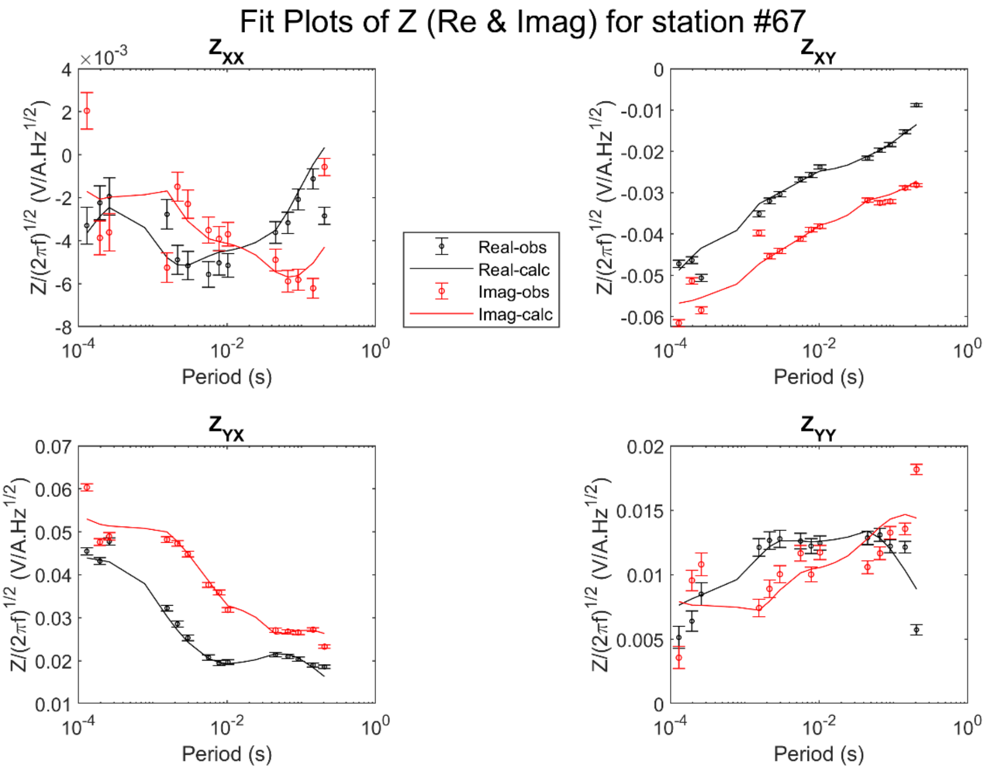
Fit Plots of Z (Re & Imag) for station #67
Z_XX
Z_XY
Z_YX
Z_YY
Z/(2πf)^1/2 (V/A.Hz^1/2)
Period (s)
Real-obs
Real-calc
Imag-obs
Imag-calc

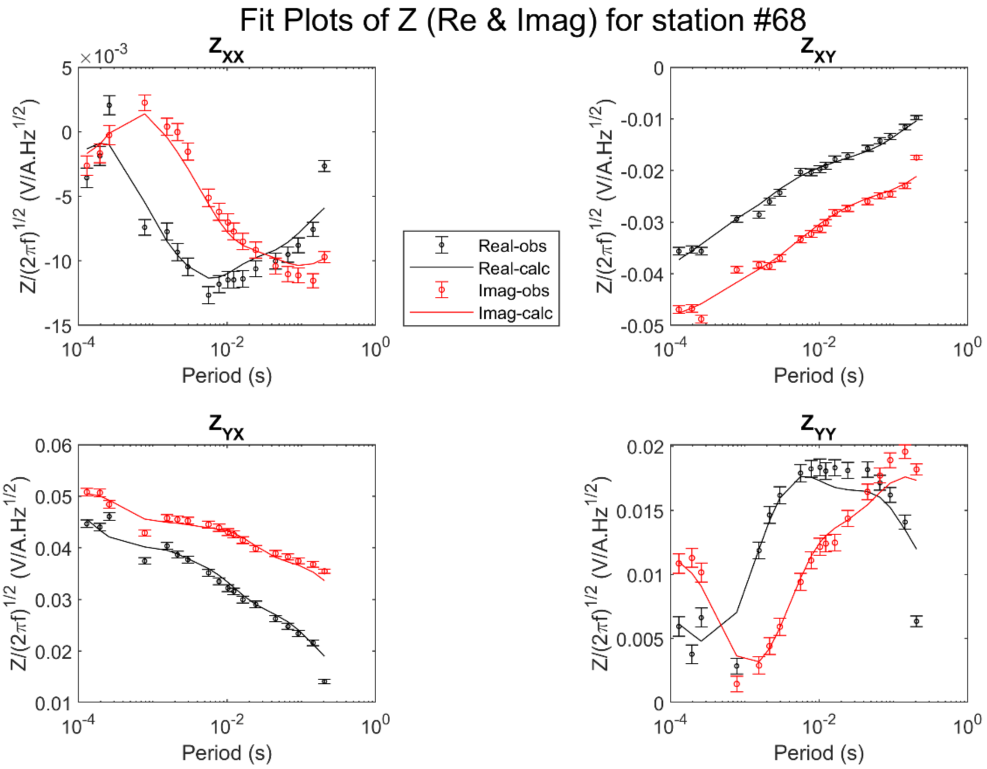
Fit Plots of Z (Re & Imag) for station #68
Z_{XX}
Z_{XY}
Z_{YX}
Z_{YY}
$\times 10^{-3}$
Real-obs
Real-calc
Imag-obs
Imag-calc
$Z/(2\pi f)^{1/2}$ (V/A.Hz$^{1/2}$)
Period (s)

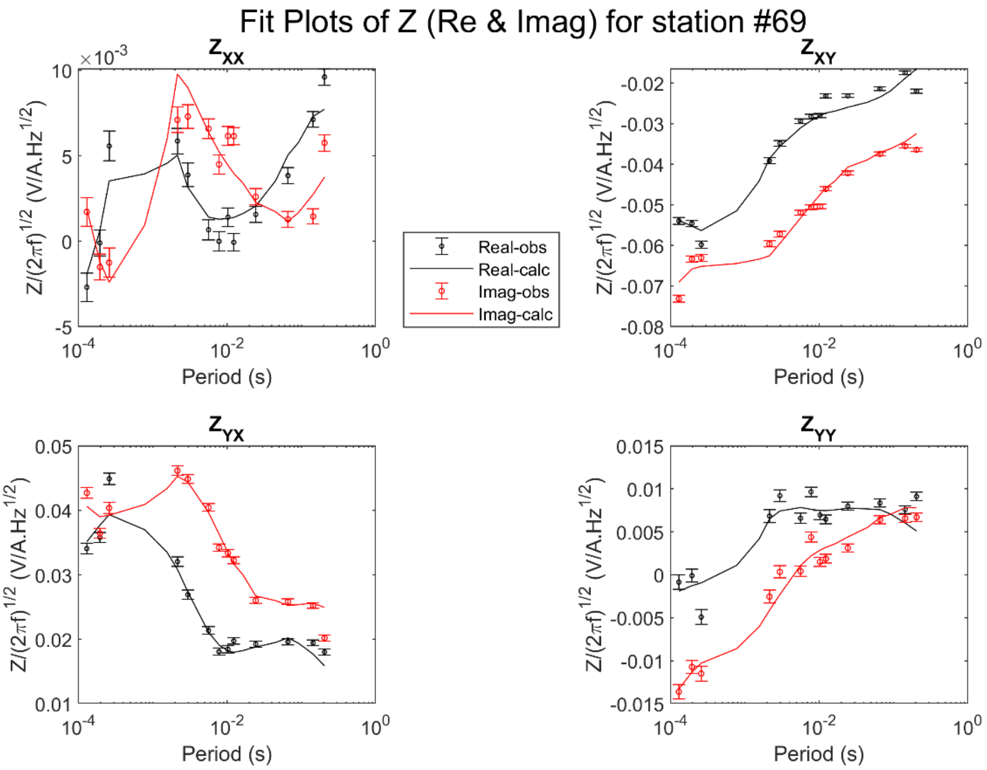
Fit Plots of Z (Re & Imag) for station #69
Z_{XX}
Z_{XY}
Z_{YX}
Z_{YY}
$\times 10^{-3}$
Real-obs
Real-calc
Imag-obs
Imag-calc
$Z/(2\pi f)^{1/2}$ (V/A.Hz$^{1/2}$)
Period (s)

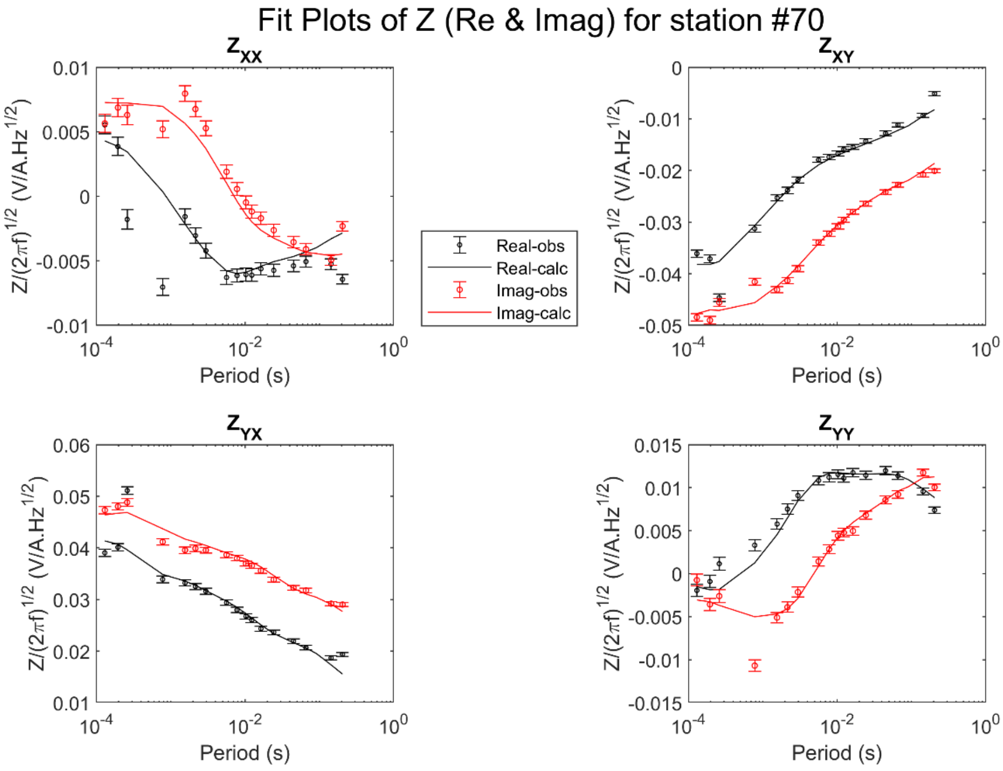

Fit Plots of Z (Re & Imag) for station #70
Z_XX
Z_XY
Z_YX
Z_YY
Z/(2πf)^1/2 (V/A.Hz^1/2)
Period (s)
Real-obs
Real-calc
Imag-obs
Imag-calc

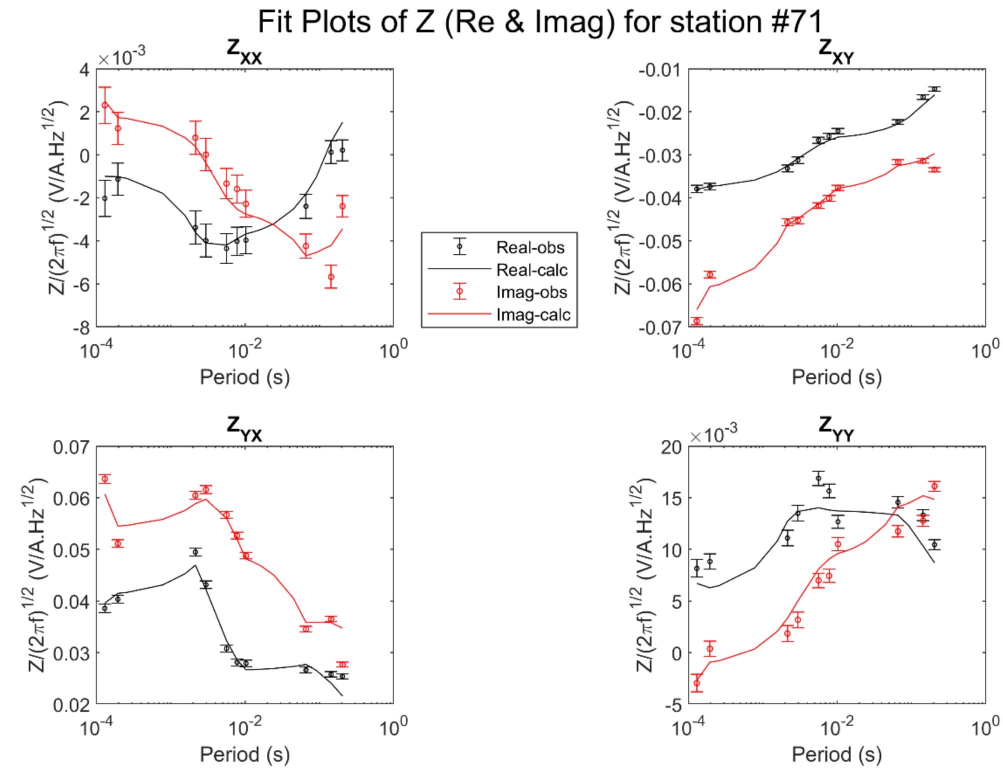

Fit Plots of Z (Re & Imag) for station #71
Z_XX
Z_XY
Z_YX
Z_YY
Z/(2πf)^1/2 (V/A.Hz^1/2)
Period (s)
Real-obs
Real-calc
Imag-obs
Imag-calc

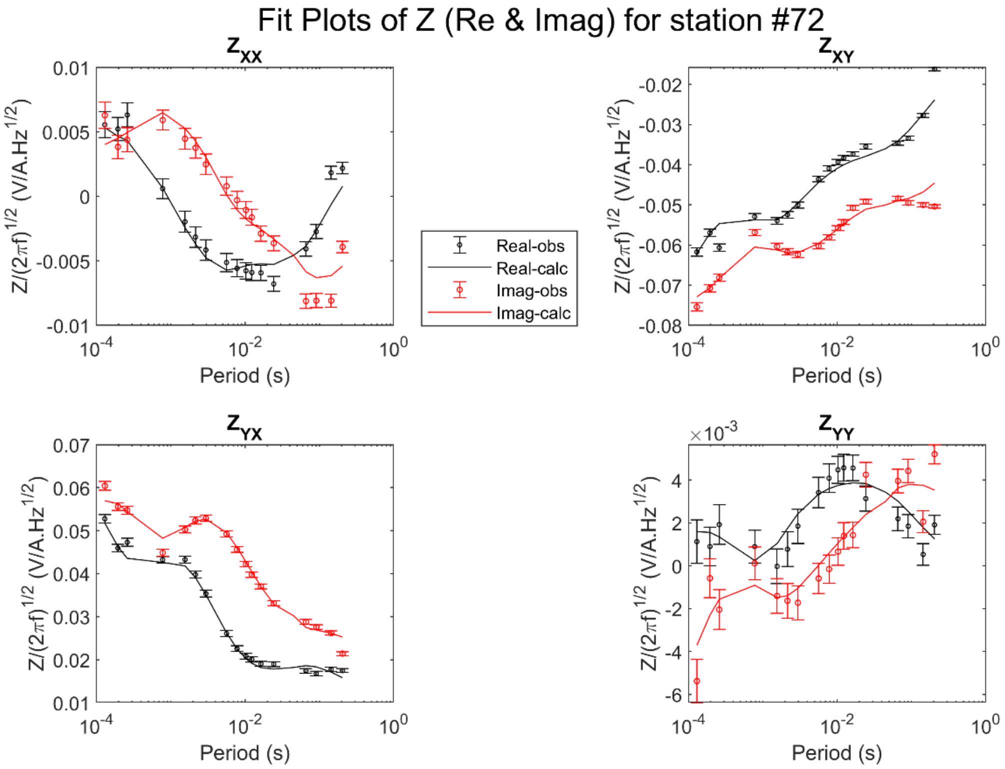
Fit Plots of Z (Re & Imag) for station #72
Z_{XX}
Z_{XY}
Z_{YX}
Z_{YY}
$Z/(2\pi f)^{1/2}$ (V/A.Hz$^{1/2}$)
Period (s)
Real-obs
Real-calc
Imag-obs
Imag-calc

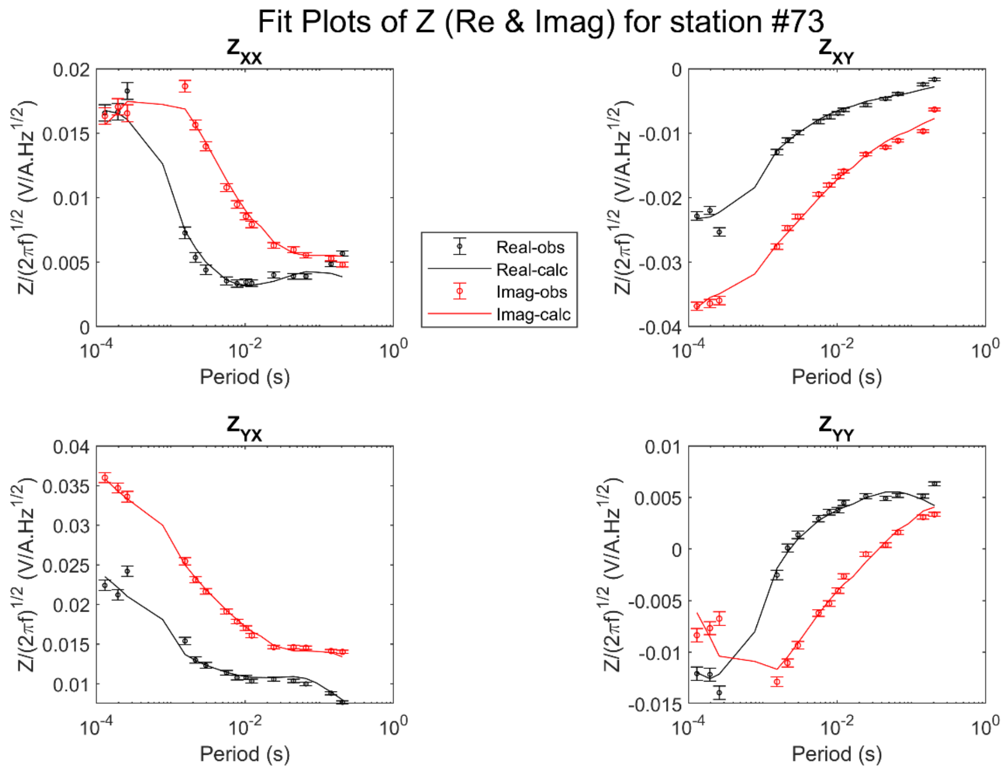
Fit Plots of Z (Re & Imag) for station #73
Z_{XX}
Z_{XY}
Z_{YX}
Z_{YY}
$Z/(2\pi f)^{1/2}$ (V/A.Hz$^{1/2}$)
Period (s)
Real-obs
Real-calc
Imag-obs
Imag-calc

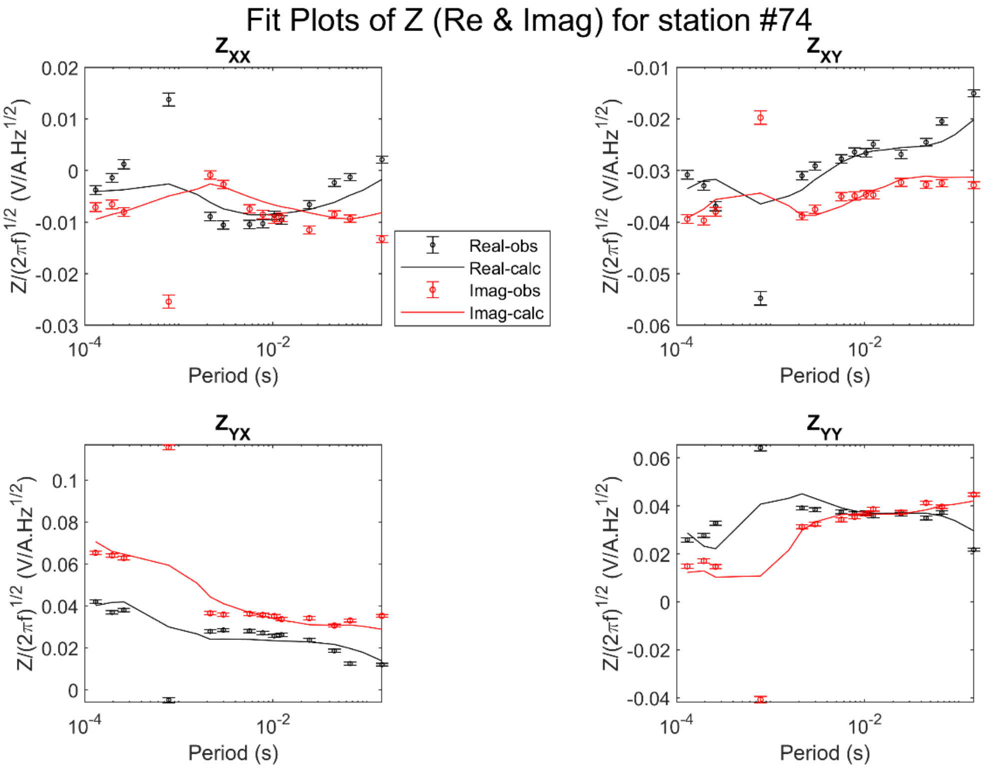

Fit Plots of Z (Re & Imag) for station #74
Z_{XX}
Z_{XY}
Z_{YX}
Z_{YY}
$Z/(2\pi f)^{1/2}$ (V/A.Hz$^{1/2}$)
Period (s)
Real-obs
Real-calc
Imag-obs
Imag-calc

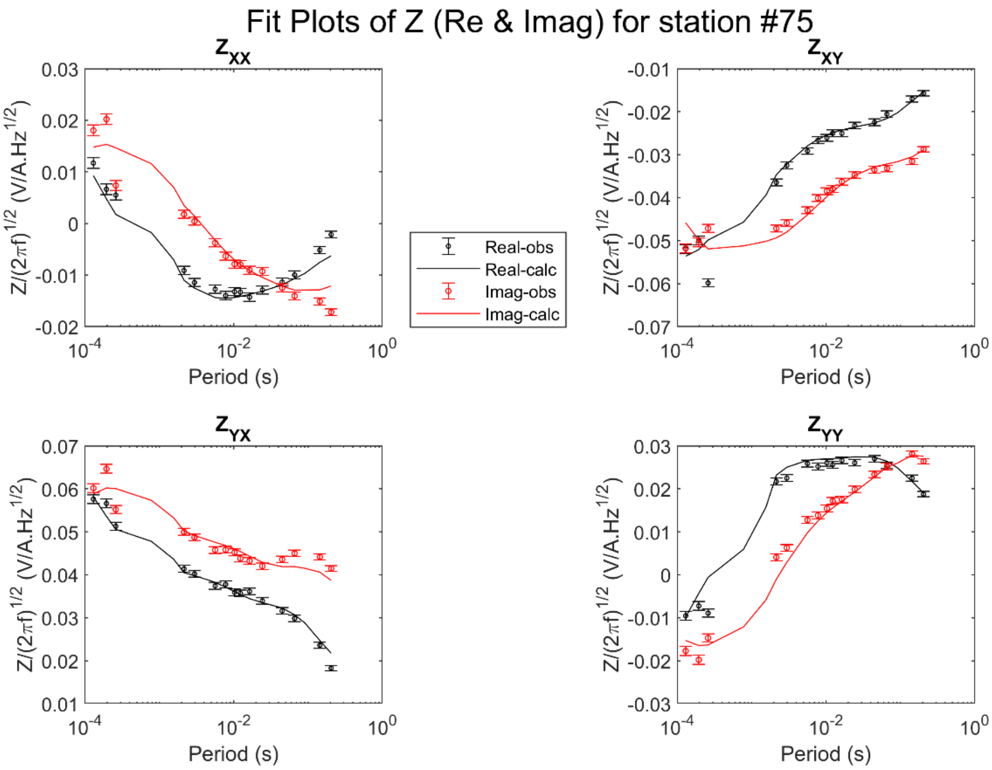

Fit Plots of Z (Re & Imag) for station #75
Z_{XX}
Z_{XY}
Z_{YX}
Z_{YY}
$Z/(2\pi f)^{1/2}$ (V/A.Hz$^{1/2}$)
Period (s)
Real-obs
Real-calc
Imag-obs
Imag-calc

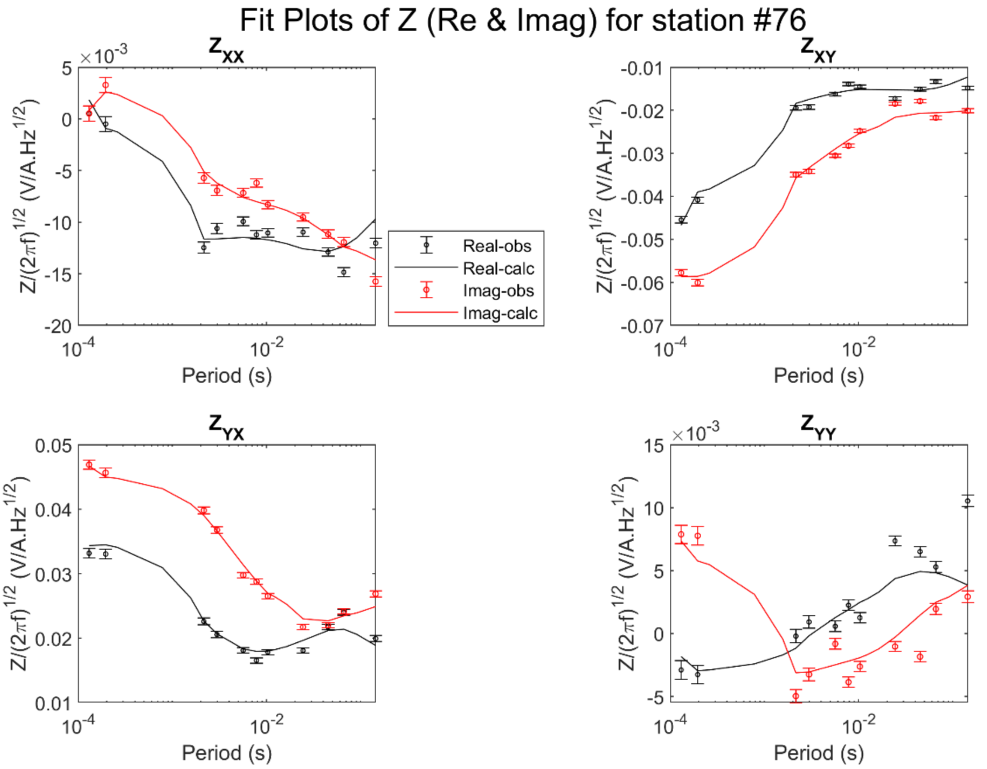
Fit Plots of Z (Re & Imag) for station #76
Z_XX
Z_XY
Z_YX
Z_YY
Z/(2πf)^1/2 (V/A.Hz^1/2)
Period (s)
Real-obs
Real-calc
Imag-obs
Imag-calc

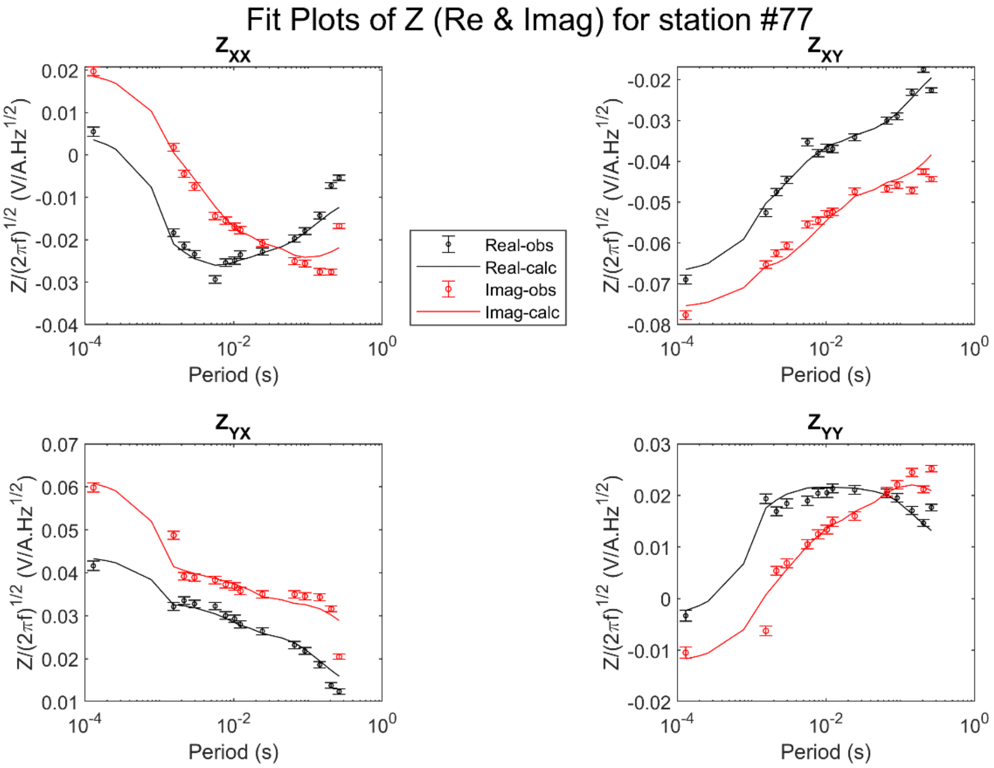
Fit Plots of Z (Re & Imag) for station #77
Z_XX
Z_XY
Z_YX
Z_YY
Z/(2πf)^1/2 (V/A.Hz^1/2)
Period (s)
Real-obs
Real-calc
Imag-obs
Imag-calc

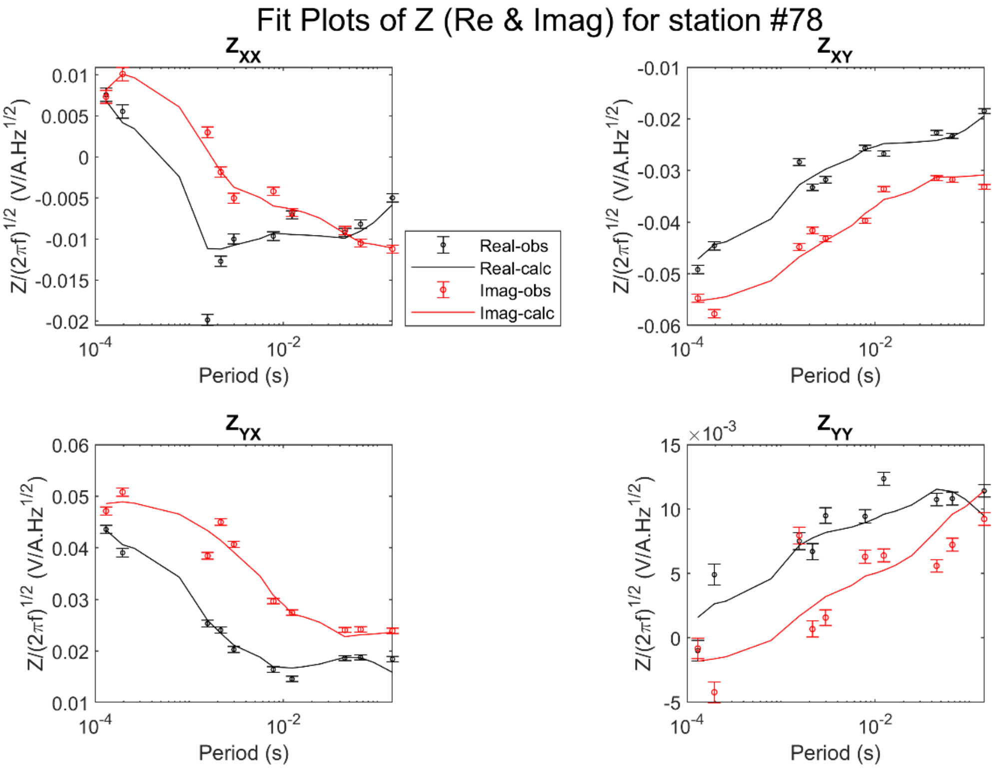
Fit Plots of Z (Re & Imag) for station #78
Z_XX
Z_XY
Z_YX
Z_YY
Z/(2πf)^1/2 (V/A.Hz^1/2)
Period (s)
Real-obs
Real-calc
Imag-obs
Imag-calc

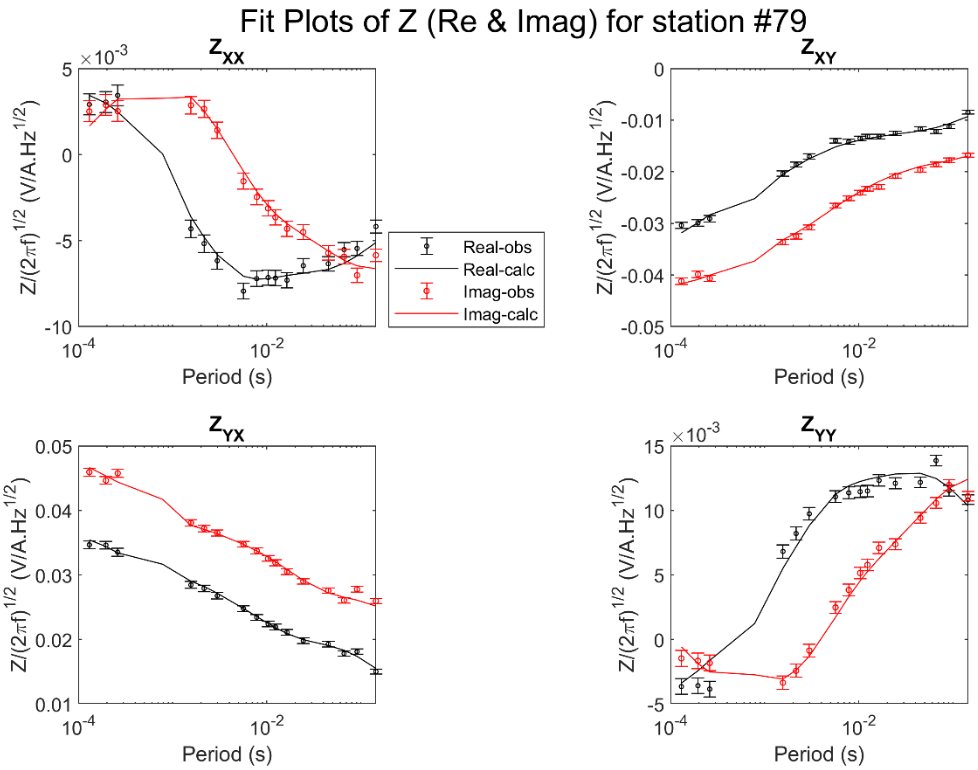
Fit Plots of Z (Re & Imag) for station #79
Z_XX
Z_XY
Z_YX
Z_YY
Z/(2πf)^1/2 (V/A.Hz^1/2)
Period (s)
Real-obs
Real-calc
Imag-obs
Imag-calc

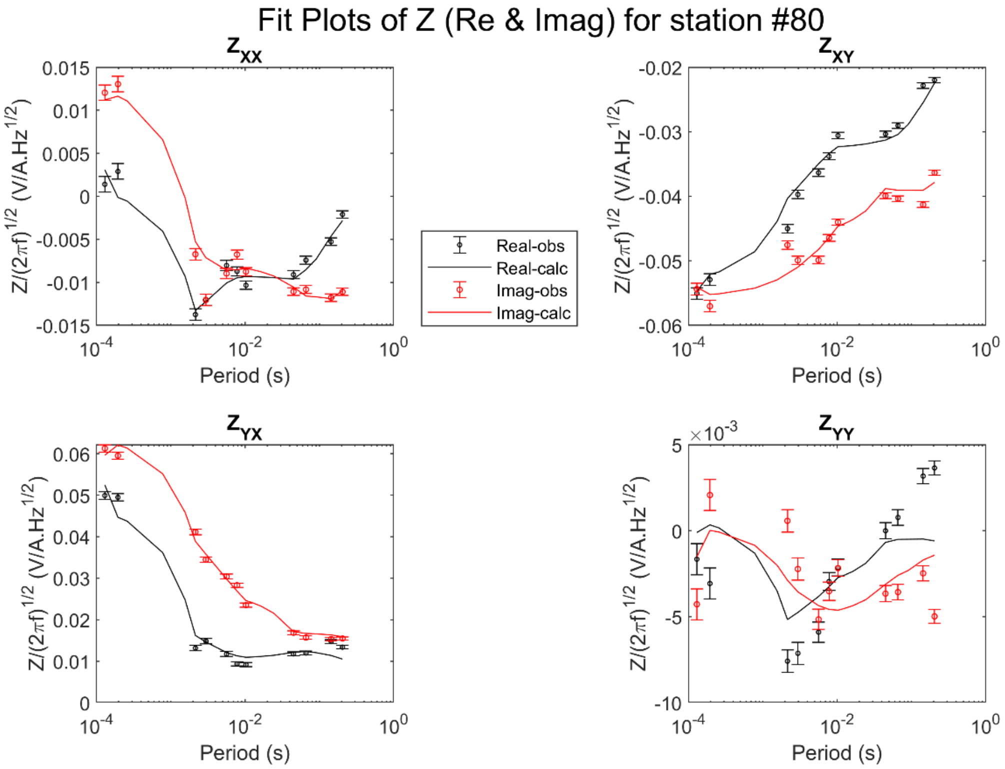
Fit Plots of Z (Re & Imag) for station #80
Z_{XX}
Z_{XY}
Z_{YX}
Z_{YY}
$Z/(2\pi f)^{1/2}$ (V/A.Hz$^{1/2}$)
Period (s)
Real-obs
Real-calc
Imag-obs
Imag-calc

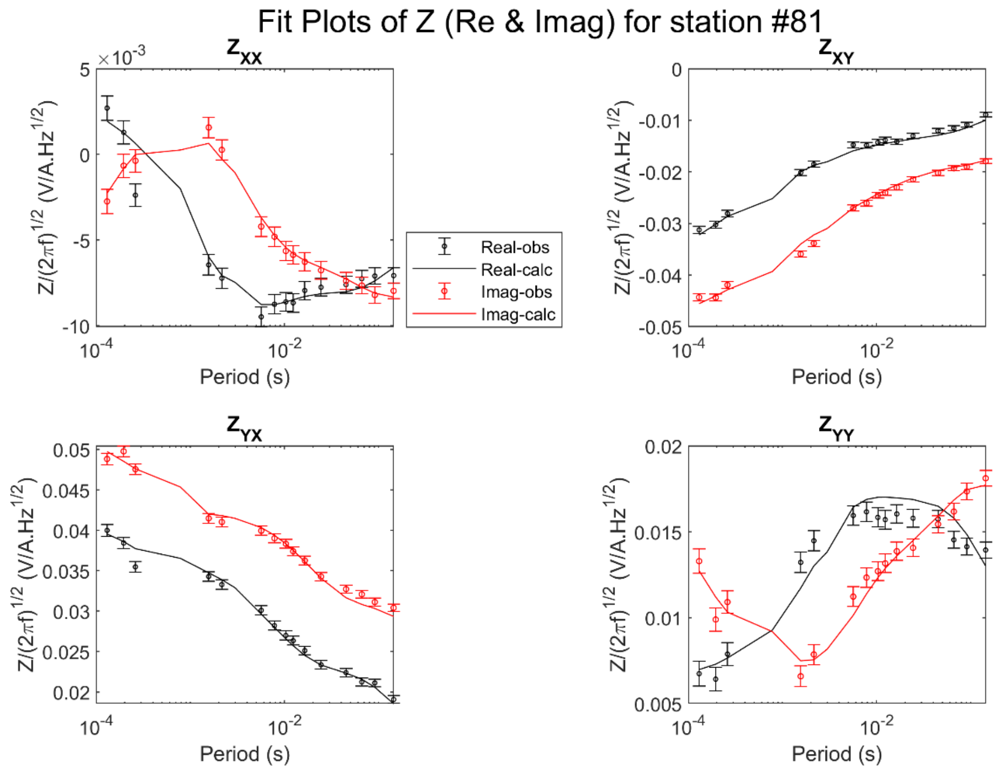
Fit Plots of Z (Re & Imag) for station #81
Z_{XX}
Z_{XY}
Z_{YX}
Z_{YY}
$Z/(2\pi f)^{1/2}$ (V/A.Hz$^{1/2}$)
Period (s)
Real-obs
Real-calc
Imag-obs
Imag-calc

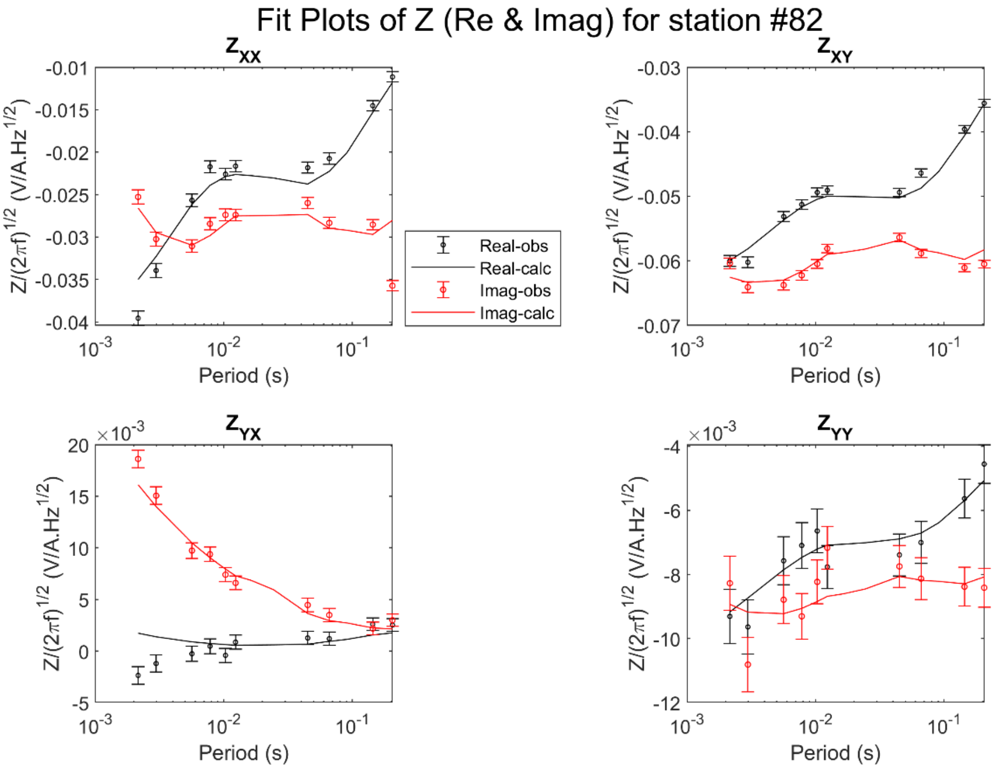
Fit Plots of Z (Re & Imag) for station #82
Z_{XX}
Z_{XY}
Z_{YX}
Z_{YY}
$Z/(2\pi f)^{1/2}$ (V/A.Hz$^{1/2}$)
Period (s)
Real-obs
Real-calc
Imag-obs
Imag-calc

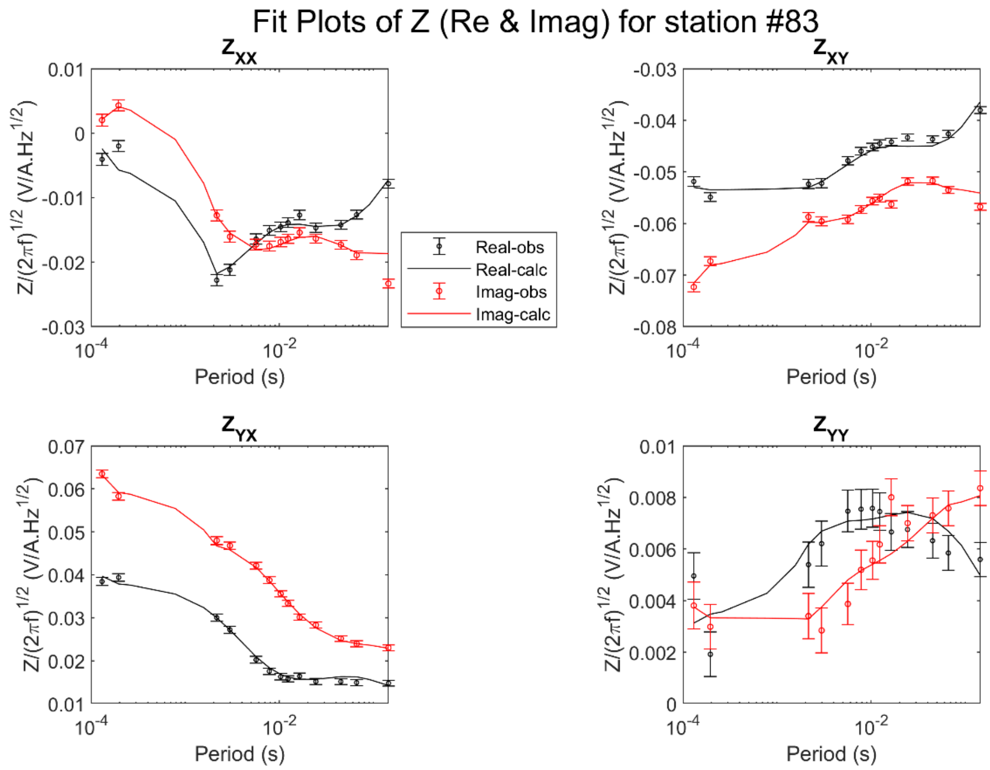
Fit Plots of Z (Re & Imag) for station #83
Z_{XX}
Z_{XY}
Z_{YX}
Z_{YY}
$Z/(2\pi f)^{1/2}$ (V/A.Hz$^{1/2}$)
Period (s)
Real-obs
Real-calc
Imag-obs
Imag-calc

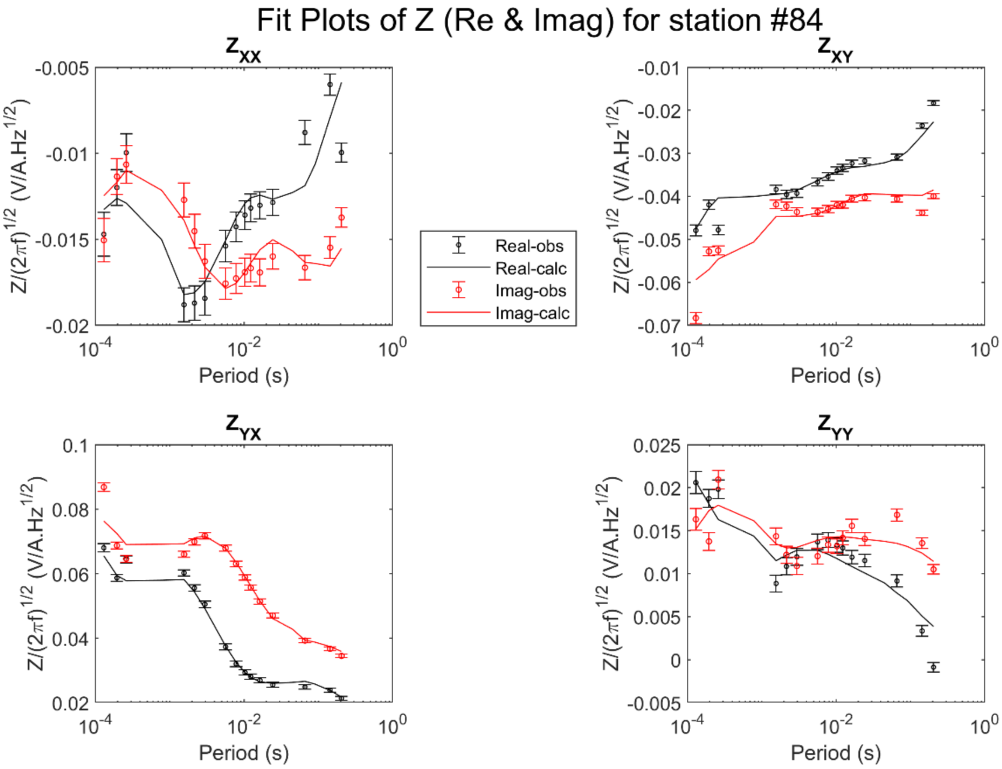

Fit Plots of Z (Re & Imag) for station #84
Z_XX
Z_XY
Z_YX
Z_YY
Z/(2πf)^1/2 (V/A.Hz^1/2)
Period (s)
Real-obs
Real-calc
Imag-obs
Imag-calc

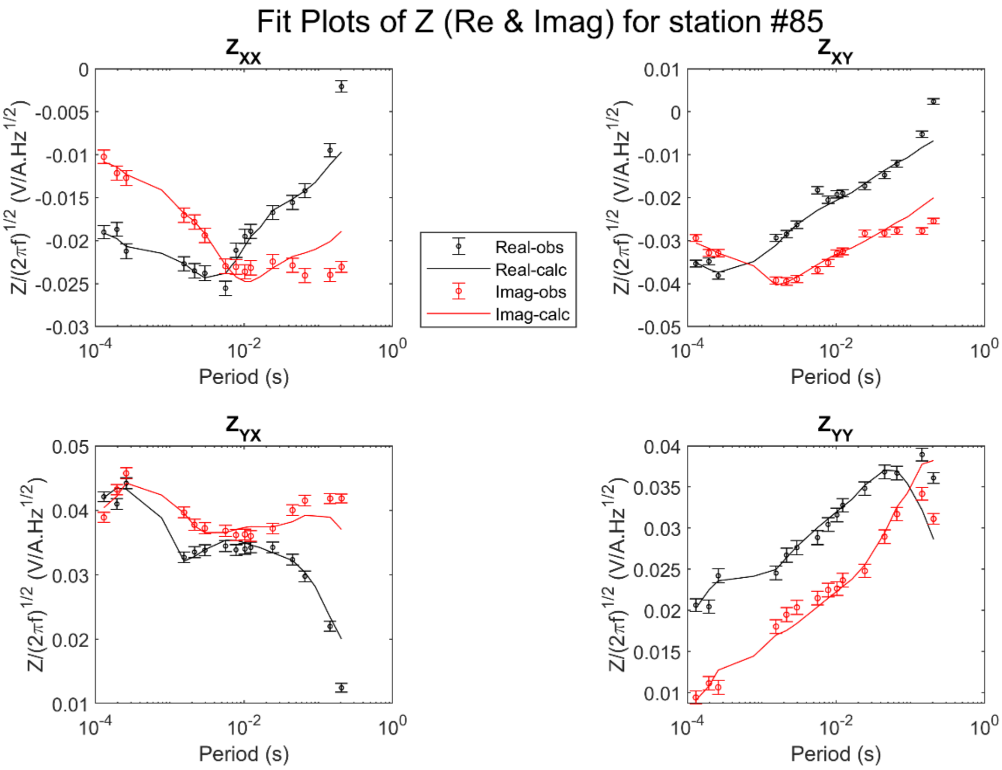

Fit Plots of Z (Re & Imag) for station #85
Z_XX
Z_XY
Z_YX
Z_YY
Z/(2πf)^1/2 (V/A.Hz^1/2)
Period (s)
Real-obs
Real-calc
Imag-obs
Imag-calc

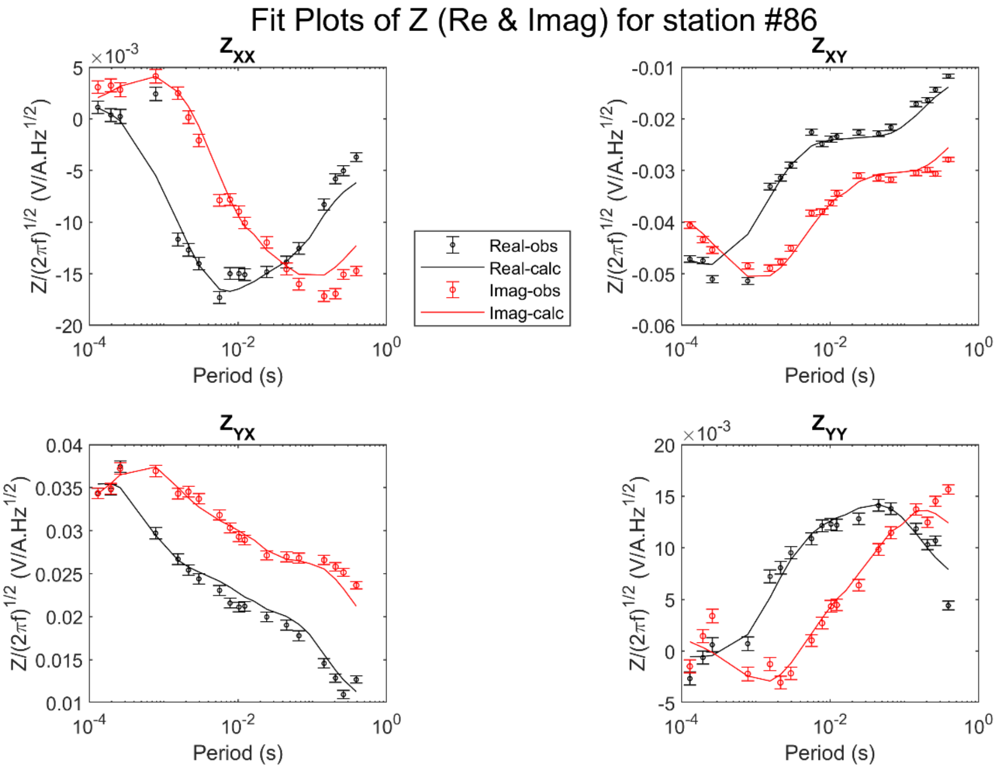
Fit Plots of Z (Re & Imag) for station #86
Z_XX
Z_XY
Z_YX
Z_YY
Z/(2πf)^1/2 (V/A.Hz^1/2)
Period (s)
Real-obs
Real-calc
Imag-obs
Imag-calc

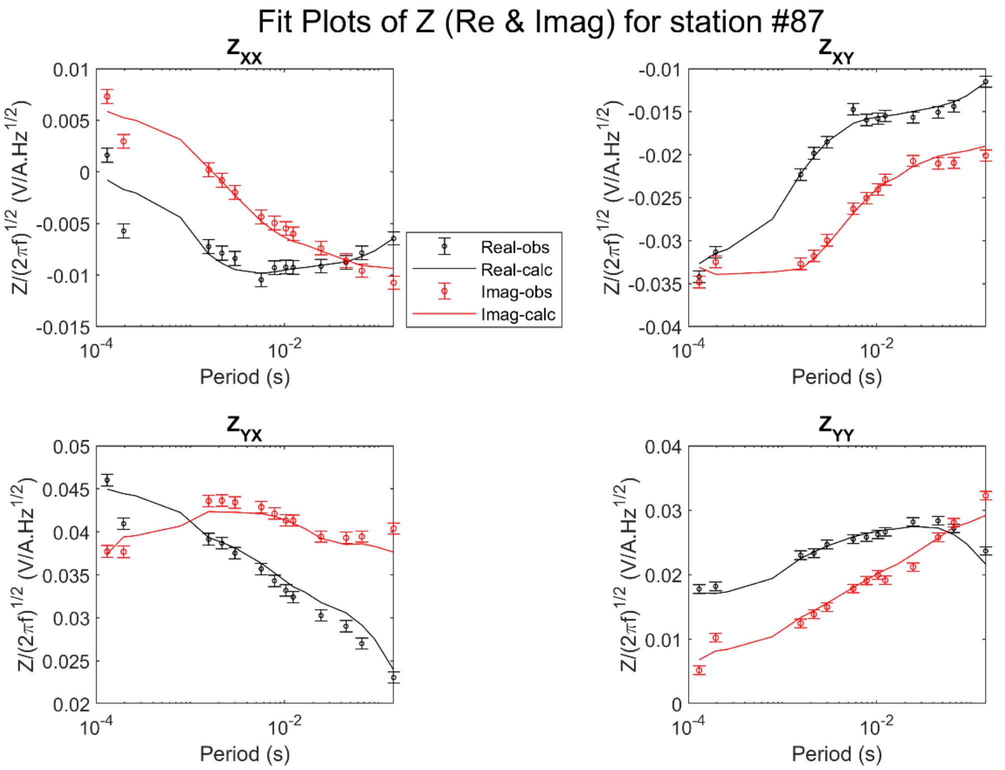
Fit Plots of Z (Re & Imag) for station #87
Z_XX
Z_XY
Z_YX
Z_YY
Z/(2πf)^1/2 (V/A.Hz^1/2)
Period (s)
Real-obs
Real-calc
Imag-obs
Imag-calc

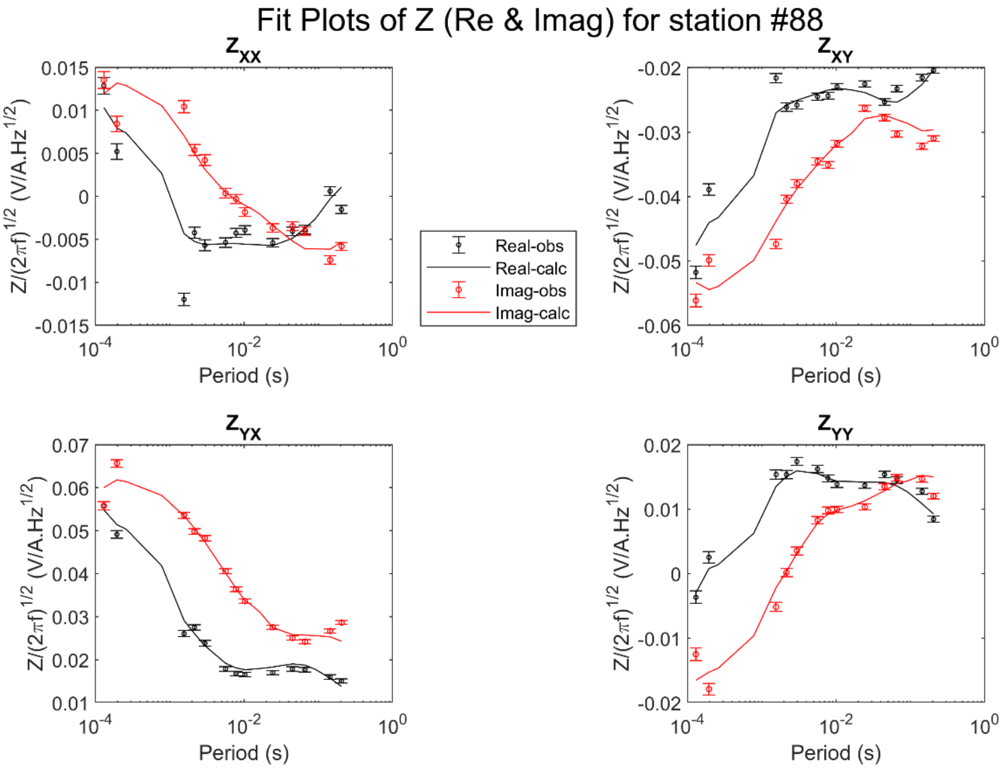
Fit Plots of Z (Re & Imag) for station #88
Z_XX
Z_XY
Z_YX
Z_YY
Z/(2πf)^1/2 (V/A.Hz^1/2)
Period (s)
Real-obs
Real-calc
Imag-obs
Imag-calc

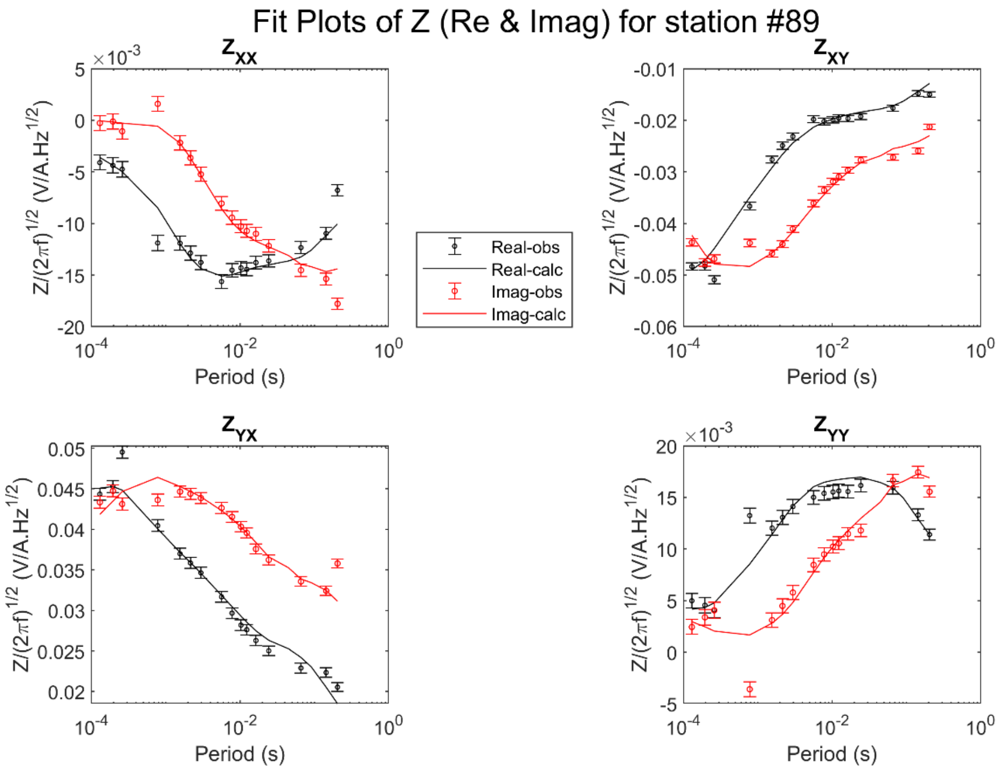
Fit Plots of Z (Re & Imag) for station #89
Z_XX
Z_XY
Z_YX
Z_YY
Z/(2πf)^1/2 (V/A.Hz^1/2)
Period (s)
Real-obs
Real-calc
Imag-obs
Imag-calc

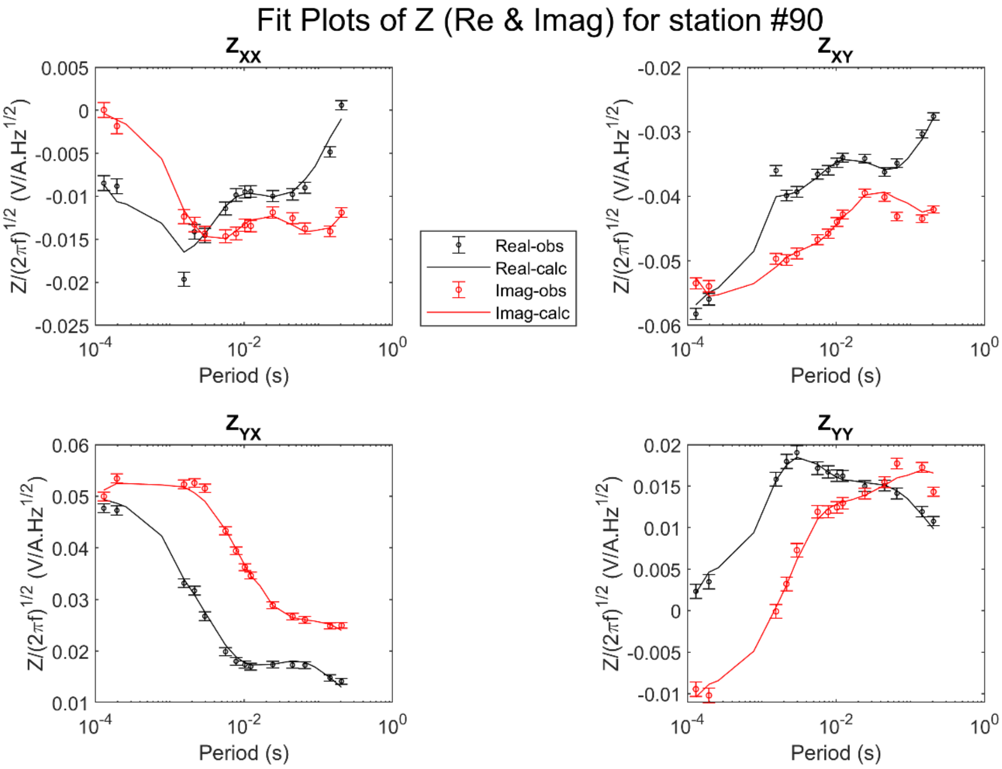
Fit Plots of Z (Re & Imag) for station #90
Z XX
Z XY
Z YX
Z YY
Z/(2πf)^1/2 (V/A.Hz^1/2)
Period (s)
Real-obs
Real-calc
Imag-obs
Imag-calc

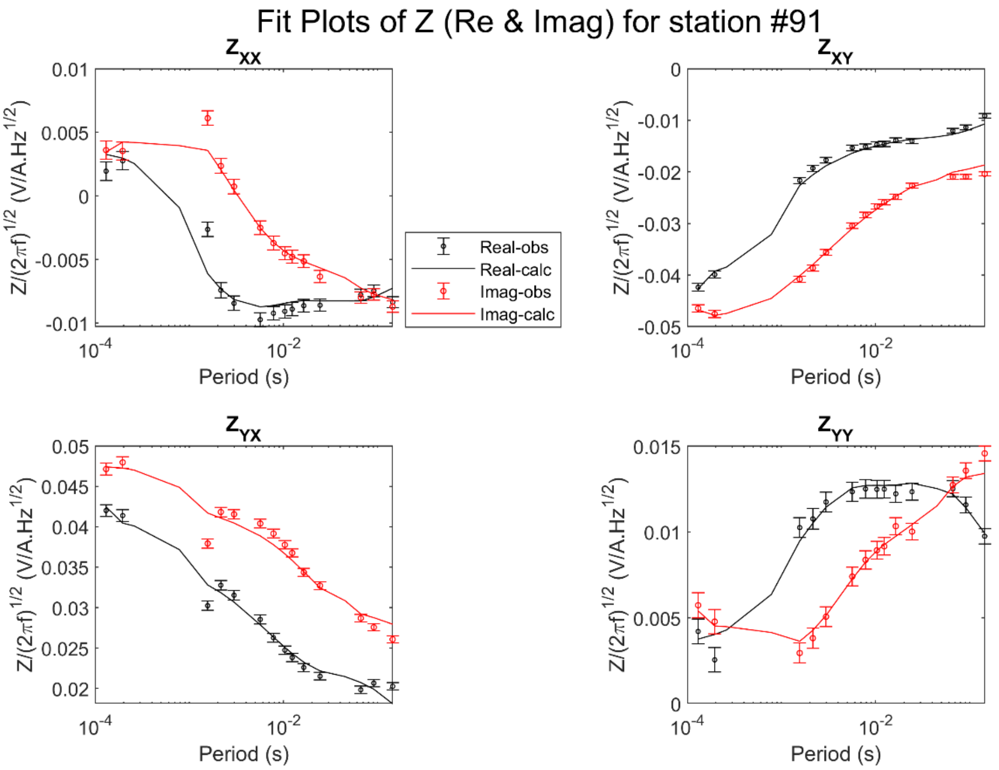
Fit Plots of Z (Re & Imag) for station #91
Z XX
Z XY
Z YX
Z YY
Z/(2πf)^1/2 (V/A.Hz^1/2)
Period (s)
Real-obs
Real-calc
Imag-obs
Imag-calc

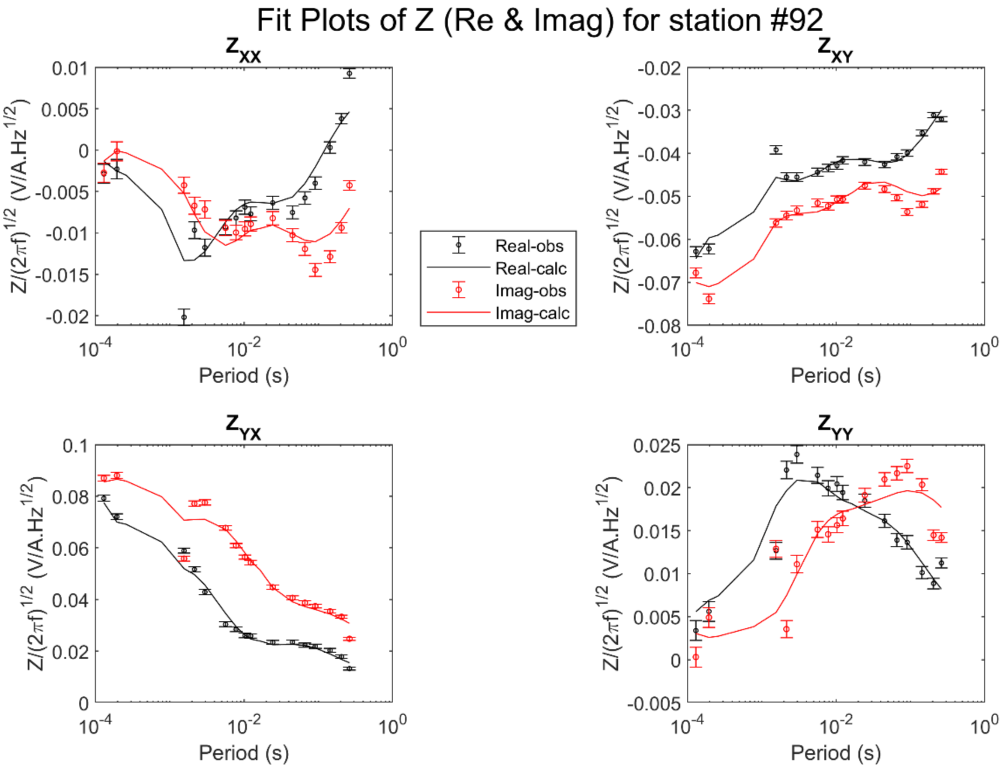
Fit Plots of Z (Re & Imag) for station #92
Z_XX
Z_XY
Z_YX
Z_YY
Z/(2πf)^1/2 (V/A.Hz^1/2)
Period (s)
Real-obs
Real-calc
Imag-obs
Imag-calc

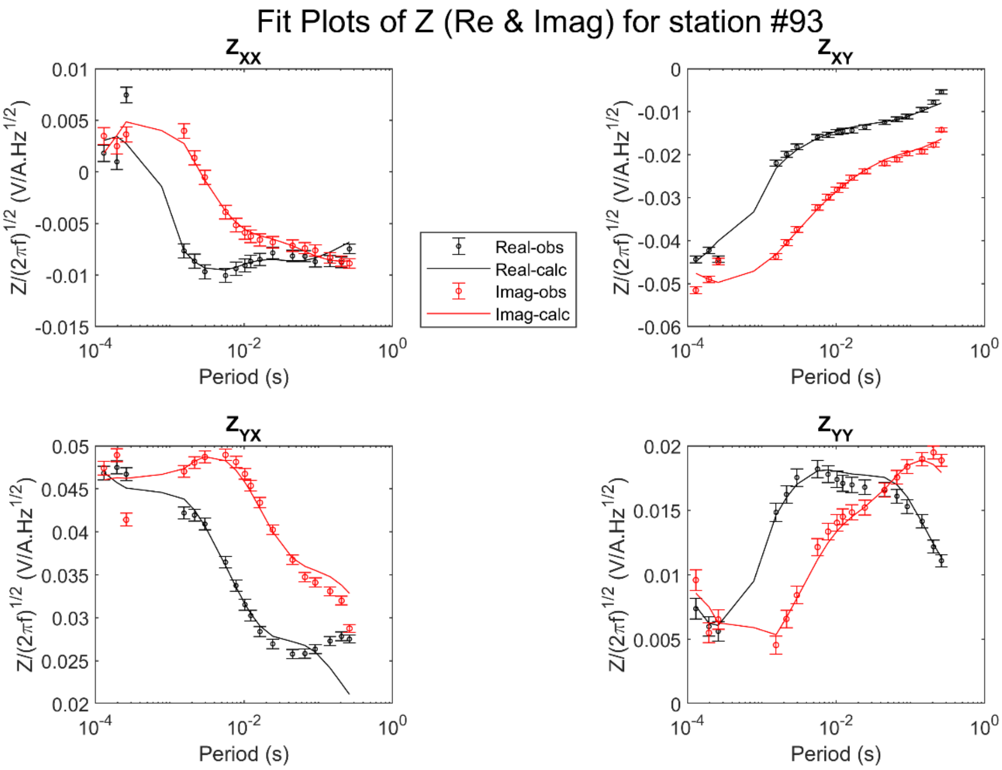
Fit Plots of Z (Re & Imag) for station #93
Z_XX
Z_XY
Z_YX
Z_YY
Z/(2πf)^1/2 (V/A.Hz^1/2)
Period (s)
Real-obs
Real-calc
Imag-obs
Imag-calc

Fit Plots of Z (Re & Imag) for station #94

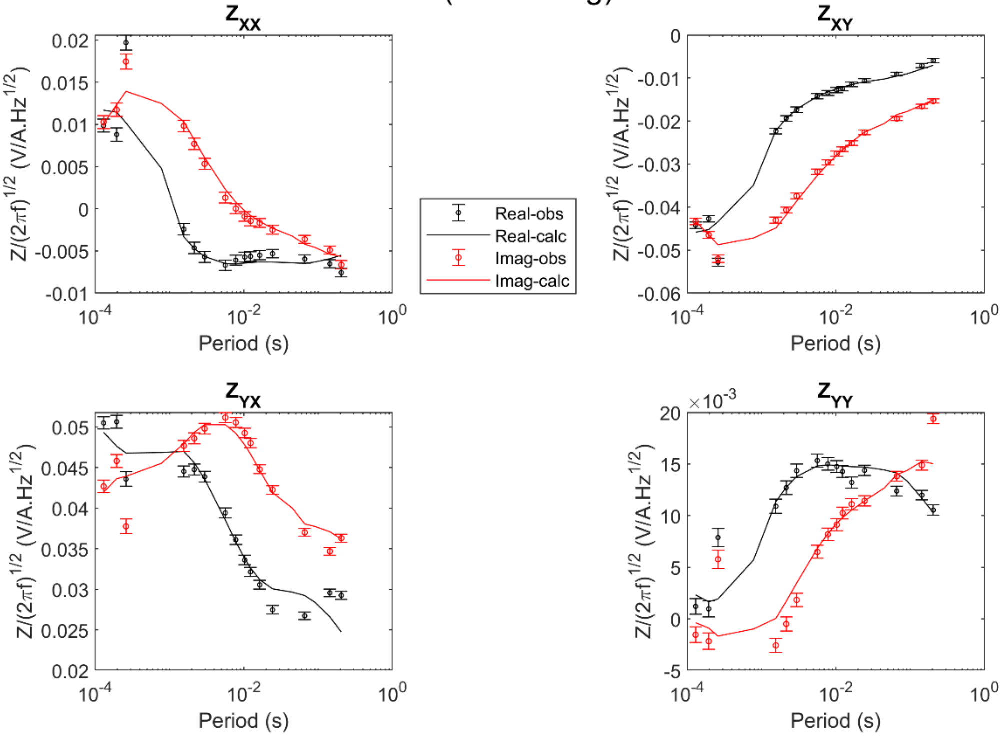

Fit Plots of Z (Re & Imag) for station #95

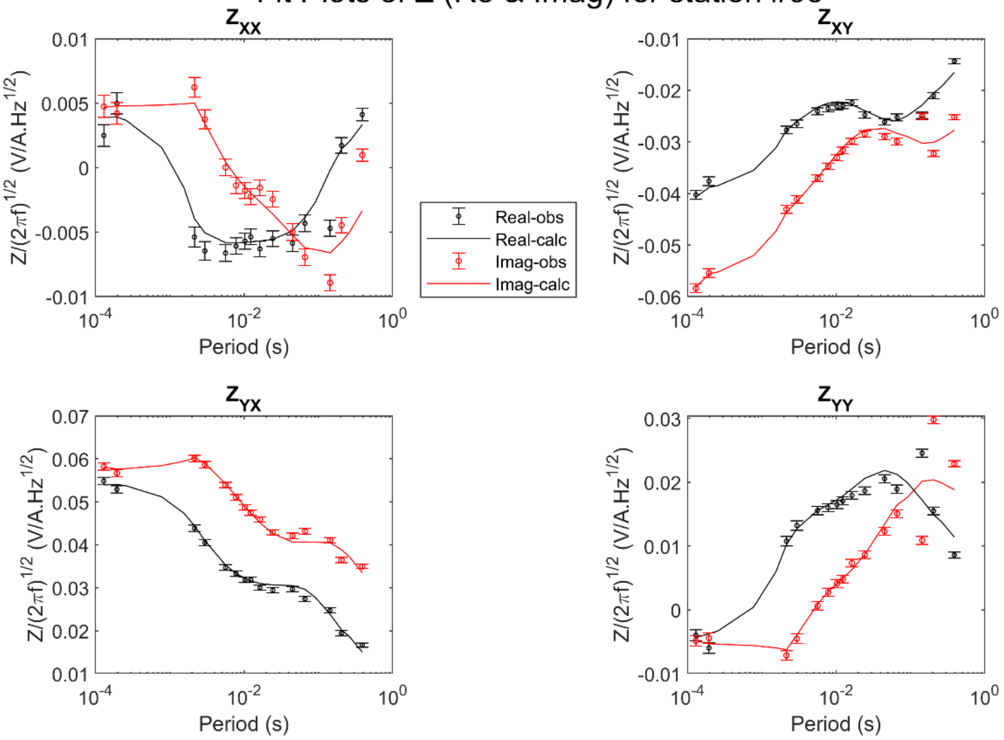

Fit Plots of Z (Re & Imag) for station #96

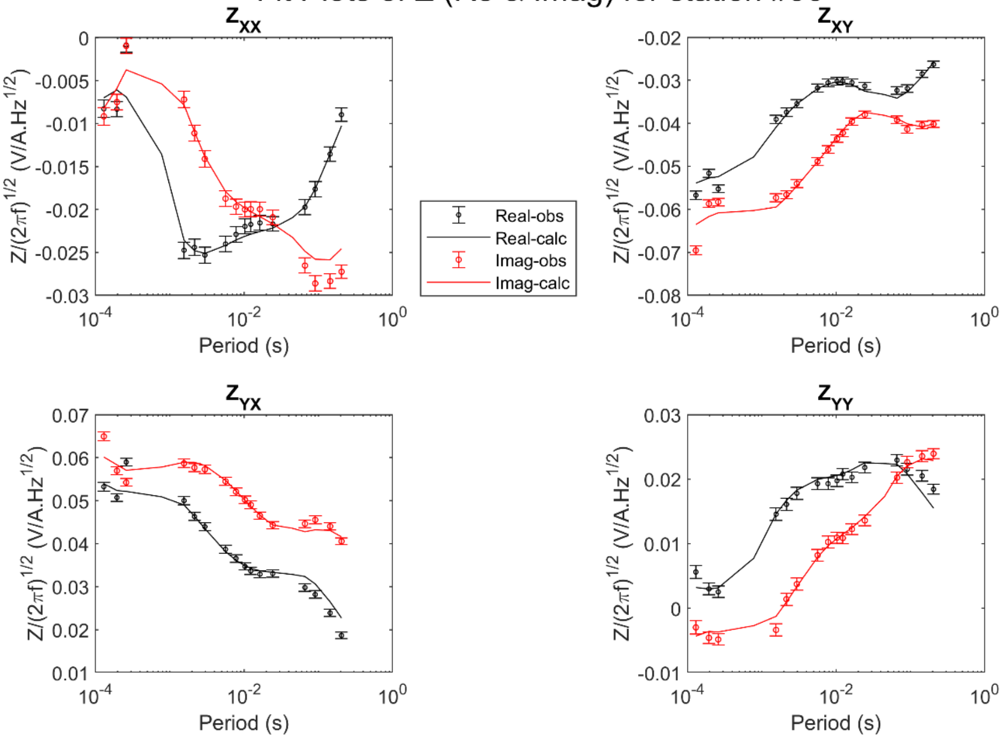

Fit Plots of Z (Re & Imag) for station #97

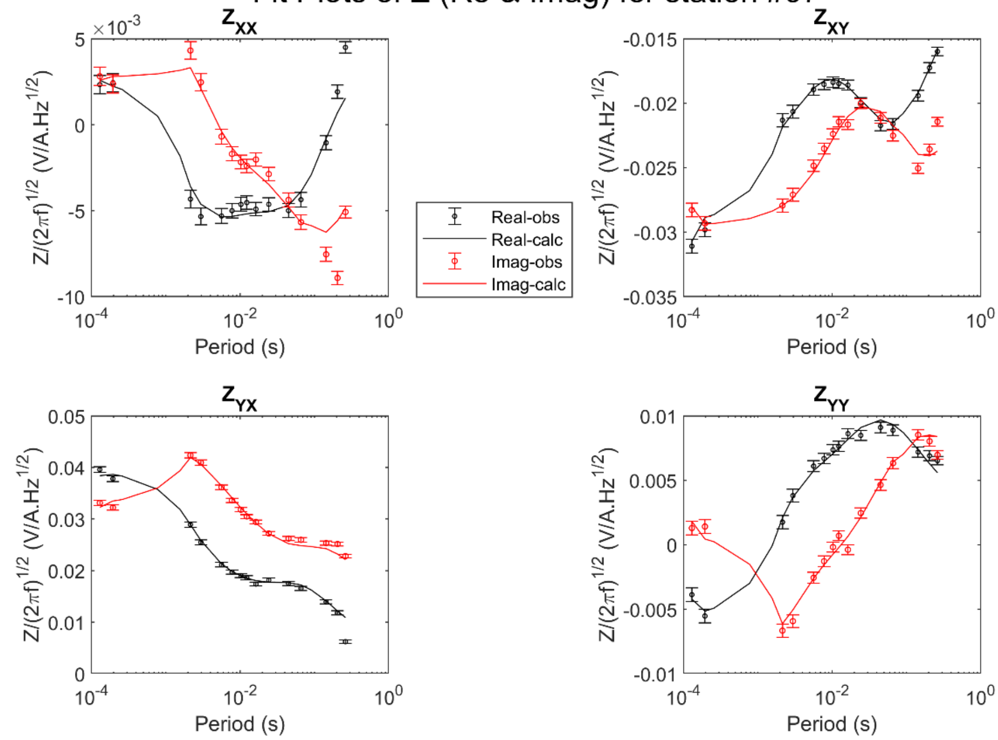

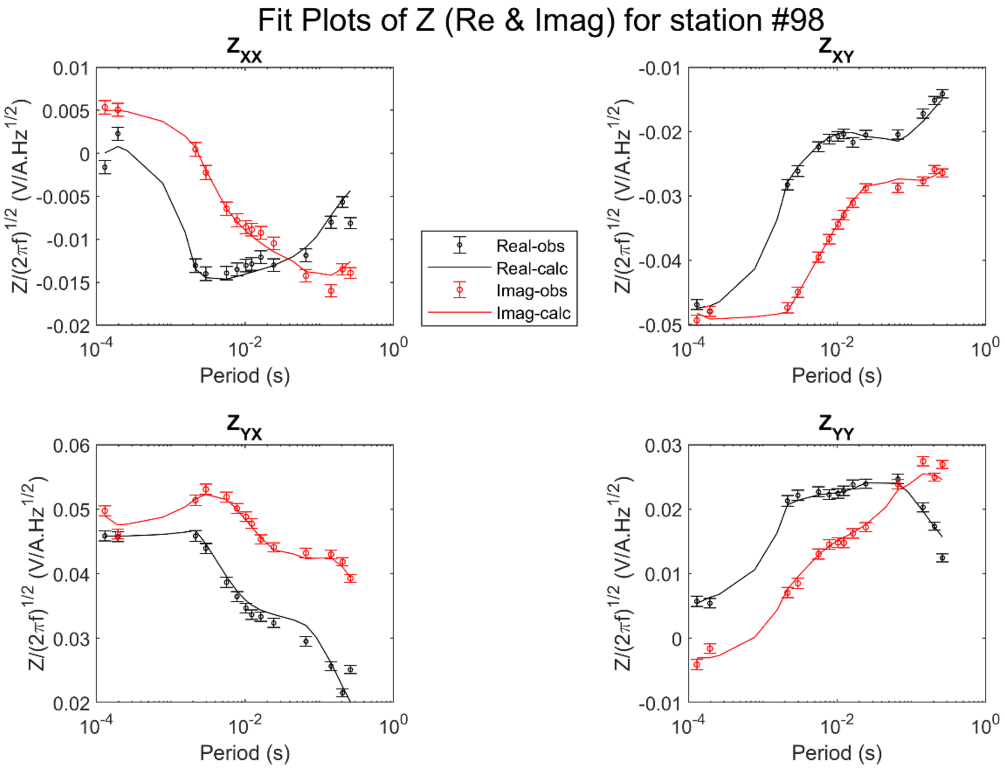
Fit Plots of Z (Re & Imag) for station #98
Z_XX
Z_XY
Z_YX
Z_YY
Z/(2πf)^{1/2} (V/A.Hz^{1/2})
Period (s)
Real-obs
Real-calc
Imag-obs
Imag-calc

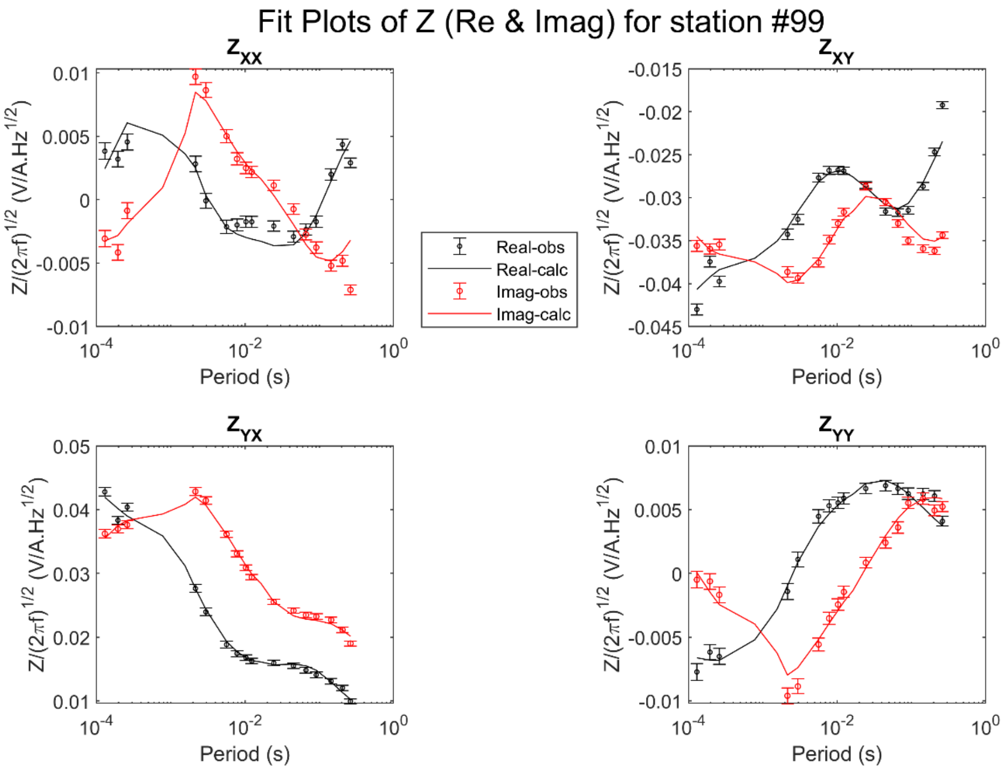
Fit Plots of Z (Re & Imag) for station #99
Z_XX
Z_XY
Z_YX
Z_YY
Z/(2πf)^{1/2} (V/A.Hz^{1/2})
Period (s)
Real-obs
Real-calc
Imag-obs
Imag-calc

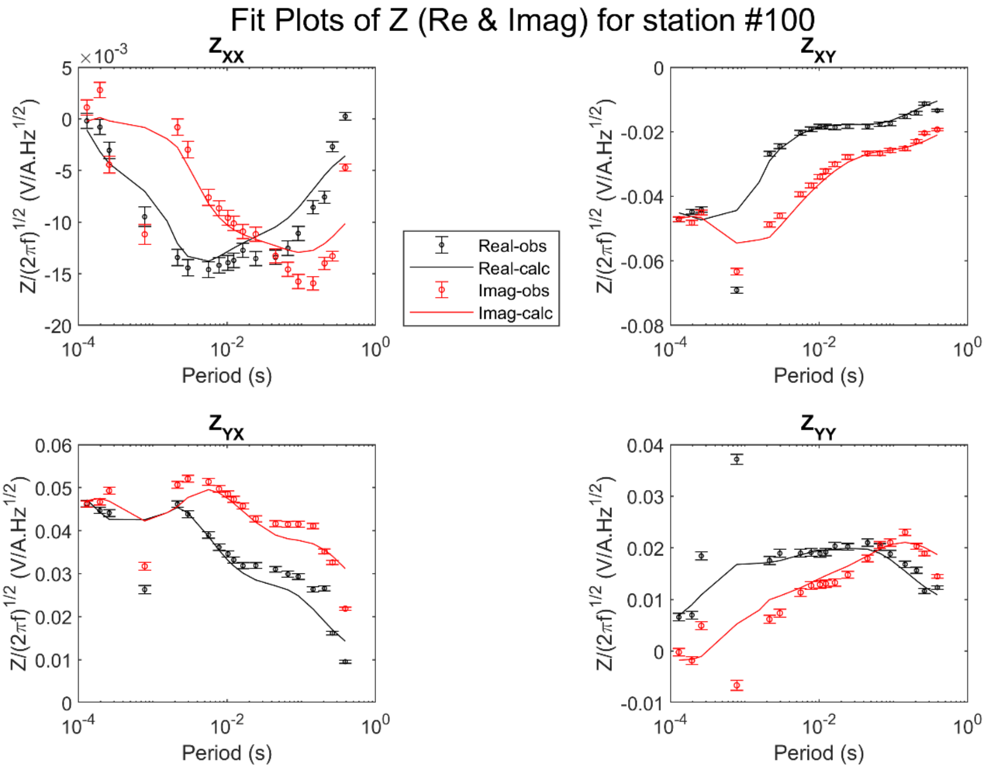
Fit Plots of Z (Re & Imag) for station #100
Z_{XX}
Z_{XY}
Z_{YX}
Z_{YY}
$Z/(2\pi f)^{1/2}$ (V/A.Hz$^{1/2}$)
Period (s)
Real-obs
Real-calc
Imag-obs
Imag-calc

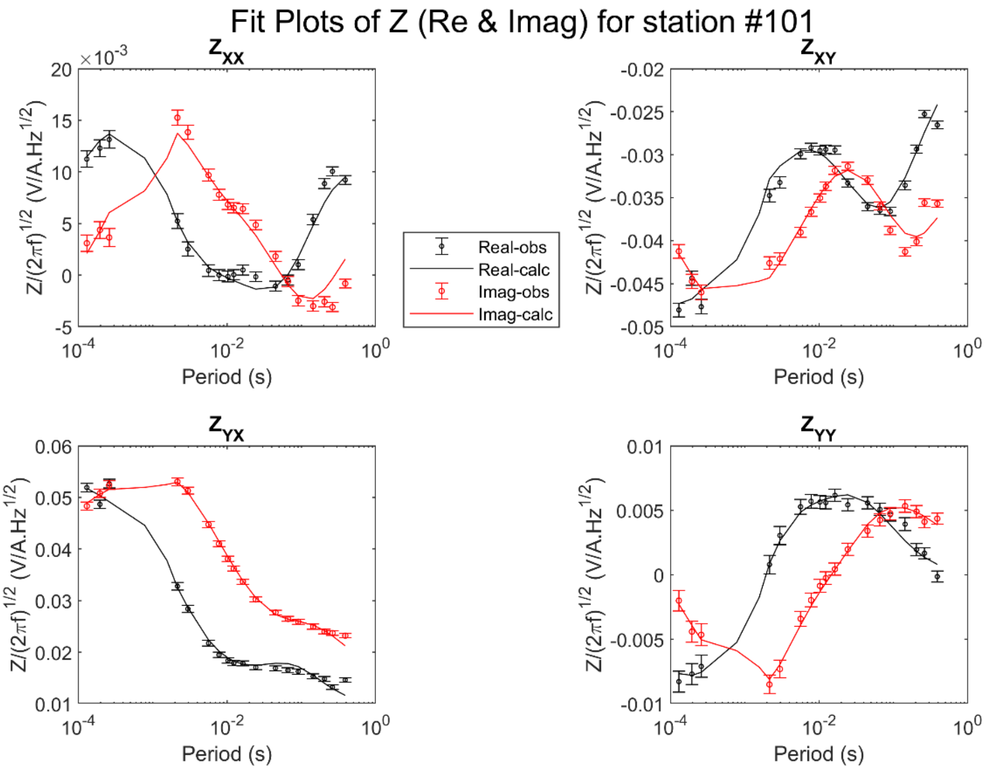
Fit Plots of Z (Re & Imag) for station #101
Z_{XX}
Z_{XY}
Z_{YX}
Z_{YY}
$Z/(2\pi f)^{1/2}$ (V/A.Hz$^{1/2}$)
Period (s)
Real-obs
Real-calc
Imag-obs
Imag-calc

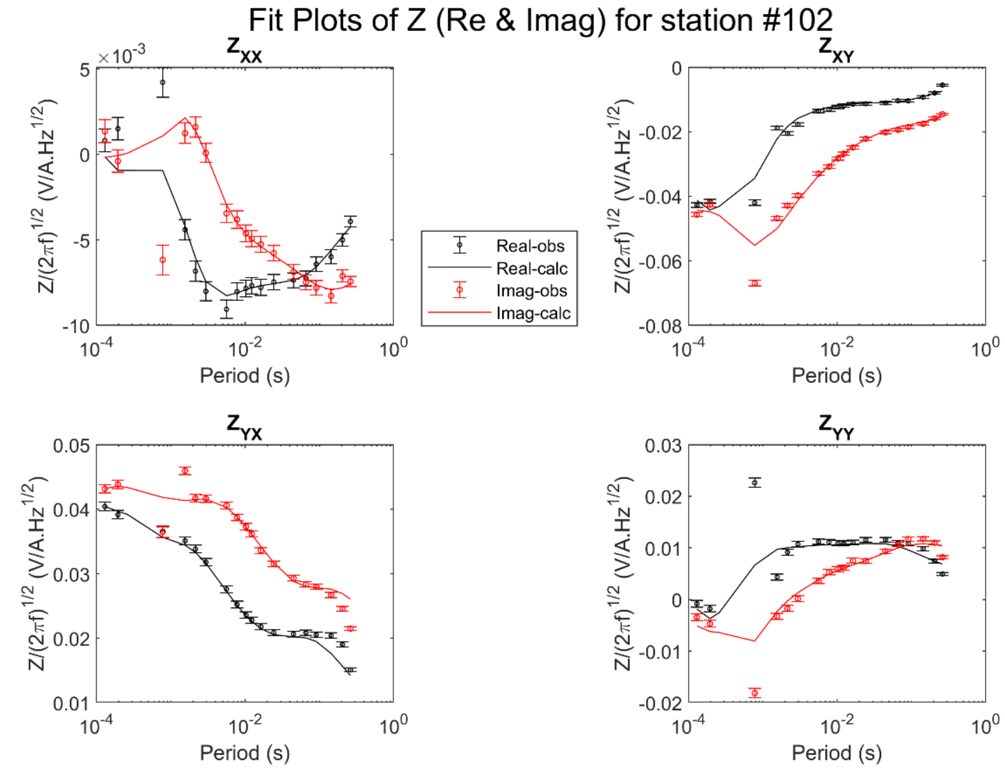

Fit Plots of Z (Re & Imag) for station #102
Z_{XX}
Z_{XY}
Z_{YX}
Z_{YY}
$\times 10^{-3}$
$Z/(2\pi f)^{1/2}$ (V/A.Hz$^{1/2}$)
Period (s)
Real-obs
Real-calc
Imag-obs
Imag-calc

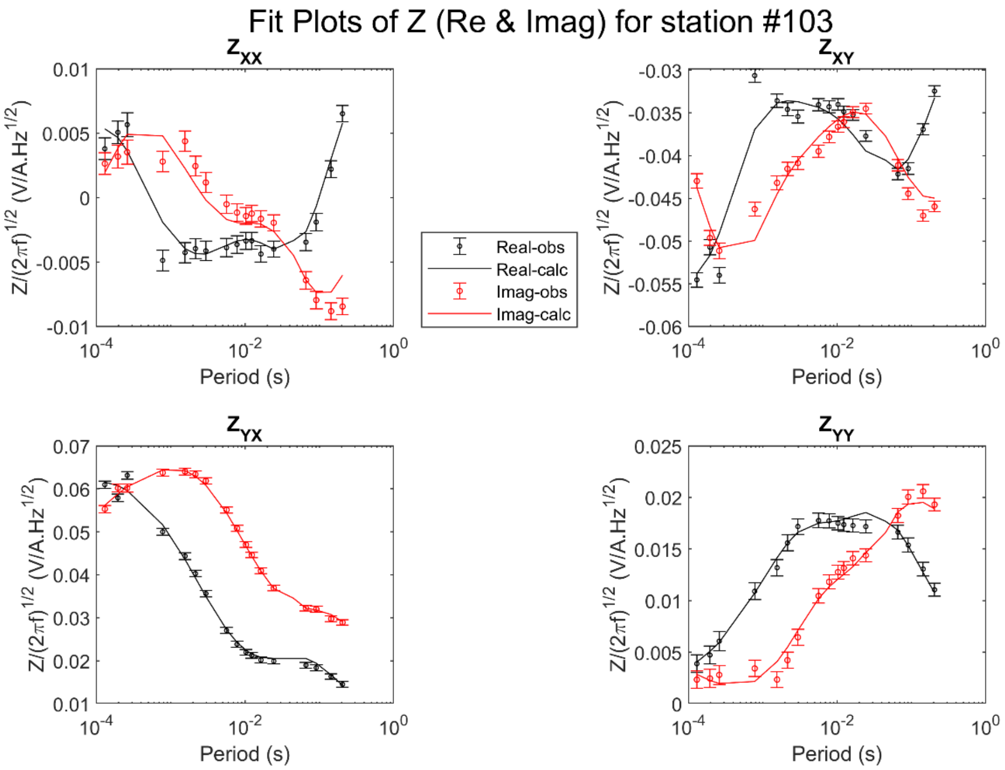

Fit Plots of Z (Re & Imag) for station #103
Z_{XX}
Z_{XY}
Z_{YX}
Z_{YY}
$Z/(2\pi f)^{1/2}$ (V/A.Hz$^{1/2}$)
Period (s)
Real-obs
Real-calc
Imag-obs
Imag-calc

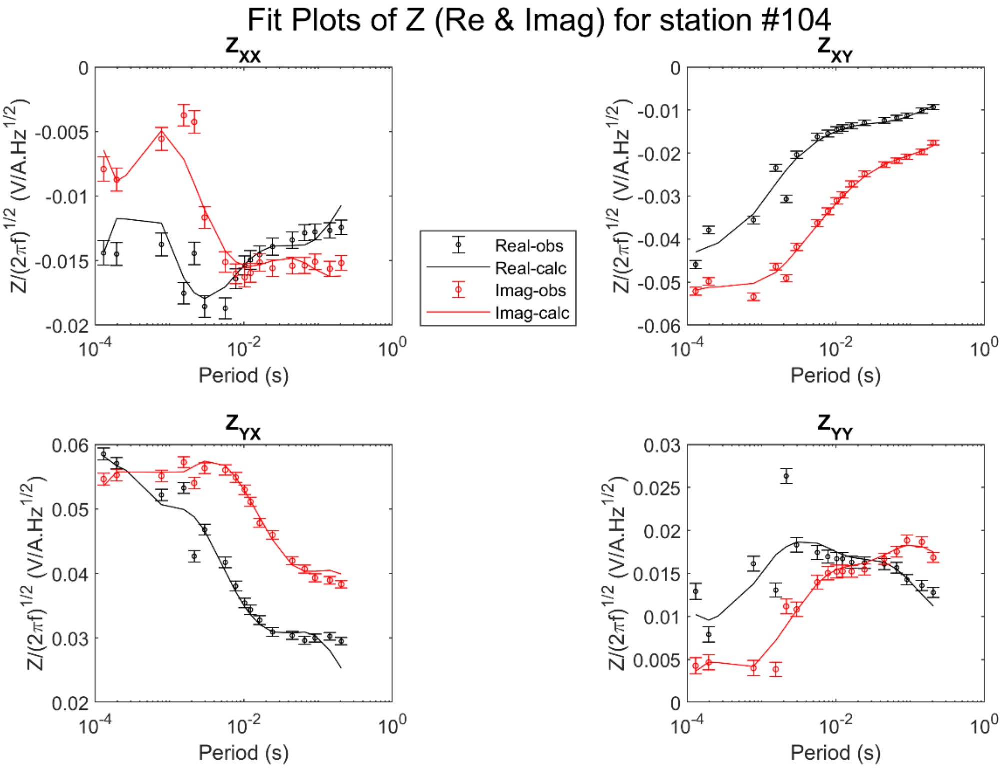
Fit Plots of Z (Re & Imag) for station #104
Z_{XX}
Z_{XY}
Z_{YX}
Z_{YY}
$Z/(2\pi f)^{1/2}$ (V/A.Hz$^{1/2}$)
Period (s)
Real-obs
Real-calc
Imag-obs
Imag-calc

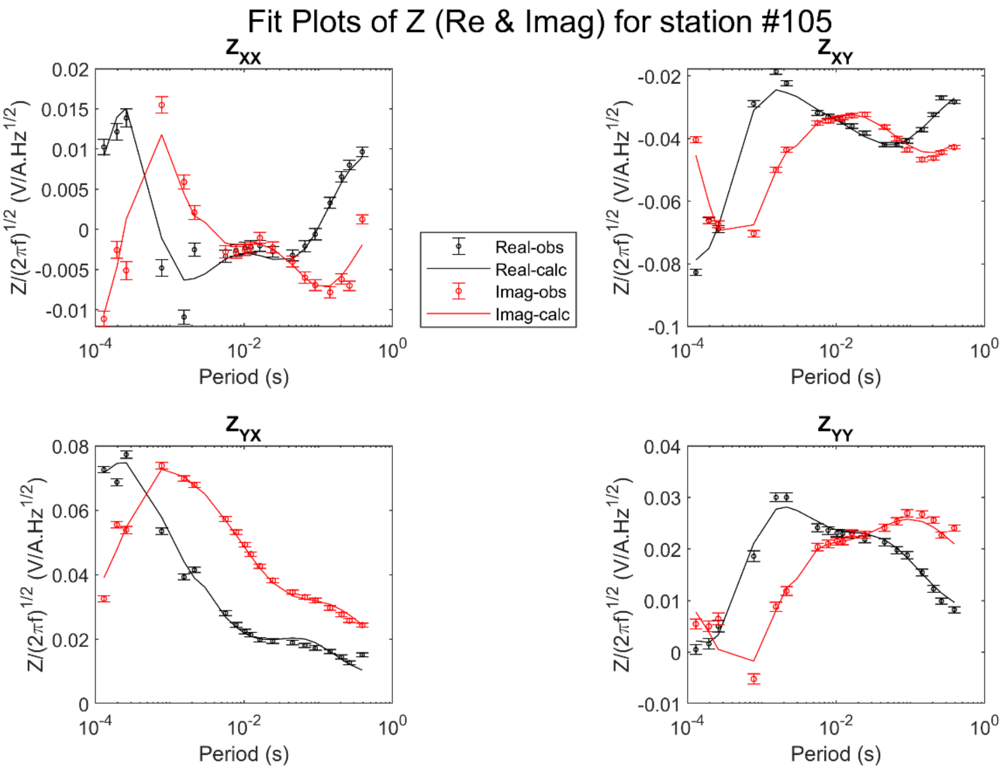
Fit Plots of Z (Re & Imag) for station #105
Z_{XX}
Z_{XY}
Z_{YX}
Z_{YY}
$Z/(2\pi f)^{1/2}$ (V/A.Hz$^{1/2}$)
Period (s)
Real-obs
Real-calc
Imag-obs
Imag-calc

Fit Plots of Z (Re & Imag) for station #106

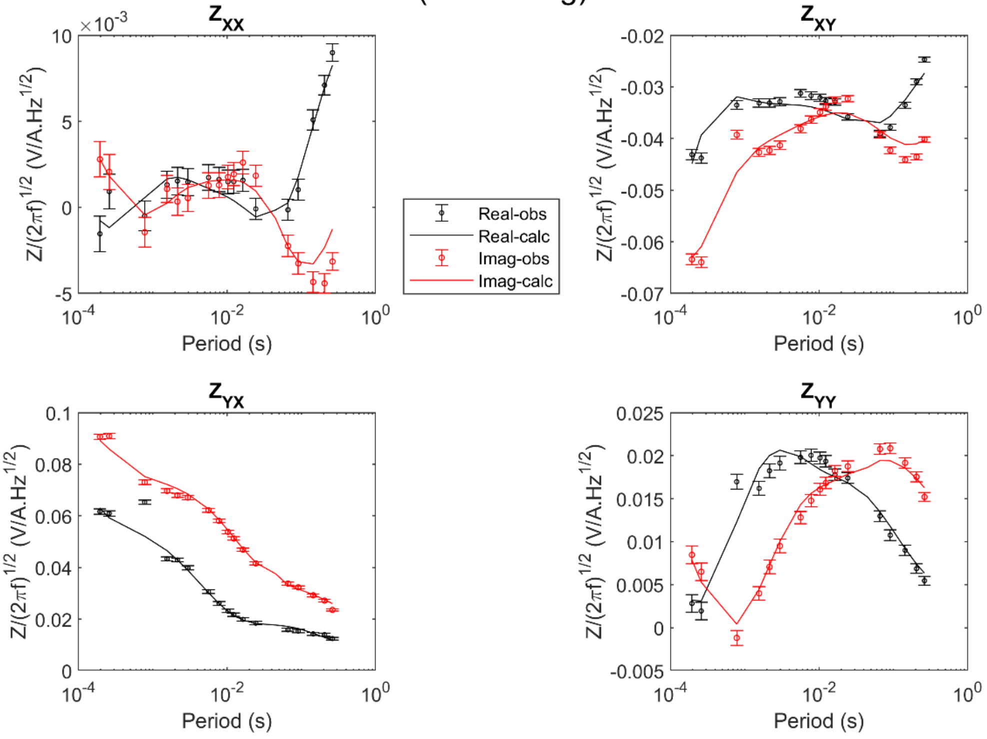

Fit Plots of Z (Re & Imag) for station #107

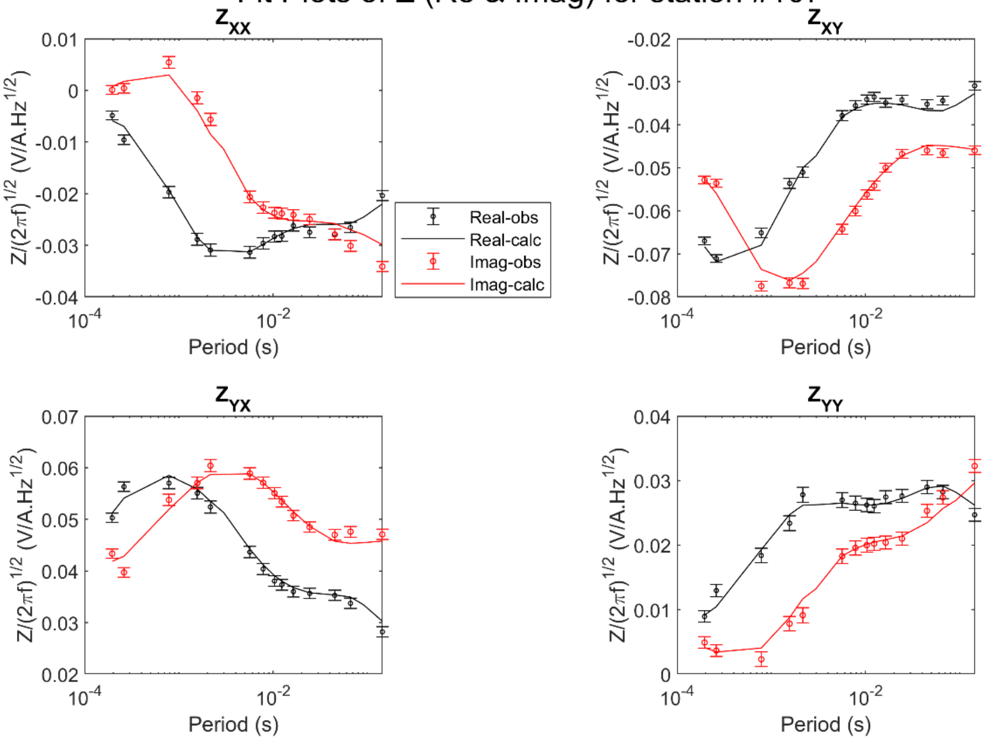

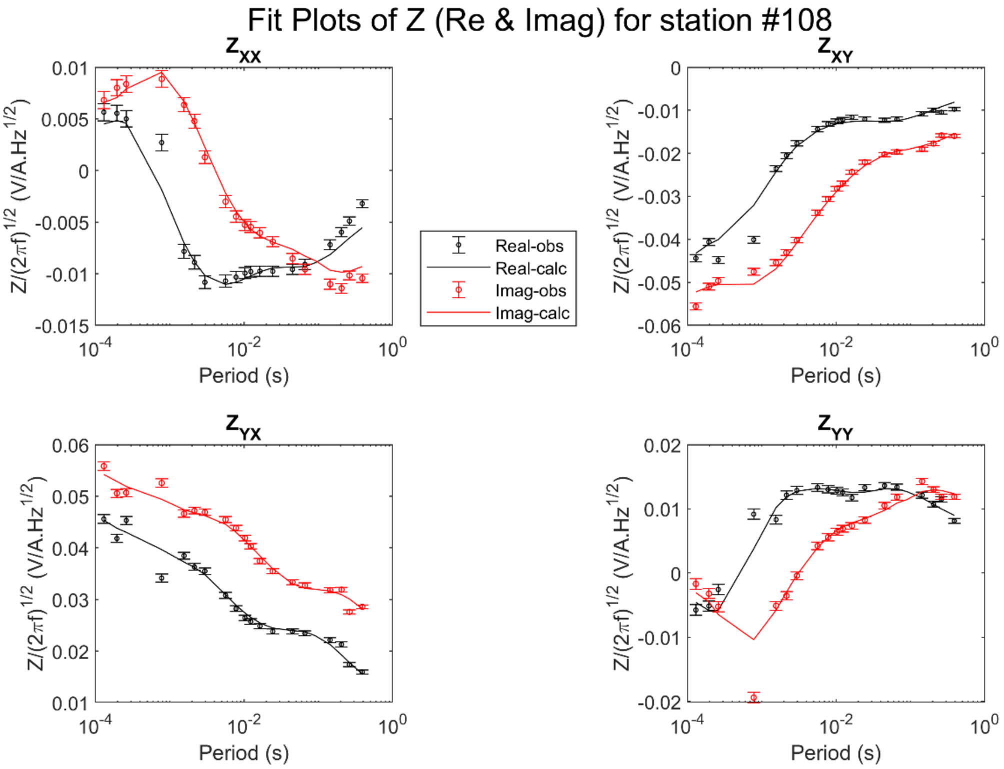
Fit Plots of Z (Re & Imag) for station #108
Z_XX
Z_XY
Z_YX
Z_YY
Z/(2πf)^1/2 (V/A.Hz^1/2)
Period (s)
Real-obs
Real-calc
Imag-obs
Imag-calc

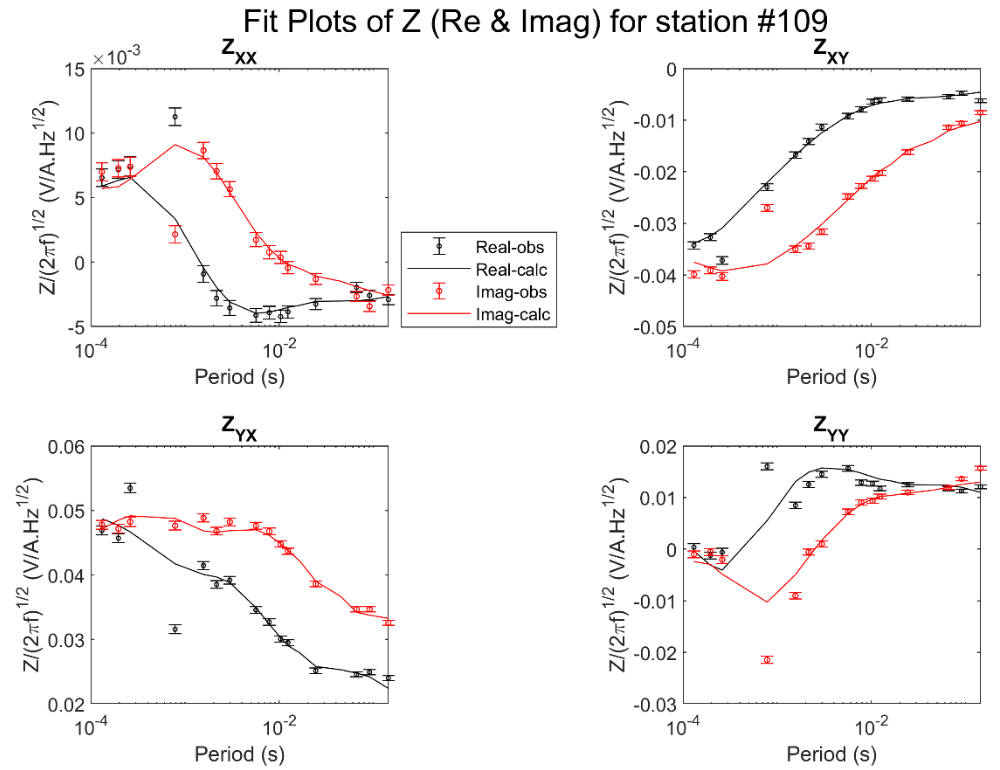
Fit Plots of Z (Re & Imag) for station #109
Z_XX
Z_XY
Z_YX
Z_YY
Z/(2πf)^1/2 (V/A.Hz^1/2)
Period (s)
Real-obs
Real-calc
Imag-obs
Imag-calc

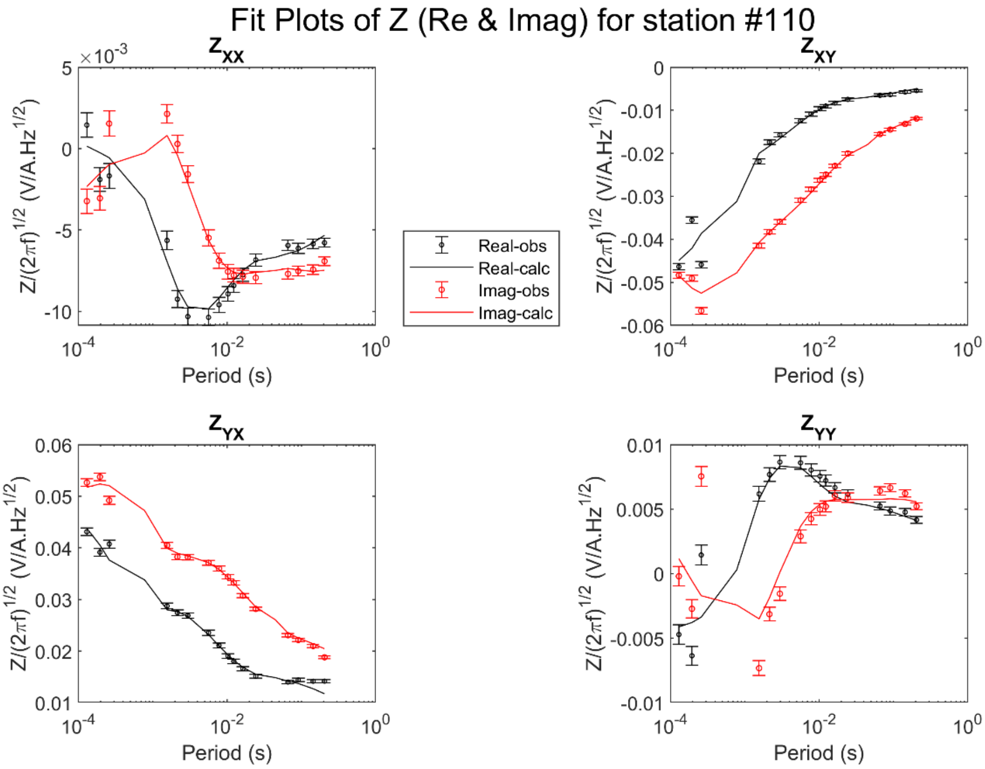

Fit Plots of Z (Re & Imag) for station #110
Z XX
Z XY
Z YX
Z YY
Z/(2πf)^1/2 (V/A.Hz^1/2)
Period (s)
Real-obs
Real-calc
Imag-obs
Imag-calc

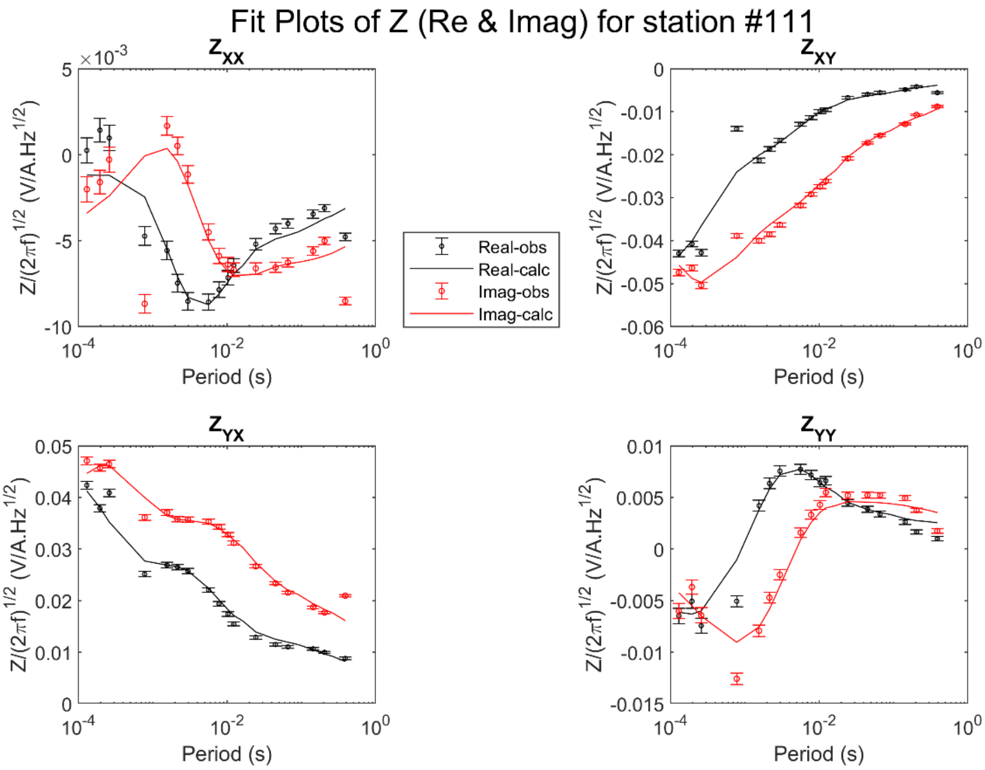

Fit Plots of Z (Re & Imag) for station #111
Z XX
Z XY
Z YX
Z YY
Z/(2πf)^1/2 (V/A.Hz^1/2)
Period (s)
Real-obs
Real-calc
Imag-obs
Imag-calc

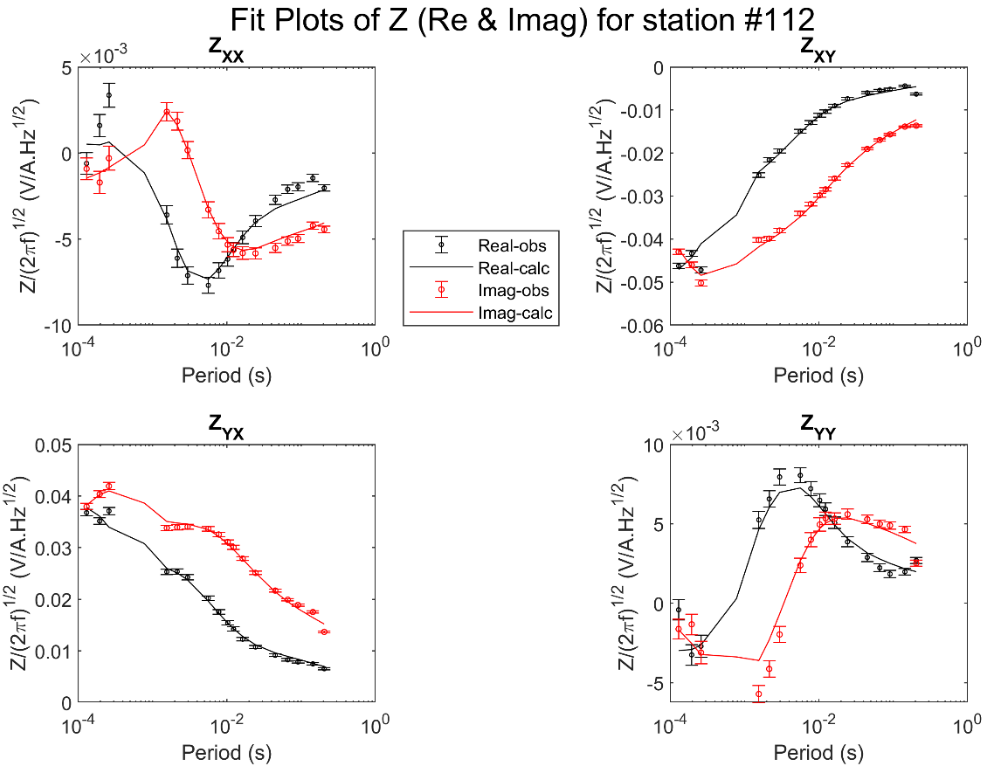
Fit Plots of Z (Re & Imag) for station #112
Z_XX
Z_XY
Z_YX
Z_YY
Z/(2πf)^1/2 (V/A.Hz^1/2)
Period (s)
Real-obs
Real-calc
Imag-obs
Imag-calc

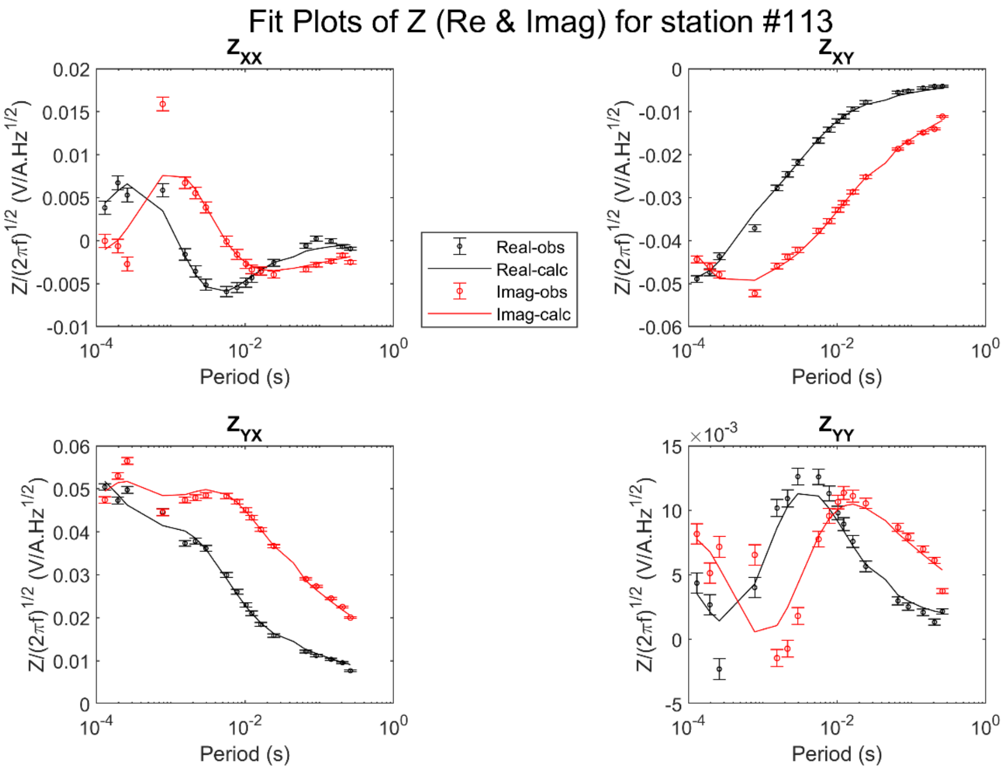
Fit Plots of Z (Re & Imag) for station #113
Z_XX
Z_XY
Z_YX
Z_YY
Z/(2πf)^1/2 (V/A.Hz^1/2)
Period (s)
Real-obs
Real-calc
Imag-obs
Imag-calc

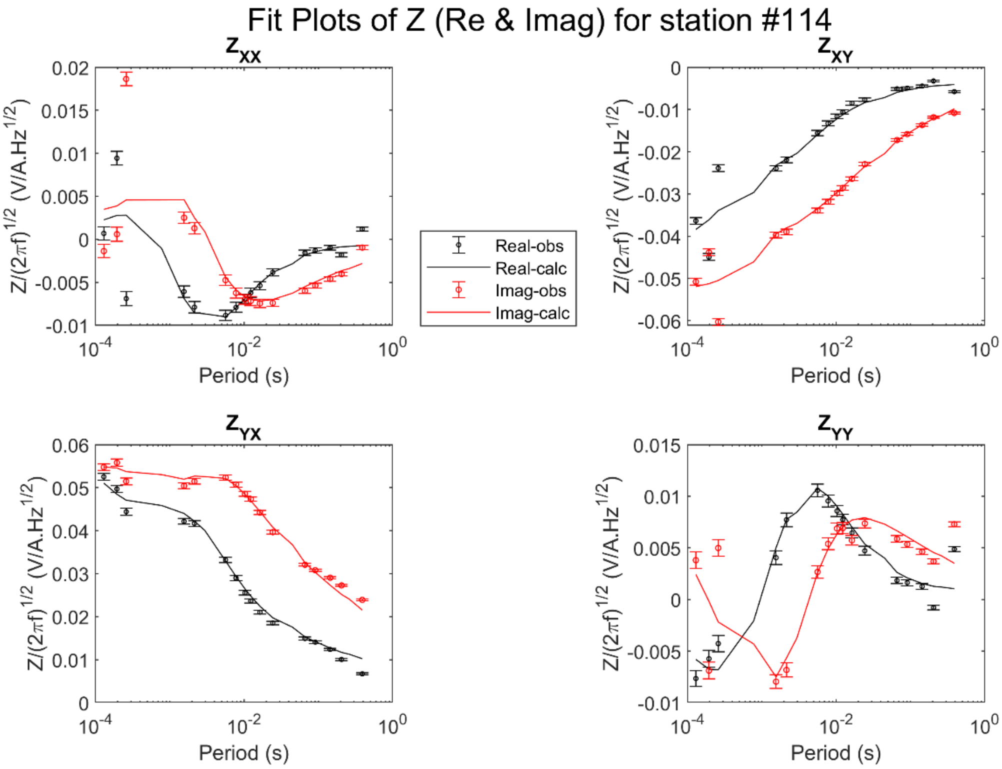
Fit Plots of Z (Re & Imag) for station #114
Z_XX
Z_XY
Z_YX
Z_YY
Z/(2πf)^1/2 (V/A.Hz^1/2)
Period (s)
Real-obs
Real-calc
Imag-obs
Imag-calc

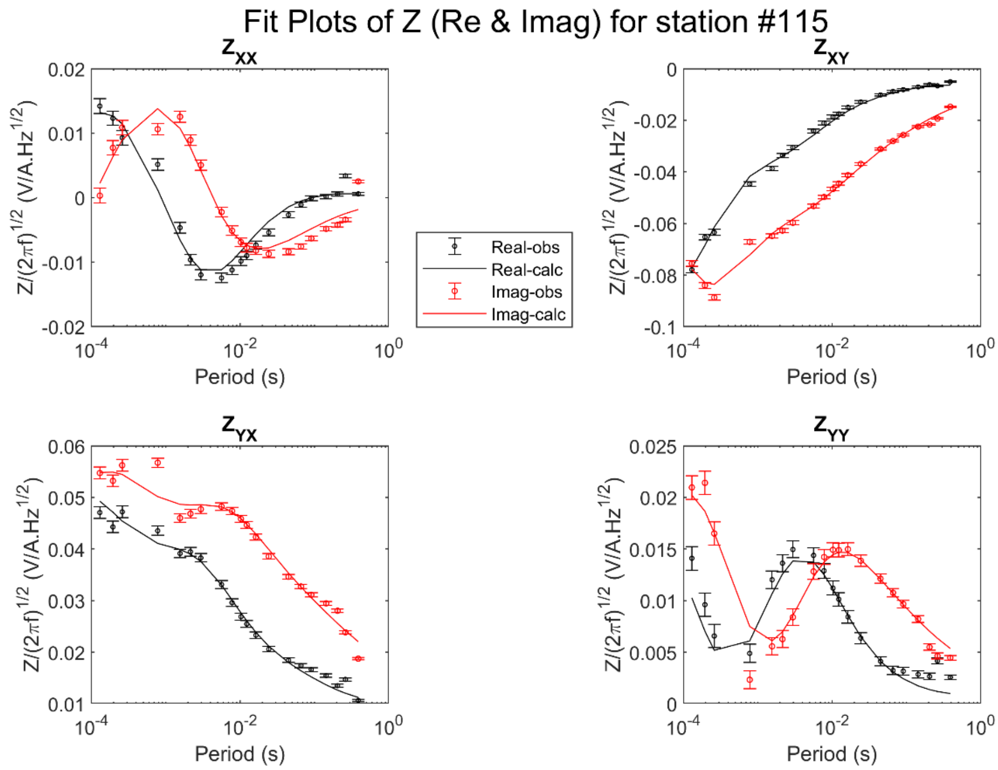
Fit Plots of Z (Re & Imag) for station #115
Z_XX
Z_XY
Z_YX
Z_YY
Z/(2πf)^1/2 (V/A.Hz^1/2)
Period (s)
Real-obs
Real-calc
Imag-obs
Imag-calc

Fit Plots of Z (Re & Imag) for station #116

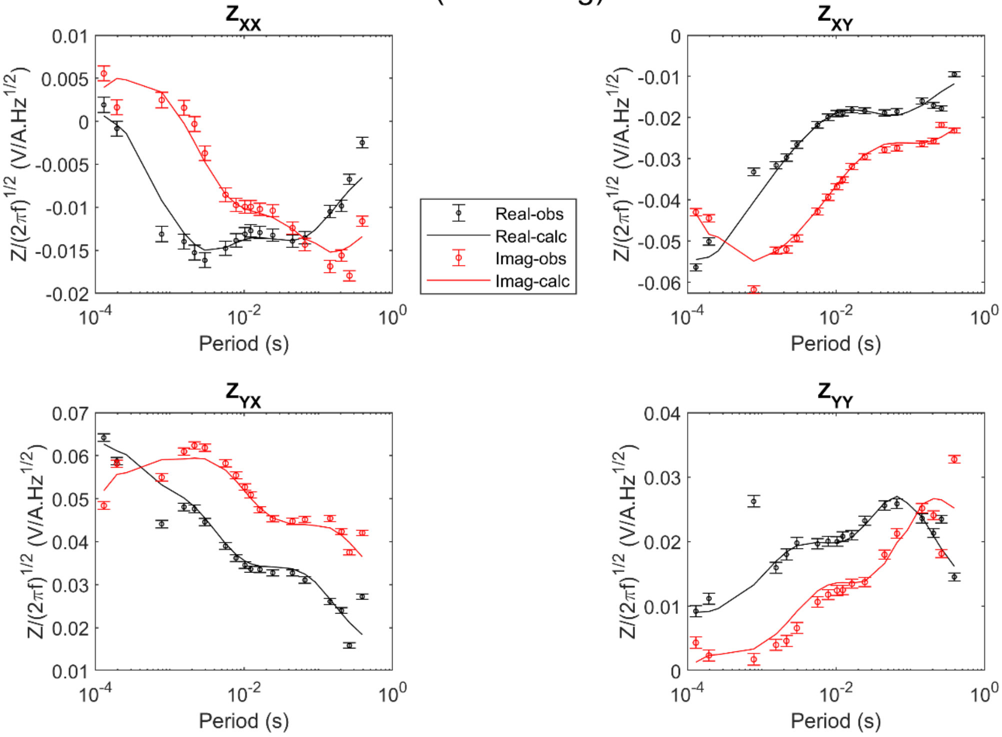

Fit Plots of Z (Re & Imag) for station #117

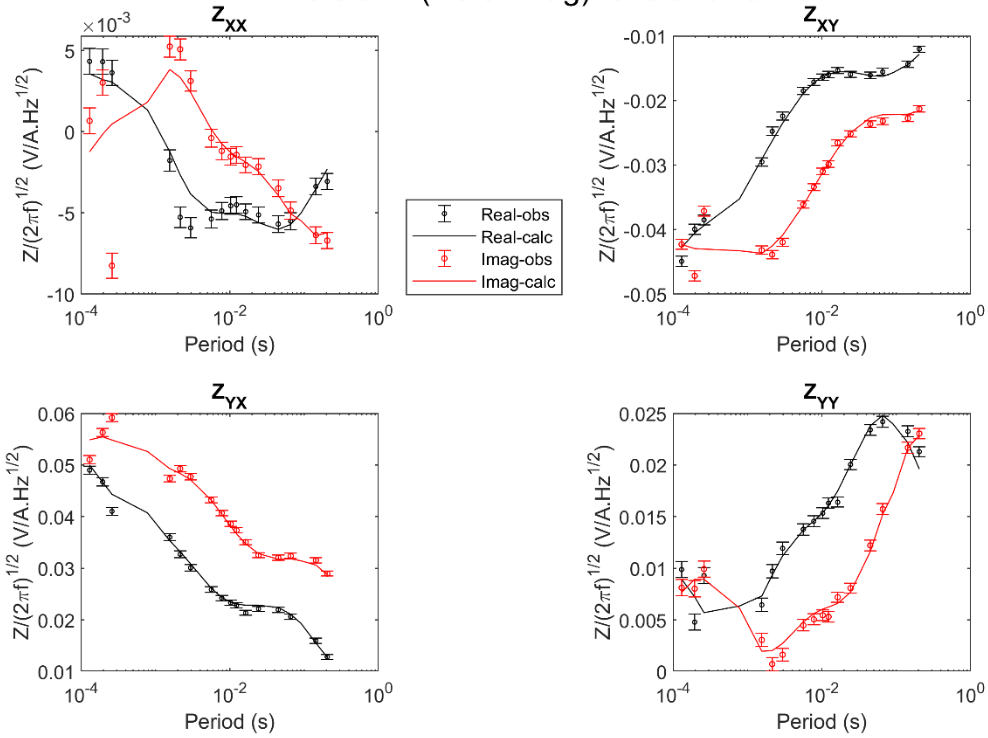

Fit Plots of Z (Re & Imag) for station #118

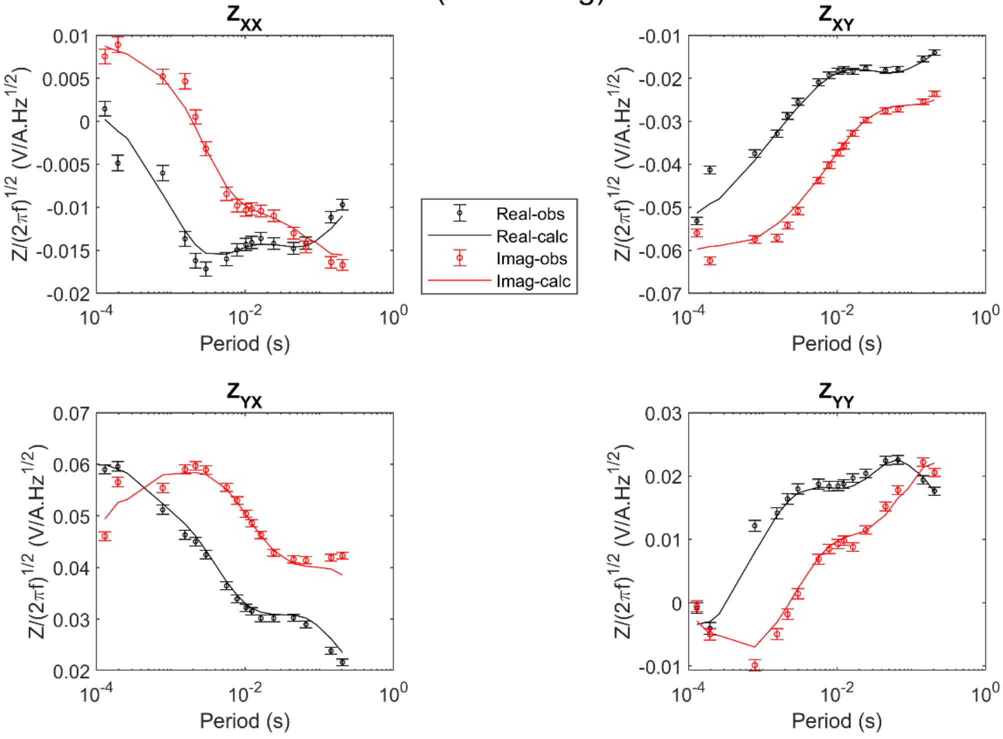

Fit Plots of Z (Re & Imag) for station #119

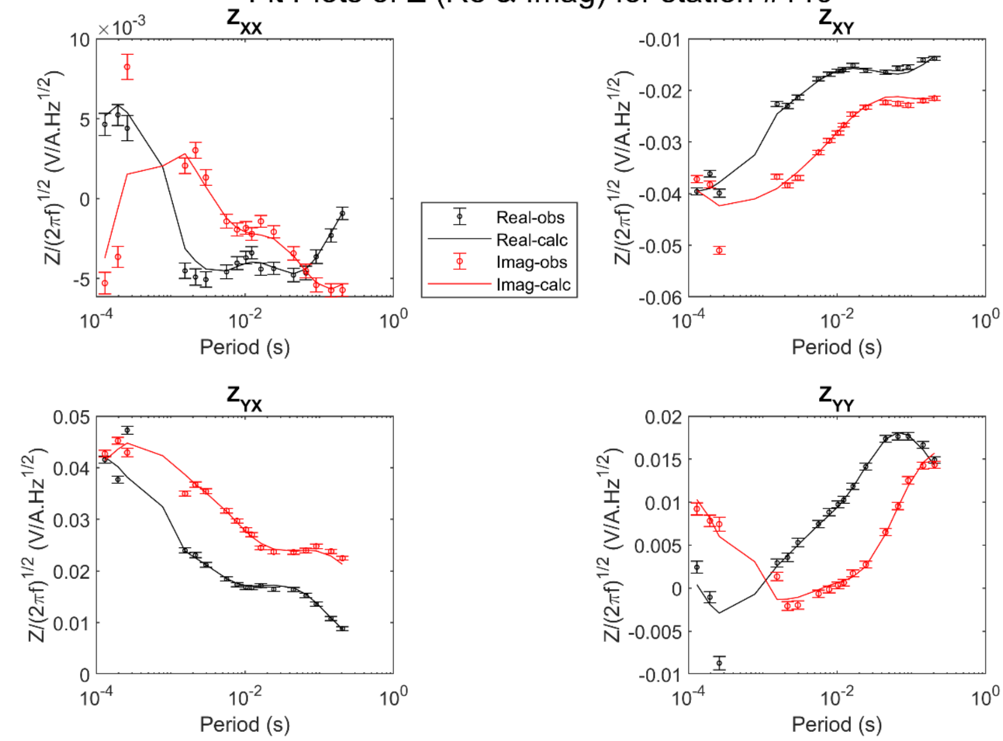

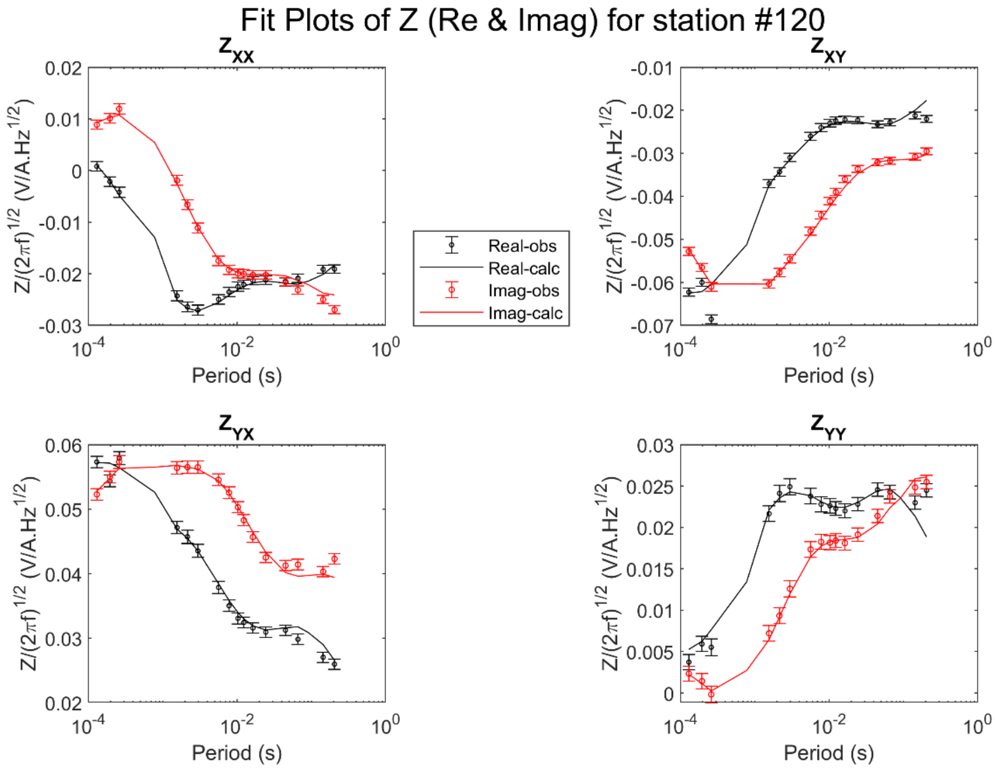
Fit Plots of Z (Re & Imag) for station #120
ZXX
ZXY
ZYX
ZYY
Z/(2πf)1/2 (V/A.Hz1/2)
Period (s)
Real-obs
Real-calc
Imag-obs
Imag-calc

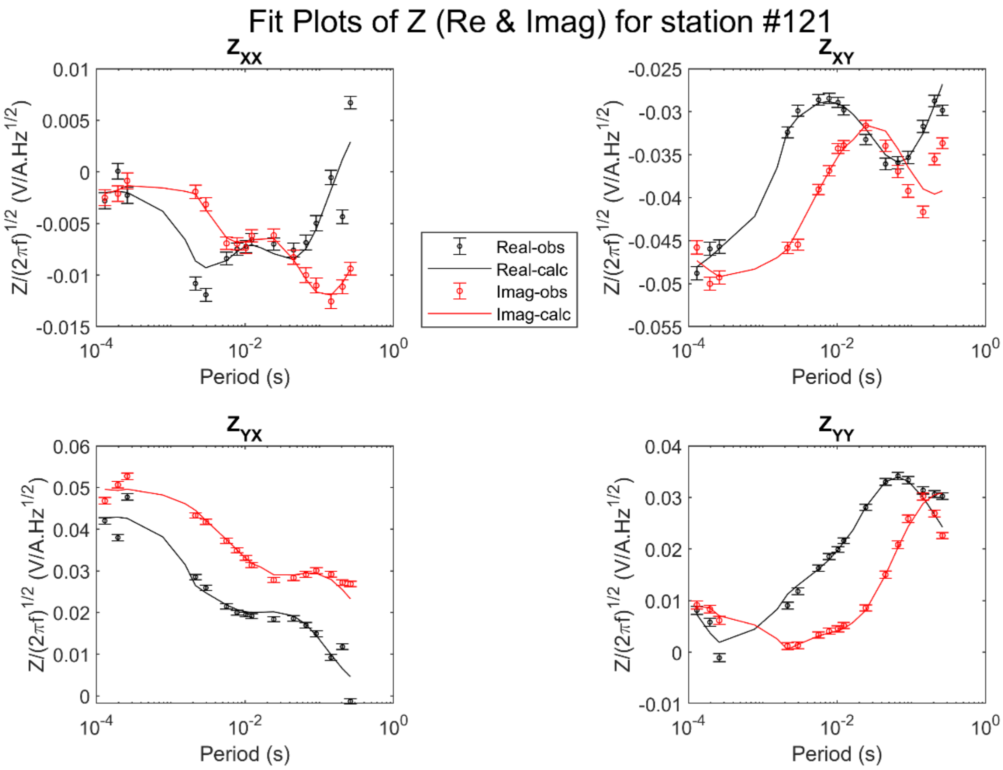
Fit Plots of Z (Re & Imag) for station #121
ZXX
ZXY
ZYX
ZYY
Z/(2πf)1/2 (V/A.Hz1/2)
Period (s)
Real-obs
Real-calc
Imag-obs
Imag-calc

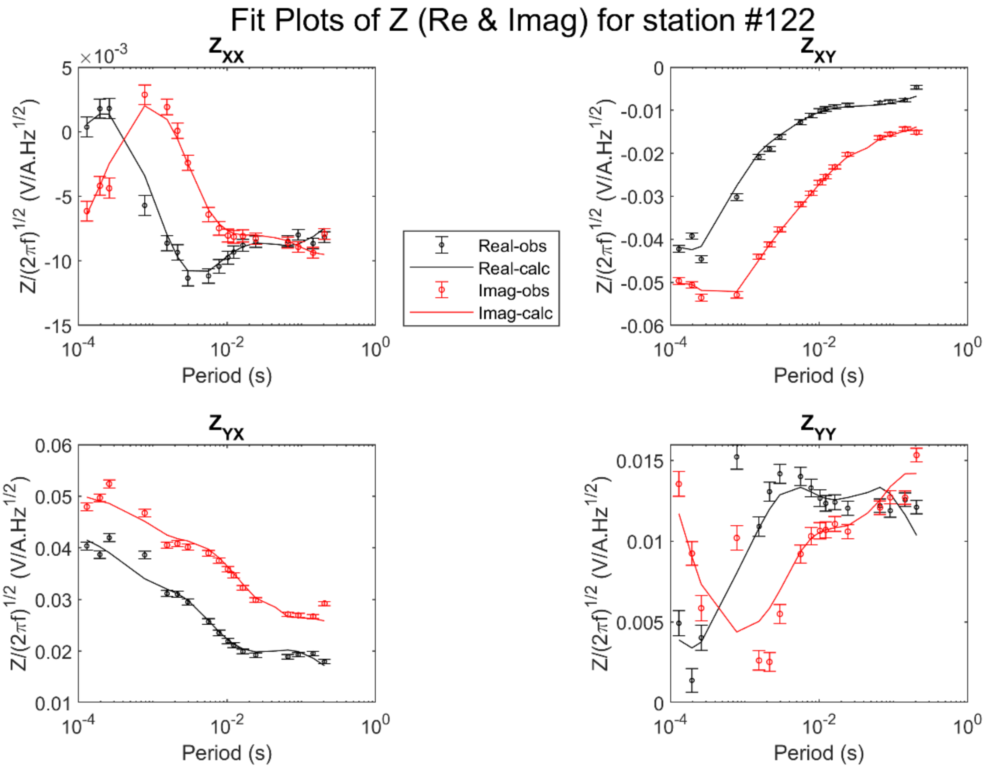
Fit Plots of Z (Re & Imag) for station #122
Z_{XX}
Z_{XY}
Z_{YX}
Z_{YY}
$\times 10^{-3}$
$Z/(2\pi f)^{1/2}$ (V/A.Hz$^{1/2}$)
Period (s)
Real-obs
Real-calc
Imag-obs
Imag-calc

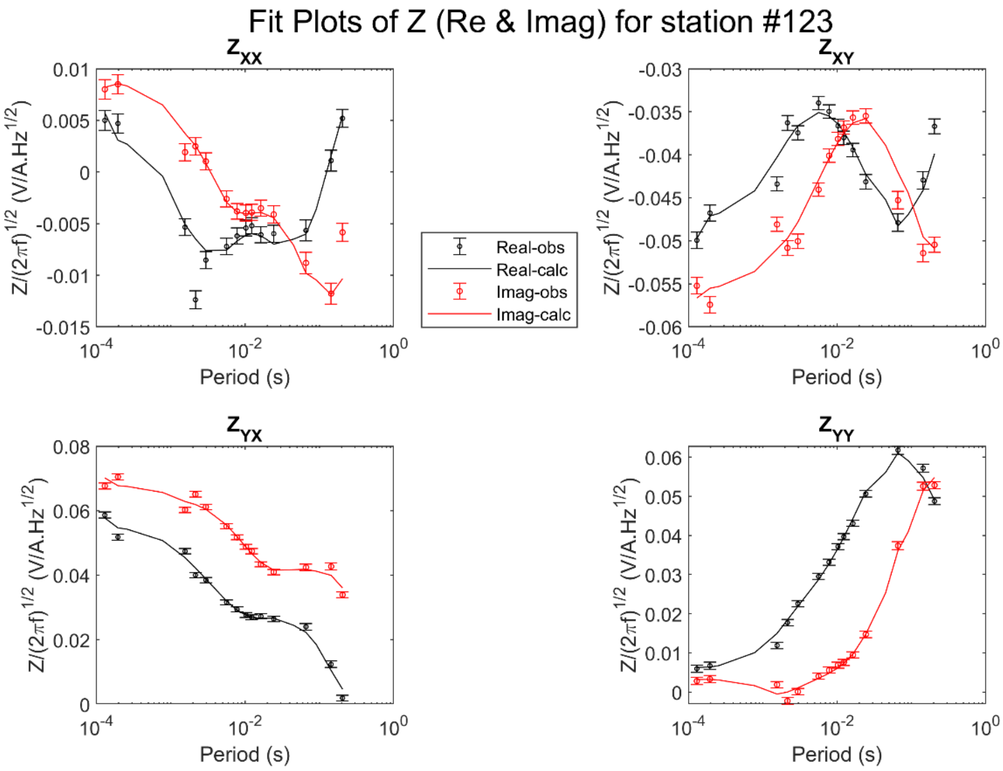
Fit Plots of Z (Re & Imag) for station #123
Z_{XX}
Z_{XY}
Z_{YX}
Z_{YY}
$Z/(2\pi f)^{1/2}$ (V/A.Hz$^{1/2}$)
Period (s)
Real-obs
Real-calc
Imag-obs
Imag-calc

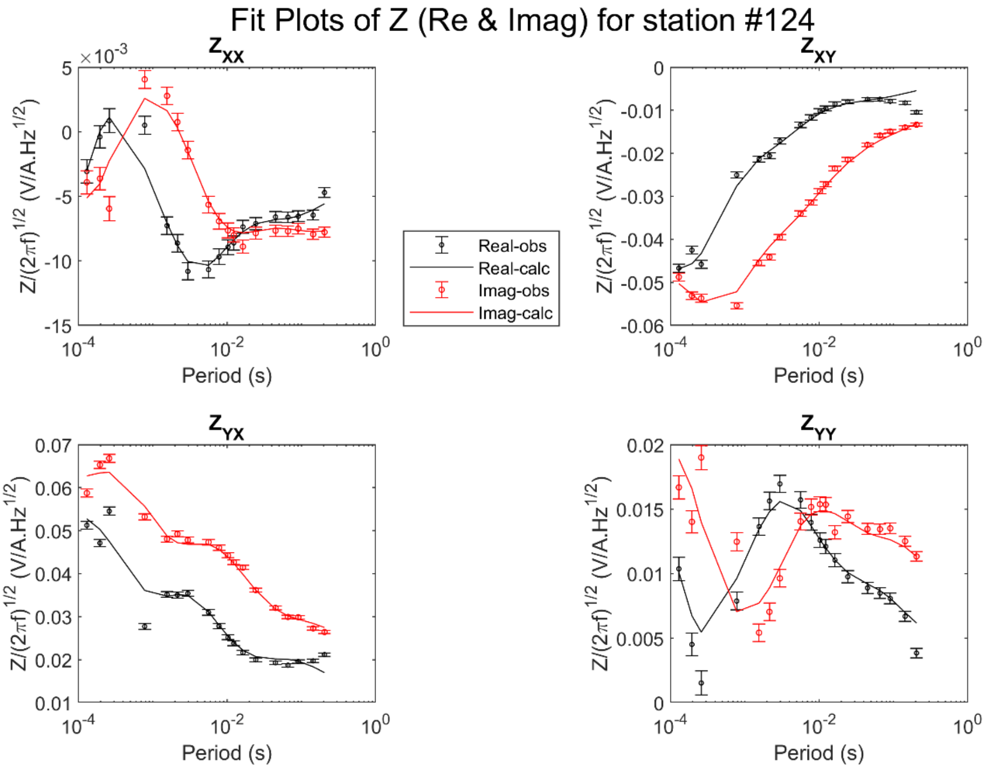
Fit Plots of Z (Re & Imag) for station #124
Z XX
Z XY
Z YX
Z YY
Z/(2πf)^1/2 (V/A.Hz^1/2)
Period (s)
Real-obs
Real-calc
Imag-obs
Imag-calc

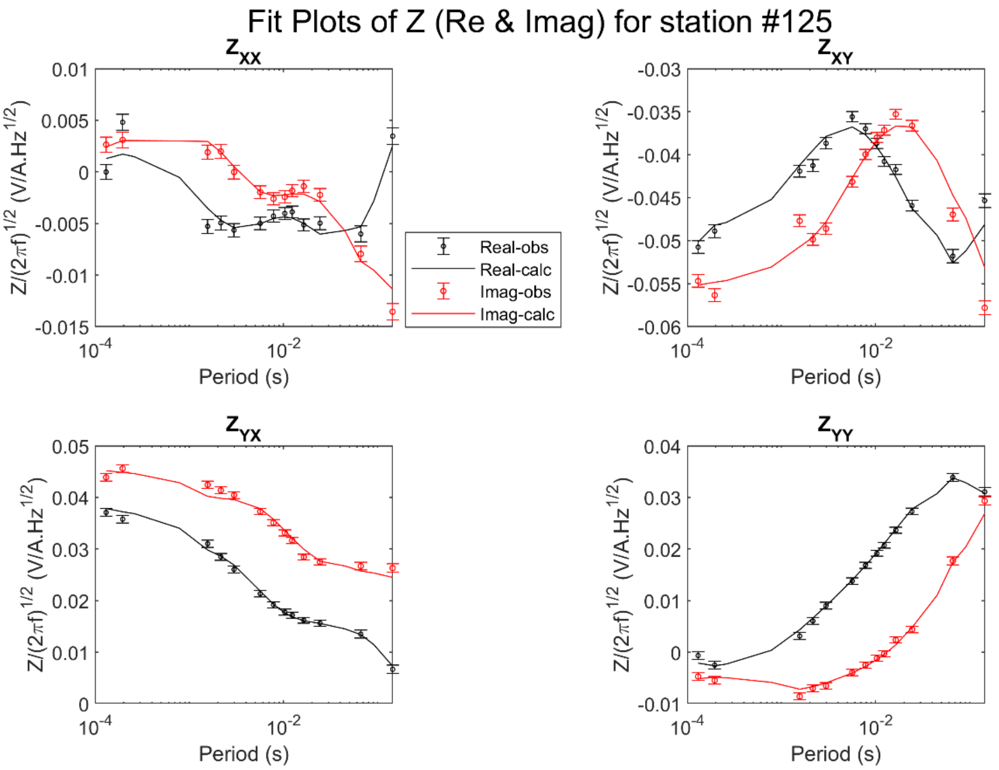
Fit Plots of Z (Re & Imag) for station #125
Z XX
Z XY
Z YX
Z YY
Z/(2πf)^1/2 (V/A.Hz^1/2)
Period (s)
Real-obs
Real-calc
Imag-obs
Imag-calc

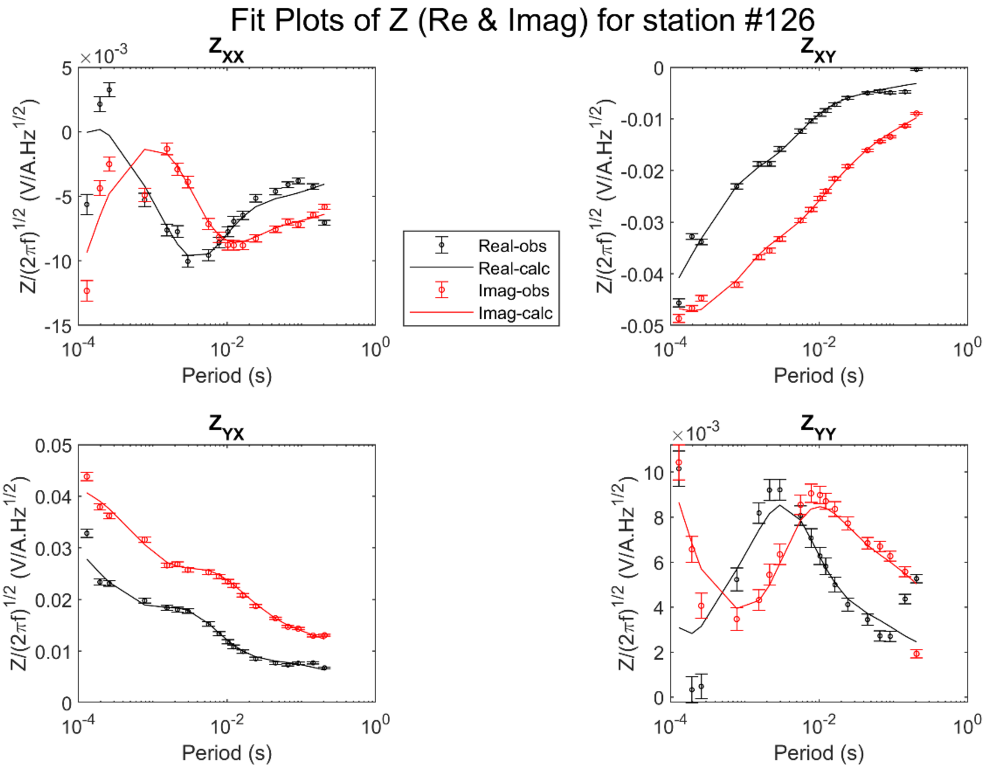
Fit Plots of Z (Re & Imag) for station #126
Z_XX
Z_XY
Z_YX
Z_YY
Z/(2πf)^1/2 (V/A.Hz^1/2)
Period (s)
Real-obs
Real-calc
Imag-obs
Imag-calc

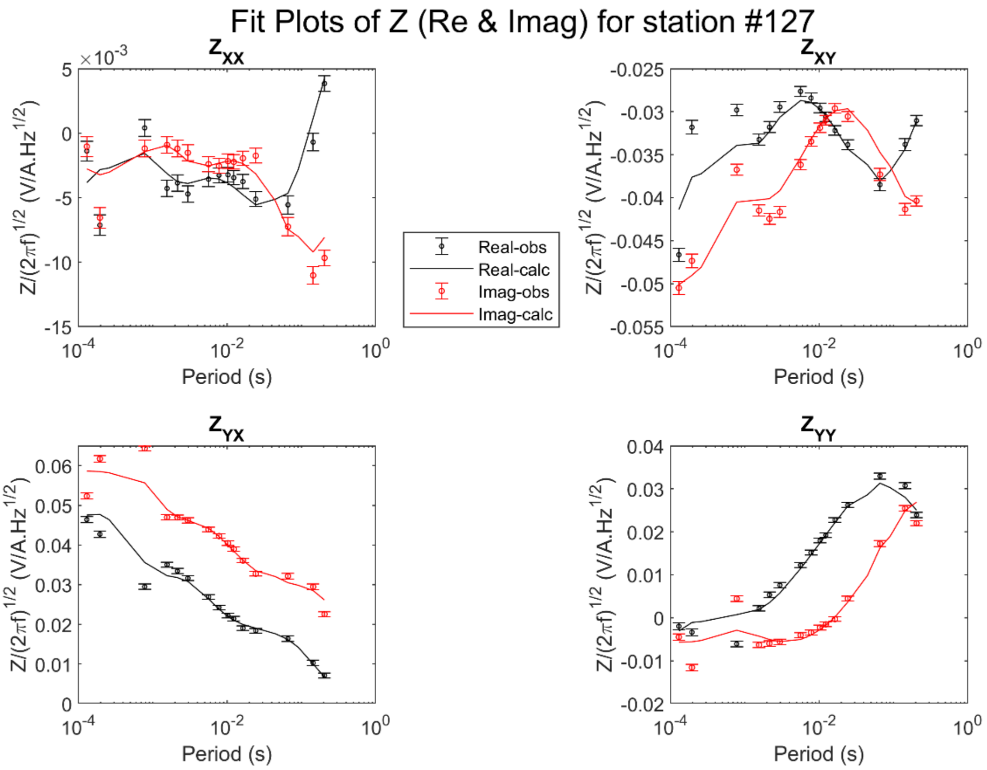
Fit Plots of Z (Re & Imag) for station #127
Z_XX
Z_XY
Z_YX
Z_YY
Z/(2πf)^1/2 (V/A.Hz^1/2)
Period (s)
Real-obs
Real-calc
Imag-obs
Imag-calc

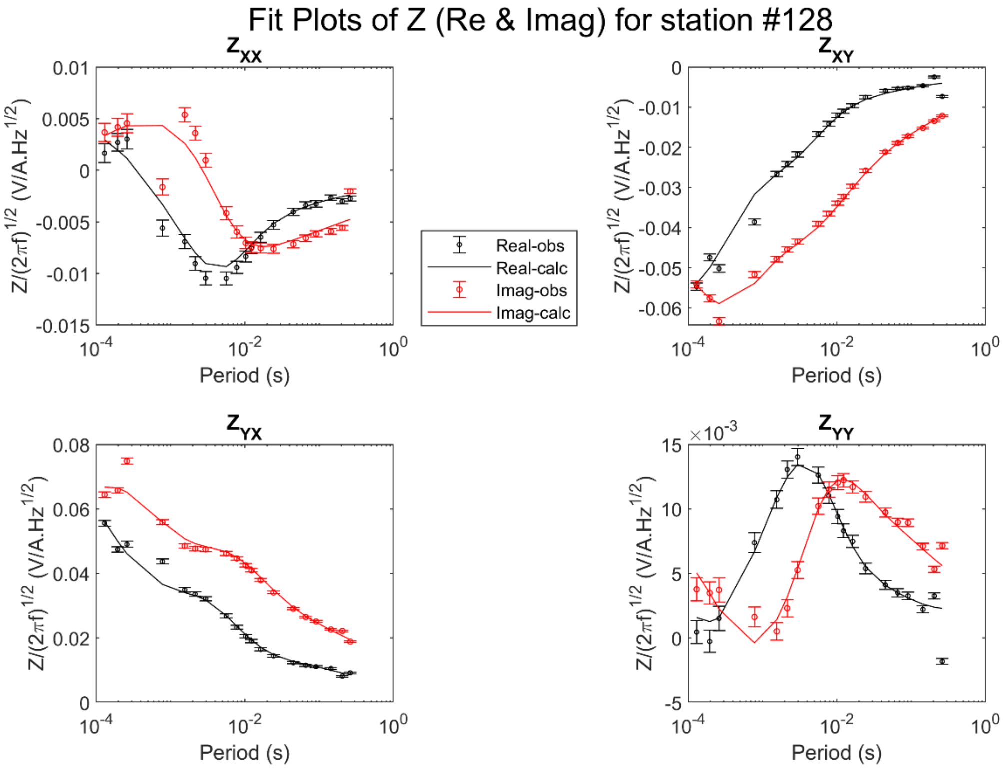
Fit Plots of Z (Re & Imag) for station #128
Z_XX
Z_XY
Z_YX
Z_YY
Z/(2πf)^1/2 (V/A.Hz^1/2)
Period (s)
Real-obs
Real-calc
Imag-obs
Imag-calc

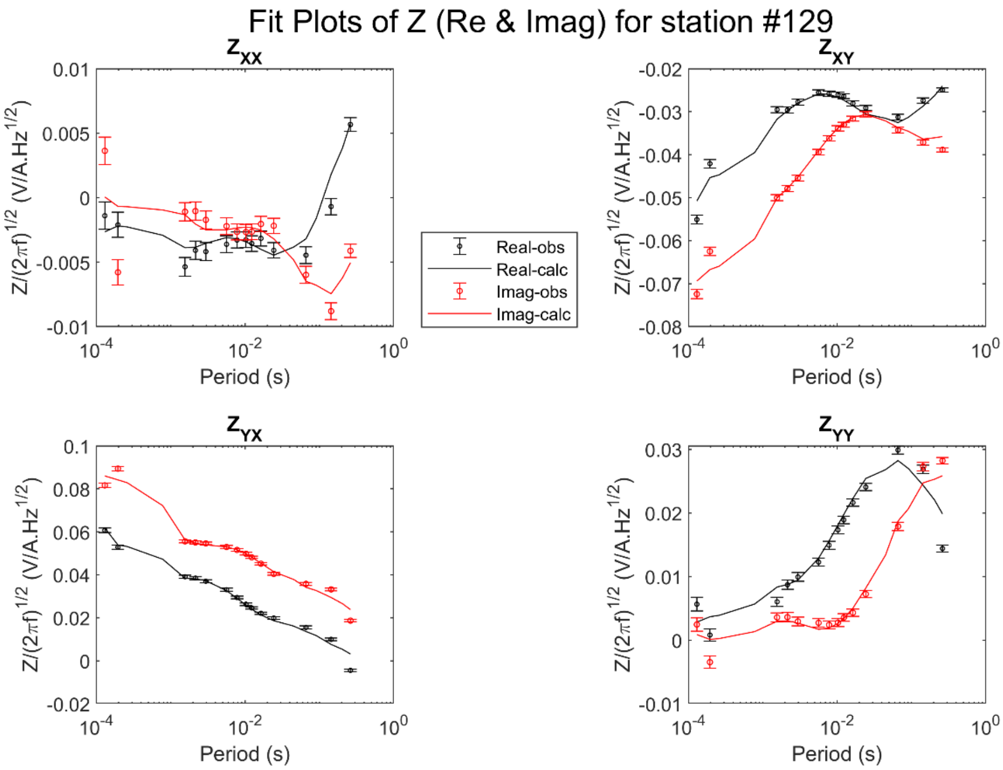
Fit Plots of Z (Re & Imag) for station #129
Z_XX
Z_XY
Z_YX
Z_YY
Z/(2πf)^1/2 (V/A.Hz^1/2)
Period (s)
Real-obs
Real-calc
Imag-obs
Imag-calc

Fit Plots of Z (Re & Imag) for station #130

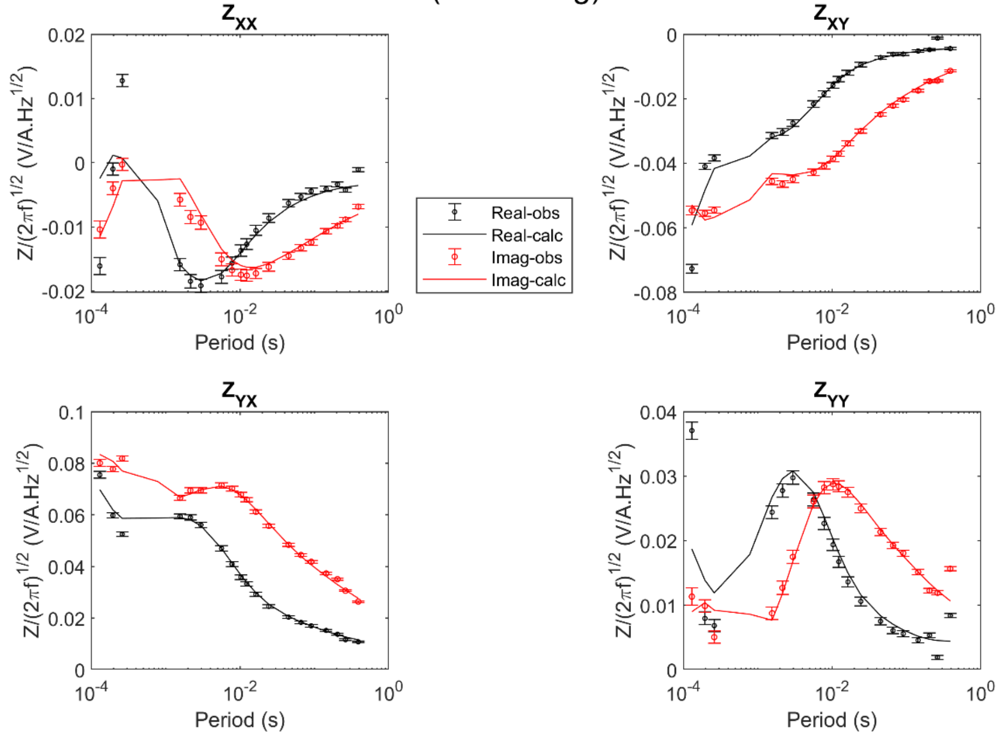

Fit Plots of Z (Re & Imag) for station #131

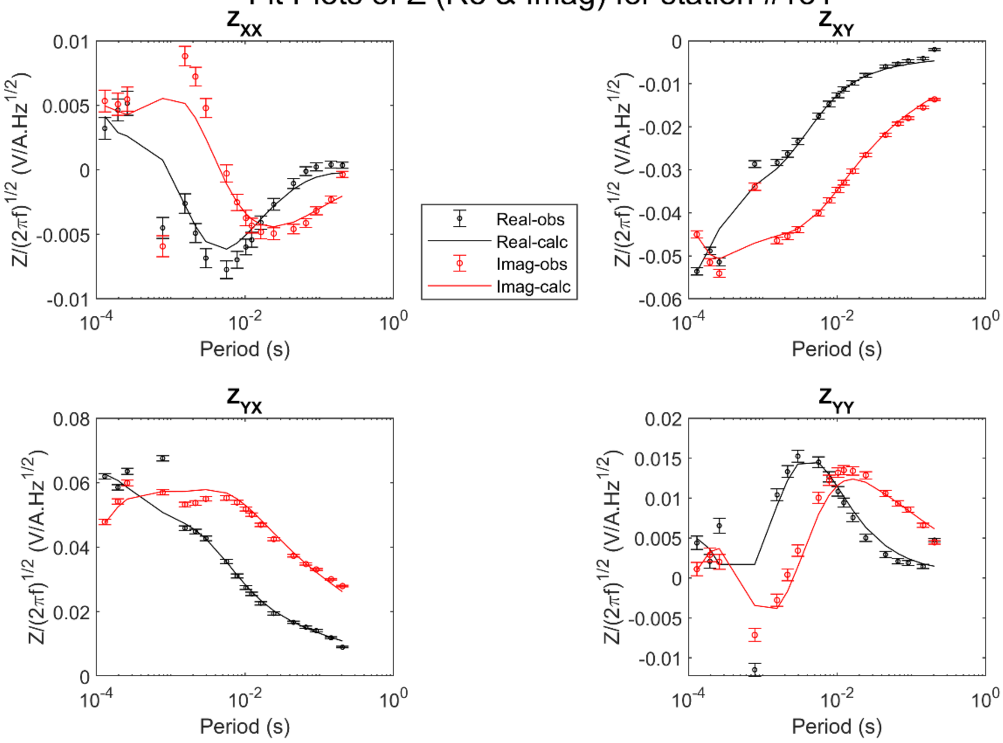

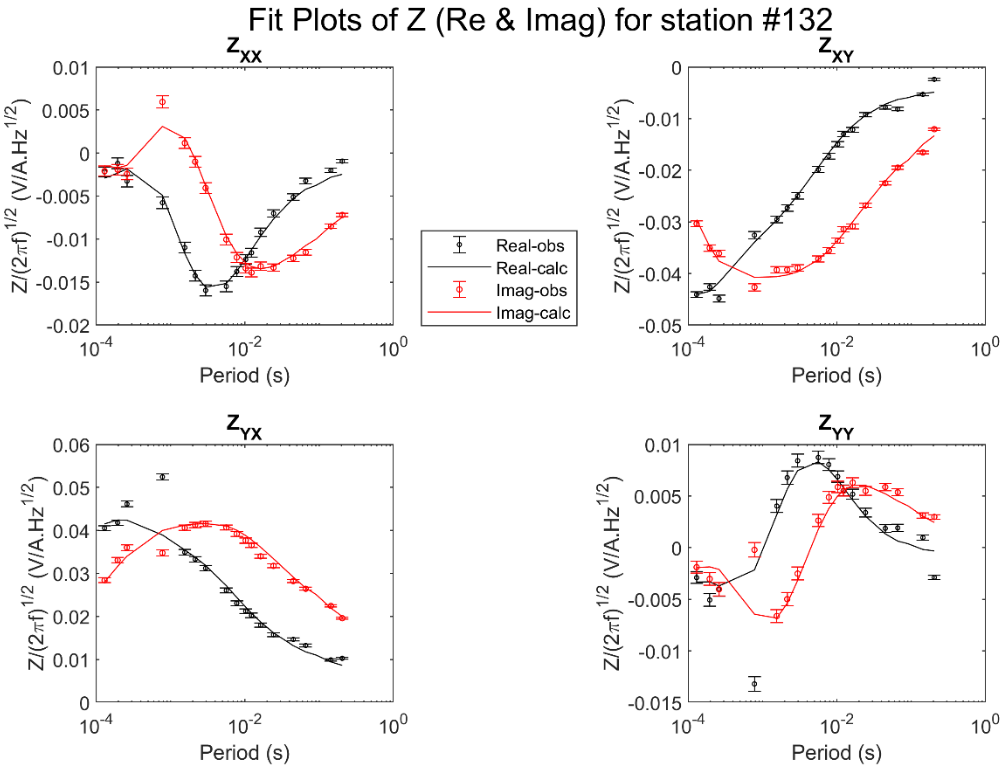

Fit Plots of Z (Re & Imag) for station #132
Z_XX
Z_XY
Z_YX
Z_YY
Z/(2πf)^1/2 (V/A.Hz^1/2)
Period (s)
Real-obs
Real-calc
Imag-obs
Imag-calc

E.2. Fit Plots of Apparent Resistivities and Phases

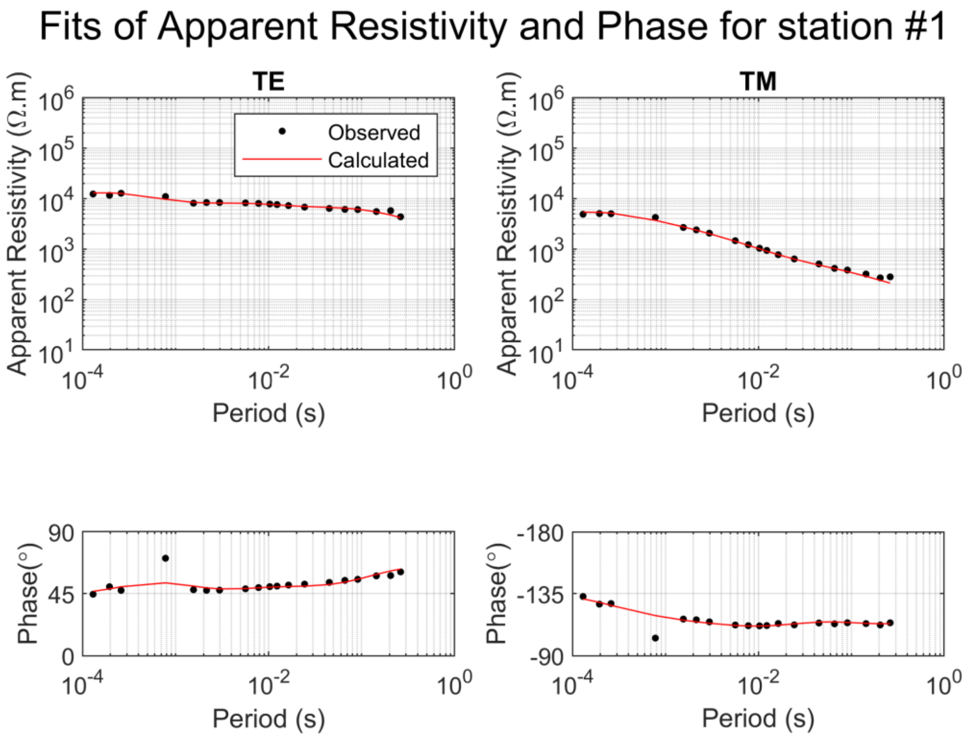

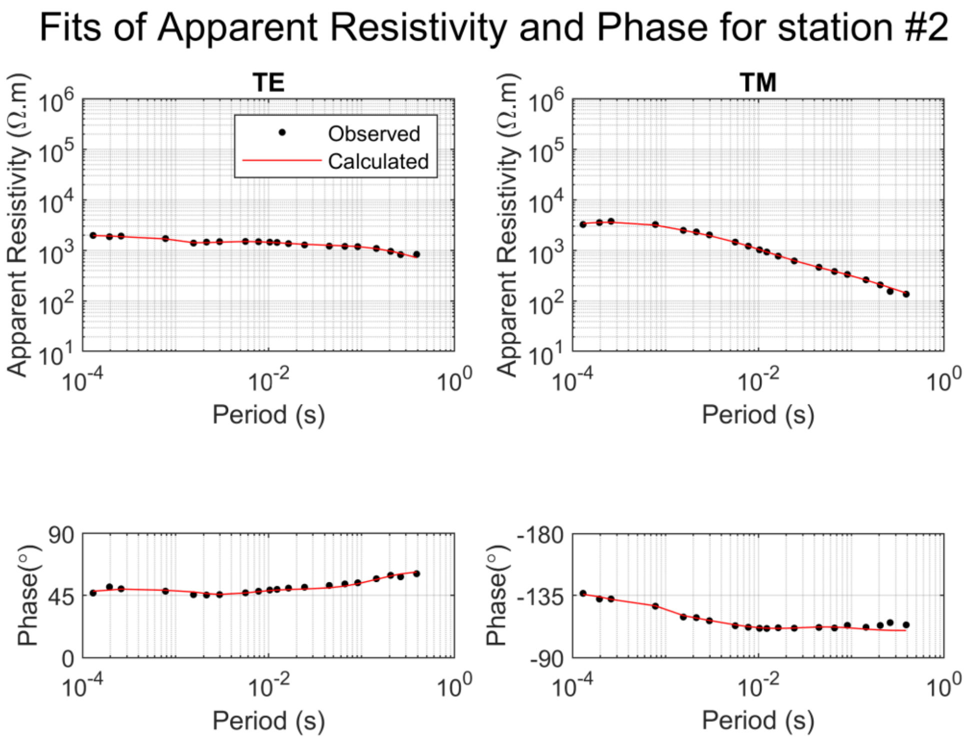

Fits of Apparent Resistivity and Phase for station #3

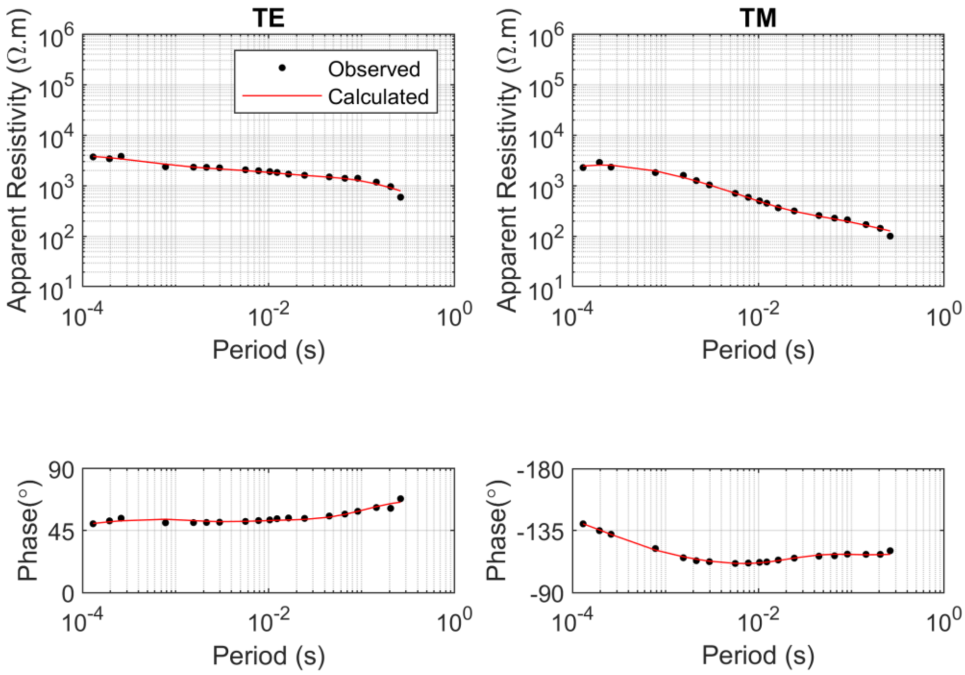

Fits of Apparent Resistivity and Phase for station #4

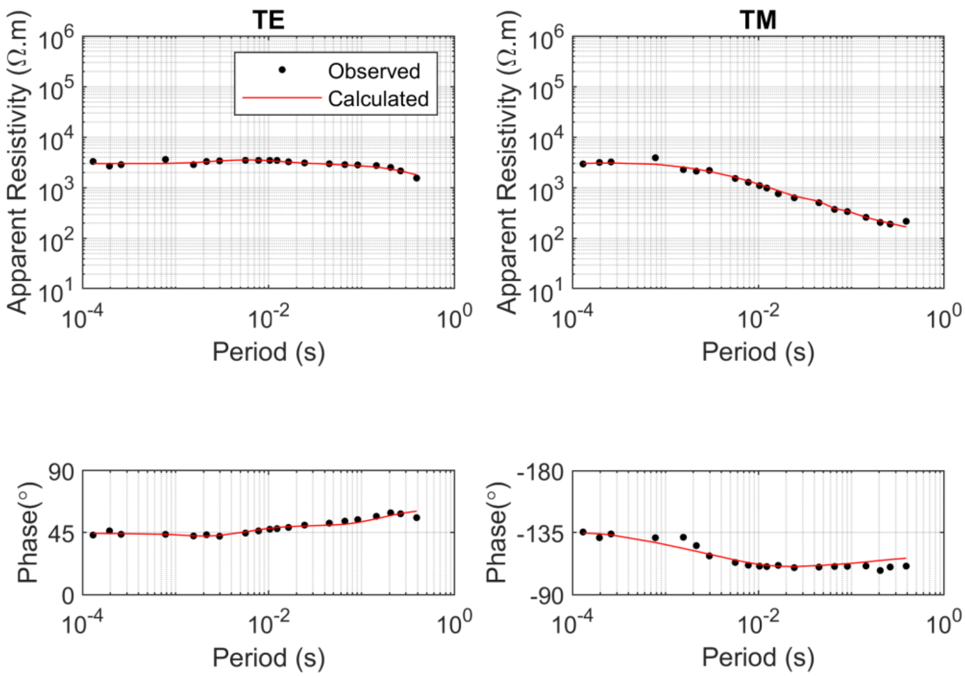

Fits of Apparent Resistivity and Phase for station #5

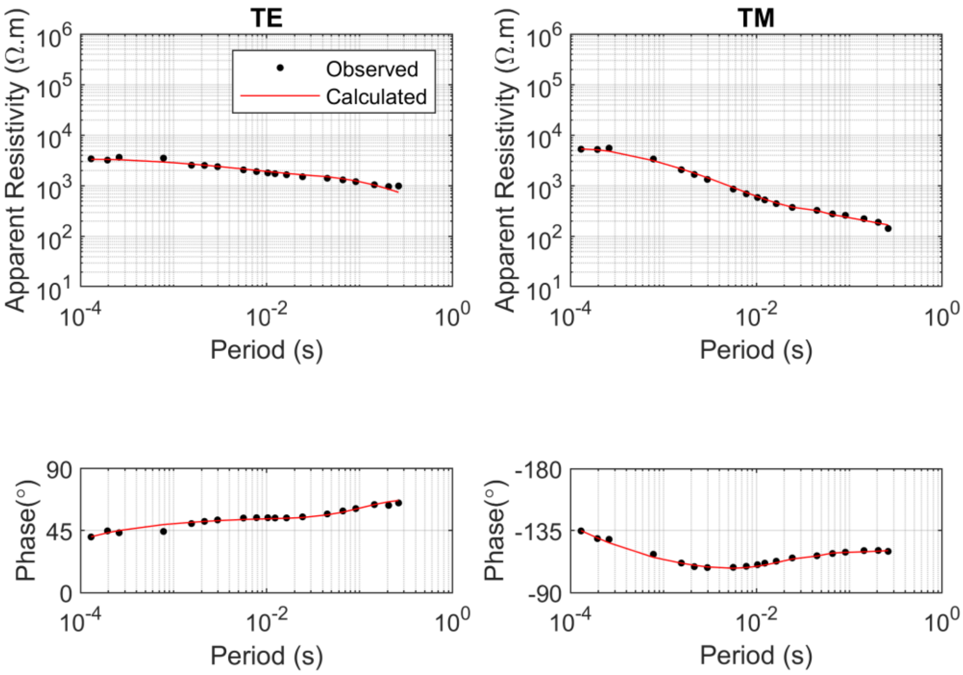

Fits of Apparent Resistivity and Phase for station #6

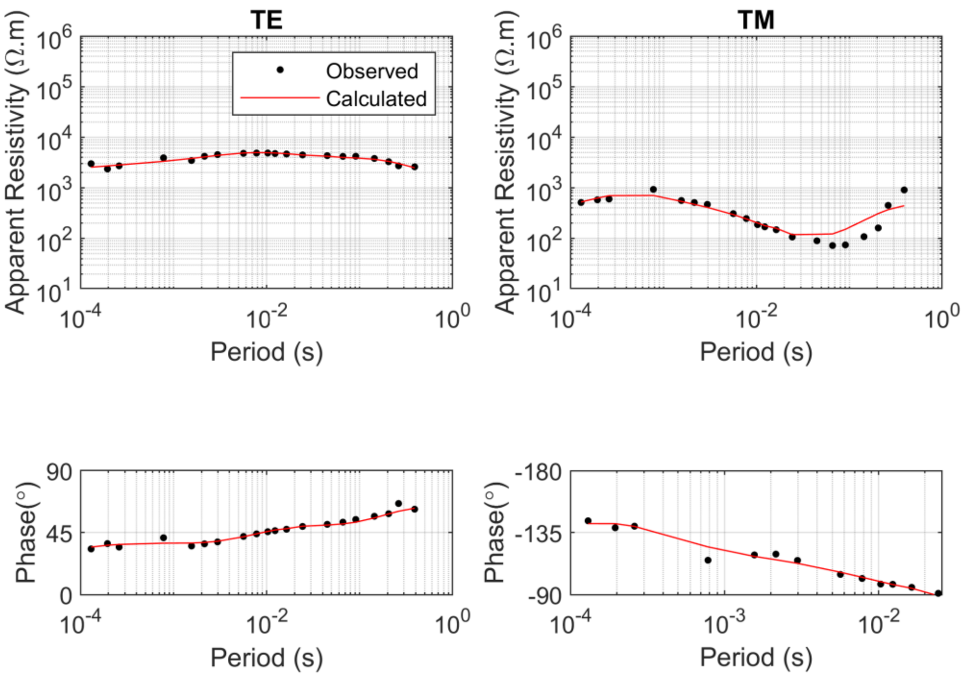

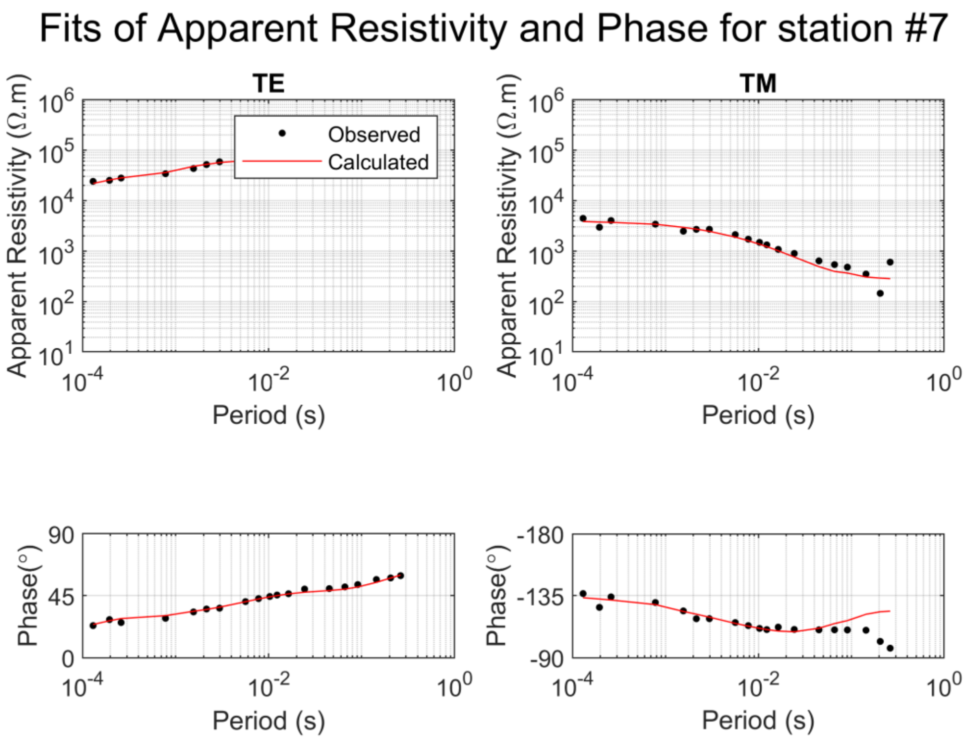

Fits of Apparent Resistivity and Phase for station #7
TE
TM
Observed
Calculated
Apparent Resistivity (Ω.m)
Phase(°)
Period (s)

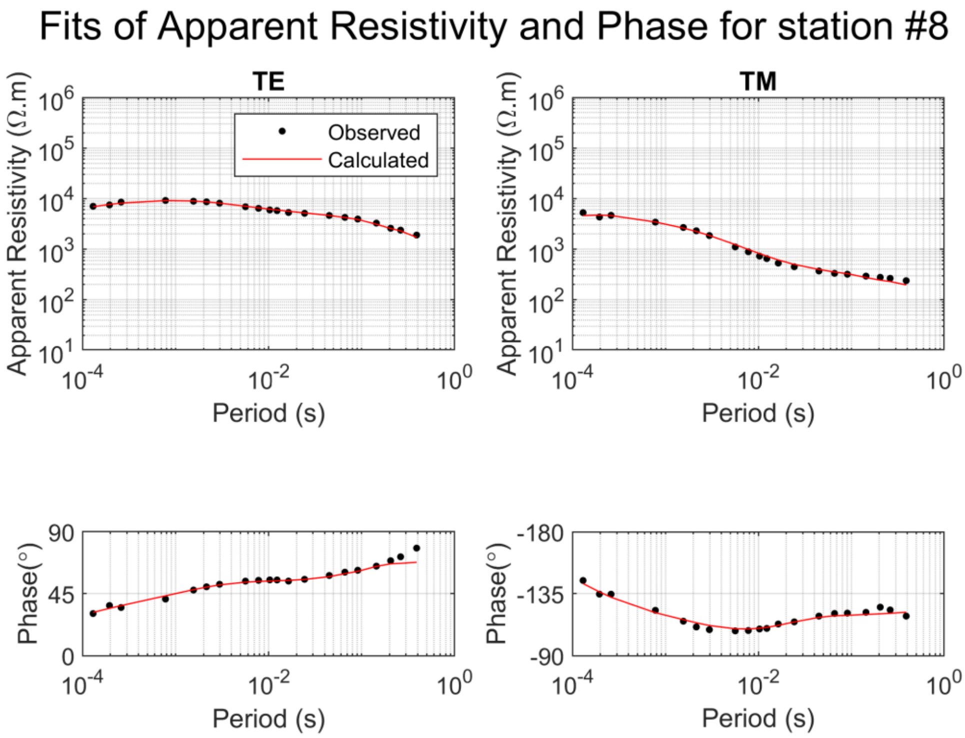

Fits of Apparent Resistivity and Phase for station #8
TE
TM
Observed
Calculated
Apparent Resistivity (Ω.m)
Phase(°)
Period (s)

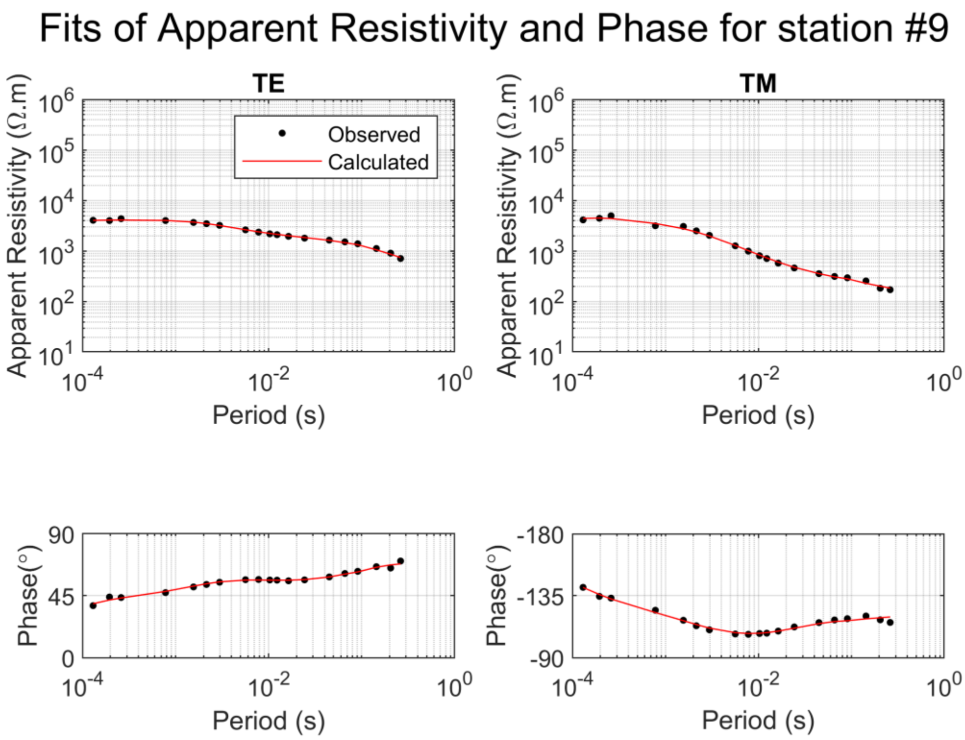
Fits of Apparent Resistivity and Phase for station #9
TE
TM
Observed
Calculated
Apparent Resistivity (Ω.m)
Phase(°)
Period (s)

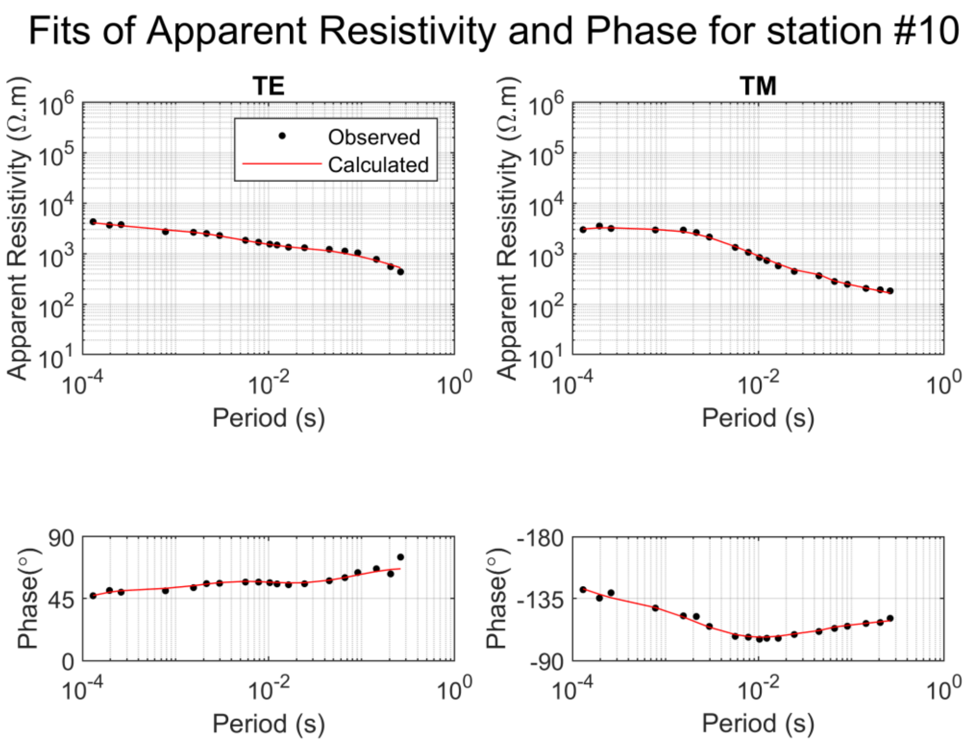
Fits of Apparent Resistivity and Phase for station #10
TE
TM
Observed
Calculated
Apparent Resistivity (Ω.m)
Phase(°)
Period (s)

Fits of Apparent Resistivity and Phase for station #11

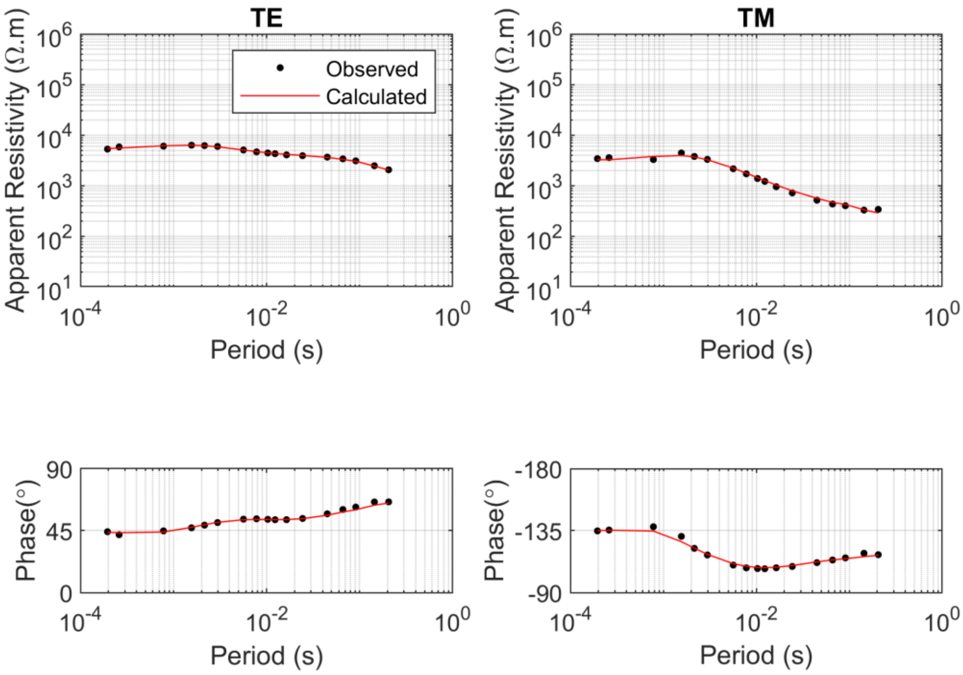

Fits of Apparent Resistivity and Phase for station #12

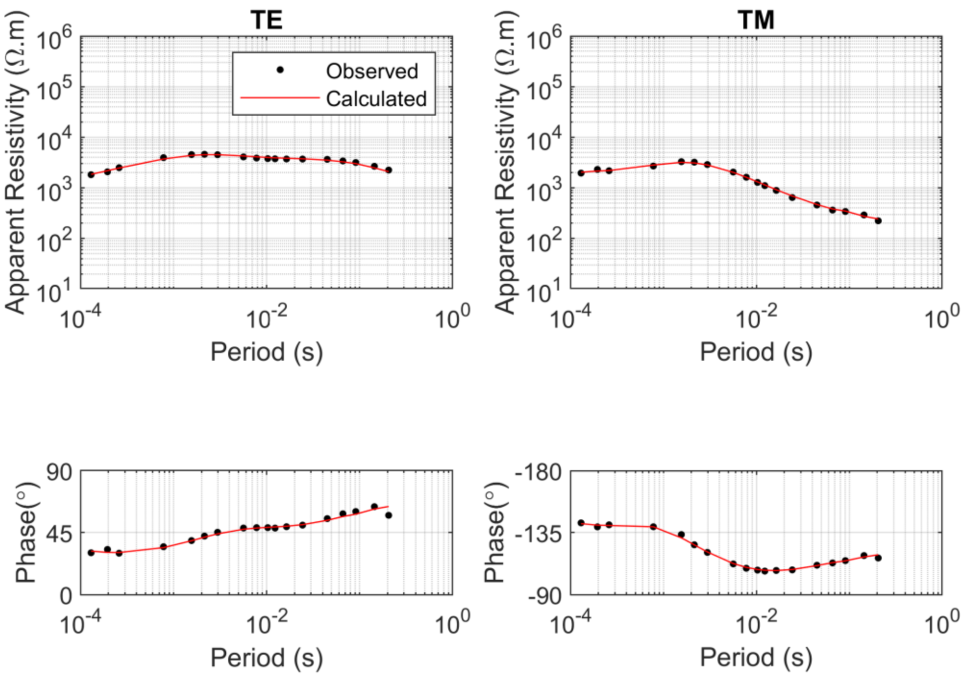

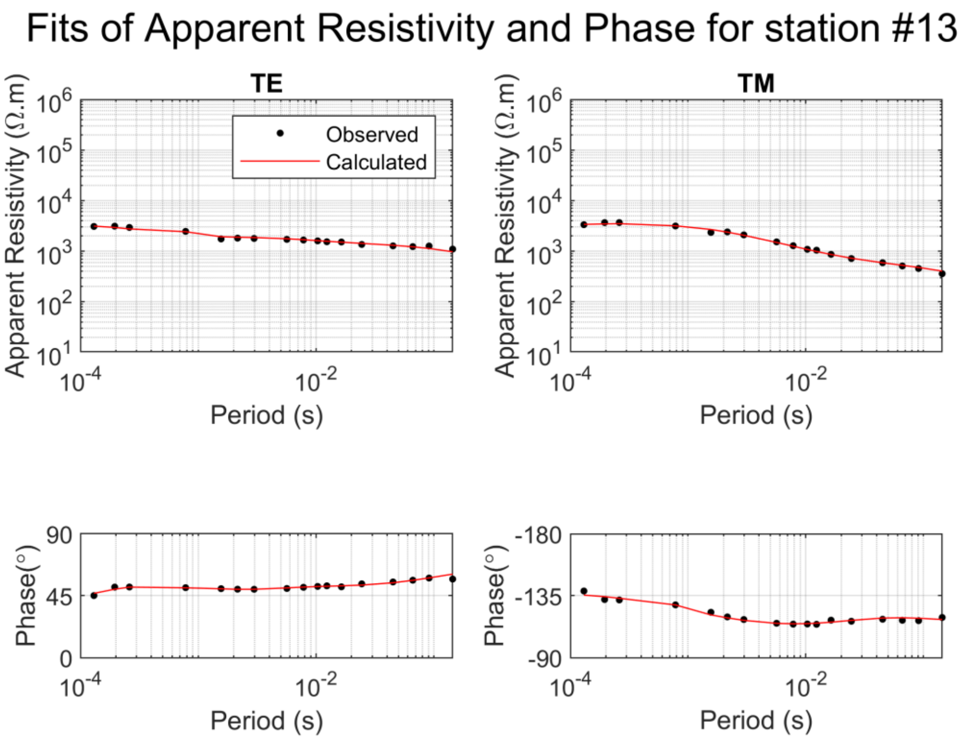
Fits of Apparent Resistivity and Phase for station #13
TE
TM
Observed
Calculated
Apparent Resistivity (Ω.m)
Period (s)
Phase(°)

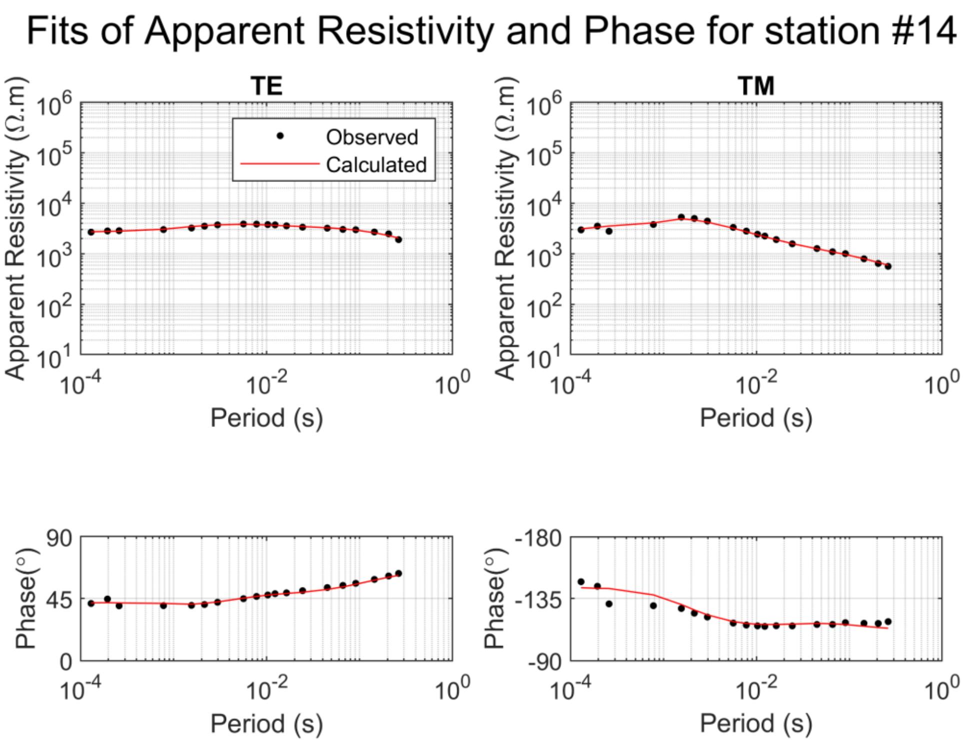
Fits of Apparent Resistivity and Phase for station #14
TE
TM
Observed
Calculated
Apparent Resistivity (Ω.m)
Period (s)
Phase(°)

Fits of Apparent Resistivity and Phase for station #15

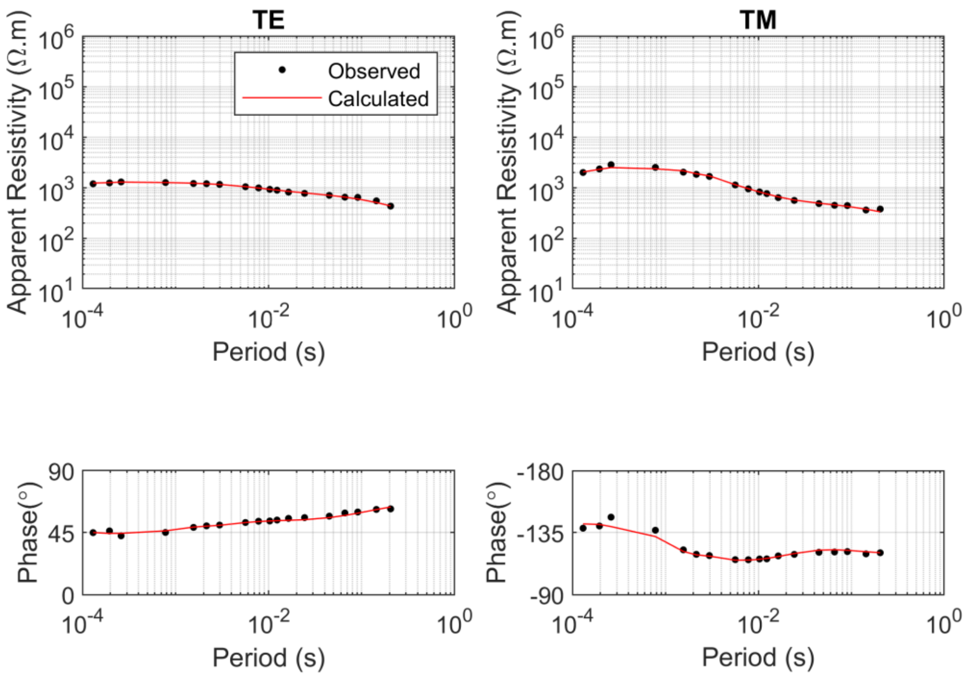

Fits of Apparent Resistivity and Phase for station #16

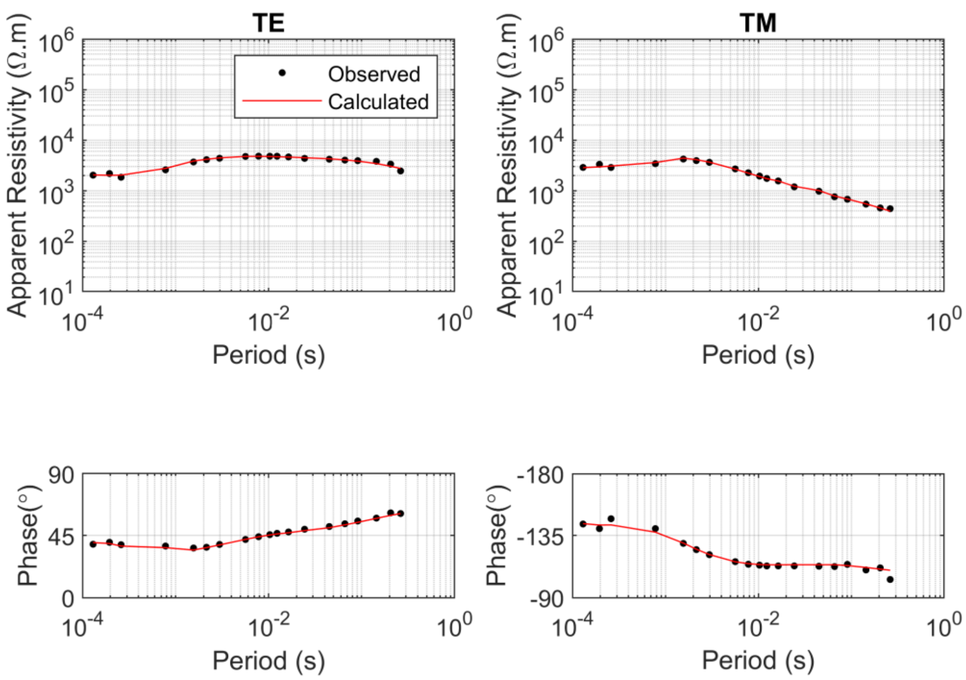

Fits of Apparent Resistivity and Phase for station #17

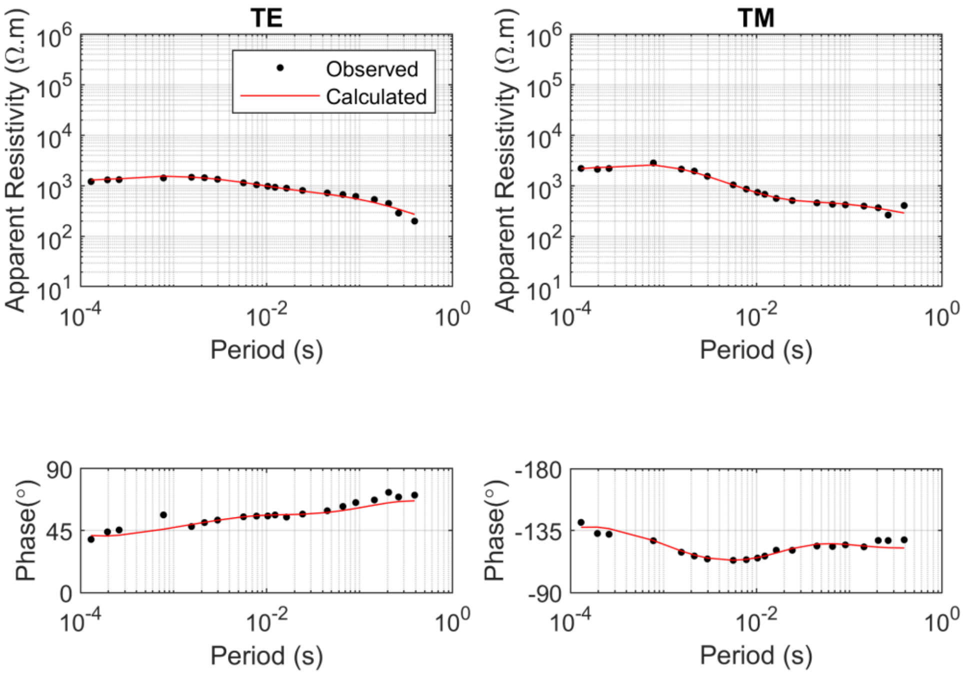

Fits of Apparent Resistivity and Phase for station #18

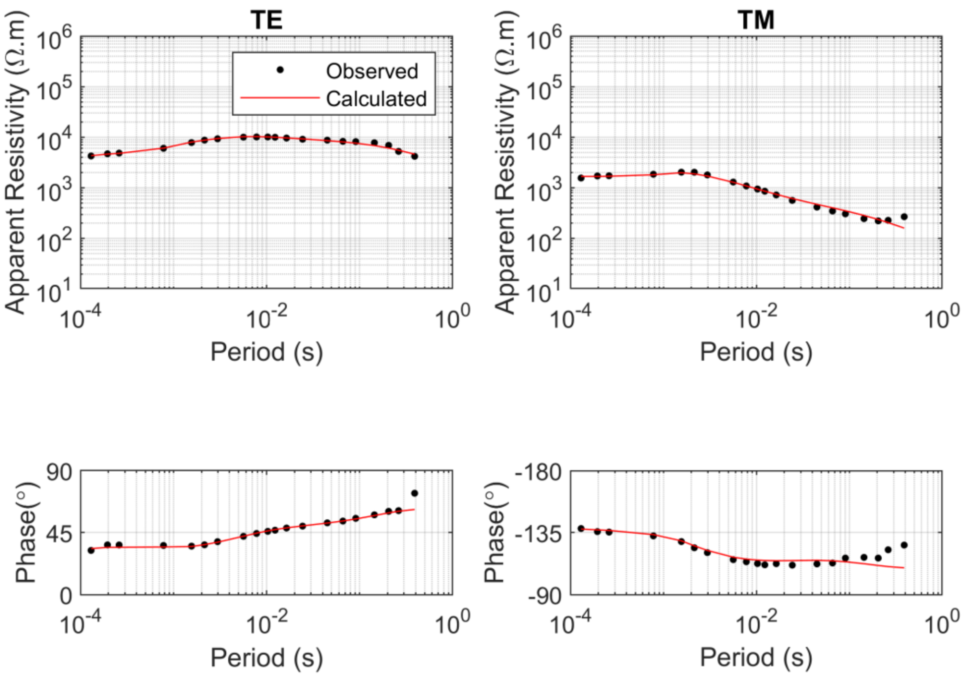

Fits of Apparent Resistivity and Phase for station #19

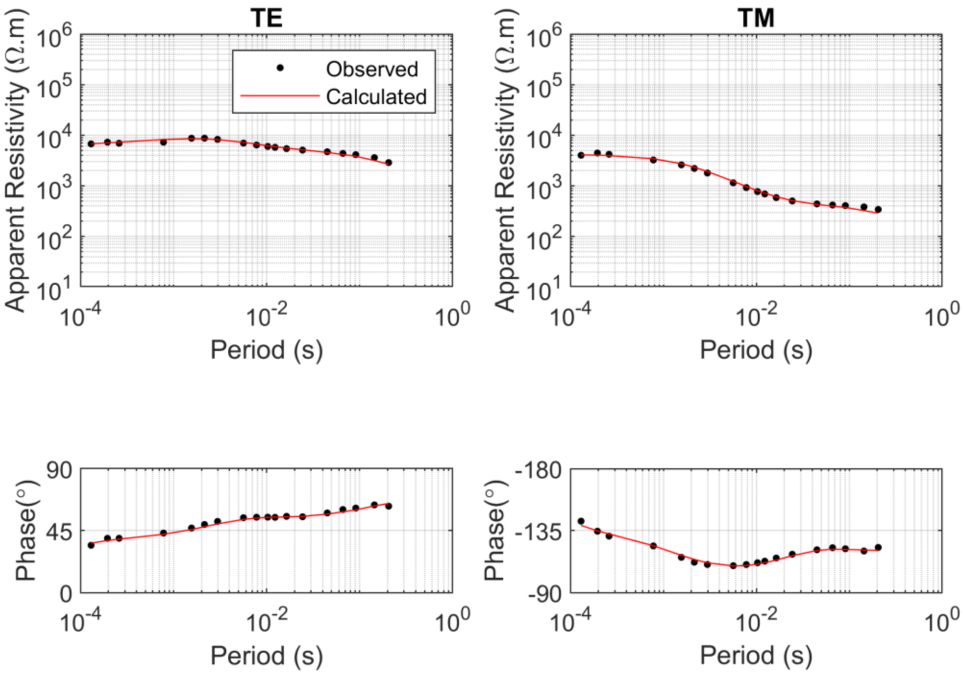

Fits of Apparent Resistivity and Phase for station #20

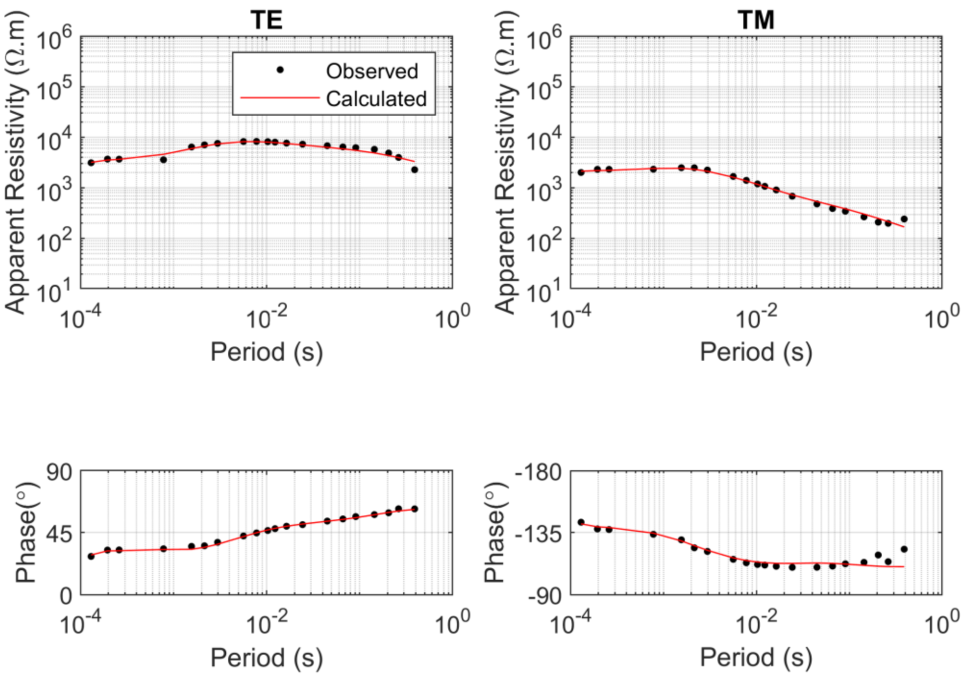

Fits of Apparent Resistivity and Phase for station #21

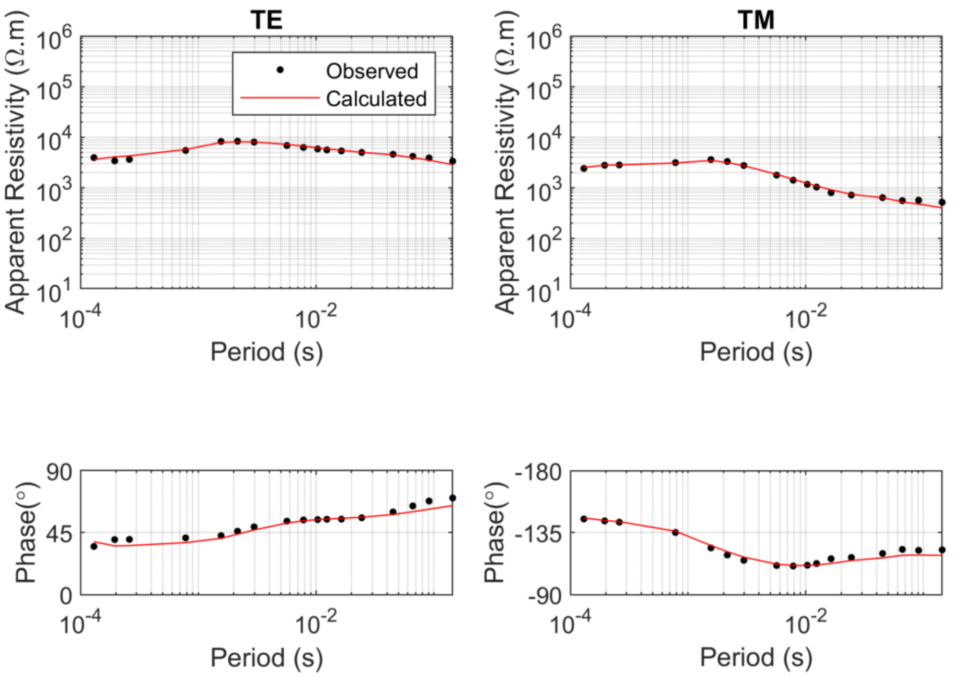

Fits of Apparent Resistivity and Phase for station #22

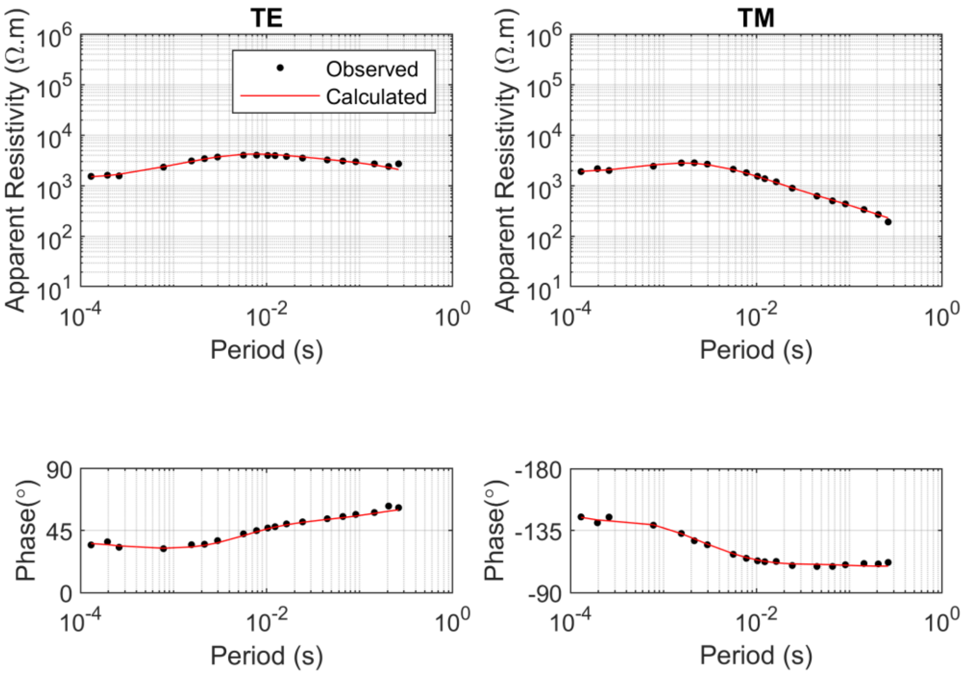

Fits of Apparent Resistivity and Phase for station #23

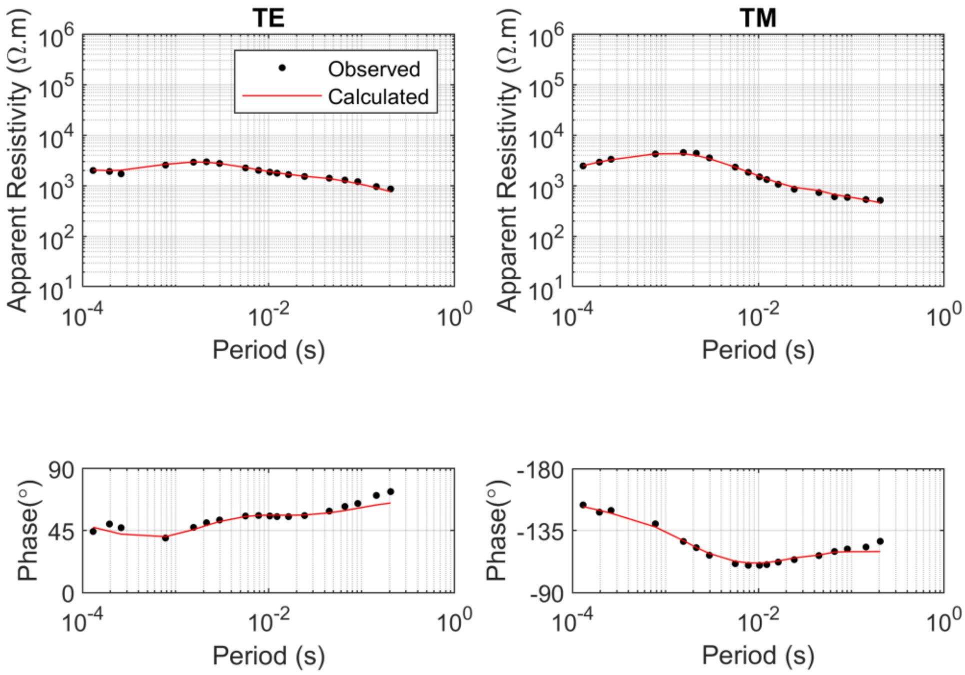

Fits of Apparent Resistivity and Phase for station #24

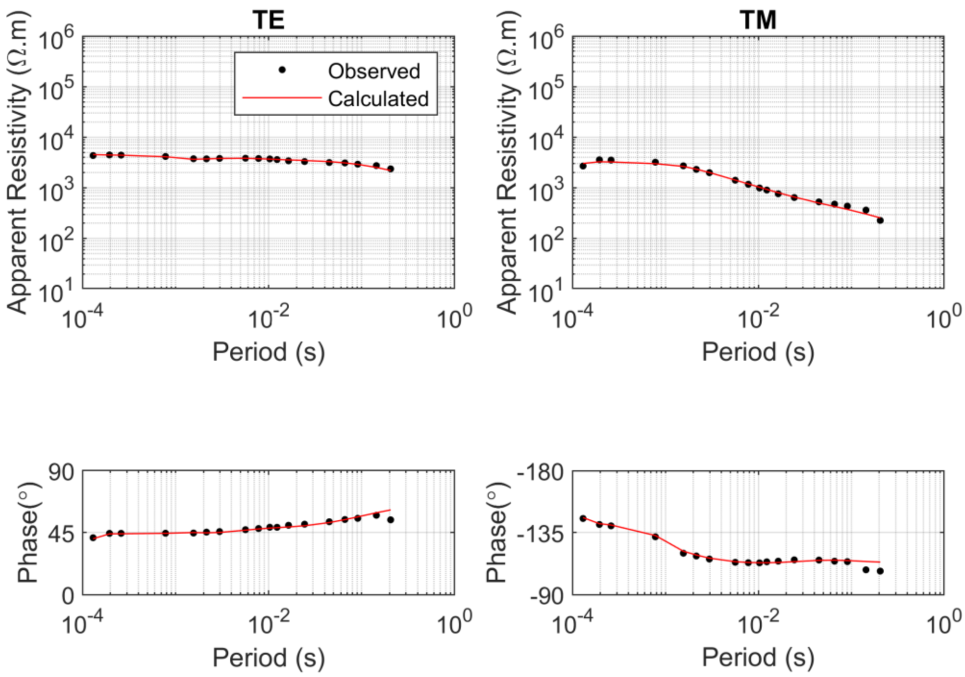

Fits of Apparent Resistivity and Phase for station #25

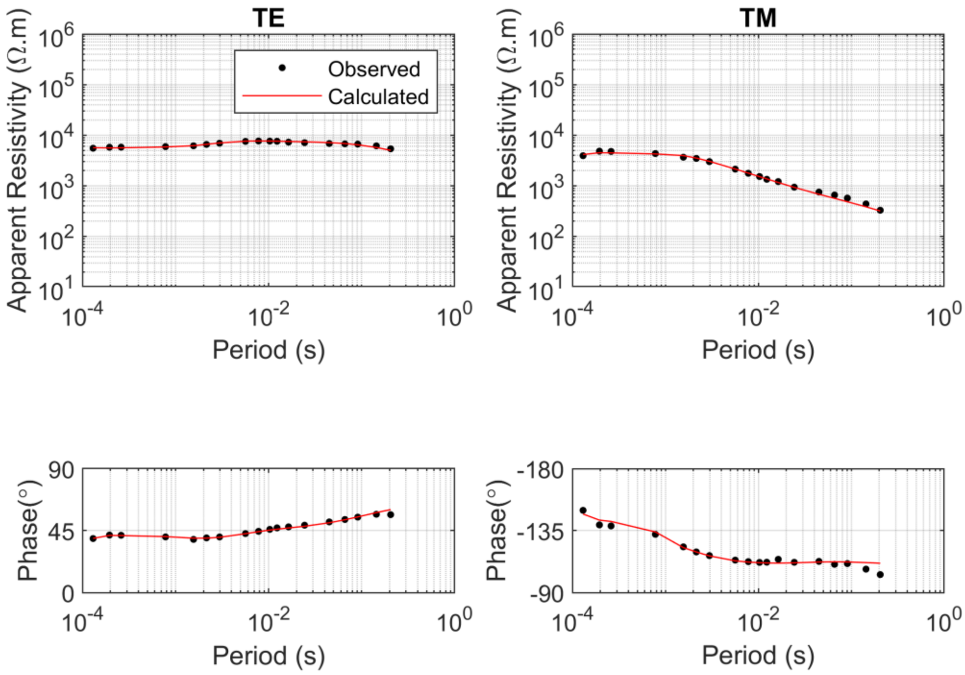

Fits of Apparent Resistivity and Phase for station #26

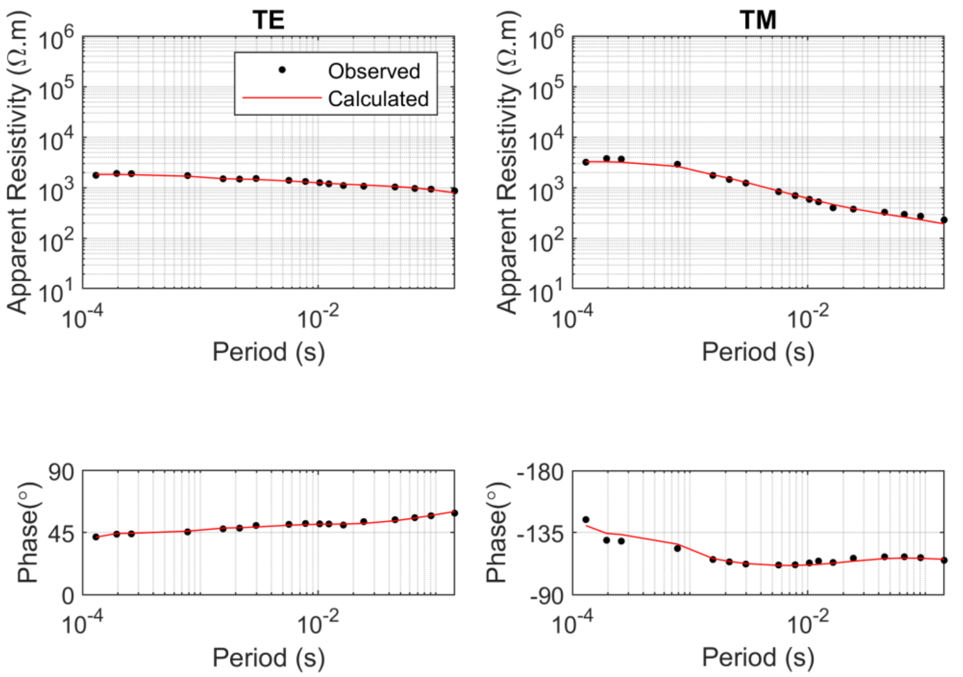

Fits of Apparent Resistivity and Phase for station #27

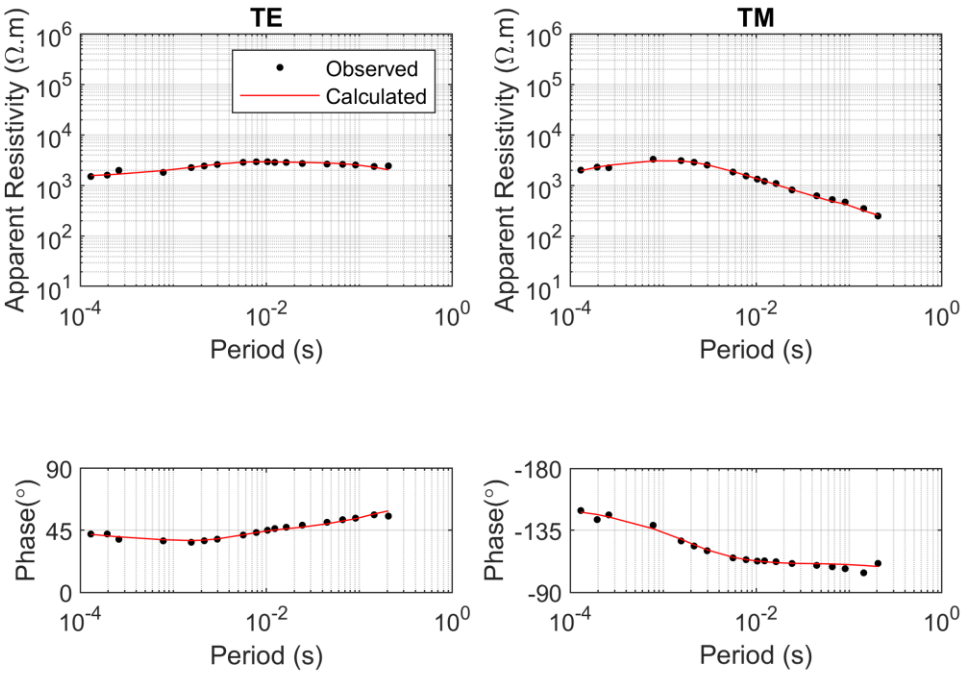

Fits of Apparent Resistivity and Phase for station #28

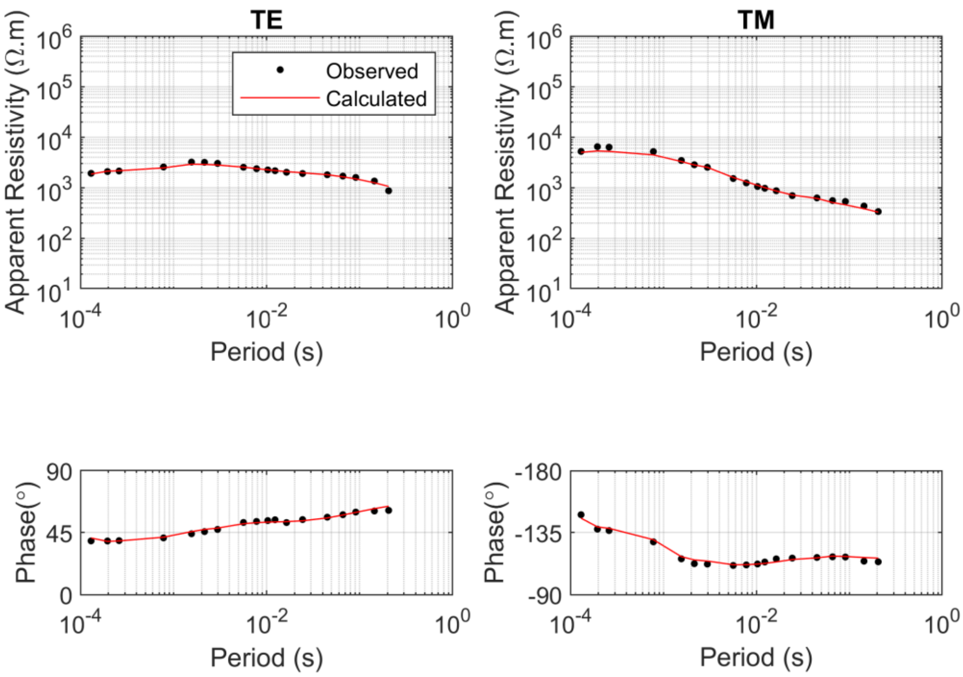

Fits of Apparent Resistivity and Phase for station #29

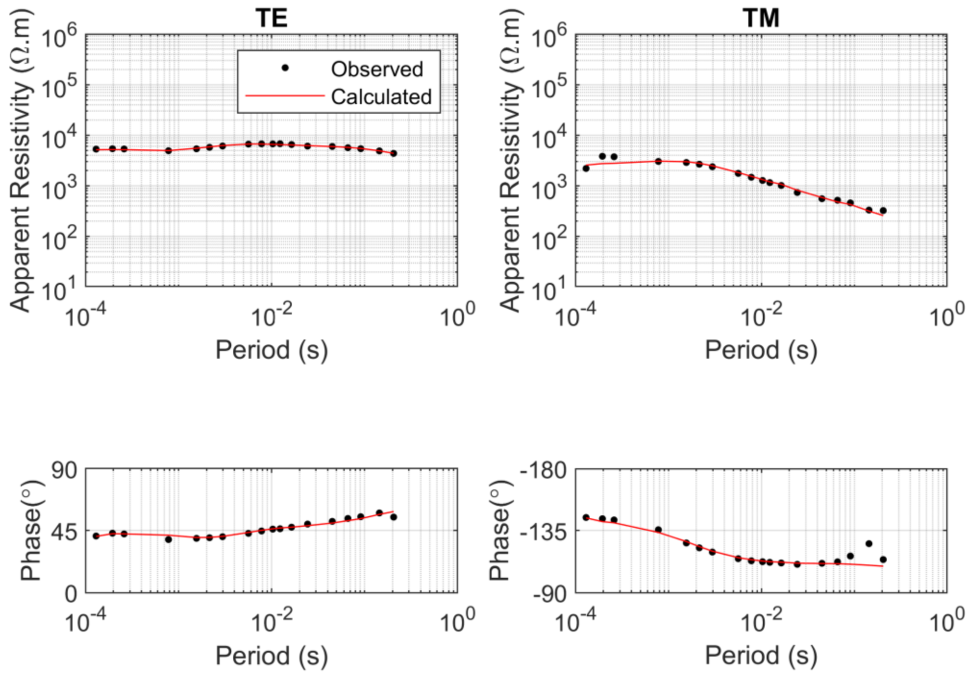

Fits of Apparent Resistivity and Phase for station #30

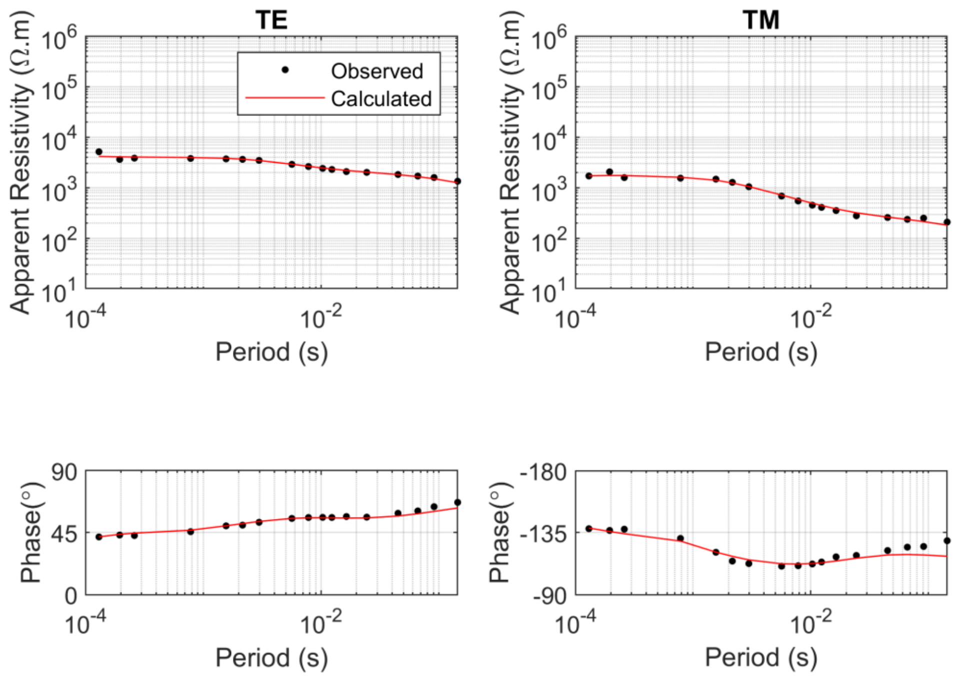

Fits of Apparent Resistivity and Phase for station #31

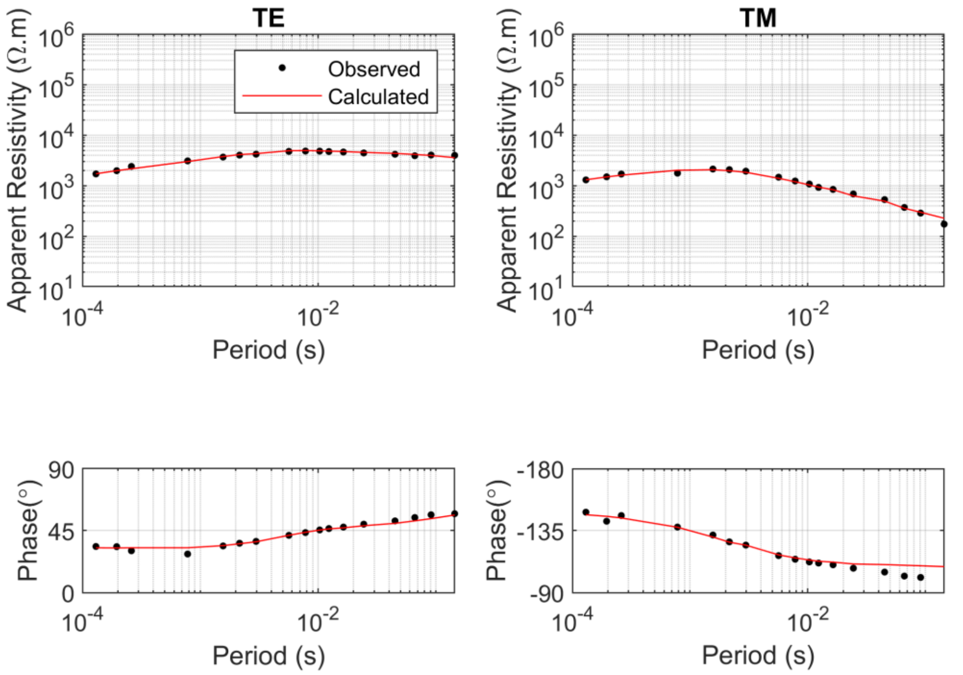

Fits of Apparent Resistivity and Phase for station #32

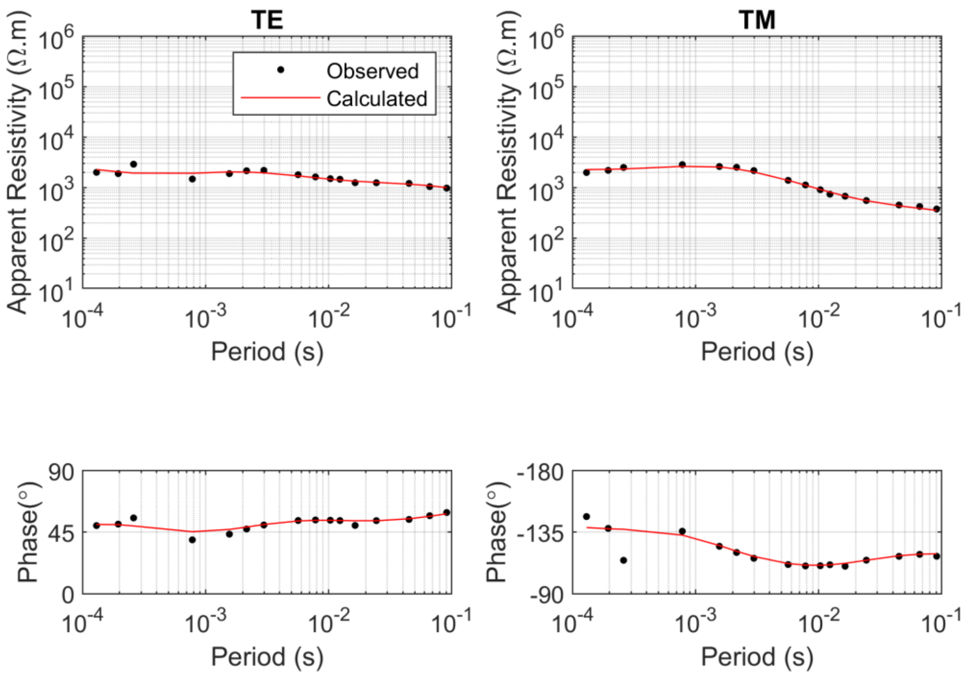

Fits of Apparent Resistivity and Phase for station #33

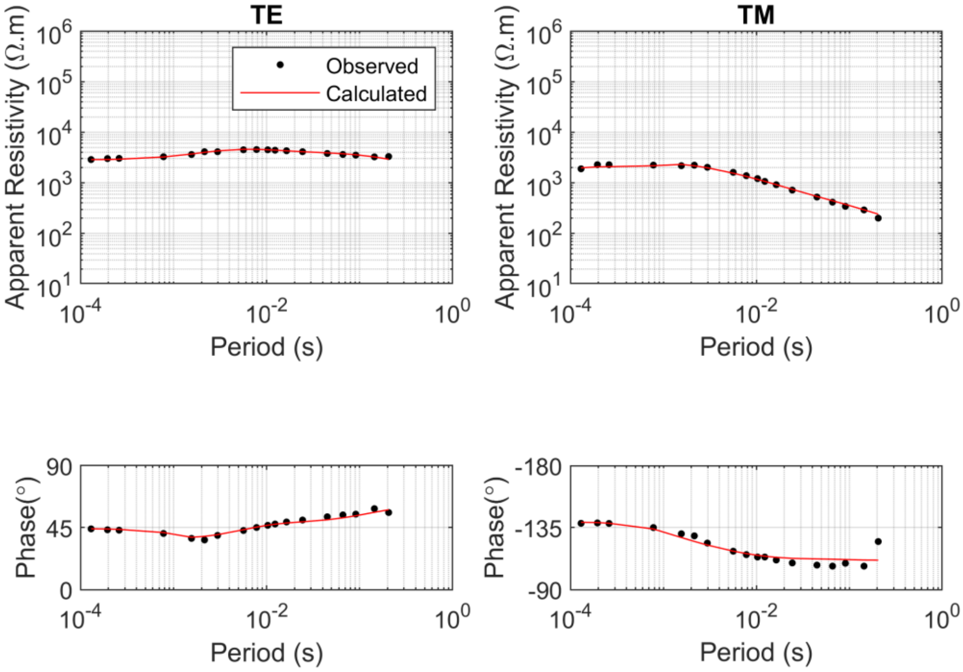

Fits of Apparent Resistivity and Phase for station #34

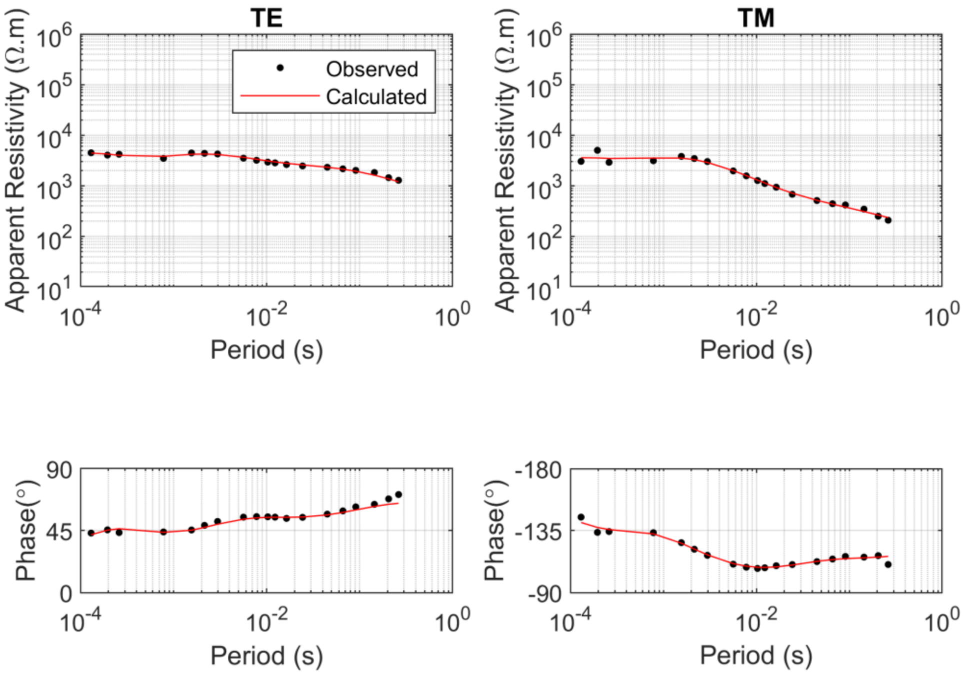

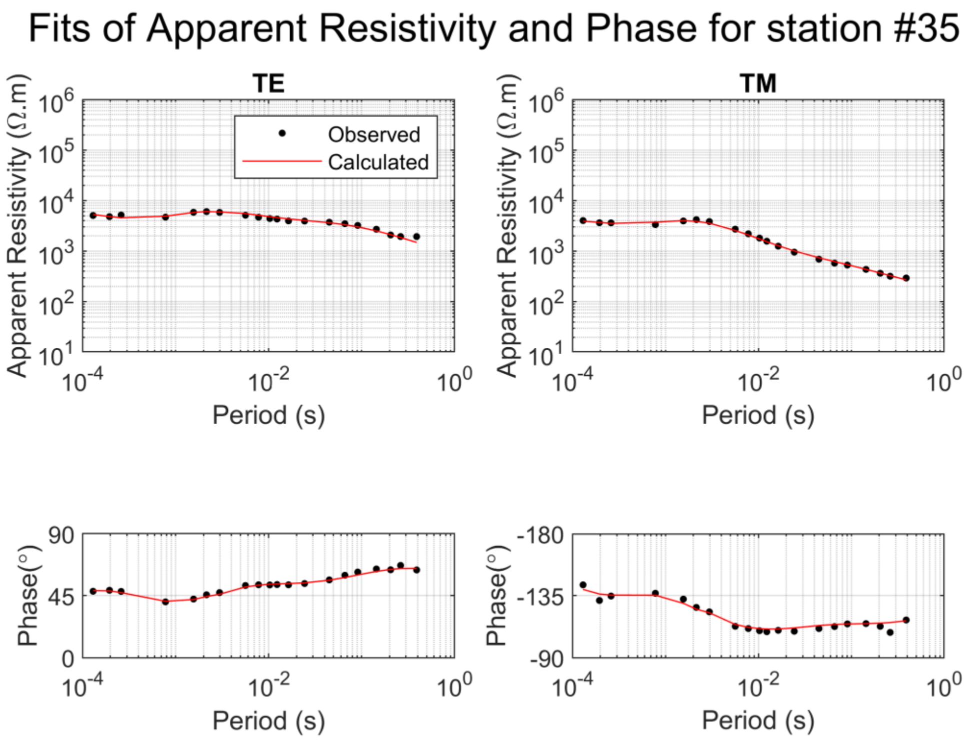
Fits of Apparent Resistivity and Phase for station #35
TE
TM
Observed
Calculated
Apparent Resistivity (Ω.m)
Period (s)
Phase(°)

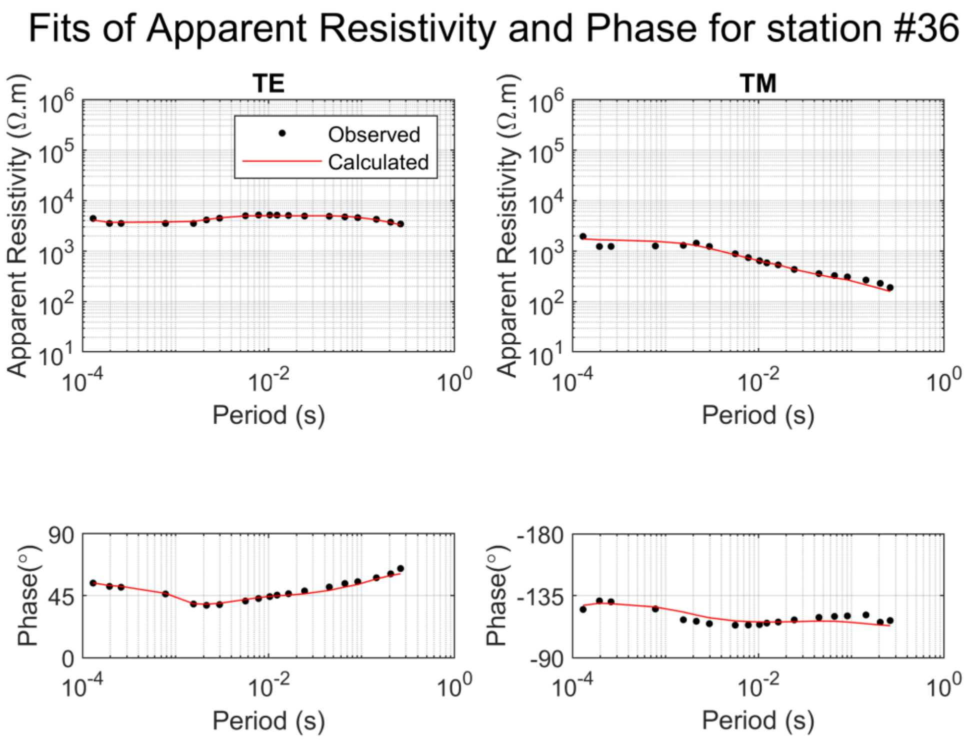
Fits of Apparent Resistivity and Phase for station #36
TE
TM
Observed
Calculated
Apparent Resistivity (Ω.m)
Period (s)
Phase(°)

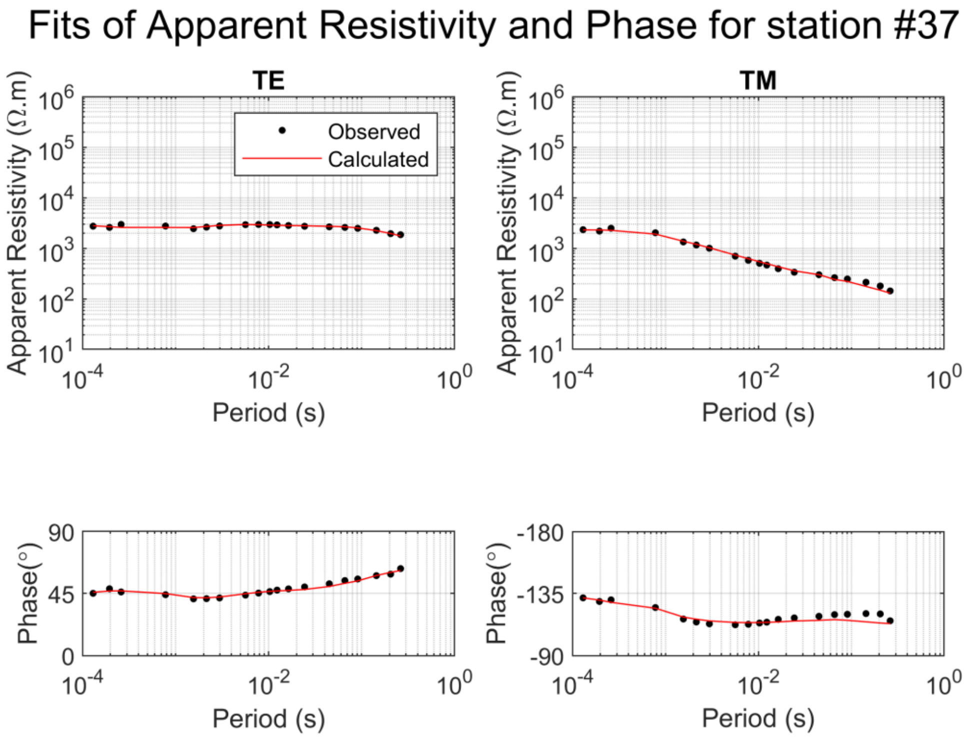
Fits of Apparent Resistivity and Phase for station #37
TE
TM
Observed
Calculated
Apparent Resistivity (Ω.m)
Phase(°)
Period (s)

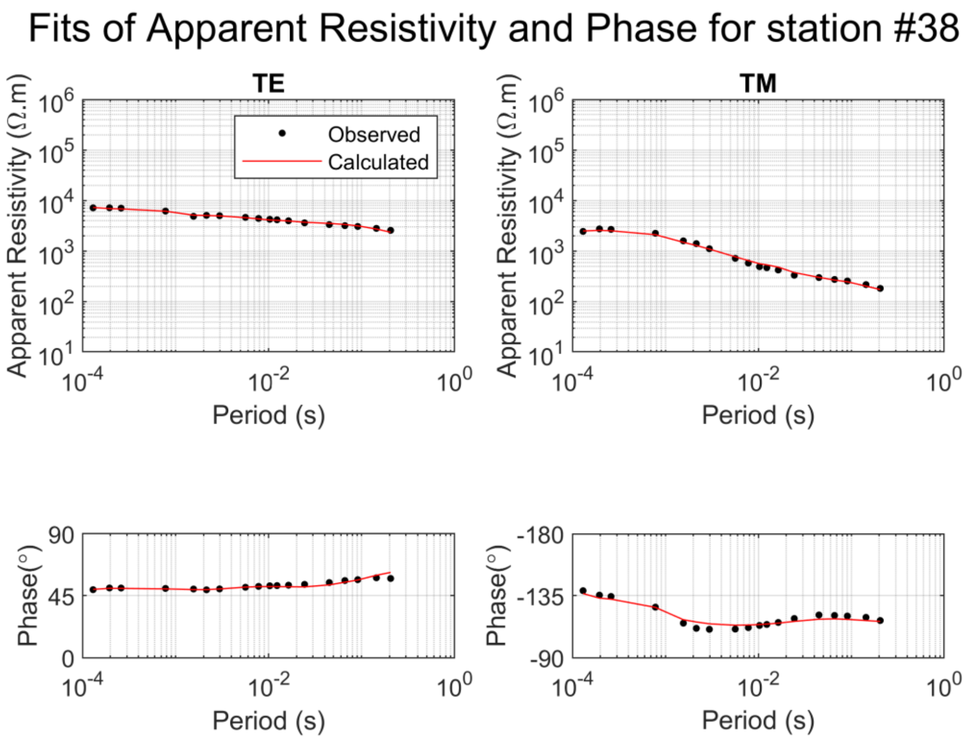
Fits of Apparent Resistivity and Phase for station #38
TE
TM
Observed
Calculated
Apparent Resistivity (Ω.m)
Phase(°)
Period (s)

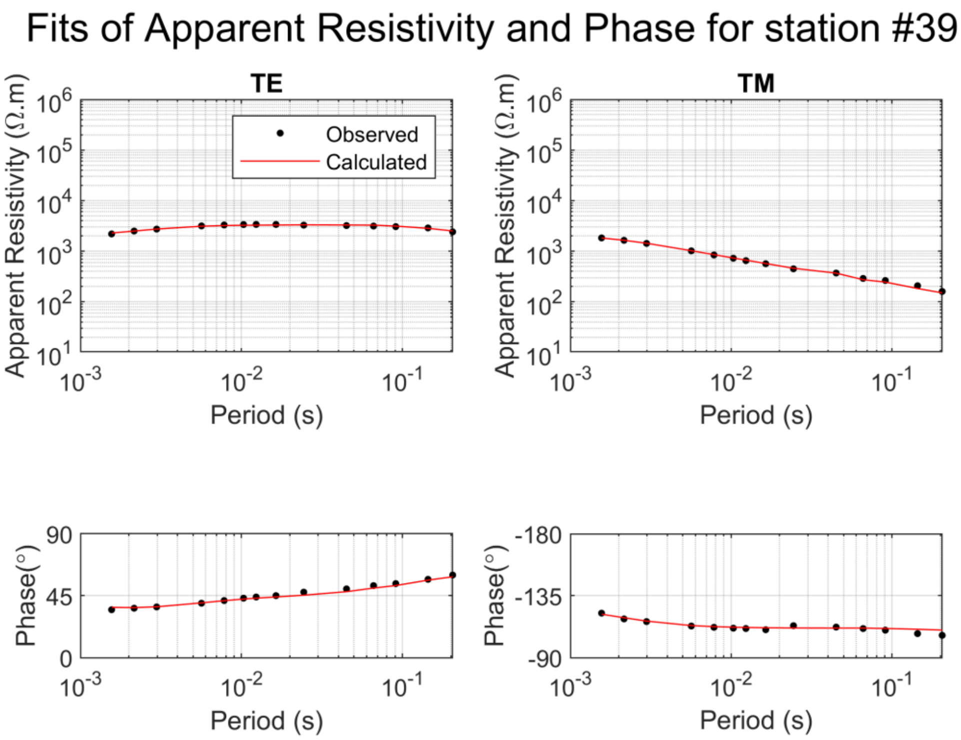
Fits of Apparent Resistivity and Phase for station #39
TE
TM
Observed
Calculated
Apparent Resistivity (Ω.m)
Phase(°)
Period (s)

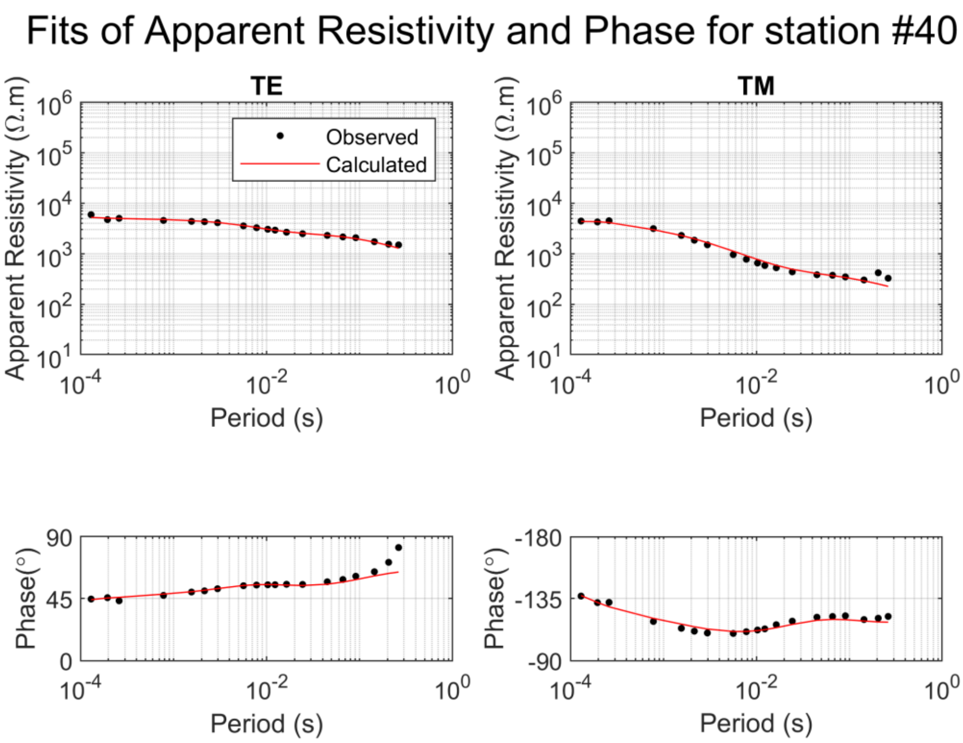
Fits of Apparent Resistivity and Phase for station #40
TE
TM
Observed
Calculated
Apparent Resistivity (Ω.m)
Phase(°)
Period (s)

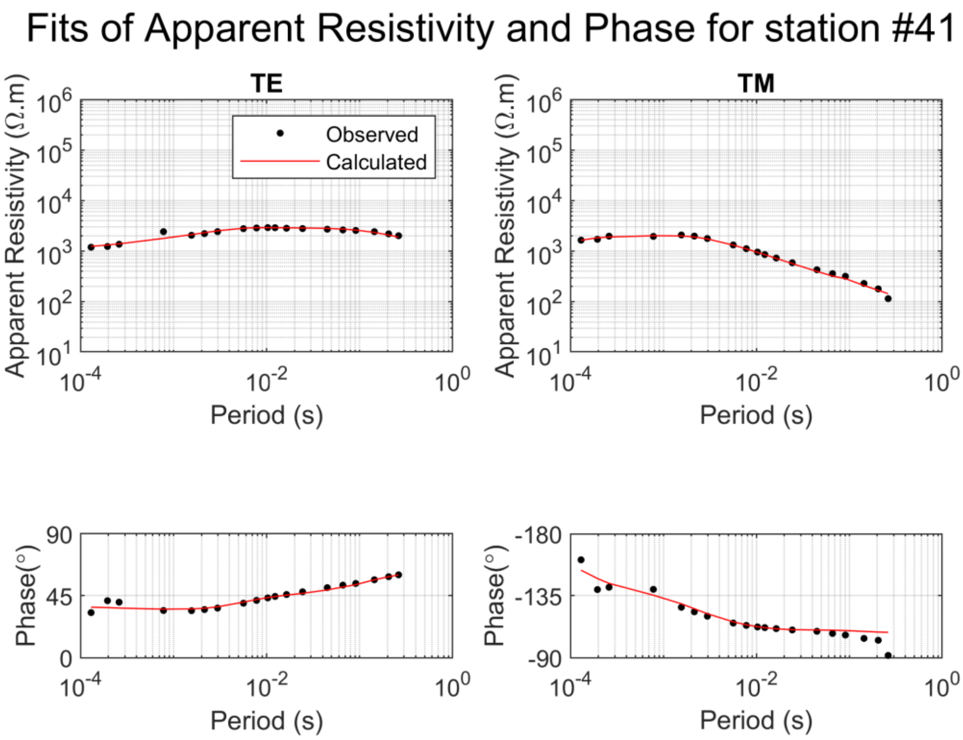
Fits of Apparent Resistivity and Phase for station #41
TE
TM
Observed
Calculated
Apparent Resistivity (Ω.m)
Phase(°)
Period (s)

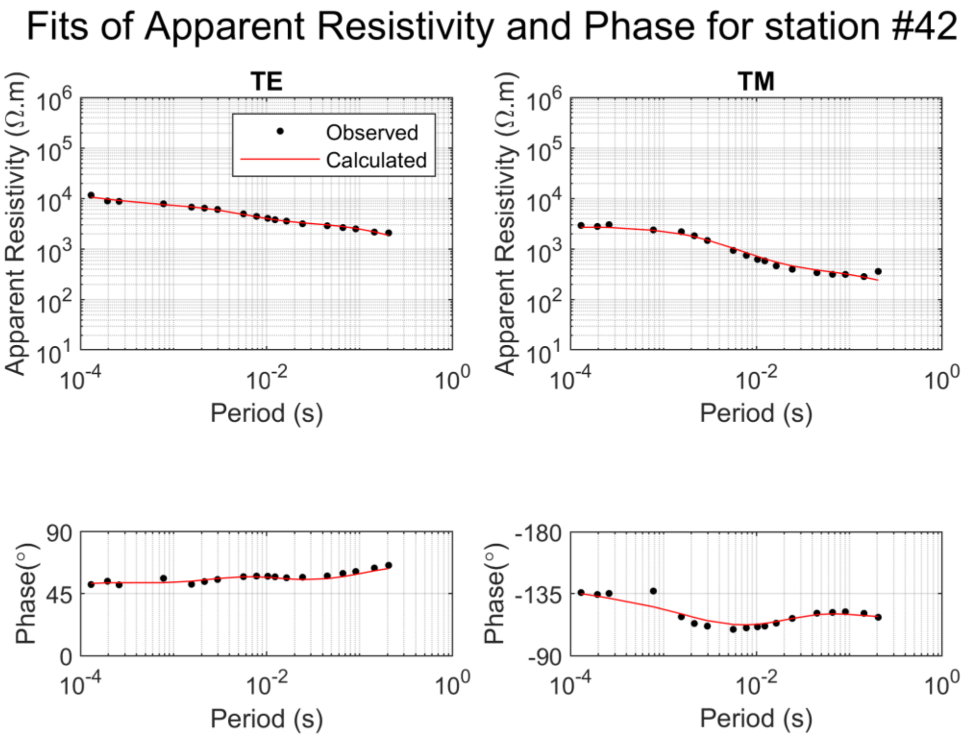
Fits of Apparent Resistivity and Phase for station #42
TE
TM
Observed
Calculated
Apparent Resistivity (Ω.m)
Phase(°)
Period (s)

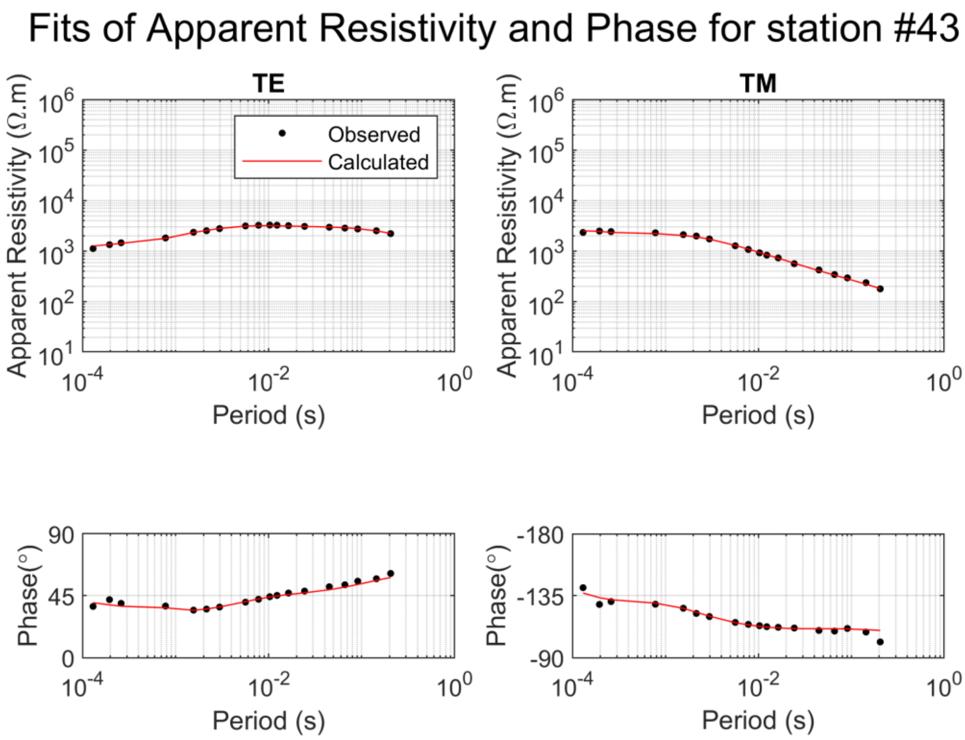
Fits of Apparent Resistivity and Phase for station #43
TE
TM
Observed
Calculated
Apparent Resistivity (Ω.m)
Phase(°)
Period (s)

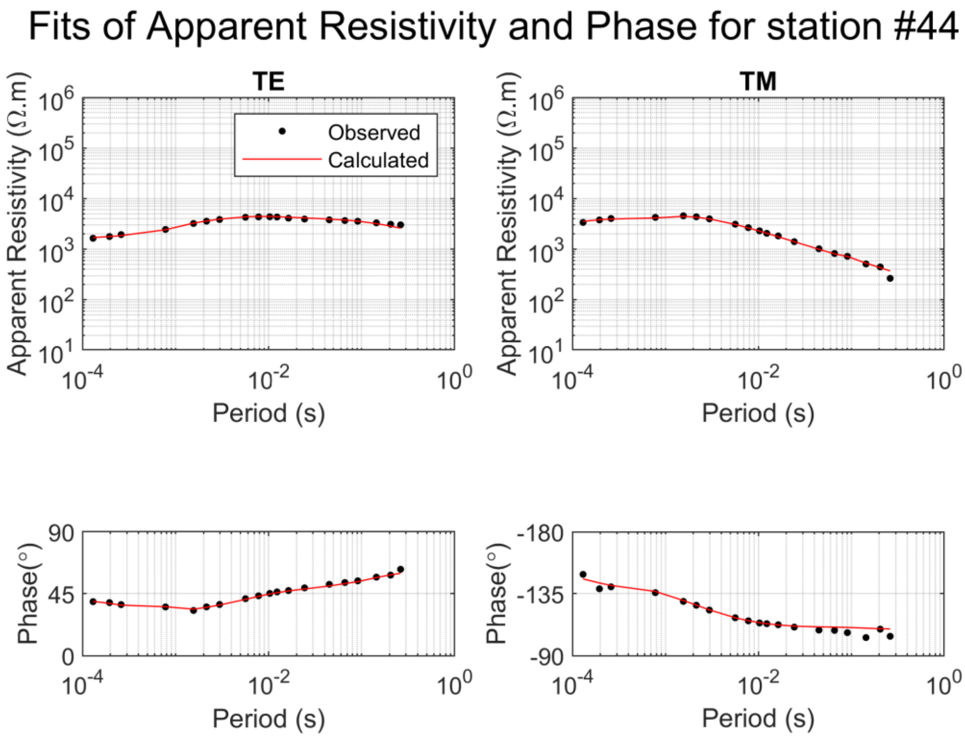
Fits of Apparent Resistivity and Phase for station #44
TE
TM
Observed
Calculated
Apparent Resistivity (Ω.m)
Phase(°)
Period (s)

Fits of Apparent Resistivity and Phase for station #45

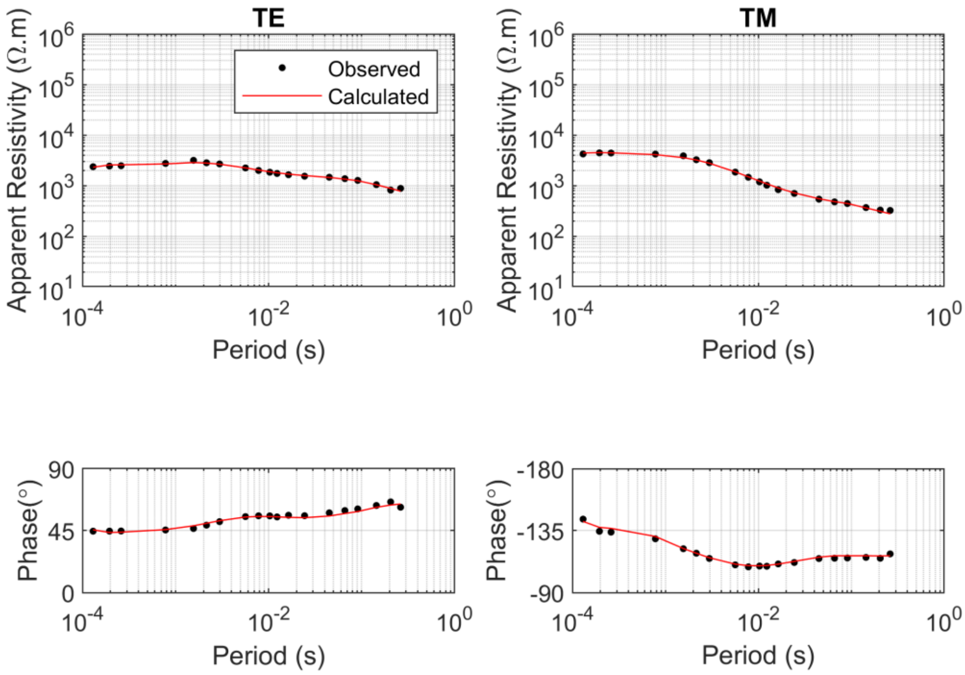

Fits of Apparent Resistivity and Phase for station #46

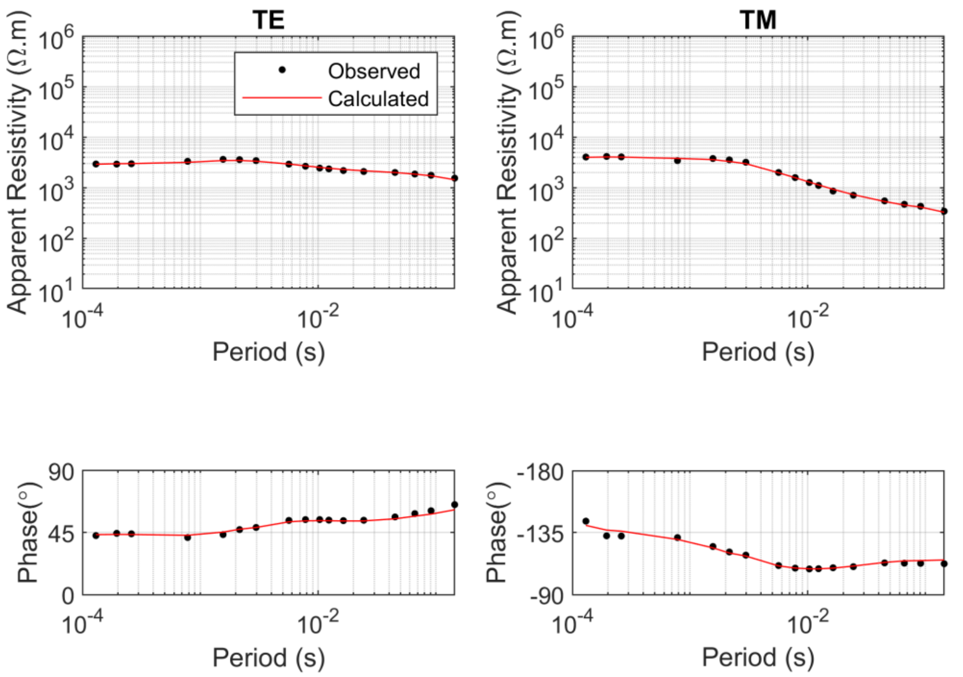

Fits of Apparent Resistivity and Phase for station #47

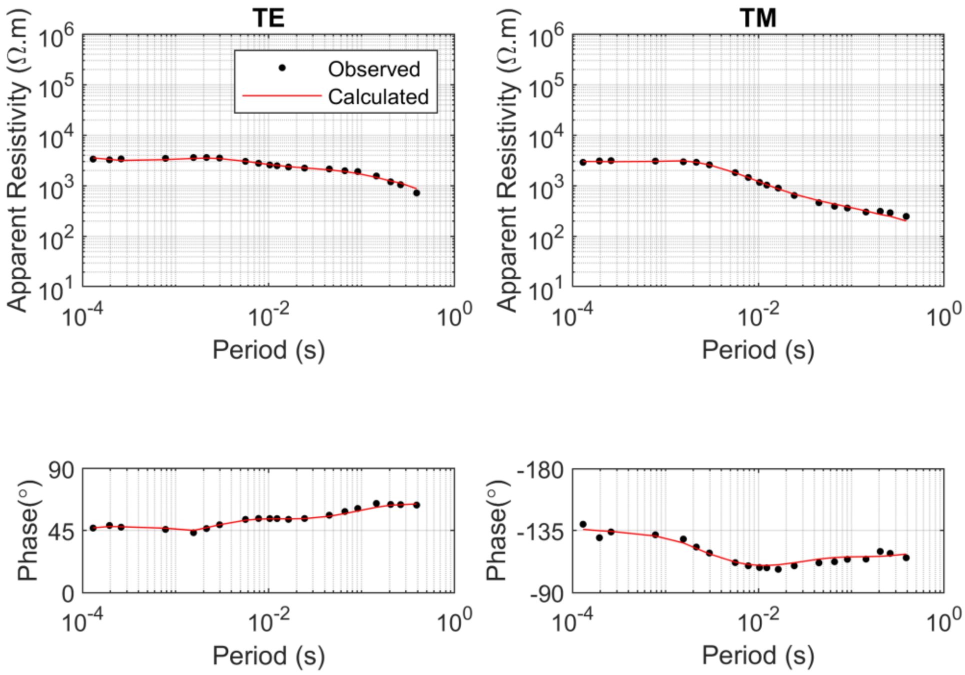

Fits of Apparent Resistivity and Phase for station #48

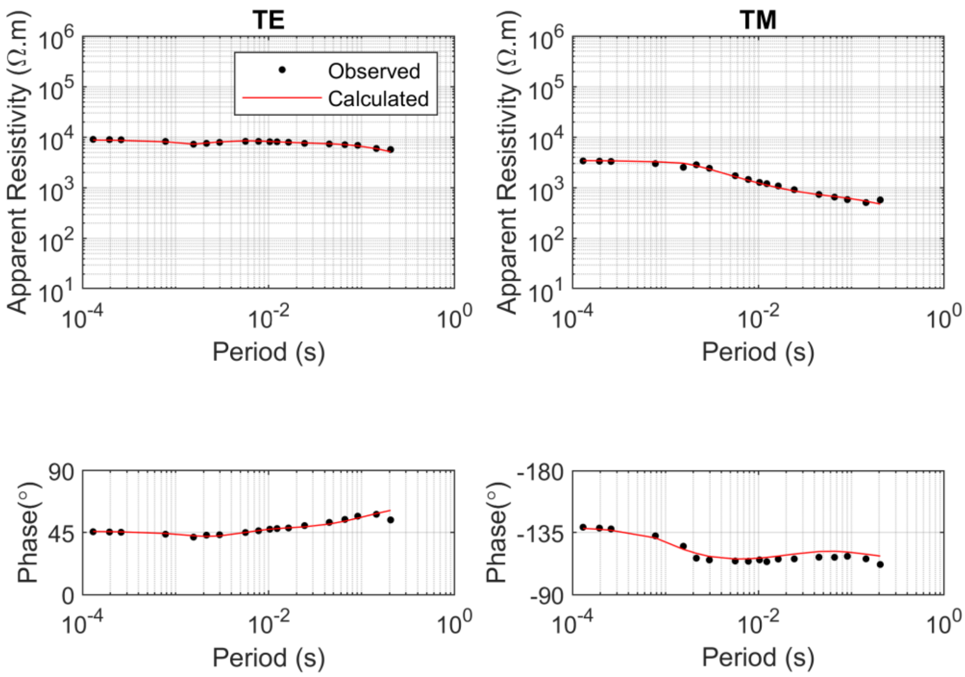

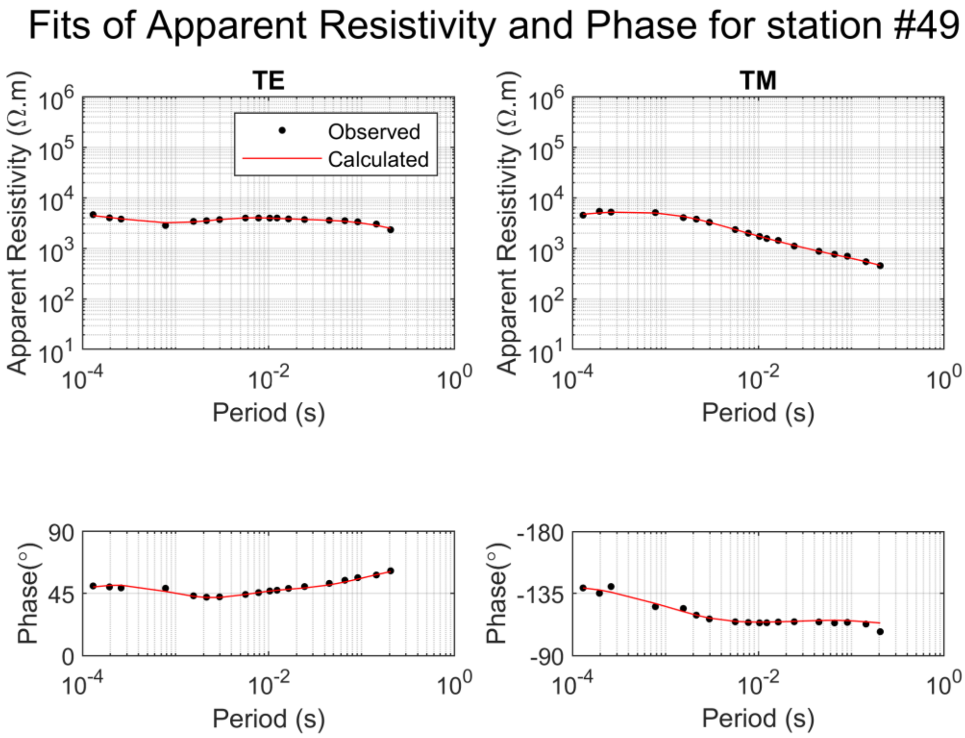
Fits of Apparent Resistivity and Phase for station #49
TE
TM
Observed
Calculated
Apparent Resistivity (Ω.m)
Phase(°)
Period (s)

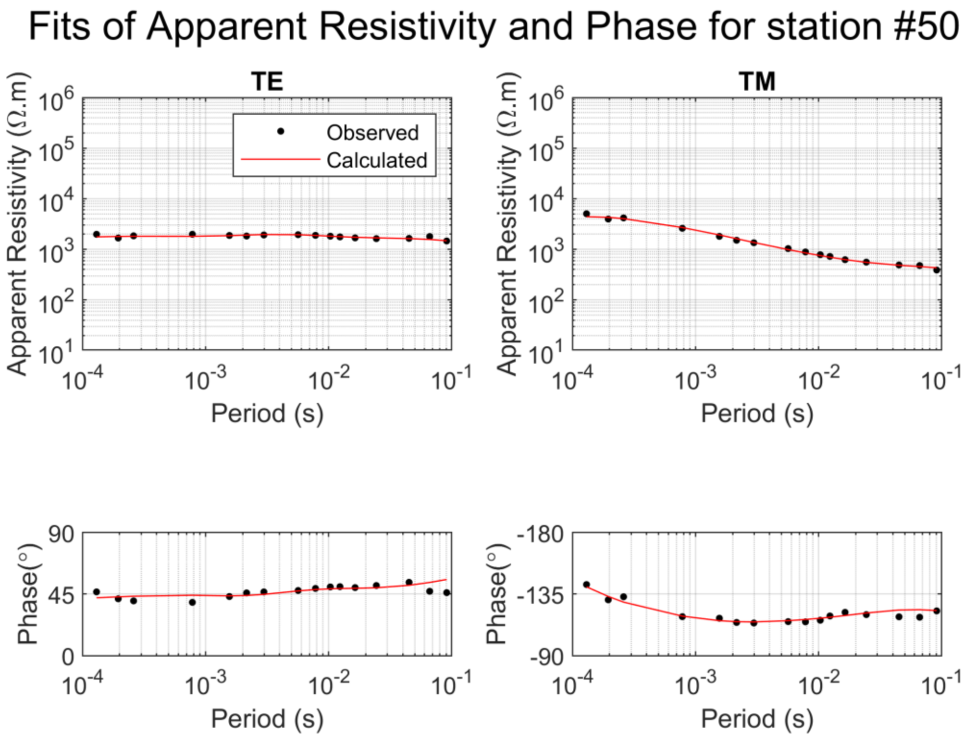
Fits of Apparent Resistivity and Phase for station #50
TE
TM
Observed
Calculated
Apparent Resistivity (Ω.m)
Phase(°)
Period (s)

Fits of Apparent Resistivity and Phase for station #51

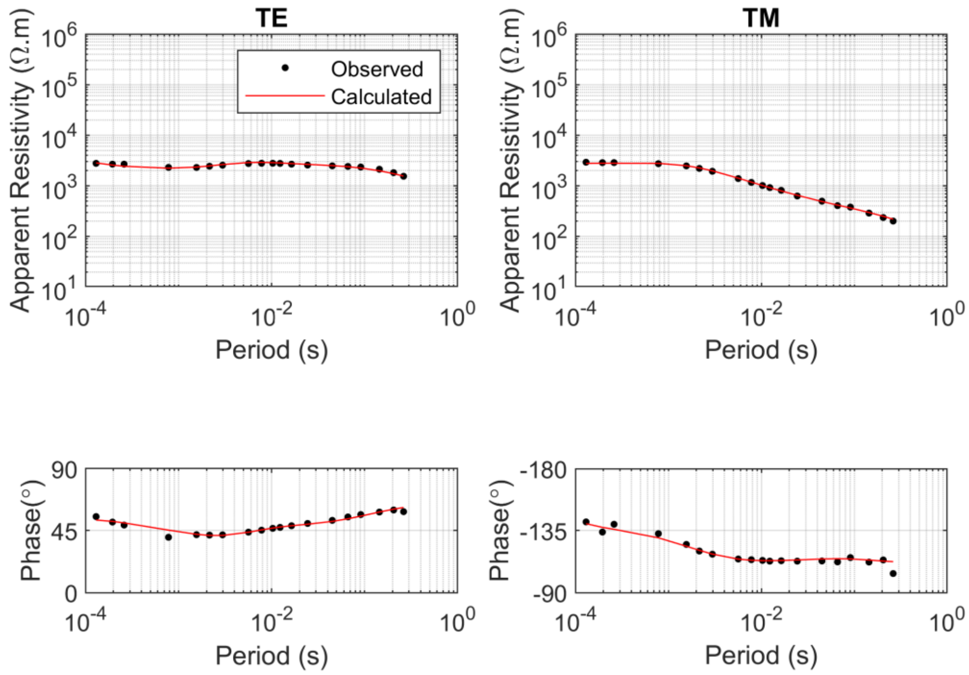

Fits of Apparent Resistivity and Phase for station #52

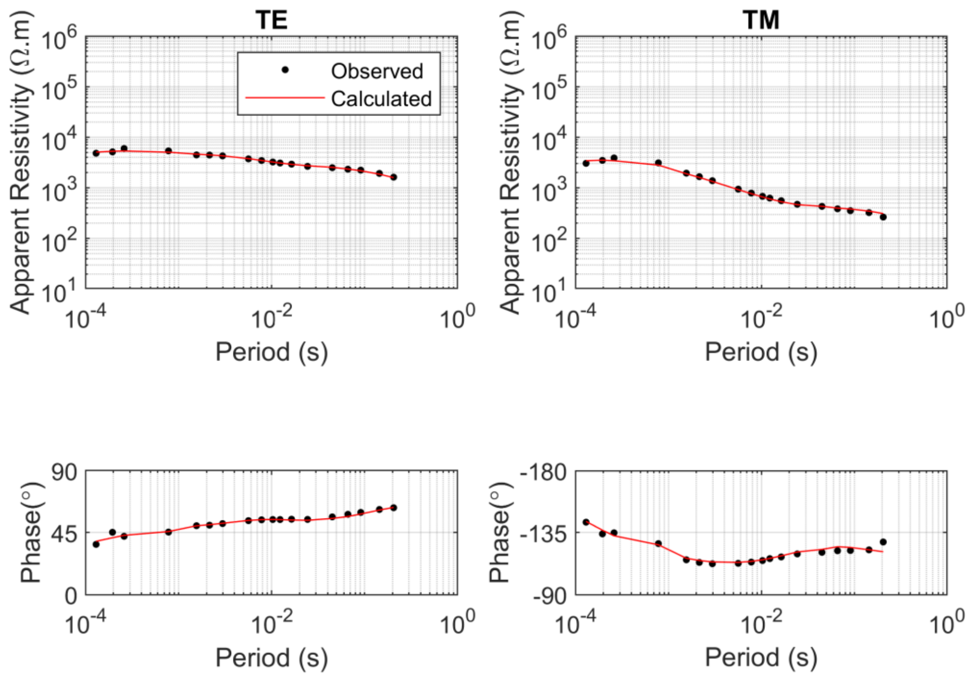

Fits of Apparent Resistivity and Phase for station #53

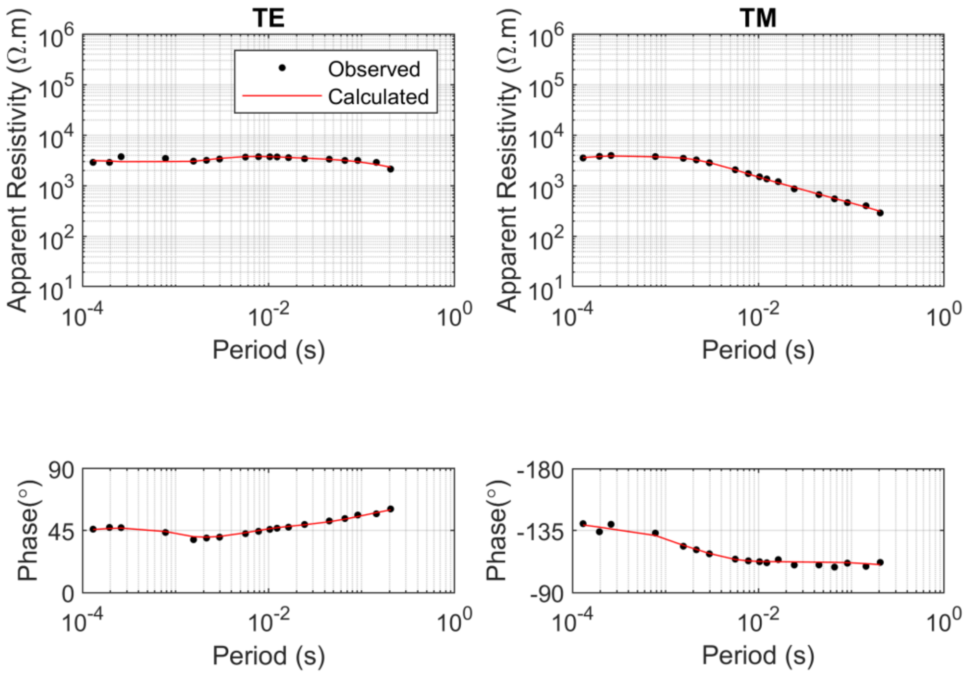

Fits of Apparent Resistivity and Phase for station #54

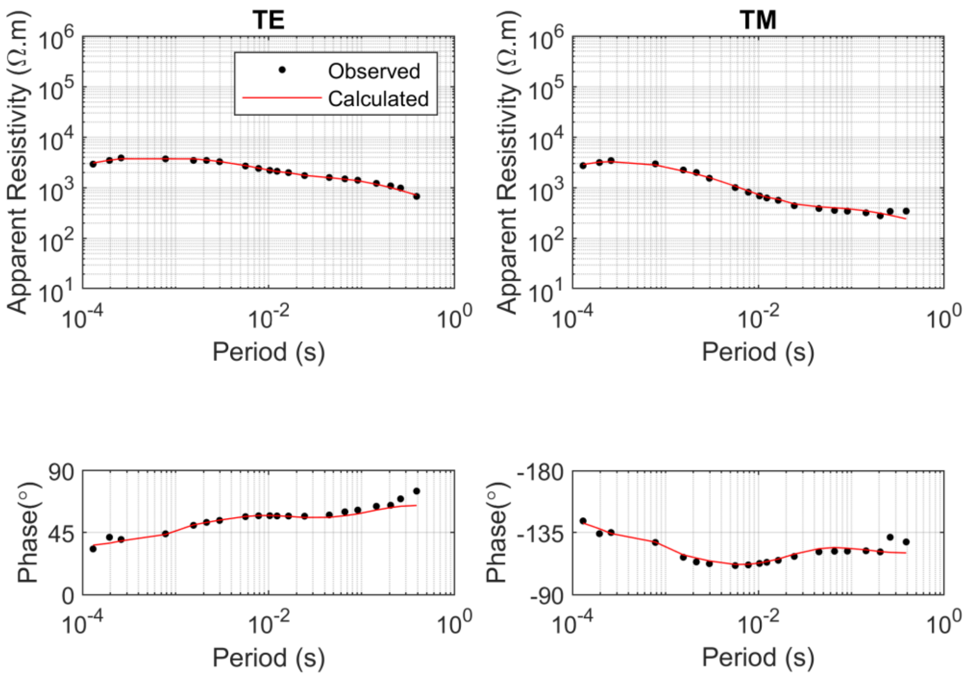

Fits of Apparent Resistivity and Phase for station #55

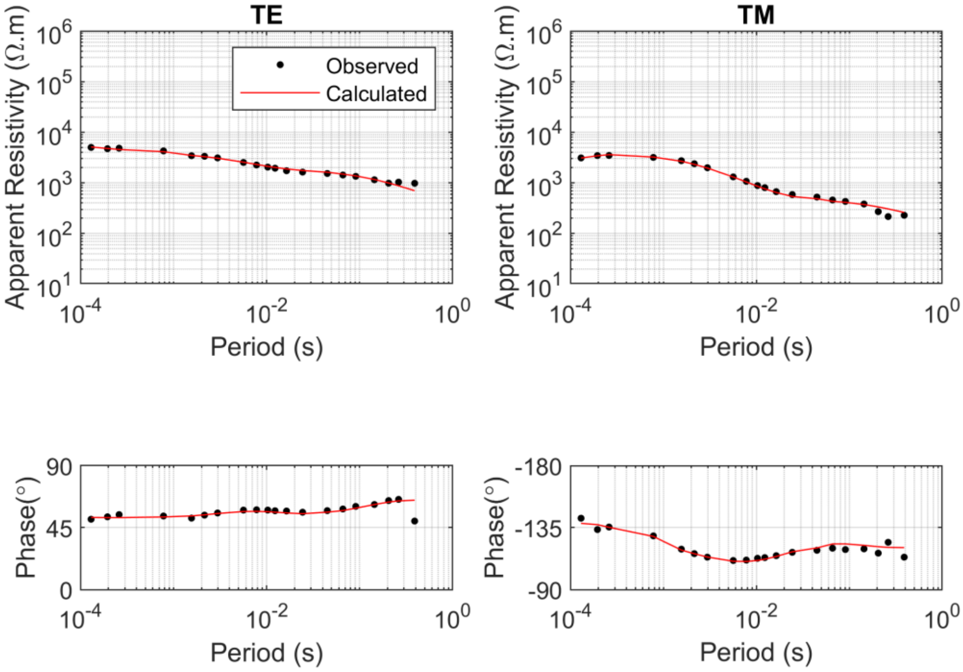

Fits of Apparent Resistivity and Phase for station #56

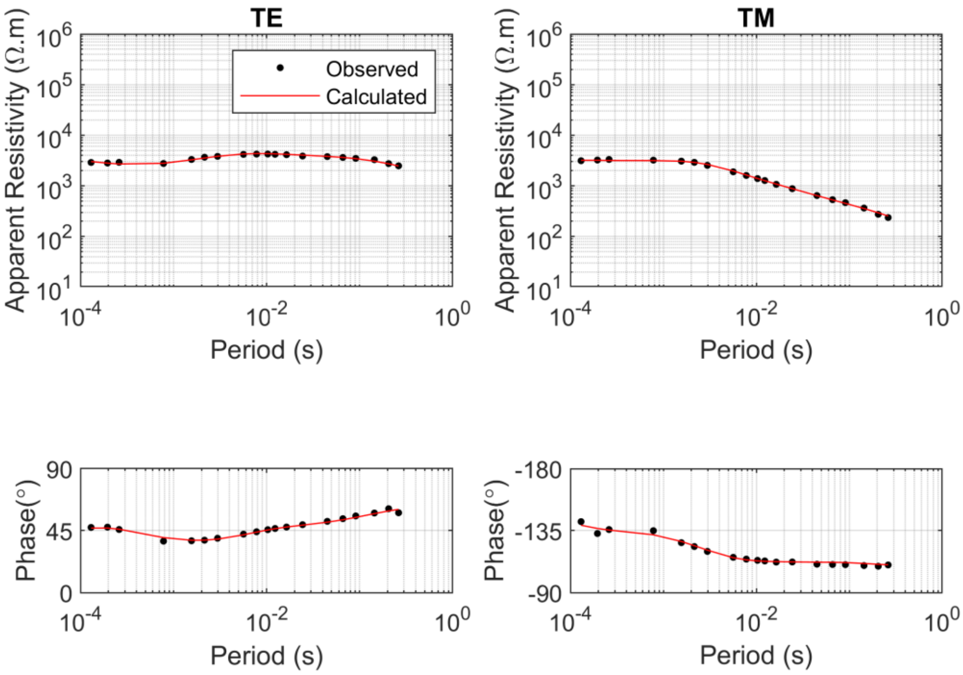

Fits of Apparent Resistivity and Phase for station #57

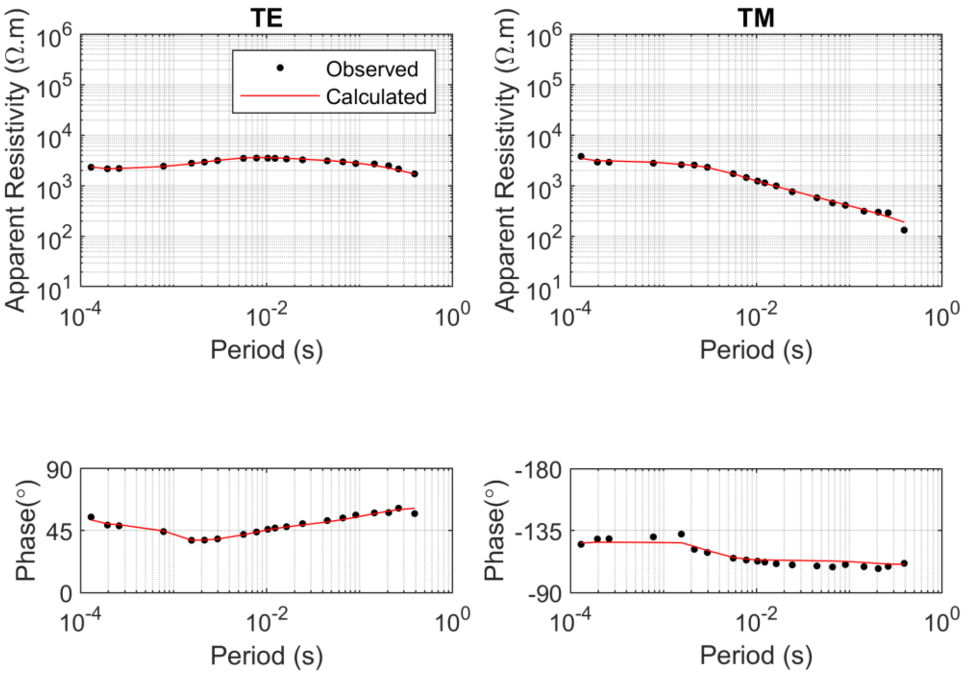

Fits of Apparent Resistivity and Phase for station #58

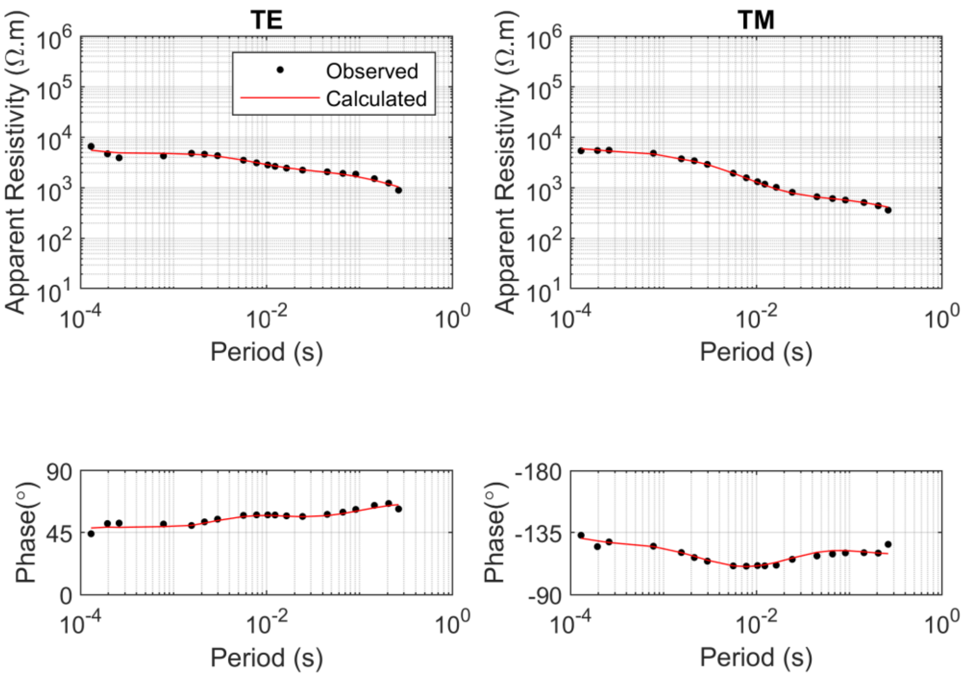

Fits of Apparent Resistivity and Phase for station #59

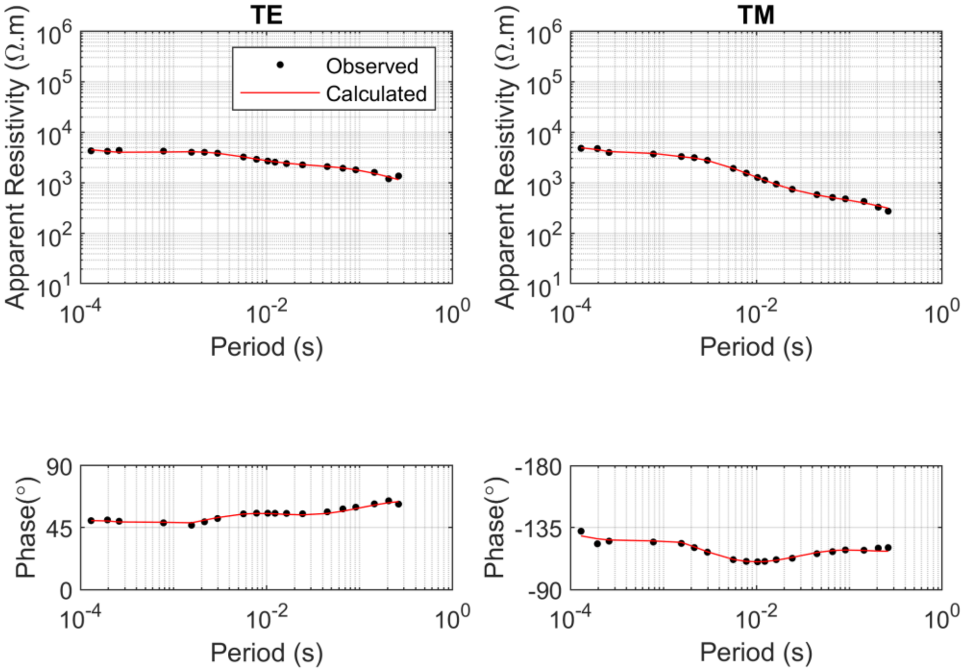

Fits of Apparent Resistivity and Phase for station #60

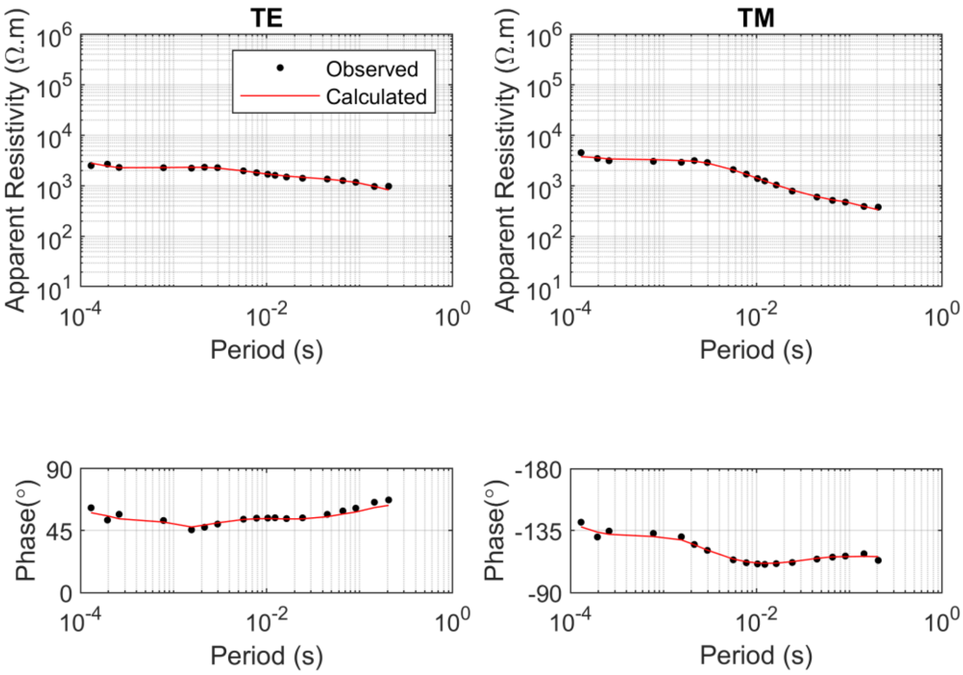

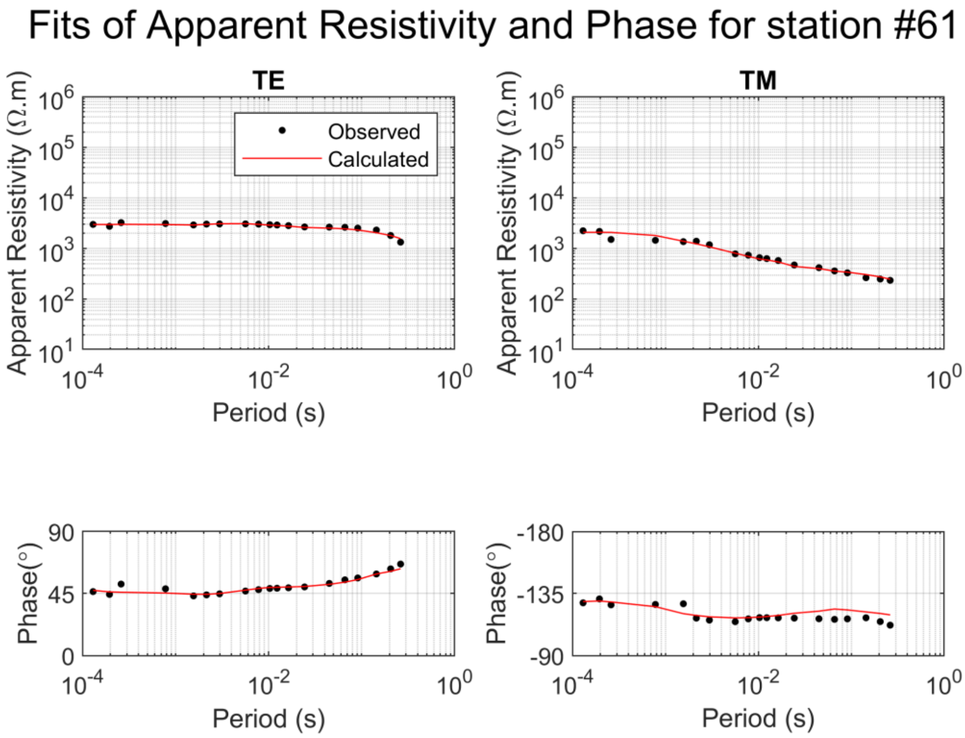
Fits of Apparent Resistivity and Phase for station #61
TE
TM
Observed
Calculated
Apparent Resistivity (Ω.m)
Period (s)
Phase(°)

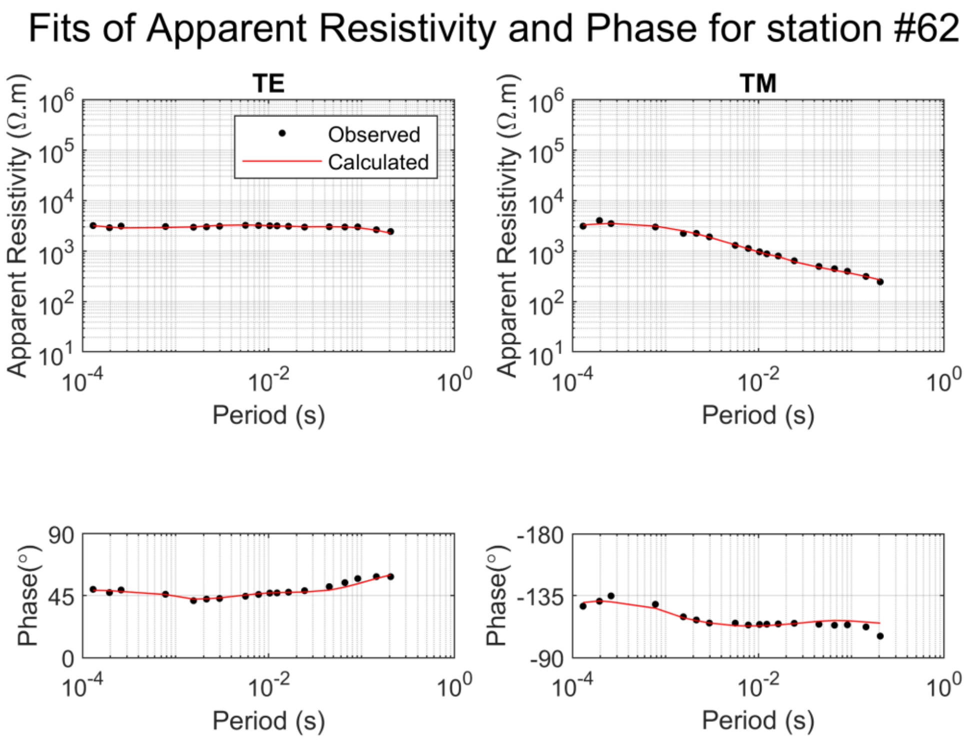
Fits of Apparent Resistivity and Phase for station #62
TE
TM
Observed
Calculated
Apparent Resistivity (Ω.m)
Period (s)
Phase(°)

Fits of Apparent Resistivity and Phase for station #63

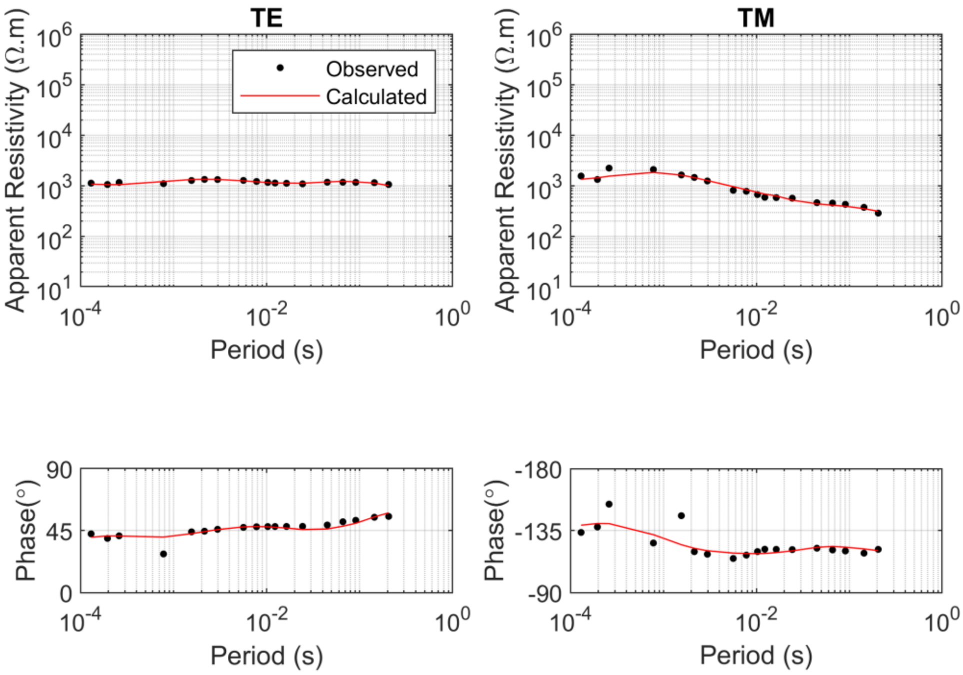

Fits of Apparent Resistivity and Phase for station #64

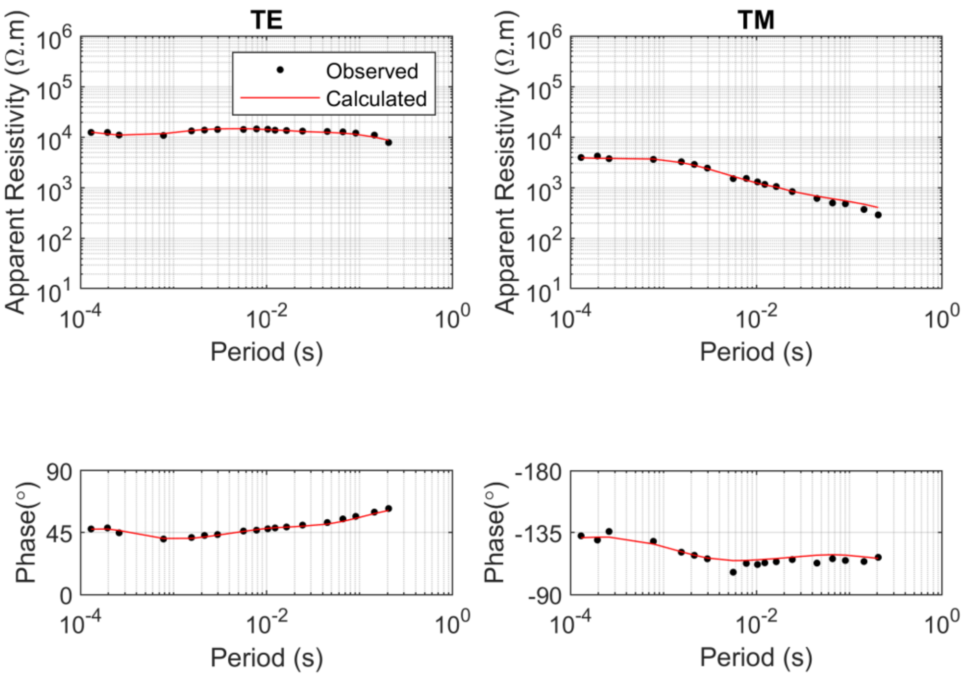

Fits of Apparent Resistivity and Phase for station #65

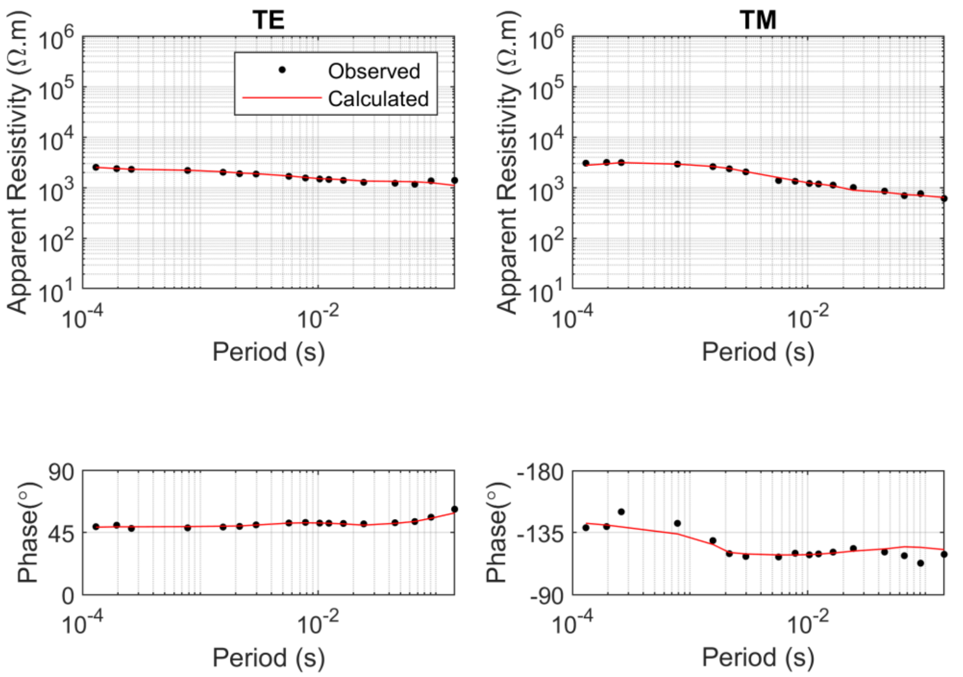

Fits of Apparent Resistivity and Phase for station #66

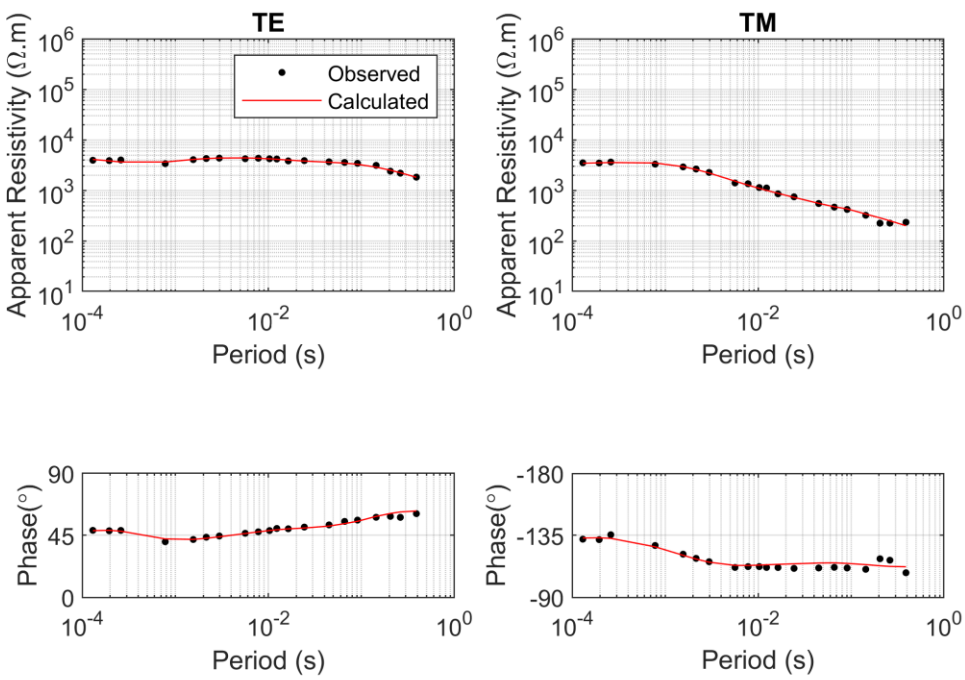

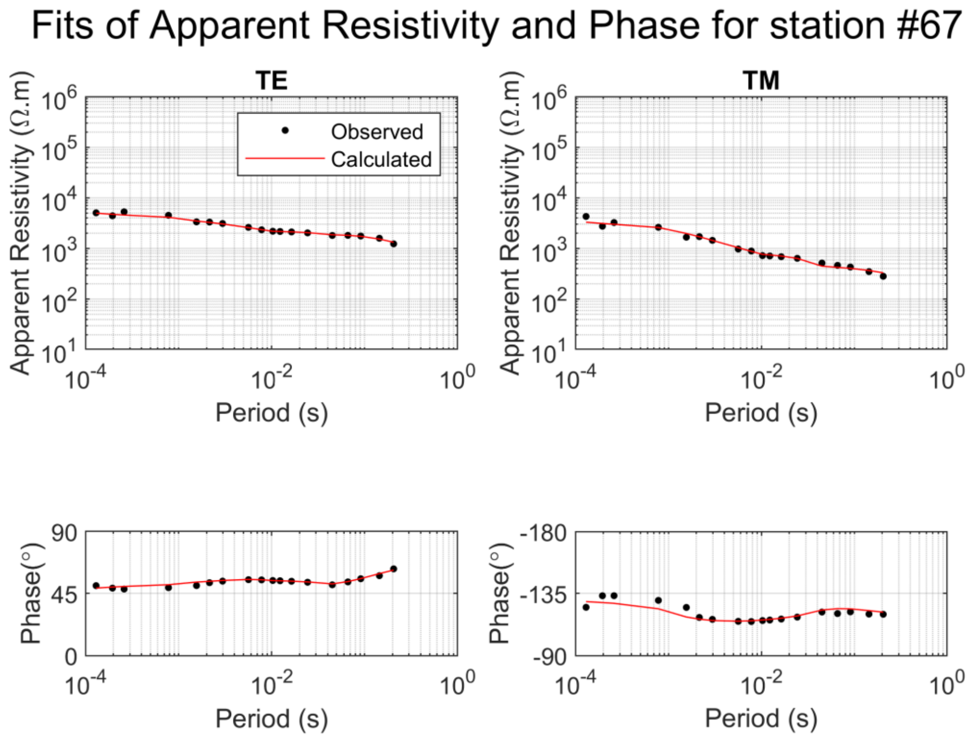
Fits of Apparent Resistivity and Phase for station #67
TE
TM
Observed
Calculated
Apparent Resistivity (Ω.m)
Phase(°)
Period (s)

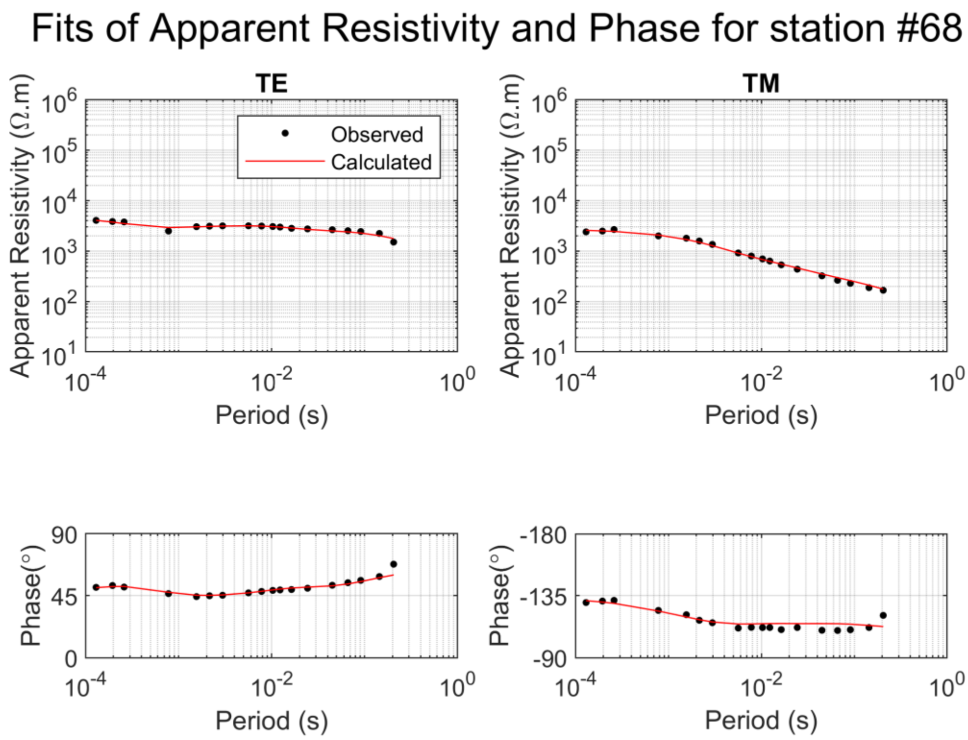
Fits of Apparent Resistivity and Phase for station #68
TE
TM
Observed
Calculated
Apparent Resistivity (Ω.m)
Phase(°)
Period (s)

Fits of Apparent Resistivity and Phase for station #69

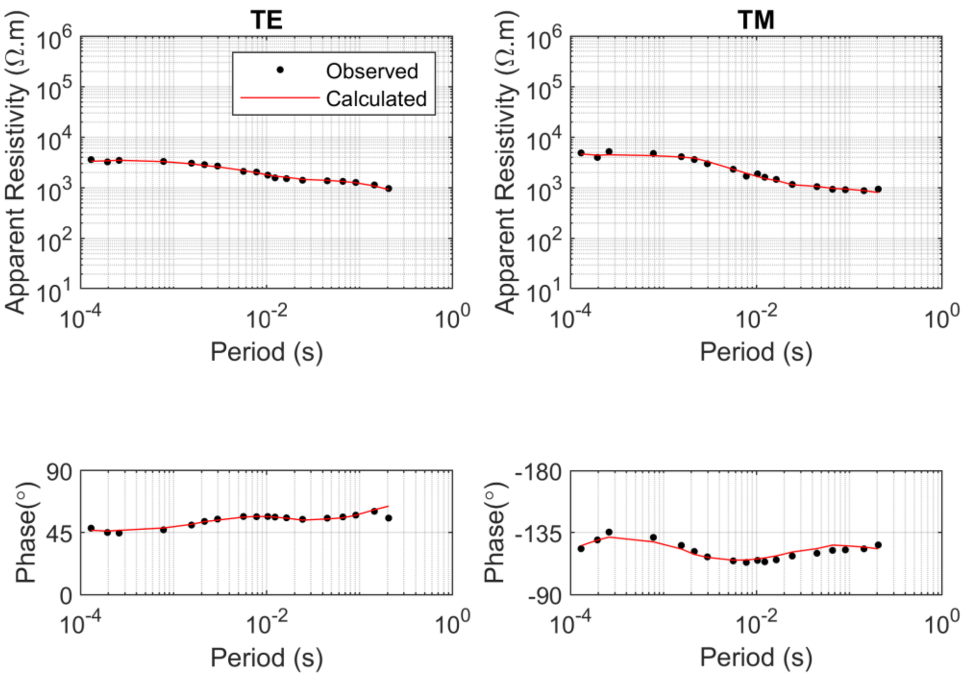

Fits of Apparent Resistivity and Phase for station #70

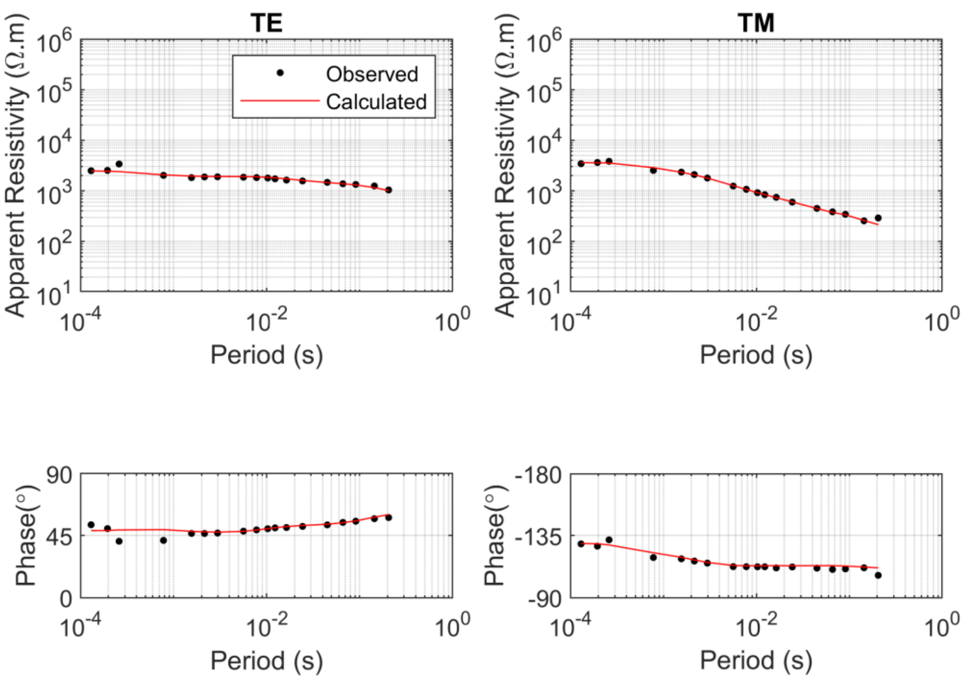

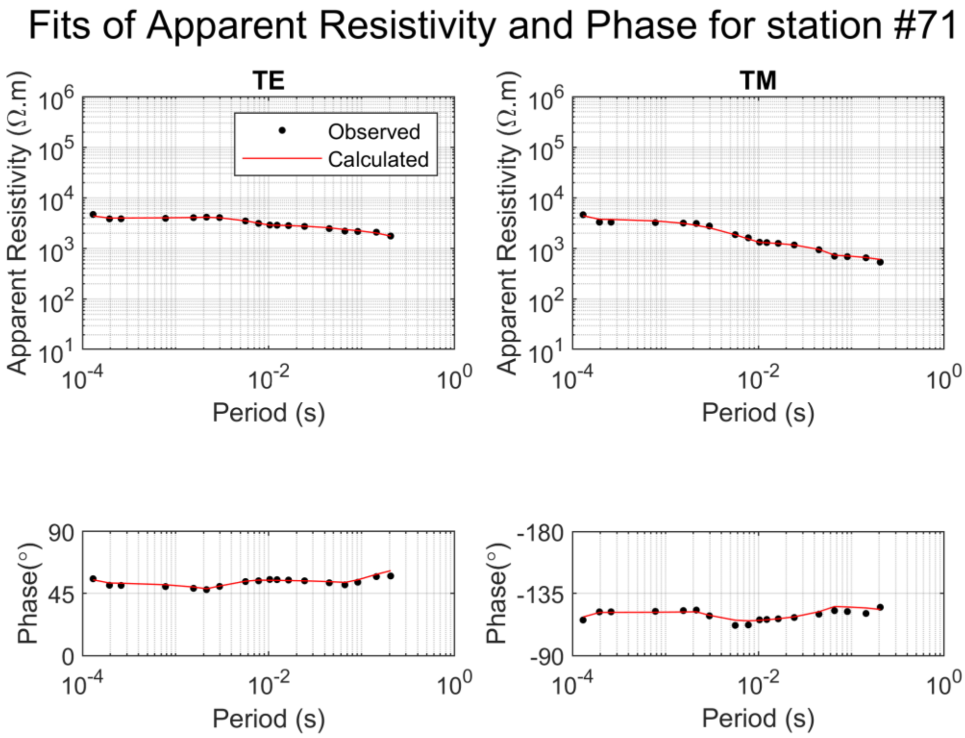
Fits of Apparent Resistivity and Phase for station #71
TE
TM
Observed
Calculated
Apparent Resistivity (Ω.m)
Period (s)
Phase(°)

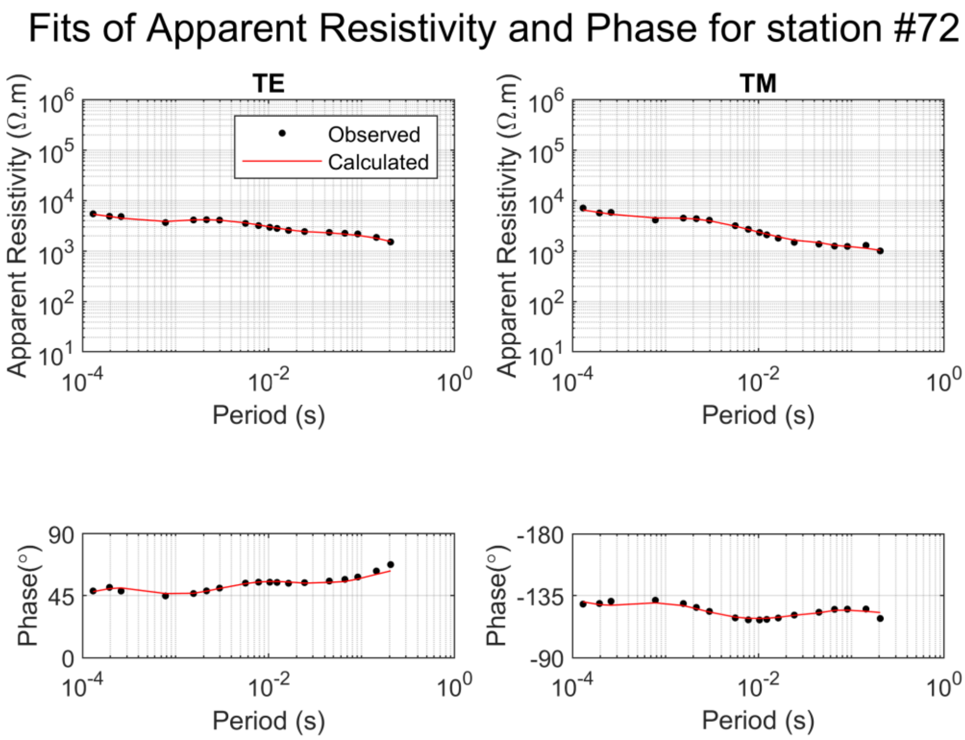
Fits of Apparent Resistivity and Phase for station #72
TE
TM
Observed
Calculated
Apparent Resistivity (Ω.m)
Period (s)
Phase(°)

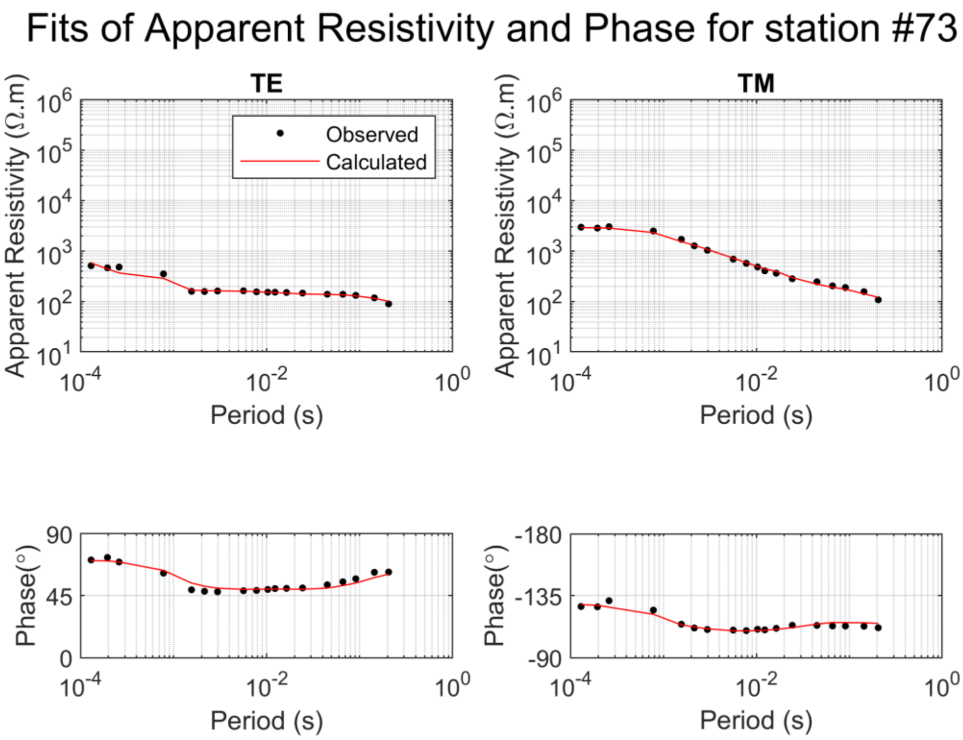
Fits of Apparent Resistivity and Phase for station #73
TE
TM
Observed
Calculated
Apparent Resistivity (Ω.m)
Phase(°)
Period (s)

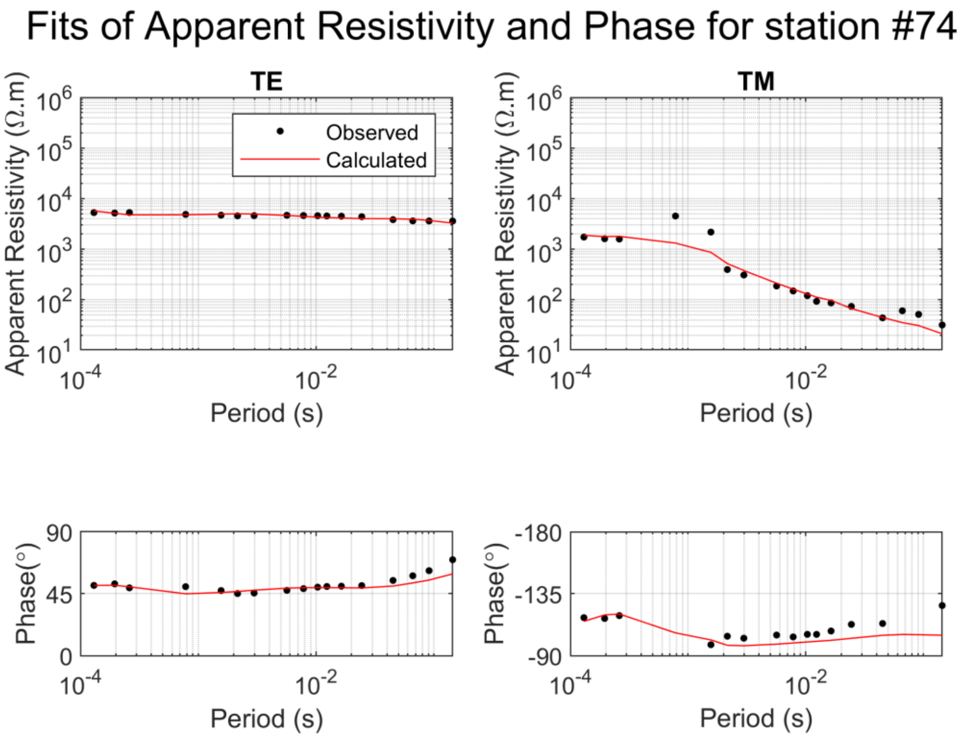
Fits of Apparent Resistivity and Phase for station #74
TE
TM
Observed
Calculated
Apparent Resistivity (Ω.m)
Phase(°)
Period (s)

Fits of Apparent Resistivity and Phase for station #75

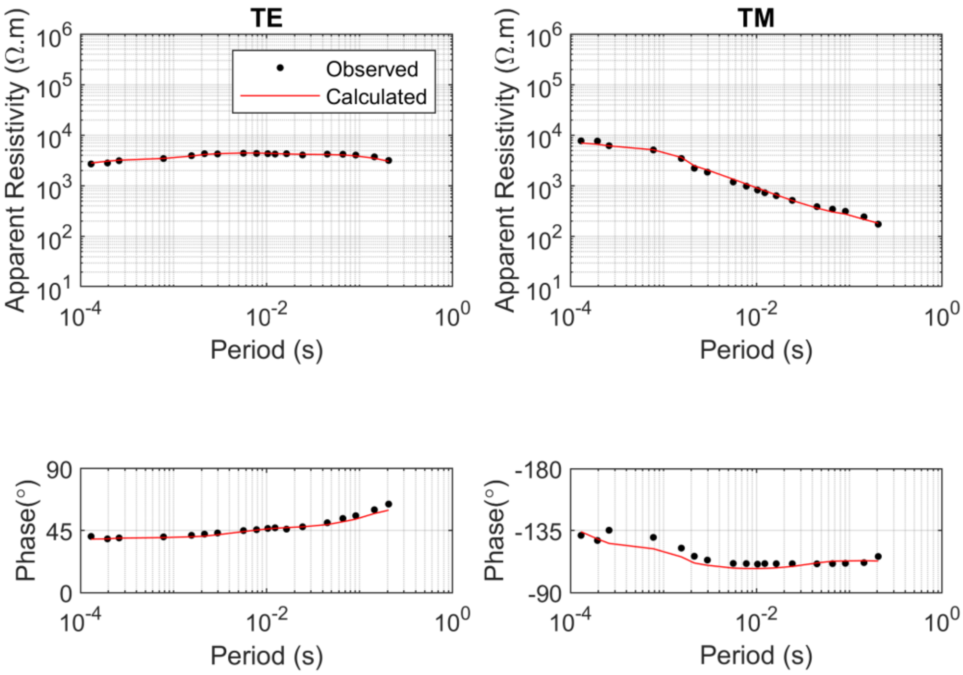

Fits of Apparent Resistivity and Phase for station #76

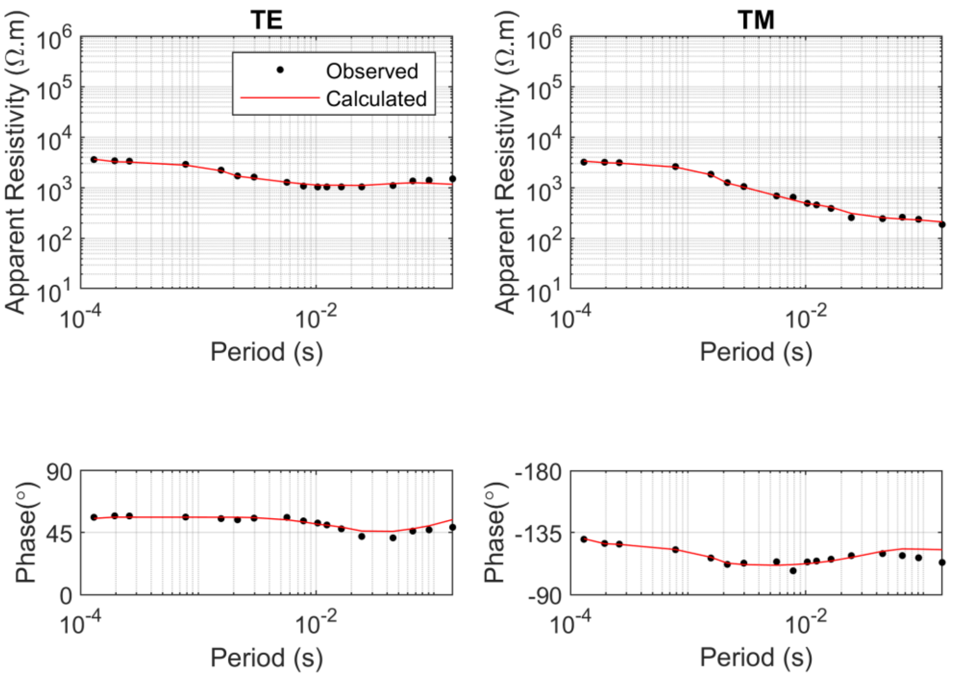

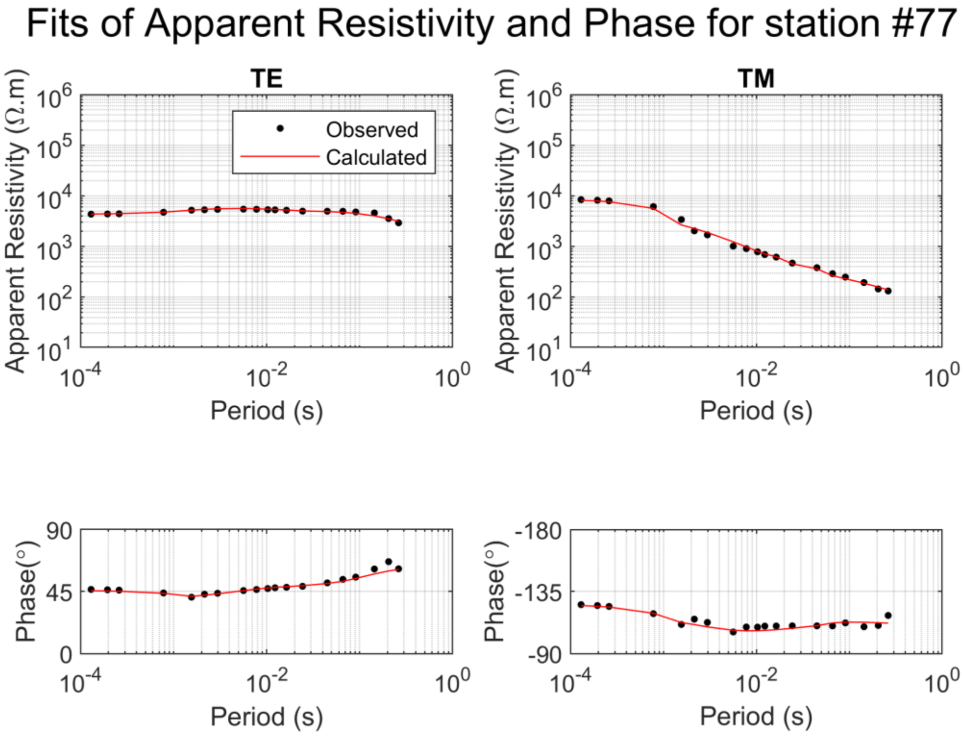
Fits of Apparent Resistivity and Phase for station #77
TE
TM
Observed
Calculated
Apparent Resistivity (Ω.m)
Phase(°)
Period (s)

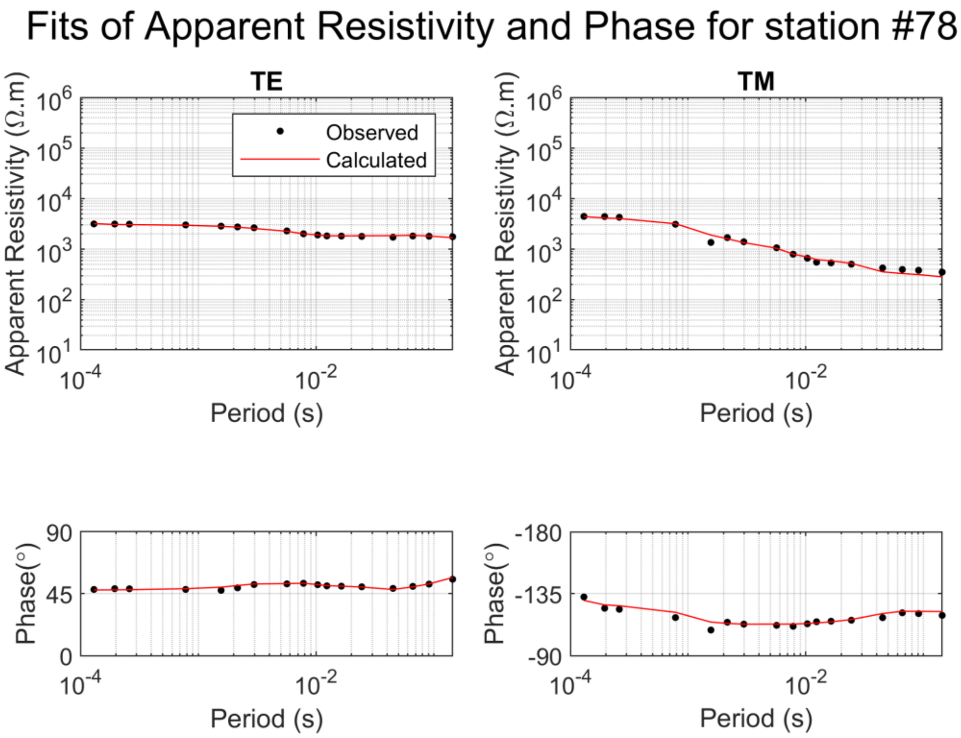
Fits of Apparent Resistivity and Phase for station #78
TE
TM
Observed
Calculated
Apparent Resistivity (Ω.m)
Phase(°)
Period (s)

Fits of Apparent Resistivity and Phase for station #79

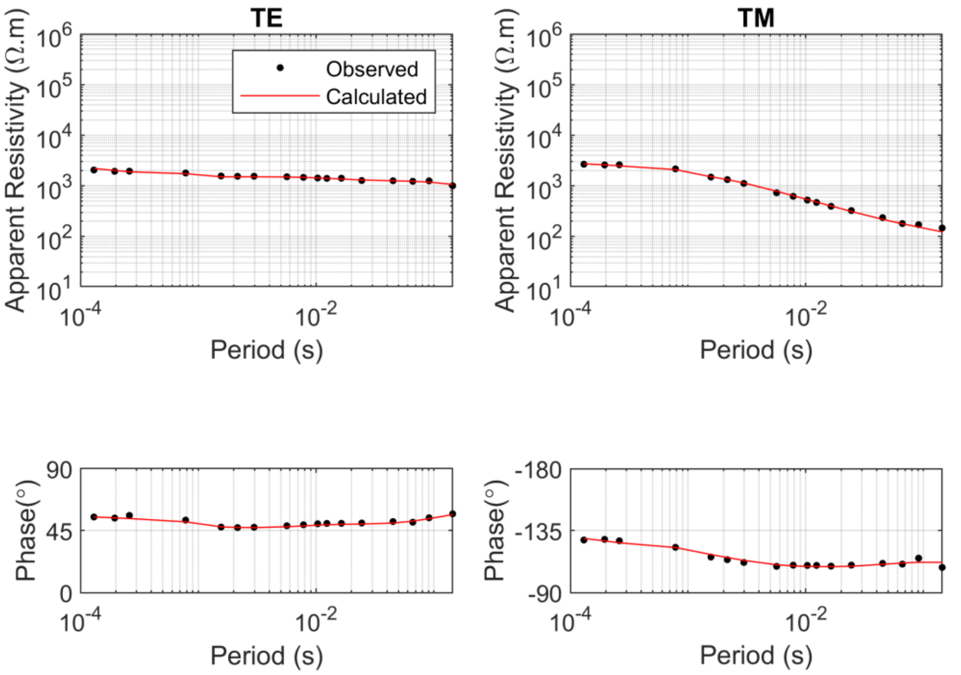

Fits of Apparent Resistivity and Phase for station #80

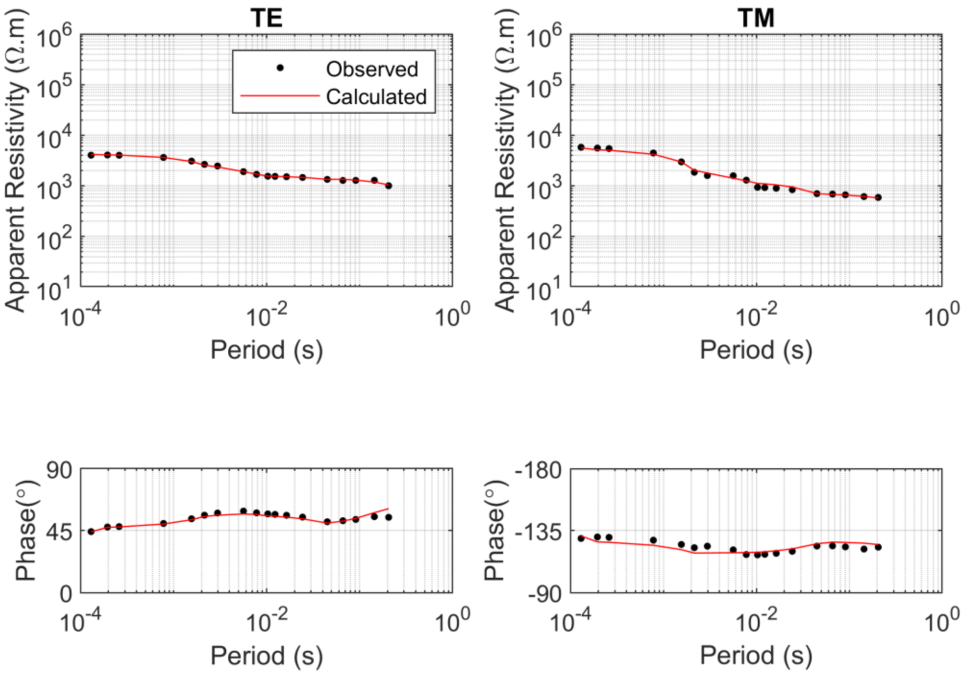

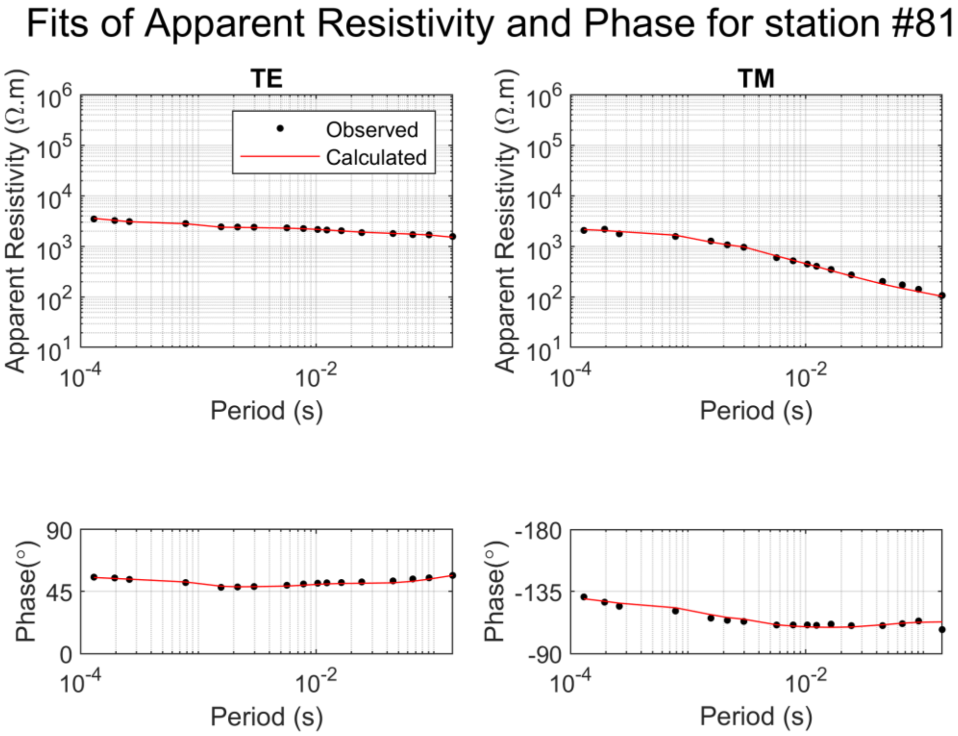
Fits of Apparent Resistivity and Phase for station #81
TE
TM
Observed
Calculated
Apparent Resistivity (Ω.m)
Phase(°)
Period (s)

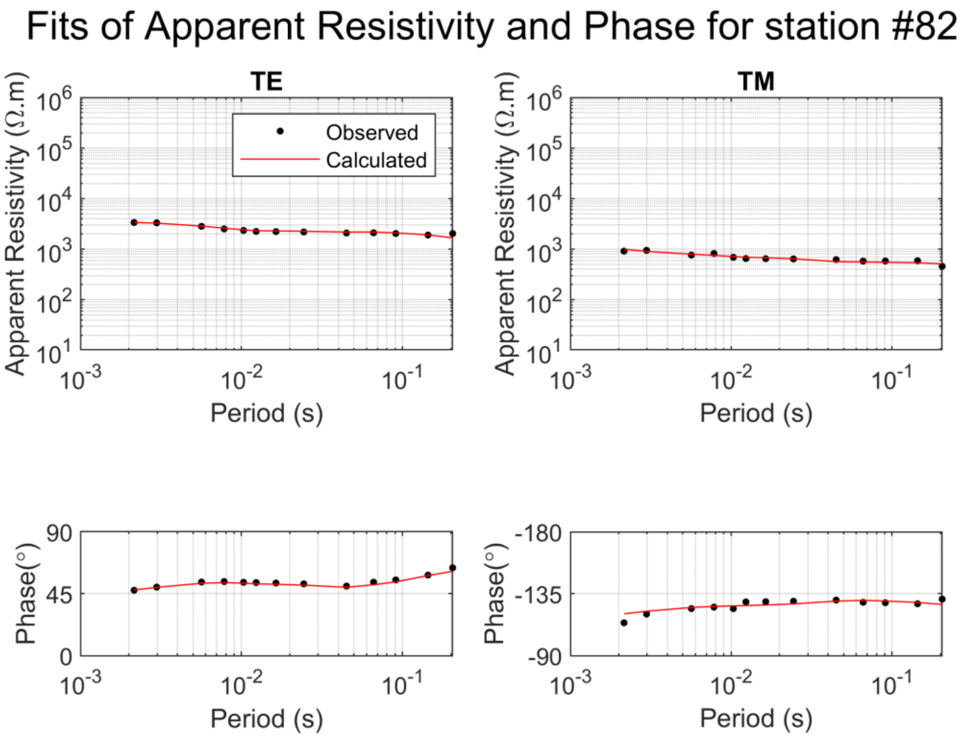
Fits of Apparent Resistivity and Phase for station #82
TE
TM
Observed
Calculated
Apparent Resistivity (Ω.m)
Phase(°)
Period (s)

Fits of Apparent Resistivity and Phase for station #83

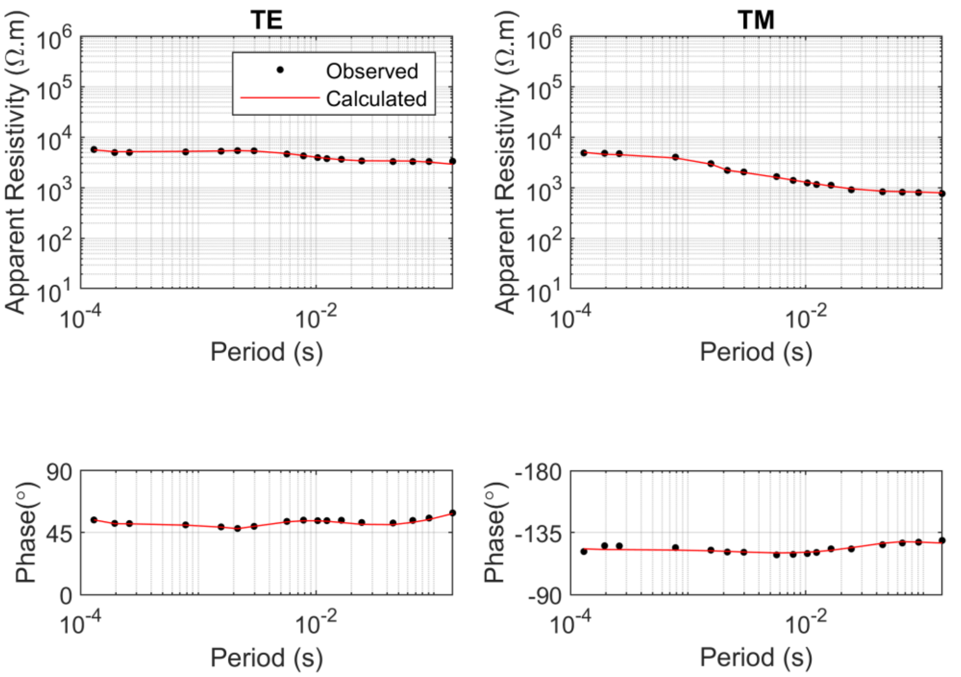

Fits of Apparent Resistivity and Phase for station #84

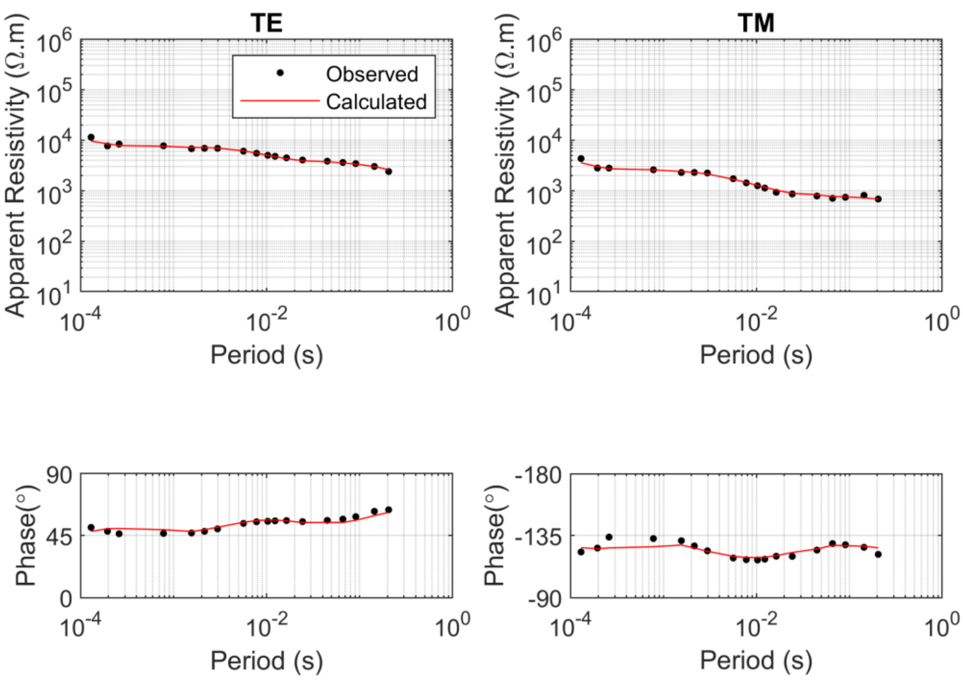

Fits of Apparent Resistivity and Phase for station #85

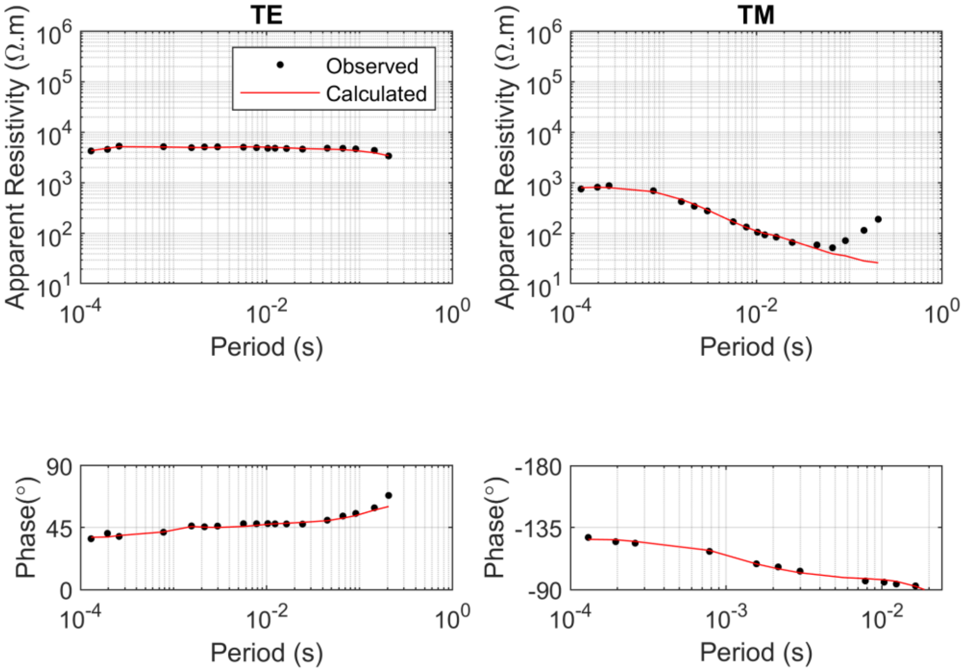

Fits of Apparent Resistivity and Phase for station #86

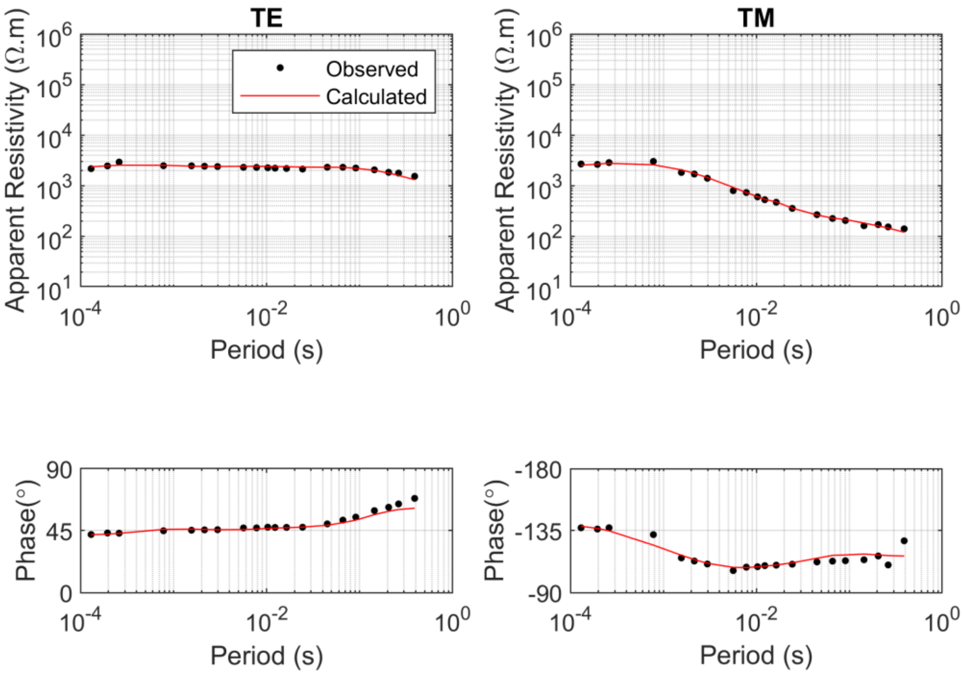

Fits of Apparent Resistivity and Phase for station #87

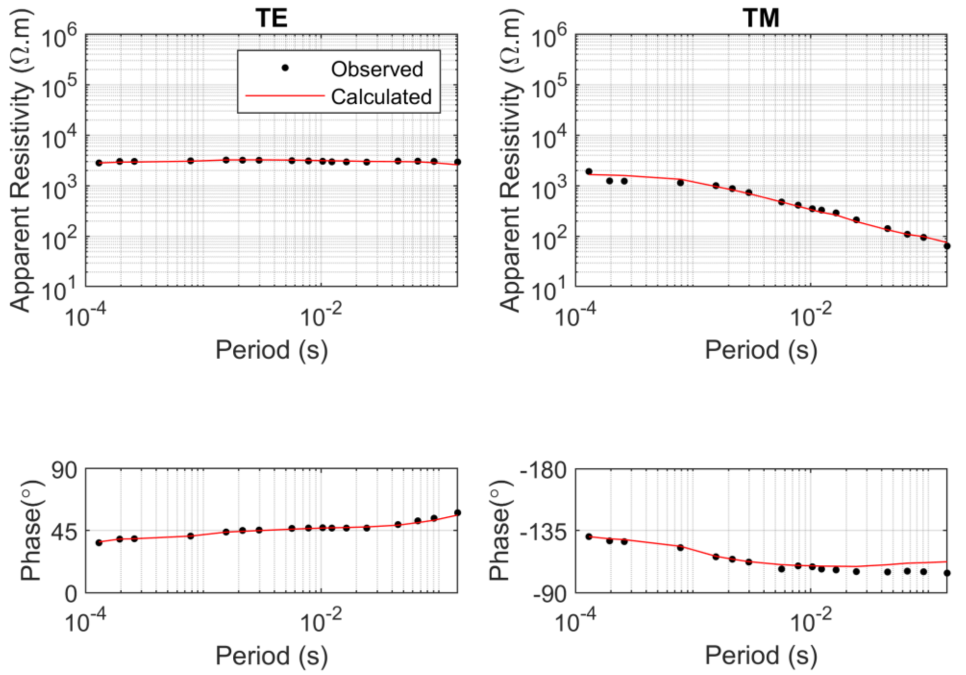

Fits of Apparent Resistivity and Phase for station #88

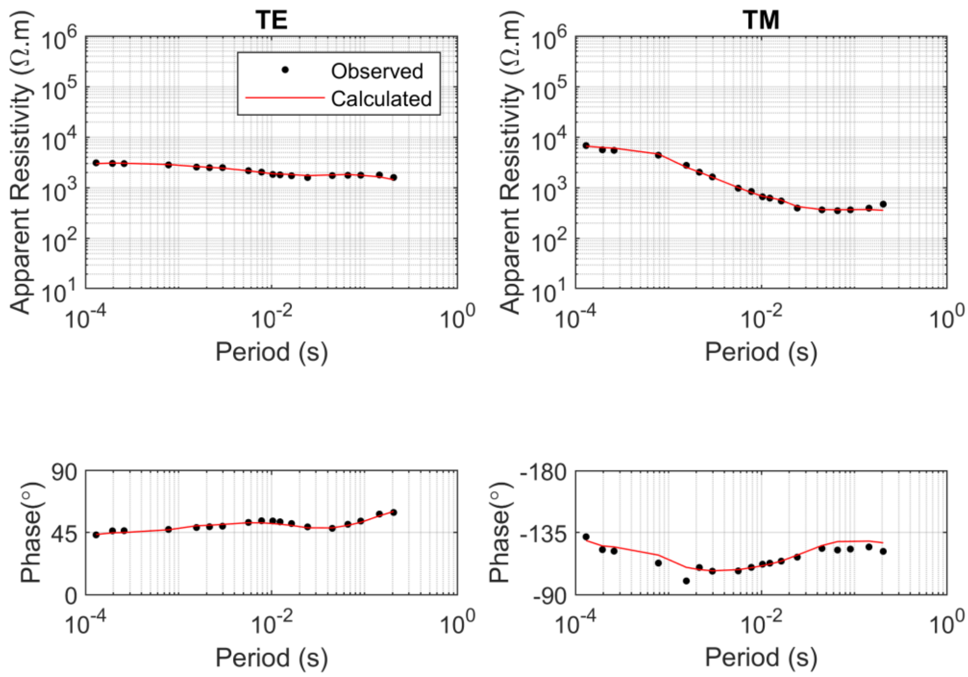

Fits of Apparent Resistivity and Phase for station #89

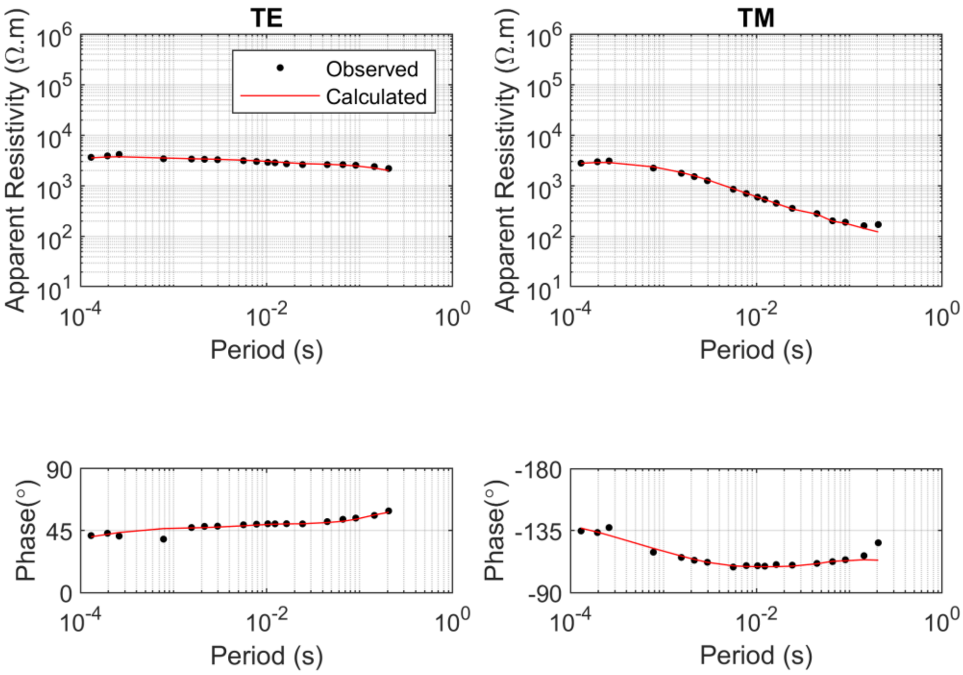

Fits of Apparent Resistivity and Phase for station #90

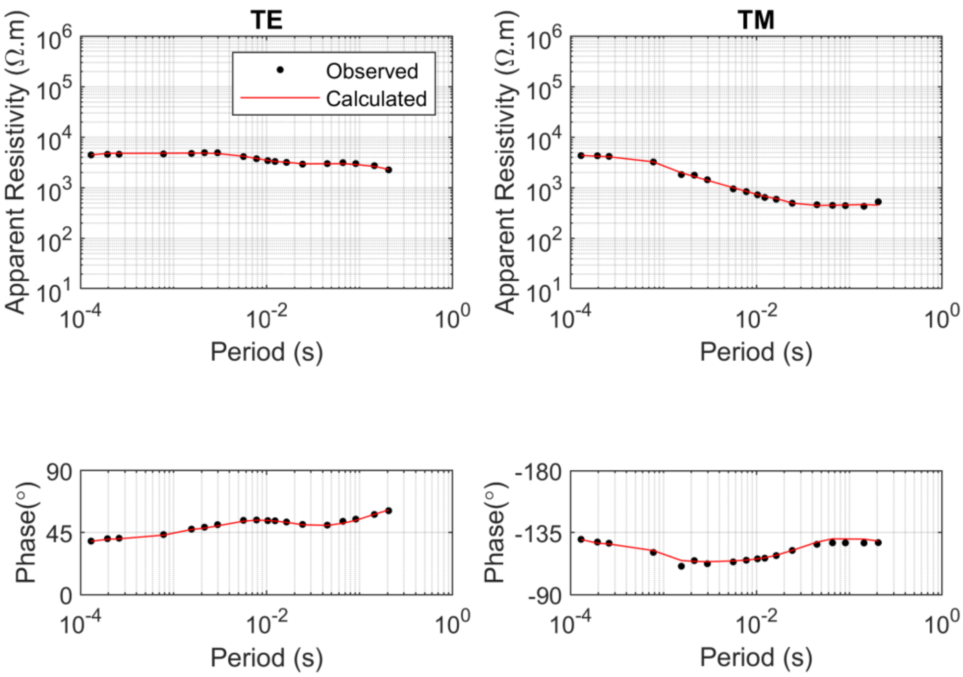

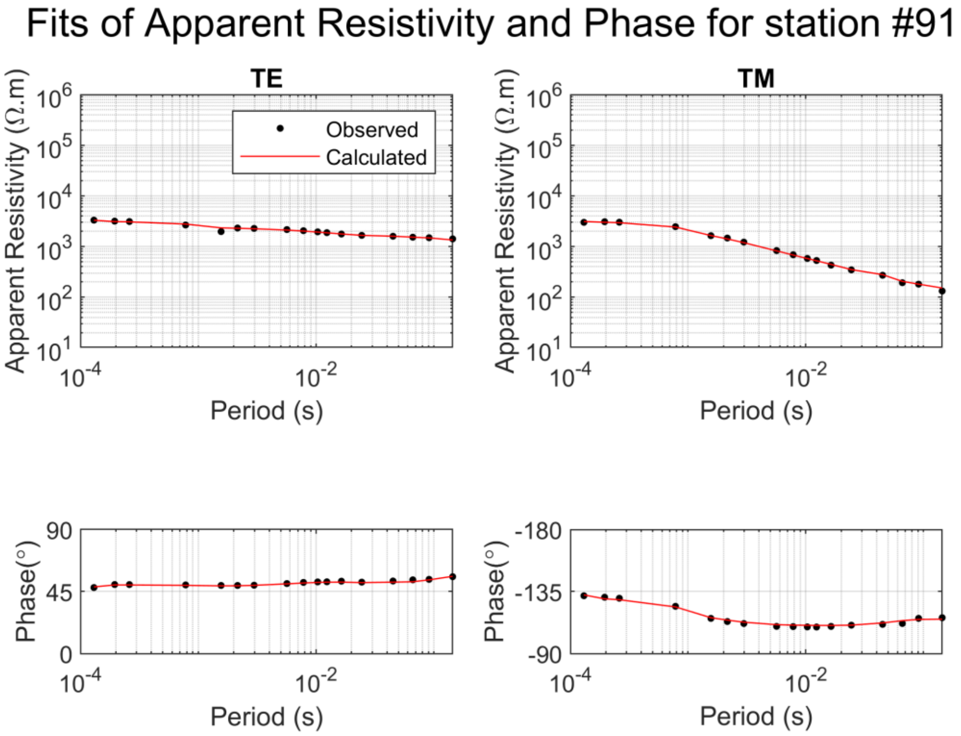
Fits of Apparent Resistivity and Phase for station #91
TE
TM
Observed
Calculated
Apparent Resistivity (Ω.m)
Phase(°)
Period (s)

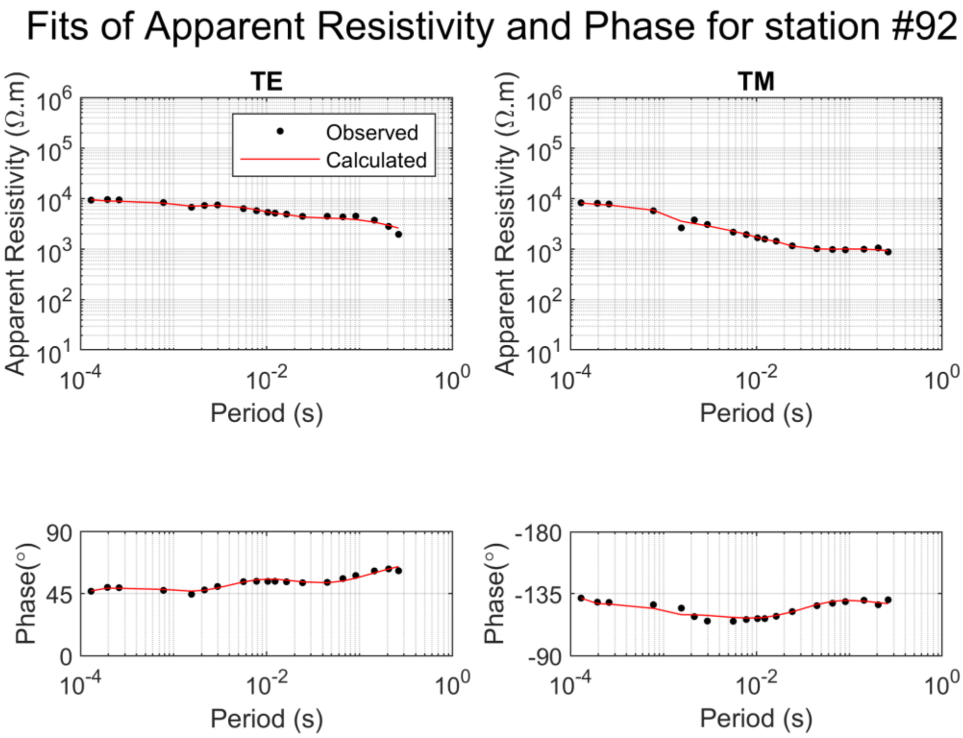
Fits of Apparent Resistivity and Phase for station #92
TE
TM
Observed
Calculated
Apparent Resistivity (Ω.m)
Phase(°)
Period (s)

Fits of Apparent Resistivity and Phase for station #93

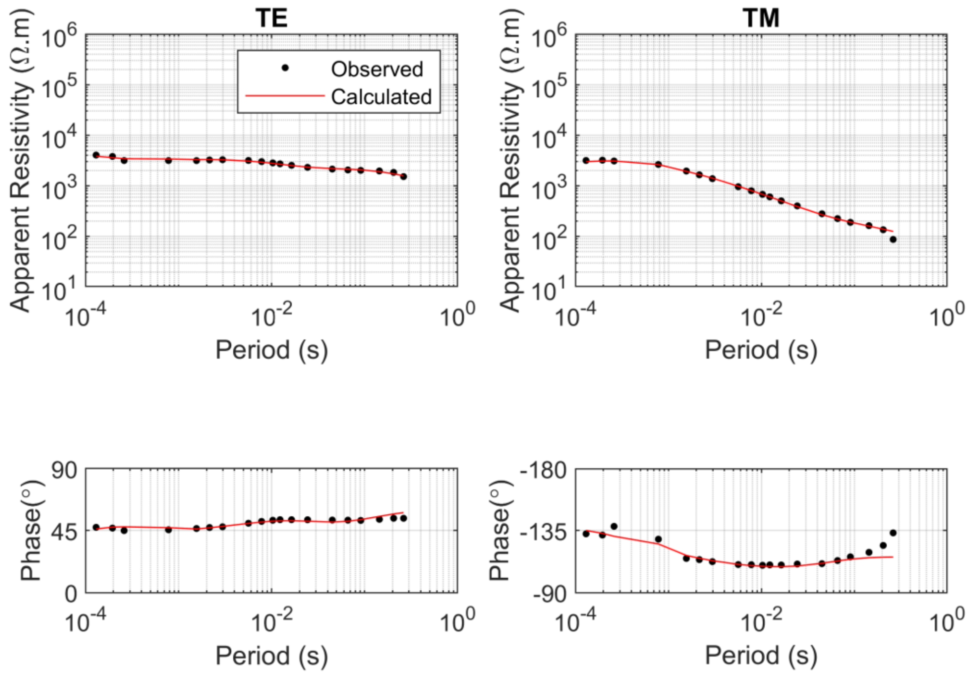

Fits of Apparent Resistivity and Phase for station #94

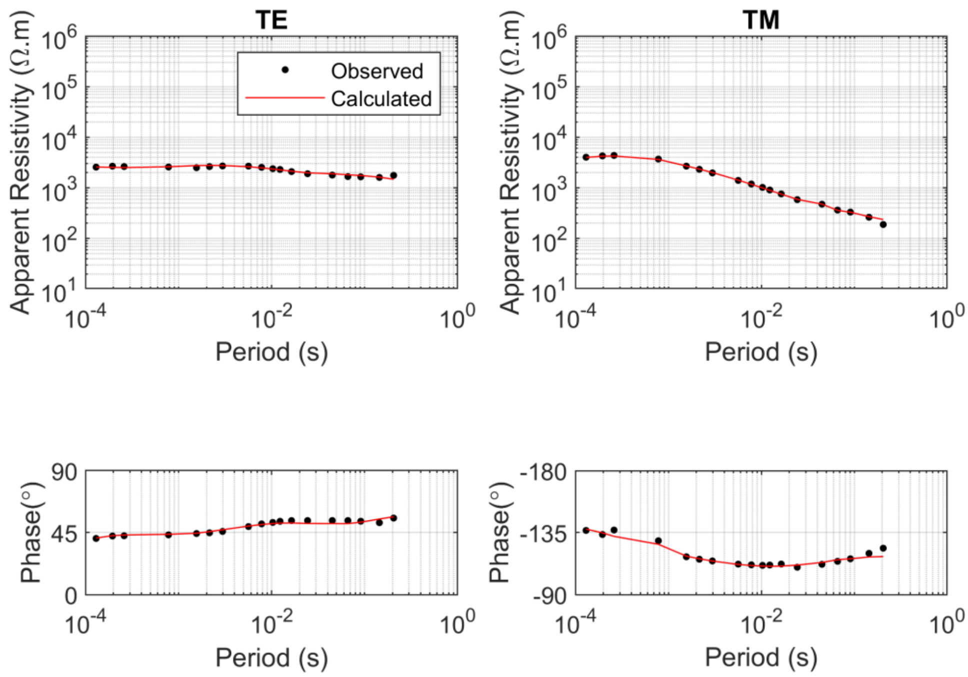

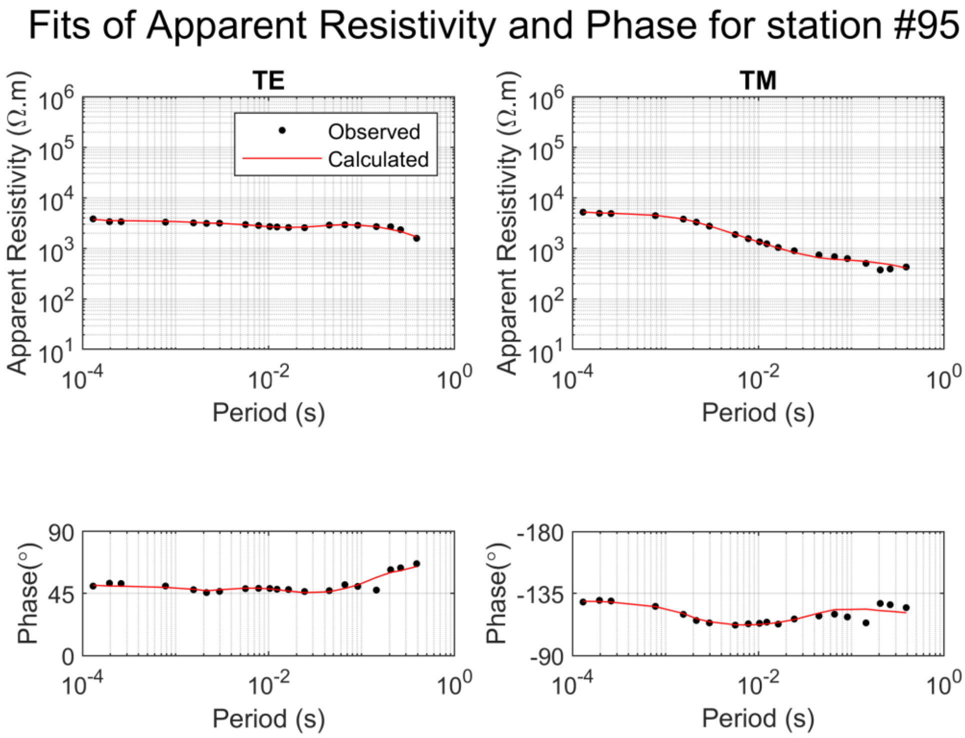
Fits of Apparent Resistivity and Phase for station #95
TE
TM
Observed
Calculated
Apparent Resistivity (Ω.m)
Phase(°)
Period (s)

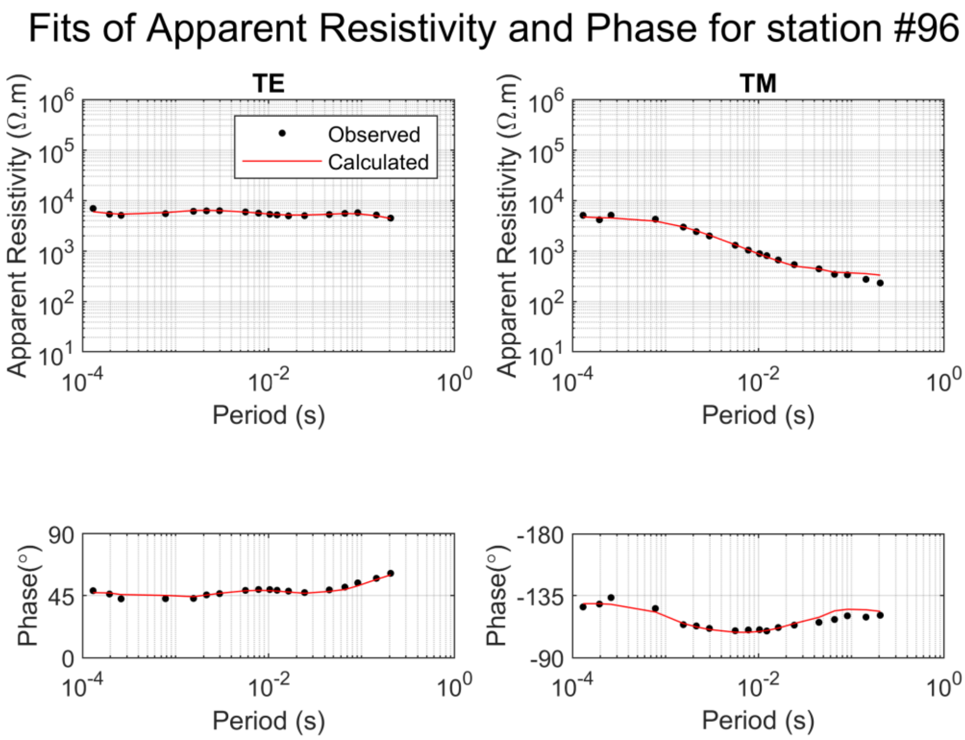
Fits of Apparent Resistivity and Phase for station #96
TE
TM
Observed
Calculated
Apparent Resistivity (Ω.m)
Phase(°)
Period (s)

Fits of Apparent Resistivity and Phase for station #97

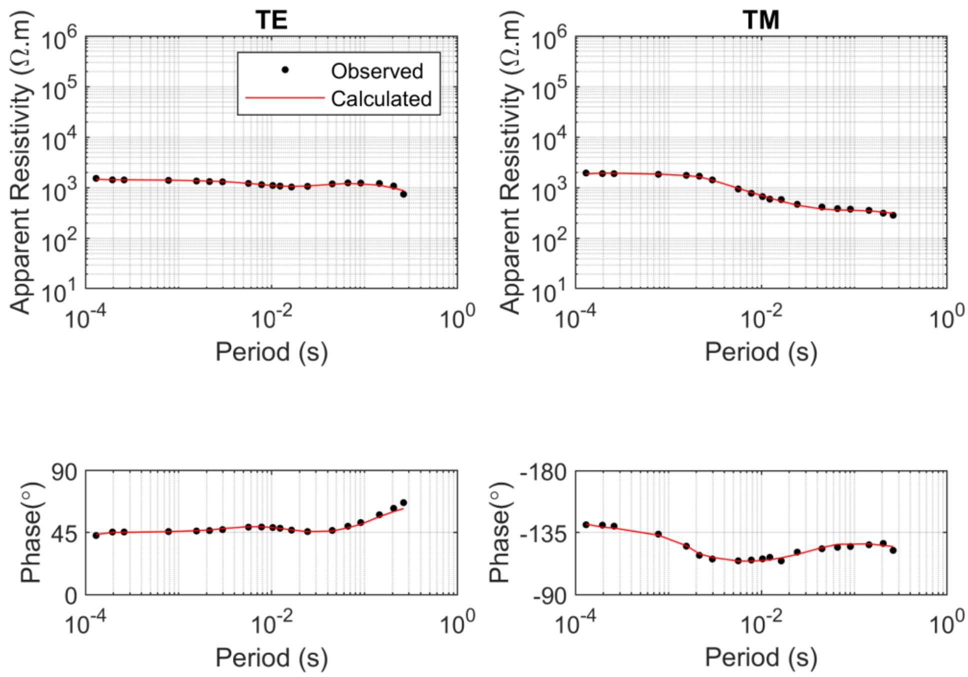

Fits of Apparent Resistivity and Phase for station #98

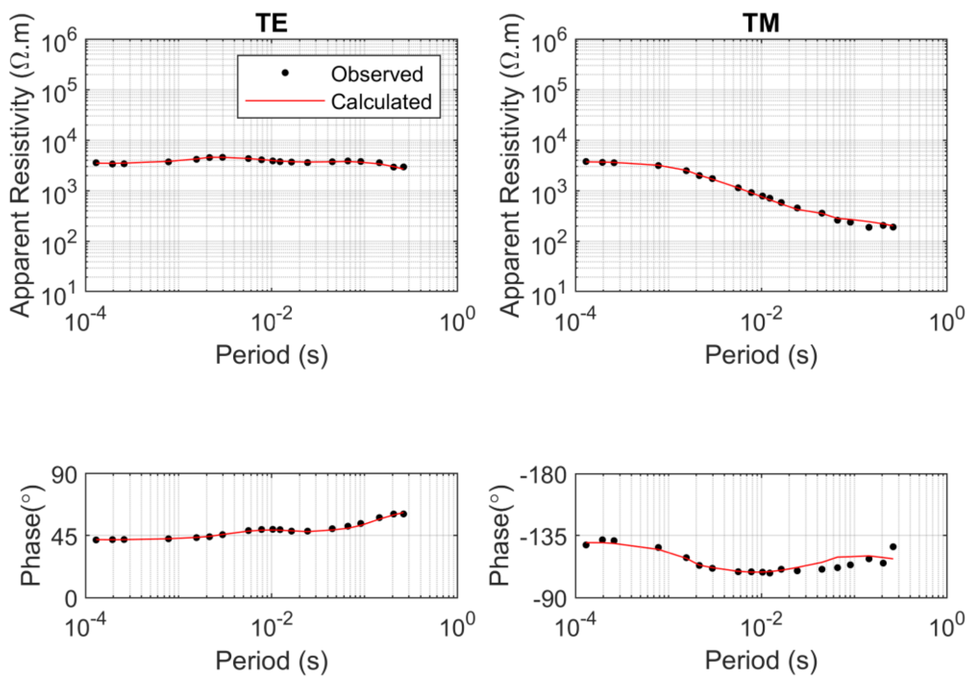

Fits of Apparent Resistivity and Phase for station #99

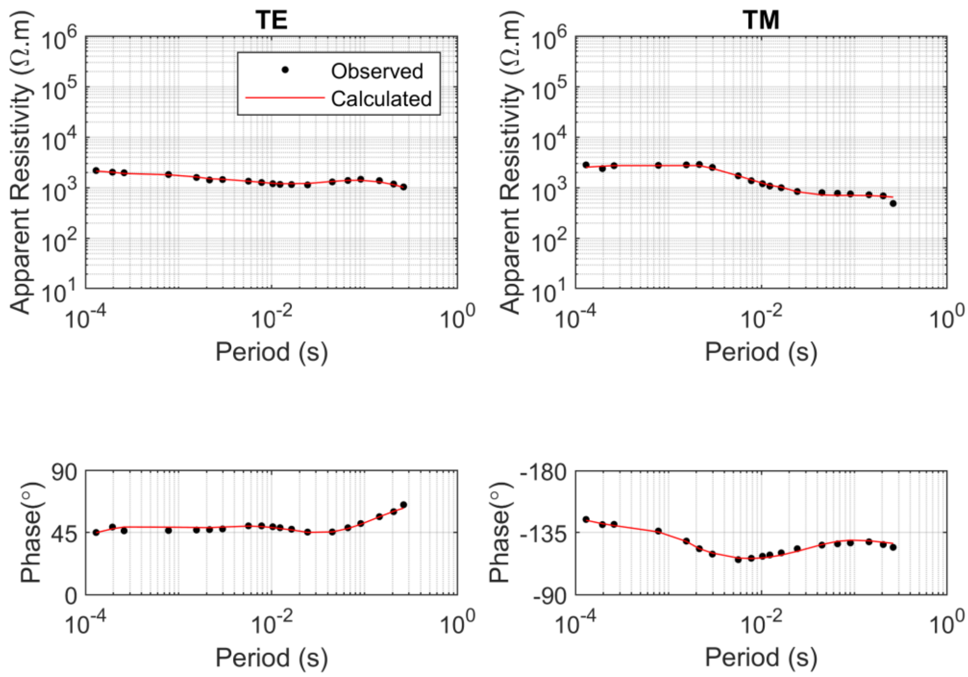

Fits of Apparent Resistivity and Phase for station #100

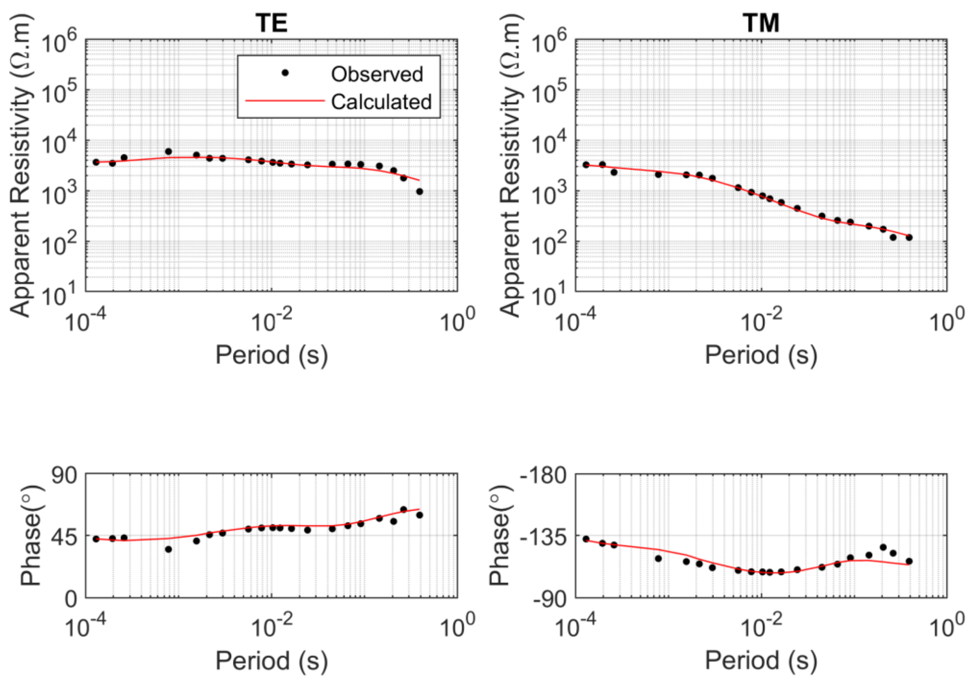

Fits of Apparent Resistivity and Phase for station #101

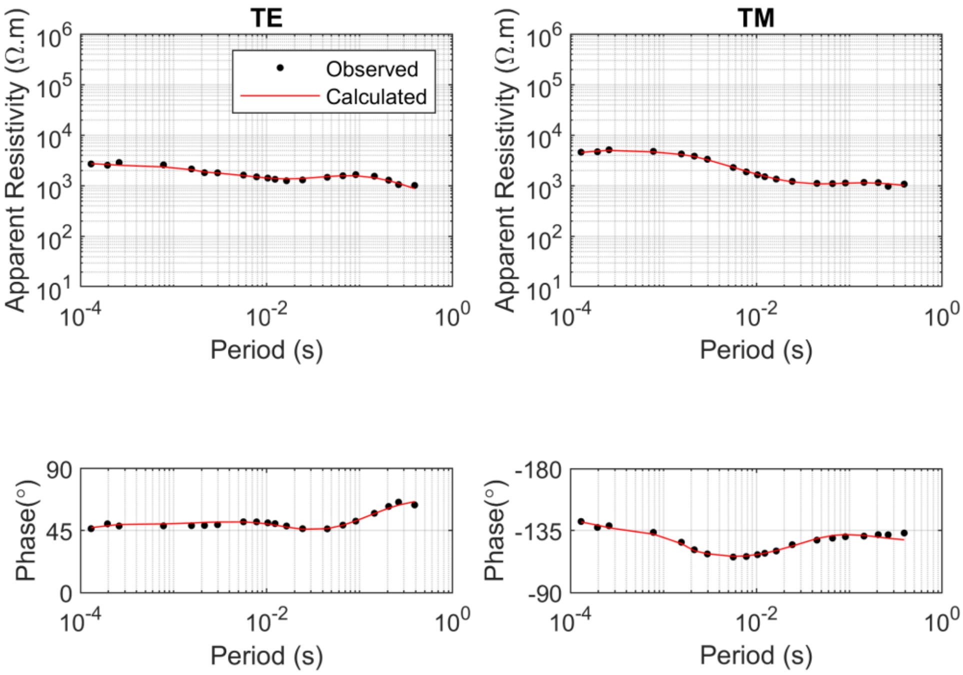

Fits of Apparent Resistivity and Phase for station #102

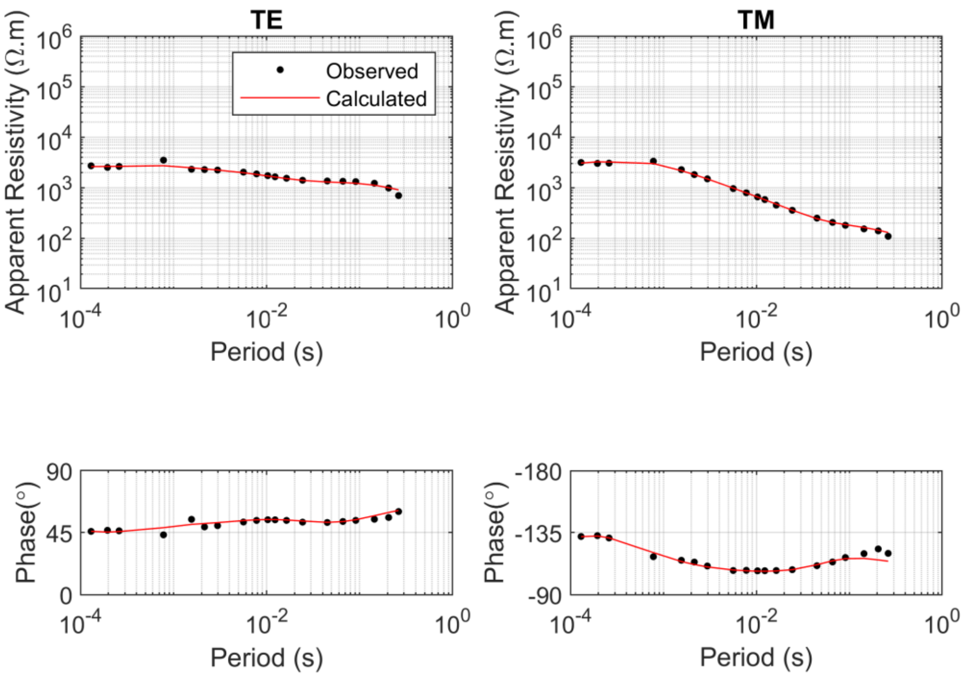

Fits of Apparent Resistivity and Phase for station #103

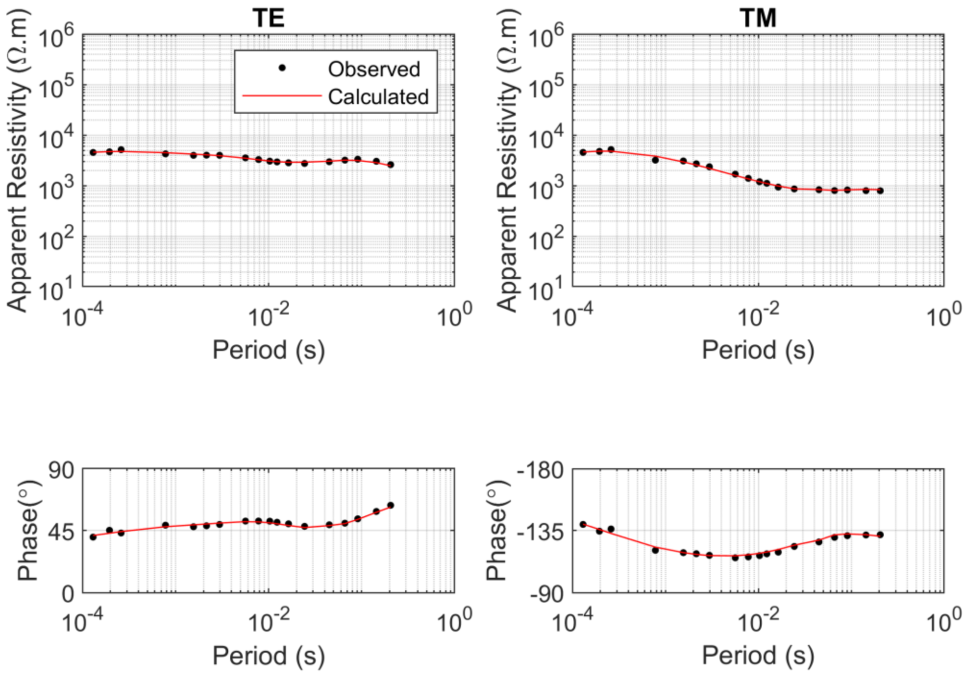

Fits of Apparent Resistivity and Phase for station #104

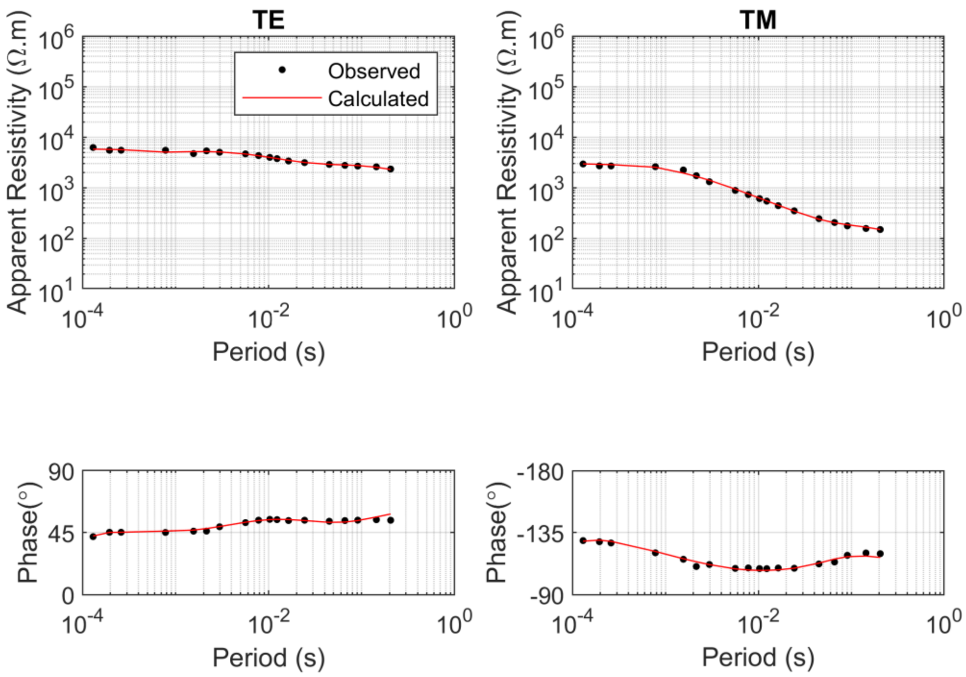

Fits of Apparent Resistivity and Phase for station #105

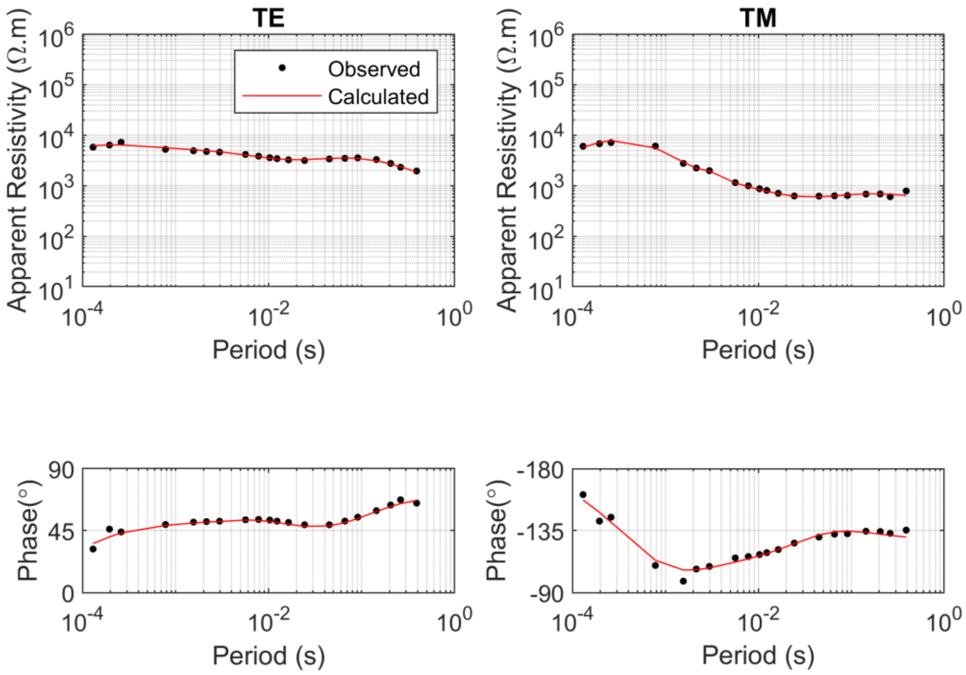

Fits of Apparent Resistivity and Phase for station #106

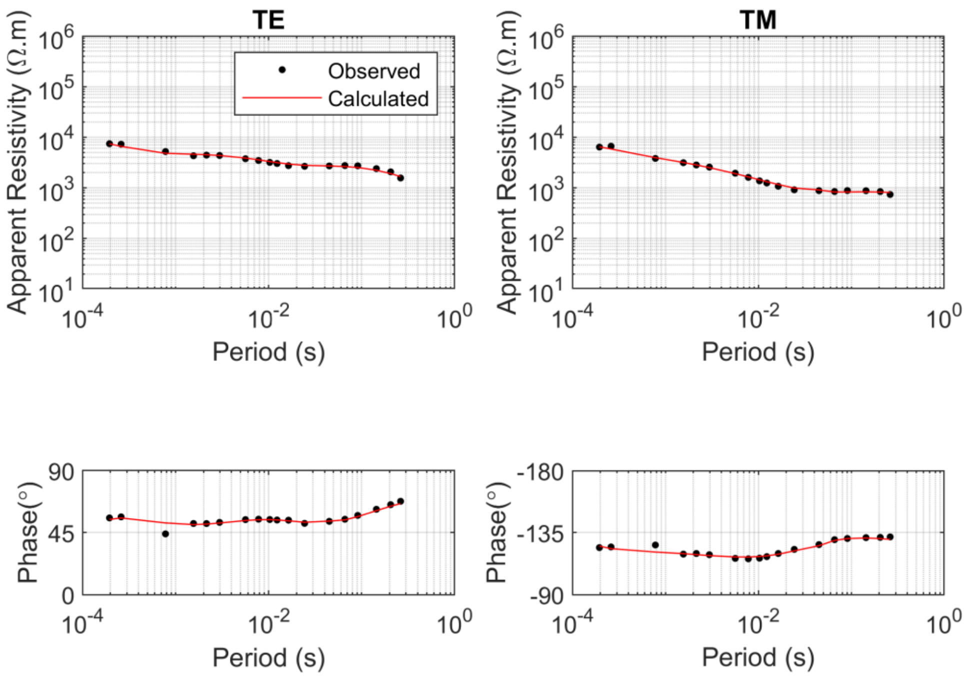

Fits of Apparent Resistivity and Phase for station #107

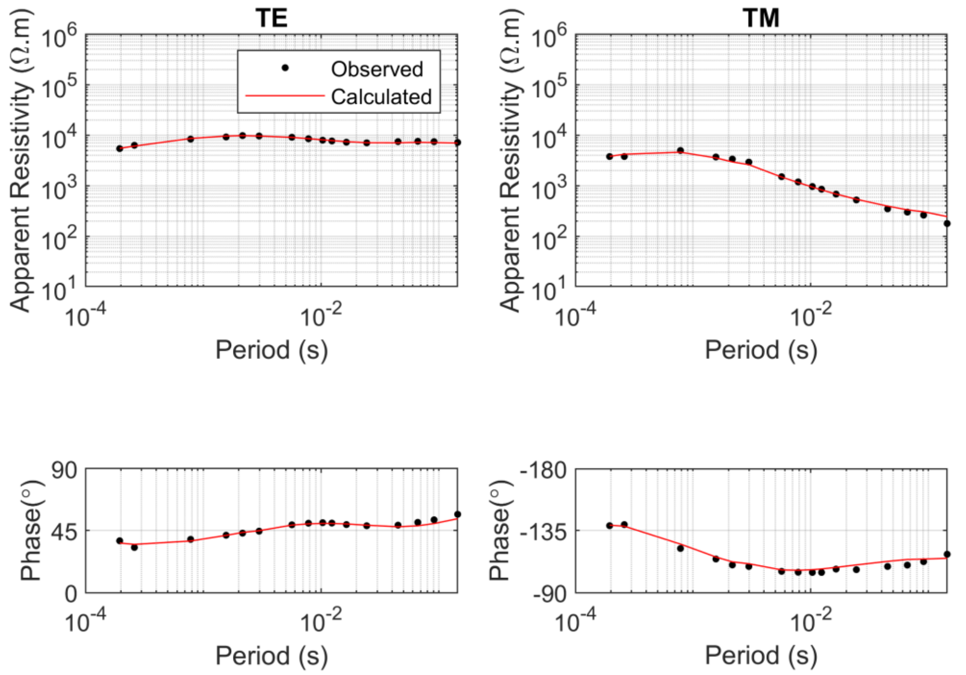

Fits of Apparent Resistivity and Phase for station #108

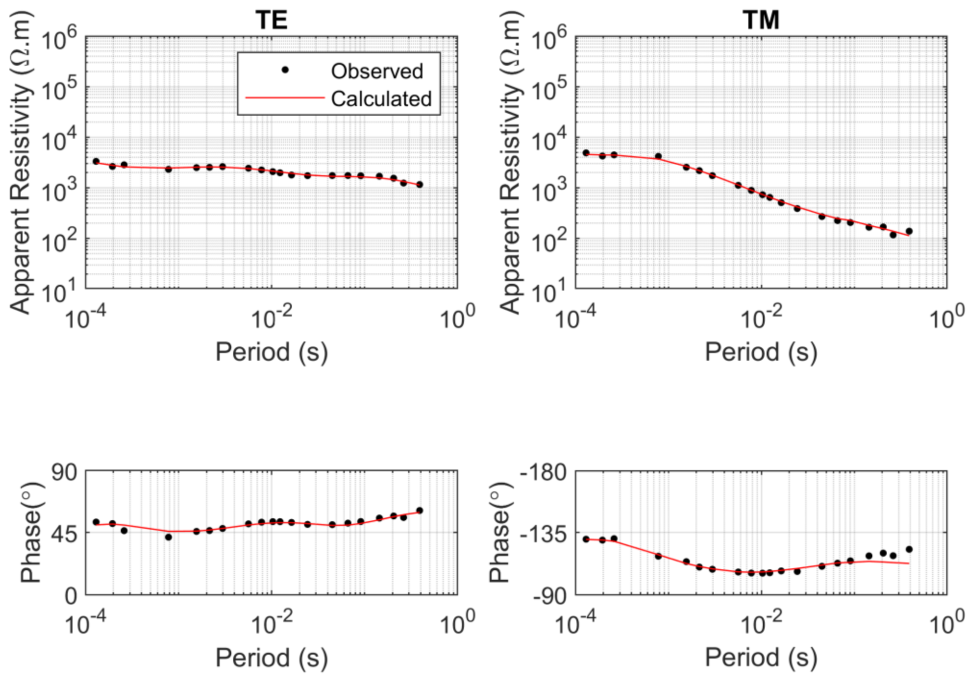

Fits of Apparent Resistivity and Phase for station #109

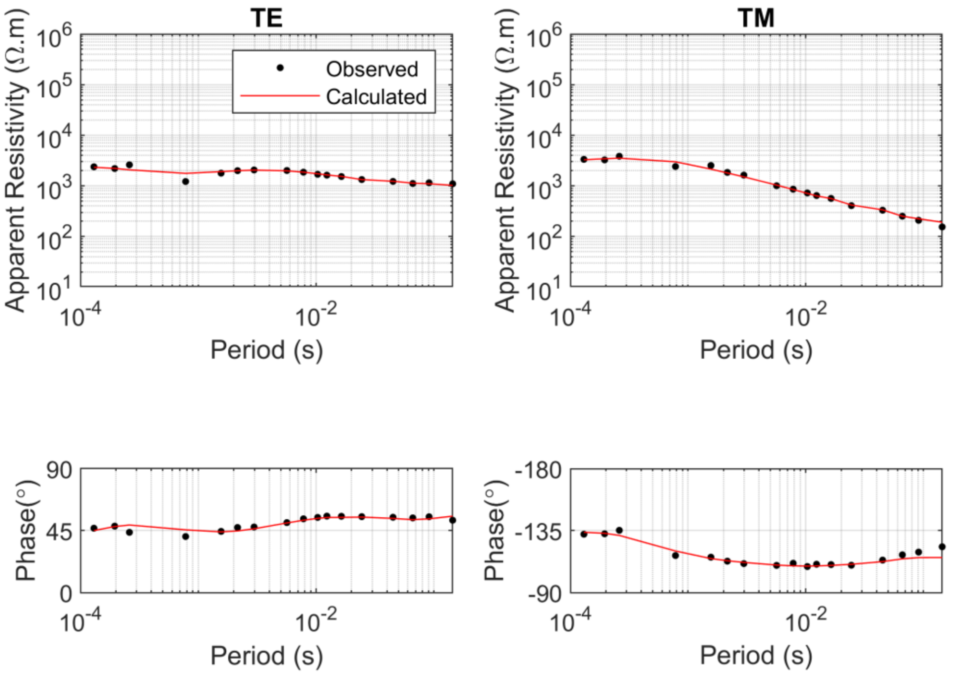

Fits of Apparent Resistivity and Phase for station #110

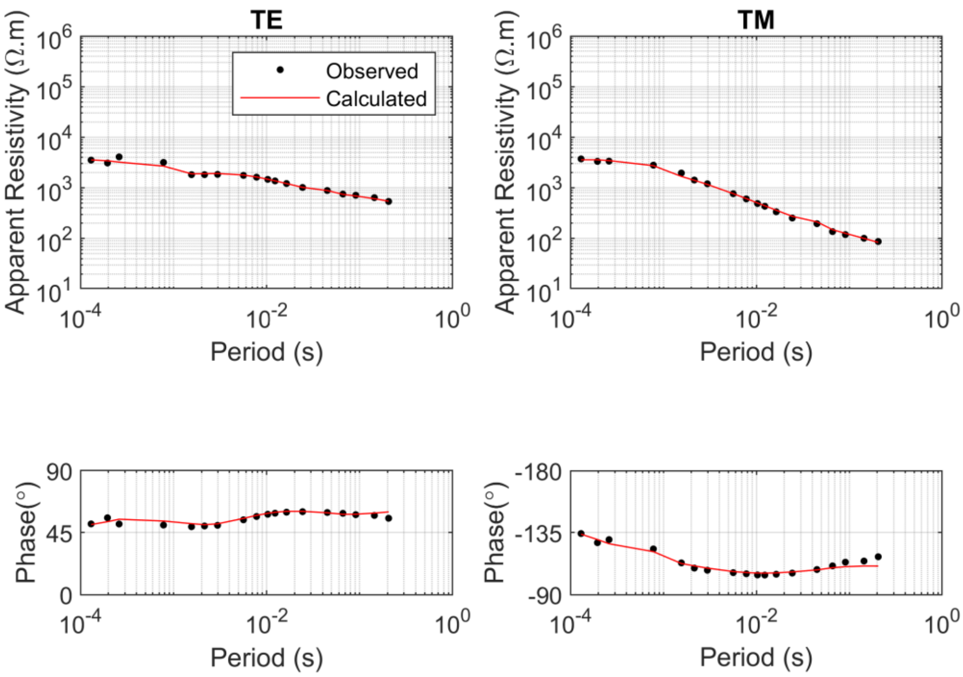

Fits of Apparent Resistivity and Phase for station #111

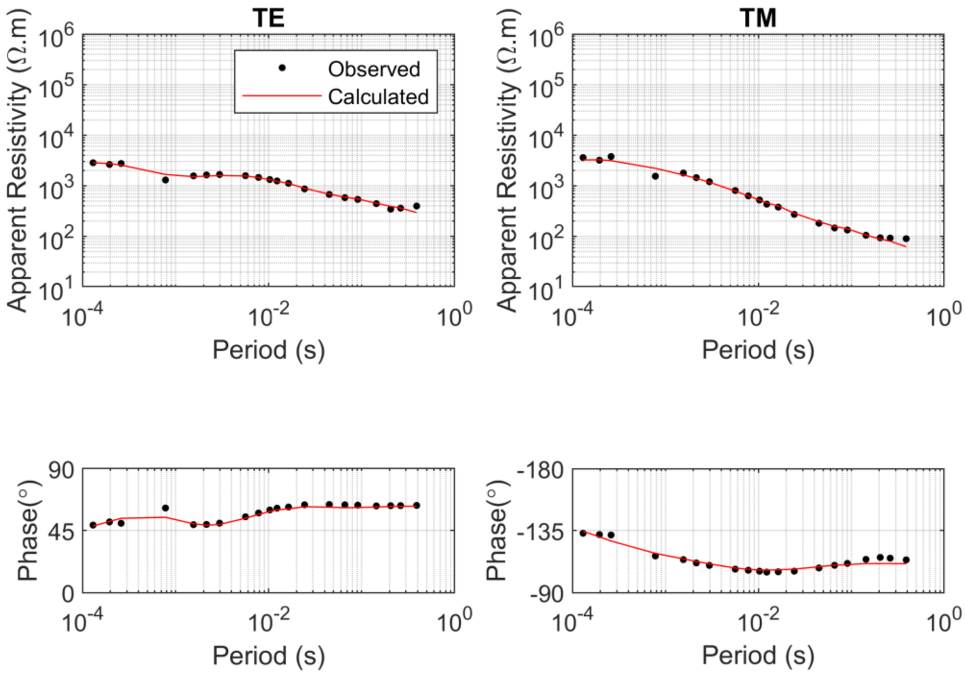

Fits of Apparent Resistivity and Phase for station #112

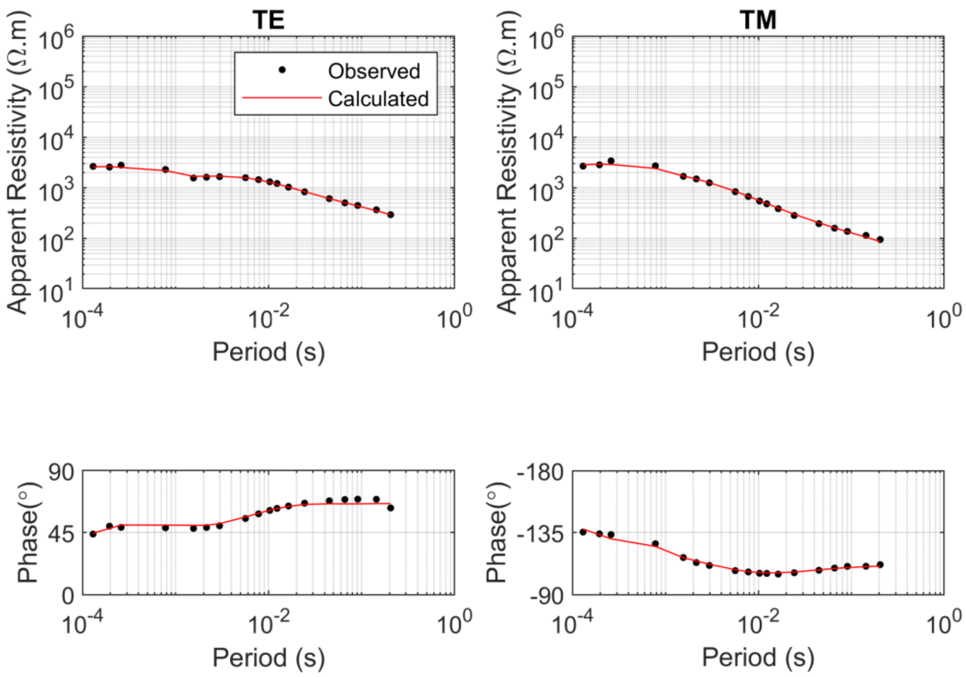

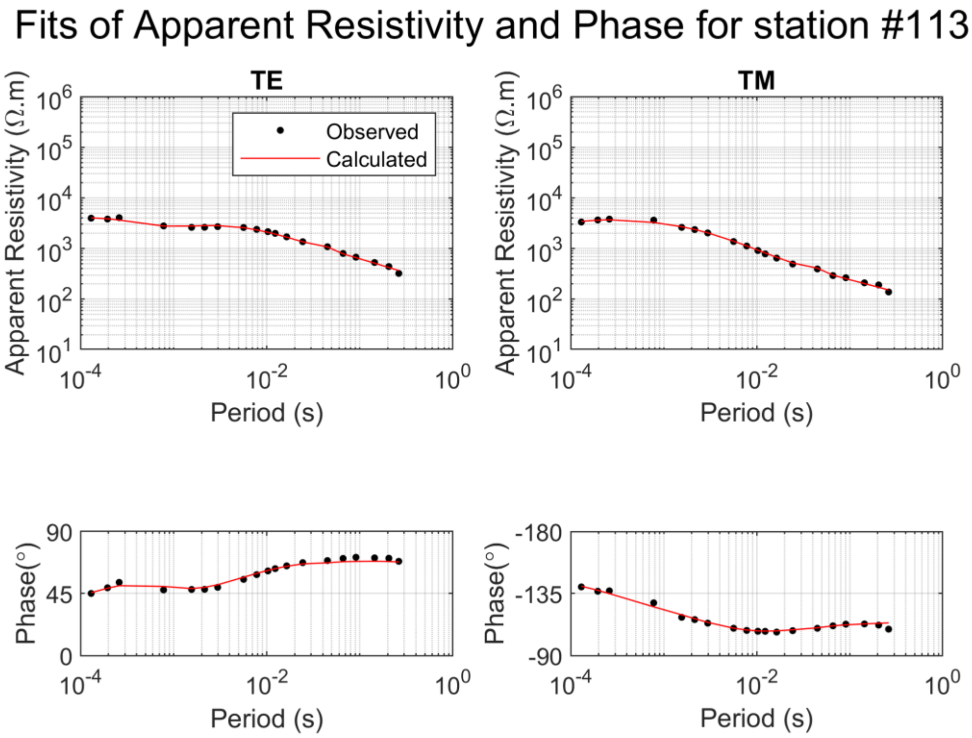

Fits of Apparent Resistivity and Phase for station #113
TE
TM
Observed
Calculated
Apparent Resistivity (Ω.m)
Period (s)
Phase(°)

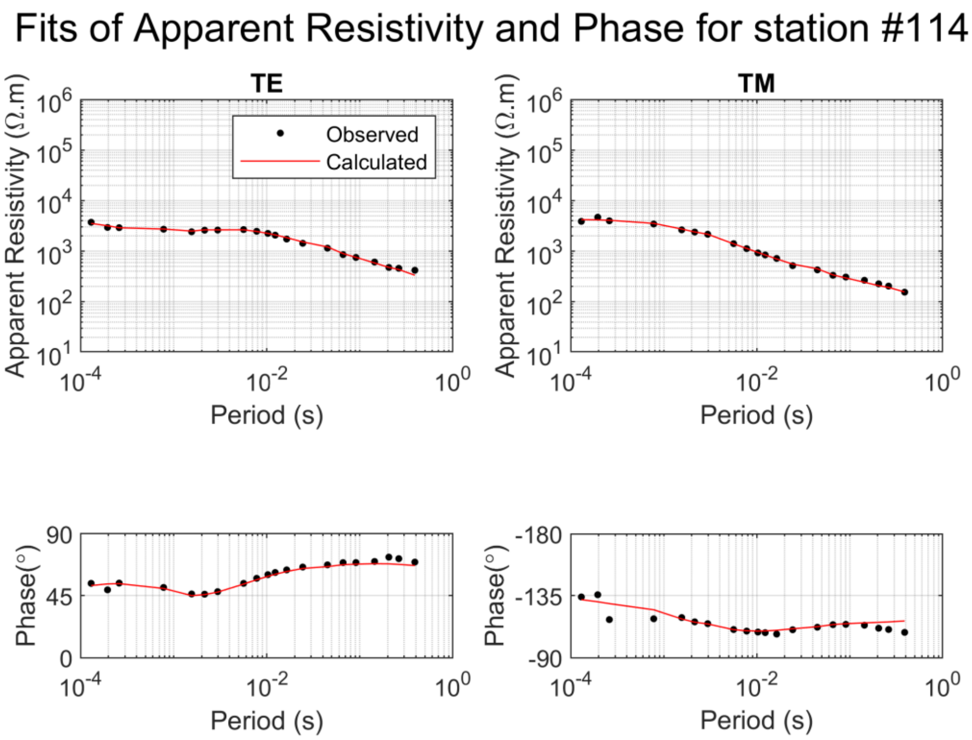

Fits of Apparent Resistivity and Phase for station #114
TE
TM
Observed
Calculated
Apparent Resistivity (Ω.m)
Period (s)
Phase(°)

Fits of Apparent Resistivity and Phase for station #115

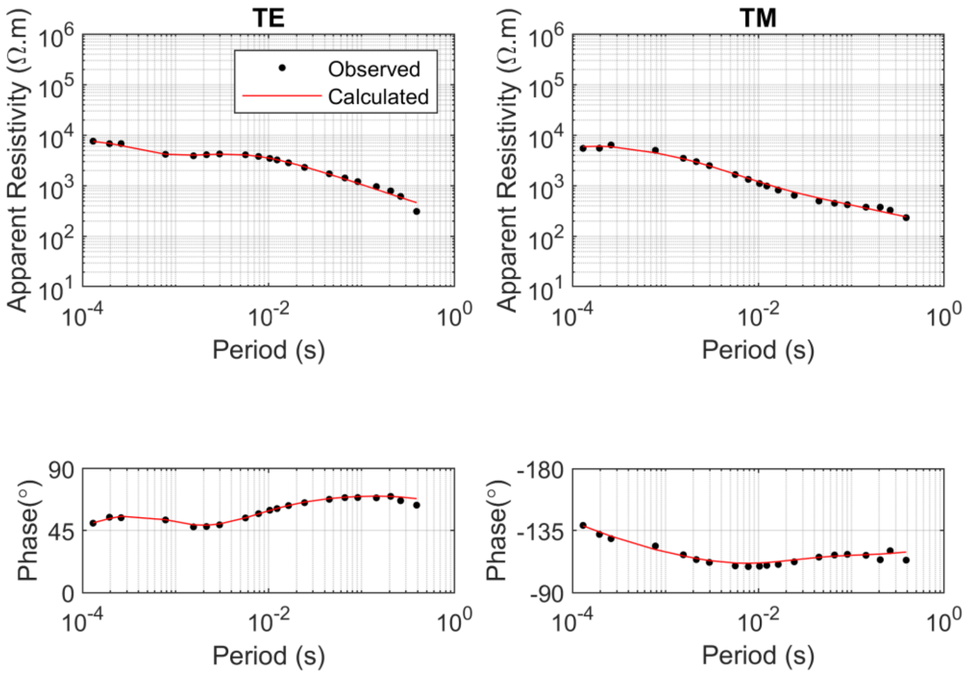

Fits of Apparent Resistivity and Phase for station #116

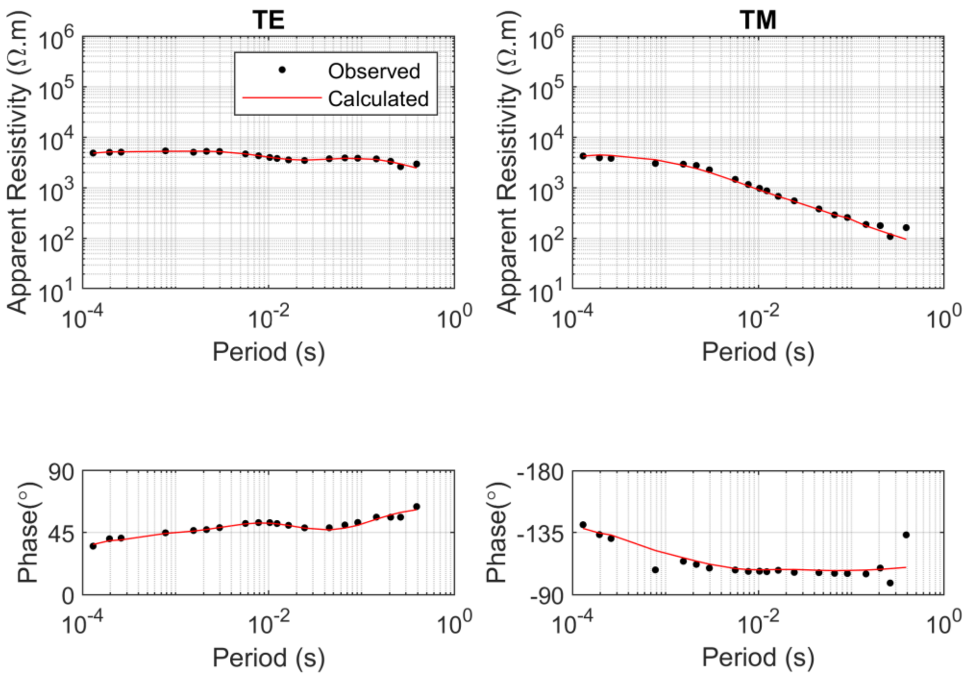

Fits of Apparent Resistivity and Phase for station #117

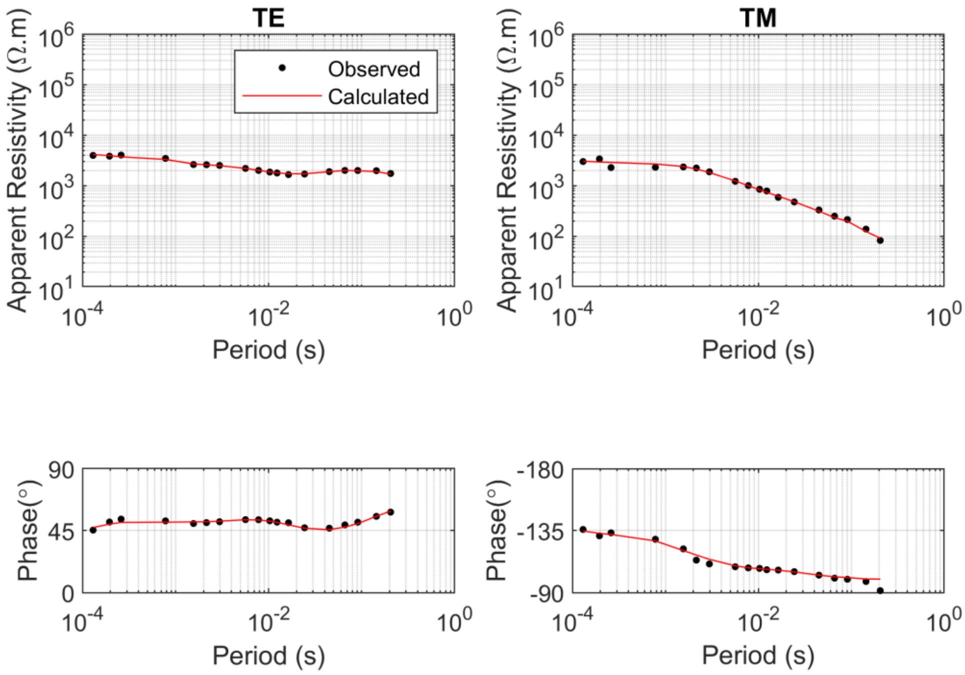

Fits of Apparent Resistivity and Phase for station #118

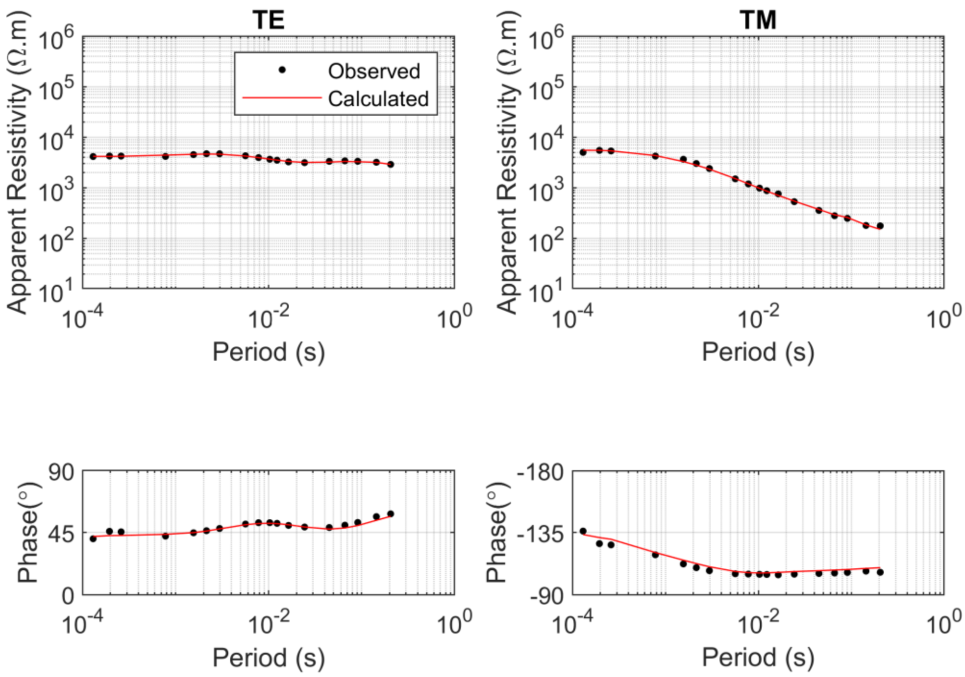

Fits of Apparent Resistivity and Phase for station #119

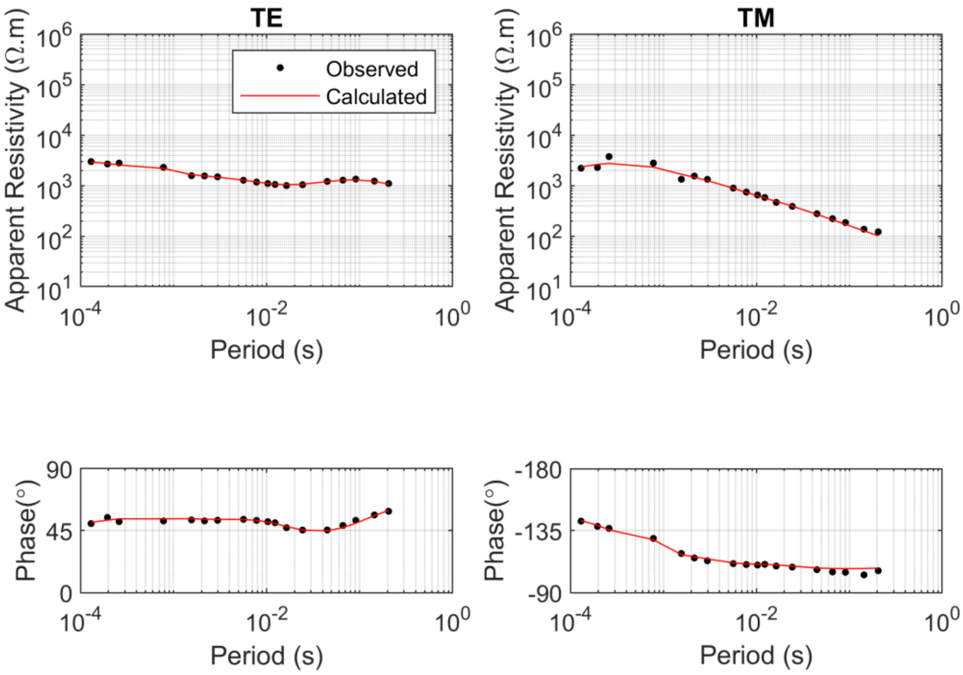

Fits of Apparent Resistivity and Phase for station #120

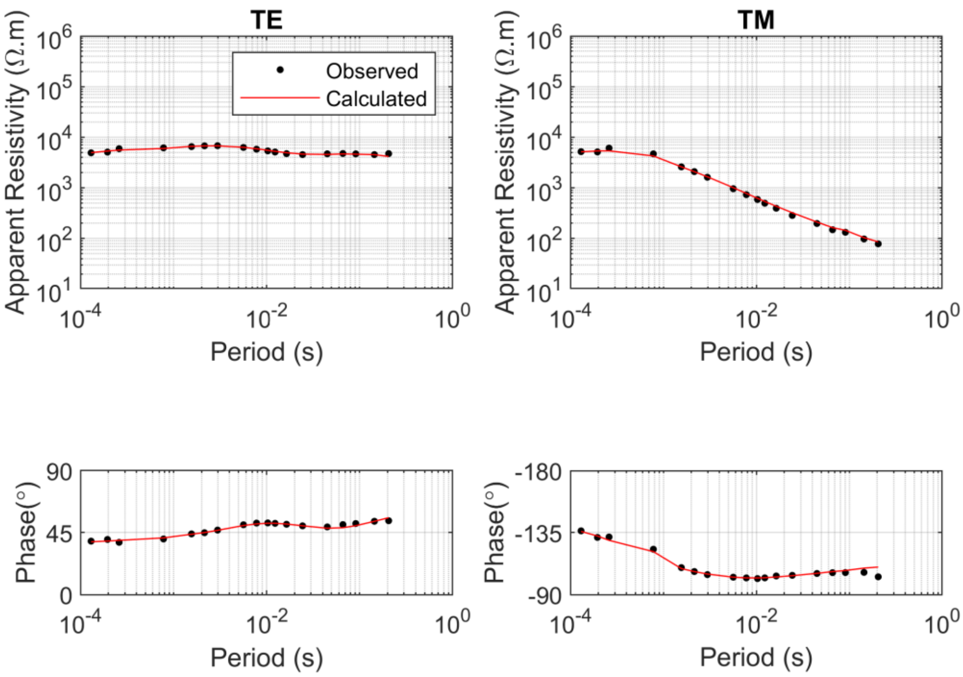

Fits of Apparent Resistivity and Phase for station #121

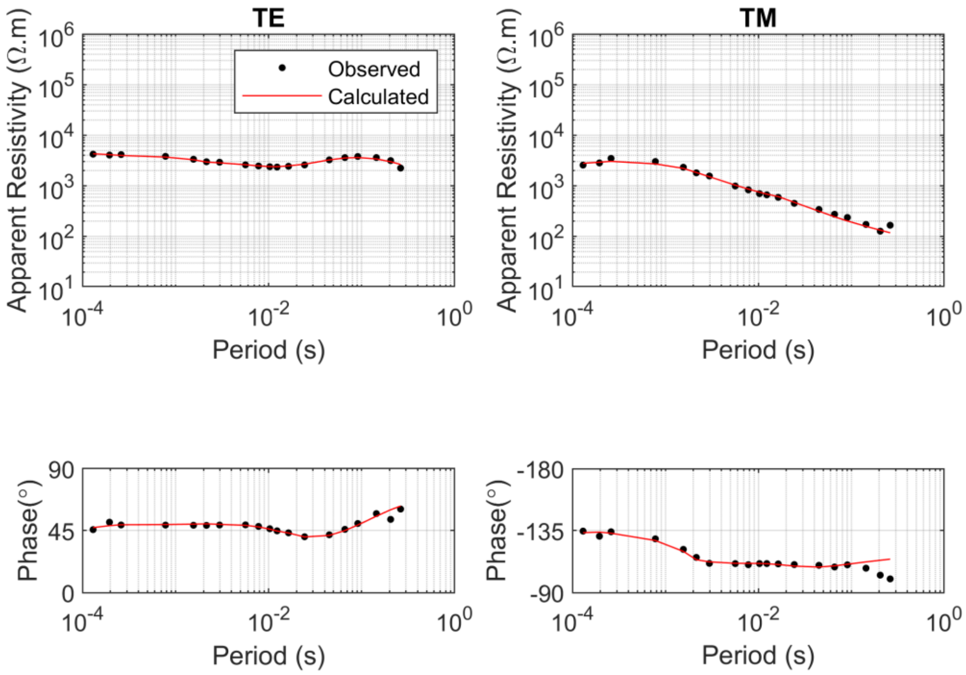

Fits of Apparent Resistivity and Phase for station #122

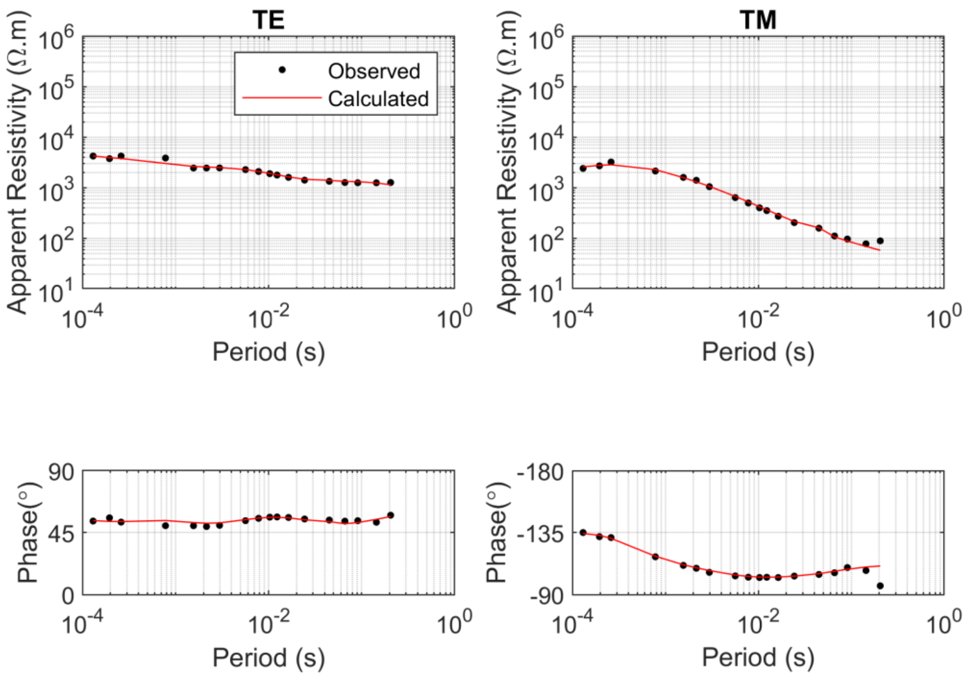

Fits of Apparent Resistivity and Phase for station #123

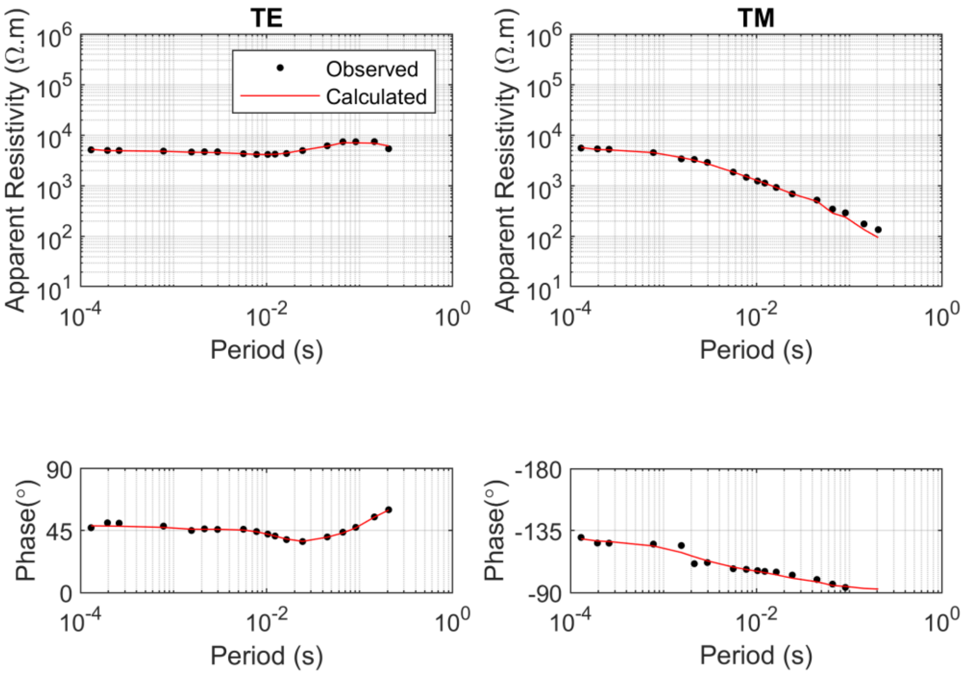

Fits of Apparent Resistivity and Phase for station #124

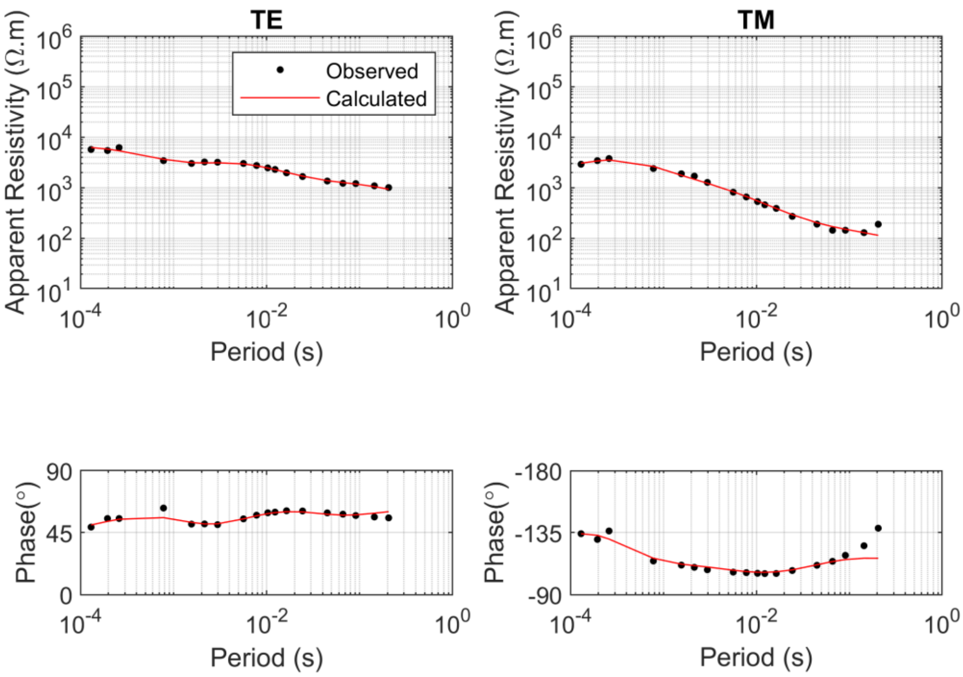

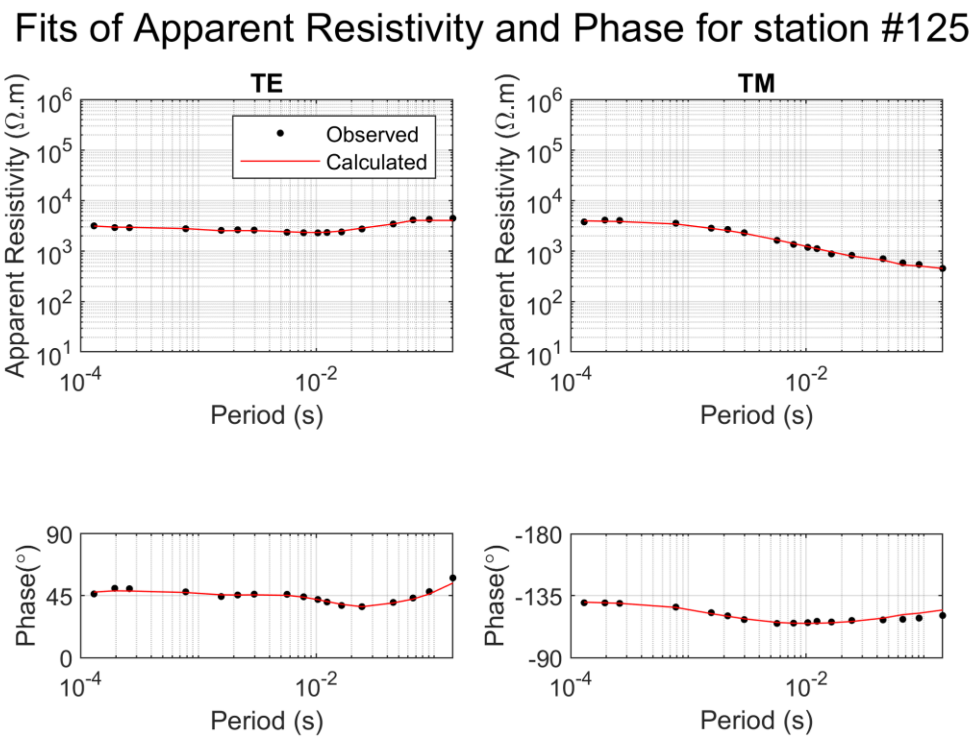
Fits of Apparent Resistivity and Phase for station #125
TE
TM
Observed
Calculated
Apparent Resistivity (Ω.m)
Phase(°)
Period (s)

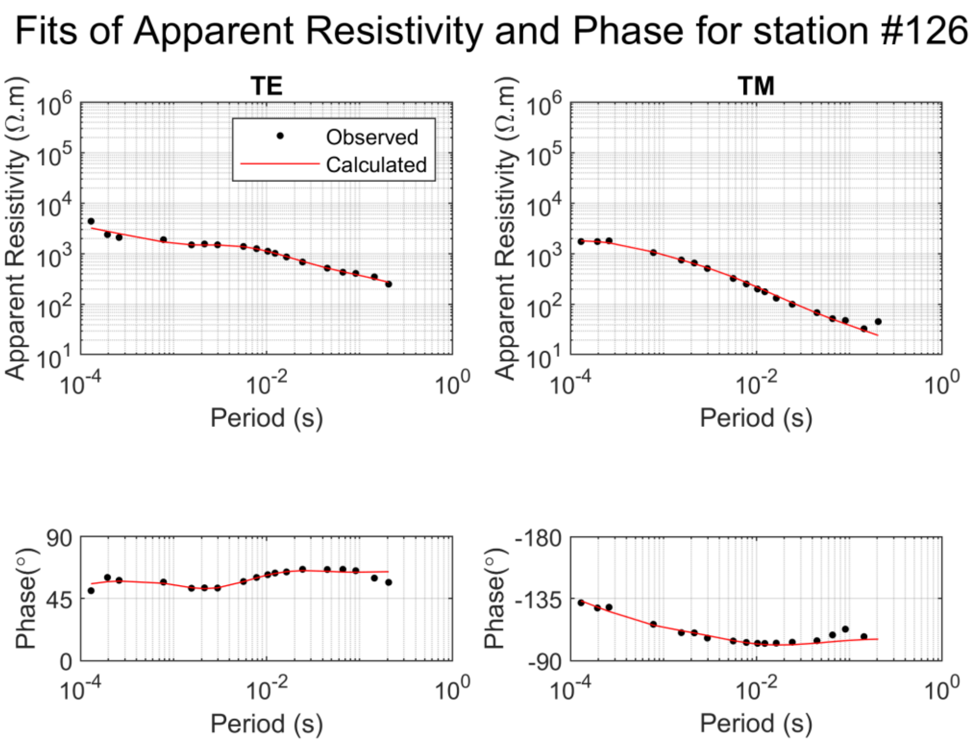
Fits of Apparent Resistivity and Phase for station #126
TE
TM
Observed
Calculated
Apparent Resistivity (Ω.m)
Phase(°)
Period (s)

Fits of Apparent Resistivity and Phase for station #127

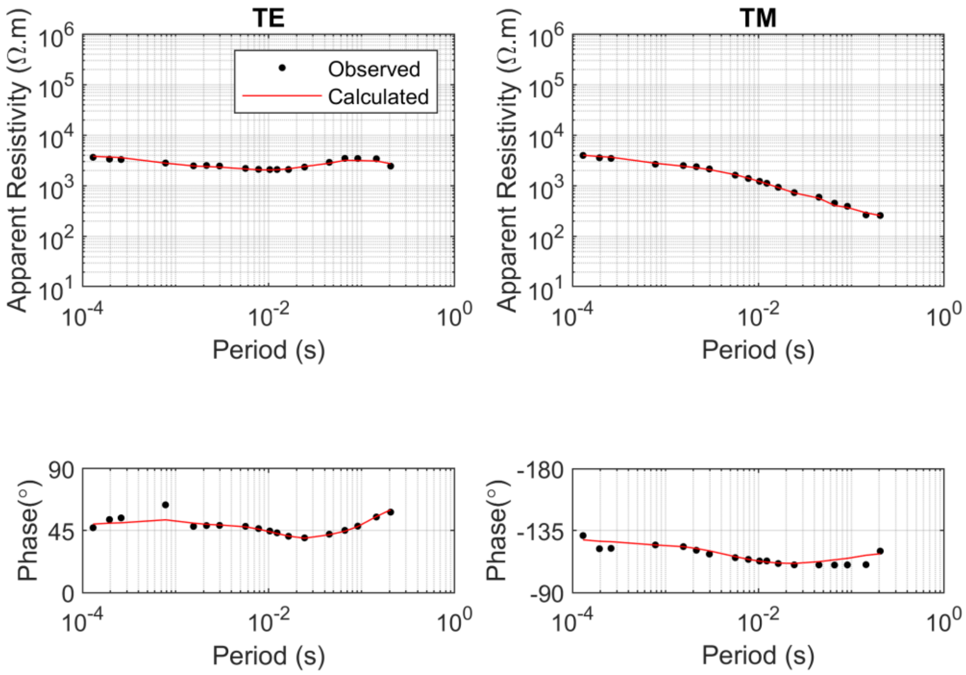

Fits of Apparent Resistivity and Phase for station #128

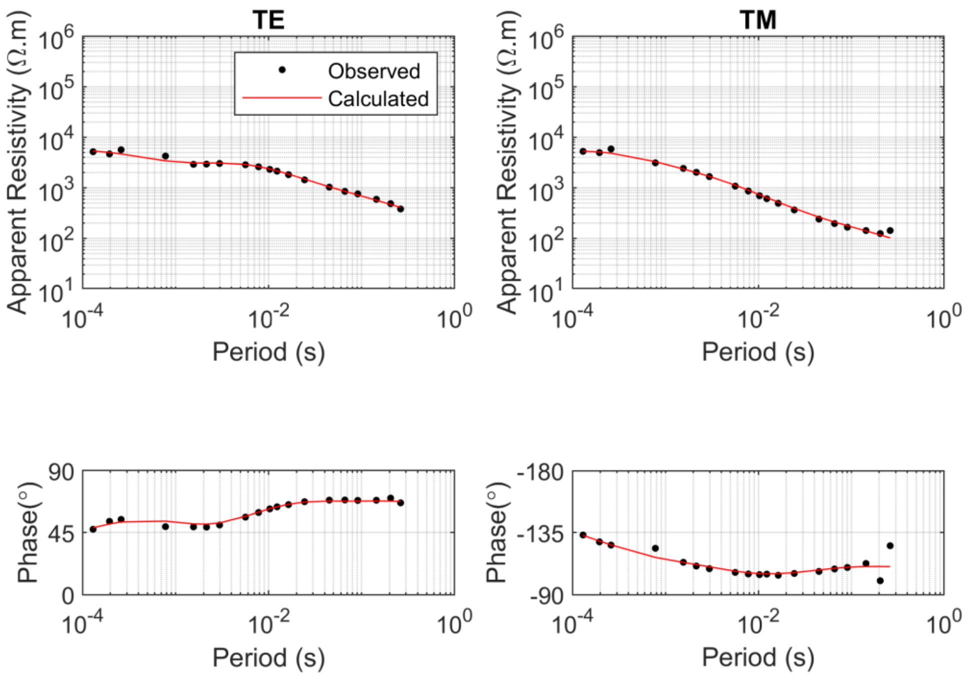

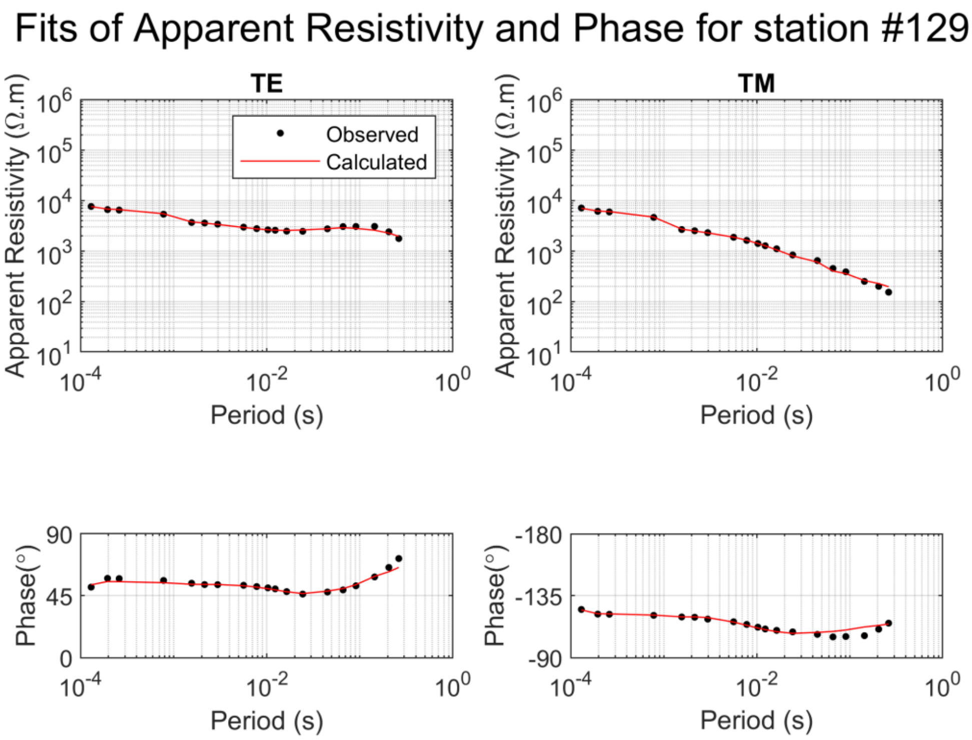
Fits of Apparent Resistivity and Phase for station #129
TE
TM
Observed
Calculated
Apparent Resistivity (Ω.m)
Period (s)
Phase(°)

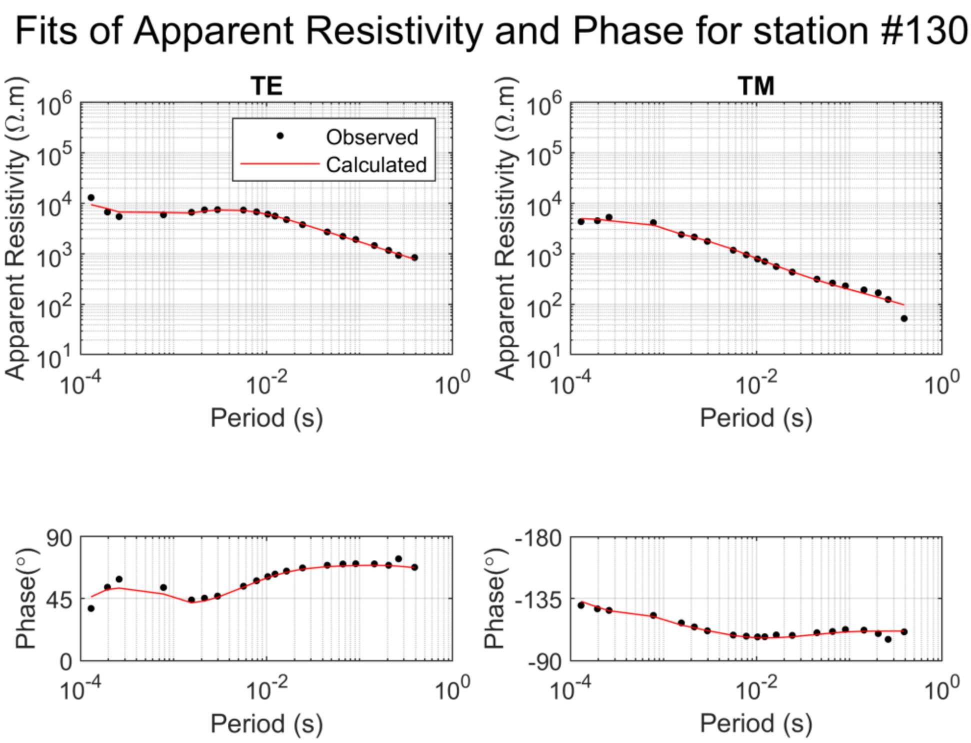
Fits of Apparent Resistivity and Phase for station #130
TE
TM
Observed
Calculated
Apparent Resistivity (Ω.m)
Period (s)
Phase(°)

Fits of Apparent Resistivity and Phase for station #131

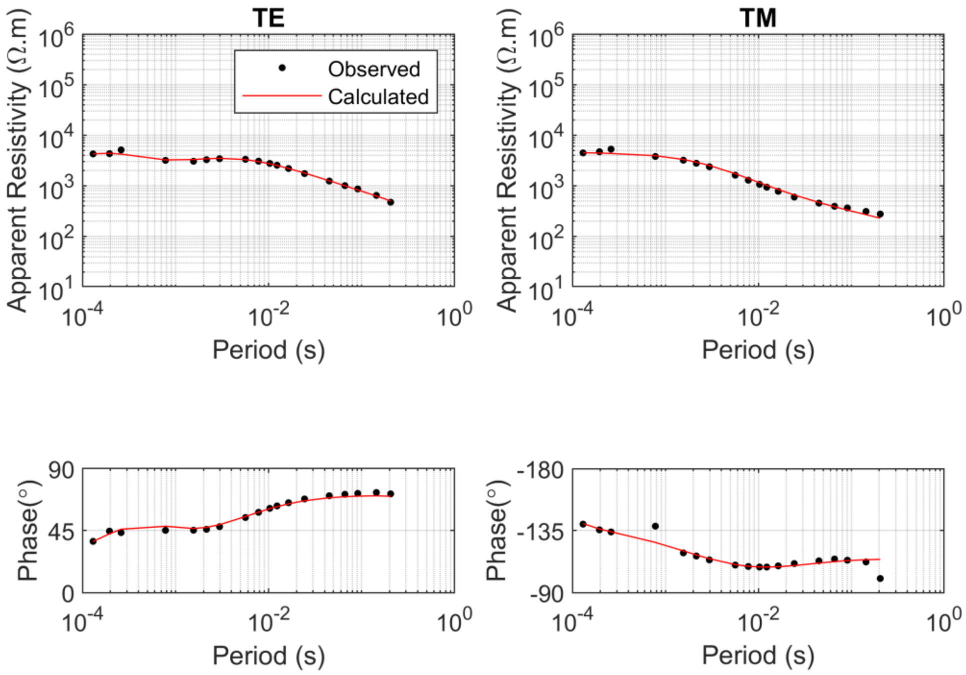

Fits of Apparent Resistivity and Phase for station #132

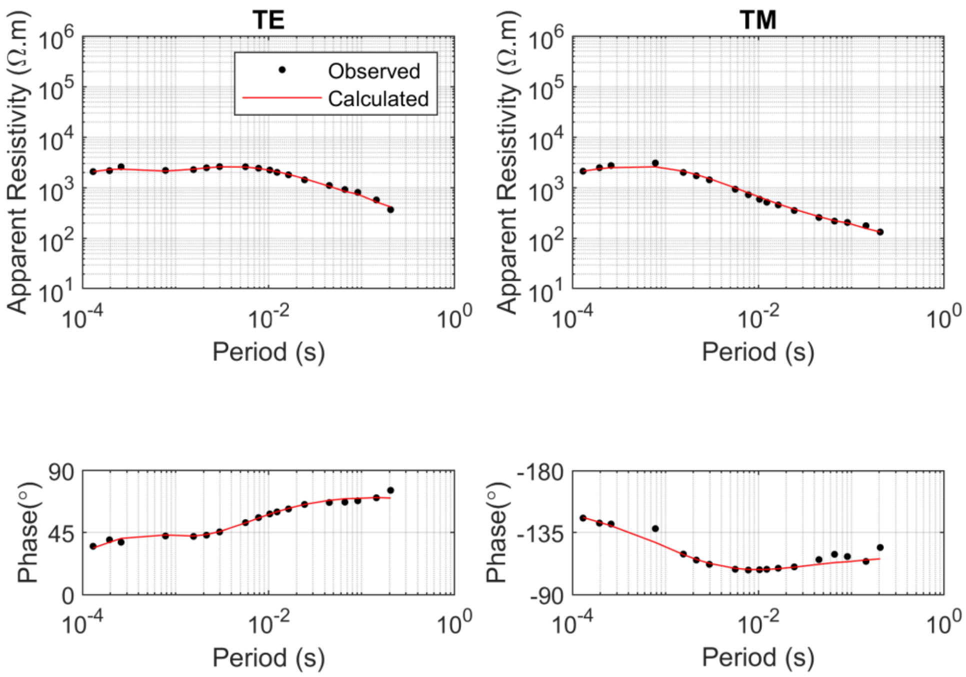

Appendix F – Fit Plots of Impedances, Apparent Resistivities and Phases for Inversion with 5% Uncertainties

F.1. Fit Plots of Impedances

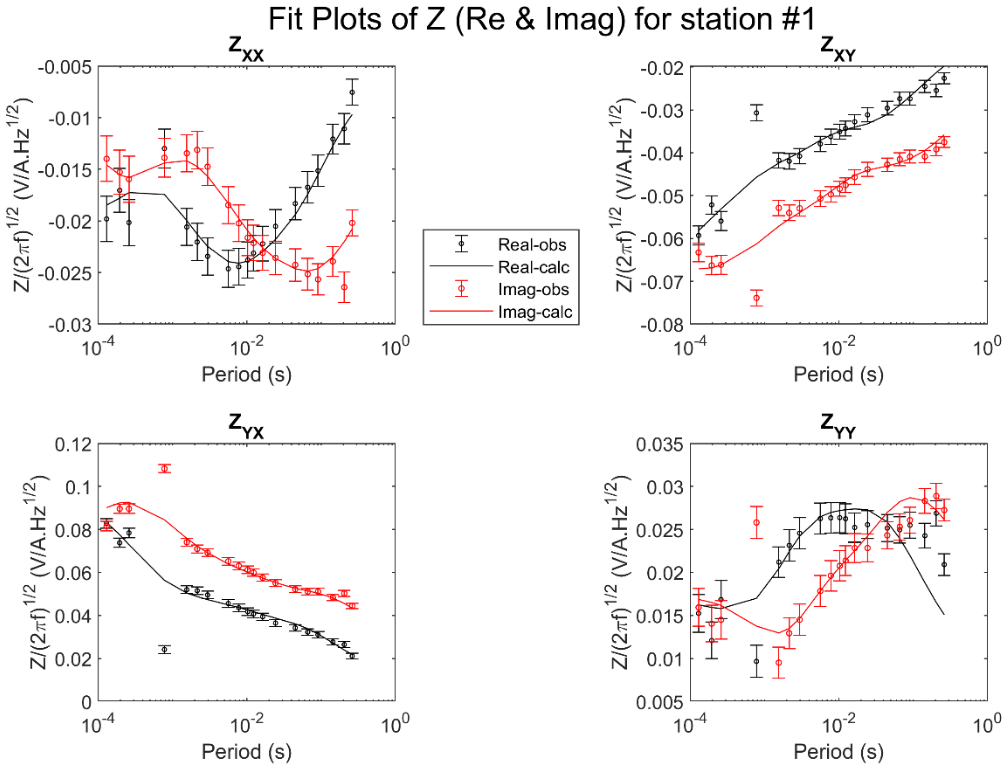

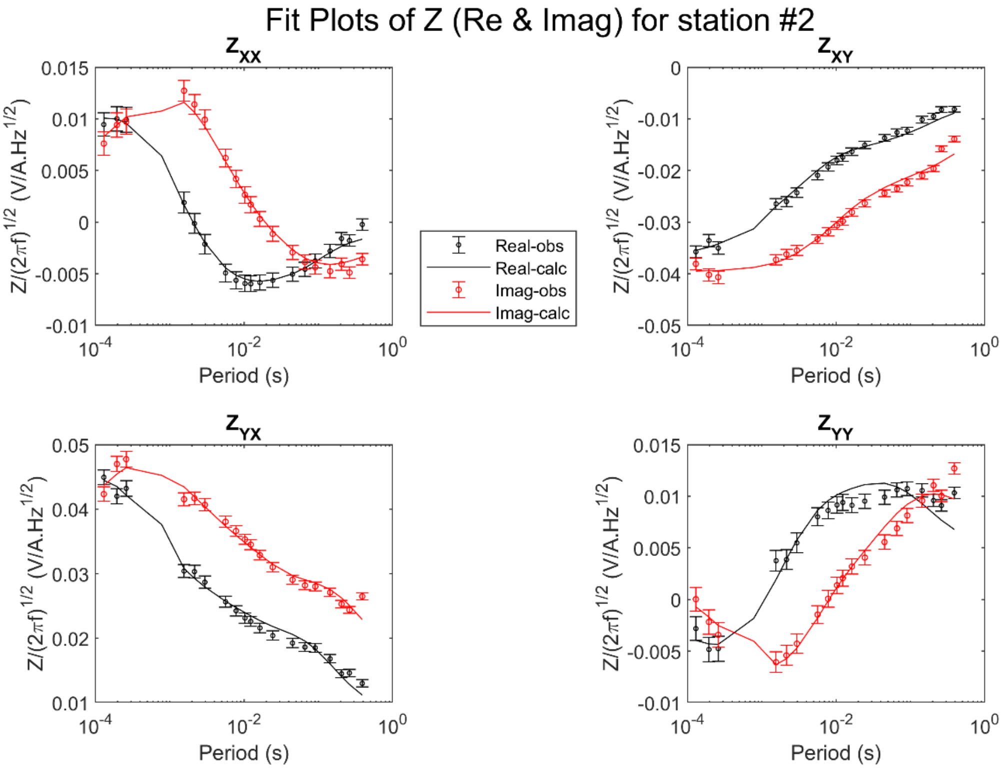
Fit Plots of Z (Re & Imag) for station #2
Z_XX
Z_XY
Z_YX
Z_YY
Z/(2πf)^1/2 (V/A.Hz^1/2)
Period (s)
Real-obs
Real-calc
Imag-obs
Imag-calc

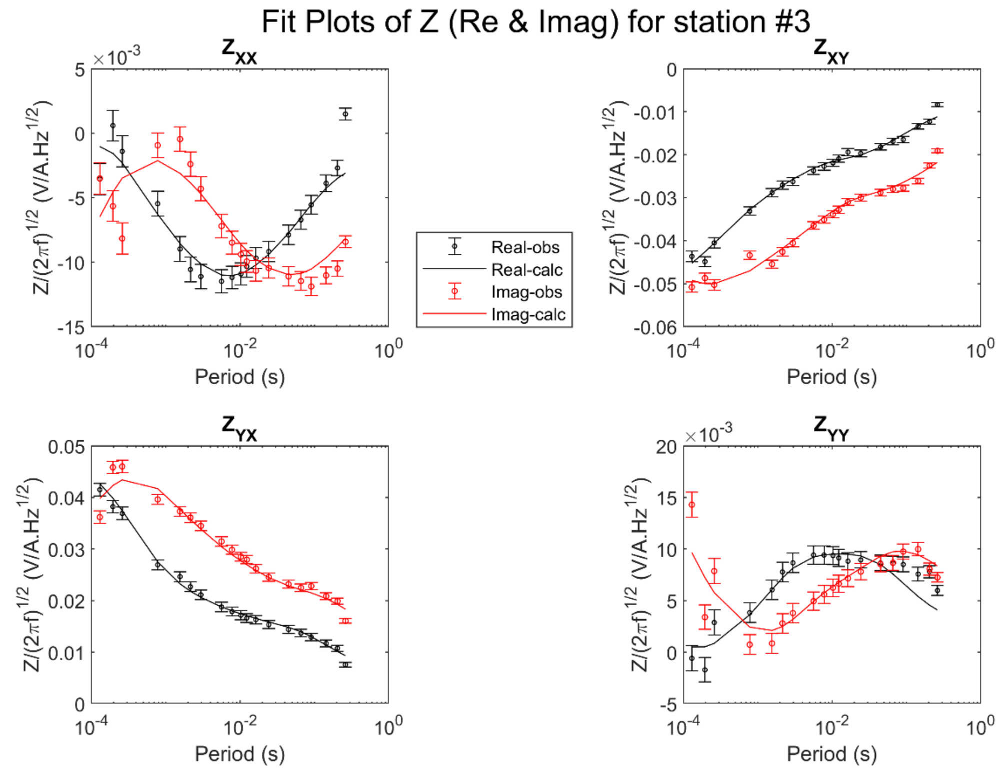
Fit Plots of Z (Re & Imag) for station #3
Z_XX
Z_XY
Z_YX
Z_YY
×10^-3
Z/(2πf)^1/2 (V/A.Hz^1/2)
Period (s)
Real-obs
Real-calc
Imag-obs
Imag-calc

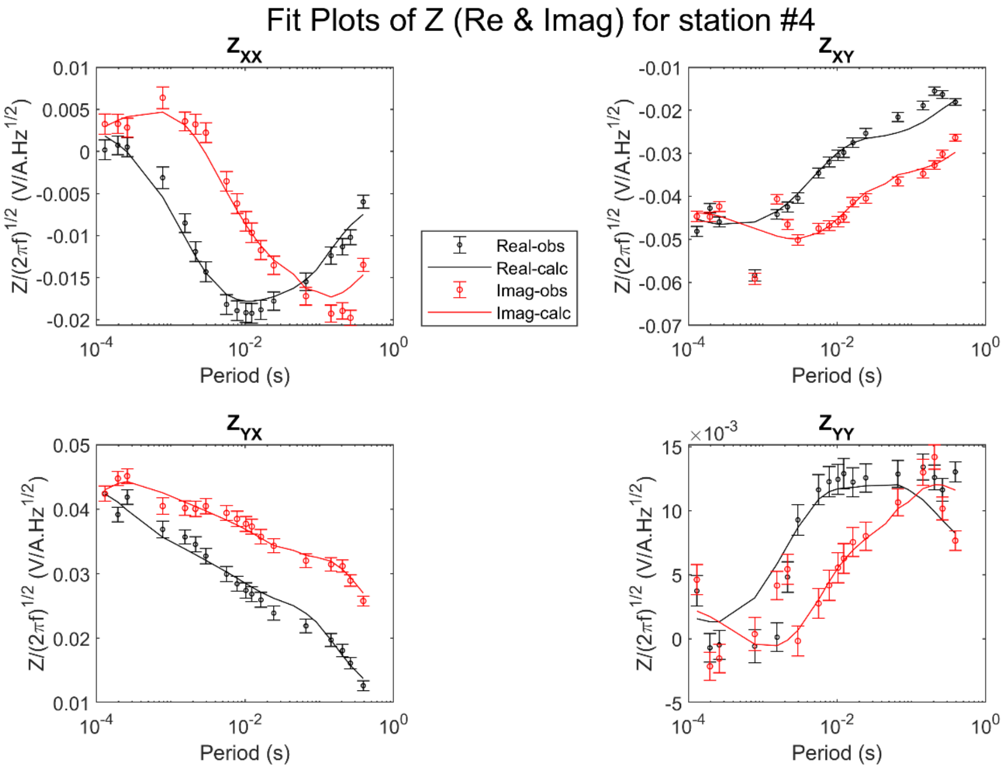
Fit Plots of Z (Re & Imag) for station #4
Z_XX
Z_XY
Z_YX
Z_YY
Real-obs
Real-calc
Imag-obs
Imag-calc
Z/(2πf)^1/2 (V/A.Hz^1/2)
Period (s)
×10^-3

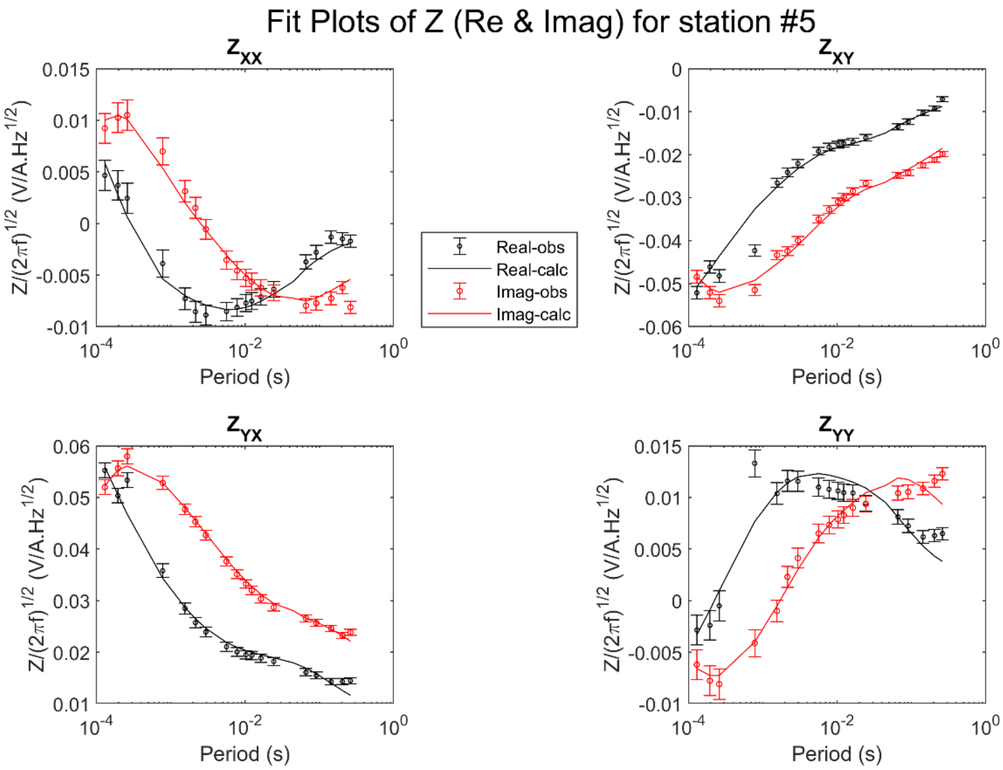
Fit Plots of Z (Re & Imag) for station #5
Z_XX
Z_XY
Z_YX
Z_YY
Real-obs
Real-calc
Imag-obs
Imag-calc
Z/(2πf)^1/2 (V/A.Hz^1/2)
Period (s)

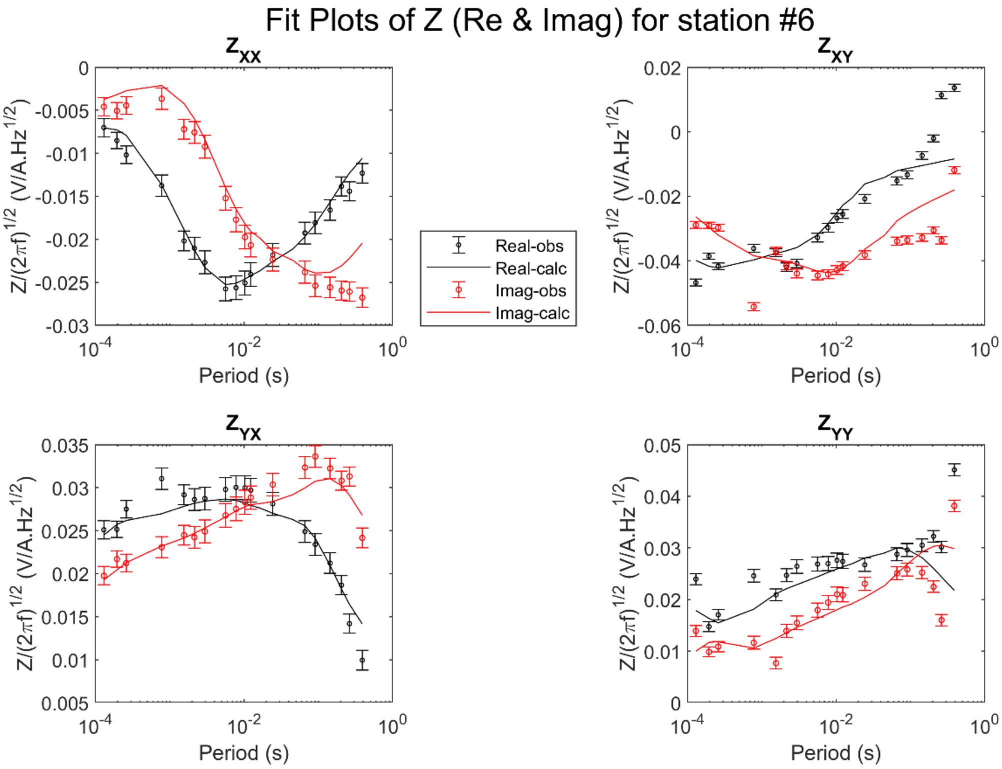
Fit Plots of Z (Re & Imag) for station #6
Z_XX
Z_XY
Z_YX
Z_YY
Z/(2πf)^1/2 (V/A.Hz^1/2)
Period (s)
Real-obs
Real-calc
Imag-obs
Imag-calc

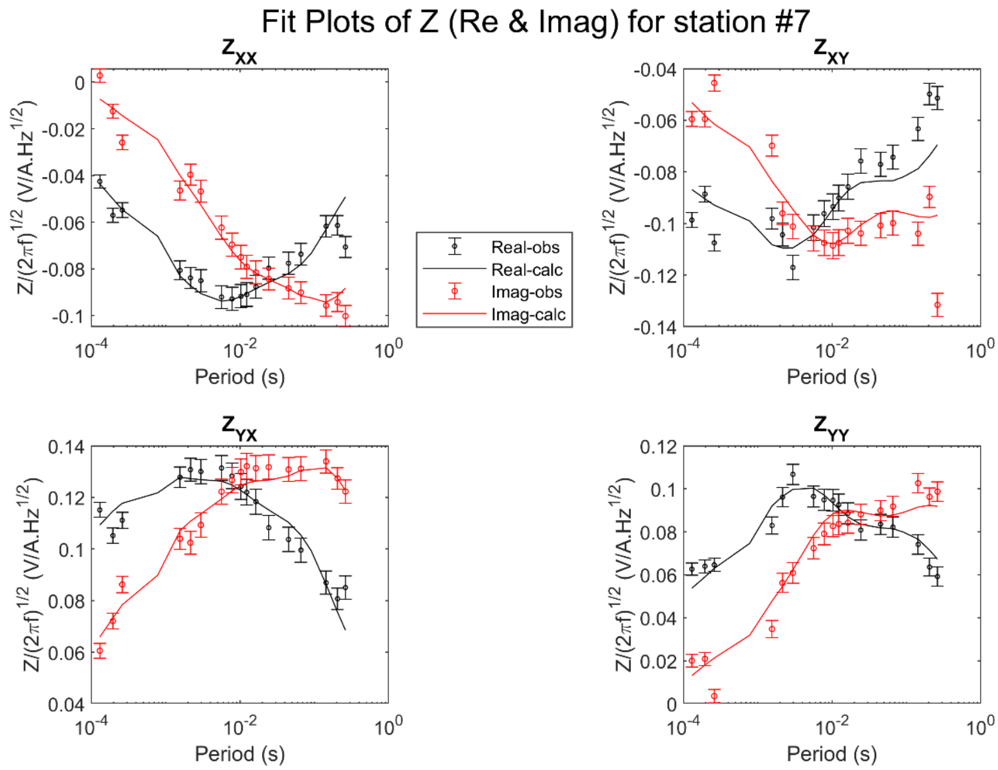
Fit Plots of Z (Re & Imag) for station #7
Z_XX
Z_XY
Z_YX
Z_YY
Z/(2πf)^1/2 (V/A.Hz^1/2)
Period (s)
Real-obs
Real-calc
Imag-obs
Imag-calc

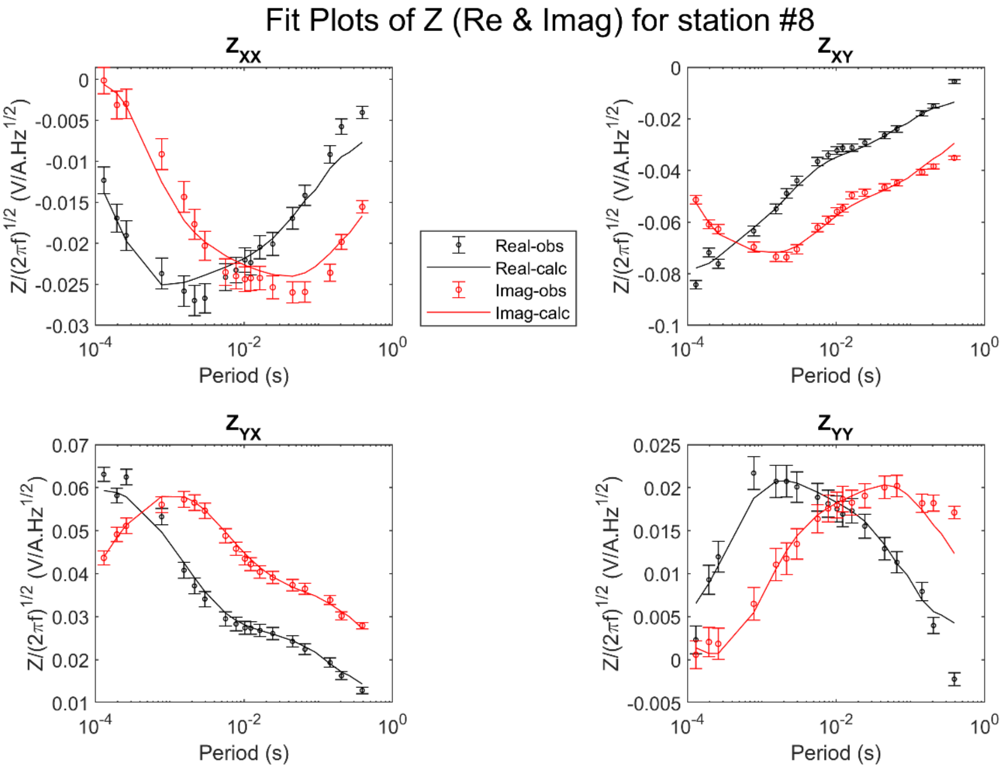
Fit Plots of Z (Re & Imag) for station #8
Z_XX
Z_XY
Z_YX
Z_YY
Z/(2πf)^1/2 (V/A.Hz^1/2)
Period (s)
Real-obs
Real-calc
Imag-obs
Imag-calc

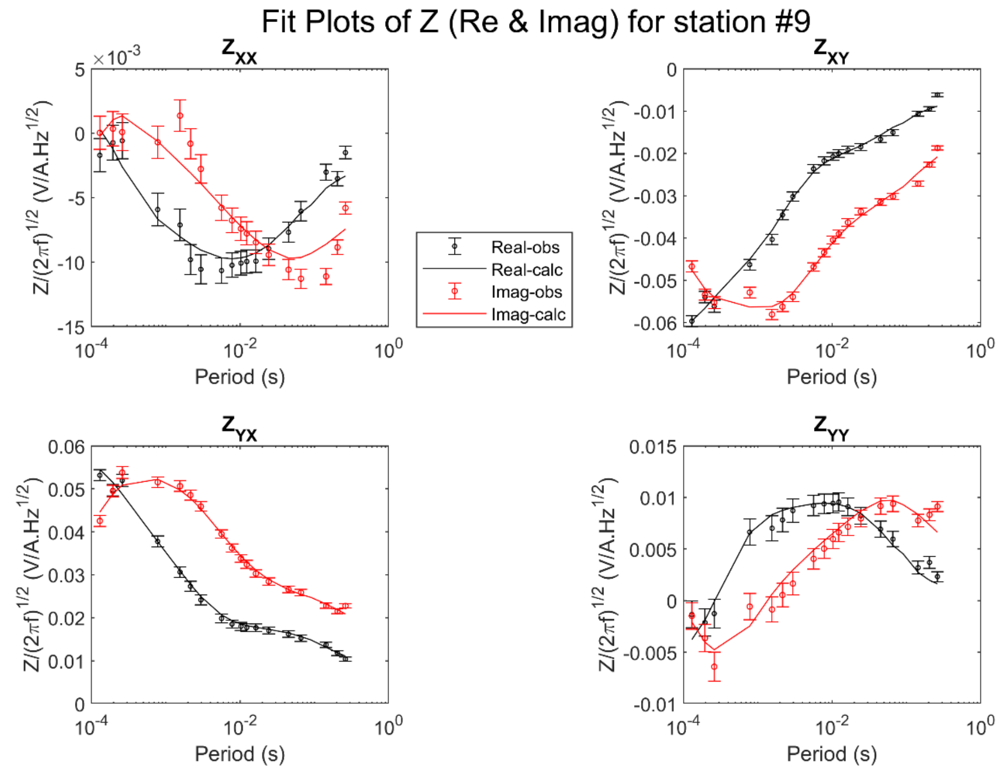
Fit Plots of Z (Re & Imag) for station #9
Z_XX
Z_XY
Z_YX
Z_YY
Z/(2πf)^1/2 (V/A.Hz^1/2)
Period (s)
Real-obs
Real-calc
Imag-obs
Imag-calc

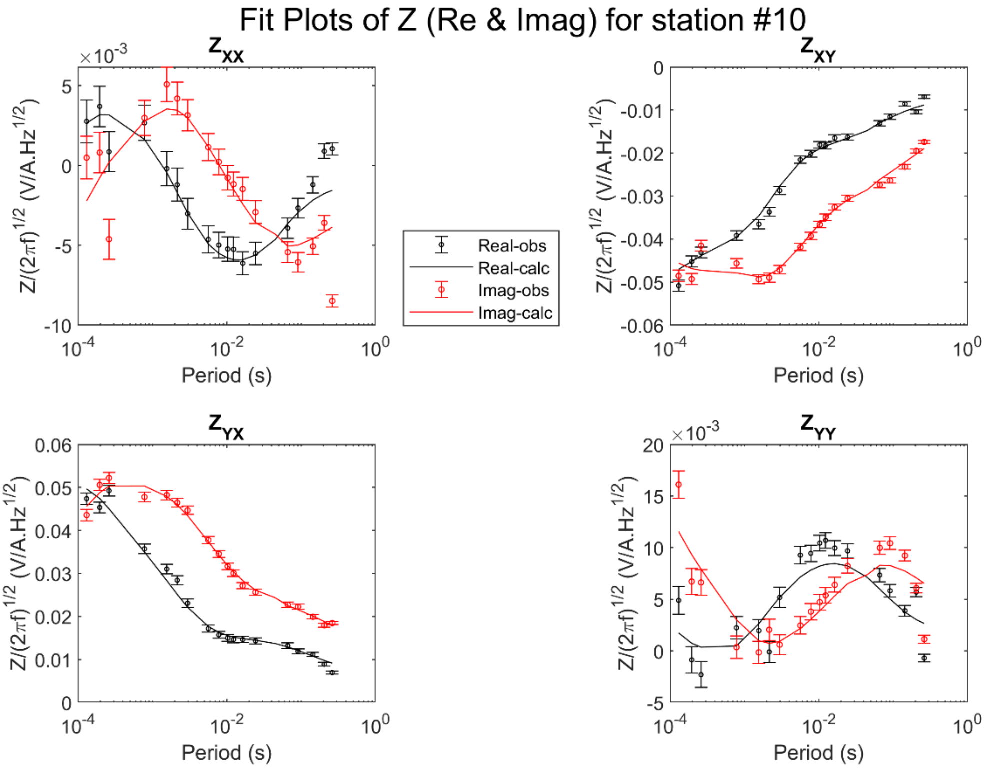
Fit Plots of Z (Re & Imag) for station #10
Z_XX
Z_XY
Z_YX
Z_YY
Real-obs
Real-calc
Imag-obs
Imag-calc
Z/(2πf)^1/2 (V/A.Hz^1/2)
Period (s)

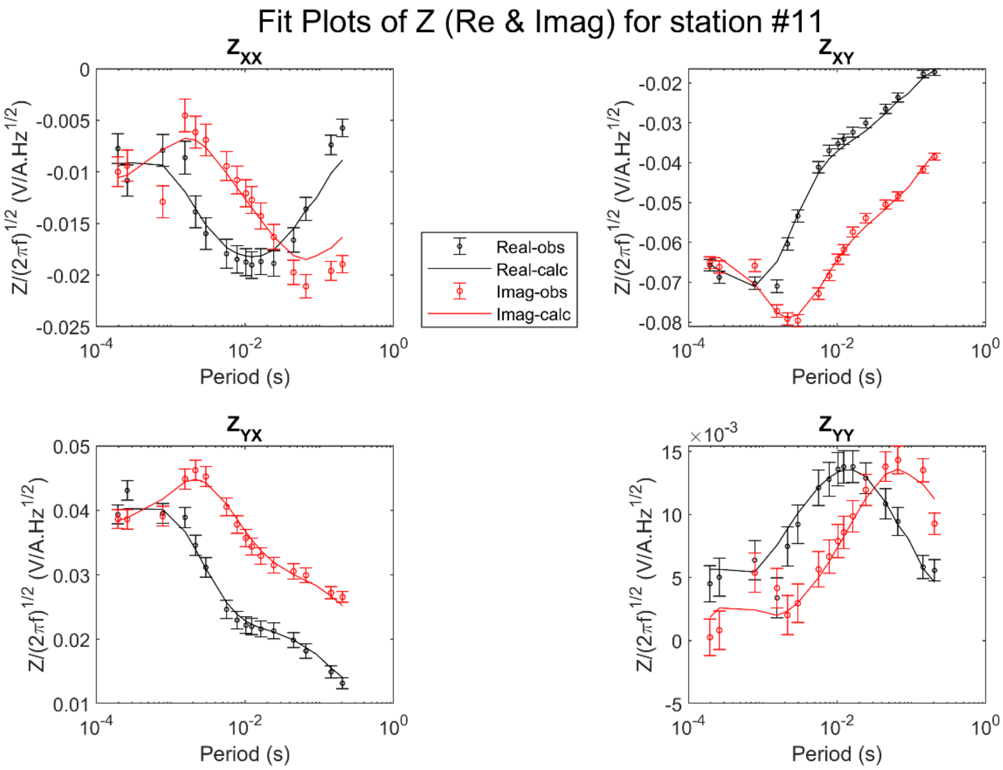
Fit Plots of Z (Re & Imag) for station #11
Z_XX
Z_XY
Z_YX
Z_YY
Real-obs
Real-calc
Imag-obs
Imag-calc
Z/(2πf)^1/2 (V/A.Hz^1/2)
Period (s)

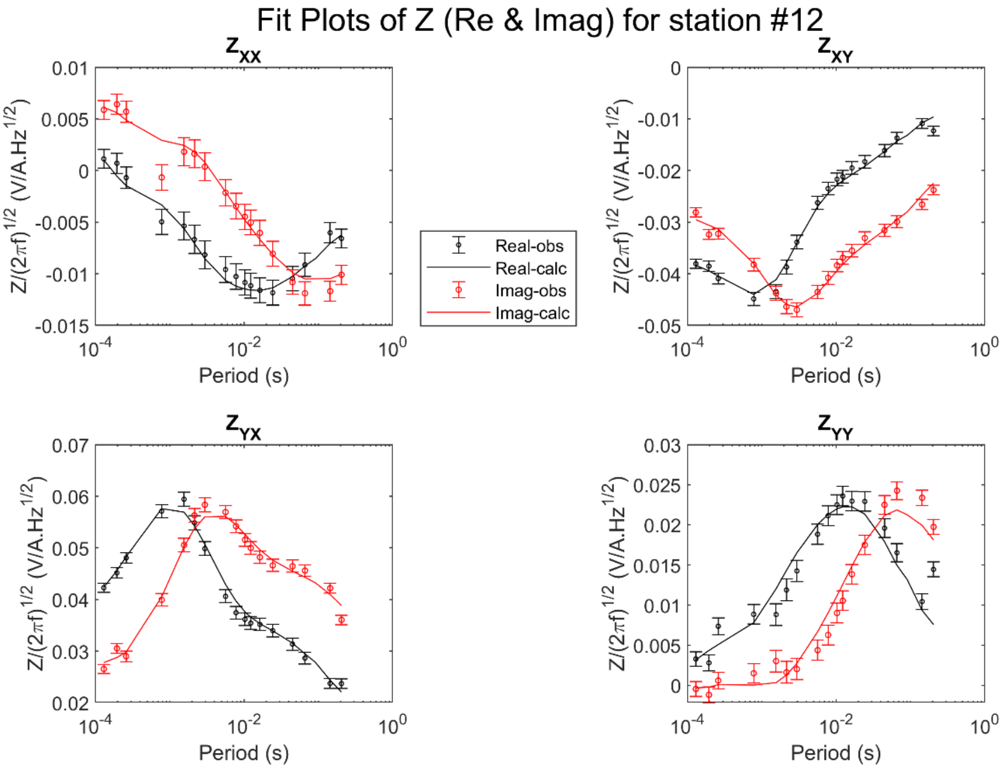
Fit Plots of Z (Re & Imag) for station #12
Z_XX
Z_XY
Z_YX
Z_YY
Z/(2πf)^1/2 (V/A.Hz^1/2)
Period (s)
Real-obs
Real-calc
Imag-obs
Imag-calc

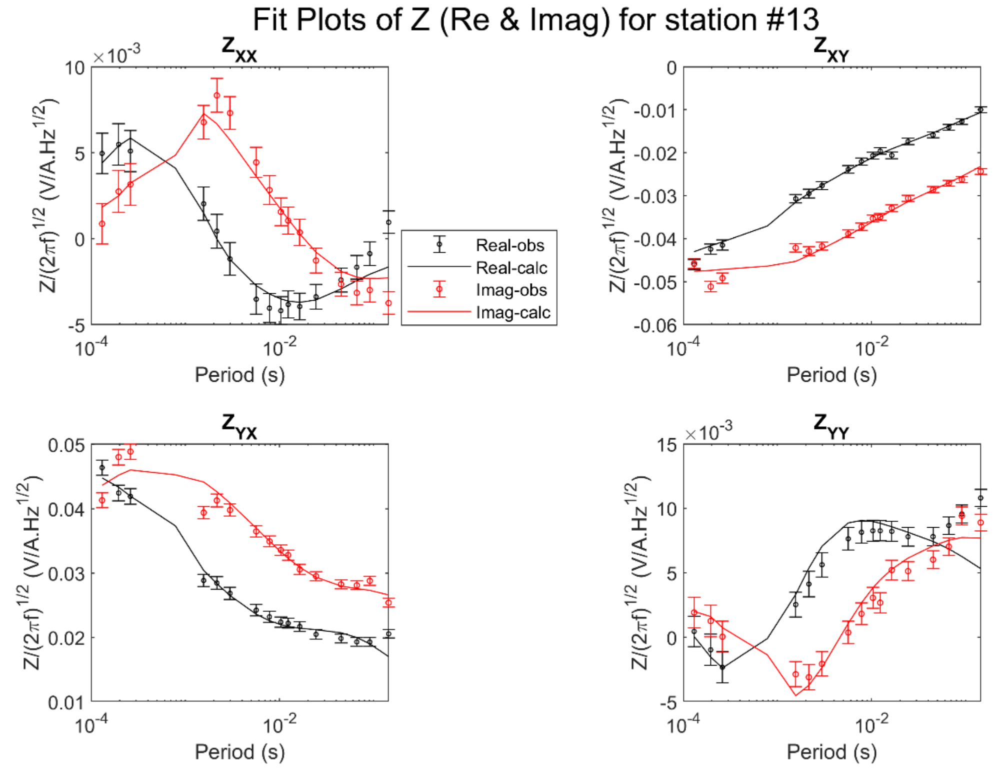
Fit Plots of Z (Re & Imag) for station #13
Z_XX
Z_XY
Z_YX
Z_YY
Z/(2πf)^1/2 (V/A.Hz^1/2)
Period (s)
Real-obs
Real-calc
Imag-obs
Imag-calc

Fit Plots of Z (Re & Imag) for station #14

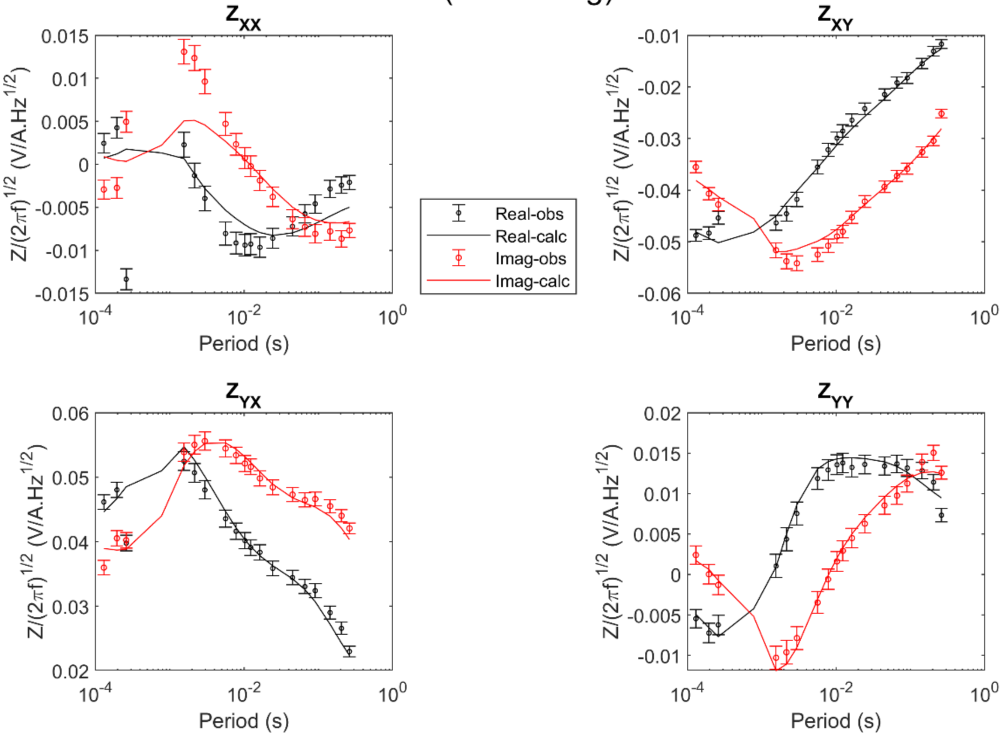

Fit Plots of Z (Re & Imag) for station #15

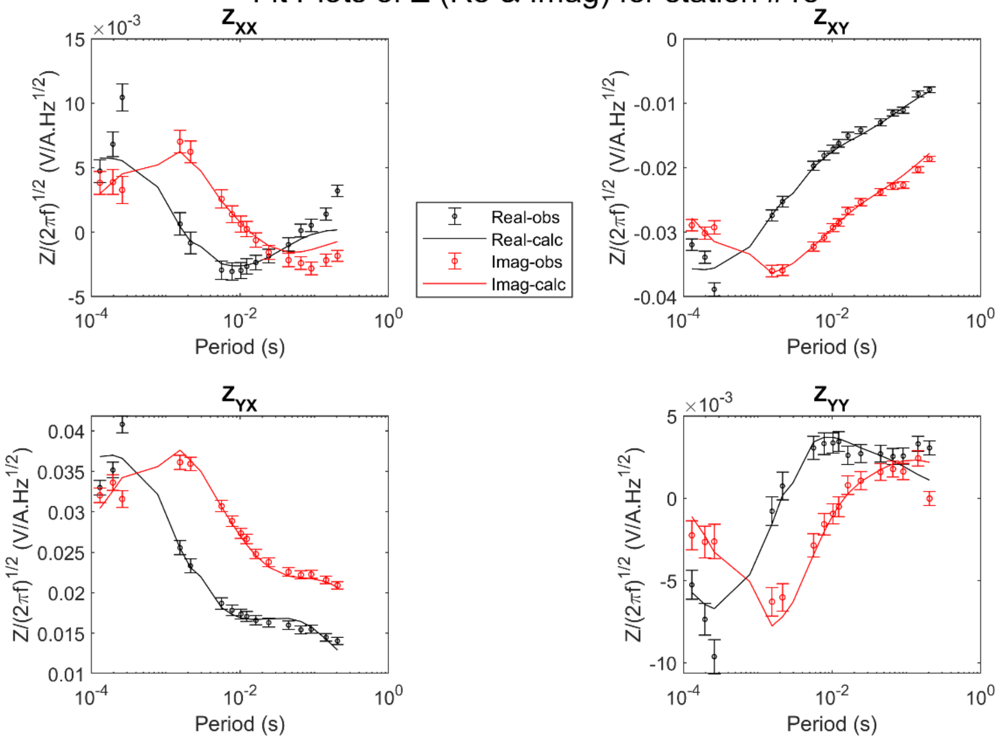

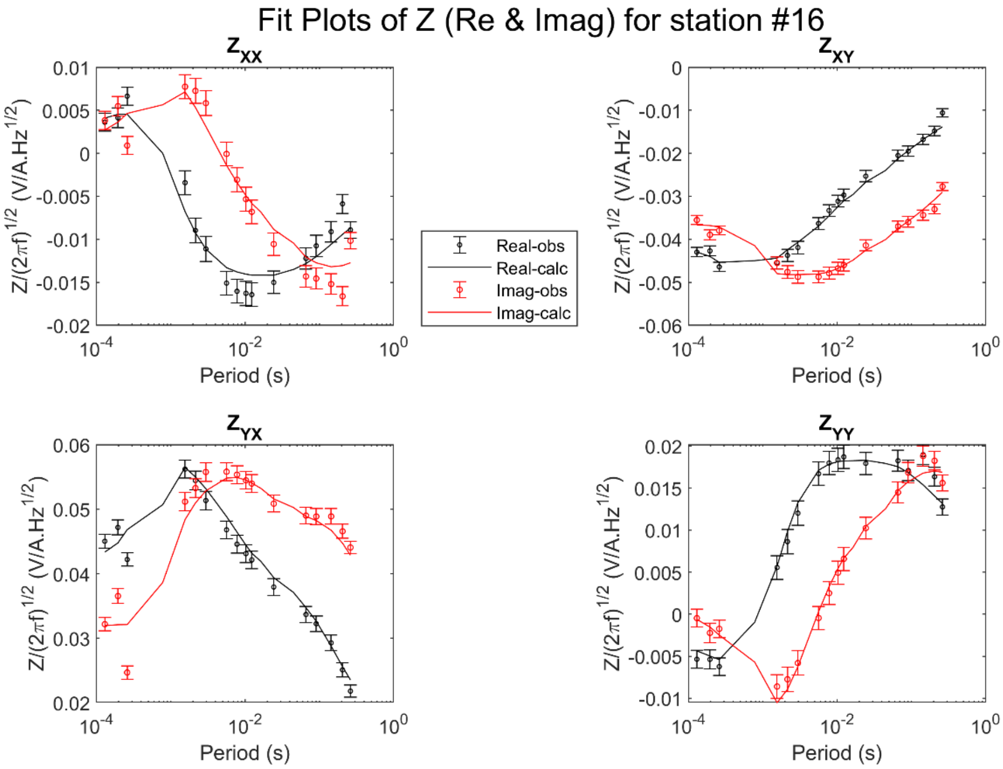
Fit Plots of Z (Re & Imag) for station #16
ZXX
ZXY
ZYX
ZYY
Z/(2πf)^1/2 (V/A.Hz^1/2)
Period (s)
Real-obs
Real-calc
Imag-obs
Imag-calc

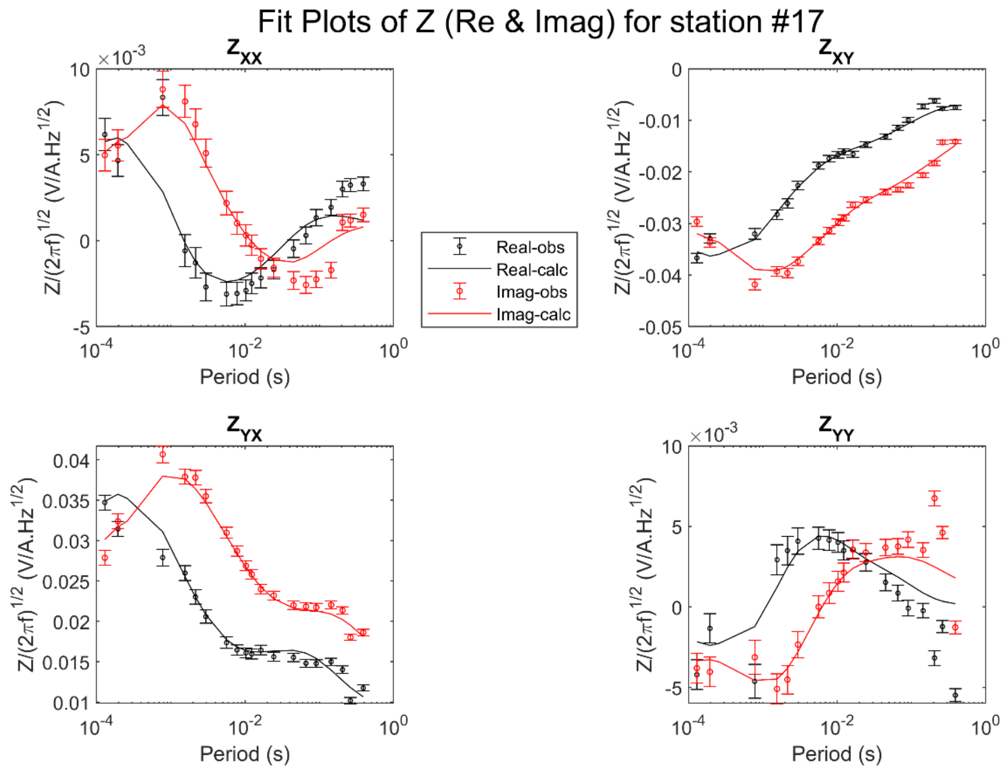
Fit Plots of Z (Re & Imag) for station #17
ZXX
ZXY
ZYX
ZYY
Z/(2πf)^1/2 (V/A.Hz^1/2)
Period (s)
Real-obs
Real-calc
Imag-obs
Imag-calc

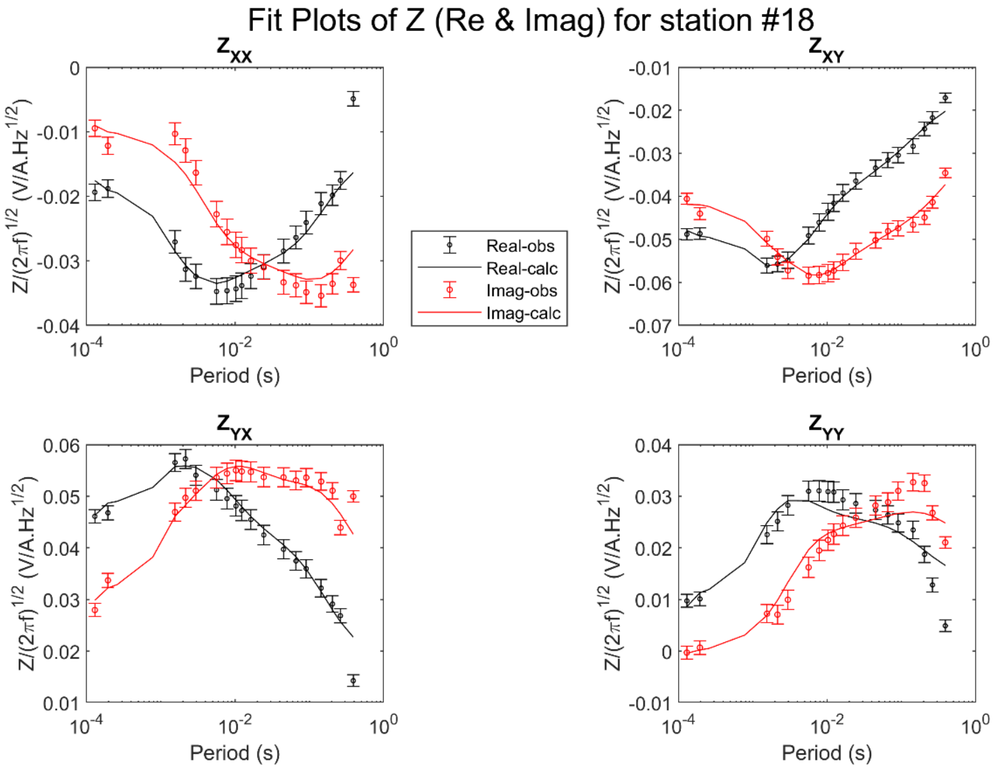
Fit Plots of Z (Re & Imag) for station #18
Z_XX
Z_XY
Z_YX
Z_YY
Z/(2πf)^1/2 (V/A.Hz^1/2)
Period (s)
Real-obs
Real-calc
Imag-obs
Imag-calc

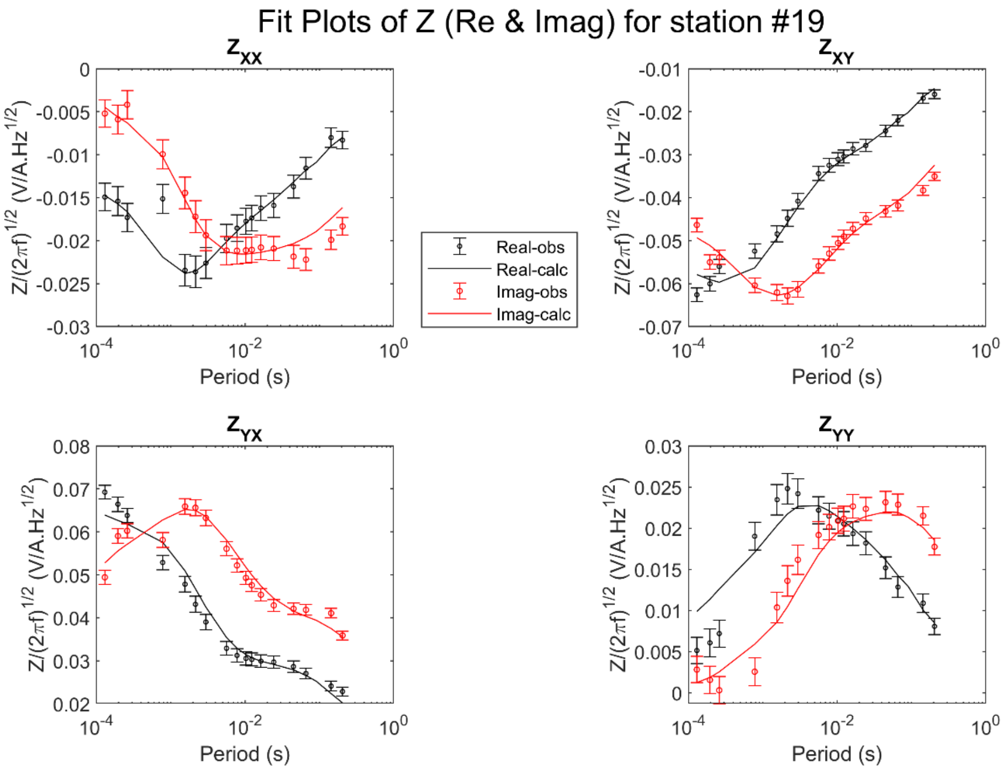
Fit Plots of Z (Re & Imag) for station #19
Z_XX
Z_XY
Z_YX
Z_YY
Z/(2πf)^1/2 (V/A.Hz^1/2)
Period (s)
Real-obs
Real-calc
Imag-obs
Imag-calc

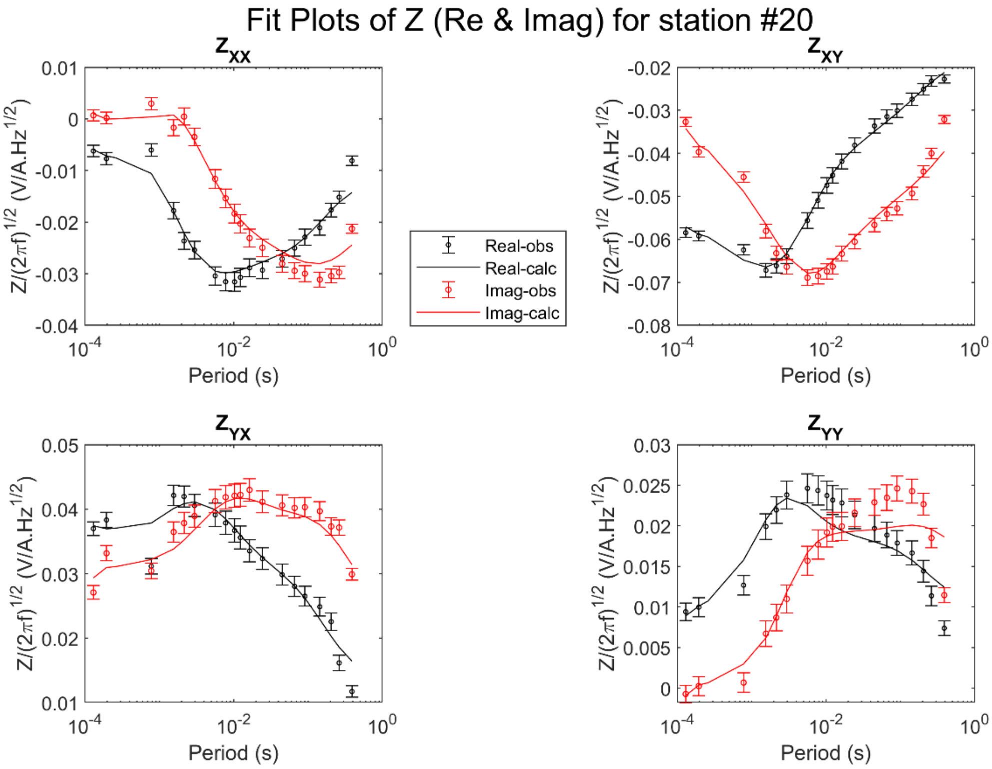
Fit Plots of Z (Re & Imag) for station #20
Z_XX
Z_XY
Z_YX
Z_YY
Z/(2πf)^1/2 (V/A.Hz^1/2)
Period (s)
Real-obs
Real-calc
Imag-obs
Imag-calc

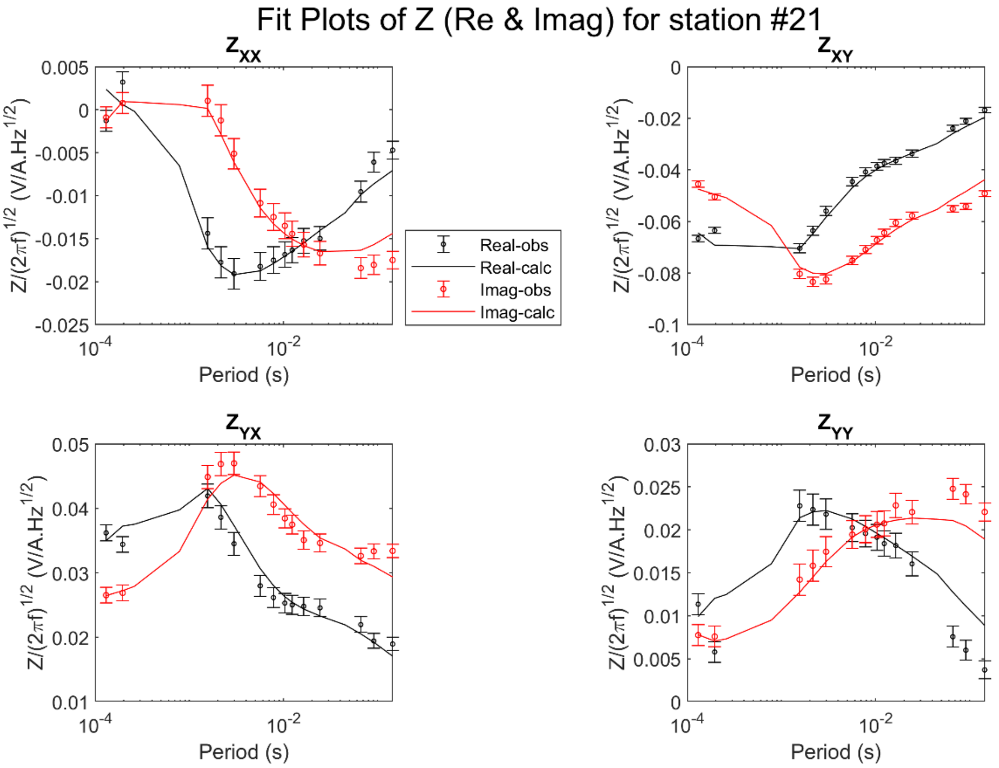
Fit Plots of Z (Re & Imag) for station #21
Z_XX
Z_XY
Z_YX
Z_YY
Z/(2πf)^1/2 (V/A.Hz^1/2)
Period (s)
Real-obs
Real-calc
Imag-obs
Imag-calc

Fit Plots of Z (Re & Imag) for station #22

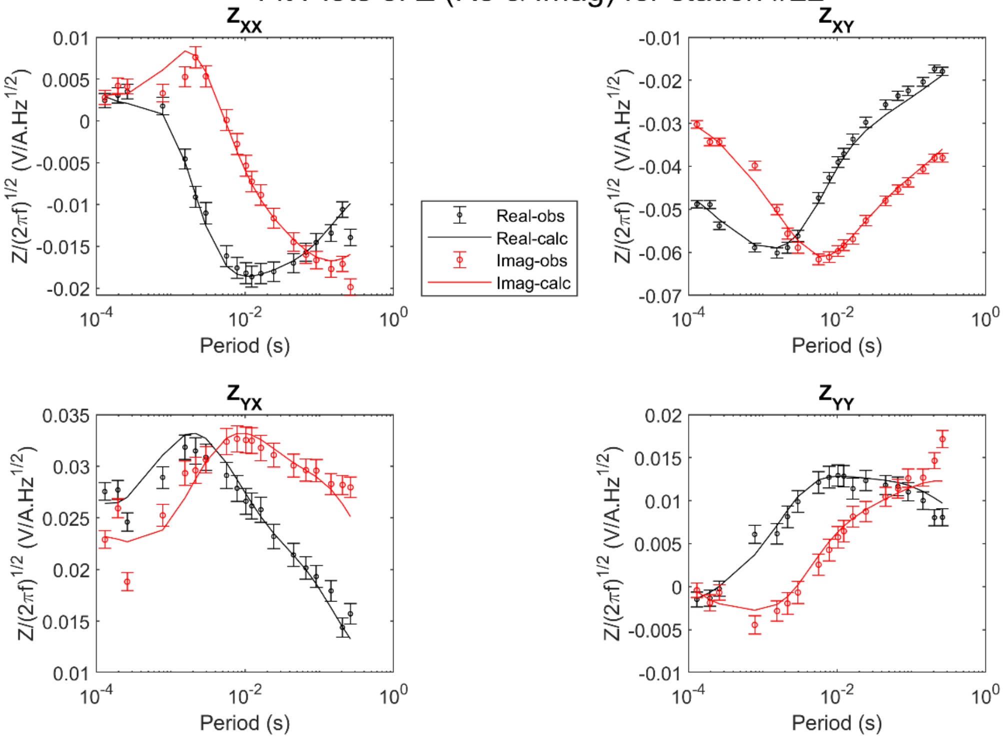

Fit Plots of Z (Re & Imag) for station #23

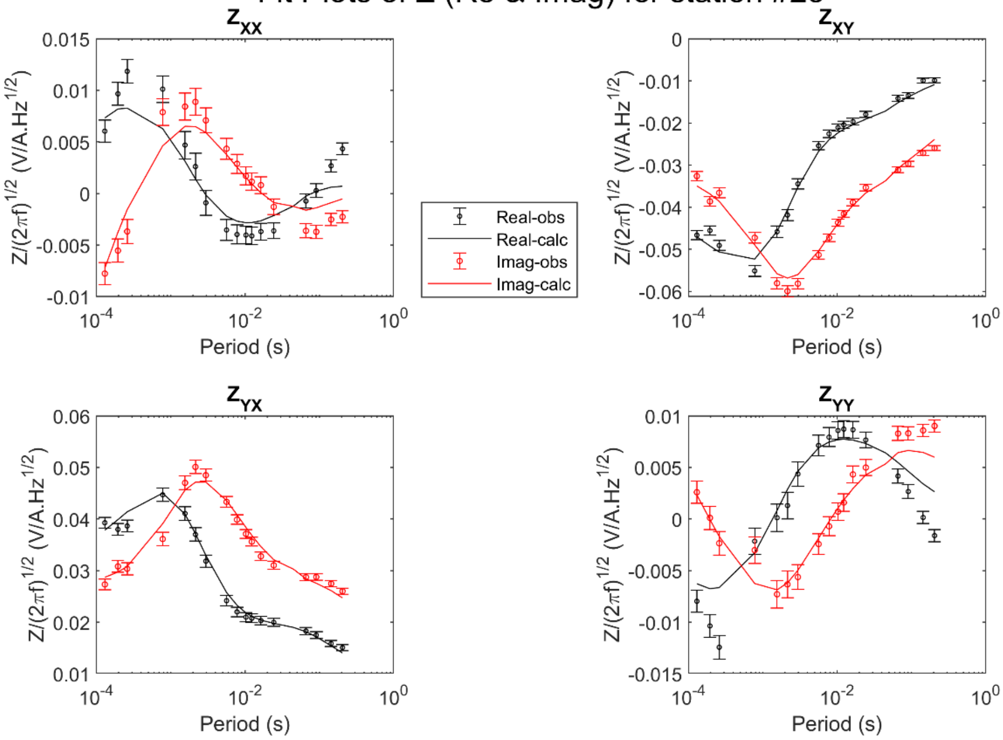

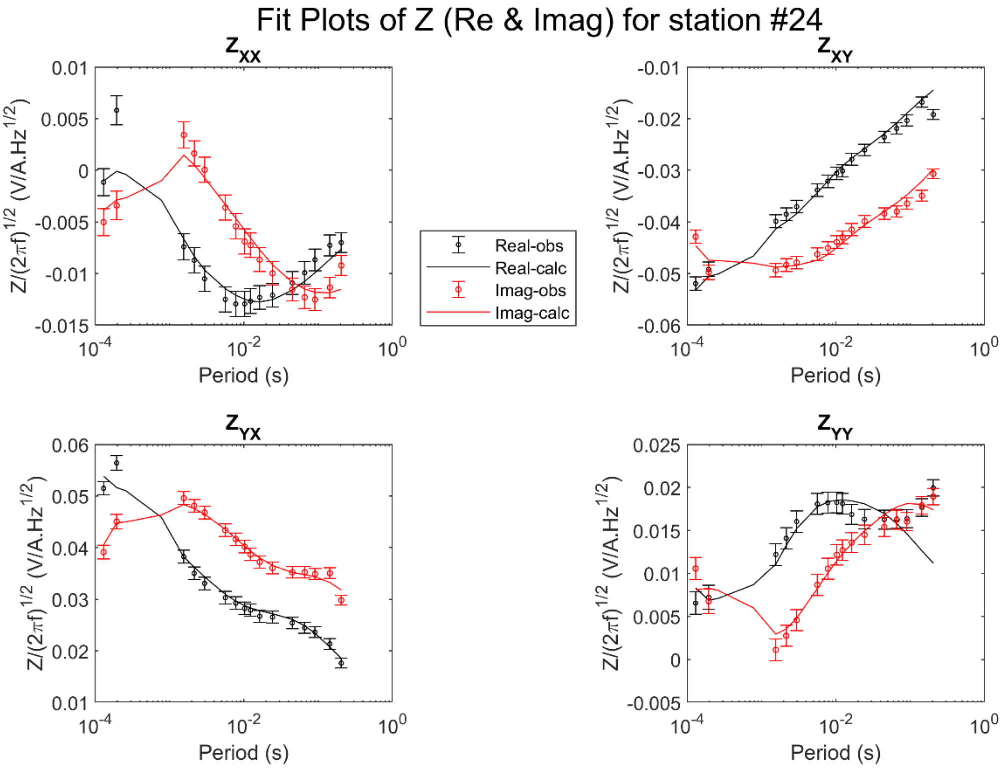
Fit Plots of Z (Re & Imag) for station #24
Z_XX
Z_XY
Z_YX
Z_YY
Z/(2πf)^1/2 (V/A.Hz^1/2)
Period (s)
Real-obs
Real-calc
Imag-obs
Imag-calc

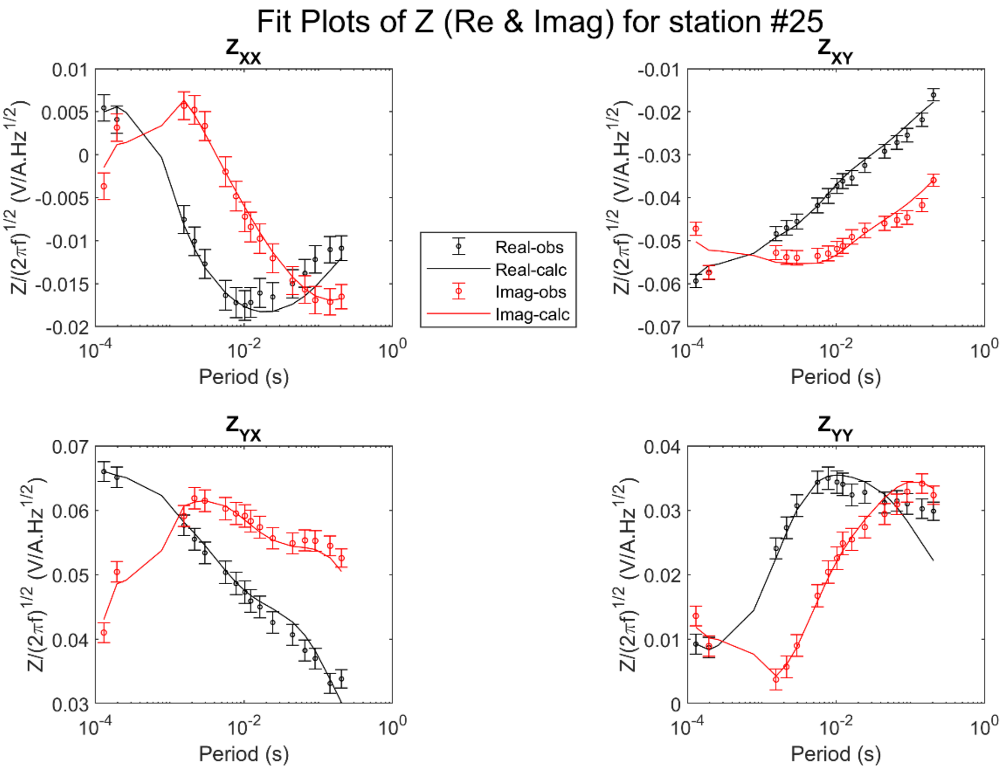
Fit Plots of Z (Re & Imag) for station #25
Z_XX
Z_XY
Z_YX
Z_YY
Z/(2πf)^1/2 (V/A.Hz^1/2)
Period (s)
Real-obs
Real-calc
Imag-obs
Imag-calc

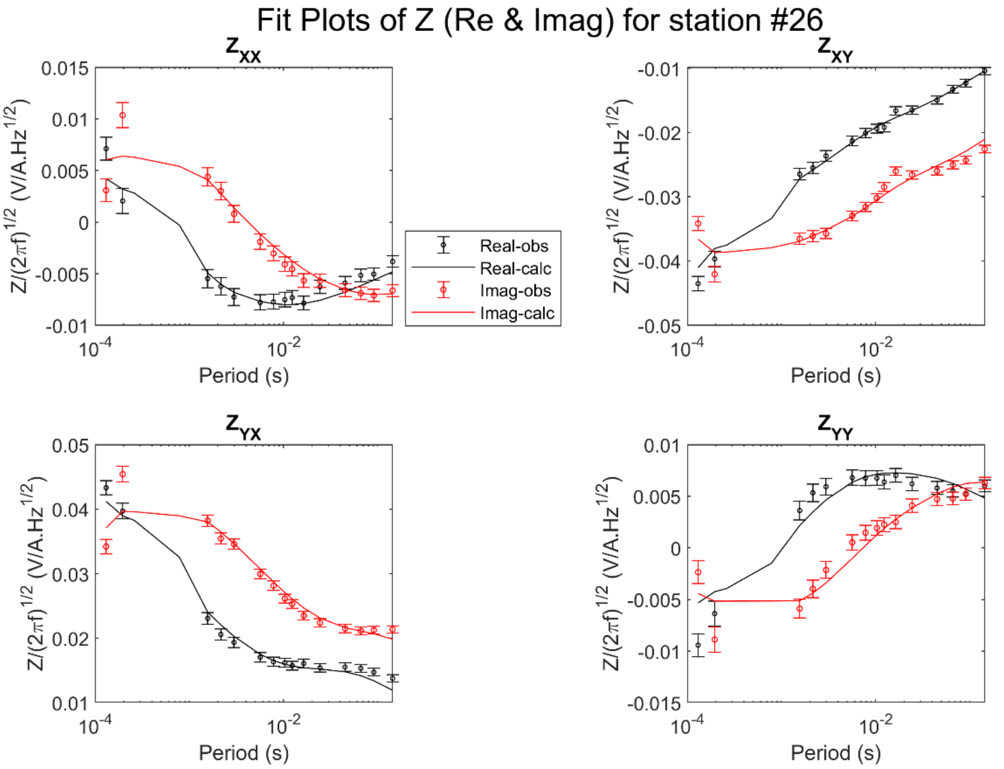

Fit Plots of Z (Re & Imag) for station #26
Z_XX
Z_XY
Z_YX
Z_YY
Z/(2πf)^1/2 (V/A.Hz^1/2)
Period (s)
Real-obs
Real-calc
Imag-obs
Imag-calc

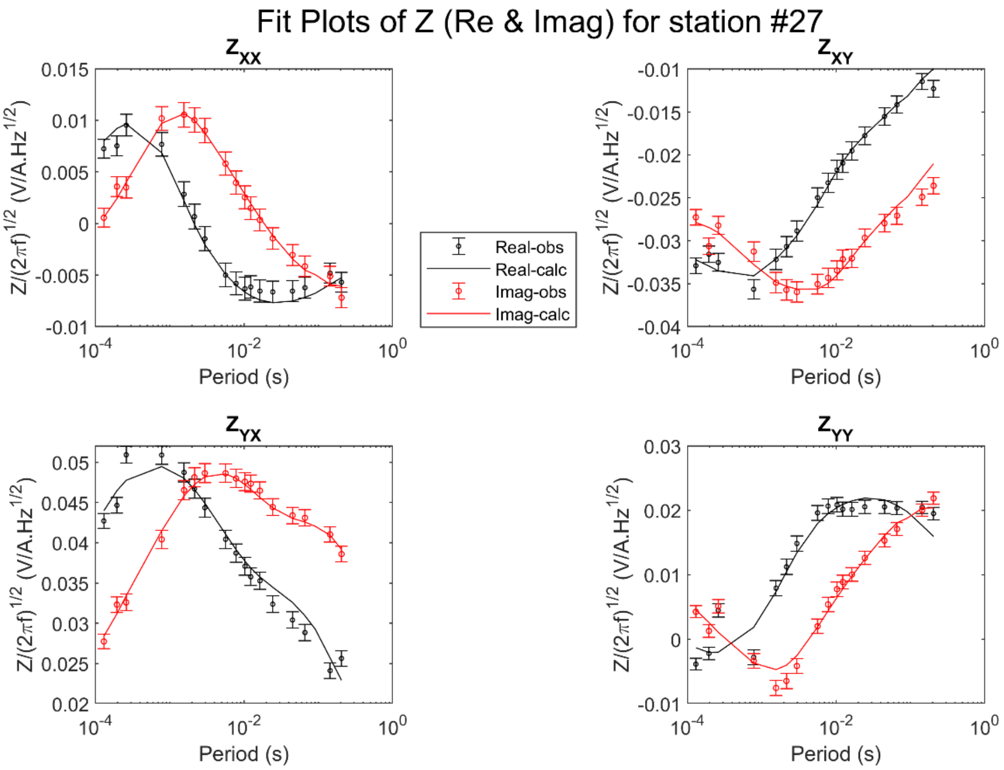

Fit Plots of Z (Re & Imag) for station #27
Z_XX
Z_XY
Z_YX
Z_YY
Z/(2πf)^1/2 (V/A.Hz^1/2)
Period (s)
Real-obs
Real-calc
Imag-obs
Imag-calc

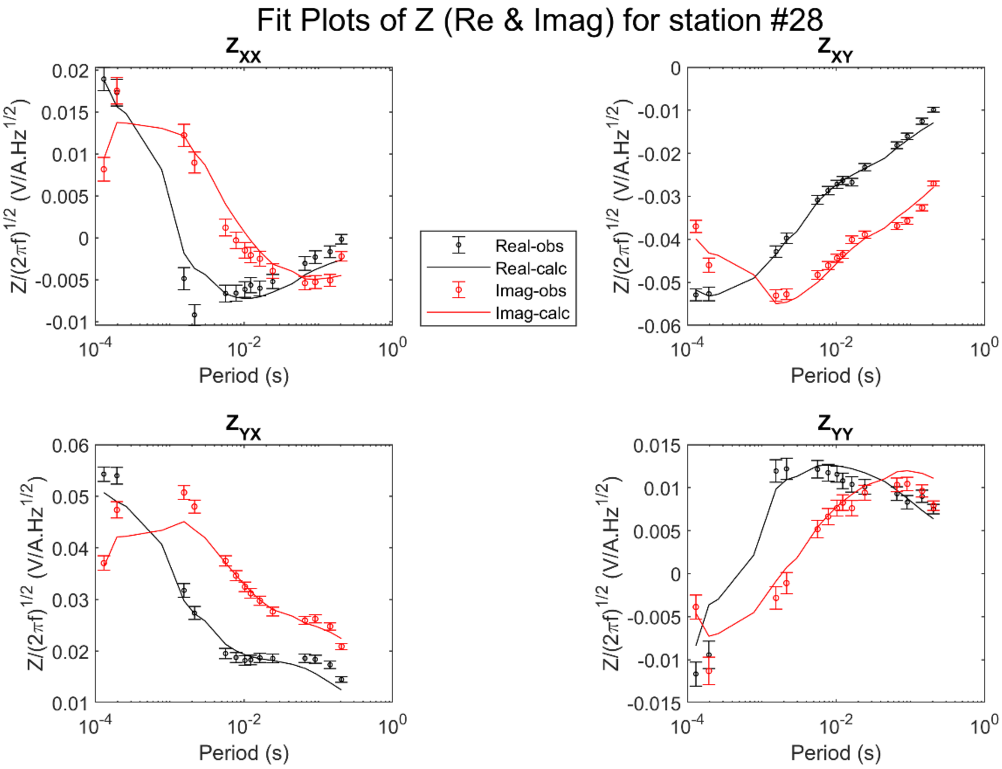
Fit Plots of Z (Re & Imag) for station #28
ZXX
ZXY
ZYX
ZYY
Z/(2πf)^1/2 (V/A.Hz^1/2)
Period (s)
Real-obs
Real-calc
Imag-obs
Imag-calc

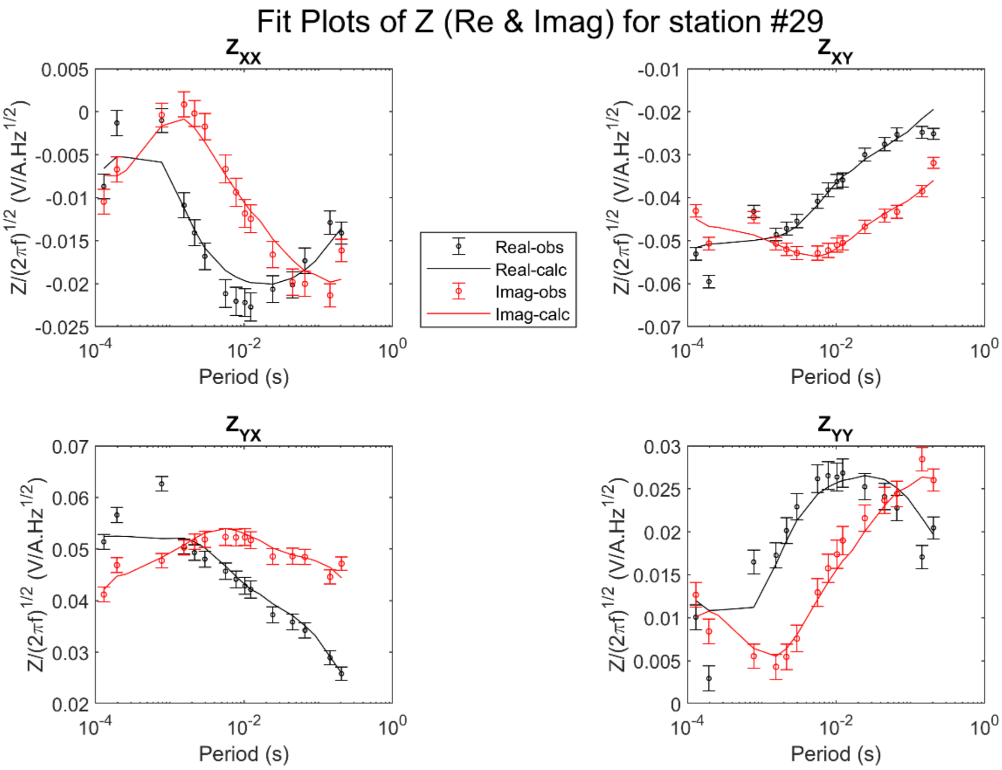
Fit Plots of Z (Re & Imag) for station #29
ZXX
ZXY
ZYX
ZYY
Z/(2πf)^1/2 (V/A.Hz^1/2)
Period (s)
Real-obs
Real-calc
Imag-obs
Imag-calc

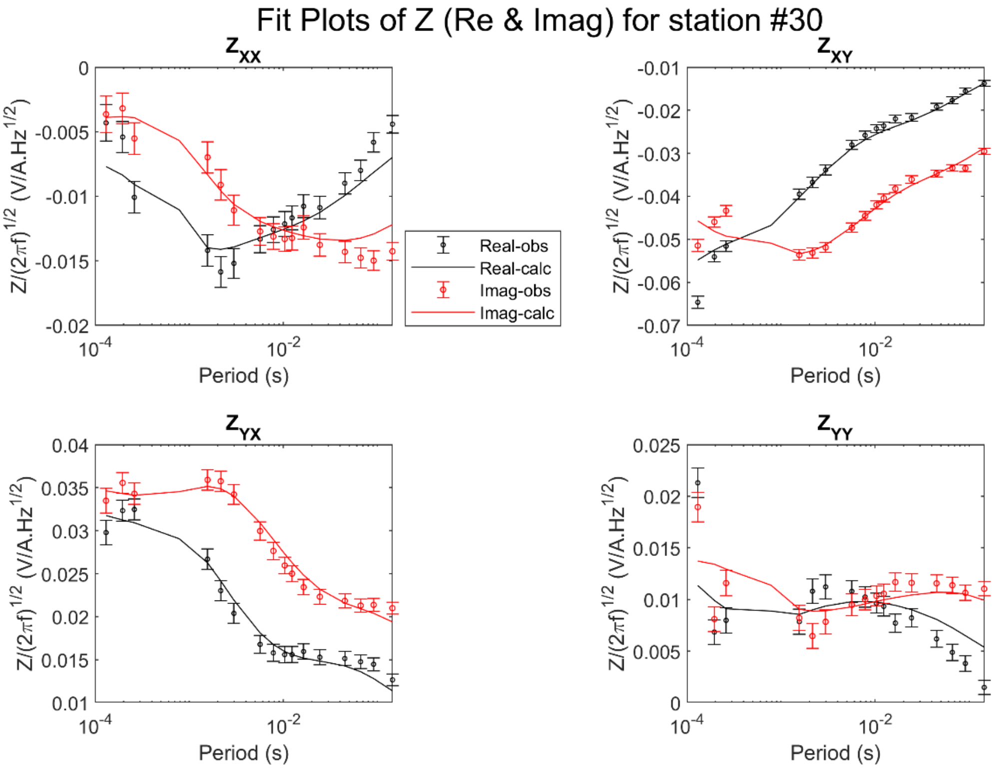
Fit Plots of Z (Re & Imag) for station #30
Z_XX
Z_XY
Z_YX
Z_YY
Z/(2πf)^1/2 (V/A.Hz^1/2)
Period (s)
Real-obs
Real-calc
Imag-obs
Imag-calc

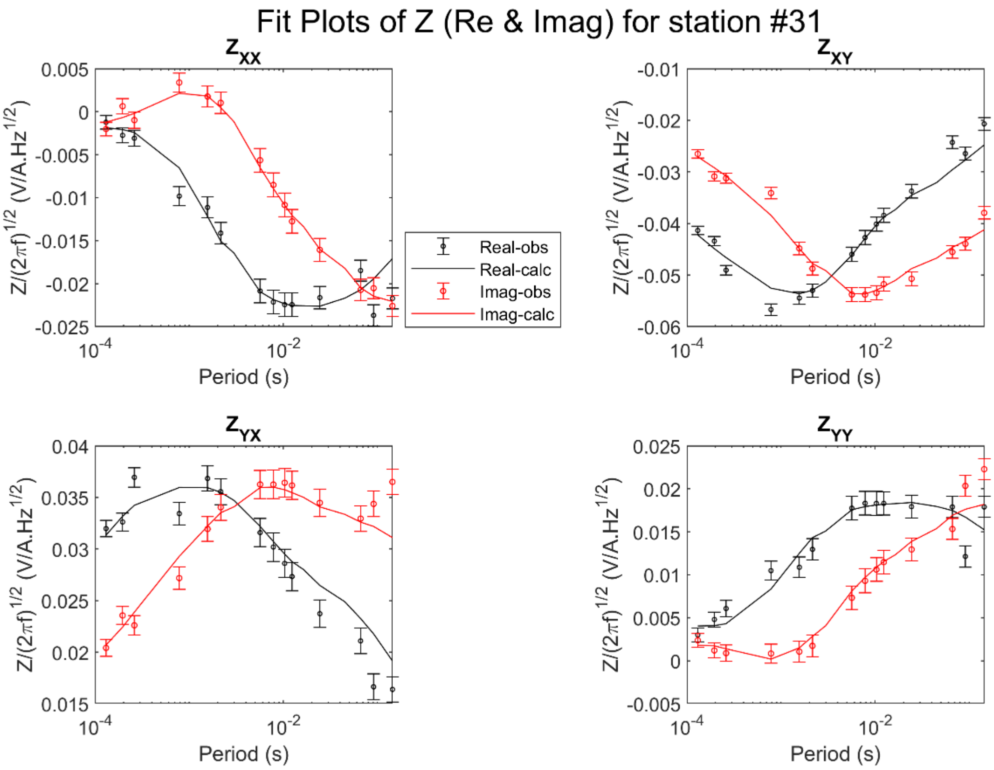
Fit Plots of Z (Re & Imag) for station #31
Z_XX
Z_XY
Z_YX
Z_YY
Z/(2πf)^1/2 (V/A.Hz^1/2)
Period (s)
Real-obs
Real-calc
Imag-obs
Imag-calc

Fit Plots of Z (Re & Imag) for station #32

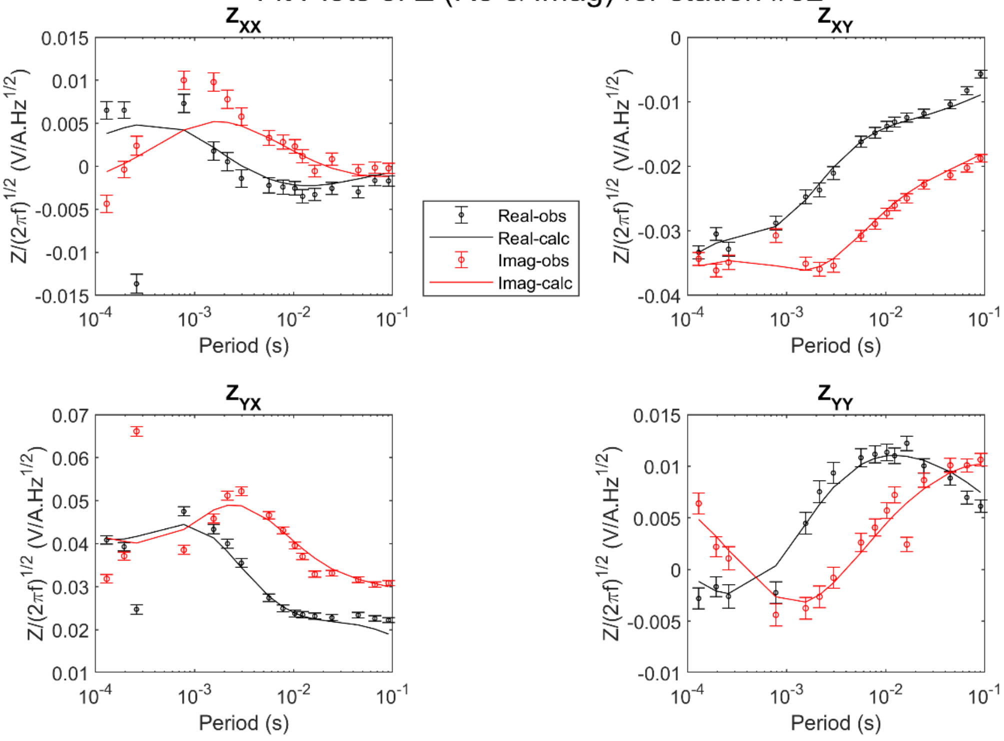

Fit Plots of Z (Re & Imag) for station #33

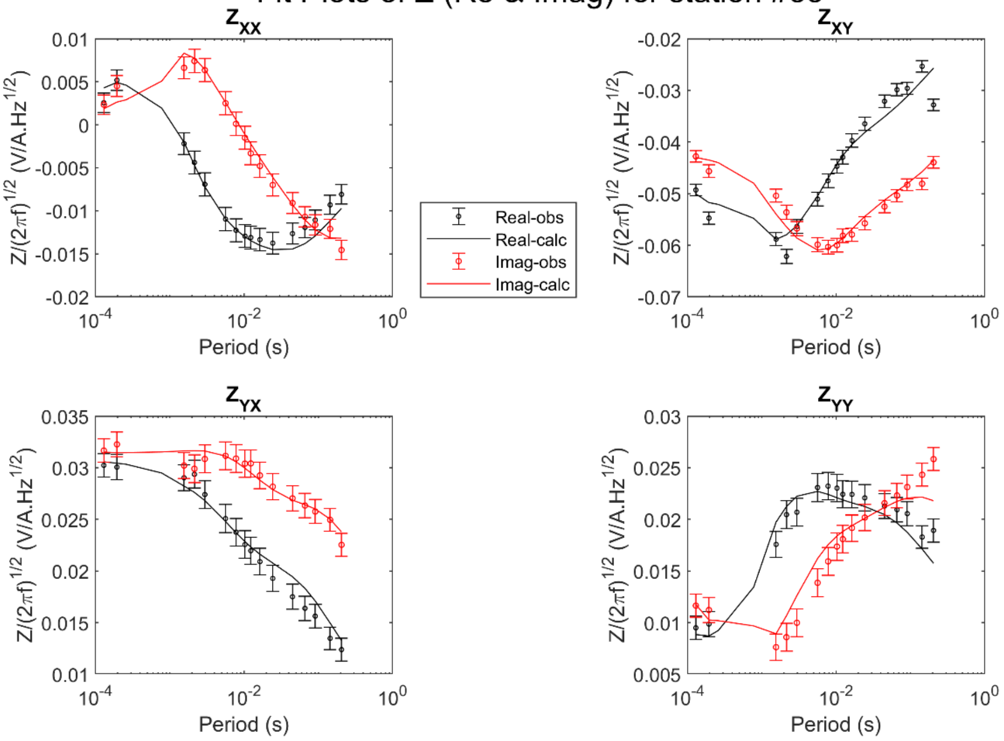

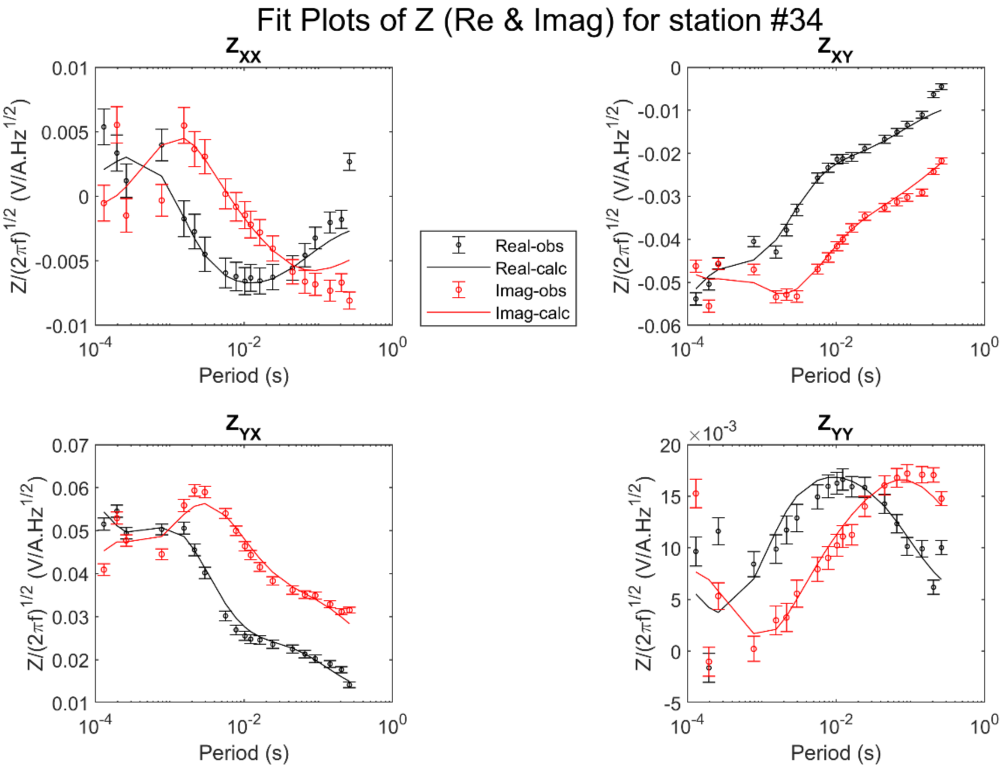
Fit Plots of Z (Re & Imag) for station #34
Z_{XX}
Z_{XY}
Z_{YX}
Z_{YY}
$Z/(2\pi f)^{1/2}$ (V/A.Hz$^{1/2}$)
Period (s)
Real-obs
Real-calc
Imag-obs
Imag-calc

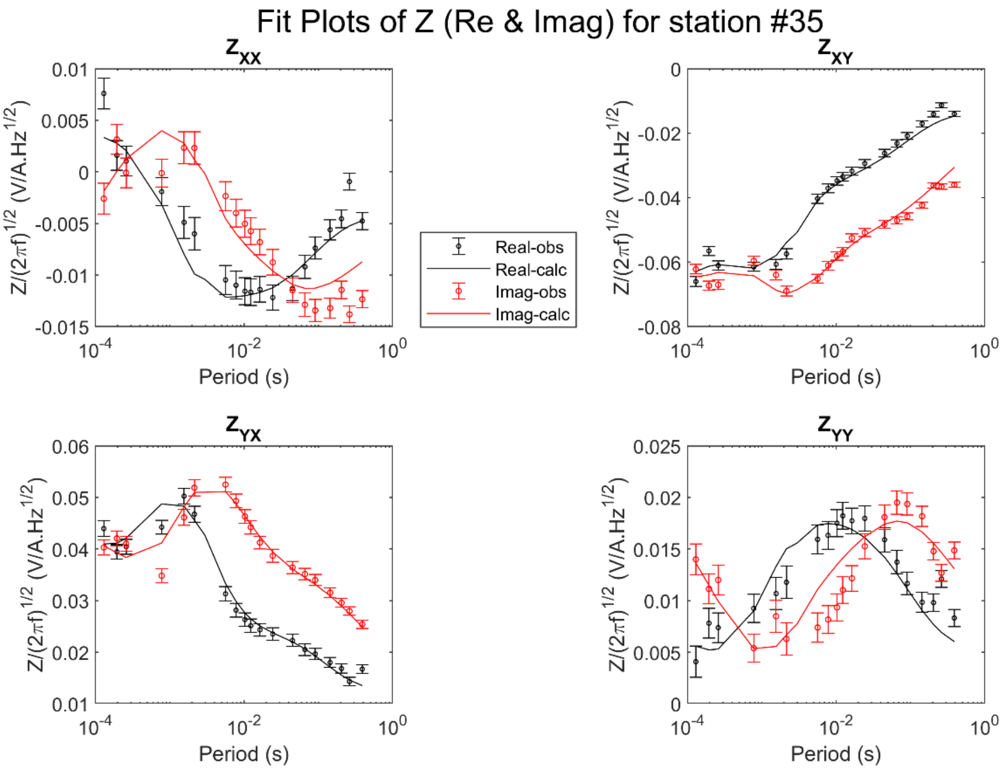
Fit Plots of Z (Re & Imag) for station #35
Z_{XX}
Z_{XY}
Z_{YX}
Z_{YY}
$Z/(2\pi f)^{1/2}$ (V/A.Hz$^{1/2}$)
Period (s)
Real-obs
Real-calc
Imag-obs
Imag-calc

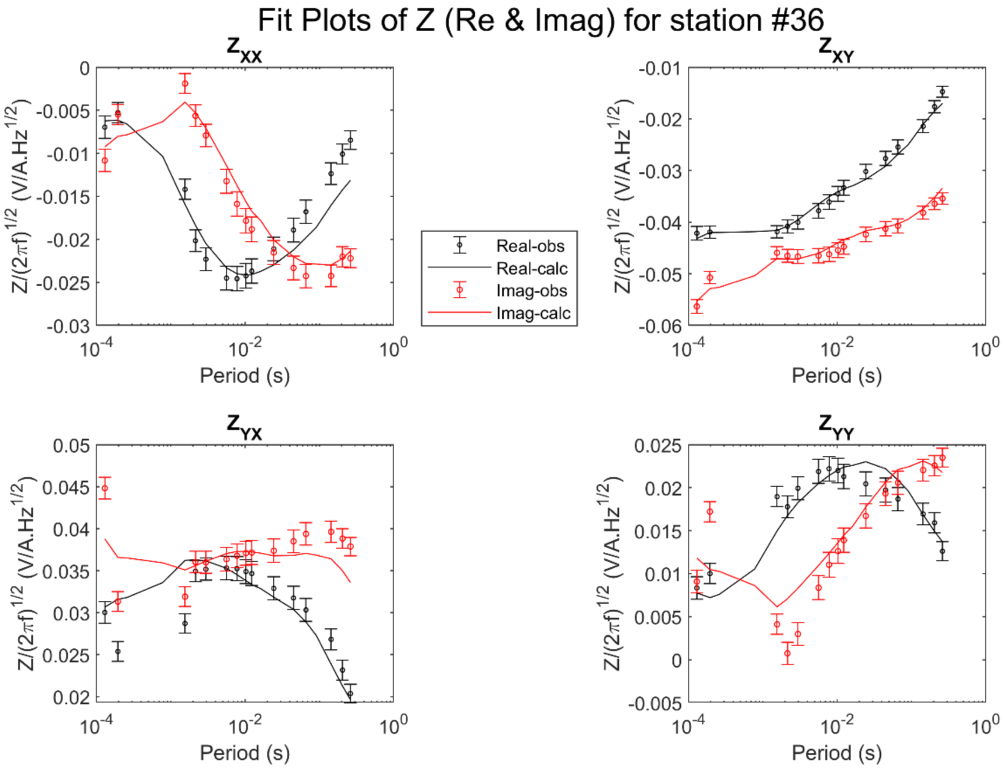

Fit Plots of Z (Re & Imag) for station #36
Z_{XX}
Z_{XY}
Z_{YX}
Z_{YY}
$Z/(2\pi f)^{1/2}$ (V/A.Hz$^{1/2}$)
Period (s)
Real-obs
Real-calc
Imag-obs
Imag-calc

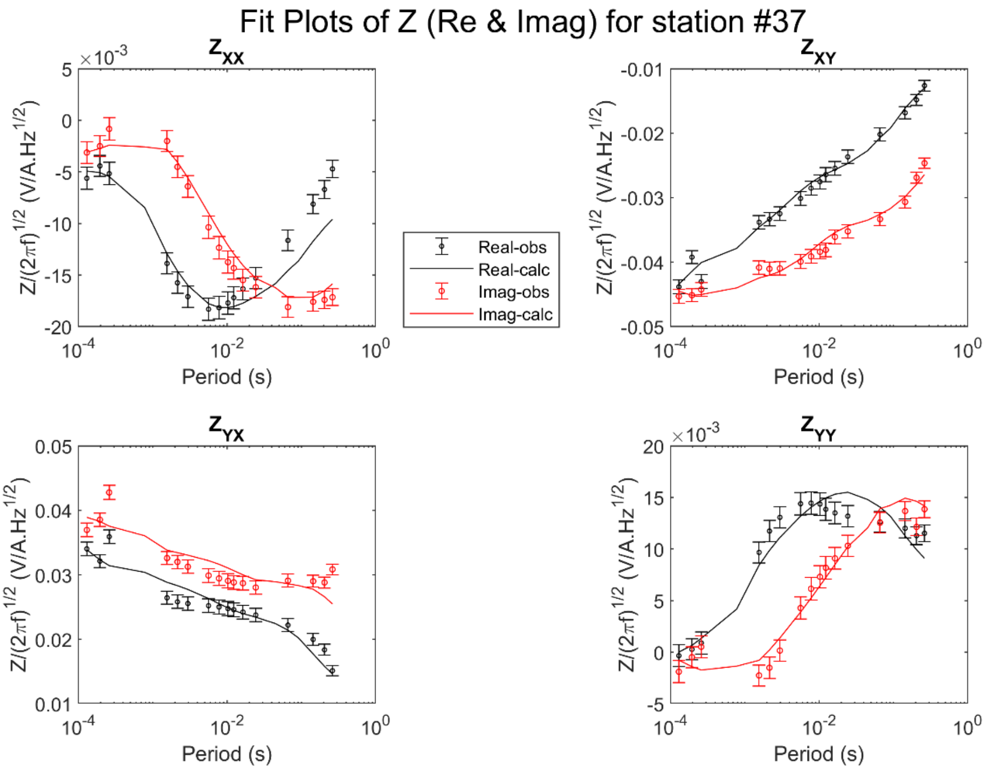

Fit Plots of Z (Re & Imag) for station #37
Z_{XX}
Z_{XY}
Z_{YX}
Z_{YY}
$\times 10^{-3}$
$Z/(2\pi f)^{1/2}$ (V/A.Hz$^{1/2}$)
Period (s)
Real-obs
Real-calc
Imag-obs
Imag-calc

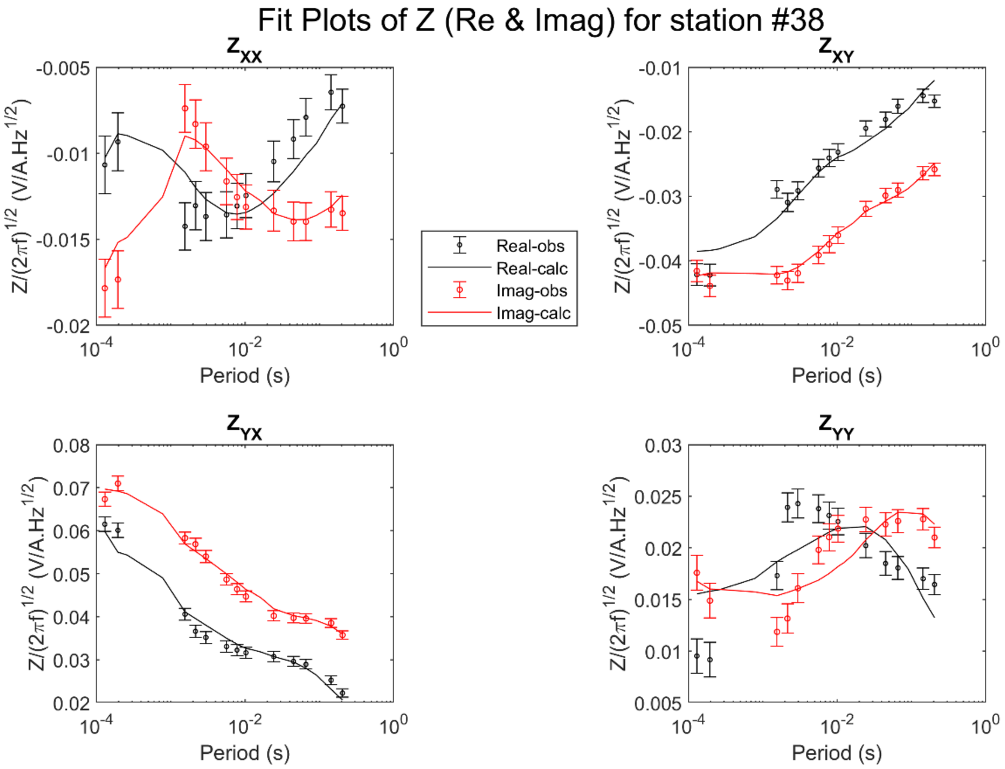
Fit Plots of Z (Re & Imag) for station #38
Z_XX
Z_XY
Z_YX
Z_YY
Z/(2πf)^1/2 (V/A.Hz^1/2)
Period (s)
Real-obs
Real-calc
Imag-obs
Imag-calc

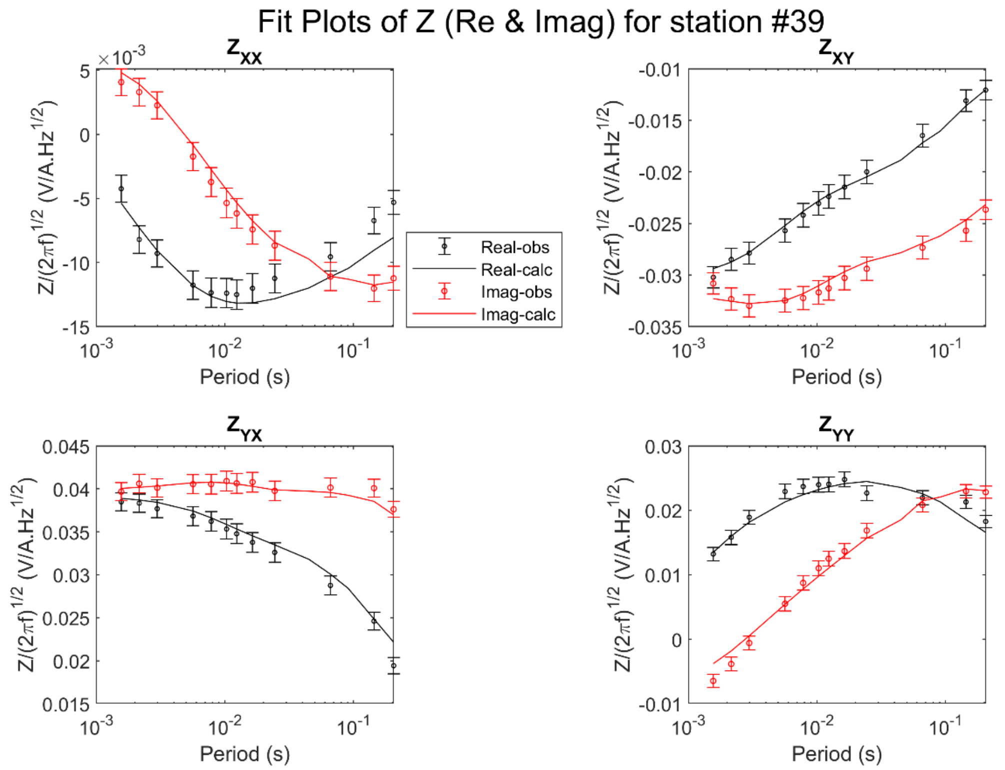
Fit Plots of Z (Re & Imag) for station #39
Z_XX
Z_XY
Z_YX
Z_YY
Z/(2πf)^1/2 (V/A.Hz^1/2)
Period (s)
Real-obs
Real-calc
Imag-obs
Imag-calc

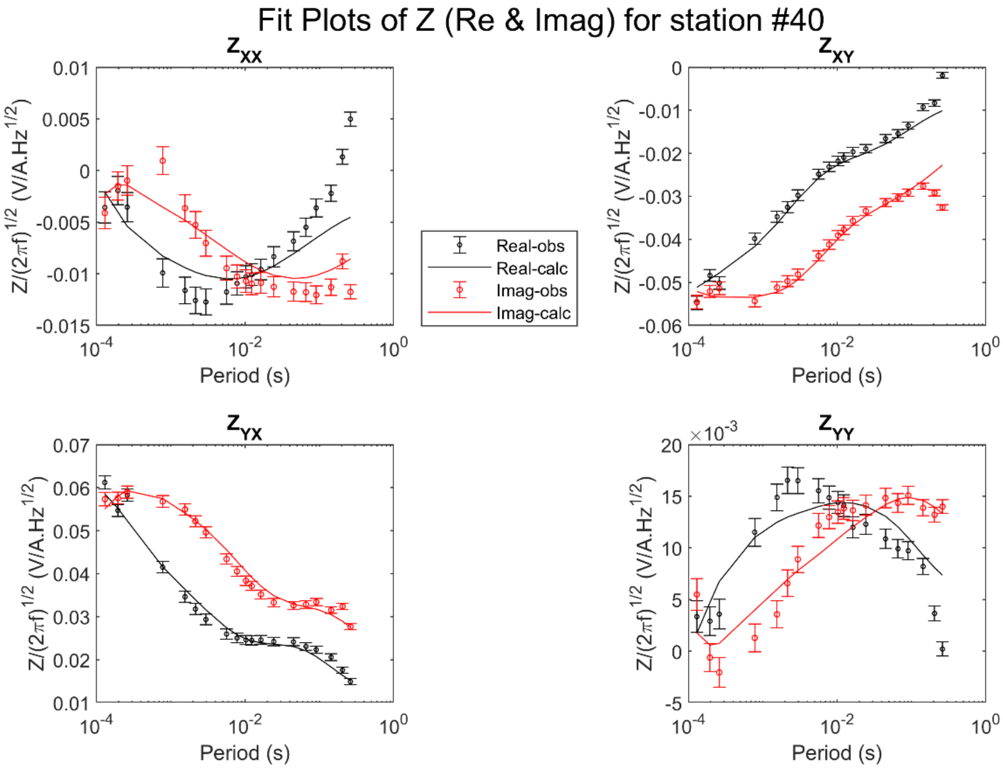

Fit Plots of Z (Re & Imag) for station #40
Z_XX
Z_XY
Z_YX
Z_YY
Real-obs
Real-calc
Imag-obs
Imag-calc
Z/(2πf)^1/2 (V/A.Hz^1/2)
Period (s)

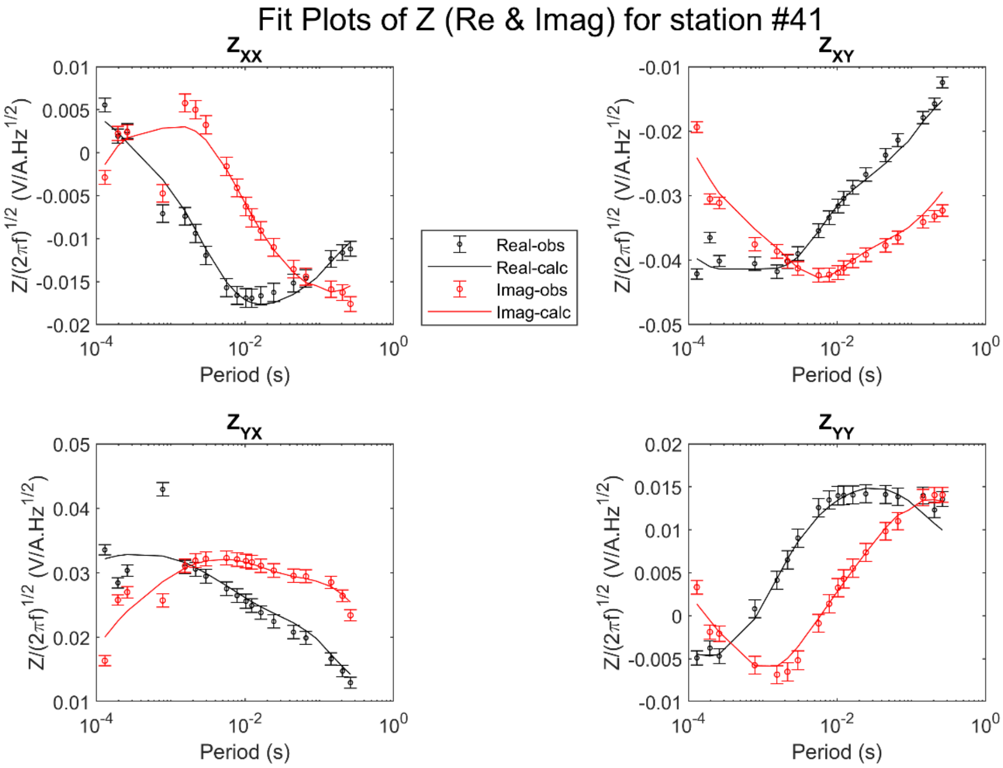

Fit Plots of Z (Re & Imag) for station #41
Z_XX
Z_XY
Z_YX
Z_YY
Real-obs
Real-calc
Imag-obs
Imag-calc
Z/(2πf)^1/2 (V/A.Hz^1/2)
Period (s)

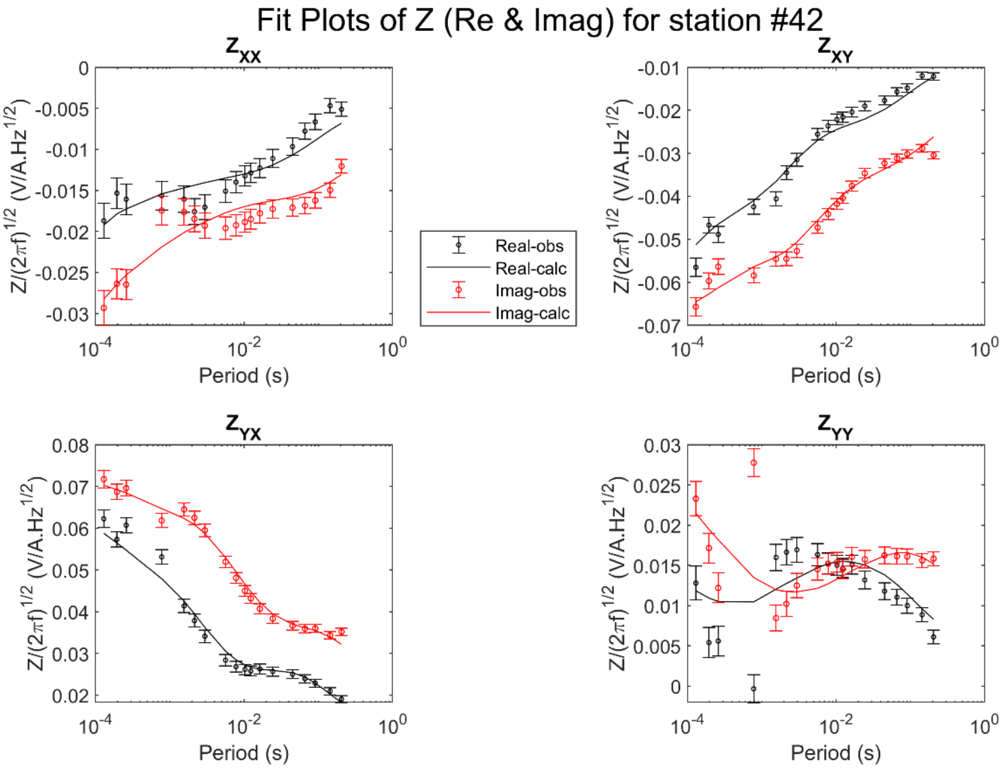
Fit Plots of Z (Re & Imag) for station #42
Z_XX
Z_XY
Z_YX
Z_YY
Z/(2πf)^1/2 (V/A.Hz^1/2)
Period (s)
Real-obs
Real-calc
Imag-obs
Imag-calc

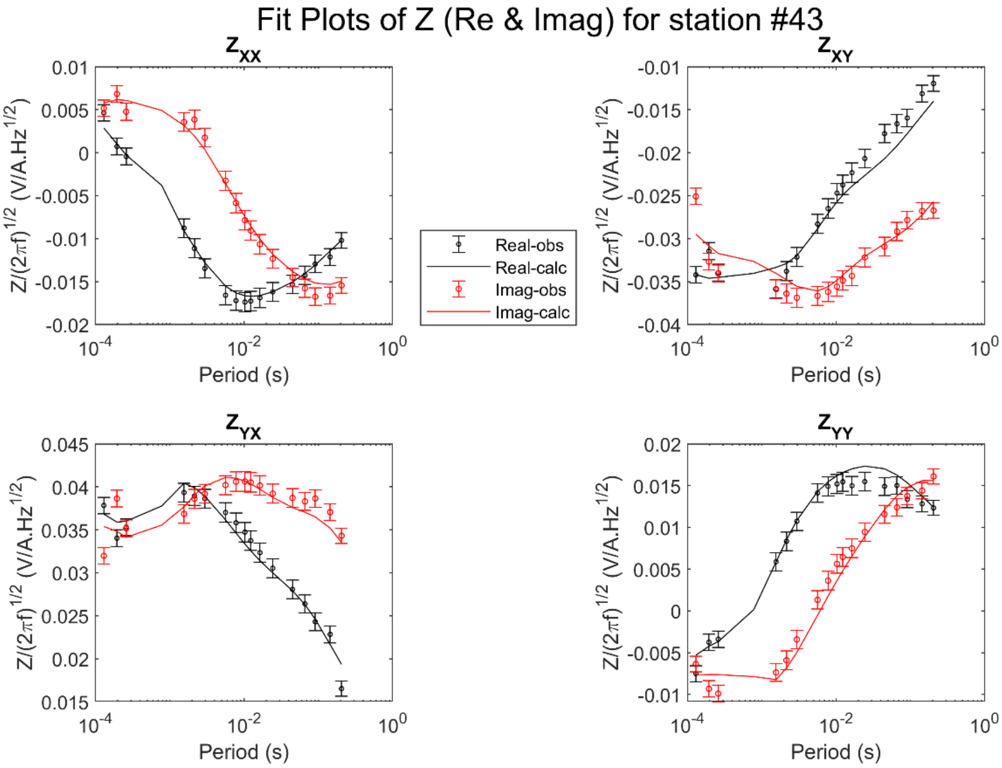
Fit Plots of Z (Re & Imag) for station #43
Z_XX
Z_XY
Z_YX
Z_YY
Z/(2πf)^1/2 (V/A.Hz^1/2)
Period (s)
Real-obs
Real-calc
Imag-obs
Imag-calc

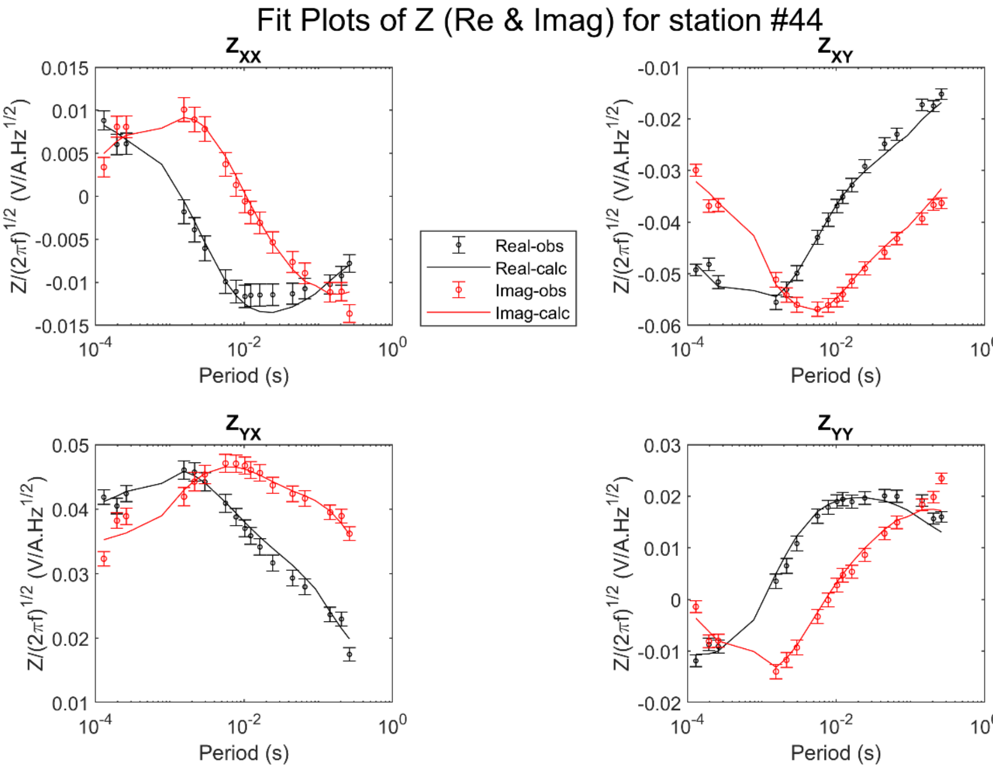
Fit Plots of Z (Re & Imag) for station #44
Z_XX
Z_XY
Z_YX
Z_YY
Z/(2πf)^1/2 (V/A.Hz^1/2)
Period (s)
Real-obs
Real-calc
Imag-obs
Imag-calc

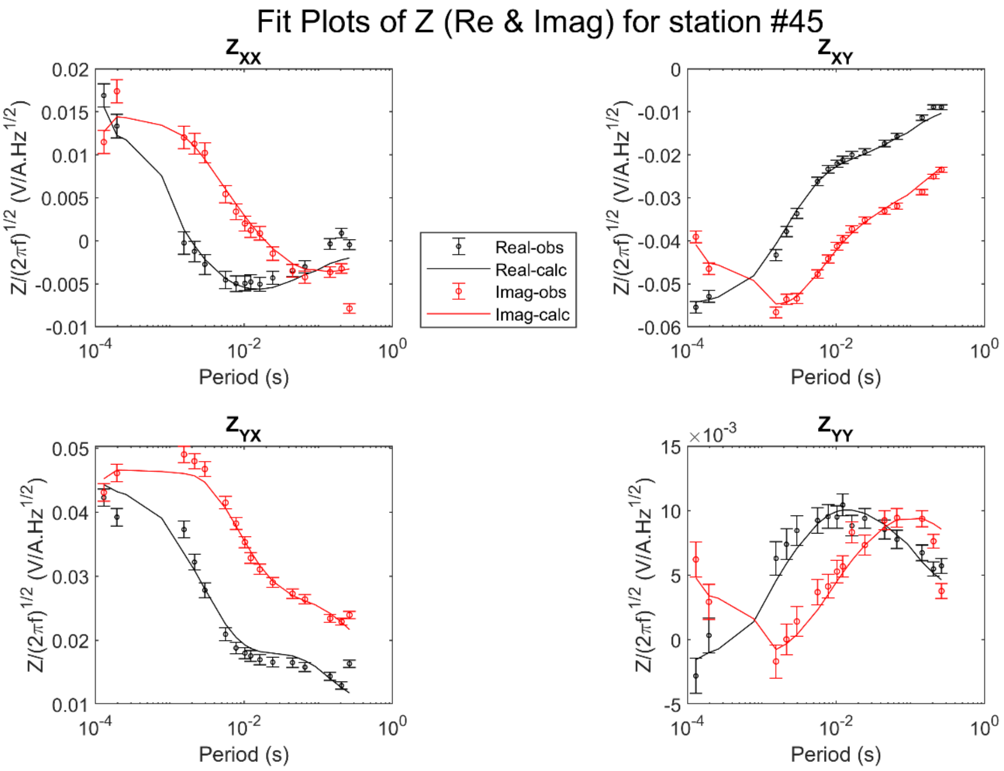
Fit Plots of Z (Re & Imag) for station #45
Z_XX
Z_XY
Z_YX
Z_YY
×10^-3
Z/(2πf)^1/2 (V/A.Hz^1/2)
Period (s)
Real-obs
Real-calc
Imag-obs
Imag-calc

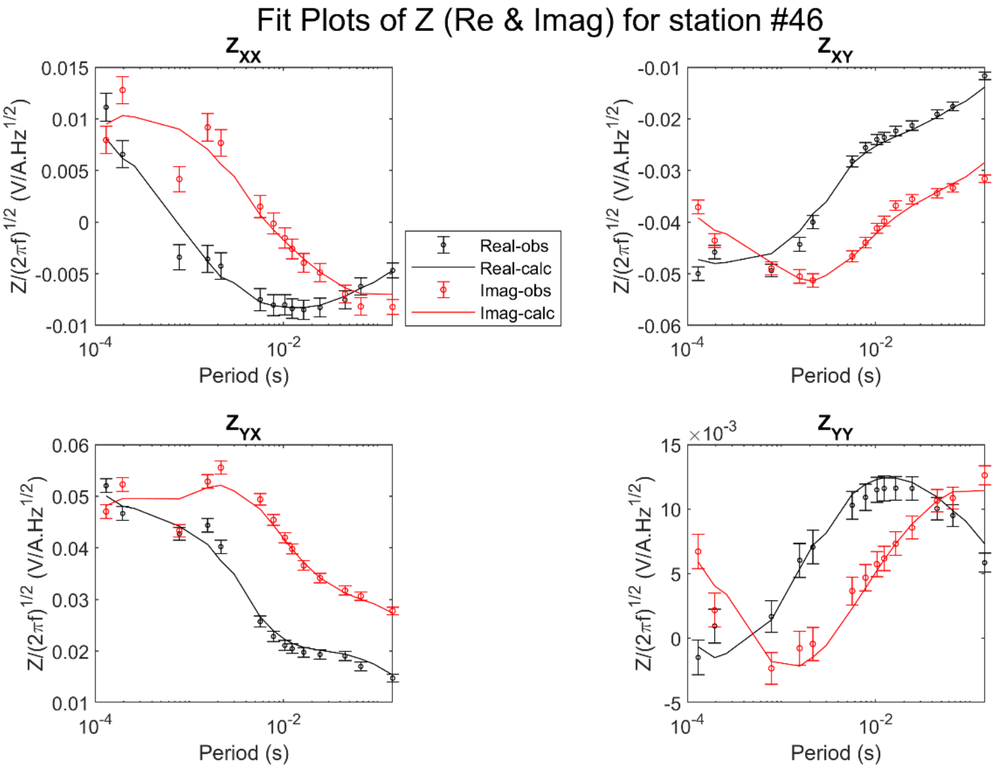
Fit Plots of Z (Re & Imag) for station #46
Z_XX
Z_XY
Z_YX
Z_YY
Z/(2πf)^1/2 (V/A.Hz^1/2)
Period (s)
Real-obs
Real-calc
Imag-obs
Imag-calc

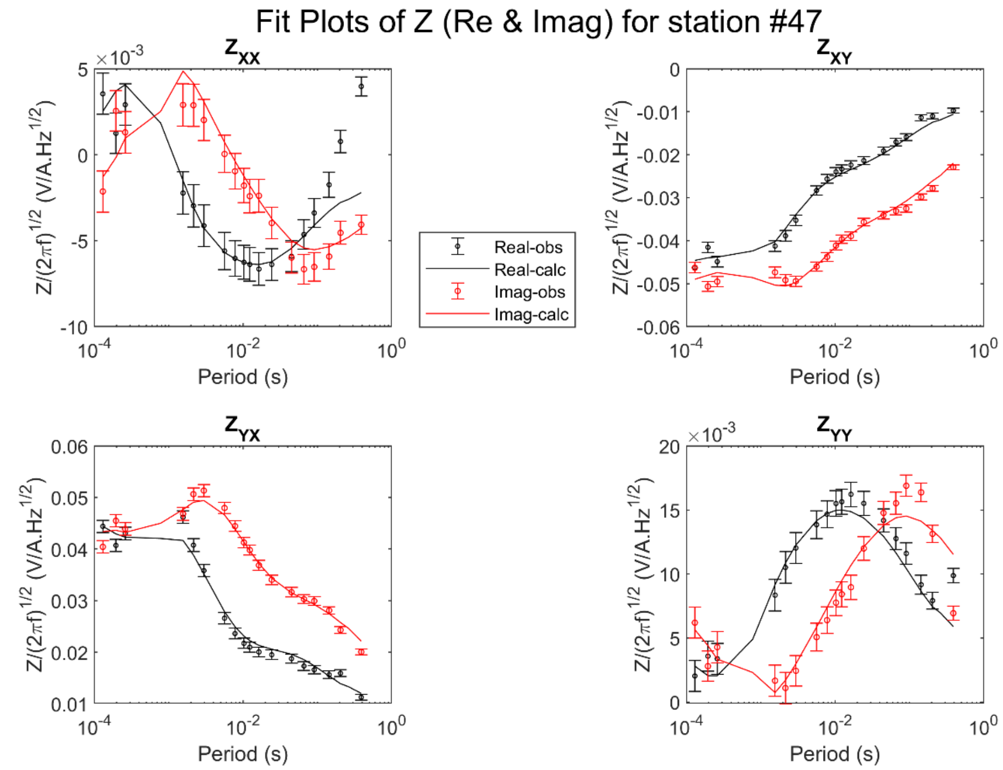
Fit Plots of Z (Re & Imag) for station #47
Z_XX
Z_XY
Z_YX
Z_YY
Z/(2πf)^1/2 (V/A.Hz^1/2)
Period (s)
Real-obs
Real-calc
Imag-obs
Imag-calc

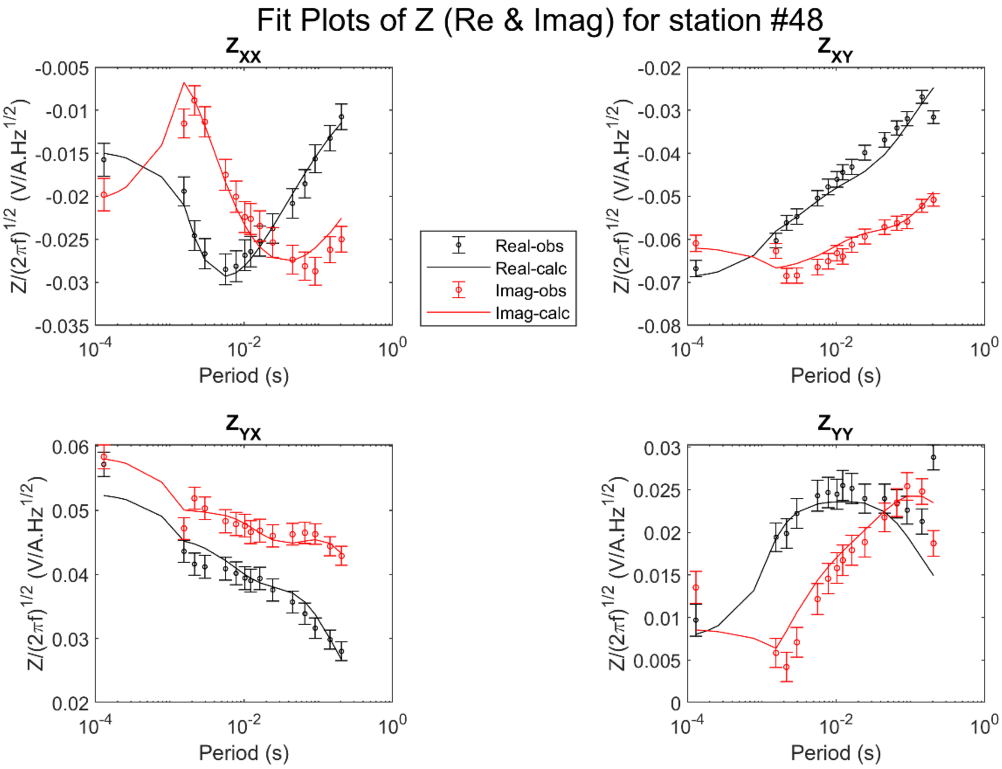
Fit Plots of Z (Re & Imag) for station #48
Z XX
Z XY
Z YX
Z YY
Z/(2πf)^1/2 (V/A.Hz^1/2)
Period (s)
Real-obs
Real-calc
Imag-obs
Imag-calc

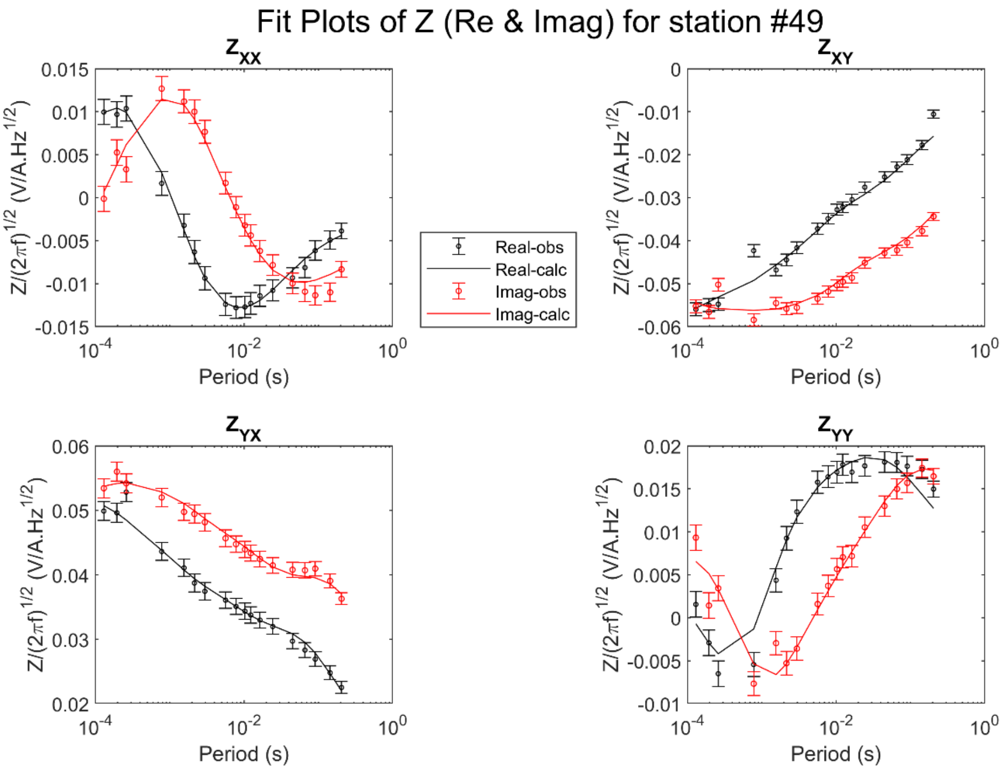
Fit Plots of Z (Re & Imag) for station #49
Z XX
Z XY
Z YX
Z YY
Z/(2πf)^1/2 (V/A.Hz^1/2)
Period (s)
Real-obs
Real-calc
Imag-obs
Imag-calc

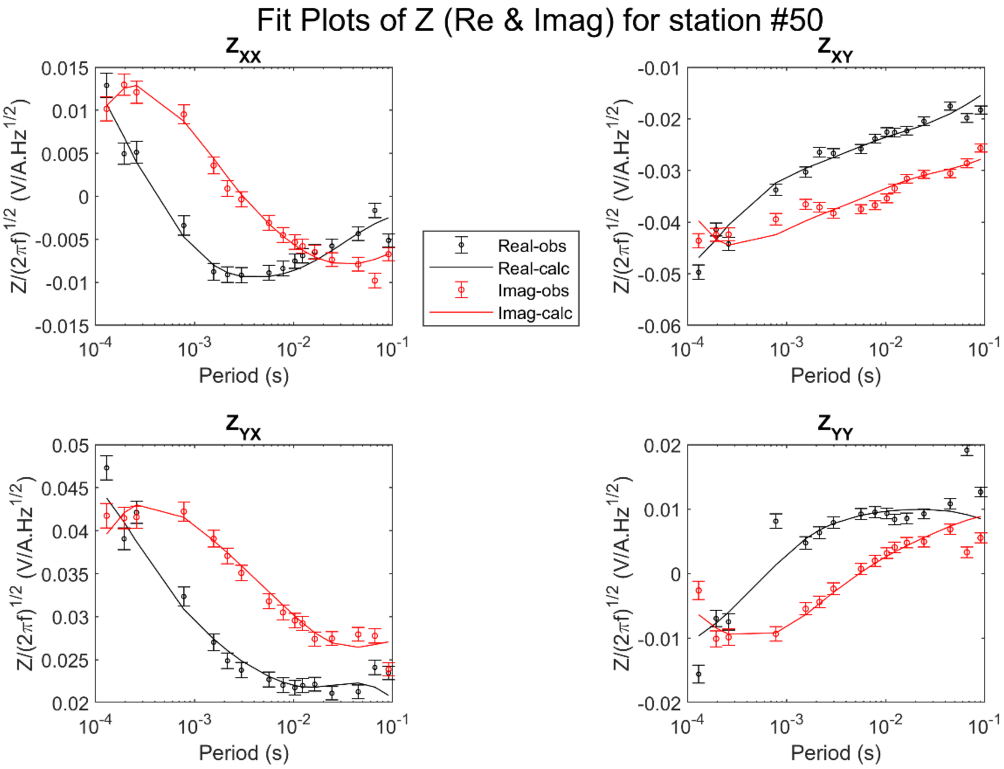
Fit Plots of Z (Re & Imag) for station #50
Z_{XX}
Z_{XY}
Z_{YX}
Z_{YY}
Real-obs
Real-calc
Imag-obs
Imag-calc
$Z/(2\pi f)^{1/2}$ (V/A.Hz$^{1/2}$)
Period (s)

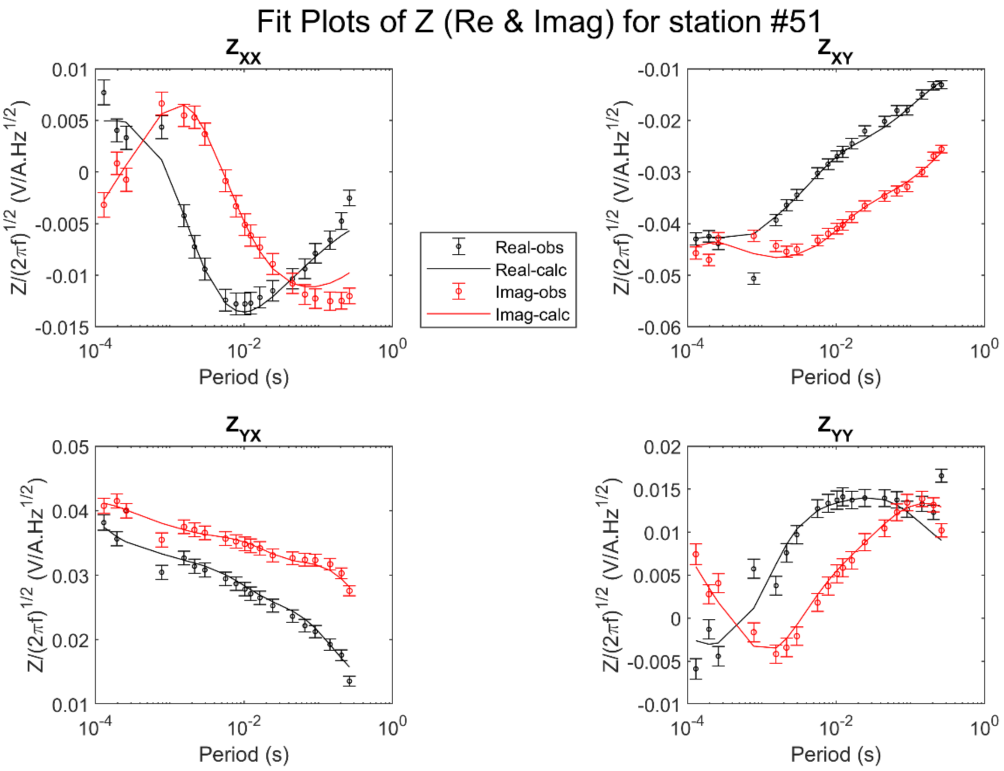
Fit Plots of Z (Re & Imag) for station #51
Z_{XX}
Z_{XY}
Z_{YX}
Z_{YY}
Real-obs
Real-calc
Imag-obs
Imag-calc
$Z/(2\pi f)^{1/2}$ (V/A.Hz$^{1/2}$)
Period (s)

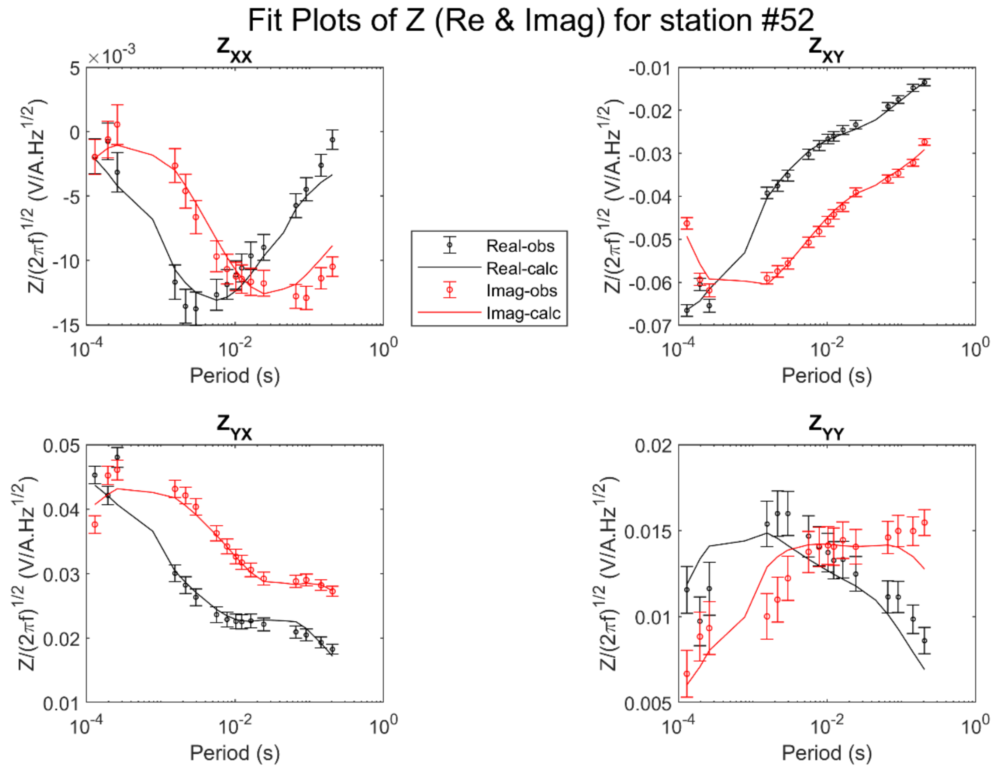
Fit Plots of Z (Re & Imag) for station #52
Z_XX
Z_XY
Z_YX
Z_YY
Z/(2πf)^1/2 (V/A.Hz^1/2)
Period (s)
Real-obs
Real-calc
Imag-obs
Imag-calc

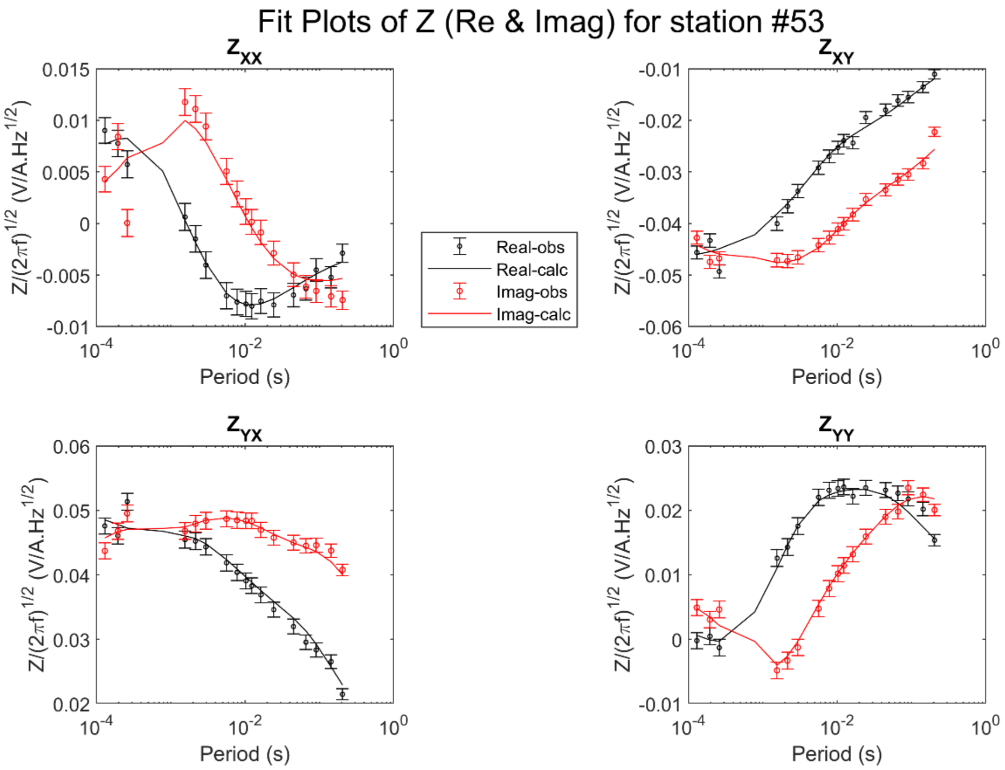
Fit Plots of Z (Re & Imag) for station #53
Z_XX
Z_XY
Z_YX
Z_YY
Z/(2πf)^1/2 (V/A.Hz^1/2)
Period (s)
Real-obs
Real-calc
Imag-obs
Imag-calc

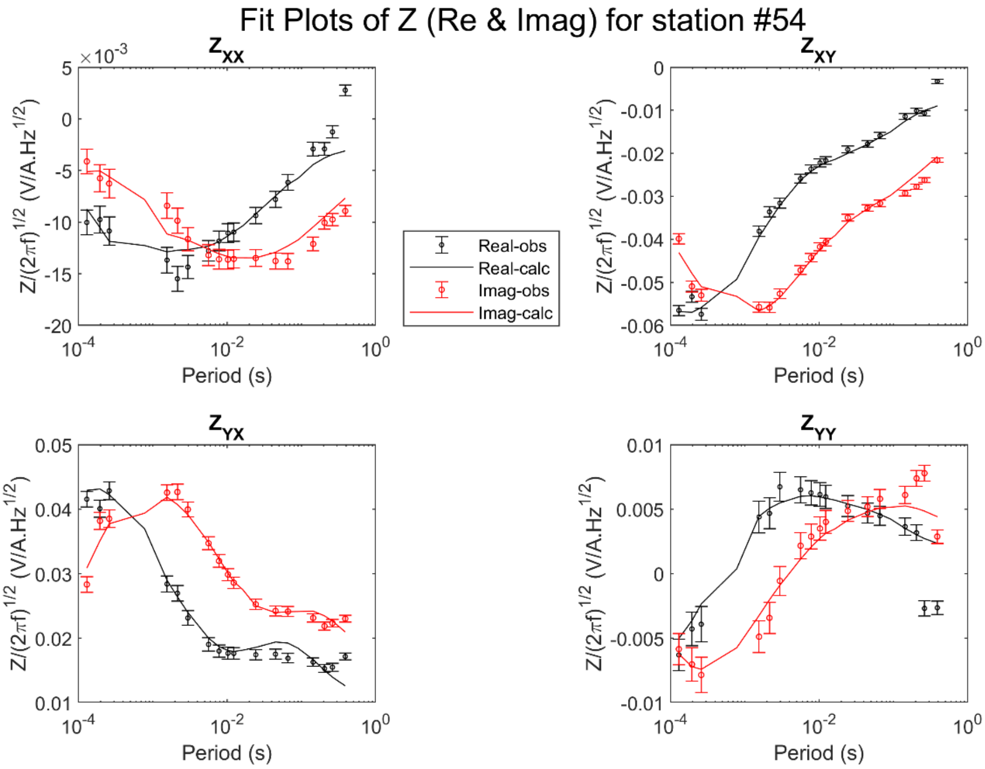
Fit Plots of Z (Re & Imag) for station #54
Z_{XX}
Z_{XY}
Z_{YX}
Z_{YY}
$Z/(2\pi f)^{1/2}$ (V/A.Hz$^{1/2}$)
Period (s)
Real-obs
Real-calc
Imag-obs
Imag-calc

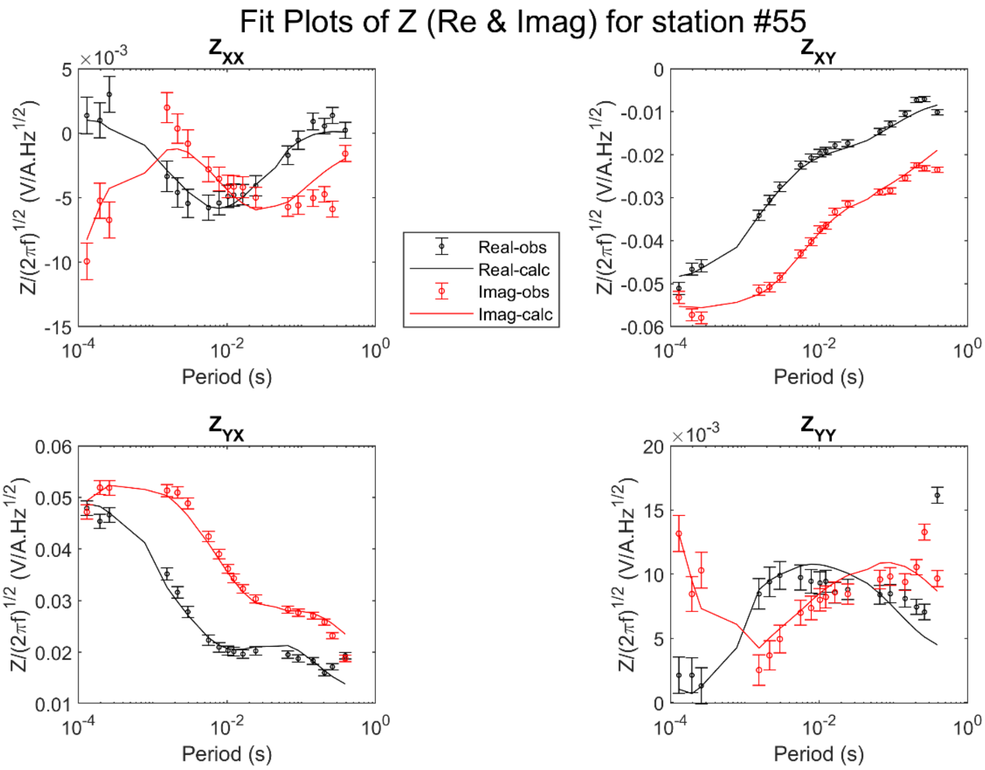
Fit Plots of Z (Re & Imag) for station #55
Z_{XX}
Z_{XY}
Z_{YX}
Z_{YY}
$Z/(2\pi f)^{1/2}$ (V/A.Hz$^{1/2}$)
Period (s)
Real-obs
Real-calc
Imag-obs
Imag-calc

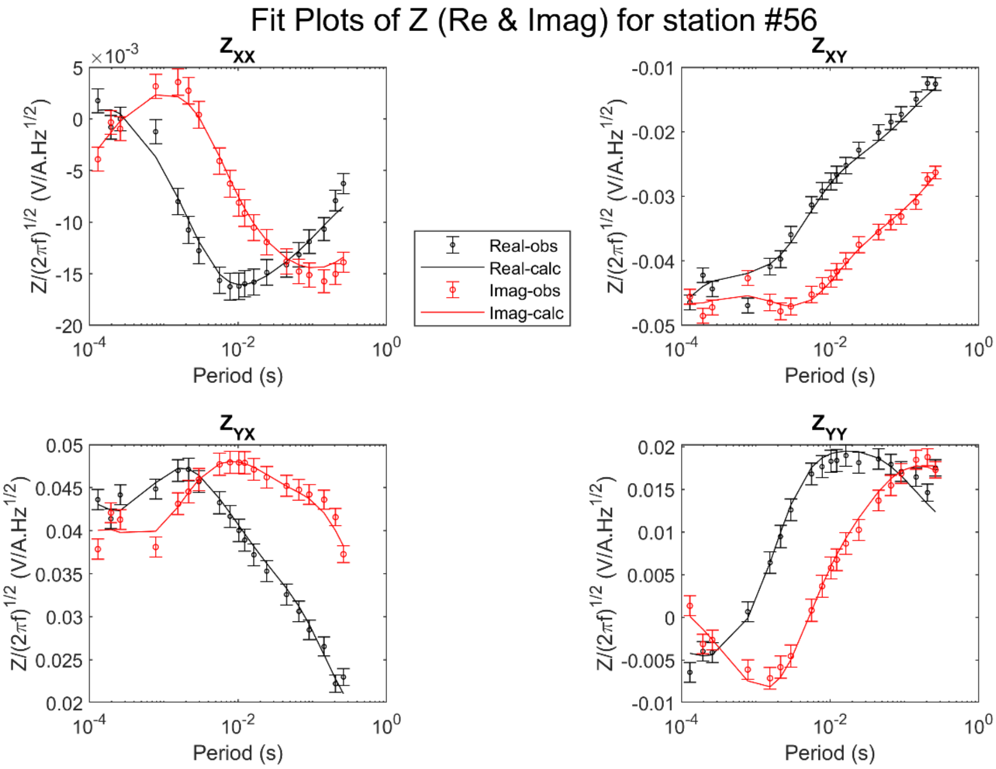
Fit Plots of Z (Re & Imag) for station #56
Z_{XX}
Z_{XY}
Z_{YX}
Z_{YY}
$Z/(2\pi f)^{1/2}$ (V/A.Hz$^{1/2}$)
Period (s)
Real-obs
Real-calc
Imag-obs
Imag-calc

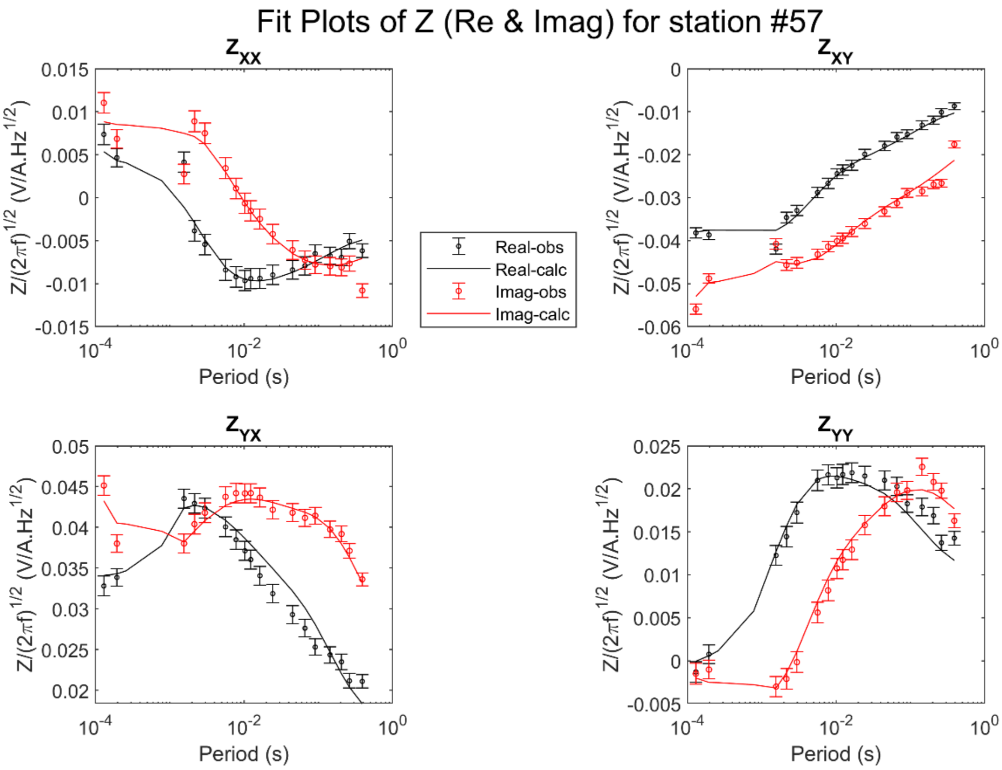
Fit Plots of Z (Re & Imag) for station #57
Z_{XX}
Z_{XY}
Z_{YX}
Z_{YY}
$Z/(2\pi f)^{1/2}$ (V/A.Hz$^{1/2}$)
Period (s)
Real-obs
Real-calc
Imag-obs
Imag-calc

Fit Plots of Z (Re & Imag) for station #58

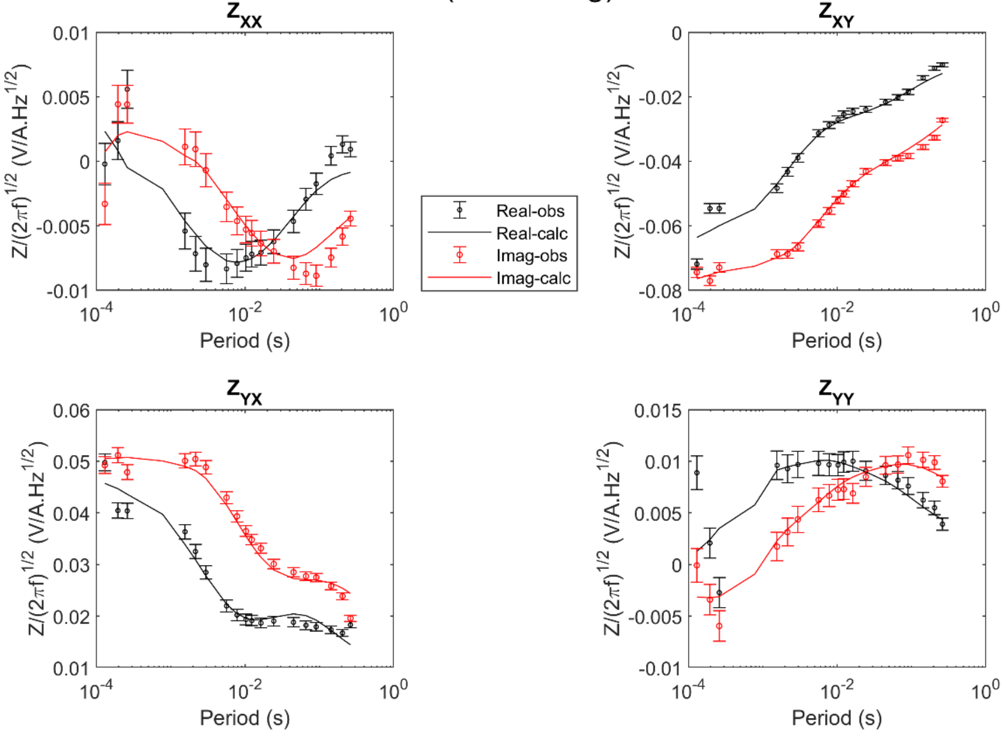

Fit Plots of Z (Re & Imag) for station #59

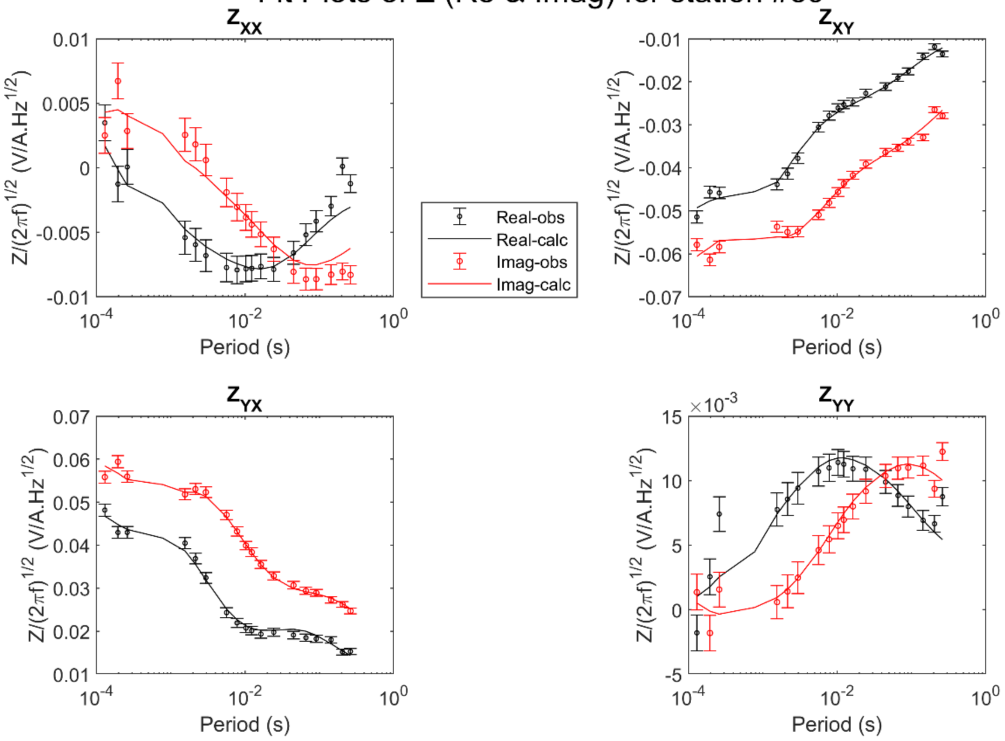

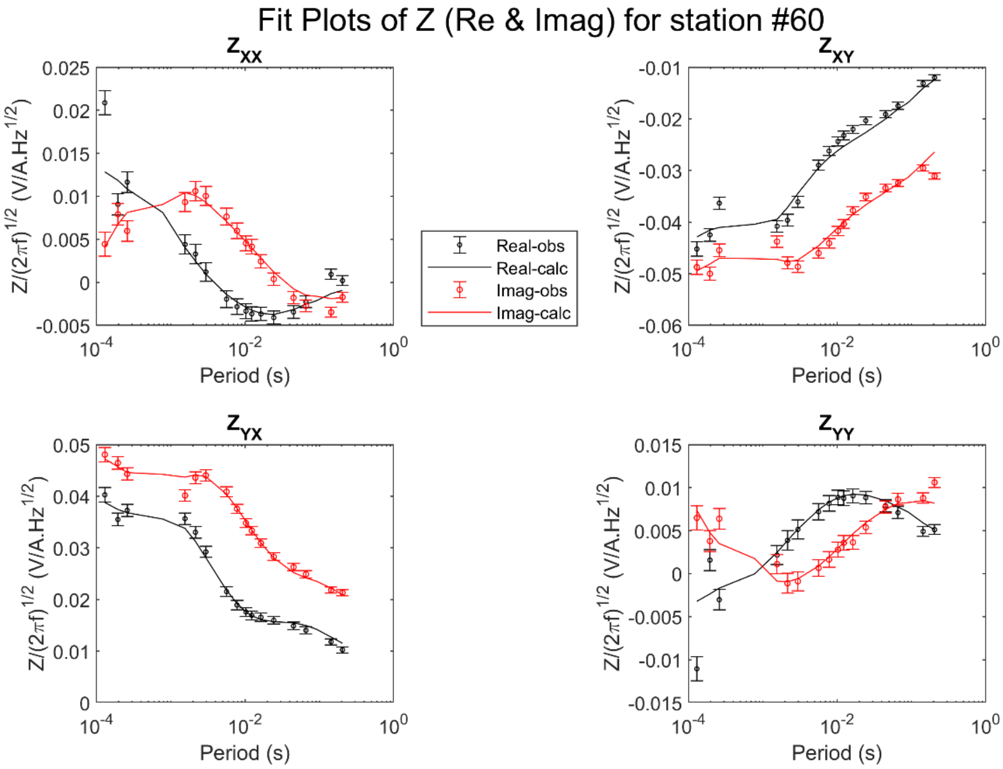
Fit Plots of Z (Re & Imag) for station #60
Z_{XX}
Z_{XY}
Z_{YX}
Z_{YY}
$Z/(2\pi f)^{1/2}$ (V/A.Hz$^{1/2}$)
Period (s)
Real-obs
Real-calc
Imag-obs
Imag-calc

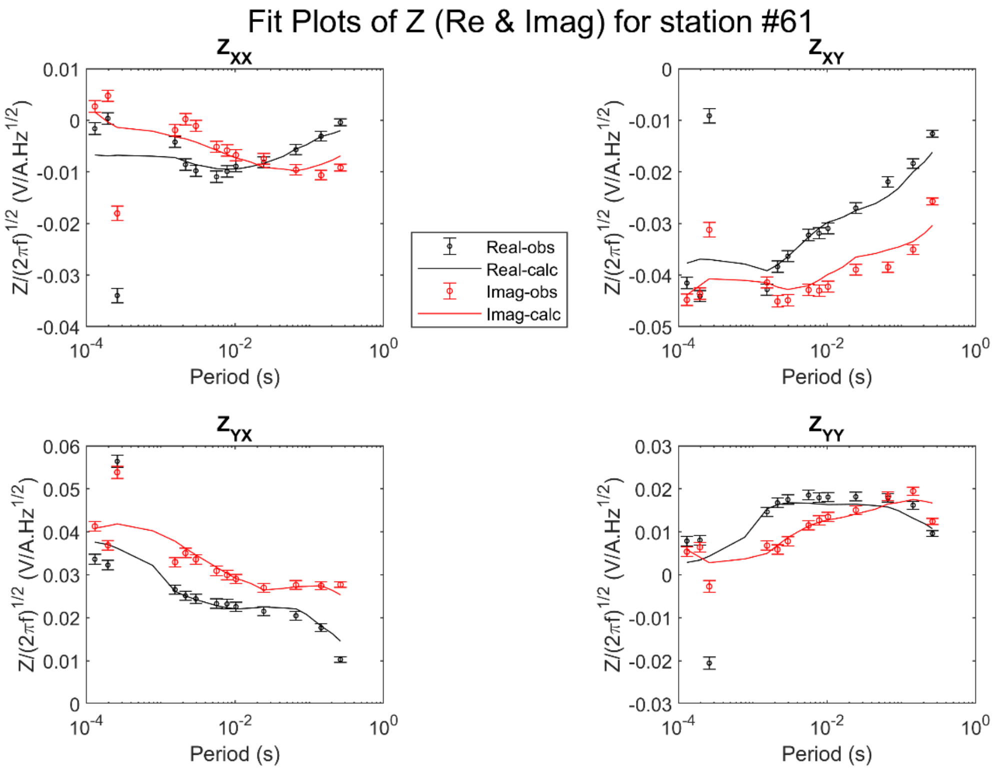
Fit Plots of Z (Re & Imag) for station #61
Z_{XX}
Z_{XY}
Z_{YX}
Z_{YY}
$Z/(2\pi f)^{1/2}$ (V/A.Hz$^{1/2}$)
Period (s)
Real-obs
Real-calc
Imag-obs
Imag-calc

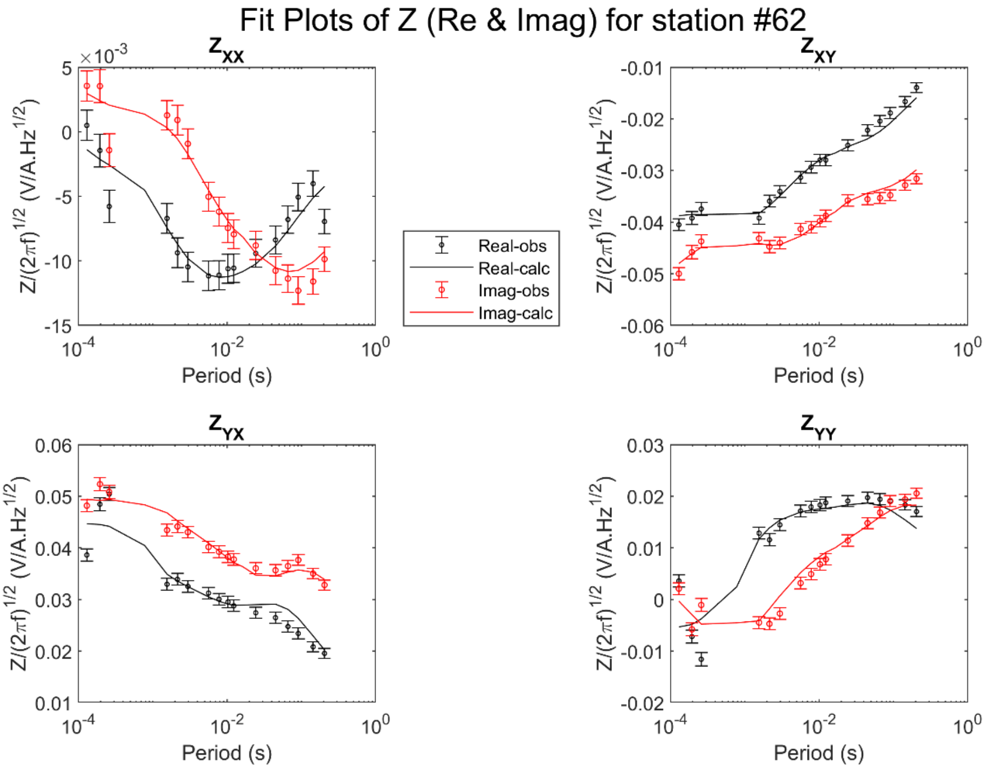
Fit Plots of Z (Re & Imag) for station #62
Z_XX
Z_XY
Z_YX
Z_YY
Z/(2πf)^1/2 (V/A.Hz^1/2)
Period (s)
Real-obs
Real-calc
Imag-obs
Imag-calc

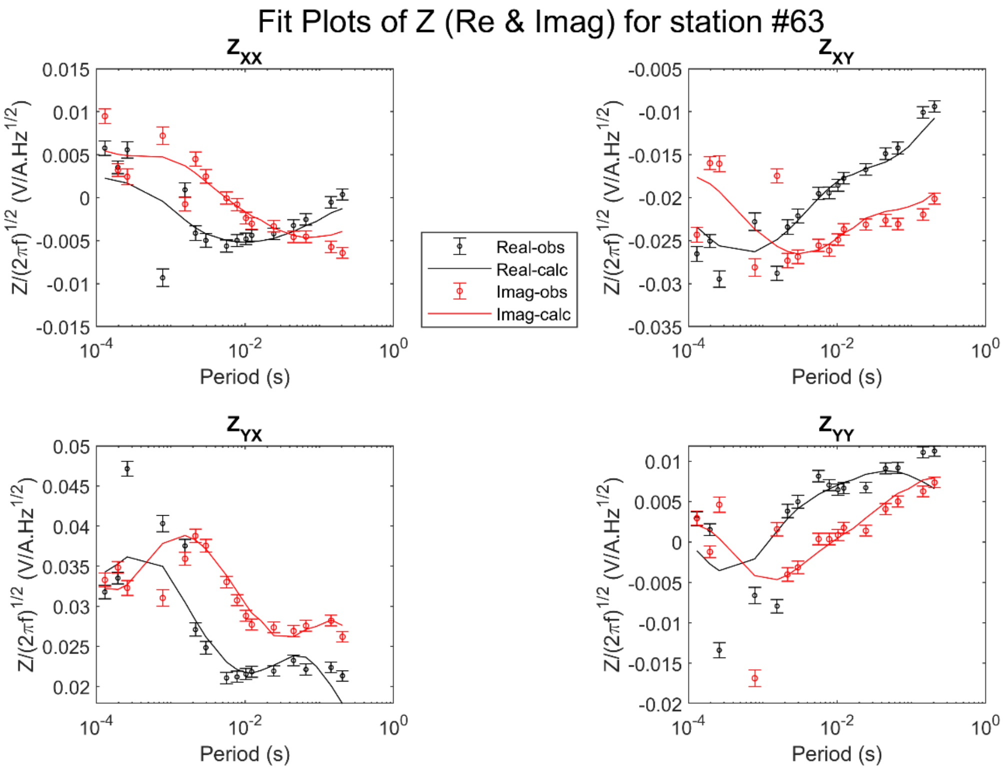
Fit Plots of Z (Re & Imag) for station #63
Z_XX
Z_XY
Z_YX
Z_YY
Z/(2πf)^1/2 (V/A.Hz^1/2)
Period (s)
Real-obs
Real-calc
Imag-obs
Imag-calc

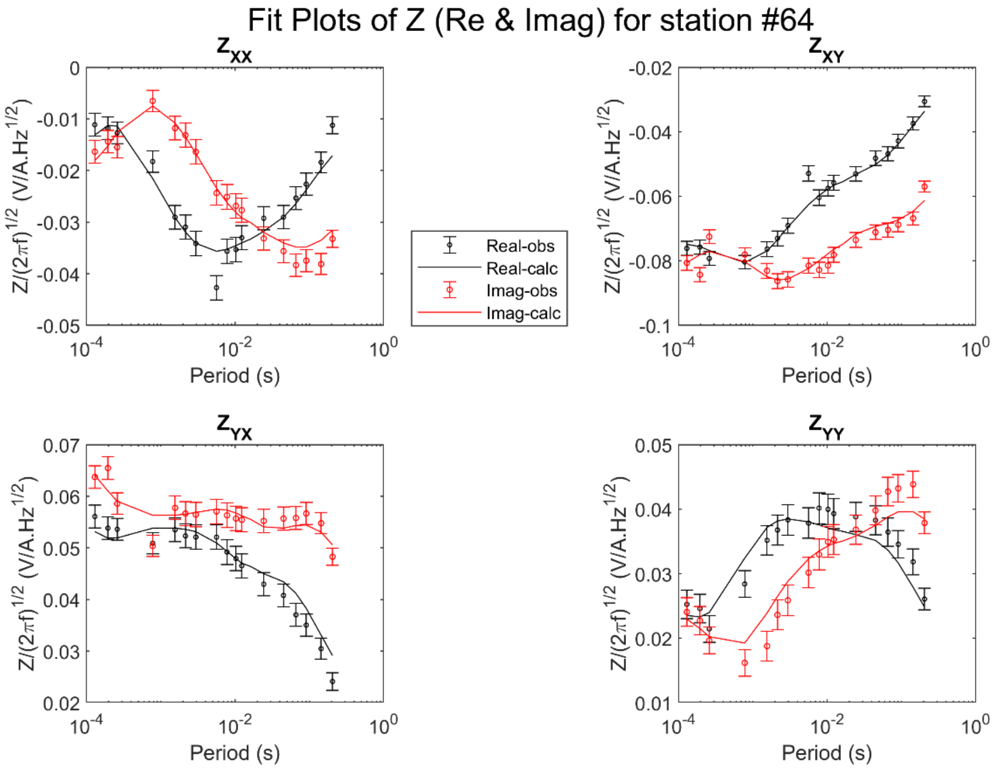
Fit Plots of Z (Re & Imag) for station #64
Z_{XX}
Z_{XY}
Z_{YX}
Z_{YY}
$Z/(2\pi f)^{1/2}$ (V/A.Hz$^{1/2}$)
Period (s)
Real-obs
Real-calc
Imag-obs
Imag-calc

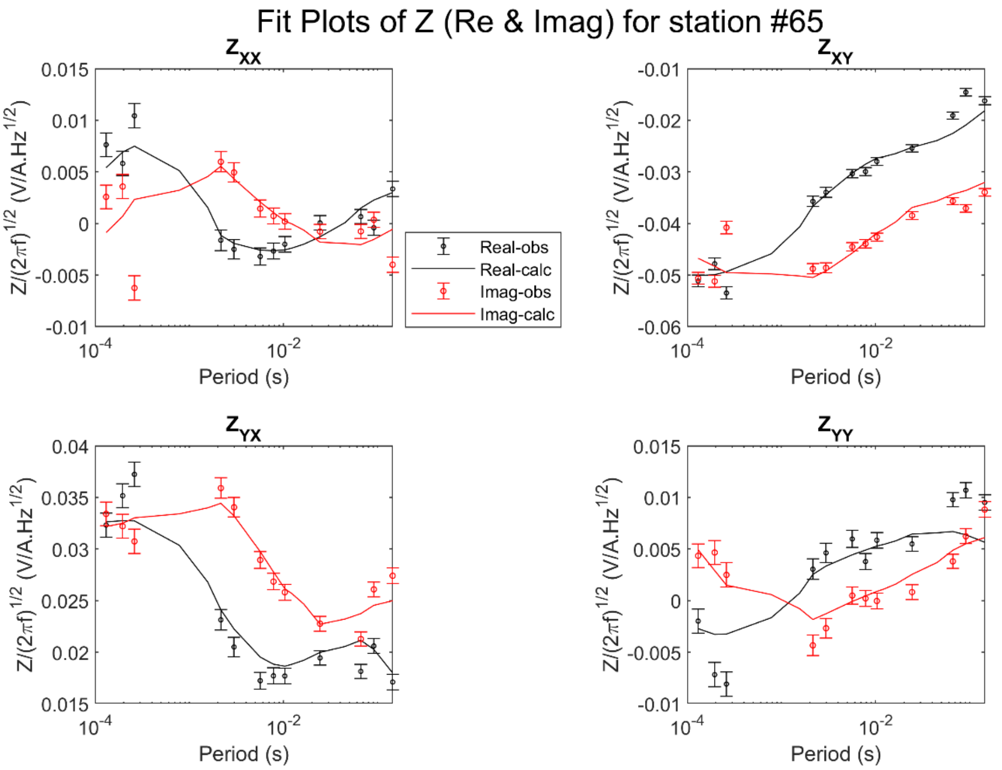
Fit Plots of Z (Re & Imag) for station #65
Z_{XX}
Z_{XY}
Z_{YX}
Z_{YY}
$Z/(2\pi f)^{1/2}$ (V/A.Hz$^{1/2}$)
Period (s)
Real-obs
Real-calc
Imag-obs
Imag-calc

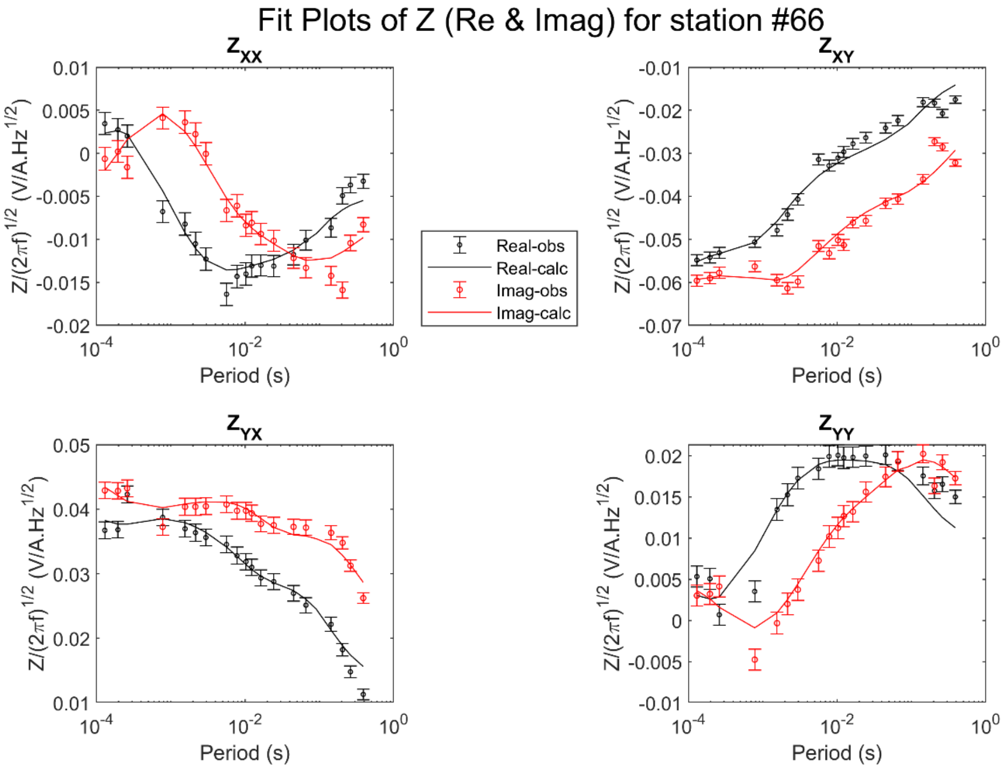
Fit Plots of Z (Re & Imag) for station #66
Z_XX
Z_XY
Z_YX
Z_YY
Z/(2πf)^1/2 (V/A.Hz^1/2)
Period (s)
Real-obs
Real-calc
Imag-obs
Imag-calc

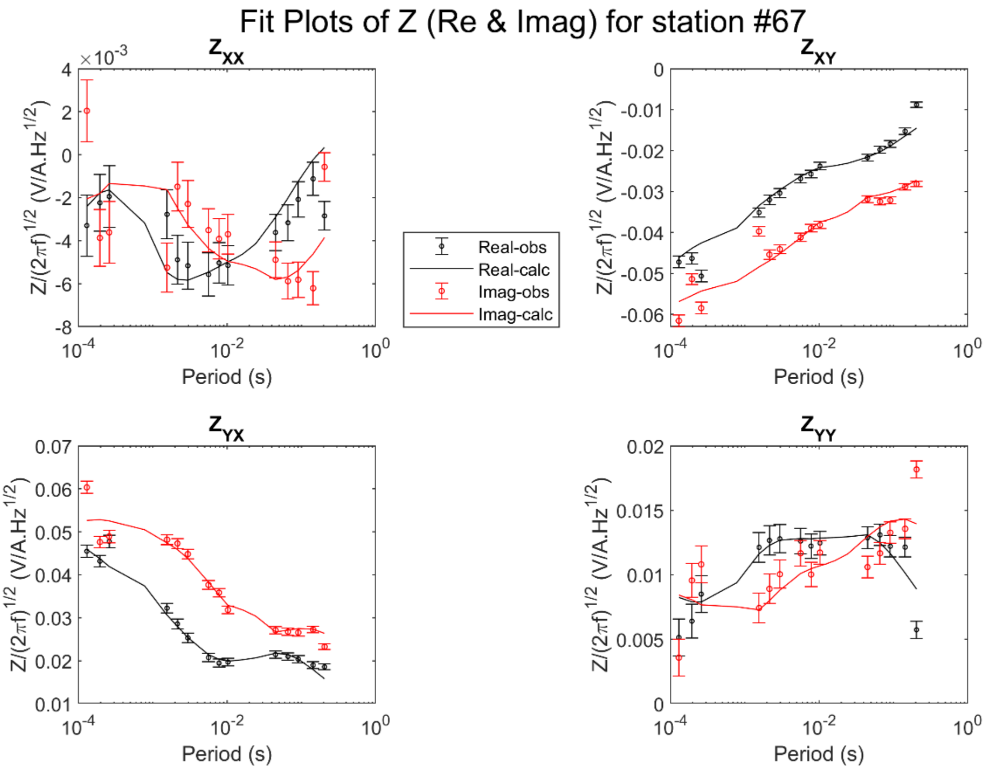
Fit Plots of Z (Re & Imag) for station #67
Z_XX
Z_XY
Z_YX
Z_YY
Z/(2πf)^1/2 (V/A.Hz^1/2)
Period (s)
Real-obs
Real-calc
Imag-obs
Imag-calc

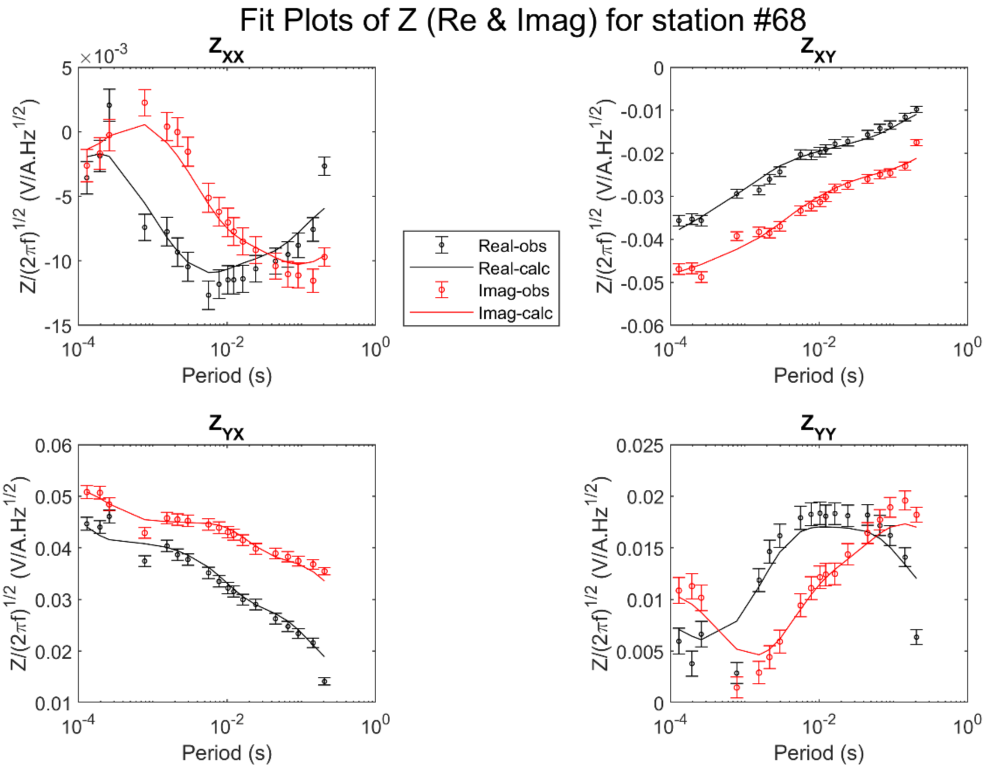
Fit Plots of Z (Re & Imag) for station #68
Z_XX
Z_XY
Z_YX
Z_YY
Real-obs
Real-calc
Imag-obs
Imag-calc
Z/(2πf)^1/2 (V/A.Hz^1/2)
Period (s)

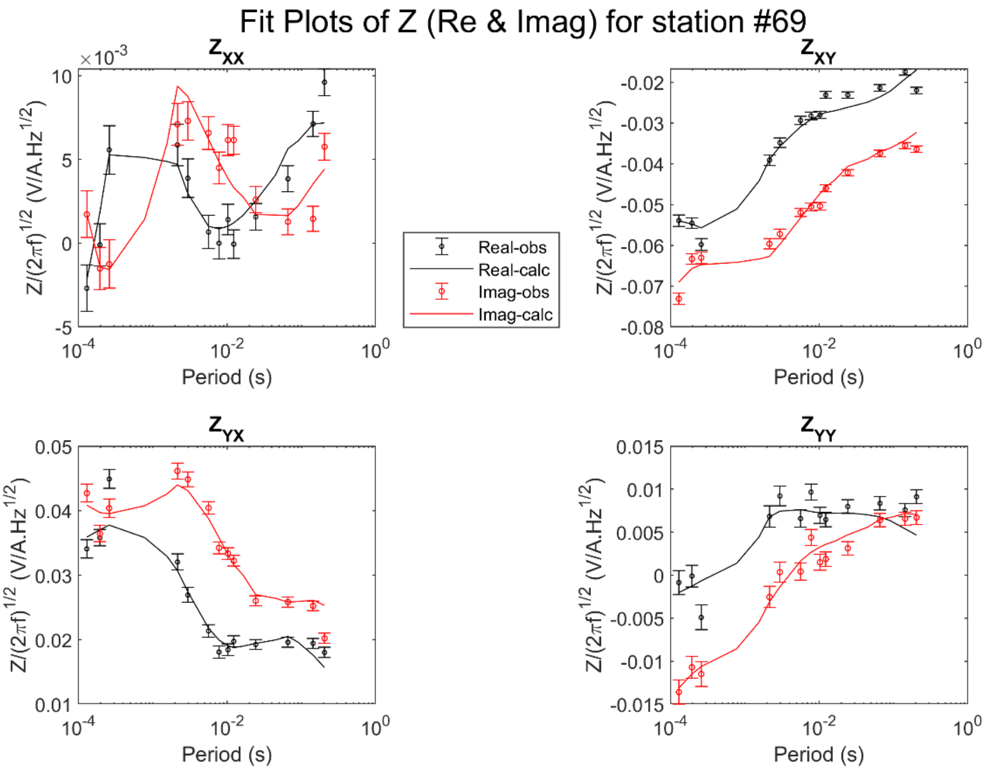
Fit Plots of Z (Re & Imag) for station #69
Z_XX
Z_XY
Z_YX
Z_YY
Real-obs
Real-calc
Imag-obs
Imag-calc
Z/(2πf)^1/2 (V/A.Hz^1/2)
Period (s)

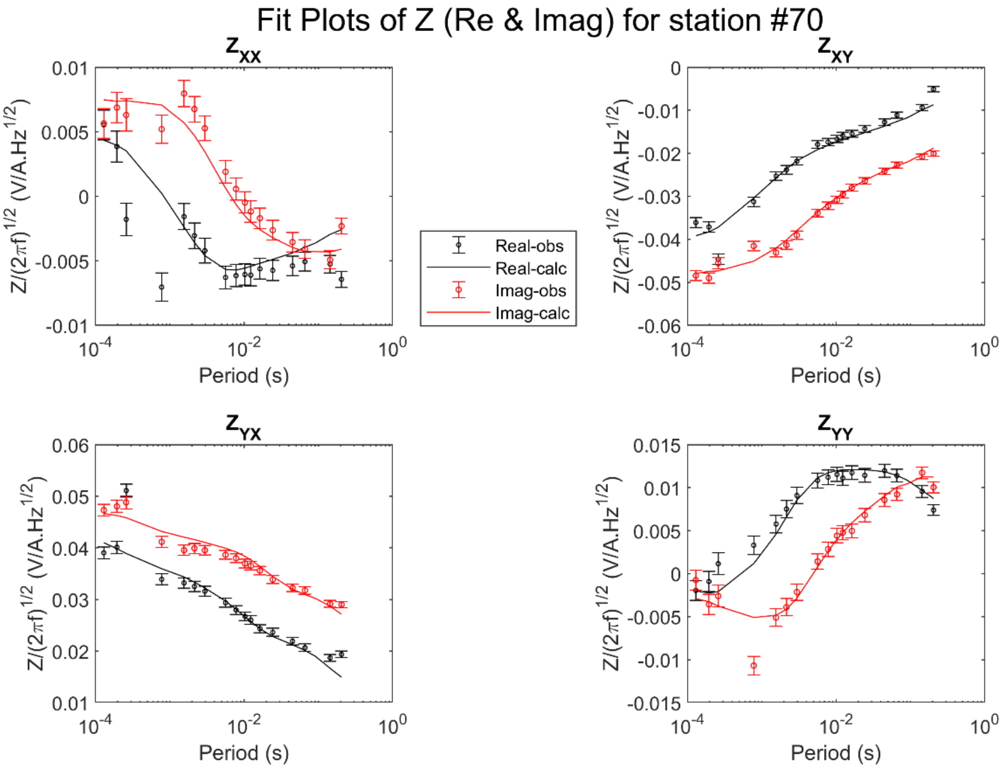
Fit Plots of Z (Re & Imag) for station #70
Z_{XX}
Z_{XY}
Z_{YX}
Z_{YY}
$Z/(2\pi f)^{1/2}$ (V/A.Hz$^{1/2}$)
Period (s)
Real-obs
Real-calc
Imag-obs
Imag-calc

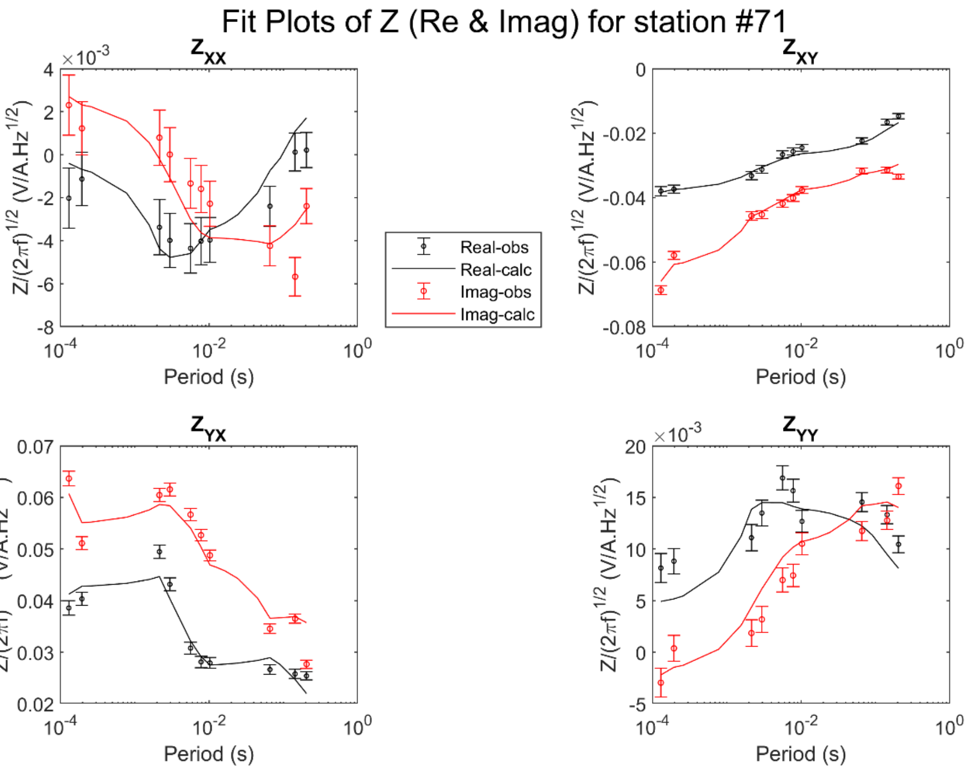
Fit Plots of Z (Re & Imag) for station #71
Z_{XX}
Z_{XY}
Z_{YX}
Z_{YY}
$\times 10^{-3}$
$Z/(2\pi f)^{1/2}$ (V/A.Hz$^{1/2}$)
Period (s)
Real-obs
Real-calc
Imag-obs
Imag-calc

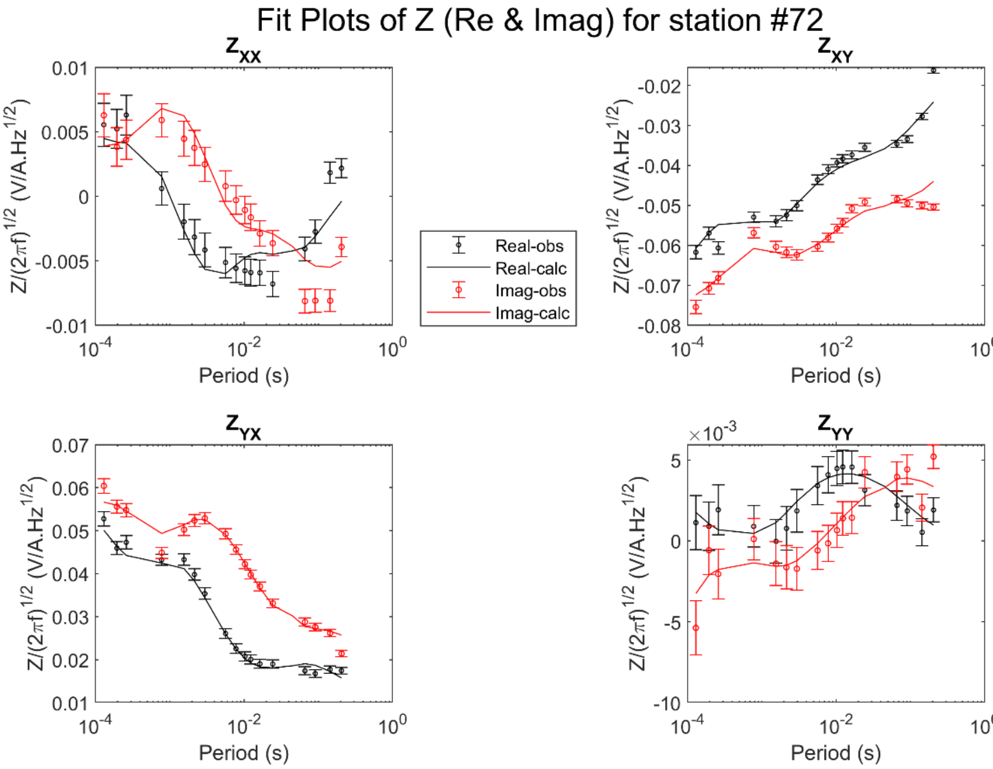
Fit Plots of Z (Re & Imag) for station #72
Z_XX
Z_XY
Z_YX
Z_YY
Z/(2πf)^1/2 (V/A.Hz^1/2)
Period (s)
Real-obs
Real-calc
Imag-obs
Imag-calc

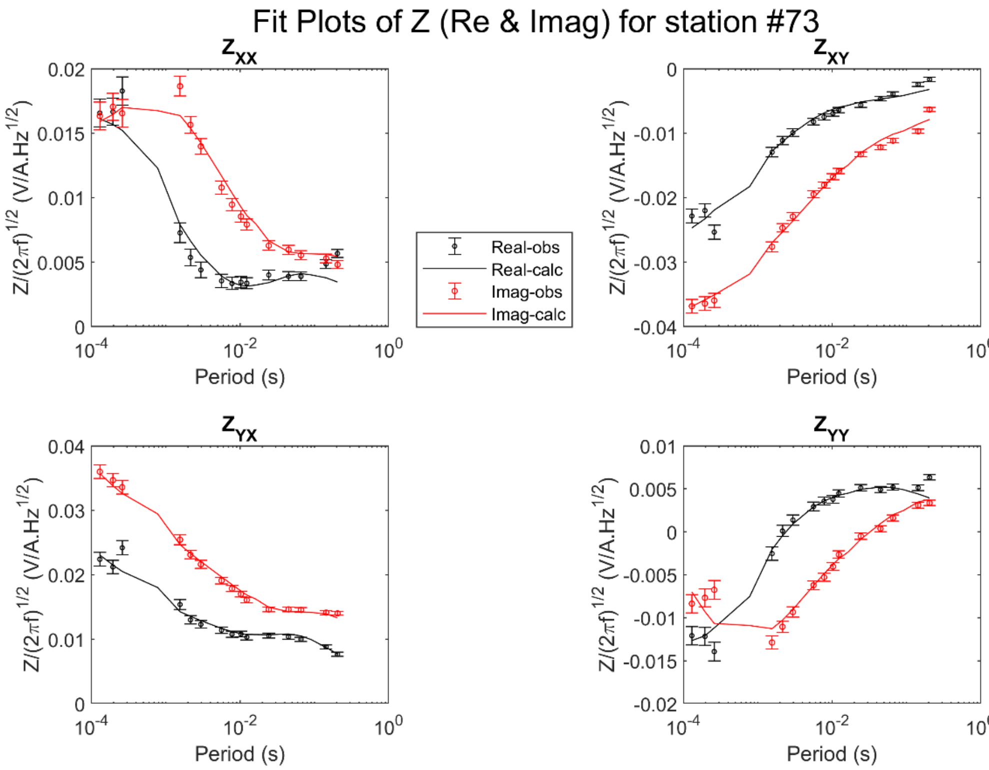
Fit Plots of Z (Re & Imag) for station #73
Z_XX
Z_XY
Z_YX
Z_YY
Z/(2πf)^1/2 (V/A.Hz^1/2)
Period (s)
Real-obs
Real-calc
Imag-obs
Imag-calc

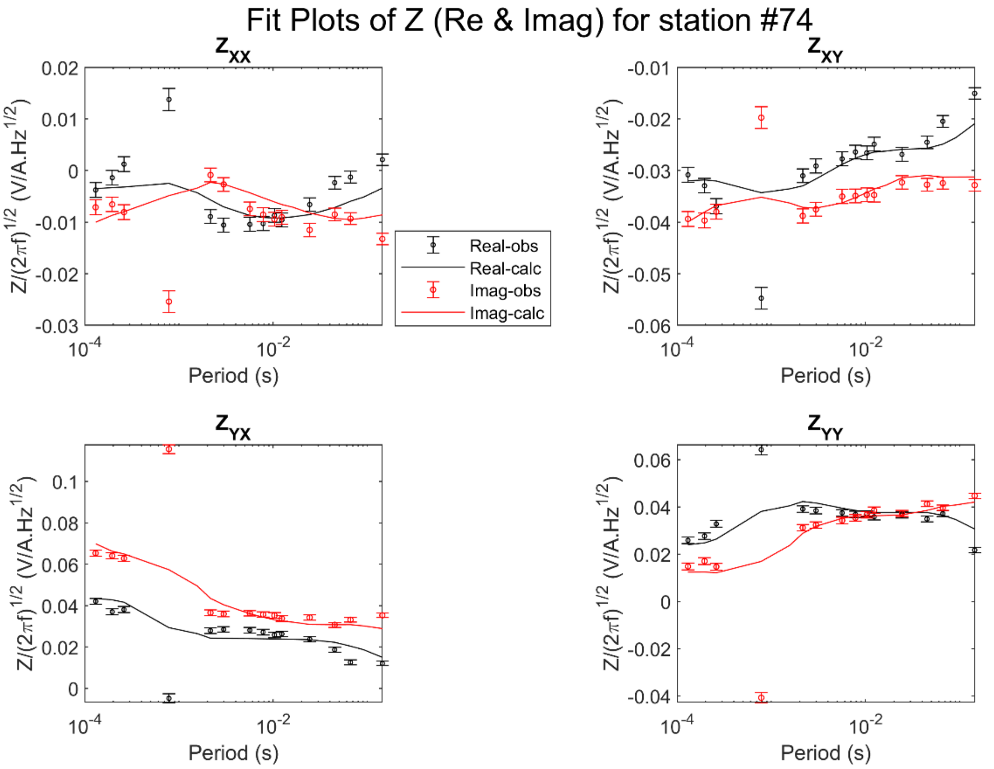
Fit Plots of Z (Re & Imag) for station #74
Z_XX
Z_XY
Z_YX
Z_YY
Z/(2πf)^1/2 (V/A.Hz^1/2)
Period (s)
Real-obs
Real-calc
Imag-obs
Imag-calc

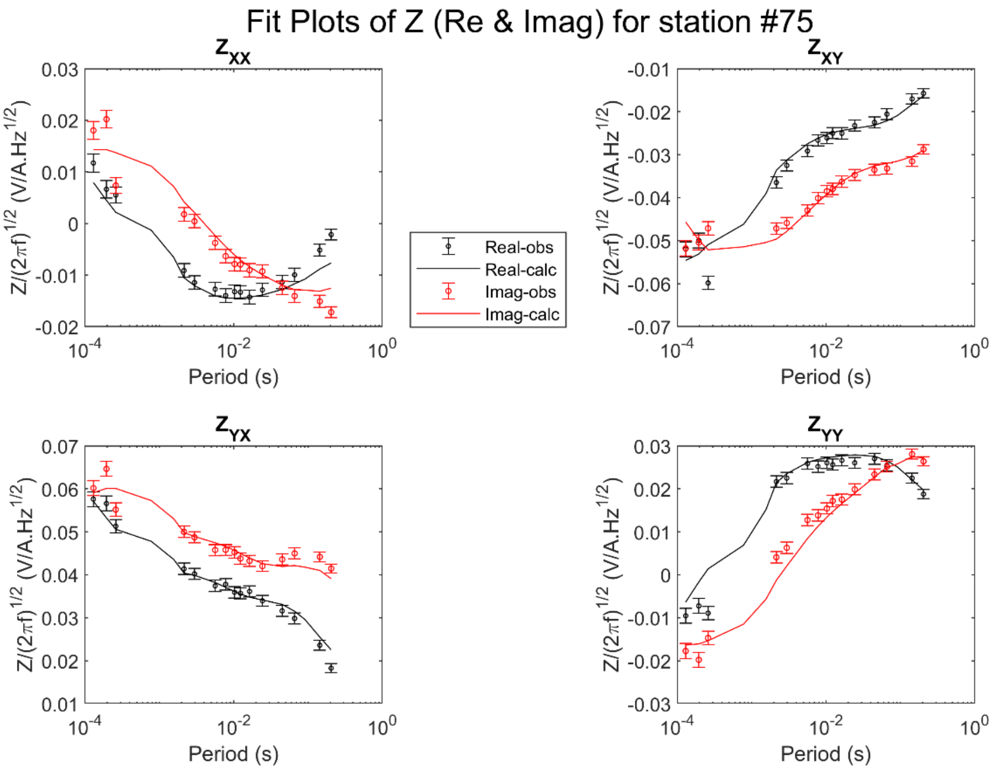
Fit Plots of Z (Re & Imag) for station #75
Z_XX
Z_XY
Z_YX
Z_YY
Z/(2πf)^1/2 (V/A.Hz^1/2)
Period (s)
Real-obs
Real-calc
Imag-obs
Imag-calc

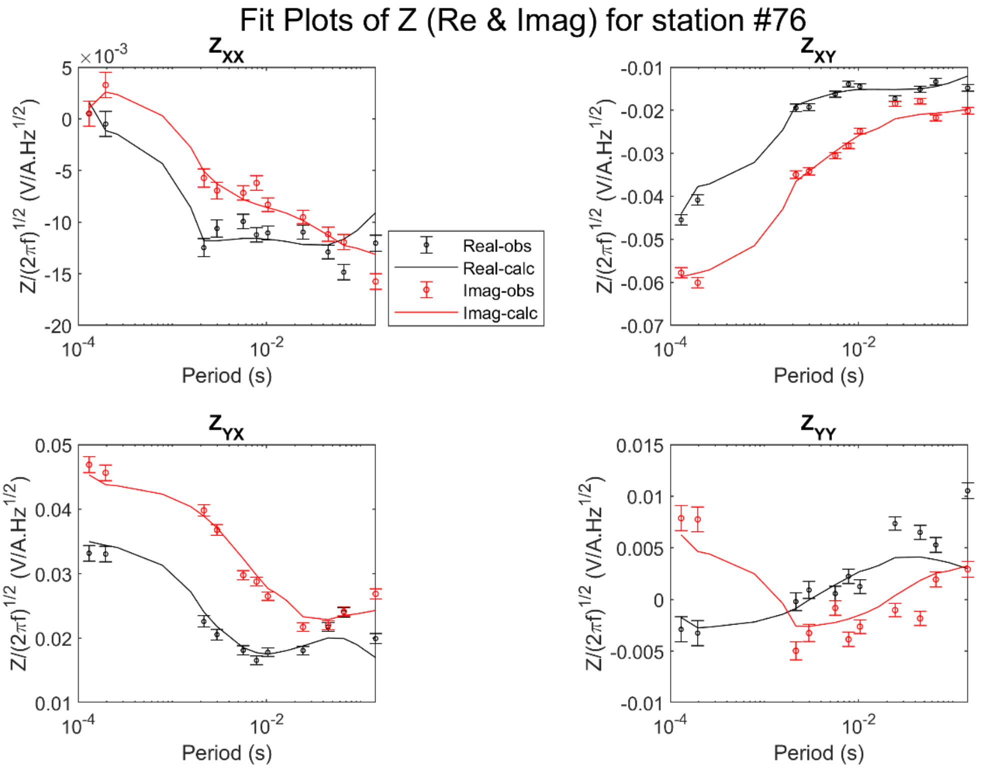
Fit Plots of Z (Re & Imag) for station #76
Z_{XX}
Z_{XY}
Z_{YX}
Z_{YY}
$Z/(2\pi f)^{1/2}$ (V/A.Hz$^{1/2}$)
Period (s)
Real-obs
Real-calc
Imag-obs
Imag-calc

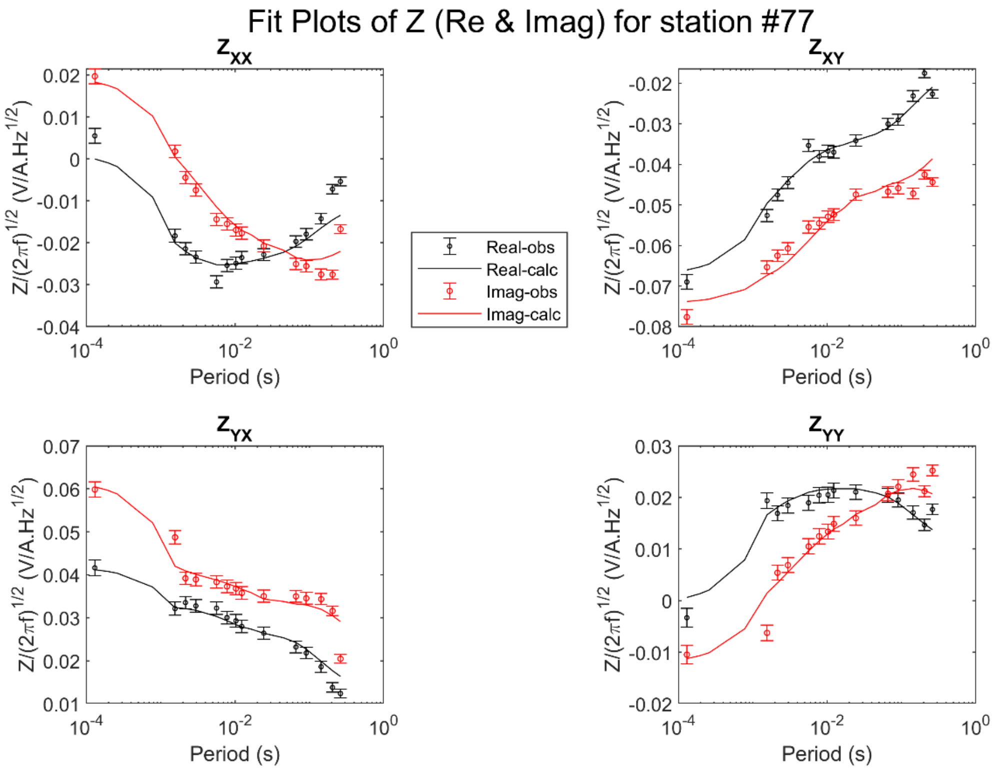
Fit Plots of Z (Re & Imag) for station #77
Z_{XX}
Z_{XY}
Z_{YX}
Z_{YY}
$Z/(2\pi f)^{1/2}$ (V/A.Hz$^{1/2}$)
Period (s)
Real-obs
Real-calc
Imag-obs
Imag-calc

Fit Plots of Z (Re & Imag) for station #78

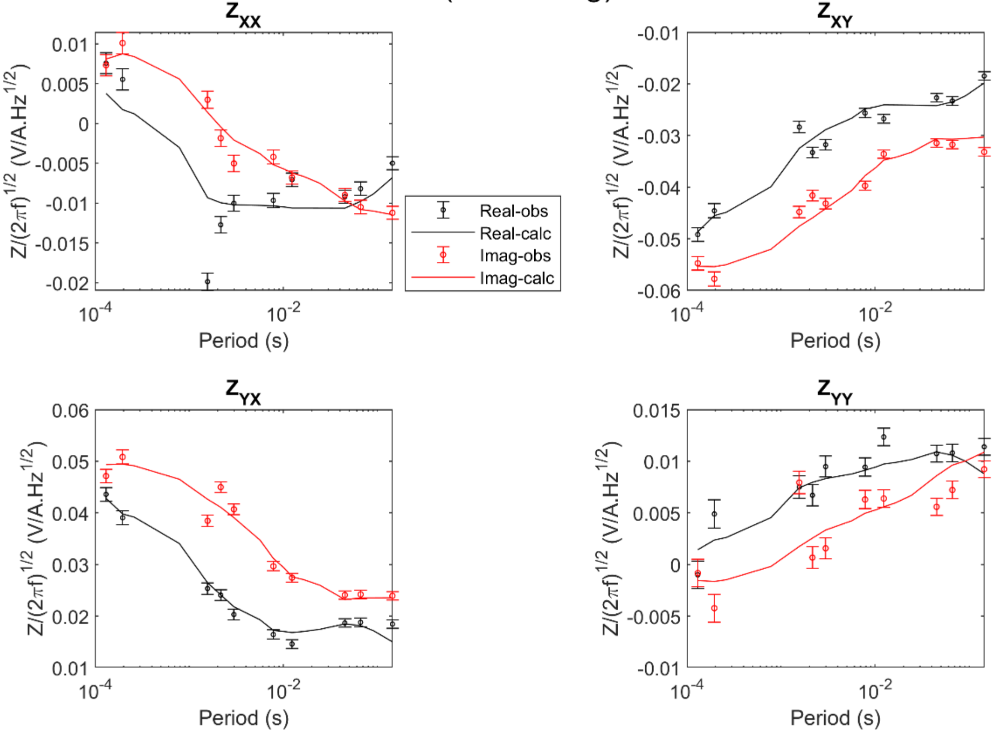

Fit Plots of Z (Re & Imag) for station #79

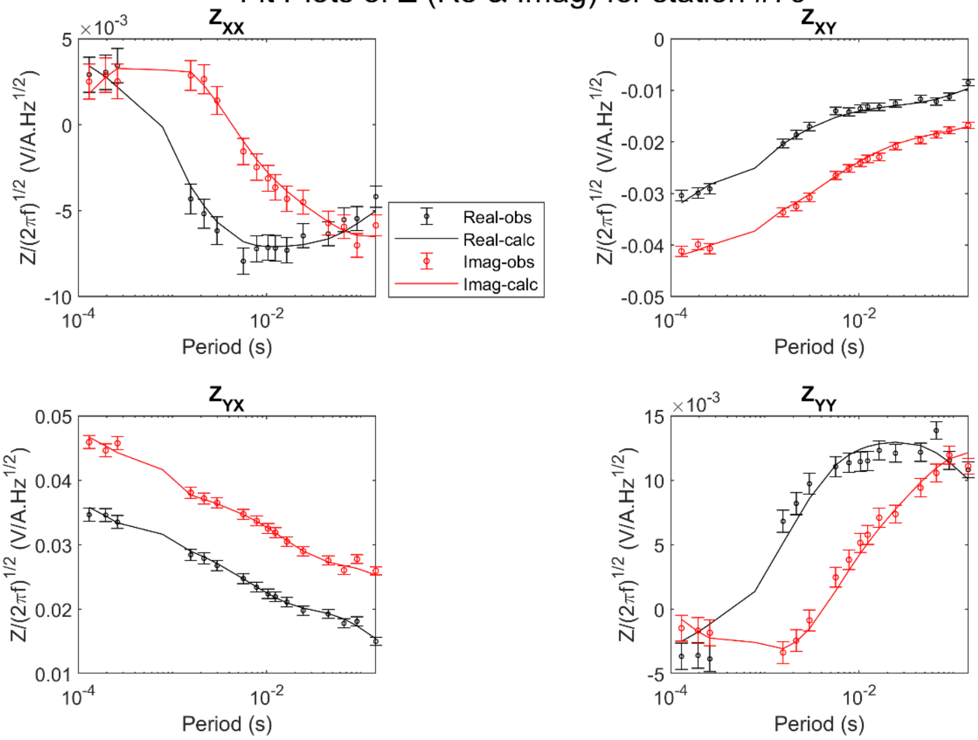

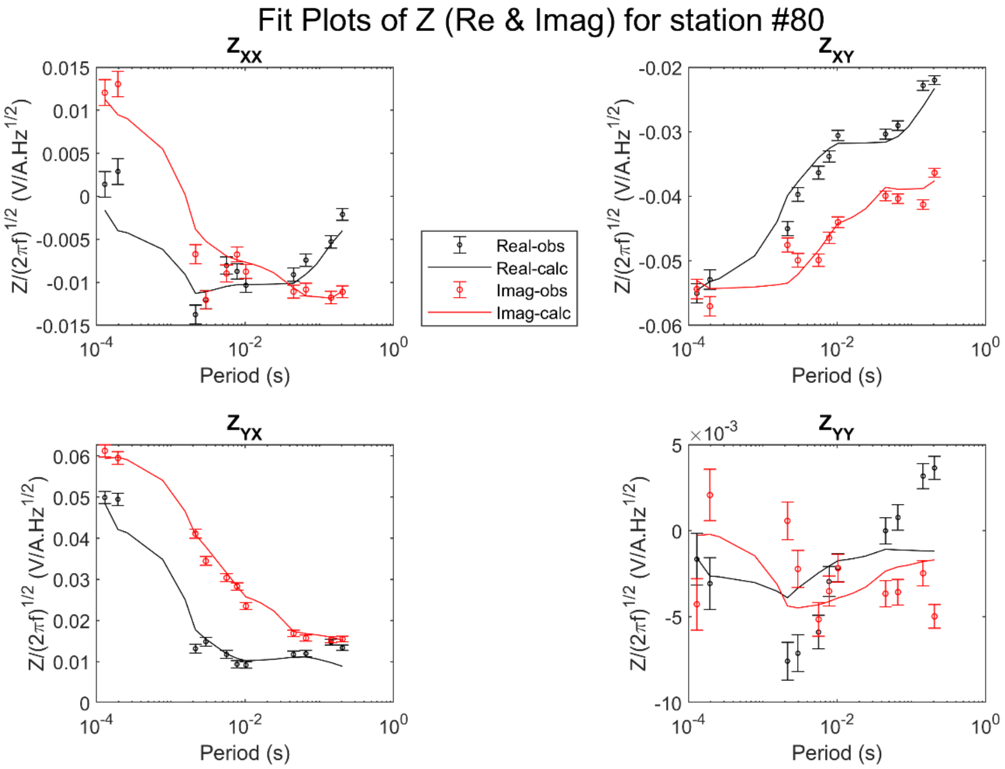
Fit Plots of Z (Re & Imag) for station #80
Z_XX
Z_XY
Z_YX
Z_YY
Real-obs
Real-calc
Imag-obs
Imag-calc
Z/(2πf)^1/2 (V/A.Hz^1/2)
Period (s)

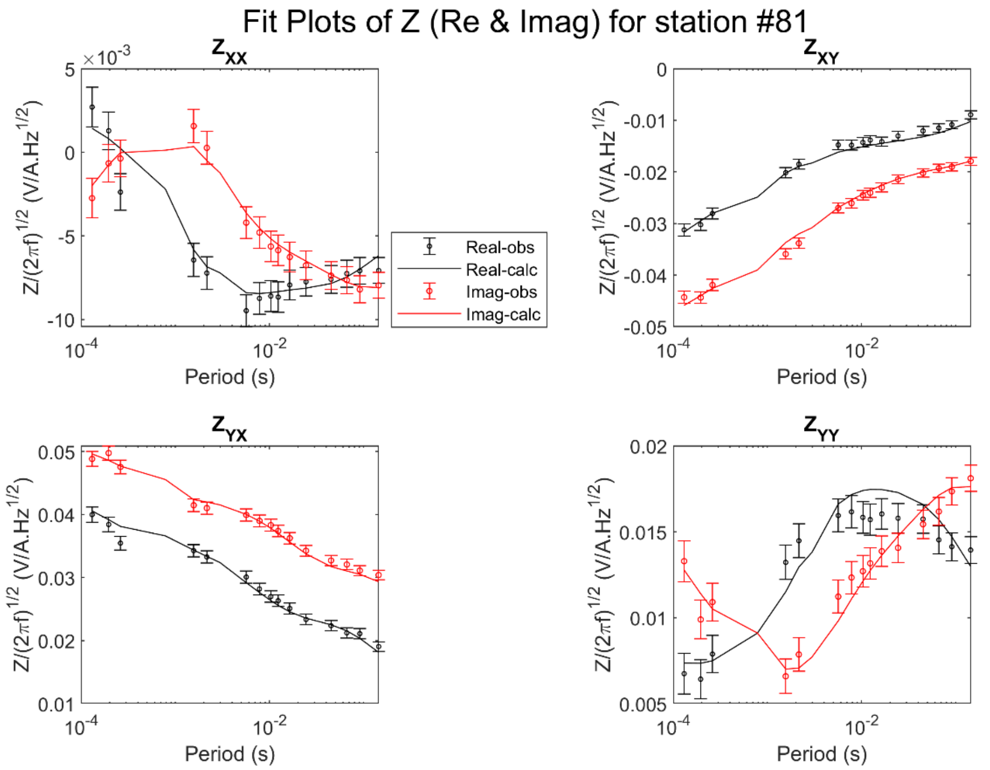
Fit Plots of Z (Re & Imag) for station #81
Z_XX
Z_XY
Z_YX
Z_YY
Real-obs
Real-calc
Imag-obs
Imag-calc
Z/(2πf)^1/2 (V/A.Hz^1/2)
Period (s)

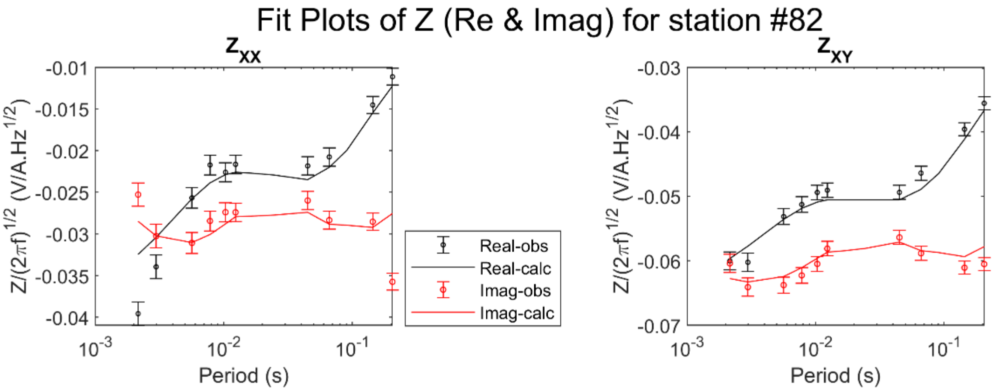
Fit Plots of Z (Re & Imag) for station #82
Z_XX
Z_XY
Z_YX
Z_YY
Z/(2πf)^1/2 (V/A.Hz^1/2)
Period (s)
Real-obs
Real-calc
Imag-obs
Imag-calc

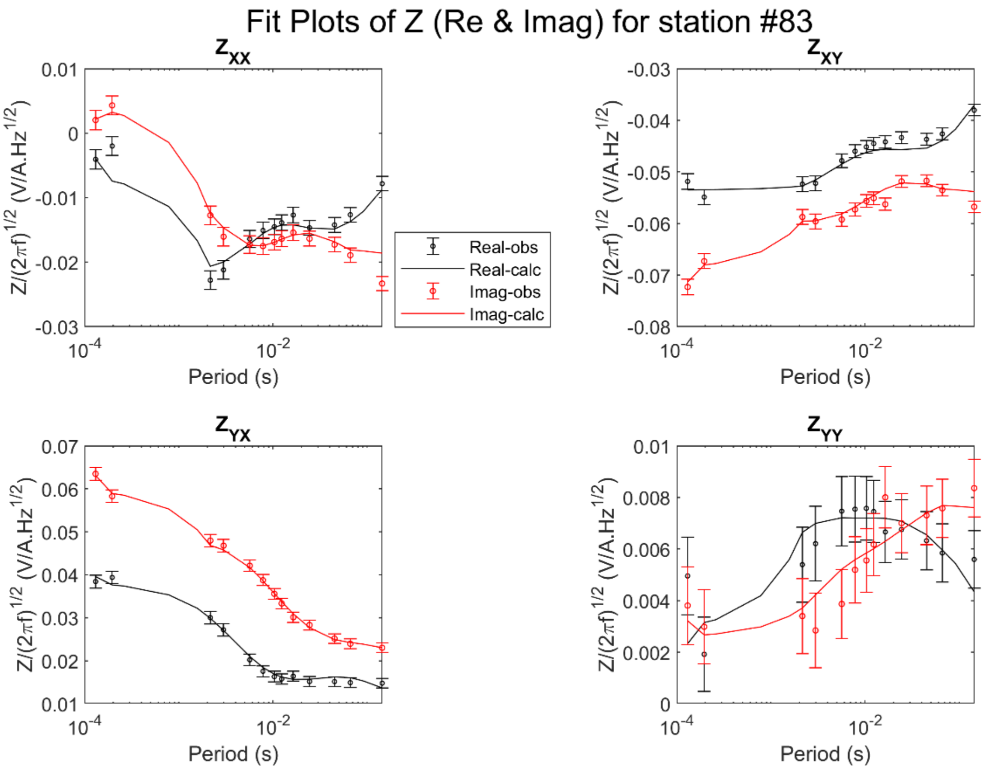
Fit Plots of Z (Re & Imag) for station #83
Z_XX
Z_XY
Z_YX
Z_YY
Z/(2πf)^1/2 (V/A.Hz^1/2)
Period (s)
Real-obs
Real-calc
Imag-obs
Imag-calc

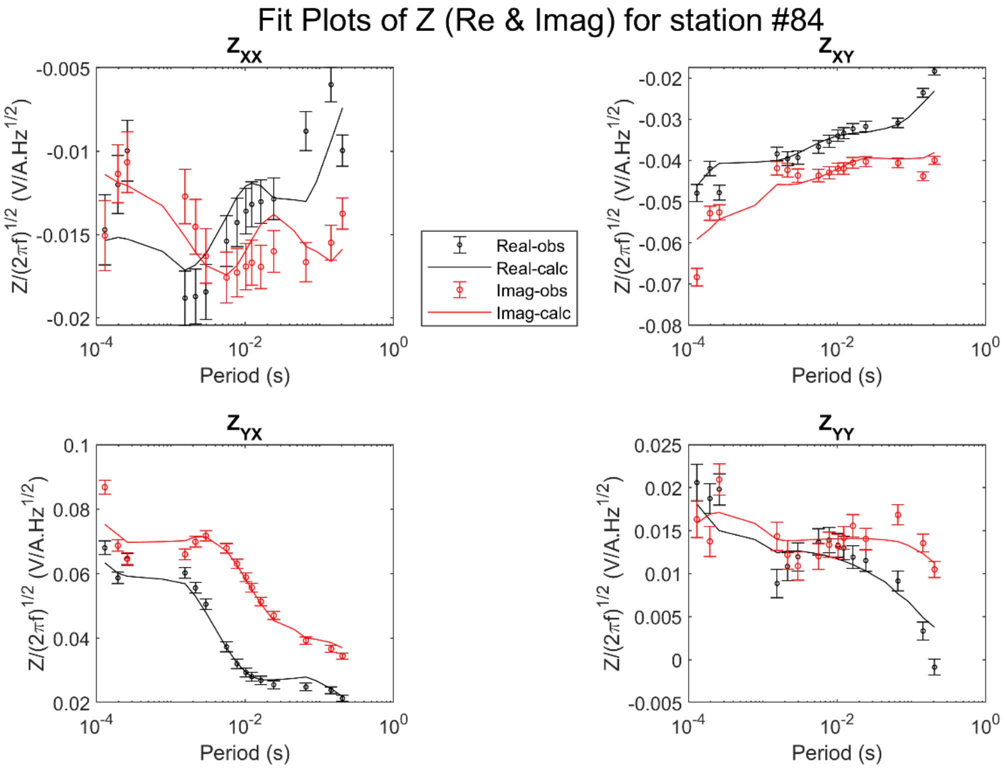
Fit Plots of Z (Re & Imag) for station #84
Z_XX
Z_XY
Z_YX
Z_YY
Z/(2πf)^1/2 (V/A.Hz^1/2)
Period (s)
Real-obs
Real-calc
Imag-obs
Imag-calc

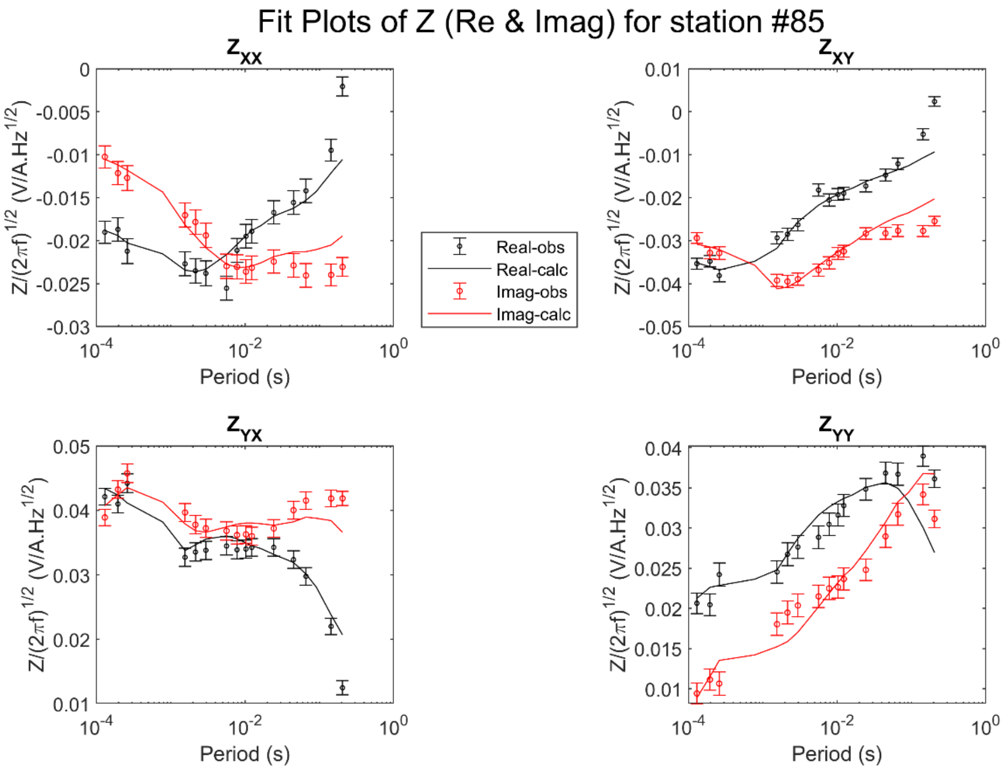
Fit Plots of Z (Re & Imag) for station #85
Z_XX
Z_XY
Z_YX
Z_YY
Z/(2πf)^1/2 (V/A.Hz^1/2)
Period (s)
Real-obs
Real-calc
Imag-obs
Imag-calc

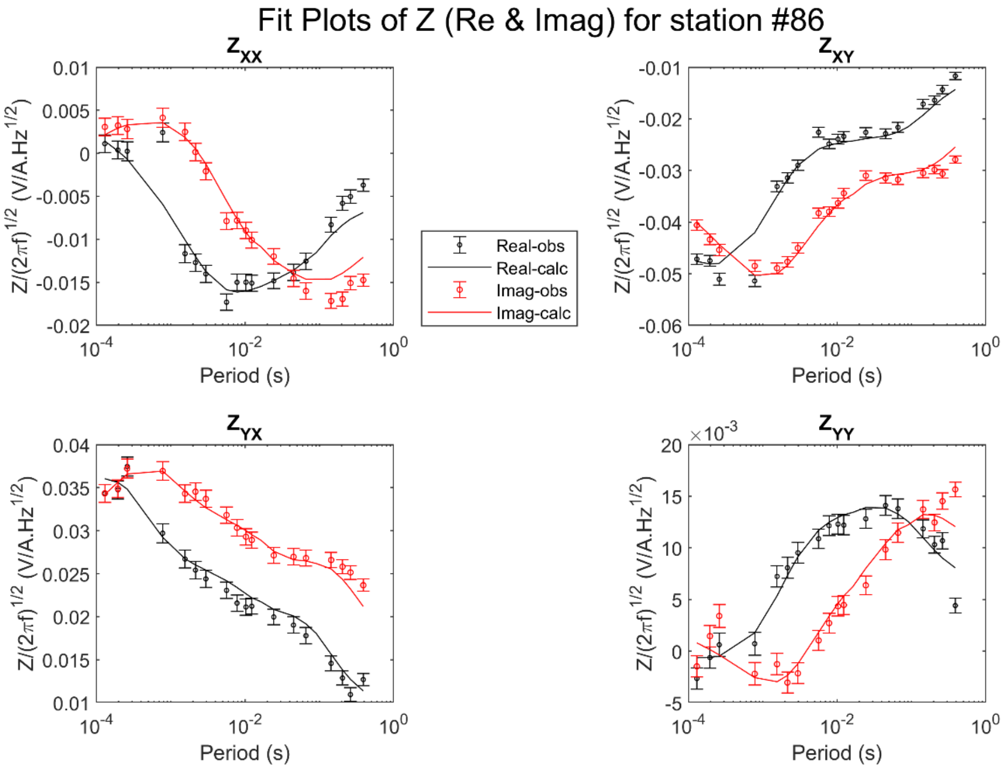

Fit Plots of Z (Re & Imag) for station #86
Z_XX
Z_XY
Z_YX
Z_YY
Real-obs
Real-calc
Imag-obs
Imag-calc
Z/(2πf)^1/2 (V/A.Hz^1/2)
Period (s)
×10^-3

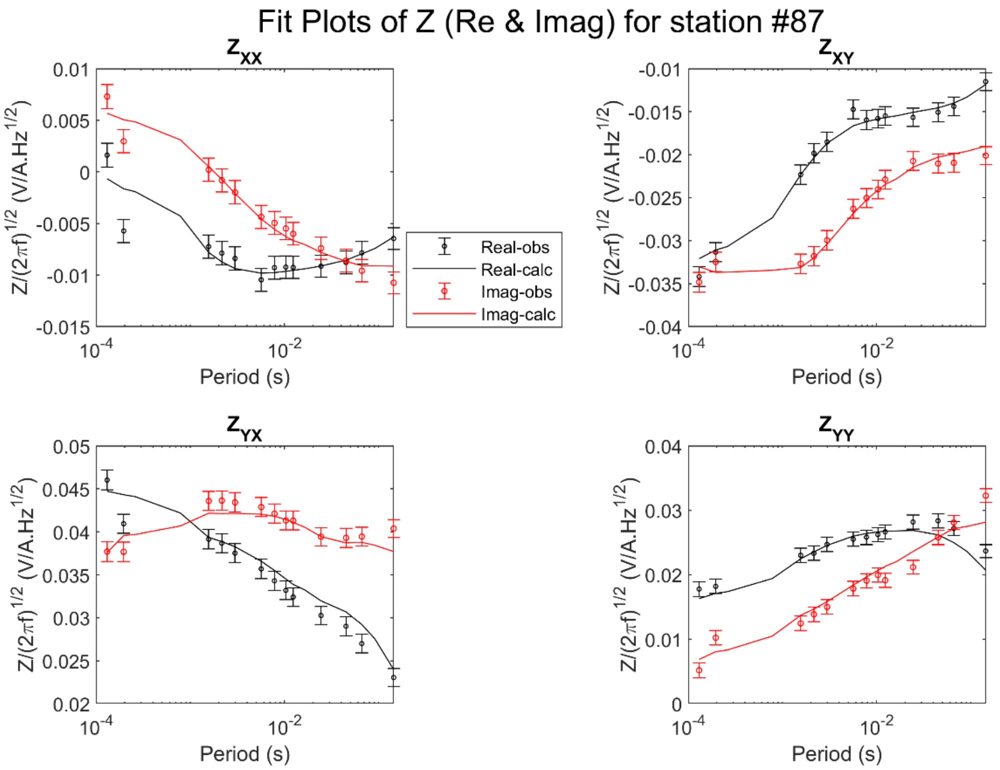

Fit Plots of Z (Re & Imag) for station #87
Z_XX
Z_XY
Z_YX
Z_YY
Real-obs
Real-calc
Imag-obs
Imag-calc
Z/(2πf)^1/2 (V/A.Hz^1/2)
Period (s)

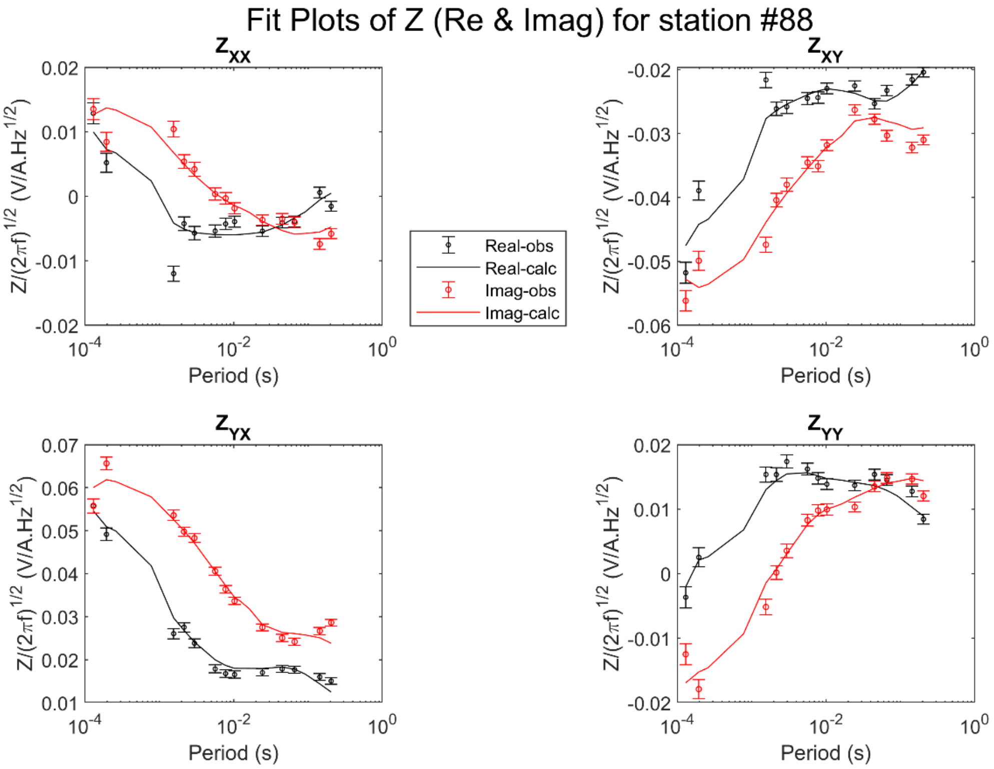
Fit Plots of Z (Re & Imag) for station #88
Z_{XX}
Z_{XY}
Z_{YX}
Z_{YY}
Real-obs
Real-calc
Imag-obs
Imag-calc
$Z/(2\pi f)^{1/2}$ (V/A.Hz$^{1/2}$)
Period (s)

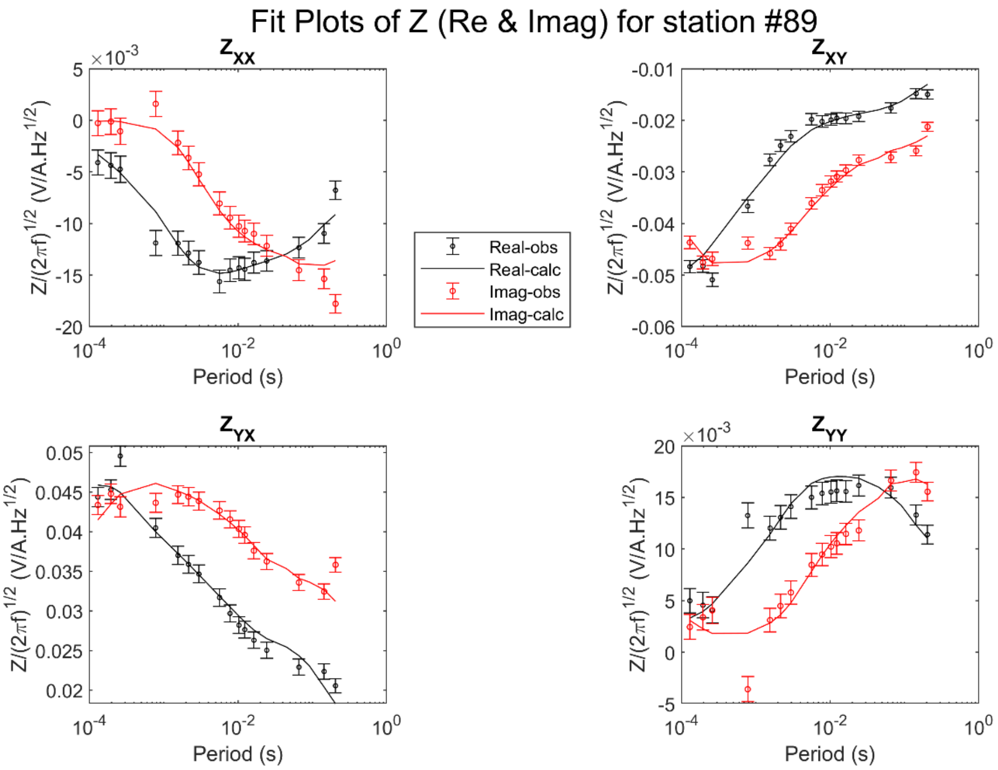
Fit Plots of Z (Re & Imag) for station #89
Z_{XX}
Z_{XY}
Z_{YX}
Z_{YY}
$\times 10^{-3}$
Real-obs
Real-calc
Imag-obs
Imag-calc
$Z/(2\pi f)^{1/2}$ (V/A.Hz$^{1/2}$)
Period (s)

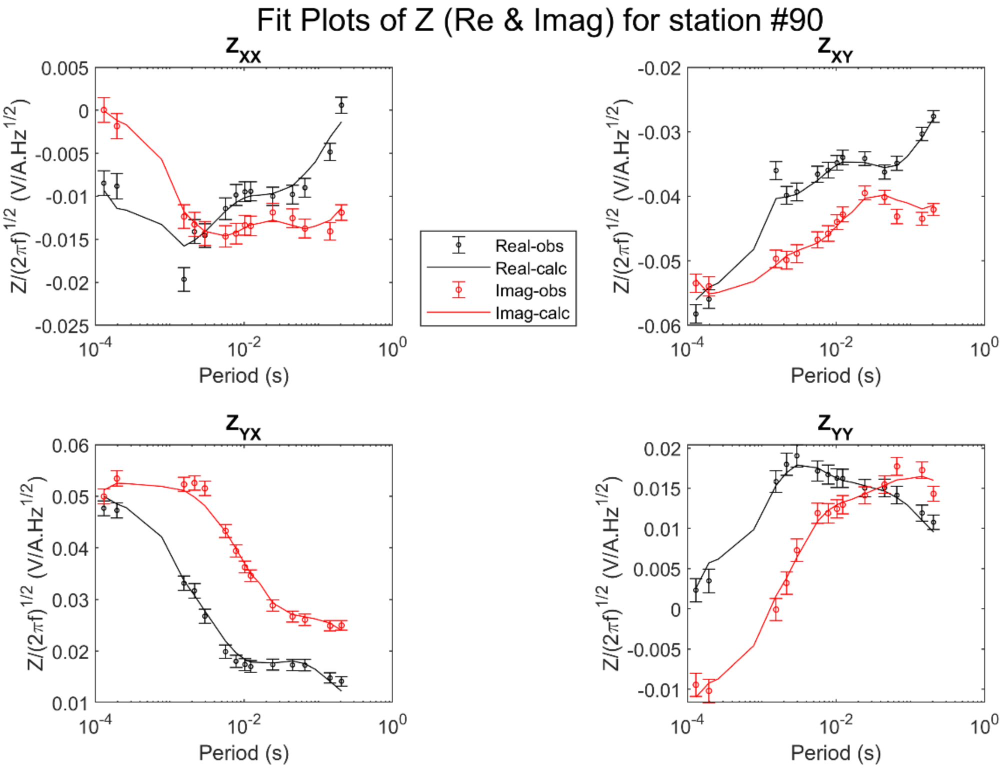

Fit Plots of Z (Re & Imag) for station #90
Z_{XX}
Z_{XY}
Z_{YX}
Z_{YY}
Real-obs
Real-calc
Imag-obs
Imag-calc
$Z/(2\pi f)^{1/2}$ (V/A.Hz$^{1/2}$)
Period (s)

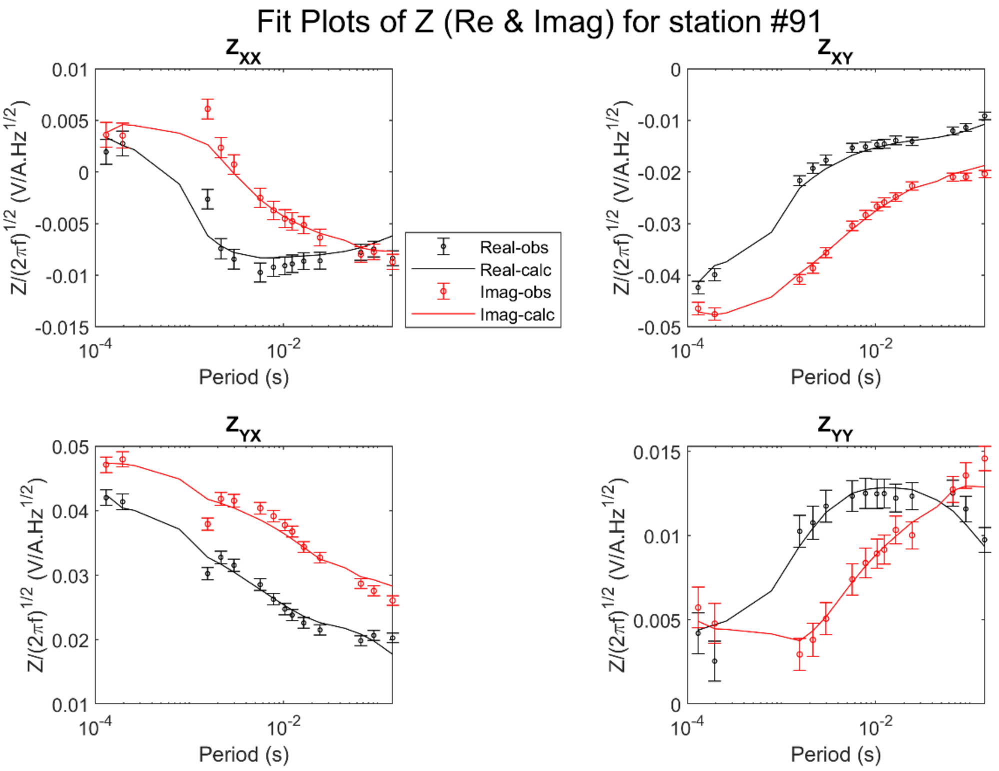

Fit Plots of Z (Re & Imag) for station #91
Z_{XX}
Z_{XY}
Z_{YX}
Z_{YY}
Real-obs
Real-calc
Imag-obs
Imag-calc
$Z/(2\pi f)^{1/2}$ (V/A.Hz$^{1/2}$)
Period (s)

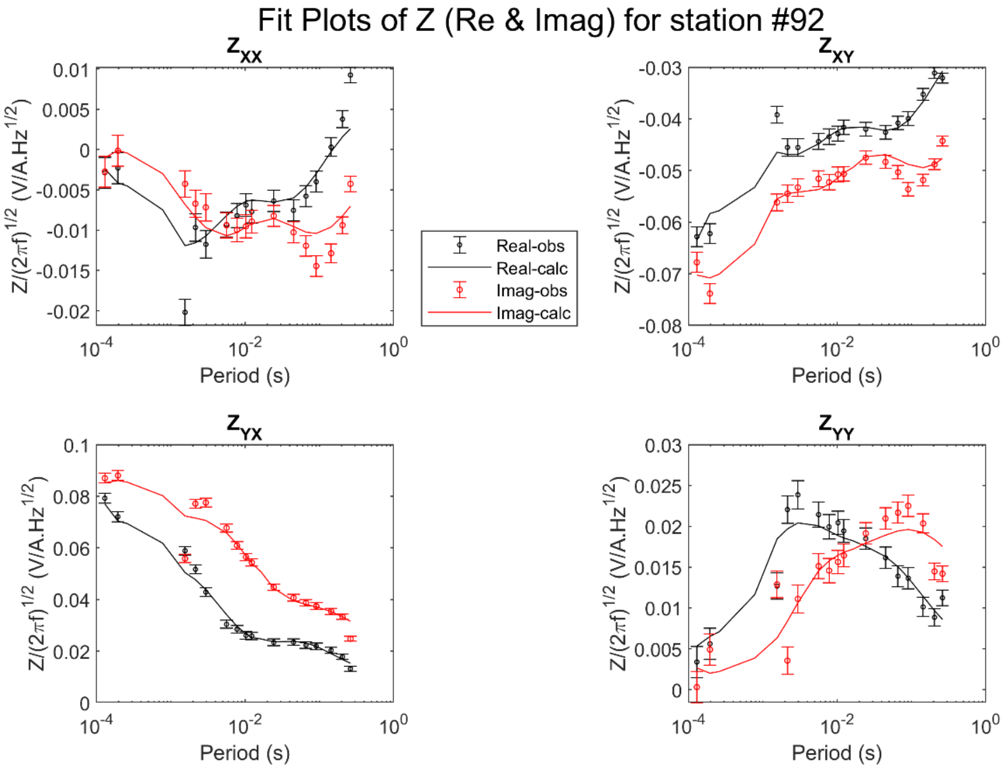
Fit Plots of Z (Re & Imag) for station #92
Z_XX
Z_XY
Z_YX
Z_YY
Z/(2πf)^1/2 (V/A.Hz^1/2)
Period (s)
Real-obs
Real-calc
Imag-obs
Imag-calc

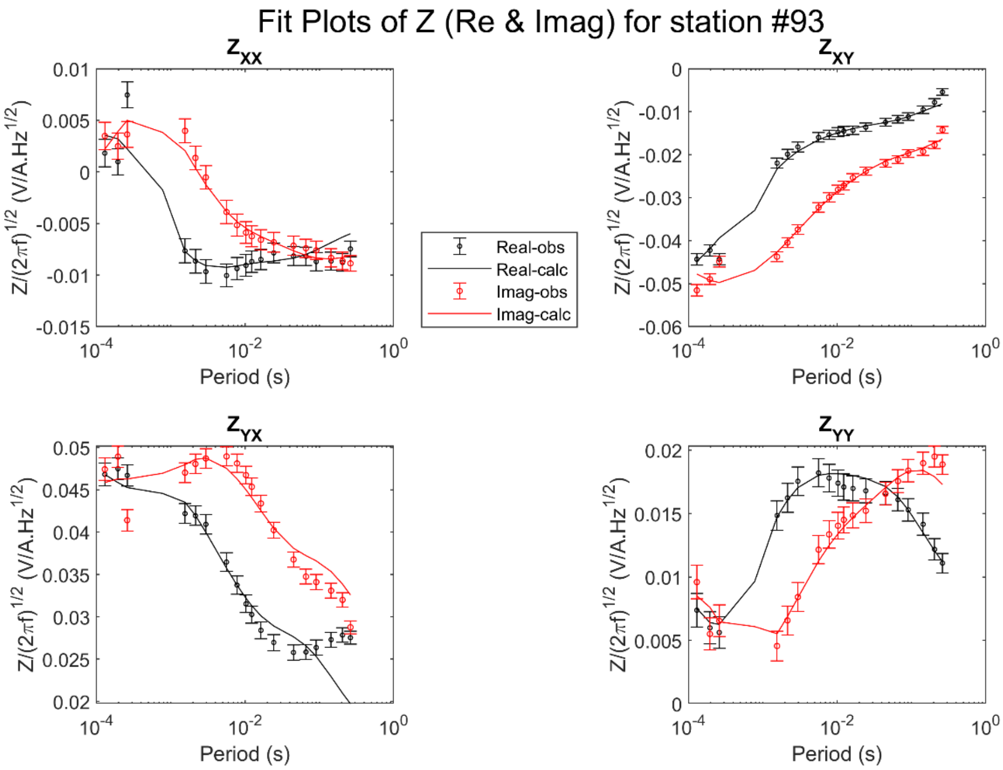
Fit Plots of Z (Re & Imag) for station #93
Z_XX
Z_XY
Z_YX
Z_YY
Z/(2πf)^1/2 (V/A.Hz^1/2)
Period (s)
Real-obs
Real-calc
Imag-obs
Imag-calc

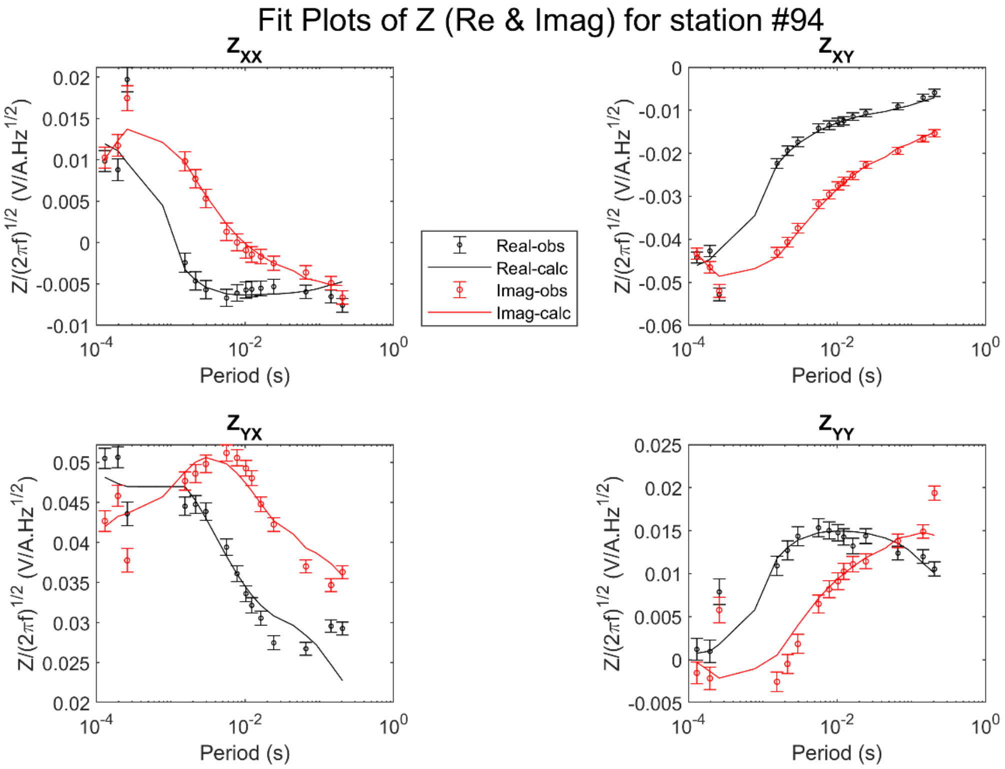
Fit Plots of Z (Re & Imag) for station #94
Z_XX
Z_XY
Z_YX
Z_YY
Real-obs
Real-calc
Imag-obs
Imag-calc
Z/(2πf)^1/2 (V/A.Hz^1/2)
Period (s)

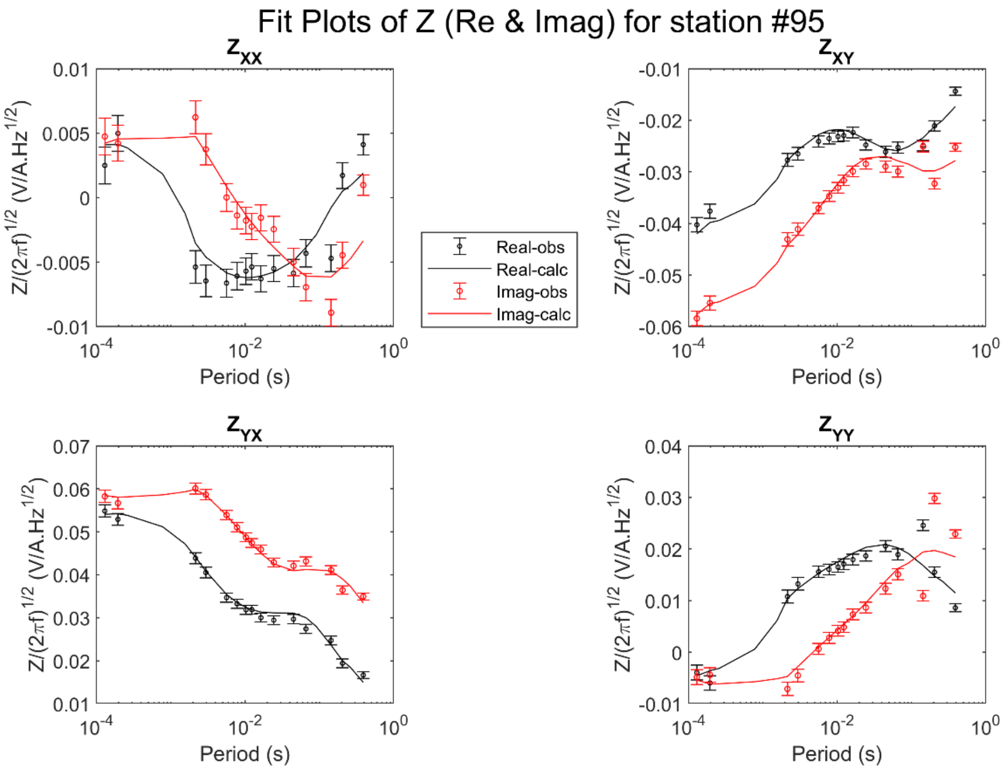
Fit Plots of Z (Re & Imag) for station #95
Z_XX
Z_XY
Z_YX
Z_YY
Real-obs
Real-calc
Imag-obs
Imag-calc
Z/(2πf)^1/2 (V/A.Hz^1/2)
Period (s)

Fit Plots of Z (Re & Imag) for station #96

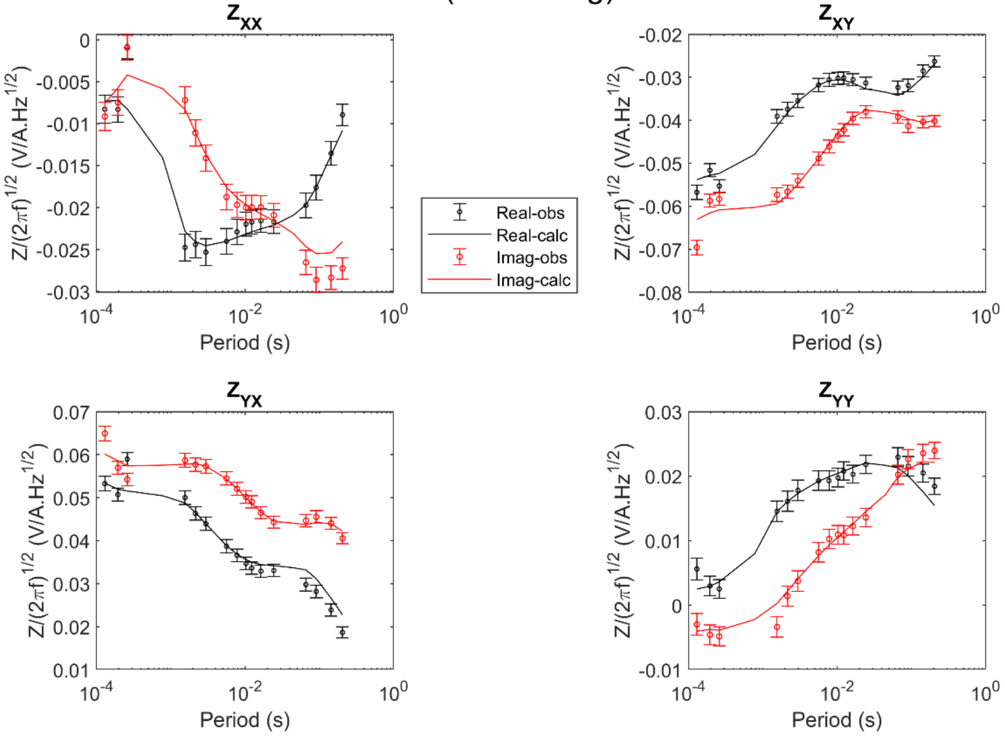

Fit Plots of Z (Re & Imag) for station #97

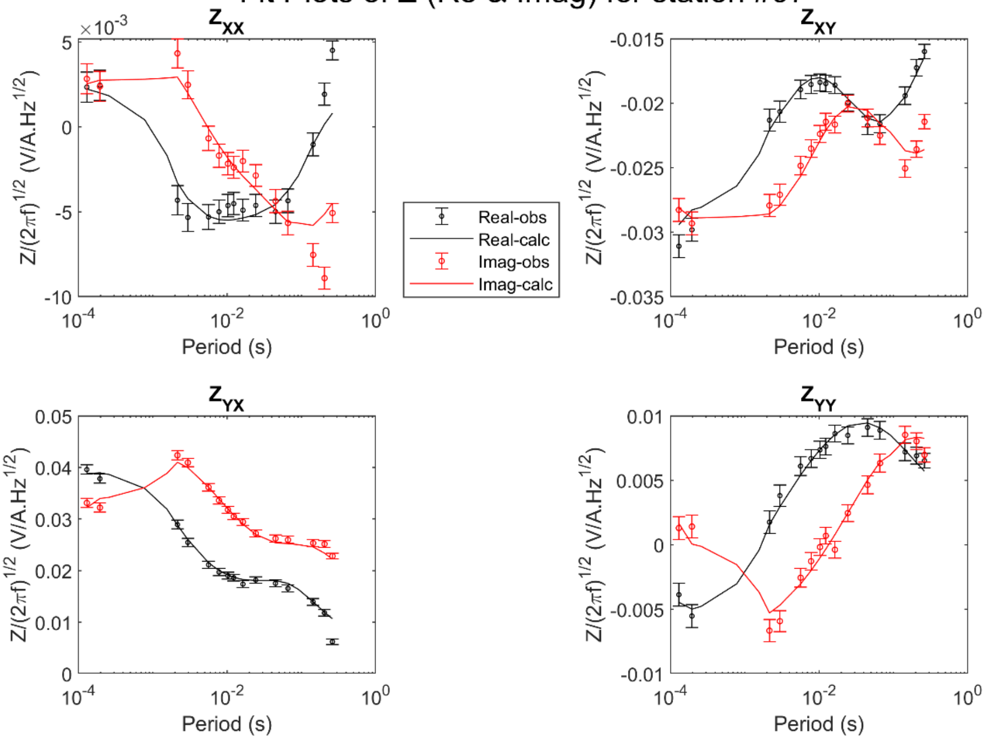

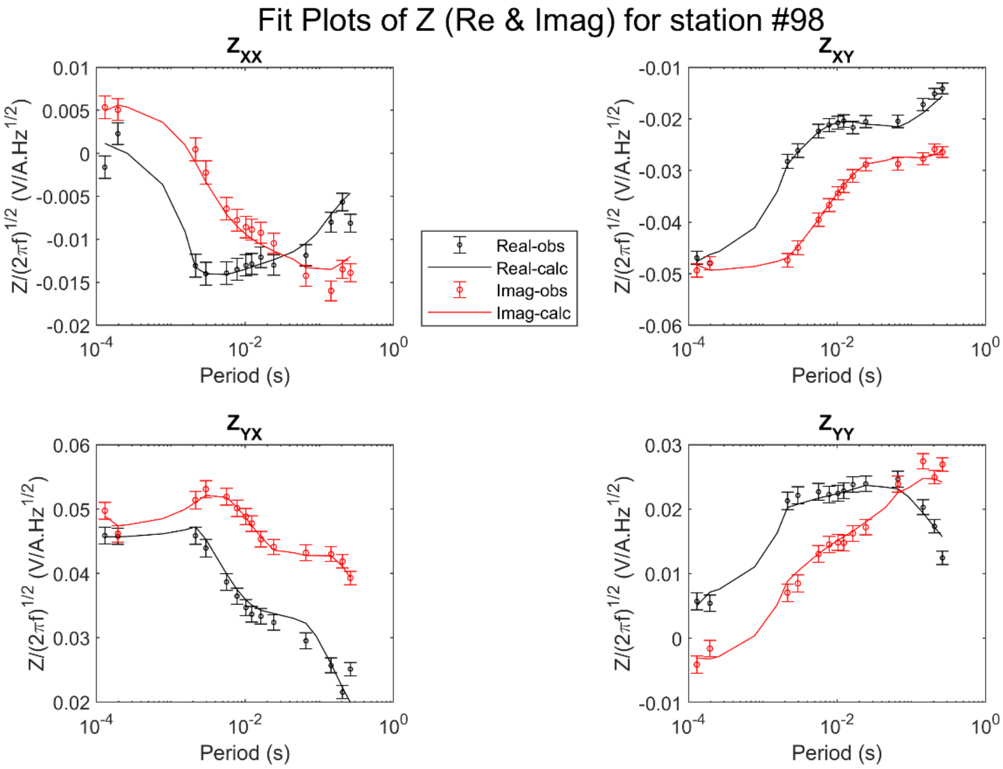

Fit Plots of Z (Re & Imag) for station #98
ZXX
ZXY
ZYX
ZYY
Z/(2πf)1/2 (V/A.Hz1/2)
Period (s)
Real-obs
Real-calc
Imag-obs
Imag-calc

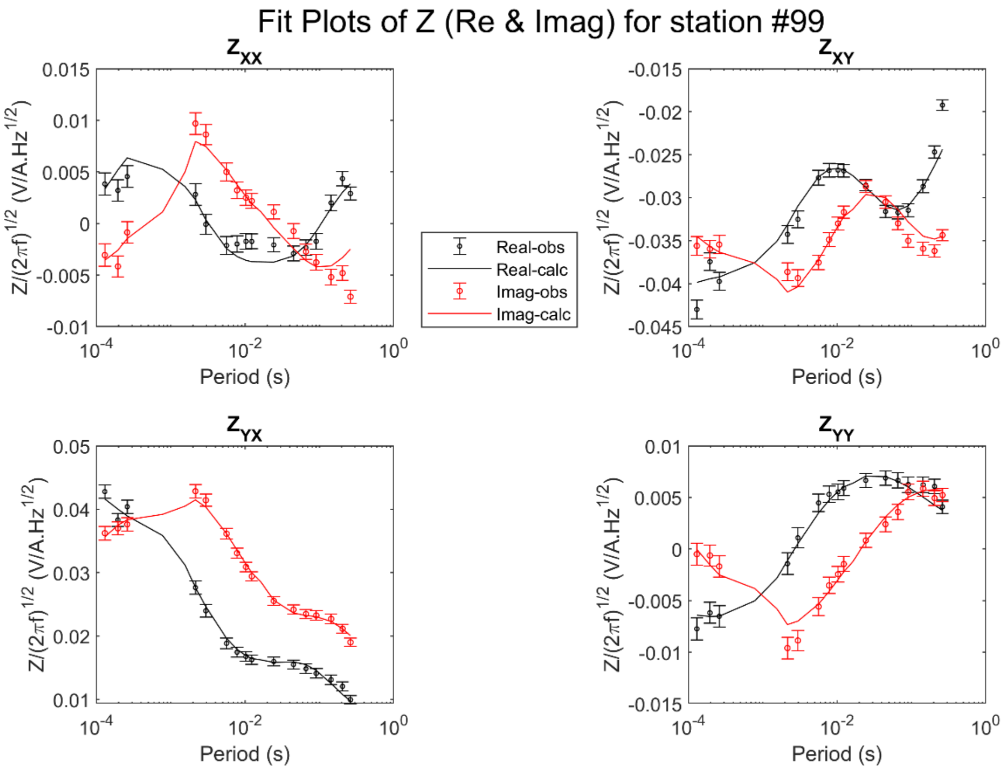

Fit Plots of Z (Re & Imag) for station #99
ZXX
ZXY
ZYX
ZYY
Z/(2πf)1/2 (V/A.Hz1/2)
Period (s)
Real-obs
Real-calc
Imag-obs
Imag-calc

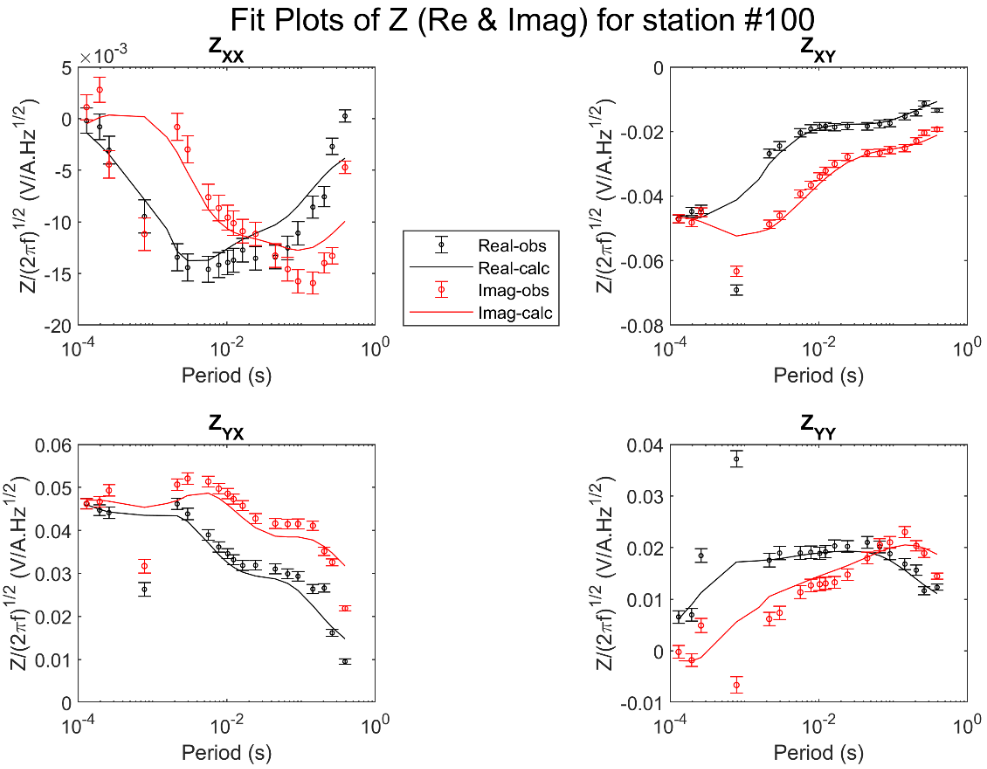
Fit Plots of Z (Re & Imag) for station #100
Z_XX
Z_XY
Z_YX
Z_YY
Real-obs
Real-calc
Imag-obs
Imag-calc
Z/(2πf)^1/2 (V/A.Hz^1/2)
Period (s)

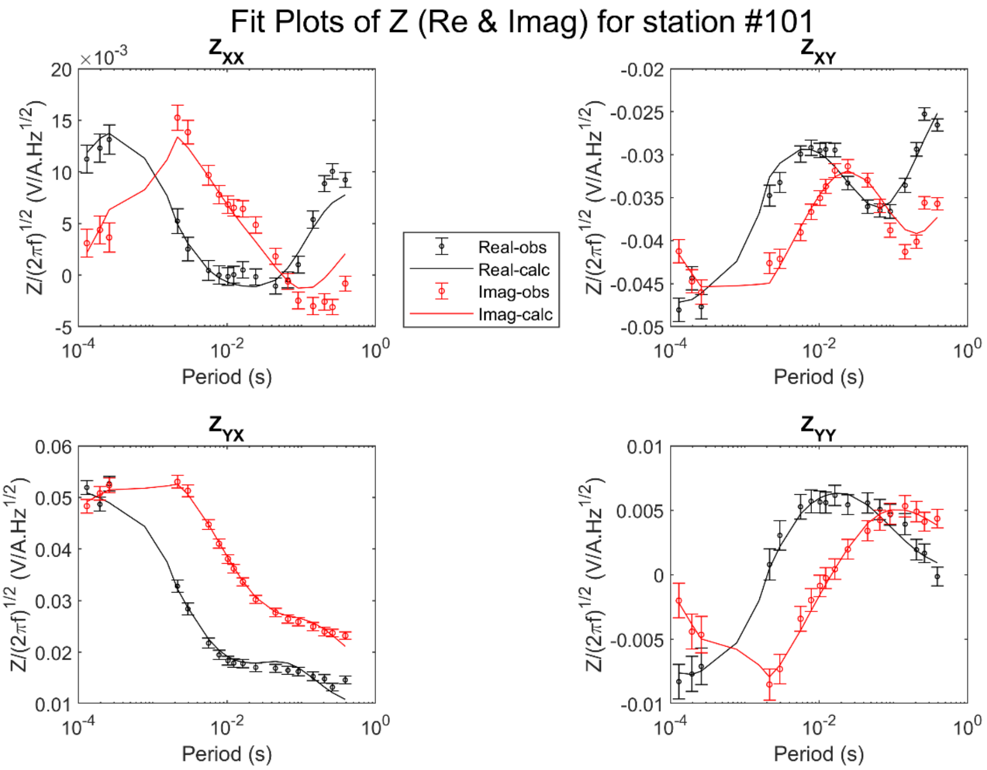
Fit Plots of Z (Re & Imag) for station #101
Z_XX
Z_XY
Z_YX
Z_YY
Real-obs
Real-calc
Imag-obs
Imag-calc
Z/(2πf)^1/2 (V/A.Hz^1/2)
Period (s)

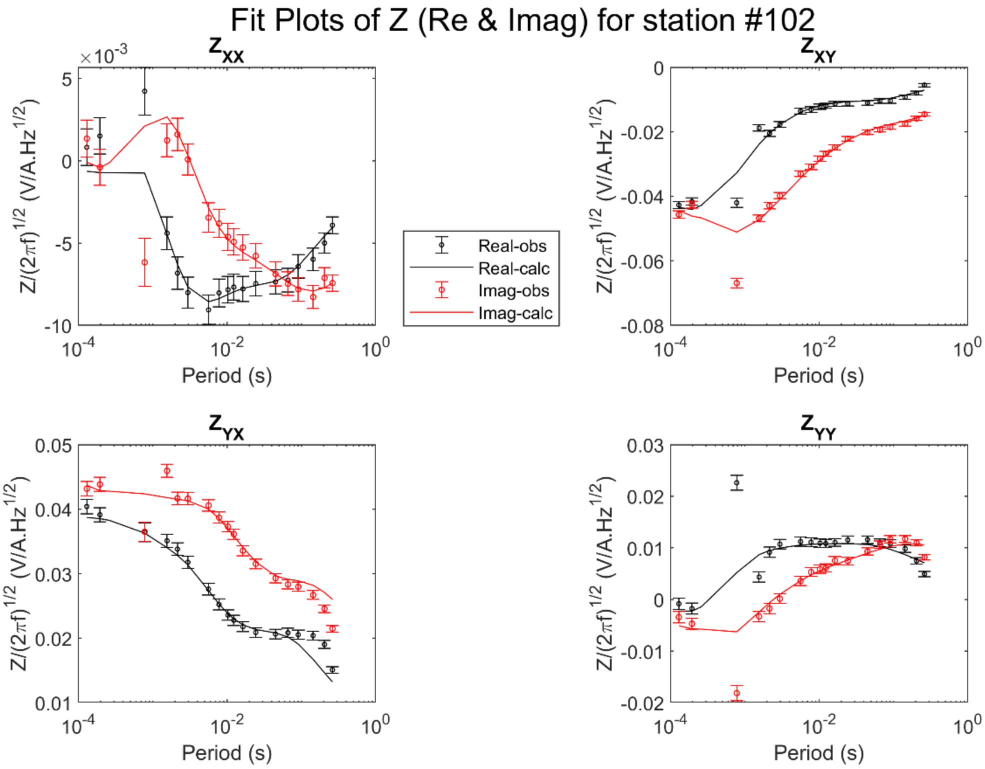
Fit Plots of Z (Re & Imag) for station #102
Z_{XX}
Z_{XY}
Z_{YX}
Z_{YY}
$\times 10^{-3}$
$Z/(2\pi f)^{1/2}$ (V/A.Hz$^{1/2}$)
Period (s)
Real-obs
Real-calc
Imag-obs
Imag-calc

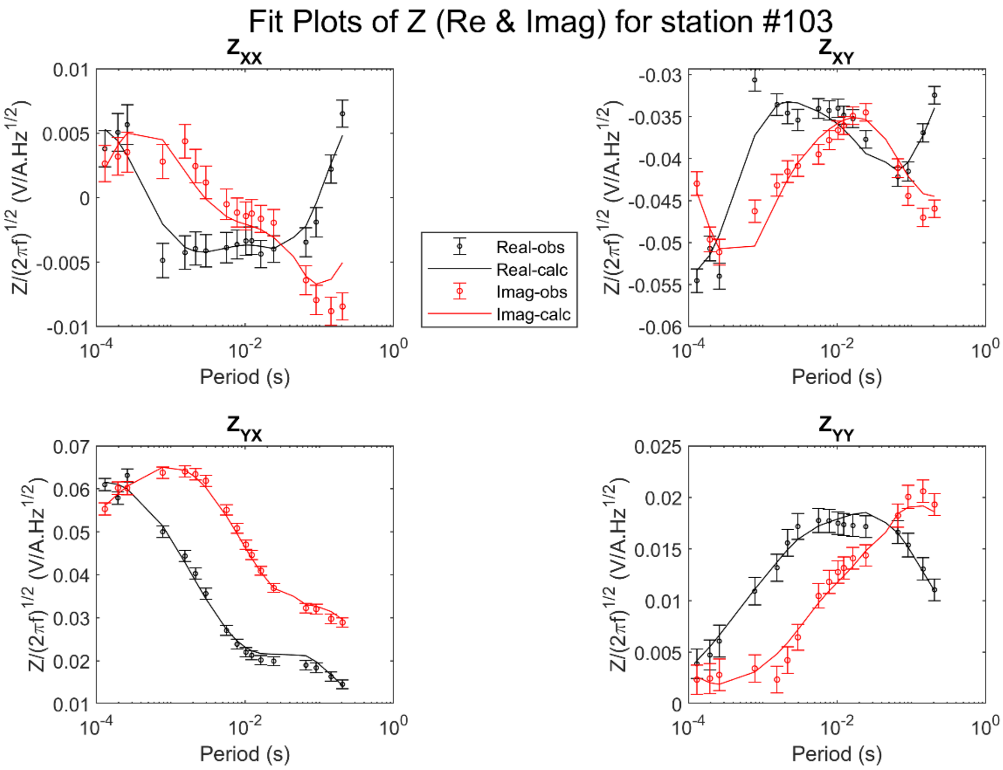
Fit Plots of Z (Re & Imag) for station #103
Z_{XX}
Z_{XY}
Z_{YX}
Z_{YY}
$Z/(2\pi f)^{1/2}$ (V/A.Hz$^{1/2}$)
Period (s)
Real-obs
Real-calc
Imag-obs
Imag-calc

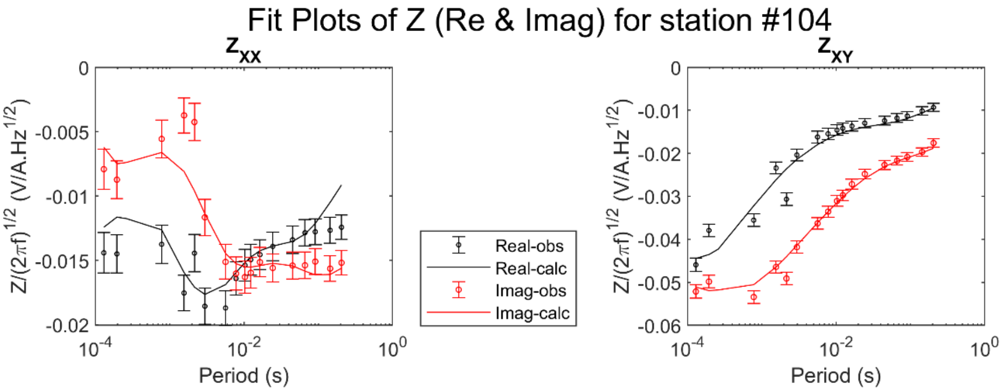

Fit Plots of Z (Re & Imag) for station #104
Z_XX
Z_XY
Z_YX
Z_YY
Z/(2πf)^1/2 (V/A.Hz^1/2)
Period (s)
Real-obs
Real-calc
Imag-obs
Imag-calc

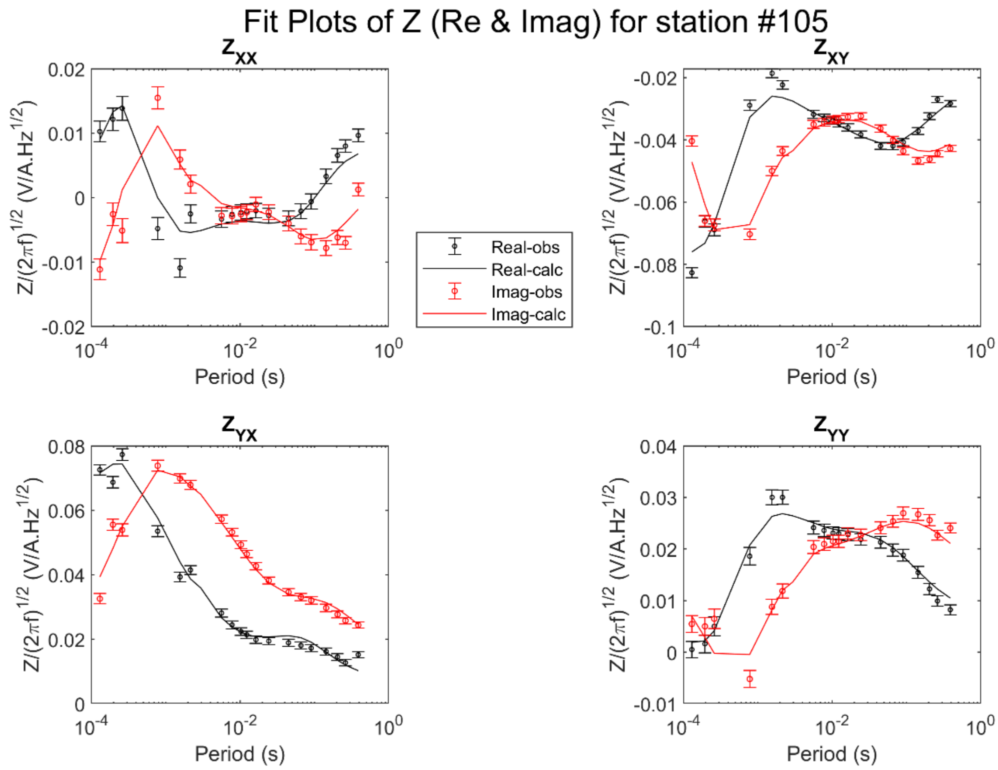

Fit Plots of Z (Re & Imag) for station #105
Z_XX
Z_XY
Z_YX
Z_YY
Z/(2πf)^1/2 (V/A.Hz^1/2)
Period (s)
Real-obs
Real-calc
Imag-obs
Imag-calc

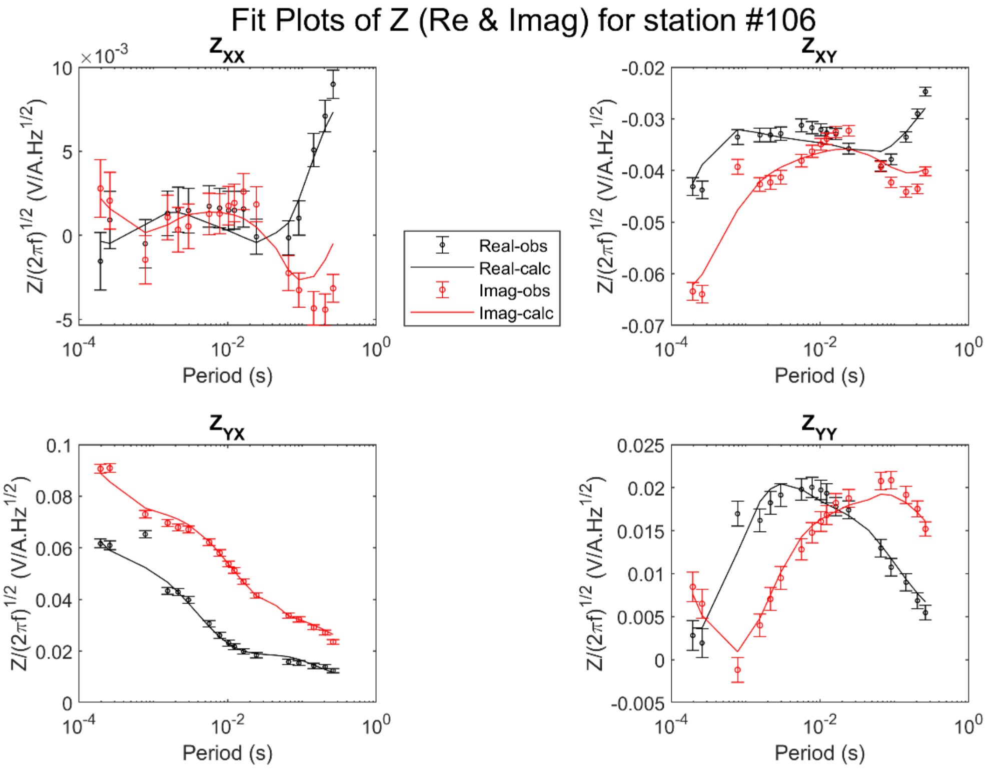
Fit Plots of Z (Re & Imag) for station #106
Z_XX
Z_XY
Z_YX
Z_YY
Z/(2πf)^1/2 (V/A.Hz^1/2)
Period (s)
Real-obs
Real-calc
Imag-obs
Imag-calc

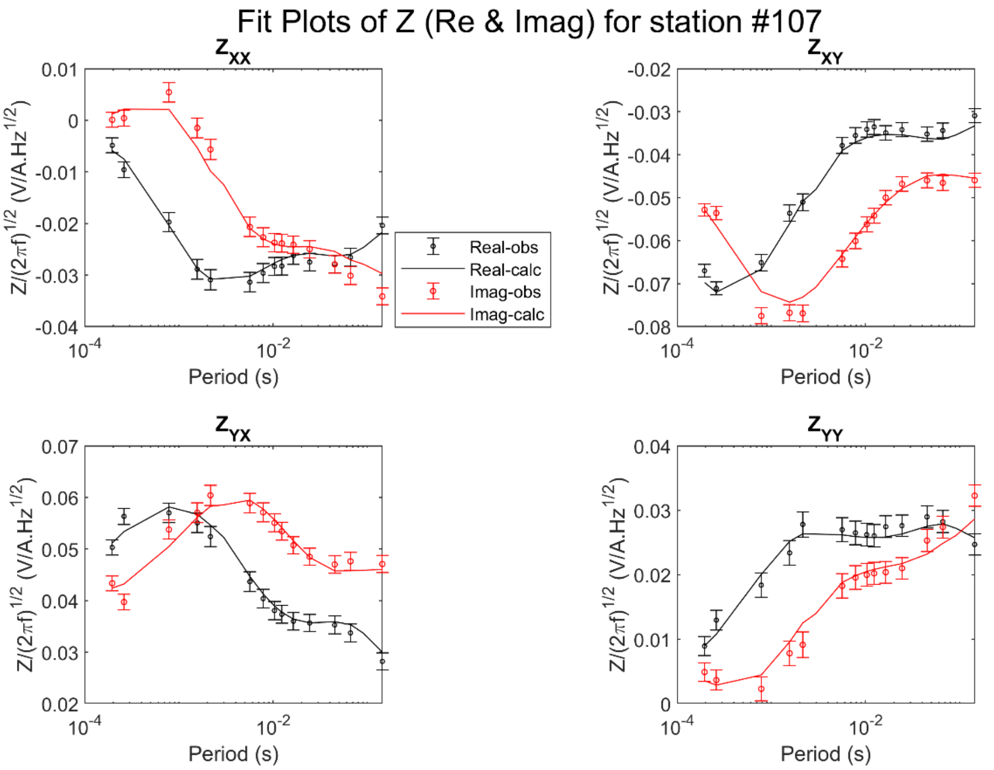
Fit Plots of Z (Re & Imag) for station #107
Z_XX
Z_XY
Z_YX
Z_YY
Z/(2πf)^1/2 (V/A.Hz^1/2)
Period (s)
Real-obs
Real-calc
Imag-obs
Imag-calc

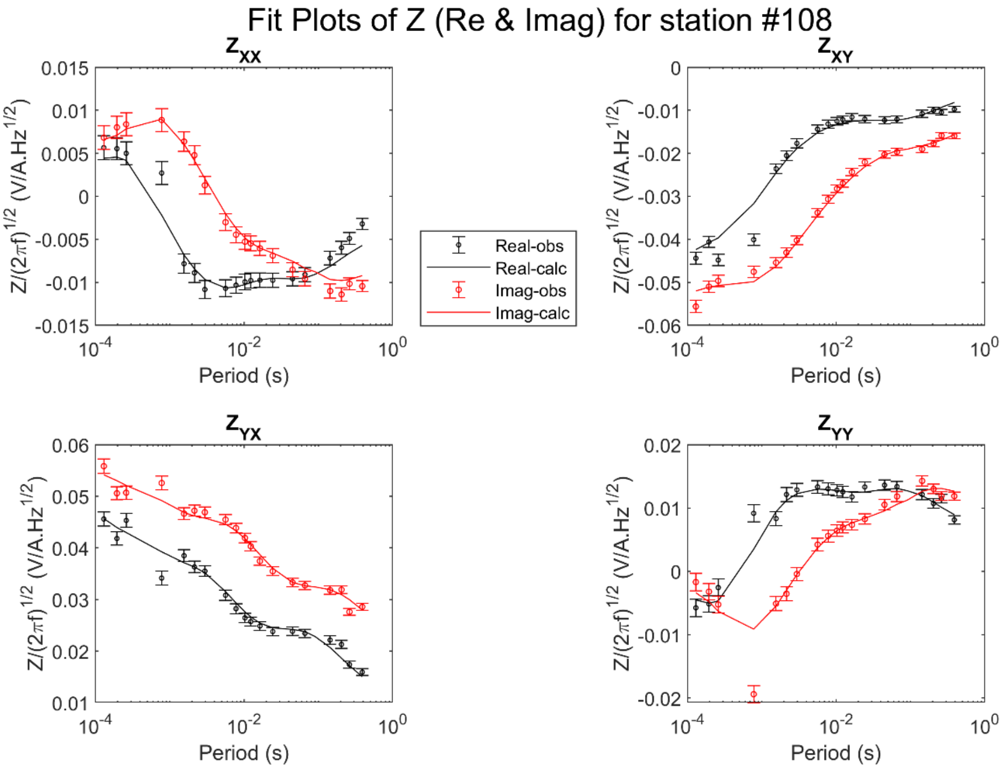
Fit Plots of Z (Re & Imag) for station #108
Z_{XX}
Z_{XY}
Z_{YX}
Z_{YY}
$Z/(2\pi f)^{1/2}$ (V/A.Hz$^{1/2}$)
Period (s)
Real-obs
Real-calc
Imag-obs
Imag-calc

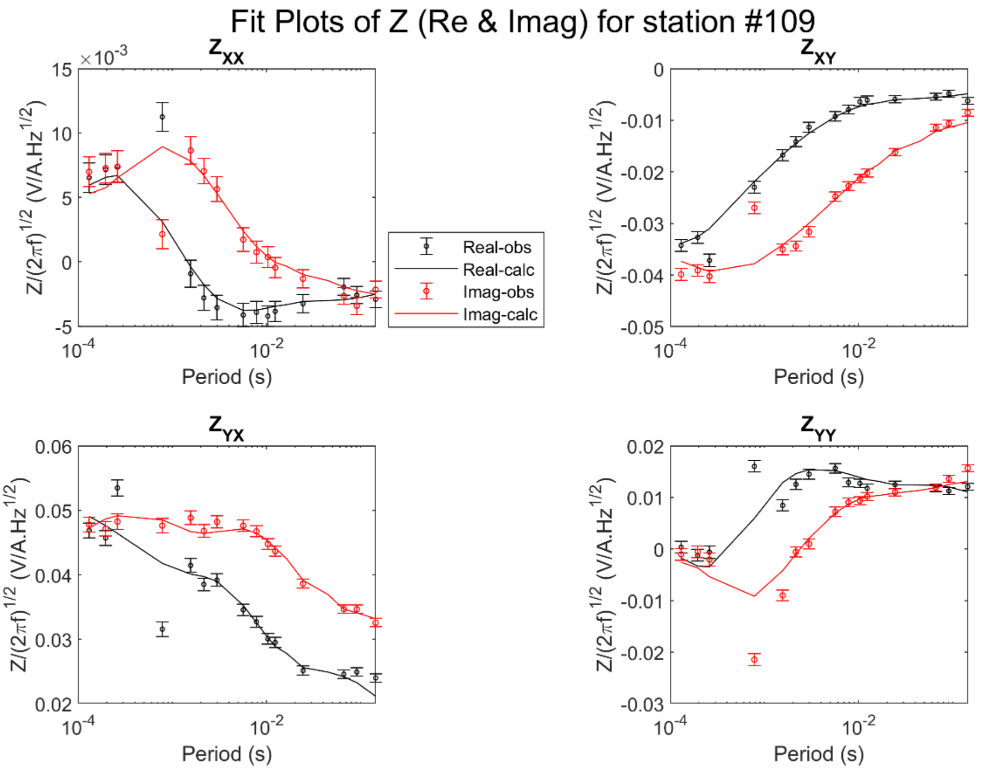
Fit Plots of Z (Re & Imag) for station #109
Z_{XX}
Z_{XY}
Z_{YX}
Z_{YY}
$\times 10^{-3}$
$Z/(2\pi f)^{1/2}$ (V/A.Hz$^{1/2}$)
Period (s)
Real-obs
Real-calc
Imag-obs
Imag-calc

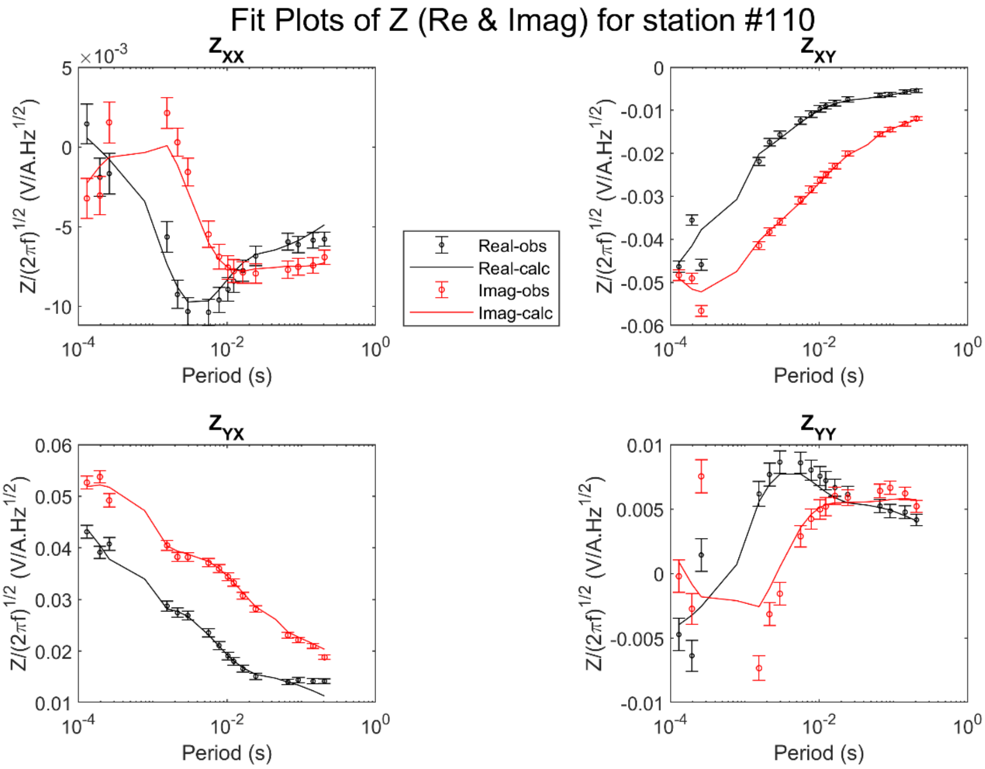
Fit Plots of Z (Re & Imag) for station #110
Z_XX
Z_XY
Z_YX
Z_YY
Z/(2πf)^1/2 (V/A.Hz^1/2)
Period (s)
Real-obs
Real-calc
Imag-obs
Imag-calc

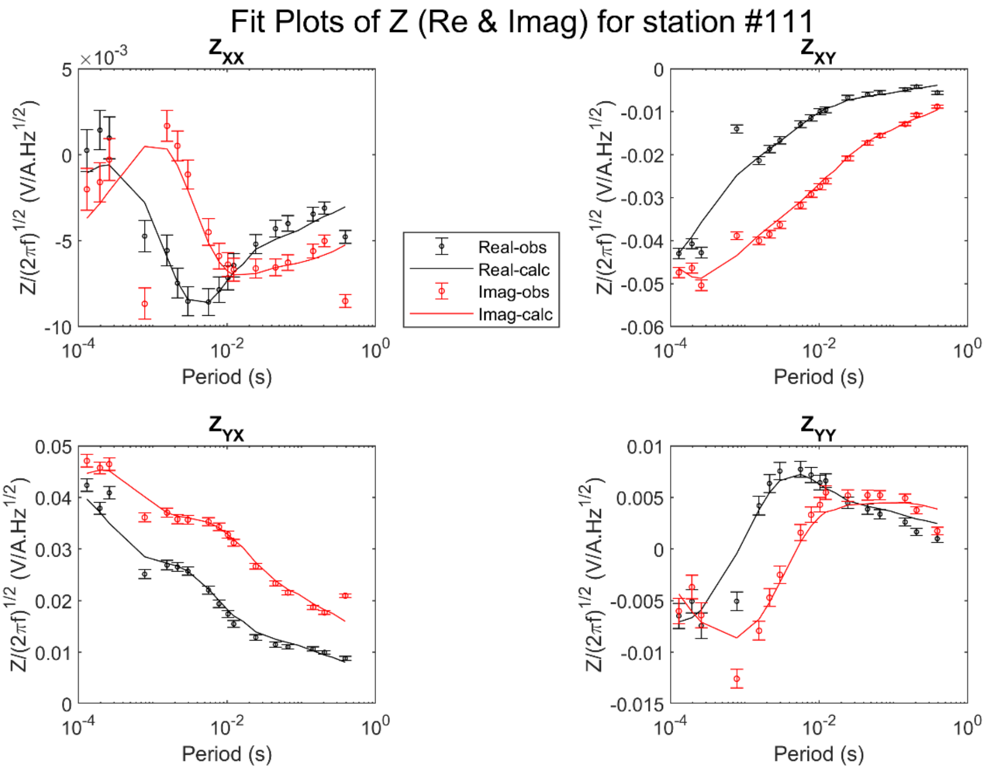
Fit Plots of Z (Re & Imag) for station #111
Z_XX
Z_XY
Z_YX
Z_YY
Z/(2πf)^1/2 (V/A.Hz^1/2)
Period (s)
Real-obs
Real-calc
Imag-obs
Imag-calc

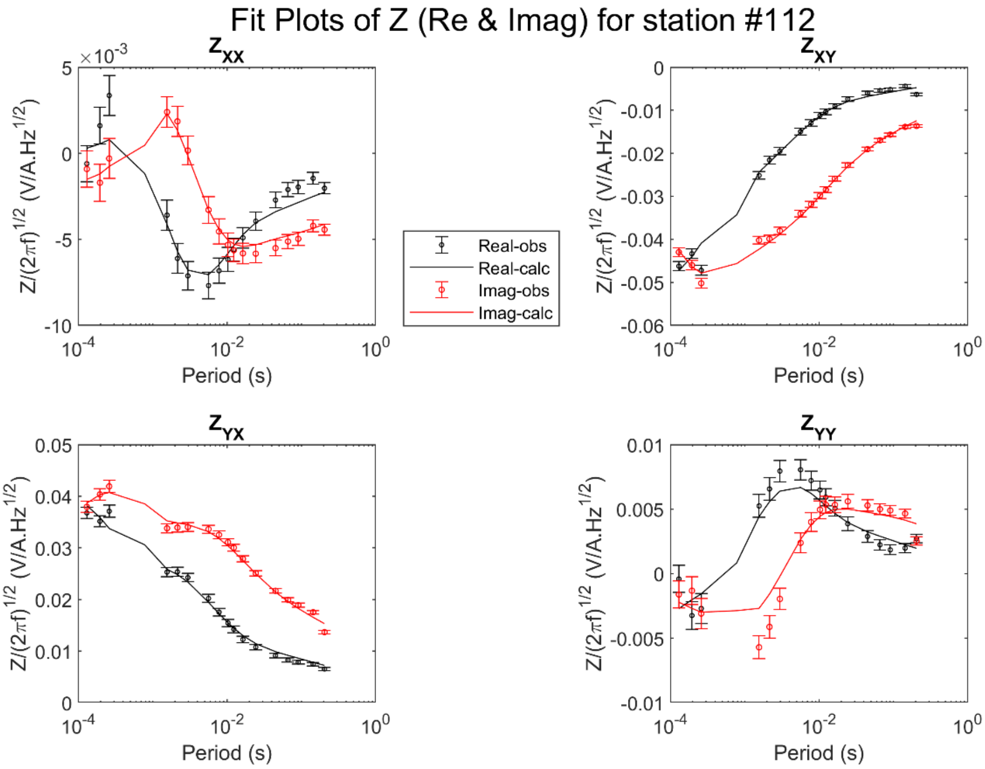
Fit Plots of Z (Re & Imag) for station #112
Z_{XX}
Z_{XY}
Z_{YX}
Z_{YY}
$\times 10^{-3}$
$Z/(2\pi f)^{1/2}$ (V/A.Hz$^{1/2}$)
Period (s)
Real-obs
Real-calc
Imag-obs
Imag-calc

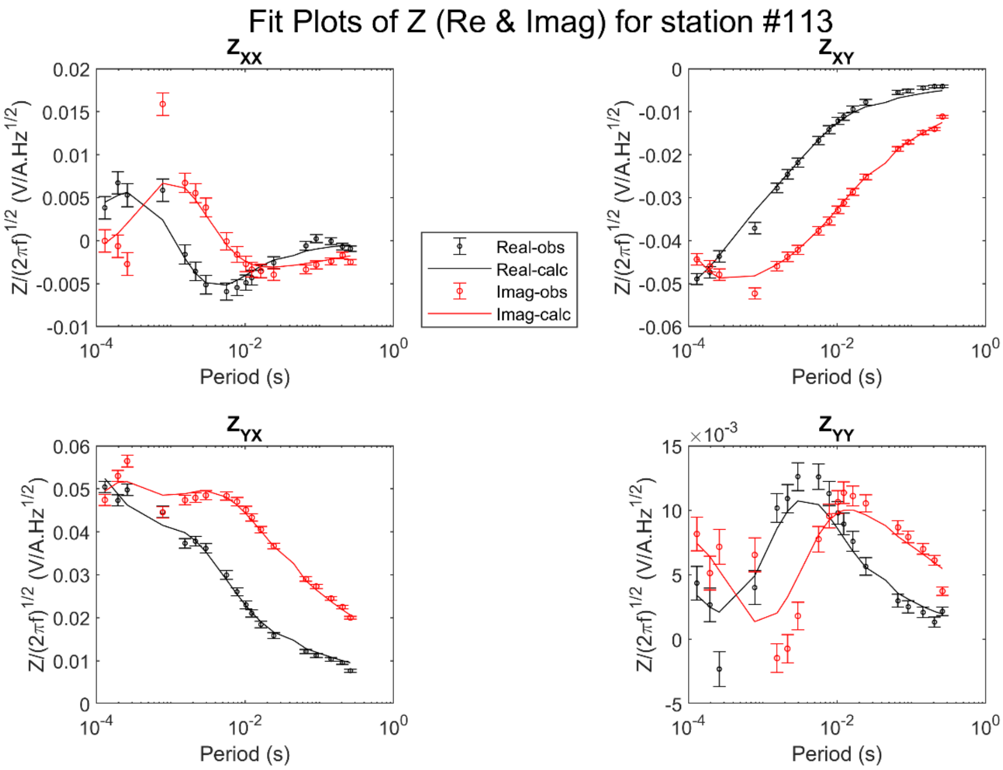
Fit Plots of Z (Re & Imag) for station #113
Z_{XX}
Z_{XY}
Z_{YX}
Z_{YY}
$\times 10^{-3}$
$Z/(2\pi f)^{1/2}$ (V/A.Hz$^{1/2}$)
Period (s)
Real-obs
Real-calc
Imag-obs
Imag-calc

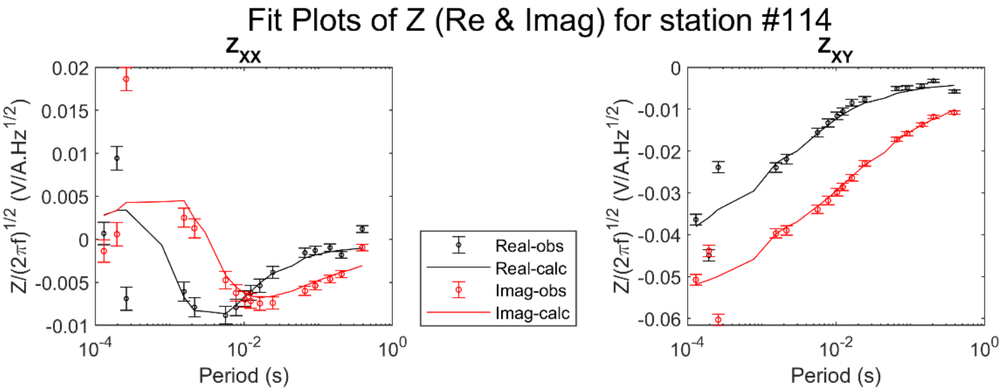
Fit Plots of Z (Re & Imag) for station #114
ZXX
ZXY
ZYX
ZYY
Z/(2πf)1/2 (V/A.Hz1/2)
Period (s)
Real-obs
Real-calc
Imag-obs
Imag-calc

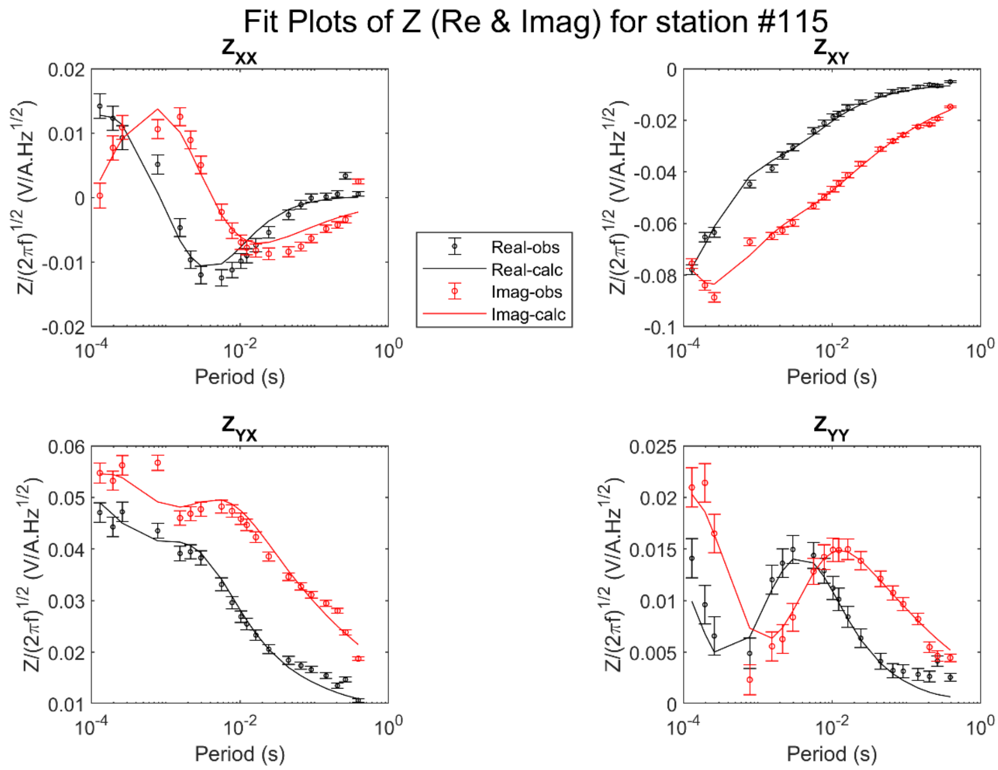
Fit Plots of Z (Re & Imag) for station #115
ZXX
ZXY
ZYX
ZYY
Z/(2πf)1/2 (V/A.Hz1/2)
Period (s)
Real-obs
Real-calc
Imag-obs
Imag-calc

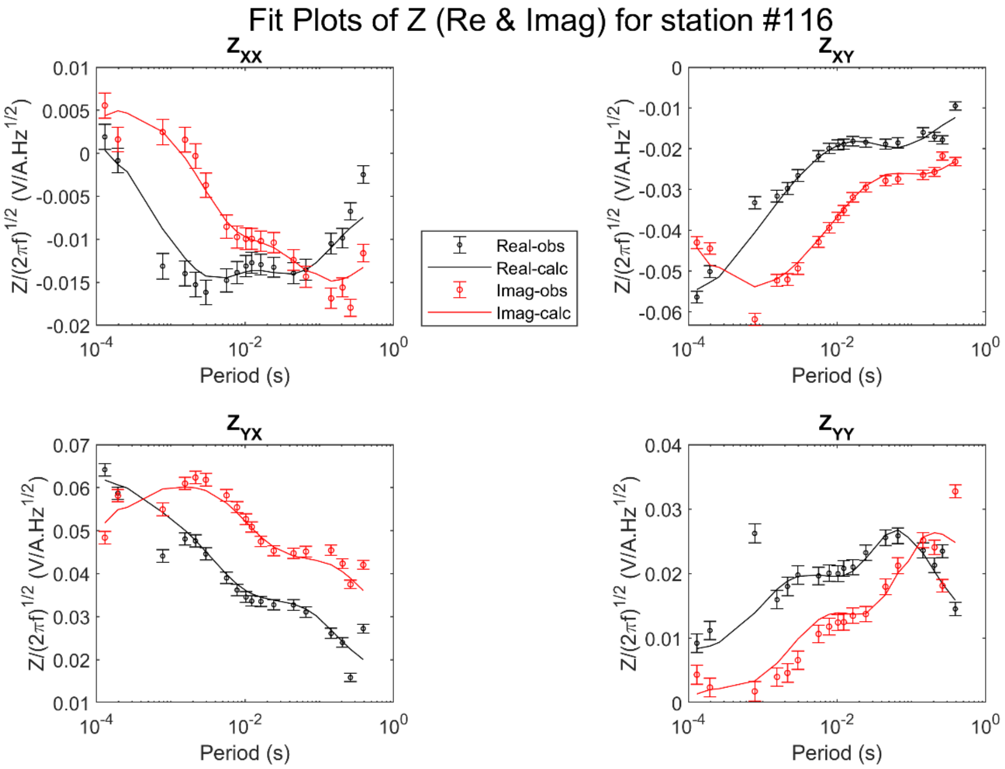
Fit Plots of Z (Re & Imag) for station #116
Z_{XX}
Z_{XY}
Z_{YX}
Z_{YY}
$Z/(2\pi f)^{1/2}$ (V/A.Hz$^{1/2}$)
Period (s)
Real-obs
Real-calc
Imag-obs
Imag-calc

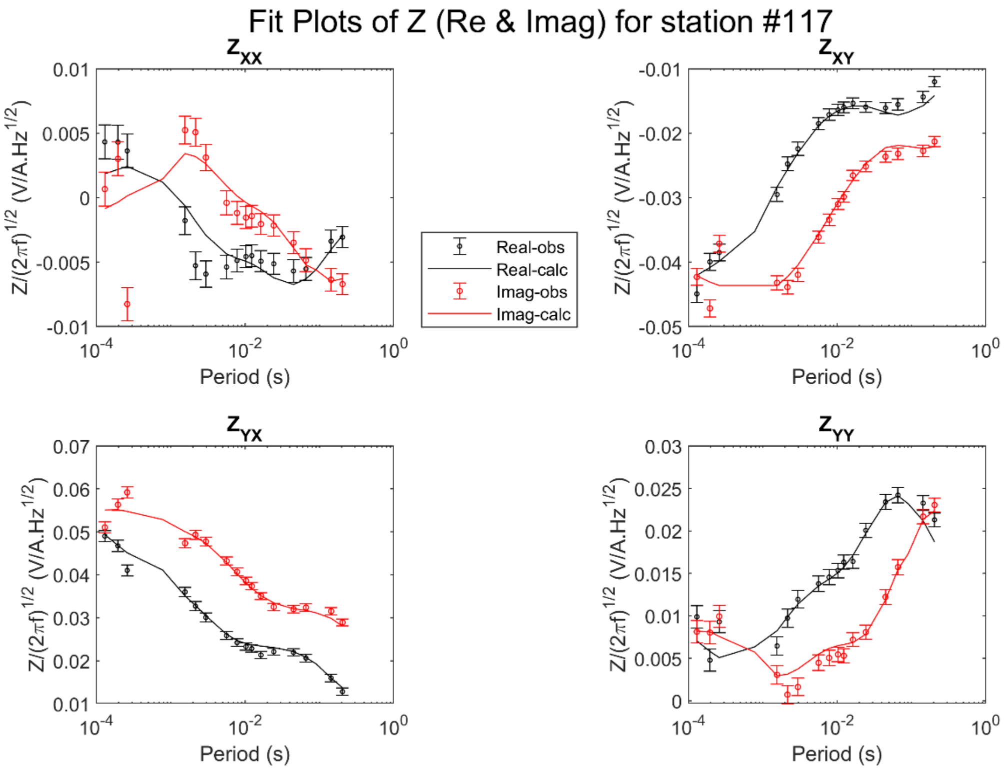
Fit Plots of Z (Re & Imag) for station #117
Z_{XX}
Z_{XY}
Z_{YX}
Z_{YY}
$Z/(2\pi f)^{1/2}$ (V/A.Hz$^{1/2}$)
Period (s)
Real-obs
Real-calc
Imag-obs
Imag-calc

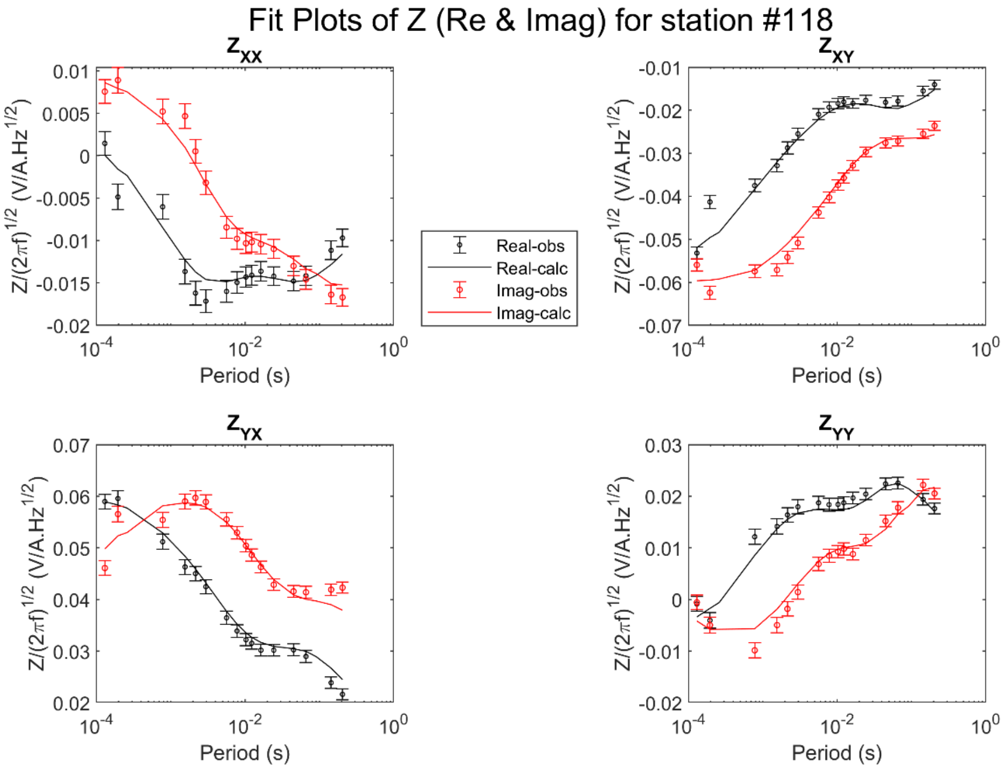
Fit Plots of Z (Re & Imag) for station #118
Z_XX
Z_XY
Z_YX
Z_YY
Z/(2πf)^1/2 (V/A.Hz^1/2)
Period (s)
Real-obs
Real-calc
Imag-obs
Imag-calc

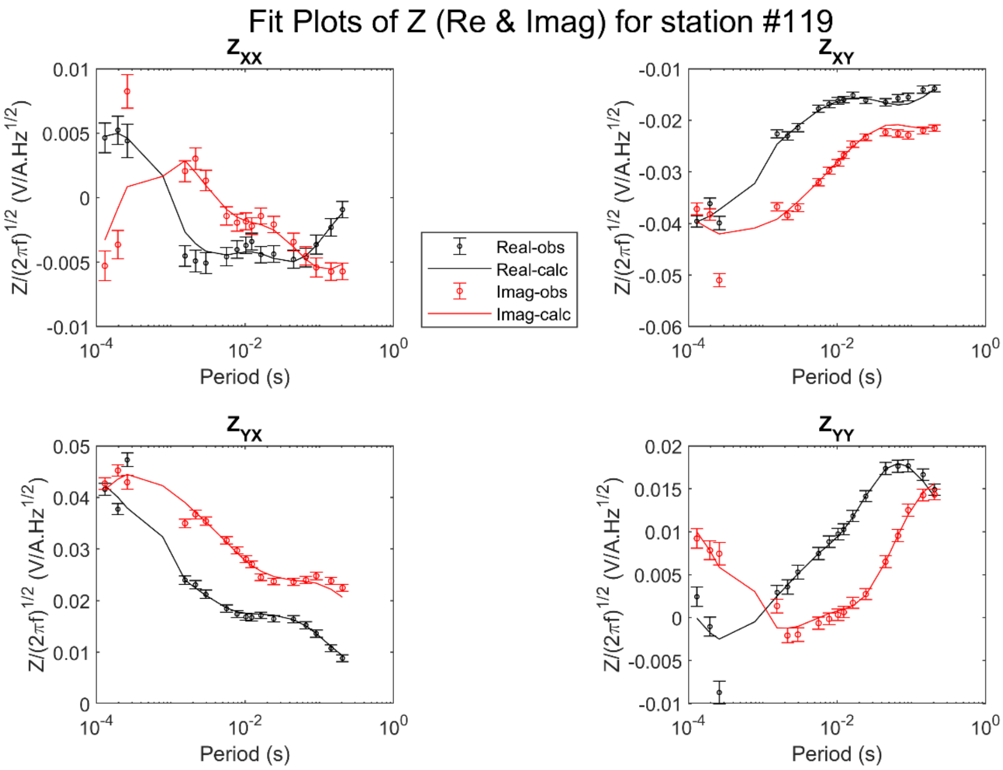
Fit Plots of Z (Re & Imag) for station #119
Z_XX
Z_XY
Z_YX
Z_YY
Z/(2πf)^1/2 (V/A.Hz^1/2)
Period (s)
Real-obs
Real-calc
Imag-obs
Imag-calc

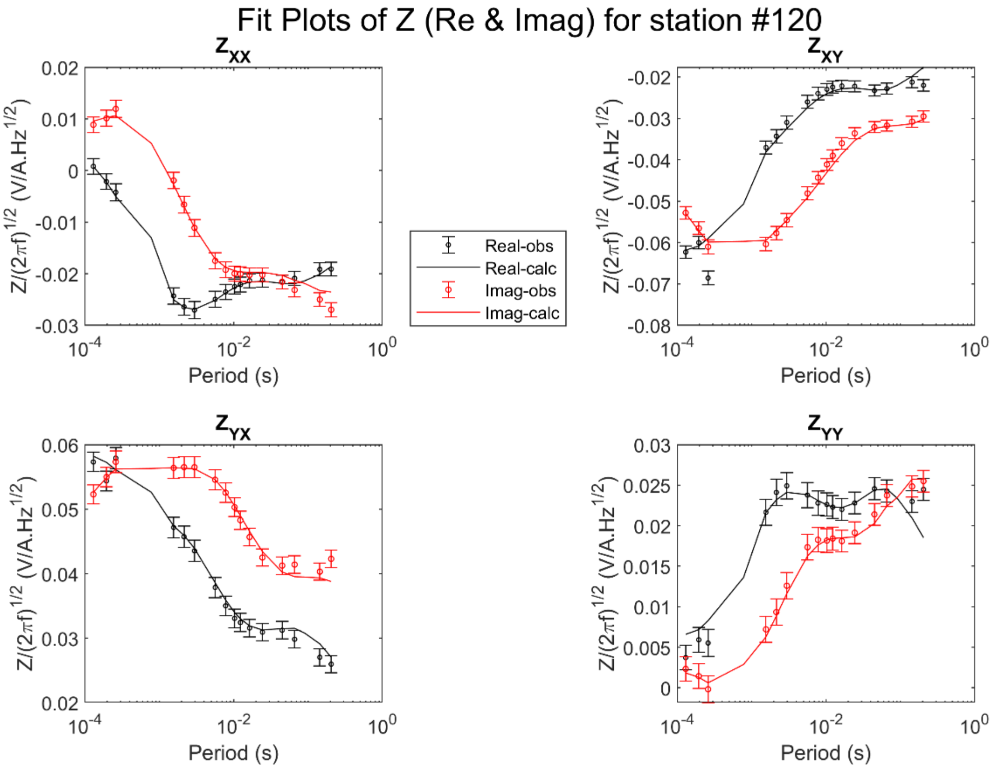

Fit Plots of Z (Re & Imag) for station #120
Z_XX
Z_XY
Z_YX
Z_YY
Z/(2πf)^1/2 (V/A.Hz^1/2)
Period (s)
Real-obs
Real-calc
Imag-obs
Imag-calc

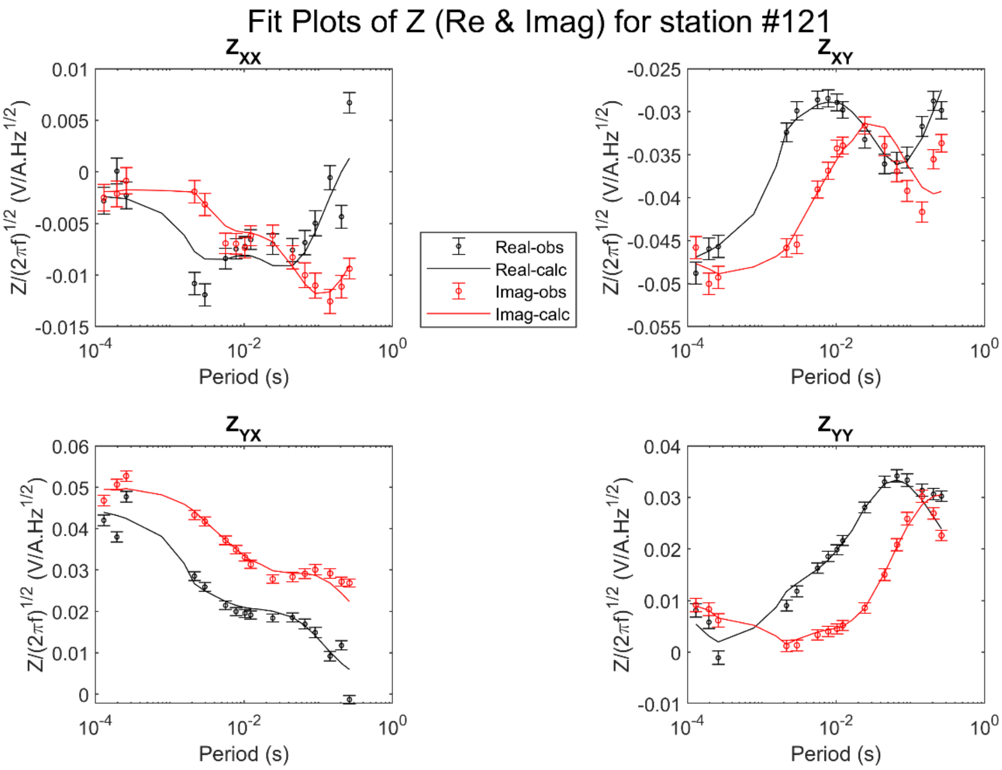

Fit Plots of Z (Re & Imag) for station #121
Z_XX
Z_XY
Z_YX
Z_YY
Z/(2πf)^1/2 (V/A.Hz^1/2)
Period (s)
Real-obs
Real-calc
Imag-obs
Imag-calc

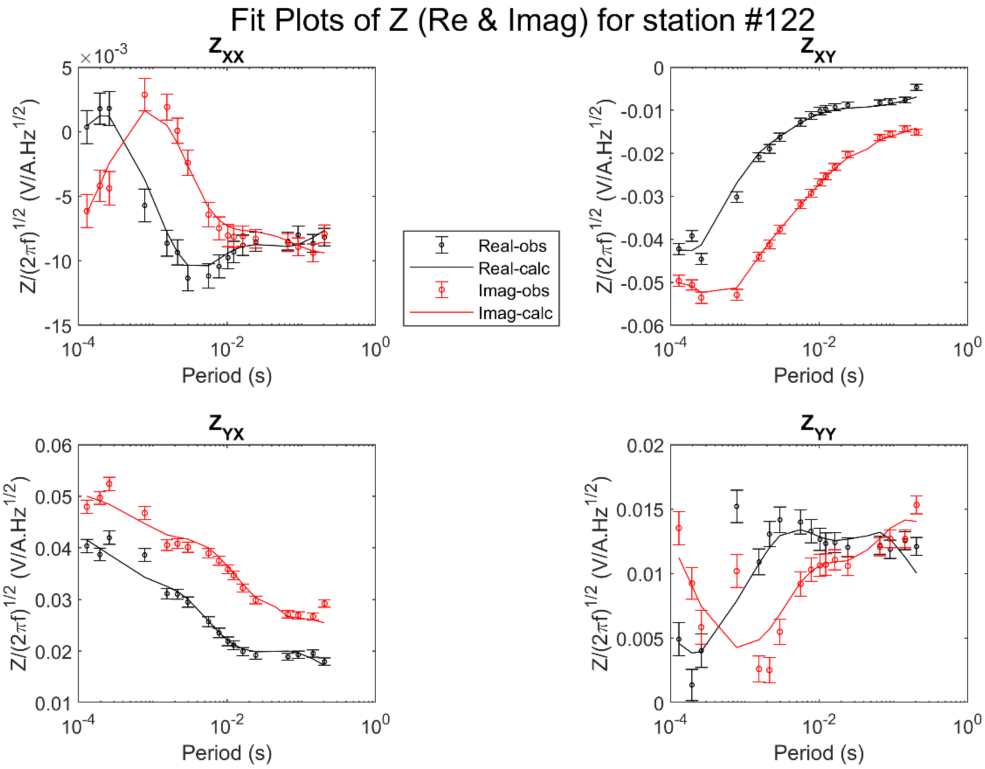
Fit Plots of Z (Re & Imag) for station #122
Z_XX
Z_XY
Z_YX
Z_YY
Z/(2πf)^1/2 (V/A.Hz^1/2)
Period (s)
Real-obs
Real-calc
Imag-obs
Imag-calc

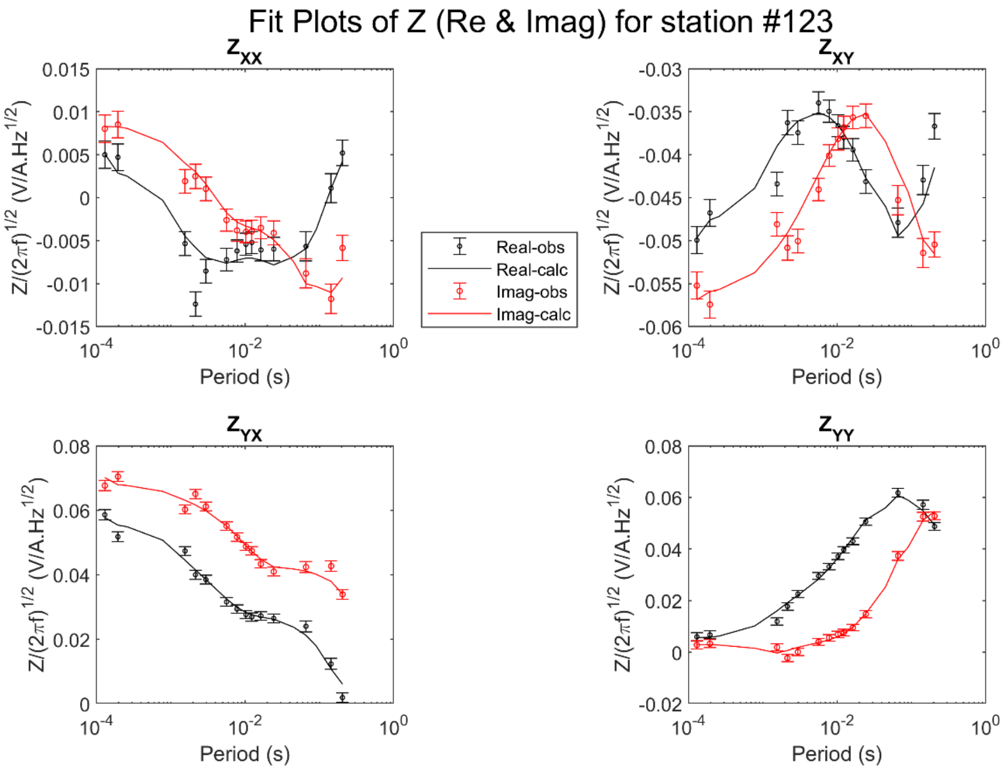
Fit Plots of Z (Re & Imag) for station #123
Z_XX
Z_XY
Z_YX
Z_YY
Z/(2πf)^1/2 (V/A.Hz^1/2)
Period (s)
Real-obs
Real-calc
Imag-obs
Imag-calc

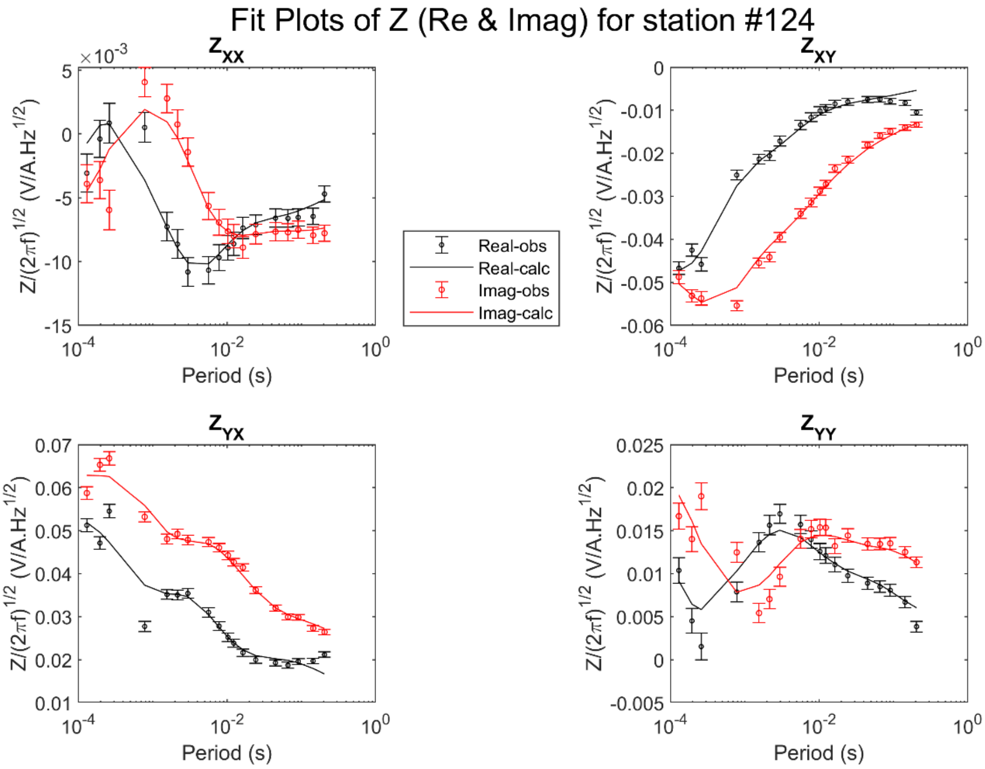
Fit Plots of Z (Re & Imag) for station #124
Z_XX
Z_XY
Z_YX
Z_YY
Z/(2πf)^1/2 (V/A.Hz^1/2)
Period (s)
Real-obs
Real-calc
Imag-obs
Imag-calc

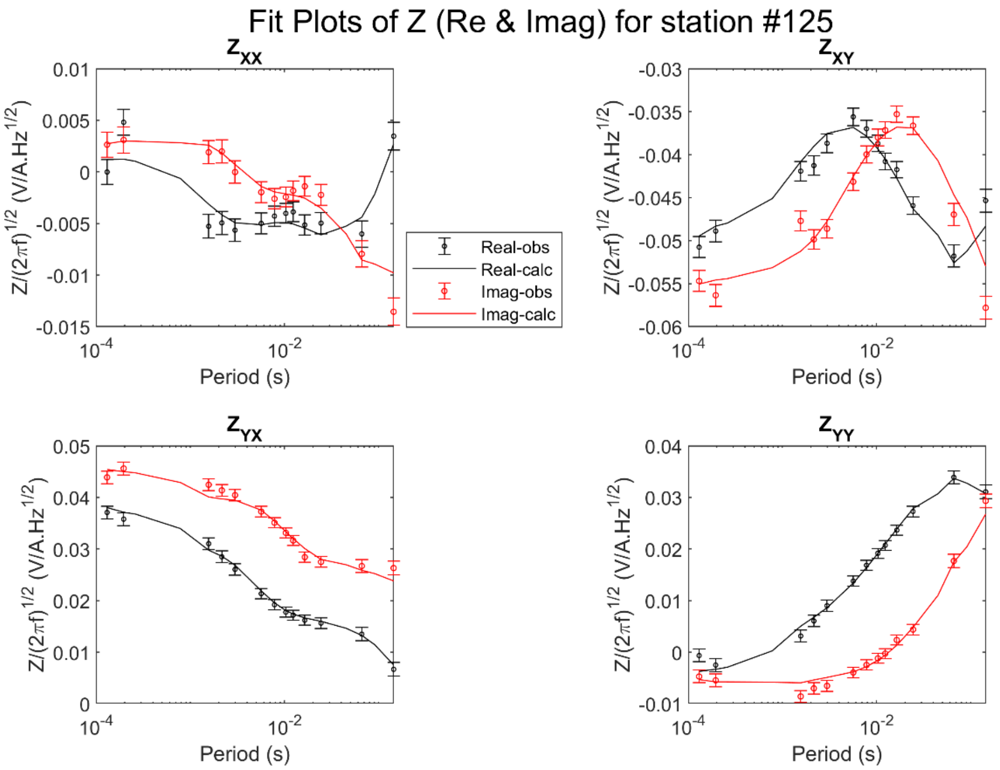
Fit Plots of Z (Re & Imag) for station #125
Z_XX
Z_XY
Z_YX
Z_YY
Z/(2πf)^1/2 (V/A.Hz^1/2)
Period (s)
Real-obs
Real-calc
Imag-obs
Imag-calc

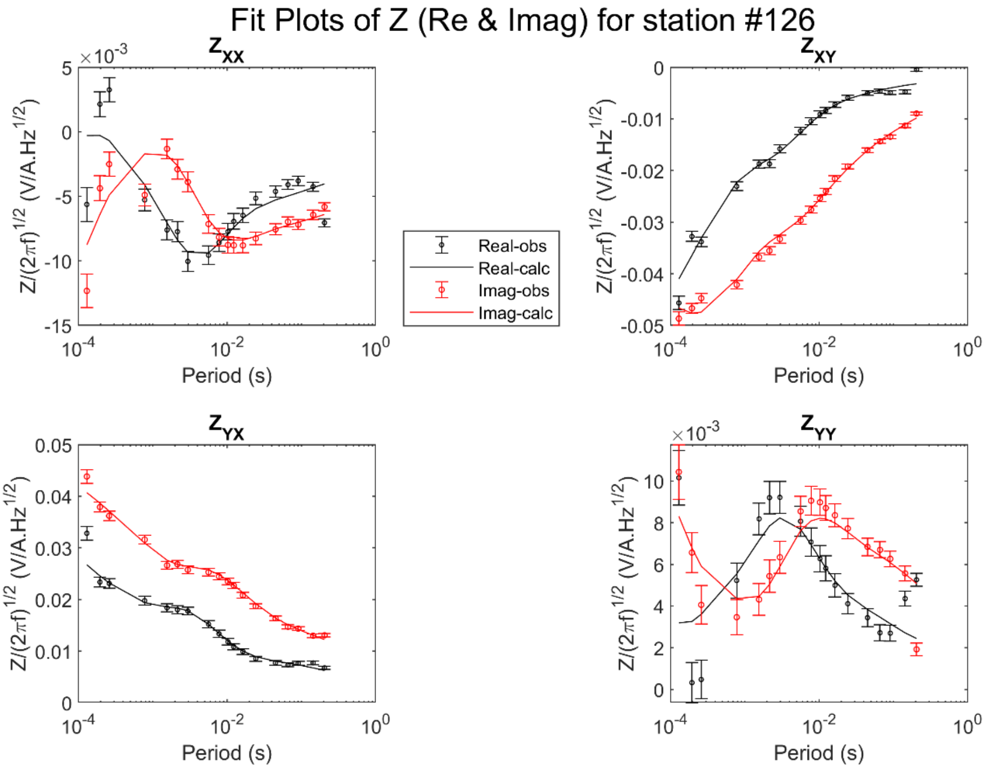
Fit Plots of Z (Re & Imag) for station #126
Z_XX
Z_XY
Z_YX
Z_YY
Z/(2πf)^1/2 (V/A.Hz^1/2)
Period (s)
Real-obs
Real-calc
Imag-obs
Imag-calc

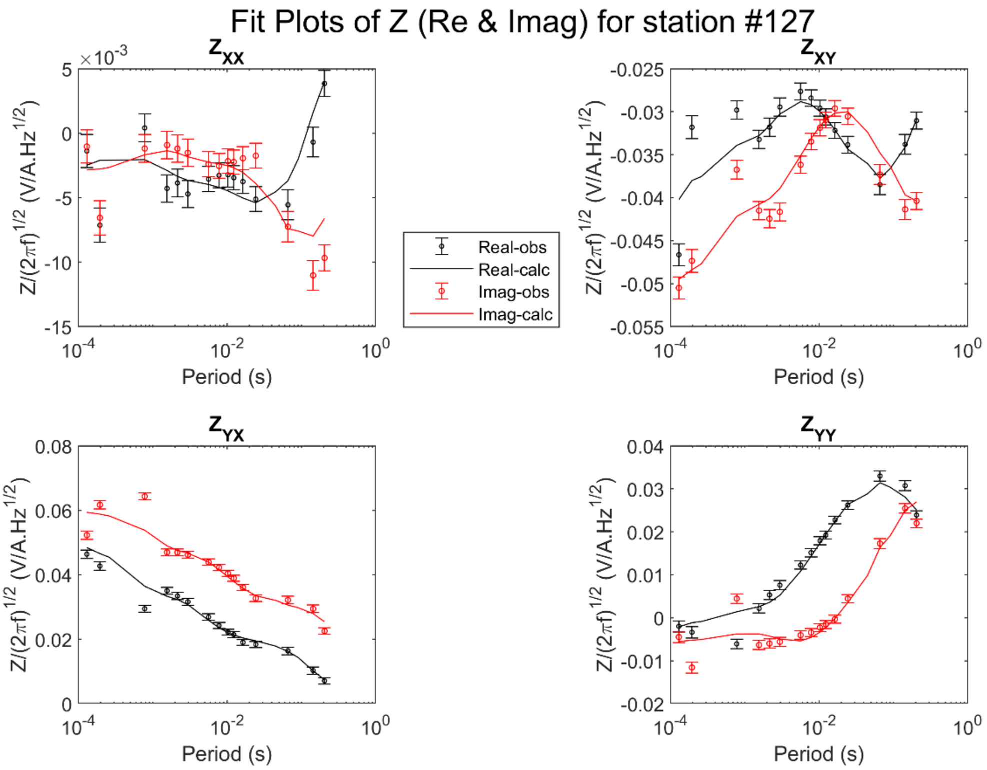
Fit Plots of Z (Re & Imag) for station #127
Z_XX
Z_XY
Z_YX
Z_YY
Z/(2πf)^1/2 (V/A.Hz^1/2)
Period (s)
Real-obs
Real-calc
Imag-obs
Imag-calc

Fit Plots of Z (Re & Imag) for station #128

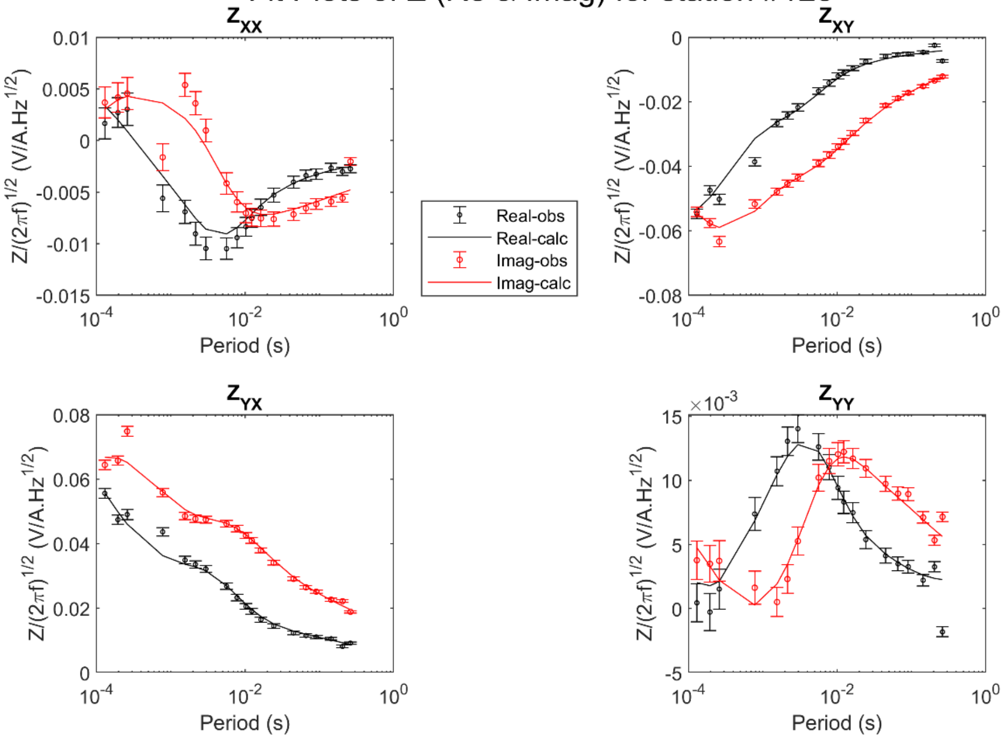

Fit Plots of Z (Re & Imag) for station #129

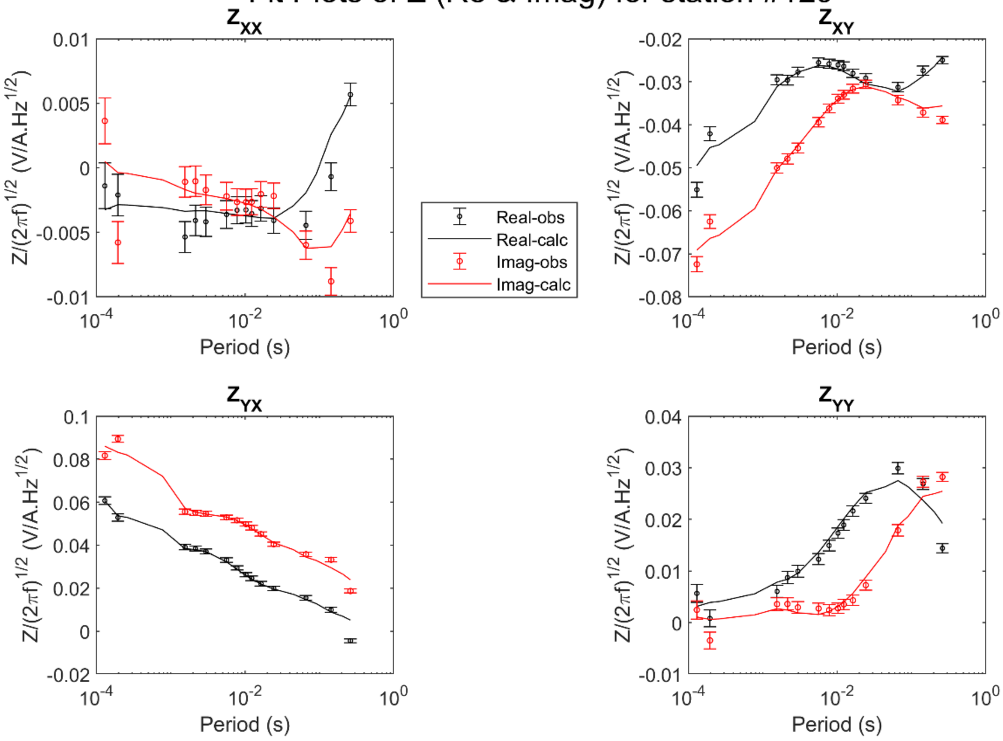

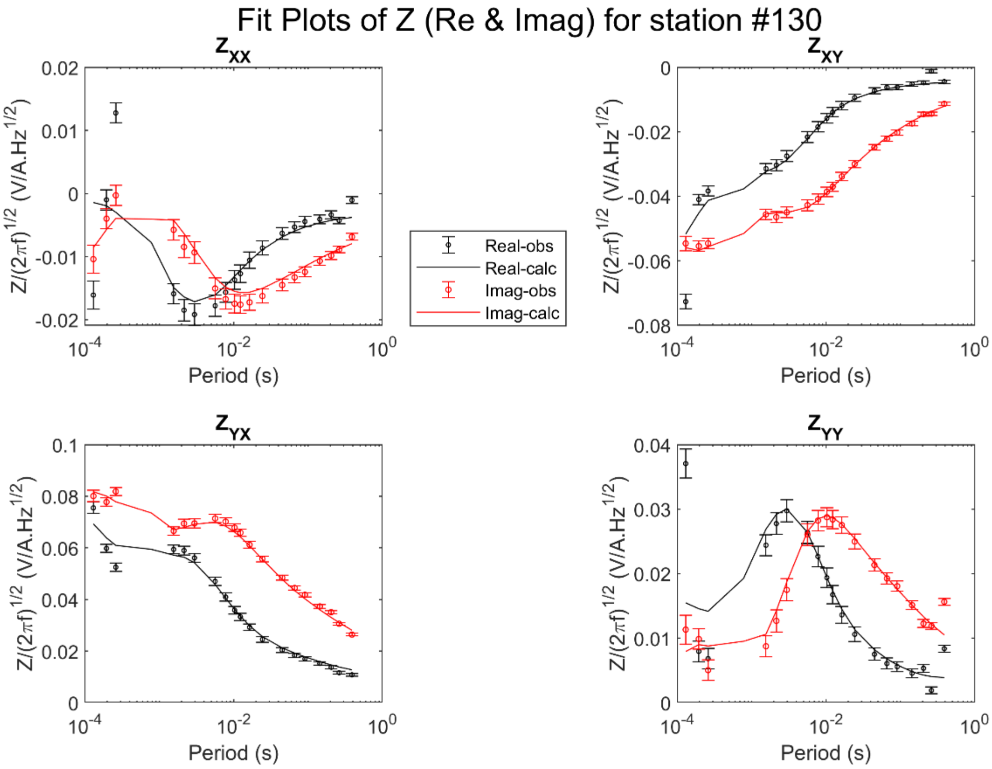
Fit Plots of Z (Re & Imag) for station #130
Z_{XX}
Z_{XY}
Z_{YX}
Z_{YY}
$Z/(2\pi f)^{1/2}$ (V/A.Hz$^{1/2}$)
Period (s)
Real-obs
Real-calc
Imag-obs
Imag-calc

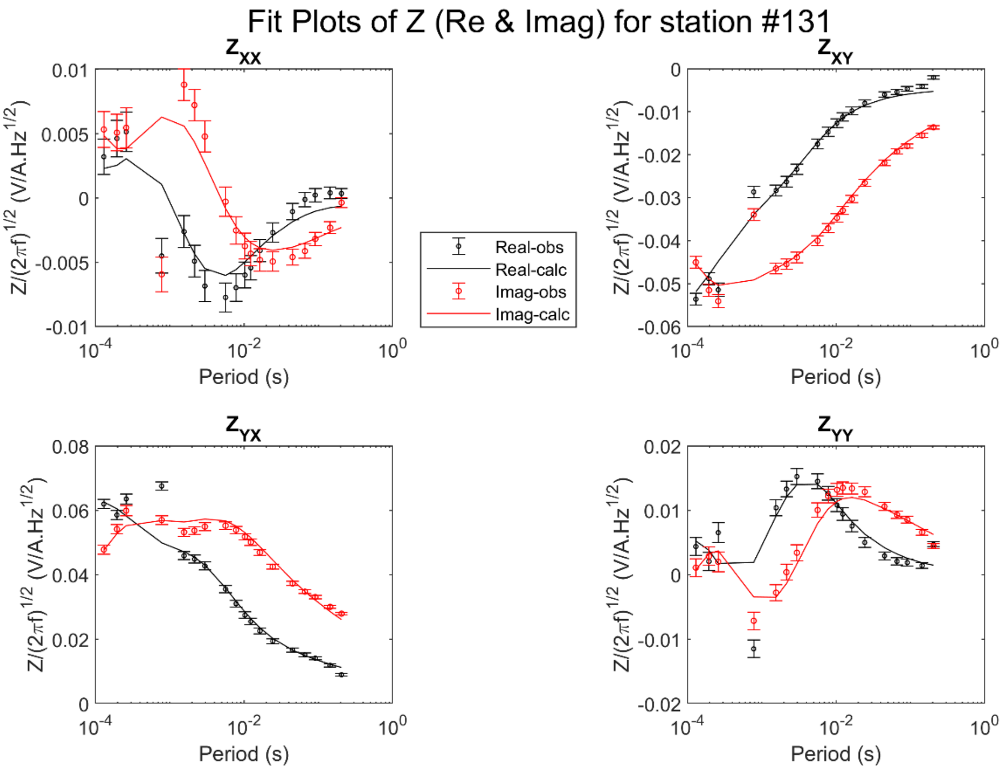
Fit Plots of Z (Re & Imag) for station #131
Z_{XX}
Z_{XY}
Z_{YX}
Z_{YY}
$Z/(2\pi f)^{1/2}$ (V/A.Hz$^{1/2}$)
Period (s)
Real-obs
Real-calc
Imag-obs
Imag-calc

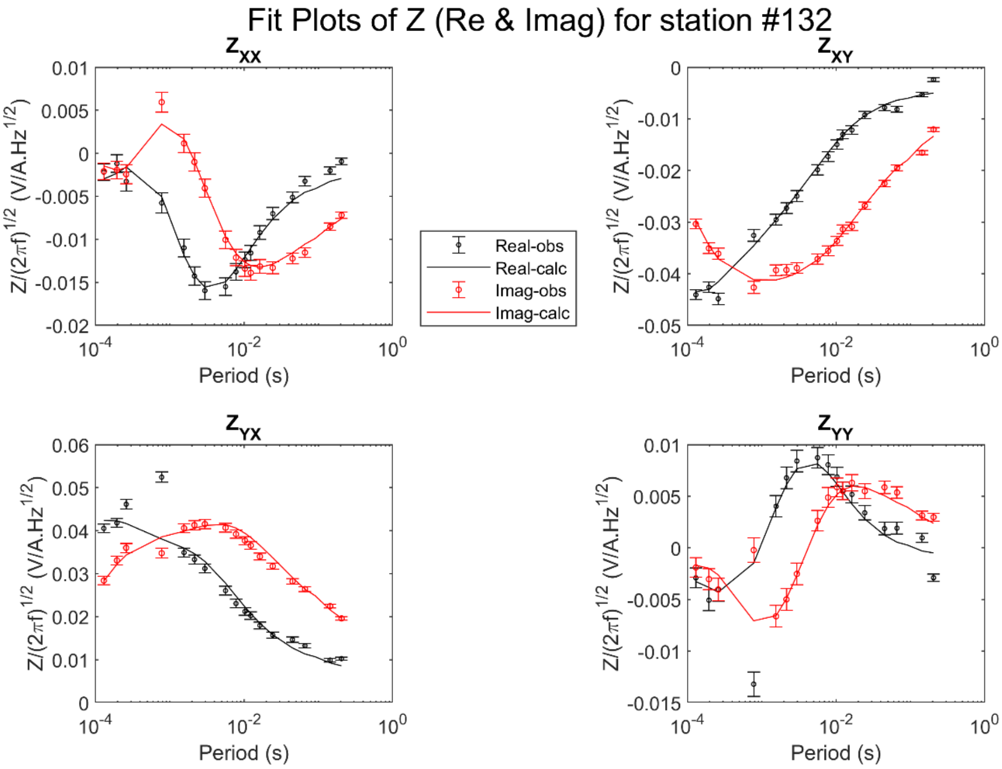

Fit Plots of Z (Re & Imag) for station #132
Z_XX
Z_XY
Z_YX
Z_YY
Z/(2πf)^1/2 (V/A.Hz^1/2)
Period (s)
Real-obs
Real-calc
Imag-obs
Imag-calc

F.2. Fit Plots of Apparent Resistivity and Phase

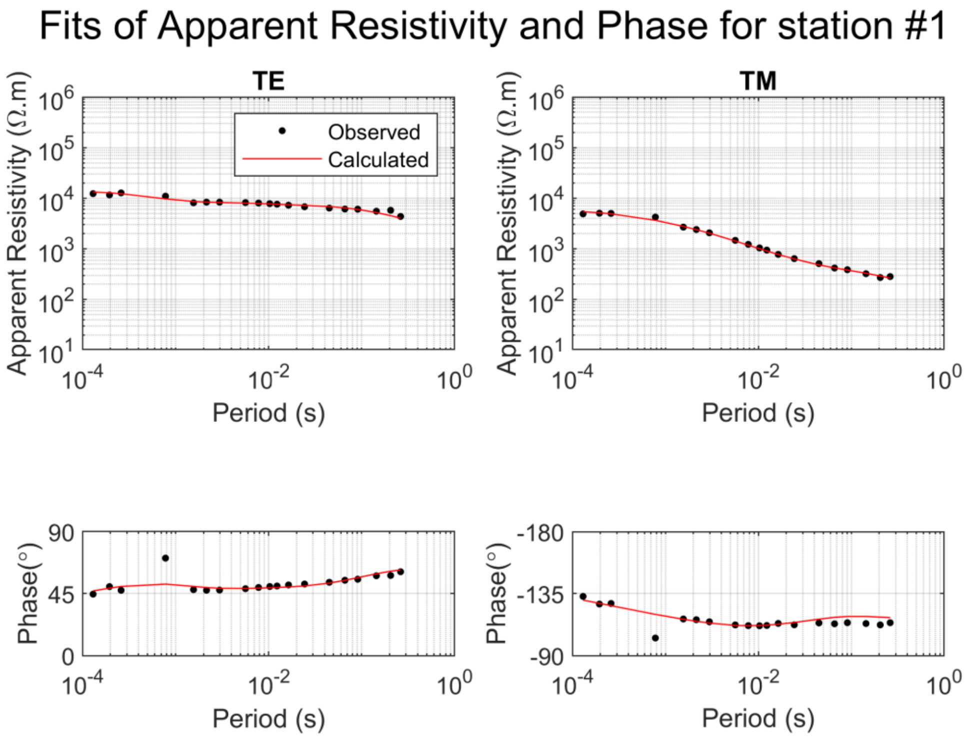

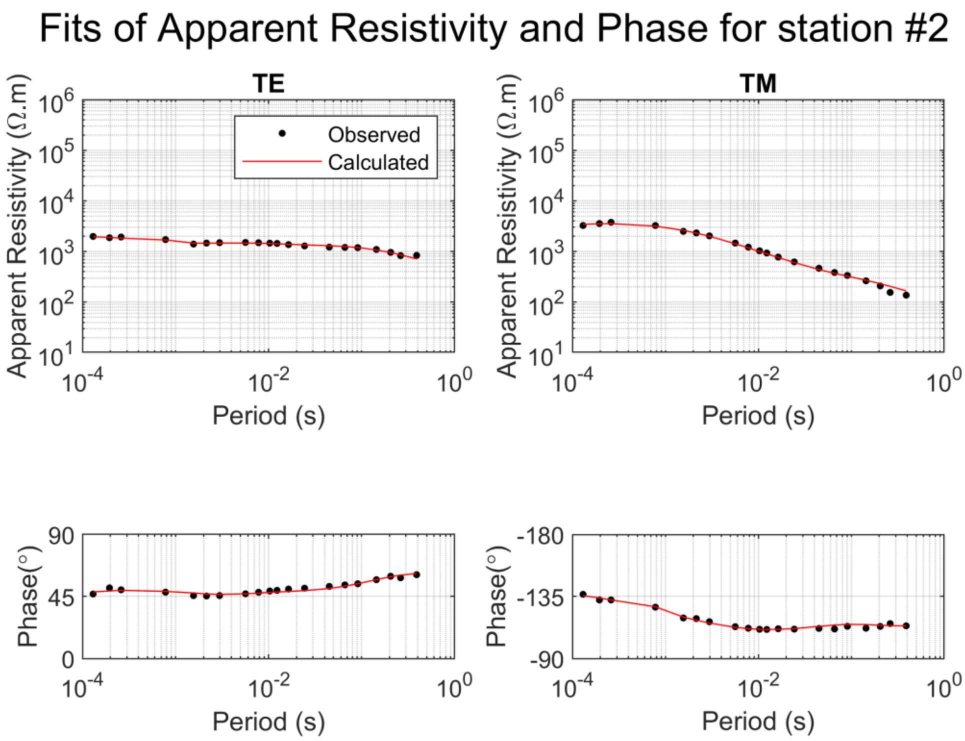

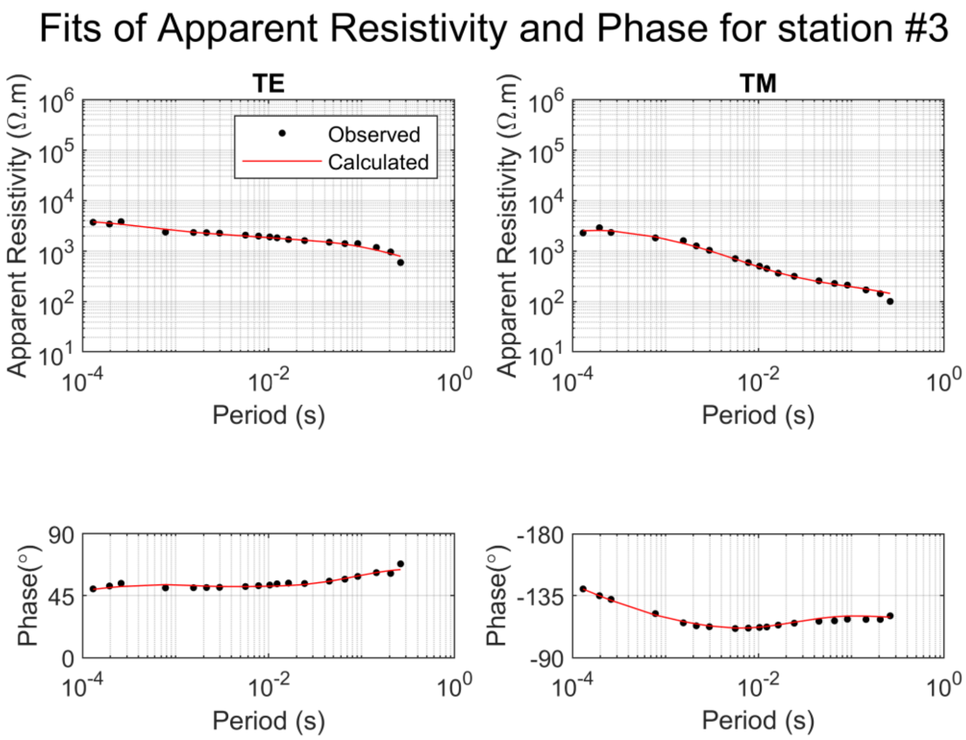
Fits of Apparent Resistivity and Phase for station #3
TE
TM
Observed
Calculated
Apparent Resistivity (Ω.m)
Phase(°)
Period (s)

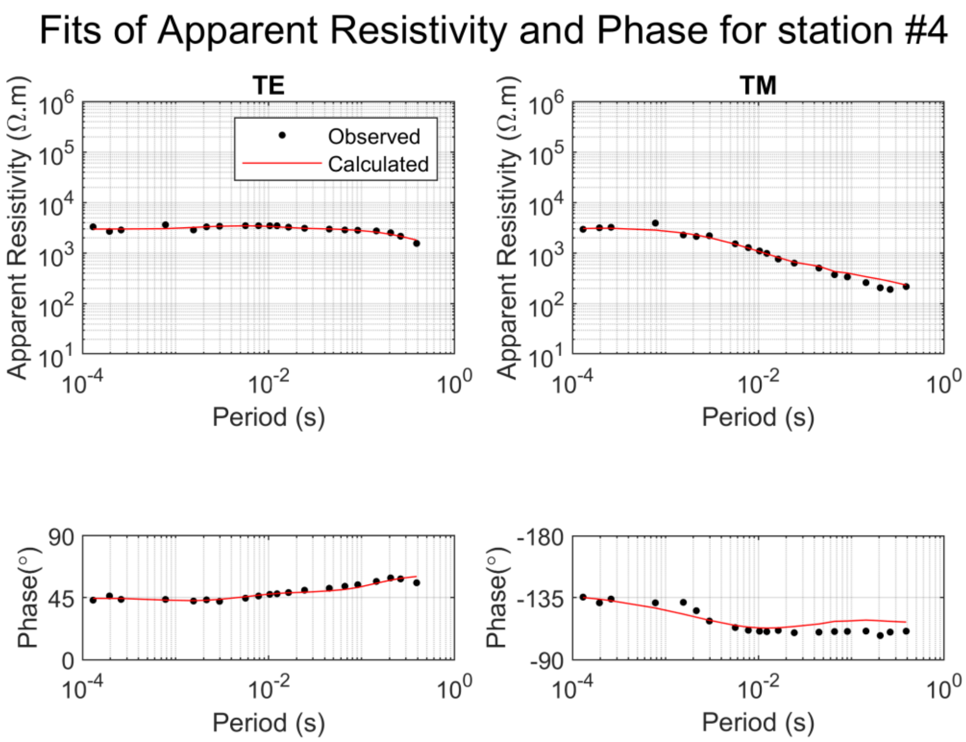
Fits of Apparent Resistivity and Phase for station #4
TE
TM
Observed
Calculated
Apparent Resistivity (Ω.m)
Phase(°)
Period (s)

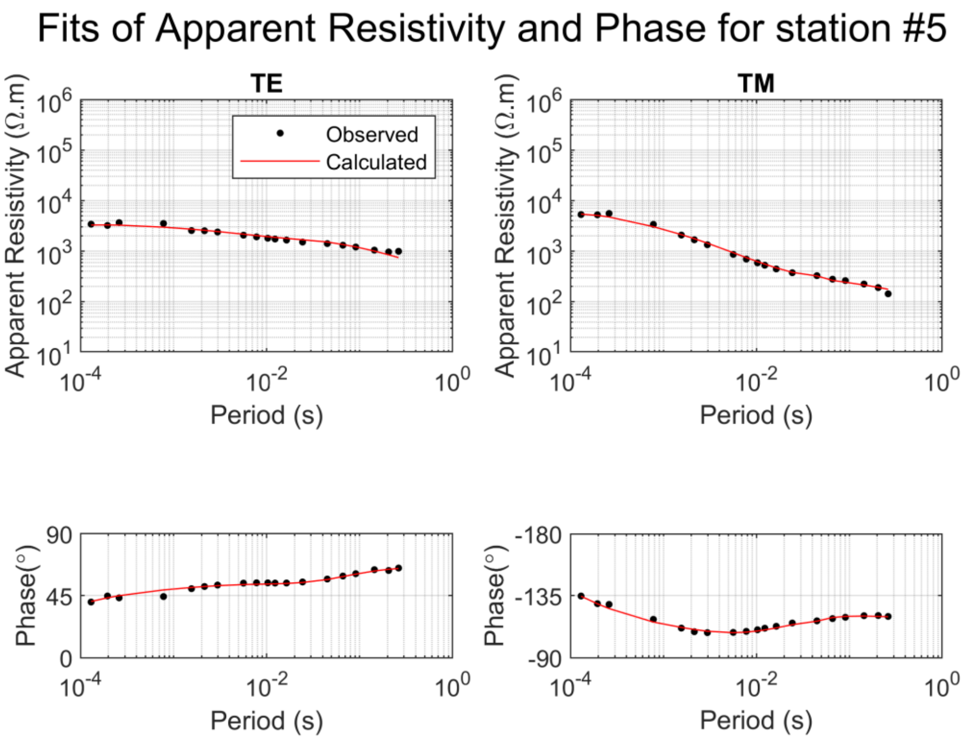
Fits of Apparent Resistivity and Phase for station #5
TE
TM
Observed
Calculated
Apparent Resistivity (Ω.m)
Phase(°)
Period (s)

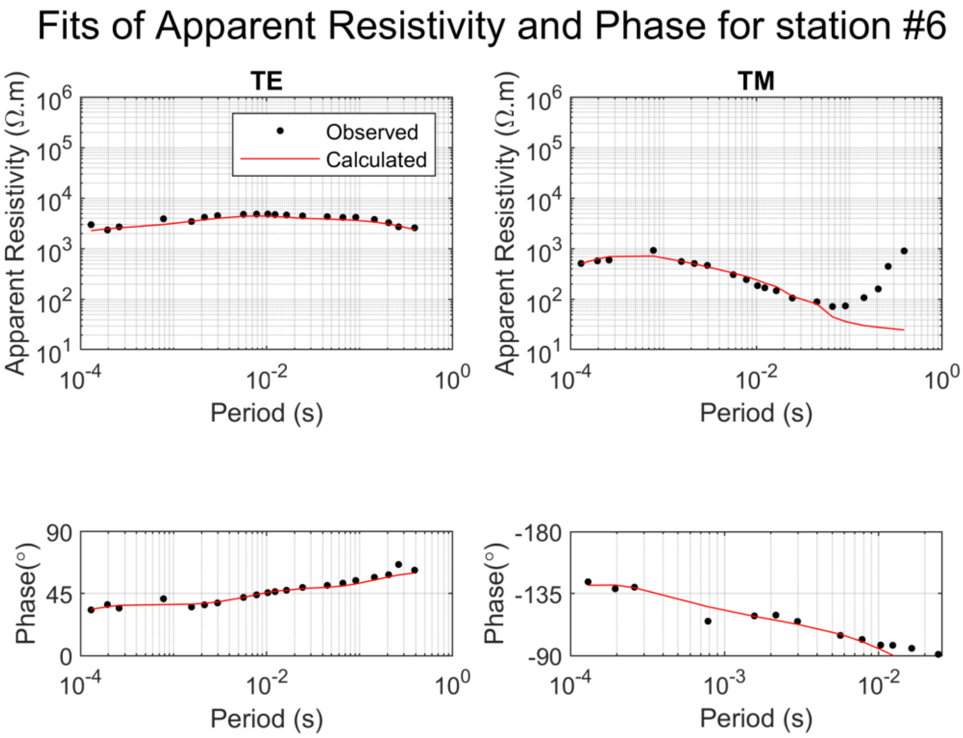
Fits of Apparent Resistivity and Phase for station #6
TE
TM
Observed
Calculated
Apparent Resistivity (Ω.m)
Phase(°)
Period (s)

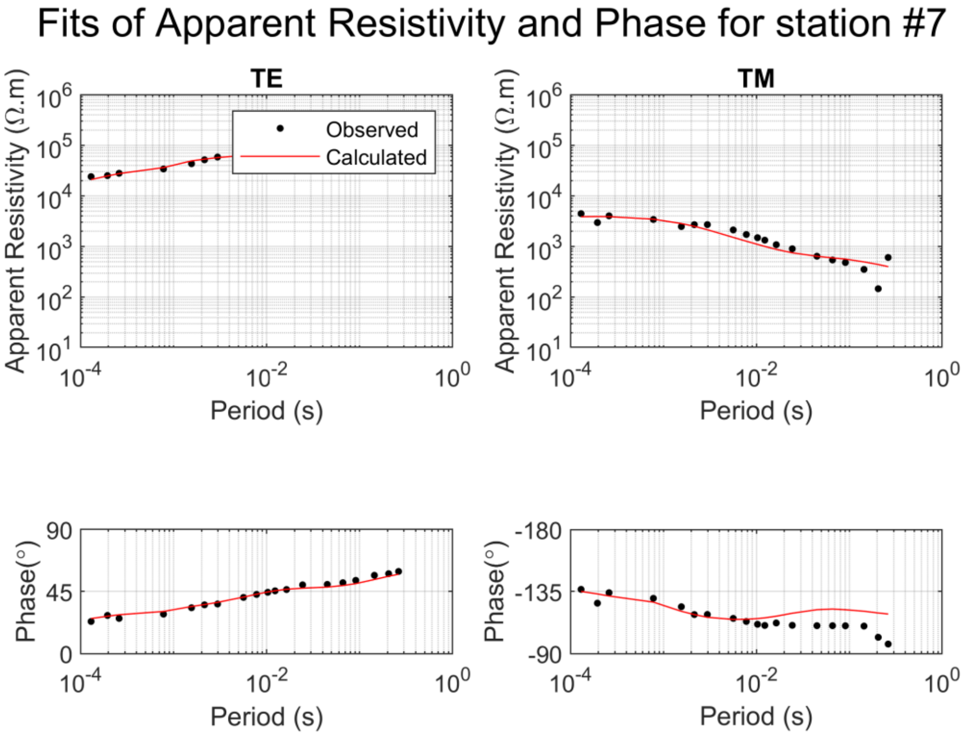
Fits of Apparent Resistivity and Phase for station #7
TE
TM
Observed
Calculated
Apparent Resistivity (Ω.m)
Phase(°)
Period (s)

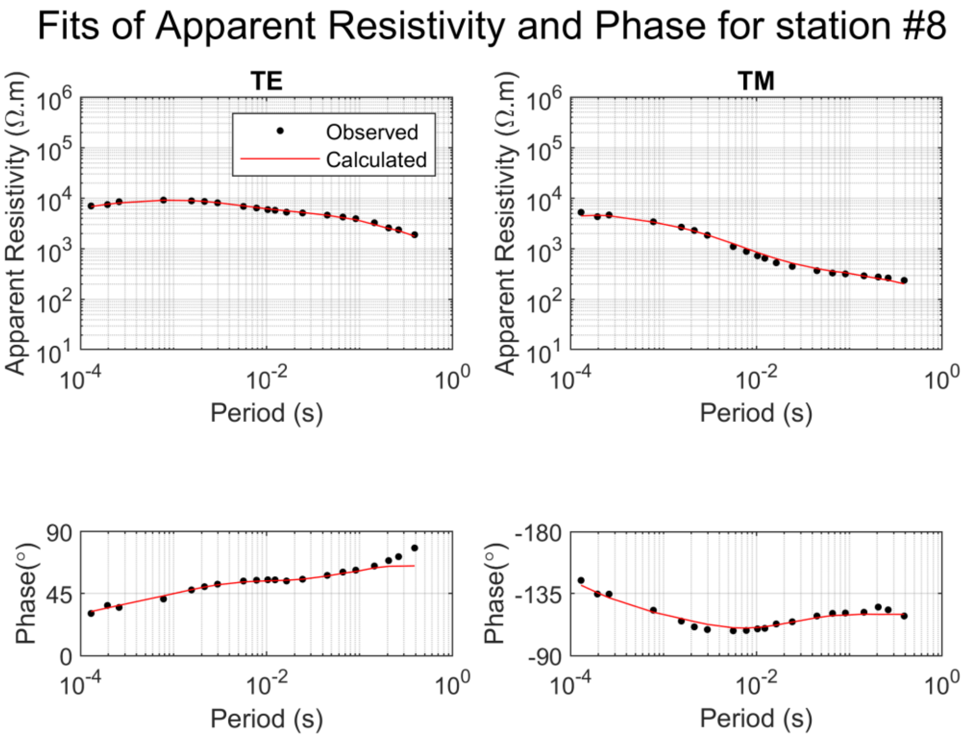
Fits of Apparent Resistivity and Phase for station #8
TE
TM
Observed
Calculated
Apparent Resistivity (Ω.m)
Phase(°)
Period (s)

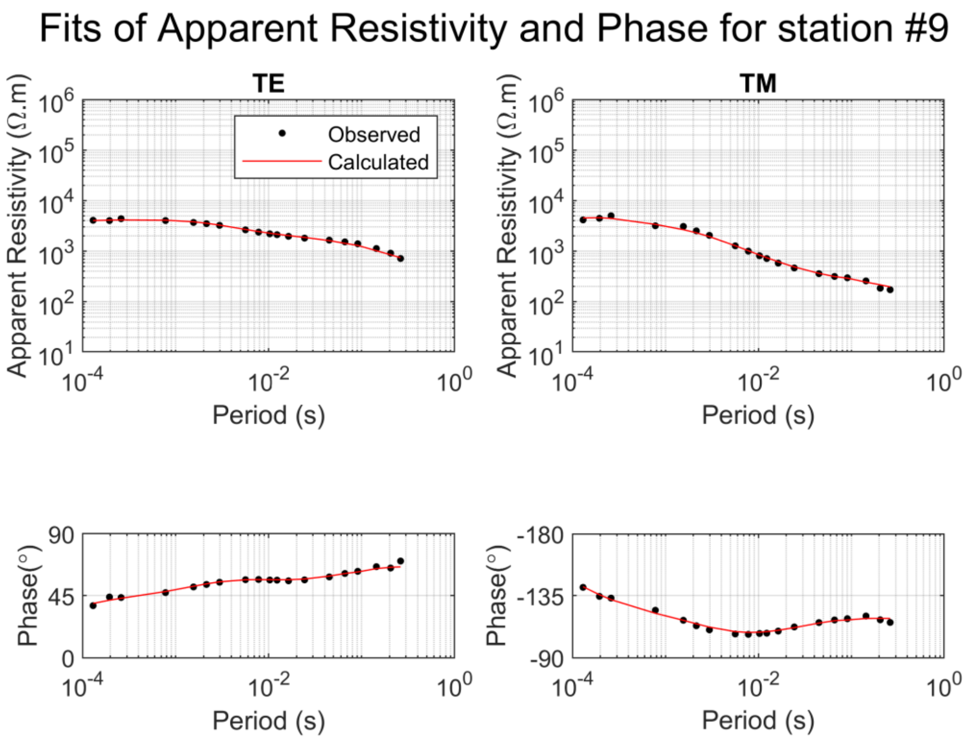
Fits of Apparent Resistivity and Phase for station #9
TE
TM
Observed
Calculated
Apparent Resistivity (Ω.m)
Phase(°)
Period (s)

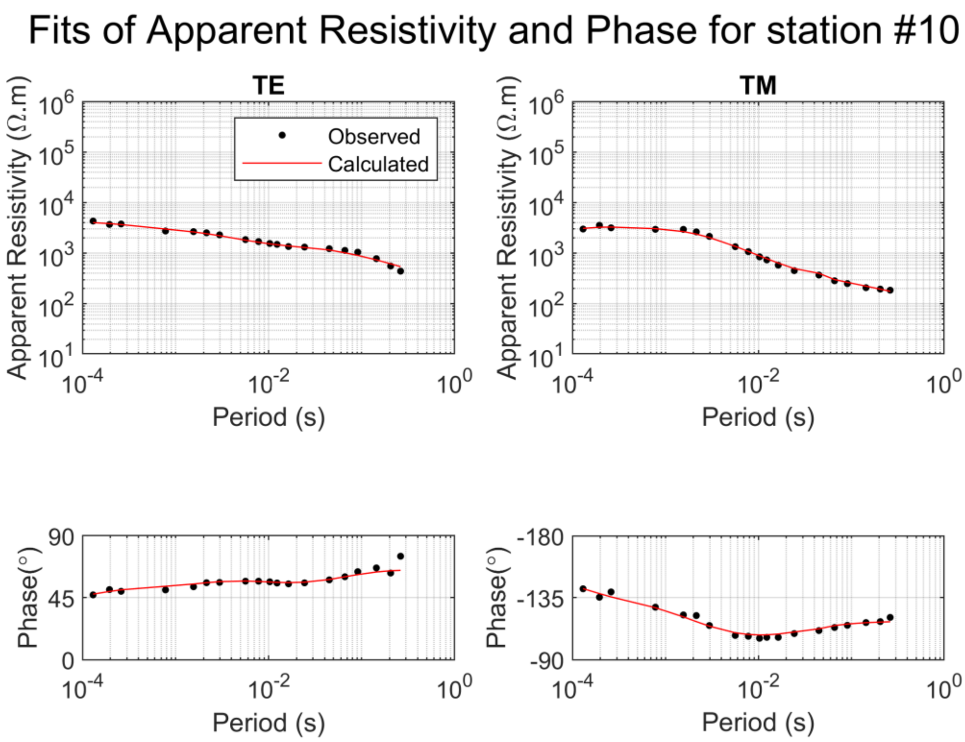
Fits of Apparent Resistivity and Phase for station #10
TE
TM
Observed
Calculated
Apparent Resistivity (Ω.m)
Phase(°)
Period (s)

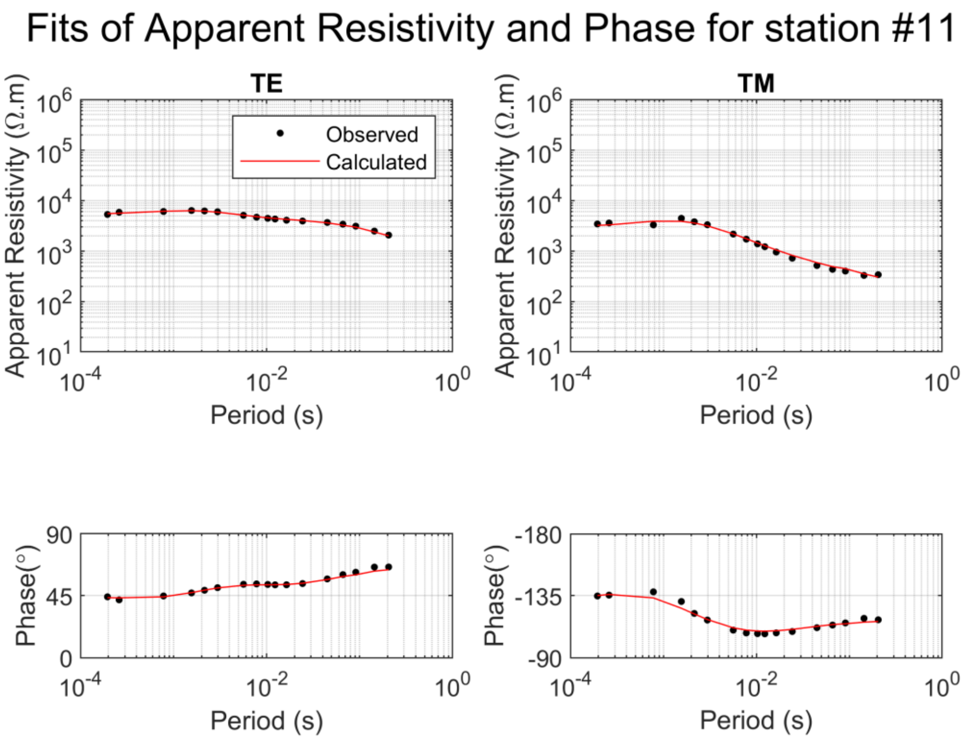
Fits of Apparent Resistivity and Phase for station #11
TE
TM
Observed
Calculated
Apparent Resistivity (Ω.m)
Phase(°)
Period (s)

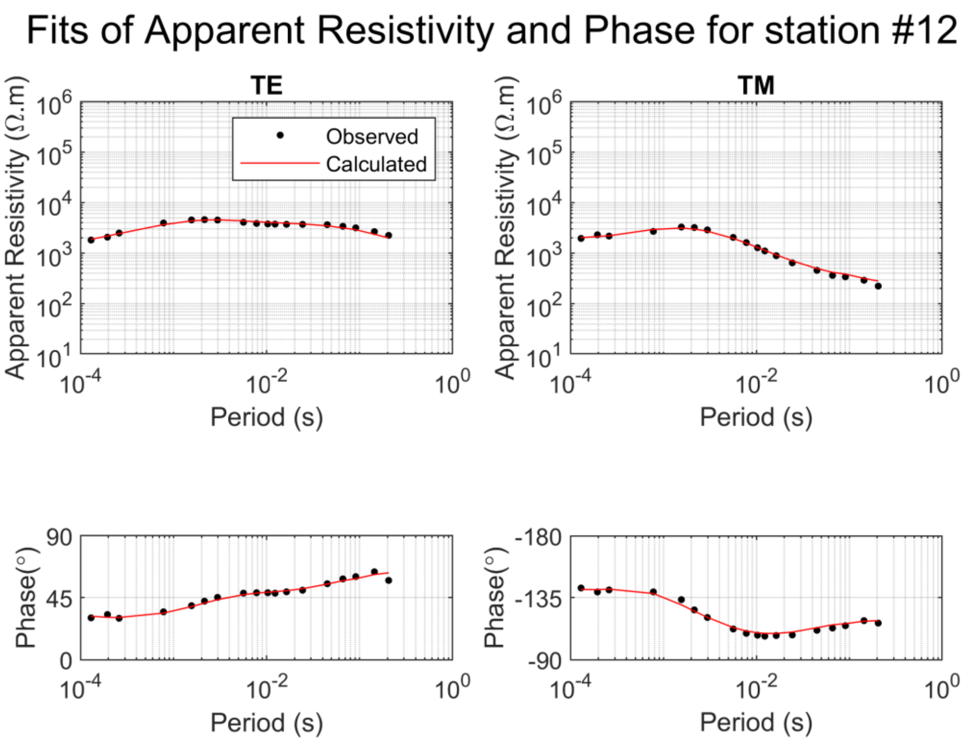
Fits of Apparent Resistivity and Phase for station #12
TE
TM
Observed
Calculated
Apparent Resistivity (Ω.m)
Phase(°)
Period (s)

Fits of Apparent Resistivity and Phase for station #13

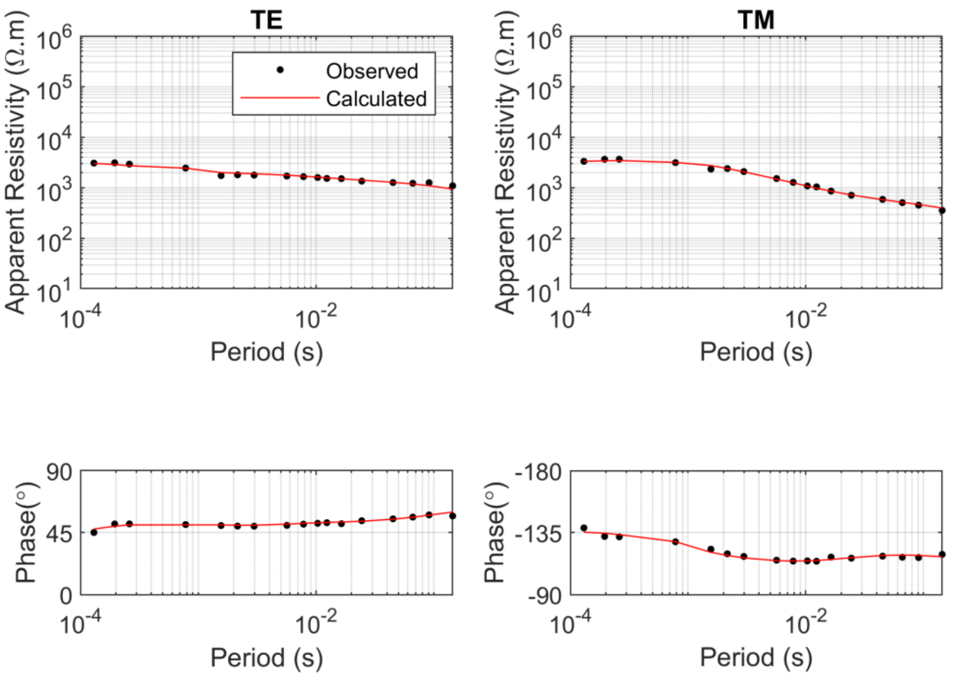

Fits of Apparent Resistivity and Phase for station #14

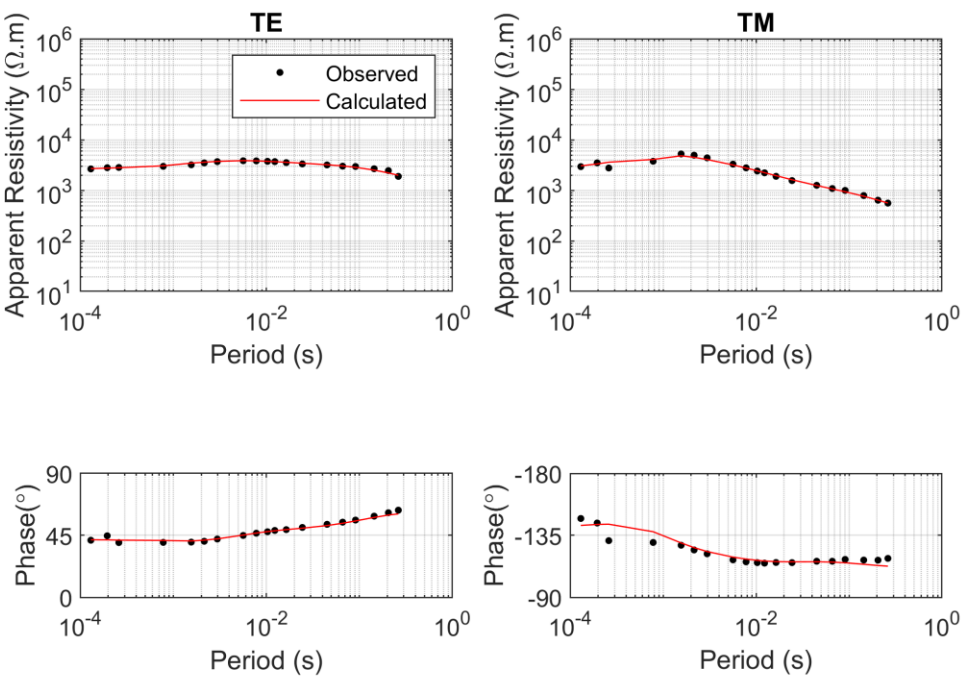

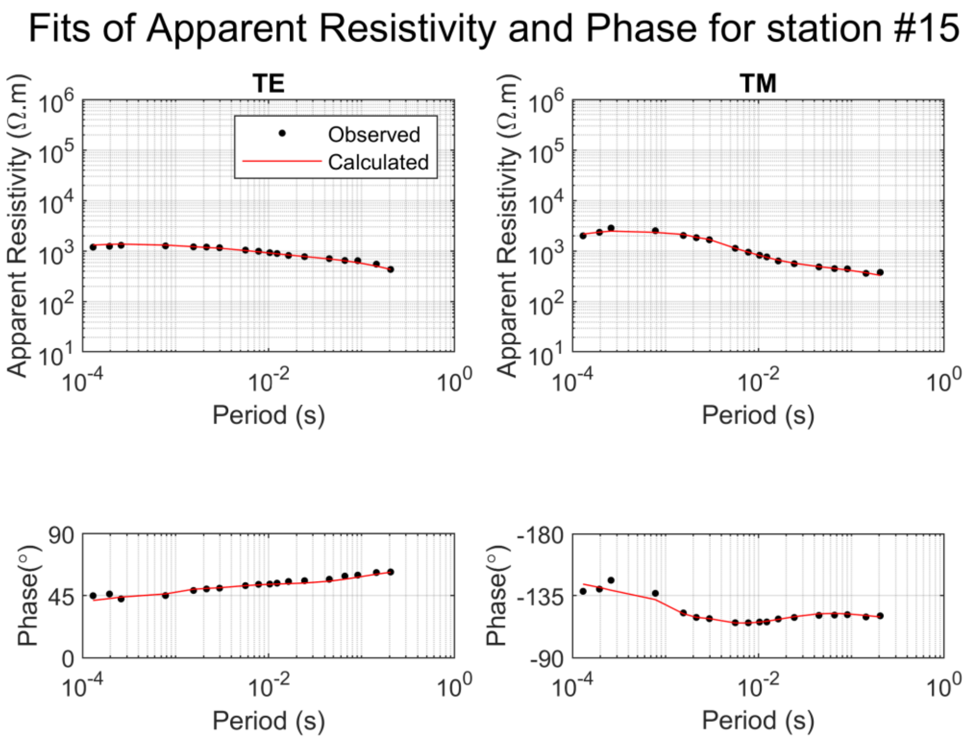
Fits of Apparent Resistivity and Phase for station #15
TE
TM
Observed
Calculated
Apparent Resistivity (Ω.m)
Period (s)
Phase(°)

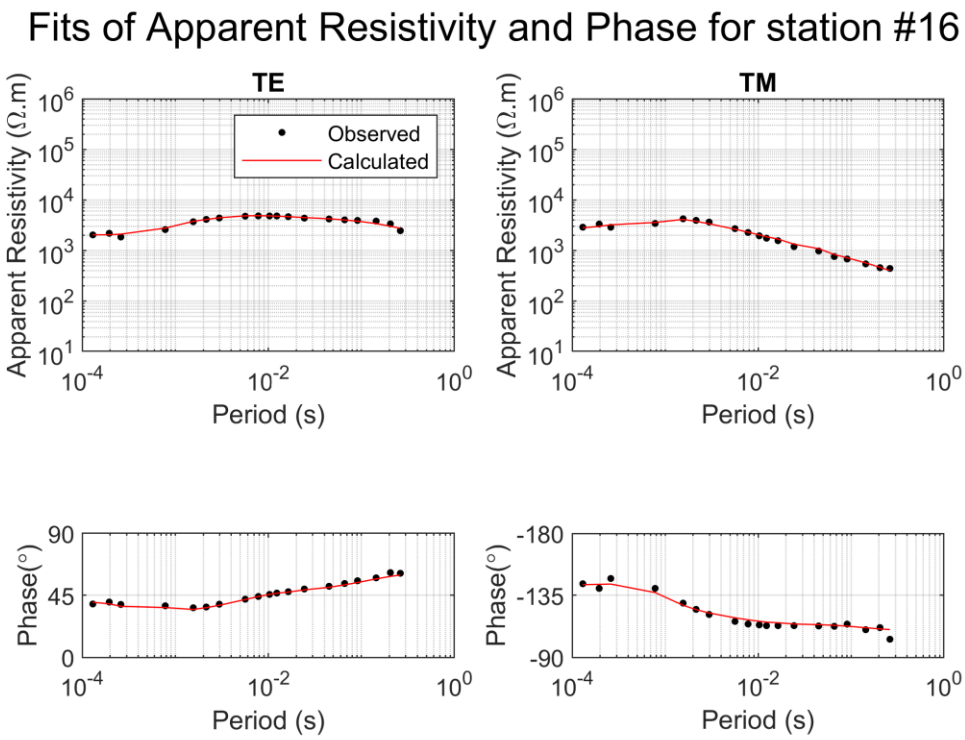
Fits of Apparent Resistivity and Phase for station #16
TE
TM
Observed
Calculated
Apparent Resistivity (Ω.m)
Period (s)
Phase(°)

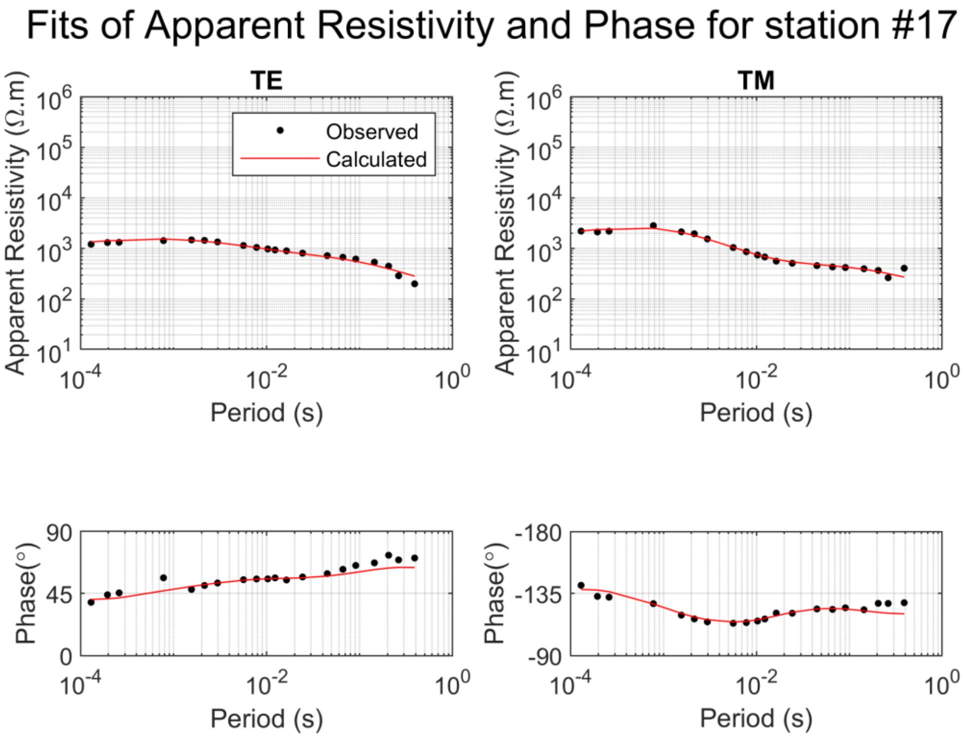
Fits of Apparent Resistivity and Phase for station #17
TE
TM
Observed
Calculated
Apparent Resistivity (Ω.m)
Phase(°)
Period (s)

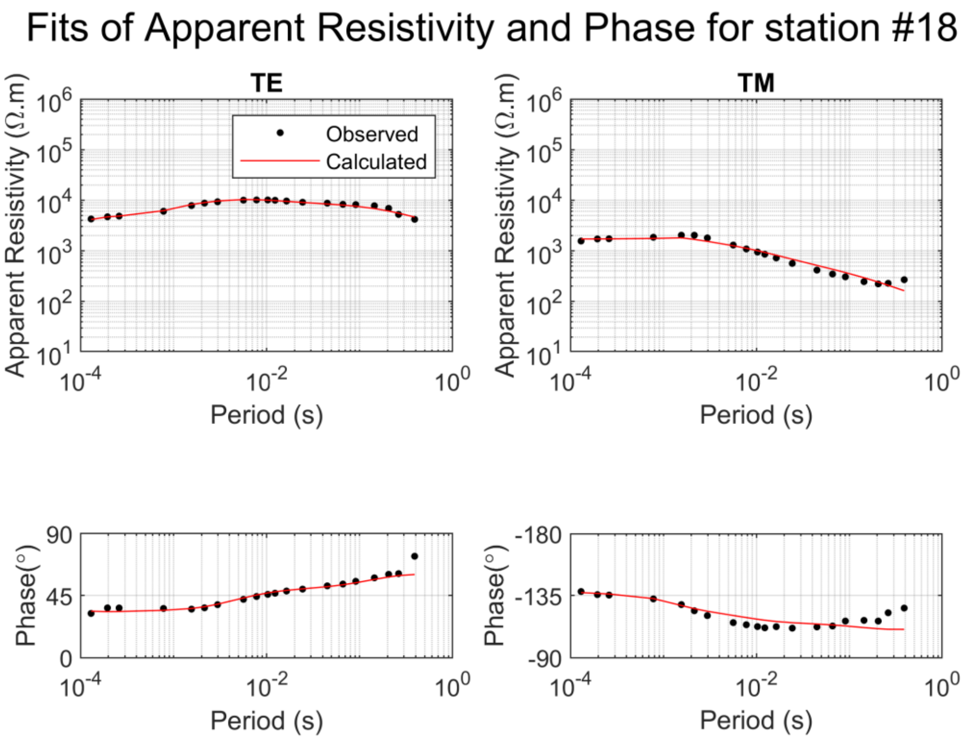
Fits of Apparent Resistivity and Phase for station #18
TE
TM
Observed
Calculated
Apparent Resistivity (Ω.m)
Phase(°)
Period (s)

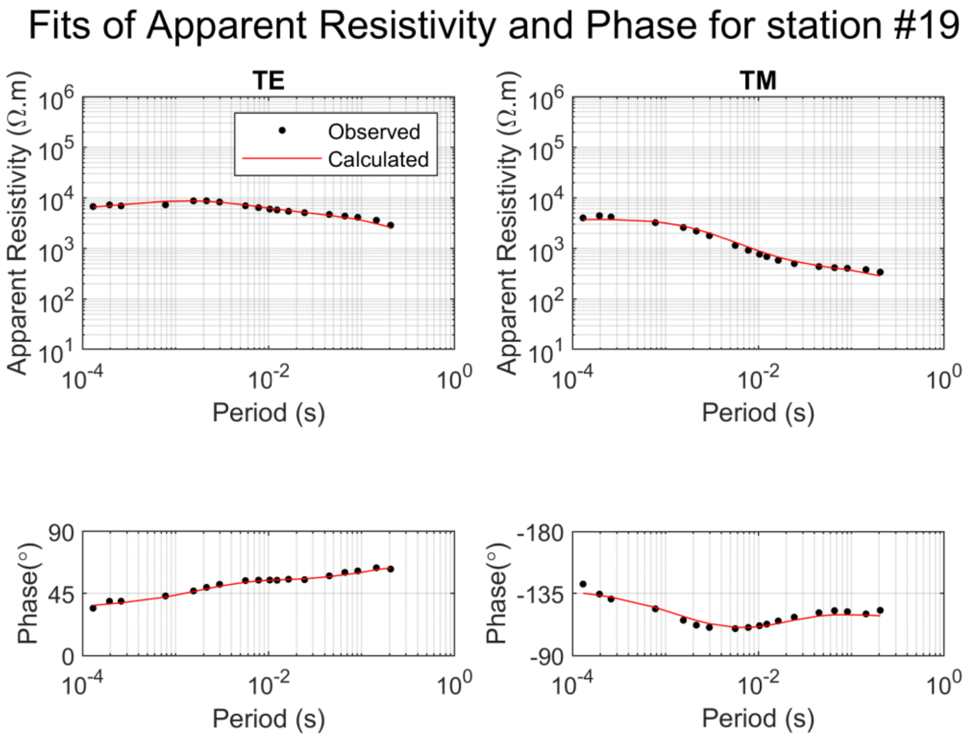
Fits of Apparent Resistivity and Phase for station #19
TE
TM
Observed
Calculated
Apparent Resistivity (Ω.m)
Period (s)
Phase(°)

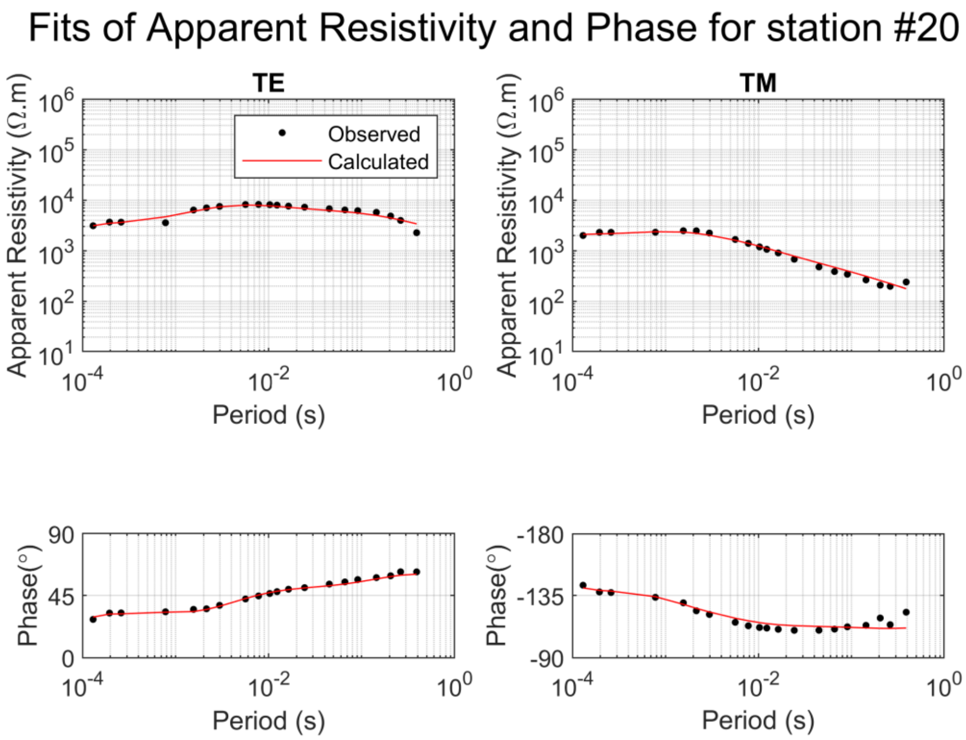
Fits of Apparent Resistivity and Phase for station #20
TE
TM
Observed
Calculated
Apparent Resistivity (Ω.m)
Period (s)
Phase(°)

Fits of Apparent Resistivity and Phase for station #21

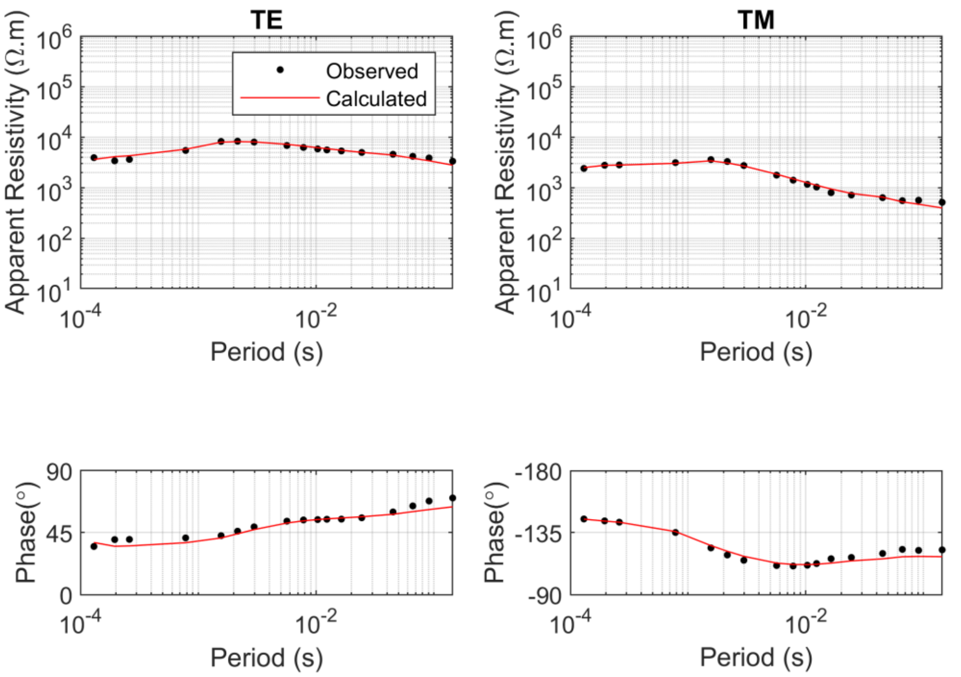

Fits of Apparent Resistivity and Phase for station #22

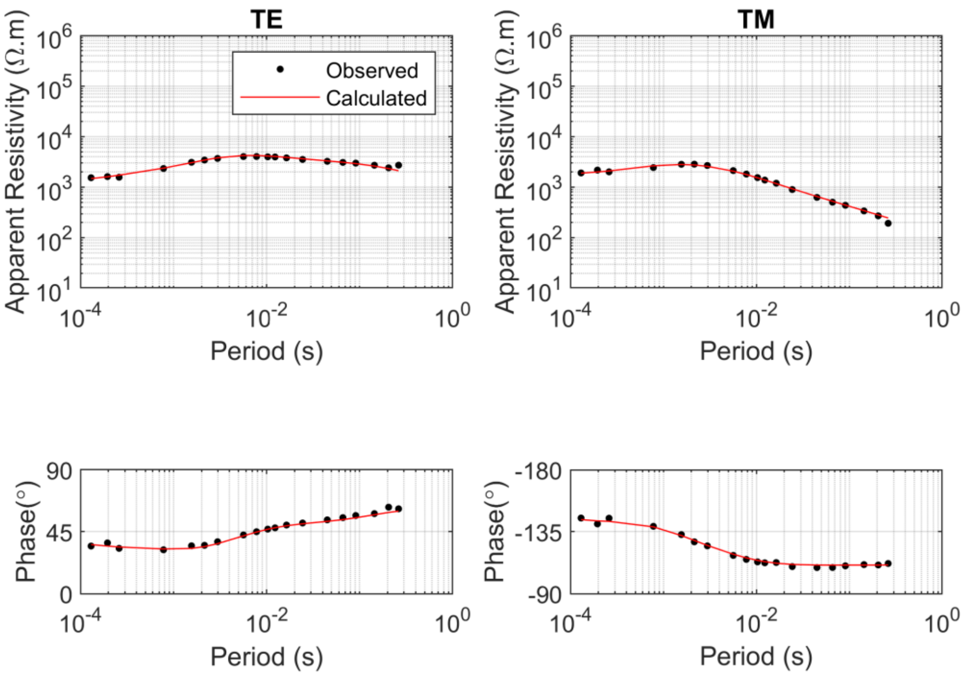

Fits of Apparent Resistivity and Phase for station #23

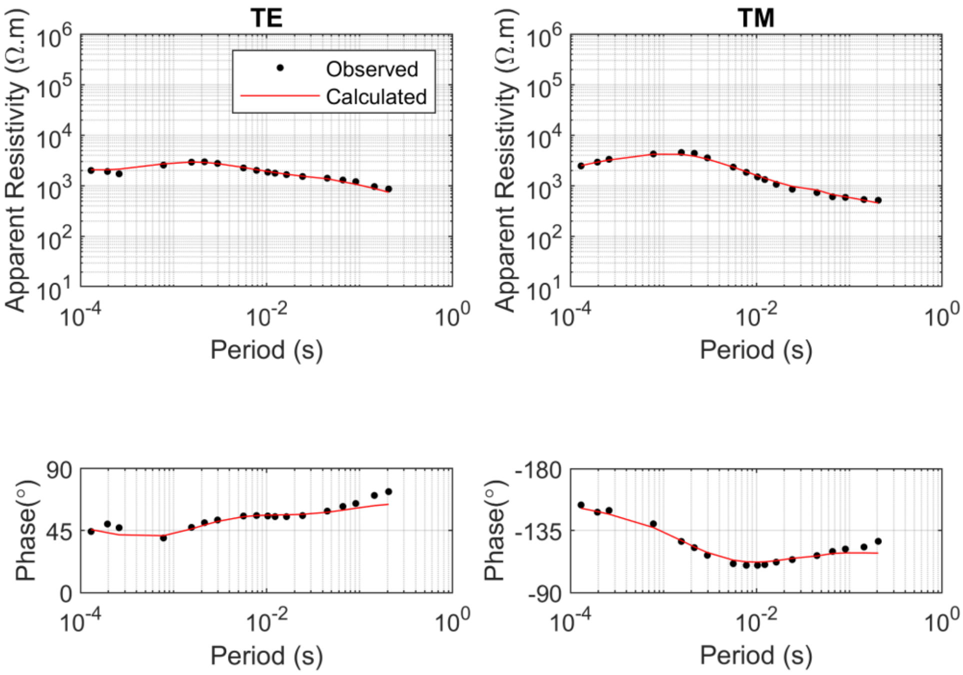

Fits of Apparent Resistivity and Phase for station #24

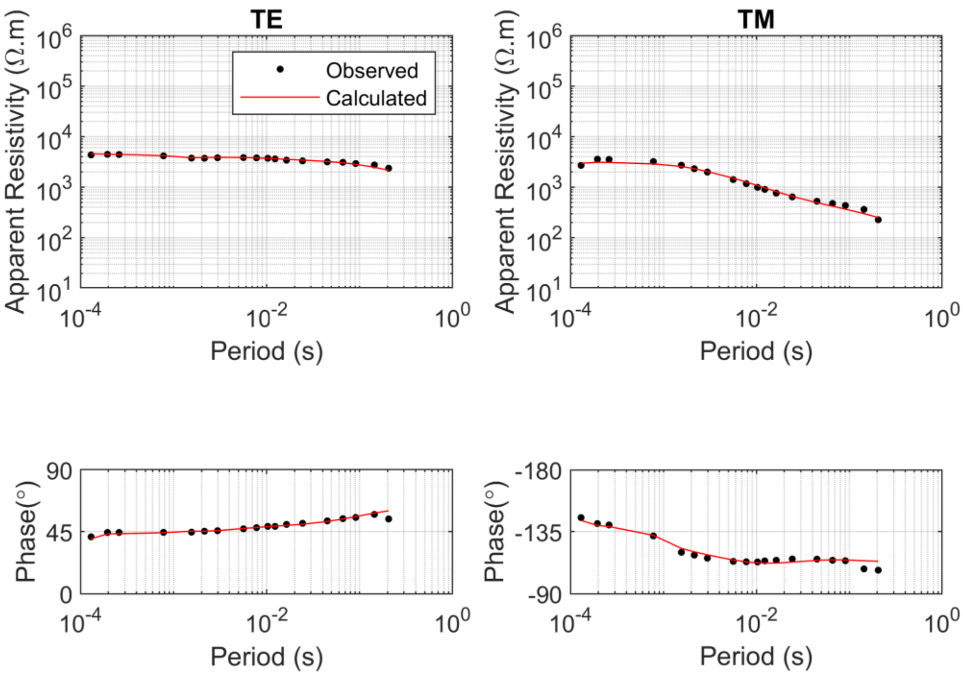

Fits of Apparent Resistivity and Phase for station #25

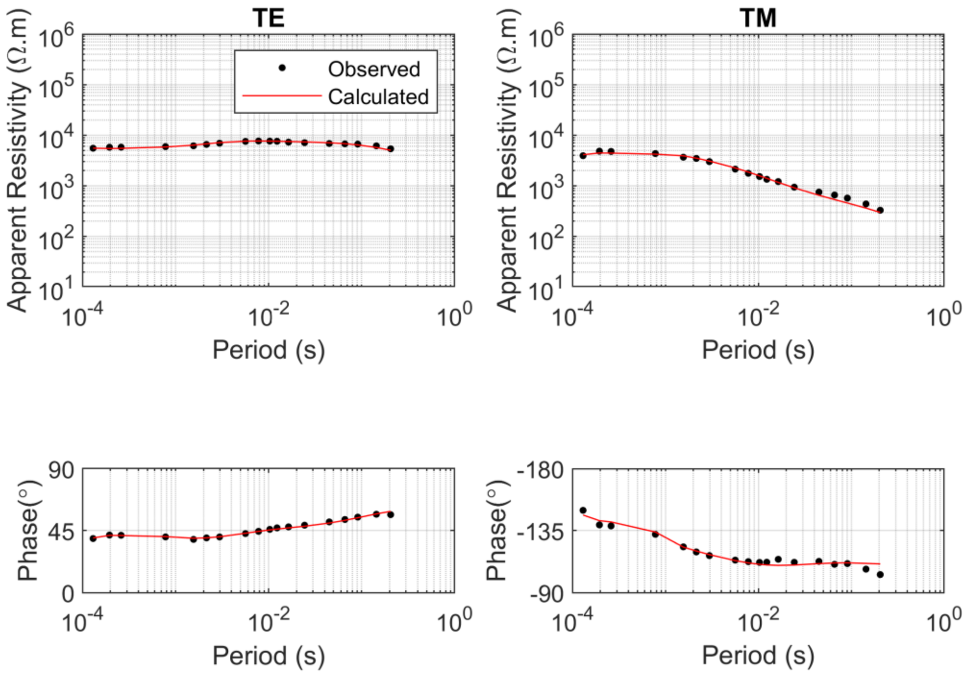

Fits of Apparent Resistivity and Phase for station #26

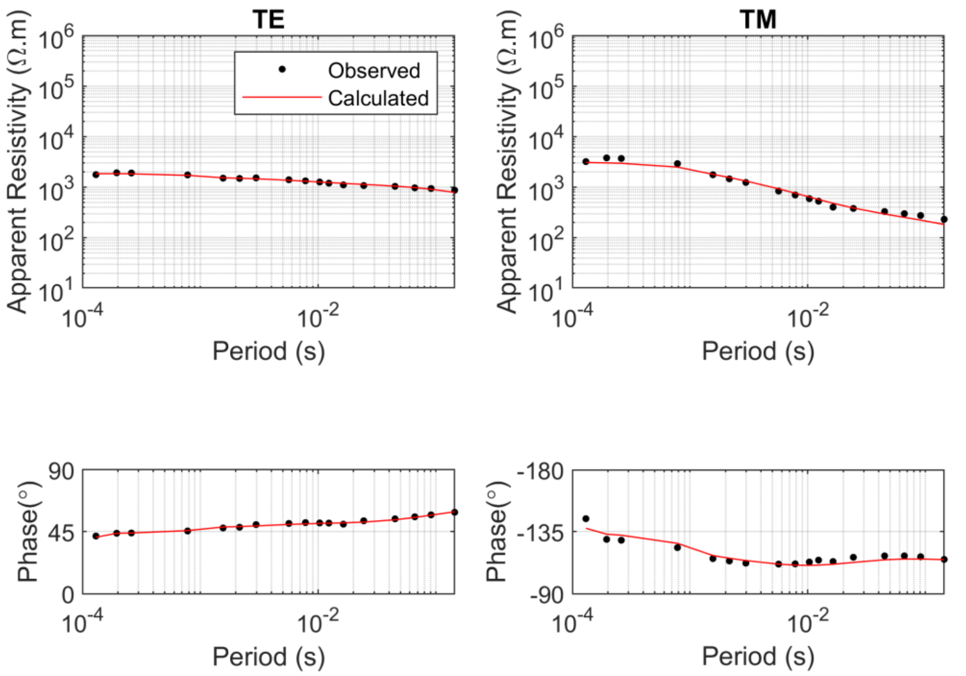

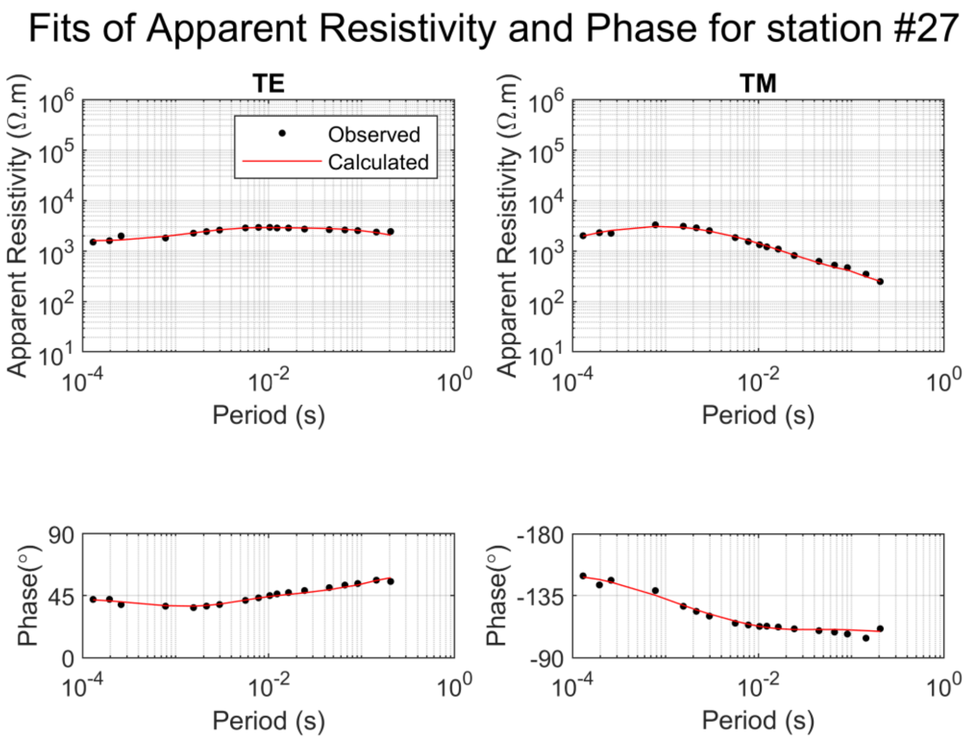
Fits of Apparent Resistivity and Phase for station #27
TE
TM
Observed
Calculated
Apparent Resistivity (Ω.m)
Phase(°)
Period (s)

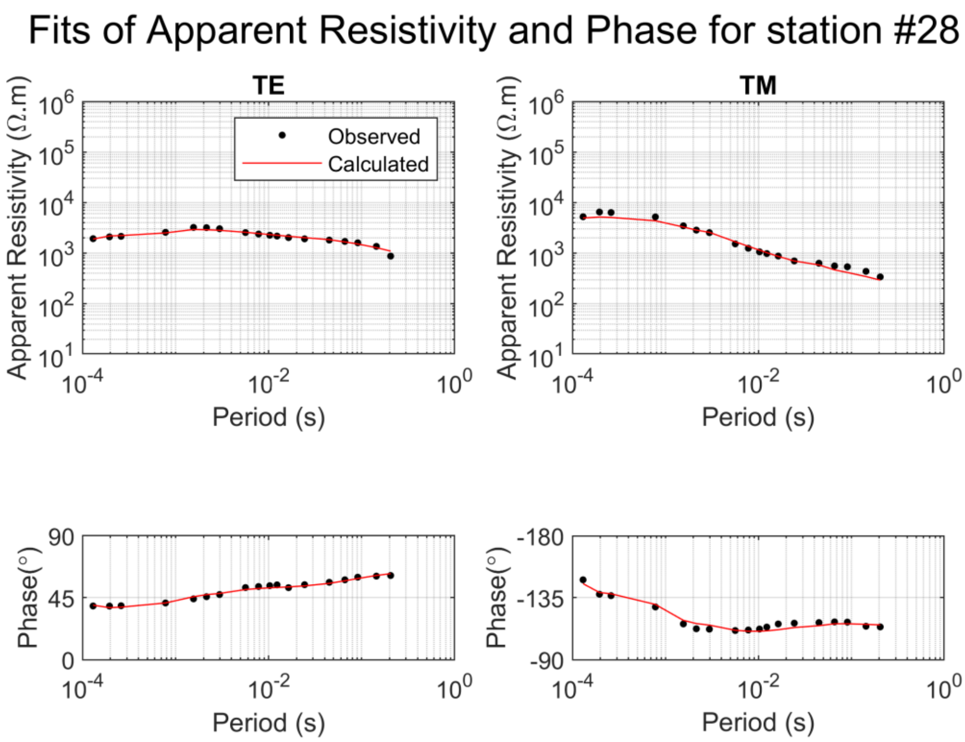
Fits of Apparent Resistivity and Phase for station #28
TE
TM
Observed
Calculated
Apparent Resistivity (Ω.m)
Phase(°)
Period (s)

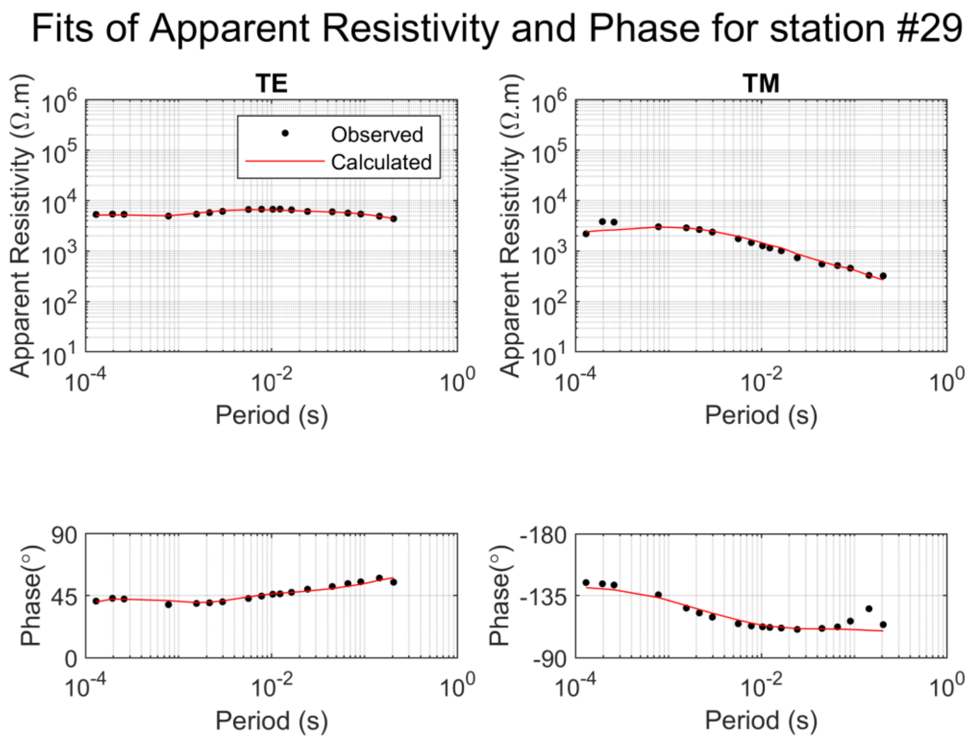
Fits of Apparent Resistivity and Phase for station #29
TE
TM
Observed
Calculated
Apparent Resistivity (Ω.m)
Period (s)
Phase(°)

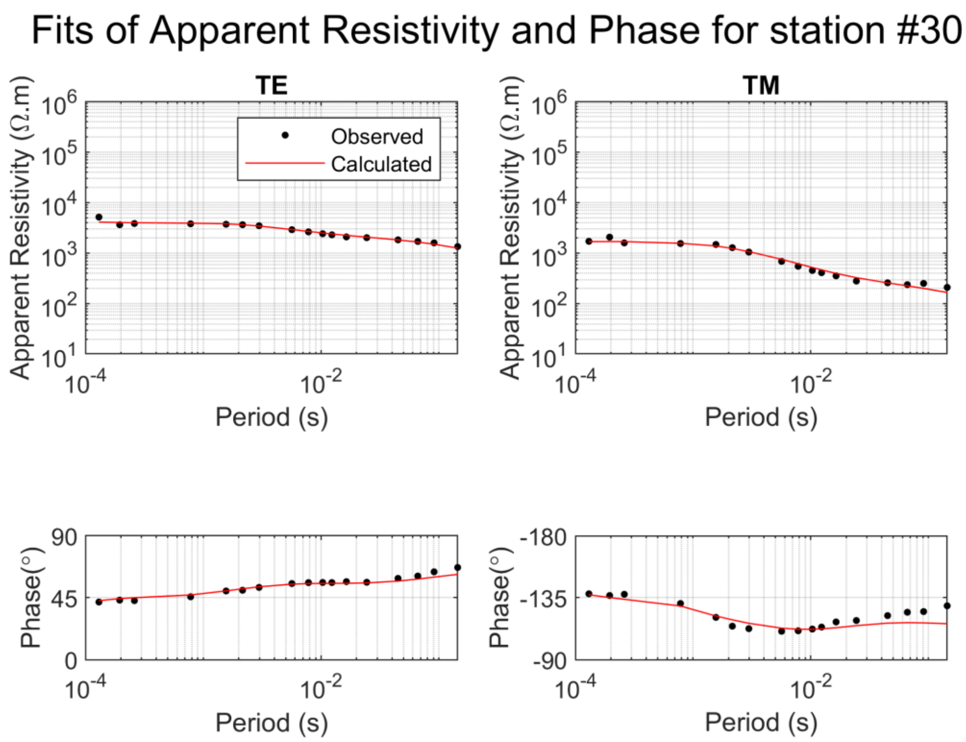
Fits of Apparent Resistivity and Phase for station #30
TE
TM
Observed
Calculated
Apparent Resistivity (Ω.m)
Period (s)
Phase(°)

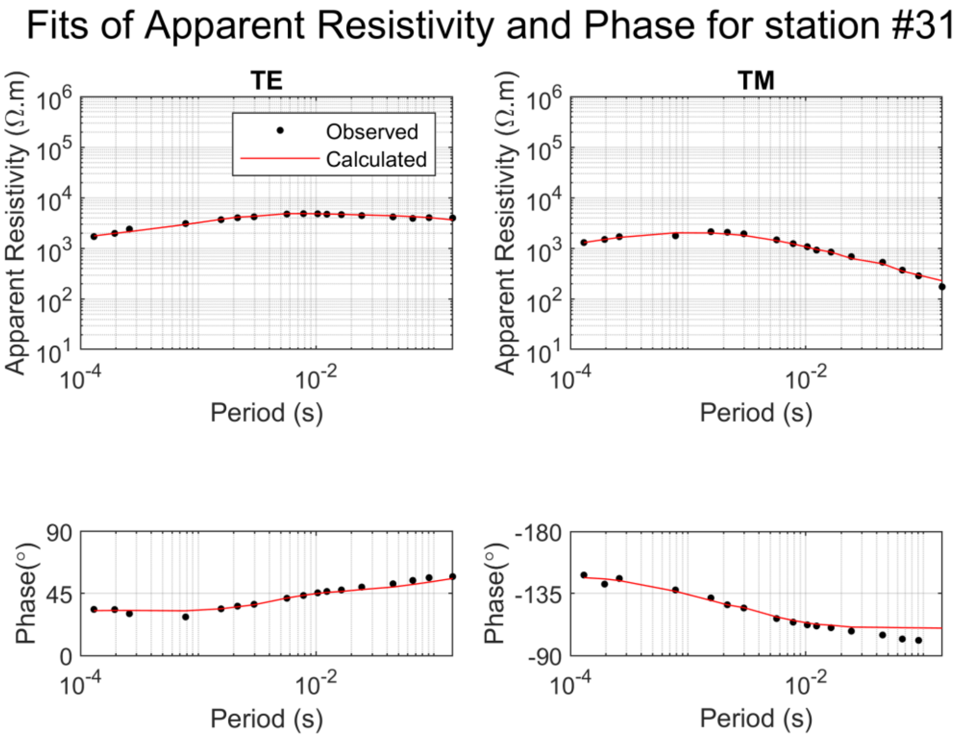
Fits of Apparent Resistivity and Phase for station #31
TE
TM
Observed
Calculated
Apparent Resistivity (Ω.m)
Phase(°)
Period (s)

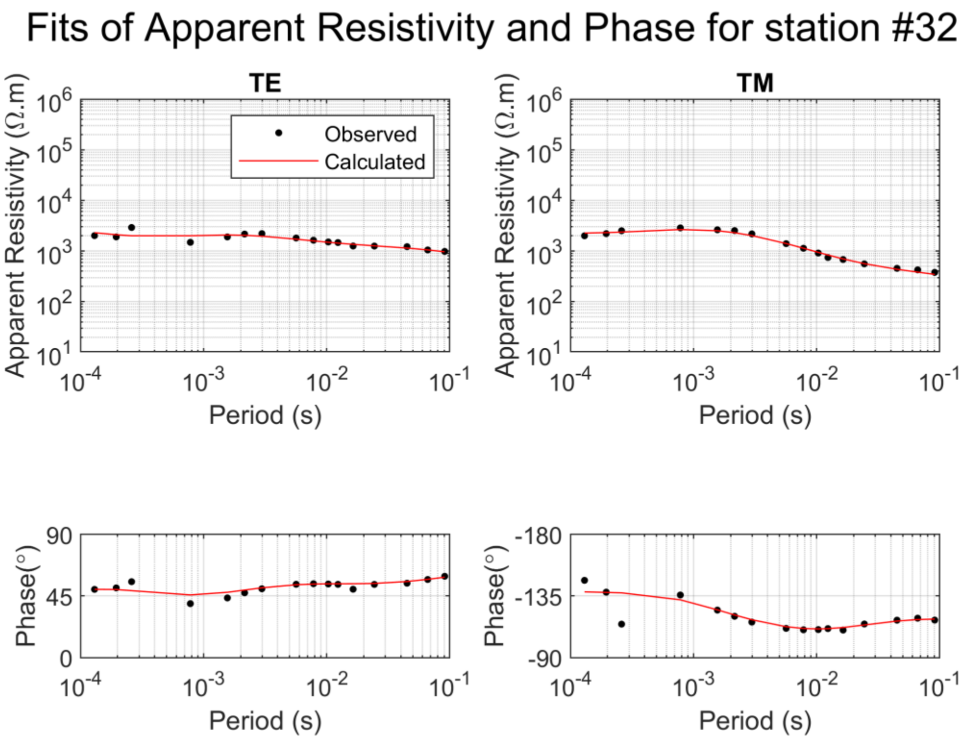
Fits of Apparent Resistivity and Phase for station #32
TE
TM
Observed
Calculated
Apparent Resistivity (Ω.m)
Phase(°)
Period (s)

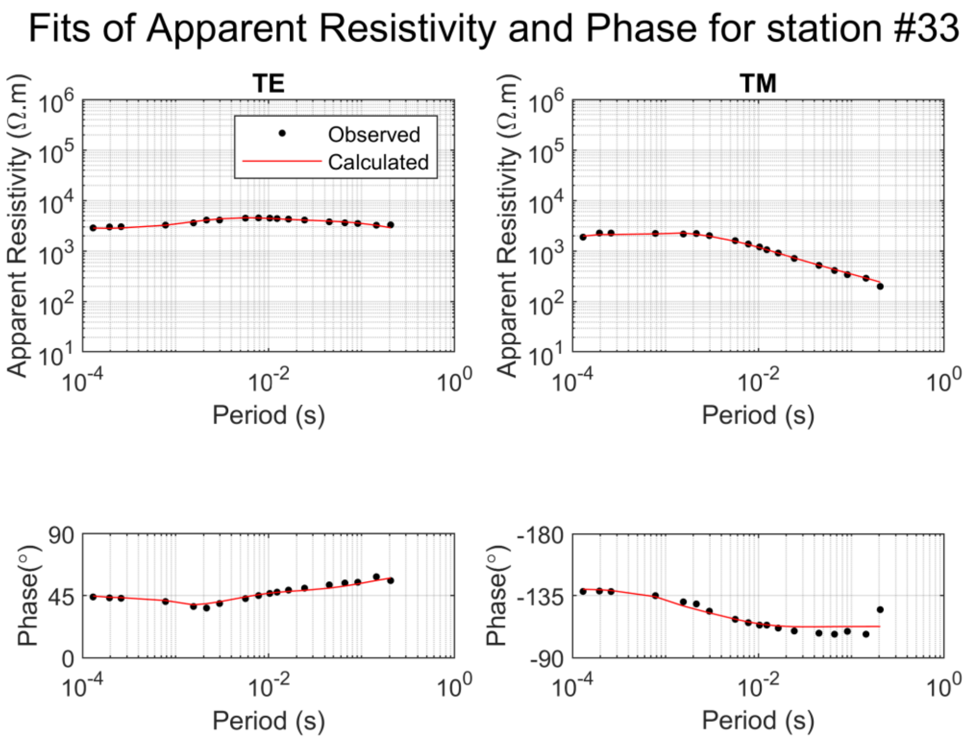
Fits of Apparent Resistivity and Phase for station #33
TE
TM
Observed
Calculated
Apparent Resistivity (Ω.m)
Phase(°)
Period (s)

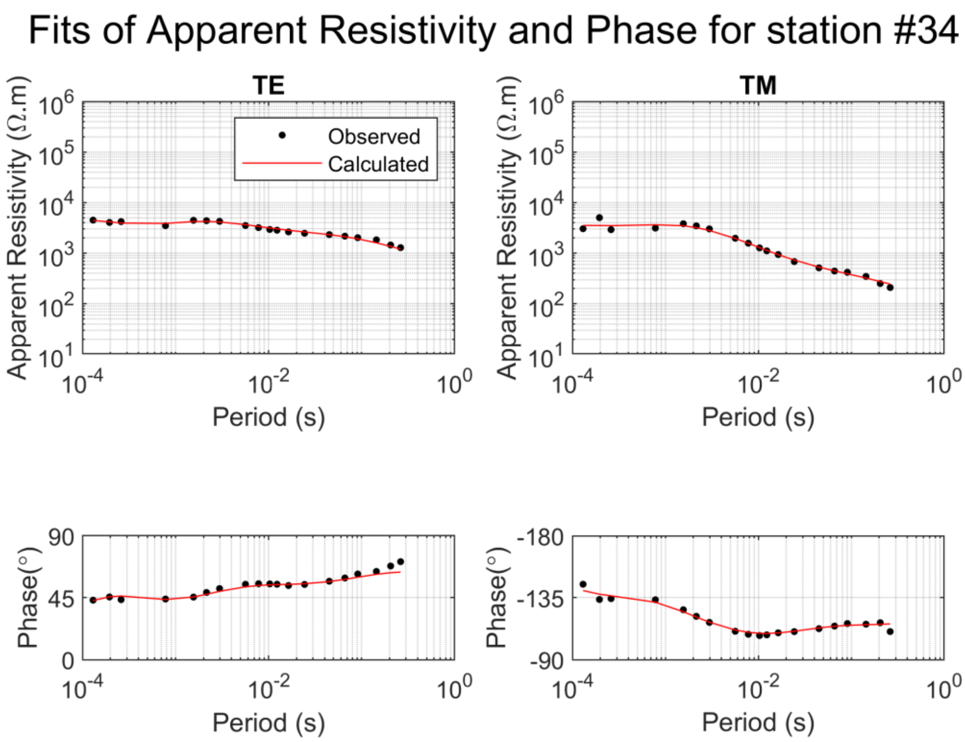
Fits of Apparent Resistivity and Phase for station #34
TE
TM
Observed
Calculated
Apparent Resistivity (Ω.m)
Phase(°)
Period (s)

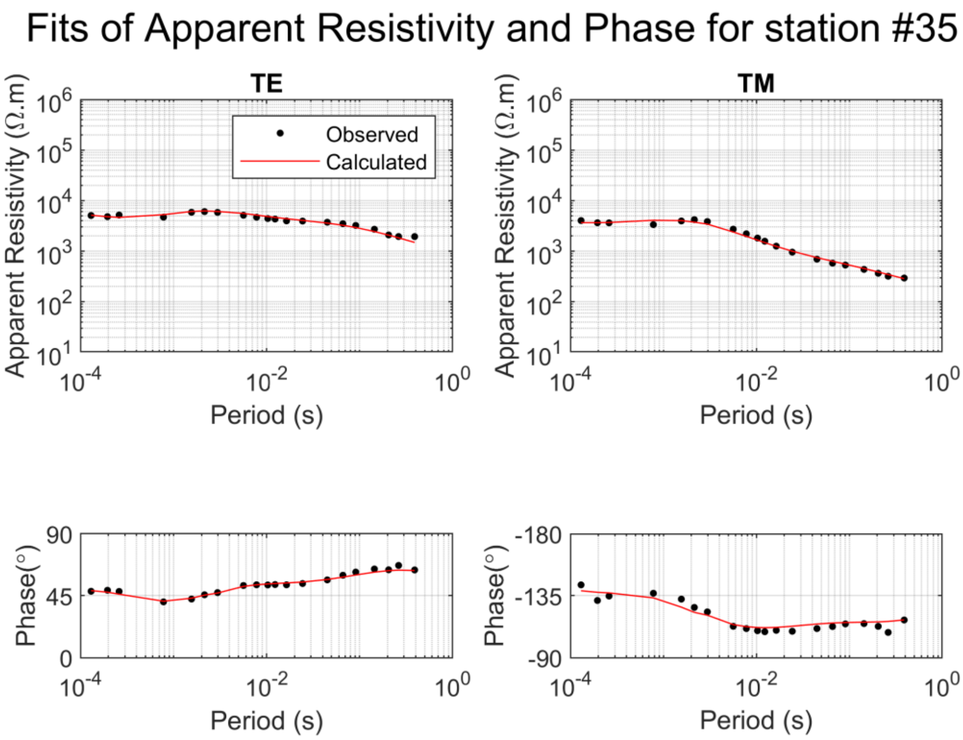
Fits of Apparent Resistivity and Phase for station #35
TE
TM
Observed
Calculated
Apparent Resistivity (Ω.m)
Period (s)
Phase(°)

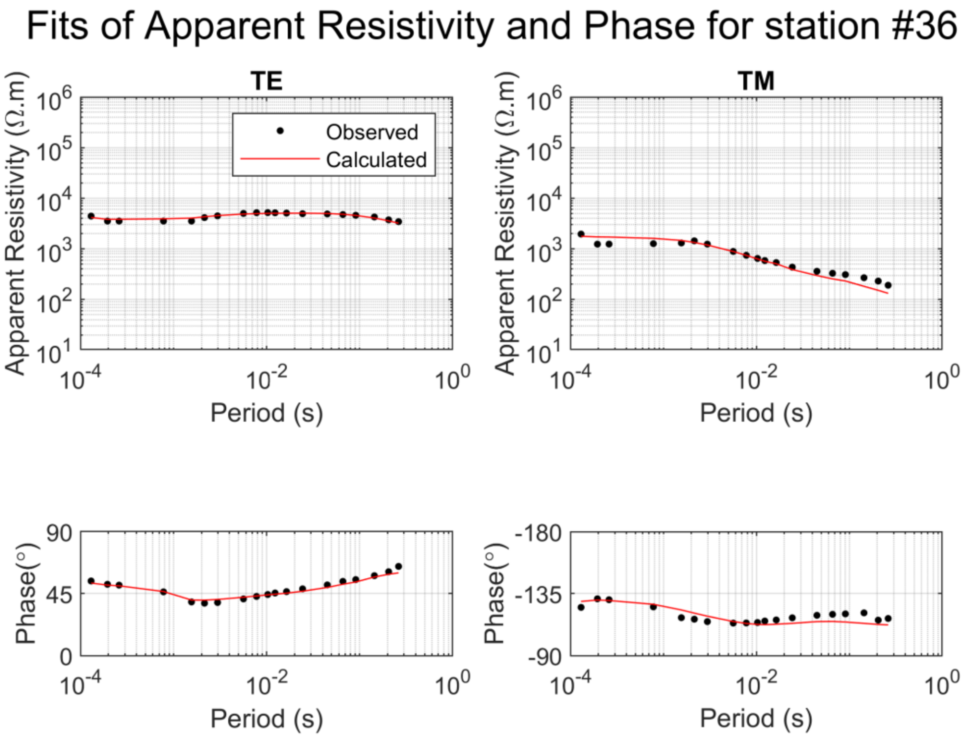
Fits of Apparent Resistivity and Phase for station #36
TE
TM
Observed
Calculated
Apparent Resistivity (Ω.m)
Period (s)
Phase(°)

Fits of Apparent Resistivity and Phase for station #37

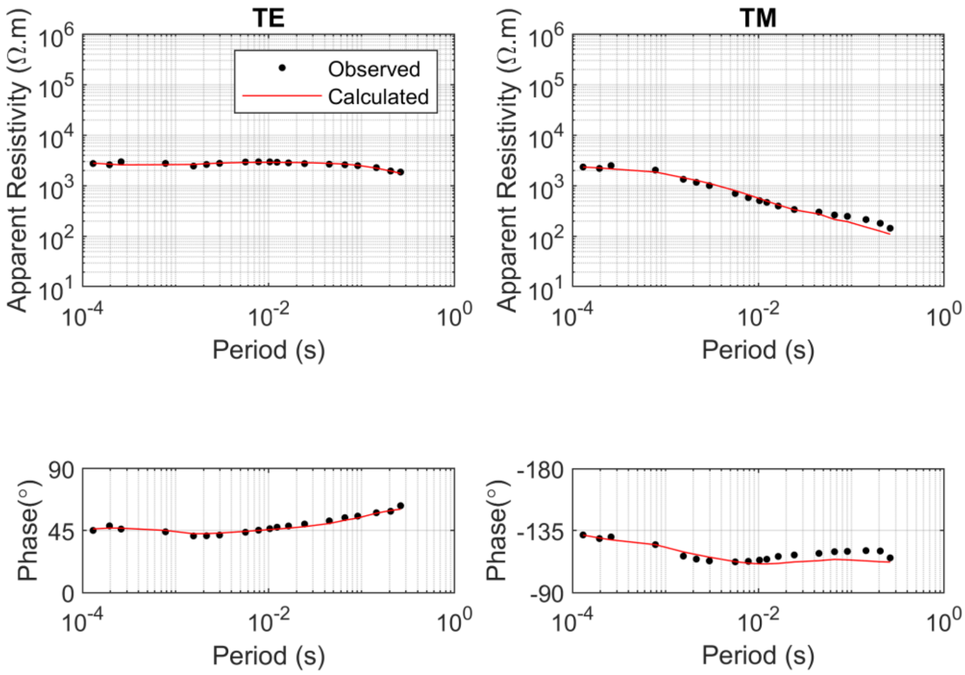

Fits of Apparent Resistivity and Phase for station #38

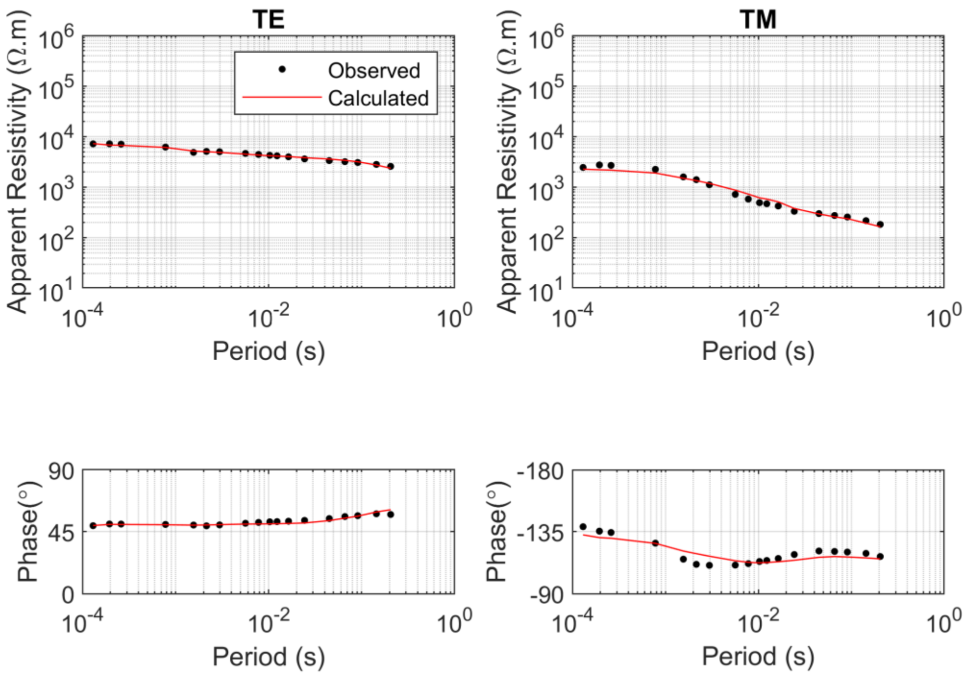

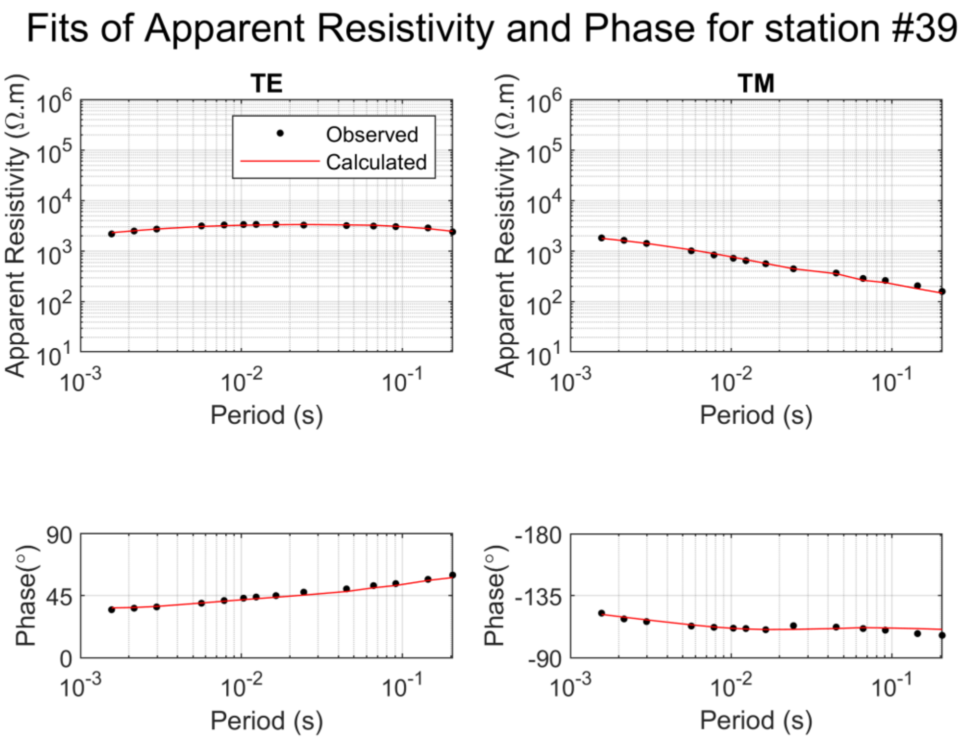
Fits of Apparent Resistivity and Phase for station #39
TE
TM
Observed
Calculated
Apparent Resistivity (Ω.m)
Phase(°)
Period (s)

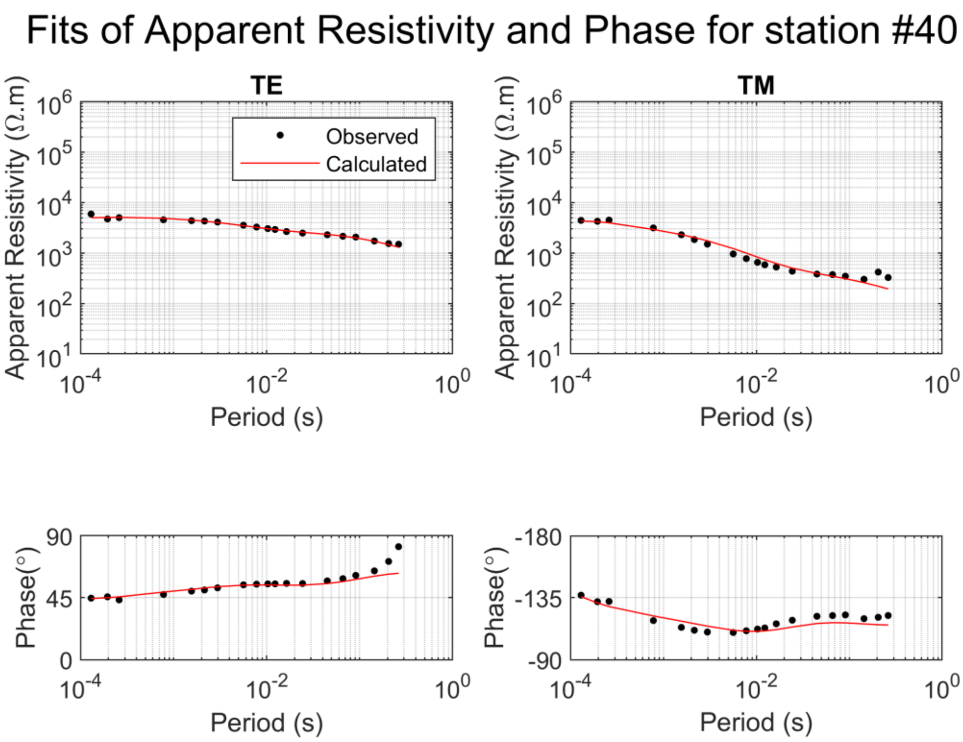
Fits of Apparent Resistivity and Phase for station #40
TE
TM
Observed
Calculated
Apparent Resistivity (Ω.m)
Phase(°)
Period (s)

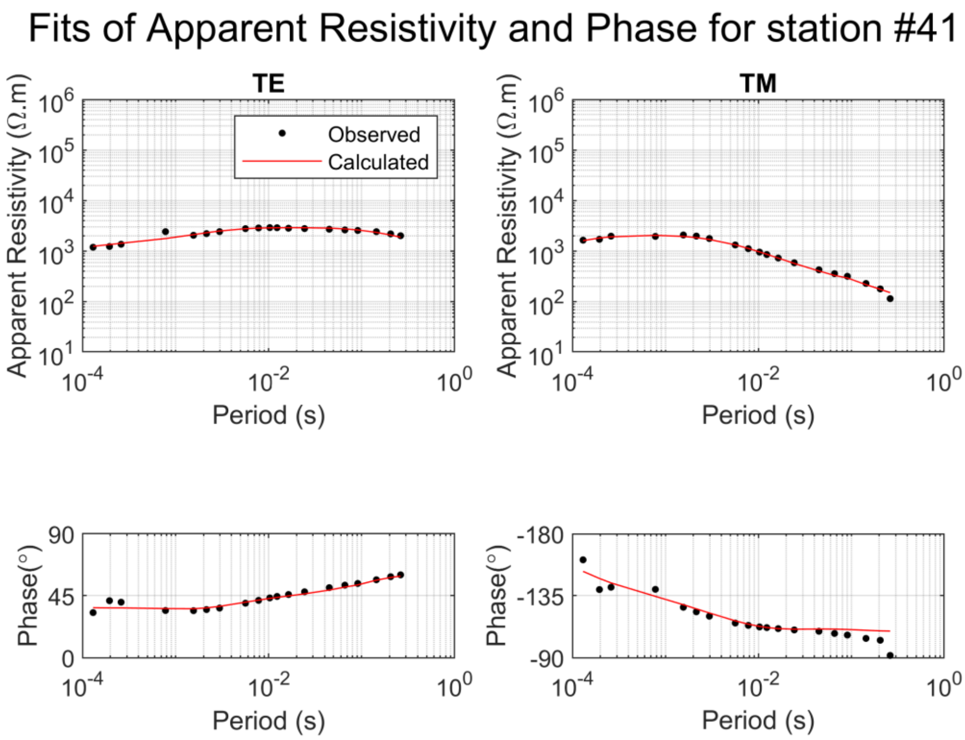
Fits of Apparent Resistivity and Phase for station #41
TE
TM
Observed
Calculated
Apparent Resistivity (Ω.m)
Phase(°)
Period (s)

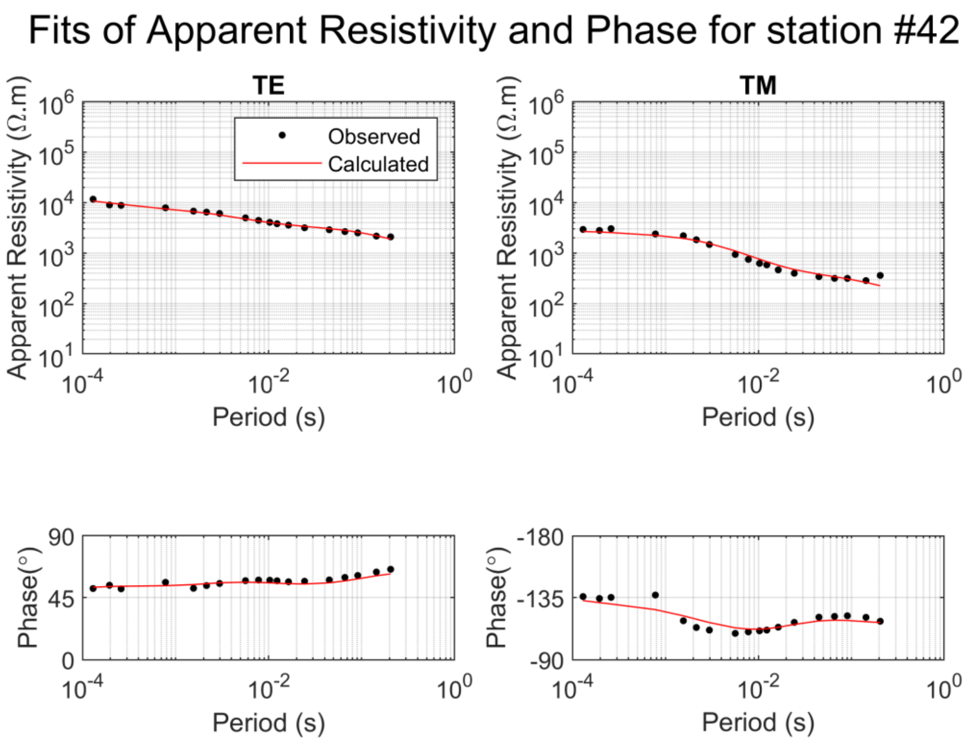
Fits of Apparent Resistivity and Phase for station #42
TE
TM
Observed
Calculated
Apparent Resistivity (Ω.m)
Phase(°)
Period (s)

Fits of Apparent Resistivity and Phase for station #43

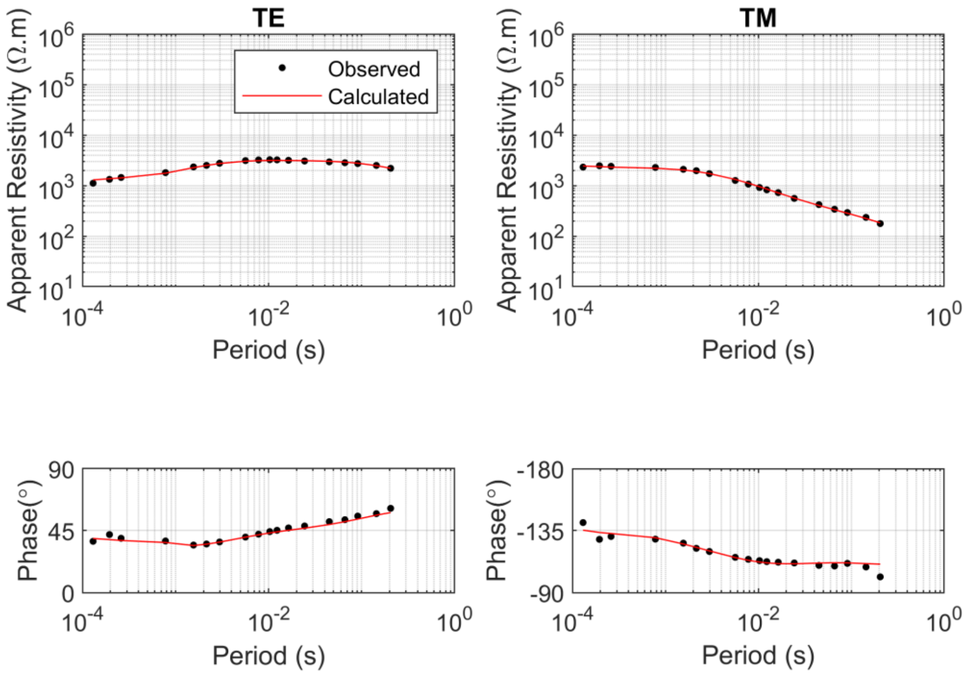

Fits of Apparent Resistivity and Phase for station #44

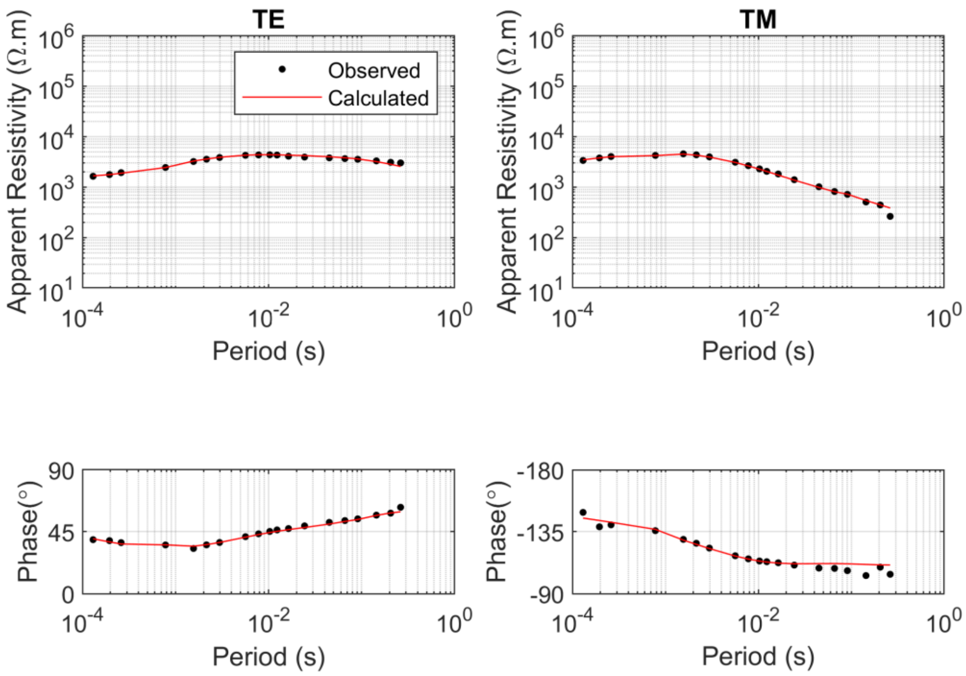

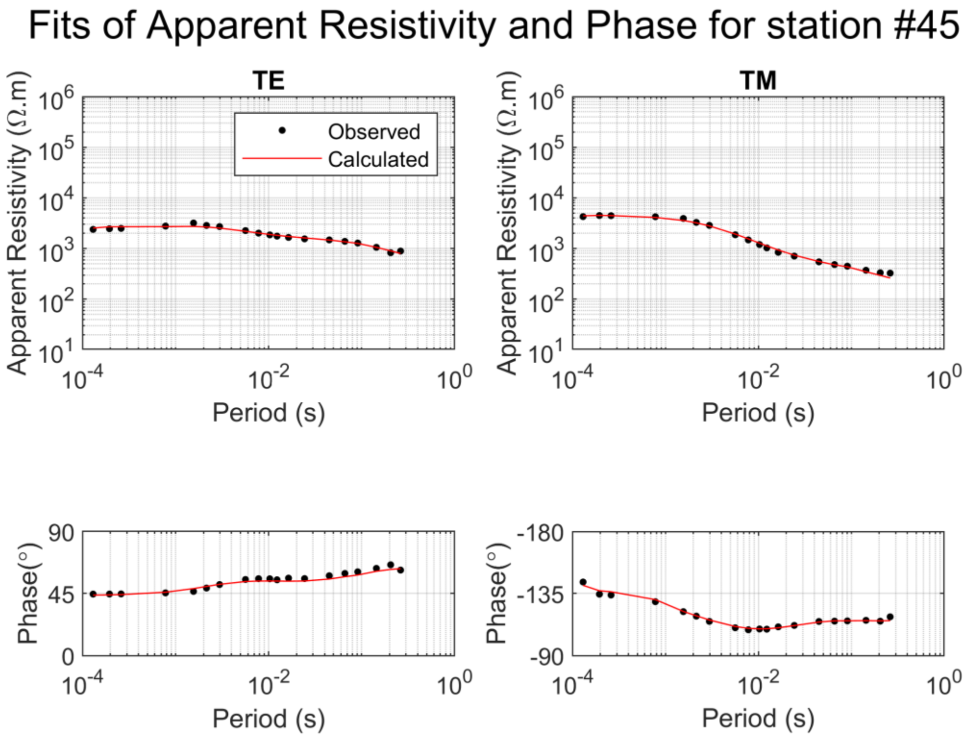
Fits of Apparent Resistivity and Phase for station #45
TE
TM
Observed
Calculated
Apparent Resistivity (Ω.m)
Phase(°)
Period (s)

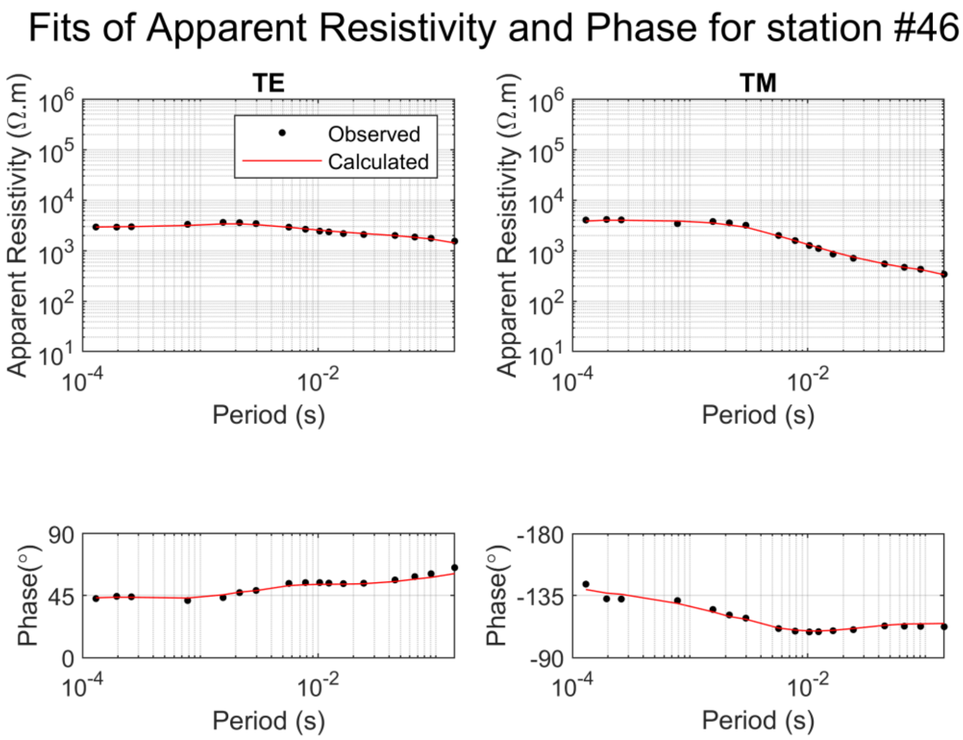
Fits of Apparent Resistivity and Phase for station #46
TE
TM
Observed
Calculated
Apparent Resistivity (Ω.m)
Phase(°)
Period (s)

Fits of Apparent Resistivity and Phase for station #47

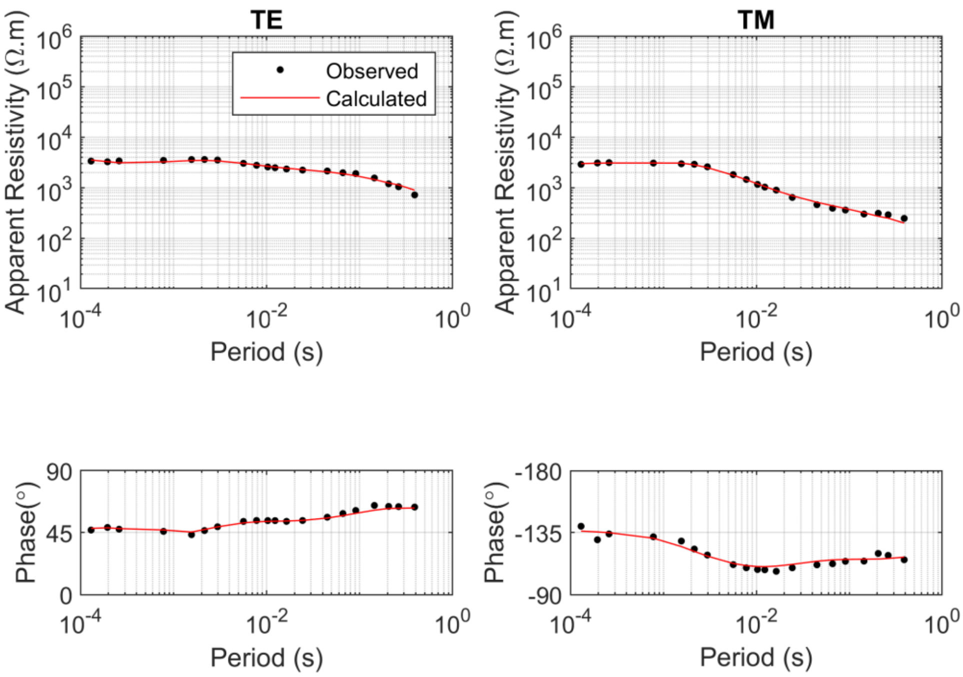

Fits of Apparent Resistivity and Phase for station #48

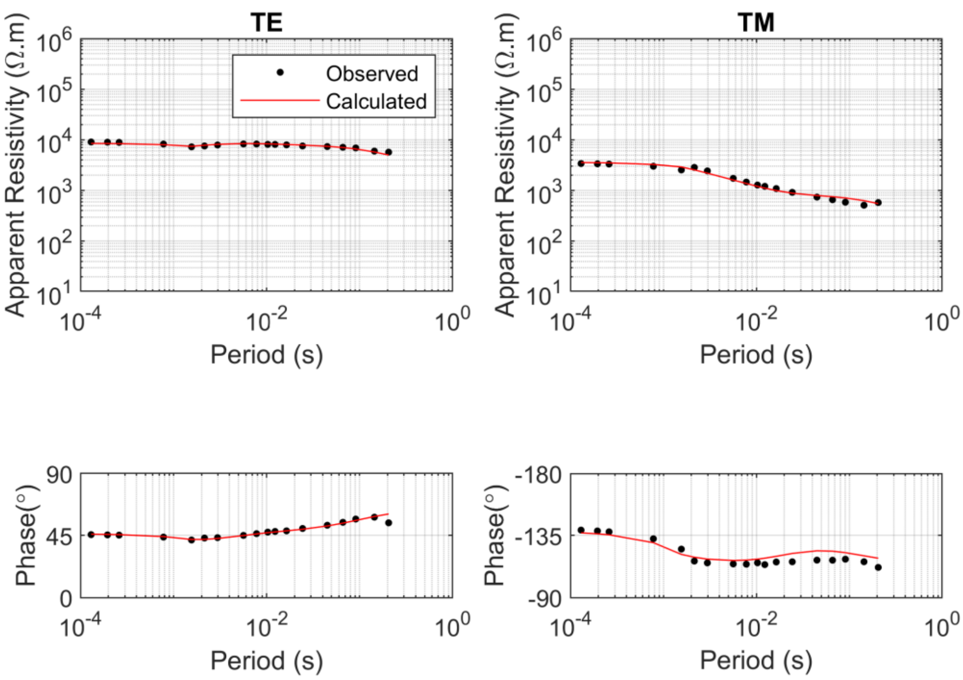

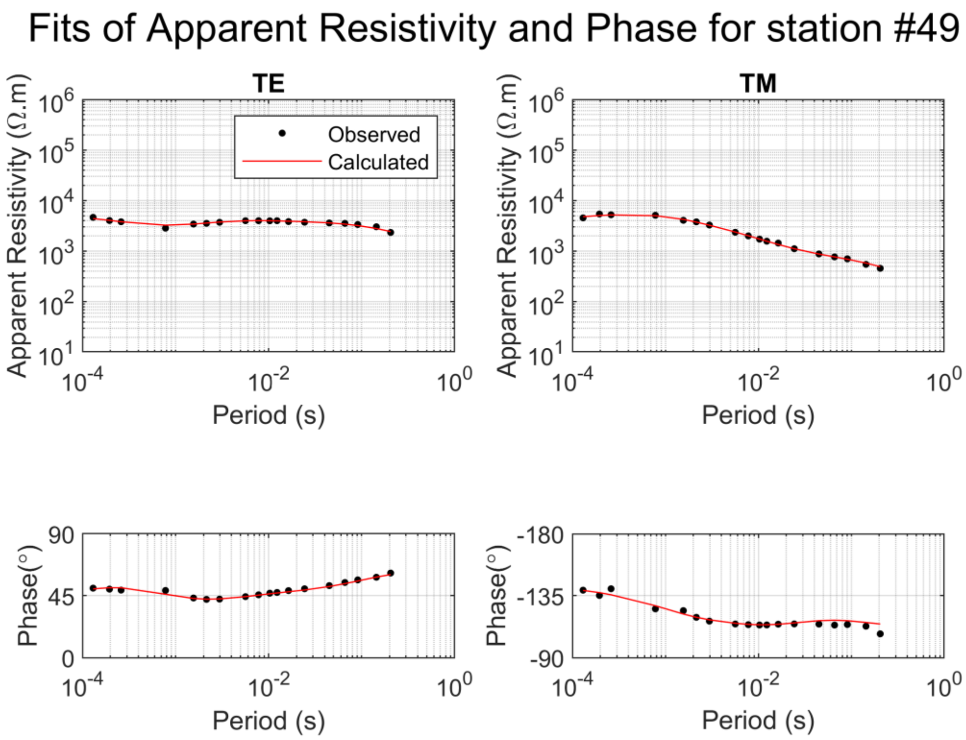
Fits of Apparent Resistivity and Phase for station #49
TE
TM
Observed
Calculated
Apparent Resistivity (Ω.m)
Period (s)
Phase(°)

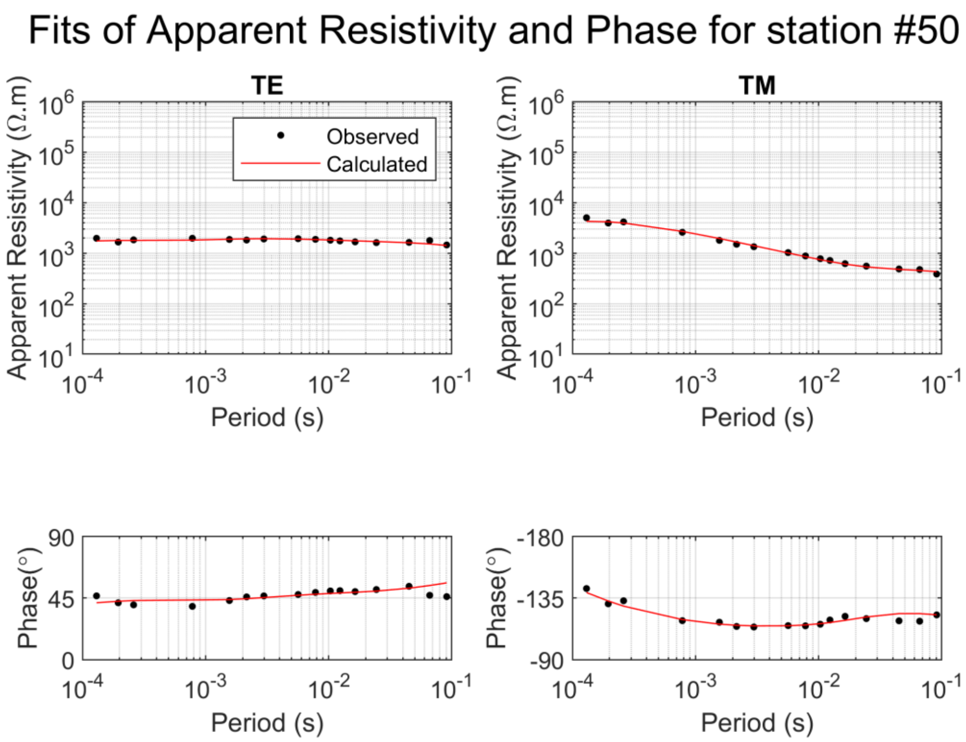
Fits of Apparent Resistivity and Phase for station #50
TE
TM
Observed
Calculated
Apparent Resistivity (Ω.m)
Period (s)
Phase(°)

Fits of Apparent Resistivity and Phase for station #51

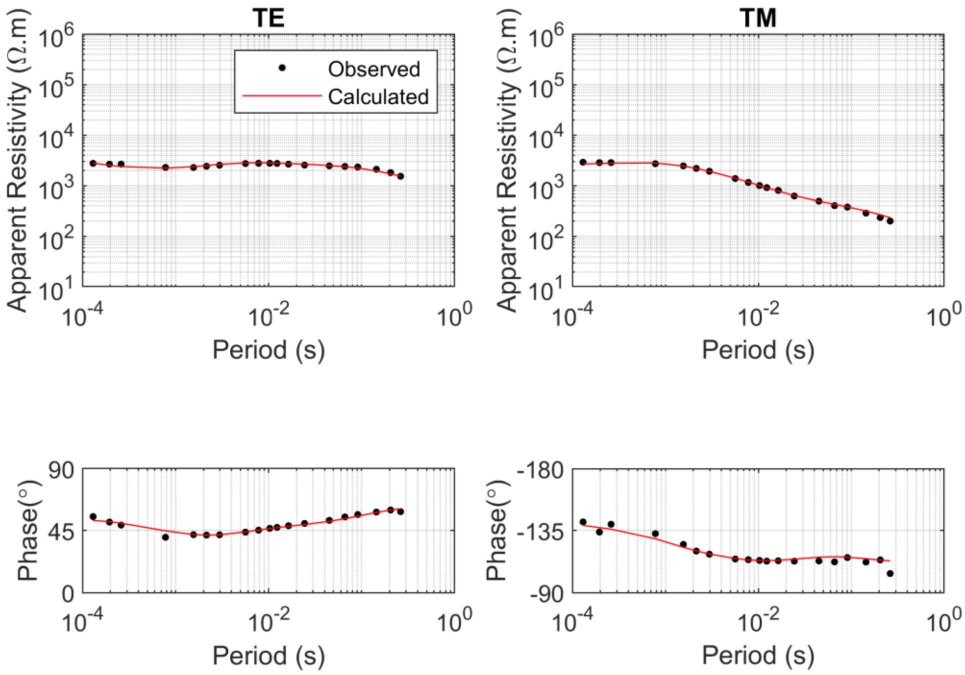

Fits of Apparent Resistivity and Phase for station #52

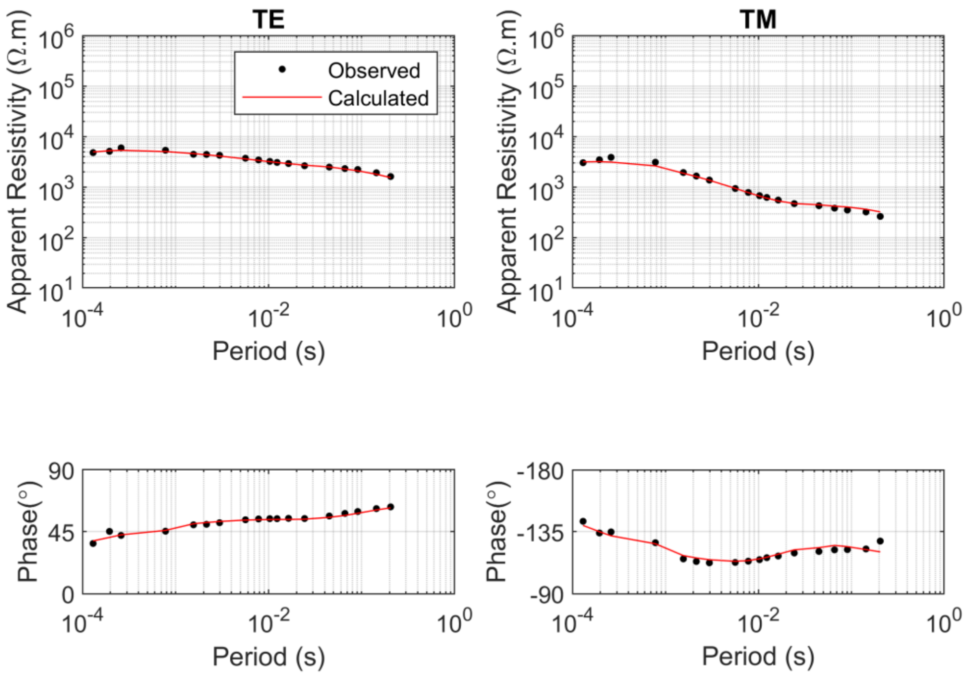

Fits of Apparent Resistivity and Phase for station #53

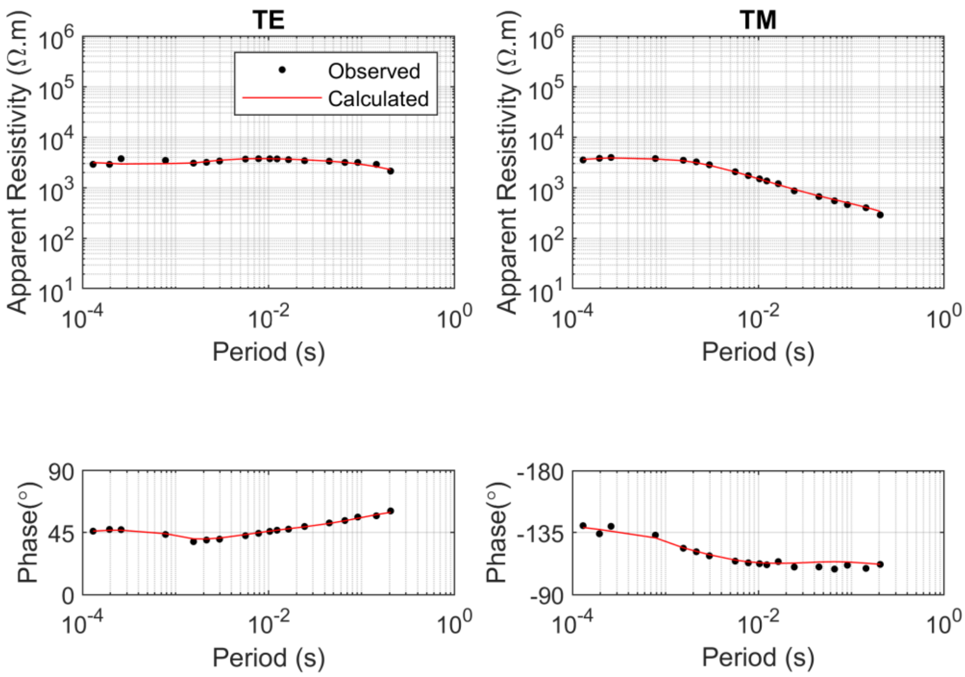

Fits of Apparent Resistivity and Phase for station #54

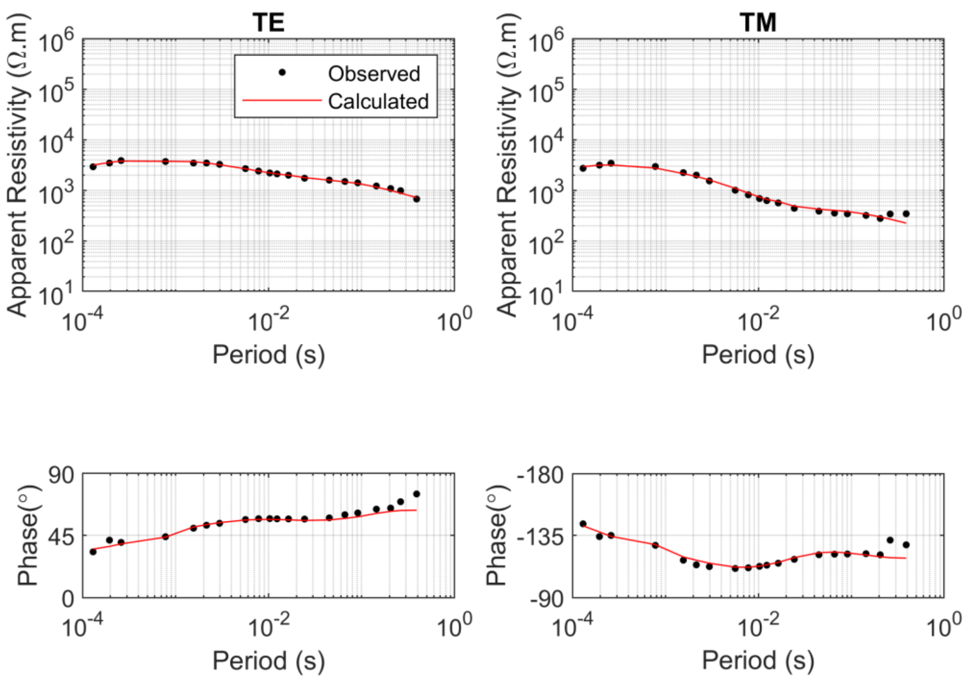

Fits of Apparent Resistivity and Phase for station #55

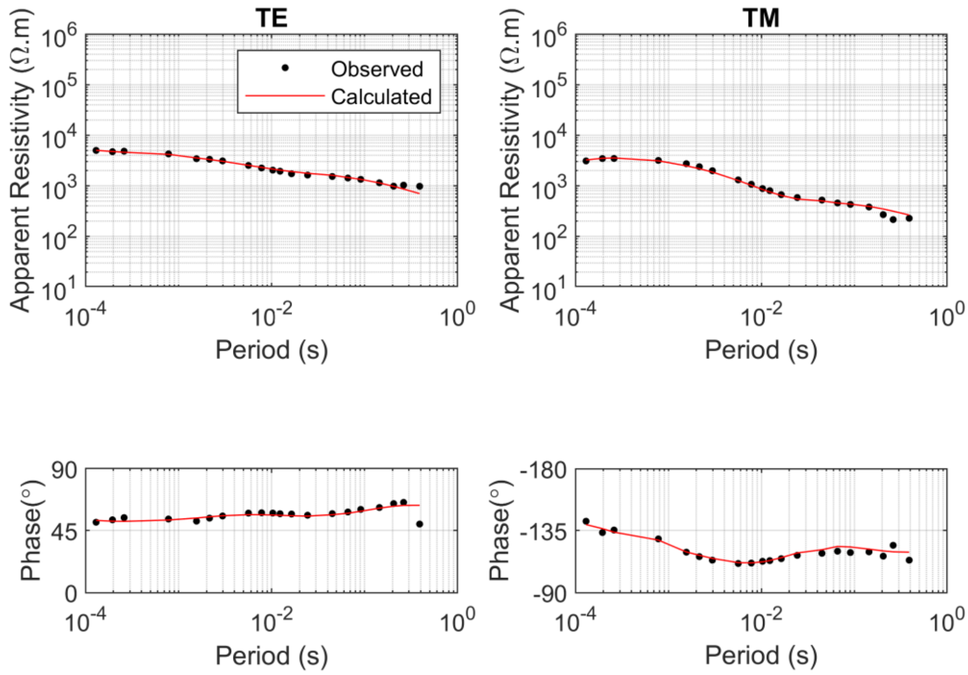

Fits of Apparent Resistivity and Phase for station #56

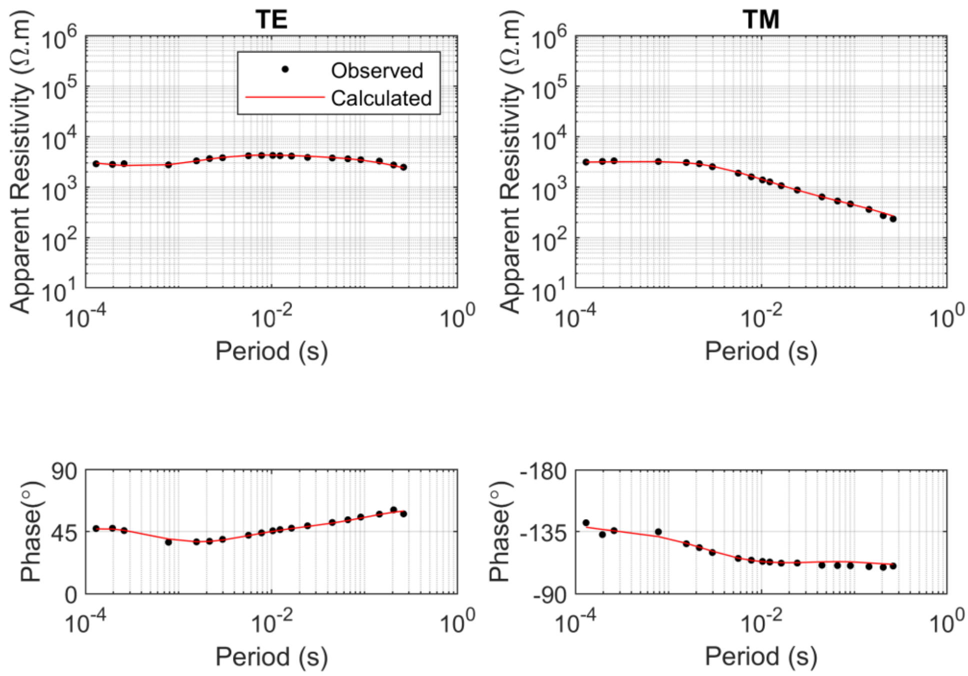

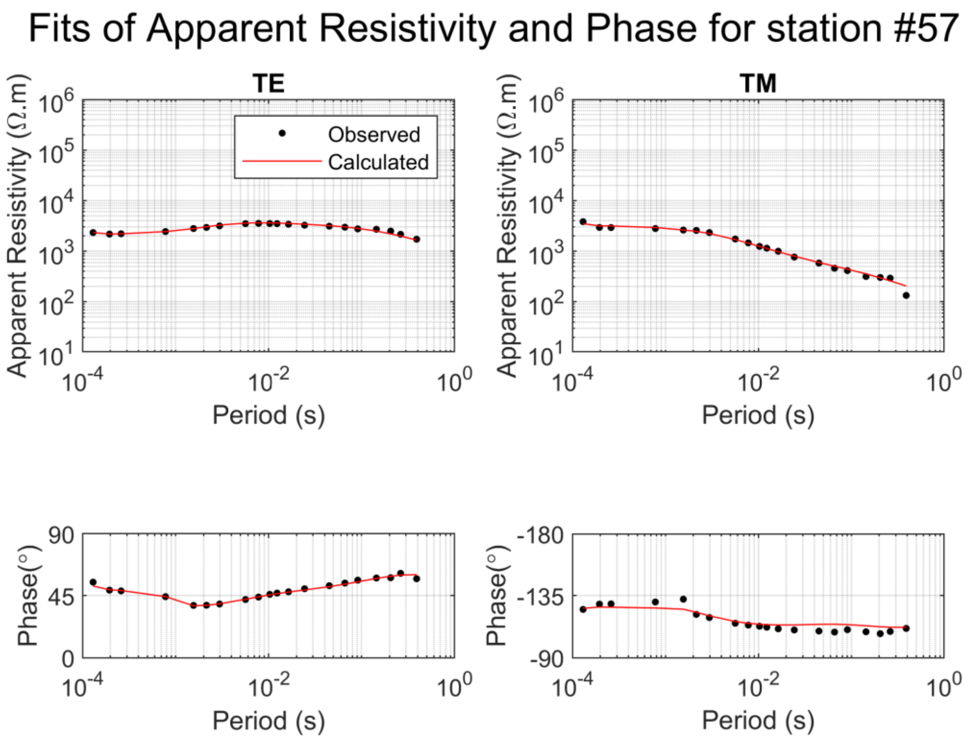
Fits of Apparent Resistivity and Phase for station #57
TE
TM
Observed
Calculated
Apparent Resistivity (Ω.m)
Phase(°)
Period (s)

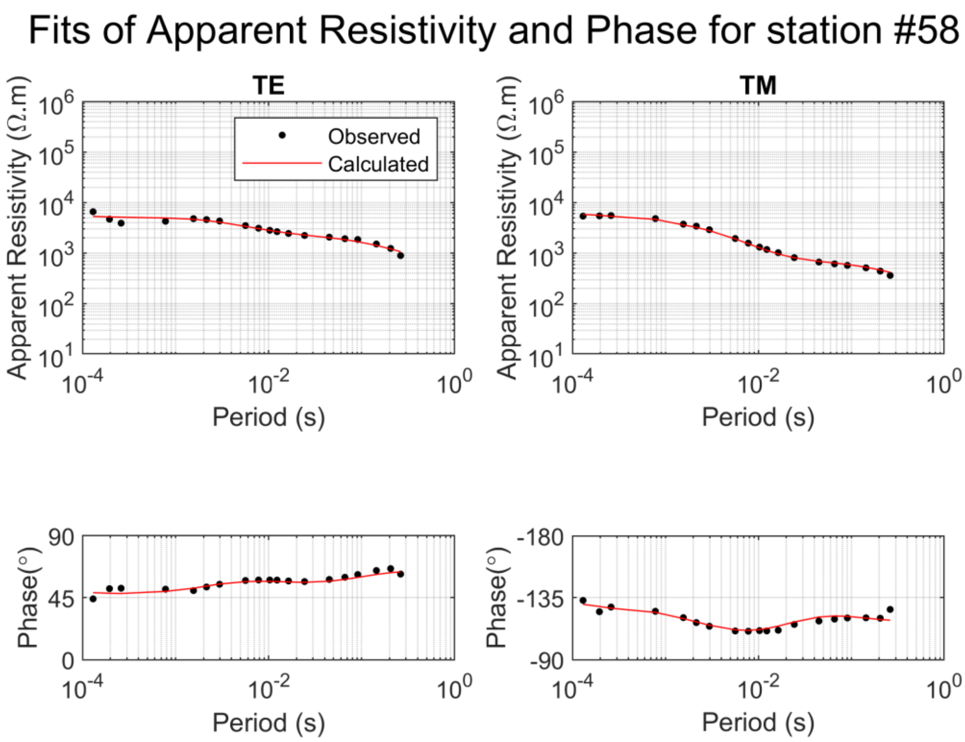
Fits of Apparent Resistivity and Phase for station #58
TE
TM
Observed
Calculated
Apparent Resistivity (Ω.m)
Phase(°)
Period (s)

Fits of Apparent Resistivity and Phase for station #59

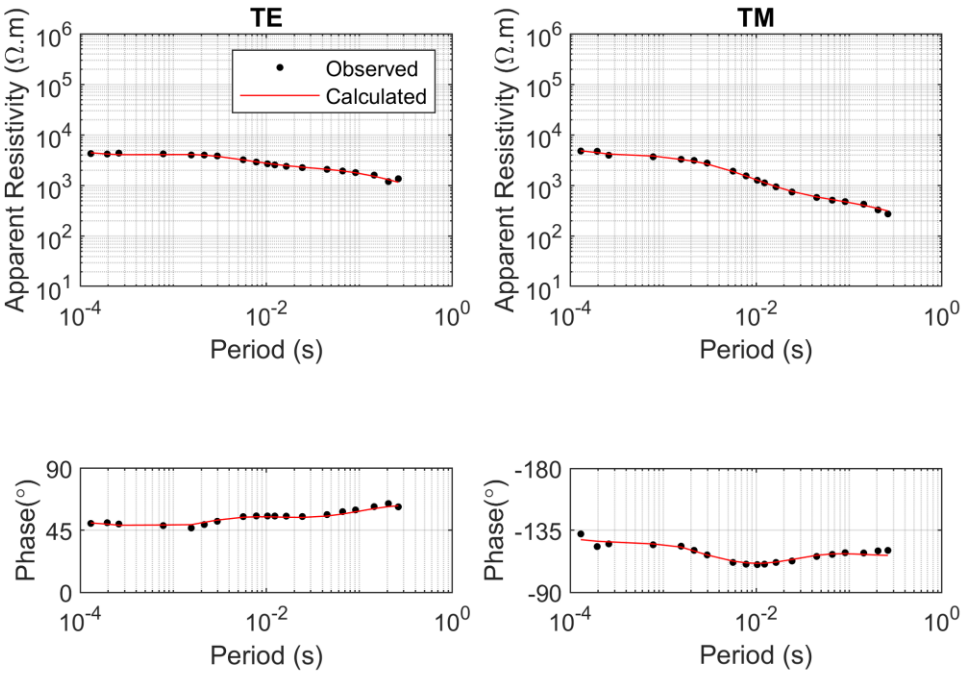

Fits of Apparent Resistivity and Phase for station #60

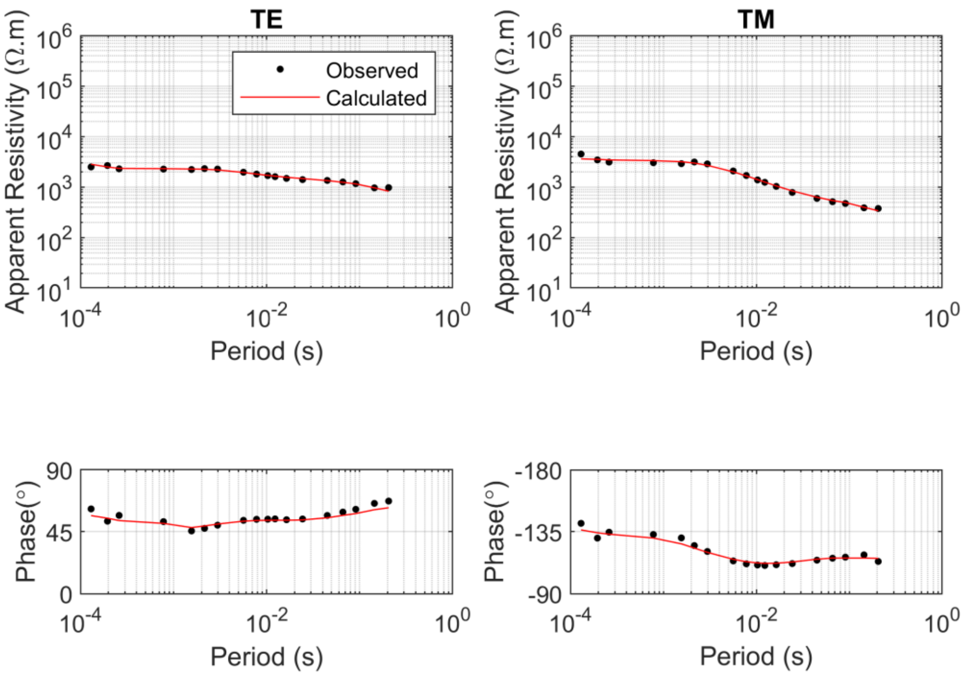

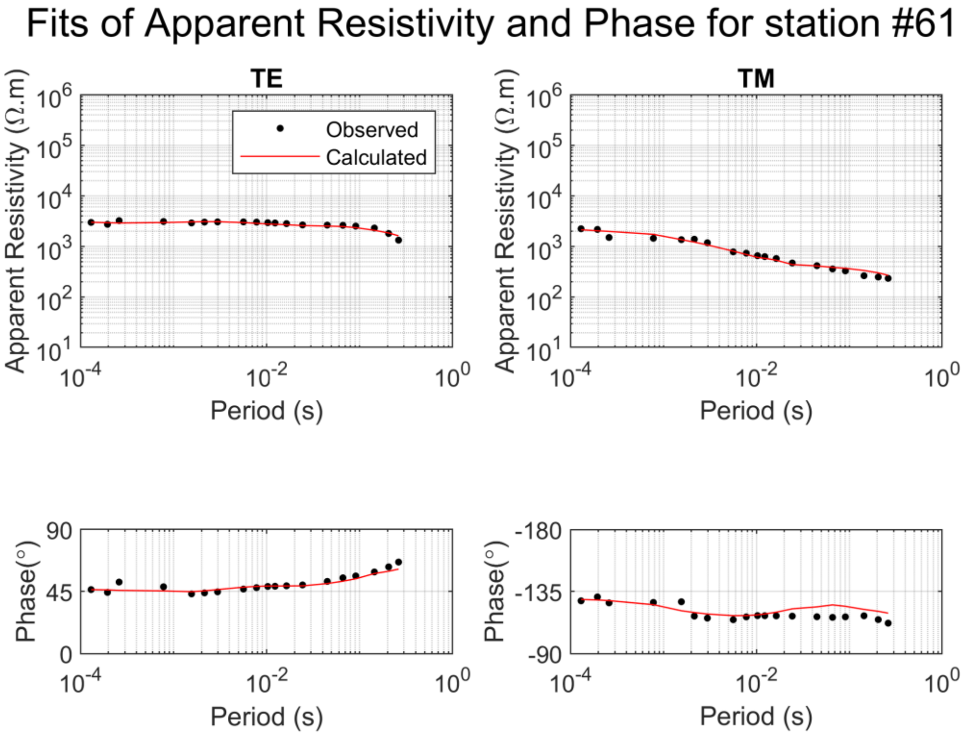
Fits of Apparent Resistivity and Phase for station #61
TE
TM
Observed
Calculated
Apparent Resistivity (Ω.m)
Phase(°)
Period (s)
10^6
10^5
10^4
10^3
10^2
10^1
10^-4
10^-2
10^0
90
45
0
-180
-135
-90

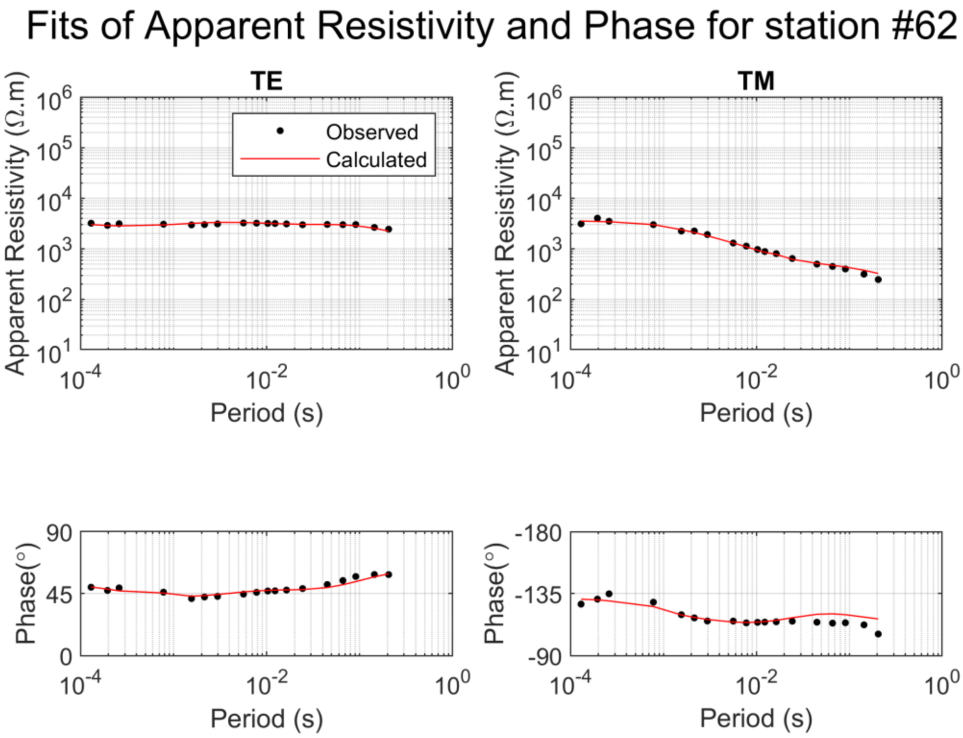
Fits of Apparent Resistivity and Phase for station #62
TE
TM
Observed
Calculated
Apparent Resistivity (Ω.m)
Phase(°)
Period (s)
10^6
10^5
10^4
10^3
10^2
10^1
10^-4
10^-2
10^0
90
45
0
-180
-135
-90

Fits of Apparent Resistivity and Phase for station #63

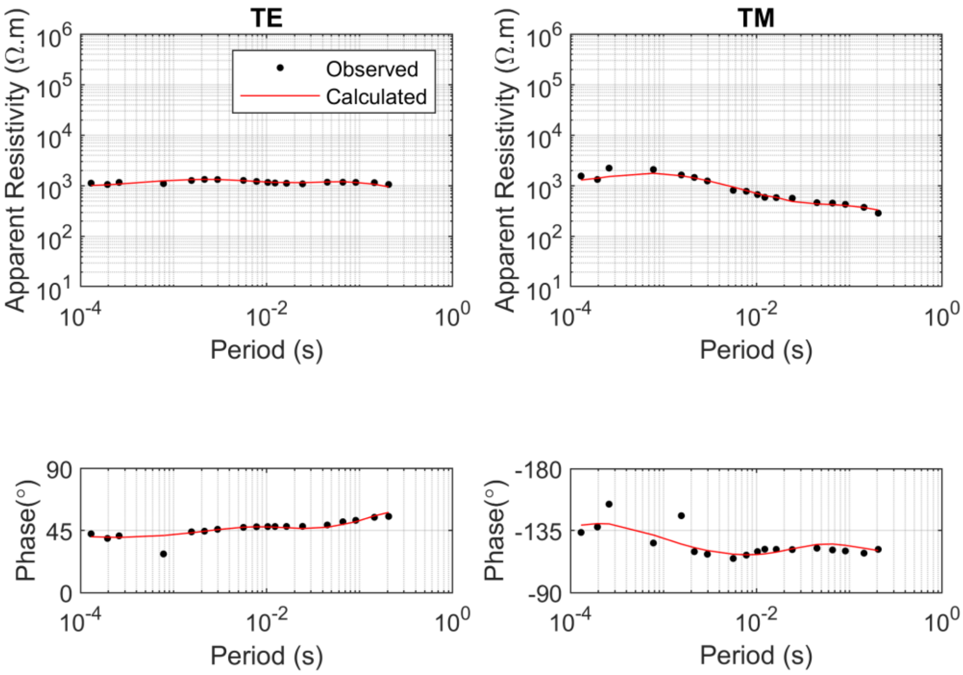

Fits of Apparent Resistivity and Phase for station #64

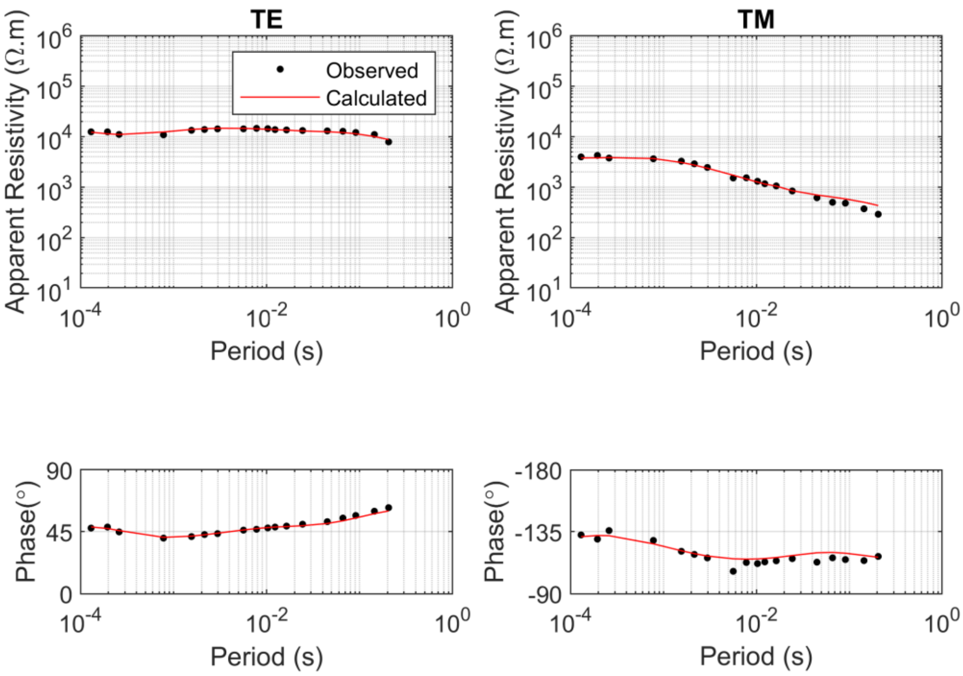

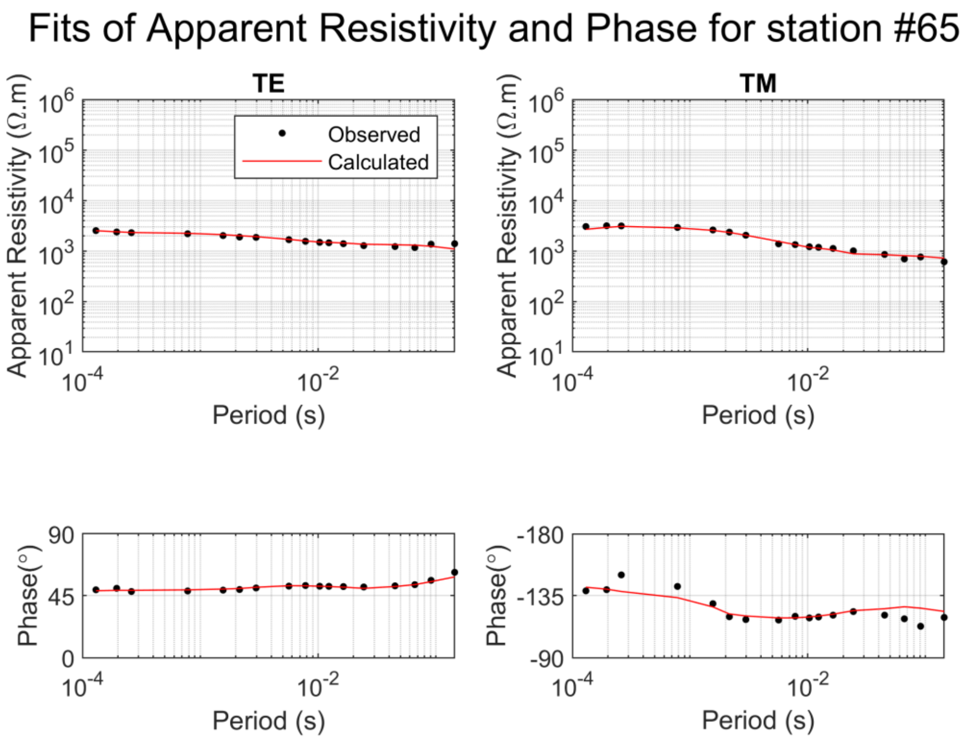
Fits of Apparent Resistivity and Phase for station #65
TE
TM
Observed
Calculated
Apparent Resistivity (Ω.m)
Phase(°)
Period (s)

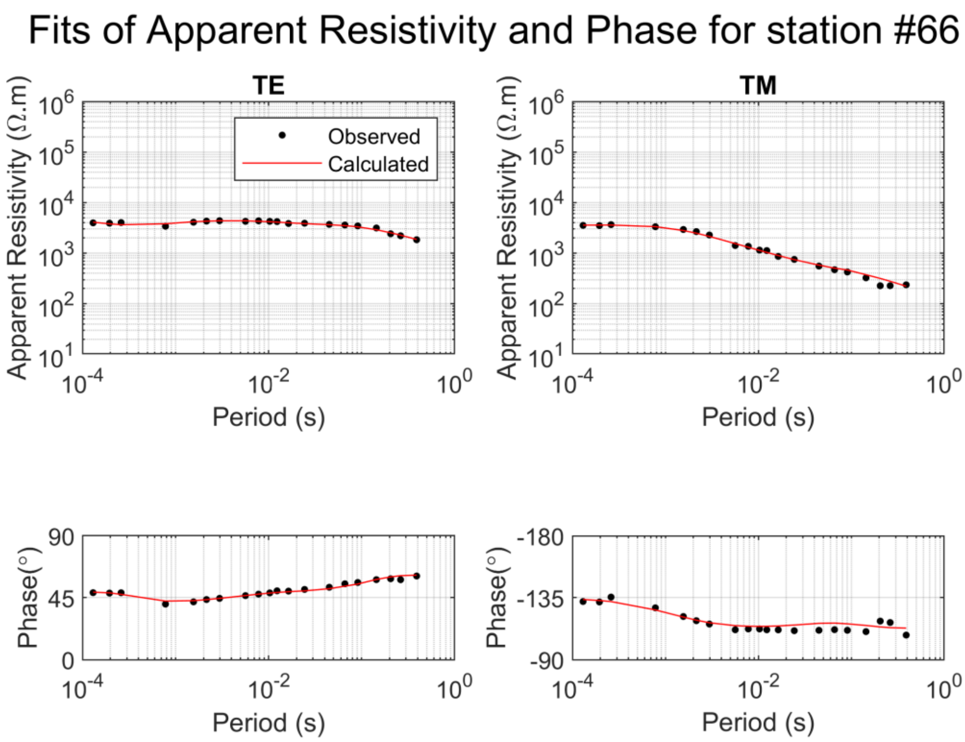
Fits of Apparent Resistivity and Phase for station #66
TE
TM
Observed
Calculated
Apparent Resistivity (Ω.m)
Phase(°)
Period (s)

Fits of Apparent Resistivity and Phase for station #67

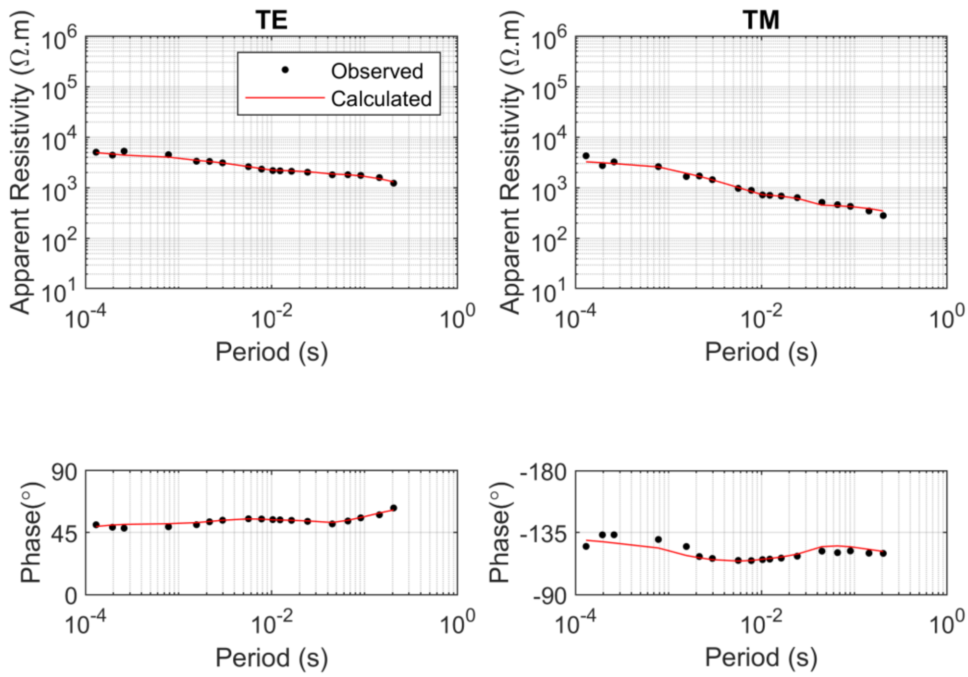

Fits of Apparent Resistivity and Phase for station #68

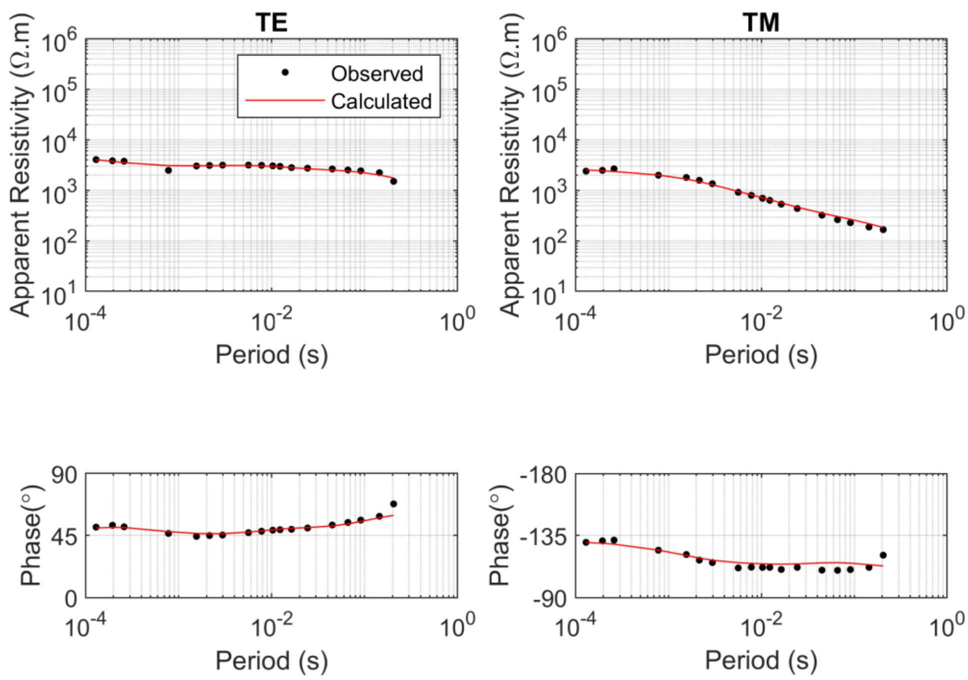

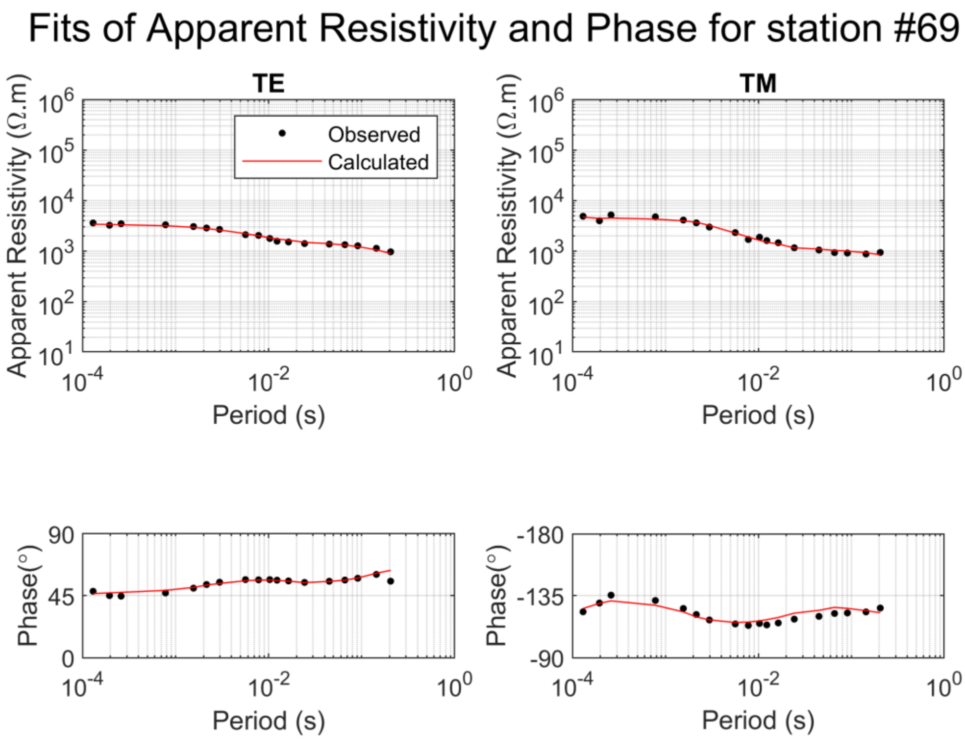
Fits of Apparent Resistivity and Phase for station #69
TE
TM
Observed
Calculated
Apparent Resistivity (Ω.m)
Period (s)
Phase(°)

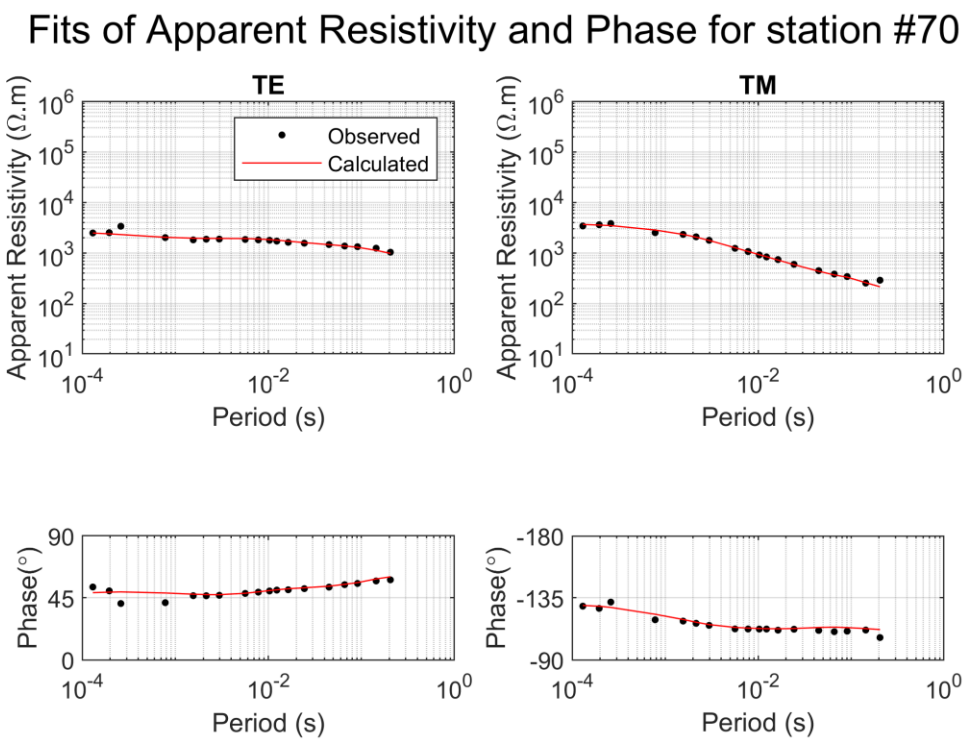
Fits of Apparent Resistivity and Phase for station #70
TE
TM
Observed
Calculated
Apparent Resistivity (Ω.m)
Period (s)
Phase(°)

Fits of Apparent Resistivity and Phase for station #71

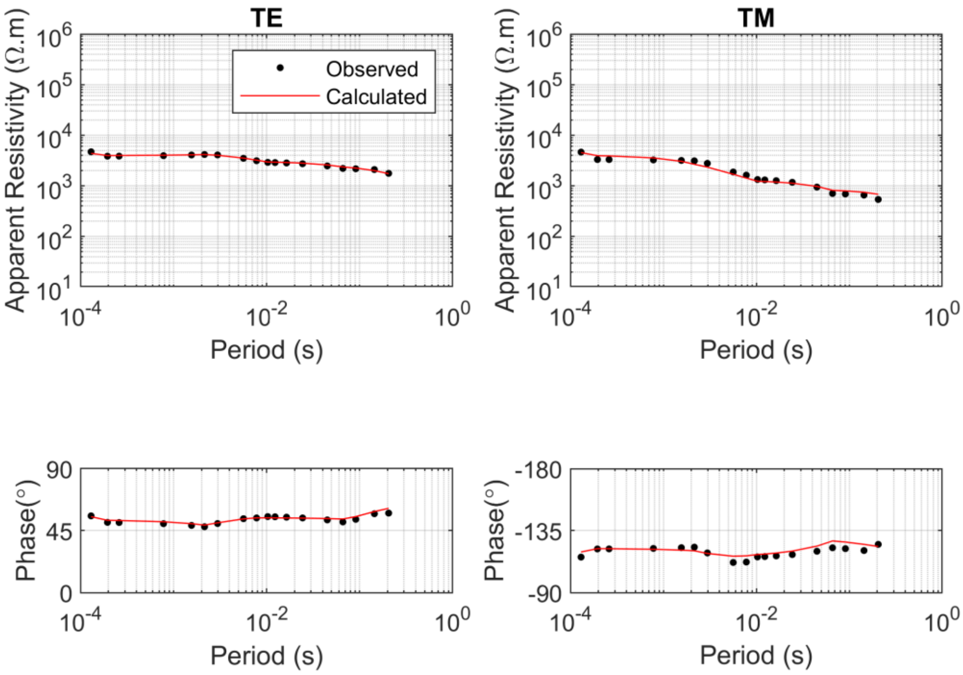

Fits of Apparent Resistivity and Phase for station #72

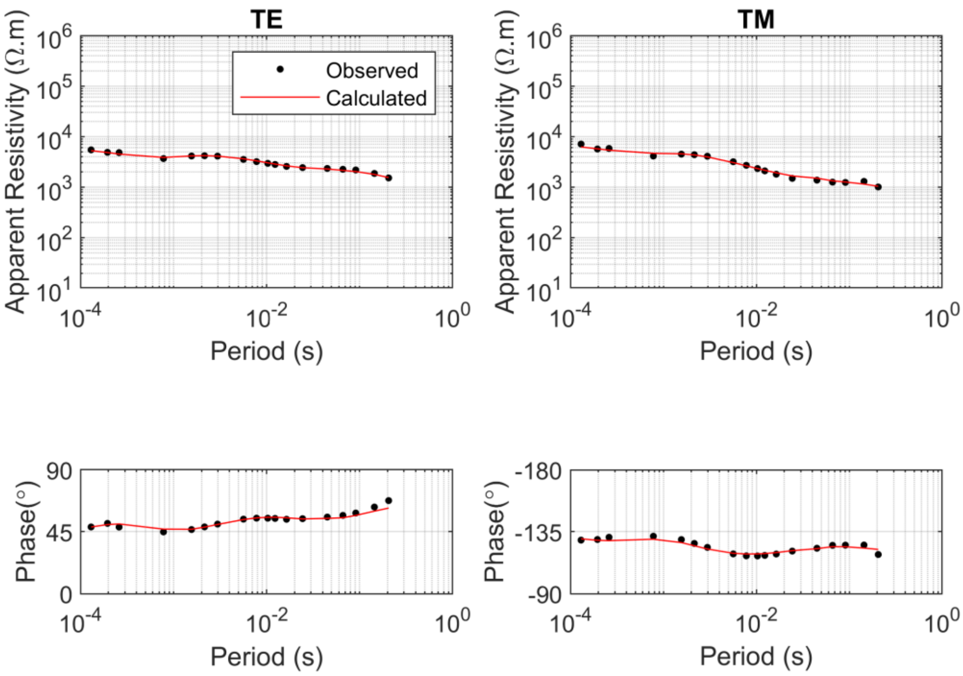

Fits of Apparent Resistivity and Phase for station #73

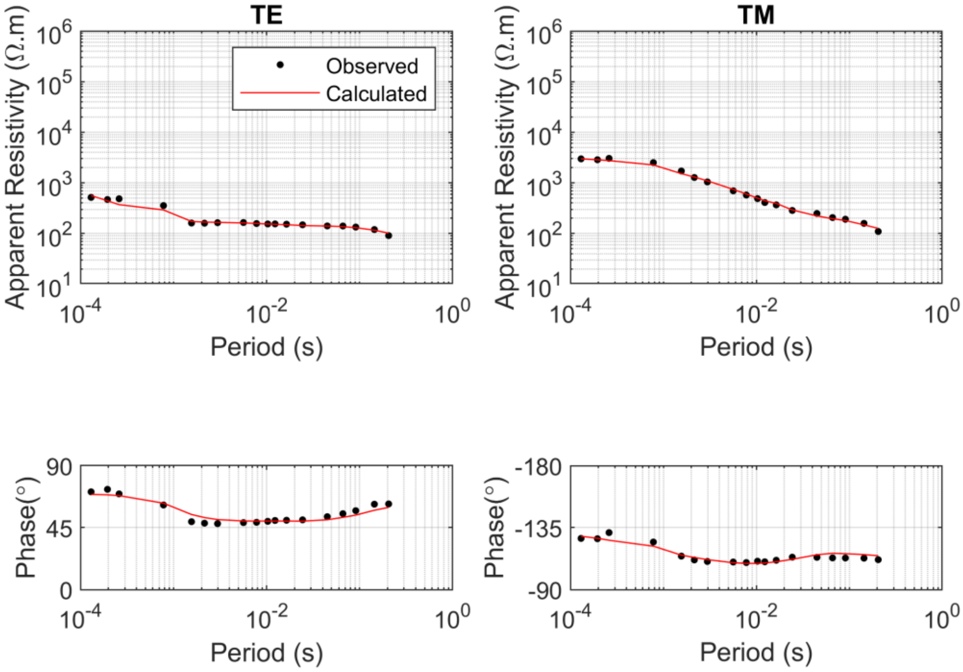

Fits of Apparent Resistivity and Phase for station #74

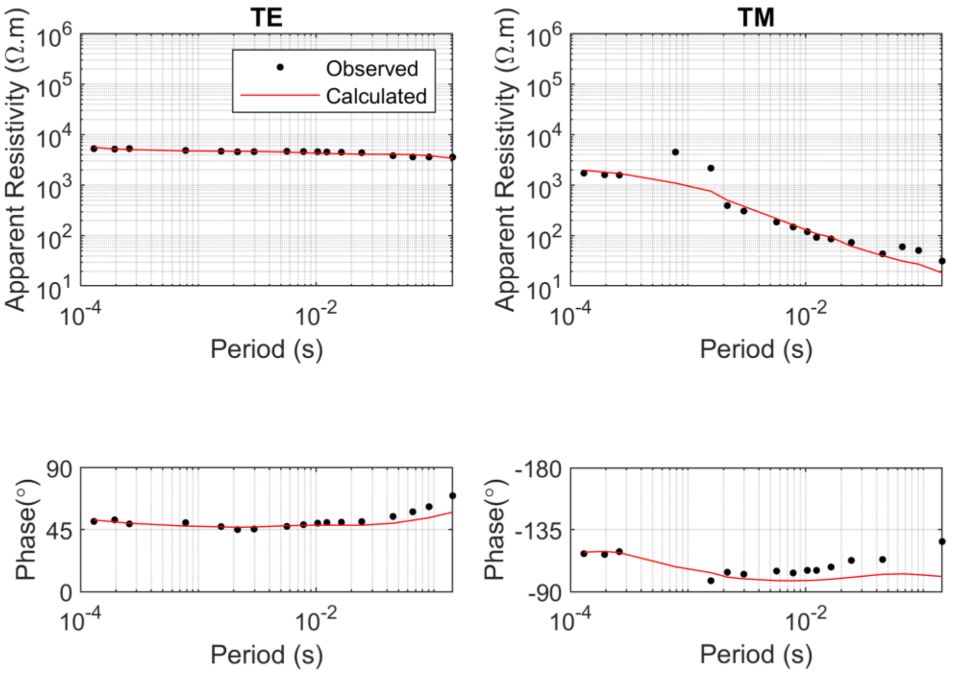

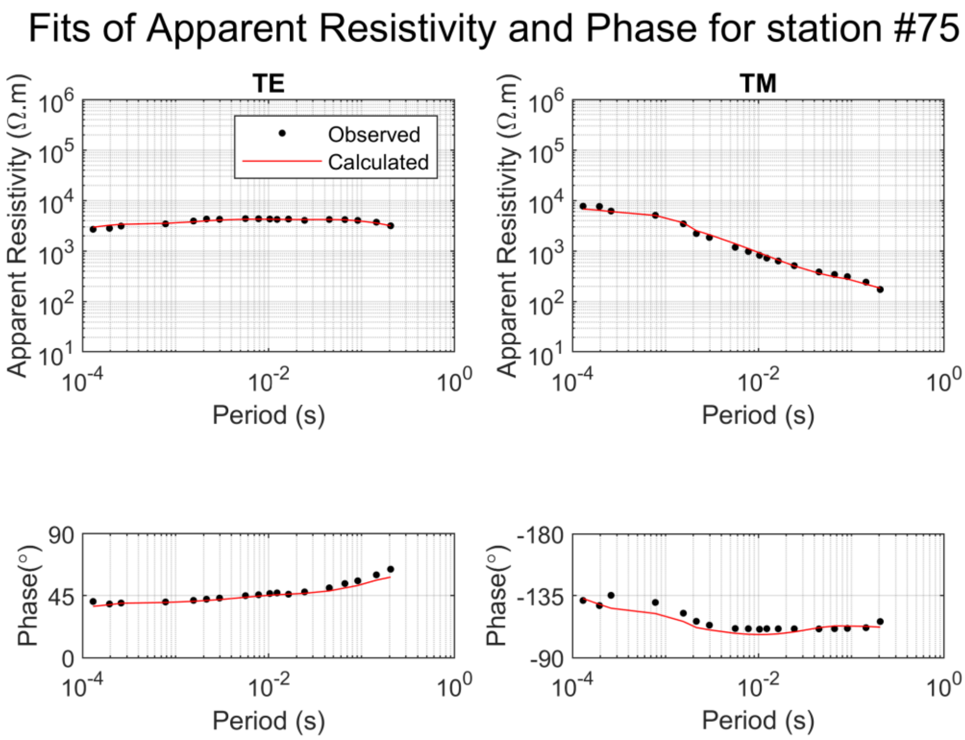
Fits of Apparent Resistivity and Phase for station #75
TE
TM
Observed
Calculated
Apparent Resistivity (Ω.m)
Phase(°)
Period (s)

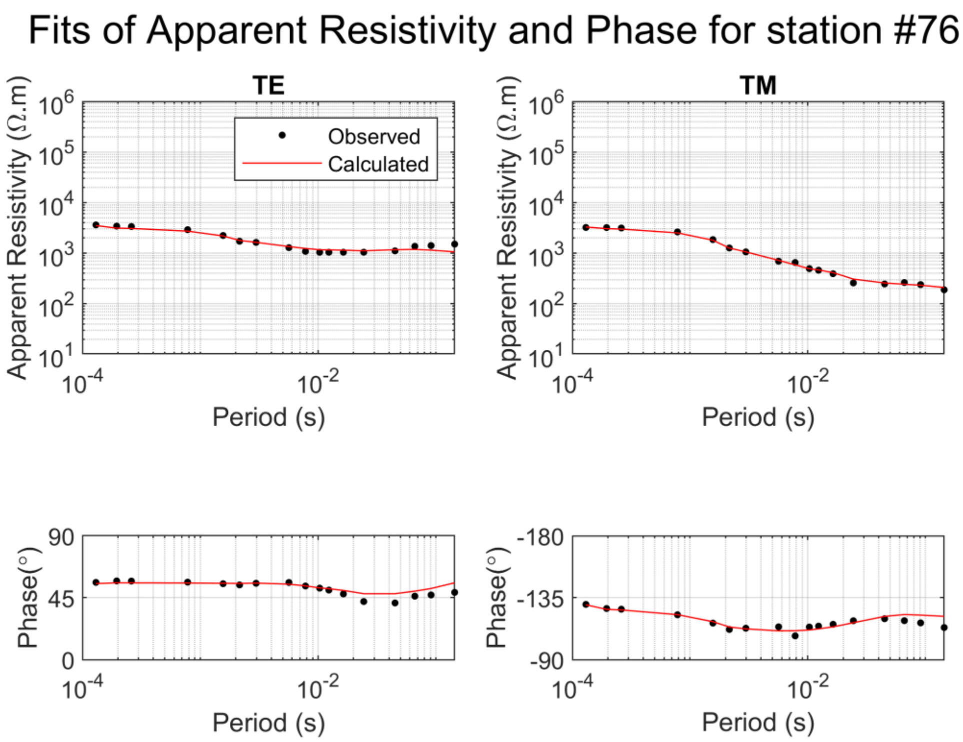
Fits of Apparent Resistivity and Phase for station #76
TE
TM
Observed
Calculated
Apparent Resistivity (Ω.m)
Phase(°)
Period (s)

Fits of Apparent Resistivity and Phase for station #77

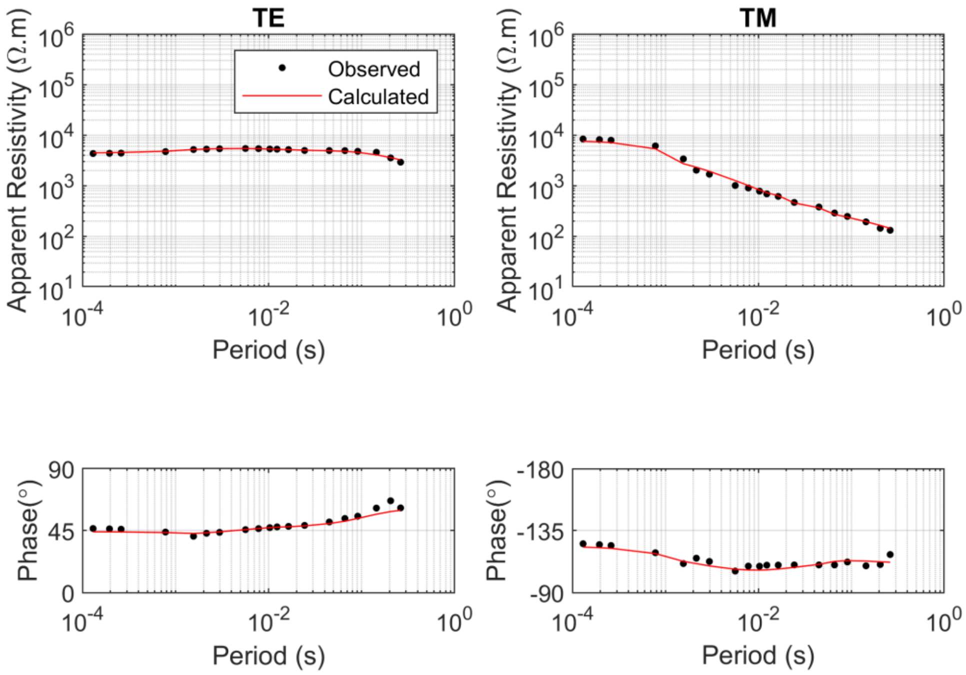

Fits of Apparent Resistivity and Phase for station #78

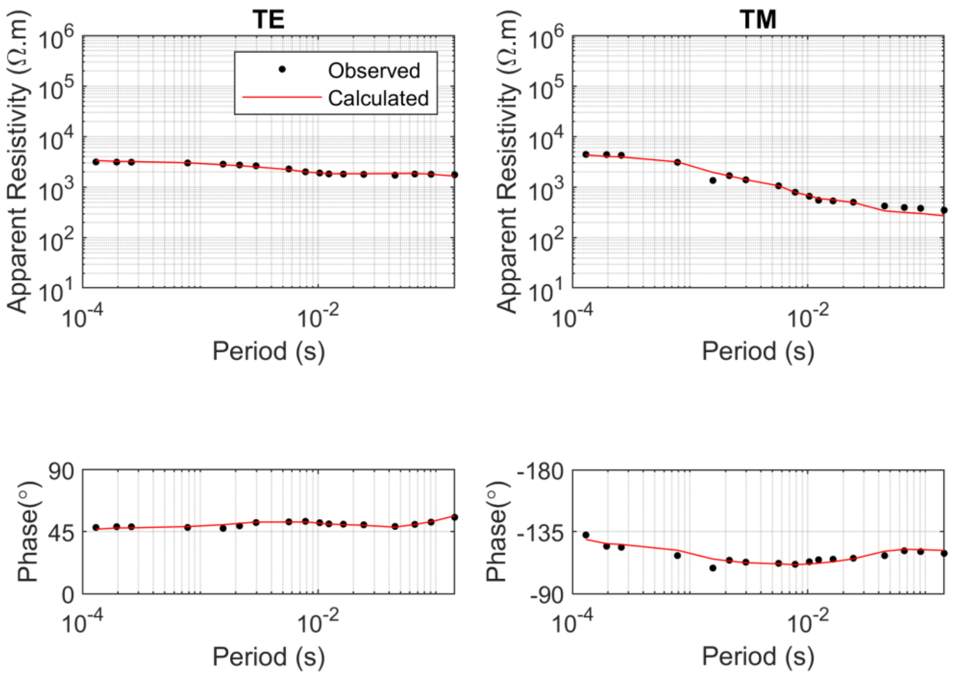

Fits of Apparent Resistivity and Phase for station #79

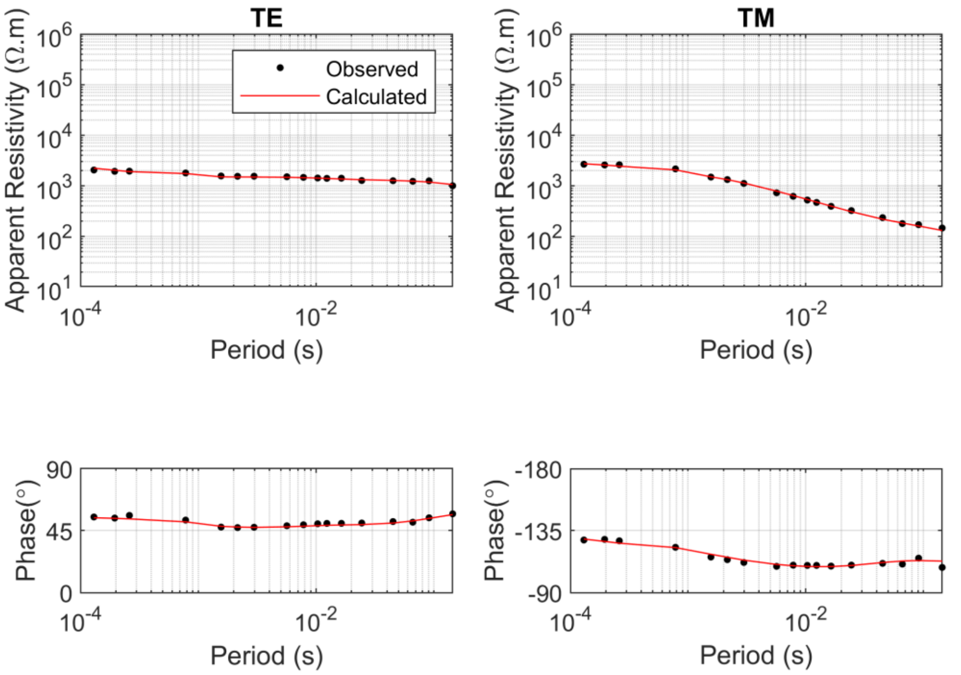

Fits of Apparent Resistivity and Phase for station #80

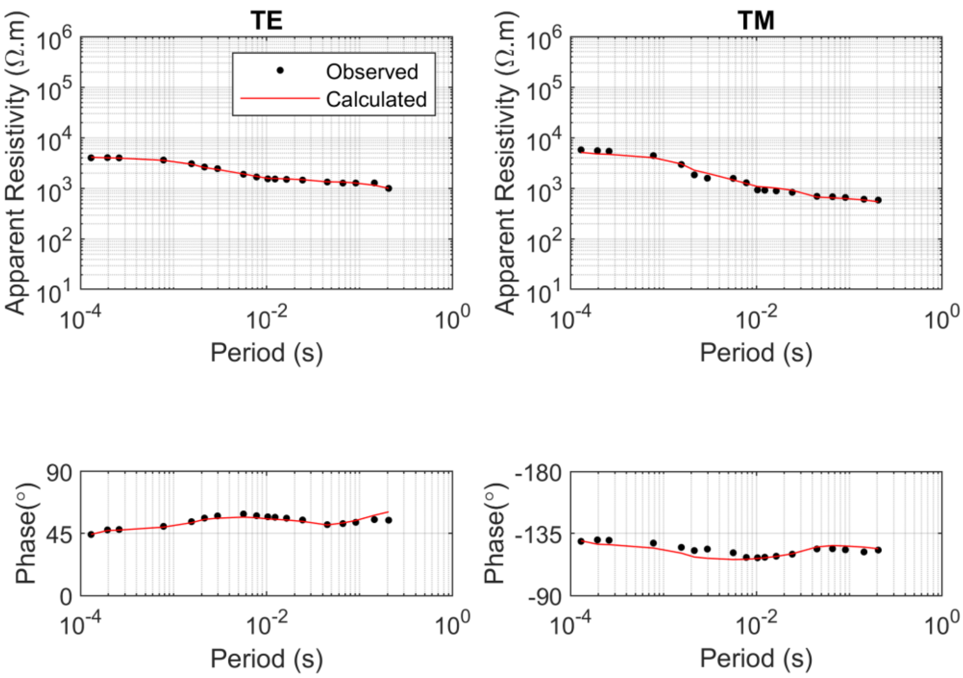

Fits of Apparent Resistivity and Phase for station #81

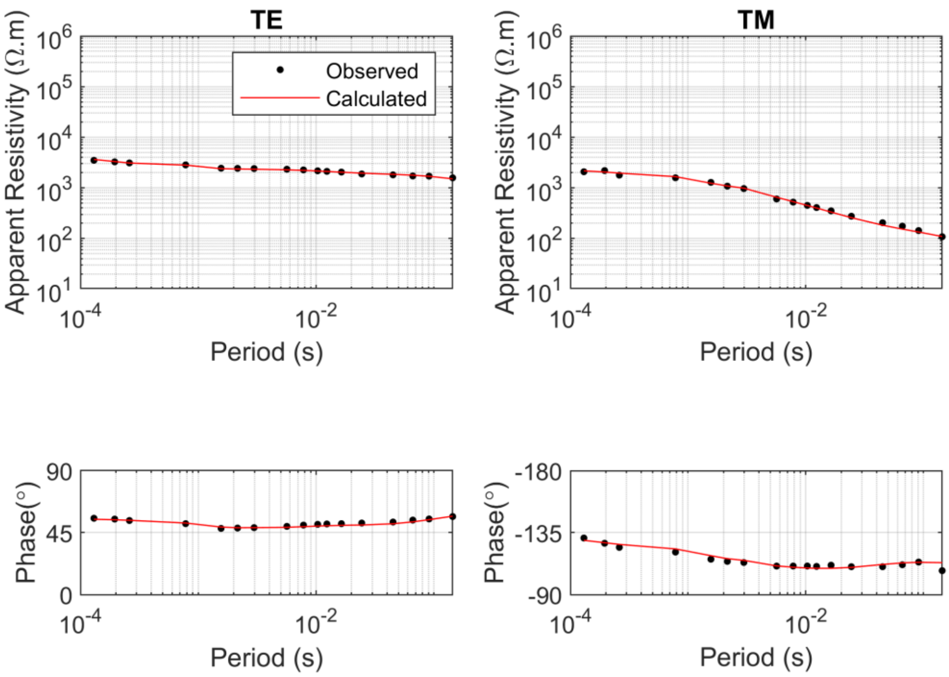

Fits of Apparent Resistivity and Phase for station #82

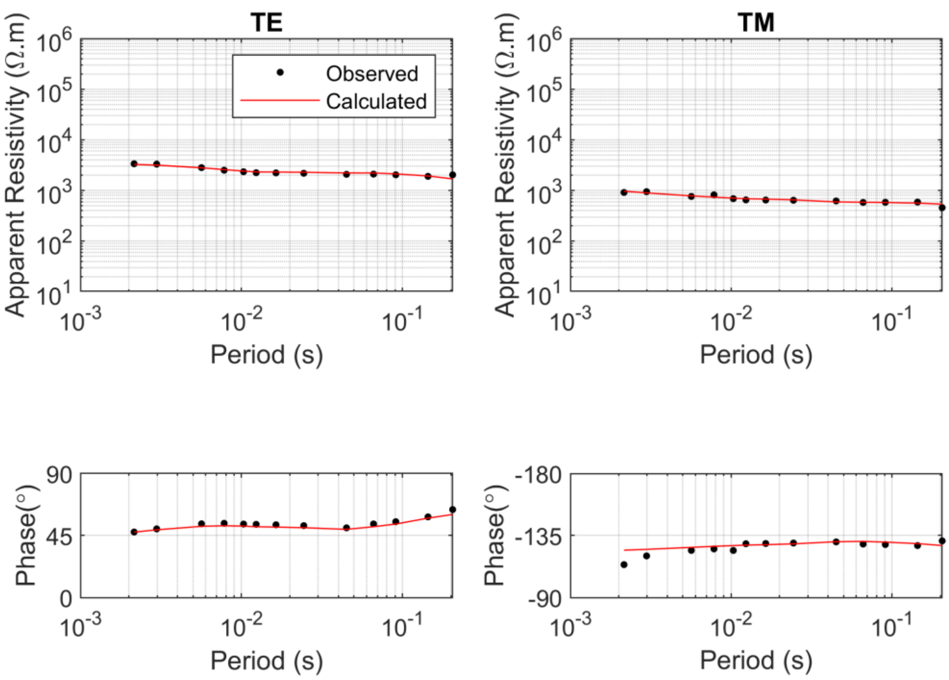

Fits of Apparent Resistivity and Phase for station #83

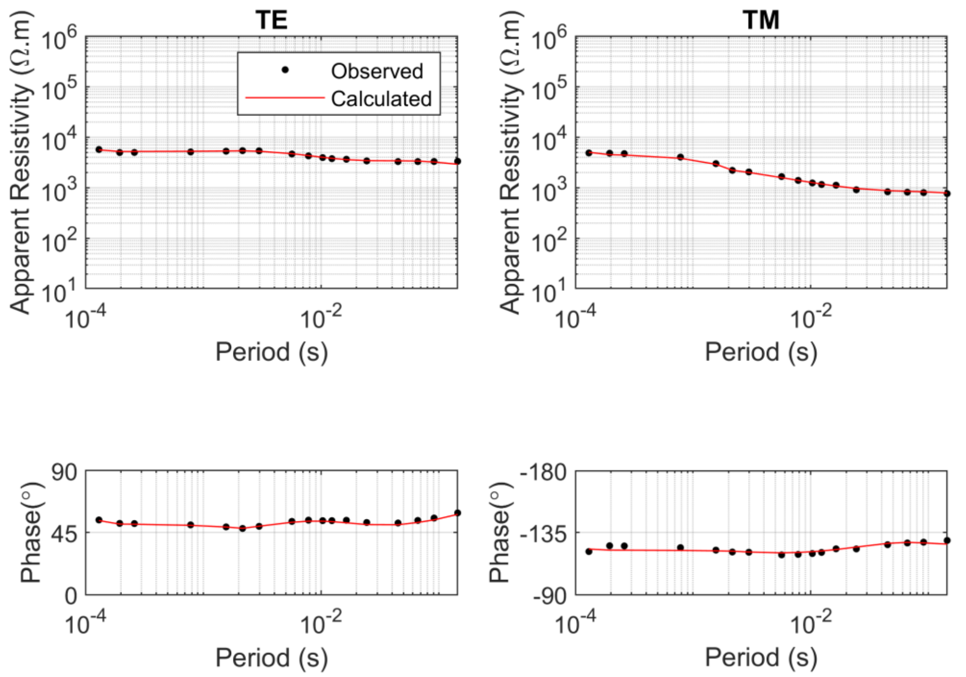

Fits of Apparent Resistivity and Phase for station #84

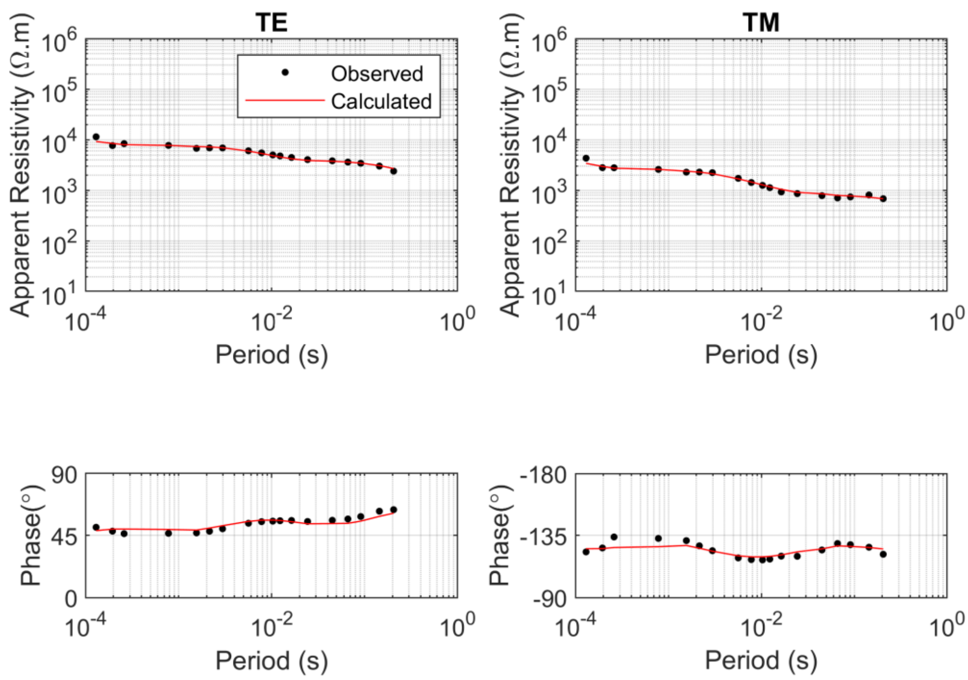

Fits of Apparent Resistivity and Phase for station #85

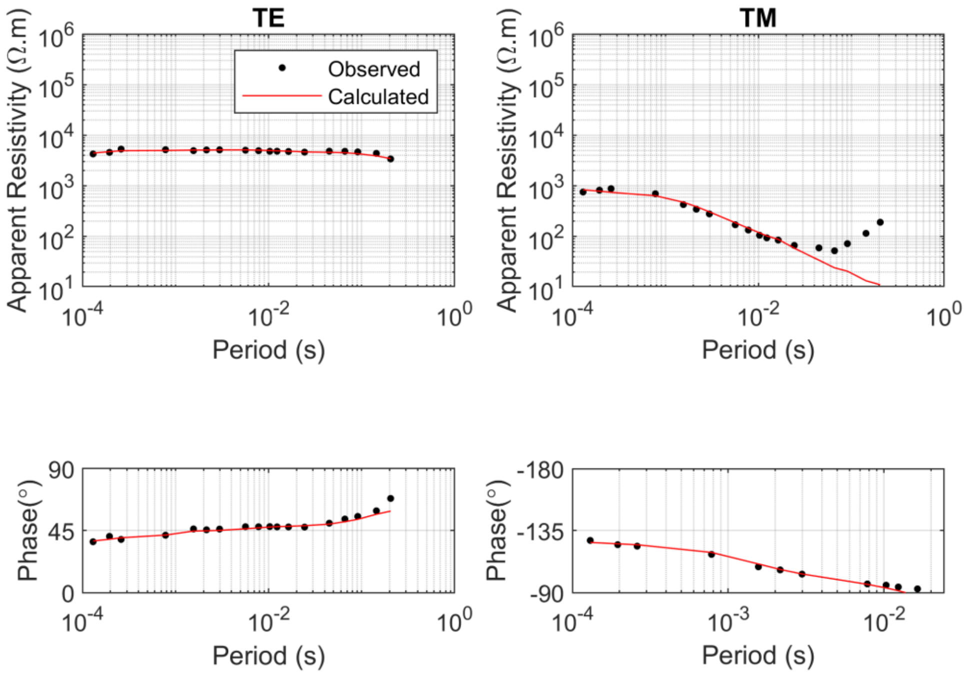

Fits of Apparent Resistivity and Phase for station #86

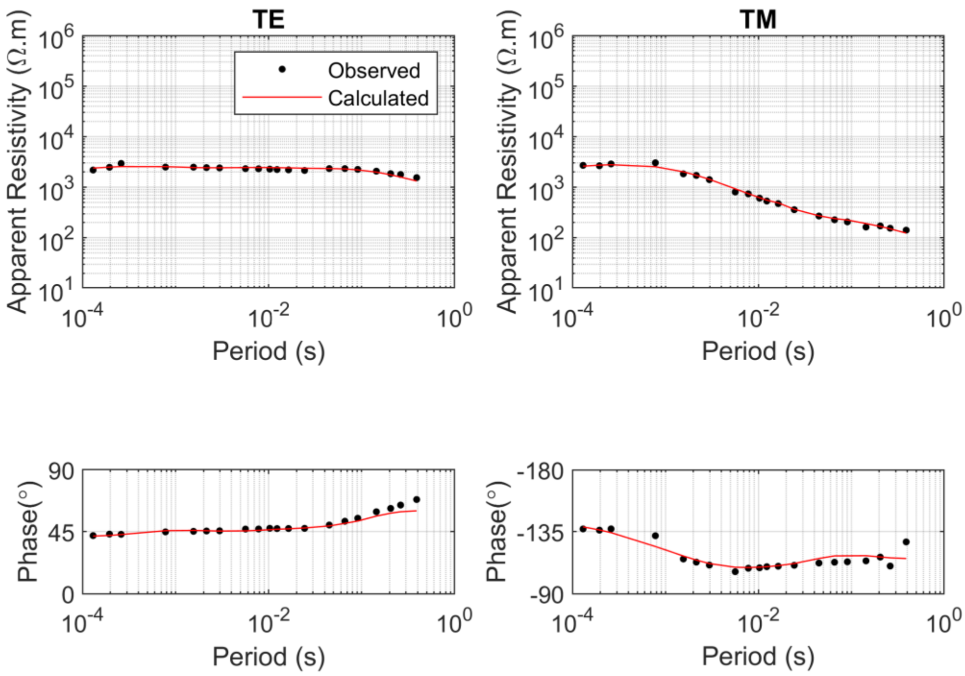

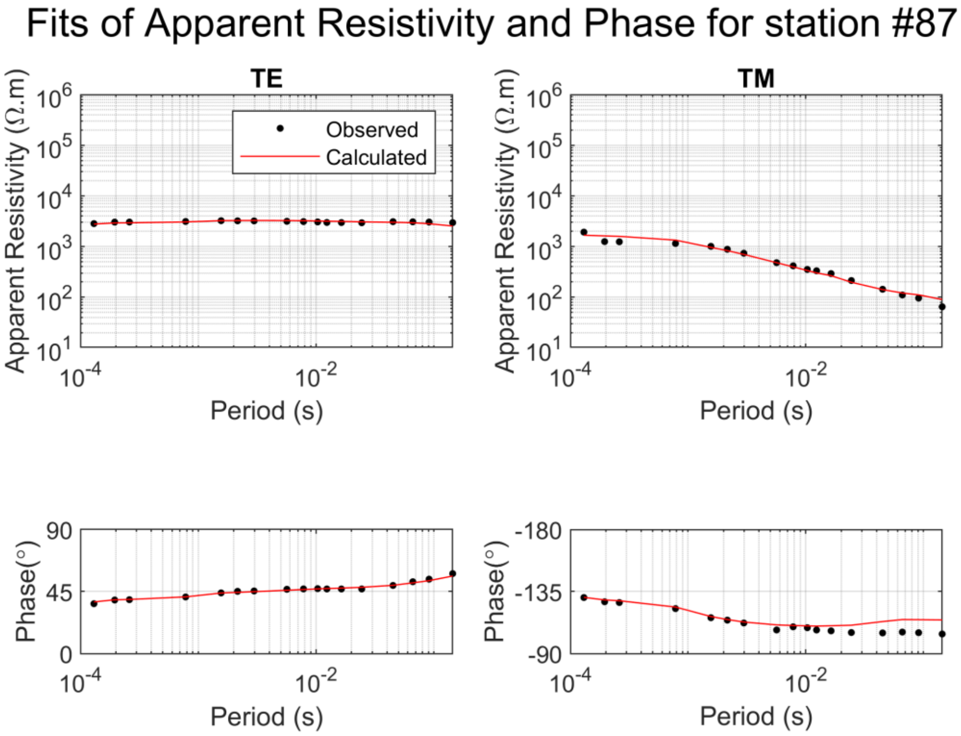
Fits of Apparent Resistivity and Phase for station #87
TE
TM
Observed
Calculated
Apparent Resistivity (Ω.m)
Period (s)
Phase(°)

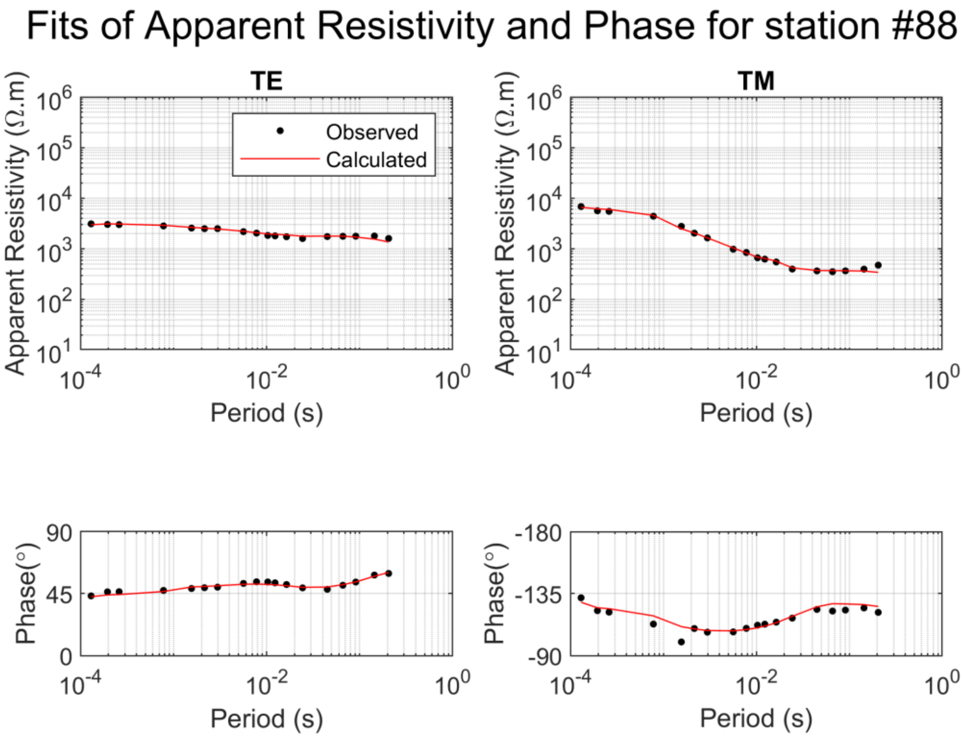
Fits of Apparent Resistivity and Phase for station #88
TE
TM
Observed
Calculated
Apparent Resistivity (Ω.m)
Period (s)
Phase(°)

Fits of Apparent Resistivity and Phase for station #89

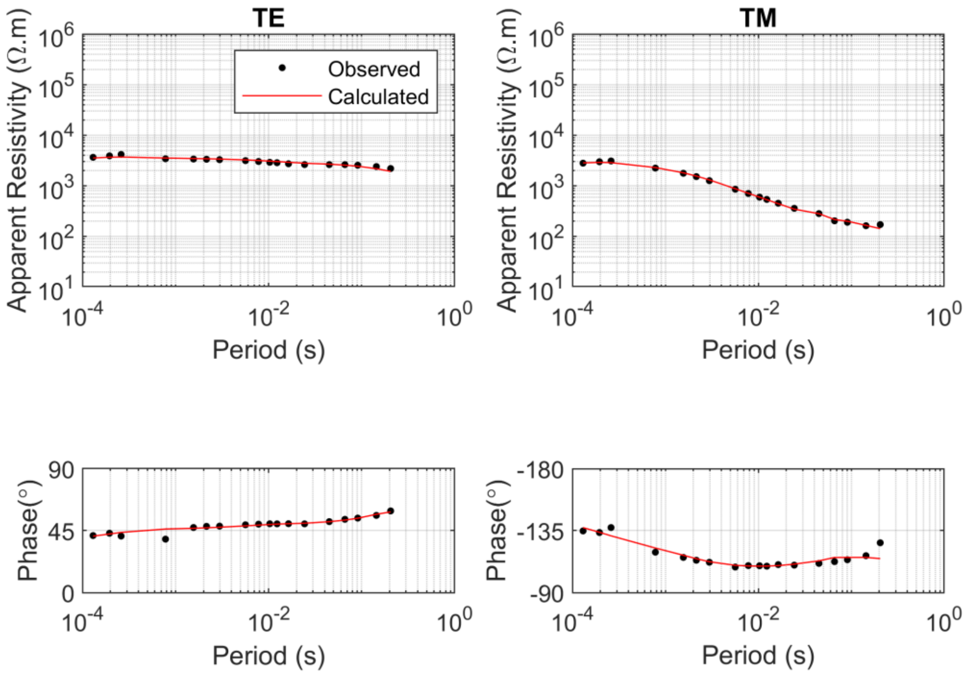

Fits of Apparent Resistivity and Phase for station #90

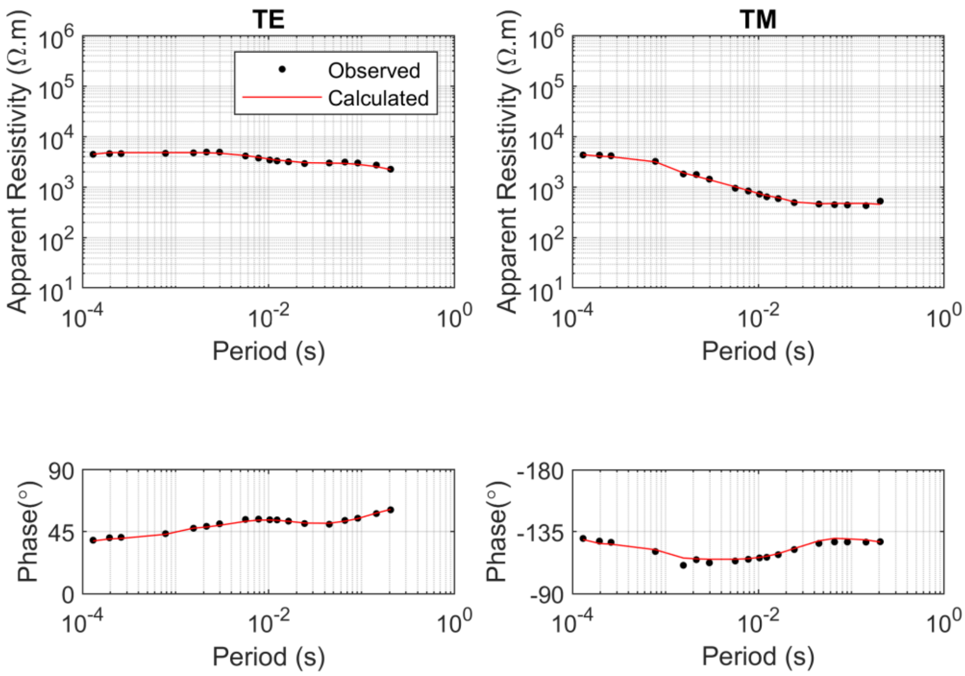

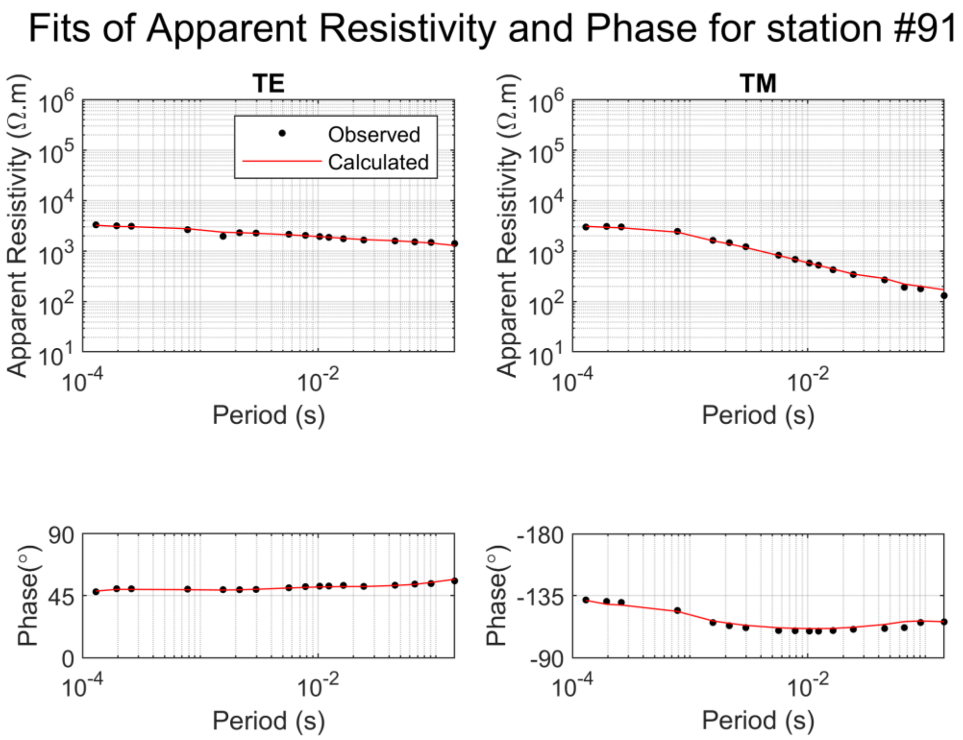
Fits of Apparent Resistivity and Phase for station #91
TE
TM
Observed
Calculated
Apparent Resistivity (Ω.m)
Phase(°)
Period (s)
10^6
10^5
10^4
10^3
10^2
10^1
10^-4
10^-2
90
45
0
-180
-135
-90

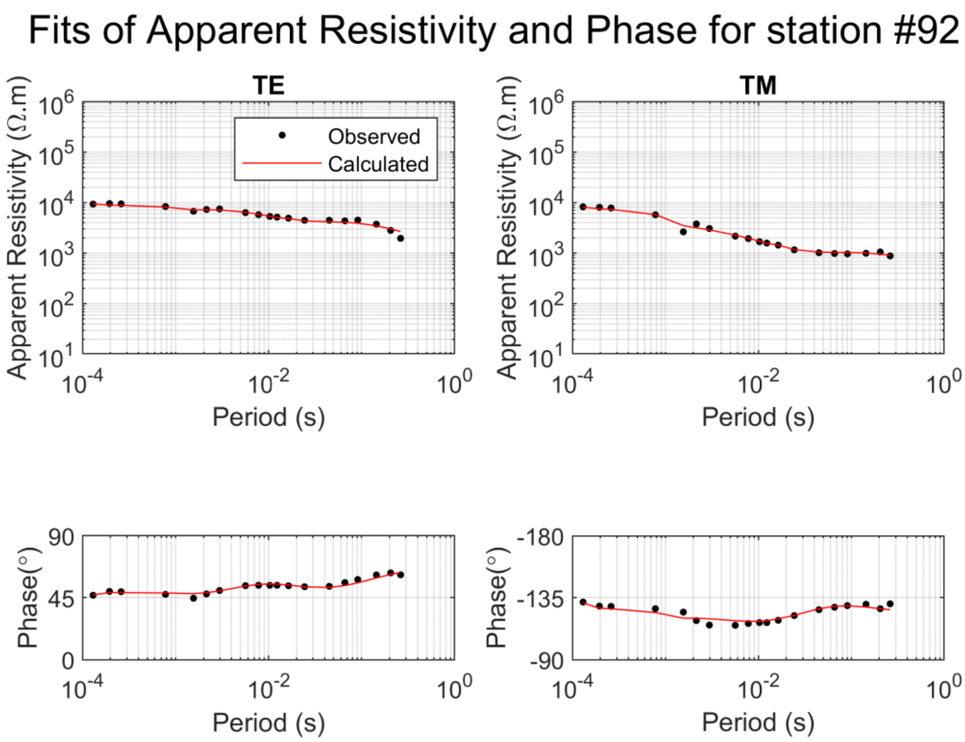
Fits of Apparent Resistivity and Phase for station #92
TE
TM
Observed
Calculated
Apparent Resistivity (Ω.m)
Phase(°)
Period (s)
10^6
10^5
10^4
10^3
10^2
10^1
10^-4
10^-2
10^0
90
45
0
-180
-135
-90

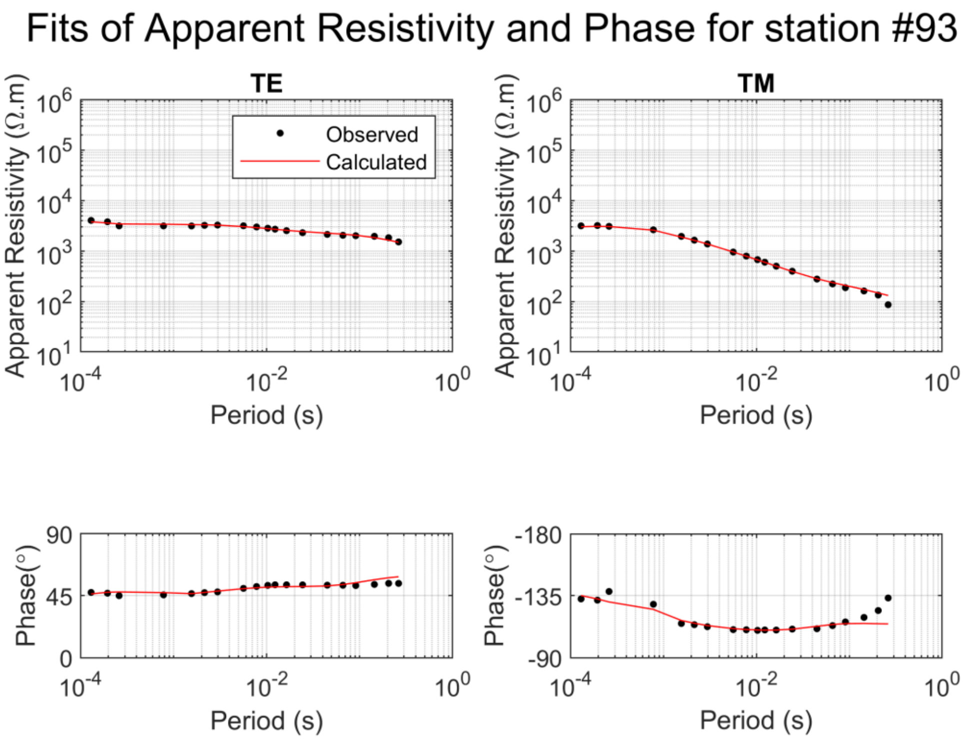
Fits of Apparent Resistivity and Phase for station #93
TE
TM
Observed
Calculated
Apparent Resistivity (Ω.m)
Phase(°)
Period (s)

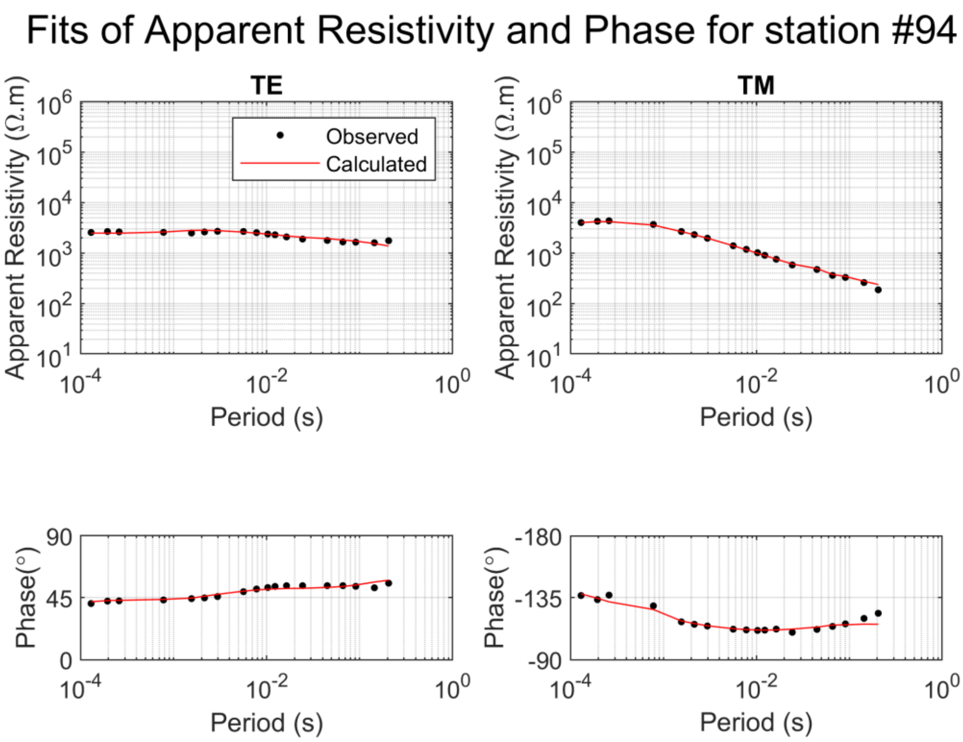
Fits of Apparent Resistivity and Phase for station #94
TE
TM
Observed
Calculated
Apparent Resistivity (Ω.m)
Phase(°)
Period (s)

Fits of Apparent Resistivity and Phase for station #95

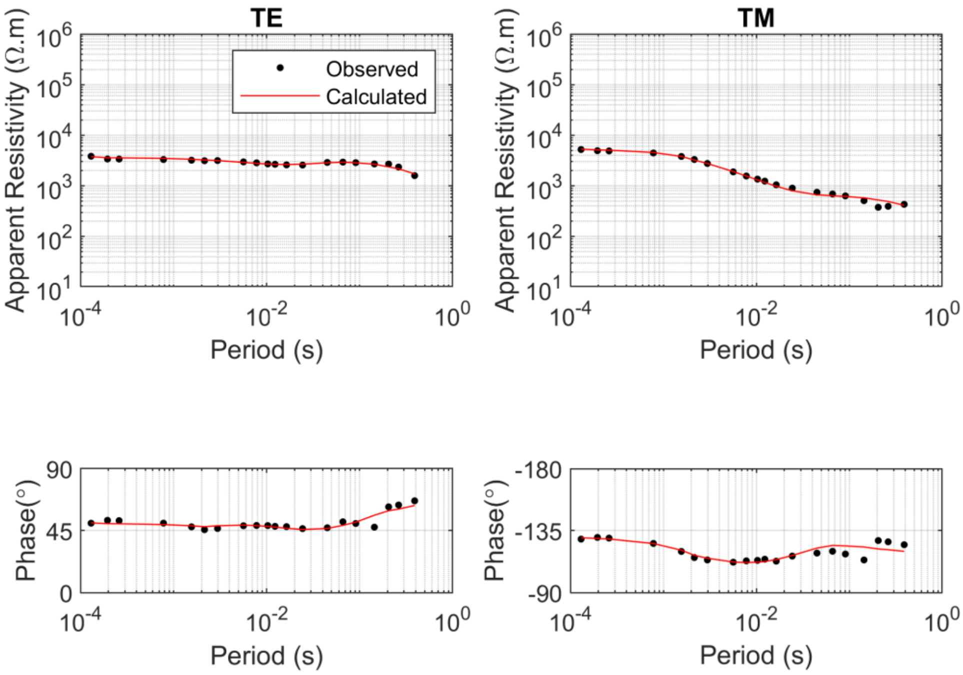

Fits of Apparent Resistivity and Phase for station #96

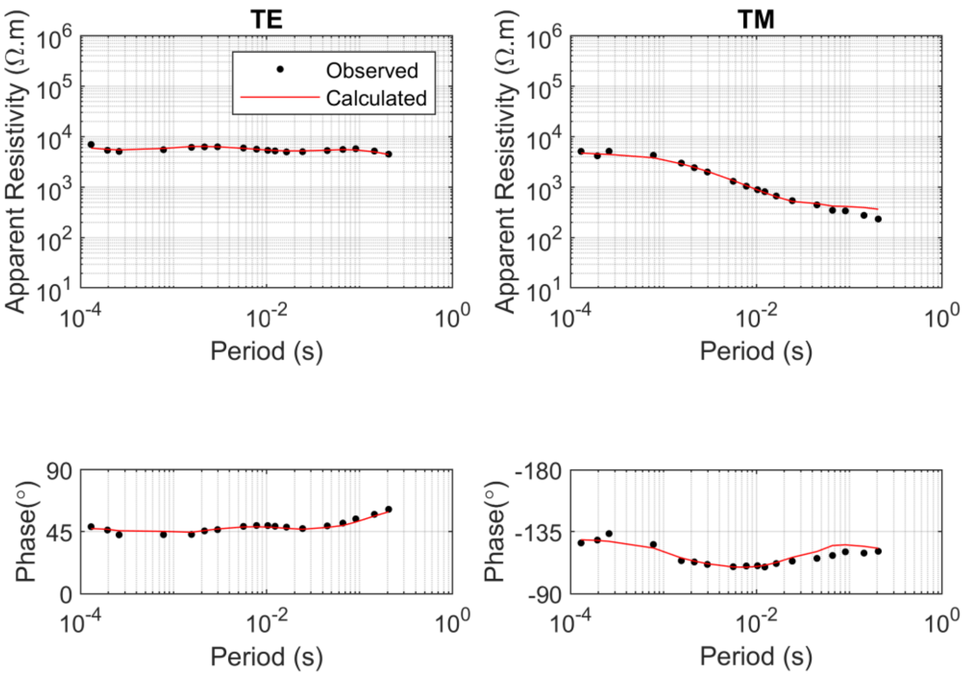

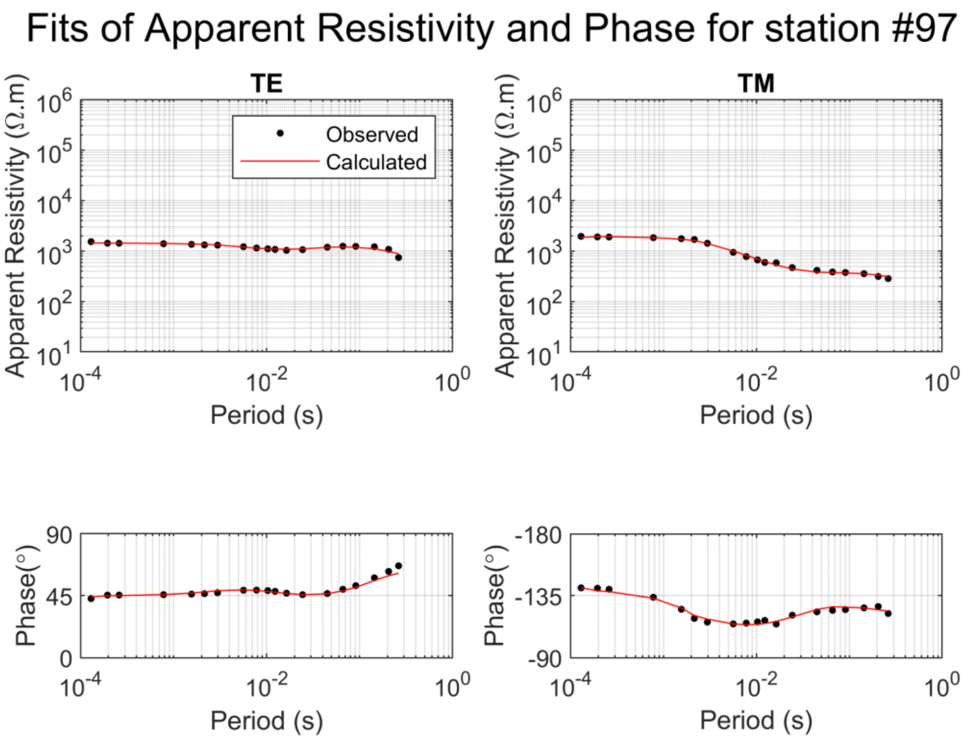
Fits of Apparent Resistivity and Phase for station #97
TE
TM
Observed
Calculated
Apparent Resistivity (Ω.m)
Phase(°)
Period (s)

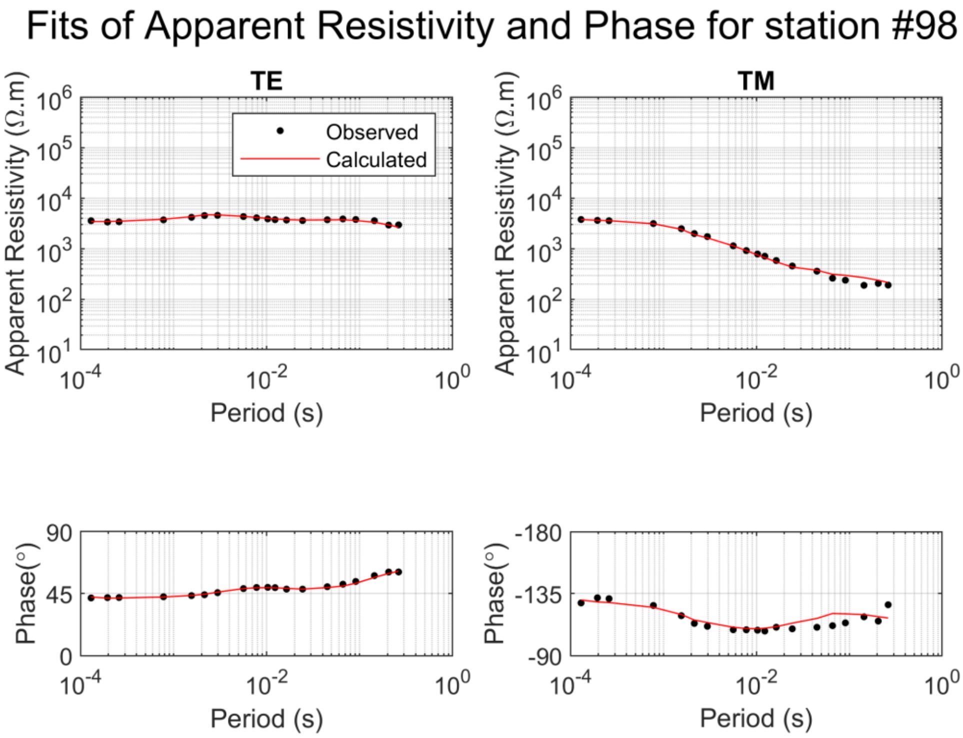
Fits of Apparent Resistivity and Phase for station #98
TE
TM
Observed
Calculated
Apparent Resistivity (Ω.m)
Phase(°)
Period (s)

Fits of Apparent Resistivity and Phase for station #99

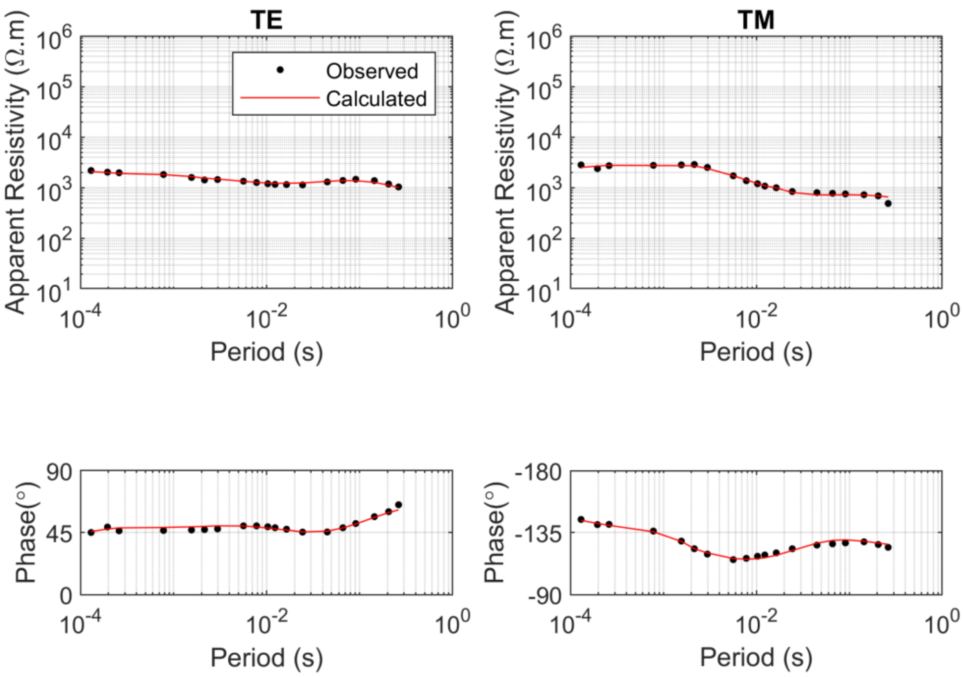

Fits of Apparent Resistivity and Phase for station #100

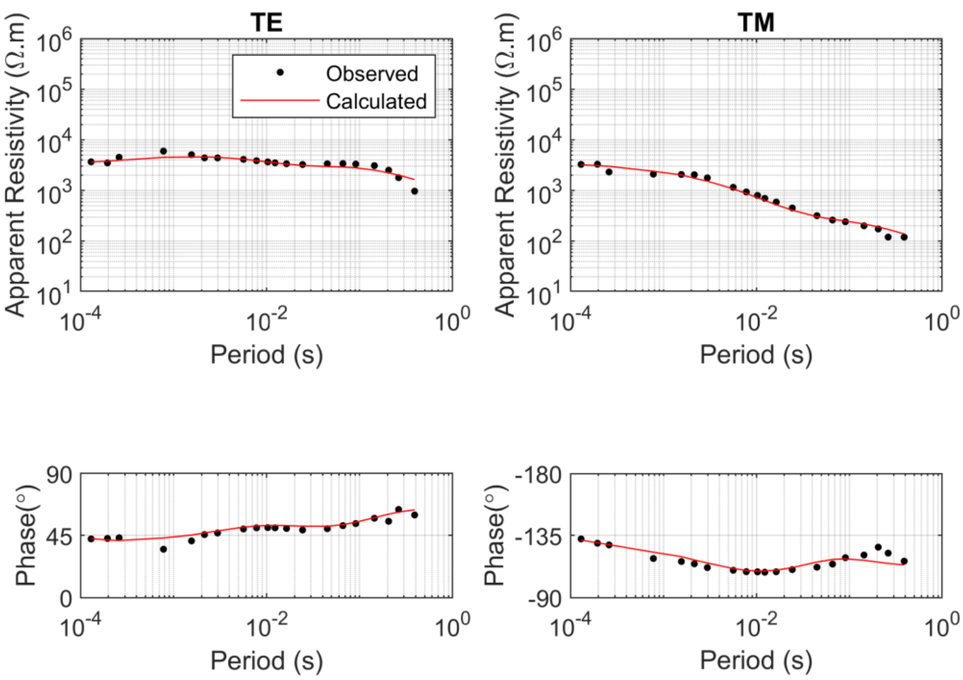

Fits of Apparent Resistivity and Phase for station #101

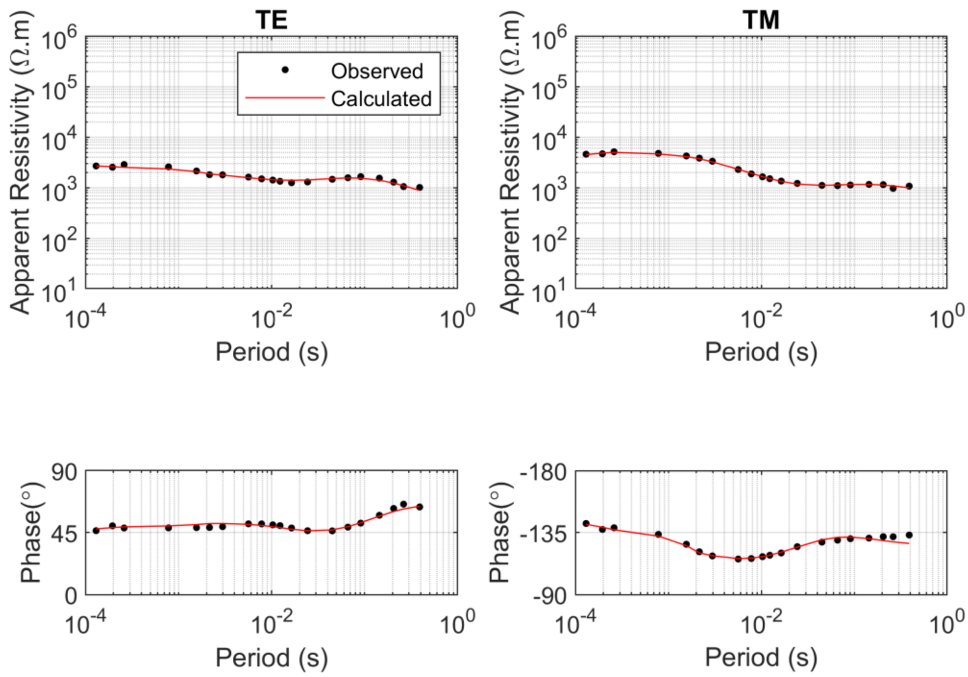

Fits of Apparent Resistivity and Phase for station #102

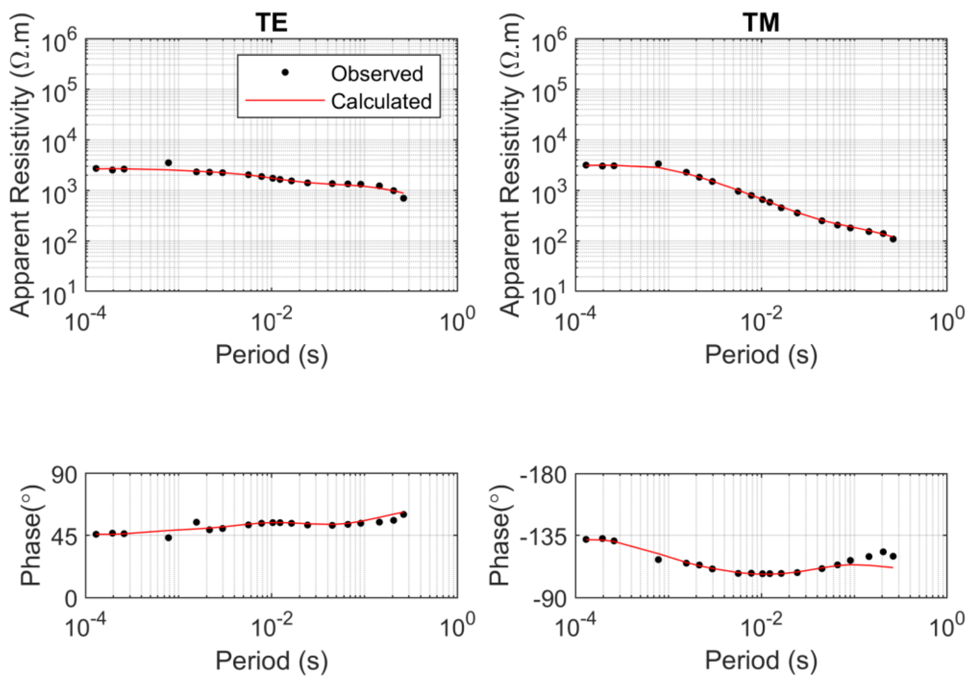

Fits of Apparent Resistivity and Phase for station #103

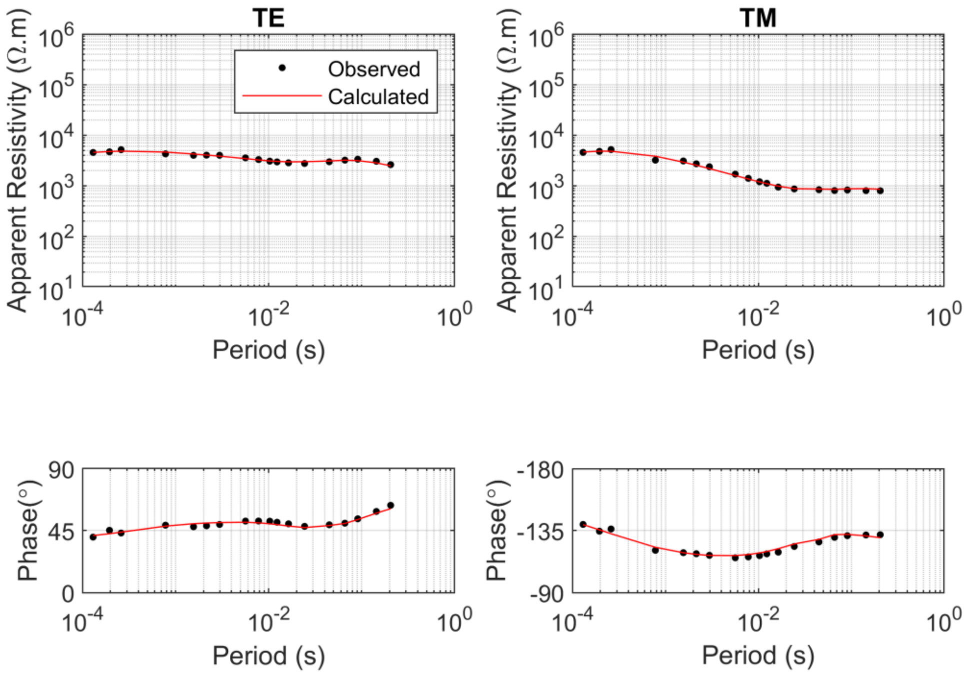

Fits of Apparent Resistivity and Phase for station #104

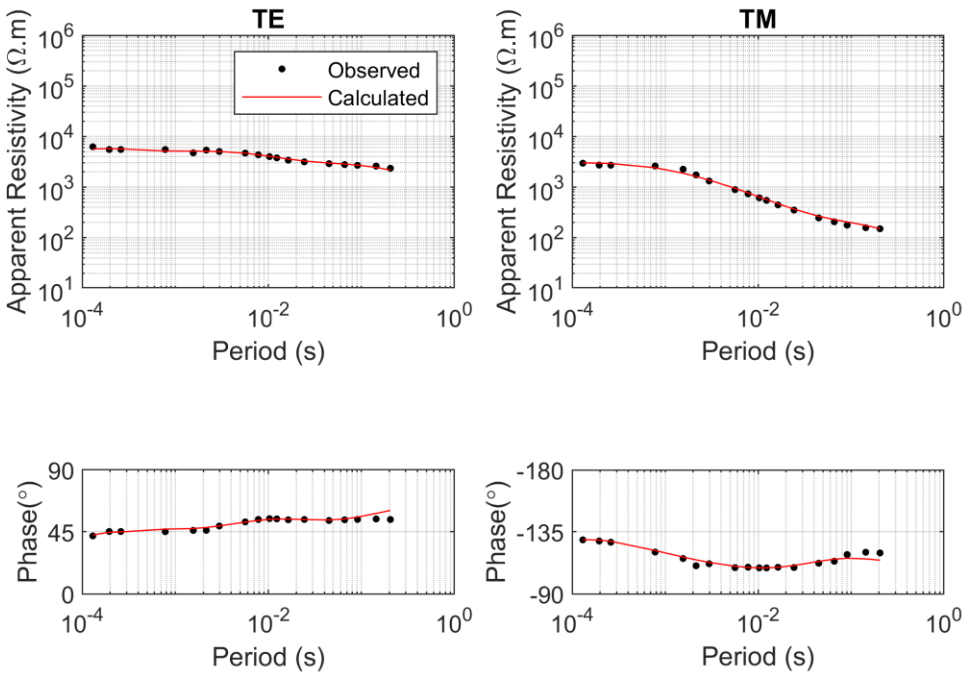

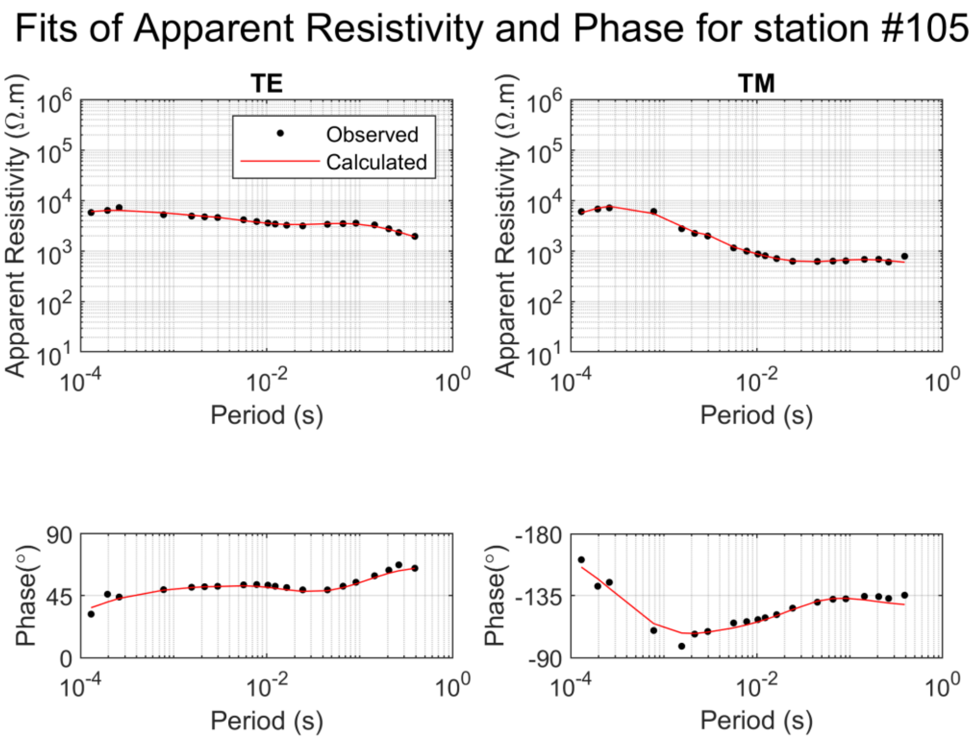
Fits of Apparent Resistivity and Phase for station #105
TE
TM
Observed
Calculated
Apparent Resistivity (Ω.m)
Phase(°)
Period (s)
10^6
10^5
10^4
10^3
10^2
10^1
10^-4
10^-2
10^0
90
45
0
-180
-135
-90

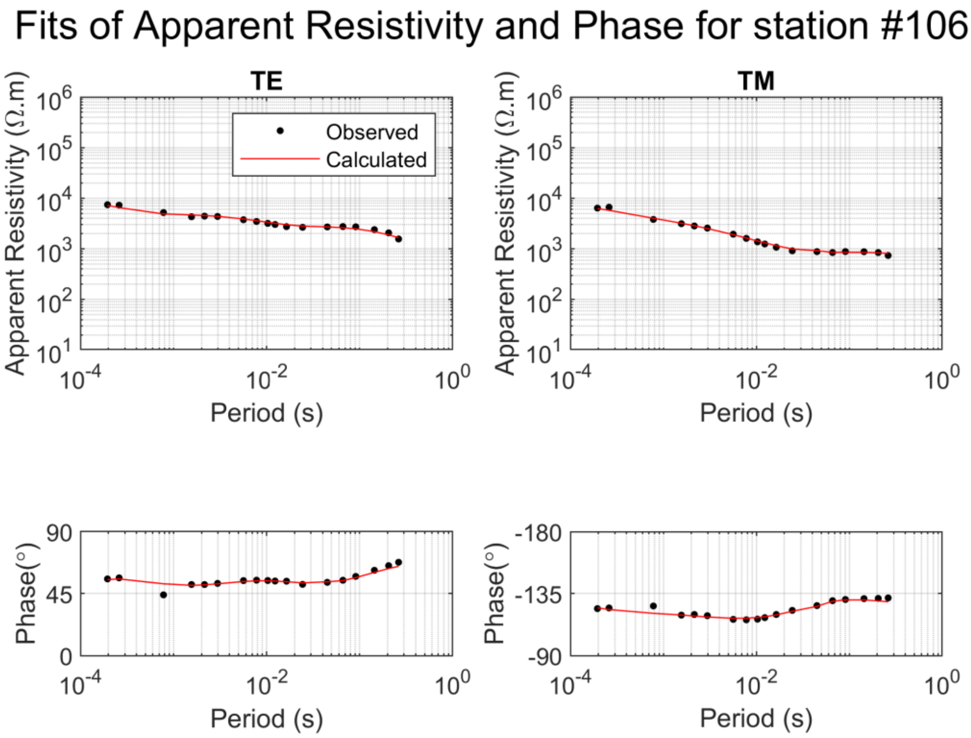
Fits of Apparent Resistivity and Phase for station #106
TE
TM
Observed
Calculated
Apparent Resistivity (Ω.m)
Phase(°)
Period (s)
10^6
10^5
10^4
10^3
10^2
10^1
10^-4
10^-2
10^0
90
45
0
-180
-135
-90

Fits of Apparent Resistivity and Phase for station #107

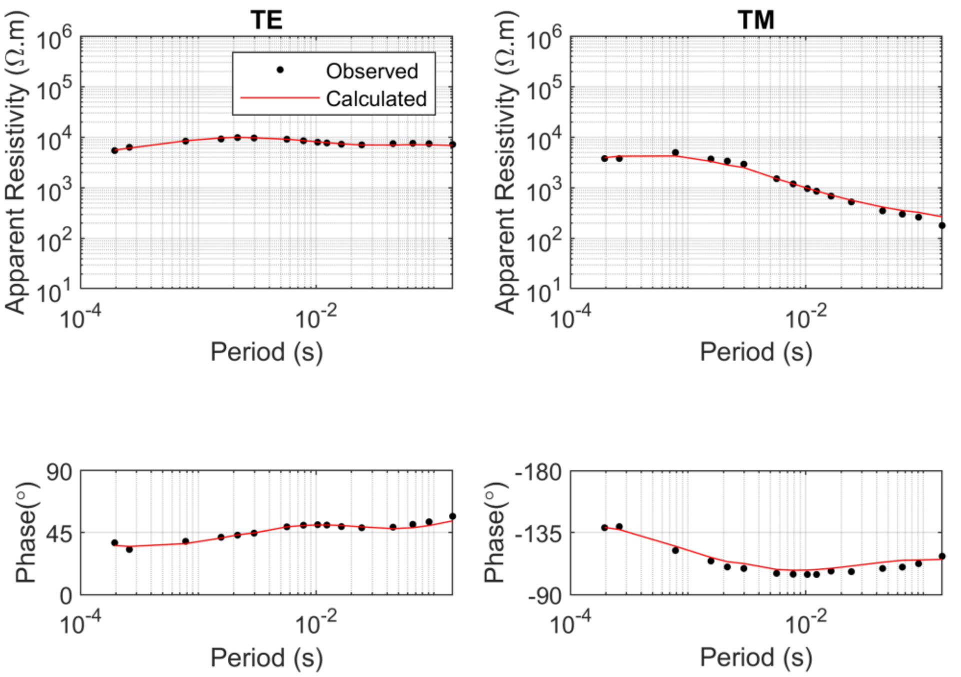

Fits of Apparent Resistivity and Phase for station #108

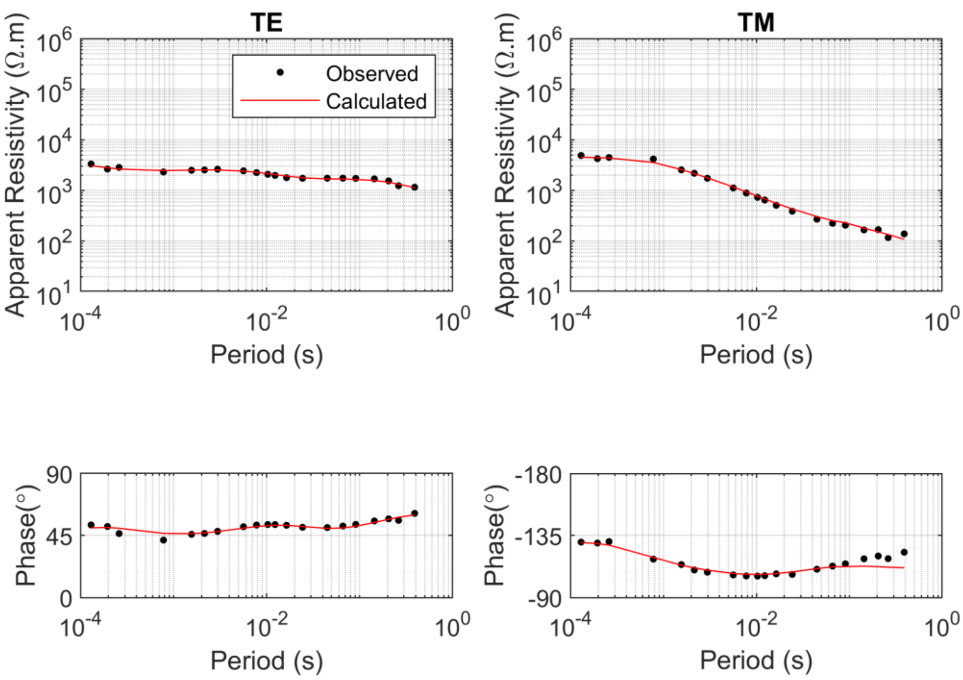

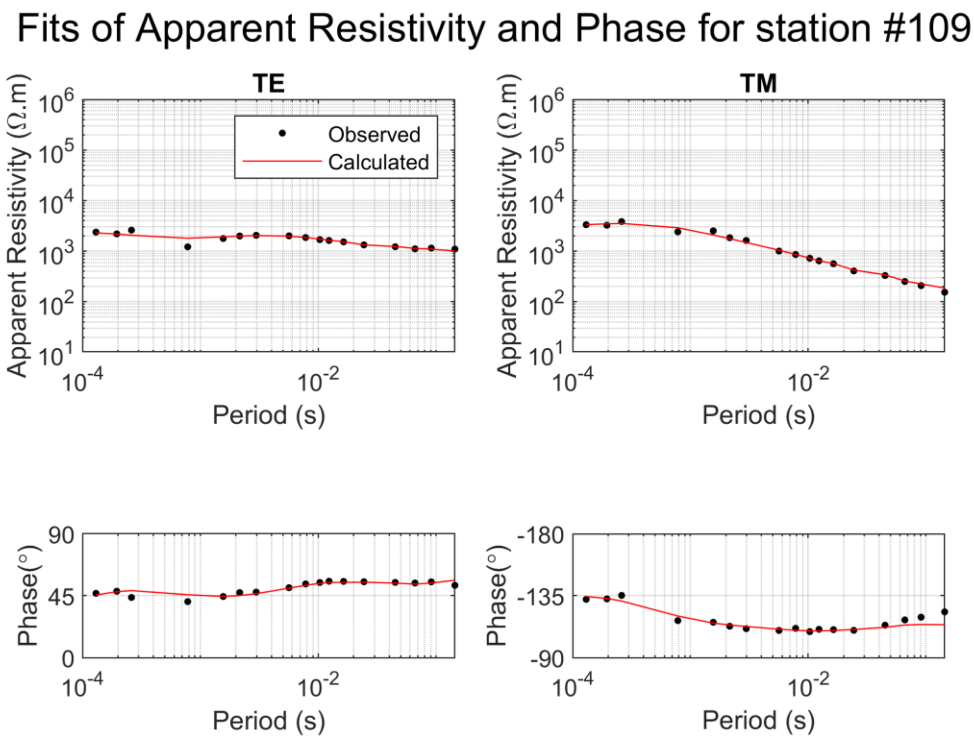
Fits of Apparent Resistivity and Phase for station #109
TE
TM
Observed
Calculated
Apparent Resistivity (Ω.m)
Phase(°)
Period (s)
10^6
10^5
10^4
10^3
10^2
10^1
10^-4
10^-2
90
45
0
-180
-135
-90

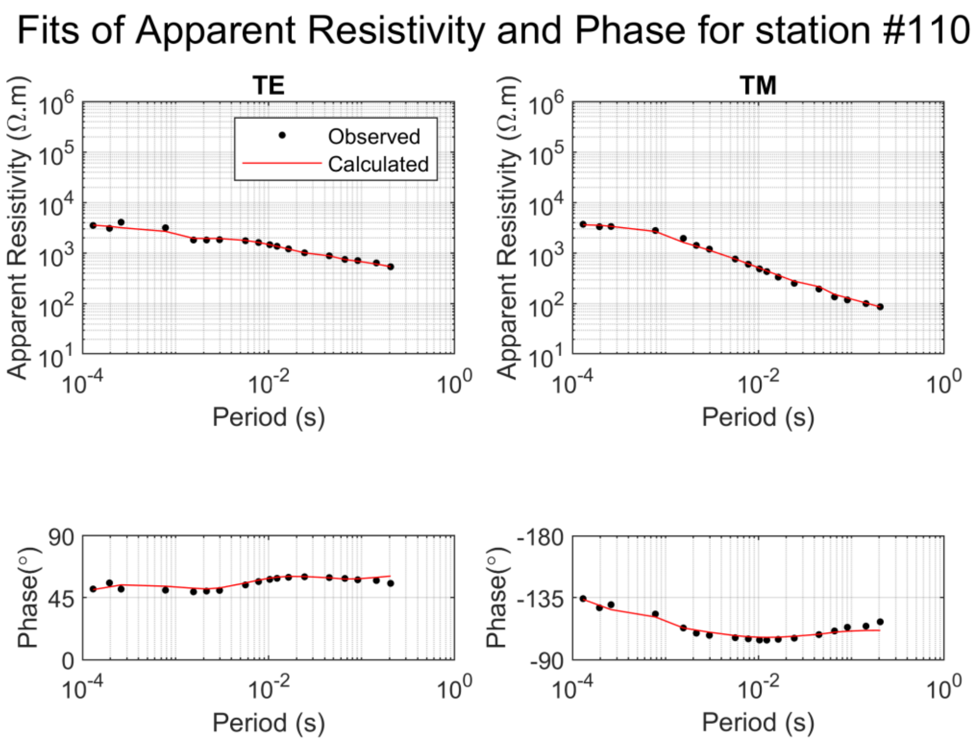
Fits of Apparent Resistivity and Phase for station #110
TE
TM
Observed
Calculated
Apparent Resistivity (Ω.m)
Phase(°)
Period (s)
10^6
10^5
10^4
10^3
10^2
10^1
10^-4
10^-2
10^0
90
45
0
-180
-135
-90

Fits of Apparent Resistivity and Phase for station #111

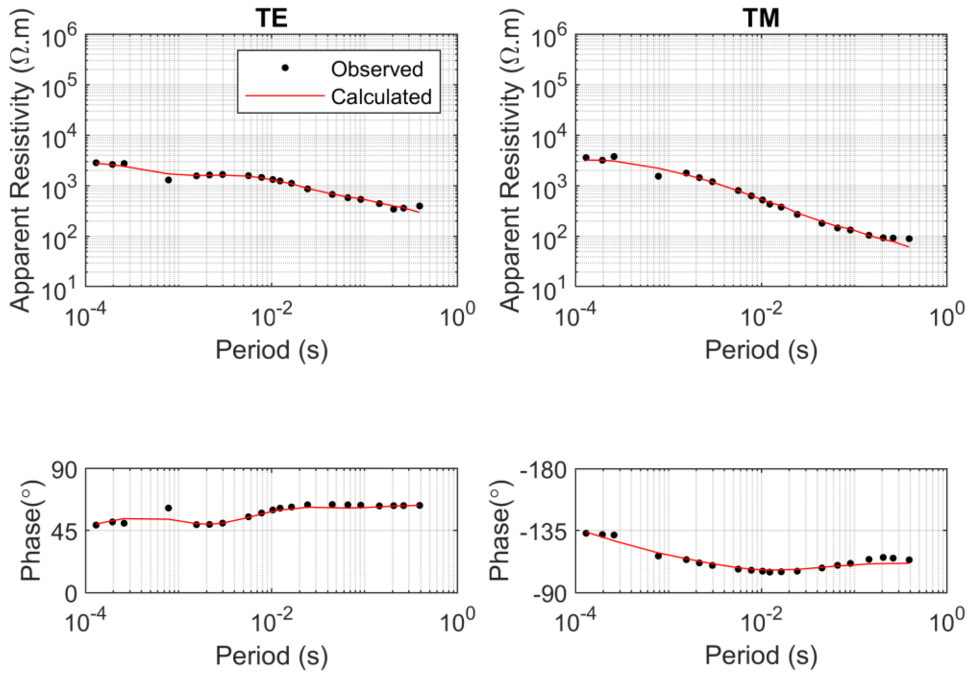

Fits of Apparent Resistivity and Phase for station #112

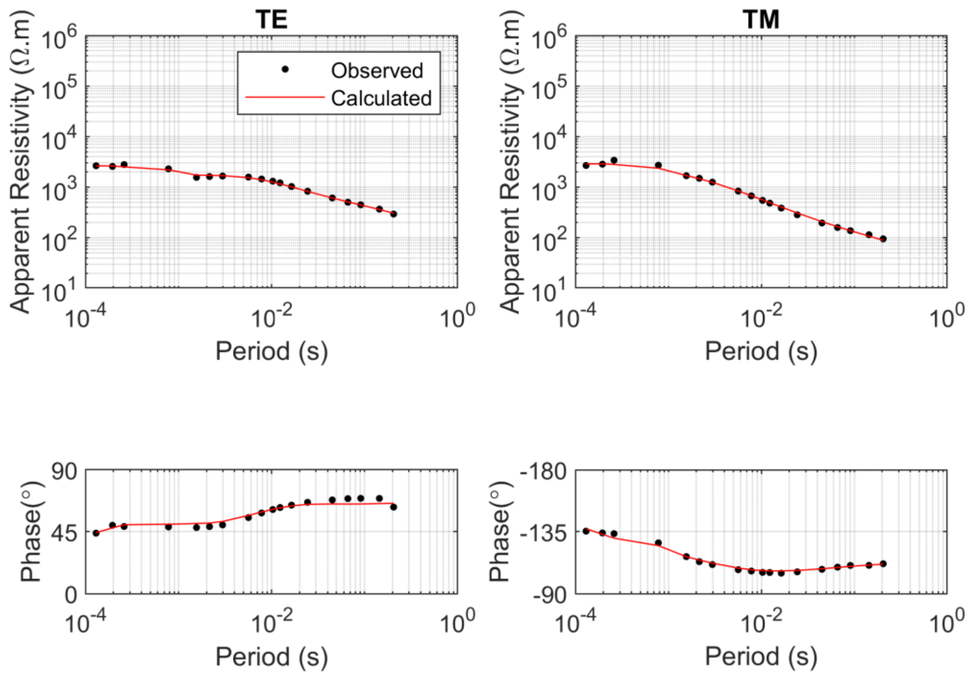

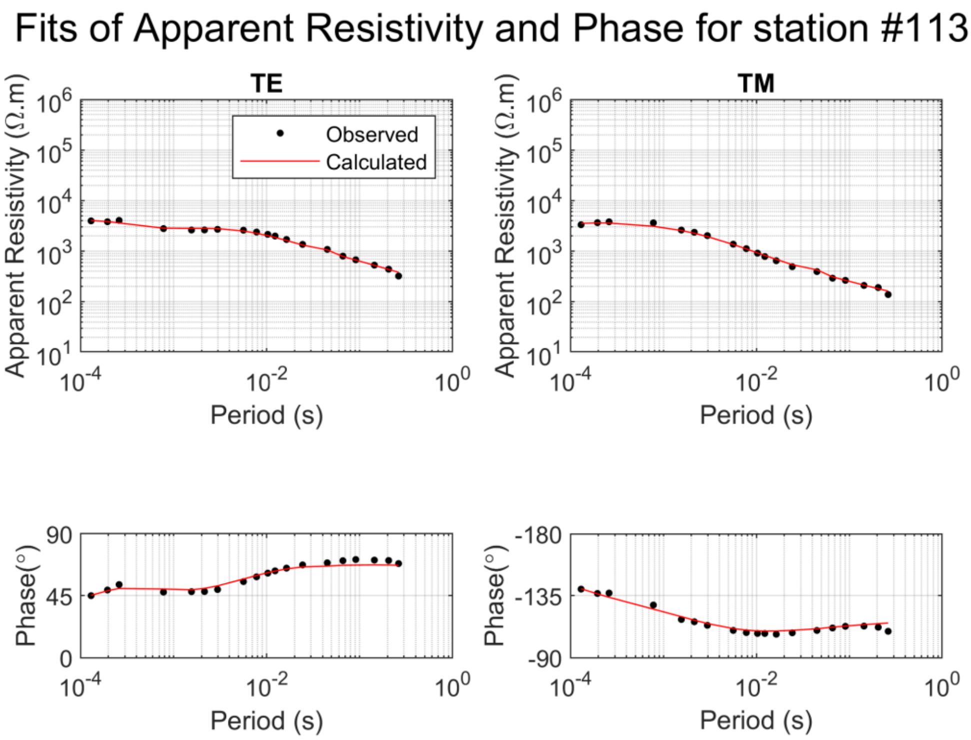
Fits of Apparent Resistivity and Phase for station #113
TE
TM
Observed
Calculated
Apparent Resistivity (Ω.m)
Period (s)
Phase(°)

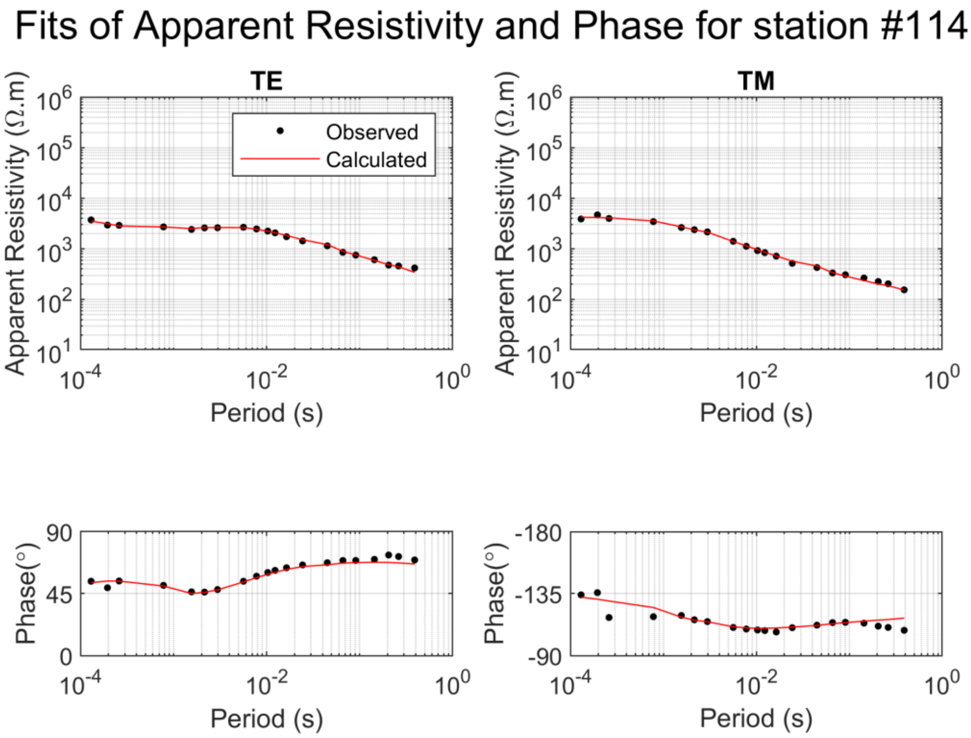
Fits of Apparent Resistivity and Phase for station #114
TE
TM
Observed
Calculated
Apparent Resistivity (Ω.m)
Period (s)
Phase(°)

Fits of Apparent Resistivity and Phase for station #115

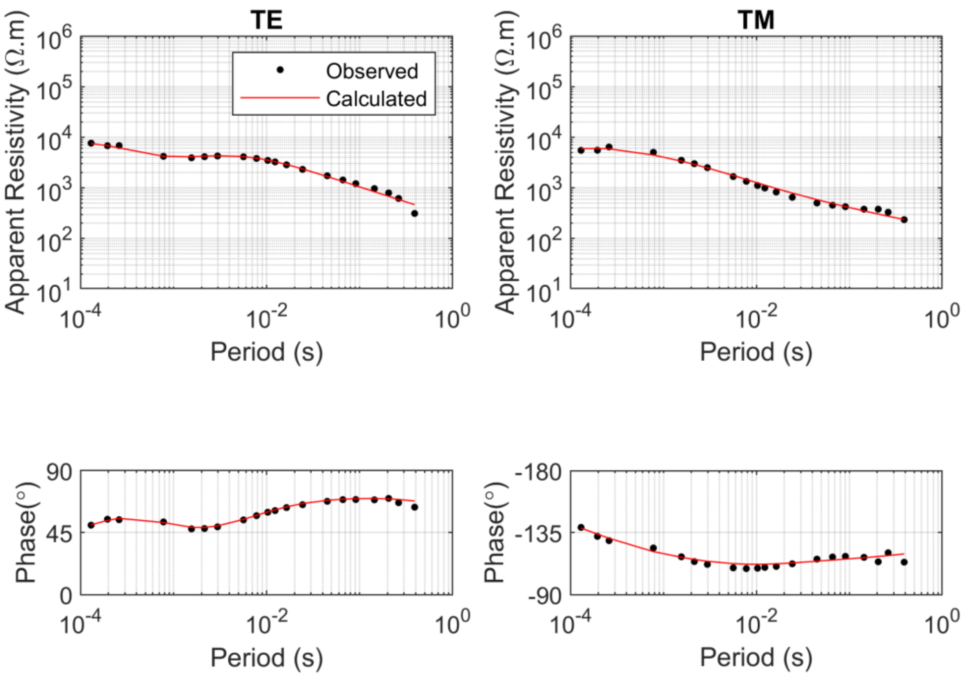

Fits of Apparent Resistivity and Phase for station #116

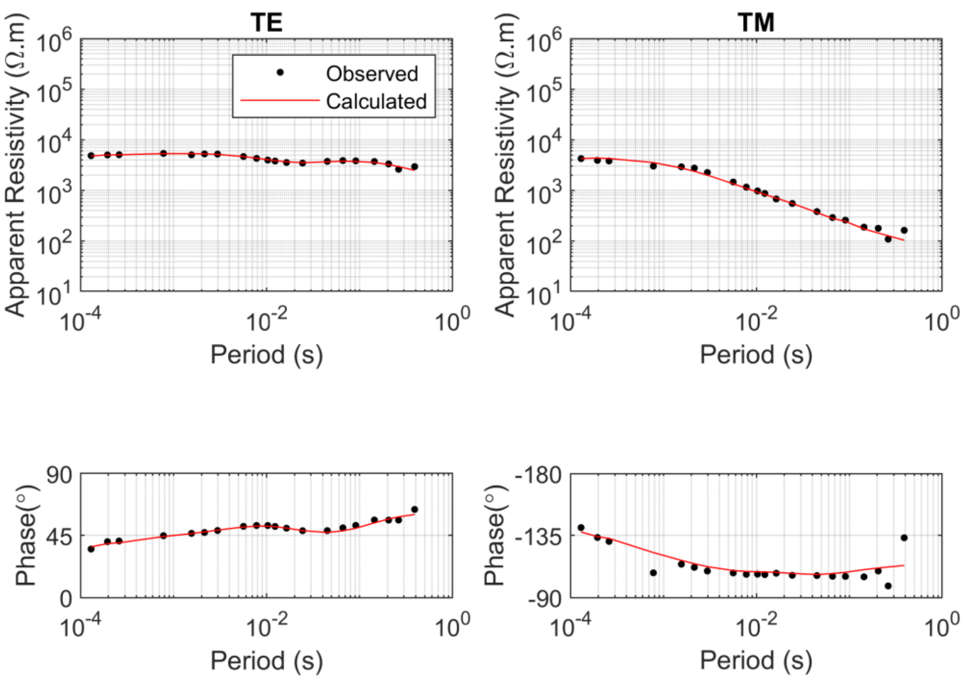

Fits of Apparent Resistivity and Phase for station #117

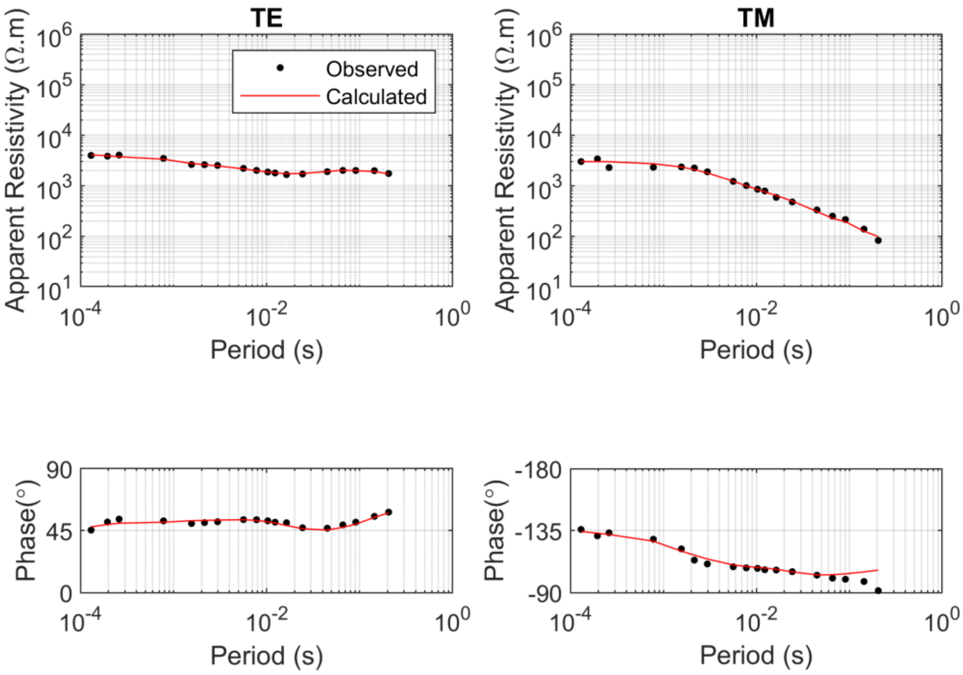

Fits of Apparent Resistivity and Phase for station #118

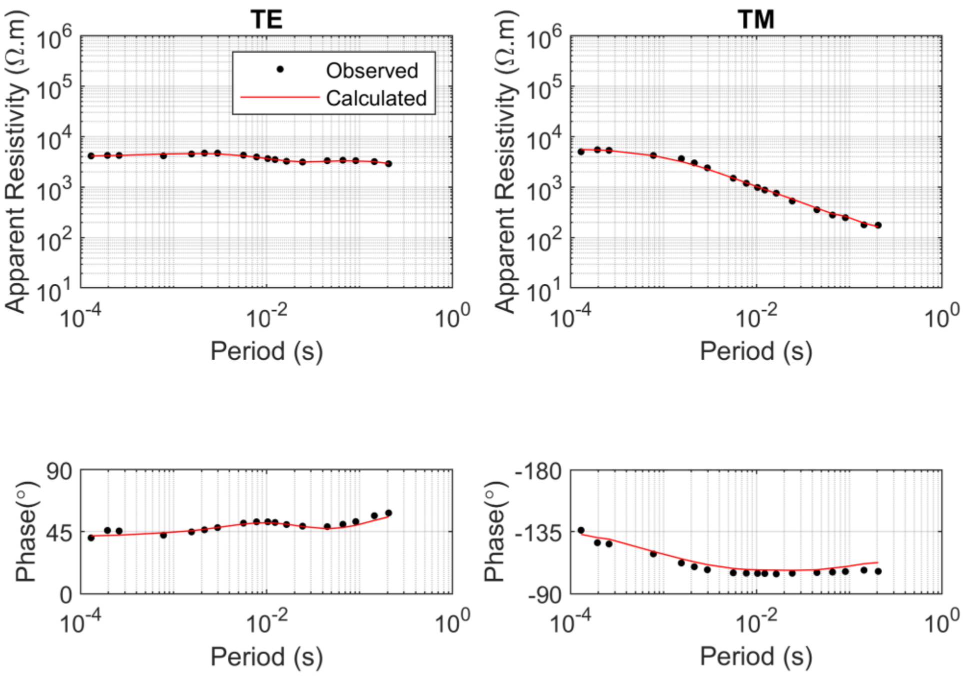

Fits of Apparent Resistivity and Phase for station #119

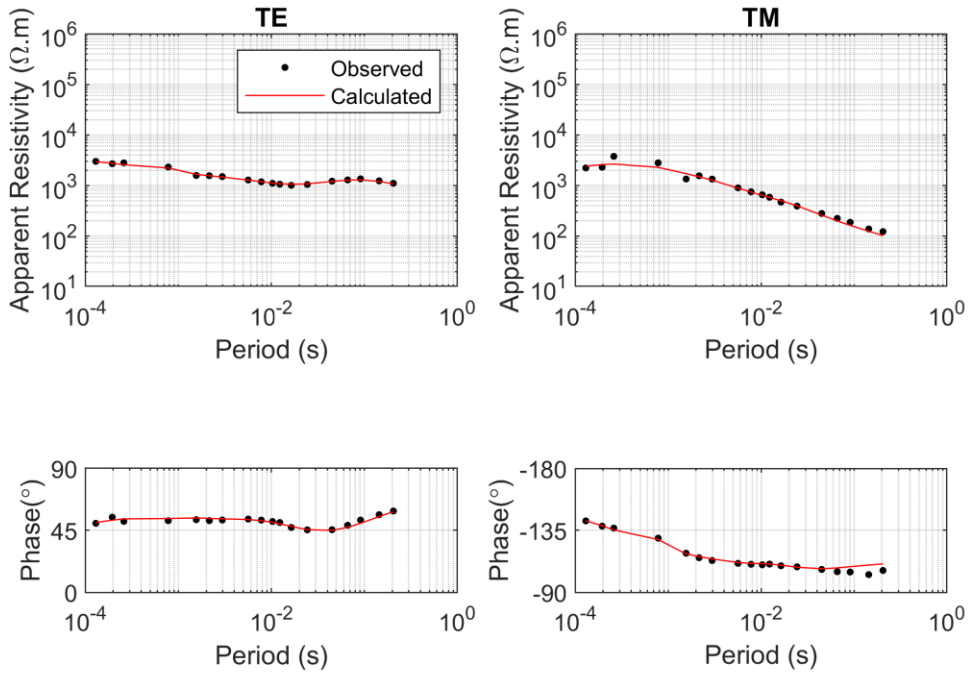

Fits of Apparent Resistivity and Phase for station #120

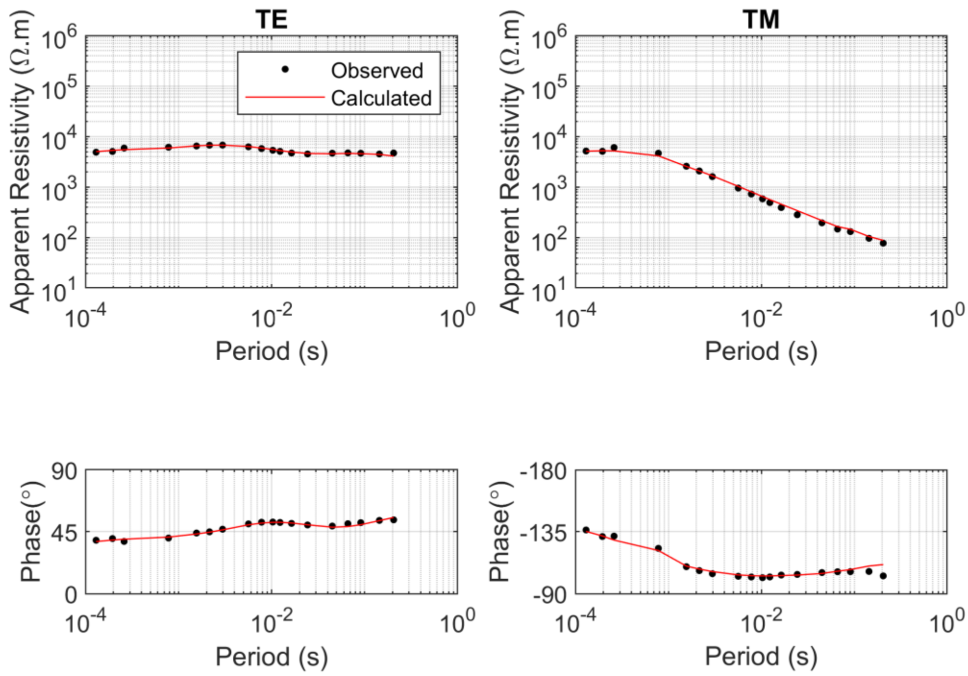

Fits of Apparent Resistivity and Phase for station #121

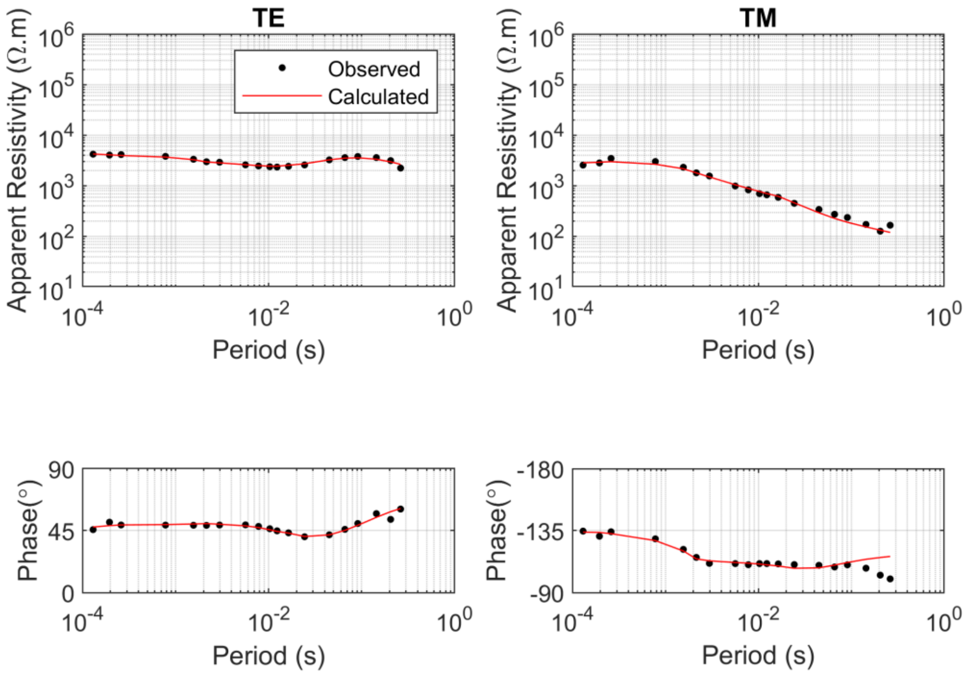

Fits of Apparent Resistivity and Phase for station #122

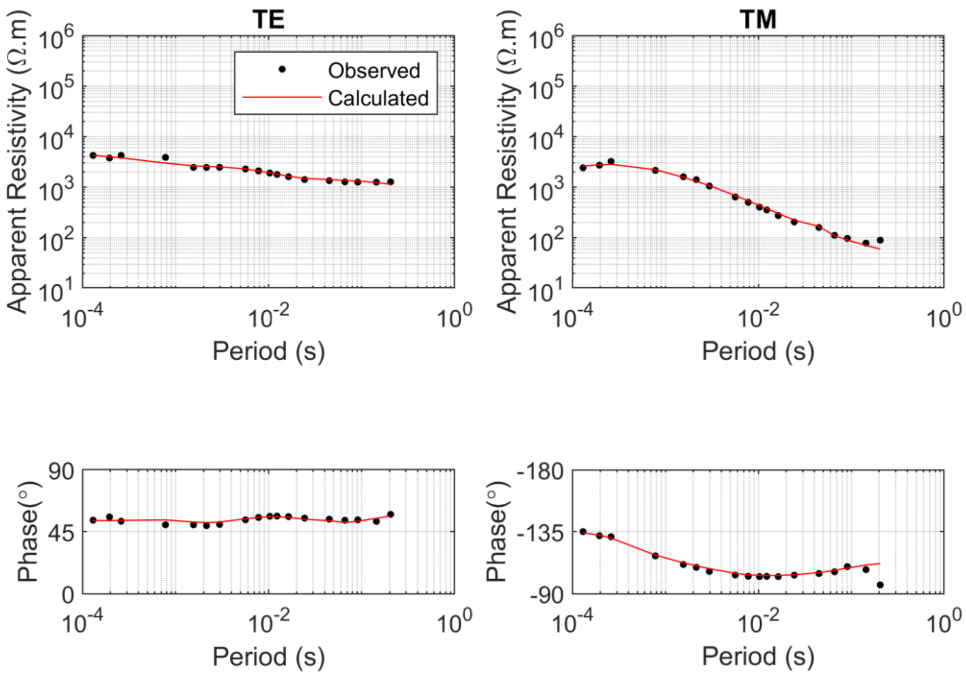

Fits of Apparent Resistivity and Phase for station #123

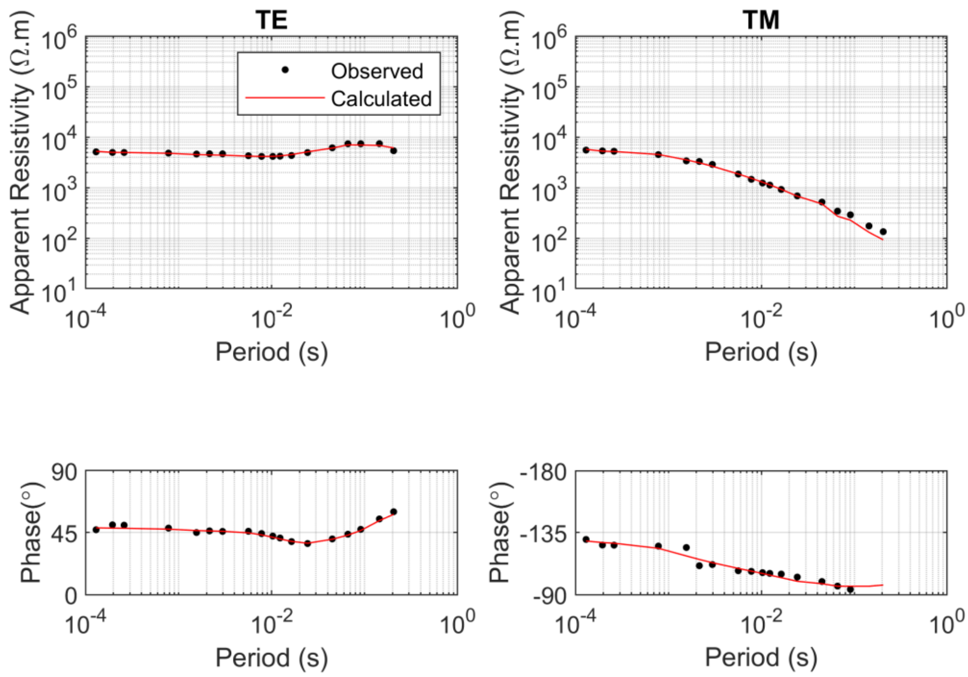

Fits of Apparent Resistivity and Phase for station #124

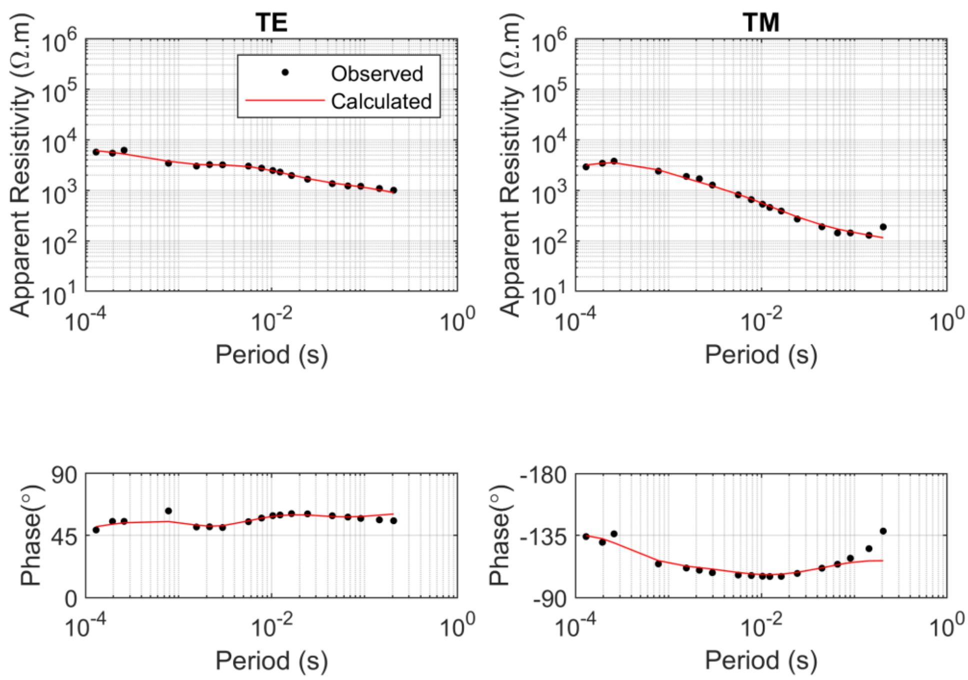

Fits of Apparent Resistivity and Phase for station #125

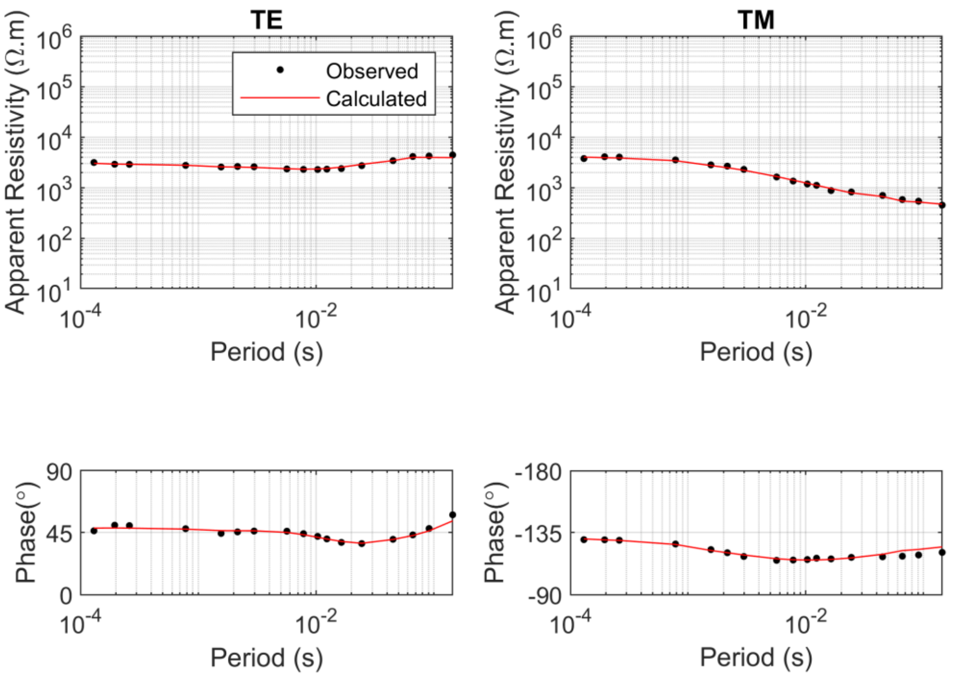

Fits of Apparent Resistivity and Phase for station #126

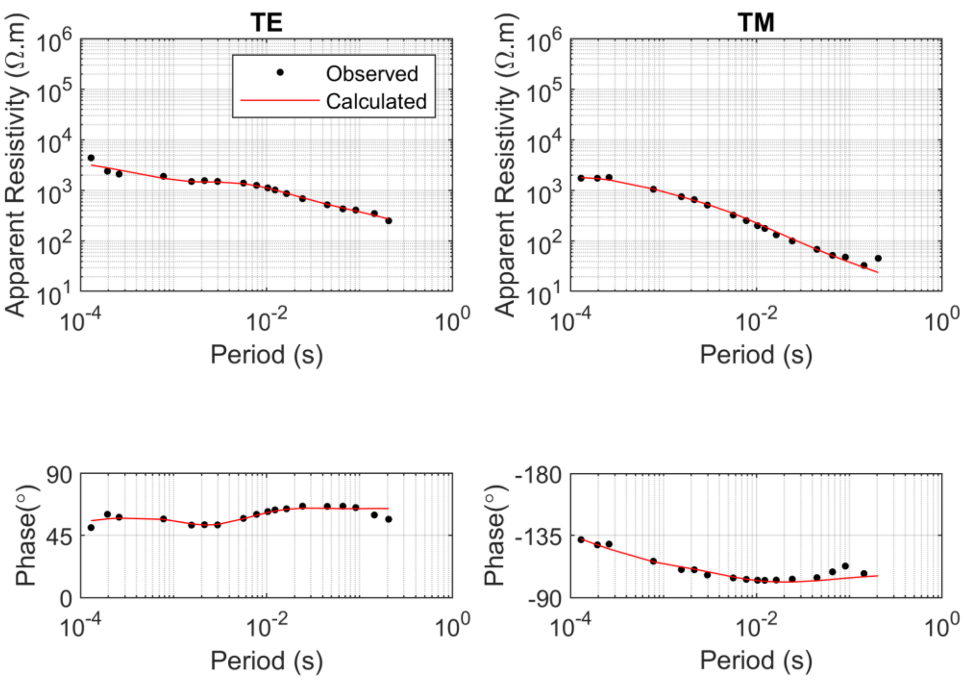

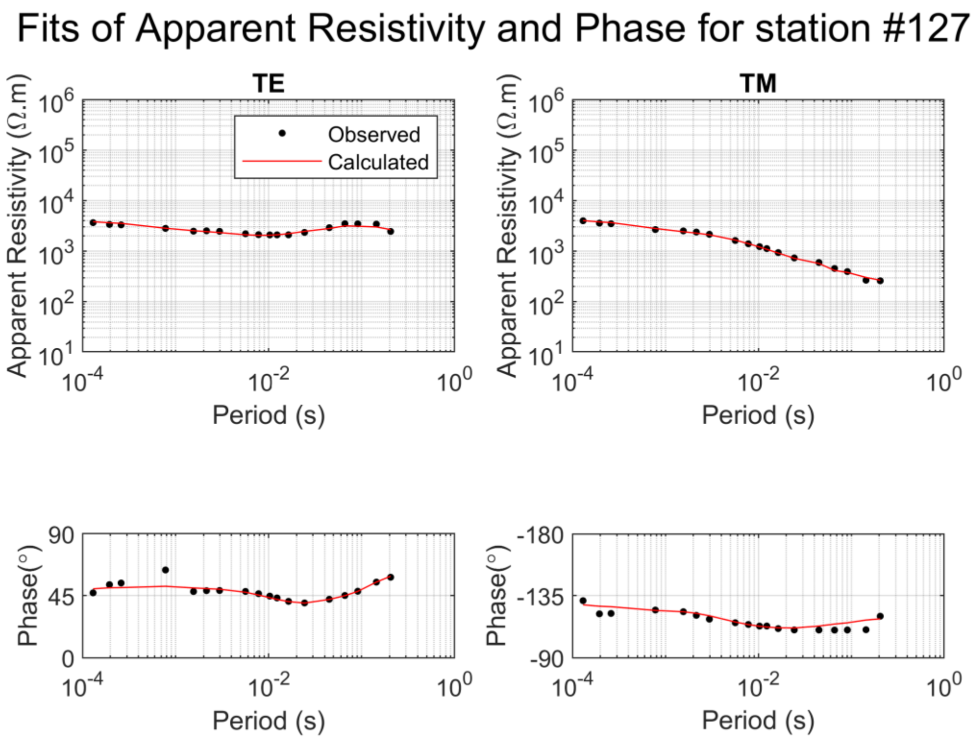
Fits of Apparent Resistivity and Phase for station #127
TE
TM
Observed
Calculated
Apparent Resistivity (Ω.m)
Phase(°)
Period (s)
10^6
10^5
10^4
10^3
10^2
10^1
10^-4
10^-2
10^0
90
45
0
-180
-135
-90

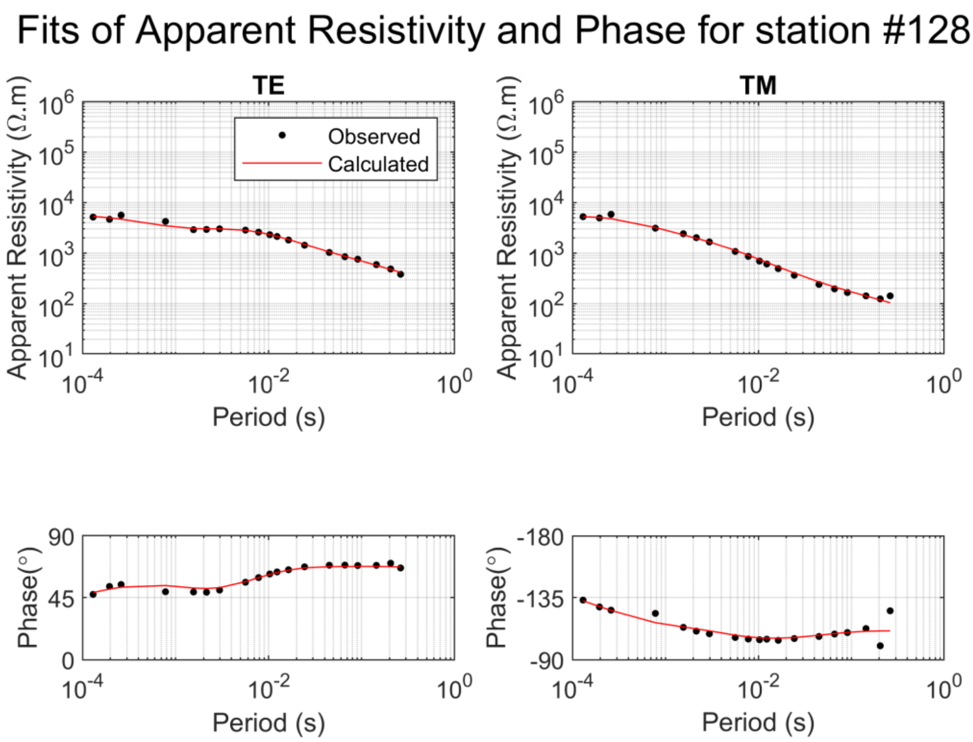
Fits of Apparent Resistivity and Phase for station #128
TE
TM
Observed
Calculated
Apparent Resistivity (Ω.m)
Phase(°)
Period (s)
10^6
10^5
10^4
10^3
10^2
10^1
10^-4
10^-2
10^0
90
45
0
-180
-135
-90

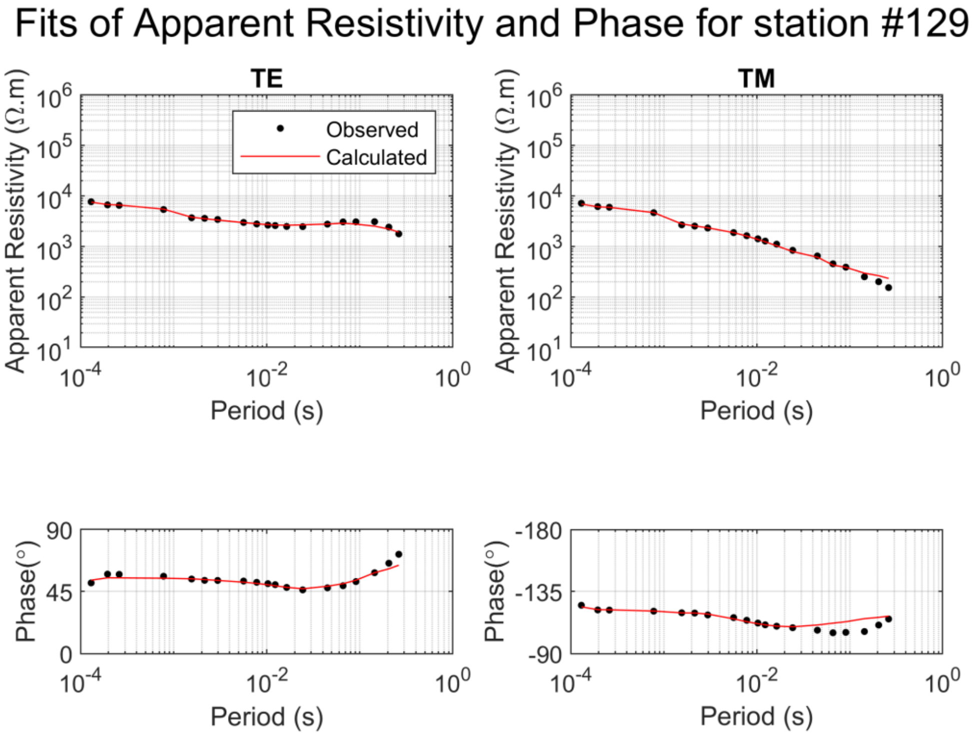
Fits of Apparent Resistivity and Phase for station #129
TE
TM
Observed
Calculated
Apparent Resistivity (Ω.m)
Period (s)
Phase(°)

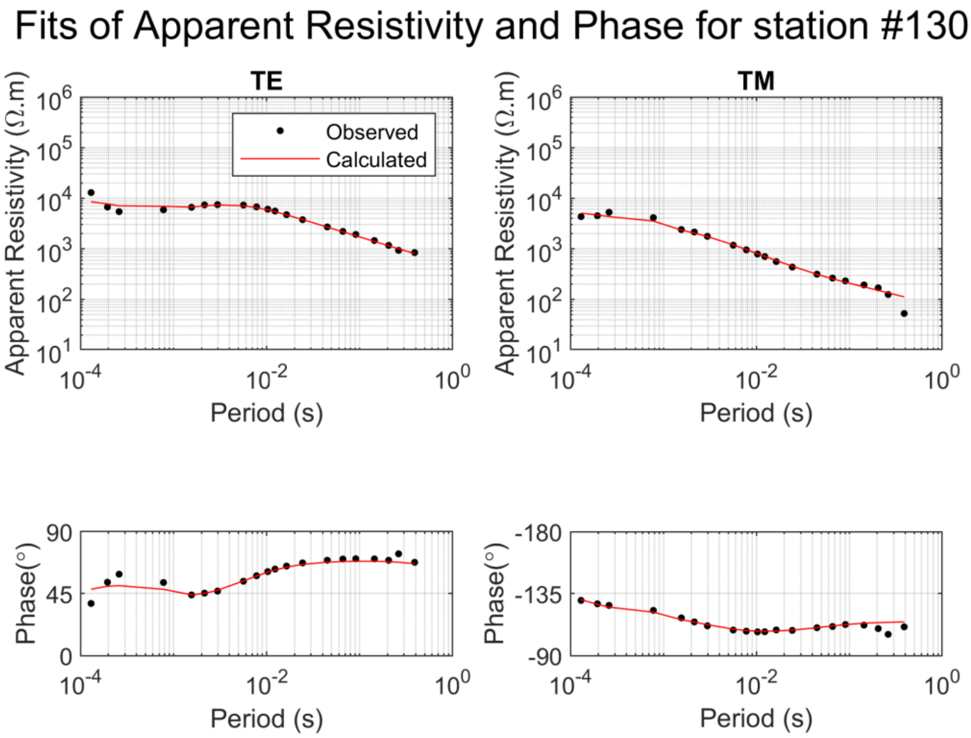
Fits of Apparent Resistivity and Phase for station #130
TE
TM
Observed
Calculated
Apparent Resistivity (Ω.m)
Period (s)
Phase(°)

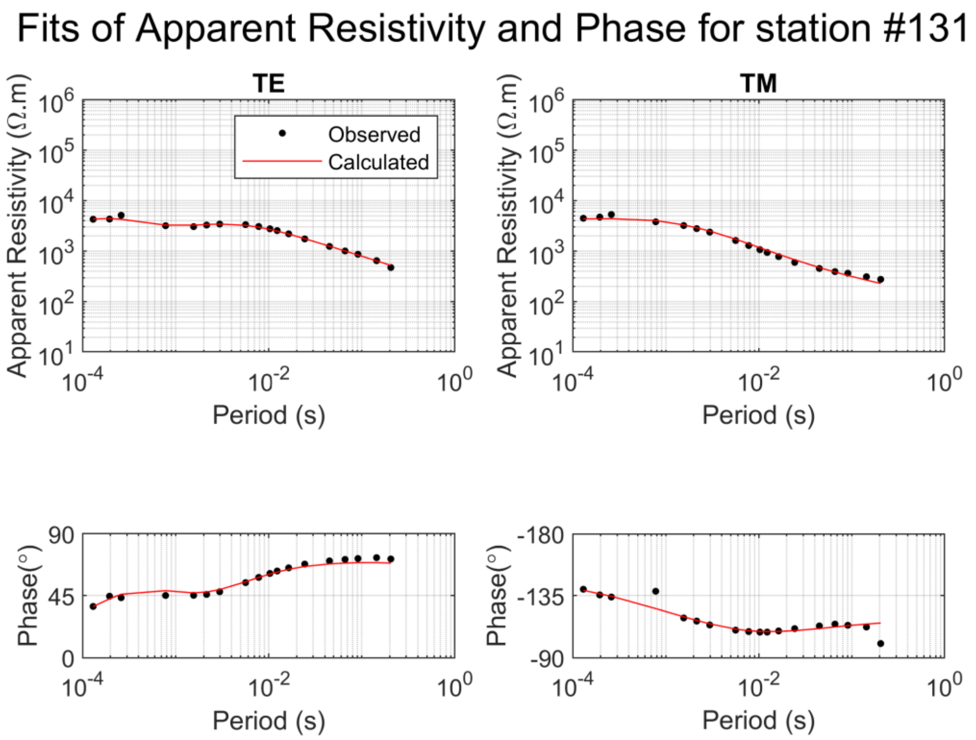
Fits of Apparent Resistivity and Phase for station #131
TE
TM
Observed
Calculated
Apparent Resistivity (Ω.m)
Phase(°)
Period (s)

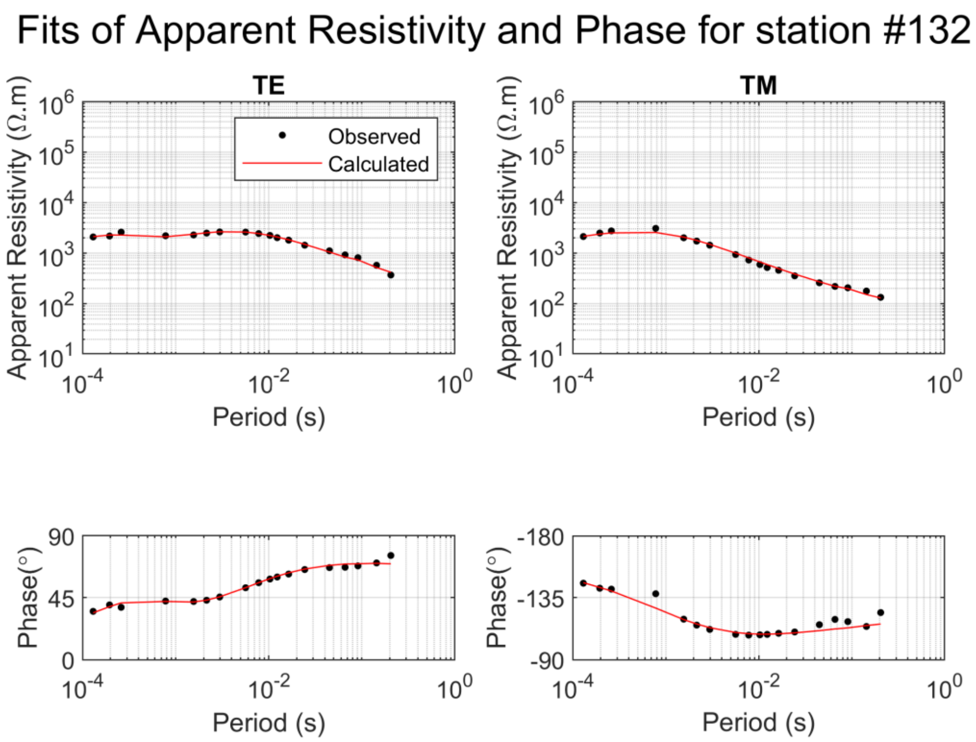
Fits of Apparent Resistivity and Phase for station #132
TE
TM
Observed
Calculated
Apparent Resistivity (Ω.m)
Phase(°)
Period (s)